ADVANCES IN STEEL STRUCTURES

ICASS '02

edited by
S.L. Chan, J.G. Teng
and K.F. Chung

ELSEVIER

www.EngineeringEBooksPdf.com

ADVANCES IN STEEL STRUCTURES

Proceedings of the
Third International Conference on Advances in Steel Structures

9-11 December 2002, Hong Kong, China

Volume II

www.EngineeringEBooksPdf.com

Elsevier Science Internet Homepage - http://www.elsevier.com

Consult the Elsevier homepage for full catalogue information on all books, journals and electronic products and services.

Elsevier Titles of Related Interest

CHAN & TENG
ICASS '99, Advances in Steel Structures. (2 Volume Set).
ISBN: 008-043015-5

FRANGOPOL, COROTIS & RACKWITZ
Reliability and Optimization of Structural Systems.
ISBN: 008-042826-6

FUKUMOTO
Structural Stability Design.
ISBN: 008-042263-2

HOLLAWAY & HEAD
Advanced Polymer Composites and Polymers in the Civil Infrastructure.
ISBN: 008-043661-7

KELLY & ZWEBEN
Comprehensive Composite Materials.
ISBN: 008-042993-9

KO & XU
Advances in Structural Dynamics. (2 Volume Set)
ISBN: 008-043792-3

LUNDQUIST, LETERRIER, SUNDERLAND & MÅNSON
Life Cycle Engineering of Plastics Technology, Economy and the Environment
ISBN: 008-043886-5

MAKELAINEN
ICSAS'99, Int. Conf. on Light-Weight Steel and Aluminium Structures.
ISBN: 008-043014-7

USAMI & ITOH
Stability and Ductility of Steel Structures.
ISBN: 008-043320-0

VASILIEV & MOROZOV
Mechanics and Analysis of Composite Materials.
ISBN: 008-042702-2

WANG, REDDY & LEE
Shear Deformable Beams and Plates.
ISBN: 008-043784-2

Related Journals

Free specimen copy gladly sent on request. Elsevier Science Ltd, The Boulevard, Langford Lane, Kidlington, Oxford, OX5 1GB, UK

Advances in Engineering Software
CAD
Composites Part A: Applied Science and Manufacturing
Composites Part B: Engineering
Composite Structures
Computer Methods in Applied Mechanics and Engineering
Computers and Structures
Computer Science and Technology
Construction and Building Materials
Engineering Failure Analysis
Engineering Fracture Mechanics
Engineering Structures
International Journal of Fatigue
International Journal of Mechanical Sciences
International Journal of Solids and Structures
Journal of Constructional Steel Research
Mechanics of Materials
Mechanics Research Communications
Structural Safety
Thin-Walled Structures

To Contact the Publisher

Elsevier Science welcomes enquiries concerning publishing proposals: books, journal special issues, conference proceedings, etc. All formats and media can be considered. Should you have a publishing proposal you wish to discuss, please contact, without obligation, the publisher responsible for Elsevier's civil and structural engineering publishing programme:

Keith Lambert
Senior Publishing Editor
Elsevier Science Ltd
The Boulevard, Langford Lane
Kidlington, Oxford
OX5 1GB, UK

Phone: +44 1865 843411
Fax: +44 1865 843931
E.mail: k.lambert@elsevier.com

General enquiries, including placing orders, should be directed to Elsevier's Regional Sales Offices – please access the Elsevier homepage for full contact details (homepage details at the top of this page).

www.EngineeringEBooksPdf.com

ADVANCES IN STEEL STRUCTURES

Proceedings of the
Third International Conference on Advances in Steel Structures

9-11 December 2002, Hong Kong, China

Volume II

Edited by
S.L. Chan, J.G. Teng and K.F. Chung
The Hong Kong Polytechnic University

Organized by
Research Centre for Advanced Technology in Structural Engineering,
Department of Civil and Structural Engineering,
The Hong Kong Polytechnic University

Sponsored by
The Hong Kong Institution of Engineers,
The Hong Kong Institution of Steel Construction

2002
ELSEVIER
Amsterdam – Boston – London – New York – Oxford – Paris
San Diego – San Francisco – Singapore – Sydney – Tokyo

www.EngineeringEBooksPdf.com

ELSEVIER SCIENCE Ltd
The Boulevard, Langford Lane
Kidlington, Oxford OX5 1GB, UK

© 2002 Elsevier Science Ltd. All rights reserved.

This work is protected under copyright by Elsevier Science, and the following terms and conditions apply to its use:

Photocopying
Single photocopies of single chapters may be made for personal use as allowed by national copyright laws. Permission of the Publisher and payment of a fee is required for all other photocopying, including multiple or systematic copying, copying for advertising or promotional purposes, resale, and all forms of document delivery. Special rates are available for educational institutions that wish to make photocopies for non-profit educational classroom use.

Permissions may be sought directly from Elsevier Science via their homepage (http://www.elsevier.com) by selecting 'Customer support' and then 'Permissions'. Alternatively you can send an e-mail to: permissions@elsevier.com, or fax to: (+44) 1865 853333.

In the USA, users may clear permissions and make payments through the Copyright Clearance Center, Inc., 222 Rosewood Drive, Danvers, MA 01923, USA; phone: (+1) (978) 7508400, fax: (+1) (978) 7504744, and in the UK through the Copyright Licensing Agency Rapid Clearance Service (CLARCS), 90 Tottenham Court Road, London W1P 0LP, UK; phone: (+44) 207 631 5555; fax: (+44) 207 631 5500. Other countries may have a local reprographic rights agency for payments.

Derivative Works
Tables of contents may be reproduced for internal circulation, but permission of Elsevier Science is required for external resale or distribution of such material.
Permission of the Publisher is required for all other derivative works, including compilations and translations.

Electronic Storage or Usage
Permission of the Publisher is required to store or use electronically any material contained in this work, including any chapter or part of a chapter.

Except as outlined above, no part of this work may be reproduced, stored in a retrieval system or transmitted in any form or by any means, electronic, mechanical, photocopying, recording or otherwise, without prior written permission of the Publisher.
Address permissions requests to: Elsevier Science Global Rights Department, at the fax and e-mail addresses noted above.

Notice
No responsibility is assumed by the Publisher for any injury and/or damage to persons or property as a matter of products liability, negligence or otherwise, or from any use or operation of any methods, products, instructions or ideas contained in the material herein. Because of rapid advances in the medical sciences, in particular, independent verification of diagnoses and drug dosages should be made.

First edition 2002

Library of Congress Cataloging in Publication Data
A catalog record from the Library of Congress has been applied for.

British Library Cataloguing in Publication Data
A catalogue record from the British Library has been applied for.

ISBN: 0 08 044017 7 (2 volume set)

♾ The paper used in this publication meets the requirements of ANSI/NISO Z39.48-1992 (Permanence of Paper).
Printed in The Netherlands.

The papers presented in these proceedings have been reproduced directly from the authors' 'camera-ready' manuscripts. As such, the presentation and reproduction quality may vary from paper to paper.

www.EngineeringEBooksPdf.com

PREFACE

These two volumes of proceedings contain 9 invited keynote papers and 130 contributed papers presented at the Third International Conference on Advances in Steel Structures (ICASS '02) held on 9 - 11 December 2002 in Hong Kong. The conference was a sequel to the First and the Second International Conferences on Advances in Steel Structures held in Hong Kong in December 1996 and 1999 respectively.

The conference provided a forum for discussion and dissemination by researchers and designers of recent advances in the analysis, behaviour, design and construction of steel structures. The papers were contributed from over 18 countries around the world. They cover a wide spectrum of topics, reporting the current state-of-the-art and pointing to future directions of structural steel research.

The organization of a conference of this magnitude would not have been possible without the supports and contributions of many individuals and organizations. The strong support from Professor J.M. Ko, Associate Vice President and Dean of Faculty of Construction and Land Use, and Professor Y.S. Li, Head of the Department of Civil and Structural Engineering, have been pivotal in the organization of this conference.

We also wish to express our gratitude to the Hong Kong Institution of Engineers and the Hong Kong Institute of Steel Construction for sponsoring the conference, and also to the Conference Advisory Committee for mobilizing support from the local construction industry and various government departments.

Thanks are due to all the contributors for their careful preparation of the manuscripts and all the keynote speakers for their special support. Reviews of papers were carried out by members of the International Scientific Committee and the Conference Organizing Committee. To all the reviewers, we are most grateful.

We would also like to thank all those involved in the day-to-day running of the organization work, including members of the Conference Organizing Committee, and both the secretarial and the technical staff of the Department of Civil and Structural Engineering.

Finally, we gratefully acknowledge our pleasant cooperation with Keith Lambert, Noël Blatchford, Lorna Canderton and Vicki Wetherell at Elsevier Science Ltd in the UK.

S.L. Chan, J.G. Teng and K.F. Chung

www.EngineeringEBooksPdf.com

This Page Intentionally Left Blank

www.EngineeringEBooksPdf.com

INTERNATIONAL SCIENTIFIC COMMITTEE

H. Akiyama	University of Tokyo	Japan
F.G. Albermani	University of Queensland	Australia
D. Anderson	University of Warwick	UK
P. Ansourian	University of Sydney	Australia
R.G. Beale	Oxford Brookes University	UK
R. Bjorhovde	University of Pittsburgh	USA
M.A. Bradford	University of New South Wales	Australia
R.Q. Bridge	University of Western Sydney	Australia
C.S. Cai	Kansas State University	USA
C.R. Calladine	University of Cambridge	UK
W.F. Chen	University of Hawaii at Manoa	USA
Y.K. Cheung	University of Hong Kong	HKSAR, China
S.P. Chiew	Nanyang Technological University	Singapore
C.K. Choi	Korea Advanced Institute of Science & Technology	Korea
K.P. Chong	National Science Foundation	USA
M. Chryssanthopoulos	University of Surrey	UK
A. Combescure	Laboratoire de Mechanique et Technologie	France
J.G.A. Croll	University College London	UK
J.M. Davies	University of Manchester	UK
G.G. Deierlein	Stanford University	USA
S.L. Dong	Zhejiang University	China
P.J. Dowling	University of Surrey	UK
D. Dubina	University of Timisoara	Romania
M. Farshad	Swiss Federal Laboratories for Materials Testing & Research	Switzerland
F.C. Filippou	University of California at Berkeley	USA
Y. Fukumoto	Fukuyama University	Japan
H.B. Ge	Nagoya University	Japan
Y. Goto	Nagoya Institute of Technology	Japan
P.L. Gould	Washington University	USA
R. Greiner	Technical University of Graz	Austria
Q. Gu	Xian University of Architecture & Technology	China
J.F. Hajjar	University of Minnesota	USA
L.H. Han	Fuzhou University	China
G.J. Hancock	University of Sydney	Australia
J.E. Harding	University of Surrey	UK
J.F. Jullien	INSA Lyon	France
S. Kato	Toyohashi University of Technology	Japan
A.R. Kemp	University of Witwatersrand	South Africa
S. Kitipornchai	City University of Hong Kong	HKSAR, China
K.C.S. Kwok	Hong Kong University of Science & Technology	HKSAR, China
R.A. LaBoube	University of Missouri-Rolla	USA
T.T. Lan	Chinese Academy of Building Research	China
G.Q. Li	Tongji University	China
S.F. Li	Tsinghua University	China
R.J.Y. Liew	National University of Singapore	Singapore
J. Lindner	Technische Universitat Berlin	Germany
Xila Liu	Tsinghua University	China
Xiliang Liu	Tianjin University	China
L.W. Lu	Lehigh University	USA

www.EngineeringEBooksPdf.com

INTERNATIONAL SCIENTIFIC COMMITTEE *(Continued)*

P. Makelainen	Helsinki University of Technology	Finland
P. Marek	Academy of Science of the Czech Republic	Czech Republic
J. Melcher	Technical University of Brno	Czech Republic
D.A. Nethercot	Imperial College of Science, Technology & Medicine	UK
D.J. Oehlers	University of Adelaide	Australia
G.W. Owens	The Steel Construction Institute	UK
J.M. Rotter	University of Edinburgh	UK
B. Samali	University of Technology, Sydney	Australia
H. Schmidt	University of Essen	Germany
G. Sedlacek	Institute of Steel Construc tion	Germany
S.Z. Shen	Harbin Institute of Technology	China
Z.Y. Shen	Tongji University	China
L.S. da Silva	Universidade de Coimbra	Portugal
T.T. Soong	State University of New York at Buffalo	USA
N.S. Trahair	University of Sydney	Australia
K.C. Tsai	National Taiwan University	Taiwan, China
C.M. Uang	University of California at San Diego	USA
T. Usami	Nagoya University	Japan
A.S. Usmani	University of Edinburgh	UK
A. Wada	Tokyo Institute of Technology	Japan
F. Wald	Czech Technical University	Czech Republic
E. Walicki	Technical University of Zielona Gora	Poland
C.M. Wang	National University of Singapore	Singapore
D. White	Georgia Institute of Technology	USA
F.W. Williams	City University of Hong Kong	HKSAR, China
Y. Xiao	University of Southern California	USA
Y.B. Yang	National Taiwan University	Taiwan, China
R. Zandonini	University of Trento	Italy
X.L. Zhao	Monash University	Australia
S.T. Zhong	Harbin Institute of Technology	China

www.EngineeringEBooksPdf.com

CONFERENCE ADVISORY COMMITTEE

Chairman	**J.M. Ko** The Hong Kong Polytechnic University
Members	
Andrew. S. Beard	Mott Connell Limited
Francis S.Y. Bond	Maunsell Consultants Asia Limited
Andrew K.C. Chan	Ove Arup & Partners (Hong Kong) Limited
L.Y.K. Choi	Shui On (Contractors) Limited
K.P. Chong	Directorate of Engineering, National Science Foundation, USA
M. Hadaway	Gammon Construction Limited
J. Kong	BHP Steel Building Products Singapore Pte Limited
C.M. Leung	Buildings Department, HKSAR
A.Y.T. Leung	City University of Hong Kong
C.K. Lau	Civil Engineering Department, HKSAR
P.K.K. Lee	The University of Hong Kong
S.H. Ng	Icfox Hong Kong Limited
S.H. Pau	Architectural Services Department, HKSAR
S. Sin	Atkin China Limited
W. Tang	The Hong Kong University of Science & Technology
V.W.S. Tong	Housing Department, HKSAR
W.H. Wong	Meinhardt Engineering Limited
I. Kimura	Nippon Steel Corporation

www.EngineeringEBooksPdf.com

CONFERENCE ORGANIZING COMMITTEE

Chairman	**S.L. Chan** The Hong Kong Polytechnic University
Co-Chairmen	**J.G. Teng** and **K.F. Chung** The Hong Kong Polytechnic University
Members	
F.T.K. Au	The University of Hong Kong
C.M. Chan	The Hong Kong University of Science & Technology
T.H.T. Chan	The Hong Kong Polytechnic University
K.M. Cheung	Buildings Department, HKSAR
R.P.K. Chu	Meinhardt (C&S) Limited
G.W.M. Ho	Ove Arup and Partners (Hong Kong) Limited
M.K.Y. Kwok	Ove Arup and Partners (Hong Kong) Limited
E.S.S. Lam	The Hong Kong Polytechnic University
J.C.W. Lau	James Lau and Associates Limited
S.S. Law	The Hong Kong Polytechnic University
J.Q.S. Li	City University of Hong Kong
M.C. Luo	Ove Arup and Partners (Hong Kong) Limited
Y.W. Mak	Housing Department, HKSAR
Y.Q. Ni	The Hong Kong Polytechnic University
A.K. Soh	The University of Hong Kong
F.M.K. Tong	Architectural Services Department, HKSAR
K.Y. Wong	Highways Department, HKSAR
Y.L. Wong	The Hong Kong Polytechnic University
Y.L. Xu	The Hong Kong Polytechnic University
F.Y.F. Yau	Maunsell Structural Consultants Limited
B. Young	The Hong Kong University of Science & Technology

www.EngineeringEBooksPdf.com

CONTENTS

VOLUME I

Preface v

International Scientific Committee vii

Conference Advisory Committee ix

Conference Organizing Committee x

Keynote Papers

Stability of High Strength G550 Steel Compression Members 3
D. Yang and G. Hancock

The Application and Development of Pretensioned Long-Span Steel Space Structures in China 15
S.L. Dong and Y. Zhao

Advanced Computer Calculations in the Design of Shell Structures 27
J.M. Rotter

Exploiting the Special Features of Stainless Steel in Structural Design 43
D.A. Nethercot and L. Gardner

Cassette Wall Construction: Current Research and Practice 57
J.M. Davies

A New Issue in Plate and Box Girder Stability Design 69
T. Usami and P. Chusilp

Monotonic and Hysteretic Behaviour of Bolted Endplate Beam-to-Column Joints 81
R. Zandonini and O.S. Bursi

Design of Steel Arches Against In-Plane Instability 95
M.A. Bradford and Y.-L. Pi

FEM Analysis of Steel Members Considering Damage Accumulation Effects Under Cyclic Loading 105
Z.Y. Shen and Z.S. Song

Beams and Columns

A Review of Recent Developments on Design of Perforated Beams 121
C.H. Ko and K.F. Chung

A New Derivation of the Buckling Theory of Thin-Walled Beams 129
G.S. Tong and L. Zhang

www.EngineeringEBooksPdf.com

Analysis of Strain Hardening in Steel Beams Using Mill Tests 139
M.P. Byfield and M. Dhanalakshmi

In-Plane Ultimate Load-Carrying Capacity of Tapered I Columns 147
Y.L. Guo and Y. Pan

Elastic Torsional-Flexural Buckling of Tapered I Beam-Columns 155
Y.L. Guo, Y. Han, W.Q. Hao and T. Liu

Load-Carrying Capacity of Box Section Beam-Column 163
T. Liu and Y.L. Guo

Multi-Directional Pseudo Dynamic Experiment of Steel Bridge Piers 171
M. Obata and Y. Goto

Connections

Shear Lag in Double Angle Truss Connections 181
D.B. Bauer and A. Benaddi

Structural Behaviour of Web Bolted Flange Welded Connection 189
T. Emi, M. Tabuchi, T. Tanaka and H. Namba

Effects of Beam Flange Width-to-Thickness Ratio on Beam Flange Fracture Caused from Scallop Root 197
T. Iguchi, M. Tabuchi, T. Tanaka and S. Kihara

Experimental Investigation of Slot Lengths in RHS Bracing Members 205
T. Wilkinson, T. Petrovski, E. Bechara and M. Rubal

Experimental Study on Cyclic Behavior of Improved Beam-Column Connections 213
Z.F. Li, Y.J. Shi, H. Chen and Y.Q. Wang

Repair/Upgrade of Steel Moment Frames in Low Rise Buildings 221
J.C. Anderson, Y. Xiao and J.X.J. Duan

Ultimate Bearing Capacity of Welded Hollow Spherical Joints in Spatial Reticulated Structures 229
Q.H. Han and X.L. Liu

Ultimate Strength of Welded Thin-Walled SHS-CHS T-Joints Under In-Plane Bending 237
F.R. Mashiri, X.L. Zhao, L.W. Tong and P. Grundy

Tests and Design of Longitudinal Fillet Welds in Very High Strength (VHS) Steel Circular Tubes 245
T.W. Ling, X.L. Zhao and R. Al-Mahaidi

Experimental Behaviour of End Plate I-Beam to Concrete-Filled Rectangular Hollow Section Column Joints 253
L.C. Neves, L. Simões da Silva and P.C.G. da S. Vellasco

Composite Connections at Perimeter Locations in Unpropped Composite Floors 261
M. Dhanalakshmi, M.P. Byfield and G.H. Couchman

www.EngineeringEBooksPdf.com

Analysis of Steel and Composite Braced Frames with Semi-Rigid Joints 269
A. Kozlowski

Numerical Evaluation of the Ductility of a Bolted T-Stub Connection 277
A.M. Girão Coelho and L. Simões da Silva

Strength and Stress Analysis of Steel Beam-Column Connections Using Finite Element Method 285
H. Chen, Y.J. Shi, Y.Q. Wang and Z.F. Li

Scaffolds and Slender Structures

Geometric Non-Linear Analysis of Flexible Supporting System 295
Z. Wang, Y.Q. Wang and Y.J. Shi

Determination of the Factors of Safety of Standard Scaffold Structures 303
B. Milojkovic, R.G. Beale and M.H.R. Godley

Sway Stability of Steel Scaffolding and Formwork Systems 311
S. Vaux, C. Wong and G. Hancock

Second-Order Analysis and Design of Steel Scaffold Using Multiple Eigen-Imperfection Modes 321
S.L. Chan, C. Dymiotis and Z.H. Zhou

Cold-Formed Steel

On the Distortional Post-Buckling Behaviour of Cold-Formed Lipped Channel Steel Beams 331
L.C. Prola and D. Camotim

GBT-Based Distortional Buckling Formulae for Thin-Walled Rack-Section Columns and Beams 341
N. Silvestre, K. Nagahama, D. Camotim and E. Batista

Testing and Numerical Analysis of Cold-Formed C-Sections Subject to Patch Load 351
R.Y. Xiao, G.P.W. Chin and K.F. Chung

Torsional Buckling Experiments on Wide-Flange Thin-Walled Z-Section Columns 357
R.A.D. Fish, M. Lee and K.J.R. Rasmussen

Structural Stability of Stainless Steel Compression Members 365
Y. Liu and B. Young

Membrane Imperfections Measured in Cold Formed Tubes 375
A. Wheeler and M. Pircher

Flexural Failure of Cold-Formed Single Channels Connected Back-to-Back 383
M. Dundu and A.R. Kemp

Ultimate Strength Design of Bolted Moment-Connections Between Cold-Formed Steel Members 391
J.B.P. Lim and D.A. Nethercot

www.EngineeringEBooksPdf.com

Analysis of Cassette Sections in Compression 401
P.A. Voutay and J.M. Davies

Performance of Wall-Stud Shear Walls Under Monotonic and Cyclic Loading 409
L.A. Fulop and D. Dubina

Direct Strength Method for the Design of Purlins 421
L. Quispe and G. Hancock

Cold-formed Purlin-Sheeting Systems 429
F. Albermani and S. Kitipornchai

An Experimental Investigation into Lapped Moment Connections Between Z-Sections 437
H.C. Ho and K.F. Chung

Practical Design of Cold-Formed Steel Z-Sections with Lapped Connections 445
H.C. Ho and K.F. Chung

Destructive Mechanism of Large Span Cold-Formed Section Roof Truss 453
Y.J. Guo, K. Li and X.X. Du

Sway Buckling of Down-Aisle Pallet Rack Structures Containing Splices 461
R.G. Beale and M.H.R. Godley

Composite Construction

Composite Action in Non-Composite Beams 471
R. Seracino and D.J. Oehlers

Effect of Concrete Infill on Non-Compact Tubes Subjected to Pure Bending 479
A. Wheeler and R. Bridge

Simplified Elastic and Elastic-Plastic Analysis of Continuous Composite Beams 487
P.A. Berry

Elastic Cross-Section Analysis of Continuous Composite Beams Affected by Web Slenderness 495
P.A. Berry

Effects of Transverse Reinforcement on Composite Beams with Precast Hollow Core Slabs 503
D. Lam and T.F. Nip

Shear Connection in Composite Beams Incorporating Profiled Steel Sheeting with Narrow Open or Closed Steel Ribs 511
M. Patrick and R.Q. Bridge

Shear Connection in Composite Beams Incorporating Open-Trough Profile Decks 519
M. Patrick and R.Q. Bridge

Research in Canada on Steel-Concrete Composite Floor Systems: An Update 527
M.U. Hosain and A. Pashan

Early Age Shrinkage and Casting Sequence Effects in Composite Steel-Concrete Girders 535
L. Dezi, G. Leoni and A. Vitali

www.EngineeringEBooksPdf.com

Shear Strength of Prestressed Concrete Encased Steel Beams with Bonded Tendons 543
S.C. Choy, Y.L. Wong and S.L. Chan

Instability Behavior of Prestressed Steel-Concrete Composite Continuous Beam 551
Y. Han, Z.Z. Fang and Y.L. Guo

Evaluation of Simplified Superposition Design Method for Composite Columns 559
J.H. Zhong and S.F. Chen

Tests on Concrete-Filled Double Skin (SHS Outer and CHS Inner) Composite Stub Columns 567
X.L. Zhao, R.H. Grzebieta, A. Ukur and M. Elchalakani

Strength of Slender Concrete Filled Columns Fabricated with High Strength Structural Steel 575
B. Uy, M. Mursi and H.B.A. Tan

Concrete-Filled Steel RHS Columns Subjected to Long-Term Loads 583
L.H. Han, W. Liu and Y.F. Yang

Hysteretic Behaviors of Concrete-Filled Steel SHS Beam-Columns 591
Z. Tao and L.H. Han

Experimental and Theoretical Studies on Steel-Concrete Hybrid Structures 599
G.Q. Li, X.M. Zhou and X. Ding

Seismic Demand Evaluation Procedure for Concrete-Filled Steel Columns 607
H.B. Ge, K.A.S. Susantha and T. Usami

VOLUME II

Preface v

International Scientific Committee vii

Conference Advisory Committee ix

Conference Organizing Committee x

Plates

Numerical Modelling of Stainless Steel Plates 617
K.J.R. Rasmussen, T. Burns, P. Bezkorovainy and M.R. Bambach

Local Buckling of Biaxially Compressed Steel Plates in Double Skin Composite Panels 625
Q.Q. Liang, B. Uy, H.D. Wright and M.A. Bradford

Ductility of High Performance Steel Rectangular Plates Under Uniaxial Compression 633
K. Niwa, I. Mikami and Y. Miyazaki

Shear-Carrying Capacity of Steel Plate Shear Wall with Cross Stiffeners 641
G.D. Chen and Y.L. Guo

www.EngineeringEBooksPdf.com

Elastic Critical Moments of I Sections with Very Slender Webs 649
A.J. Wang and K.F. Chung

Shells

An Efficient Strategy for the Evaluation of the Reliability of 3D Shells in Case of Non Linear Buckling 659
A. Combescure and A. Legay

Case Study of a Medium-Length Silo Under Wind Loading 667
M. Pircher, R.Q. Bridge and R. Greiner

Buckling of Thin Pressurized Cylindrical Shells Under Bending Load 675
A. Limam and *J.F. Jullien*

Stability of Thin-Walled Cylindrical Shells Subjected to Lateral Patch Loads 683
E. Feifel and H. Saal

Buckling of Circular Steel Silos Subject to Eccentric Discharge Pressures – Part I 693
C.Y. Song and J.G. Teng

Buckling of Circular Steel Silos Subject to Eccentric Discharge Pressures – Part II 703
C.Y. Song and J.G. Teng

Aspects of Corrugated Silos 713
P. Ansourian and M. Gläsle

Buckling Experiments on Transition Rings in Elevated Steel Silos 721
Y. Zhao and J.G. Teng

Buckling Strength of Cylinders with a Consistent Residual Stress 729
J.M.F.G. Holst and J.M. Rotter

Buckling Behaviour of Extensively-Welded Steel Cylinders Under Axial Compression 737
X. Lin and J.G. Teng

Experiment on a Model Steel Base Shell of the Comshell Roof System 745
H.T. Wong and J.G. Teng

Effect of Cracks on Vibration, Buckling and Parametric Instability of Cylindrical Shells 755
A. Vafai, M. Javidruzi, J.F. Chen and J.C. Chilton

An Experimental Study for Seismic Reinforcement Method on Existing Cylindrical Steel Piers by Welded Rectangular Steel Plates 763
K. Chu and T. Sakurai

Bridges

Metal Forms Replace Reinforcement in Bridge Deck Slabs 773
B. Bakht, A.A. Mufti and G. Tadros

Analysis of the Camber at Prestressing of a New Kind of Composite Railway Bridge Deck 783
S. Staquet, H. Detandt and B. Espion

www.EngineeringEBooksPdf.com

Evaluation of Typhoon Induced Fatigue Damage Using Health Monitoring Data 791
T.H.T. Chan, Z.X. Li and J.M. Ko

Fatigue Stress Analysis of Suspension Bridges Using FEM 799
T.H.T. Chan, L. Guo and Z.X. Li

Curved Steel Box-Girder Bridges at Construction Phase 807
G.C.M. Lee, K.M. Sennah and J.B. Kennedy

Numerical Study of Characteristic Behavior of Steel Plate Girder Bridges 815
E. Yamaguchi, K. Harada, M. Nagai and Y. Kubo

Nonlinear Seismic Response Analysis of a Deck-Type Steel Arch Bridge 823
T. Yamao, H. Harada and Y. Muramoto

The Unit Load Method - Some Recent Applications 831
D. Janjic, M. Pircher and H. Pircher

Global Analysis of Steel and Composite Highway Bridges - Development of Improved Spatial Beam Models 839
H. Unterweger

Dynamics

Field Comparative Tests of Cable Vibration Control Using Magnetorheological (MR) Dampers in Single- and Twin-Damper Setups 849
Y.F. Duan, J.M. Ko, Y.Q. Ni and Z.Q. Chen

Evaluation of Ride Comfort of Road Vehicles Running on a Cable-Stayed Bridge Under Crosswind 857
W.H. Guo and Y.L. Xu

Comparison of Buffeting Response of a Suspension Bridge Between Analysis and Aeroelastic Test 865
Y.L. Xu, D.K. Sun and K.M. Shum

Dynamic Response of the Cable to Moving Mass 873
Y.L. Guo, H. Wang and G.X. Ren

Traffic-Induced Microvibration Mitigation of High Tech Equipment Inside a Building Using Passive/Active Platform 881
Z.C. Yang and Y.L. Xu

Dynamic Analysis of Coupled Train-Bridge Systems Under Fluctuating Wind 889
Y.L. Xu, H. Xia and Q.S. Yan

Modal Parameter Identification of Tsing Ma Bridge During Typhoon Victor: EMD-HT Approach 897
J. Chen, Y.L. Xu and R.C. Zhang

Dynamic Load from Pedestrian Footsteps 905
S.S. Law

www.EngineeringEBooksPdf.com

Frictional Joint in the Dynamic Analysis of a Portal Frame 913
S.S. Law, Z.M. Wu and S.L. Chan

Formulas for Vibration Period of Steel Buildings in Taiwan Derived from Ambient Vibration Data 921
L.J. Leu, C.Y. Liu, C.W. Huang and S.H. Yeh

Impact Mechanics

Some Recent Studies on Energy Absorption of Metallic Structural Components 931
G. Lu

Crash Analysis of Automobile Bumpers with Pedestrians 939
B. Wang and G. Lu

A Theoretical Model for Axial Splitting and Curling of Circular Metal Tubes 947
X. Huang, G. Lu and T.X. Yu

Experiment and Analysis of a Scaled-Down Guardrail System Under Static and Impact Loading 955
J.T.Y. Hui, T.X. Yu and X.Q. Huang

Crashworthiness of Motor Vehicle and Luminaire Support in Frontal Impact 963
M. Samaan and K. Sennah

Effects of Welding

Experimental and Numerical Uni-Axial Tests at High Temperature - Analysis of Models 973
Y. Vincent and J.F. Jullien

A Two Scale Model for the Simulation of Residual Stresses Due to Welding of a Metallic Multiphase Material 981
A. Combescure and M. Coret

Influence of Welding Details on the Performance of Beam to Column Connections of Steel MRFs in Seismic Areas 989
D. Dubina and A. Stratan

Fatigue and Fracture

Correlation of Fatigue Life of Fillet Welded Joints Based on Stress at 1mm in Depth 1001
Z.G. Xiao and K. Yamada

Fatigue Strength Prediction for Misaligned Welded Joints by Stress Field Intensity Method 1009
D.Q. Guan, W.J. Yi and L. Li

Failure of a Steel Plate Containing a Circular Rivet Hole with an Emanating Crack 1017
K.T. Chau and S.L. Chan

A Method to Estimate P-S-N Curve of Welded Joints Under General Stress Ratio 1025
D.Q. Guan, W.J. Yi and Q. Wang

www.EngineeringEBooksPdf.com

Fatigue Crack Propagation of Tubular T-Joints Under Combined Loads 1033
S.P. Chiew, S.T. Lie and Z.W. Huang

High-Cycle Fatigue Behaviour of Welded Thin SHS-CHS T-Joints Under In-Plane Bending 1043
.R. Mashiri, X.L. Zhao, L.W. Tong and P. Grundy

On the Analysis of Fracture Phenomena Observed in Steel Structures During the Kobe Earthquake 1051
H. Fujiwara, Y. Goto and M. Obata

Fire Performance

Assessment of Structures for Fire Safety - Insights on Current Methods and Trends 1061
J.Y.R. Liew and H.X. Yu

World Trend for the Development of Performance-Based Fire Codes for Steel Structures 1071
M.B. Wong

A New Method to Determine the Ultimate Load Capacity of Composite Floors in Fire 1079
A.S. Usmani and N.J.K. Cameron

Graphical Method for Design of Steel Structures in Fire 1089
M.B. Wong

High Temperature Transient Tensile Properties of Fire Resistant Steels 1095
W. Sha and T.M. Chan

Mechanical Properties of Structural Steel at Elevated Temperatures 1103
J. Outinen and P. Mäkeläinen

Structural Response of a Steel Beam Within a Frame During a Fire 1111
Z.F. Huang, K.H. Tan and S.K. Ting

Effect of External Bending Moment on the Response of Boundary-Restrained Steel Column in Fire 1119
K.H. Tan and Z.F. Huang

Concrete-Filled HSS Columns after Exposure to the ISO-834 Standard Fire 1127
L.H. Han, J.S. Huo and Y.F. Yang

An Experimental Study and Calculation on the Fire Resistance of Concrete-Filled SHS and RHS Columns 1135
L.H. Han, L. Xu and Y.F. Yang

Analysis and Design

A Unified Analysis Method to Predict Long-Term Mechanical Performance of Steel Structures Considering Corrosion, Repair and Earthquake 1145
Y. Goto and N. Kawanishi

A Higher Order Formulation for Geometrically Nonlinear Space Beam Element 1153
J.X. Gu, S.L. Chan and Z.H. Zhou

www.EngineeringEBooksPdf.com

Unified Analytical Method of Gliding Cables in Structural Engineering – Frozen-Heated Method 1161
Y.L. Guo and X.Q. Cui

Large Deflection Analysis of Tensioned Membrane Structures Allowing for Support Flexibility 1169
J.J. Li and S.L. Chan

Torsional Analysis of Asymmetric Proportional Building Structures Using Substitute Plane Frames 1177
W.P. Howson and B. Rafezy

On Some Problems of Analytical and Probability Approaches to Structural Design 1185
J.J. Melcher

Design of Steel Frames Using Calibrated Design Curves for Buckling Strength of Hot-Rolled Members 1193
S.L. Chan and S.H. Cho

Analysis of the Bending Strength of U-Section Steel Sheet Piles Crimped in Pairs 1201
M.P. Byfield and R.J. Crawford

A Textbook for the New Canadian Standard - *Strength Design in Aluminum* 1209
D. Beaulieu

Index of Contributors I1

Keyword Index I3

www.EngineeringEBooksPdf.com

PLATES

www.EngineeringEBooksPdf.com

This Page Intentionally Left Blank

www.EngineeringEBooksPdf.com

Advances in Steel Structures, Vol. II
Chan, Teng and Chung (Eds.)
© 2002 Elsevier Science Ltd. All rights reserved.

NUMERICAL MODELLING OF STAINLESS STEEL PLATES

K.J.R. Rasmussen, T. Burns, P. Bezkorovainy and M.R. Bambach

Department of Civil Engineering, University of Sydney, Australia

ABSTRACT

The paper describes the development of numerical models for analysing stainless steel plates in compression. Material tests on coupons cut in the longitudinal, transverse and diagonal directions are included as are the results of tests on stainless steel plates. Detailed comparisons are made between the experimental and numerical ultimate loads and load-displacement curves. It is shown that excellent agreement with tests can be achieved by using the compressive stress-strain curve pertaining to the longitudinal direction of loading.

The effect of anisotropy is investigated using elastic-perfectly-plastic material models, where the anisotropic material model is based on Hill's theory. The models indicate that the effect of anisotropy is small and that it may not be required to account for anisotropy in the modelling of stainless steel plates in compression.

KEYWORDS

Plates, stainless steel, finite elements, plasticity, anisotropy, tests.

INTRODUCTION

Stainless steel alloys are found in a wide range of structural applications, including two and three dimensional truss structures, canopy structures and other roof structures featuring the aesthetic appeal of the material, including roof sheeting. The thickness is often kept at a minimum to reduce the relatively high material cost and achieve solutions with high strength to weight ratios. Many structural applications are cold-formed and may suffer from local or distortional buckling in their ultimate limit state.

Despite the prevalence of local buckling in the design of stainless steel structural members, little research data exists and the available research (Johnson and Winter 1966, van den Berg 2000, SCI 2000) is primarily experimental. The present paper forms part of an ongoing investigation into the strength of stainless steel plate elements. It describes the development of finite element models which incorporate the material characteristics of stainless steel alloys. The models are shown to produce good agreement with tests on stainless steel plates. They are currently being used to produce data for the design of stainless steel plates in compression, as will be described in a companion paper.

www.EngineeringEBooksPdf.com

Stainless steel alloys are characterized by having different properties in compression and tension and different properties in the transverse and longitudinal directions. These characteristics require careful material modelling particularly in the case of plated structures in compression which develop two-dimensional stress states during buckling. Furthermore, in contrast to structural steels, which have a yield plateau and may be modelled as elastic-perfectly-plastic, stainless steel alloys have nonlinear stress-strain curves featuring low proportionality stress, no yield plateau and extensive strain-hardening capability.

In numerical analyses, the modelling of nonlinear stress-strain curves is straightforward in most finite element packages, including Abaqus which has been used for the present study. However, these material models assume isotropic nonlinear hardening and as such cannot model stainless steel alloys accurately. Abaqus includes a facility for modelling anisotropy based on Hill's theory (Hill 1950) which has been used in the present paper to study the effect of anisotropy on the buckling of plates. However, the anisotropic theory assumes the material is elastic-perfectly-plastic and cannot account for strain hardening.

The purpose of this paper is to present test results and the development of finite element models for stainless steel plates. Recent tests on simply supported plates in uniform compression are described and comparisons are made between the experimentally and numerically obtained load-displacements curves. To obtain data for the anisotropic material model, results are included for compression and tension tests on coupons cut in the longitudinal, diagonal and transverse directions.

TESTS

Plate Tests

Two tests were conducted on single plates cut from nominally 3 mm thick UNS31803 stainless steel plate, popularly known as Duplex 2205. The nominal widths were chosen as 125 mm and 250 mm, which corresponded to plate slenderness values ($\lambda=\sqrt{\sigma_y/\sigma_{cr}}$) of 1.03 and 2.06 respectively when using nominal values of yield stress and initial Young's modulus of 440 MPa and 200,000 MPa respectively. The nominal length of the plates was 750 mm which produced aspect ratios of 6 and 3 for the 125 mm and 250 mm wide plates respectively. The plates were guillotined to size. They were simply supported along all four edges in the test rig.

The measured value of thickness was 3.02 mm. The widths were measured as 126.0 mm and 250.7 mm for the nominally 125 mm and 250 mm wide plates respectively. The measured material properties are detailed in the section following. The 125 mm and 250 mm wide test specimens have been referred to as SS125 and SS250 respectively.

The plate test rig used the "finger principle" developed at Cambridge University to a) provide simple supports at the longitudinal supports and b) ensure that the axial thrust was not transferred to the longitudinal supports. The fingers supported the plates at a distance of 4 mm from the longitudinal edges. Bearings were used at the loaded ends to allow flexural rotations. The plates were subjected to uniform compression and tested under stroke control until failure. Full details of the rig are given in Bambach and Rasmussen (2000).

A displacement transducer frame was placed over the rig to measure the deflection along the centre of the plate. A transducer was mounted on a plate sliding along linear bearings so that by taking frequent readings the longitudinal profile of the plate deflection could be obtained. The deflections were also measured prior to the test to obtain the initial out-of-flatness.

The ultimate loads of test specimens SS125 and SS250 were 155.6 kN and 170.5 kN respectively. Specimen SS125 failed by inelastic buckling with negligible deflections developing until after the ultimate load. Specimen SS250 formed three nearly symmetric buckles prior to reaching the ultimate load.

www.EngineeringEBooksPdf.com

Material tests

The material properties of the stainless steel alloy S31803 were obtained from coupon tests of small sample plates cut from the same larger plates as those used for the plate test specimens. Tension and compression coupons were cut from each sample plate in the longitudinal, transverse and diagonal directions so as to obtain data for the anisotropic properties of the material. The full set of stress-strain curves are shown in Rasmussen et al. (2002).
The mechanical properties are summarised in Table 1. They include the initial elastic modulus (E_0), the ultimate tensile strength (σ_u), and the Ramberg-Osgood parameter (n) calculated as,

$$n = \frac{\ln(20)}{\ln(\sigma_{0.2} / \sigma_{0.01})} \tag{1}$$

where $\sigma_{0.01}$ and are $\sigma_{0.2}$ are the 0.01% and 0.2% proof stresses respectively.

TABLE 1: MECHANICAL PROPERTIES OF S31803 ALLOY FROM TEST DATA

Specimen	E_o (MPa)	$\sigma_{0.01}$ (MPa)	$\sigma_{0.2}$ (MPa)	σ_{ult} (MPa)	n
TT	215250	430	635	831	7.7
LT	200000	310	575	740	4.8
DT	195000	376	565	698	7.4
TC	210000	380	617	-	6.2
LC	181650	275	527	-	4.6
DC	205000	460	610	-	10.6

NUMERICAL MODELS

General

The aims of the numerical modelling were a) to develop accurate finite element (F.E.) models validated against the experimental plate test results, and b) to investigate the effects of material anisotropy and the shape of the initial geometric imperfection.

Four F.E. models were made of each of the tested plates, distinguished only by their material modelling and geometric imperfection. The material models were isotropic nonlinearly hardening, isotropic elastic-perfectly-plastic and anisotropic elastic-perfectly-plastic. The geometric imperfection was as-measured, or in three half-waves (plate SS250) or six halfwaves (plate SS125) according to the elastic buckling mode. Abaqus version 5.7 (Hibbit et al. 1997) was used for the F.E. analyses.

Geometric Details

Each of the four models was simply supported on all edges and loaded in uniform compression. The test plates buckled into three (SS250) or six (SS125) half-waves and post-ultimate localisation was observed. To allow localisation to occur, the full length of the test plates was modelled. Supported by the test observations, only half the plates was modelled by utilising symmetry along the longitudinal centreline. The measured dimensions of the test plates were used. Consistent with the test conditions, the longitudinal boundary restraints modelling the longitudinal finger supports were applied along a row of nodes 4 mm from the edge, as shown in Fig. 1. The same figure shows the model geometry and support conditions. The 4-node reduced integration shell element 4SR of the Abaqus element library was used for all calculations.

www.EngineeringEBooksPdf.com

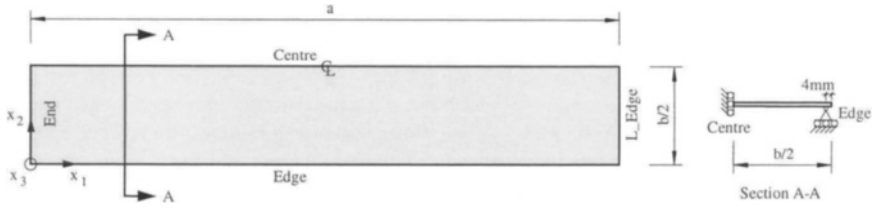

Figure 1: Model geometry

Imperfection Modelling and Elastic Buckling Analysis

Two imperfection types were used. The first imperfection was six or three identical half-waves for test plates SS125 and SS250 respectively, corresponding to the first eigenmode for the test plates as obtained from an elastic buckling analysis. The elastic buckling loads for test plates SS125 and SS250 were 169.4 kN and 78.3 kN respectively based on the total width. The amplitudes of each buckle was set to 0.5 mm and 1 mm for test plates SS125 and SS250 respectively, which were also the geometric imperfections measured at the centre of the plates.

The second imperfection represented the measured imperfection and was in the form of a single slightly asymmetric single half-wave with amplitudes 0.5 mm and 1.0 mm for test plates SS125 and SS250 respectively. The imperfections were generated in a separate load step by applying forces perpendicular to the plate along the centerline. The magnitudes of the forces were adjusted to produce close agreement with the measured imperfections of the test specimens. The deflected shapes obtained from this load step were used as the geometry of the plate in the subsequent nonlinear analysis.

Material Modelling

Three material models were employed: isotropic strain hardening, isotropic perfect plasticity and anisotropic perfect plasticity. The isotropic nonlinearly hardening material model was based on the average compressive stress-strain curve for the longitudinal direction (LC). Notwithstanding that this material model (Iso-sh-1hw) did not account for anisotropy, it was the most realistic of the three material models.

The stress-strain curve was modelled as a multi-linear curve of true stress against true plastic strain. The conversion from engineering stress and strain into true stress and true plastic strain was obtained by the well-known formulae, $\sigma_t=\sigma_e(1+\varepsilon_e)$ and $\varepsilon_{tp}=\ln(1+\varepsilon_e)-\sigma_t/E_0$, where the subscripts t and e refer to "true" and "engineering" respectively, and ε_{tp} is the true plastic strain.

As mentioned in the Introduction, the anisotropic model implemented in Abaqus assumes perfect plasticity. The model (Aniso-pp-1hw) could therefore not represent the actual stress-strain curves but did facilitate a means of assessing the effect of anisotropy on the behaviour and strength of stainless steel plates. To make this comparison, the anisotropic model has been compared with an isotropic elastic-perfectly-plastic model (Iso-pp-1hw) using the same as-measured geometric imperfection. The isotropic elastic-perfectly-plastic model was a bilinear stress-strain curve with elastic modulus taken from the longitudinal compression (LC) coupon test, see Table 1. The yield stress was defined as the 0.2% proof stress obtained from the LC coupon test.

The anisotropic perfect plasticity model defines the yield surface in the form (Hill 1950),

$$f(\boldsymbol{\sigma}) = \left[F(\sigma_{22}-\sigma_{33})^2 + G(\sigma_{33}-\sigma_{11})^2 + H(\sigma_{11}-\sigma_{22})^2 + 2L\tau_{23}^2 + 2M\tau_{13}^2 + 2N\tau_{12}^2\right]^{\frac{1}{2}} \quad (2)$$

where F, G, H, L, M and N are defined in terms of the yield stresses, eg,

www.EngineeringEBooksPdf.com

$$F = \frac{\sigma_0^2}{2}\left(\frac{1}{\sigma_{0,22}^2}+\frac{1}{\sigma_{0,33}^2}-\frac{1}{\sigma_{0,11}^2}\right)=\frac{1}{2}\left(\frac{1}{R_{22}^2}+\frac{1}{R_{33}^2}-\frac{1}{R_{11}^2}\right) \text{ and } N=\frac{3}{2}\left(\frac{\tau_0}{\tau_{0,12}}\right)^2=\frac{3}{2}\frac{1}{R_{12}^2} \quad (3)$$

Similar equations (involving cyclic rotation of indices) exist (Hill 1950) for G, H, L and M. In Eqn. (3), $\sigma_{0,ii}$ ($\tau_{0,ij}$) is the measured yield stress when σ_{ii} (τ_{ij}) is applied as the only nonzero stress, σ_0 is a reference yield stress, $\tau_0 = \sigma_0/\sqrt{3}$ and R_{ij} is the yield stress ratio,

$$R_{11}=\frac{\sigma_{0,11}}{\sigma_0};\quad R_{22}=\frac{\sigma_{0,22}}{\sigma_0};\quad R_{33}=\frac{\sigma_{0,33}}{\sigma_0};\quad R_{12}=\frac{\tau_{0,12}}{\tau_0};\quad R_{13}=\frac{\tau_{0,13}}{\tau_0};\quad R_{23}=\frac{\tau_{0,23}}{\tau_0} \quad (4)$$

The longitudinal direction (X1) has been nominated as the reference direction in the present study so that σ_0=527 MPa and R_{11}=1. The shear yield stress $\tau_{0,12}$ for the X1-X2 plane has been approximated by $\sigma_{0D}/\sqrt{3}$ where σ_{0D} is the yield stress for the diagonal direction. Furthermore, the yield stress for the through-thickness direction has been assumed equal to σ_0.

The yield stresses have been taken as the 0.2% proof stresses for compression given in Table 1. Hence, the following yield stress ratios were used,

$$R_{11}=1;\quad R_{22}=\frac{617}{527}=1.17;\quad R_{33}=1;\quad R_{12}=\frac{610/\sqrt{3}}{527/\sqrt{3}}=1.16;\quad R_{13}=1;\quad R_{23}=1 \quad (5)$$

COMPARISON OF F.E. AND EXPERIMENTAL RESULTS

Validation of FE models

Tables 2a and 2b compare numerical ultimate loads with test values for plates SS125 and SS250 respectively. For the strain-hardening models Iso-sh-3hw and Iso-sh-1hw, the numerical ultimate loads were 7.4% and 3.6% less than the test value respectively for plate SS125, and were 0.4% and 1.1% greater than the test value for plate SS250. It follows that for fairly stocky plates with $\lambda \approx 1$, it is necessary to model the actual imperfection to obtain good agreement with test while for more slender plates, which develop appreciable local buckles prior to reaching the ultimate load, the ultimate load is virtually unchanged whether the actual imperfection is modelled or the imperfection is assumed to be in the shape of the elastic buckling mode.

TABLE 2A: NUMERICAL MODELS AND ULTIMATE LOADS OF TEST PLATE SS125

Model	Imperfection Type	Material Type	Ult. Load (kN)	Error* (%)
Iso-sh-3hw	3 symm. Half-waves	Isotropic strain hardening	144.1	-7.4
Iso-sh-1hw	1 asymm. Half-wave	Isotropic strain hardening	150.0	-3.6
Iso-pp-1hw	1 asymm. Half-wave	Isotropic perfect plasticity	169.3	8.8
Aniso-pp-1hw	1 asymm. Half-wave	Anisotropic perfect plasticity	168.0	8.0

* Relative to test value, P_u=155.6 kN

TABLE 2B: NUMERICAL MODELS AND ULTIMATE LOADS OF TEST PLATE SS250

Model	Imperfection Type	Material Type	Ult. Load (kN)	Error* (%)
Iso-sh-3hw	3 symm. Half-waves	Isotropic strain hardening	171.2	0.4
Iso-sh-1hw	1 asymm. Half-wave	Isotropic strain hardening	172.4	1.1
Iso-pp-1hw	1 asymm. Half-wave	Isotropic perfect plasticity	179.9	5.5
Aniso-pp-1hw	1 asymm. Half-wave	Anisotropic perfect plasticity	181.2	6.3

* Relative to test value, P_u=170.5 kN

The elastic-perfectly-plastic models Iso-pp-1hw and Aniso-pp-1hw produce significantly higher ultimate loads than the test values, as could be expected. For the more slender plate SS250, the effect of anisotropy is to increase the ultimate load by 0.8% compared to the isotropic model. However, for

www.EngineeringEBooksPdf.com

the stockier plate SS125, the effect of anisotropy is to *decrease* the ultimate load by 0.8% compared to the isotropic model. It is not clear how the ultimate load can decrease by incorporating anisotropic mechanical properties which are higher in the transverse direction than in the longitudinal reference direction. It is possible that different numerical schemes are used in Abaqus for isotropic and anisotropic yielding. In any event, the difference in ultimate load between the isotropic and anisotropic cases is small, suggesting that it may not be required to account for the effect of anisotropy in the modelling of stainless steel plates in compression. However, this conclusion is drawn for elastic-perfectly-plastic material models and may not apply equally to strain hardening models.

The experimental and F.E. load *vs* axial shortening curves for test plates SS125 and SS250 are compared in Figs 2a and 2b respectively. The axial shortening is the decrease in the distance between the loaded ends and the load is the total load on the plate, which is that recorded in the tests and twice that obtained from an F.E. analysis of half of the plate. The Iso_sh_1hw model is generally in close agreement with the test, while the Iso_sh_3hw model is too flexible, particularly for test plate SS125. The elastic-perfectly-plastic models Iso_pp_1hw and Aniso_pp_1hw are nearly coincident demonstrating negligible influence of material anisotropy.

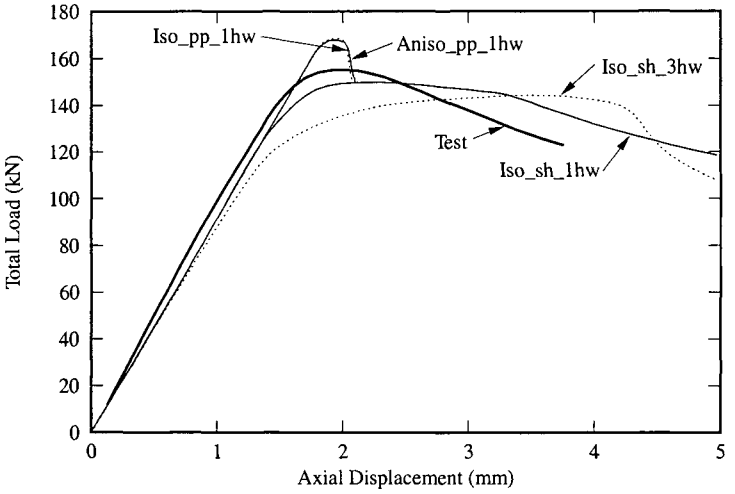

Figure 2a: Load vs Axial Displacement for Plate SS125 and Abaqus Models

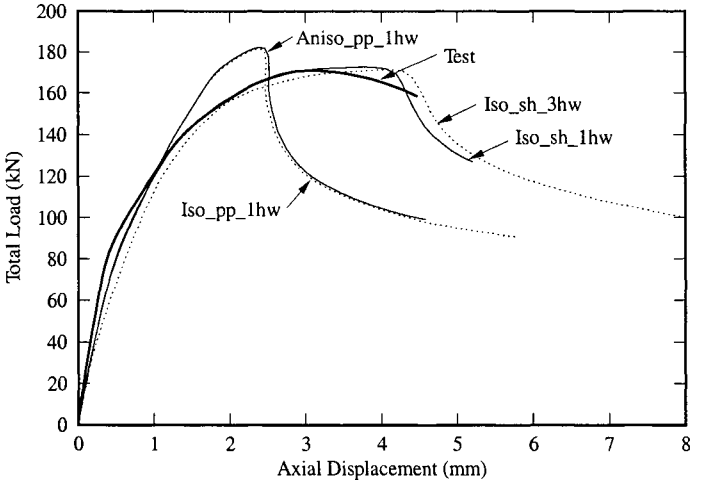

Figure 2b: Load vs Axial Displacement for Plate SS250 and Abaqus Models

www.EngineeringEBooksPdf.com

The curves of load *vs* lateral displacement at the centre are compared in Fig. 3 for test plate SS250. The agreement is good for the strain-hardening models up to and slightly beyond the ultimate load when localization occurred. In the test, localization occurred in the central buckle and so the central deflection increased monotonically until the conclusion of the test, as shown in Fig. 3. However, in the F.E. analysis, localization occurred in one of the buckles at the loaded edges and was associated with elastic unloading of the two other buckles. Accordingly, the displacement decreased at the centre when localization occurred, as shown in Fig. 3. For test plate SS125, the central deflection was small throughout the test and has not been compared with analytical results.

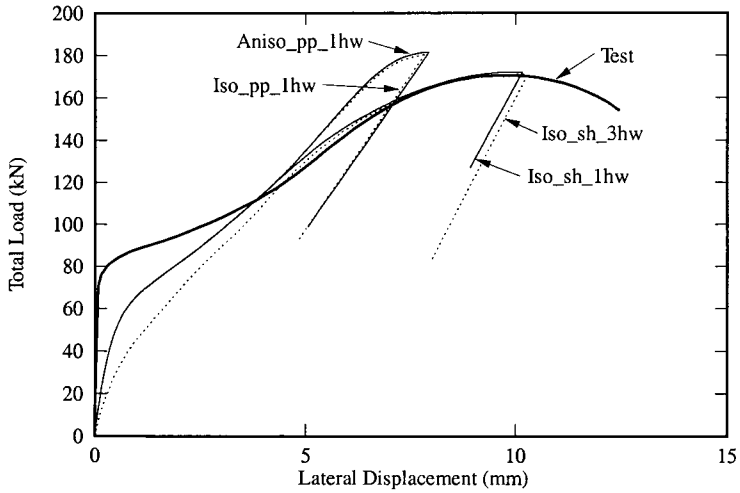

Figure 3: Load vs Lateral Disp. at centre for test plate SS250 and Abaqus Models

Further comparison between experimental and numerical results is included in Rasmussen et al. (2002) in the form of profiles of plate deflection at the longitudinal centerline for increasing levels of loading, and load-strain curves. These comparisons also show that good agreement can be achieved using the Iso_sh_1hw model.

Effect of Initial Imperfection

The ultimate loads predicted by the Iso-sh-3hw and Iso-sh-1hw models differed by 3.8% and 0.7% for test plates SS125 and SS250 respectively, as shown in Tables 2a and 2b. As mentioned above, it is necessary to model the actual imperfection to obtain close agreement with test for fairly stocky plates with $\lambda \approx 1$, while for more slender plates, which develop appreciable local buckles prior to reaching the ultimate load, the ultimate load is virtually unchanged whether the actual imperfection is modelled or the imperfection is assumed to be in the shape of the elastic buckling mode. However, there is some difference in the load-displacement and load-strain curves of the two models, as shown in Fig. 3. The difference is most pronounced near the local buckling load where the as-measured single half-wave imperfection delays the development of local buckles and produces better agreement with tests.

Effect of Material Anisotropy

By examining the load-displacement curves for Abaqus models Iso-pp-1hw and Aniso-pp-1hw shown in Figs 2 and 3, it can be concluded that the effect of anisotropy in plates with perfect plasticity is negligible: The difference between ultimate loads predicted by the two models is only ±0.8% and the load *vs* displacement are nearly coincident. However, further study into the effects of anisotropy on stainless steel plates with strain hardening could be warranted considering the fact that models Iso-pp-1hw and Aniso-pp-1hw were premised on elastic-perfectly-plastic material modelling.

www.EngineeringEBooksPdf.com

CONCLUSIONS

Finite element models have been presented for the analysis of stainless steel plates in compression. It has been shown that excellent agreement with tests can be achieved by using the stress-strain curve for longitudinal compression, assuming isotropic hardening, and modelling the as-measured geometric imperfection (Iso_sh_1hw). The ultimate load obtained using this model was 3.6% less and 1.2% more that the experimental ultimate loads for test plates SS125 and SS250 respectively. Furthermore, the load *vs* axial shortening and load *vs* lateral displacement curves closely resemble the experimental curves, particularly for the slender test plate SS250.

The effect of anisotropy has been investigated on the basis of elastic-perfectly-plastic material models. In the anisotropic model, the yield stress for the transverse direction was 17% higher than for the longitudinal direction. The load *vs* displacement curves showed that anisotropy had negligible effect on the load *vs* displacement curves with a maximum difference in ultimate load of 0.8%. However, the effect of anisotropy may be more pronounced in a strain hardening model where anisotropy plays a role at significantly lower stresses than in elastic-perfectly-plastic models.

Comparing the elastic-perfectly-plastic models (Iso-pp-1hw) with the strain hardening models (Iso-sh-1hw) it is evident that it is important to model the nonlinear stress-strain curve in numerical analyses. The ultimate loads obtained using the elastic-perfectly-plastic material model were 8.8% and 5.5% higher than the experimental values for test plates SS125 and SS250 respectively, as shown in Table 2. Furthermore, the displacements are generally underestimated whereas close agreement was obtained using the strain hardening models.

In summary, stainless steel plates can be accurately modelled by using nonlinear strain hardening material models which are based on compression coupon tests for the longitudinal direction. The present study indicates that anisotropy may *not* be important for numerical analyses.

REFERENCES

Bambach, MR and Rasmussen, KJR, "Experimental Techniques for Testing Unstiffened Plates in Compression and Bending", *Thin-walled Structures, Advances and Developments*, eds J. Zaras, K. Kowal-Michalska and J. Rhodes, Proceedings of the Third International Conference on Thin-walled Structures, Elsevier, pp. 719-727.

Burns, T and Bezkorovainy, P, (2001), *Buckling of Stiffened Stainless Steel Plates*, BE (Honours) Thesis, Department of Civil Engineering, University of Sydney.

Hibbitt, Karlsson and Sorensen, Inc., (1997), "ABAQUS Standard, Users Manual", Vols 1 and 2, Ver. 5.7, USA.

Hill, R, (1950), *The Mathematical Theory of Plasticity*, Ch. XII, Oxford Science Publications, Clarendon Press, Oxford.

Johnson, AL, and Winter, G, (1966), "Behaviour of Stainless Steel Columns and Beams", *Journal of the Structural Division*, American Society of Civil Engineers, Vol. 92, No. ST5, pp. 97-118.

Rasmussen, KJR, Burns, T, Bezkorovainy, P, and Bambach, MR, (2002), "Numerical Modelling of Stainless Steel Plates", *Research Report No R 813*, Department of Civil Engineering, University of Sydney.

SCI, (2000), "Development of the Use of Stainless Steel in Construction", Main Work Package Reports – Vol. 1, Document RT810, Ver. 01. Work Package 2: Cross-sections – Welded I-sections and Cold-formed Sheeting, *Steel Construction Institute*, London.

Van den Berg, GJ, (2000), "The Effect of Non-linear Stress-strain Behaviour of Stainless Steel on Member Capacity", *Journal of Constructional Steel Research*, Vol. 54, No. 1, pp135-160.

www.EngineeringEBooksPdf.com

Advances in Steel Structures, Vol. II
Chan, Teng and Chung (Eds.)
© 2002 Elsevier Science Ltd. All rights reserved.

LOCAL BUCKLING OF BIAXIALLY COMPRESSED STEEL PLATES IN DOUBLE SKIN COMPOSITE PANELS

Q. Q. Liang,[1] B. Uy,[1] H. D. Wright[2] and M. A. Bradford[1]

[1] School of Civil and Environmental Engineering, The University of New South Wales, Sydney, NSW 2052, Australia
[2] Department of Civil Engineering, University of Strathclyde, Glasgow, G4 0NG, UK

ABSTRACT

Steel plates in double skin composite (DSC) panels may buckle locally between shear connectors when subjected to biaxial compression. The local and post-local buckling behaviour of biaxially compressed steel plates restrained by discrete stud shear connectors in DSC panels is studied in this paper by using the finite element method. The shear stiffness effect of stud shear connectors is considered in the determination of elastic local buckling coefficients. The post-local buckling strength of steel plates in biaxial compression is investigated by performing a geometric and material nonlinear analysis. The initial imperfections, material stress-strain relationship and shear-slip behaviour of stud shear connectors are taken into account in the post-local buckling analysis. Biaxial strength interaction curves and design formulas are developed for the design of steel plates in DSC panels under biaxial compression.

KEYWORDS

Biaxial compression, composite construction, double skin composite panels, finite element analysis, local buckling, post-local buckling, strength, stud shear connectors, steel plates.

INTRODUCTION

In a double skin composite panel, the concrete core is sandwiched by two steel plates welded with headed stud shear connectors at a regular spacing, as shown in Fig. 1. Stud shear connectors are designed to resist the shear between steel skins and the concrete core, and separation at the interface. Steel plates serve as permanent formwork and biaxial steel reinforcement for the concrete. Experimental behaviour of DSC elements has been investigated by Wright et al. (1991a). Research conducted by Wright et al. (1991b) showed that DSC elements could be analyzed and designed in

www.EngineeringEBooksPdf.com

accordance with the conventional theory for doubly reinforced concrete elements and composite structures, providing that the effects of local buckling and shear connections are taken into account.

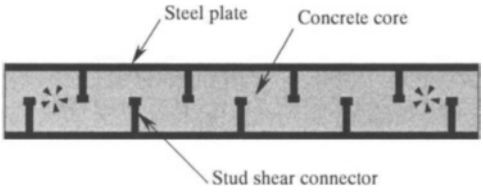

Figure 1: Cross-section of double skin composite panel

The local buckling and strength of concrete-filled steel box columns have been investigated by Ge and Usami (1992). Wright (1995) derived limiting width-to-thickness ratios for plates with various boundary conditions. Experimental and numerical studies have been performed on the strength of composite steel-concrete members incorporating local buckling effects by Uy and Bradford (1995) and Uy (2000, 2001). Liang and Uy (2000) proposed effective width models for the design of steel plates in concrete-filled box columns.

Elastic buckling solutions of biaxially loaded steel plates that can buckle bilaterally were given in the book by Bulson (1970). Valsgard (1980) reported that biaxial strength design formulas for steel plates in biaxial compression should be generated on the basis of a proportional load increment scheme in a nonlinear finite element analysis. The finite difference approach has been used by Dier and Dowling (1984) to generate the biaxial strength interaction curves of simply supported steel plates. Moreover, tests of steel plates under biaxial forces have been conducted by Bradfield et al. (1992).

In this paper, the local and post-local buckling behaviour of biaxially compressed steel plates in DSC panels is investigated by using the finite element code STRAND7 (2000). Finite element models for buckling analysis are described. Elastic local buckling coefficients of plates with various boundary conditions are presented. Biaxial strength interaction curves and design formulas are developed for the design of steel plates in DSC panels.

FINITE ELEMENT MODELS

Boundary conditions

Steel plates in DSC panels are restrained to buckle in a unilateral mode between stud shear connectors. To determine the critical stud spacing and strength of steel plates in DSC panels, the structural model is considered to be a single plate field between studs, as shown in Fig. 2. The edge restraint of a plate field located inside a DSC panel depends on the stiffness of adjacent plate fields. It could be argued that the edges of the plate field are restrained from rotation by the adjacent plate fields and concrete, but the degree of rotation is not complete, as adjacent plate fields are usually not stiff enough to provide a fully clamped boundary condition. It is assumed that the edges of the plate field between studs at a worst case are simply supported while its four corners are restrained by studs with finite shear stiffness. The rotations at the corners are constrained whilst their in-plane translations are defined by the shear-slip relationship. This boundary assumption for plate fields located inside DSC panel yields conservative results. If a plate field is located at the panel boundary, which is fully clamped by the connected concrete elements, the edge at the boundary should be assumed as clamped.

www.EngineeringEBooksPdf.com

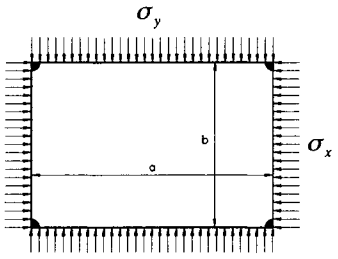

Figure 2: Single plate field restrained by stud shear connectors

Initial imperfections

The initial imperfections of steel plates are considered in the post-local buckling analysis. The form of initial geometric imperfections is taken as the first local buckling mode in the analysis. The maximum magnitude of initial geometric imperfections at the plate centre is taken as $w_0 = 0.003b$. Residual stresses due to welding of stud shear connectors at discrete positions are insignificant in DSC panels. Their effects are indirectly incorporated within the geometric imperfections.

Material stress-strain relationship

The material stress-strain relationship for steel plates in the post-local buckling analysis is defined by the Ramberg-Osgood formula (1943) that is expressed by

$$\varepsilon = \frac{\sigma}{E}\left[1 + \frac{3}{7}\left(\frac{\sigma}{\sigma_{0.7}}\right)^n\right] \tag{1}$$

where σ and ε are stress and strain respectively, E is the Young's modulus, $\sigma_{0.7}$ is the stress corresponding to $E_{0.7} = 0.7E$, and n is the knee factor that defines the sharpness of the stress-strain curve. The knee factor $n = 25$ is used here to account for the isotropic strain hardening of steel plates.

Shear-slip behaviour of headed stud shear connectors

The shear connection affects the strength of steel plates in DSC panels. The local buckling of slender steel plates may occur before the failure of stud shear connectors. The shear connection may fail before the onset of the local buckling or yielding of stocky plates. This effect is considered in the analysis by the shear-slip model of stud shear connectors. The model proposed by Ollgaard et al. (1971) is adopted in the present study, which is expressed by

$$Q = Q_u\left(1 - e^{-18\delta}\right)^{0.4} \tag{2}$$

where Q is the longitudinal shear force, Q_u is the ultimate shear strength of a stud shear connector, and δ is the longitudinal slip. The ultimate shear strength of headed studs can be calculated in accordance with AS 2327.1 (1996). In the linear buckling analysis, a stud shear connector is modeled

www.EngineeringEBooksPdf.com

by elastic springs. The tangent modulus of the shear-slip curve generated by Eqn. 2 is taken as the spring stiffness. A spring-type beam element is used in the post-local buckling analysis to model stud shear connectors, whose nonlinear shear-slip relationship is defined by Eqn. 2.

Validation of finite element models

Finite element models developed for local buckling analysis of steel plates restrained by shear connectors are calibrated with experimental results given by Smith (1998). In the tested specimens, two steel plates (b = 300 mm, t = 3 mm) were connected to the concrete core by three 10-mm diameter bolts at each loaded edge. The loading was applied to two steel plates only in the test. In the linear buckling analysis, the shear stiffness of bolts was taken as $k_s = 1.458\times10^6$ N/mm. It can be seen from Fig. 3 that finite element solutions agree well with experimental results.

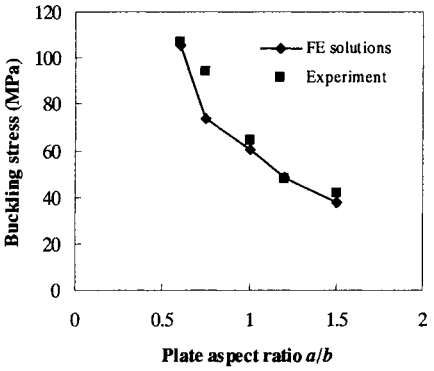

Figure 3: Comparison of FE solutions with experimental results

ELASTIC LOCAL BUCKLING BEHAVIOUR

Buckling coefficients

The linear buckling analysis is undertaken to investigate the elastic local buckling behaviour of perfectly flat plates under biaxial compression. In the analysis, buckling coefficients are determined by varying the plate aspect ratios and biaxial loading. The elastic buckling coefficient (k_x) in the x direction is calculated by the following equation (Bulson 1970)

$$\sigma_{xcr} = \frac{k_x \pi^2 E}{12\left(1-\nu^2\right)(b/t)^2} \tag{3}$$

where σ_{xcr} is the critical buckling stress in the x direction. The elastic local buckling coefficient in the y direction (k_y) can be obtained by substituting σ_{ycr} and a in Eqn. 3. The configurations of plates used in the numerical analyses are b = 500 mm, t = 10 mm, E = 200 GPa and ν = 0.3. The shear stiffness $k_s = 4.52\times10^6$ N/mm is used for a stud shear connector that resists shear from a single plate field, whilst $\frac{1}{2}k_s$ is used for a stud shear connector that resists shear from two adjacent plate fields.

www.EngineeringEBooksPdf.com

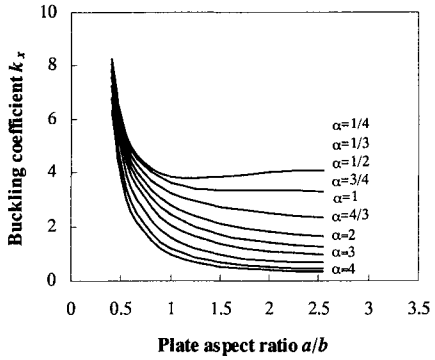

Figure 4: Buckling coefficients of plates in biaxial compression (S-S-S-S+SC)

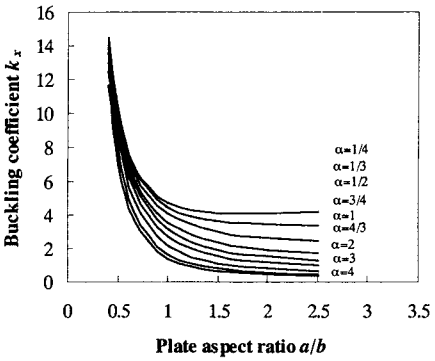

Figure 5: Buckling coefficients of plates in biaxial compression (C-S-S-S+SC)

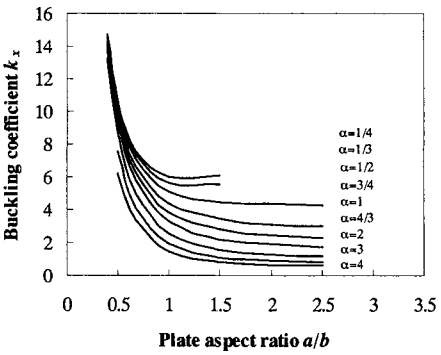

Figure 6: Buckling coefficients of plates in biaxial compression (C-C-S-S+SC)

www.EngineeringEBooksPdf.com

The elastic buckling coefficients of plates with the boundary condition of S-S-S-S+SC (S = Simply supported, SC = Shear Connectors) are presented in Fig. 4. It can be observed from Fig. 4 that whthe biaxial stress ratio ($\alpha = \sigma_y / \sigma_x$) is greater than 1/3, the buckling coefficient of a plate decreases with an increase in the plate aspect ratio *a*/*b*. The transverse compressive stresses (σ_y) significantly reduce the critical local buckling stresses. Shear connectors considerably increases the stability of a steel plate between stud shear connectors. The buckling coefficient of a square plate restrained by shear connectors under equal compression forces in two directions is 2.404, whilst it is only 2.0 for plates unrestrained by shear connectors (Bulson 1970). The studs therefore provide a considerable effect to the in-plane boundary condition.

Fig. 5 shows the buckling coefficients of plates with one clamped edge, and the buckling results of plates with two clamped adjacent edges are presented in Fig. 6. It can be observed that clamped edges considerably increase the critical buckling stresses of plates in biaxial compression. When the difference between applied compressive stresses in two directions is large, clamped edges may cause the shortening of the buckling half-wavelength.

Limiting width-to-thickness ratios for steel plates

Elastic buckling coefficients obtained can be used to determine limiting width-to-thickness ratios for steel plates in DSC panels. The relationship between critical buckling stress components at yield can be expressed by the von Mises yield criterion as

$$\sigma_{xcr}^2 - \sigma_{xcr}\sigma_{ycr} + \sigma_{ycr}^2 = \sigma_0^2 \tag{4}$$

where σ_0 is the yield stress of steel plates. If the material properties E = 200 GPa and ν = 0.3, and the plate aspect ratio $\varphi = a / b$ are assumed, the limiting width-to-thickness ratio can be derived as

$$\frac{b}{t}\sqrt{\frac{\sigma_0}{250}} = 26.89\left(k_x^2 - \frac{k_x k_y}{\varphi^2} + \frac{k_y^2}{\varphi^4}\right)^{1/4} \tag{5}$$

POST-LOCAL BUCKLING BEHAVIOUR

Biaxial strength interaction curves

The post-local buckling strength of biaxially compressed steel plates with the boundary condition of S-S-S-S+SC is studied by undertaking a geometric and material nonlinear analysis. The strength interaction curve of a plate under biaxial compression is determined by varying applied biaxial loads in the analysis. The proportional load increment scheme is employed. Square steel plates (b = 400 mm) with a yield strength of 300 MPa are studied. The 19-mm diameter headed studs are used as shear connectors in the DSC panel filled with the concrete with a compressive strength of 32 MPa. Due to symmetry, only a quarter of the plate field is modeled. Half of the ultimate shear strength of a stud shear connector is used in Eqn. 2 to account for the effect of the adjacent plate field.

Fig. 7 shows the biaxial strength interaction curves of square plates with various *b*/*t* ratios. It can be observed that the ultimate strength of a biaxially compressed plate decreases with an increase in its *b*/*t*

www.EngineeringEBooksPdf.com

ratio. The presence of transverse loading (σ_y) reduces the longitudinal ultimate strength of plates (σ_{xu}). It is noted that a steel plate attains the same ultimate strength in two directions when subjected to the same biaxial loads. Biaxial strength interaction curves of stocky steel plates are parabolic whilst the interaction curves of slender steel plates are closed to straight lines.

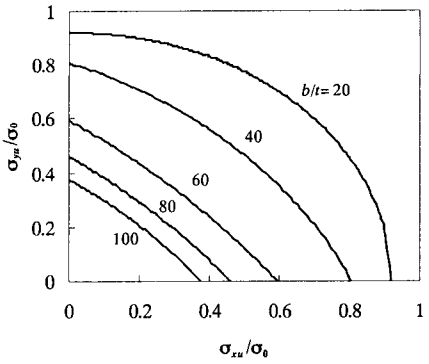

Figure 7: Biaxial strength interaction curves of square plates

Design formulas for strength interaction

It can be observed from Fig. 7 that the shapes of biaxial strength interaction curves strongly depend on the plate slenderness. Biaxial strength interaction relationships of steel plates in DSC panels can be expressed by the general form of a von Mises yield ellipse. The general strength interaction formula is proposed as

$$\left(\frac{\sigma_{xu}}{\sigma_0}\right)^{\xi} + \eta\left(\frac{\sigma_{xu}\sigma_{yu}}{\sigma_0^2}\right) + \left(\frac{\sigma_{yu}}{\sigma_0}\right)^2 = \gamma \quad (\gamma \le 1) \tag{6}$$

where the shape factor ξ of the interaction curve depends on the plate aspect ratio and slenderness, η is a function of the plate slenderness, and γ is the uniaxial strength factor. The shape factor η can be used to define any shapes of interaction curves from a straight line ($\eta = 2$) to the von Mises ellipse ($\eta = -1$). Based on numerical results, parameters defining strength interaction formulas are proposed and given in Table 1. If biaxial applied stresses are known, the biaxial ultimate strengths of a plate can be determined using Eqn. 6 and parameters presented in Table 1.

TABLE 1
PARAMETERS FOR STRENGTH INTERACTION FORMULAS, $\xi = 2$

b/t	η	γ
20	0	0.846
40	0.8	0.65
60	1.45	0.353
80	1.47	0.211
100	1.4	0.14

www.EngineeringEBooksPdf.com

CONCLUSIONS

This paper has investigated the local and post-local buckling behaviour of steel plates in double skin composite panels under biaxial compression by using the finite element method. Elastic buckling coefficients for steel plates with various boundary conditions have been given. Biaxial strength interaction curves have been generated using the proportional load increment approach in the geometric and material nonlinear analysis. Buckling coefficients presented can be used to proportion stud spacing and plate thickness. Strength interaction formulas proposed can be used to determine the ultimate strength of steel plates in DSC panels under biaxial compression.

REFERENCES

AS 2327.1 (1996). *Composite Structures, Part I: Simply Supported Beams*. Standards Australia, Sydney.

Bradfield C. D., Stonor R. W. P. and Moxham K. E. (1992). Tests of long plates under biaxial compression. *Journal of Constructional Steel Research,* 25-56.

Bulson P. S. (1970). *The Stability of Flat Plates*. Chatto and Windus, London.

Dier A. F. and Dowling P. J. (1984). The strength of plates subjected to biaxial forces. In *Behaviour of Thin Walled Structures* (Rhodes J. and Sperce J., eds), Elsevier Applied Science Publishers, London.

Ge H. B. and Usami T. (1992). Strength of concrete-filled thin-walled steel box columns: experiment. *Journal of Structural Engineering,* ASCE, **118:11**, 3036-3054.

Liang Q. Q. and Uy B. (2000). Theoretical study on the post-local buckling of steel plates in concrete-filled box columns. *Computers & Structures,* **75:5**, 479-490.

Ollgaard J. G., Slutter R. G. and Fisher J. W. (1971). Shear strength of stud shear connectors in lightweight and normal-weight concrete. *AISC Engineering Journal,* **8**, 55-64.

Ramberg W. and Osgood W. R. (1943). Description of stress-strain curves by three parameters. *NACA Technical Note*, No. 902.

Smith S. T. (1998). Local buckling of steel side plates in the retrofit of reinforced concrete beams. Ph.D. thesis, The University of New South Wales, Australia.

STRAND7. (2000). G + D Computing Pty Ltd, Sydney.

Uy B. (2000). Strength of concrete-filled steel box columns incorporating local buckling. *Journal of Structural Engineering,* ASCE, **126:3**, 341-352.

Uy B. (2001). Local and postlocal buckling of fabricated steel and composite cross sections. *Journal of Structural Engineering,* ASCE, **127:6**, 666-677.

Uy B. and Bradford M. A. (1995). Local buckling of thin steel plates in composite construction: experimental and theoretical study. *Proceedings of the Institution of Civil Engineers, Structures & Buildings,* **110**, 426-440.

Valsgard S. (1982). Numerical design prediction of the capacity of plates in biaxial in-plane compression. *Computers & Structures,* **12**, 729-739.

Wright H. D. (1995). Local stability of filled and encased steel sections. *Journal of Structural Engineering,* ASCE, **121:10**, 1382-1388.

Wright H. D., Oduyemi T. O. S. and Evans H. R. (1991a). The experimental behaviour of double skin composite elements. *Journal of Constructional Steel Research*, **19:2**, 97-110.

Wright H. D., Oduyemi T. O. S. and Evans H. R. (1991b). The design of double skin composite elements. *Journal of Constructional Steel Research*, **19:2**, 111-132.

www.EngineeringEBooksPdf.com

Advances in Steel Structures, Vol. II
Chan, Teng and Chung (Eds.)
© 2002 Elsevier Science Ltd. All rights reserved.

DUCTILITY OF HIGH PERFORMANCE STEEL RECTANGULAR PLATES UNDER UNIAXIAL COMPRESSION

K. Niwa [1], I. Mikami [2], and Y. Miyazaki [3]

[1] Japan Information Processing Service Co., Ltd.,
Osaka, 532-0011, JAPAN
[2] Department of Civil Engineering, Kansai University,
Osaka, 564-8680, JAPAN
[3] Graduate Student, Department of Civil Engineering, Kansai University,
Osaka, 564-8680, JAPAN

ABSTRACT

It is very important that the structures have the ductility after ultimate state. In order to possess the ductility of thin-walled steel structures, the high performance steels whose material properties can be controlled may practically be used in lieu of the ordinary steels. In this paper, the elasto-plastic finite displacement analyses are carried out for uni-axial compressed steel rectangular plate with initial imperfections of deflection and residual stress. The inelastic behavior on the ultimate state and thereafter of these steel plates with various aspect ratios and width-thickness ratios are parametrically examined for the yield plateau length and the strain-hardening gradient. The influences of both the parameters on ductility are discussed from many analytical results. It follows that their two material properties are opportunely controlled for possessing ductility of uniaxial compressed rectangular steel plates. Additionally, the required values of their parameters (the yield plateau length and the strain-hardening gradient) are cleared by the illustrations in order to efficiently possess the ductility of rectangular steel plates. It is found that the high performance steel is a significant material for our infrastructure.

KEYWORDS

High performance steel, ductility, rectangular plate, uniaxial compression, yield plateau length, strain-hardening gradient

INTRODUCTION

Urban structures should be designed as the tenacious structures which never crash under heavy earthquake, even if they are damaged such as the deterioration of geometric integrity in those structures. For

www.EngineeringEBooksPdf.com

that purpose, it is very important that the structures have not only ultimate strength but also ductility after ultimate state (Mikami et al. 1993).

Some researches have been reported for possessing the ductility of steel bridge piers. The following geometrical improvements of ductility are suggested: partially filling with concrete (Kitada et al. 1993; Usami et al. 1995), rigidifying longitudinal stiffeners (Suzuki et al. 1995; Watanabe et al. 1999), rounding corners of cross section (Watanabe et al. 1992), and thickening the main plate (Mikami et al. 1993; Usami 1997). On the other hand, some studies have been made on the effective parameters of material properties for possessing ductility of steel plate elements, members, or structures: the yield to tensile ratio (Kato 1986; Toyoda et al. 1990), the strain-hardening gradient (Kawakami et al. 2000; Ono and Yoshida 1998), the uniform elongation (Toyoda et al. 1990; Moriwaki 1993; Nara et al. 1993), and the yield plateau length (Moriwaki 1993; Nara et al. 1993). However, little is known about required values of material properties for efficiently possessing ductility.

It was reported by The Kozai Club (1998) that the following steels have higher performance than ordinary steels: the high strength steel which has high tensile strength for reducing the weight of steel in the structure; the constant-yield-strength steel which varies narrowly in the yield strength regardless of its thickness; the high fracture toughness steel which provides a high resistance to brittle fracture occurring in cold districts; the little or no pre-heating steel which is improved weldability; the weathering steel which is able to perform without painting under normal atmospheric conditions. In this study, the high performance steel is defined as having various values of material properties: the yield stress-to-tensile strength ratio, the strain-hardening gradient, the uniform elongation, and the yield plateau length.

The authors (Mikami et al. 2000) showed that the high performance steel could possess ductility of the square plate under uniaxial compression by controlling the yield plateau length and strain-hardening gradient.

In this paper, many elasto-plastic finite displacement analyses are carried out for the rectangular high performance steel plates under uniaxial compression by using the finite element software MARC (*MARC* 1997). The inelastic behavior on the ultimate state and thereafter of the rectangular steel plates with various aspect ratios and width-thickness ratios are parametrically examined for the yield plateau length and the strain-hardening gradient of the high performance steel. The influences of both the effective parameters (the yield plateau length and strain-hardening gradient) on ductility are discussed from many numerical solutions. Additionally, the required values of the two effective parameters are presented by the illustrations for efficiently possessing ductility of the high performance steel plates under uniaxial compression.

STEEL PLATE UNDER UNIAXIAL COMPRESSION

Figure 1 shows the analytical model for the high performance steel plate which is subjected to uniaxial compression and simply supported along the four edges.

This steel plate has the length a, width b, thickness t, yield stress $\sigma_Y = 240\,\mathrm{N/mm^2}$ (approximated to grade SS400 in JIS 2001), elastic modulus $E = 205{,}800\,\mathrm{N/mm^2}$, and Poisson's ratio $\nu = 0.3$. The following non-dimensional parameters are used to indicate the geometric shapes: the aspect ratio $\alpha = a/b$ and equivalent width-thickness ratio $R = (b/t)\sqrt{12(1-\nu^2)\sigma_Y / 4\pi^2 E}$.

The stress-strain curve of high performance steel is modeled in tri-linear function as shown in Fig. 2, given in terms of true stress and logarithmic strain. The controlled values of material properties, the yield plateau length $\epsilon_{st}/\epsilon_Y - 1$ and strain-hardening gradient E_{st}/E, are parametrically examined for possessing

www.EngineeringEBooksPdf.com

ductility of the high performance steel plate, where ϵ_Y is the yield strain. The form of the yield condition adopts the von Mises criterion.

The elasto-plastic finite displacement analyses are carried out by using the finite element software MARC. Many numerical solutions are used for the investigation of the non-linear behavior on the ultimate state and thereafter of uniaxial compressed rectangular plates.

It is assumed that the analyzing models have the initial imperfections. The one is the initial out-of-plane deflection w_0. For steel plates with $\alpha > 1.0$, the lowest ductility of the plates may not be estimated by using the initial deflection mode as elastic buckling mode (Timoshenko and Gere 1961). Therefore, as the initial deflection, both one half-wave mode and two half-waves mode are taken into consideration, which are represented as follows:

$$w_0(x, y) = w_{0,\max} \cdot \cos\frac{\pi}{a}x \cdot \cos\frac{\pi}{b}y \tag{1a}$$

$$w_0(x, y) = w_{0,\max} \cdot \sin\frac{2\pi}{a}x \cdot \cos\frac{\pi}{b}y \tag{1b}$$

where the maximum value of the initial deflection, $w_{0,\max}$, is $b/150$ (JRA 1996).

The other initial imperfection is the residual stress from welding as shown in Fig. 3 (Mikami et al. 1993). The maximum tensile residual stress σ_{rt} and maximum compressive residual stress σ_{rc} are taken as σ_Y and $-0.2\sigma_Y$, respectively. The residual stresses in the loading direction are approximately modeled at each integration point as shown in Fig. 4.

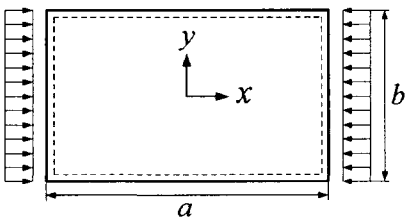

Fig. 1: Steel plate under uniaxial compression

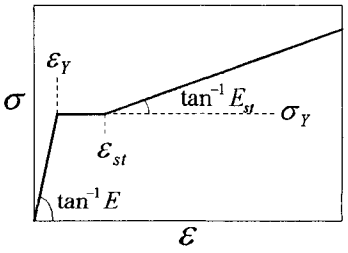

Fig. 2: Stress-strain curve of high performance steel

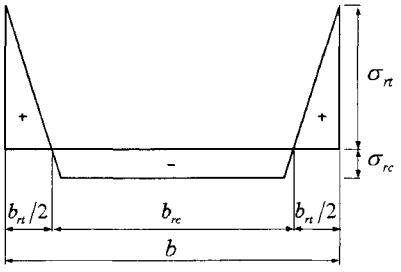

Fig. 3: Considered residual stress

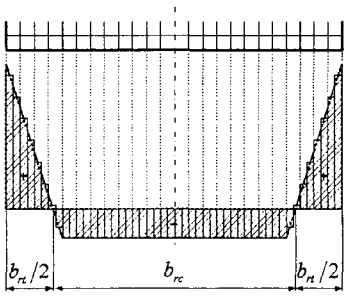

Fig. 4: Modeled residual stress in FEA

www.EngineeringEBooksPdf.com

EVALUATION OF DUCTILITY

In this study, the ductility of high performance steel plates under uniaxial compression can be evaluated by using the relation between $\overline{\sigma}/\sigma_Y$ and $\overline{\epsilon}/\epsilon_Y$, where $\overline{\sigma}$ and $\overline{\epsilon}$ are the averaged compressive stress and averaged shortening strain at the loading edges, respectively.

Possession of ductility may be judged from the two criteria by using the relation between $\overline{\sigma}/\sigma_Y$ and $\overline{\epsilon}/\epsilon_Y$, as shown in Figs. 5 and 6, respectively. Figure 5 can be seen that after ultimate state, $\overline{\sigma}/\sigma_Y$ steadily decreases as $\overline{\epsilon}/\epsilon_Y$ increases. The first criterion is determined that the average compressive stress $\overline{\sigma}$ corresponding with $\overline{\epsilon} = 20 \cdot \epsilon_Y$ is greater than $0.95 \cdot \overline{\sigma}_u$, where $\overline{\sigma}_u$ is the ultimate strength. Figure 6 can be seen that $\overline{\sigma}/\sigma_Y$ falls right down to the lowest point, then, changes into increasing. The second criterion is determined that the average stress $\overline{\sigma}_{min}$ at the minimum point is greater than $0.95 \cdot \overline{\sigma}_u$.

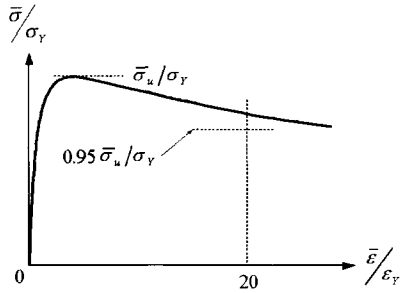

Fig. 5: First criterion for evaluation of ductility

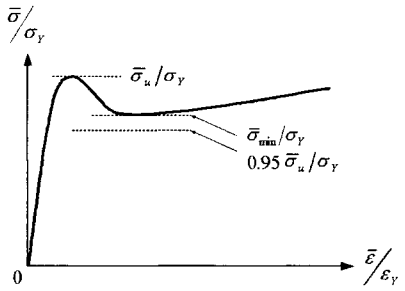

Fig. 6: Second criterion for evaluation of ductility

RELATION BETWEEN DUCTILITY AND MATERIAL PROPERTIES

The yield plateau length $\epsilon_{st}/\epsilon_Y - 1$ and the strain-hardening gradient E_{st}/E affect the inelastic behavior after ultimate state of the high performance steel plates. The behavior is discussed by using the relation between $\overline{\sigma}/\sigma_Y$ and $\overline{\epsilon}/\epsilon_Y$ for the model with $\alpha = 0.7$, $R = 0.4$.

Relation between Ductility and Yield Plateau Length

Figure 7 shows the three relation curves between $\overline{\sigma}/\sigma_Y$ and $\overline{\epsilon}/\epsilon_Y$ for the above mentioned model with the constant strain-hardening gradient $E_{st}/E = 0.0284$: the first case is the yield plateau length $\epsilon_{st}/\epsilon_Y - 1 = 0$ (no yield plateau); the second case is $\epsilon_{st}/\epsilon_Y - 1 = 4$; the third case is $\epsilon_{st}/\epsilon_Y - 1 = 9$ (equivalent to grade SS400). The average compressive stress $\overline{\sigma}/\sigma_Y$, in the case of $\epsilon_{st}/\epsilon_Y - 1 = 0$, scarcely decreases after ultimate state. While, $\overline{\sigma}/\sigma_Y$, in the other case of $\epsilon_{st}/\epsilon_Y - 1 = 9$, decreases. It is found from Fig. 7 that the yield plateau length affects the decreasing rate of $\overline{\sigma}/\sigma_Y$ after ultimate state. It seems that the yield plateau length had better be shortened to possess ductility.

Relation between Ductility and Strain-hardening Gradient

Figure 8 shows the relation between $\overline{\sigma}/\sigma_Y$ and $\overline{\epsilon}/\epsilon_Y$ for the following three cases of the strain-hardening gradient, $E_{st}/E = 0.02$, 0.038, and 0.06, with the constant yield plateau length $\epsilon_{st}/\epsilon_Y - 1 = 5$. It can be seen that all cases have the same ultimate strength. In the case of $E_{st}/E = 0.02$, $\overline{\sigma}/\sigma_Y$ keeps decreasing after ultimate state. While, as E_{st}/E increases, $\overline{\sigma}/\sigma_Y$ tends to increase. It is found that the strain-hardening gradient affects the increasing rate of $\overline{\sigma}/\sigma_Y$ after once decreasing.

From the above mentioned insight, it is deduced that both the yield plateau length and the strain-

www.EngineeringEBooksPdf.com

hardening gradient should be opportunely controlled in order to possess ductility of uniaxial compressed plates.

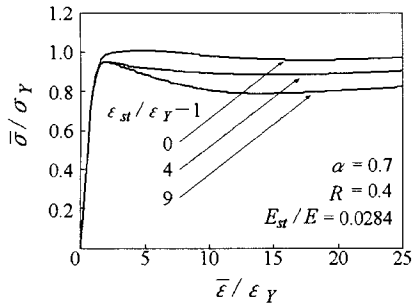

Fig. 7: Influence of yield plateau length

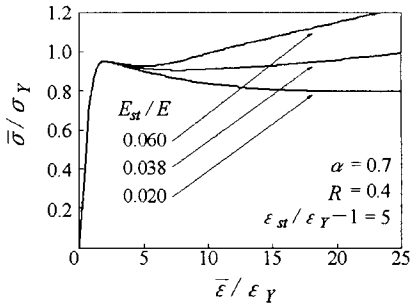

Fig. 8: Influence of strain-hardening gradient

REQUIRED MATERIAL PROPERTIES FOR POSSESSION OF DUCTILITY

The ordinary steel plates with α = 0.7 and $R \leq 0.31$ have enough ductility (Usami et al. 1995; Usami 1997). In this study, the high performance steel plates are numerically analyzed with α = 0.3 to 2.0, and R = 0.32 to 0.7.

For possessing ductility, the required values of the yield plateau length $\epsilon_{st}/\epsilon_Y - 1$ and the strain-hardening gradient E_{st}/E are given by parametric examinations, and illustrated as required curves for each aspect ratio, as shown in Figs. 9 to 21. The curves represent the area of the two material properties of high performance steel to be able to possess ductility of the rectangular plates. The applicable area can be determined as follows: 1) the yield plateau length $\epsilon_{st}/\epsilon_Y - 1$ should be shorter than the values on each required curve, and 2) the strain-hardening gradient E_{st}/E should be also larger than the values on each required curve. If the yield plateau is set to be long, the strain-hardening gradient must be controlled to have relatively high value. For all cases of aspect ratio, the area of material properties for possessing ductility becomes small as the equivalent width-to-thickness ratio increases. It causes that the choice of material properties for possessing ductility is reduced as the plate becomes slender.

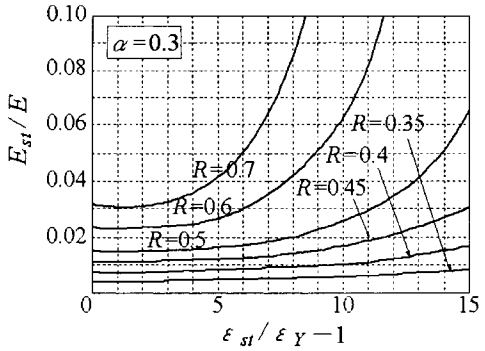

Fig. 9: Required values for α = 0.3

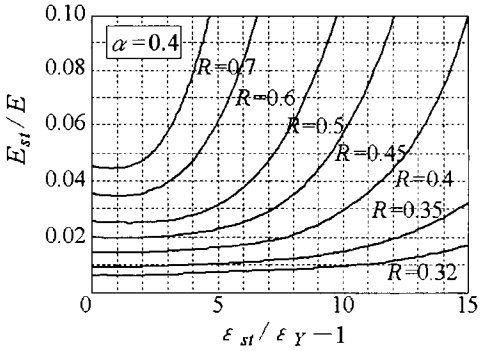

Fig. 10: Required values for α = 0.4

www.EngineeringEBooksPdf.com

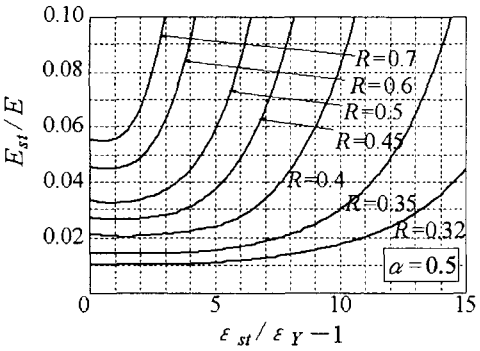

Fig. 11: Required values for α = 0.5

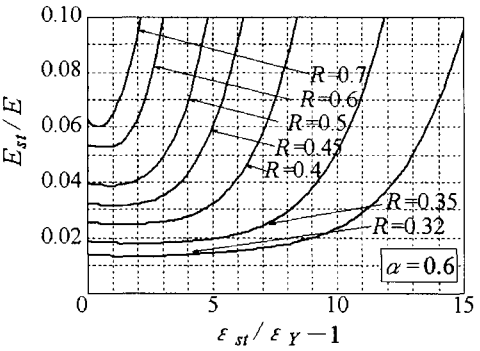

Fig. 12: Required values for α = 0.6

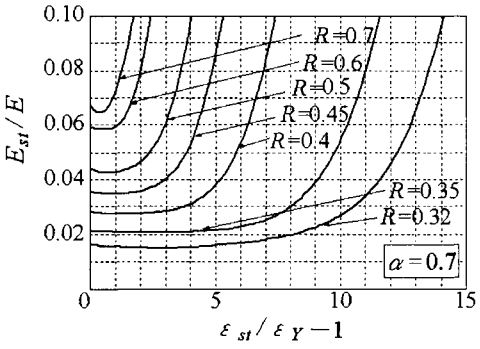

Fig. 13: Required values for α = 0.7

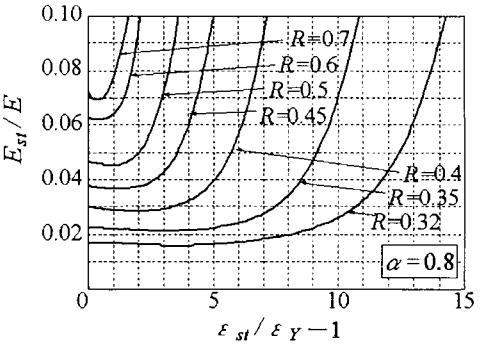

Fig. 14: Required values for α = 0.8

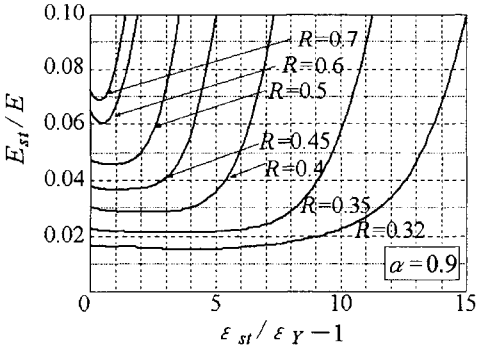

Fig. 15: Required values for α = 0.9

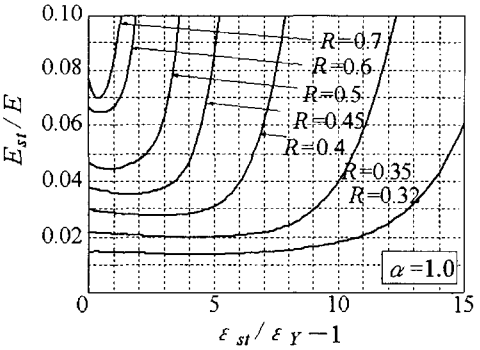

Fig. 16: Required values for α = 1.0

www.EngineeringEBooksPdf.com

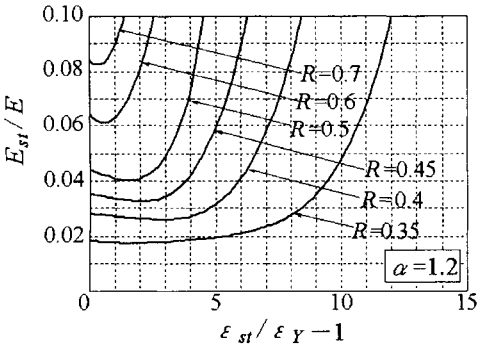

Fig. 17: Required values for α = 1.2

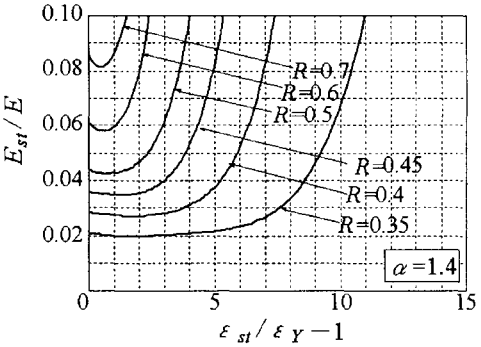

Fig. 18: Required values for α = 1.4

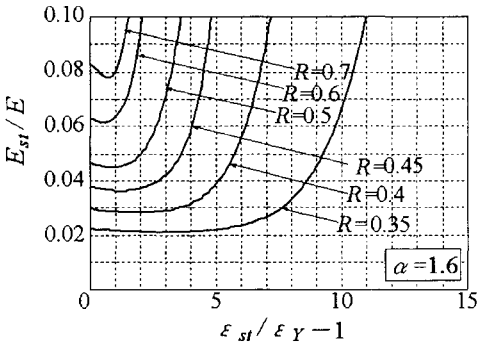

Fig. 19: Required values for α = 1.6

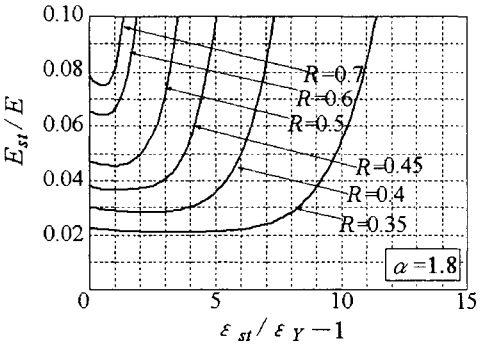

Fig. 20: Required values for α = 1.8

CONCLUSIONS

In this study, the inelastic behavior of the high performance steel plates under uniaxial compression are parametrically examined by elasto-plastic finite displacement analyses. It is found that the high performance steel can effectively possess the ductility of the rectangular plates under compression by controlling the material properties, the yield plateau length and strain-hardening gradient. Additionally, for possessing ductility, the required values of the yield plateau length and strain-hardening gradient are illustrated for various aspect ratios and various equivalent width-thickness ratios.

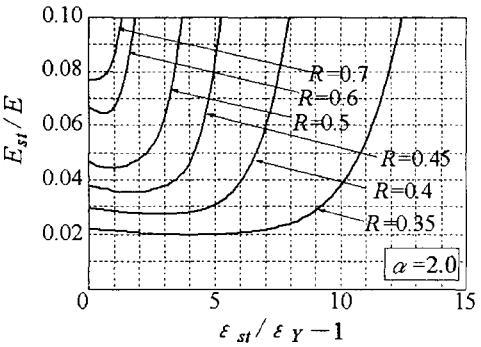

Fig. 21: Required values for α = 2.0

In order to possess ductility of thin-walled steel structures, the high performance steel, whose effective parameters of material properties are carefully controlled, can be practically applied to the important parts of structures in lieu of the ordinary steels. It is found that the high performance steel is a significant material for our infrastructure.

www.EngineeringEBooksPdf.com

REFERENCES

Japan Road Association (JRA). (1996). *Specifications for Highway Bridges* (in Japanese).

JIS. (2001). *Ferrous Material & Metallurgy II-2001*, Japanese Standards Association.

Kato, B. (1986). On the Yield Ratio of the Structural Steel Used for Building Frames. *Iron and Steel* **74:No.6,** 11-21 (in Japanese).

Kawakami, M., Shirahata, H., Suzuki, K., and Masuda, N. (2000). A Basic Investigation Regarding the Influence of the Stress-strain Relation of Steel Material on the Energy Absorption of a Plate Subjected to In-plane Cyclic Loading. *Papers of Study of Utilization for Bridges of High Performance Steel,* 224-233 (in Japanese).

MARC. (1997). *Volume A~D.* Version K7, MARC Analysis Research Corporation.

Mikami, I., Tsuji, S., Nakano, T., and Takehara, K. (1993). Ductility and Width-Thickness Ratio of Steel Cylindrical Panels Subjected to Circumferential Compression. *Jour. Struct. Engrg.* **39:A,** 37-50 (in Japanese).

Mikami, I., Niwa, K., and Miyanishi, A. (2000) Ductility over Ultimate Strength of Compressive Plate Using High Performance Steel and Material Properties of Steel. *Proc. of First Symposium on Improvement of Protection against Earthquake Disasters through the Elucidation of the Fracture Process of Structures,* 87-90 (in Japanese).

Moriwaki, Y. (1993). Ultimate Compressive Strength and Plastic Deformation Capacity of Steel Plate in Consideration of Material Properties. *Jour. Struct. Engrg.* **39:A** 115-124 (in Japanese).

Nakai, H., Kitada, T., Yoshikawa, O., Nakanishi, K., and Oyama, T. (1993). Experimental Study on Ultimate Strength and Ductility of Concrete Filled Steel Box Columns. *Jour. Struct. Engrg.* **39:A,** 1347-1360 (in Japanese).

Nara, S., Umemura, T., Hattori, M., Moriwaki, Y. (1993). Ultimate Strength and Ductility of Compressive Plates with Various Steel Properties. *Jour. Struct. Engrg.* **39:A,** 125-132 (in Japanese).

Ono, T., Yoshida, T. (1998). Effects of Material Properties on Deformation Capacity of H-section Stub-columns Part 1. *J. Struct. Constr. Eng.* **No.503** 125-129 (in Japanese).

Suzuki, M., and Usami, T. (1995). An Analytical Study on the Strength and Ductility of Box Section Steel Cantilever Columns Subjected to Compression and Transverse Loads. *Jour. Struct. Engrg.* **41:A,** 265-276 (in Japanese).

The Kozai Club. Research Group on Steel Bridges. (1998). *Summary of High Performance Steel (for a Bridge)*(in Japanese).

Timoshenko, S. and Gere, J. (1961). *Theory of Elastic Stability*. 2nd ed., McGraw-Hill.

Toyoda, M., Koi, M., Hagiwara, Y., and Seto, A. (1990) Significance of Yield to Tensile Ratio and Uniform Elongation of Steels Based on Deformability of Welded Frame-Structures. *Journal of the Japan Welding Society* **8:No.1,** 119-125 (in Japanese).

Usami, T., Suzuki, M., Mamaghani, I. H. P., and Ge, H. B. (1995). A Proposal for Ultimate Earthquake Resistance of Partially Concrete-filled Steel Bridge Piers. *Proc. of Japan Society of Civil Engineers* **No.525: I -33,** 69-82 (in Japanese).

Usami, T. (1997). High Ductility Steel Bridge Piers. *Bridge and Foundation Engineering* **31:No.6,** 30-36, June (in Japanese).

Watanabe, E., Sugiura, K., Harimoto, S., and Hasegawa, T. (1992). The Effective Cross Section of Bridge Piers for Strength and Ductility. *Jour. Struct. Engrg.* **38:A,** 133-142 (in Japanese).

Watanabe, T., Ge, H. B., and Usami, T. (1999). Analytical Study on Strength and Ductility of Steel Stiffened Plates under Cyclic Loading. *Jour. Struct. Engrg.* **45:A,** 185-195 (in Japanese).

www.EngineeringEBooksPdf.com

Advances in Steel Structures, Vol. II
Chan, Teng and Chung (Eds.)
© 2002 Elsevier Science Ltd. All rights reserved.

SHEAR-CARRYING CAPACITY OF STEEL PLATE SHEAR WALL WITH CROSS STIFFENERS

G. D. Chen and Y.L. Guo

Department of Civil Engineering, Tsinghua University,
Beijing, 100084, CHINA

ABSTRACT

Since 1980s, many theoretical and experimental investigations on monotonic and hysteretic behavior of thin steel plate shear wall (SPSW) have been conducted. However, to the author's knowledge, very few researches have been found in the thin or moderate thick SPSW with cross stiffeners. Inelastic large displacement FE method by using ANSYS package is employed in this paper to reveal influence of three main parameters on shear carrying capacity of stiffened steel plate shear wall. Three main parameters are as follows: slenderness ratio of panel λ, stiffness ratio of stiffener to panel η and column stiffness β.

From the numerical result obtained, some important conclusions can be drawn that steel plate shear wall with cross stiffeners has higher strength, and higher initial shear stiffness, compared with that of unstiffened thin SPSW, and that λ and η give rise to the qualitative change of shear-carrying capacity from thin panel to thick or moderate thick panel, while the parameter β causes only the quantitative change. Two parameters λ and η can not be separated from each other in investigating theorectically the behavior of steel plate shear wall. The optimal value of stiffener stiffness η is 30, which is effective and economic in the design of the SPSW. First yield criteria for shear stress beyond the elastic buckling load for the design of SPSW is proposed and the formulas that are used to estimate the shear carrying capacity of the panels with various λ, η and β is then put forward.

KEYWORDS

Shear-carrying capacity, steel plate shear wall, cross stiffener, first yield criteria

www.EngineeringEBooksPdf.com

INTRODUCTION

For the past few decades, experimental and analytical researches have been conducted on the use of thin steel plate shear walls to resist the lateral loads acting on buildings. In current Chinese codes, web of girders and thin plate shear walls are designed not allowing the plate local buckling and the post buckling strength is therefore ignored. However, early studies done by Wagner in 1931 found that the buckling of plates does not mean their failure; the plates with stronger surrounding frame exhibit much higher strength beyond the elastic buckling. Works done by Basler, Porter and Rockey etc. have paid many attentions on the post-buckling behavior of web in plate girder under shear, and many kinds of analysis models[1][4] have been proposed to calculate ultimate shear strength of webs. The researchers such as G. L. Kulak, R.G. Driver[5][6], M. Elgaaly, V. Caccese[7]-[10] and A.S. Lubell[11] etc. conducted monotonic and hysteretic experiment on unstiffened steel plate shear wall. Kulak's tension strip model has been widely used to calculate the ultimate strength of the test.

However, their works are limited to the unstiffened thin steel plate shear wall, the proposed diagonal tension strip model are not suitable to thick or mid-thick panel with or without stiffeners under shear, and the researches[2][3] on the behavior of shear plate with stiffeners are very few. The purpose of this paper is to investigate the post buckling behavior of cross-stiffened panel ranging from thin plate to thick plate, and to propose designing criteria for utilizing post buckling strength and to determinate the optimal value of stiffener's stiffness. Here, panels are stiffened to prevent local buckling and to increase the elastic buckling load, and to increase shear-carrying capacity and shear stiffness, and to reduce out-of-plane deformation in the panel.

ANALYSIS MODEL AND PARAMETERS

Three assumptions are made in analysis model that the local buckling is not allowed in flanges and web of columns, and the stiffened or unstiffened steel plate is framed by surrounding pin-connected square steel frame, where the beams in steel frame is assumed as rigid bar pin-connected with columns, as shown in figure 1. It is assumed that the out of plane displacement of the panel at its top and bottom edges is prohibited.

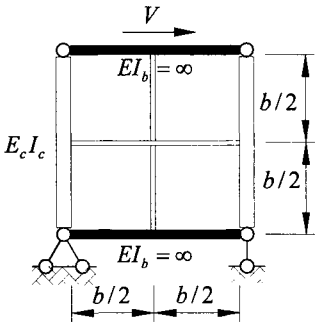

Figure 1: Model of cross-stiffened SPSW

ANSYS package is employed in analyzing the inelastic nonlinear problems embedded in the steel plate shear wall. Two element types, BEAM188 and SHELL 181 involved in ANSYS, are selected to simulate the frame members and panel and/or stiffeners, respectively. Pin connection at four corners of frame is reached by using node couple technology. The von Mises yielding criteria and associated flow rule are included to estimate ultimate load-carrying capacity. Kinematical hardening rule for the elastic-plastic hardening structural steel material is involved in the study, and the effective stress movement on the plastic yielding surface due to material yielding could be accounted for automatically. The effect of residual stress weren't taken into account because of its small influence on strength and stiffness of steel plate shear wall from previous study[12]. In FE calculation, the modified Newton-Raphson (MNR) is used to get the ultimate

www.EngineeringEBooksPdf.com

load and subsequent load-deflection curve.

Three main parameters are included in the analysis. It is well known that the slenderness ratio b/t is one of the main parameters affecting the characteristic of panel. Therefore, b/t is then suggested here to represent the panel slenderness ratio λ. For cross-stiffened panel, flexural stiffness ratio of stiffener to panel η is defined as

$$\eta = \frac{EI_s}{Db}$$

Where, I_s is the flexural stiffness of stiffener about the panel horizontal axis or vertical axis. D is the cylinder stiffness of panel, which equals to

$$D = \frac{Et^3}{12(1-\nu^2)}$$

The last parameter is the stiffness of column β, which is defined as

$$\beta = \frac{1}{\lambda_c^2} = \frac{N_{cr}}{N_y} = \frac{\pi^2 EI_c}{l_c^2 A_c f_y}$$

POST-BUCKLING BEHAVIOR

Steel Plate Shear Wall Framed by Rigid and Elastic Column

In this section of discussion, the column surrounding the panel is assumed to be fully rigid, which means elastic and plastic deformation is prohibited in the column during loading. The objective of this assumption is to focus on the investigation of the shear capacity of infill panel itself. Shear-lateral displacement curve as shown in figure 2 reflects the effect of parameter λ, β and η on the post-buckling behavior of steel plate shear wall. It can be seen that when column is rigid enough, the $V-\Delta$ curves exhibit bi-linear property and the effect of parameter η has neglectable influence on the panel post-buckling behavior. No matter what slenderness ratio η is for the panel, the panel strength may reach shear-yielding stress τ_y, which equals to $f_y/\sqrt{3}$. The reason for ratio τ/τ_y greater than one in the figure 2 for plate with λ equals to 100 is from material hardening. In figure 2, τ is the ratio of shear capacity V to horizontal cross section area of steel panel A_p.

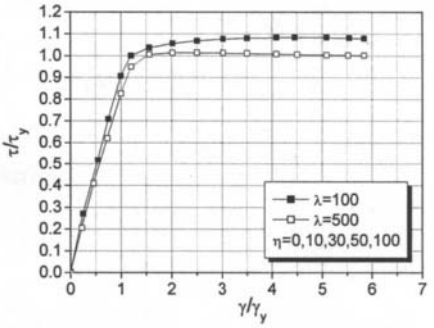

Figure 2. Shear-displacement curve with infinite rigid and elastic column

Steel Plate Shear Wall Framed by Flexural and Inelastic Column

The columns in precious discussion are assumed to be infinite rigid, but columns in reality have a limited flexural stiffness E_cI_c and cross section area A_c, and the yielding of column under combined axial loading and transverse loading result from diagonal tension strip would result in great decrease in

www.EngineeringEBooksPdf.com

bending and axial stiffness of the columns. For thin panels, the diagonal tension field developed is completely anchored on the boundary members of steel frame; weaker column would naturally result in a decrease in the shear carrying capacity of thin steel plate shear wall. For panels with moderate slenderness ratio η, the interaction of elastic buckling load τ_{cr} and post-buckling tension field σ_t^y could be interpreted by following formula developed by K.C. Rockey in 1970s which is based on von Mises yielding criteria.

$$\frac{\sigma_t^y}{f_y} = \sqrt{1-\left(\frac{\tau_{cr}}{\tau_y}\right)^2\left(1-\frac{3}{4}\sin^2 2\theta\right)} - \frac{\sqrt{3}}{2}\frac{\tau_{cr}}{\tau_y}\sin 2\theta \tag{1}$$

In formula 1, τ_{cr} is the elastic buckling load. Thick plate has higher elastic buckling τ_{cr} that may larger than τ_y, in this case no tension field forms. But for thin steel plate, tension field σ_t^y develops completely and reaching the yielding stress of material at limit load.

The numerical results obtained indicate that inelastic behavior of steel plate shear wall is determined by panel slenderness ratio λ. Inelastic behavior of thick plate is the result of the yielding of panel and column, and inelastic behavior of thin plate is due to the formation of diagonal tension field and yielding of column. This conclusion coincides with the test results done by Caccese & Elgaaly (USA, 1993). Therefore, the collapse type of steel plate shear wall could be divided into two types according to slenderness ratio λ: truss model (Figure 3a) for thin panel and beam model (Figure 3b) for thick panel.

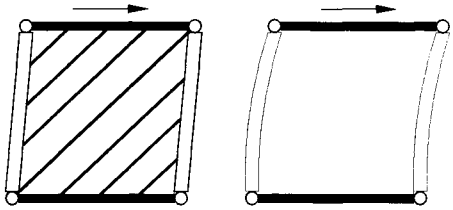

(a) Truss model (b) Beam model

Figure 3: Models for Steel Plate Shear Wall

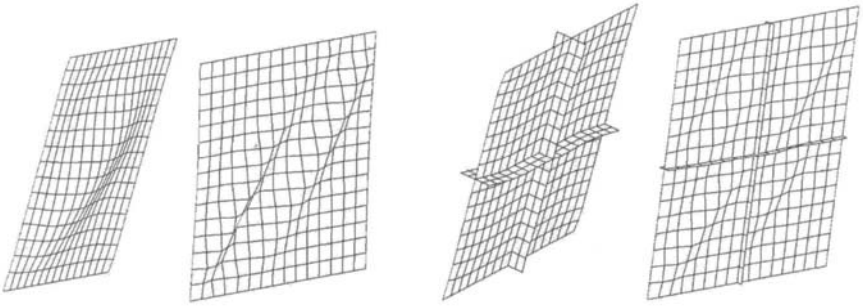

(a) $\lambda = 100$ (b) $\lambda = 500$ (c) $\lambda = 100$、$\eta = 30$ (d) $\lambda = 500$、$\eta = 30$

Figure 4: Collapse mode of steel plate shear wall with or without cross stiffeners

In the case of thick panel with λ equals to 100, the parameter η has no effect on the post-buckling behavior, this is because the stiffener buckling occurs before the panel completely develops its post-buckling strength (fig.4c). For thin panel with λ equals to 300 and 500, stiffeners subdivide thin panel into four smaller panels as shown in fig.4d, as a result, four smaller panels behave as thick or moderate thick panel which increase the elastic buckling load and thus decrease the tension field action;

www.EngineeringEBooksPdf.com

the dependence of panel collapse on column properties decrease with the increase of stiffener's stiffness η and slenderness ratio λ as shown in figure 5.

It is obvious from figure 5 that column stiffness β plays an important role in shear carrying capacity of steel plate shear wall. The small column stiffness β leads to the lower shearing capacity of panel. For thin plate with weaker columns ($\lambda = 500, \beta = 6.55$), the situation is the worst because the weak column could not sustain the tension field of thin panel, and the decrease of shear capacity occurs. For steel panel with cross stiffeners discussed above, the influence of column decrease with the increase of stiffener stiffness η. Hence, two functions of stiffener are that, first, to increase the buckling load, second, to reduce indirectly the requirement of column stiffness. Two parameters λ and η can not be separated from each other in studying the behavior of steel plate shear wall.

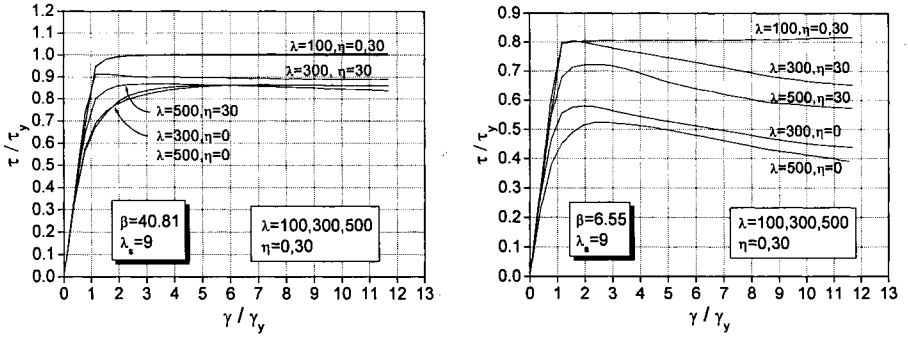

Figure 5: Load-lateral displacement curve of parameters λ, η and β

The influence of three parameters (λ, η and β) on shear stiffness is listed in table 1, and the initial stiffness ratios for each panel relative to $\beta = 6.55$ are shown in parenthesis. Table 1 shows that the shear stiffness increases in the panels is in a much lower rate than the stiffness increase in the columns. The column stiffness β contributes more to the shear stiffness of thin wall than that of thicker one.

TABLE 1

INITIAL SHEAR STIFFNESS OF STEEL PLATE SHEAR WALL KS ($\times 10^6$ KN/m)

Ks	β	λ =100	λ =300	λ =500
η =0	40.81 (6.23)	1.955 (1.25)	0.579 (1.29)	0.347 (1.55)
	20.33 (3.10)	1.801 (1.15)	0.534 (1.19)	0.313 (1.39)
	6.55 (1.00)	1.564 (1.00)	0.447 (1.00)	0.224 (1.00)
η =30	40.81 (6.23)	1.955 (1.25)	0.652 (1.45)	0.379 (1.69)
	20.33 (3.10)	1.801 (1.15)	0.585 (1.31)	0.346 (1.54)
	6.55 (1.00)	1.564 (1.00)	0.569 (1.27)	0.338 (1.51)

www.EngineeringEBooksPdf.com

First Yield Criteria for Cross-Stiffened Steel Plate Shear Wall

The first yield criteria for steel plate shear wall could be proposed based on the load-displacement curves as shown in figure 2 and figure 5. At first yield state, where γ equals to average shear yielding strain γ_y, load-displacement curves remain almost elastic. Therefore the proposed limit state can be easily used in design.

Relationship Between τ and λ, η and β

Some relationships between τ and parameters (λ , η and β) are drawn in figure 6. Figure 6a indicates that first yield shear capacity of unstiffened panel decreases with the increase of λ. However, for stiffened thin panel, the first yield shear capacity increases when the larger stiffener stiffness is employed, but for thick panel with $\lambda = 100$, the contribution of stiffener could be neglected. As can be noted from figure 6a that stiffener stiffness η equals to 30 could steadily increase the first yield shear capacity τ_1 / τ_y, and τ_1 / τ_y remains almost unchanged when η equals to 30 and λ less than 300. Therefore, $\eta = 30$ could be treated as optimum value for cross stiffener panel. Numerical analysis shows that the variation of slenderness ratio λ and stiffener stiffness η could result in the qualitative change in load-carrying capacity of steel plate shear wall.

Although the influence of columns stiffness on the post-buckling behavior of the panels is complicated with the change of slenderness ratio λ, linear relationship still exists between τ_1 / τ_y and column stiffness β as shown in figure 6b. Therefore, the effect of column stiffness β on shear carrying capacity of the panels can be treated as quantitative change, and further the linear relationship could greatly simplify analysis process.

Figure 6c shows that relationship between the shear-carrying capacity of the panels and stiffener stiffness η. As can be noted, the shear-carrying capacity increases rapidly with the increase of η when panel is thin, while it doesn't in thick panel. The increase of shear-carrying capacity remains unchanged when stiffener's stiffness η equals to 30.

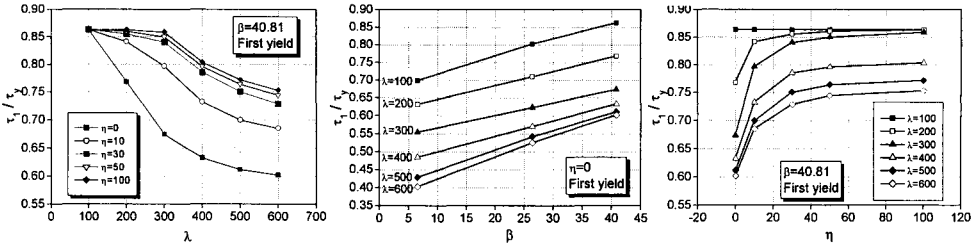

(a) $\lambda - \tau / \tau_y$ (b) $\beta - \tau / \tau_y$ (c) $\eta - \tau / \tau_y$

Figure 6: Relationship between the shear capacity and individual parameter

Formulas of Shear-Carrying Capacity for First Yield Criteria

Formulas of shear-carrying capacity of steel plate shear wall can be proposed based on the first yield criteria. The form of formulas is similar to that proposed for post-buckling shear capacity of web of

www.EngineeringEBooksPdf.com

girder in EC3 (1993).

Because the column stiffness β only causes the quantitative change, and slenderness ratio λ and stiffener stiffness η cause qualitative change in shear-carrying capacity, the formulas of first yield criteria and shear capacity can be shown as follows

$$\tau_1 / \tau_y = C(\beta) \cdot \tau(\eta, \lambda_s) \tag{2}$$

$$V_s = \tau_1 \cdot b \cdot t_p \tag{3}$$

Where, $C(\beta)$ is the column stiffness coefficient β

$$C(\beta) = 1.16 - (71 - \beta)/180 \tag{4}$$

for $\beta \geq 71$, $\beta = 71$.

Among the three parameters affecting the shear-carrying capacity of the panels, the slenderness ratio of panel is the most important one because the loading property of the steel panel changes by the change of λ. The stiffener stiffness η also affects the panel behavior when the panel varies from thin plate to moderate or thick plate. First yield shear strength τ is given by curve fitting, the proposed formulas agree very well with the FEM numerical results.

For $0 \leq \eta \leq 10$:

when $\lambda_s \leq 2.121$,

$$\tau = 0.86 - (0.1315 - 0.00869\eta) \times (\lambda_s - 0.707) \tag{5.1}$$

when $\lambda_s > 2.121$,

$$\tau = 0.592 + 0.0079\eta + (0.673 + 0.0435\eta) \cdot e^{-\lambda_s} \tag{5.2}$$

For $10 < \eta \leq 30$:

when $\lambda_s \leq 2.121$,

$$\tau = 0.86 - [0.0446 - 0.00153(\eta - 10)] \times (\lambda_s - 0.707) \tag{5.3}$$

when $\lambda_s > 2.121$,

$$\tau = 0.671 + 0.0024(\eta - 10) + [1.108 - 0.003(\eta - 10)] \cdot e^{-\lambda_s} \tag{5.4}$$

For $30 < \eta \leq 50$:

when $\lambda_s \leq 2.121$,

$$\tau = 0.86 - [0.0141 - 0.00071(\eta - 30)] \times (\lambda_s - 0.707) \tag{5.5}$$

when $\lambda_s > 2.121$,

$$\tau = 0.719 + 0.0011(\eta - 30) + [1.048 - 0.0033(\eta - 30)] \cdot e^{-\lambda_s} \tag{5.6}$$

Where

$$\lambda_s = \sqrt{\frac{f_{vy}}{\tau_{cr}}} = \frac{1}{37\sqrt{K_s}} \cdot \left(\frac{b}{t_p}\right) \cdot \sqrt{\frac{f_y}{235}} \tag{6}$$

For square panels with λ equals to 300, $K_s = 14.58$ and $\lambda_s = 2.121$.

www.EngineeringEBooksPdf.com

CONCLUSIONS

One important conclusion obtained from this study is that there are two kinds of collapse modes corresponding to thin and thick panels, respectively, namely the nonlinear behavior of thick plate mainly owing to the panel material yielding, and the nonlinear behavior of thin panel due to both its material yielding and its diagonal tension field formation. The requirement for the column stiffness and stiffener stiffness are determined by these two collapse modes, respectively. Overall, thick panel can stand itself under shear loading, so the requirement for column stiffness and stiffener stiffness is relatively relaxed. But for thin panel the diagonal tension field should be anchored on the boundary members such as beams and columns. The column stiffness, therefore, has great effect on the post-buckling behavior of thin panel.

The thin panel stiffened by cross stiffener behaves as moderate thick or thick panel because its cylinder stiffness is enhanced. Numerical results obtained show that stiffener stiffness equals to 30 can be effective and economic to increase the shear-carrying capacity.

The design formulas of steel plate shear wall for first yield criteria are proposed by the curve fitting, which are base on the linear range of load-displacement curve that would greatly simplify the use of its post-buckling strength.

REFERENCES

1. D.M. Porter, K.C. Rockey and H.R. Evans (1975). The Collapse Behavior of Plate Girders Loaded in Shear. The Structural Engineering. No.98, Vol.53, 313-326.
2. G.S. Stanway, J.C. chapman and P.J. Dowling (1993). Behavior of a Web Plate in Shear with an Intermediate Stiffener. Proc Instn Civ Engrs Structs & bldgs, 1993,99 327-344.
3. O. Mijuskovic, B. Coric and M.N. Pavlovic. (1999). Transverse-Stiffener Requirements for the post-Buckling Behavior of a Plate in Shear. Thin-Walled Structures. Vol.34, 43-63.
4. H.R. Evans. (1983). Plate Structures, Stability and Strength, Narayanan. Applied Sciences.
5. R.G. Driver, G.L. Kulak, A.E. Elwi and D.J.L. Kennedy (1998). FE and Simplified Models of Steel Plate Shear Wall. Journal of Structural Engineering. Vol.124, No.2, 121-130.
6. R.G. Driver, G.L. Kulak, D.J.L. Kennedy and A.E. Elwi (1998). Cyclic Test of Four-Story Steel Plate Shear Wall. Journal of Structural Engineering. Vol.124, No.2, 112-120.
7. M. Elgaaly and Yinbo Liu. (1997). Analysis of Thin-Steel-Plate Shear Walls. Journal of Structural Engineering. Vol.123, No.11, 1487-1496.
8. M. Elgaaly. (1998). Thin Steel Plate Shear Walls Behavior and Analysis. Thin-Walled Structures. Vol.32, 151-180.
9. M. Elgaaly, V. Caccese and C. Du. (1993). Post-Buckling Behavior of Steel-Plate Shear Walls under Cyclic Loads. Journal of Structural Engineering. Vol.119, No.2, 588-605.
10. V. Caccese, M. Elgaaly and Ruobo Chen. (1993). Experimental Study of Thin Steel Plate Shear Walls under Cyclic Load. Journal of Structural Engineering. Vol.119, No.2, 573-587.
11. A.S. Lubell, H.G.L. Prion, H.G.L. Prion, C.E. Ventura and M. Rezai. Unstiffened Steel Plate Shear Wall Performance under Cyclic Loading. Journal of Structural Engineering. Vol.126, No.4, 453-460.
12. Guodong Chen and Yanlin Guo (in press). Ultimate Shear-carrying Capacity of Unstiffened Panels. Engineering Mechanics (in Chinese).

www.EngineeringEBooksPdf.com

Advances in Steel Structures, Vol. II
Chan, Teng and Chung (Eds.)
© 2002 Elsevier Science Ltd. All rights reserved.

ELASTIC CRITICAL MOMENTS OF I SECTIONS WITH VERY SLENDER WEBS

A. J. Wang and K.F. Chung

Department of Civil and Structural Engineering,
the Hong Kong Polytechnic University, Hong Kong, China.

ABSTRACT

An analytical elastic distortional buckling theory is formulated to investigate the elastic structural behaviour of I sections with very slender webs where cross section distortion in terms of local buckling of the web-plate and overall distortional buckling of the I sections are fully incorporated. Through a standard eigenvalue analysis, the elastic critical moments of these sections are obtained, and comparison with finite strip results are also presented. Moreover, an extensive parametric study on I sections with practical ranges of geometrical dimensions is also reported to assess the importance of distortional buckling for I sections susceptible to lateral torsional buckling. It is found that cross-section distortion may be apparent in I sections with depth to web thickness ratios larger than 60, resulting in significant reduction in their elastic critical moments. Moreover, distortional buckling is found to be very significant in short to medium span beams with very slender webs, and specific design rules should be developed in assessing their structural behaviour against distortional buckling.

KEYWORDS

Distortional buckling, I sections with slender webs, Structural instability, Lateral torsional buckling.

INTRODUCTION

In most hot rolled I sections buckling between points of restraints, the members may undergo lateral torsional buckling in which large lateral and rotational displacements of the cross section is found. The cross sections of hot rolled I sections are generally assumed to be rigid as there is insignificant distortion in the cross sections. However, for I sections fabricated from thin plates or cold formed sections with webs of large depth to thickness ratios, there is always significant distortion in the cross section during buckling which may be termed collectively as *distortional buckling* (Chung, 1997), as shown in Figure 1. Further classification on the structural behaviour of I sections with very slender webs is necessary to distinguish the instability characteristics of the web-plates and the compression flanges. If the compression flanges buckle in an overall fashion with differential lateral deflection together with buckled web-plate, it is proposed to refer the deformation as *overall distortional buckling*. This buckling mode is very similar to *lateral torsional buckling* expect that local curvature is found in the web-plates and the flanges have different lateral deflections and longitudinal rotations.

www.EngineeringEBooksPdf.com

If buckling occurs solely in the web-plate while the web-flange junctions remain nearly straight, it is proposed to refer the deformation as *the local plate buckling*.

DISTORTIONAL BUCKLING MODEL

An I section with a very slender web may be considered as a thin web-plate connected longitudinally with two stocky bars of rigid cross section (Chung, 1989) as presented in Figure 2. The deflection profile of the web-plate, w , may be discretized into a number of cosine curves in the longitudinal direction, each with a high order algebraic polynomial in the transverse direction as follows:

$$w = \sum_{m}^{N} cos(\frac{m\pi x}{b}) \sum_{r=0}^{n} c_{mr}\, \eta^{r} \qquad where \quad \eta = \frac{y}{b} \qquad [1]$$

The coefficients c_{mr} are the only unknowns to be solved. Through the governing equation of the classical large deformation plate theory as follows:

$$\nabla^4 F = E\left[\frac{\partial^2 w}{\partial x^2}\frac{\partial^2 w}{\partial y^2} - \left(\frac{\partial^2 w}{\partial x\, \partial y}\right)^2\right] \qquad [2]$$

the membrane stress system, F, is coupled up with the out-of-plane deflection, w :

$$F = \frac{E}{2}\sum_{m=1}^{N}\sum_{n=1}^{N} \Phi_{1mn} cos\,\alpha_{mn}x + \Phi_{2mn} cos\,\beta_{mn}x \qquad [3]$$

where Φ_{1mm} and Φ_{2mm} are high order hyperbolic functions in terms of c_{mr} . Due to deformation compatibility along the top and the bottom edges of the web-plate, the deflection profiles of both the top and the bottom flanges, w_T and w_B are given as follows:

$$w_T = \sum_{m} cos(\frac{m\pi x}{a}) \sum_{r=0}^{n} c_{mr} \;;\; w_B = \sum_{m} cos(\frac{m\pi x}{b})\, c_{m0} \qquad [4]$$

Boundary Conditions

Consideration of force and moment equilibrium between both the web-plate and the flanges along the top and the bottom edges of the web-plate results in the formulation of two linear and two non-linear boundary conditions, and detailed derivation of these boundary conditions is reported by Chung (1989).

Total Potential Energy

Through analytical integration, the total stain energy and the external work of the I section under combined compression and bending are formulated in terms of the polynomial coefficients, c_{mr} :

Strain energy

Web plate:
$$V = \frac{D}{2}\int_0^b \int_{-\frac{a}{2}}^{\frac{a}{2}} \left\{\left[\frac{\partial^2 w}{\partial x^2} + \frac{\partial^2 w}{\partial y^2}\right]^2 - 2(1-v)\left[\frac{\partial^2 w}{\partial x^2}\frac{\partial^2 w}{\partial y^2} - \left(\frac{\partial w}{\partial x\, \partial y}\right)^2\right]\right\} dx dy \qquad [5]$$

www.EngineeringEBooksPdf.com

$$\textit{Top flange:} \quad V_T\big|_{y=b} = \frac{EI_y{}^f}{2}\int_{-\frac{a}{2}}^{\frac{a}{2}}\left(\frac{\partial^2 w^f}{\partial x^2}\right)^2 dx + \frac{GJ^f}{2}\int_{-\frac{a}{2}}^{\frac{a}{2}}\left(\frac{\partial^2 w^f}{\partial x \partial y}\right)^2 dx \qquad [6]$$

$$\textit{Bottom flange:} V_B\big|_{y=0} = \frac{EI_y{}^f}{2}\int_{-\frac{a}{2}}^{\frac{a}{2}}\left(\frac{\partial^2 w^f}{\partial x^2}\right)^2 dx + \frac{GJ^f}{2}\int_{-\frac{a}{2}}^{\frac{a}{2}}\left(\frac{\partial^2 w^f}{\partial x \partial y}\right)^2 dx \qquad [7]$$

External work done

$$W = \frac{1}{2}N_0\int_0^b\int_{-\frac{a}{2}}^{\frac{a}{2}}\left(1-2\frac{y}{b}\right)\left(\frac{\partial w}{\partial x}\right)^2 dx\,dy - \frac{1}{2}\frac{N_0 BT}{t}\int_{-\frac{a}{2}}^{\frac{a}{2}}\left[\left(\frac{\partial w_T}{\partial x}\right)^2 - \left(\frac{\partial w_B}{\partial x}\right)^2\right]dx \qquad [8]$$

Total potential energy

$$V = V + V_T + V_B - W \qquad [9]$$

For post-buckling behaviour of the I section, numerical optimisation on the total potential energy may be carried out (Chung and Owens, 1990; Chung, 1997) to solve for the values of c_{mr} at specific end rotations subjected to linear and non-linear constraint equations which are derived from the boundary conditions. However, in order to evaluate the elastic critical moment of the I section, the problem may be reduced into a conventional eigenvalue analysis through standard analysis procedure as follows:

$$[K_S - \lambda K_G]\Delta = [K_{cr}]\Delta = 0 \qquad [10]$$

where K_S and K_G are the stiffness and the stability matrices respectively, λ is the eigenvalue, and Δ is the deformation matrix of the I section in terms of c_{mr} . For simplicity, the eigenvalue expression is modified with $[K_{cr}]$which is the critical stiffness matrix. For non-trivial solution at bifurcation, the critical stiffness matrix $[K_{cr}]$ should be equal to zero. The critical stiffness matrix $[K_{cr}]$ of a I section with a single cosine curve in the longitudinal direction, i.e. $m = 1$, and a fourth order polynomial in the transverse direction, i.e. $N = 4$, is presented in Appendix. Through numerical calculation, the eigenvalue problem is solved, and both the elastic critical moment, M_{DB} , and the deflection profile of the I section undergoing distortional buckling are obtained. It should be noted that due to the nature of the eigenvalue analysis, the boundary conditions are not considered.

A close inspection on the critical stiffness matrix shows that for I sections with practical geometrical dimensions, the leading term in the critical stiffness matrix is $\pi^4 EI^f/a^3$, demonstrating the importance of the out-of-plane flexural rigidity of the compression flange in distortional buckling, especially for I sections with wide flanges and short spans. The term $\pi^2 GJ^f/ab^2$ is also important which describes the effect of the torsional rigidity of the flanges in the I sections.

In order to assess the accuracy of the proposed theory for I sections with very slender webs, the elastic critical moments of I sections under distortional buckling, M_{DB} , are compared with those obtained from finite strip buckling analyses, M_{FSM} , through the use of the computer program THIN-WALL (Papangelis and Hancock, 1995). Table 1 summarises the comparisons for I sections with different cross section dimensions and beam spans. It is shown that the values of M_{DB} and M_{FSM} are very close, demonstrating the validity and accuracy of the proposed method.

www.EngineeringEBooksPdf.com

PARAMETRIC STUDIES

In order to examine the importance of distortional buckling in I sections with practical geometrical dimensions, an extensive parametric study with the proposed theory is carried out. The ranges of the geometrical dimensions of I sections covered in the current study are summarised in Figure 2 while the elastic critical moments, M_{DB} , of the I sections are summarised in Table 1. The elastic critical buckling moments of I sections undergoing lateral torsional buckling, M_{LTB} , are also presented in Table 1 for direct comparison. It is shown that the values of M_{DB} is always significantly smaller than M_{LTB}, in particular, for those I sections with medium spans and very slender webs, and this suggests that there is significant reduction in the elastic critical moments whenever cross section distortion in I sections is incorporated.

In practical design, member instability is often assessed through the use of slenderness ratios, such as λ to allow for flexural buckling in columns, and λ_{LT} to allow for lateral torsional buckling in beams (Kirby and Nethercot, 1979; BS5950, 2000). Figure 3 presents the comparisons between the equivalent slenderness ratios obtained by the proposed theory and the lateral torsional buckling theory for I sections with various beam spans and depth to web thickness ratios. It is shown that in Figures 3a) to 3d), the equivalent slenderness ratios obtained from the proposed distortional buckling theory are typically 10% to 25% larger than those from the lateral torsional buckling theory. Moreover, as shown in Figure 3e), for short span I sections with a depth to web thickness ratio of 200, distortional buckling becomes so important that the equivalent slenderness ratios obtained by the proposed distortional buckling theory are roughly 1.5 to 2.0 times of those obtained from the lateral torsional buckling theory.

CONCLUSIONS

An eigenvalue analysis is established to assess the elastic critical moments of I-sections with very slender webs undergoing distortional buckling. Comparison on the elastic critical moments obtained from the proposed theory and the finite strip method is also presented. Based on the results of an extensive parametric study, it is found that for I sections with depth to web thickness ratios larger than 60, distortional buckling is apparent, especially in beams with short to medium spans. Consequently, distortional buckling should be allowed for in practical design of I sections with very slender webs.

REFERENCES

BS5950: Structural Use of Steelwork in Building. Part 1: Code of practice for design in simple and continuous construction: Hot rolled sections. British Standards Institution, 2000.

Chung K.F. (1989). *The Elastic Distortional and Local Plate Buckling of Very Slender Web Beams*, PhD Thesis, Imperial College, University of London.

Chung K.F. and Owens G.W. (1990). Distortional Instability of Very Slender Web Beams. *Proceedings of the Forth Rail Bridge Centenary Conference*, Edinburgh, U.K., 747-757.

Chung K.F. (1997). Cross Section Distortion and Mode-switching in Distortional Buckling of Beams with Very Slender Webs. *Proceedings of the Fifth International Colloquium on Stability and Ductility of Steel Structures*, Nagoya, Japan, 539-546.

Kirby P.K. and Nethercot D.A. (1979). *Design for Structural Stability*, Granada Publisher, London, U.K.

Papangelis J.P. and Hancock G.J. (1995). Computer Analysis of Thin-Walled Structural Members, *Computers and Structures*, **56: 1**, 157-176.

www.EngineeringEBooksPdf.com

APPENDIX Critical Stiffness Matrix ($m = 1$ and $N = 4$)

$$
\begin{bmatrix}
\left(\frac{D\pi^4 b}{2a^3}+\frac{EI^f\pi^4}{a^3}\right) & \left(\frac{D\pi^4 b}{4a^3}+\frac{EI^f\pi^4}{2a^3}+\frac{N_0\pi^2 b}{12a}+\frac{\pi^2 N_0 BT}{2at}\right) & \left(\frac{D\pi^4 b}{6a^3}-\frac{D\pi^2}{ab}+\frac{D(1-\nu)\pi^2}{ab}+\frac{EI^f\pi^4}{2a^3}+\frac{N_0\pi^2 b}{12a}+\frac{\pi^2 N_0 BT}{2at}\right) & \left(\frac{D\pi^4 b}{8a^3}-\frac{3D\pi^2}{2ab}+\frac{3D(1-\nu)\pi^2}{2ab}+\frac{EI^f\pi^4}{2a^3}+\frac{3N_0\pi^2 b}{40a}+\frac{\pi^2 N_0 BT}{2at}\right) & \left(\frac{D\pi^4 b}{10a^3}-\frac{2D\pi^2}{ab}+\frac{2D(1-\nu)\pi^2}{ab}+\frac{EI^f\pi^4}{2a^3}+\frac{N_0\pi^2 b}{15a}+\frac{\pi^2 N_0 BT}{2at}\right) \\
\cdots & \left(\frac{D\pi^4 b}{6a^3}+\frac{D(1-\nu)\pi^2}{ab}+\frac{\pi^2 N_0 BT}{2at}+\frac{EI^f\pi^4}{2a^3}+\frac{GJ^f\pi^2}{ab^2}+\frac{N_0\pi^2 b}{12a}\right) & \left(\frac{D\pi^4 b}{8a^3}-\frac{D\pi^2}{2ab}+\frac{3D(1-\nu)\pi^2}{2ab}+\frac{EI^f\pi^4}{2a^3}+\frac{GJ^f\pi^2}{ab^2}+\frac{3N_0\pi^2 b}{40a}+\frac{\pi^2 N_0 BT}{2at}\right) & \left(\frac{D\pi^4 b}{10a^3}-\frac{D\pi^2}{ab}+\frac{2D(1-\nu)\pi^2}{ab}+\frac{EI^f\pi^4}{2a^3}+\frac{3GJ^f\pi^2}{2ab^2}+\frac{N_0\pi^2 b}{15a}+\frac{\pi^2 N_0 BT}{2at}\right) & \left(\frac{D\pi^4 b}{12a^3}-\frac{3D\pi^2}{2ab}+\frac{5D(1-\nu)\pi^2}{2ab}+\frac{EI^f\pi^4}{2a^3}+\frac{2GJ^f\pi^2}{ab^2}+\frac{5N_0\pi^2 b}{84a}+\frac{\pi^2 N_0 BT}{2at}\right) \\
\cdots & \cdots & \left(\frac{D\pi^4 b}{10a^3}-\frac{2D\pi^2}{3ab}+\frac{2aD}{b^3}+\frac{\pi^2 N_0 BT}{2at}+\frac{2D(1-\nu)\pi^2}{ab}+\frac{EI^f\pi^4}{2a^3}+\frac{2GJ^f\pi^2}{ab^2}+\frac{N_0\pi^2 b}{15a}\right) & \left(\frac{D\pi^4 b}{12a^3}-\frac{D\pi^2}{ab}+\frac{3aD}{b^3}+\frac{5D(1-\nu)\pi^2}{2ab}+\frac{EI^f\pi^4}{2a^3}+\frac{3GJ^f\pi^2}{ab^2}+\frac{5N_0\pi^2 b}{84a}+\frac{\pi^2 N_0 BT}{2at}\right) & \left(\frac{D\pi^4 b}{14a^3}-\frac{7D\pi^2}{5ab}+\frac{4aD}{b^3}+\frac{3D(1-\nu)\pi^2}{2ab}+\frac{EI^f\pi^4}{2a^3}+\frac{4GJ^f\pi^2}{ab^2}+\frac{3N_0\pi^2 b}{56a}+\frac{\pi^2 N_0 BT}{2at}\right) \\
\cdots & \textbf{(SYM)} & \cdots & \left(\frac{D\pi^4 b}{14a^3}-\frac{6D\pi^2}{5ab}+\frac{6aD}{b^3}+\frac{3D(1-\nu)\pi^2}{2ab}+\frac{EI^f\pi^4}{2a^3}+\frac{9GJ^f\pi^2}{2ab^2}+\frac{3N_0\pi^2 b}{56a}+\frac{\pi^2 N_0 BT}{2at}\right) & \left(\frac{D\pi^4 b}{16a^3}-\frac{3D\pi^2}{2ab}+\frac{9aD}{b^3}+\frac{7D(1-\nu)\pi^2}{2ab}+\frac{EI^f\pi^4}{2a^3}+\frac{6GJ^f\pi^2}{ab^2}+\frac{7N_0\pi^2 b}{144a}+\frac{\pi^2 N_0 BT}{2at}\right) \\
\cdots & \cdots & \cdots & \cdots & \left(\frac{D\pi^4 b}{18a^3}-\frac{12D\pi^2}{7ab}+\frac{72aD}{5b^3}+\frac{4D(1-\nu)\pi^2}{ab}+\frac{EI^f\pi^4}{2a^3}+\frac{8GJ^f\pi^2}{ab^2}+\frac{2N_0\pi^2 b}{45a}+\frac{\pi^2 N_0 BT}{2at}\right)
\end{bmatrix}
\times
\begin{bmatrix} c_0 \\ c_1 \\ c_2 \\ c_3 \\ c_4 \end{bmatrix} = 0
$$

Note: N_0 is the maximum bending stress applied to the end of the section at bifurcation.

www.EngineeringEBooksPdf.com

TABLE 1
SUMMARY OF ELASTIC CRITICAL MOMENTS

d = 500 mm t = 6 mm

L = 5 m

Label	M_{DB} (kNm)	M_{FSM} (kNm)	$\frac{M_{DB}}{M_{FSM}}$	M_{LTB} (kNm)	$\frac{M_{DB}}{M_{LTB}}$
25	26.5	26.8	0.99	30.0	0.88
35	113.2	114.6	0.99	131.3	0.86
45	291.3	294.2	0.99	344.7	0.85
55	598.5	611.5	0.98	724.6	0.83
65	1827.7	1837.3	0.99	2244.3	0.81
75	4161.5	4050.5	1.02	5323.9	0.78
32	22.4	22.7	0.99	23.1	0.97
33	45.2	45.5	0.99	48.0	0.94
34	75.6	78.2	0.97	83.4	0.91
35	113.2	114.6	0.99	131.3	0.86
36	153.0	155.6	0.98	192.1	0.80
37	265.1	263.8	1.00	454.4	0.58

d = 1000 mm t = 6 mm

L = 5 m

Label	M_{DB} (kNm)	M_{FSM} (kNm)	$\frac{M_{DB}}{M_{FSM}}$	M_{LTB} (kNm)	$\frac{M_{DB}}{M_{LTB}}$
25	32.1	32.3	0.99	35.3	0.91
35	159.2	160.1	0.99	178.9	0.89
45	472.9	473.8	1.00	528.9	0.89
55	1064.8	1067.8	1.00	1191.0	0.89
65	3483.9	3472.7	1.00	3887.0	0.90
75	8121.3	7888.8	1.03	9178.1	0.88
32	39.8	39.9	1.00	40.1	0.99
33	76.0	76.0	1.00	78.0	0.97
34	116.5	116.6	1.00	124.1	0.94
35	159.2	160.1	0.99	178.9	0.89
36	200.9	203.8	0.99	244.5	0.82
37	319.5	322.2	0.99	514.1	0.62

L = 7.5 m

Label	M_{DB} (kNm)	M_{FSM} (kNm)	$\frac{M_{DB}}{M_{FSM}}$	M_{LTB} (kNm)	$\frac{M_{DB}}{M_{LTB}}$
25	17.6	17.7	0.99	19.5	0.90
35	71.3	71.5	1.00	80.2	0.89
45	171.0	172.4	0.99	196.6	0.87
55	332.6	334.5	0.99	390.1	0.85
65	921.4	910.2	1.01	1119.5	0.82
75	2000.7	1985.8	1.01	2548.4	0.79
32	12.5	12.5	1.00	12.8	0.98
33	25.6	25.6	1.00	27.0	0.95
34	45.1	45.5	0.99	49.1	0.92
35	71.3	71.5	1.00	80.2	0.89
36	101.2	102.3	0.99	120.2	0.84
37	199.8	206.4	0.97	294.0	0.68

L = 10 m

Label	M_{DB} (kNm)	M_{FSM} (kNm)	$\frac{M_{DB}}{M_{FSM}}$	M_{LTB} (kNm)	$\frac{M_{DB}}{M_{LTB}}$
25	14.9	14.4	1.03	15.9	0.94
35	61.6	61.1	1.01	66.6	0.92
45	157.2	154.0	1.02	171.1	0.92
55	323.5	317.5	1.02	354.0	0.91
65	964.6	969.1	1.00	1062.5	0.91
75	2178.8	2145.2	1.02	2419.5	0.90
32	13.4	13.1	1.02	13.5	0.99
33	25.1	25.1	1.00	25.8	0.97
34	41.2	41.8	0.99	43.0	0.96
35	61.6	61.1	1.01	66.6	0.92
36	85.6	86.6	0.99	96.5	0.89
37	164.2	163.0	1.01	226.4	0.73

L = 10 m

Label	M_{DB} (kNm)	M_{FSM} (kNm)	$\frac{M_{DB}}{M_{FSM}}$	M_{LTB} (kNm)	$\frac{M_{DB}}{M_{LTB}}$
25	13.2	13.5	0.98	14.5	0.91
35	52.0	52.9	0.98	58.0	0.90
45	122.0	123.1	0.99	137.7	0.88
55	229.0	229.6	1.00	263.8	0.87
65	596.0	590.0	1.01	714.9	0.83
75	1235.0	1252.9	0.99	1566.0	0.79
32	8.6	8.8	0.98	8.8	0.98
33	17.8	18.1	0.98	18.7	0.95
34	32.5	32.7	0.99	35.0	0.93
35	52.0	52.9	0.98	58.0	0.90
36	76.0	76.2	1.00	88.0	0.86
37	161.0	163.0	0.99	218.0	0.74

L = 15 m

Label	M_{DB} (kNm)	M_{FSM} (kNm)	$\frac{M_{DB}}{M_{FSM}}$	M_{LTB} (kNm)	$\frac{M_{DB}}{M_{LTB}}$
25	9.9	10.1	0.98	10.4	0.95
35	38.5	39.1	0.98	40.9	0.94
45	91.9	92.4	0.99	98.4	0.93
55	178.0	182.4	0.98	191.9	0.93
65	488.3	500.7	0.98	532.6	0.92
75	1053.2	1072.6	0.98	1162.1	0.91
32	7.9	7.8	1.01	7.9	1.00
33	14.6	14.9	0.98	15.0	0.97
34	24.7	24.3	1.02	25.7	0.96
35	38.5	39.1	0.98	40.9	0.94
36	55.1	55.9	0.99	60.7	0.91
37	118.8	120.4	0.99	146.9	0.81

Notes:

M_{DB} is the elastic critical moment obtained by the proposed theory.
M_{FSM} is the elastic critical moment obtained by finite strip method.
M_{LTB} is the elastic critical moment obtained by lateral torsional buckling theory.

www.EngineeringEBooksPdf.com

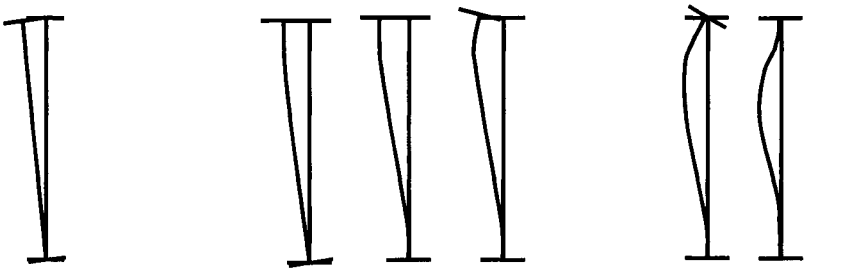

Lateral torsional buckling | Overall distortional buckling | Local plate buckling

Figure 1: Instability in I sections

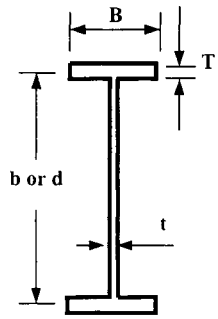

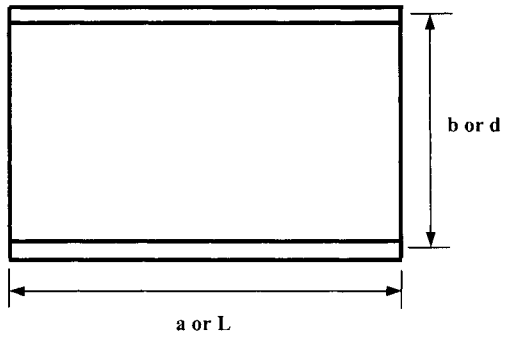

Long to medium span beams | Short span beams

Label	B (mm)	T (mm)
25	50	20
35	100	20
45	150	20
55	200	20
65	300	20
75	400	20
32	100	5
33	100	10
34	100	15
35	100	20
36	100	25
37	100	40

L	= 5 m = 7.5 m = 10 m = 15 m
d	= 500 mm = 1000 mm
t	= 6 mm = 8 mm = 10 mm

L	= 1 m = 1.5 m = 2 m
d	= 1000 mm
t	= 5 mm

Figure 2: Geometrical dimensions of I sections

www.EngineeringEBooksPdf.com

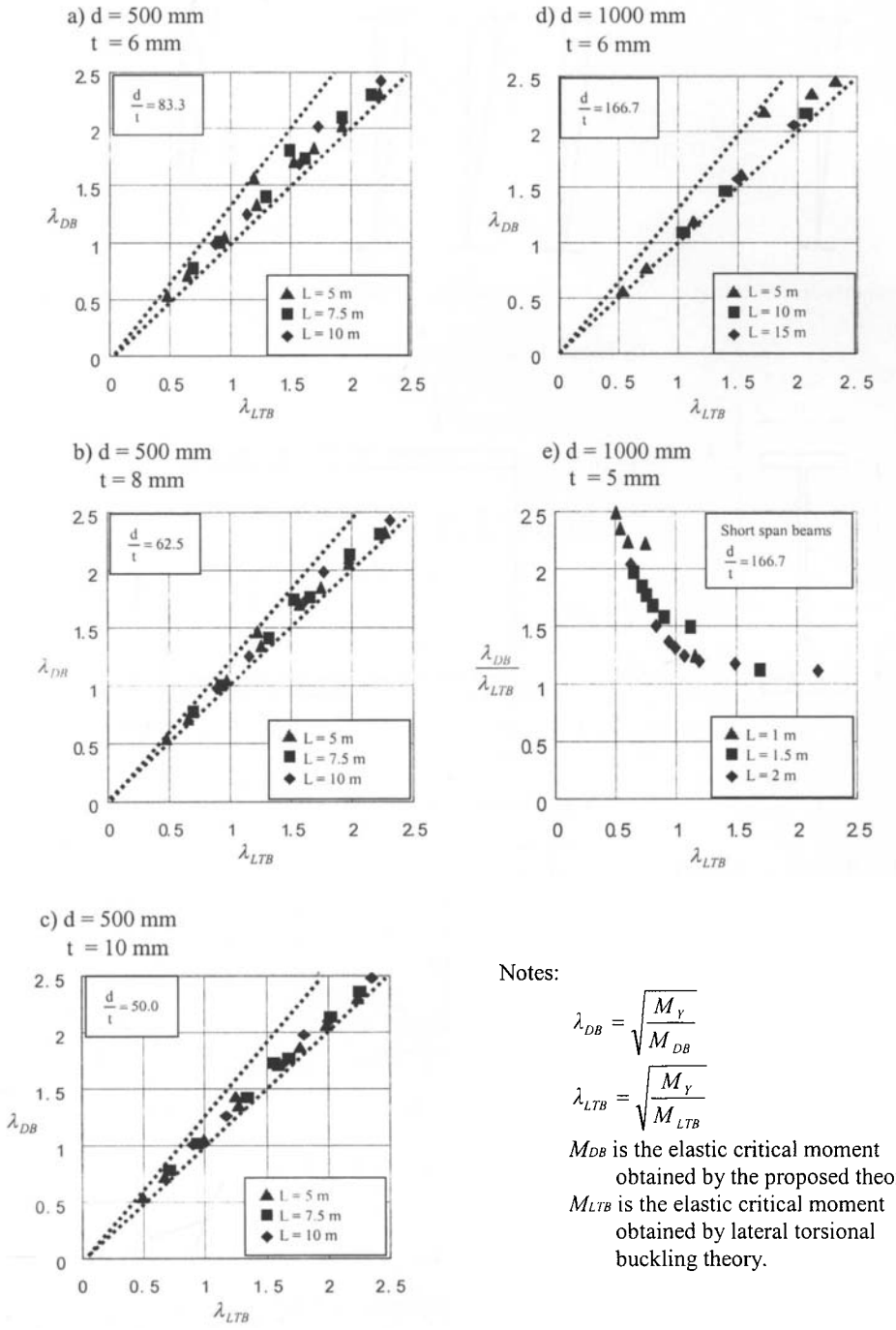

Notes:

$$\lambda_{DB} = \sqrt{\frac{M_Y}{M_{DB}}}$$

$$\lambda_{LTB} = \sqrt{\frac{M_Y}{M_{LTB}}}$$

M_{DB} is the elastic critical moment obtained by the proposed theory.

M_{LTB} is the elastic critical moment obtained by lateral torsional buckling theory.

Figure 3: Comparison on equivalent slenderness ratios

www.EngineeringEBooksPdf.com

SHELLS

www.EngineeringEBooksPdf.com

This Page Intentionally Left Blank

www.EngineeringEBooksPdf.com

Advances in Steel Structures, Vol. II
Chan, Teng and Chung (Eds.)
© 2002 Elsevier Science Ltd. All rights reserved.

AN EFFICIENT STRATEGY FOR THE EVALUATION OF THE RELIABILITY OF 3D SHELLS IN CASE OF NON LINEAR BUCKLING

A Combescure, A Legay

LMC-INSA Lyon
18-20 allée des sciences
69621 Villeurbanne cedex France

ABSTRACT

The object of this paper is to propose a new efficient computing strategy for the study of the reliability of 3D shells in case of non linear buckling. Two aspects are presented in the paper. For the reliability analysis a lot of non linear analysis has to be performed when the parameters are varied. The usual practice is simply to rerun the full non linear computation for every set of parameters: this method works well but is very computer time consuming. We propose an algorithm which allows computing once the nonlinear response for the mean set of parameters, to store the states and the tangent stiffness matrices for this case, and to predict the responses for the modified parameters using the results and matrices stored in the mean value prediction. This method is very efficient and it will be demonstrated in the paper. The second part is the presentation of a new massive 3D shell element which is very efficient for 3D shell computations and which is again used in this context.

KEYWORDS

Nonlinear buckling, shells, finite elements, reliability, axisymmetric, efficient algorithms

1 INTRODUCTION

In this paper we present a new method for the computation of parametric prediction of non linear instability of shell structures. The method is applied to axisymmetric shells with non axisymmetric imperfections using COMU elements (Combescure 1986) as well as on general 3D shell using either DKT (Batoz 1992) shell element, or a new massive 8 node shell element denoted SHB8PS, which is briefly introduced in the paper. The efficient method is described in

www.EngineeringEBooksPdf.com

details in the paper of Legay (2002) and will be briefly presented in this paper. The principle of the method shall be first introduced, then the SHB8PS element shall be briefly introduced, and finally application examples shall be given in order to evaluate the efficiency of the method.

2 THE EFFICIENT METHOD

21 The idea of the method

We want to compute the non linear instability of a structure under compressive applied loads including pressures, with a set of varying parameters (EG Young's modulus, yield stress, thicknesses, geometrical imperfections, loads), in order to evaluate its reliability. Some methods are developed for linear reliability analysis but are not appropriate for the evaluation of non linear responses. New methods have been recently proposed for the direct prediction of the set of limit or bifurcation points, in case of elastic non linear buckling (Erickson 1999, Baguet 2000). These methods are very nice from a theoretical point of view, but they have two drawbacks: the first one is that they impose to derive explicitly the derivatives of the tangent matrices with the variable parameters, and the second is that they cannot be used for elastoplastic material laws, because the proposed methods suppose that the state do not depend on the history of the stresses and strains at the point. The method we propose here has not these drawbacks, and is in this sense, more general. It is rather usual nowadays to use Riks method (adding a constraint to the equilibrium equations) to get the response in the post-buckling range. The constraint equation is of the type:

$$f(\Delta \underline{U}, \Delta\lambda, \Delta a) = 0 \qquad (2.1)$$

where $\Delta \underline{U}$ is the displacement increment in the load step, $\Delta\lambda$ the load parameter increment, and Δa some control variable increment. Let us suppose that we have computed the response of the structure using the mean values of the parameters and have stored the tangent matrices at each step n as well as the material state, and the arc length of the step a_n: we shall denote this case the reference case. We now want to compute the non linear response of a modified parameter case using the results of the reference computation. We shall always use the Riks' constraint equation (2.1). We shall have to solve the equilibrium equations of the modified case using the tangent matrices of the reference case. This is possible if we use the residual loads to check that the equilibrium of the modified structure is verified, and a "good" tangent matrix to perform the equilibrium iterations. Let us suppose that we have an arc length b_m at the beginning of the step m+1 of the modified computation. We shall choose to iterate for the equilibrium equations at step m+1 using the tangent matrix of the reference computation step n such that the arc length a_n is the closest to b_m. This method leads to a larger number of iterations than if we had used the appropriate tangent matrix, but it avoids the computation and inversion of this matrix. We shall see on significant 3D cases that it is preferable because it leads to a much lower computing cost. The method can be used in three manners. The most obvious one is to compute the whole modified curve from the reference one (see figure 1) and to stop the modified computation as soon as the load parameter decreases (we have got the new critical parameter (limit point, or bifurcation point).

www.EngineeringEBooksPdf.com

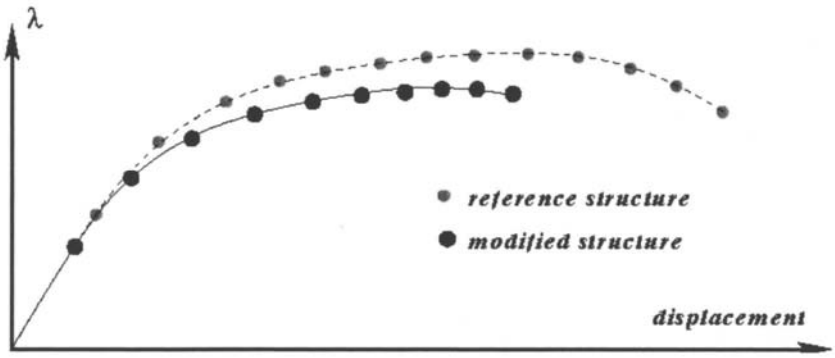

Figure 1 : Parametric method computation of the complete modified curve

A second method consists to compute only one part of the modified curve i.e. the part which is close to the maximum. In order to achieve this, when the material behaviour is elastic, there are two strategies. First we can start the modified response curve from one point of the reference curve and go on as before from this starting point (see figure 2)

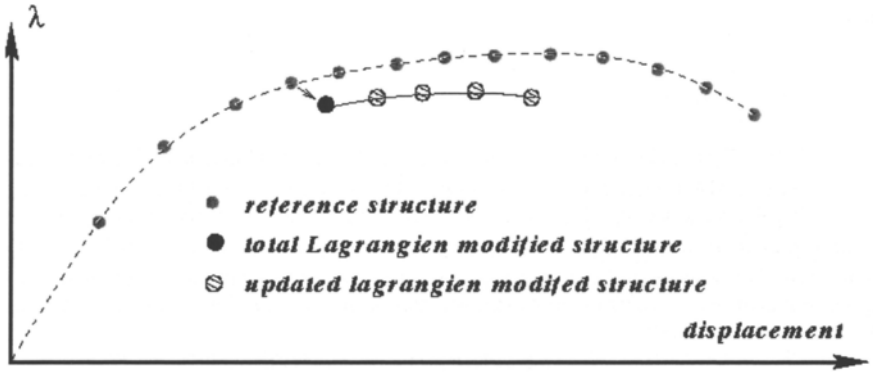

Figure 2: start the modified computation from any point of the reference curve

We also can approximate the modified response curve starting from three or four points of the reference curve to get three or four time he first point of the modified response curve. This will give an approximate modified curve, which is often sufficient for the following reliability analysis (see figure 3).

www.EngineeringEBooksPdf.com

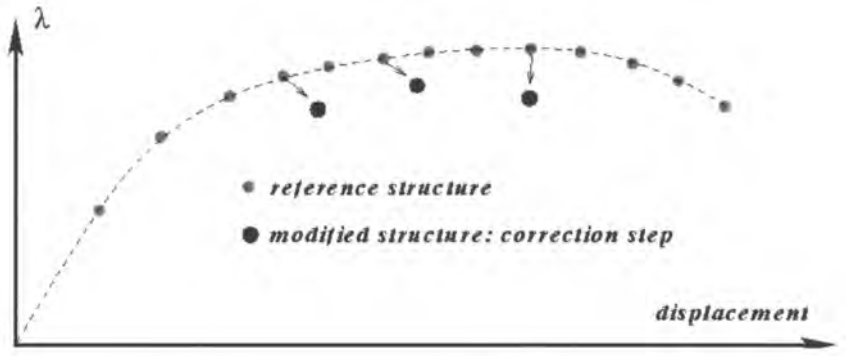

Figure 3: point by point modified curve

Let us quote that these two last methods are only valid if the material behaviour is elastic. In case of elastoplastic response the first of the two last methods can still be used if the start and final state of the first step are in the elastic domain.
This method has some limitations if the instability modes of the modified structure are different from those of the original one, the method fails, but one can shift automatically in this case to the full usual non linear computation. We need to have a large memory available to store all the tangent matrices.

22 The SHB8PS finite element

The proposed method can be applied very efficiently for axisymmetric structures with initial non axisymmetric imperfections using the COMU finite element (Combescure 86 or Combescure 99). But this method needs a few Fourier modes to be really competitive and cannot be applied to real 3D structures. In order to overcome these limitations the DKT element (Batoz 1992) has been introduced in the Stanlax code, but this element is limited to thin shells. A new element denoted SHB8PS has been introduced in the code in order to simulate the behaviour of thick shells. This element is based on the assumed strain concept. It is an extension to shells of the 8 node brick element proposed by T Belytschko and Bindeman (Belytschko 1993). The element is presented in details in the paper of A Meraim (A Meraim, A Combescure 2002). It is an 8 node brick for which a thickness direction ς is specified. The other local directions are denoted ξ, η. The integration uses a set of 5 gauss points across the thickness $(\xi = 0, \eta = 0)$. Figure 4 describes the element geometry and Gauss points:

www.EngineeringEBooksPdf.com

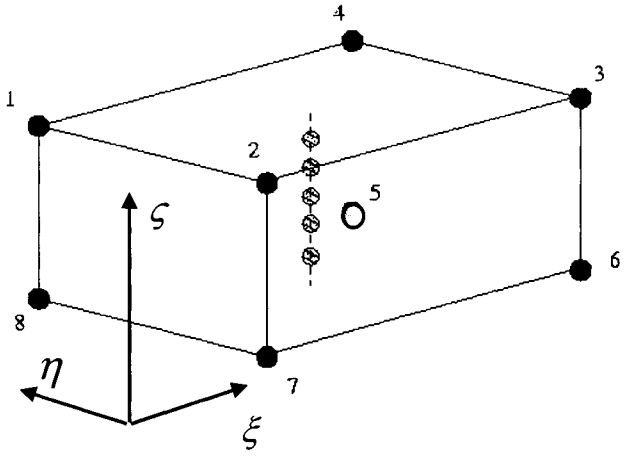

Figure 4: SHB8PS geometry and Gauss points

As this element is under integrated an hourglass control has to be introduced. This control uses the assumed strain concept: an additional strain energy, denoted hourglass energy, activated only by the hourglass modes is added to the usual strain energy to suppress the hourglass modes. This leads to add to the usual stiffness matrix, a stabilisation matrix, given by the following equation:

$$K^{stab} = E\begin{bmatrix} K_{11}^{stab} & 0 & 0 \\ 0 & K_{22}^{stab} & 0 \\ 0 & 0 & K_{33}^{stab} \end{bmatrix} \tag{2.2}$$

where the submatrices are complex combinations of the hourglass modes. Let us observe that the stabilisation matrix is proportional to the Young's modulus E. The physically controlled element uses a tangent modulus concept to control the increment of hourglass energy when the element is in the elastoplastic regime. This simple idea permits to have an efficient element which adapts automatically when the element is elastic or elastoplastic.

3 Application examples

31 Cylindrical panel under point load: SHB8PS element

This example is one of the classical examples for 3D snap through problems. Figure 5 describes the problem. The material behaviour is here elastic. The reference values are: $\alpha = 0.1$ rad, length L = 254mm, radius R=2540mm, thickness h=12.7mm, Young's modulus=3102.75 Mpa, and Poisson's ratio=0.3. Young's modulus is the variable parameter and the modified value is 2500MPa. The reference example and solutions are given for instance in Klinkel and Wagner (Klinkel 1997). The mesh of one quarter of panel has 100 elements. The response is highly non linear. The efficient method results are compared on figure 6. The dotted curve is the non linear

www.EngineeringEBooksPdf.com

response with the standard nonlinear response, whereas the large circle points are computed from the small circle points using parallel independent computations and the efficient method. The method proposed here is 30 times faster than the whole computation of the modified curve.

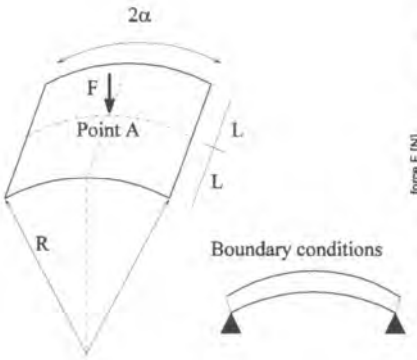

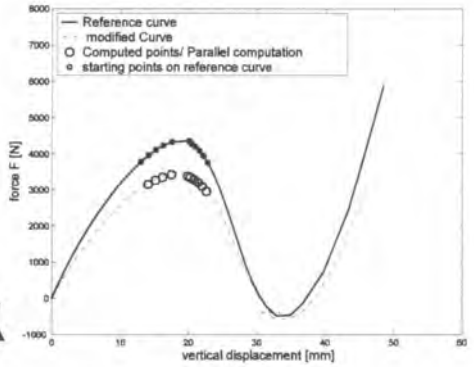

Figure 5: cylindrical panel SHB8PS element **Figure 6:** load displacement response

32 Large 3D computation: submarine under external pressure

A whole main shell of submarine is meshed using 312 COMU elements and an initial imperfection either on mode 2 or on mode 4 of 10% of the thickness. Figure 7 displays one portion of the imperfect cylindrical part of the submarine. One can observe that this imperfection implies twisting of the stiffeners. The submarine is submitted to a uniform external pressure (follower force). Reference values are thickness 24mm Young's modulus 200000MPa, Yield stress 390MPa. These values are decreased to 23mm, 190000MPa, and 370MPa respectively. The linear buckling pressure is 9.16MPa. The elastoplastic limit pressure with the nominal values is 3.43MPa.

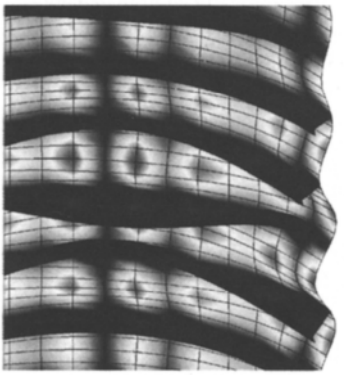

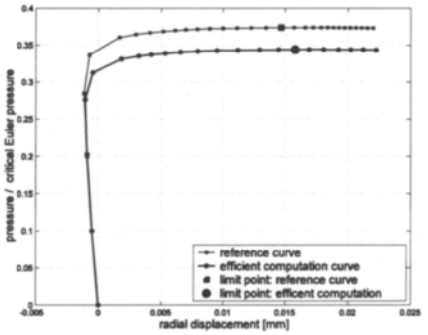

www.EngineeringEBooksPdf.com

With the modified parameters the limit load is decreased to 3.15MPa. The radial load-displacement curves of the two structures (reference and modified) are plotted on figure 8. The computing time necessary to obtain the modified curve is twice smaller than the standard computation. The method is interesting but not very efficient for this case because the stiffness matrix obtained with the COMU element is already very well optimised.

33 imperfect thickness ring under external pressure using the reliability algorithm

We use the DKT element in this case. The variable is the thickness of each element. The thickness is supposed to vary by 10%. We use a classical reliability algorithm (see Legay 2002 for details) to search what is the non uniform thickness repartition which leads to the minimum buckling pressure. It is known that it is a mode 4 thickness reduction which is the most critical. The answer of the reliability algorithm is compared to the theoretical solution on figure 9. The answer is quite acceptable.

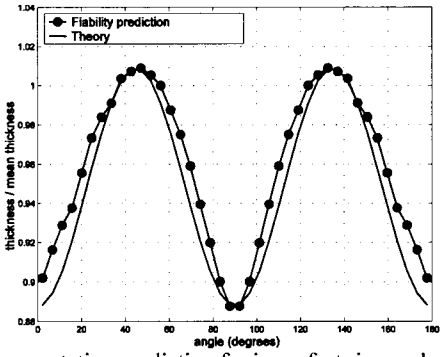

Figure 9: theory computation prediction for imperfect ring under external pressure

4 CONCLUSIONS

The results of this paper can be summarised as follows: the new element SHB8PS is an elegant way to develop a shell from a continuum mechanics usual element. The efficient method permits a computation of the modified non linear answer which is between 2 and 50 times faster then the full non linear computation of the modified curve. The method is more efficient for computations involving large matrices. The main drawbacks of the proposed methodology are the need of a large memory to store the tangent matrices at each step and the fact that this method is not appropriate, when the modified structure buckles with different modes than the reference one. This way of computing the full non linear response of the modified curve is very useful for the fast computation of the reliability of a structure in case of non linear buckling for instance. This method is not limited to buckling predictions but can be used also to evaluate the reliability of a different type of damage of a non linear structure.

www.EngineeringEBooksPdf.com

REFERENCES

A Combescure (1986)
Static and dynamic buckling of large thin shells
Nuclear Engng Design Vol 92, pp 339-354

J. L. Batoz, G. Dhatt (1992)
Modélisation des structures par elements finis, Vol 3, HERMES

A. Legay, A. Combescure (2002)
Efficient algorithms for parametric non-linear instability analysis
Int. Journal of Non-linear Mechanics, Vol. 37, Issues 4-5, pp 709-722

A Erickson, C. Pacoste, A Zdunek (1999)
Numerical analysis of complex instability behaviour using incremental-iterative strategies
Computer methods in applied mech. And Engrg. Vol 179, pp 265-305

S. Baguet, B. Cochelin (2000)
Direct computation of paths of limit points using asymptotic numerical method
Computational methods for shell and spatial structures, IASS-IACM 2000, Athens, Greece, Papadrakis, A Samartin, E Onate

A. Combescure (1999)
Are the static post-buckling predictions conservative?
Advances in steel structures ICASS'99, Vol. 2, Elsevier editors SL Chan, J G Teng, pp 713-720

T. Belytchko, L. P. Bindeman (1993)
Assumed strain stabilisation of the eight node hexahedral element
Comp. Meth. Applied mech. And Engrg, Vol 105, pp 225-260

A. Meraim, A. Combescure (2002)
SHB8PS a new adaptative assumed strain continuum mechanics shell element for impact analysis
To appear in Computers and structures.

S. Klinkel, W Wagner (1997)
A geometrical non linear brick element based on the EAS method
Int. J. for num. Meth. in engrg, Vol 40, pp 4529-4545

www.EngineeringEBooksPdf.com

Advances in Steel Structures, Vol. II
Chan, Teng and Chung (Eds.)
© 2002 Elsevier Science Ltd. All rights reserved.

CASE STUDY OF A MEDIUM-LENGTH SILO UNDER WIND LOADING

M. Pircher[1], R.Q. Bridge[1] and R. Greiner[2]

[1] Centre for Construction Technology and Research, University of Western Sydney, Locked Bag 1797, Penrith South DC, NSW 1797, Australia
[2] Institut für Stahlbau, Holzbau und Flächentragwerke, Technical University of Graz, Rechbauerstr 12, 8010 Graz, Austria

ABSTRACT

Depending on the geometry of a cylindrical structure three different stability failure modes under wind loading can be observed. In low cylinders the radial compression at the meridian facing into the wind causes a buckling mode similar to cylinders under constant radial compression while very long cylinders display a failure characterised by buckling in the lower third of the structure at the side which faces away from the wind. Both these failure modes have received a certain amount of interest by the research community and design rules and proposals against both these failure modes exist. However, the failure of medium-height cylinders is characterised by a number of horizontal ripple-like buckles in the upper half of the meridian which faces into the wind. This buckling mode has received comparatively little attention although it has been observed in previous studies.

A case study using a finite element model of a cylinder displaying this particular failure mode will be presented in this paper. The governing parameters for this rather unexpected behaviour are identified and an explanation for this rather unexpected structural behaviour is given.

KEYWORDS

Thin-walled cylinder, silo, tank, wind load, stability

INTRODUCTION

Depending on the geometry of a cylindrical structure three different stability failure modes can be observed (Figure 1). In low cylinders the radial compression in the area near the meridian facing into the wind causes tangential membrane forces N_φ which govern a buckling mode similar to cylinders under radial compression (mode 1 in Figure 1). Closed form solutions for cylinders under constant radial compression exist and have been used as a basis for design rules against this

www.EngineeringEBooksPdf.com

failure mode under wind load (eg. Deutsche Norm 1990, Lindner et al. 1994). Very long cylinders display a distinctly different failure mode whereby the compressive axial forces N_x at the base of the meridian facing away from the wind trigger buckling in the lower third of the structure (mode 3 in Figure 1). A detailed analysis of this failure mode and some recommendations regarding design rules are given in Schneider & Thiele (1998).

Mode 2 in Figure 1 is characterised by a number of ripple-like circumferential buckles in the upper half of the meridian facing into the wind, causing a rather unexpected failure mode. This buckling mode was first mentioned by Feder (1975) who described a similar failure mode for small PVC-specimens in a wind tunnel test with additional axial loading. Greiner & Derler (1995) presented results of a numerical investigation of cylinders under wind load which also displayed this failure characteristic. In this paper a case study of a thin-walled cylinder displaying this particular failure mode will be presented and an explanation for this behaviour will be given.

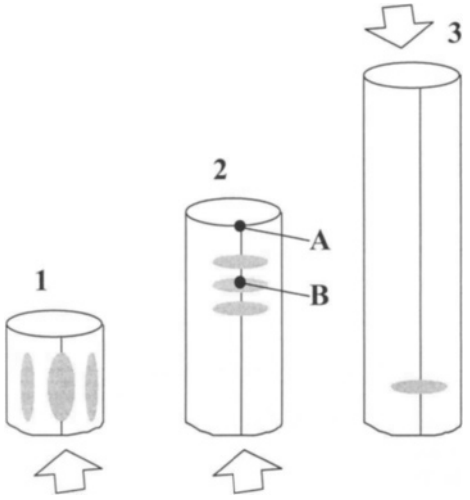

Figure 1. Buckling of thin-walled cylinders under wind loading.

THE COMPUTER MODEL

1.1 Wind Loading

A thorough discussion of many of the factors involved in wind pressure on circular cylindrical structures can be found in Esslinger (1971) and Kwok (1985). The radial wind pressure varies around the circumference and up the height of the cylinder. For this paper the governing radial component of the wind loading around the circumference is given by

$$p_{Wind}(\varphi) = \sum_{m=1}^{n} p_m \cos(m\varphi) = p_r \cdot \sum_{m=1}^{n} c_m \cos(m\varphi) \qquad (1)$$

where p_r is the actual wind pressure onto the meridian facing the wind, c_m are the amplitudes of the Fourier waves, m is the number of the individual Fourier waves and $p_{Wind}(\varphi)$ is the resulting wind

www.EngineeringEBooksPdf.com

load. Figure 2 illustrates the structural significance of the various load waves: Wave m=0 describes the axi-symmetric component of the load; wave m = *1* stands for the loading effect of the wind force on the cylinder as a whole and all waves with $m > 1$ comprise the cross-section-deforming portions of the wind load. Different design codes give different values for the individual wave-dependent coefficients c_m. The material developed for this paper uses values for c_m which have been suggested by Greiner & Derler (1995) as shown in Figure 2. Wind pressure up the height of the cylinder was assumed to be constant and the roof was not loaded.

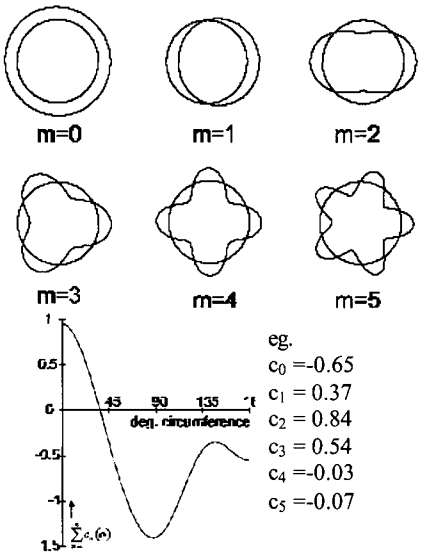

Figure 2. Fourier-analysis of wind loading, factors c_m after Greiner & Derler (1993).

1.2 Structural Model

The work presented in this paper refers to a thin-walled cylindrical shell with fixed bottom support and a diaphragm roof or rigid ring stiffener restricting movement in the tangential and radial direction at the top. Tanks, silos or chimneys are commonly constructed in this manner. Figure 3 captures the geometric properties R_0, L and t of the described structural system and also gives the naming conventions for the membrane section forces N_x, N_φ, $N_{x\varphi}$ and displacements u, v, w.

For this paper a finite element model of a cylinder displaying failure mode 2 (Figure 1) was built to study and develop an explanation for the buckling under wind loading. The geometry of the cylinder analysed for this example is given by R_0 = 10m, R/t = 400 and L/R = 10. Elastic material properties to resemble the behaviour of steel with a Youngs modulus E = 2.1E8 kN/m^2 and a Poissons ratio of ν= 0.3 were defined. A commercial finite element code called ABAQUS (Hibbit et al. 1998) was used.

www.EngineeringEBooksPdf.com

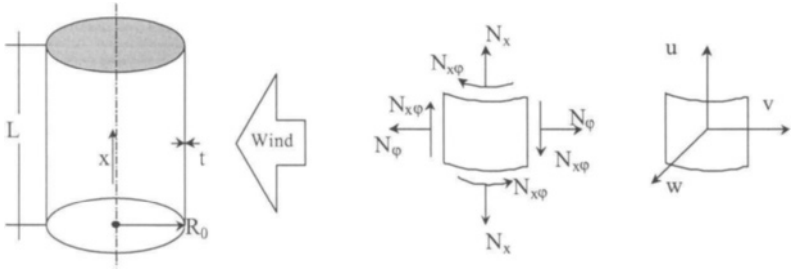

Figure 3. Structural system, membrane section forces and displacements.

LINEAR-ELASTIC ANALYSIS

As a first approximation it could be assumed that a cylindrical shell structure of sufficient length should behave somewhat similar to a cantilever with a ring-shaped cross section. This is not the case for thin-walled cylinders due to the detrimental effects of cross-sectional deformation. Procedures and tools to compute section forces in thin-walled cylinders under wind load using linear-elastic shell theories have been given in the past (e.g. Greiner 1980, 1983, Pircher et al. 2001). Applying these tools, the following general picture of the distribution of the axial section force N_x in thin-walled cylinders under wind load can be drawn (Figure 4). Most notably, a region of compressive axial section forces occurs in the upper half of the cylinder around the meridian facing into the wind. Ovalisation of the initially circular cross-section leads to a local increase of the radius $\rho(\varphi=0)$ of the shell structure in this region. Using the discrete radial displacements $w_0 = w(\varphi=0)$ and $w_1 = w(\varphi>0)$ the local radius $\rho(\varphi=0)$ along the meridian facing into the wind can be approximated taking into account symmetry at the meridian and assuming $w << R_0$:

$$\rho(\varphi=0) \approx R_0 + w_1 + 2\frac{w_1 - w_0}{\Delta\varphi^2} \tag{2}$$

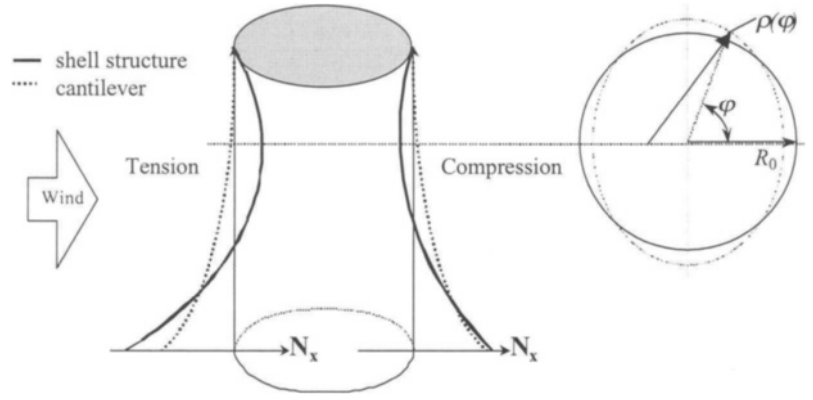

Figure 4. Membrane force N_x for meridians facing into and away from the wind and ovalisation.

www.EngineeringEBooksPdf.com

The buckling strength of a thin-walled cylinder under axial load assuming perfect initial geometry, simple supports, linear elastic material behaviour and membrane stress distribution in the pre-buckling region (eg. Timoshenko 1910) is commonly referred to as the "classical buckling σ_{cl}) and is widely used as a reference value. By substituting the radius of the unloaded structure R_0 with the local radius $\rho(\varphi=0)$ of the displaced structure $\sigma_{cl,\,local}$ can be defined as follows:

$$\sigma_{cl} = \frac{E \cdot t}{R_0 \sqrt{3(1-\nu^2)}} \approx 0.605 \frac{E \cdot t}{R_0}$$
$$\sigma_{cl,local} \approx 0.605 \frac{E \cdot t}{\rho(\varphi = 0)} \qquad (3)$$

Figure 5 qualitatively shows the consequences of ovalisation along the meridian facing the wind. Under the assumption that the area of compression is large enough so the formula for σ_{cl} (Equation 3) can be applied, critical wind loads can be defined where the compressive axial stresses N_x/t equals σ_{cl} and $\sigma_{cl,local}$ respectively. For the given example these critical loads were computed to be $p_{r,cr}$ = 16.10 kN/m^2 and 12.39 kN/m^2 respectively. This represents a significant reduction due to the ovalisation of the cylinder cross-section.

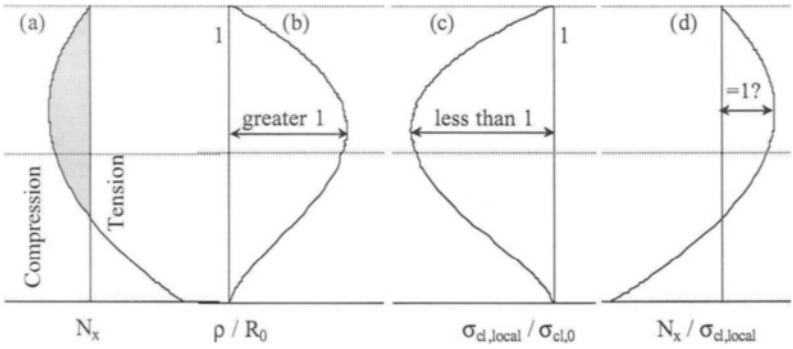

Figure 5. Consequences of cross-sectional deformation along the meridian facing the wind.

GEOMETRICALLY NON-LINEAR ANALYSIS

An FE-analysis which took into account geometric non-linear effects was performed on the same shell structure of the present case study. In the following all loads are given for a factor λ which is a multiplier for the reference load of p_{ref} = 1.0 kN/m^2. The points marked LD1 to LD6 in Figure 6 help illustrate the non-linear response of the cylinder under wind load. A first bifurcation point was recorded at point LD3 after which accelerated inward deflections were recorded for a large area around the upper half of the meridian facing the wind, eventually followed by another bifurcation point (LD4) where the formation of the buckling pattern shown in mode 2 in Figure 1 occured. A load maximum was reached at λ = 5.83 between LD3 and LD4. The load-displacement curves given in Figure 6 (point "A" in Figure 1) and Figure 7 (point "B" in Figure 1) illustrate this behaviour. The displaced shapes of the meridian facing the wind for given points along these load-displacement curves are plotted in Figure 8.

www.EngineeringEBooksPdf.com

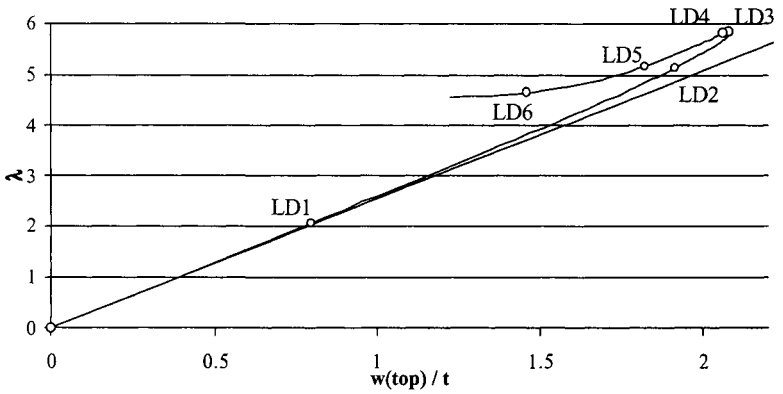

Figure 6. Radial displacement at the top of the meridian facing the wind (point „A").

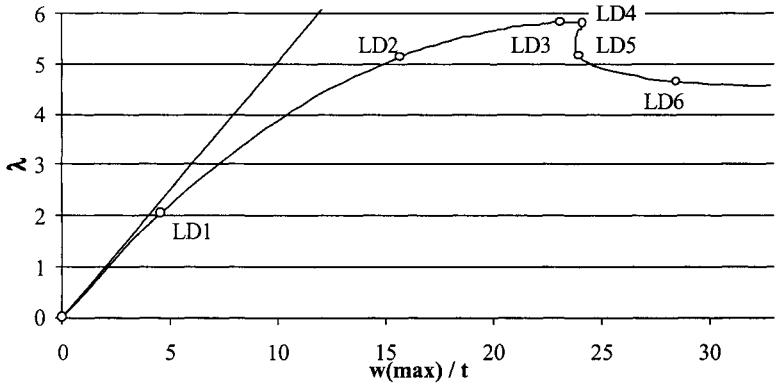

Figure 7. Maximum radial displacement along the meridian facing the wind (point „B").

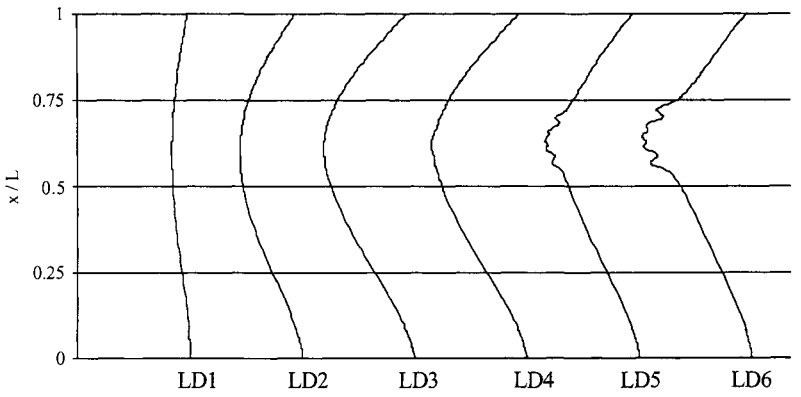

Figure 8. Displaced shapes of the meridian facing the wind at selected points along the load-displacement path.

www.EngineeringEBooksPdf.com

Comparing the results of the linear analysis with the geometrically non-linear analysis reveals two detrimental effects in the structural behaviour of the shell structure. Firstly, the rate at which the local radius ρ is increased in the critical upper half of the cylinder is much greater for the model which takes into account geometric non-linearity, drastically reducing the buckling resistance under axial load (Figure 9); and secondly, the maximum axial membrane forces N_x along "meridian A" are also increased for the model which takes into account geometric non-linearity. The thin line in Figure 6, Figure 7, Figure 9, Figure 10 shows the results of the linear analysis.

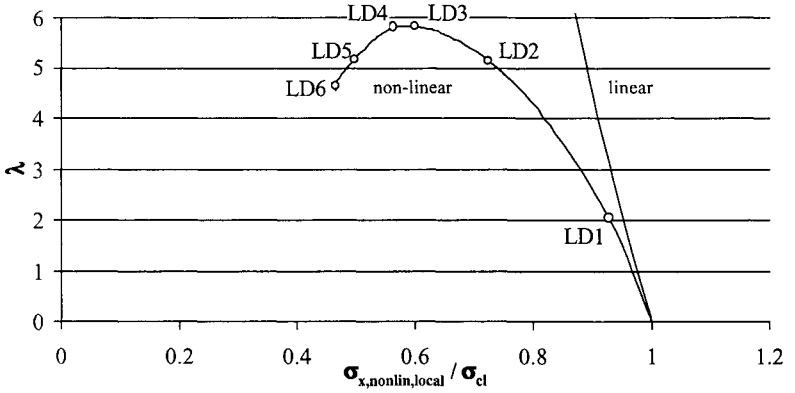

Figure 9. Local buckling resistance under axial compression at point B.

The ratio of the maximum axial membrane force and the local buckling resistance under axial stress along the loading path is given in Figure 10. It can be seen that after the load maximum is reached between points LD3 and LD4 this ratio is still increased due to the large local increase in radius at this stage. Once the buckling pattern as shown in mode 2 in Figure 1 has formed the load and the local membrane force drops off considerably (LD6). The maximum local stress level due to axial compression reaches 0.765 of $\sigma_{cl,local}$. Assuming that the structure fails mainly due to axial compression in a localised area an explanation must be given for the fact that the stress level remains well below $\sigma_{cl,local}$. Figure 8 shows that the deflections in the critical region between x=0.5L and x=0.75L of the meridian facing the wind can be looked at as an additional imperfection. This "imperfection" along with interaction between the longitudinal and tangential axial membrane force can be made responsible for the fact that axial membrane stresses in the given example only reach the given level of 0.765 of $\sigma_{cl,local}$.

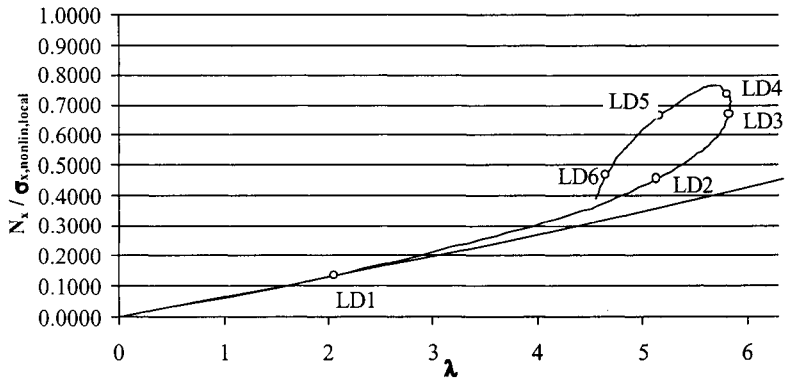

Figure 10. Ratio of maximum axial membrane force Nx and buckling resistance at „meridian A".

www.EngineeringEBooksPdf.com

CONCLUSIONS

A case study for a thin-walled cylindrical shell structure under wind loading has been presented. The geometric parameters of the cylinder were chosen so that a particular buckling pattern occurred. This pattern is characterised by horizontal ripple-like buckles in the upper half of the side of the cylinder facing the wind. In this area considerable axial compression occurs. These axial compressive stresses were recorded for a finite-element model and compared to the critical axial buckling stress for constant axial loading. Two critical factors were identified: firstly, the ovalisation at the critical cross-section; and, secondly the disproportional increase of axial compression due to geometrically non-linear effects. Further reductions of the expected buckling resistance were suspected to be caused by interaction with tangential compression in the area and additional displacements.

REFERENCES

Deutsche Norm (1990). *Stahlbauten, Stabilitätsfälle, Schalenbeulen, DIN 18 800, Teil 4*, Beuth Verlag, Berlin, Germany (in German)

Esslinger M. (1971). Stationäre Windbelastung offener und geschlossener kreiszylindrischer Silos. *Der Stahlbau* **12**, 361-368 (in German)

Feder G. (1975). Einige qualitative Bemerkungen zum Beulen von stehenden Behältern unter Windlast. *Sonderheft der Deutschen Forschungs- und Versuchsanstalt für Luft- und Raumfahrt*, Esslinger M. & Geier B. (editors), Braunschweig, (in German)

Greiner R. (1980). *Ingenieurmässige Berechnung dünnwandiger Kreiszylinderschalen*. Research Report, Heft 1, Institute of Steel, Timber and Shell Structures, Technical University Graz, Austria (in German)

Greiner R. (1983). *Zur ingenieurmässigen Berechnung und Konstruktion zylindrischer Behälter aus Stahl unter allgemeiner Belastung*. Wissenschaft und Praxis, Band 31, Fachhochschule Biberach, Germany (in German)

Greiner R., Derler P. (1995). Effect of Imperfections on Wind-Loaded Cylindrical Shells. *Thin-Walled Structures* **23**, 271-281

Hibbit, Karlsson & Sorensen (1998). *ABAQUS Version 5.8-1: Standard User's Manual*, Pawtucket, RI, USA

Kwok K.C.S. (1985). Wind Loads on Circular Storage Bins. *Proceedings: Joint U.S.-Australian Workshop on Loading, Analysis and Stability of Thin Shell Bins, Tanks and Silos*, University of Sydney, pp 49-54

Lindner J., Scheer J., Schmidt H. (1994). *Stahlbauten – Erläuterungen zu DIN 18 800 Teil 1 bis Teil 4*, Beuth Verlag, Berlin, Germany (in German)

Pircher M., Guggenberger W., Greiner R. (2001). Stresses in Elastically Supported Cylindrical Shells under Wind Load and Foundation Settlement. *Advances in Structural Engineering* **4**(3), 159-167

Schneider W., Thiele R. (1998). Tragfähigkeit schlanker wind-belasteter Kreizylinderschalen. *Der Stahlbau* **67**:6, 434-441 (in German)

www.EngineeringEBooksPdf.com

Advances in Steel Structures, Vol. II
Chan, Teng and Chung (Eds.)
© 2002 Published by Elsevier Science Ltd.

BUCKLING OF THIN PRESSURIZED CYLINDRICAL SHELLS UNDER BENDING LOAD

LIMAM Ali *, JULLIEN Jean François *

* INSA de Lyon, 20 Avenue Albert Einstein, 69621 Villeurbanne Cedex, France
ali.limam@insa-lyon.fr
Jean-Francois.Jullien@insa-lyon.fr

ABSTRACT

Design standards dealing with thin cylindrical shells subjected to bending, axial compression and internal pressure are based on analytical formulations and knock down factors from experimental investigations. This contribution gives some explanations on the behavior of such loaded structures; in particular, the case of combined loads as internal pressure and bending, or pressure, bending and shear is investigated. Parametrical experimental study highlights the stabilizing effect of internal pressure; in the simulation only the large displacement approach confirms the enhancement of the load capacity due to the pressurization. The importance of the coupling between shear and bending is shown using parametric numerical studies.

KEYWORDS

Elastic buckling, Cylindrical shells, Bending load, Internal pressure, Combined loads, Finite element.

INTRODUCTION

Thin cylindrical shells are used as structural components in many aeronautical and aerospace structural systems ; these components are often submitted to interacting loads including compression, bending and internal pressure. It is therefore essential that their buckling behavior be properly understood so that suitable design methods can be established and structures can be optimized. Although the buckling of cylindrical shells under axial compression has been extensively studied, few works deal with bending. We can note, in particular, the studies of Gorman and Evan-Iwanowski (1970), Hutchinson (1965), Weingarten et al (1965), Lo et al (1951) carried out on the interaction between pressure and compression ; they conclude, in the case of elastic buckling, that pressure has a benefic effect ; the reduced effect of geometrical imperfections allows the buckling stress to reach the classical stress which remains the upper bound ;

$$\sigma_{CL} = \frac{1}{\sqrt{3(1-\nu^2)}} \frac{Et}{R} \tag{1}$$

www.EngineeringEBooksPdf.com

Rotter (1990) extended these studies to the plastic buckling case, giving a simplified design method. Plasticity effect leads generally to a collapse in an axisymmetric mode, confined near the boundaries ; these results confirm all experimental and numerical work conducted by Limam (1991). Then Teng and Rotter (1992) largely completed the work in the elastic buckling range, by conducting a parametrical numerical study, gauging the effects of imperfections.

In the case of bending load, Seide and Weingarten (1961) have shown that the classical stress was a good estimate of the buckling stress. Their results obtained by a Galerkin method did not agree with the analysis of Timoshenko (1932) and Flügge (1932) and in particular didn't corroborate the experimental results which seemed to confirm a buckling stress higher than the classical stress. Our results confirm Weingarten's work. In the case of bending and internal pressure interaction, studies are rare compared to other load cases, on the other hand the results are disseminated which leads to wrong conclusions. Generally bending is induced by a transverse force applied at a certain distance of the shell's boundaries. We show that by coupling shear and bending (even if it is a weak coupling) gives appreciable differences in the behavior. For instance, the gaps found experimentally, which have led to contradictory conclusions, can be explained by loading processes different from one experimental set-up to another. We finally confirm the stabilizing effect of internal pressure, this result needs calculations considering large displacements. The gain on the critical load remains restricted in the case of pure bending, but can be relatively important in the case of the interaction between shear and bending. In this last case our experimental results corroborate those coming from numerical simulation. While good agreement between experimental tests and numerical simulations is quite easy in the case of quasi-perfect shells, the conservative nature of design requires the consideration of geometrical imperfections. Hence, we show that the localized axisymmetric default allows to a lower bound collapse load to be reached.

LINEAR ANALYSIS

Pure bending – Influence of internal pressure

Simulations are conducted with the ABAQUS code, (element S8R5). The study is done for different values of R/t, knowing that the radius R is kept constant (R=135 mm) and corresponds to the tested shells' radius. Pure bending is applied on the top of the shell and boundary conditions are clamped. We compare the critical stress $\tilde{\sigma}$ to the classical buckling stress,

$$\tilde{\sigma} = \frac{\sigma_F - PR/2t}{\sigma_{CL}} \tag{2}$$

σ_F is the axial membrane stress induced by the bending load, PR/2t corresponds to the end effects, for the pressure we use the dimensionless variable :

$$\tilde{P} = \frac{\sigma_\theta}{\sigma_{CL}} = \frac{PR/t}{\sigma_{CL}} \tag{3}$$

where σ_θ represents the circumferential membrane stress.

For pure bending, our results correspond to Seide and Weingarten's ; the critical stress is equal to the classical stress within 1%. The beneficial effect of pressure is observed, and depends on the R/t

www.EngineeringEBooksPdf.com

parameter, but the load increase remains limited. For example, for R/t=1350 and P=2400 mbars that means $\tilde{P}$ =5.5, the enhancement is about 6% of σ_{CL} .

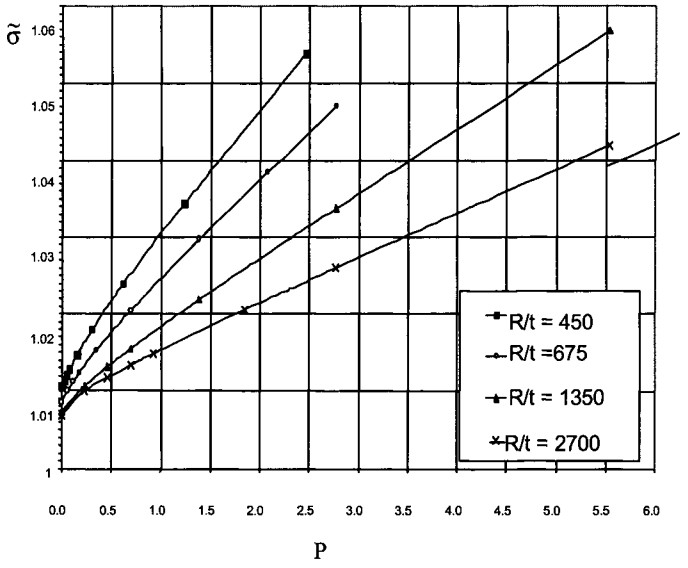

Figure 1 : Pure bending – Effect of internal pressure

Bending and shear interaction – effect of internal pressure

Generally, experimentally speaking, the bending load is obtained by shear load via a lever arm. This implies direct coupling between bending and shear loads. Our experimental set-up configuration is given below.

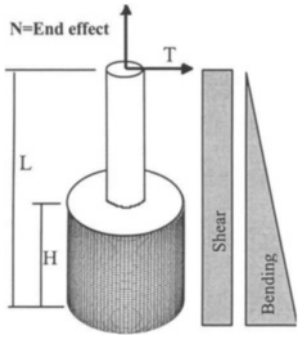

Characteristics :

- E = 126500 MPa, ν = 0.38,
- t=0.1 mm, R=135 mm, H=270 mm,
- λ=L/R=13.6 P : variable.
- $\sigma_{Cr} = \frac{T_{Cr} L}{\pi R^2 t}$, bending
- $\tau_{Cr} = \frac{T_{Cr}}{\pi R t}$, shear

Figure 2 : Experimental set-up – INSA

www.EngineeringEBooksPdf.com

In order to gauge the effect of the coupling of bending and shear, numerical simulations were considered at variable internal pressure, for different values of the dimensionless parameter $\lambda = \frac{L}{R}$ which represents the lever arm dimensions.

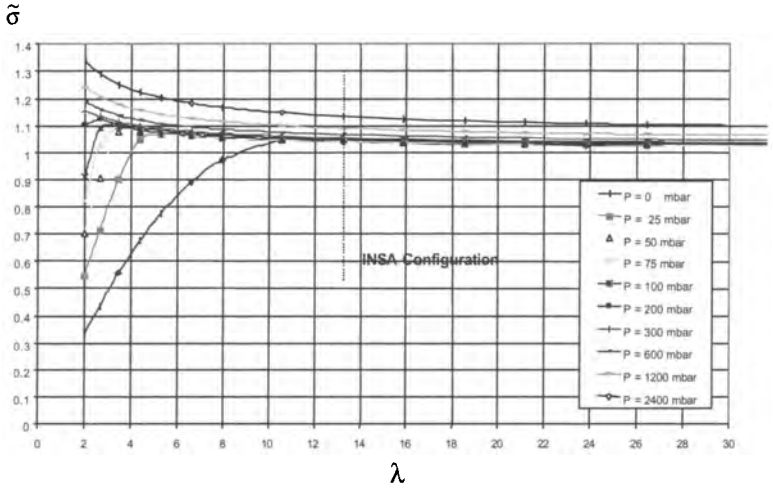

Figure 3 : Effect of coupling Bending and Shear

Pressure increases critical loads, the enhancement is more important in the case of bending induced by lever arm than in the case of pure bending, the gap is all the more important when shear predominates. For $P \leq 200$ mbars, the value $\lambda = 10$ represents a threshold between a shear and a bending buckling ; beyond this pressure intensity, the critical mode corresponds to bending load configuration. When $\lambda \geq 20$ the behavior tends to pure bending. These results show the sensitivity to a loading process and can explain the scattering of experimental results reported in literature.

GEOMETRICAL NON LINEAR ANALYSIS

Suer and Harris (1958) results as well as ours' Antoine (2000) show that collapse loads of cylindrical shells under pressure and bending combined to shear, are much higher than the classical stress. The enhancement of 14% obtained for P=2400 mbars via linear modeling is far from the 50% experimentally observed for a lower pressure (1200 mbars). The geometrical non linear analysis leads to critical loads higher than the ones given by a linear analysis.

www.EngineeringEBooksPdf.com

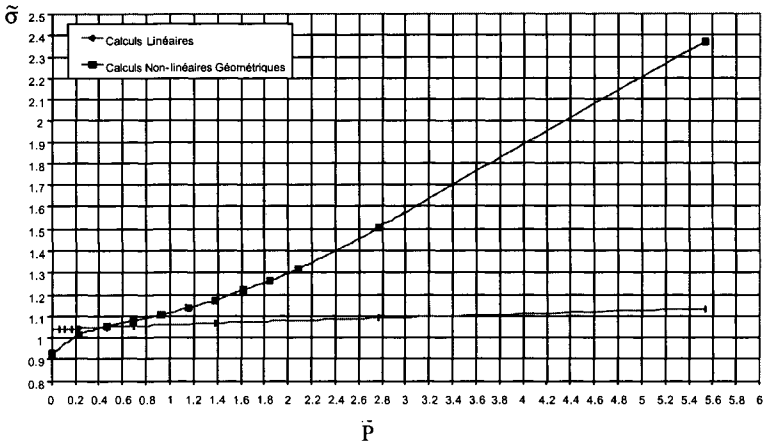

Figure 4 : Effect of internal pressure, linear and large displacements analysis

In the case of no internal pressure , pre-critical rotations near the boundaries involve a drop of the critical stress, according to Yamaki's results (1984). Increasing the internal pressure enhances the gap between Euler's analysis and the non linear geometrical calculation. Only a calculation with a re-estimate of the tangent stiffness matrix allows to corroborate the stabilizing effects of pressure, noted experimentally (figure 5) going from unstable post-critical behavior for P<400 mbars to stable behavior beyond (figure 6).

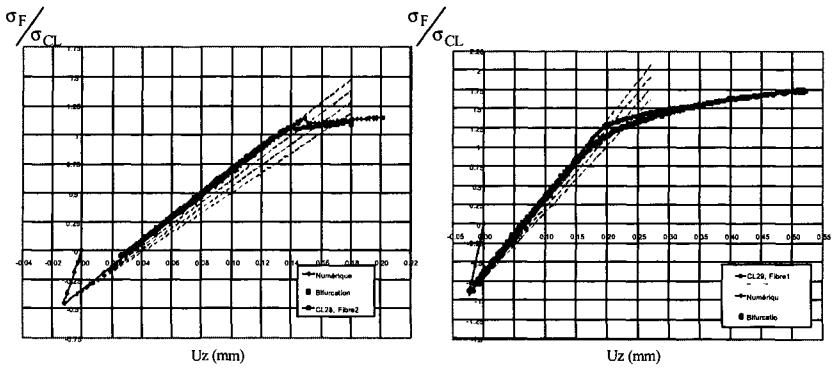

Figure 5 : Load deflection curves. Tests and Simulations

www.EngineeringEBooksPdf.com

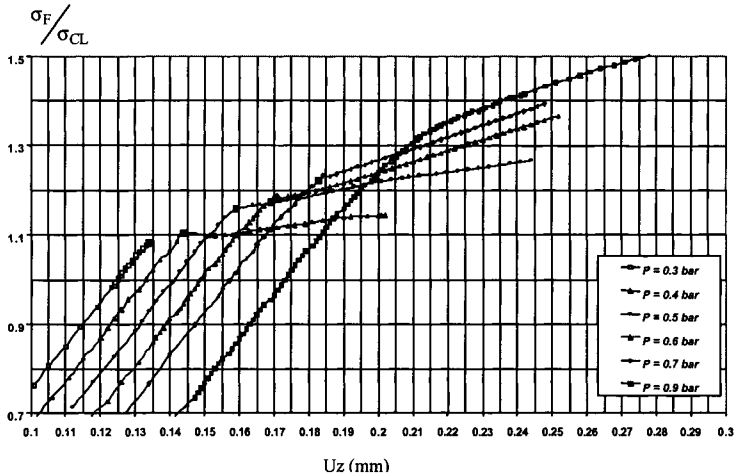

Figure 6 : Load shortening curves – Simulations (R/t=1350)

The good agreement between tests and numerical simulations is yet correct only for quasi-perfect specimens. The tested shells are obtained by Electro-deposition, which avoids in particular welding joints and the shells have hence little geometrical imperfections. In order to validate a design approach, it is however necessary to consider the effect of geometrical imperfections coupled to plasticity.

TOWARDS A DESIGN APPROACH : EFFECT OF IMPERFECTIONS

Every thin structure includes geometrical defaults which are generally inherent to manufacturing processes. If simulations on perfect shells corroborate the observed phenomenon during experimental tests and suitably capture the effects of the different parameters, the comparison between collapse loads is not yet systematically satisfactory, especially for shells having shape imperfections with a high magnitude ($A/t > 0.1$). In order to allow the design with a numerical approach, we compare the effect of different geometrical imperfections, the Euler defect, corresponding to the bifurcation mode of a perfect structure, and the local axisymmetric defect corresponding to a generator's perturbation by the cosine function. Only a half-structure model is considered. For low defaults' magnitudes ($A/t<0.25$) the Euler's defect has the most drastic effect, whereas for higher magnitudes, the cosine default is the most harmful.

This result puts to the fore that it is impossible to determine a unique critical imperfection. To confirm that the design remains conservative, it is necessary to choose a particular shape of the defect depending on the magnitude (manufacturing tolerance). A conservative approach would consist in taking a minimum envelop curve. On the other hand, pressure tends to blur inextensional modes, and hence has less effect on an axisymmetric mode.

www.EngineeringEBooksPdf.com

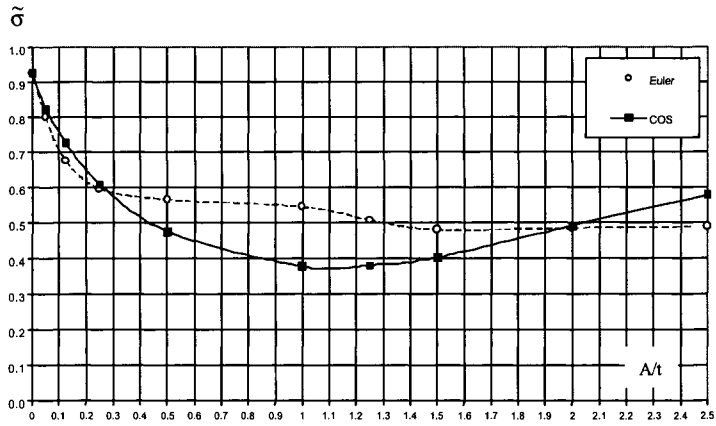

Figure 7 : Effect of localized Axisymmetric and Euler's defect

We can conclude that the axisymmetric default has the most drastic effect; and in order to guaranty the conservative nature of the design, we keep this geometrical imperfection with a magnitude of A/t=1.

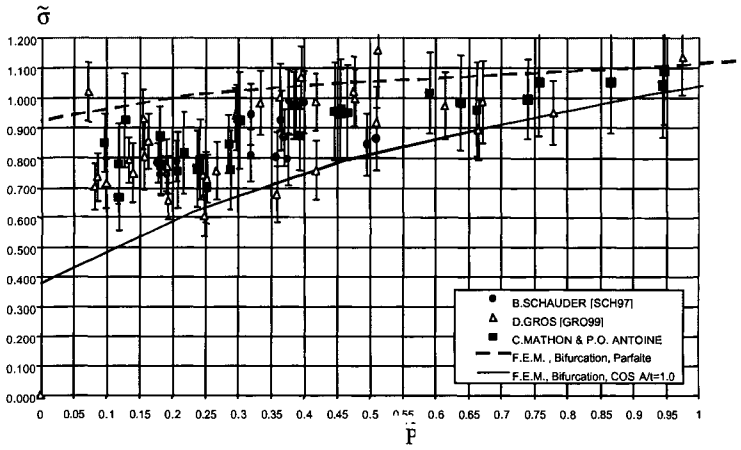

Figure 8 : Comparison between Experimental tests and Numerical simulation

This approach conduces to a lower bound of most experimental results.

CONCLUSION

Under pure bending, the critical stress is equivalent to the classical stress. The strengthening effect of pressure found experimentally is corroborated only by large displacements calculations. Taking into account a localized axisymmetric imperfection allows a dimensioning approach.

www.EngineeringEBooksPdf.com

REFERENCES

Antoine P.O. (2000). "Comportement des coques cylindriques minces sous chargements combinés : vers une amélioration du dimensionnement sous flexion et pression interne", *Thèse de Doctorat, INSA de LYON*, 171 p

Flügge W., (1932). "Die stabilitat der kreiszylinderschale", *Ingenieur-Archiv*, **Vol. 3**, pp 463-506

Gorman D.J., Evan-Iwanowski R.M., (1970). "An Analytical and Experimental Investigation of the Effects of Large Prebuckling Deformations on the Buckling of Clamped Thin-Walled Circular Cylindrical Shells Subjected to Axial Loading and Internal Pressure", *Developments in Theoretical and Applied Mechanics*, **Vol. 4**, pp. 415-426

Hutchinson J., (1965). "Axial Buckling of Pressurized Imperfect Cylindrical Shells", *AIAA Journal*, **Vol. 3, N°8**, pp. 1461-1466

Limam A., (1991). "Flambage de coques cylindriques sous combinaison de chargements : pression interne et compression axial", *Thèse de Doctorat, INSA de LYON*, 211 p

Lo H., Crate H., Schwartz E.B., (1951). "Buckling of Thin-Walled Cylinder under Axial Compression and Internal Pressure", *Langley: NASA*, **NASA Report 1027**, pp 647-655.

Rotter M., (1990). "Local Collapse of Axially Compressed Pressurized Thin Steel Cylinders", *Journal of Structural Engineering*, **Vol. 116, N°7**

Rotter M., Teng J.G., (1992). "Buckling of pressurized axisymmetrically imperfect cylinders under axial loads", *Journal of Structural Engineering, American Society of Civil Engineers*, **Vol. 118, N°2**

Seide P., Weingarten V.I., (1961). "On The Buckling of Circular Cylindrical Shells under Pure Bending", *ASME*, p112-p116

Suer H.S., Harris L.A., Skene W.T., Benjamin R.J., (1958). "The Bending Stability of Thin-Walled Unstiffened Circular Cylinders Including the Effects of Internal Pressure", *Journal of the Aeronautical Sciences*, **Vol. 25, N°5**, pp. 281-287

Timoshenko S, (1932). "Theory of Elastic Stability", *McGraw-Hill Book Company*, Inc, New York, pp 463-467

Weingarten V.I.; Morgan E.J.; Seide P., (1965). "Elastic Stability of Thin-Walled Cylindrical and Conical Shells under Combined Internal Pressure and Axial Compression", *AIAA Journal*, **Vol. 3, N°6**, pp. 1118-1125

Yamaki N., (1984). "Elastic Stability of Circular Cylindrical Shells", *Amsterdam: North Holland*, 558 p.

www.EngineeringEBooksPdf.com

Advances in Steel Structures, Vol. II
Chan, Teng and Chung (Eds.)
© 2002 Published by Elsevier Science Ltd.

STABILITY OF THIN-WALLED CYLINDRICAL SHELLS SUBJECTED TO LATERAL PATCH LOADS

E. Feifel and H. Saal

Lehrstuhl für Stahl- und Leichtmetallbau, Universität (TH) Karlsruhe
D-76128 Karlsruhe, Germany

ABSTRACT

Cylindrical tanks and other large shell structures are subjected to local loads from attached piping. The dominating effects are caused by radial forces and moments. For large R/t ratios the load displacement behaviour is nonlinear at higher load levels even for elastic shells. This paper investigates this geometric nonlinear behaviour including stability phenomena. The Finite Element analysis has been verified by comparison with experimental results for spherical caps. This shows the beneficial influence of the stiffness of the nozzle. For radial forces P a nondimensional load parameter P* is used for the cylindrical shells as in earlier investigations of the buckling behaviour of spherical caps. The critical load P^*_{crit} is obtained by considering the first maximum of the load displacement curve as well as the load P* at which the maximum radial displacement u_0 attains a value which is six times the shell thickness t. This critical load P^*_{crit} increases almost linearly with the nondimensional diameter d* of the loaded area. The load deformation curves show stable behaviour at deformations far beyond P*. This is also true for the moment loading which is represented by the nondimensional parameter M*. The moment rotation curves become independent of R/t if M* is plotted versus α^* which is obtained from the rotation α by multiplication with $(R/t)^{0.5}$. They then only depend upon the nondimensional diameter d* of the area loaded by the nozzle. The nonlinearity of these curves increases with increasing d* and thereby load maxima with unstable equilibrium occur.

KEYWORDS

Cylinders, tanks, buckling, nozzle, reinforcement, patch loading, local moments, local forces

INTRODUCTION

The design of piping should minimize the forces and moments transferred to shell structures because they may induce high local stresses at their connection to the shell. Despite this construction principle for the piping the unavoidable supporting forces and moments will in many cases be of such size that their effect on the shell can not be neglected. With shells of small and moderate R/t ratios like pressure vessels the design may focus on stresses and strains which may promote fatigue problems. However, with large R/t ratios local buckling has to be considered which may occur due to the supporting forces

www.EngineeringEBooksPdf.com

and moments. In both cases the major concern is with the radial forces and the moments in the tangential plane whereas the forces in the tangential plane and the moment with the vector normal to the tangential plane may be disregarded because they are much less harmful.

The first investigation of this type of stability problem was performed by Biezeno (1935) with a spherical cap subjected to a radial load P. In the middle of the 20th century there were numerous investigations of this problem, both analytical and experimental, as have been summarized by Fitch (1968). These investigations revealed that in the case of elastic buckling the critical load P_{crit} may be expressed by a nondimensional load parameter $P^*_{crit} = (P_{crit}R)/(Et^3)$. It was shown that the load could be increased in the postbucklig range with increasing wave numbers. In the experiments the load was applied by steel cylinders of small diameter. No increase of the shell stiffness in the area of load application - as may be due to nozzles for the connected piping - was considered neither in the analytical or the experimental investigations.

At about the same time Bijlaard investigated the stresses due to forces and moments from the piping connected to cylindrical (1955) and spherical shells (1957). His work was the basis for the design rules suggested by Wichman et. al. (1965) and was also included in PD5500 (2000). Due to the pressure vessels with their moderate R/t ratios as the intended field of application it was sufficient to use linear shell theory.

For the large R/t ratios occuring in tank structures it may be necessary to consider the stability problem of cylindrical shells due to lateral patch loads. This investigation shall account for the fact that these lateral loads are introduced by the attached pipe and sometimes even a reinforcing pad which will improve the situation compared to that of a separate load as was used in the aforementioned investigations of spherical shells.

VERIFICATION OF THE FINITE ELEMENT MODEL

The Finite Element program ANSYS 5.6 was used for the geometric nonlinear, elastic analysis with shell element type 43. The isoparametric 4-node shell elements are based on a large displacement and large strain formulation. The arc-length method was used to trace the load-deflection curve of the structure. To determine bifurcation-points on the load displacement-path, eigenvalues were searched on specified load levels.

The first step of the verification of the Finite Element model was that by test results. Since such test results were only available for spherical caps the first Finite Element modelling was for these caps. The meshing density, the element type and the type of analysis had to be verified with these models which differed by the double curvature and the boundary conditions from the situation with the cylindrical shells of this investigation. The clamping of the boundary of the spherical cap will not interfere with this verification because of the governing local character of the situation. Due to the different types of curvature the global behaviour of the cylindrical shell will be different from that of the spherical shell. However, because of the governing local character of the situation this is also not significant for the verification. Figure 1 shows the Finite Element model for aluminium test specimen AL-29(2) from Penning (1966) with R/t = 1770 and b/R = 0,198.

www.EngineeringEBooksPdf.com

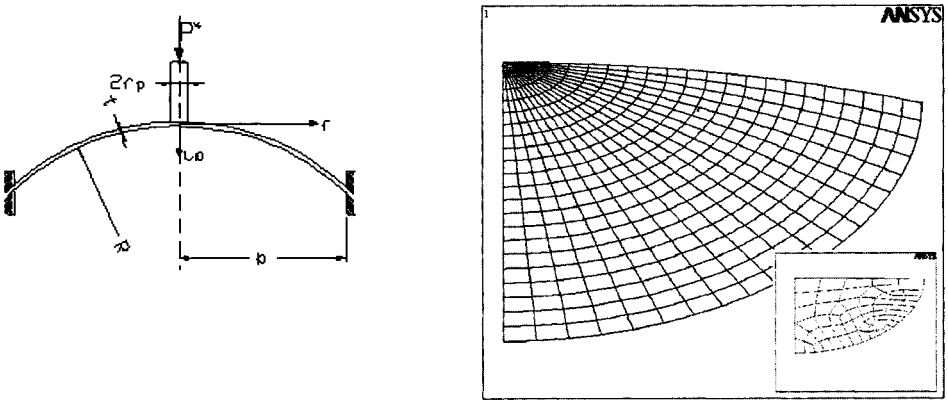

Figure 1: Finite-Element-model for aluminium test specimen AL-29(2) from Penning (1966)

The boundaries are clamped and the load introduction is over an area with radius r_p= 14,0t. Figure 2 shows the load displacement curve with the experimental results and the numerical results.

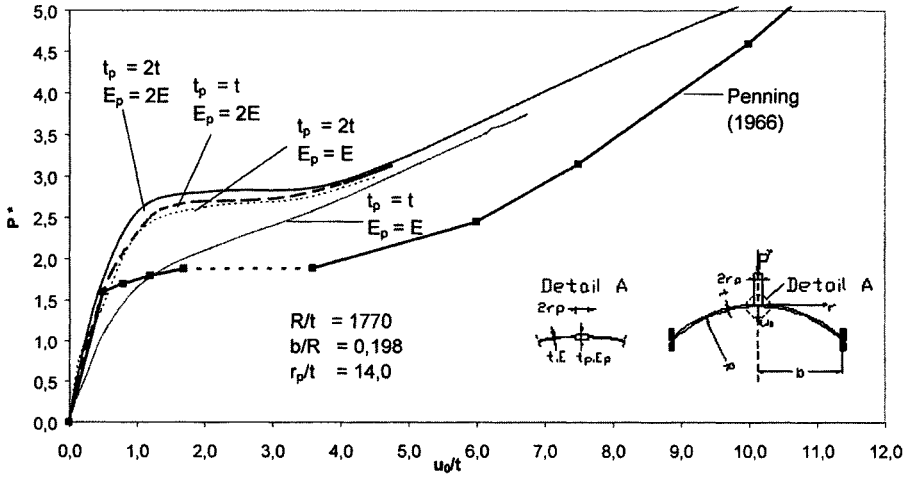

Figure 2: Experimental and analytical load displacement curve for cap according to Figure 1

In the shell structure (pressure vessel or tank) the load will usually be introduced by a nozzle or pipe. This means that the out-of-plane stiffness of this area is large compared to that of the shell. Therefore the numerical results are given for four different stiffnesses of the loaded area. These different stiffnesses are modelled by the modification of Youngs modulus E_p and the thickness t_p of the shell in the loaded area. The analysis with $E_p = 2E$ and $t_p = 2t$ represents the practically rigid loaded area which is comparable to the situation with the nozzle or pipe whereas the analysis with $E_p = E$ and $t_p = t$ represents the situation in the experiments of Penning (1966) with a load tip. The buckling phenomenon in the experiments is indicated by the horizontal part of the load displacement curve. From Figure 2 it is obvious that with the analysis of the nozzle situation the critical load is about 50% larger than that for the situation with the load tip in the experiments. With decreasing stiffness of the

www.EngineeringEBooksPdf.com

loaded area the analytical results approach the experimental result. A second example has been taken from Penning and Thurston (1965). Figure 3 shows the load displacement curve for their aluminium shell B36(3) with R/t = 3030, b/R = 0,200 and r_P/t = 75,8. The boundaries are again clamped. This experimental curve agrees well with the analytical results. It is improved when the shell thickness in the loaded area is increased by 20%.

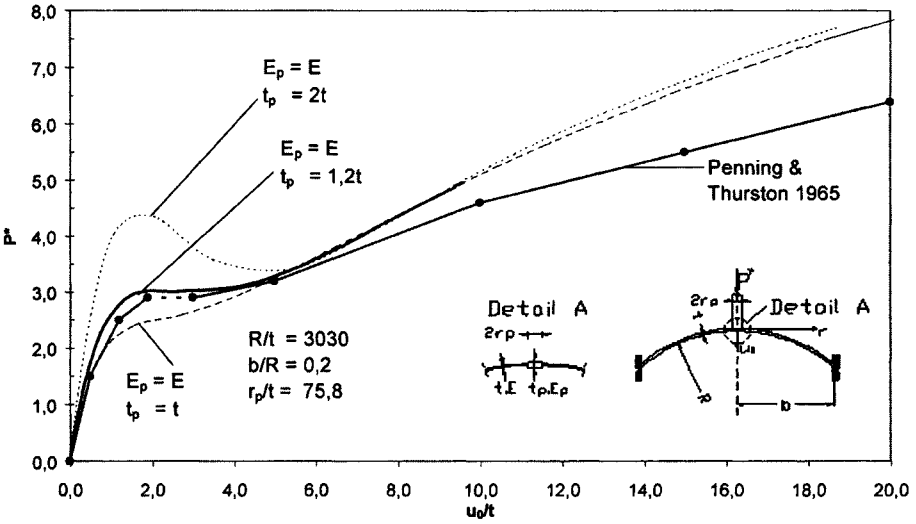

Figure 3: Experimental and analytical load displacement curve for aluminium cap B36(3) from Penning and Thurston (1965)

In the cylindrical shell - in contrast to the spherical shell where the global stresses decay with the distance from the load - the local load causes a global stress state depending even upon the remote boundary conditions of the cylindrical shell. However, these global stresses and the respective displacements are expected to be much less than those in the loaded area. Since the implication of such remote boundary conditions and the related global stress state would increase the parameters of the analysis a cylindrical shell with two opposite self equilibrating radial forces according to Figure 4 was chosen for the Finite Element analysis. The end sections are simply supported.

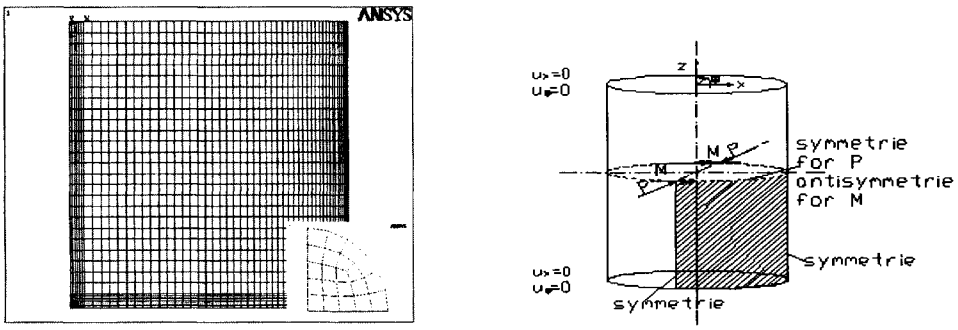

Figure 4: Finite Element model for patch loaded circular cylindrical shells

www.EngineeringEBooksPdf.com

Figure 5 gives the maximum radial displacement u_0 at the load normalized to the shell thickness t for a shell with R/t = 4000 subjected to two opposite loads and for the same shell with four equidistant loads around the circumference.

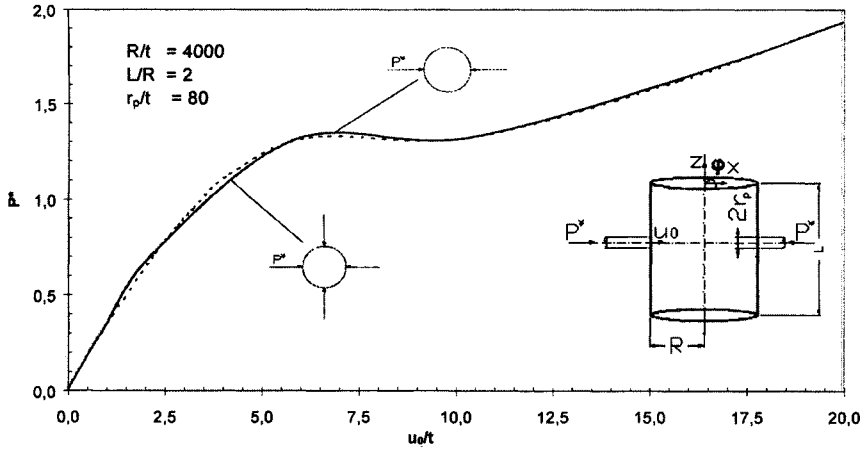

Figure 5: Maximum radial displacement u_0/t at the load for a cylinder with R/t = 4000 subjected to two and for four equidistant loads around the circumference respectively

The coincidence of the two load displacement curves demonstrates the local character of the situation and justifies the model with two opposite loads for the investigation of the dominating situation with a singular radial load. The stiffness of the loaded area is represented by $E_p = 2E$ and $t_p = 2t$. This applies also for all of the following investigations.

The local character of the dominating stresses and displacements was checked in the axial direction by plotting the curvature κ of the meridian in the symmetry axis under the load versus the nondimensional coordinate $x/(Rt)^{0,5}$ along the meridian. This plot in Figure 6 for shells with R/t = 2000, 4000 and 5000 respectively shows that the large values of curvature are restricted to an area with about distance $6(Rt)^{0,5}$ from the load.

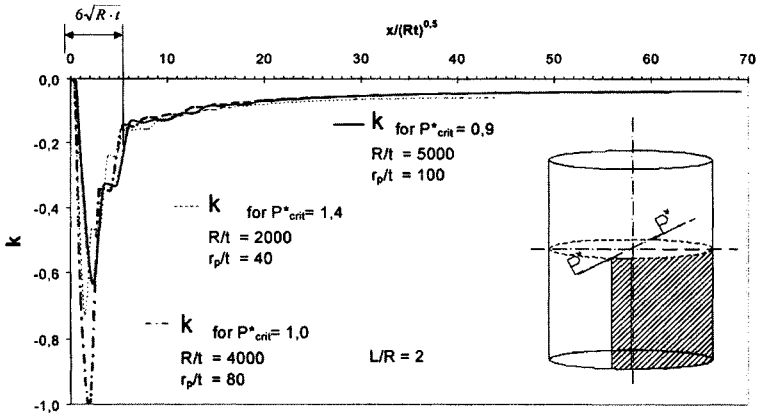

Figure 6: Curvature κ of the meridian in the symmetry axis under the load versus the nondimensional coordinate $x/(Rt)^{0,5}$ along the meridian

www.EngineeringEBooksPdf.com

This means that the results of the following investigation should be valid if the distance of the load to the boundary of the shell or any other local loaded area is less than this distance. This is conservative compared to PD5500 (2000) which with respect to the stress analysis states that the stresses in loaded areas may influence each other if their distance is less than $2{,}5(R\ t)^{0,5}$.

CYLINDRICAL SHELL SUBJECTED TO A RADIAL FORCE

The nondimensional load parameter $P^* = (P\ R)/(Et^3)$ is plotted in Figure 7 versus the nondimensional radial displacement $u^* = u_0/t$ at the load for the shells according to Figure 4.

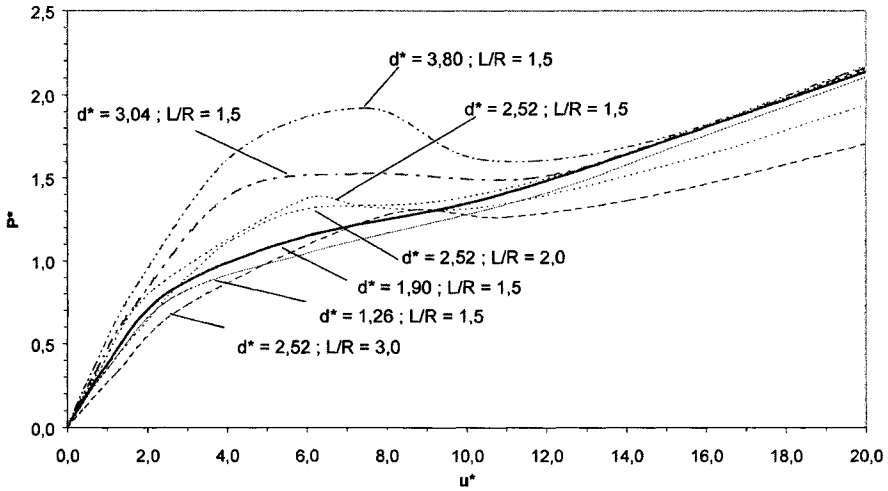

Figure 7: Nondimensional load displacement curves with $P^* = (P\ R)/(Et^3)$ and $u^* = u_0/t$ for the shells according to Figure 4 with R/t = 4000 with different d* and L/R

With these shells the R/t ratio is 4000 whereas the nondimensional diameter $d^* = 2r_p/(Rt)^{0,5}$ of the loaded area is varied from 1,26 to 3,80. All load displacement curves are linear for P* smaller than 0,80. The displacements increase more or less progressively beyond this load. For the smaller values of d* these curves have a distinct knee which is followed by an almost linear part of the load displacement curve with a reduced slope. For the larger values of d* the nonlinearities of the load displacement curve occur at higher values of P*. The load P* attains maximum after which it drops and increases again at about u* =10. Because of this load deformation behaviour it was decided to consider as well the first maximum of the load deformation curve as the load where the nondimensional displacement u* attains a certain value in defining the critical load P^*_{crit}. This value was chose as u* = 6 and the critical load P^*_{crit} was obtained as minimum of the two values mentioned before. For the curves in Figure 8 the criterion u* = 6 is governing in all cases but it gives values close to the load maxima for the larger values of d*. The same is true for Figure 8 where not only d* but also R/t varies with the load displacement curve.

www.EngineeringEBooksPdf.com

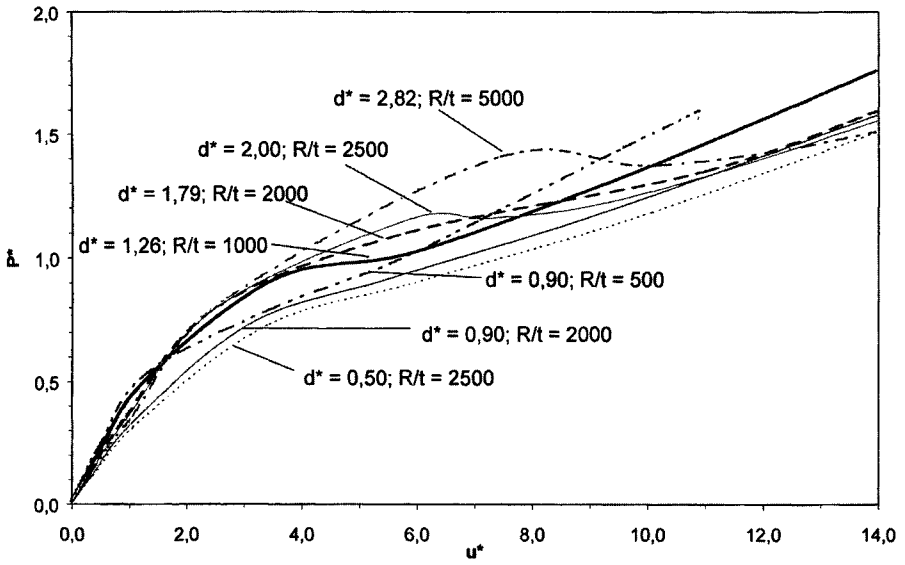

Figure 8: Nondimensional load displacement curve with $P^* = (P\ R)/(Et^3)$ and $u^* = u_0/t$ for the shells according to Figure 4 with different R/t and d* values and L/R = 2

Figure 9 shows that the nondimensional critical loads P^*_{crit} increases with the nondimensional diameter d* of the loaded area. The influence of R/t seems to be insignificant in this relation.

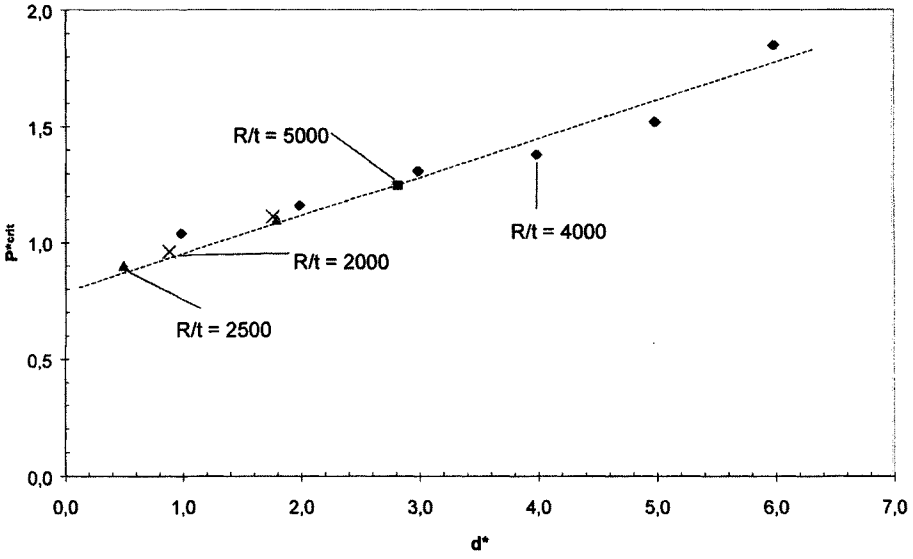

Figure 9: Critical loads P^*_{crit} based on deformation criterion P*(u*=6) and stability criteron

www.EngineeringEBooksPdf.com

CYLINDRICAL SHELL SUBJECTED TO A CIRCUMFERENTIAL MOMENT

Moments due to dead loads will predominantly have a vector in the horizontal direction. For cylindrical shells with vertical axis this moment vector will be in the circumferential direction. For this reason the second loading type of this investigation is a circumferential moment M. The nondimensional load parameter for this moment loading is chosen to be $M^* = (M)/(Et^3)(R/t)^{0,5}$. This is in line with Wichman et. al. (1965), where for the determination of stresses the geometry part of the nondimensional moment also differs from that for the nondimensional force by a factor $(R/t)^{0,5}$. The Finite Element model for this load case is identical with that for the radial force except for the boundary conditions at the cross section at half length of the cylinder (x = 0) where now antisymmetric boundary conditions are prescribed instead of the symmetric boundary conditions used before. The area with the nozzle diameter $d = 2r_p$ again is modelled with $E_p = 2E$ and $t_p = 2t$ to represent a rigid part within the shell. Due to this and to the antisymmetric boundary conditions it is sufficient to describe the circumferential moment M by a radial force on the symmetric boundary in this rigid area. $d^* = 2r_p/(Rt)^{0,5}$ is the nondimensional expression for the diameter of the area with $E_p = 2E$ and $t_p = 2t$ representing the nozzle.

The work of Bijlaard 1957 shows that for the spherical shell the rotation α of the rigid area depends only on M^* and d^* if it is multiplied by $(R/t)^{0,5}$. Therefore the nondimensional load parameter M^* is plotted in Figures 10 and 11 versus the rotation $\alpha^* = \alpha(R/t)^{0,5}$ of the rigid area for $d^* = 1,5$ and 2,0 with R/t varying from 2000 to 5000.

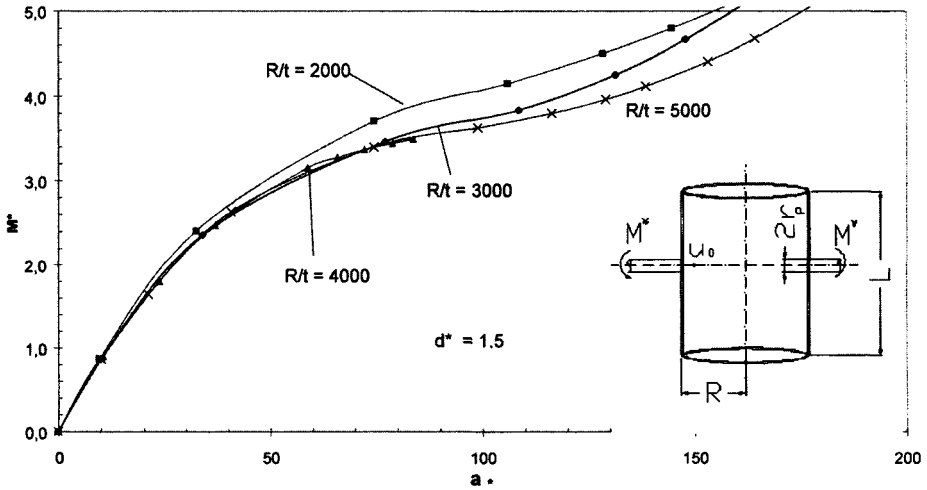

Figure 10: Nondimensional moment rotation curve for $d^* = 1,50$

www.EngineeringEBooksPdf.com

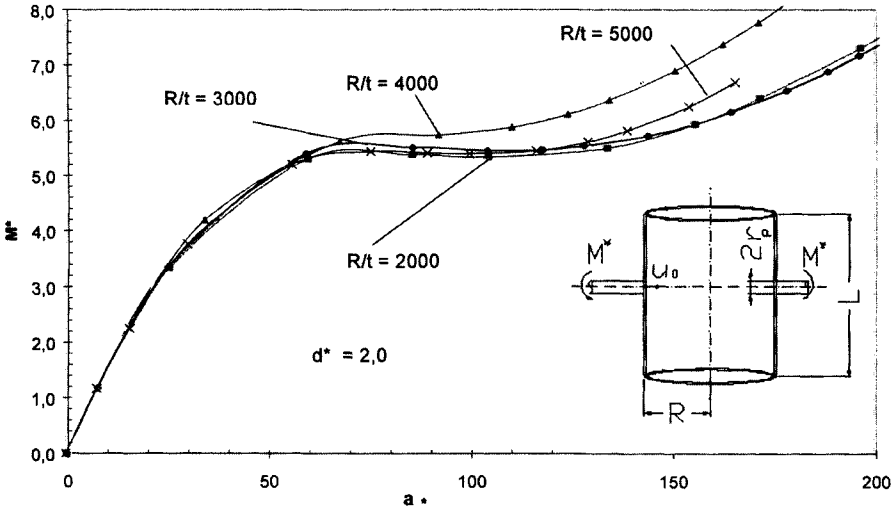

Figure 11: Nondimensional moment rotation curve for d* = 2,00

These plots confirm the missing or minor influence of R/t on this result. The nondimensional diameter d* is the dominating parameter. The solution of the problem is almost linear for small values of d*. The nonlinearity increases with increasing d*. With increasing nonlinearity there occurs a maximum in the load deformation curves which is associated with unstable equilibrium. The moment rotation curves beyond this maximum may be realised by deformation controlled actions, e.g. thermal expansion of the piping. The nondimensional moment rotation curves may be essentially characterised by the slope of the initial linear part C_0 and the moment values M_1* at the end of this linear part and M^*_{max} the first maximum of the curve. These values are plotted in Figure 12 together with the nondimensional load parameters M^*_{50} and M^*_{100} where the nondimensional rotation α^* is 50° and 100° respectively. With this Figure it must be kept in mind that for the values M^*_{max} exceeding M^*_{50} and M^*_{100} these latter values are in the postbuckling range.

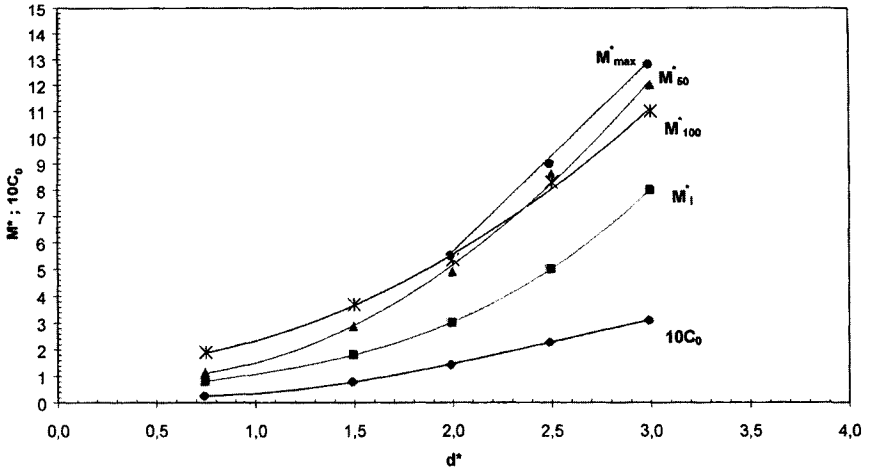

Figure 12: Parameters of the nondimensional moment rotation curves

www.EngineeringEBooksPdf.com

CONCLUSION

For elastic circular cylindrical shells subjected to radial loads and moment loads within a rigid circular area representing nozzles or mountings the nonlinear load deformation behaviour is investigated. If a nondimensional presentation is used the load deformation behaviour depends strongly upon the diameter of this rigid area whereas the R/t value is of negligible influence. The nonlinear load deformation curves have continuous positive slope for small values of the nondimensional diameter d* of the loaded area. They show a distinct knee when this parameter increases and with further increase a maximum with a subsequent stable postbuckling range. The nonlinear load displacement curves from this investigation may serve for spring models in the calculation of the loads, e.g. from thermal expansion, transferred to the shell and as basis for the design criterion, e.g. limitation of displacements.

REFERENCES

Biezeno C.B. (1935). Über die Bestimmung der Durchschlagkraft einer schwachgekrümmten kreisförmigen Platte. *Zeitschrift für angewandte Mathematik und Mechanik.* **15:10**, 10-22.

Bijlaard P.P. (1955). Stresses from local loadings in cylindrical pressure vessels. *Transactions of the ASME.* **77**, 805-816.

Bijlaard P.P. (1957). Computation of the stresses from local loads in spherical pressure vessels or pressure vessel heads. *Welding Research Council Bulletin.* **34**.

Fitch J.R. (1968) The buckling and post-buckling behaviour of spherical caps under concentrated load. *International Journal of Solids and Structures*. **4,** 421-446.

PD5500 (2000). *Specification for unfired fusion welded pressure vessels, Appendix G.* British Standards Institution.

Penning A. and Thurston G.A. (1965). The stability of shallow spherical shells under concentrated load. *NASA Contract Report 265.*

Penning F.A. (1966). Experimental buckling modes of clamped shallow shells under concentrated load. *Transactions of the ASME, Journal of Applied Mechanics.*297-304.

Wichman K.R., Hopper A.G.and Mershon J.L. (1965). Local stresses in spherical and cylindrical shells due to external loadings. *Welding Research Council Bulletin.* **107**.

www.EngineeringEBooksPdf.com

Advances in Steel Structures, Vol. II
Chan, Teng and Chung (Eds.)
© 2002 Elsevier Science Ltd. All rights reserved.

BUCKLING OF CIRCULAR STEEL SILOS SUBJECT TO ECCENTRIC DISCHARGE PRESSURES-PART I

C.Y. Song and J.G. Teng

Department of Civil and Structural Engineering
The Hong Kong Polytechnic University, Hong Kong, China

ABSTRACT

The buckling strength of steel silos subject to eccentric discharge has been a subject of great interest to designers and researchers in this area. This paper presents a finite element study on the buckling behaviour and strength of an example circular steel silo subject to code-specified eccentric discharge pressures. Four well-known silo loading codes, namely the Australian code, the German code, the ISO code and the European code, are employed to predict wall pressures in silos during eccentric discharge, which lead to very different wall pressures. These differences are passed on to the linear bifurcation buckling loads. The Australian code leads to the lowest bifurcation load, while the German code the highest. The latter is 2.7 times the former for the example silo. The effect of geometric nonlinearity on the buckling load is shown to depend on the sources of the meridional membrane compressive stress. A great beneficial effect is found when bending deformation due to non-uniformity of horizontal pressures is a major source. Imperfection-sensitivity analysis of the silo demonstrates that the linear bifurcation modes do not provide the worst imperfection form, as an axisymmetric weld depression is much more detrimental.

KEYWORDS

Silos, Shells, Buckling, Eccentric Discharge, Patch Loads, Imperfection Sensitivity, Silo Loading Codes

INTRODUCTION

Buckling of the cylindrical shell wall under axial compressive stresses is a common failure mode for circular steel silos (e.g. Ross *et al.* 1980; Ravenet 1981; Rotter *et al.* 1989; Allen 1989; Clercq 1990; Pavlovic 1997; Wood 1997). Steel silos subject to eccentric discharge are particularly vulnerable to buckling failures of this kind, so silo designers have often been advised to avoid eccentric discharge if at all possible (e.g. AS3774 Supp1-1997, 1997). However, practical considerations such as the cost and ease of access often require the use of eccentric discharge. On the other hand, even for silos designed for concentric discharge, eccentric discharge effects are difficult to avoid due to factors such as material segregation (Rotter 2001a) and the sequential opening and closing of multiple outlets.

A well-known consequence of eccentric discharge is the development of non-uniform horizontal pressures. This pressure non-uniformity produces circumferential as well as meridional bending, and associated membrane actions. The stress state in a silo subject to eccentric discharge is very complex

www.EngineeringEBooksPdf.com

(Brown 1996; Guggenberger 1996; Rotter 1996; Rotter 2001a, 2001b), so simplified analytical methods such as those employed for wind loads (e.g. Pecknold 1989) can only provide approximate solutions. In terms of possible failure modes, yielding of the silo wall as a result of severe bending has been suggested as a possibility (Jenike 1967; Roberts and Ooms 1983), but a buckling failure is generally expected due to the development of high local axial compressive stresses at the base of the silo (Buchert 1967; Rotter 1986).

Despite many studies on pressure distributions in silos subject to eccentric discharge, the development of a widely accepted pressure model is still some time away. As a result, instead of the adoption of a sophisticated but still inaccurate pressure model, recent silo loading codes have opted for the patch load approach. In this approach, a patch load with a continuous circumferential distribution or a pair of isolated patch loads is specified to account for the effects of pressure non-uniformity of actual eccentric discharge pressures (DIN1055-6 1987; ISO11697 1995; ENV1991-4 1995). Different loading codes specify patch loads which differ greatly in their size, position and location, which is at least partly attributable to the lack of precise information on pressures in eccentrically discharged silos. The Australian code (AS3774-1996 1996) on the other hand specifies a pressure pattern intended to approximate real discharge pressures. For simplicity, the additional pressure blocks specified by the Australian code for eccentric discharge are also referred to as patch loads in this and the companion paper (Song and Teng 2002).

In general, the specification of patch loads to represent the effect of real eccentric discharge pressures has been done without a rigorous assessment of their structural consequences. Indeed, very limited research has been carried out on the structural response of steel silos subject to these patch loads (Rotter 1986, 1996, 2001a; Guggengerber 1996). The few existing studies have either been based on linear finite element analysis (Rotter 1986, 2001a) or concentrated on perfect silos (Guggengerger 1996; Rotter 2001a). A rigorous non-linear numerical study of the buckling behaviour and strength of steel silos subject to eccentric discharge pressures is therefore urgently needed, both for a better understanding of structural behaviour and for an assessment of the different consequences of different pressure patterns specified by the existing loading codes. In this paper, four different pressure patterns from the Australian code (AS3774-1996 1996), the German code (DIN1055-6 1987), the ISO code (ISO11697 1995) and Part 4 of Eurocode 1 (ENV1991-4 1995) respectively are first compared. Results from a hierarchy of buckling analyses of a silo under these pressures are next presented and compared. All four loading codes are well recognised and widely referred to by the international silo design community. The four pressure patterns are referred to simply as the AS pressures, the DIN pressures, the ISO pressures and the Eurocode pressures hereafter. It should be noted that Part 4 of Eurocode 1 is referred to as the Eurocode or the European code for convenience. Two parts of Eurocode 3 (ENV1993-1-6 1999; ENV 1993-4-1 1999) are also referred to in both this paper and the companion paper (Song and Teng 2002); they are more precisely referenced for differentiation from the silo loading code.

PRESSURES IN ECCENTRICALLY DISCHARGED SILOS

Bulk Solid Properties

Before pressures in a silo can be predicted, the relevant properties of the stored solid have to be defined first. The key properties of a bulk solid for the structural design of silos are its unit weight γ, angle of wall friction ϕ_w ($\mu = \tan\phi_w$), effective angle of internal friction ϕ_i, and horizontal/vertical pressure ratio κ. For frequently encountered bulk solids such as wheat, all four loading codes under consideration give characteristic values of these properties. Conversions of characteristic values into design values differ from code to code.

Table 1 lists the upper and the lower characteristic value given in the Australian code (AS3774-1996 1996) for both ϕ_w and ϕ_i to cover the range of values that wheat may exhibit, with the wall roughness being Type D2 which is appropriate for a painted carbon steel surface.

www.EngineeringEBooksPdf.com

Table 2 lists the material properties of wheat from the DIN, ISO and European codes. The DIN code directly specifies bulk solid properties for design use. The ISO and European codes provide mean values of κ and μ and then use two conversion factors (0.9 and 1.15) to obtain values that represent extremes of the material properties, in order to account for the inherent variability of bulk solid properties. In both Tables 1 and 2, the value for the unit weight γ is the upper limit which is recommended by all four codes for use in the calculation of wall pressures.

TABLE 1
CHARACTERISTIC VALUES OF MATERIAL PROPERTIES
OF WHEAT FROM THE AUSTRALIAN CODE

Unit weight	ϕ_w		ϕ_i	
γ	Lower	Upper	Lower	Upper
9.0kN/m^3	18°	30°	26°	32°

TABLE 2
MATERIAL PROPERTIES OF WHEAT FROM
THE DIN, ISO AND EUROPEAN CODES

DIN			ISO			Eurocode		
γ	k	μ	γ	κ_m	μ_m	γ	κ_m	μ_m
9.0 kN/m^3	0.60	0.25	8.5 kN/m^3	0.60	0.30	9.0 kN/m^3	0.55	0.30

Load Cases

For large size thin-walled steel silos subject to eccentric discharge, the main failure mode is expected to be buckling of the silo wall. This buckling is due to the axial compressive stresses, which arise from both the wall frictional pressure and the complex bending action produced by non-uniform horizontal pressures. If other load effects are not important, the stability assessment of silos subject to eccentric discharge should consider the following two load cases: (a) Load Case I: maximum frictional pressures with corresponding horizontal wall pressures, plus patch loads; and (b) Load Case II: maximum horizontal wall pressures with corresponding frictional pressures, plus patch loads. Tables 3 lists values of bulk solid properties appropriate for use for the two load cases according to the Australian, European and ISO codes.

TABLE 3
DESIGN VALUES OF BULK SOLID PROPERTIES
ACCORDING TO THE AUSTRALIAN, ISO AND EUROPEAN CODES

	AS			ISO and Eurocode	
Parameter	ϕ_w	κ	ϕ_i	κ	μ
Load Case I	Upper	Upper	Lower	$1.15\kappa_m$	$1.15\mu_m$
Load Case II	Lower	Upper	Lower	$1.15\kappa_m$	$0.9\mu_m$

The axisymmetric internal pressure (excluding patch loads) in a steel silo is generally beneficial to the buckling strength unless it becomes very high. However, this beneficial effect can only be utilized when the internal pressure can be guaranteed to co-exist with the axial compression; otherwise, it will lead to the overestimation of the buckling strength. For a safe design, the Australian code defines a minimum reliable horizontal wall pressure for the assessment of buckling strength of steel silos subject to concentric discharge, which is 0.8 times the horizontal wall pressure calculated according to the procedure outlined above. For eccentric discharge, it has been recommended that professional advice should be sought on the minimum reliable wall pressure (AS3774 Supp1-1997, 1997). In the present study, without any better

www.EngineeringEBooksPdf.com

information, the minimum horizontal wall pressure was also taken to be 0.8 times the horizontal wall pressure normally calculated.

For checking the buckling and bulging strength of steel silos, the German code requires that the wall frictional pressure be increased by 10% and the horizontal wall pressure be simultaneously reduced by a factor of $0.5(1\text{-}2e/D) \geq 0.167$ where D is the diameter of the silo and e is the eccentricity of discharge outlet (i.e. the radial distance between the centre of the silo and the centre of the outlet).

Wall Pressures in the Example Silo

Based on the information given above and additional information given in the four loading codes, the wall pressures in a silo can be predicted without difficulty. For a silo subject to eccentric discharge, the wall pressures consist of two components: an axisymmetric component which is the same as that for a silo subject to concentric discharge and an unsymmetric component (the patch load component) which is intended to account for the effect of discharge eccentricity. Figures 1 and 2 show the axisymmetric

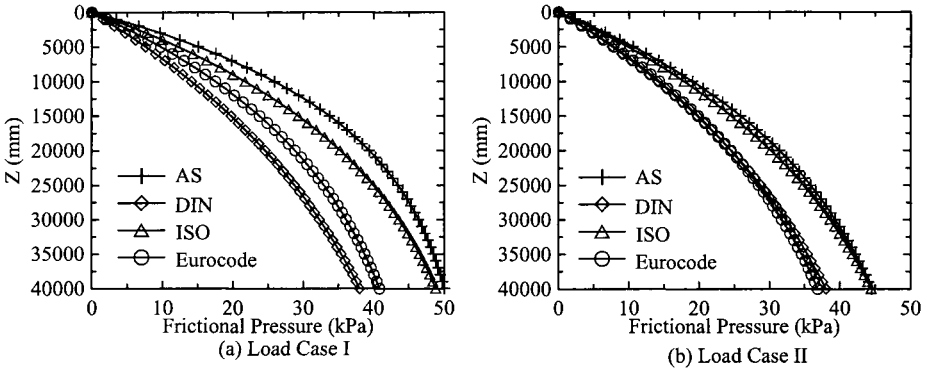

Figure 1: Frictional pressures predicted by different silo loading codes

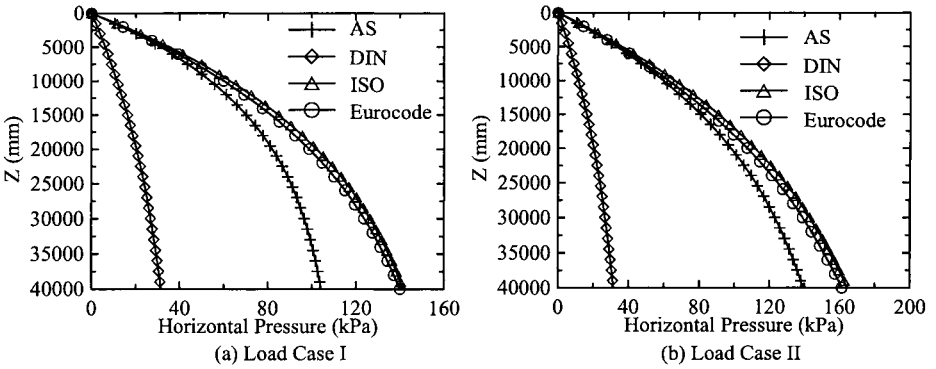

Figure 2: Horizontal pressures predicted by different silo loading codes

component predicted by the four silo loading codes for an example silo with a diameter D of 20 metres and a height-to-diameter ratio of 2 (i.e. H/D = 2) for Load Case I and Load Case II respectively. The vertical distributions of downward frictional pressures are shown in Figure 1, where substantial differences between the four different codes are seen. The AS code predicts the highest frictional pressures for both load cases. The DIN code predicts the lowest values for Load Case I and almost the lowest for Load Case II.

www.EngineeringEBooksPdf.com

The vertical distributions of horizontal wall pressures for both Load Case I and Load Case II as predicted by the four loading codes are shown in Figure 2. The predictions of the ISO code agree closely with those of the Eurocode for both load cases, while the DIN code predicts much lower horizontal wall pressures as this code recommends a reduction of horizontal wall pressures by a factor of 0.5(1-2e/D). The present example silo was assumed to have a discharge eccentricity of 0.25D, which means that this reduction factor is 0.25. The horizontal wall pressures recommended by the AS code are also lower than those of the ISO code and the Eurocode.

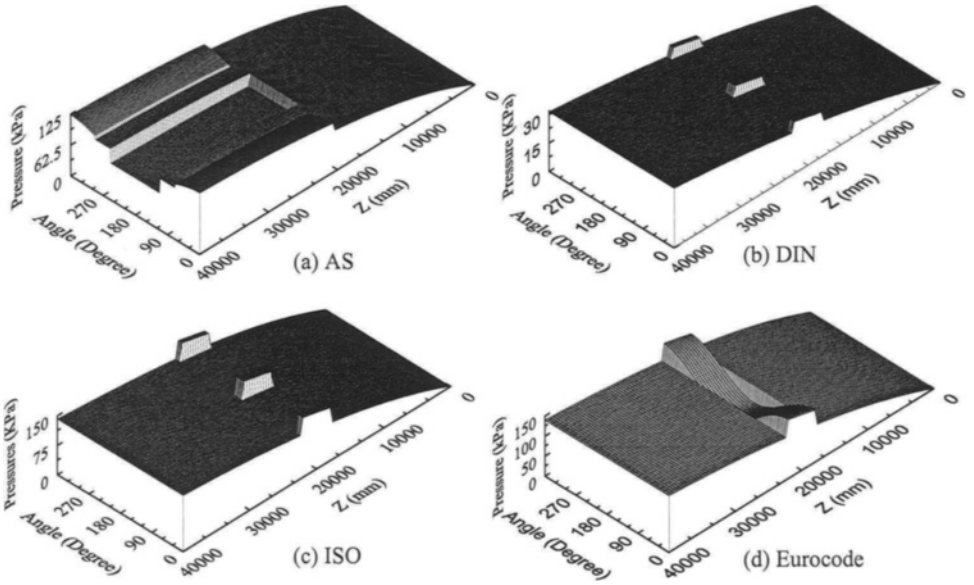

Figure 3: Horizontal wall pressure distributions predicted by different silo loading codes for Load Case I

Three-dimensional views of the distributions of horizontal wall pressures for Load Case I, including patch loads as specified by the four loading codes, are shown in Figure 3. In general, the DIN, ISO and European codes require consideration of the patch loads placed anywhere over the silo height. Simplified treatments for the position of patch loads are also suggested in the ISO and European codes. For simplicity, the patch loads in the present study are assumed to be centred at the mid-height of the silo wall for pressures predicted by the DIN, ISO and European codes. This simplification is consistent with the recommendations of these codes. For the AS pressures, the patch loads are distributed in strict accordance to the specification of the code.

FINITE ELEMENT BUCKLING ANALYSIS

Silo Geometry and Material Properties

In the present study, numerical investigations were carried out for an example simply supported flat-bottomed steel silo using the well-known general purpose package ABAQUS (Hibbit, Karlsson & Sorensen 1998). The height and diameter of the example silo are defined in the preceding section (i.e. D = 20 m and H/D = 2). For this example silo, the code-specified eccentric discharge wall pressures are

www.EngineeringEBooksPdf.com

shown in Figures 1-3. The wall thickness of the silo t was determined to be 25 mm according to the wall loads predicted by the Australian code (AS3774-1996 1996) with the recommendations of Part 1-6 of Eurocode 3 (ENV1993-1-6 1999) on the strength and stability of steel shells without considering the effect of patch loads. The meridional membrane stress and the internal pressure required to determine the silo thickness are those at the base of the silo where buckling is expected to occur for a silo of constant wall thickness. The steel of the silos was assumed to be elastic-perfectly plastic and to have the following properties: elastic modulus $E = 2 \times 10^5$ MPa, yield stress $f_y = 250$ MPa, and Poisson's ratio $\upsilon = 0.3$.

Finite Element Modelling

As a result of the differences in patch load distributions predicted by different loading codes, the finite element models employed also differ. With the DIN and ISO pressures, the patch loads act on two diametrically opposite square areas (Figures 3b and 3c), so a quarter-structure model was employed. With the Eurocode and AS pressures, the patch loads possess only one axis of symmetry (Figures 3a and 3d), so the finite element models included a symmetric half of the structure. The wall pressures were transformed into equivalent nodal loads. The 4-node thin shell element S4R5 was employed. The roof was omitted in the finite element model, so only a cylindrical shell was modelled. At the bottom end of the cylinder, the radial, circumferential, and meridional displacements were all prevented, while at the top end of the cylinder, only radial and circumferential displacements were restrained. The rotational degrees of freedom on the two ends of the cylinder were treated as suggested in Song (2002) to suppress the possible spurious modes associated with them.

Types of Buckling Analysis

The following four types of analysis were conducted for the example silo:

1) LBA—Linear Bifurcation Analysis of the perfect silo;
2) GNA—Geometrically Non-linear elastic Analysis of the perfect silo;
3) GMNA—Geometrically and Materially Non-linear Analysis of the perfect silo;
4) GMNIA — Geometrically and Materially Non-linear Imperfect silo Analysis

These analysis types (LBA, GNA, GMNA and GMNIA) are all recommended by Part 1-6 of Eurocode 3 (ENV1993-1-6 1999) for the determination of load carrying capacity when checking the buckling limit state, although the LBA type is only part of the LA (Linear elastic Analysis) type recommended by Eurocode 3. It is well known that the buckling strength of shells is generally sensitive to fabrication imperfections and thus the quality of construction. In the present study, quality classes specified in Eurocode 3 (ENV1993-1-6 1999) are referred to. The particular quality class a shell belongs to determines the amplitude of equivalent geometric imperfections for use in GMNIA and GNIA types of analysis.

FINITE ELEMENT BUCKLING LOADS

LBA Results

The linear bifurcation loads of the example silo subject to eccentric discharge pressures predicted by the four silo loading codes are shown in Figure 4. Only Load Case I, as defined earlier, consisting of maximum frictional pressures and corresponding horizontal wall pressures in addition to patch loads, is considered here due to space limitation, as Song (2002) has demonstrated that Load Case I is generally more detrimental than Load Case II. The vertical axis in Figure 4 is the load factor over the base wall loads P_{base} which are wall loads during discharge predicted by the four loading codes. The base wall loads vary from code to code, but they represent the loads expected to be present in a fully filled silo during eccentric discharge.

www.EngineeringEBooksPdf.com

It can be observed from Figure 4 that large differences exist between the linear bifurcation loads of the silo subject to pressures predicted by the four silo loading codes. The highest load factor is around 2.7 times the lowest one. The AS pressures lead to the lowest linear bifurcation load and the DIN pressures the highest. While the magnitudes of the linear bifurcation loads have the same trend as that of the frictional pressures in the example silo (Figure 1), the former show much larger differences as a result of additional differences due to the different patch loads. Figure 5 shows the corresponding linear bifurcation modes of the silo. The buckling deformation is concentrated near the base of the silo. The linear bifurcation mode due to the Eurocode pressures is less localised than those due to the other three pressure patterns, consistent with the circumferential distributions of path loads.

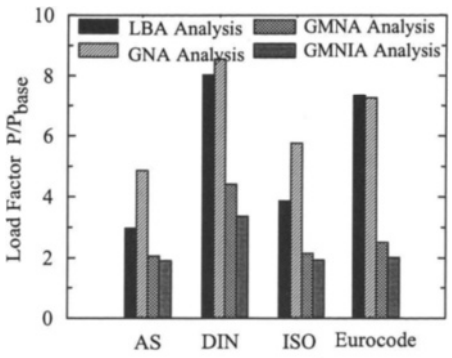

Figure 4: Buckling loads of the example silo from different analysis types

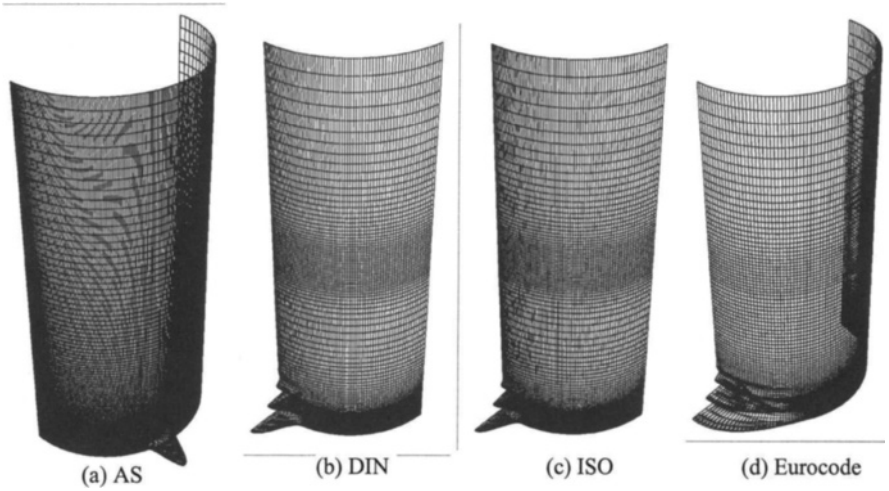

Figure 5: Linear bifurcation buckling modes

GNA and GMNA Results

The results of geometrically non-linear analysis (GNA) are also presented in Figure 4. This figure demonstrates that the DIN pressures still lead to the highest value while the AS pressures still the lowest. The ratio between the highest and the lowest buckling load is however substantially reduced to 1.8 from 2.7 for the linear bifurcation loads. These results show that geometric nonlinearity may have a beneficial effect (for the AS, DIN, ISO pressures) or a deleterious effect (for the Eurocode pressures) on the buckling load.

Figure 6 shows the ratios of the GNA loads to the LBA loads. These ratios are a measure of the effect of geometric non-linearity. It is seen that this effect is very strong and beneficial for the AS and ISO pressures, resulting in increases of more than 60% in the buckling load. For the DIN pressures, this effect is small (6.5%) but also beneficial. For the Eurocode pressures, the effect of geometrical non-linearity leads to a slight reduction in the buckling load.

www.EngineeringEBooksPdf.com

Figure 7 shows the relative contributions to the maximum meridional membrane compressive stress by the frictional pressures and the patch loads from linear analysis for each of the four pressure patterns. Around 54% and 45% of the maximum axial membrane compressive stress are due to the patch loads in the cases of the AS and ISO pressures respectively, but for the DIN pressures, this is only 11.7%. For the Eurocode pressures, only 1.3% is from the patch loads. From Figure 7, it can be concluded that a larger beneficial effect from geometric non-linearity is available if a larger part of the meridional membrane compressive stress comes from the bending deformation due to patch loads.

The limit point buckling loads from GMNA analyses in Figure 4 show that material non-linearity is important. Large reductions are observed for all four pressure patterns.

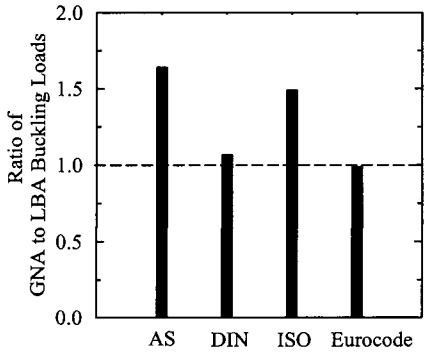

Figure 6: Ratios of GNA to LBA buckling loads

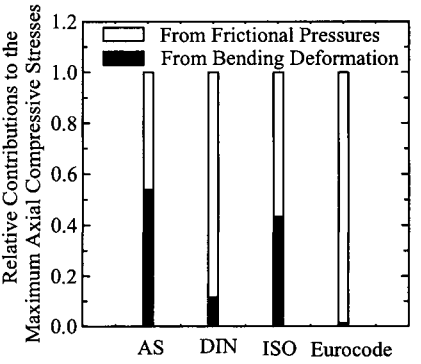

Figure 7: Sources of the maximum axial compressive stress

GMNIA Results

The buckling loads of the silo with assumed imperfections found from GMNIA analyses are also included in Figure 4. These buckling loads were obtained with imperfections in the form of the linear bifurcation mode (LBM imperfections) (Figure 5). The imperfection amplitude was determined according to Part 1-6 of Eurocode 3 (ENV1993-1-6 1999) assuming normal fabrication quality, which yielded an imperfection amplitude of $\delta/t = 2.5$.

Figure 4 shows that the silo is not very sensitive to imperfections of this sort when it is subject to the AS and ISO pressures. The DIN and Eurocode pressures lead to a rather different scenario: the silo is now significantly more sensitive to LBM imperfections. The buckling loads from GMNIA analyses suggest that the LBM imperfection is probably not the worst imperfection form.

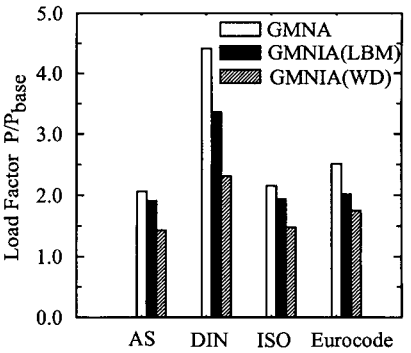

Figure 8: Limit point loads from the GMNA and GMNIA analyses

Figure 8 compares the buckling loads of the silo from GMNA analyses and two sets of GMNIA calculations corresponding to two types of geometric imperfections: LBM imperfections and weld depression (WD) imperfections. The exact form of the latter type of imperfections was assumed to be that of the Type A weld depression (WD) of Rotter and Teng (1989), which was proposed to represent axisymmetric depressions associated with continuous circumferential welded joints between circular strakes in steel silos and tanks. The WD imperfections were centred at one linear meridional bending half-wavelength away from the base to avoid

www.EngineeringEBooksPdf.com

a significant load eccentricity at the base, and considering that the first circular strake of a silo is at least as long as this half wavelength and the high meridional compressive stresses are localized near the support. Weld depressions centred at higher positions were briefly explored, which confirmed that a weld centre height of one meridional bending half wavelength is appropriate. The comparison in Figure 8 demonstrates that the WD imperfections have a much more detrimental effect on the buckling load than the LBM imperfections for the same fabrication quality class.

CONCLUSIONS

This paper has been concerned with the buckling behaviour of an example steel silo subject to wall loads predicted by four well-known silo loading codes: the Australian code (AS3774-1996 1996), the German code (DIN1055-6 1987), the ISO code (ISO11697 1995) and the part 4 of Eurocode 3 (ENV1991-4 1995). The following conclusions can be drawn:

1. Wall loads in a silo subject to eccentric discharge predicted by the four well-known loading codes vary greatly from code to code. As a result, great differences exist between the linear bifurcation loads of the perfect silo subject to wall loads predicted by the four different loading codes. These large differences are however substantially reduced once the effect of geometric nonlinearity is taken into account in a more sophisticated buckling analysis.
2. Geometric nonlinearity can reduce or increase the buckling load, depending on the sources of the meridional membrane compressive stress in the silo. If a large percentage of the axial membrane compressive stress is from patch loads, geometric nonlinearity substantially increases the buckling load.
3. Material non-linearity reduces the buckling load substantially, even though the silo considered is a very thin shell (R/t=400).
4. The buckling strength is sensitive to geometric imperfections. Imperfections in the form of the linear bifurcation mode however have a much smaller effect on the buckling load except for the DIN pressure pattern than axisymmetric weld depressions.

The first conclusion appears to suggest that the patch loads as specified by existing silo loading codes to represent the effect of discharge eccentricity are likely to be much less important as may be gauged from a linear stress analysis or a linear bifurcation analysis. A comprehensive study of this issue will be presented in the companion paper (Song and Teng 2002) where the buckling resistances of steel silos deduced from finite element calculations are also discussed.

ACKNOWLEDGMENTS

The work described here forms part of the project "Buckling Strength of Steel Cylindrical Shells under a General State of Non-uniform Stresses" funded by the Research Grants Council of the Hong Kong SAR (Project No. PolyU 5081/97E), with additional support from The Hong Kong Polytechnic University. The authors are grateful to both organizations for their financial support.

REFERENCES

Allen, M.F. (1989). Testing, evaluation and repair methods for structural stability of coal silos. *Proc., the 51th American Power Conference*, pp. 788-797.

AS3774-1996 (1996). *Loads on Bulk Solids Containers.* Standards Australia, Sydney.

AS3774 Supplement 1-1997 (1997). *Loads on Bulk Solids Containers - Commentary.* Standards Australia, Sydney.

www.EngineeringEBooksPdf.com

Brown, C.J. (1996). *Effect of Patch Loads on Rectangular Metal Silos and Annex*. Department of Mechanical Engineering, Brunel University, Uxbridge, UK.

Buchert, K.P. (1967). Discussion of 'Denting of circular bins with eccentric drawpoints', by Jenike, A.W. *J. Struct. Div., ASCE*, **93:3**, 318-319.

Clercq, H. De. (1990). Investigation into stability of a silo with concentric and eccentric emptying. *Civil Engineer in South Africa*, **32:3**, 103-107.

DIN1055-6 (1987). *Design Loads for Buildings: Loads in Silo Bins*, Deutsches Institut fur Normung, Berlin, May.

ENV1991-4 (1995). *Eurocode 1: Basis of Design and Actions on Structures, Part 4: Actions in Silo and Tanks*. European Committee for Standardisation, Brussels.

ENV1993-1-6 (1999). *Eurocode 3: Design of Steel Structures, Part 1-6: General Rules-Supplementary Rules for the Strength and Stability of Shell Structures.* European Committee for Standardisation, Brussels.

ENV1993-4-1 (1999). *Eurocode 3: Design of Steel Structures, Part 4-1: Steel Silos*. European Committee for Standardisation, Brussels.

Guggenberger, W. (1996). *Patch Loads and Their Use in Metal Silo Design—Strand 3: Effect of Patch Loads on Stiffened Circular Cylindrical Silos*. Institute for Steel, Timber and Shell Structures, Technical University of Graz, Austria.

Hibbit, Karlsson & Sorensen (1998). ABAQUS/Standard *Theory and User's Manuals*.

ISO11697 (1995). *Bases for Design of Structures—Loads Due to Bulk Materials*.

Jenike, A.W. (1967). Denting of circular bins with eccentric drawpoints. *J. Struct. Div., ASCE*, **93:ST1**, 27-35.

Pavlovic, P. (1997). The testing and repair of steel silo. *Construction and Building Materials*, **34**, 101-109.

Pecknold, D.A. (1989). Load transfer mechanisms in wind-loaded cylinders. *J. Eng. Mech., ASCE*, **115:11**, 2353-2367.

Ravenet, J. (1981). Silo problems. *Bulk Solid Handling*, **1:4**, 667-679.

Roberts, A.W. and Ooms, M. (1983). Wall loads in large steel and concrete bins and silos due to eccentric draw-down and other factors. *Proc., 2nd Int. Conf. on Design of Silos for Strength and Flow*, Strstford-Upon-Avon Hilton, 7-9, Nov., pp. 151-170.

Ross, I.J., Moore, D.W., Lower, O.J. White, G.M. (1980). Model studies of grain bin failure. *Paper No. 80-2-264, Winter Meeting, ASAE,* Chicago, Dec.

Rotter, J.M. (1986). The analysis of steel bins subject to eccentric discharge. *Proc., 2nd Int. Conf. on Bulk Material Storage, Handling and Transportation*, Wollongong, 7-9 Jul., pp. 264-271.

Rotter, J.M. (1996). Patch load effects in unstiffened steel silos. *Proc., CA-Silo Project on the Effect of Patch Loads on Metal Silos,* CA-Silo, Edinburgh, pp. 5-195.

Rotter, J.M. (2001a). *Guide for Economic Design of Circular Metal Silos*. Spon, London.

Rotter, J.M. (2001b). Pressures, stresses and buckling in metal silos containing eccentrically discharging solids. *60th Birthday Celebration for Univ.-Prof. Dipl.-Ing. Dr.techn. Richard Greiner*, Oct. 12, 2001, Institute for Steel, Timber and Shell Structures, Technical University Graz, Austria.

Rotter, J.M., Jumikis, P.T., Fleming, S.P. and Porter, S.J. (1989). Experiments on the buckling of thin-walled model silo structure. *J. Construct. Steel Res.*, **13**, 271-299.

Rotter, J.M. and Teng, J.G. (1989). Elastic stability of cylindrical shells with weld depressions. *J. Struct. Engrg., ASCE*, **115:5**, 1244-1263.

Song, C.Y. (2002). *Buckling of Shells under Non-uniform Stress States*. Ph.D. Thesis, Department of Civil and Structural Engineering, The Hong Kong Polytechnic University.

Song, C.Y. and Teng, J.G. (2002) Buckling of circular steel silos subject to eccentric discharge pressures – Part II. *Proc., 3rd Int. Conf. on Advances in Steel Structures,* December, Hong Kong, China.

Wood, J.G.M. (1997). Silos: evolution by failure. *Structural Engineering International*, **7:2**, 116-117.

www.EngineeringEBooksPdf.com

Advances in Steel Structures, Vol. II
Chan, Teng and Chung (Eds.)
© 2002 Elsevier Science Ltd. All rights reserved.

BUCKLING OF CIRCULAR STEEL SILOS SUBJECT TO ECCENTRIC DISCHARGE PRSESURES-PART II

C.Y. Song and J.G. Teng

Department of Civil and Structural Engineering
The Hong Kong Polytechnic University, Hong Kong, China

ABSTRACT

The eccentric discharge pressures specified by leading silo loading codes include an axisymmetric component which is the same as that for a silo subject to concentric discharge and an unsymmetric component in the form of patch loads which is intended to represent the detrimental effect of discharge eccentricity. Little information is currently available on the effect of these patch loads on the buckling strength of a circular steel silo, but results presented in the companion paper appear to suggest that the patch loads as specified by existing silo loading codes are likely to be much less important as may be gauged from a linear stress analysis or a linear bifurcation analysis. In this paper, finite element buckling loads from different types of analysis are first presented to clarify the effect of patch loads. Buckling resistances derived from finite element buckling loads according to the procedures given in Eurocode 3 are next presented and compared.

KEYWORDS

Silos, Shells, Buckling, Eccentric Discharge, Patch Loads, Buckling Resistance, Silo Loading Codes

INTRODUCTION

In the companion paper (Song and Teng 2002), the pressures in and the buckling behaviour of an example steel silo subject to code-specified eccentric discharge pressures were examined. It was shown there that eccentric discharge pressures as predicted by four well-known silo loading codes (AS3773-1996 1996; DIN1055-6 1987; ISO11697 1995 and ENV1991-4 1995) are very different, which also lead to very different linear bifurcation loads. These large differences in buckling loads, however, become much smaller once geometric nonlinearly is taken into account in the buckling analysis, pointing to the possibility that the patch loads used to represent the effect of discharge eccentricity may not be effective if buckling loads are determined using one of the more sophisticated types of analysis instead of a linear bifurcation analysis. In this paper, finite element buckling loads from different types of analysis are first presented to clarify the effect of patch loads. Buckling resistances derived from finite element buckling loads according to the procedures given in Eurocode 3 (ENV1993-1-6 1999; ENV 1993-4-1 1999) are next presented and compared.

www.EngineeringEBooksPdf.com

SELETED SILO GEOMETRIES

In order to evaluate the effect of patch loads on the buckling strength of circular steel silos, steel silos of three typical aspect ratios were selected for investigation: H/D = 1, 2, and 4, where H is the height and D the diameter of the silo which is fixed to be 20 metres. The steel of the silos and the stored wheat have properties as detailed in the companion paper (Song and Teng 2002). The thicknesses of the silos were determined to correspond to reasonable load factors over the base wall loads in a fully-filled silo to cause buckling failures according to the recommendations of Part 1-6 of Eurocode 3 (ENV1993-1-6 1999) without considering the effect of patch loads. The meridional membrane stress and the primary pressure (i.e. excluding patch loads) required to determine the silo thickness are those at the base of the silo where buckling is expected to occur for a constant thickness over the height. The chosen wall thicknesses and the corresponding load factors to cause buckling failures of these silos subject to wall loads from the Australian code (AS3773-1996 1996) are shown in Table 1. During these calculations, the partial safety factor, which is used to define a design buckling resistance from a characteristic buckling resistance, was ignored. While only silos of constant thickness are considered, the three silos studied here can be interpreted to represent the behaviour of different sections of a tall silo in which the wall thickness reduces up the height. These three silos are referred to as thin, medium and thick silos respectively according to their thicknesses, with the medium silo being the example silo examined in the companion paper (Song and Teng 2002).

TABLE 1
LOAD FACTORS OF SILOS SUBJECT
TO PRIMARY WALL LOADS FROM THE AUSTRALIAN CODE

H/D	1	2	4
Thickness t (mm)	10	25	40
Load factor	1.09	1.64	1.50

Table 2 lists the three buckling failure load factors for the medium silo when subject to primary wall loads predicted by the other three loading codes (i.e. the DIN, ISO and European codes). All three load factors are greater than that for the AS primary wall loads, indicating that the AS primary wall loads lead to the most conservative design, while the most un-conservative design results from the Eurocode primary wall loads, with the former load factor being 70% of the latter. These results illustrate that there are substantial differences in the predicted load factor even for a silo subject to axisymmetric primary wall loads due to differences between the loading codes.

TABLE 2
LOAD FACTORS OF THE MEDIUM SILO SUBJECT
TO PRIMARY WALL LOADS OF THREE SILO LOADING CODES

Code	DIN1055-6 (1987)	ISO11697 (1995)	ENV1991-4 (1995)
Load factor	1.79	2.01	2.34

EFFECT OF PATCH LOADS ON FINITE ELEMENT BUCKLING LOADS

The patch loads considered here are those predicted by the four silo loading codes (AS3773-1996 1996; DIN1055-6 1987; ISO11697 1995; ENV1991-4 1995) for a discharge eccentricity e=0.25D as considered in the companion paper (Song and Teng 2002). The patch loads determined using the DIN, ISO and European codes were assumed to be centred at the mid-height of the silo for simplicity and because the position of patch loads only has a limited effect on the stress state in a silo as shown in Song (2002). The patch loads of the Australian code are distributed in strict accordance to the specification of the code.

www.EngineeringEBooksPdf.com

Buckling analyses of five types, including the four types (LBA, GNA, GMNA, GMNIA) recommended in Eurocode 3 (ENV1993-1-6 1999) as well geometrically nonlinear analyses with imperfections (GNIA) were carried out for the three silos. The corresponding buckling loads are designated as LBA, GNA, GMNA, GNIA and GMNIA buckling loads. The effect of patch loads on these buckling loads is evaluated by comparing two sets of buckling loads: one for silos subject to

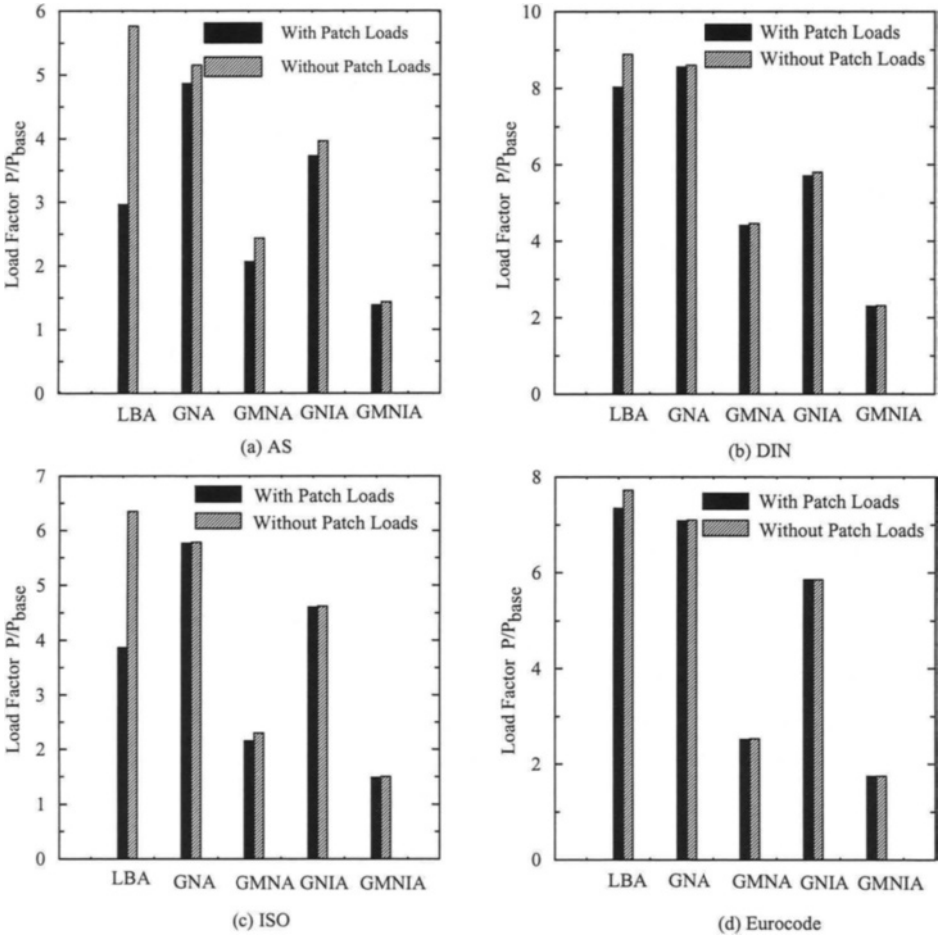

Figure 1: Buckling loads of the medium silo subject to wall loads predicted by different silo loading codes

eccentric discharge pressures which consist of the primary wall loads plus the eccentric discharge patch loads and the other for silos subject to primary wall loads alone. Figures 1a-1d show the buckling loads of the medium silo. In the GNIA and GMNIA analyses, the geometric imperfection used is that of Rotter and Teng's (1989) Type A weld depression, as this imperfection is more detrimental than one in the form of the linear bifurcation mode (Song and Teng 2002). The imperfection is centred at a distance of one linear meridional bending half wavelength from the base as was adopted in Song and Teng (2002). Assuming that the fabrication quality is of the normal class, the amplitude of imperfection is 2.5 times the wall thickness (i.e. δ/t=2.5), according to Part 1-6 of Eurocode 3 (ENV1993-1-6 1999). Figures 1a-d show that the patch loads have the largest effect on the

www.EngineeringEBooksPdf.com

LBA results. Once geometrical non-linearity is taken into account, the effect of patch loads becomes very small, regardless of the inclusion of geometric imperfections. This observation is consistent with the observation made in Song (2002) that axial compressive stresses due to patch loads reduce greatly when geometric non-linearity is taken into account.

The effect of patch loads on the other two silos is shown in Figure 2. Only the patch loads from the Australian code are considered as they have the greatest effect among the patch loads of the four codes (Figure 1).

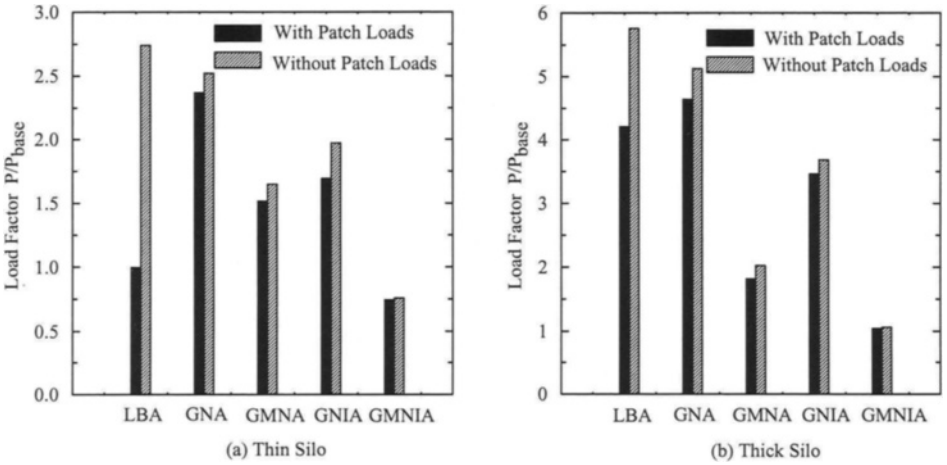

Figure 2: Buckling loads of thin and thick silos subject to the AS pressures

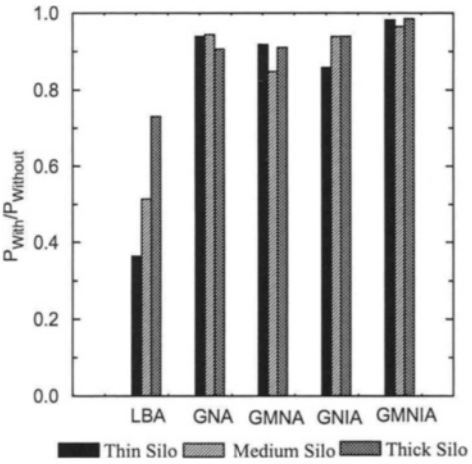

Figure 3: Effect of patch loads on the buckling loads of silos from different types of analysis

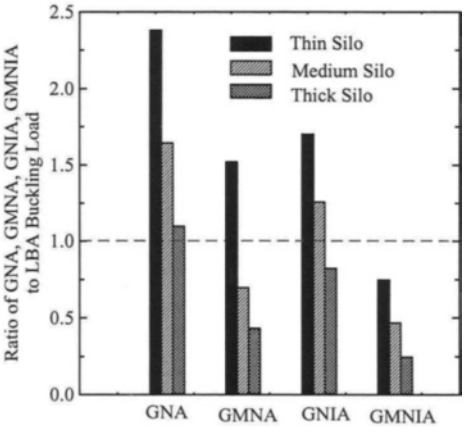

Figure 4: Ratios of GNA, GMNA, GNIA, GMNIA to LBA buckling loads

www.EngineeringEBooksPdf.com

Figure 3 presents the buckling load ratios between wall loads including patch loads and those without patch loads, with the wall pressures being those of the Australian code. From Figure 3, it can again be observed that the patch loads have a great influence on the linear bifurcation load, while their effect on buckling loads from GNA, GMNA, GNIA and GMNIA analyses is small (less than 20%). The effect of patch loads is seen to be larger in the thin silo than in the thick silo. Figure 4 provides the ratios of the buckling loads from GNA, GMNA, GNIA, GMNIA analyses and to the LBA buckling load for all three silos subject to the AS pressures. The beneficial effect of geometrical non-linearity is seen to be large, especially for the thin silo. It is worth noting that for both the thin silo and the medium silo, even with the effect of imperfection taken into account, the GNIA buckling load is still higher than the linear bifurcation load due to the strong beneficial effect of geometric non-linearity.

BUCKLING RESISTANCES FROM EUROCODE METHODS

General

When a silo is subject to eccentric discharge pressures, the unsymmetry of loading means that an assessment of the buckling resistance of the shell is complicated. Part 4-1 of Eurocode 3 (ENV 1993-4-1 1999) for the structural design of steel silos provides a method for the assessment of the design buckling resistance based on the results of a linear elastic stress analysis employing shell bending theory. Alternatively, the buckling resistance can be obtained by a suitable interpretation of the various numerical buckling loads employing procedures given in Part 1-6 of Eurocode 3 (ENV1993-1-6 1999). Ideally, these different methods should lead to similar buckling resistances, but no rigorous assessment of the consistency of the different approaches has been made, at least with regard to steel silos subject to code-specified eccentric discharge pressures. This section presents such an assessment using the finite element buckling loads from the preceding sections for the medium silo. The various methods for calculating buckling resistances are first outlined below. Only the characteristic buckling resistances, with the relevant partial safety factor omitted, are discussed.

Buckling Resistances Based on Linear Stress Analysis

Part 4-1 of Eurocode 3 (ENV 1993-4-1 1999) provides a method for the assessment of the design buckling resistance of a silo subject to meridional compressive membrane stresses of non-uniform distribution as typically found when subject to eccentric discharge pressures. The maximum compressive membrane stress resultant is employed as the design stress resultant n_{xSd}, which should satisfy the condition that

$$n_{xSd} \leq t\sigma_{xRd}$$

where t is the thickness of the silo, and σ_{xRd} is the design buckling membrane stress determined as

$$\sigma_{xRd} = \sigma_{xRk} / \gamma_{M3}$$

where $\gamma_{M3} = 1.10$ is a partial factor for the resistance of silo wall to buckling, σ_{xRk} is the characteristic buckling strength, which is related to the material yield strength f_y through a reduction factor χ_x as

$$\sigma_{xRk} = \chi_x f_y$$

The reduction factor χ_x is determined using the following equations:

www.EngineeringEBooksPdf.com

$$\chi_x = 1 \qquad (\bar{\lambda}_x \le \bar{\lambda}_0)$$

$$\chi_x = 1 - 0.6\left(\frac{\bar{\lambda}_x - \bar{\lambda}_0}{\bar{\lambda}_p - \bar{\lambda}_0}\right) \qquad (\bar{\lambda}_0 < \bar{\lambda}_x < \bar{\lambda}_p)$$

$$\chi_x = \frac{\alpha}{\bar{\lambda}_x^2} \qquad (\bar{\lambda}_p \le \bar{\lambda}_x)$$

with

$$\bar{\lambda}_x = \sqrt{\frac{f_y}{\sigma_{xRc}}}, \quad \bar{\lambda}_0 = 0.2, \quad \bar{\lambda}_p = \sqrt{2.5\alpha}$$

The critical buckling stress of an isotropic elastic cylinder is calculated as

$$\sigma_{xRc} = \frac{E}{\sqrt{3(1-\nu^2)}}\frac{t}{R}$$

where R is the radius of the cylinder. The imperfection factor α is determined considering both the effects of the internal pressure in a cylinder and material non-linearity. For an un-pressurized cylinder, the elastic imperfection factor α_0 is

$$\alpha_0 = \frac{0.62}{1 + 1.9\psi\left(\frac{w_{ok}}{t}\right)^{1.44}}, \qquad w_{ok} = \frac{1}{Q}\sqrt{Rt}$$

where Q is the quality parameter depending on the fabrication tolerance. For a pressurized cylinder, the elastic imperfection factor α_{pe} is

$$\alpha_{pe} = \alpha_o + (1-\alpha_o)\left(\frac{\bar{p}}{\bar{p} + \frac{0.3}{\sqrt{\alpha}}}\right), \qquad \text{with } \bar{p} = \frac{pR}{t\sigma_{xRc}}$$

where p is the minimum reliable local value of the internal pressure.

For a pressurized cylinder, a plastic imperfection factor α_{pp} is evaluated as

$$\alpha_{pp} = \left\{1 - \left(\frac{\bar{p}}{\bar{\lambda}_x^2}\right)^2\right\}\left[1 - \frac{1}{1 + 1.12 + s^{1.5}}\right]\left[\frac{s^2 + 1.21\bar{\lambda}_x^2}{s(s+1)}\right]$$

with

$$\bar{p} = \frac{pR}{t\sigma_{xRc}}, \quad s = \left(\frac{1}{400}\right)\left(\frac{R}{t}\right), \quad \bar{\lambda}_x^2 = \frac{f_y}{\sigma_{xRc}}$$

where p is the maximum local value of internal pressure. The smaller of the elastic imperfection factor and the plastic imperfection factor controls the strength of a pressurised cylinder.

The parameter ψ in the un-pressurized elastic imperfection factor α_0 represents the effect of the non-uniformity of the meridional compressive membrane stress around the circumference. It is determined from the distribution of the meridional compressive stress from a linear elastic stress analysis based on shell bending theory. The non-uniformity of the compressive membrane stress in the meridional direction is ignored.

To evaluate the buckling strength of a silo subject to a non-uniform (or circumferentially varying) meridional compressive stress distribution, ENV1993-4-1 (1999) recommends that the stress

www.EngineeringEBooksPdf.com

distribution should be transformed into the form shown in Figure 5. The design value of the meridional compressive membrane stress $\sigma_{x,Ed}$ in question is the peak value $\sigma_{xo,Ed}$. The parameter ψ is determined by deducing an equivalent harmonic from the stress distribution, which is expressed as

$$\psi = \frac{(1-b_1 j)}{(1+b_2 j)}$$

with

$$j = 0.25\sqrt{\frac{R}{t}}\cos^{-1}\left(\frac{\sigma_{x1,Ed}}{\sigma_{xo,Ed}}\right)$$

$$b_1 = 0.5\sqrt{\frac{t}{R}}$$

$$b_2 = \frac{(1-b_1)}{\psi_b} - 1$$

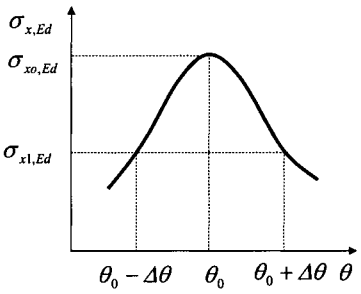

Figure 5: Representation of local distribution of meridional membrane stress around the circumference

where ψ_b is the effective reduction factor due to representative imperfections for a global bending condition, which may be taken to be 0.40. The design value of the meridional compressive membrane stress $\sigma_{x1,Ed}$ in the expression for the determination of the equivalent harmonic j is the value at a point with the same axial coordinate as that of the peak value $\sigma_{xo,Ed}$, but separated in the circumferential direction by the distance $R\times\Delta\theta = 4\sqrt{Rt}$. Rotter (2001) suggested that this distance may be too large when the procedure is applied to a highly localized stress distribution. An alternative distance was suggested by him to be $R\times\Delta\theta_g$, where $\Delta\theta_g$ is the angle of a point separated from the point in question, where the meridional compressive membrane stress $\sigma_{xg,Ed}$ is half the peak value $\sigma_{xo,Ed}$. The equivalent harmonic j can then be expressed as

$$j = \frac{1}{\Delta\theta_g}\cos^{-1}\left(\frac{\sigma_{xg,Ed}}{\sigma_{xo,Ed}}\right)$$

In the present study, the procedure recommended in Part 4-1 of Eurocode 3 (ENV1993-4-1 1999) was employed to evaluate the buckling resistance of the medium silo subject to wall loads determined according to the recommendations of the four silo loading codes.

Buckling Resistances Based on Finite Element Buckling Loads

Apart from the method described above based on stresses from a linear elastic stress analysis, the buckling resistance of a silo can alternatively be determined using the result of a numerical buckling analysis such as an LBA analysis. ENV1993-1-6 (1999) provides recommendations on how to convert numerical buckling loads into design buckling resistances; these numerical buckling loads can be determined by LBA, GNA, GMNA and GMNIA analyses respectively. Details of these procedures are not repeated here but a few points are noted below.

When the numerical buckling loads are from LBA and GNA analyses, a plastic reference resistance R_{pl} is required to define the overall relative slenderness. Following the recommendations of Part 1-6 of Eurocode 3, a linear stress analysis was first conducted for each silo in the present study. The maximum von Mises equivalent stress at the mid-surface of the silo was checked and compared with the yield stress to determine the plastic reference resistance R_{pl} in terms of a load factor over the base wall loads. When the numerical buckling load is from a GMNA analysis, the buckling resistance was obtained by multiplying the GMNA buckling load by an imperfection reduction factor which was

www.EngineeringEBooksPdf.com

calculated with the same procedure as used for cylindrical shells under uniform axial compression. The GMNIA numerical buckling load needs to be multiplied by a calibration factor. In this study, the ratio between the buckling resistance evaluated by the stress design approach of Part 1-6 of Eurocode 3 and the GMNIA buckling load for a silo subject to the primary wall loads only was calculated for each of the four loading codes and the average of these ratios is taken as the calibration factor.

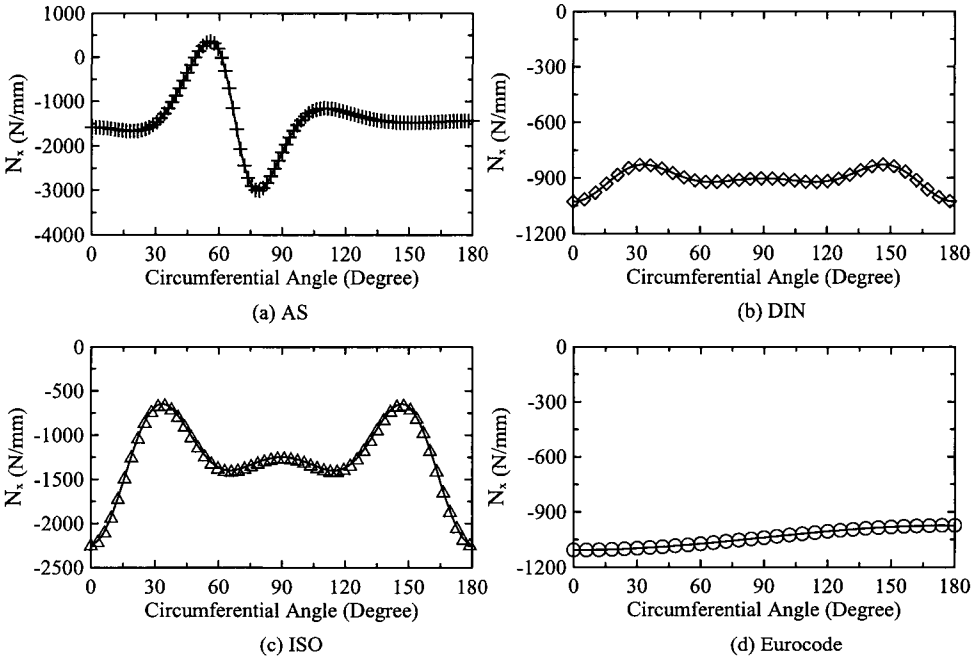

Figure 6: Distributions of meridional membrane stress resultant at the base of the medium silo

COMPARISON OF BUCKLING RESISTANCES FROM DIFFERENT APPROACHES

The buckling resistances of the medium silo determined according to the different approaches described in the preceding section are compared in this section. The distributions of the meridional membrane stress resultant at the base of the silo subject to eccentric discharge pressures predicted by the four different loading codes are shown in Figure 6.

Detailed views of these distributions near the maximum value are shown in Figure 7 for two cases. These results are from linear elastic stress analyses (LA) with the silo being under the base wall loads. There are two different types of distributions: symmetric about the peak stress point (the DIN, ISO and Eurocode pressures) and non-symmetric about the peak stress point (the AS pressures). For the non-symmetric distributions, the equivalent harmonic needs to be defined using the stress at either point A or point B shown in Figure 7. Numerical results showed that a different choice of this point leads to a difference of about 5% in the elastic buckling load. The medium silo subject to the AS pressures was found to be controlled by the plastic imperfection factor, so this did not become an issue for this silo.

www.EngineeringEBooksPdf.com

Table 3 compares the buckling resistances of the medium silo in terms of load factors over the base wall loads determined according to the Eurocode 3 approaches based on the linear stress analysis (LA) and the numerical buckling loads determined by LBA, GNA, GMNA and GMNIA analyses.

TABLE 3
BUCKLING RESISTANCES OF THE MEDIUM SILO

	AS	DIN	ISO	Eurocode
LA	1.12	2.85	1.50	2.60
LBA	0.50	1.37	0.65	1.25
GNA	0.79	1.46	0.96	1.21
GMNA	0.62	0.95	0.730	0.85
GMNIA	1.54	2.55	1.65	1.94

The results of Table 3 show that there are large differences between the buckling resistances predicted by different approaches for the same wall loads, and between the buckling resistances predicted by the same approach for different wall loads. The former differences demonstrate that for silos subject to eccentric discharge pressures as specified by existing loading codes, the Eurocode 3 recommendations do not lead to consistent buckling resistances for different types of analysis. Given that the effect of patch loads on the numerical buckling loads is small except when LBA loads are considered, most of the differences in buckling resistance between wall loads from different loading codes can be attributed to the differences in the primary wall loads.

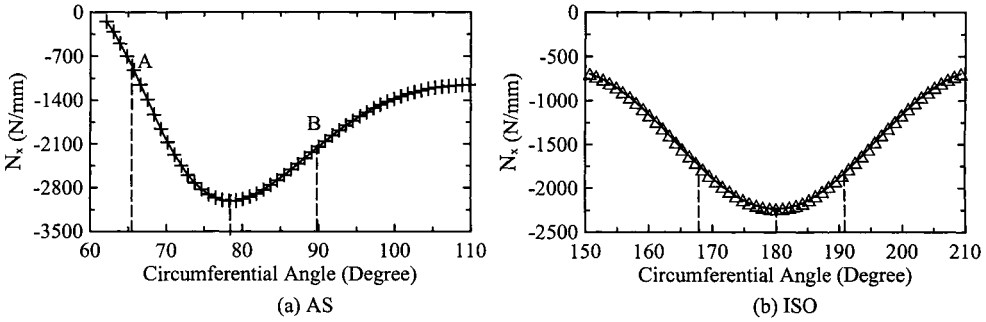

Figure 7: Detailed views of stress distributions

CONCLUSIONS

A parametric study was carried out to investigate the effect of patch loads as specified by existing silo loading codes to represent discharge eccentricity on the buckling loads of silos. The study showed that these patch loads have a great effect on linear bifurcation loads. This effect is substantially reduced if geometrical non-linearity is considered. The axisymmetric primary wall loads have been found to control the buckling loads from non-linear analysis, in which the patch loads play only a small role. It can thus be concluded that the patch loads specified in existing silo loading codes are inadequate in representing the effect of discharge eccentricity if this effect is important in reality, when the specified loads are used in a non-linear buckling analysis. If this effect is as small as shown by the nonlinear buckling loads presented in this paper, then this effect can be easily covered by a small increase in the primary wall loads which represents a much simpler approach.

www.EngineeringEBooksPdf.com

Eurocode 3 (ENV1993-4-1 1999) provides procedures for converting numerical buckling loads into design buckling resistances. These procedures were adopted in the present study to produce the buckling resistances of a silo subject to eccentric discharge pressures. Very different results were obtained from different analysis types for the buckling resistance, which means that improvements to these procedures are required. Very different results were also obtained for wall loads specified by different loading codes. Given that the effect of patch loads on the numerical buckling loads is small except when LBA loads are considered, most of these differences in buckling resistance can be attributed to the differences in the primary wall loads.

The results presented in this and the companion paper (Song and Teng 2002) are believed to have important implications for the future development of silo loading codes and shell stability design codes in terms of adequate representation of a complex loading condition. One of the most important implications is that in the specification of loads to represent the equivalent effect of actual loads which are not yet well defined, there needs to be close coordination between writers of the loading code and the structural design code so that the resulting deigns does not become either unnecessarily conservative or unsafe as a result of a different choice of analysis techniques.

ACKNOWLEDGEMENTS

The work described here forms part of the project "Buckling Strength of Steel Cylindrical Shells under a General State of Non-uniform Stresses" funded by the Research Grants Council of the Hong Kong SAR (Project No. PolyU 5081/97E), with additional support from The Hong Kong Polytechnic University. The authors are grateful to both organizations for their financial support.

REFERENCES

AS3774-1996 (1996). *Loads on Bulk Solids Containers*. Standards Australia, Sydney.

DIN1055-6 (1987). *Design Loads for Buildings: Loads in Silo Bins*, Deutsches Institut fur Normung, Berlin, May.

ENV1991-4 (1995). *Eurocode 1: Basis of Design and Actions on Structures, Part 4: Actions in Silo and Tanks*. European Committee for Standardisation, Brussels.

ENV1993-1-6 (1999). *Eurocode 3: Design of Steel Structures, Part 1-6: General Rules-Supplementary Rules for the Strength and Stability of Shell Structures.* European Committee for Standardisation, Brussels.

ENV1993-4-1 (1999). *Eurocode 3: Design of Steel Structures, Part 4-1: Steel Silos*. European Committee for Standardisation, Brussels.

ISO11697 (1995). *Bases for Design of Structures—Loads Due to Bulk Materials*.

Rotter, J.M. and Teng, J.G. (1989). Elastic stability of cylindrical shells with weld depressions. *J. Struct. Engrg., ASCE*, **115:5**, 1244-1263.

Rotter, J.M. (2001). Pressures, stresses and buckling in metal silos containing eccentrically discharging solids. *60th Birthday Celebration for Univ.-Prof. Dipl.-Ing. Dr.techn. Richard Greiner*, Oct. 12, 2001, Institute for Steel, Timber and Shell Structures, Technical University Graz, Austria.

Song, C.Y. (2002). *Buckling of Shells under Non-uniform Stress States*. Ph.D. Thesis, Department of Civil and Structural Engineering, The Hong Kong Polytechnic University.

Song, C.Y. and Teng, J.G. (2002). Buckling of circular steel silos subject to eccentric discharge pressures-Part I. *Proc., 3rd Int. Conf. on Advances in Steel Structures,* December, Hong Kong, China.

www.EngineeringEBooksPdf.com

Advances in Steel Structures, Vol. II
Chan, Teng and Chung (Eds.)
© 2002 Elsevier Science Ltd. All rights reserved.

ASPECTS OF CORRUGATED SILOS

Peter Ansourian[1], Mathias Gläsle[2]

[1] Department of Civil Engineering, The University of Sydney, Sydney 2006, Australia
[2] University of Karlsruhe, Kaiserstr. 12 , 76128 Karlsruhe, Germany

ABSTRACT

The failure of partially stiffened corrugated silos is investigated. Methods of analysis are given. It is recommended that where stiffening is required, it should be extended to the full height of the silo, unless careful analysis is made of the local stresses where the stiffening is curtailed. Care should also be taken in the design of the bolting of the stiffeners.

KEYWORDS

Cylindrical shell, silo, corrugation, stiffener, yielding, stability.

INTRODUCTION

For the storage of products from the primary and mining industries, large-scale silos are often constructed of steel, where the wall may be either of plain sheet or corrugated. In the case of plain sheet, extensive research has clarified many of the stability problems under external pressure loading (e.g. Ansourian et Al (1995), Vodenitcharova & Ansourian (1996, 1998)). In the case of corrugated sheets, the corrugations may run in either the vertical or horizontal direction, and may be stiffened by thin-walled members running perpendicular to the corrugations. They represent a highly economical structure of light steel tonnage. Their design is however complex. A significant problem is local failure of the corrugations. Extensive finite element analysis of the stiffened and unstiffened corrugated shell has shown that high risk of failure exists unless the stiffening is carried through for the entire height of the silo. In this presentation, the significant failure modes that have been observed in corrugated silos are analysed, and important features of their design investigated; recommendations are advanced for their long-term service and stability.

Vertical compression failure of the corrugations under vertical loading may not cause catastrophic collapse but may cause lean of the structure and out-of-roundness, effectively requiring major repair. It can also lead to buckling failure of the stiffeners, with potentially catastrophic results. The vertical load arises primarily through frictional drag of the bulk solids partly against the wall and partly against itself, exacerbated by flow overpressures. In this paper, the stability of the corrugations is evaluated taking account of the eccentricity of the load, and the amplification of stresses that occurs through the second-order effects. Failure occurs by yielding at the critical section defined by a trough of the

www.EngineeringEBooksPdf.com

corrugations under a biaxial stress system including axial, bending and circumferential stresses; amplification of the vertical moment arises from additional deflection of the curved shell.

FAILURE OF CORRUGATIONS UNDER COMBINED LOADS

Major silos constructed of corrugated steel sheets where the corrugation runs vertically are often stiffened with vertical members but for economy the stiffeners do not always run the full height of the wall. As a result, failure may occur by collapse of the corrugations, most commonly at or just above the level where the stiffeners terminate (Figure 1).

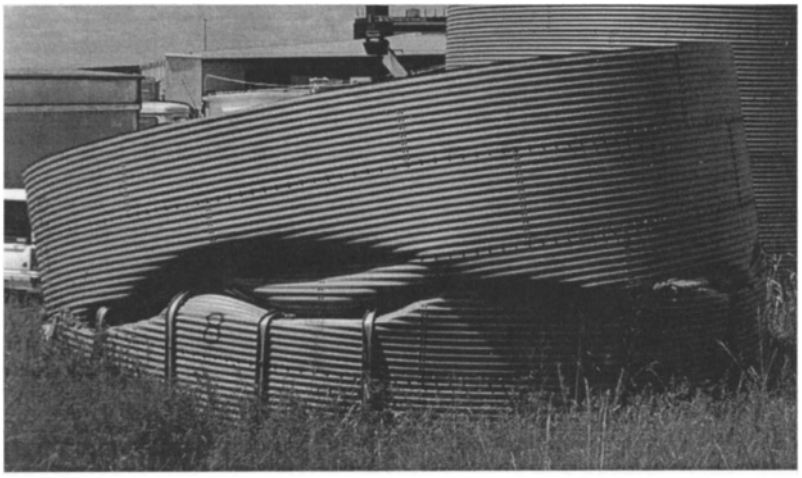

(a) Sectional view

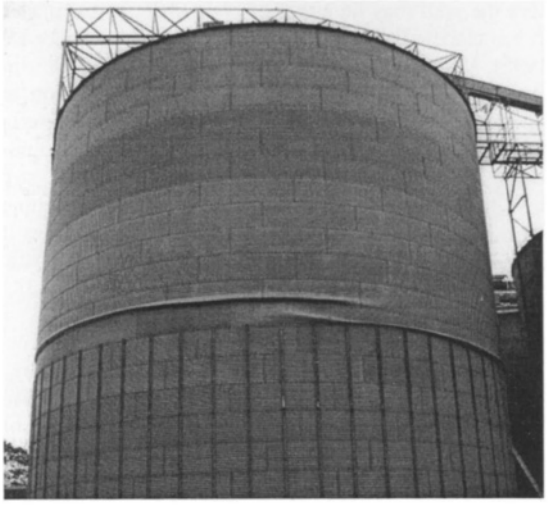

(b) Full silo

Figure 1: Two examples of corrugation failure at stiffener end

www.EngineeringEBooksPdf.com

Referring to Figures 2 and 3, assume that the critical section located at the trough of the corrugation is fully plastic under the action of the vertical friction force P, acting at eccentricity 'e'.

Take moments about the neutral axis:

$$Pe+P\left(d_c-\frac{t}{2}\right)=F_{y,eff}\left[\frac{d_c^{\,2}}{2}+\frac{(t-d_c)^2}{2}\right] \quad (1)$$

where t is the thickness of the section, $F_{y,eff}$ the effective yield stress under combined axial and circumferential stresses, and d_c defines the neutral axis. The axial load P is the resultant force acting on the section, and therefore:

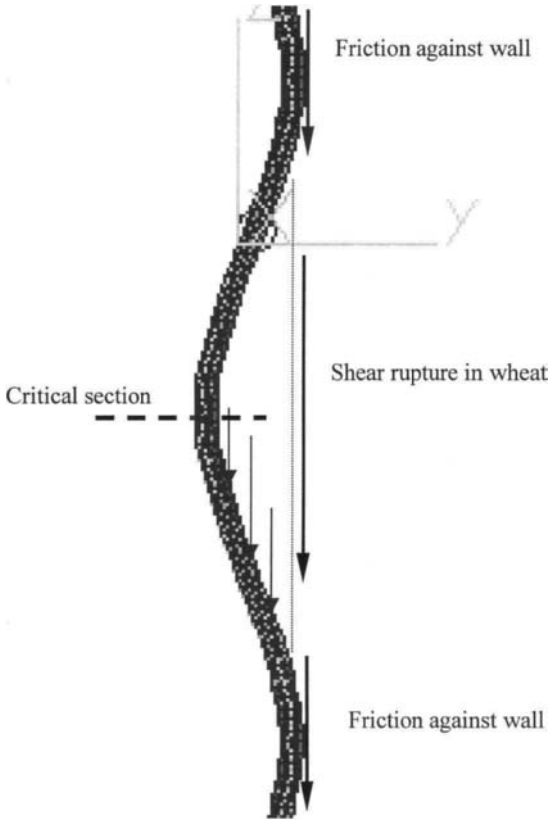

Figure 2: Friction force components on corrugated wall

$$P=2F_{y,eff}\left(d_c-\frac{t}{2}\right) \quad (2)$$

www.EngineeringEBooksPdf.com

The neutral axis is located at:

$$d_c = \frac{P}{2F_y} + \frac{t}{2} \tag{3}$$

Substitution into equation 1 results in the expression:

$$Pe = \frac{t^2}{4F_{y,eff}} \left[F_{y,eff}{}^2 - \left(\frac{P}{t} \right)^2 \right] \tag{4}$$

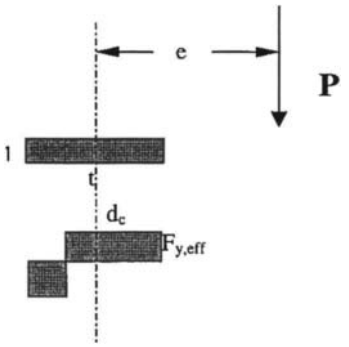

Figure 3: Critical section of corrugation

Solving for P:

$$P = \left(\sqrt{4e^2 + t^2} - 2e \right) F_{y,eff} \tag{5}$$

Now, the effective yield stress of the material under the combination of axial stress $F_{y,eff}$ and circumferential stress (hoop tension caused by bulk material pressure) σ_h is given by the von Mises yield criterion:

$$F_{y,eff} + \sigma_h{}^2 + \sigma_h F_{y,eff} = F_y{}^2 \tag{6}$$

where F_y is the yield stress under uniaxial stress. Solving the quadratic equation for the effective yield stress gives:

$$F_{y,eff} = \frac{1}{2} \left(\sqrt{4F_y{}^2 - 3\sigma_h{}^2} - \sigma_h \right) \tag{7}$$

If the lateral pressure of the bulk material is p_h, and the ratio of the actual height of the corrugations to the developed height is denoted by c, we have:

www.EngineeringEBooksPdf.com

$$\sigma_h = \frac{cp_n R}{t} \tag{8}$$

and the axial force ultimate capacity is finally given by:

$$P = \frac{1}{2}\left(\sqrt{4e^2 + t^2} - 2e\right)\left(\sqrt{4F_y{}^2 - \frac{3c^2 p_h{}^2 R^2}{t^2}} - \frac{c p_h R}{t}\right) \tag{9}$$

At the critical steel section corresponding to a trough of a corrugation (Figures 2-3), the vertical downward frictional force is eccentric relative to the centreline of the critical section. This eccentricity may be evaluated approximately using some of the method of Appendix B, Australian Standard AS 3774 - 1996. The total vertical force is applied in part by direct friction of the grain against the steel, and in part through shear rupture within the grain. The respective parts may be approximated in a typical case as 20% in direct friction and 80% in rupture. The eccentricity 'e' of the resultant vertical force relative to the centroid of the critical section may therefore be estimated; in a typical case, it is about 30% greater than the half corrugation depth.

More refined analysis would include the 2nd order effects of the eccentric axial force, which amplify the 1st order moment. A lower bound to this amplification may be evaluated on the assumption that the corrugation remains elastic for most of the loading history. On this assumption, the new eccentricity becomes:

$$e_{max} = \frac{e}{1 - \dfrac{12P(0.7L)^2}{\pi^2 E t^3}} \tag{10}$$

where L is the average height of the corrugations (trough to trough), and 0.7 is the factor to approximate the effective height; E is the modulus of elasticity of steel. In a typical situation, the amplification of the eccentricity is in order of 10%.

VERTICAL COMPRESSION FAILURE OF CORRUGATIONS

Because of economy, stiffening of corrugated silos has in the past not always continued to the top. This fact has had a negative influence on stability, as several examples of failures have shown (e.g. Figures 1(a) and 1(b)). Detailed finite element analysis was carried out to investigate the vertical compression failure and to present a proposal for improving the structural response. The following development relates to stiffening curtailed at the level of the first bolt between stiffener and sheet.

Due to compression and exterior eccentricity of the stiffener, the corrugated sheet immediately above the first bolt translates inwards (Figures 4, 5). Since the stiffener carries a substantial proportion of the total compressive load, the friction force generates tensile stresses just below the bolt (Figure 6). In combination with the eccentricity of the stiffener, the corrugated sheet now translates outwards. A further increase in axial load below the bolt develops compressive stress in the sheet again.

www.EngineeringEBooksPdf.com

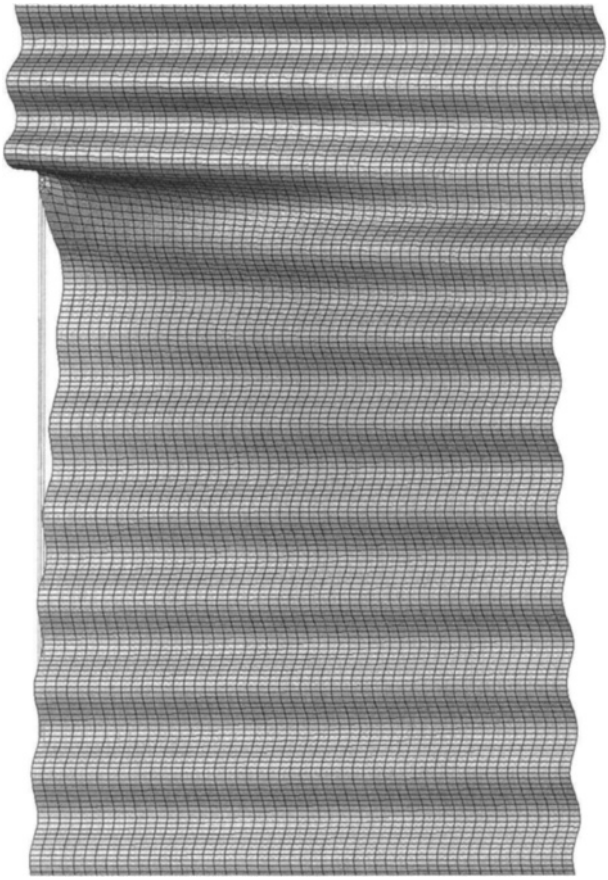

Figure 4: Deformed shape of corrugated sheeting at start of stiffening (view from inside of silo)

At the start of stiffening (first bolt), the compressive stress in the sheet rises sharply (Figure 6). Immediately below the bolt, high tensile stress exists. This is attributed to the fact that the stiffener at the height of the bolt keeps the corrugation in place, whereas the friction load below the bolt pulls the corrugation down, causing tension. Since a major part of the axial load runs down the stiffener to the ground, the membrane stress in the corrugated sheet decreases in value towards the bottom.

It is concluded that the abrupt introduction of stiffening causes very high local stress in the corrugated sheet. The von Mises stress in this area under assumed linear conditions is more than five times the yield stress σ_y of 450 N/mm^2. The area around the first bolt therefore yields and precipitates failure of the sheeting.

The highly stressed areas at the location beneath the first bolt (Figure 7) indicate regions of the structure stressed beyond the elastic limit σ_y = 450 N/mm^2. These areas are also subjected to large deformations and will most likely trigger collapse. Of course, in the circumferential direction, the influence of the stiffener decreases, but local failure beneath the first bolt is likely to cause lean of the structure, buckling of the stiffener and potentially total collapse.

www.EngineeringEBooksPdf.com

The above problem is eliminated if the stiffeners are extended up to the top of the silo, as the introduction of load to the stiffeners will increase only slowly from zero.

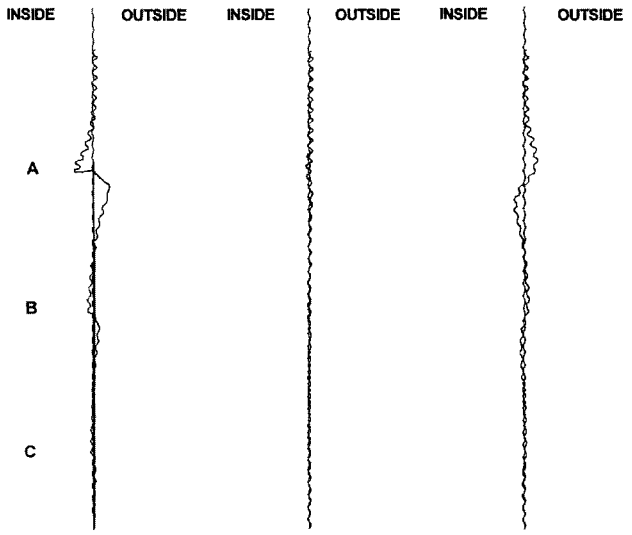

Figure 5: Deformed elevation of corrugated wall at 0°, 3.75° and 7° from stiffener

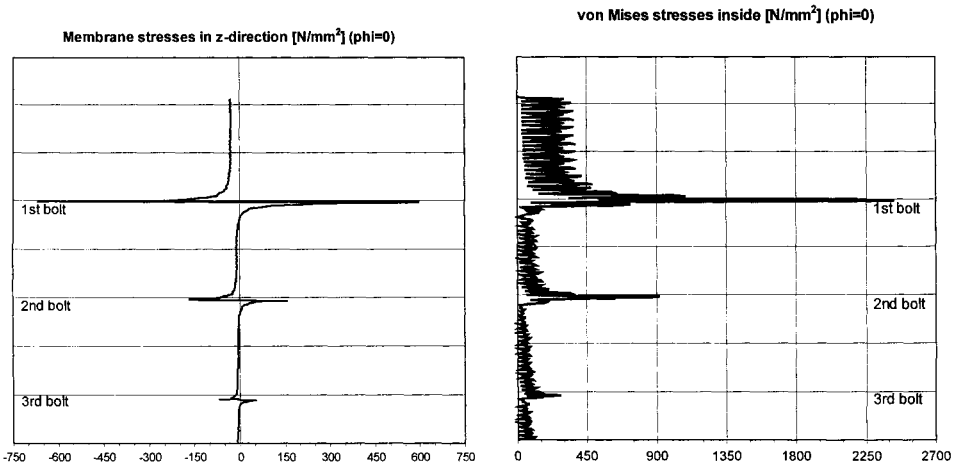

Figure 6: Membrane stresses in vertical direction and von Mises stresses

www.EngineeringEBooksPdf.com

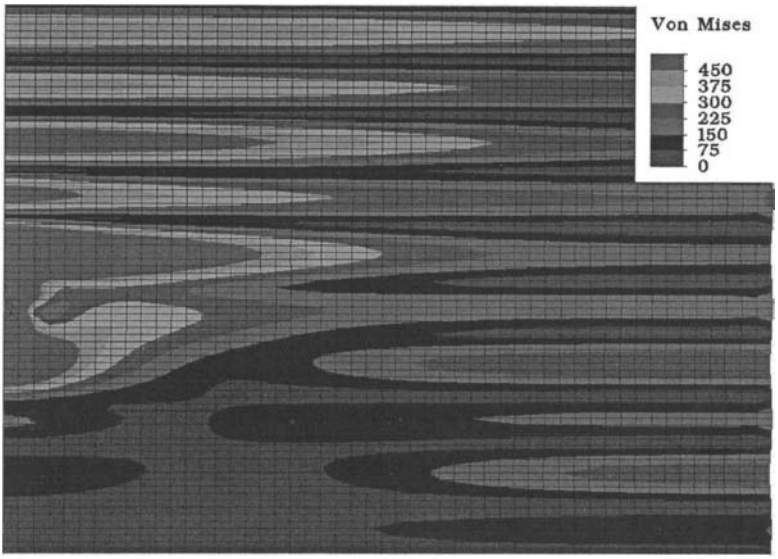

Figure 7: Von Mises stresses at and below first bolt

The stiffeners are prevented from bending by the restraint of the silo, and their maximum capacity is their squash load. They carry the difference between the total applied vertical force and the ultimate axial capacity of the sheeting calculated above.

CONCLUSIONS

In this paper, the effects of combined lateral pressure and longitudinal compression on vertically corrugated silo walls have been investigated and expressions derived for ultimate capacity. Finite Element analysis has shown that if stiffening of the silo is required, then it should extend over the full silo height unless very careful analysis of local stresses is undertaken. Moreover a closer bolting reduces stresses and deformations significantly.

REFERENCES

Ansourian, P., Showkati, H., Sengupta, M. & Vodenitcharova, T. (1995). Analysis, Computation and Experiments for Cylindrical Shells under Uniform and Non-uniform External Pressure. *Proc. Intl. Conf. on Struct. Stab. and Design, Sydney*, Oct. 1995, Balkema, Rotterdam, 385-390.

Vodenitcharova, T. and Ansourian, P. (1996). Buckling of Circular Cylindrical Shells Subject to Uniform Lateral Pressure. *Engineering Structures*, Vol. 18, No. 8, 1996, 604 - 614.

Vodenitcharova, T. and Ansourian, P. (1996). Non-uniform Lateral Pressure Solutions for Containment vessels. Proc. ICASS'96 Intl. Conf. on Advances in Steel Structures, Hong Kong, Dec. 1996, ed. SL Chan and JG Teng, Pergamon, Vol.2, 753-758.

Vodenitcharova, T.M. and P. Ansourian. (1998). Hydrostatic, Wind and Non-Uniform Lateral Pressure Solutions for Containment Vessels. *Thin-walled Structures*, Vol. 31, No. 1-3, May-July 1998, 221-236.

www.EngineeringEBooksPdf.com

Advances in Steel Structures, Vol. II
Chan, Teng and Chung (Eds.)
© 2002 Elsevier Science Ltd. All rights reserved.

BUCKLING EXPERIMENTS ON TRANSITION RINGS IN ELEVATED STEEL SILOS

Y. Zhao[1] and J. G. Teng[2]

[1]Department of Civil Engineering, Zhejiang University, Hangzhou 310027, P. R. China
[2]Department of Civil and Structural Engineering, The Hong Kong Polytechnic University, Hong Kong, P. R. China

ABSTRACT

Large elevated steel silos for the storage of bulk solids general consist of a cylindrical vessel, a conical discharge hopper and a skirt. The cone-cylinder-skirt junction is subject to a large circumferential compressive force which is derived from the horizontal component of the meridional tension in the hopper, so either a ring is provided or the shell walls are locally thickened to strengthen the junction. Many theoretical studies have examined the buckling and collapse strengths of these junctions, but no previous experimental study has been reported due to the great difficulties associated with testing these thin-shell junctions at model scale. This paper presents the results of a series of tests on cone-cylinder-skirt-ring junctions in steel silos under simulated bulk solid loading. In addition to the presentation of test results including geometric imperfections and failure behavior, the determination of buckling modes and loads based on displacement measurements is examined.

KEYWORDS

Steel Silos, Transition Junctions, Rings, Buckling, Stability, Experiments, Shells, Imperfections

INTRODUCTION

Large elevated steel silos for the storage of bulk solids general consist of a cylindrical vessel, a conical discharge hopper and a skirt (Figure 1). The cone-cylinder-skirt junction is subject to a large circumferential compressive force which is derived from the horizontal component of the meridional tension in the hopper, so either a ring is provided or the shell walls are locally thickened to strengthen the junction. Under the compressive force, the strength of the transition junction with a ring may be limited by plastic collapse of the junction (Figure 2a) or by elastic or plastic out-of-plane buckling of the ring (Figure 2b). Many theoretical studies have examined the buckling and collapse strengths of these junctions, leading to theoretically based design proposals. A summary of research on steel silo transition junctions undertaken before 1992 was given by Teng and Rotter (1992). A more recent review of research on steel shell junctions including steel silo transition junctions can be found in Teng (2000).

www.EngineeringEBooksPdf.com

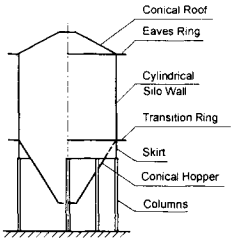

Figure 1: Typical elevated steel silo

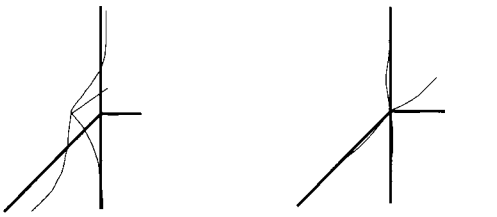

(a) Plastic collapse of the junction (b) Out-of-plane buckling of the ring

Figure 2: Failure modes of steel silo transition junctions

Despite the many theoretical studies, no previous experimental study on steel silo transition junctions has been reported due to the great difficulties associated with testing these thin-shell junctions at model scale. To rectify this deficiency, a major experimental program has recently been undertaken at The Hong Kong Polytechnic University. In this program, a sophisticated shell buckling facility was first developed with particular attention to the testing of shell junctions, as detailed in Teng *et al.* (2001). An experimental study of the related buckling problem of internally-pressurized cone-cylinder junctions using this facility has been presented elsewhere (Zhao and Teng 2001). This paper provides a summary of the experimental results of a series of tests conducted on cone-cylinder-skirt-ring transition junctions in steel silos under simulated bulk solid loading.

MODEL JUNCTIONS AND MATERIAL PROPERTIES

This test series includes five cone-cylinder-skirt-ring junctions subjected to simulated bulk solid loading. The nominal junction dimensions are given in Table 1, where α is the cone apex half angle, R the junction radius, and l and t the length and thickness of a given shell segment as defined by the subscript. The width-to-thickness ratio of the ring was the main variable under investigation, and this parameter determines how important buckling of the ring is to the integrity of the junction. Actual thicknesses of steel sheets were measured and are given in Table 2. All junctions were fabricated using the method of sheet rolling followed by seam welding. Careful fabrication techniques were employed to produce model junctions of high quality (Teng *et al.* 2001). Two types of steel sheets (1 mm and 2 mm) were used in fabricating these model junctions. The Young's modulus and the yield stress obtained from tensile tests are 2.04×10^5 MPa and 253 MPa for the 1 mm sheets and 1.99×10^5 MPa and 165 MPa for the 2 mm sheets, respectively. Tensile test results also showed that while rolling had little effect on the material properties, welding increased the yield stress of the steel near the weld significantly (Zhao and Teng 2001).

TABLE 1
NOMINAL GEOMETRIES OF MODEL JUNCTIONS

Specimen	R (mm)	α (degree)	$l_{cylinder}$ (mm)	l_{skirt} (mm)	$t_{cylinder}$ (mm)	t_{cone} (mm)	t_{skirt} (mm)	$B \times T$ (mm×mm)
CCSR-1	500	40	300	200	1	1	1	20 × 1
CCSR-2	500	40	300	200	1	1	2	30 × 1
CCSR-3	500	40	300	200	1	1	2	20 × 2
CCSR-4	500	40	300	200	1	1	2	40 × 1
CCSR-5	500	40	300	200	1	1	2	30 × 2

EXPERIMENTAL SET-UP

Figure 3 shows the overall view of the experimental set-up which was developed as a multi-purpose test rig for shell buckling experiments with special attention to the testing of steel silo transition junctions. This facility included a measurement system employing a laser displacement meter for accurate

www.EngineeringEBooksPdf.com

measurement of geometric imperfections and deformations. The laser sensor head was mounted on a measurement frame, rotated around and moved up and down the test specimen to provide a three-dimensional survey of the specimen. All the movements were effected using stepping motors controlled by a computer which also recorded the measurement results. A detailed description of the experimental facility has been given by Teng et al. (2001).

In order to simulate realistically bulk solid loading in silos, the model junction was filled with sand and a surcharge load was applied through a thick circular plate which was loaded by a hydraulic jack (Figure 3). This loading method led to realistic pressures on the junction without having to build a tall silo. Furthermore, the total load supported by the hopper could be estimated accurately as the part of the applied load supported by friction between the short cylinder wall and the solid was small.

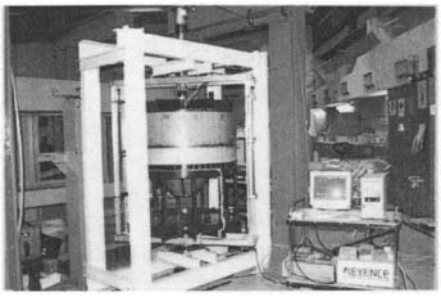

Figure 3: Experimental set-up

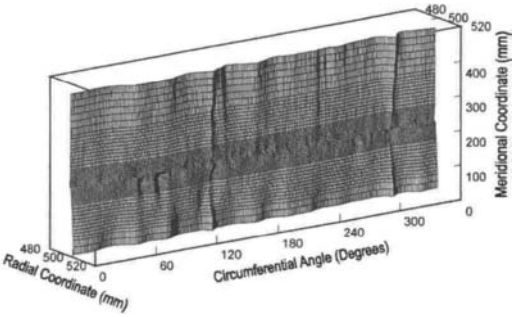

Figure 4: Initial surface of Junction CCSR-1

GEOMETRIC IMPERFECTIONS

Before each test, a careful three-dimensional survey was conducted on the specimen to obtain the initial imperfect shape. It should be noted that imperfections in the hopper could not be measured as it was behind the skirt and the vertical supports. This was not a major concern as the hopper, being subject to meridional tension, was not expected to be the most critical part of the buckling event.

As an example, Figure 4 shows the initial surface of Junction CCSR-1 excluding the ring. A nearly axisymmetric circumferential weld shrinkage depression can be identified at the cylinder-to-skirt welded joint. This depression was caused by the three passes of circumferential welding at the transition required to form a cone-cylinder-skirt-ring junction. A localised ridge can also be seen along each meridional weld (2 in the cylinder and 2 in the skirt). In addition, short-wave imperfections of a smaller amplitude in the critical area near the transition and longer-wave imperfections of a greater amplitude away from the transition are seen. The initial surfaces of the other four model junctions featured similar patterns. Table 2 gives the mean and maximum normal geometric deviations of all grid points from the nominal surface in the vicinity of the transition (within 2λ from the transition, where λ is the linear elastic bending half-wavelength) for each junction.

The initial surface of the ring was also determined, but only the outer part of the ring could be accessed by the laser beam as there was a small distance between the edge of the sensor head and the transmitter of the sensor head, from which the laser beam emitted. The initial shapes of the scanned circumferences are plotted as the dashed lines in Figure 6. In subsequent finite element modelling of these junctions not reported here, it was assumed that the inner edge of the ring was on a perfect horizontal plane, and the radial profile of the ring was a straight line originating from the inner edge and passing through the monitored circumference.

www.EngineeringEBooksPdf.com

TABLE 2
MEASURED THICKNESSES AND INITIAL DEVIATIONS OF MODEL JUNCTIONS

Specimen		Actual Thickness t (mm)	Deviation	
			Mean $\bar{\delta}/t$	Maximum δ_{max}/t
CCSR-1	Cylinder & Hopper	0.950	1.75	4.39
	Skirt	0.950	1.14	4.29
CCSR-2	Cylinder & Hopper	0.950	1.33	5.31
	Skirt	1.965	0.54	1.34
CCSR-3	Cylinder & Hopper	0.950	0.90	4.33
	Skirt	1.965	0.53	1.57
CCSR-4	Cylinder & Hopper	0.950	0.67	2.72
	Skirt	1.965	0.28	0.98
CCSR-5	Cylinder & Hopper	0.950	0.76	2.67
	Skirt	1.965	0.39	1.16

EXPERIMENTAL OBSERVATIONS

Overall Behavior

During the loading process of Junction CCSR-1, the deformations were initially nearly axisymmetric and increased linearly with the applied load. At a total load of about 170 kN, some short-wave buckles could be seen on the ring by naked eyes. The model junction failed suddenly by the buckling of the skirt at a total load of 230 kN (Figure 5). Skirt buckling did not occur in the other four junctions. They displayed similar behavior which can be summarized as follows. Linear and dominantly axisymmetric behavior was displayed in the initial stage of loading. As the load increased, non-symmetric deformations were developed and short-wave buckles of similar wavelengths could be observed on the ring by naked eyes. Buckles of similar wavelengths but smaller amplitudes were also found at the bottom of the cylinder. The development of these buckles was not associated with a reduction in the load carrying capacity. That is, a stable postbuckling path was displayed. In the late stage of loading, nearly axisymmetric inward deformations could be clearly seen near the transition. Final failure was by the formation of a plastic collapse mechanism with nearly uniform plastic deformations over a large part of the circumference. Figure 5 shows these junctions after final failure. The collapse loads of all five junctions are listed in Table 3.

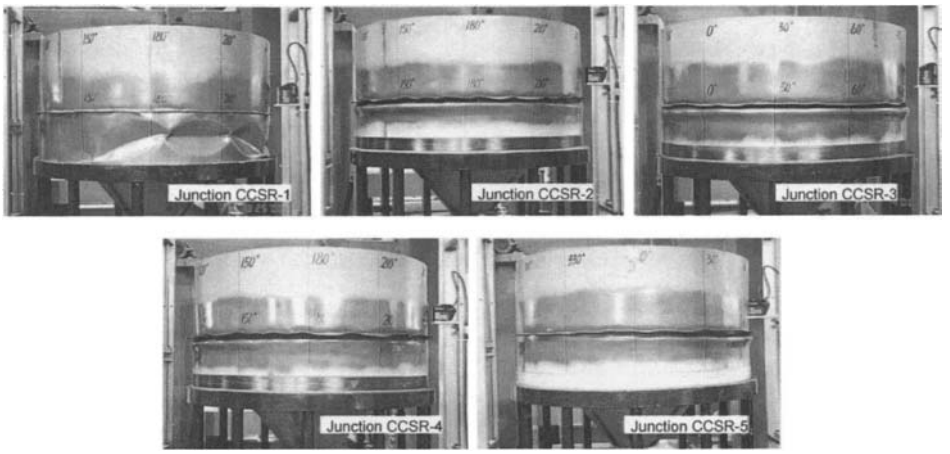

Figure 5: Model junctions after final failure

www.EngineeringEBooksPdf.com

TABLE 3
EXPERIMENTAL COLLAPSE AND BUCKLING LOADS OF MODEL JUNCTIONS

Specimen	Collapse Load (kN)	Buckling Load (kN)	Buckling Wave Number
CCSR-1	230	160	35
CCSR-2	410	250	31
CCSR-3	434	340	20
CCSR-4	442	160	29
CCSR-5	477	325	27

Growth of Ring Deformations

In a steel silo transition junction with a ring, the ring is generally the critical component in the buckling process of the junction. In all five tests, displacements at one selected circumference on the ring were scanned at each load level to monitor changes in the deformed shape of the ring during the test. Figure 6 shows the scanned results for all model junctions where the dashed lines represent the initial shapes. The positions of the radial welds on the ring are also indicated in Figure 6. It is seen from Figure 6 that deformations on the ring developed gradually as the load increased. For Junction CCSR-1, although some short-wave buckles on the ring could be seen by naked eyes as mentioned above, at the time of failure by skirt buckling, the measured deformations on the ring are quite small and the deformation waves are not very obvious. The development of roughly uniform short-wave buckles can be seen more clearly in the ring displacements of Junctions CCSR-2 and CCSR-4, due to the slenderness of the ring in these two junctions (with width-to-thickness ratios of 30 and 40 respectively). All scanned results show that most of the short-wave buckles were amplified from the initial geometric imperfections, especially for the two thinner rings in Junctions CCSR-2 and CCSR-4. It is also seen that the radial welds on the ring had only a small effect on the deformation modes.

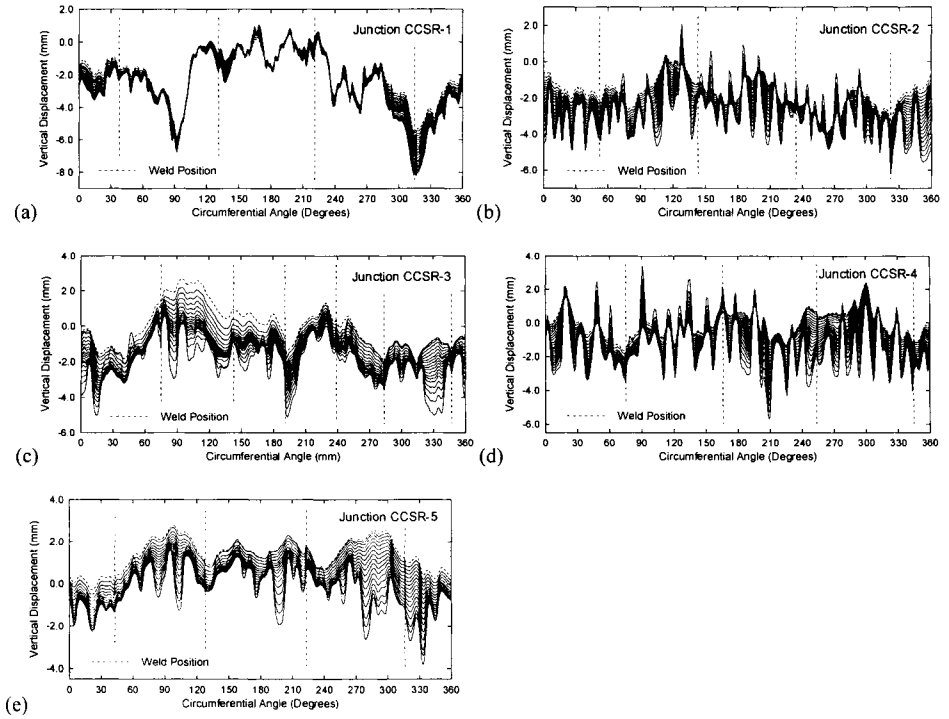

Figure 6: Deformed shapes of the ring

www.EngineeringEBooksPdf.com

DETERMINATION OF BUCKLING MODE AND LOAD

General

In all five tests, buckling of the ring was associated with a stable postbuckling behavior. Due to the stable postbuckling path, the buckling load cannot be easily defined but the effect of imperfections is believed to be limited. For these junctions, the buckling load of the corresponding perfect structure is believed to be a good measure of its integrity, as was found for internally-pressurized cone-cylinder junctions (Zhao and Teng 2001), but the direct determination of this buckling load from a test is not so straightforward. The determination of experimental buckling modes and loads based on displacement measurements of the ring was examined in this study as presented below.

Fourier Analyses of Imperfections and Deformations

Theoretically speaking, the buckling mode of a perfect transition junction under axisymmetric loading is in the form of a single harmonic mode around the circumference, but in a test, due to the presence of imperfections, many modes may be involved. A well-established way of interpreting geometric imperfection and deformation measurements to identify the dominant harmonic modes and their relationship is to carry out Fourier decompositions. Such decompositions were carried out for the imperfection and deformation measurements of all model junctions (shown in Figure 6), and the results at selected load levels for Junction CCSR-2 are shown in Figure 7 for the total amplitude A_n ($=\sqrt{a_n^2+b_n^2}$, where a_n and b_n are the coefficients of the cosine and sine terms respectively, and n is the Fourier harmonic number).

Figure 7 shows that the initial imperfect shape of the ring is dominated by low harmonic terms. This means that the imperfection in the ring was predominantly out-of-flatness. However, the coefficients of these low harmonic terms are seen to be much more stable than certain other harmonic modes which showed rapid growth with load. Some coefficients, such as those for terms 2, 4, 5 and 6 even reduced as the load increased. The rapid-growth terms including terms 20, 25 and 30 can be regarded as the main harmonic terms describing the buckling mode shapes. The Fourier analysis results for other four junctions showed similar behavior (Zhao 2001) and are not given here due to space limitation.

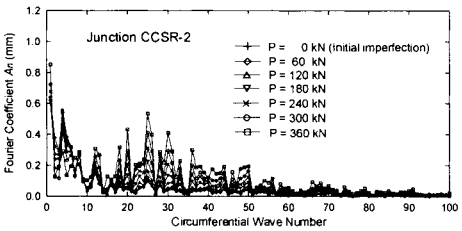

Figure 7: Growth of Fourier coefficients

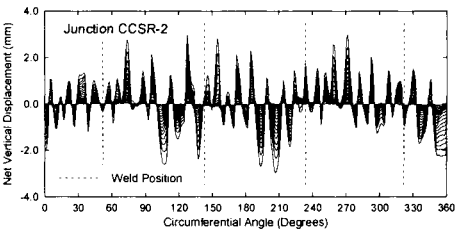

Figure 8: Load-induced deformations of the ring with harmonic modes 0 and 1 excluded

Buckling Mode

By removing the initial imperfections from the deformed shapes, plots showing only load-induced deformations could be obtained. As the low harmonic modes are believed to have little effect on the development of non-symmetric deformations, the components in harmonic modes 0 and 1 were omitted in these plots. Figure 8 shows such a plot for Junction CCSR-2. This plot shows a clear process of the development of buckles with loading, and the number of periodical waves counted from this figure is 31. The buckling wave numbers for the other four junctions were obtained using the same approach and the

www.EngineeringEBooksPdf.com

results are listed in Table 3. These numbers are in general agreement with the results of Fourier decomposition.

Buckling Load

Nonlinear finite element analyses of the model junctions showed that for a nearly perfect junction, the load-displacement curves of the nodal points within a buckling half wave on the ring are initially coincidental, and then start to differ from each other, and at the same time experience a sudden change in slope at a load close to the bifurcation buckling load of the perfect junction (Zhao 2001). The load-displacement curves of points on the ring of a test junction do not generally show such behavior due to the presence of significant initial imperfections. However, as a single half wave occupies only a small portion of the ring circumference, if a small nearly-perfect portion of the ring can be identified, the development of displacements of this small portion can then be examined to define the buckling load of the perfect ring quite accurately. To identify those points on a ring with a sudden slope change or sudden divergence from each other in their load-displacement curves, sets of load-displacement curves of points falling within each half wave were first plotted. In addition, load-displacement curves of all points at or near wave crests and troughs were also plotted to identify points showing an obvious slope change (Zhao 2001). Due to space limitation, only a single set of curves, which was used for the determination of buckling loads, is shown in Figure 9 for each model junction.

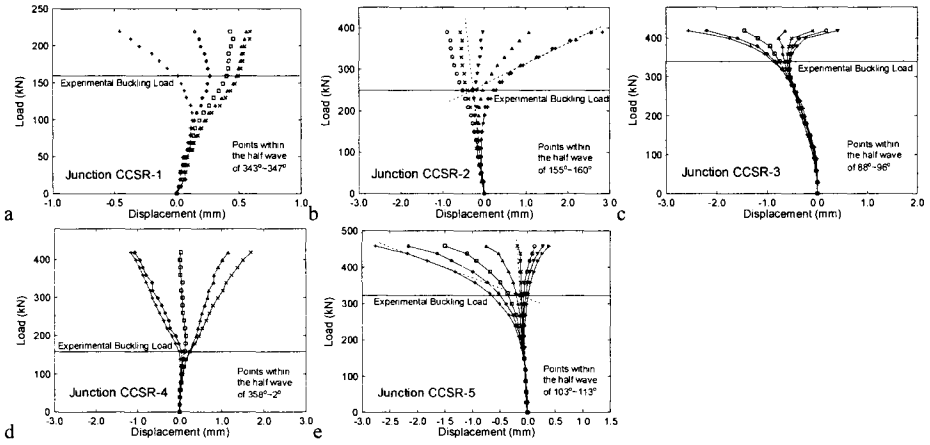

Figure 9: Load-displacement curves for the determination of buckling loads

For both Junctions CCSR-3 and CCSR-4 (Figures 9c and 9d), the load-displacement curves almost coincide with each other, before a sudden slope change or reversal occurs in some of the curves. In these curves, sudden divergence in displacements is rather obvious at a certain load level. This load is taken as the experimental buckling load, which is 340 kN for CCSR-3 and 160 kN for CCSR-4. For Junctions CCSR-2 and CCSR-5, the load-displacement curves show a somewhat different type of behavior (Figures 9b and 9e). In these curves, the displacements of different points are initially similar, but diverge gradually with increases of load. A load corresponding to a sudden divergence or an obvious change of slope cannot be identified. Instead, to determine the buckling load, the curve showing the most obvious slope change was identified, and the intercept of the initial slope of this curve and a tangent to a suitable portion of the postbuckling (i.e. post-slope change) part of the curve is taken as the buckling load, as shown in Figures 9b and 9e for these two junctions respectively. The buckling loads so obtained are 250 kN for Junction CCSR-2 and 325 kN for Junction CCSR-5. This method of determination of buckling loads bears some similarity to what is done for plate buckling experiments (Singer *et al.* 1998). As Junction CCSR-1 failed by skirt buckling in the initial postbuckling stage of the ring, most of the load-

www.EngineeringEBooksPdf.com

displacement curves are nearly linear. A load corresponding to a sudden divergence or an obvious change of slope cannot be identified (Figure 9a). In addition, the lack of deep postbuckling data means that the intercept of the initial slope of the curve with the most obvious slope change and a tangent to a suitable portion of its postbuckling (i.e. post-slope change) part is unlikely to deliver a reliable prediction of the buckling load. For these reasons, the buckling load is taken as the load when a relatively obvious slope change occurs in two of the curves shown in Figure 9a, and this load is 160 kN.

The experimental buckling loads as well as the circumferential buckling wave numbers are summarized in Table 3. Despite some uncertainty, these loads are believed to be rational approximations to the buckling loads of rings in corresponding perfect transition junctions.

CONCLUSIONS

This paper presented the results of five tests on cone-cylinder-skirt-ring junctions under simulated bulk solid loading. For each model junction, the initial imperfect surface was carefully surveyed before loading. The deformed shape of a circumference on the ring was monitored during the loading process. These measurements of initial shapes and deformed shapes were interpreted by Fourier decomposition, and led to the conclusion that most of the short-wave buckles were amplified from initial geometric imperfections. For all model junctions, buckling of the ring was associated with a stable postbuckling behavior. Final failure was by either skirt buckling when the skirt was thin or plastic collapse when the skirt was thicker. Due to the stable postbuckling path, the buckling loads of these junctions cannot be easily determined. This paper has shown that by making appropriate use of displacement measurements on the ring, both buckling modes and loads of these junctions can be rationally determined. Such buckling modes and loads have been presented for all five model junctions.

ACKNOWLEDGEMENT

The work described here forms part of the project "Stability and Strength of Steel Silo Transition Junctions" supported by a grant from the Research Grants Council of the Hong Kong SAR (Project No. PolyU 66/96E), with additional support from The Hong Kong Polytechnic University.

REFERENCES

Singer J., Arbocz J. and Weller T. (1998). *Buckling Experiments: Experimental Methods in Buckling of Thin-Walled Structures*. John Wiley & Sons, Chichester, England.

Teng J.G. (2000). Intersections in Steel Shell Structures. *Progress in Structural Engineering and Materials* **2:4**, 459-471.

Teng J.G. and Rotter J.M. (1992). Recent Research on the Behaviour and Design of Steel Silo Hoppers and Transition Junctions. *Journal of Constructional Steel Research* **23,** 313-343.

Teng J.G., Zhao Y. and Lam L. (2001). Techniques for Buckling Experiments on Steel Silo Transition Junctions. *Thin-Walled Structures* **39:8**, 685-707.

Zhao Y. (2001). *Stability and Strength of Steel Silo Transition Junctions*. PhD Thesis, The Hong Kong Polytechnic University, China.

Zhao Y. and Teng J.G. (2001). Buckling Experiments on Cone-Cylinder Intersections under Internal Pressure. *Journal of Engineering Mechanics, ASCE*, **127:12**, 1231-1239.

www.EngineeringEBooksPdf.com

Advances in Steel Structures, Vol. II
Chan, Teng and Chung (Eds.)
© 2002 Published by Elsevier Science Ltd.

BUCKLING STRENGTH OF CYLINDERS WITH A CONSISTENT RESIDUAL STRESS STATE

J.M.F.G. Holst and J.M. Rotter

School of Civil and Environmental Engineering, Division of Engineering,
University of Edinburgh, Edinburgh EH9 3JN, United Kingdom

ABSTRACT

The sensitivity of metal cylinder strength to geometric imperfections is well known. Because different imperfection forms and different amplitudes have quite different effects on cylinder strength, there has been a long search for the 'most serious' imperfection, constrained by the fact that this imperfection must be, in some sense, reasonably likely to be detected in a real structure after construction. The 'worst' imperfections currently known are far from practical. The search for practically useful and credible modes of imperfections has led to this study of the geometric imperfections arising from misfits of construction. Imperfections in the form of residual stresses have only rarely been investigated, and the challenges facing a rigorous treatment of them have often not been faced. This paper adopts a rigorous treatment technique to investigate residual stresses and their effect on the axial compression buckling strength under elastic conditions. It achieves this by considering consistent stress and displacement fields arising from local geometrical incompatibilities, and adopting their consequent geometric imperfections. The calculations of the strength of imperfect shells with residual stresses are compared with corresponding calculations for the same imperfections but with the residual stresses "annealed" out of the analysis. The results show that consistent residual stresses generally appear to strengthen a thin shell relative to the corresponding strength with only geometric imperfections present.

KEYWORDS

Buckling, cylindrical shell, dimple, fabrication misfit, imperfection, residual stress, silo, tank

1. INTRODUCTION

Buckling failure under axial compression is the controlling design consideration for most metal silos and many other shell structures. The buckling strength of a thin cylindrical shell under axial compression is well known to be very sensitive to the magnitude and shape of imperfections, which may be geometric, related to boundary conditions, or caused by residual or "locked in" stresses

www.EngineeringEBooksPdf.com

(Yamaki, 1984; Calladine, 1995). Geometric imperfections and imperfections in the boundary conditions have been widely studied over the last five decades. However, residual stresses have, until recently, received very little attention. This paper presents part of a rigorous numerical study of the relationship between misfits of geometry, residual stresses, induced geometric imperfections, and a resulting change in buckling strength (Holst, Rotter & Calladine, 1996, 1997, 1999, 2000).

The geometry of a real misfit is often in a form that is difficult to characterise, so it seems best to begin studies of the effects of fabrication misfits by using idealised forms. Here the idealised form is a local zone in which there is too little or too much material, and where the misfit may be in either the meridional or the circumferential direction, or both. These idealised forms provide a first step into a rather complicated field and their generalisation is then illustrated. It is not a simple matter to model fabrication misfits using finite element analysis. The introduction of excess or insufficient material seems to be best achieved by representing a small part of the shell as swelling or shrinking to the extent of the desired misfit. This strategem allows a variety of different misfit forms to be studied relatively simply.

The first part of this paper examines the effect of varying the radius to thickness ratio of thin metal cylindrical shells on the local imperfection form under shrinkage or swelling applied to a small square patch. The second part investigates the subsequent behaviour of the shell under externally applied axial loading. The sensitivity of the shell buckling strength to the length of a circumferential misfit strip is also discussed.

2. MISFITS OF GEOMETRY

Shell structures such as metal silos and tanks are frequently constructed from a set of curved panels or plates (Martens, 1988*b*). The seam between different plates is the major source of deviation from a truly cylindrical form (Fig. 1). These deviations or imperfections may be a result of the welding process and they may also be caused by a lack of fit between plates. A schematic detail of a fabrication misfit is shown in Fig. 1. In order to align the different plates to give a neat fit, the edges of the plates must be subjected to certain displacements. Whilst the magnitude of the lack of fit in the plane of the plate may be much less than one shell thickness, it gives rise to a significant bulging normal to the shell and large associated stresses.

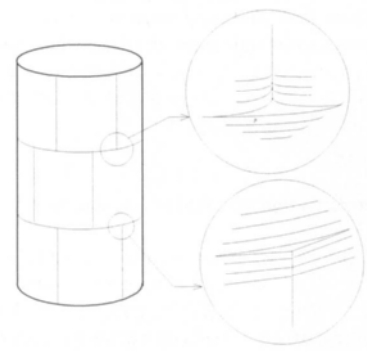

Fig. 1. Schematic drawing of a plated cylindrical shell structure with details of geometrical misfits

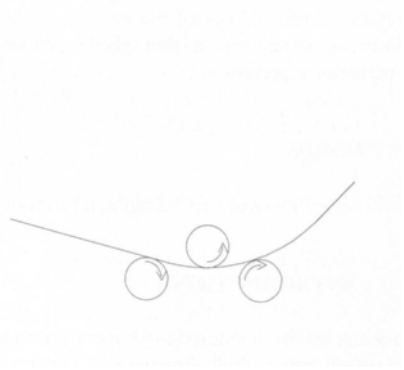

Fig. 2. Schematic drawing of the roller system for manufacturing curved metal panels.

www.EngineeringEBooksPdf.com

One of the main causes for misfits such as those depicted in Fig. 1 is the process by which the panels are curved (Lacher & Haspel, 1980; Martens, 1988*a*). These are generally produced from flat plates by feeding them through a system of rollers. Unfortunately this process results in small sections at both sides of the plate remaining flat (Fig. 2). Whilst these flat sections are removed in certain high precision applications, they are left in place for general structural components. In a constructed shell structure such as a silo or tank, the flat sections of the curved panels constitute a deviation from the cylindrical form.

Limited observations of full-scale silos suggest that fabrication misfits are nonuniform in practice. The actual misfit is highly complex and can take many different forms. As this is the first study of the problem, a stylised misfit geometry, which will give similar results to a first approximation and can be expanded to cover other forms, is investigated here. Thus a uniform lack of fit is applied to a small area of the shell over a local strip.

Two types of misfit are used in this paper: a small localized misfit and one in which one of the dimensions is significantly greater than the other. The simplest possible form of local misfit from a theoretical viewpoint is a single point source. This form is representative of a hotspot or a localized impact. The misfit may be biaxial, where there is a lack of fit in two orthogonal directions, or uniaxial. The second type of misfit of extended length will generally be uniaxial in character. This type of misfit may be a result of weld shrinkage or a lack of fit in fabrication.

Misfits in real structures are generally more complex in form, but a study of these is beyond the scope of the present paper. However, Holst *et al.* (2000) demonstrated that superposition of local patch misfits can be used to predict imperfections arising from general misfits along a circumferential or meridional seam. The localized and extended misfits are modelled here by applying a uniform shrinkage strain to a rectangular patch on the shell. A uniaxial lack of fit of Δa is simulated by applying a shrinkage strain $\Delta\varepsilon$ across the patch width a, where

$$\Delta\varepsilon = \frac{\Delta a}{a} \tag{1}$$

In a similar manner, a biaxial misfit is modelled by applying a lack of fit of $\Delta a = \Delta b$ in two orthogonal directions.

All analyses performed were geometrically nonlinear and static using the modified Riks method to determine the equilibrium curves (ABAQUS User's Manual, 1997). Nonlinear analyses had to be used both to ensure that all geometrically nonlinear effects were detected; and to discover whether a linear regime of behaviour could be found in which superposition rules might apply.

3 FINITE-ELEMENT ANALYSIS PROCEDURE

The commercial finite-element package ABAQUS was chosen for the present analysis; and elements of type S4R were used. These are 4-noded doubly curved thin shell elements. Steel cylindrical shell structures were examined in purely elastic analyses. Many different cylinder geometries were investigated. The reference cylinder described here had a radius $R = 5.0$ m, thickness $t = 10.0$ mm (i.e. $R/t = 500$), and height $H = 10.0$ m. The geometry of the undeformed shell is shown schematically in Fig. 3. A cylindrical co-ordinate system was used, where the position of a point on the shell middle surface is described by the co-ordinates θ in the hoop direction and x in the axial direction (measured on the undeformed cylinder).

www.EngineeringEBooksPdf.com

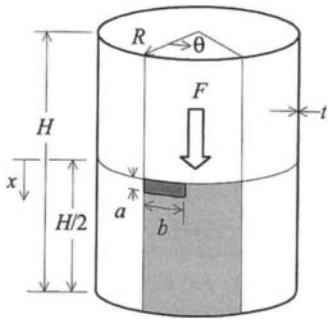

Figure 3. Schematic drawing of the loading and undeformed geometry for the shell.

To reduce the time required for computations, mirror symmetry boundary conditions were imposed such that only a segment of the shell needed to be analysed numerically, namely one of height $H/2$ and circumferential angle $\theta_{seg} = 45°$. This segment is indicated in Fig. 3 by means of a shaded area. The material, corresponding to steel, was assumed to be isotropic linear elastic, with a Young's modulus of elasticity $E = 2\times10^5$ MPa, and a Poisson's ratio $\nu = 0.3$.

The general procedure for analysis was as follows. In an initial step (Step 1), a strain of value $\Delta\varepsilon$ was imposed on the shell over a small rectangular patch of dimensions $a\times b$ (indicated by a trellis pattern in Fig. 3). Taking into account the mirror symmetry used, this corresponds to the imposition on a complete cylindrical shell of four rectangular shrinkage patches of dimensions $2a\times2b$. Throughout this paper, a positive value of $\Delta\varepsilon$ indicates an imposed shrinkage strain, whereas a negative value implies swelling. As a result of this strain and the associated stresses developed both within the patch and near it, a local dimple or bulge was formed. The second step then followed: an axial load F (total load on segment) was applied to the upper circular edge of the segment shown in Fig. 3 such that this edge of the shell displaced uniformly in the axial direction. Two distinct cases were examined in Step 2. In the first case (Analysis R) both the deformed geometry and the equilibrium residual stress state at the end of Step 1 were retained as the initial conditions for the second step. In the second case (Analysis A) only the deformed geometry after Step 1 was used at the start of the second step, corresponding to an analysis in which the residual stresses have been annealed out of the cylinder.

During Step 1, symmetry boundary conditions were imposed on the two edges parallel to the axis and at the upper circumferential boundary (at $x = 0$ in Fig. 3). The lower circumferential edge was radially and circumferentially restrained, but free to move axially. The symmetry boundary conditions used in Step 1 along the meridional edges were preserved during Step 2. The upper circumferential boundary was forced to displace under the imposed axial load by an amount $-u$ in the x direction, whilst the boundary conditions in the other translational and rotational degrees of freedom were retained. The lower boundary was fully restrained against translation and rotation.

4 BIAXIAL SHRINKAGE ON A SQUARE PATCH

In the first series of analyses a small square patch ($2a\times2a$) was subjected to a uniform isotropic or biaxial shrinkage $\Delta\varepsilon$ in Step 1. Holst *et al.* (1999) demonstrated that for the reference shell geometry ($R/t = 500$) the form of the geometric imperfection resulting from such a prescribed local misfit is described well by

www.EngineeringEBooksPdf.com

$$w = \frac{\pi R}{2}\frac{\Delta a}{\lambda} e^{-\pi\left(\frac{\eta}{2}+\xi\right)}\left(\sin\left(\pi\left(\frac{\eta}{2}+\xi\right)\right)+\cos\left(\pi\left(\frac{\eta}{2}-\xi\right)\right)\right) \tag{2}$$

if the dimensions of the square misfit patch are small enough ($a << \lambda$). Here the co-ordinates along the shell middle surface have been made dimensionless using the relationships $\xi = x/\lambda$ and $\eta = R\theta/\lambda$, and $\lambda \cong 2.44\sqrt{Rt}$ is the linear bending half-wavelength for the shell. Fig. 4 plots Eq. 2 together with data from a wide range of thin shells ($150 \le R/t \le 4000$) and for a wide range of applied strains. It is clear that Eq. 2 is also valid for here provided that the shrinkage area

$$\frac{A\Delta\varepsilon}{t^2} = 4\left(\frac{a}{t}\right)^2 \Delta\varepsilon \le 1 \tag{3}$$

Holst *et al.* (1999) showed that the applied strain-displacement relationship is practically linear for a small square misfit patch, if the shrinkage area is limited by Eq. 3. At larger shrinkage areas (as with the smallest misfit patches), the strain-displacement relationship becomes significantly nonlinear and the resulting imperfection pattern changes completely.

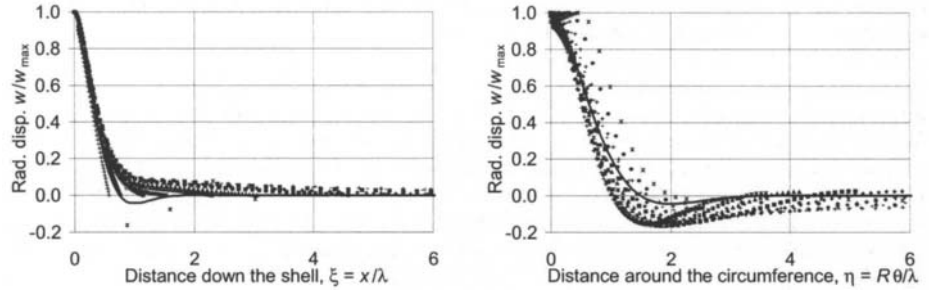

(*a*) along the line $\eta = 0$ (*b*) along the line $\xi = 0$

Figure 4. Normalised radial displacement for a wide range of R/t ratios (Step 1)

When the shell is subjected to a uniform axial load (Step 2) the form of the geometric imperfection changes substantially. Fig. 5 illustrates the evolution of the deformation pattern by plotting the normalised radial displacement at the end of Step 1, at the buckling load in Analysis R, and in the post-buckling domain in Analyses R and A. Initially, prior to buckling, only the amplitude of the imperfection increases.

The pattern after buckling is markedly different: the imperfection amplitude increases much more rapidly and a mode change also occurs when the extent of the dimple increases suddenly. The form of the dimple in the postbuckling domain is, however, the same whether or not residual stresses have been included in the buckling calculation.

www.EngineeringEBooksPdf.com

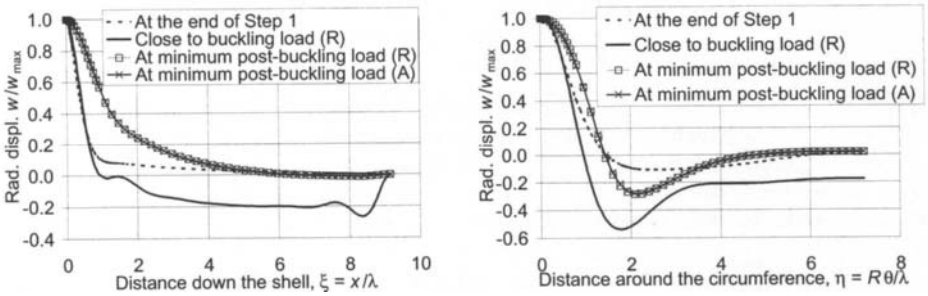

(*a*) along the line $\eta = 0$ (*b*) along the line $\xi = 0$

Figure 5. Dimensionless radial displacement for the reference cylinder (Step 2)

Even at the point of buckling, the essential form of the dimple remains the same as beforehand. Only away from the dimple peak does the form diverge from that at the end of Step 1. Beyond the gross locality of the dimple the deformed geometry is evidently unstable, displaying frequent changes of curvature particularly in the meridional direction. The plots of radial displacement in Fig. 5 point to a continuing linear deformation behaviour in the prebuckling regime when a uniform axial load is applied in Step 2. This is confirmed by the load-displacement diagram (Fig. 6) where the onset of nonlinear behaviour occurs at the buckling load.

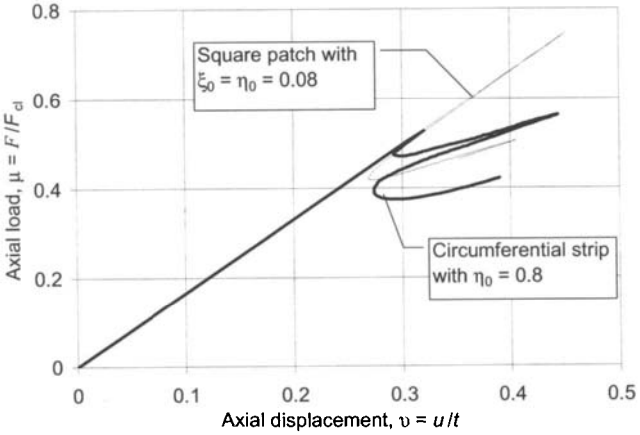

Figure 6. Normalized axial load against normalized axial displacement

Figure 6 shows a plot of the total axial load against the axial displacement $\upsilon = u/t$ at the upper edge for an Analysis R, including residual stresses. The total axial load, F, is normalized with respect to the axial load F_{cl} corresponding to the classical elastic critical buckling stress, $\sigma_{cl} = 0.605Et/R$. Thus for a segment of 45°

$$\mu = \frac{F}{F_{cl}} = \frac{4}{\pi} \frac{F}{0.605Et^2}. \tag{4}$$

www.EngineeringEBooksPdf.com

5 UNIAXIAL SHRINKAGE ON A CIRCUMFERENTIAL STRIP

The previous analyses have focused on a rather idealised misfit: a small local square zone in which too little material led to geometric imperfections and residual stresses. A more realistic condition is that in which the edge of a plate does not reach to the desired position and either clamps or weld shrinkage lead to misfits. A series of analyses was conducted in which a uniaxial lack of fit was applied to thin circumferential strip of varying length with a meridional lack of fit.

Holst *et al.* (1999) found that due to the approximate linearity of the problem, the deformed geometry of the shell for any misfit strip length can be obtained by adding the displacements resulting from a set of local misfits. Holst *et al.* (2000) went on to show that, for a particular long misfit of $\eta_0 = b/\lambda = 0.8$, the imperfection amplitude w_{max} increases almost linearly with increasing applied shrinkage strain. Whilst the load-displacement relationship is initially the same as for the case of a small square misfit patch, the buckling load is somewhat lower and the subsequent drop in strength is smaller (Fig. 6).

The variation of the buckling strength μ_{cr} (maximum load in Fig. 6) with imperfection amplitude is shown on a logarithmic scale in Fig 7. As the amplitude of the initial imperfection increases the buckling strength decreases, as expected, before the load-displacement behaviour changes fundamentally (Holst *et al.*, 2000). It is clear from Fig. 7 that for both strip lengths shown, the buckling strength is consistently greater when residual stresses are present than when they have been annealed out of the cylinder. This is directly related to the stress state of the shell at the end of Step 1 (Holst *et al.*, 2000). The difference in buckling strength between the two analysis types varies significantly. Where there is a very large difference (say 20 % or greater) it is recommended that the residual stresses be included in the buckling calculation so that the predicted strength is not excessively conservative. The imperfection amplitude at which the greatest difference is observed varies for different lengths of circumferential strip.

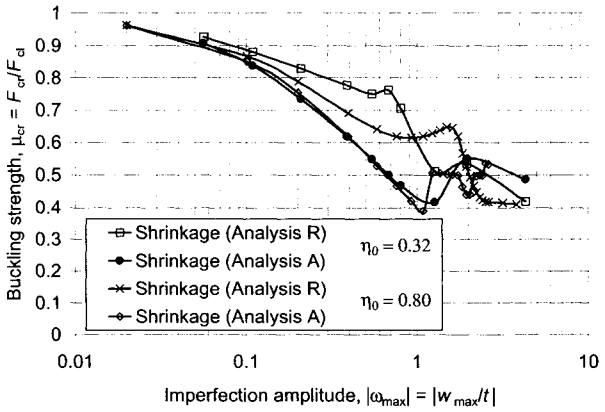

Figure 7. Variation of buckling strength with amplitude of imposed imperfection

6 CONCLUSIONS

a) For a small square misfit subject to biaxial strain, the form of the dimple or imperfection is uniform in the gross vicinity of the misfit.
b) The form remains constant over a wide range of shell geometries and levels of applied strain.

www.EngineeringEBooksPdf.com

c) The form of the dimple remains approximately constant in the prebuckling regime under applied external loading.
d) Buckling precipitates sudden changes to the dimple amplitude and mode.
e) The postbuckling drop in the load carrying capacity is less severe for a long narrow strip of uniaxial strain than for a small square misfit of biaxial strain.
f) The removal of the residual stress field in a shell significantly changes its behaviour under axial load. Thus in the cases examined in this paper, the buckling strength is significantly increased when the residual stresses are included in the buckling calculation. The imperfection amplitude for which the buckling strength calculation is most conservative varies as the strip length changes.

7 REFERENCES

1) ABAQUS User's Manual (1997). *ABAQUS/Standard Users's Manual, Volume 1, Version 5.7.* Pawtucket, Rhode Island: Hibbitt, Karlsson & Sorenson, Inc.
2) Calladine, C.R. (1995). Understanding imperfection-sensitivity in the buckling of thin-walled shells. *Thin Walled Structures: Special Issue on Imperfection-Sensitive Shells*, ed. G.D. Galletly, **23**, 215-235 (based on papers presented at the Euromech Colloquium 317, Liverpool, UK, 21-23 March 1994).
3) Holst, J.M.F.G., Rotter, J.M. & Calladine, C.R. (1996). Geometric imperfections and consistent residual stress fields in elastic cylinder buckling under axial compression. In *Proceedings of the International Workshop on Imperfections in Metal Silos: Measurement, Characterisation, and Strength Analysis*, 199-216 (based on lectures presented at the CA-Silo workshop, Lyon, France, 19 April 1996).
4) Holst, J.M.F.G., Rotter, J.M. & Calladine, C.R. (1997). Characteristic geometric imperfection forms for cylinders derived from misfit calculations. In *Carrying Capacity of Steel Shell Structures* (Proceedings of the International Conference, Brno, Czech Republic, 1-3 October 1997), eds V. Krupka & P. Schneider, 333-339.
5) Holst, J.M.F.G., Rotter, J.M. & Calladine, C.R. (1999). Imperfections in cylindrical shells resulting from fabrication misfits. *Journal of the Engineering Mechanics Division, Proceedings of the American Society of Civil Engineers*, **125**, 4, 410-418.
6) Holst, J.M.F.G., Rotter, J.M. & Calladine, C.R. (2000). Imperfections and buckling in cylindrical shells with consistent residual stresses. *Journal of Constructional Steel Research,* **54**, 265-282.
7) Lacher, G. & Haspel, H. (1980). Baustellenmaßnahmen zur Erzielung der Maßhaltigkeit bei einem großen Zementklinkersilo. *Der Stahlbau*, **49**, 65-69.
8) Martens, P. (1988a). Stahl- und Aluminiumsilos. In *Silo-Handbuch,* ed. P. Martens. Wilhelm Ernst & Sohn, Berlin, Germany, 255-341.
9) Martens, P. (1988b). Bauausführung: Ausführung in Stahl. In *Silo-Handbuch,* ed. P. Martens. Wilhelm Ernst & Sohn, Berlin, Germany, 460-463.
10) Teng, J.G. & Rotter, J.M. (1992). Buckling of pressurized axisymmetrically imperfect cylinders under axial loads. *Journal of Engineering Mechanics, ASCE*, **118**, no. 2, 229-247.
11) Yamaki, N. (1984). *Elastic Stability of Circular Cylindrical Shells*. Amsterdam, North Holland, Elsevier Applied Science Publishers.

www.EngineeringEBooksPdf.com

Advances in Steel Structures, Vol. II
Chan, Teng and Chung (Eds.)
© 2002 Elsevier Science Ltd. All rights reserved.

BUCKLING BEHAVIOUR OF EXTENSIVELY-WELDED STEEL CYLINDERS UNDER AXIAL COMPRESSION

X. Lin and J.G. Teng

Department of Civil and Structural Engineering
The Hong Kong Polytechnic University,
Hong Kong, China

ABSTRACT

Thin cylindrical shells in large steel silos and tanks are generally constructed from a large number of rolled panels with many circumferential and meridional welds. This extensive use of welding is expected to lead to unique imperfections and residual stresses that can greatly reduce the buckling strength of these shells when subject to axial compression. While many studies have examined the buckling strength of cylindrical shells with one or more circumferential welds, no previous study has considered the buckling strength of cylindrical shells with multiple circumferential welds together with a large number of short meridional welds as found in large civil engineering steel shells. This paper presents the results of the first two tests on laboratory models of such extensively welded shells. The experimental procedure is described first. Typical test results are then summarized and compared with finite element predictions which do not account for the effect of welding-induced residual stresses. These comparisons indicate that the effect of residual stresses in these shells may be considerable, and may be either detrimental or beneficial.

KEYWORDS

Buckling, Experiments, Cylindrical Shells, Cylinders, Silos, Axial Compression, Imperfections, Residual Stresses

INTRODUCTION

Steel silos and tanks are common civil engineering steel shell structures. Axial compression very often dominates the design of the thin cylindrical shell wall of these structures. For cylindrical shells in large steel silos and tanks, the method of rolling a single sheet (or a small number of sheets) and welding (or riveting) along the meridional seam (referred to as the rolling and seaming method hereafter) is not a feasible method of fabrication. Instead, they are commonly constructed from a large number of curved panels joined by many continuous circumferential and short meridional welds (referred to as the panel method hereafter). A large steel silo constructed by the panel method is shown in Figure 1. The rolling and seaming method is however commonly used for fabricating specimens in laboratory tests and smaller cylinders for many other applications.

www.EngineeringEBooksPdf.com

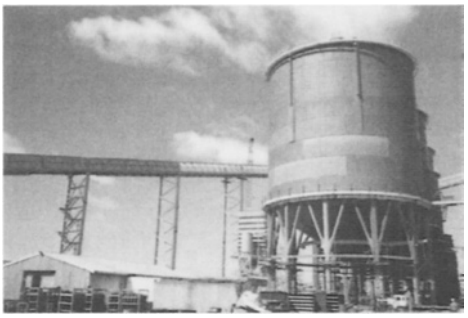

Figure 1: Steel silo constructed by the panel method

The buckling strength of axially compressed cylindrical shells is highly sensitive to initial geometric imperfections. Existing research suggests that both the magnitude and form of geometric imperfections are important in reducing the buckling strength (Teng, 1996; Rotter, 1998), and the form of imperfections depends on the fabrication process (Arbocz, 1982; Chryssanthopoulos *et al.*; 1991; Rotter *et al.*, 1992). This has serious consequences for large civil engineering steel cylindrical shells as found in steel silos and tanks: existing test results for un-stiffened thin cylinders almost exclusively relate to laboratory specimens constructed using the rolling and seaming method, which is not representative of shells constructed using the panel method. Doubt therefore exists about the relevance of existing laboratory test results and design provisions based on these results to these large civil engineering cylinders.

The extensive use of welding in the panel method leads to unique geometric imperfections which may be significantly more detrimental than those from the rolling and seaming method (e.g. Schmit and Swadlo, 1996). The associated residual stresses may further reduce the buckling strength. An important feature of the imperfections from the panel method is a nearly axisymmetric weld depression at each circumferential weld, consequently a number of recent studies have been carried out on thin cylinders with a single or multiple weld depressions (e.g. Rotter & Teng, 1989; Teng & Rotter, 1992; Rotter, 1996; Berry *et al.*, 2000; Pircher & Birdge, 2001a, 2001b; Pircher *et al.*, 2001). These studies showed that even the axisymmetric weld depressions alone can lead to buckling strengths which are lower than those of other known forms of practically credible geometric imperfections of the same magnitude.

While the existing studies on cylindrical shells with axisymmetric weld depressions have shed insightful light on the buckling behaviour of cylindrical shells constructed by the panel method, a fuller understanding can only be achieved by considering both the axisymmetric and non-symmetric components of geometric imperfections as a well as the associated residual stresses. Both theoretical and experimental studies are required, and are being undertaken in an on-going project at The Hong Kong Polytechnic University. This paper presents the results of the first two tests that have been completed together with the experimental procedure. Comparisons between the test and finite element results are also presented to evaluate the effect of residual stresses.

FABRICATION OF MODEL SHELLS

Fabrication of small-scale model shells that closely reassemble large real cylinders is a great challenge. In real construction using the panel method, flat plates of relatively small sizes are rolled into circular panels and then joined to form circular strakes. These circular strakes are then assembled to form the complete cylinder using circumferential welds. If exactly the same technique is adopted in the laboratory, the process becomes very tedious and there is a great deal of difficulty in assembling all pieces to fit together smoothly. An innovative two-stage fabrication method has been developed by the authors for fabricating small-scale models for laboratory bucking experiments (Teng and Lin, 2002). In Stage I, two steel sheets

www.EngineeringEBooksPdf.com

are rolled into a cylindrical surface and then joined with two meridional welds to form a cylinder. Ring stiffeners providing radial restraints are then added to both ends to maintain circularity before the Stage II operation. In Stage II, 'pattern welding' in the form of controlled heat input in a required pattern of circumferential and meridional 'welds' (the quotation marks are dropped hereafter) is then carried out on the central portion of the shell surface, producing a specimen (Figures 6 and 7) with its central portion being similar to the cylindrical shell in a real steel silo or tank. By analogy to real shells, the areas enclosed by welds are referred to as panels, while the circumferential rows of panels are referred to as strakes. The two real meridional welds are referred to as the meridional weld seams to differentiate them from the short meridional welds from pattern welding. Further details of this two stages technique are described in Teng and Lin (2002).

TEST SET-UP

The tests were carried out using an existing shell buckling test facility (Teng *et al.*, 2001) with necessary modifications (Figure 2). The upgraded facility was designed for displacement control during loading using an MTS Actuator. Load transfer from the actuator to the cylinder is effected through a universal joint, a shallow loading cone and a loading ring with a knife edge to ensure uniform loading on the end ring.

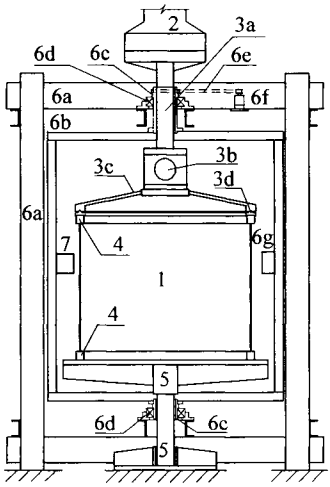

1-Specimen
2-MTS Swivel Head
3-Load Transfer System
3a-Load transfer cylinder
3b-Universal joint
3c-Loading cone
3d-Loading ring
4-End Ring
5-Support
6-Measurement System
6a-Supporting frame
6b-Rotating frame
6c-Rotating shaft
6d-Spherical roller bearing
6e-Timing belt
6f-Stepping motor
6g-Laser meter
7-Welding Carriage

Figure 2: Overall view of the buckling test set-up

The facility includes a measurement system for precise surveys of geometric imperfections and deformations of the test specimen (Teng *et al.*, 2001). This measurement system rotates a laser displacement meter around and moves it up and down the test specimen to provide a three dimensional survey automatically. These movements are effected by two stepping motors controlled by a computer which also records the measurement results.

Four dial gauges were installed inside the test specimen to measure the relative displacements between the two end rings (i.e. axial shortening). Details of the setup for these dial gauges are given elsewhere (Lin and Teng 2002). Strain gauges were placed on the inner surface of the cylinder to avoid any interference with shape surveys on the external surface. Details of the strain gauge layouts and strain readings are given in Lin and Teng (2002). Two holes were made on the loading cone for the cables of the dial gauges and the wires of the stain gauges to pass through.

www.EngineeringEBooksPdf.com

TEST RESULTS AND OBSERVATIONS

Specimens and Material

Two specimens, identified as 09P0624 and 09P0404 within the overall test program (Lin and Teng 2002) but simply referred to as Specimens A and B herein, have so far been tested. Both models contained three strakes in the middle portion produced by pattern welding (Figures 6 and 7). Specimen A had rectangular panels with a panel height of $6\sqrt{Rt}$ and a panel width of $24\sqrt{Rt}$, while Specimen B had square panels with a width of $4\sqrt{Rt}$. The nominal radius of the models is 500 mm, while the nominal height of the models is 750 mm (excluding the end portions in the rings). The short meridional welds on one strake were offset from those on the next strake by half-width of the panels. Material properties of the steel sheets used in these models were determined from tensile tests according to the British Standard (BSEN10002-1:1990). Eight coupons were cut from two randomly selected steel sheets for tensile tests, with two cut along the meridional direction and two along the circumferential direction in terms of the rolled shape from each of the two selected sheets. The obtained stress-strain curves are almost elastic-perfectly plastic, with a small amount of strain hardening. As both the Young's modulus and the yield stress of one of the coupons from the meridional direction deviate from those of the other seven coupons by about 5%, the results of this coupon are excluded from consideration. The average values of the other seven test coupons, which were employed in subsequent numerical analyses, are as follows: thickness = 0.874mm; yield stress = $189.15\,N/mm^2$; and Young's modulus = $205{,}274\,N/mm^2$. The average tangent modulus of the stress-strain curve in the initial post-yield stage, which was used in subsequent buckling analyses, was found to be $3207\,N/mm^2$.

Geometric Imperfections

The external surfaces of both specimens were precisely surveyed before and after pattern welding. The results for specimen A are shown in Figures 3 and 4. In determining these surfaces, measurements on the test specimen were compared with those on a 'perfect' machined calibration cylinder. It is obvious that there exists considerable ovalization in the top part of the cylinder in both surfaces. However, these deviations are associated with the lowest 2 harmonic modes (0 or 1) in the circumferential direction and are unlikely to have significantly affected imperfections in the oscillating pattern or the buckling strength.

Figure 5 shows distortions due to pattern welding in Specimen A. This was obtained simply by subtracting the coordinates of the external surface before pattern welding from those of the external surface after pattern welding. It shows that the welding induced distortions are confined to the middle portion of the cylinder where pattern welding was applied. Welding induced imperfections are mainly inward distortions and are closely associated with the welds. The imperfections induced by pattern welding in Specimen B are much larger than those in Specimen A due to the much closer spacing of meridional welds in the latter (Lin and Teng 2002).

Buckling Behaviour

The two specimens were loaded in uniform axial compression to failure in the buckling test facility. Buckles first appeared in the pattern-welded portions, within the circumferential ranges of 210^0 to 270^0 and 120^0 to 180^0 respectively in specimens A and B. Buckling of Specimen A happened suddenly when the MTS actuator displacement was held constant for a while. The test facility was found ineffective in implementing displacement control during the failure process, due to various constraints which led to a loading frame of insufficient rigidity. In both specimens, buckles first appeared at some distance from the two continuous meridional weld seams, and then propagated circumferentially and somewhat meridionally during postbuckling deformations. These observations indicate that the two meridional weld seams were not critical despite the large associated imperfections. Many buckles were confined to the middle portions of the specimens, confirming the detrimental effect of the patterned

www.EngineeringEBooksPdf.com

welds. The post-buckled shapes of the two specimens are shown in Figures 6 and 7 respectively, with the load-displacement curves given in Figure 8 where the displacements are those of the top edge.

The buckling load of Specimen A is 213.7kN, which is 36.9% of the classical buckling load of a corresponding perfect cylinder (Figure 8), whereas the buckling load of Specimen B is 98.1kN, being only 16.5% of the classical buckling load of a corresponding perfect cylinder. It is of interest to note that specimen B could take another 6kN after buckling before final collapse occurred. These results indicate the severity of the imperfections in these specimens.

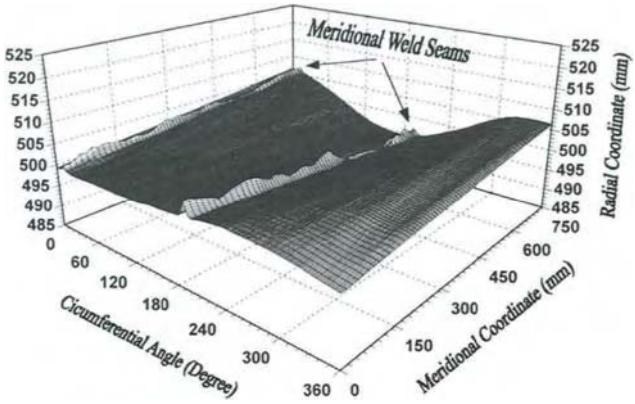

Figure 3: External surface of Specimen A before pattern welding

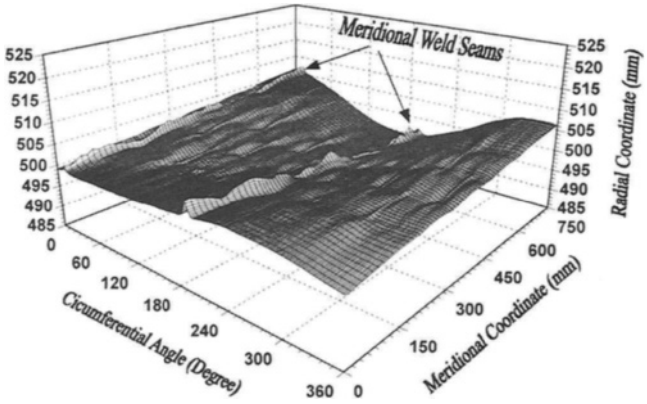

Figure 4: External surface of Specimen A after pattern welding

www.EngineeringEBooksPdf.com

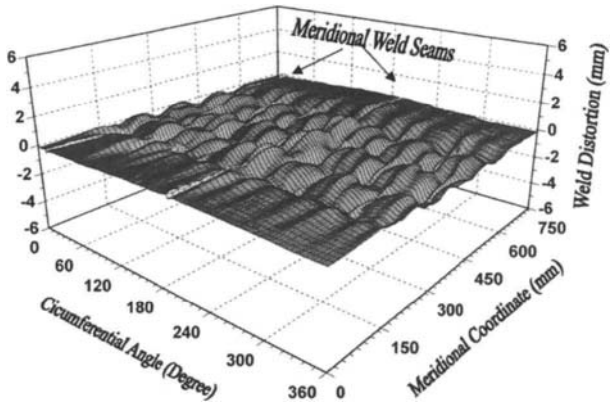

Figure 5: Imperfections in Specimen A induced by pattern welding

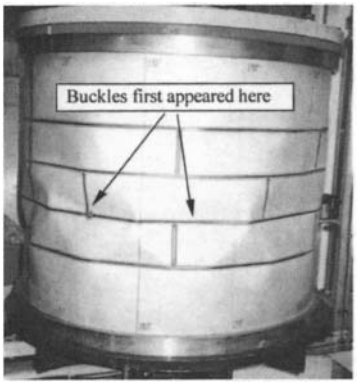

Figure 6: Postbuckled shape of Specimen A

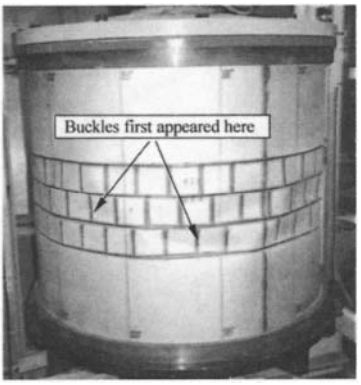

Figure 7: Postbuckled shape of Specimen B

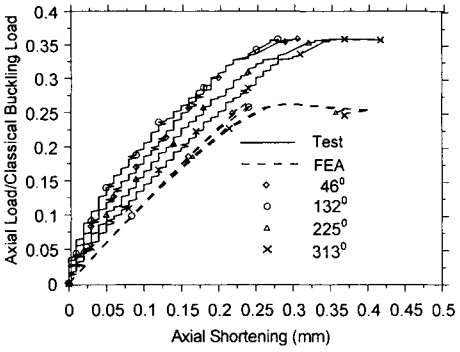

(a) Specimen A

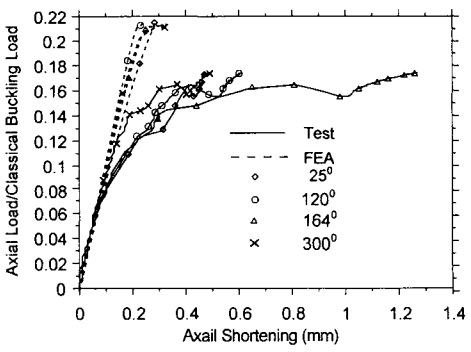

(b) Specimen B

Figure 8: Load-displacement curves

www.EngineeringEBooksPdf.com

NONLINEAR FINITE ELEMENT PREDICTIONS

Non-linear analyses of the two test specimens including the measured geometric imperfections after pattern welding were carried out considering both geometric and material nonlinearities. The analyses were carried out using the S4 element of the well-known finite element package ABAQUS. The steel was modelled as an elastic-plastic material with a bilinear stress-strain curve. In the finite element analysis, the shell was clamped at the bottom edge, but at the top edge, the rigid ring was explicitly modelled using a shell element with a large stiffness (Lin and Teng 2002).

The load-axial displacement curves of selected nodes on the top edge are shown in Figure 8 for both specimens. Apart from other differences between test and finite element results, it can be seen that the test buckling load of Specimen A is higher than that from finite element analysis, whereas the test buckling load of Specimen B is lower than that from finite element analysis. The finite element analysis underestimated the buckling load of Specimen A by 26.66% but overestimated the buckling load of Specimen B by 29.7%. These discrepancies are believed to be due to the omission of residual stresses in the finite element models, which demonstrates that residual stresses in these shells can be either significantly beneficial or significantly detrimental.

CONCLUDING REMARKS

This paper has been concerned with the buckling behaviour of laboratory models of large steel cylindrical shells featuring many welds, as found in large civil engineering shell structures such as steel silos and tanks. An innovative method for the fabrication of laboratory models has been introduced, together with the test set-up. The fabrication method successfully produced models with an oscillating pattern of imperfections and these imperfections had a severe effect on the buckling strengths as revealed by the buckling tests and nonlinear finite element analyses. While it remains to be established that the geometric imperfections in these models are closely similar to those in real structures, a task that will be attempted by the authors in the near future, the limited test results have illustrated the role of the residual stresses in determining the buckling strength of such model shells: they have a significant effect which can be either beneficial or detrimental. The effect of residual stresses will continue to be a focus in the on-going project on these shells.

ACKNOWLEDGEMENTS

The work described here forms part of the project "Buckling Strength of Axially Compressed Cylinders Built from Many Welded Panels" supported by a grant from the Research Grants Council of the Hong Kong Special Administrative Region (Project No. PolyU 5045/98E), with additional support from The Hong Kong Polytechnic University. The authors are grateful for this support. The technicians of the Heavy Structures Laboratory of the Department are thanked for their strong technical support.

REFERENCES

Arbocz, J. (1982). The imperfection data bank, a means to obtain realistic buckling loads. In *Buckling of shells*, E. Ramm, ed., Springer Verlag, New York, 535-567.

Berry, P.A., Rotter, J.M. and Bridge, R.Q. (2000). Compression tests on cylinders with circumferential weld depressions. *Journal of Engineering Mechanics, ASCE,* **126:4,** 405-413.

BSEN10002-1. (1990). *Tensile Testing of Metallic Materials: Part 1. Method of Test at Ambient Temperature*. British Standard Institution

www.EngineeringEBooksPdf.com

Chryssanthopoulos, M.K., Baker, M.J. and Dowling, P.J. (1991). Statistical analysis of imperfections in stiffened cylinders. *Journal of Structural Engineering, ASCE*, **117:7**, 1979-1997.

Lin X. and Teng, J.G. (2002). Buckling experiments on extensively-welded cylinders under axial compression. To be published.

Pircher, M., Berry, P.A., Ding, X. and Bridge, R.Q. (2001). The shape of circumferential weld-induced imperfections in thin-walled steel silos and tanks. *Thin-Walled Structures,* **39:**999-1014

Pircher, M. and Bridge, R. (2001a). The influence of circumferential weld-induced imperfections on the buckling of silos and tanks. *Journal of Construction Steel Research,* **57**:569-580.

Pircher, M. and Bridge R.Q. (2001b). Buckling of thin-walled silos and tanks under axial load-some new aspects. *Journal of Structural Engineering, ASCE,* **127:10**, 1129-1136.

Rotter, J.M. (1996). Buckling and collapse in internally pressurized axially compressed silo cylinders with measured axisymmetric imperfections: imperfections, residual stresses and local collapse. *Proceedings, International Workshop on Imperfections in Metal Silos*, INSA, Lyon, France, 119-139.

Rotter, J.M. (1998). Shell structures: the new European standard and current research needs. *Thin-Walled Structures*, **31:1-3**, 3-23.

Rotter, J.M., Coleman, R., Ding, X.L. and Teng, J.G. (1992). The measurement of imperfections in cylindrical silos for buckling strength assessment. *Proceedings, 4th International Conference on Bulk Materials Storage, Handling and Transportation*, IEAust, Wollongong, Australia, 473-479.

Rotter, J.M. and Teng J.G. (1989). Elastic stability of cylindrical shells with weld depression. *Journal of Structural Engineering, ASCE*, **115:5**, 1244-1263.

Schmidt, H. and Swadlo, P. (1996). Two buckling tests demonstrating the influence of the pattern of geometrical and structural imperfections on the axial compressive buckling strength of cylindrical shells. *Proceedings, International Workshop on Imperfections in Metal Silos*, INSA, Lyon, France, 181-190.

Teng, J.G. (1996) Buckling of thin shells: recent advances and trends. *Applied Mechanics Reviews, ASME*, **49:4**, 263-274.

Teng, J.G. and Lin X. (2002). Fabrication of small models of large cylinders with extensive welding for buckling experiments, *Proceedings, SSRC Annual Stability Conference*, Seattle, USA, April, 2002, 245-266.

Teng, J.G. and Rotter, J.M. (1992). Buckling of pressurized axisymmetrically imperfect cylinders under axial loads. *Journal of Engineering Mechanics, ASCE,* **118:2**, 229-247.

Teng, J.G., Zhao, Y. and Lam, L. (2001). Techniques for buckling experiments on steel silo transition junctions. *Thin-Walled Structures* **39:8**, 685-707.

www.EngineeringEBooksPdf.com

Advances in Steel Structures, Vol. II
Chan, Teng and Chung (Eds.)
© 2002 Elsevier Science Ltd. All rights reserved.

EXPERIMENT ON A MODEL STEEL BASE SHELL OF THE COMSHELL ROOF SYSTEM

H.T. Wong and J.G. Teng

Department of Civil and Structural Engineering
The Hong Kong Polytechnic University, Hong Kong, China

ABSTRACT

The popularity of thin concrete shell roofs has gradually declined over the past few decades, despite their many advantages. The main reason for this decline has been the costly and labour-intensive process of constructing and removing the necessary formwork and falsework. To overcome this difficulty, a new shell roof system, referred to herein as the Comshell system, has recently been proposed. A Comshell roof is constructed from a steel base shell formed by bolting together a large number of standard size modular units and cast in-situ concrete. The steel base shell serves as both the permanent formwork and the tensile reinforcement. A main design issue of Comshell roofs is the buckling strength of the bolted steel base shell during the construction stage under wet concrete loading. Due to the many bolted connections, the behaviour of these bolted base shells is complicated, so experiments are required to gain structural insight and the necessary test data for subsequent verification of numerical models. This paper is concerned with the experimental behaviour of these base shells at model scale, presenting both the experimental set-up and the results of the first experiment.

KEYWORDS

Shells, Roofs, Concrete Shells, Bolted Steel Shells, Composite Construction, Modular Construction, Wet Concrete Loading, Buckling, Design

INTRODUCTION

Many thin concrete shells have been built around the world as large span roofs, but their use has gradually declined over the past few decades. This decline has been due mainly to the high cost of construction and removal of temporary formwork and associated falsework for concrete casting in the construction of a thin concrete shell. This labour intensive and costly process of construction, coupled with the increasing ease in analysing complex skeletal spatial structures offered by advances in computer technology, has made concrete shells much less competitive than they were a few decades ago.

Over the years, there have been several attempts aimed at eliminating the need for temporary formwork in constructing thin concrete shell roofs, but these have met with only limited success. An excellent review of these attempts and other developments of thin concrete shell roofs has been given by Medwadowski (1998) who concluded that forming "remains the great, unsolved problem of construction of concrete thin shell roofs. Any and all ideas should be explored, without prejudice." The latest development in the

www.EngineeringEBooksPdf.com

forming of thin concrete shell roofs is the Comshell roof system proposed by Teng (2001) which is believed to be a very promising solution to this difficult problem.

For the Comshell system to be widely used in practice, many issues have to be studied to establish a sound understanding of the behaviour and strength of these shells, and to develop suitable design methods. At the present, a number of failure modes have been identified, and each needs a great amount of research. These failure modes are associated with either the construction stage or the service stage and are currently being investigated at The Hong Kong Polytechnic University in collaboration with Shanghai Jiaotong University and Zhejiang University. A main design issue of Comshell roofs is the buckling strength of the bolted steel base shell during the construction stage under wet concrete loading. Due to the many bolted connections, the behaviour of these bolted base shells is complicated, so experiments are required to gain structural insight and the necessary test data for subsequent verification of numerical models. This paper is concerned with the experimental behaviour of these base shells at a model scale, presenting both the experimental set-up and the results of the first experiment.

THE COMSHELL SYSTEM

A Comshell roof is a steel-concrete composite shell roof formed by pouring concrete on a thin stiffened steel base shell which serves as both the permanent formwork and the tensile steel reinforcement. A brief description of the system is given here, but further details are available elsewhere (Teng, 2001).

The steel base shell is constructed by bolting together modular steel units in the form of an open-topped box consisting of a flat or slightly curved base plate surrounded by edge plates (Figure 1). By adopting different shapes for the base, different shell forms can be achieved but this paper is limited to cylindrical shell roofs only (Figure 2) as they are the easiest to construct by this modular approach.

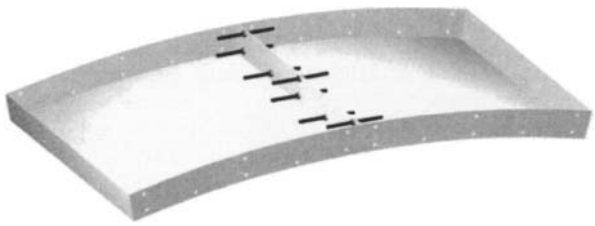

Figure 1: Modular units and bolted connection

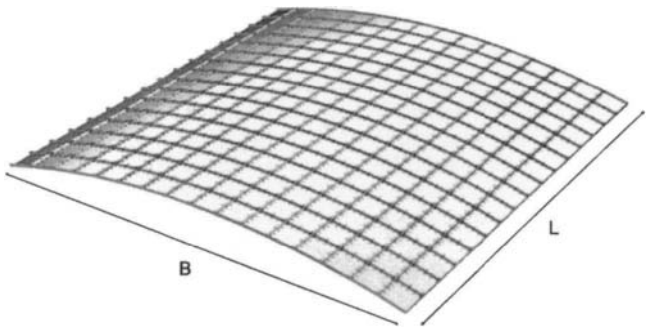

Figure 2: Steel base shell formed from modular units

www.EngineeringEBooksPdf.com

BUCKLING EXPERIMENTS ON BOLTED BASE SHELLS: OVERALL CONSIDERATIONS

During the construction stage, the wet concrete acts as loading on the bolted steel base shell which can fail by either local buckling or overall buckling. Local buckling can be in one of two modes: buckling of the bolted stiffeners formed from edge plates and bucking of the base plates of the modular units. Overall buckling of the bolted base shell involves global shape changes, while local buckling only involves deformations of either the stiffeners or the base plates or both.

With the availability of powerful computer software for nonlinear analysis of shells, the purpose of experiments is mainly to calibrate numerical models instead of providing a parametric behavioural study. Such calibration is essential when there are theoretical uncertainties in numerical modelling. Typical uncertainties in modelling the buckling behaviour of steel structures include geometric imperfections, residual stresses and connection behaviour. All these aspects are present in the bolted base shell of a Comshell roof, but the uncertainty of the connection behaviour is the most important aspect.

With the above considerations in mind, four buckling experiments on these steel base shells have been planned, with particular attention to connection details and behaviour. Two of the experiments are for the local buckling mode while the other two are for the overall buckling mode. Two experiments have been planned for each failure mode to enhance the confidence in the experimental results. Only the first experiment has been completed at the time of writing, so in the rest of the paper, only results from this experiment together with the experimental procedure are presented.

A difficulty with the testing of model shell roofs lies in the proper scaling of real dimensions. As the present experiments are for the calibration of future numerical models, emphasis has been placed on the appropriate simulation of the anticipated buckling behaviour, particularly the effects of connection flexibility on buckling behaviour. As a result, the dimensions of the local buckling test specimens were obtained by scaling down the dimensions of a prototype roof by a factor of 10 without regard to the scaling of the sheeting thickness and the height of edge plates. Table 1 provides the dimensions of the first local buckling specimen versus the dimensions of a possible full scale steel base shell.

TABLE 1
DIMENSIONS OF TEST SPECIMEN AND PROTOTYPE SHELL

	Span (L)	Chord width (B)	Radius (r)	Rise (f)	Height of edge plates (h)	B/f
Prototype (m)	15	22	18	4	0.1	5.5
Specimen (m)	1.500	2.218	1.750	0.396	0.06	5.6

FABRICATION OF THE FIRST TEST SPECIMEN

The first bolted steel base shell specimen has been tested. It was fabricated by bolting together 40 modular units into 5 rows in the transverse direction and 8 columns in the longitudinal direction (Figure 3). Each modular unit had a base size of 300 mm x 300 mm and a height of edge plate of 60 mm (Figure 4). Two of the edge plates were inclined to the base, while the other two edge plates were perpendicular to the base. The alternative of using modular units with a curved base (Figure 1) was not adopted to enable simpler fabrication.

Zinc-galvanized cold-formed steel sheets with a nominal thickness of 1mm were used to fabricate the modular units. These steel sheets were chosen to fabricate the specimen, as this thickness is commonly available and suitable for the necessary welding involved in fabrication. The height of the edge plates was chosen to accommodate two rows of bolts with washers (Figures 3 and 4). Table 2 provides material

www.EngineeringEBooksPdf.com

properties of the steel sheet averaged from the results of 4 tensile tests, where the percentage elongation after fracture is for a 50 mm gauge length. The stress-strain curves are detailed in Wong and Teng (2002).

TABLE 2
MATERIAL PROPERTIES OF THE STEEL USED

Thickness $t(mm)$	Elastic modulus E_p (GPa)	0.2% proof stress $\sigma_{0.2}$ (MPa)	Tensile strength σ_u (MPa)	Elongation after fracture ε_u (%)
1.03	193.03	285	340	29.6

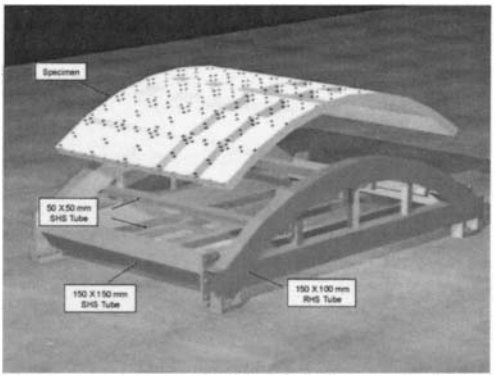

Figure 3: Comshell specimen and support frame (computer–generated mage)

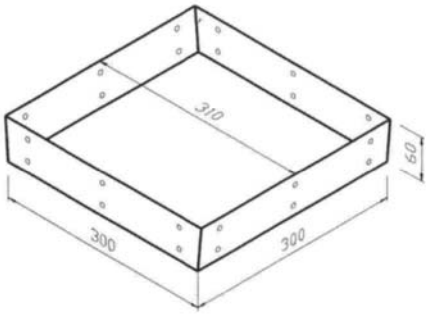

Figure 4: Dimensions of modular units for use in the first experiment

(a) Steel sheet during punching

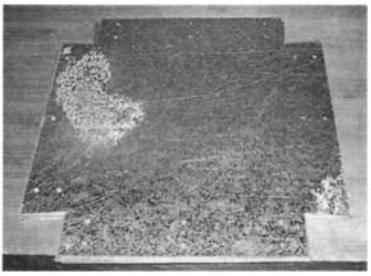

(b) Square sheet with corners cut off

(c) Corner welding

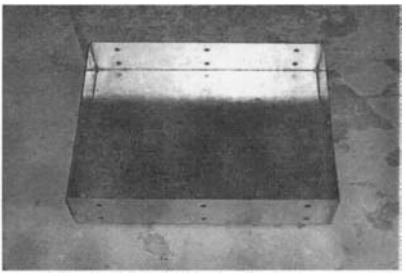

(d) Final product

Figure 5: Fabrication process of open-topped box modular unit

www.EngineeringEBooksPdf.com

While stamping is expected to be the forming process for the modular unit in future practical applications, and can be easily realized by a commercial manufacturer if a large number of units are required, the fabrication of the experimental modular units had to follow a simpler approach. The fabrication of these experimental modular units involved the steps of cutting, punching, bending and welding. First, a square steel sheet with four corner cut-outs and pre-drilled holes were obtained accurately by a numerically controlled machine (Figures 5a and 5b). Second, a bending machine also controlled by a computer was employed to fold the four edge plates to specified angles of inclination. Finally, the four corners were welded to obtain a modular unit in the form of an open-topped box (Figure 5c and 5d). To achieve high quality welding, a TRANSTIG 16Pi pulse TIG (Tungsten Inert Gas) welding machine was employed. This machine provided smooth and clean welds. During welding, the corner was restrained by a small former covered with a copper sheet which provided a heat sink to reduce welding-induced distortions to the unit. This procedure of fabrication enabled modular units of accurate dimensions to be achieved. Following the fabrication of all 40 modular units, the model steel base shell was assembled from these units with bolts.

EXPERIMENTAL SET-UP

An overall view of the test frame is shown in Figure 3. This test frame was fabricated mainly using $150\times100mm$ rectangular hollow section (RHS) tubes and $150\times150mm$ square hollow section (SHS) tubes. Moreover, $50\times50mm$ SHS tubes were employed in both the longitudinal and transverse directions, both to enhance the stiffness of the test frame and to prevent the test specimen from total collapse. The peripheral edge plates of the test specimen were bolted to the longitudinal beams and transverse arches which had pre-drilled holes. The stiff edge beams and arches were adopted to ensure that the boundary conditions of the base shell can be easily defined in subsequent finite element modelling work. Further details of the test frame design can be found elsewhere (Wong and Teng 2002).

The configuration of instrumentation is shown in Figure 6. In Figure 6, for ease of reference, each row of units is denoted by a letter while each column by a number. A unit can be referred to by the row and the column it belongs to, while a stiffener can be defined by referring to the two adjacent units. For example, unit C1 sits at the intersection of row C and column 1, while stiffener B4-C4 sits between units B4 and C4. The two edge plates of the same stiffener can also be differentiated, for example, as plate B4-C4 and plate C4-B4 for stiffener B4-C4, with plate B4-C4 belonging to unit B4.

The instrumentation consisted of 29 linear variable differential transformers (LVDTs) for the measurement of both horizontal and vertical displacements, with most of them being placed along row C and column 4 (Figure 6). The other LVDTs were employed to monitor support movements. Fourteen strain gauges were installed on the base plates of units C1 to C4 and stiffeners B4–C4 and C4–D4. Two-element strain rosettes were installed at the centres of modular units, while single-element gauges were installed on the stiffeners. The latter were placed as closely as possible to their upper edges.

During the construction stage, a real steel base shell is under gravity loading from the wet concrete. This loading was simulated in the present study using an innovative pulley-based loading system which provides an easy and convenient way of loading at a large number of points. For the present test, 28 point loads were applied. As a new loading system, a calibration test was conducted first to verify its effectiveness and accuracy. Pulleys with a diameter of 52mm were used in the calibration test. The input loads was achieved using standard weights, while the output load was measured using two TCLP-5B tension and compression load cells. An overall view of the calibration set-up is shown in Figure 7a. Results of this calibration test are shown in Figure 7b. It is seen here that the mechanical loss of this system is almost zero at the beginning but increases with the input load. However, even with an input load of about 3kN which is above the load capacity required in this test, the error is less than 5%. This pulley system was thus concluded to be of sufficient accuracy. It should be noted that pulleys of a larger size should be used if larger loads are to be applied.

www.EngineeringEBooksPdf.com

During the buckling experiment, four load cells were installed along the mid-span to monitor the applied loads. Further details of this innovative loading system are described elsewhere (Wong *et al.* 2002).

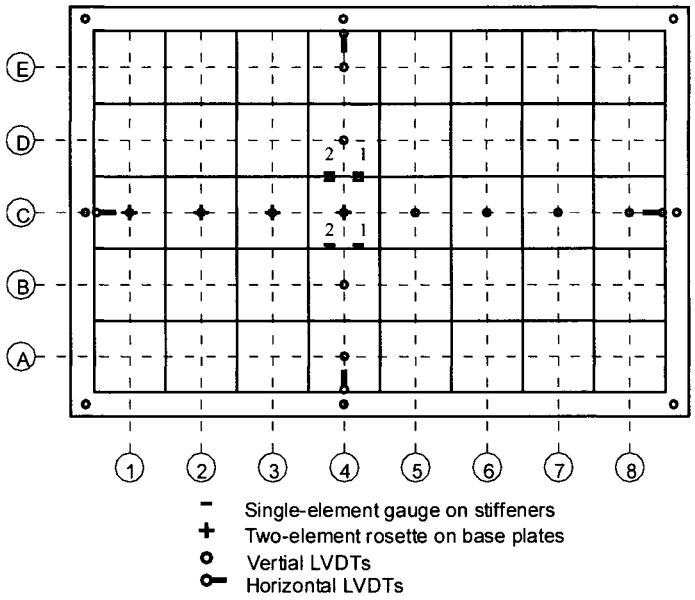

Figure 6: Configuration of instrumentation

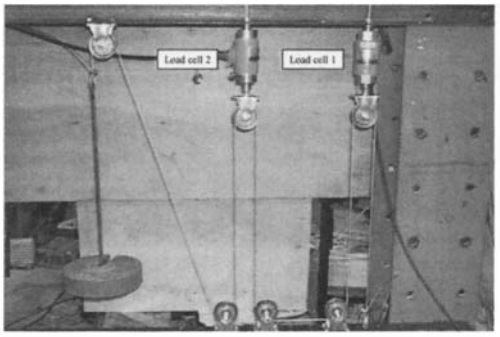

(a) Test set-up

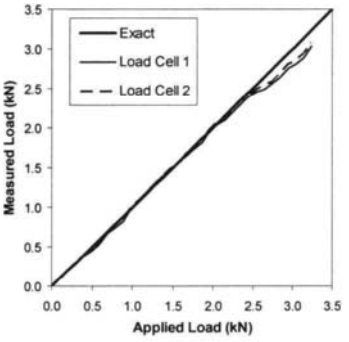

(b) Test results

Figure 7: Calibration test of loading system

EXPERIMENTAL OBSERVATIONS

Loading was applied through 14 hangers, 7 on each side of the test specimen (Figure 8). At a load of about 1.0 kN per loading point, small lateral deformations could be observed on stiffeners by naked eyes. It should be pointed out that these deformations appeared first on transverse stiffeners and subsequently on longitudinal stiffeners, but the time difference is small. These deformations continued to grow with further loading, leading to obvious short-wave buckles of similar wavelengths. The magnitudes of these buckles were larger on some stiffeners than others. As the applied load reached about 80% of the ultimate load, significant lateral deformations were observed on the stiffeners. It was quite interesting that two

www.EngineeringEBooksPdf.com

different deformation shapes of the stiffeners were found (Figure 9): the two edge plates forming the stiffener either deformed together or separated from each other. This phenomenon indicates that these two modes of buckling deformations have similar resistances.

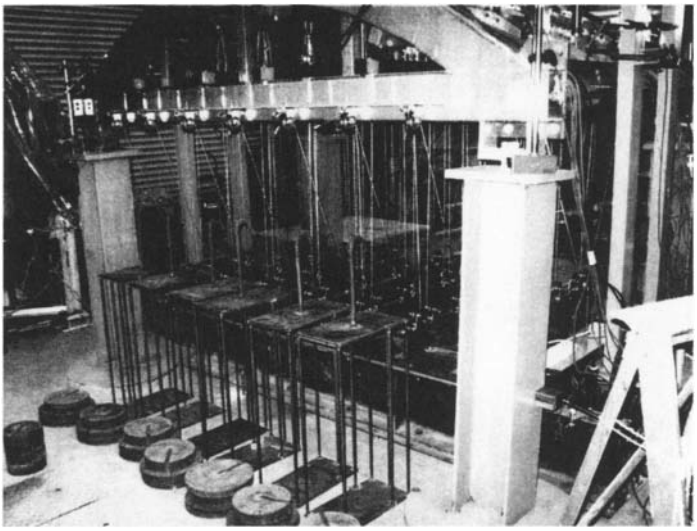

Figure 8: An overall view of the loading system

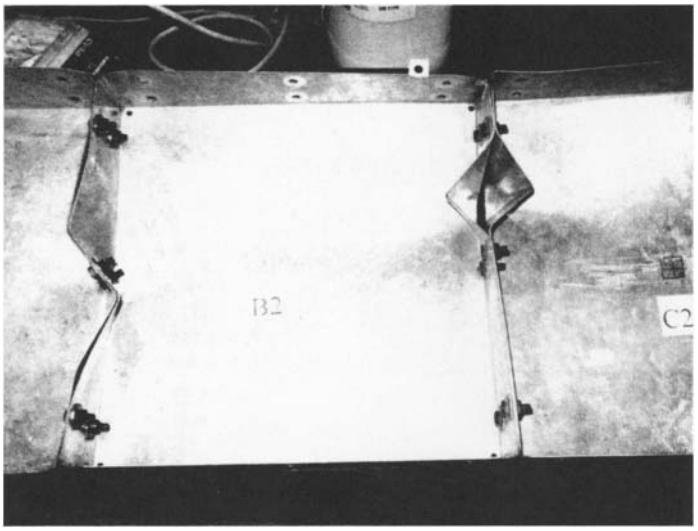

Figure 9: Two different deformation shapes of the stiffeners.

Figures 10a and 10b show the variations of strains on both the base plates and the stiffeners. The numbers 1 and 2 are used to represent the two strain gauges on the edge plate (Figures 6 and 10). Both the longitudinal and transverse strains on the base plates increase almost linearly with the applied load until the load per loading point reaches about 2 kN. Rapid increases are then seen in some of the strain

www.EngineeringEBooksPdf.com

readings. The trends of strain readings on the stiffeners indicate divergence around a load of 1.0 kN. This is the load level corresponding to the local buckling of the stiffeners. This local buckling mode has a stable postbuckling path, so the shell continued to deform with its overall stiffness little affected (Figures 10a and 11). At a load of 2 kN, plastic deformations in the stiffeners ended the stable postbuckling deformation process, which triggered a large reduction in the overall stiffness of the shell (Figures 10a and 11). Final collapse soon followed during the process of adding weights to achieve a load of 2.39 kN per loading point.

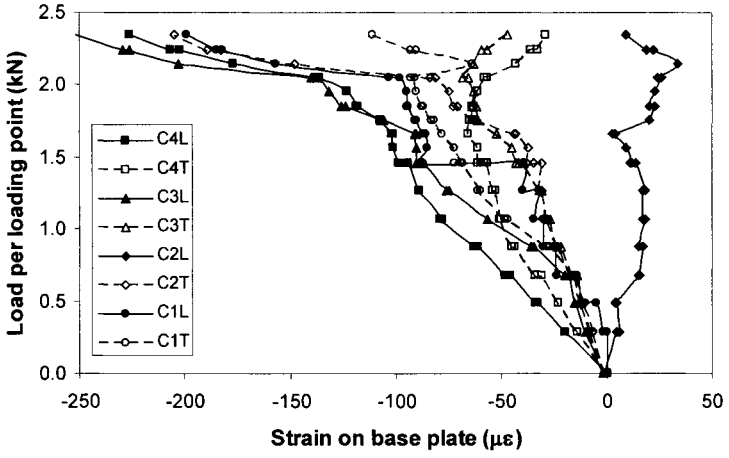

(a) Base plates

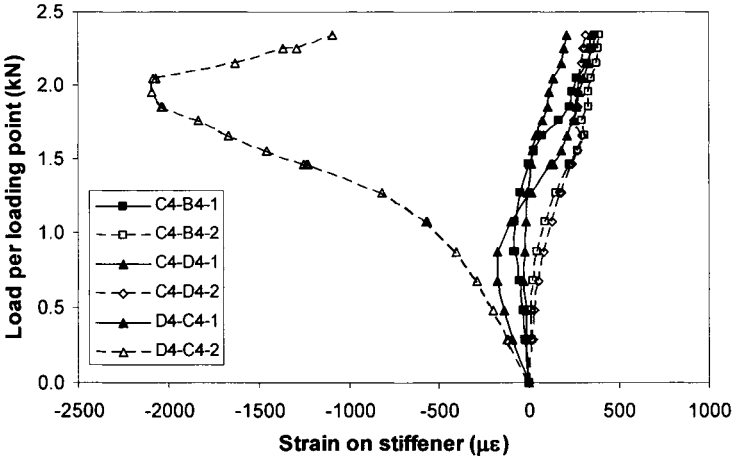

(b) Stiffeners

Figure 10: Load-strain curves

Selected load-deflection curves are plotted in Figure 11, where the deflections are those measured at the centres of units C1-C4. Deflection profiles across row C and column 4 under selected load levels are also

www.EngineeringEBooksPdf.com

plotted in Figure 12. It is clear that the deformation shape of the specimen is predominantly symmetric during the initial stage. As the load increased, non-symmetric deformations grew until it collapsed suddenly. An overall view of the failure mode of the base shell test specimen is shown in Figure 13.

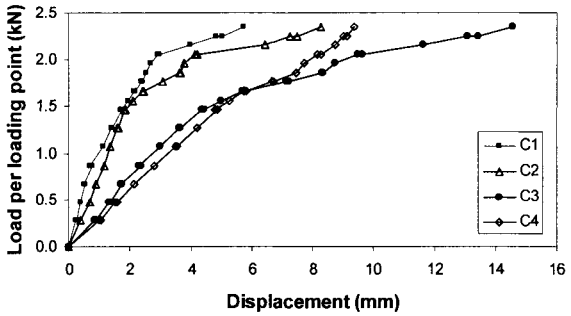

Figure 11: Selected load-displacement curves

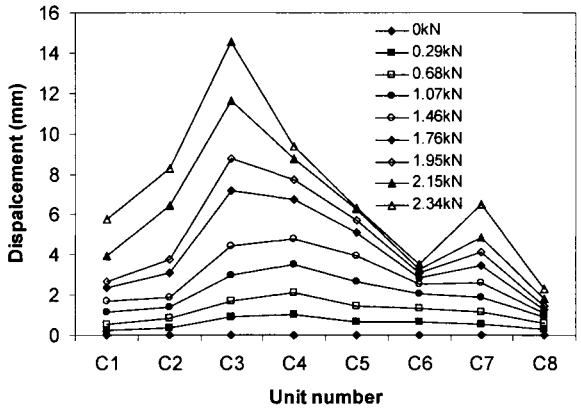

(a) Displacement profile along row C

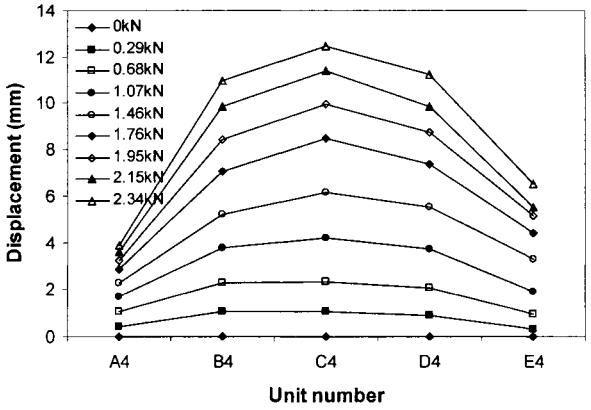

(b) Displacement profile along column 4

Figure 12: Displacement profiles under selected load levels

www.EngineeringEBooksPdf.com

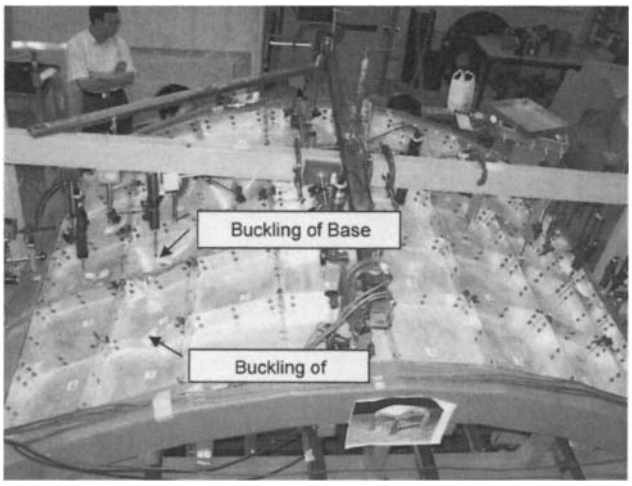

Figure 13: An overall view of the failure mode of the base shell.

CONCLUSIONS

A Comshell roof consists of a bolted steel base shell and cast in-situ concrete. A key design issue is the buckling strength of the steel base shell under wet concrete loading during construction. An experimental program involving the tests of 4 laboratory model base shells is under way to study this buckling problem. This paper has presented the results from the first experiment on a model bolted steel shell as well the experimental procedure. A method for the laboratory fabrication of modular units was established, which allowed the in-house construction of model bolted base shells. A new pulley-based loading system for the application of a large number of concentrated loads of equal value was designed and found to perform well. In the test of the first specimen, it was found that local buckling of the stiffeners occurred first, followed by stable postbuckling deformations. Final failure of the shell occurred by overall buckling.

ACKNOWLEDGEMENTS

This work has been supported by the Research Grants Council of the Hong Kong Special Administrative Region, China (Project No: PolyU 5059/99E), with additional support provided through a research studentship for Mr. H.T. Wong. The authors are grateful for this support. The authors also wish to thank Professor S.L. Dong and Dr. Z.C. Wang for their helpful discussions and comments.

REFERENCES

Medwadowski, S.J. (1998). Concrete Thin Shell Roofs at the Turn of the Millennium. *Current and Emerging Technologies of Shell and Spatial Structures, Proceedings of an IASS Symposium*, April, pp. 9-22.

Teng J.G. (2001). Steel-Concrete Composite Shells for Enclosing Large Spaces. *Proceedings, International Conference on Steel and Composite Structures*, Pusan, Korea, 14-16 June, pp. 403-409.

Teng J.G. (2002). Steel-Concrete Composite Shells: a New Structural System for Enclosing Large Spaces. To be published.

Wong, H.T. and Teng, J.G. (2002) Local Buckling in Bolted Steel Base Shells of Comshell Roofs. To be published.

Wong, H.T., Teng, J.G. and Wang, Z.C. (2002). Innovative Pulley-based System for the Simulation of Distributed Loading on Shell Roof Structures. To be published.

www.EngineeringEBooksPdf.com

Advances in Steel Structures, Vol. II
Chan, Teng and Chung (Eds.)
© 2002 Elsevier Science Ltd. All rights reserved.

EFFECT OF CRACKS ON VIBRATION, BUCKLING AND PARAMETRIC INSTABILITY OF CYLINDRICAL SHELLS

A. Vafai[1], M. Javidruzi[1], J.F. Chen[2] and J.C. Chilton[3]

[1] Department of Civil Engineering,
Sharif University of Technology, Tehran, Iran
[2] Institute for Infrastructure and Environment
School of Engineering and Electronics Edinburgh University, Edinburgh, UK
[3] School of the Built Environment, Nottingham University, Nottingham, UK

ABSTRACT

This paper presents a study on the vibration, buckling and parametric instability behaviour of a circular cylindrical shell with a crack, subject to axial periodic loading. The effects of crack length and orientation are analysed using the finite element method. The results show that, under tension load, the frequency of the shell initially increases with the load, but then decreases as the load further increases, which leads to local buckling near the crack. The size and the orientation of the crack and the loading parameters all have significant effect on the dynamic stability behaviour of the shell under both compressive and tensile loading.

KEYWORDS

Cylindrical shells, Crack, Buckling, Vibration, Dynamics, Parametric instability

INTRODUCTION

Cylindrical shell structures are widely used in various applications of engineering design. Initiation and propagation of cracks during the service life of these structures, especially when subjected to dynamic loads, are very common. A variety of modes of static and dynamic behaviour are possible for thin shells with a crack. A problem of interest in static analysis is associated with out-of-plane deformations, which accompany buckling, and post-buckling [1-3]. Dynamic studies on this class of problems usually involve lateral vibration in the absence or presence of an initial axial stress [4]. The presence of cracks can further increase the lateral vibration and lead to parametric instability.

Parametric instability of cracked plates has been the subject of several previous investigations [5,6]. Whilst plates may be considered as a special case of cylindrical shells with zero curvature, to the best knowledge of the authors no previous research has been conducted on dynamic stability of cracked general cylindrical shells.

www.EngineeringEBooksPdf.com

This paper is concerned with the vibration, buckling and parametric instability of cylindrical shells with a crack. The effects of several parameters such as static load factor, crack size and orientation, on the vibration, buckling and parametric instability behaviour, are investigated.

DYNAMIC INSTABILITY

A cylindrical shell with fixed supports and a crack, subjected to a parametric loading $N_x(t)=N_s+N_t\cos\theta t$ is depicted in Fig.1.

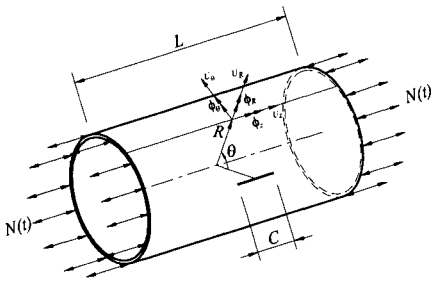

Fig. 1: Geometry and loading

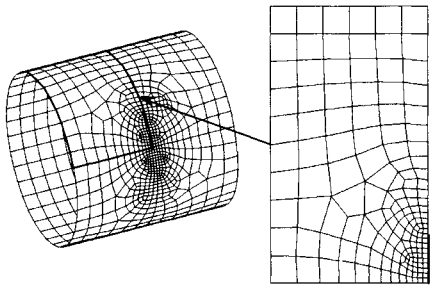

Fig.2: Crack zone meshing scheme

With the first order of approximation, the boundaries of the principal regions of instability can be obtained from the following Eqn. [7]:

$$\left(\frac{\theta^2}{4}\mathbf{M}-\left(\mathbf{K}_e-(\alpha\pm\frac{1}{2}\beta)N_{cr}\mathbf{K}_G\right)\right)\mathbf{q}=\mathbf{0} \tag{1}$$

where

$$\alpha=N_s/N_{cr};\qquad \beta=N_t/N_{cr} \tag{2}$$

α and β are static and dynamic loading factors, N_{cr} is the critical buckling load, $\mathbf{M}$ is the consistent mass matrix, $\mathbf{K}_e$ is the elastic stiffness matrix and $\mathbf{K}_G$ is the stress stiffness matrix.

Eqn. (1) reduces to a static buckling problem if $N(t)$ is a static axial load λ

$$(\mathbf{K}_e-\lambda\mathbf{K}_G)\mathbf{q}=\mathbf{0} \tag{3}$$

and reduces to a free vibration problem when $N(t)=0$ and the modal displacement vector $\mathbf{q}$ is expressed in the form of $\mathbf{q}=A\sin\omega t$

www.EngineeringEBooksPdf.com

$$\left(\omega^2\mathbf{M}+\mathbf{K}_e\right)\mathbf{q}=\mathbf{0} \tag{4}$$

Eqns. (3) and (4) are eigenvalue problems. The eigenvalues of Eqn. (3) represent the buckling loads (λ_i) and those of Eqn. (4) represent the squares of the natural frequencies of free vibration (ω^2_i). The corresponding eigenvectors give the buckling modes and vibration modals respectively.

FINITE ELEMENT MODEL OF CRACKED SHELLS

ANSYS *5.7.1* [8] was used in this study to analyse a thin cylindrical shell as shown in Fig. 1. The shell has a length *L*, thickness *h* and radius *R*. The shell material has a modulus of elasticity E, Poisson's ratio ν and unit volume mass m. The eight-node isoparametric quadratic shell element in ANSYS was used to model the structure. The element is suitable for modelling curved structures. It assumes that the normal to the central plane remains straight after deformation but does not necessarily remain normal to the centre plane. It is thus capable of avoiding shear locking. A *2x2x2* Gaussian integration scheme was used to evaluate all the elastic stiffness, stress stiffness and mass matrices. A two-point integration was used to calculate the load vector. Both transverse and rotary inertia is included in the consistent mass matrix. The subspace iteration technique was adopted to extract eigenvalues and eigenvectors. More details can be found in [9,10].

In cracked shells, a fine FE mesh was adopted in the region near the crack (the so-called "*crack zone*"). A previous study has shown that the first ring of elements around the crack tip should have a radius of not greater than *C/8* in order to achieve reasonable results [11]. The size of elements increases gradually outward from the crack tip (Fig. 2) by incorporating an automatic mesh generation routine.

RESULTS AND DISCUSSION

A cylindrical shell with fixed supports and a crack, subjected to uniform axial loading was studied. The effects of the crack length *C* and its orientation (longitudinal or circumferential crack), the magnitude, nature and frequency of the axial load on the vibration, buckling and parametric instability behaviour of the shell were examined. The results are discussed as follows.

Free Vibration

Figure 3 shows the effect of a circumferential crack on the first three natural frequencies (which have been normalised against the fundamental frequency of free vibration of the corresponding perfect shell ω_1^*). The presence of the crack reduces all the first three frequencies. This reduction is initially gradual as the crack length increases but becomes very rapid when the crack length exceeds about 15% of the circumference of the shell.

www.EngineeringEBooksPdf.com

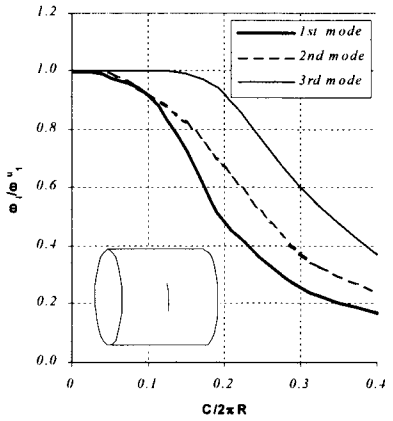

Fig. 3: Effect of circumferential crack on normalised natural frequencies

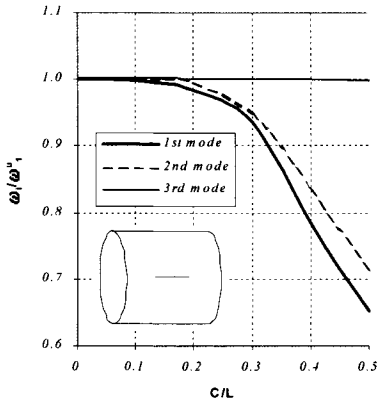

Fig. 4: Effect of longitudinal crack on normalised natural frequencies

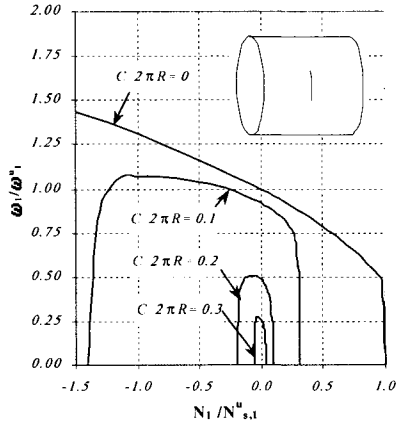

a) With a circumferential crack

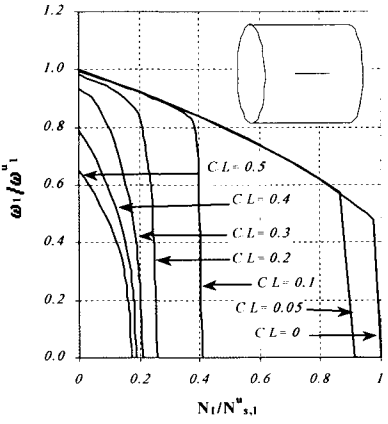

b) With a longitudinal crack

Fig. 5: Fundamental frequency of cracked cylindrical shells

The effect of a longitudinal crack (Fig. 4) is similar to but less marked than that of a circumferential crack. A crack length of 20% of the shell length significantly reduces the first two vibration frequencies. However, the third vibration frequency is hardly affected by a crack of half the length of the shell.

www.EngineeringEBooksPdf.com

Figure 5 shows the effect of the applied axial loading N_s on the fundamental frequency ω_1 in a shell with a circumferential or longitudinal crack. For ease of comparison, N_s and ω_1 have been scaled here by the critical buckling load $N^u_{s,1}$ and the fundamental frequency ω^u_1 of the corresponding perfect shell, respectively.

Under compressive axial load, the frequency decreases almost linearly as the load increases in non-cracked shells ($C/2\pi R=0$ or $C/L=0$). When the load is about 95% of the static buckling load ($N_s / N^u_{s,1} = 0.95$), the frequency reduces to about half the initial value ($\omega_1 / \omega^u_1 \cong 0.5$). When the load further increases ($N_s / N^u_{s,1} \geq 0.95$), the frequency decreases very rapidly, falling to zero when the load reaches the buckling load The presence of a crack very significantly reduces the buckling load. When there is a circumferential crack 10% of circumference of the shell, the buckling load is reduced to about 30% of the corresponding value for a perfect shell. Similarly, a longitudinal crack of 10% of the shell length reduces the buckling load to about 40% of that of the corresponding perfect shell. The presence of axial compressive load on a cracked shell also has a more marked effect on the fundamental frequency than it does on a perfect shell.

Under tensile axial load (negative $N_1/N^u_{c,1}$ values, Fig. 5a), the fundamental natural frequency of cracked shells initially increases with the load but after a certain load level it starts to decrease and rapidly reduces to zero. The initial increase of natural frequency can be attributed to the increase of the overall stiffness of the structure under tensile axial load. However, when the tensile load further increases, the stress in the compressive zone adjacent to the crack becomes relatively larger, which decreases the local stiffness. When this local stiffness reduction exceeds the stiffness increase elsewhere, the fundamental frequency starts to decrease. The frequency reduces to zero when local buckling occurs.

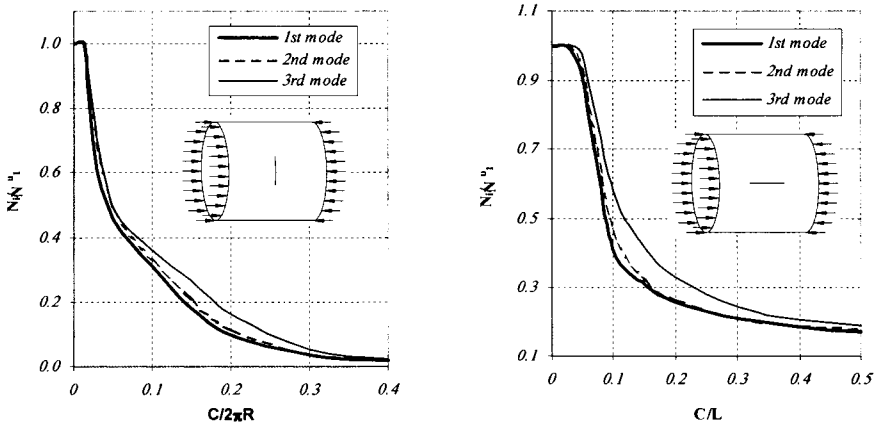

a) Circumferential crack b) Longitudinal crack

Fig. 6: Effect of crack size on buckling load for cylindrical shells under compressive axial loading

www.EngineeringEBooksPdf.com

Static Buckling Behaviour

A shell with a circumferential crack may buckle under either compressive or tensile axial loading. For a longitudinally cracked shell, only compressive axial load is investigated here because the longitudinal crack does not significantly disturb the tensile stress field. Figure 6 shows the effect of crack size on the critical buckling load of the shells under compressive axial loading. Clearly, the presence of either a circumferential or a longitudinal crack very significantly reduces the buckling load.

Figure 7 shows the effect of crack size on the static buckling load in circumferentially cracked shells under tensile axial loading. Again there is a general tendency for the critical load to decrease rapidly with the increase of crack size. Because it is usually not required to take buckling failure into account in structural design of a cylindrical shell under axial tensile loading, this type of crack can lead to an unexpected condition of failure.

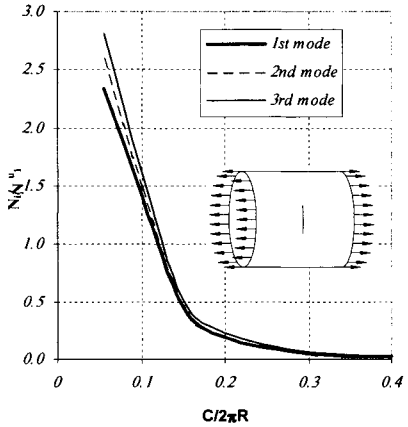

Fig.7: Effect of crack size on critical load for cylindrical shells under tensile axial loading

Parametric Instability

This section examines the parametric instability of a cracked shell with fixed supports and under either axial compressive or axial tensile loading. Figure 8 shows the fundamental region of instability for a non-cracked shell. The static loading factor α clearly has significant effect on the fundamental region of instability. The size of this region increases and its position on the vertical axis (the exciting frequency of the dynamic load) moves downwards as the value of α increases, leading to a more vulnerable situation for dynamic instability in general.

Figures 9 to 11 show the fundamental region of instability for a shell with either a circumferential or a longitudinal crack. The circumferential and longitudinal crack lengths are $C/2\pi R=0.2$ and $C/L=0.2$ respectively. A common feature for the cracked shells is that the boundaries of the instability regions become much curved than those for a perfect shell. In comparison with a perfect shell, the vertical position of instability regions becomes lower and their size much smaller for a shell with a circumferential crack (Fig. 9). Under tensile axial

www.EngineeringEBooksPdf.com

load, the size of the instability region is also considerably smaller than that of a perfect shell (Fig. 10). Its vertical position is also much lower but slightly higher than that of the same cracked shell under compressive load. This may reflect the behaviour that the overall stiffness of the structure under a static tensile load is higher than that under a static compressive load with the same magnitude.

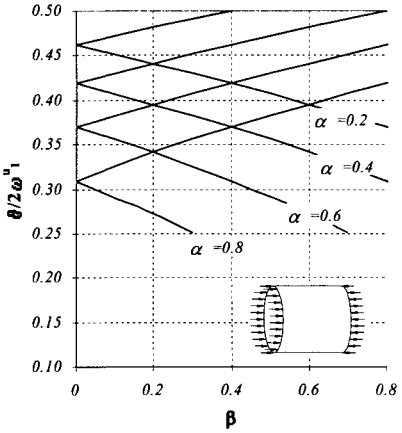

Fig. 8: Fundamental instability region for a perfect cylindrical shell under compressive load

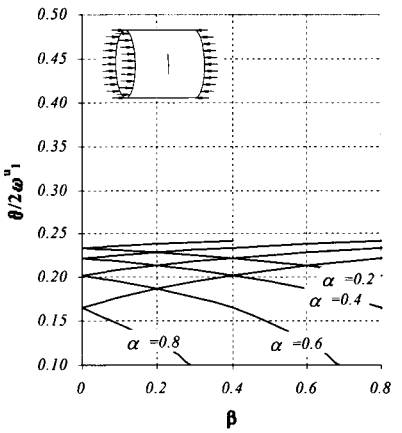

Fig. 9: Fundamental instability region for a circumferentially cracked shell under compressive load

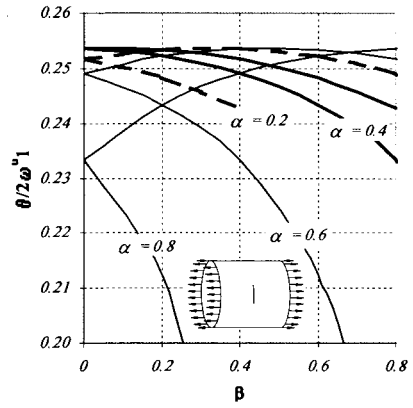

Fig. 10: Fundamental instability region for a circumferentially cracked shell under tensile load

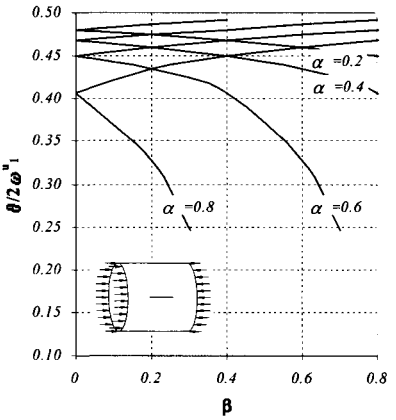

Fig. 11: Fundamental instability region for a longitudinally cracked shell under compressive load

www.EngineeringEBooksPdf.com

The effect of a longitudinal crack is somewhat different from that of a circumferential crack, as the instability region decreases for a small value of α but increases for a large value of α. Furthermore, its vertical position is slightly higher than that of a perfect shell (Fig. 11).

CONCLUSIONS

This paper has presented a study on the vibration, static and dynamic instability behaviour of cylindrical shells with different crack types subject to uniform periodic compressive or tensile axial loading. The results can be summarised as follow:

1. The fundamental frequency of the shell is affected by the size and type of the crack. Natural frequencies decrease as the compressive load increases and the fundamental frequency becomes zero at the buckling load of the shell. Under tensile load, the natural frequencies initially increase with the load, but begin to fall beyond a certain load level and rapidly approach zero as the cracked zone buckles locally.
2. For perfect shells under compressive periodic loading, the size of the instability region increases and its vertical position (on the exciting frequency axis) becomes lower as the static load factor increases. Under tensile periodic loading, the width of the instability regions decrease and they move upward on the frequency ratio axis as the static load factor increases. The presence of a crack has very significant effect on both the size and the vertical position of the fundamental region of instability. Both the size and the orientation of the crack are important factors.

REFERENCES

1. Dyshel' M.SH. (1989). Stability of a Cracked Cylindrical Shell in Tension. *Soviet Applied Mechanics* **25**, 542-548 [English Translation by Prikladnaya Mekhanika].
2. Estekanchi H.E. and Vafai A. (1999). On the Buckling of Cylindrical Shells with Through Cracks under Axial Load. *Thin-Walled Structures* **35**, 255-274.
3. Starnes J.H. Jr. and Rose C.A. (1998). Buckling and Stable Tearing Responses of Unstiffened Aluminium Shells with Long Cracks. *Collection of Technical Papers - AIAA/ASME/ASCE/AHS/ASC Structures, Structural Dynamics & Materials Conference* **3**, 2389-2402.
4. Tang, F.Q. and Huang T.C. (1983). Modal Analysis of a Cylindrical Shell with a Longitudinal Crack. *AMD (Symposia Series) (ASME, Applied Mechanics Division)* **59**, 77-84.
5. Vafai A., Javidruzi M. and Estekanchi H.E. (2002). Parametric Instability of Edge Cracked Plates. *Thin-Walled Structures* **40**, 29-44.
6. Vafai A., Javidruzi M. and Estekanchi H.E. (2001). Crack Influences on the Vibration, Buckling and Parametric Instability of Plates. *Vibration and Control of Mechanical Systems, Proceedings of the ASME International Mechanical Engineering Congress and Exposition, November 11-16, New York.*
7. Bolotin, V.V. (1964). *The Dynamic Stability of Elastic Systems*, San Francisco, Holden-Day.
8. ANSYS/University high option ®5.7.1, Copyright 2000 SAS IP, Inc.
9. Ahmad S., Irons B.M., and Zienkiewicz O.C. (1970). Analysis of Thick and Thin Shell Structures by Curved Finite Elements. *International Journal for Numerical Methods in Engineering* **2**, 419-451.
10. Cook R.D. (1981). *Concepts and Applications of Finite Element Analysis*. Second Edition, John Wiley and Sons, New York.
11. Tracey D.M. (1973). Finite Elements for Three Dimensional Elastic Crack Analysis. *Nuclear Engineering and Design* **26**.

www.EngineeringEBooksPdf.com

Advances in Steel Structures, Vol. II
Chan, Teng and Chung (Eds.)
© 2002 Elsevier Science Ltd. All rights reserved.

AN EXPERIMENTAL STUDY FOR SEISMIC REINFORCEMENT METHOD ON EXISTING CYLINDRICAL STEEL PIERS BY WELDED RECTANGULAR STEEL PLATES

Kazuo Chu[1] and Takamasa Sakurai[2]

[1]Department of Civil Engineering , Toyota National College of Technology,
Eisei-cho 2-1, toyota-city,Aichi,JAPAN
[2]Department of Civil Engineering , Toyota National College of Technology,
Eisei-cho 2-1, toyota-city,Aichi,JAPAN

ABSTRACT

A lot of existing cylindrical steel piers suffered serious damage from Hansin/Awaji great earthquake in 1995.

In this paper the purpose of reinforcement of existing piers is for improvement of ductility of piers. At the same time the increase of horizontal bearing capacity of piers needs to be kept in limited value because of protecting the anchor part of the pier from destruction.

Welded rectangular steel plates on base zone of the pier were used for the reinforcement method. On the other hand the plates were kept unwelded at the limited part on the base zone. After reinforcement of the pier, the local buckling will be occurred at the part and increase of horizontal bearing capacity will be kept limited and the ductility of piers is able to increase. We call this reinforcement system as "Fuse Structure".

Reduction models of existing cylindrical steel piers (a diameter of 216mm, full length 900mm, cylinder thickness 2.5mm) were used. This study was carried out by experimental and analytical method. The result of the study is that the increase of horizontal bearing capacity of the pier could be kept less than 15% and the increase of ductility was improved by 40%.

KEYWORDS

Buckling, Cylindrical Steel Pier, Reinforcement , Seismic Design , Ductility, Cyclic Loading

1. INTRODUCTION

On Hanshin/Awaji great earthquake occurred in January, 1995, to many cylindrical steel piers, local buckling took place at the part where plate thickness changes in the pier or at the part where stress concentration occurs in the base of the pier and even some piers collapsed. From the experience of the earthquake, existing piers were necessitated to be reinforced, and it was pointed out that the pier reinforcement shall be not imposing excessive loads to its basement, and enhancing its ductility of the pier. Some study results on reinforcing methods for the existing cylindrical steel pier in accordance with this purpose.[1),2),3),4),5)]

This research studied on the reinforcing method to limit the enhanced horizontal bearing capacity of the pier to an extent in order not for the collapse to take place at the anchor part of the pier, and to improve the ductility in the plastic region. The reinforcing method proposed here is to let local buckling take place surely at the predicted point where local buckling would occur due to the horizontal force at earthquake, and to improve the ductility of the pier at the same time. Evaluation of the reinforcing effects was studied from the characteristics of the horizontal bearing capacity and those of the ductility.

www.EngineeringEBooksPdf.com

In this research, experimental study and numerical analysis were carried out by focusing on the comparison of the horizontal bearing capacities due to the monotonous loading and the cyclic loading, and on the characteristics of the ductility in the plastic region.

2. EXPERIMENTAL ANALYSIS

2.1 SPECIMEN AND TENSILE TEST

Tensile test of the material was carried out on the JIS No.5 test pieces cut from the cylinder specimen. For the steel pipe used as specimen, two different kinds of material were used, which were designated as Type A and Type B. The result is shown in Fig.3 in terms of the relationship between the true stress and the logarithmic strain. Table-1 shows basic data of the specimen and the properties of the material.

The experiment focused on the base zone where local buckling was expected to occur, and dimensions of the model used for the experiment was one tenth of the actual bridge. View of the test specimen is shown in Fig.-1. The picture in the left end of Fig.-1 is for the case without reinforcement. Pictures shown in the right of Fig.-1 are the specimens of which lower 200 mm part are reinforced by three methods. For example, explanation for the clearance.1 (BE1) shown at the center bottom of Fig.-1 is such that reinforcing plate to be attached had the same thickness, 2.5 mm as the mother steel pipe. The plates were attached in the circumference direction at four locations symmetrical to the two axes and the width of a plate in the circumferential direction was 1/12 of the circumference. The height where local buckling occur at the pier specimen without reinforcement is 0.3 times of the radius from the fixed end of the pier, and one wavelength of the local buckling is approximately 0.1 times of the radius. In order to reduce the horizontal bearing capacity of the pier within a certain limit by the reinforcement, a part (clearance) where reinforcing plate was not attached was provided in the lower pier as shown in Fig.1, and local buckling was designed to occur at this point. The length of this clearance was determined based on one wavelength of the local buckling without reinforcement. The clearance.1 (BE1) shown in Fig.1 is for the case where the clearance width is one wavelength, and 0 (BE0) and 2 (AE2) in other figures are for the case without clearance, and the case with two wavelengths clearance, respectively. Designation of the specimens are such that A, B represent the material classification, and 0,1,2 represent different types of the clearance. N stands for the case without reinforcement. Clearance 0,1,2 stand for the case without clearance, the case with clearance spacing V/R=0.1, and V/R=0.2, respectively, where V is the clearance length and R is the radius of the cylinder. For example, AEN is of material A, for experiment E, and without reinforcement N. The specimens used for the experiment are 1) type AEN, without reinforcement, 2) type BE0, reinforced without clearance, 3) type BE1, V/R=0.1 provided for the reinforcing steel plate, and 4) type AE2, clearance V/R=0.2 provided for the reinforcing steel plate. Steel pipe material was continuous welded steel pipe available in market (material, STKR400), and its foot 200 mm from the base was cut and formed into a shape as shown in Fig.1. For its base zone, control specimen (representing the existing pier) was made of a cylindrical steel pipe with 8.2 mm thickness, and ground evenly from both inner and outer sides to the thickness of 2.5 mm. To weld reinforcing plate to the steel pipe, 3 mm clearance was provided to the base of the steel pipe as shown in Fig.2. The dimensions of the steel pipe was determined to have the same parameters such as the radii-thickness ratio parameter as those of the actual structure, by referring not only the actual structure, but Design Guideline for Steel Structure [6),7)] and other previous studies.

2.2 LOADING TEST

Loading test machine used was a hydraulic servo fatigue test machine of 30 tonf. As the test was carried out by setting the pier horizontal as shown in Fig.4, horizontal load (H) was applied in the vertical direction, and a constant axial force (P:15 % of fully plastic state axial force) equivalent to the dead load of the pier is applied in the horizontal direction.

Loading test was done by controlling the displacement in the H direction at the point 700 mm apart from the base of the specimen. For the cyclic loading, the yield horizontal displacement δ y obtained by the monotonic loading was defined as the basic control displacement, and it was increased gradually such as $\pm$ 1.0 δ y, $\pm$ 2.0 δ y, $\cdots$, up to $\pm$ 5.0 δ y, and test was carried out by one cycle at each displacement level. As the horizontal displacement of the specimen had to be measured by eliminating the rotation effect, actual displacement of the specimen was measured by a gauge attached to a rigid bar as shown in Fig.4.

www.EngineeringEBooksPdf.com

TABLE 1
DIMENSION AND MATERIAL PROPERTY
OF TEST SPECIMENS

Pier length (L) mm		900.0
Diameter (D) mm		209.7
Thickness (t) mm	BE0・BE1・B0・B1	2.58
	AEN・AE2・AN・A2	2.42
Radii-Thickness Ratio param. (Rt)	BE0・BE1・B0・B1	0.122
	AEN・AE2・AN・A2	0.120
Yield stress (σy) MPa	BE0・BE1・B0・B1	398.9
	AEN・AE2・AN・A2	374.0
Young's Modulus (E) GPa	BE0・BE1・B0・B1	209.1
	AEN・AE2・AN・A2	223.4
Poisson's ratio (ν)	BE0・BE1・B0・B1	0.247
	AEN・AE2・AN・A2	0.274
Yield load (Hy) KN	BE0・BE1・B0・B1	32.34
	AEN・AE2・AN・A2	28.52
Yield displacement (δy) mm	BE0・B0	1.74
	BE1・B1	1.77
	AE2・A2	1.53
	AEN・AN	1.86
	BEN・BN	2.15

$$Rt = \frac{\sigma y}{\sigma e} = 1.65 \times \frac{\sigma y}{E} \times \frac{r}{tf}$$

R t : Radii-Thickness Ratio Parameter
σe : Compressive buckling stress of cylindrical shell
E : Young's Modulus (GPa)
t : Thickness of steel pipe(cm)
r : Radii of steel pipe(cm) (from core to edge)
f : Coefficient by stress declivity
Hy:0.85σy× (W/L)
δy :Horizontal displacement calculated as elastic cantilever beam under load Hy
W:Section modulus

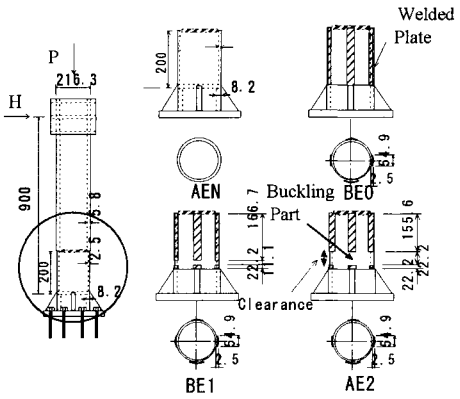

Fig.1 Test Speimen

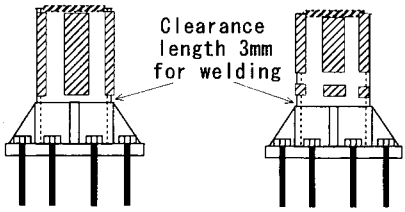

Fig.2 Base zone of test specimen

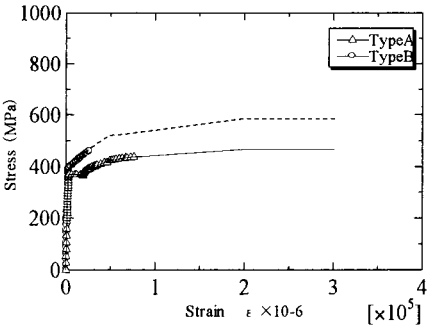

Fig.3 Stress-Strain curve

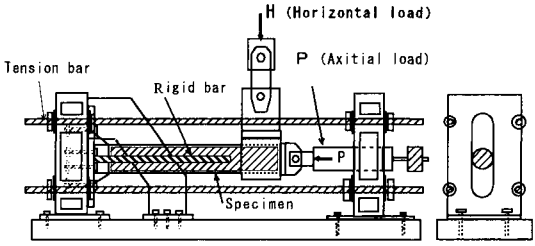

Fig.4 An experimental device

www.EngineeringEBooksPdf.com

3. NUMERICAL ANALYSIS

Numerical analysis was carried out to compare with the experimental results. Analysis models used were the same 4 types as the test specimens. Designation of the analysis models corresponds with those for the test specimens, except that the symbol E representing experiment was not shown. Therefore, the analysis models are 4 types, 1) type AN, BN without reinforcement, 2) type A0, B0, reinforced without providing clearance, 3) type A1, B1, with reinforcing steel plate having V/R=0.1, and 4) type A2, B2 with reinforcing steel plate having clearance V/R=0.2.

By using finite element method, elastic-plastic finite displacement analysis was carried out by using kinematic work-hardening rule under the Von Mises' yield condition. Calculation was carried out by a generic structural analysis program called MSC.MARC, and 4-nodes thick shell element was used with division into 7 layers in the thickness direction. The stress-strain curve used for the analysis was the one obtained by the tensile test as shown in Fig.3.

4. RESULTS AND DESCUSSIONS

Fig.5a and 5b show deformed conditions where local buckling occurred by the cyclic loading for type A, without reinforcement (AEN, AN), respectively. Local buckling took place at 0.3 times radius apart from the fixed end of the pier bottom, as "elephant foot" type, and the calculation and experiment results corresponded well each other with regard to its shape and position. Fig.6a and 6b show conditions of local buckling by the cyclic loading for type B, with clearance 1 (BE1, B1), respectively. Different from Fig.5, buckling took place with deflection of sink shape at the clearance part. Table.2 shows conditions of the section where local buckling occurred for other cases with reinforcement. It became a star-like-shape for the clearance 1 case, whereas for other cases, it became circular (elephant foot types). As will be discussed later, difference in the type of the local buckling is considered to influence on the ductility of the pier.

Fig.7 shows load-displacement curves at monotonic and cyclic loading cases for type A without reinforcement (AEN, AN). Vertical axis is horizontal load divided by the yield horizontal load, and horizontal axis is the horizontal displacement at the 700 mm from the fixed end of the pier divided by the yield horizontal displacement, and thus both axes are normalized. This figure includes both experimental and calculation results. Fig.8 shows the results for the cases with clearance 1 (BE1, B1) in the same manners as Fig.7. When comparing decrease in the bearing capacity after the maximum load, for the monotonic loading and the cyclic loading at 4 th cycle for the cyclic loading, the cyclic loading case shows 30 % to 50 % decrease compared to the monotonic loading case. It appears that ductility decreases considerably for the cyclic loading case compared to the monotonic loading case.

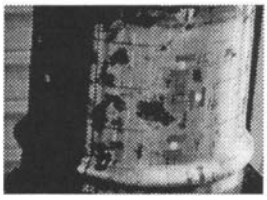

Fig.5a Defomation pattern of buckling (AEN)

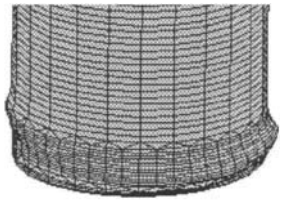

Fig.5b Defomation pattern of buckling (AN)

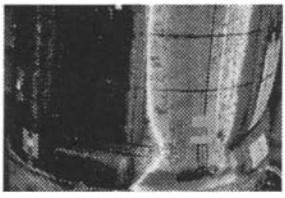

Fig.6a Defomation pattern of buckling (BE1)

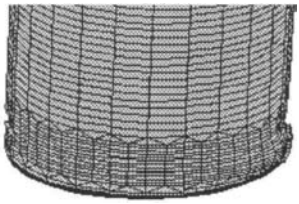

Fig.6b Defomation pattern of buckling (B1)

www.EngineeringEBooksPdf.com

TABLE 2
PATTERN OF BUCKLING

Type	Mono.	Cyclic	EF Type S Type
AEN	EF	EF	
AN	EF	EF	
AE2	EF	EF	
A2	EF	EF	
BE0	EF	EF	
B0	EF	EF	
BE1	S	S	
B1	S	S	
EF: Elephant foot pattern S : Star-shape pattern			

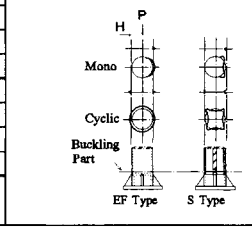

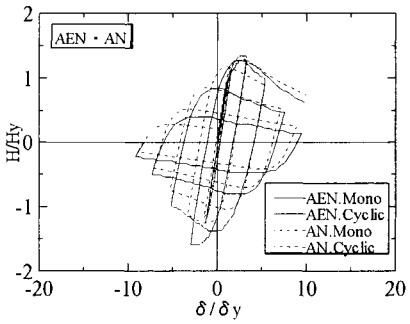

Fig.7 Load - displacement curves (AEN・AN)

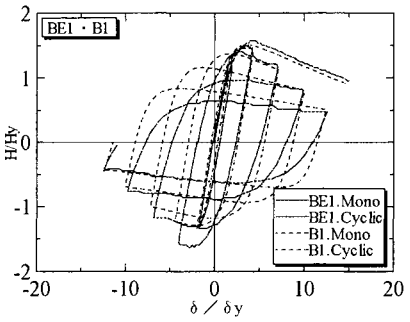

Fig.8 Load - displacement curves (BE1・B1)

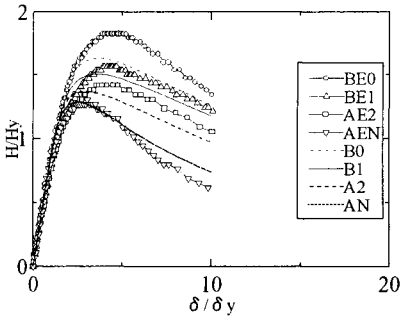

Fig.9 Load - displacement curves (Monotonous)

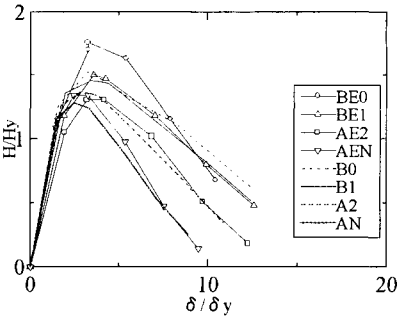

Fig.10 Envelope of Load - displacement curves

Fig.9 shows load-displacement curves of the experimental and calculation results for the monotonic loading cases. Fig.10 shows envelopes of the load-displacement curves for the cyclic loading cases, similar to Fig.9. In both figures, experiment and calculation results correspond well each other except the case without clearance (BE0, B0).

For cases without clearance, at the maximum load, the experiment case (BE0) is larger by 12 % to 16 % than the calculation case (B0). This error is caused due to the small clearance of 3 mm left in order to weld the reinforcing plate to the fixed part of the pier bottom as shown in Fig.2. In the

www.EngineeringEBooksPdf.com

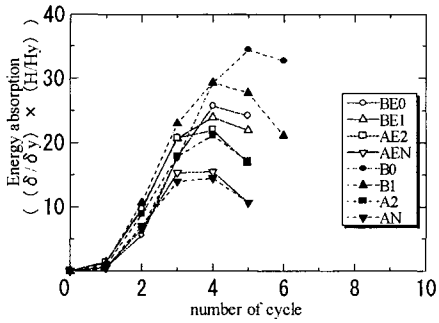

Fig.11 Energy absorption capacity per cycle

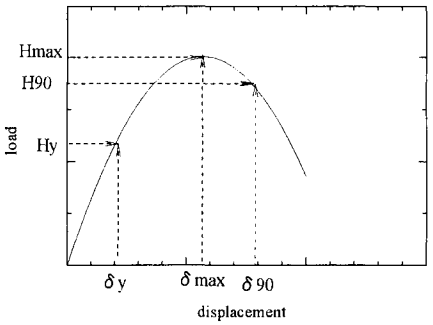

Fig.12 Definition of ductility

TABLE 3
RELATIONSHIP BETWEEN CLEARANCE, BEARING CAPACITEY, AND PLASTICITY RATIO

		κ=Hmax/Hy					μ=δ90/δy				
		Hy	Monotonous		Cyclic		δy	Monotonous		Cyclic	
		KN	F	FF	F	FF	mm	F	FF	F	FF
Type A	AEN	28.5	1.30(1.02)		1.34(1.05)		1.86	4.37(0.97)		4.02(1.05)	
	AN	28.5	1.28(1.00)	1.28(1.00)	1.28(1.00)	1.28(1.00)	1.86	4.50(1.00)	4.50(1.00)	3.82(1.00)	3.82(1.00)
	AE2	28.5	1.41(1.10)		1.30(1.02)		1.53	7.04(1.56)		5.39(1.41)	
	A2	28.5	1.37(1.07)	1.42(1.11)	1.37(1.07)	1.40(1.09)	1.53	5.86(1.30)	6.76(1.50)	4.87(1.28)	5.15(1.35)
	A1	28.5	1.51(1.18)	1.60(1.25)	1.50(1.17)	1.58(1.23)	1.51	6.49(1.44)	7.94(1.76)	5.27(1.38)	5.85(1.53)
	A0	28.5	1.63(1.27)	1.88(1.47)	1.57(1.23)	1.89(1.48)	1.49	6.21(1.38)	8.35(1.85)	4.99(1.31)	6.27(1.64)
Type B	BEN	32.3			1.31(0.98)		2.15			3.54(0.86)	
	BN	32.3	1.36(1.00)	1.36(1.00)	1.34(1.00)	1.34(1.00)	2.15	5.85(1.00)	5.85(1.00)	4.11(1.00)	4.11(1.00)
	B2	32.3	1.36(1.00)	1.42(1.04)	1.31(0.98)	1.34(1.00)	1.79	6.22(1.06)	7.35(1.26)	4.98(1.21)	5.12(1.25)
	BE1	32.3	1.57(1.15)		1.50(1.12)		1.77	7.13(1.22)		5.39(1.31)	
	B1	32.3	1.50(1.11)	1.58(1.16)	1.46(1.09)	1.51(1.13)	1.77	7.06(1.21)	8.58(1.47)	5.50(1.34)	5.86(1.43)
	BE0	32.3	1.82(1.34)		1.76(1.31)		1.74	7.14(1.22)		5.65(1.37)	
	B0	32.3	1.63(1.20)	1.84(1.35)	1.52(1.14)	1.81(1.35)	1.74	6.88(1.18)	8.89(1.52)	5.02(1.22)	5.94(1.45)

F Type : make clearance 3mm for welding zone (Fig.2)
FF Type :do not make the clearance (Fig.2)
( ) :Ratio for unit in the case AN or BN

numerical analysis, it is considered that this welding part was modeled as 3 mm clearance, which is considered not appropriate, and thus that excessive stress concentration took place at this point and the maximum load became smaller than that demonstrated in the experiment. In order to study this effect, a case where 3 mm clearance was provided (F type) in the numerical analysis, and the other case without the clearance (FF type), were analyzed and compared with the experimental results. It is then confirmed that the experimental result of this reinforcement case without clearance lies between the calculated value for type F and that for type FF.

Fig.11 shows the energy absorption in relation with the number of cycle for each reinforcing method obtained both by experiment and by calculation. The energy absorption during one cycle can be represented by the area for one cycle under the load-displacement curve at the cyclic loading as shown in Fig.7 or Fig.8, for example. It is revealed in Fig. 11 that the energy absorption decreases when going beyond 4th or 5th cycle. It is also confirmed that the narrower the clearance is, the energy absorption becomes larger and the ductility is improved.

Evaluation of the improved ductility due to the reinforcement shall be expressed by the plasticity ratio $\mu = \delta 90/\delta y$.[8] $\delta 90$ is the horizontal displacement, reached after passing the maximum horizontal load, Hmax peak, and corresponding to 90 % of the Hmax, as shown in Fig.12. Table.3 shows the maximum load ratio κ = Hmax/Hy, obtained by dividing Hmax by the yield horizontal load Hy, and the plasticity ratio μ, for each reinforcing method.

www.EngineeringEBooksPdf.com

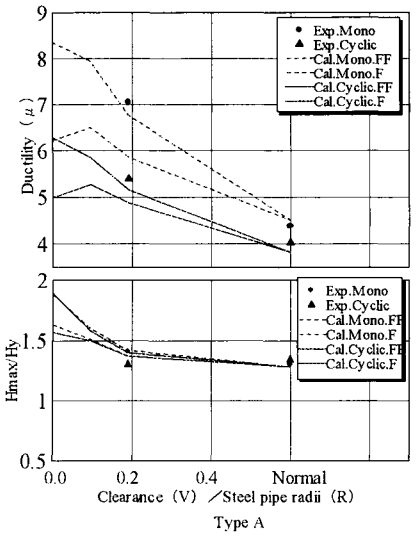

Fig.13 Relationship between clearance, ductility, and bearing capacity

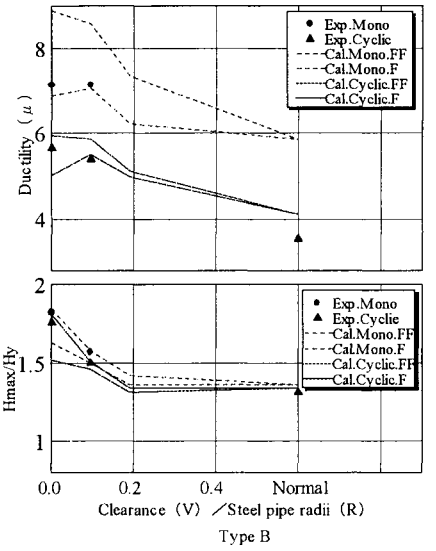

Fig.14 Relationship between clearance, ductility, and bearing capacity

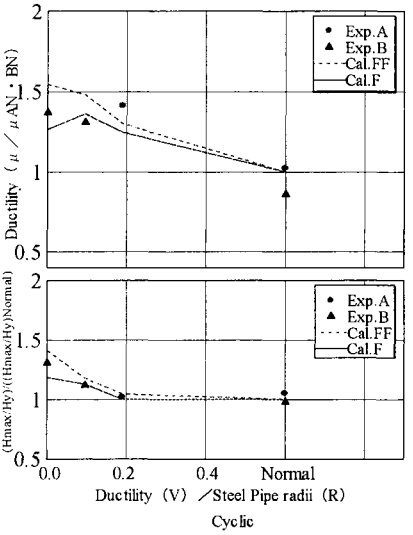

Fig. 15 Relationship between clearance, ductility, and bearing capacity (cyclic loading)

Two different material type A and type B were used as specimens for the experiment. Results are summarized by these materials in Table.3. In addition, the symbol F in the table stands for the case where 3 mm clearance was provided at the pier bottom as shown in Fig.2, and the symbol FF stands for the case without the clearance. The experiment was carried out for type F.

Using the results shown in Table.3, the relationships between clearance width (V/R) and the ductility μ, and bearing capacity ratio κ, for type A, are illustrated in Fig.13. The same relationships for type B are shown in Fig.14. By calculation, the difference in the maximum load ratio, κ, due to the difference between type F and type FF, was 6 % at its maximum among A1, A2, B1, B2. Whereas that for zero clearance (A0, B0) was 19 % at its maximum. This is because local buckling took place at the clearance for welding at the pier bottom as shown in Fig.2. As for the difference in the ductility, μ, due to the difference between type F and type FF, that for type FF was about 20% larger than that for type F, among A1, A2, B1, B2. Whereas for A0, B0, that for type FF was about 30 % larger than that for type F. In short, for type A0 and B0, the clearance for welding significantly affects the values μ and κ. Therefore, in order to increase the ductility, the reinforcing plate and the fixed end at the pier bottom are necessary to be connected rigidly (type FF).

In Fig.13 and 14, experimental results for monotonous loading are represented by ● mark, and those for cyclic loading are by ▲ mark. Most of the experimental results are between type F and type FF. This signifies that intermediate type between F and FF is better to be taken as a model for

www.EngineeringEBooksPdf.com

the lower welding part in the numerical analysis.

From the viewpoint of seismic resistant reinforcement, results in the cyclic loading test are checked. In Fig.15, κ or μ for the cyclic loading is normalized by the calculated value for the no reinforcement case, and expressed by an average value of type A and B, with the same clearance, for each reinforcing method. Using the average of type A and B means that the values κ or μ are evaluated by averaging the difference in the steel material as shown in Fig.3.

For this figure's results, it is discussed by an average value of type F and FF for each clearance. As shown in the figure, the maximum load ratio for κ increases linearly from clearance 2 to clearance 0 reinforcement, however increasing ratio of the ductility μ within this range, is almost constant. Increasing ratio of κ for clearance 1 is 17 %, and that of μ is 41%. On the contrary, increasing ratio of κ for clearance 0 is 36 %, and that of μ is 41%. In short, for the cases without clearance, the maximum load increases by 36 % and ductility increases by 41 %; while by providing clearance 1, increase in the maximum load is able to be limited to 17 % and the ductility can be increased to approximately the same level as the clearance 0 case.

5.CONCLUSIONS

The following results were obtained by experiment, and by numerical analysis.

1. In order to achieve the purpose of this study, when attaching the reinforcing plate, a part without reinforcement was provided and local buckling was induced to take place at this part. As local buckling, two types, an elephant foot type buckling and star-shape buckling, generally take place. When the clearance width is as narrow as 0.1 times the pier radii, star-shape buckling takes place; while other cases, elephant foot type buckling take place. When the buckling is of star-shape type, it is considered that development of the buckling is slowed down compared to the elephant-foot type buckling, and that ductility is enhanced.

2. For those piers investigated in this study, the horizontal bearing capacity for the reinforcing case without clearance, increases by 36 %, and the ductility increases by 41 %. While for the case with clearance of 0.1 times the radii of the pier, its ductility was about the same, and the horizontal bearing capacity was limited to 17 %. This result signifies that by providing a clearance proposed in this study, an increase in the horizontal bearing capacity can be limited and enhanced ductility can be realized.

3. Experimental results and calculations coincide each other within a reasonable range, and effectiveness of this structure is considered to be verified according to this result.

REFERENCES

1) Nisikawa.N,Yamamoto and Natori.T,etc.(1996),Experimental Study on Improvemennt of Seismic Performance of Existing Steel Bridge Piers, *Journal of Structural Engineering*, vol.42A,pp.975-985

2) Iura.M,Kumagai.Y and Komaki.O(1998),Strength and Ductility of Cylindrical Steel Piers Subjected to Cyclic Lateral Load, *Journal of Structural Mechanics and Earthquake Engineering*, No.598, I -44,125-135

3) Sakurai.T,Chu.K and Miura.H(1998), A Stiffening Method for Existing Cylindrical Steel Piers by Fuse Structures, *The 18th MARC Users' Meeting* , PP.163-166

4) Mizutani.S,Aoki.T,Itoh.Y and Okamoto.T(1996), An Experimental Study on the Cyclic Elasto-Plastic Behavior of Steel Tubular Members, *Journal of Structural Engineering*,vol.42a, pp.105-115

5) Matumura.M,Kitada.T,Sawanobori.Y and Nakabara.Y(2001), Experimental Study on Seismic Retrofitting Method by Filling Concrete with Empty Gap into Existing Bridge Piers, *Journal of Structural Engineering*, vol.47A,pp.35-pp.44

6) Japan Society of Civil Engineers, *Desigen Code for Steel Structures Part A, Structures in General*

7) Japan Road Association(1996), Specification for highway bridge :V Earthquake-resistant design

8) Metoropolitan Expressway Public Corporation(1996),The Earthquake Performance Enhancement Design Point of Existing Steel Piers (a Provisional Plan)

www.EngineeringEBooksPdf.com

BRIDGES

www.EngineeringEBooksPdf.com

This Page Intentionally Left Blank

www.EngineeringEBooksPdf.com

Advances in Steel Structures, Vol. II
Chan, Teng and Chung (Eds.)
© 2002 Elsevier Science Ltd. All rights reserved.

METAL FORMS REPLACE REINFORCEMENT IN BRIDGE DECK SLABS

Baidar Bakht[1] Aftab A. Mufti[2] and Gamil Tadros[3]

[1]JMBT Structures Research Inc.
Toronto, Ontario, Canada M1V 3G1
[2]ISIS Canada, University of Manitoba
Winnipeg, Manitoba, Canada R3T 5V6
[3]JMBT Structures Research Inc.
Calgary, Alberta, Canada T3L 1W7

ABSTRACT

Research in Canada and elsewhere has shown that the strengths of composite concrete deck slabs of girder bridges are governed by transverse confinement, which can be provided internally in the form of bottom transverse reinforcement, or externally by means of steel straps connected to the top flanges of the girders. Stay-in-place forms made of thin galvanized steel sheets are being used in the USA to cast concrete deck slabs. It is generally believed that because of the lack of bond between concrete and the galvanized surface of the metal form, the form does not participate in the load carrying action of the slab. It is shown that with simple modifications in design, the metal form can be made to confine the deck slab transversely; the modifications comprise the provision of transverse continuity in the metal form across the bridge width. Thus all the tensile reinforcement in the slab can be removed, except that required for transverse negative moments induced by loads on the deck slab overhangs. A full-scale model is under construction to confirm the above hypothesis. In current designs, the metal forms cease to be useful after the casting and setting of the slab, because of which, the durability of the form is of little consequence to the safety of these slabs. The same is not the case in the proposed design. It is suggested that the problem of metal form corrosion can be solved by one of three means: (a) using a fibre reinforced polymer form, (b) providing bottom transverse reinforcement, which could take over after the form has corroded, or (c) installing steel straps when the form begins to corrode.

KEYWORDS

Arching, bridge deck, deck slab, metal deck, slab, stay-in-place form, steel-free deck slab

www.EngineeringEBooksPdf.com

INTRODUCTION

It is now well established that the strength of a concrete deck slab composite with parallel longitudinal girders is governed by the axial stiffness of its transverse confinement. As demonstrated experimentally by Khanna et al. (2000), in conventional reinforced concrete (RC) deck slabs the bottom transverse reinforcement provides the transverse confinement. It is also shown in the same reference that the axial stiffness of the bottom transverse reinforcement, rather than its axial strength, governs the failure load of the slab. The transverse confinement to a concrete deck slab can also be provided externally by means of steel straps attached to the top flanges of the girders. Bakht and Mufti (1998) have described five bridges in Canada, in each of which the slab is generally free of tensile reinforcement; this slab is referred to as the steel-free deck slab. Recent research has confirmed earlier findings: that a well-confined deck slab develops an internal arching action, because of which its strength is significantly larger than that of the slab acting in only flexure (for example, Mufti et al. 1993; Mufti and Newhook 1998; Matsui et al. 2001; and Newhook et al. 2001).

For concrete deck slabs of girder bridges on busy roads, stay-in-place forms made of corrugated thin steel sheets are being used again in many states of the USA. The main reasons for the revival of metal forms are improvement in their durability, economy and the need to minimize or eliminate traffic disruption below the bridge.

It is generally assumed that the metal forms do not participate in the load carrying action of the slab, because their smooth galvanized surface keeps them from acting compositely with concrete (for example, Taly 1998). This assumption would be justifiable if the deck slab acted only in flexure. As discussed in many of the references cited above with respect to arching in deck slabs, transversely-confined composite deck slabs develop an arching action after they have developed a system of cracks by first 'failing' in flexure. It is argued in this paper that after minor modifications, the stay-in-place metal form can serve the same function as the bottom transverse reinforcement in RC slabs, or as the steel straps in steel-free deck slabs.

TRANSVERSE CONFINEMENT

The bending failure of an unreinforced concrete deck slab supported on two steel girders and subjected to a central concentrated load can be seen in the photograph presented in Figure 1. A transverse free edge of the slab is at the bottom of the picture, and the two girders below the slab run perpendicular to the transverse edge. The longitudinal crack in the slab is wide and becomes wider at the transverse free edge; this can happen only when the top flanges of the supporting girders move laterally away from the longitudinal crack. It was realised that the horizontal forces generated by the transverse arching action of the slab moved apart the top flanges of the girders (Mufti et al., 1993). When the relative lateral movement of the top flanges of adjacent girders is restrained by tying them together by some means, the arching action in the deck slab is harnessed in the transverse direction of the bridge.

The Canadian Highway Bridge Design Code (CHBDC, 2000) contains design provisions for deck slabs made with fibre reinforced concrete (FRC), which may be devoid of tensile reinforcement. The FRC deck slabs are also known as the steel-free deck slabs. The CHBDC requires that the FRC deck slabs be confined transversely by means of discrete transverse straps connected to the top flanges of

www.EngineeringEBooksPdf.com

the supporting girders. The minimum cross-sectional area of each strap, A, is given by the following equation in mm^2.

$$A = \frac{F_s S^2 S_l}{Et} 10^9 \qquad (1)$$

where the factor F_s is 6.0 and 5.0 MPa for outer and inner panels of the deck slab, respectively. It is noted that the spacing of the supporting beams, S, is in m; the spacing of the straps, S_l, is in m; the modulus of elasticity of the strap material, E, is in MPa, and the thickness of the deck slab, t, is in mm. The presence of E in the denominator of the right-hand side of Equation (1) confirms that this requirement relates to the stiffness, rather than the strength, of the straps. The direct or indirect connection of a strap to the supporting beams is required to have a strength in Newtons of at least $200A$. For steel straps, the required connection strength is about half the axial strength of the strap.

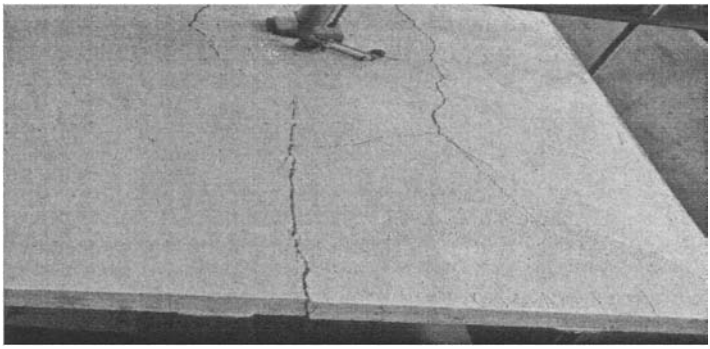

Figure 1. Bending failure of an unreinforced deck slab supported on two girders

Discrete straps of steel, designed by the above CHBDC provision, have already been provided in several FRC deck slabs (e.g., Bakht and Mufti, 1998; Newhook et al., 2001). The steel straps on the girders of the Salmon River Bridge in Nova Scotia, Canada, can be seen in Figure 2, before the steel-free deck slab was cast; this slab has no tensile reinforcement.

Figure 2. Steel straps welded to the top flanges of girders to confine the deck slab transversely

www.EngineeringEBooksPdf.com

CURRENT USE OF METAL FORMS

In the USA, the industry for manufacturing thin metal forms for slabs is fairly large. The Steel Deck Institute (SDI), with 12 'Member' Companies and 13 'Associate Member' Companies, has its own design manual (SDI, 2000). The companies affiliated with SDI manufacture a variety of metal decks, some of which are illustrated in Fig. 3. The metal forms are used for bridge deck slabs as well as for slabs in buildings.

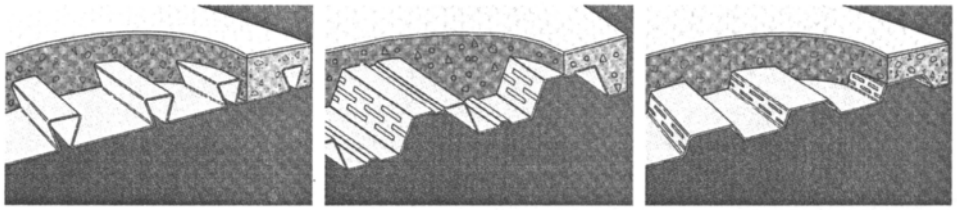

Figure 3. Various available metal forms

The use of metal decks as stay-in-place forms for bridge deck slab is regulated by the Departments of Transportation (DOT's) of the various states. For example, the Road and Bridge Specifications of Virginia DOT, in their Clause 404.03 (a) 1.a require that the minimum gauge thickness of the metal form should be 20 Gauge (0.94 mm). The same clause requires that design loading for the form should not be less than 120 pounds/ft^2 (5.75 kN/m^2), under which loading the maximum form deflection should not exceed 1/180 of the span of the form, nor 0.5 inch (12.7 mm).

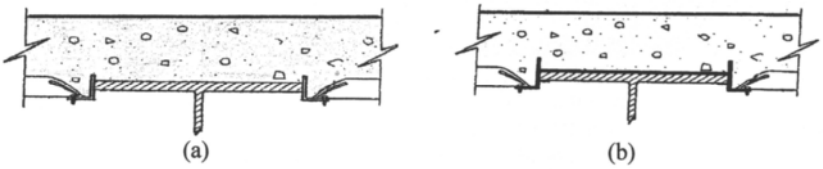

Figure 4. Deck form connections to steel beams: (a) support angles welded to girder flanges; (b) support angles connected to girder flanges by mechanical means

In Clause 404.03 (a) 1.b, the Virginia Specifications require that "Form sheets shall not rest directly on the top of the stringer or floor beam flanges." Notwithstanding this requirement, in order to maintain the specified longitudinal profile of the deck slab, the distance between the metal deck and top of girders has to be adjusted in the field. This adjustment is done by attaching the metal form to 2.65 mm thick cold-formed support angles. Some states do not permit the welding of the support angles to girder flanges; others do but only if the flanges are in compression, in which case the connection of the metal form to the girders can be as shown in Fig. 4 (a). When welding of the support angle is not permitted, the support angles are connected to the girder flanges by mechanical means, as shown in Fig. 4 (b). Metal forms are also permitted on concrete girders, but their connections are similar to those shown in Fig. 4 (b). The connections shown in Fig. 4 have the support angles in **L** position, in which case the form is lower than the girder flanges. When the form has to be above the girder flanges, the support

www.EngineeringEBooksPdf.com

angles are in 7 position. Typical metal form connections permitted by New York DOT are shown in Fig. 5 (a) with the support angles in 7 position. Mainly to reduce the dead weight of concrete and possibly to enhance the durability of the metal form, this state does not permit concrete in the valleys of the metal form (Fig. 5 b). The valleys are filled with preformed styrofoam blocks. A metal form under the deck slab of a bridge in North Carolina can be seen in Fig. 6.

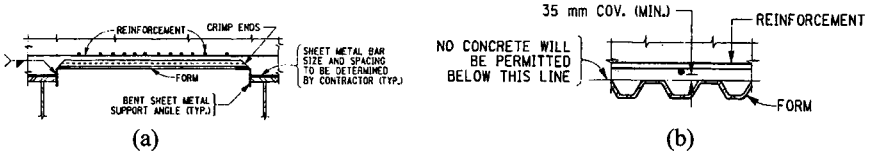

Figure 5. Typical details of a deck slab on metal forms, permitted by New York DOT: (a) partial cross-section; (b) partial longitudinal section

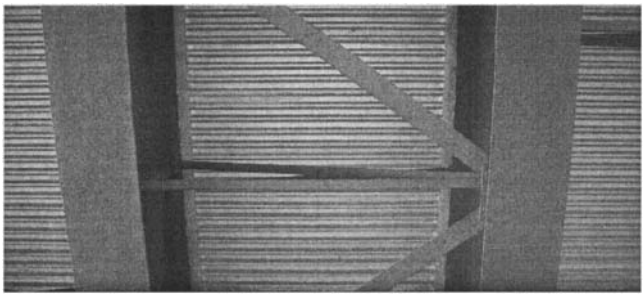

Figure 6. The underside view of a relatively new bridge in North Carolina

TRANSVERSE CONFINEMENT BY METAL FORMS

Bakht (1987) has reported on the testing of the non-composite concrete deck slab of the Champlain Bridge in Ottawa. The 150 mm thick concrete deck slab is cast on light-gauge metal forms, and is supported directly on longitudinal stringers, which are in turn supported on a system of transverse floor beams and longitudinal girders (Figure 7). The bridge was designed for non-truck traffic and could sustain only light passenger car wheels. For one particular construction project, the bridge was required to be used by concrete mix trucks, for which the steel beams were found to have adequate strength. The deck slab, analyzed for bending, however was found to have substantially lower strength than required for the wheels of concrete mix trucks.

During the test, the deck slab of the Champlain Bridge was subjected to a wheel load of 200 kN at six different locations, and a wheel load of 245 kN at two different locations; no sign of distress was observed under any test (Bakht, 1987). It is recalled that (a) the factored design failure wheel load including impact is about 200 kN, and (b) the maximum expected wheel load on a Canadian bridge during its lifetime is about 170 kN (Mufti et al., 2002). On the basis of the tests, concrete mix trucks were permitted on the Champlain Bridge.

www.EngineeringEBooksPdf.com

At the time of the test on the Champlain Bridge, the extra strength provided by the 'arching' action was accepted as an article of faith. There was little information available to identify the main source of arching, nor to quantify its contribution. Considerable research done on the behaviour of steel-free deck slabs since the work of Mufti et al. (1993) has provided some clues to the arching action of the Champlain Bridge deck slab.

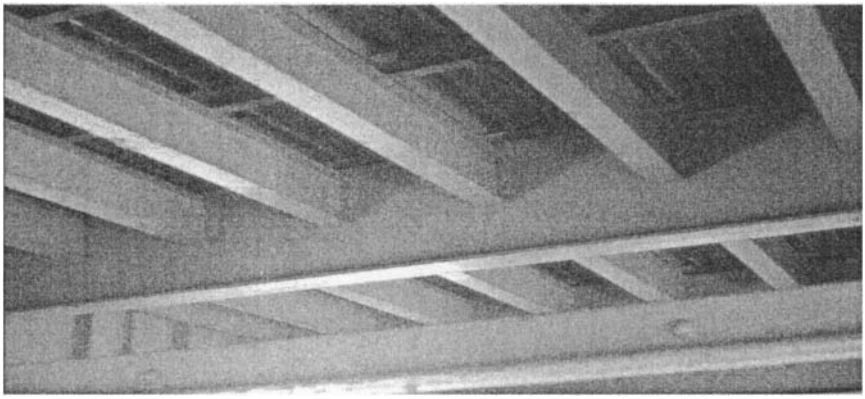

Figure 7. The deck of the Champlain Bridge viewed from below

It is hypothesised that the metal form in a non-composite deck slab, running continuously over longitudinal stringers (Fig. 7), can provide the transverse restraint, provided that there is some bond between the form and the stringers, as for example provided by tack-welding. The horizontal thrust T generated by the arching action in the transverse direction is illustrated in Fig. 8 (a). It has been shown by several researchers (e.g. Mufti and Newhook, 1998), that the stresses in the straps generated by the force T even under the heaviest expected wheels are fairly low in magnitude. In this case, even a relatively weak bond between the metallic form and the beams can transfer the arching forces in the slab to the beams.

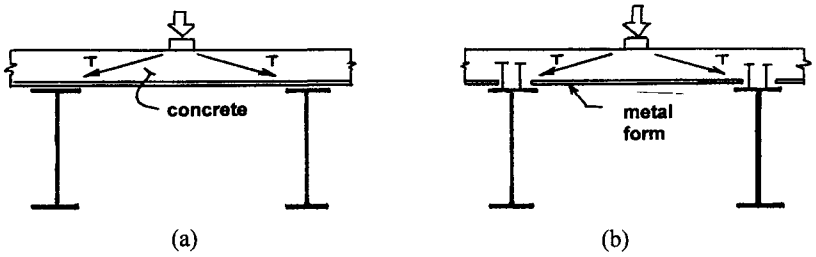

(a) (b)

Figure 8. Illustration of transfer of forces generated by the arching action in the transverse direction: (a) deck with continuous metal form in a non-composite slab; (b) deck with simply supported metal form in a composite slab

www.EngineeringEBooksPdf.com

Unlike the case in the Champlain Bridge, modern stay-in-place metallic forms are simply supported over the girders, as can be seen in the photograph of the underside of a relatively new bridge in North Carolina (Figure 6). While the RC slabs of these bridges are made composite with the girders, the metal forms are not connected directly to the top flanges of the girders. As can be appreciated from Figure 8 (b), the arching force T cannot be resisted by the metallic form unless it is attached by some means to the top flanges of the girders. A realistic connection of a metal form to a girder flange, through a support angle in 7 position, is shown in Fig. 9; this figure also illustrates the undesirable deformations of the support angle under the horizontal force generated by arching. Because of this undesirable movement of the support angle, a deck slab without reinforcement cannot be expected to develop the arching action; such a slab would fail in bending, similar to the slab shown in Figure 1.

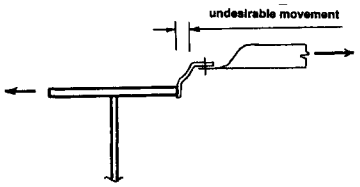

Figure 9. Deformations of a support angle under the horizontal force generated by the arching action

In order to mobilize the axial stiffness of the metal decks in the transverse direction of the bridge and to generate the arching action in the deck slab, the scheme illustrated in Fig. 10 (a) is proposed. The metal forms on each side of the internal girders are proposed to be inter-connected by means of glued sheets of metal or carbon fibre reinforced polymer (CFRP) strips. The connection of the metal deck to outer girders is proposed by means of similar glued strips, which are mechanically tied to shear connectors on the girders (Fig. 10 b).

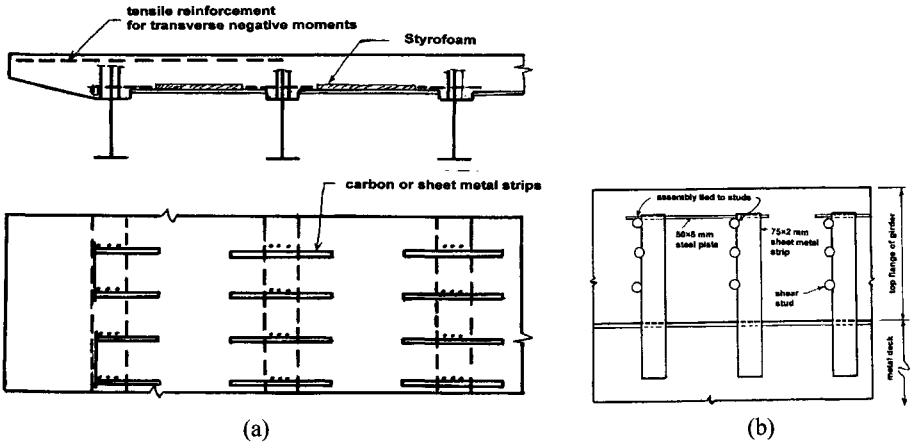

Figure 10. A scheme for mobilizing the axial stiffness of metal decks in the transverse direction: (a) plan and cross-section; (b) detail in plan of strip assemblies for connecting metal form to an external girder

www.EngineeringEBooksPdf.com

A 25mm thick styrofoam sheet is proposed to be laid over the metal forms to receive the cast-in-place concrete mixed with low modulus synthetic fibres. Other than that required for transverse negative moments due to loads on cantilever overhangs, the slab would not need any tensile reinforcement. As with the steel-free deck slabs, the concrete for the proposed slab should be mixed with low-modulus fibres to control early cracking in the concrete.

The provision of the styrofoam sheet would not only reduce the dead weight of concrete, but would also hasten the development of micro-cracks in the concrete, so that the arching action can be mobilized early in the life of the slab. Insulating the metal form from concrete is also expected to enhance the durability of the form. At the time of this writing, a full-scale model of a deck slab with metal forms, and without tensile reinforcement, is being constructed. The model, the cross-section of which is shown in Fig. 11, will be tested to failure to verify the hypothesis presented in the paper. Since there are only two girders in the model, the connection of the metal form to both the girders is the same as proposed for external girders in Fig. 10 (b). The 2.65mm thick sheet metal strips would be bonded to the metal form by a combination of glue and screws.

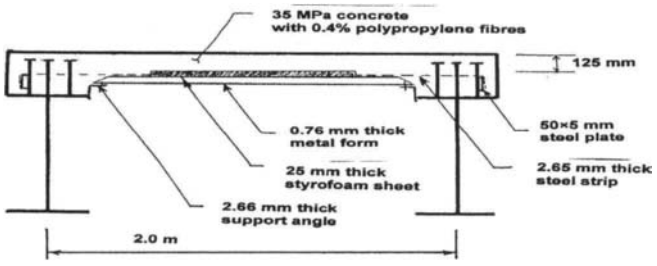

Figure 11. Cross-section of the full-scale model with metal form

DURABILITY AND ECONOMY

Currently, for deck slabs exposed to deicing salts or other aggressive agents, the top layer of reinforcement is generally protected with a large depth of cover, thus necessitating a minimum slab thickness of about 225 mm. If the reinforcing steel is removed in accordance with the scheme proposed above, then the slab thickness could be reduced to about 175 mm in most cases. The insertion of the styrofoam sheet would have the effect of reducing the net concrete thickness even further. The cost savings affected by the reduced amount of concrete and virtual elimination of all steel reinforcement are expected to be more than the additional cost of metal or CFRP strips and their assemblies.

The removal of steel reinforcement from concrete, which would become saturated with chloride, is expected to enhance the durability of the deck slab considerably. There is one aspect of durability, however, which requires particular attention – the durability of the metal form. In current designs with RC deck slabs, the metal forms are useful only till the concrete has set. Thereafter, the safety of the slab is not affected even if the forms are lost completely to corrosion. The same cannot be said about

www.EngineeringEBooksPdf.com

the proposed deck slab, in which the metal form is one the two main structural components, the other being concrete. An obvious solution to the problem is to improve the durability of the metal deck by such means as expansive foam, which could keep water out of its valleys and insulate the form from concrete. Three other possible solutions are proposed.

FRP Forms. Carbon fibre reinforced polymer (CFRP), although expensive, is extremely resistant to chemicals which cause steel to corrode in reinforced concrete. Since the modulus of elasticity of CFRP is comparable to that of steel, metal forms can be replaced by CFRP forms without changing the details significantly. A reinforcement-free deck slab with permanent CFRP forms is expected to be maintenance-free. Glass fibre reinforced polymer (GFRP) is significantly cheaper than CFRP. However, because of its low modulus of elasticity the GFRP form is expected to be much thicker.

Bottom Transverse Reinforcement. As noted earlier, the bottom transverse reinforcement also confines the slab effectively. As a safety precaution, a nominal layer of transverse bars of steel, or other suitable material, could be provided near the bottom face of the slab. Instead of four layers of steel reinforcement, as for example shown in Figs. 5 (a) and (b), only one layer of reinforcement need be provided. Enough reinforcement should be provided to confine the slab suitably without the metal form. For added durability, CFRP bars could be provided instead of steel bars.

Future Addition of Steel Straps. If the metal forms are expected to be durable, then there is no need to take precautionary measures at the time of construction. Should the form begin to corrode unexpectedly in future, the confinement can be provided later by means of straps welded to the underside of the top flanges of steel girders. In the case of concrete girders, transverse holes near the top can be left in the webs. Should the need arise in future, transverse confinement can be reinstated by means of threaded bars, described by Bakht and Lam (2000).

CONCLUSIONS

It is hypothesised that the stay-in-place metal forms, currently being used for composite concrete deck slabs of girder bridges, could be used with advantage to harness the arching action in the slab in the transverse direction of the bridge. A minor detailing change is proposed in design: that the forms be inter-connected by discrete strips of either sheet metal of CFRP. It is expected that this minor, but significant, change in design would permit the removal of the tensile reinforcement in the deck slab, and enhance its load carrying capacity significantly. The proposed concept is soon to be verified with the help of laboratory tests on a full-scale model. Proposed details of design would be formalised after these tests.

ACKNOWLEDGEMENTS

ISIS Canada and the Natural Sciences and Research Council of Canada have supported the research on which this paper is based. The authors are also grateful to (a) Leonard W. Bell for his valuable input in the proposed concept, and for his permission to reproduce the photograph presented in Figure 6; (b) to Steve May of Consolidated Systems Inc., Memphis, Tennessee, for his help in developing the details of the full-scale model; and (c) engineers of DOT's of New York and Virginia for providing design

www.EngineeringEBooksPdf.com

details permissible in their respective jurisdictions. The full-scale model is being constructed with the significant help of Moray McVey; his contribution is also acknowledged gratefully.

REFERENCES

Bakht, B. 1987. Bridge Evaluation by Proof Testing, l987. Structural Assessment, the Use of Full and Large Scale Testing, Butterworth, London, pp. l97-204.

Bakht, B. and Lam, C. 2000. Behaviour Of Transverse Confining Systems For Steel-Free Deck Slabs. ACSE Journal of Bridge Engineering. 5(2), pp. 139-147.

Bakht, B. and Mufti, A.A. (1998) Five Steel-free Deck Slabs in Canada. Structural Engineering International, 8(3), pp. 196-200.

CHBDC. (2000) Canadian Highway Bridge Design Code, Canadian Standards Association, Toronto.

Khanna, O.S., Mufti, A.A. and Bakht, B. 2000. Experimental Investigation of the Role of Reinforcement in the Strength of Concrete Deck Slabs. Canadian Journal of Civil Engineering. 27(3), pp. 475-480.

Matsui, S.; Tokai, D.; Higashiyama, H.; and Mizukoshi, M., 2001, "Fatigue Durability of Fiber Reinforced Concrete Decks Under Running Wheel Load," *Proceedings, Third International Conference on Concrete under Severe Conditions*, Vancouver, V. 1, pp. 982-991.

Mufti, A.A. Jaeger, L.G. Bakht, B. and Wegner, L.D. (1993) Experimental Investigation of FRC deck slabs without internal steel reinforcement. Canadian Journal of Civil Engineering. 20 (3), pp. 398 - 406.

Mufti, A.A., Memon, A.H., Bakht, B., and Banthia, N. 2002. Fatigue investigation of steel-free bridge deck slabs, ACI SP-206, pp. 61-70.

Mufti, A.A.; and Newhook, J.P. (1998) Punching Shear Strength of Restrained Bridge Deck Slabs, ACI Structures Journal, 8(3), pp. 375-381.

Newhook, J.P., Bakht, B., Mufti, A.A., and Tadros, G. (2001) A Novel Fibre-reinforced Marine Structure in Nova Scotia, Concrete International.

SDI (2000) Design Manual for Composite Decks, Form Decks, and Roof Decks. Steel Deck Institute, Fox River Grove, Il, USA.

Taly, N. (1998) *Design of Modern Highway Bridges*, McGraw Hill, New York, NY, USA, p. 571.

www.EngineeringEBooksPdf.com

Advances in Steel Structures, Vol. II
Chan, Teng and Chung (Eds.)
© 2002 Elsevier Science Ltd. All rights reserved.

ANALYSIS OF THE CAMBER AT PRESTRESSING OF A NEW KIND OF COMPOSITE RAILWAY BRIDGE DECK

S. Staquet[1], H. Detandt[1, 2] and B. Espion[1]

[1]Department of Civil Engineering, University of Brussels,
1050 Brussels, BELGIUM
[2]Bridge Department, Tucrail s.a.,
1070 Brussels, BELGIUM

ABSTRACT

Up to 300 composite railway bridge decks of a new kind belonging to the trough type with U shaped cross section have been constructed in Belgium since ten years. They seem to perform according to expectations. However, we have some concerns about the variability between the measured and computed camber of these bridge decks just after the transfer of prestressing. In order to explain this variability, a statistical analysis was made with a sample of 42 bridge decks using 10 variables like the concrete compressive strength, the heat cure, the type of steel girder (hot-rolled or welded) and the age of concrete at prestressing. Usual statistical tools were used: ANOVA (analysis of variance) and the linear regression. Thanks to the correlation matrix, the significant variables to enter in the linear regression models were detected. The ratio between maximum tensile stress and yield strength in the steel girders at the preflexion and the type of steel girder were found to be the most significant variables to explain the variability. If the steel girder is hot-rolled and the tensile stress/yield strength ratio in the steel girders at the preflexion is high then the difference between the measured and computed cambers is high too. So, the construction process of the steel girders is important due to its influence during the elastification phase. The purpose of the paper is to report on this statistical analysis in order to explain the influence of each of these variables on the behaviour of these composite railway bridge decks.

KEYWORDS: composite bridge, prestressing, high strength concrete, camber, numerical modelling, hot-rolled girder, welded girder, statistical analysis.

1 INTRODUCTION

A new kind of bridge deck has been developed recently in Belgium for the replacement of old steel railway bridges with moderate spans and for the construction of multi-spans viaducts for the new high speed lines. Up to now, these bridge decks have been used (single track) for simply supported spans up to 26 m (Staquet *et al.*, 2001). The bridge decks are prefabricated in workshops and transported by train to the construction site where they are placed on their supports by cranes. These

www.EngineeringEBooksPdf.com

composite steel-concrete structures belong to the trough type with U shaped cross section and have a breadth of 4m (Figure 1). The two steel hot-rolled (HEA1000 or HEB1000) or welded I-girders are bent at the mill or in plant to produce an initial camber. Then, the first step in the workshop is the elastification phase of the steel girders. In order to remove the residual stresses, two local loads are applied at ¼ and ¾ of the span of the steel girders and released several times until the precamber does not change any more. Then, the construction begins by applying two local loads again on each steel girder at ¼ and ¾ of the span in order to straighten the girders and to obtain at this stage a camber equal to zero. The stress level in the steel girders during this preflexion phase is limited to 80% of the yield strength. These two girders will be parts of the webs of the bridge. Then, the bottom slab of the deck is constructed: reinforcing bars (transversally) and naked tendons (longitudinally) are disposed and stressed in the space that will be filled by the concrete bottom slab (slab depth: 0.25m). The bottom slab is concreted some hours after the preflexion of the steel girders. A part of the bridge decks are heated at 45°C during the first day after casting. At two (for the decks with heat cure) or three (for the non heated ones) days of age, the bottom slab is prestressed by releasing the preflexion of the steel girders and by transferring the prestressing force from the tendons. On the following day, the remaining naked (upper) parts of the steel girders are enclosed in a 2nd phase concrete to complete the webs of the deck. This kind of deck has been designed, among other reasons, to minimize construction depth.

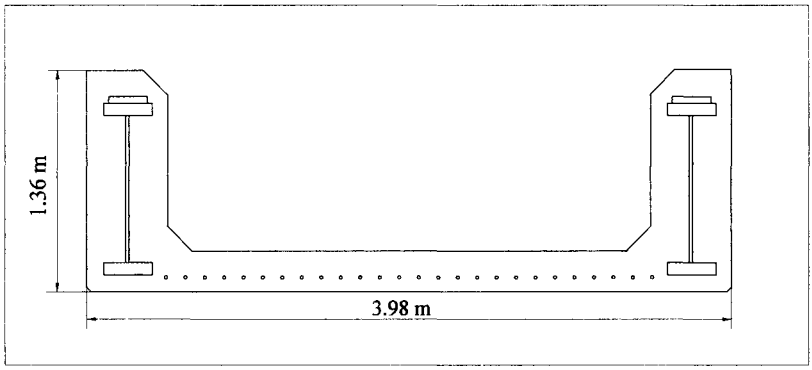

Figure 1: Typical trough shaped cross section of a bridge

Prestressing is transferred at an early age (2 or 3 days) and at high stress levels (around 0.5 $f_{c,\,cube}$) on high strength concrete ($f_{c,\,cube}$ = 45MPa at the age of transfer). The composite character of the construction, with the association of the steel of the girders (S355), the steel of the prestressing tendons (grade 1840 MPa) and the two-phases concreting should also be noted. Up to 300 of these bridge decks have now been constructed since ten years and seem to perform according to expectations (Couchard and Detandt, 2000). However, we have observed some variability between the measured and computed camber of these bridge decks just after the transfer of prestressing. The purpose of this investigation is to detect the parameters that influence significatively the variability of the camber at prestressing.

2 DESCRIPTIONS OF THE SIGNIFICANT VARIABLES

Before proceeding with the statistical analysis, the different variables assumed to be linked to the camber must be determined. The first step in order to understand the behaviour of this particular structure is to analyze the characteristics of the concretes (grade C60) casted in it. The concrete

www.EngineeringEBooksPdf.com

compressive strength f_c was measured on cubes. The formulation is identical for both concrete phases and is composed by:

-Sand (from Maas river, 0/5): 715 kg/m³
-Aggregates (crushed limestone, 7/14): 1140 kg/m³
-Portland cement (CEM I 52.5 R LA, ASTM III and class 3 CEB-MC90): 380 kg/m³
-Total water: 137 liters/m³
-Water reducing admixture (Visco 4): 7 kg/m³.

The histogram given in Figure 2 shows the distribution of the age of the first phase concrete (in hours) when the preflexion of the steel girders is released and the prestressing force from the tendons transferred. As mentioned previously, there are two peaks: the first one at 40 hours for the bridge decks heated at 45°C during the first day after mixing and the second one at 62 hours corresponding mainly to non-heated bridge decks. The minimal, mean and maximal values of the age of concrete at prestressing are 30, 60 and 126 hours.

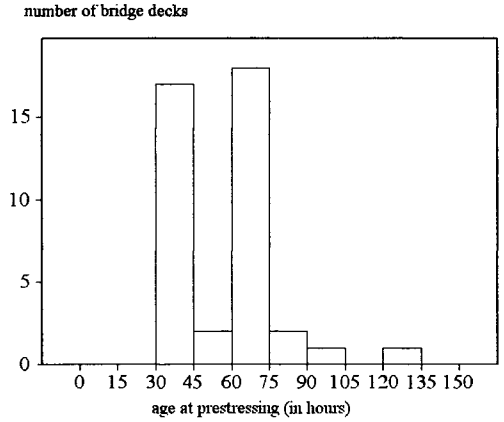

Figure 2: Histogram of the distribution of the age of the first phase concrete at prestressing

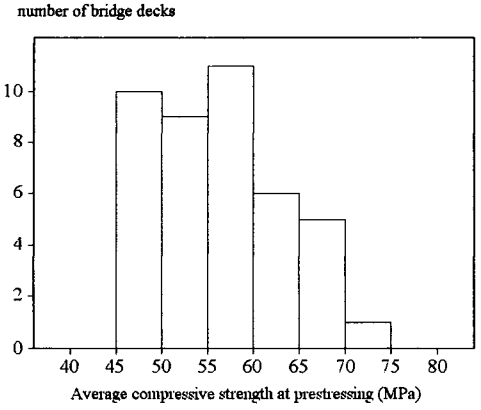

Figure 3: Average cubic compressive strength of the 1st phase concrete at prestressing (MPa)

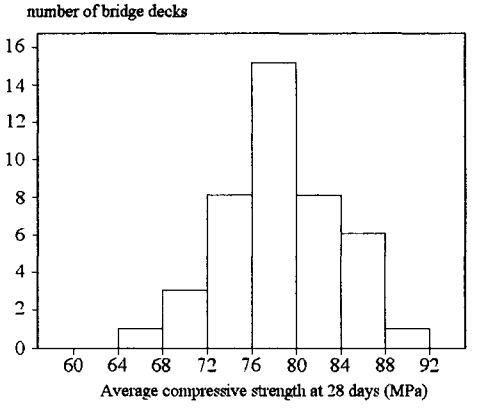

Figure 4: Average cubic compressive strength of the 1st phase concrete at 28 days (MPa)

www.EngineeringEBooksPdf.com

The histogram given in Figure 3 shows the variation of the average cubic compressive strength of the first phase concrete at prestressing. Figure 4 shows the variation of the average cubic compressive strength of the concrete at 28 days. The minimal, mean and maximal values of the compressive strength at prestressing and at 28 days are respectively 46, 55.8, 74.5 and 67.5, 78.3, 88 MPa. The standard deviation of the compressive strength at prestressing is 7 MPa and at 28 days, 5 MPa.

In order to understand exactly the influence of the heat cure on the compressive strength of the first phase concrete at prestressing and at 28 days, an analysis of variance was made which consists in a test on the equality of the mean values for both groups: without heat cure and with heat cure. The compressive strength at 28 days was slightly linked to the heat cure (P-value equal to 0.055). The P-value is the probability that there is no difference between the mean values. Usually, a difference between the mean values can be considered as significant when P-value < 0.05. However, for the compressive strength at prestressing, no difference was found between heated or non-heated first phase concrete (P-value equal to 0.828). For the next statistical analysis, the data were divided in two groups: the first group for non-heated concretes and the second group for heated concretes. The box plot given by Figure 5 shows the average compressive strength of the first phase concrete at prestressing for both groups. The mean values and the standard deviation for the non-heated and heated concretes at prestressing are respectively 56.2, 6.4 MPa and 55.7, 7.4 MPa. However, the box plot given by Figure 6 shows that the distribution of the average compressive strength of the first phase concrete at 28 days depends on the curing method: curing at 20°C or heat cure at 45°C. The minimal, mean and maximal values of the average compressive strength of the first phase concrete at 28 days without and with heat cure are respectively 75, 80.5, 88 MPa and 67.5, 77, 87 MPa. The standard deviations without and with heat cure are 3.7 and 5.3 MPa. The scatter of the results at 28 days is thus larger for concrete with heat cure than for concrete with curing at 20°C.

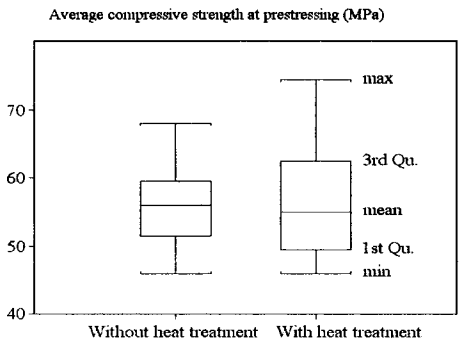

Figure 5: Compressive strength of the concrete at prestressing (MPa)

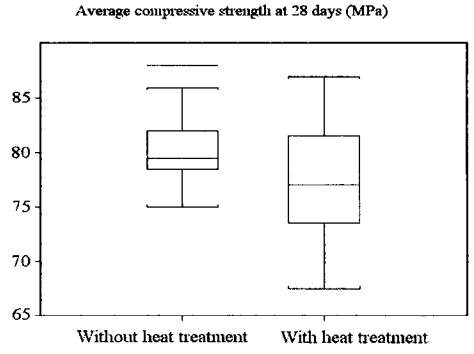

Figure 6: Compressive strength of the concrete at 28 days (MPa)

Another variable parameter linked to the concrete and suspected to have an influence on the camber at prestressing is the ratio between the stress in the first phase concrete at the bottom fiber at mid-span and the average cubic compressive strength of the first phase concrete at prestressing. A statistical analysis was made for all the data. The minimal, mean and maximal values in percentage found in this case were 23.5, 39.5 and 50.2% and the standard deviation was 6.4%. For a part of these bridge decks, this ratio can reach very high values, especially if we remember that the concrete compressive strength is measured on cubes. In fact, for this ratio, all the data can be

www.EngineeringEBooksPdf.com

divided in two groups according to the type of the steel girder: welded or hot-rolled. The box plot given by Figure 7 shows that the mean value of this ratio is higher for bridge decks with welded steel girders (44.7%) than the mean value for bridge decks with hot-rolled steel girders (37.5%).

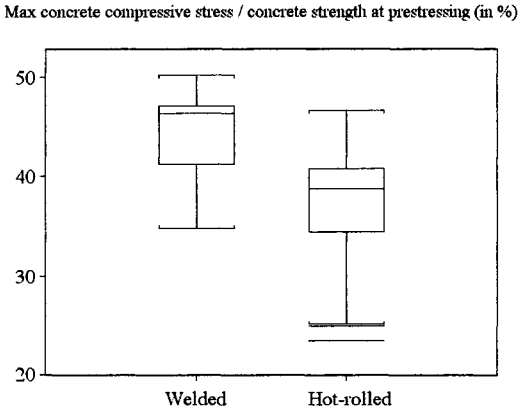

Figure 7: Ratio between the stress in the concrete at the bottom fiber at mid-span and the average cubic compressive strength at prestressing (in %)

Three others continuous variables suspected to be significant have been selected. The first one is the ratio between the maximum tensile stress in the steel girders and the yield strength at the preflexion. The minimal, mean and maximal values in percentage were 41.1, 67.1 and 74%. But all the data can be divided again in two groups according to the type of the steel girder. The minimal, mean and maximal values of this ratio for the group of welded steel girders and for the group of hot-rolled steel girders were respectively 41.1, 50.6, 69.5% and 71.2, 72, 74%. The standard deviations for the group of welded steel girders and for the group of hot-rolled steel girders were 14 and 0.8 %. This ratio is thus strongly dependent on the type of the steel girders.
The second continuous variable is the ratio between the maximum compressive stress in the steel girders and the yield strength at the preflexion. The minimal, mean and maximal values in percentage were 32.9, 53.4 and 74 %. If the data are divided in two groups according to the type of the steel girders, the minimal, mean and maximal values are respectively 32.9, 40.2, 54.9 % and 53.2, 57.2, 74 %. This ratio is also strongly dependent on the type of the steel girders. The third continuous variable is the ratio between the external bending moment due to prestressing and the sum of the external bending moment due to preflexion and the external bending moment due to prestressing. The minimal, mean and maximal values of this ratio in percentage are 55.9, 71.7 and 79% and the standard deviation is equal to 6.2 %.

3 STATISTICAL ANALYSIS OF THE CAMBER AT PRESTRESSING

In order to explain the variability of the relative difference (X) between measured and computed camber after prestressing, a statistical analysis was made with a sample of 42 bridge decks using the following continuous or discrete variables: 1) the bottom slab concrete strength at the age of prestressing transfer (A), 2) hot cure, 3) the bottom slab concrete strength at 28 days (B), 4) the age of concrete at the transfer of prestressing (C), 5) the type of steel girder, 6) reinforcement of the upper flanges of the steel girders, 7) ratio: maximum tensile stress/ yield strength in the steel girders at the preflexion (D), 8) ratio: maximum compressive stress/ yield strength in the steel girders at the preflexion, 9) ratio: bending moment due to prestressing / (bending moment due to preflexion +

www.EngineeringEBooksPdf.com

bending moment due to prestressing) (E), 10) ratio: maximum compressive stress in the first phase concrete/ first phase concrete strength at the transfer of prestressing (F). An analysis of the principal components was made for the continuous variables A, B, C, D, E and F in order to detect in the correlation matrix the pertinent variables to be entered in the linear regression models. Table 1 below shows the results of the correlation matrix.

TABLE 1
RESULTS OF THE CORRELATION MATRIX BETWEEN THE VARIABLES A, B, C, D, E, F AND X

	A	B	C	D	E	F
X	0.07	**- 0.255**	**0.218**	**0.47**	- 0.09	- 0.166

The most significant variables are D, B and C. Figure 8 that shows the correlation between the continuous variables confirms it. The variable X is strongly correlated to variable D.

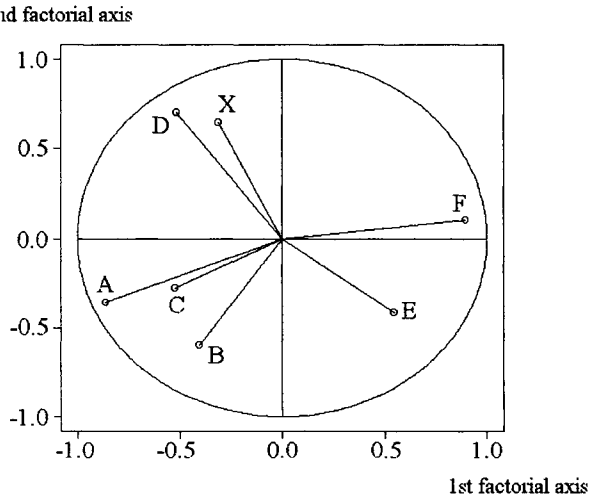

Figure 8: Representation of the continuous variables A, B, C, D, E, F and X

The continuous variables B, C, D and one discrete variable, namely the type of the steel girders, were considered in a linear regression model in order to explain the variability of the camber at prestressing. The P-value is the probability that the variable is not significant in order to explain the variable (X). Usually, the P-value can be considered as significant when P-value < 0.05. Tables 2 and 3 show the results for two simulations.

TABLE 2
RESULTS OF THE LINEAR REGRESSION MODEL WITH THE VARIABLES B, C, D AND X

X	B	C	D
P-value	0.058	0.077	**0.002**

TABLE 3
RESULTS OF THE LINEAR REGRESSION MODEL WITH THE VARIABLES B, C, THE TYPE OF GIRDER AND X

X	B	C	Type of steel girder
P-value	0.033	0.068	**0.005**

www.EngineeringEBooksPdf.com

The maximum tensile stress/ yield strength ratio in the steel girders at the preflexion (variable D) and the type of steel girders are the most significant variables to explain the variability of the camber at prestressing. If the steel girder is hot-rolled and the tensile stress/yield strength ratio in the steel girders at the preflexion is high then the difference between the measured and computed cambers after prestressing is high too. For maximum tensile stress higher than 70% of the yield strength, the yield strength can be exceeded locally due to the presence of residual stresses. Furthermore, the hot-rolled steel girders are bent just after rolling. They contain more internal stresses than the welded steel girders. So, the construction process of steel girders is significant due to its influence during the elastification phase.

The box plot given in Figure 9 shows the variability of the camber at prestressing in function of the type of the steel girders. The mean values of the variability for the bridge decks with hot-rolled steel girders and with welded steel girders are respectively 5.57% and – 0.35%.

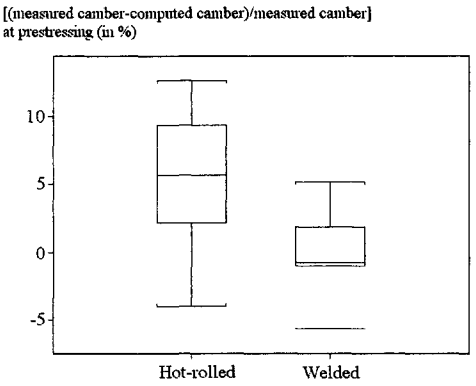

Figure 9: Ratio between (measured camber – computed camber) and measured camber at prestressing for hot-rolled and welded steel girders

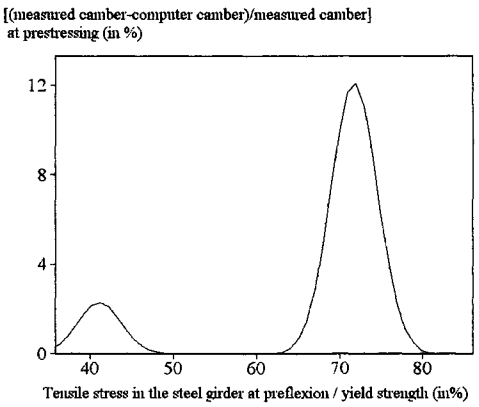

Figure 10: [(measured camber – computed camber) / measured camber] in % at prestressing in function of the [tensile stress in the steel girder / yield strength] ratio in %

Figure 10 shows the variability of the camber in function of the maximum tensile stress/yield strength ratio in the steel girders at the preflexion. The results of the previous statistical analysis are confirmed. In consequence of these results, the loss of camber by elastification must be taken into account according to these two variables in the design process of such composite structures.

The box plot given in Figure 11 confirms these conclusions. The measured permanent loss of camber in the steel girders after the elastification phase is higher for hot-rolled girders (mean value: 9.68%) than for welded steel girders (mean value: 5.21%).

www.EngineeringEBooksPdf.com

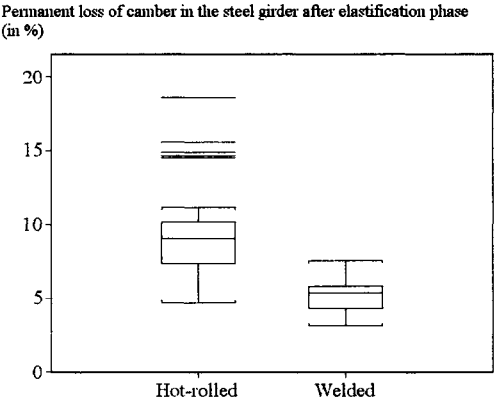

Figure 11: Measured loss of camber in the hot-rolled and welded steel girders after elastification

4 CONCLUSIONS

For a sample of 42 composite prestressed railway bridge decks, variability was observed between the measured camber at prestressing and the camber computed by a classical computation method using a pseudo-elastic analysis with modular ratios. The construction of this new kind of bridge deck is rather complex with preflexion of steel girders, prestressing of a concrete slab and two-phases concreting. Not less than ten variables, including the concrete compressive strength, the heat cure, the type of steel girder (hot-rolled or welded) and the age of concrete at prestressing were selected and handled in the statistical analysis. For the compressive strength of the first phase concrete at prestressing, no difference was found between heated and non-heated bridge decks. However, the compressive strength of the first phase concrete at 28 days was found being slightly influenced by the heat cure. But neither the compressive strength of the first phase concrete at prestressing nor the compressive strength of the first phase concrete at 28 days were found to have an influence on the variability of the camber at prestressing. In fact, the most significant variables that explain the variability of the camber at prestressing are the maximum tensile stress / yield strength ratio in the steel girders at the preflexion and the type of steel girders. Actually, the measured permanent loss of camber in the steel girders after the elastification phase is higher for hot-rolled girders than for welded steel girders. In order to increase the accuracy of the computed camber at prestressing, the computation method must take into account the type of steel girders for the evaluation of the loss of camber after the elastification phase.

REFERENCES

COUCHARD I. and DETANDT H., Entrance of the high-speed line in the Brussels South Station, Proceedings of the 16th IABSE Congress, Lucerne, Switzerland, 2000.

STAQUET S., DETANDT H. and ESPION B., Time-dependent behaviour of a railway prestressed composite bridge deck, Proceedings of the international conference Concreep-6@MIT, F.-J. Ulm, Z.P. Bažant & F.H. Wittmann editors, Elsevier, pp.373-378, 2001.

ACKNOWLEDGEMENTS

Part of this research is financed by a grant funded by the Belgian National Foundation for Scientific Research, which is gratefully acknowledged. We also wish to thank C. Jadoul[1, 2] and the companies RONVEAUX s.a. and TUCRAIL s.a. for their collaboration.

www.EngineeringEBooksPdf.com

Advances in Steel Structures, Vol. II
Chan, Teng and Chung (Eds.)
© 2002 Elsevier Science Ltd. All rights reserved.

EVALUATION OF TYPHOON INDUCED FATIGUE DAMAGE USING HEALTH MONITORING DATA

Tommy H. T. Chan[1], Z. X. Li[2] and J. M. Ko[1]

[1]Department of Civil and Structural Engineering, The Hong Kong Polytechnic University, Hung Hom, Kowloon, Hong Kong
[2]College of Civil Engineering, Southeast University, Nanjing, China, 210096

ABSTRACT

This paper aims to evaluate the effect of a typhoon on fatigue damage in steel decks of long-span suspension bridges. The strain-time histories at critical locations of deck sections of long-span bridges during a typhoon passing the bridge area are investigated by using on-line strain data acquired from the structural health monitoring system installed on the bridge. The fatigue damage models based on Miner's law and the continuum damage mechanics are applied to calculate the increment of fatigue damage due to the action of a typhoon. It is found that for the case of Tsing Ma Bridge the stress spectrum generated by a typhoon is much different than that by the normal traffic and its histogram shapes can be described approximately as a Rayleigh distribution. The influence of typhoon loading on accumulative fatigue damage is more significant than that due to normal traffic loading. The increment of fatigue damage generated by hourly stress spectrum for the maximum typhoon loading may be much greater than those for normal traffic loading. It concludes that it is necessary to evaluate typhoon induced fatigue damage for the purpose of accurately evaluating accumulative fatigue damage for the long-span bridge located at the typhoon prone region.

KEYWORDS

Typhoon, Long-span bridge, Fatigue damage, Stress spectrum, Health monitoring

INTRODUCTION

Some studies have been made on the estimation of wind-induced fatigue damage in cable-stayed bridges, e.g. Virlogeux (1992) and Gu et al (1999). These works were carried out by evaluating firstly wind load with different speed and direction, and then calculating buffeting response of the bridge. Although the wind load model was developed by considering many factors and including buffeting due to wind, still it is not enough to obtain an accurate evaluation of realistic response for a bridge under the passage of a typhoon. The best way to obtain the realistic response of a bridge under a typhoon is to carry out a field measurement for the bridge. However, it is difficult to carry out field testing when a typhoon or severe tropical storm passes over the bridge to be tested since all actions on the bridge have to be stopped during a typhoon.

www.EngineeringEBooksPdf.com

With the development of the structural health monitoring system for long-span suspension bridges (Aktan et al 1998), it becomes possible to obtain field data of dynamic response induced by a typhoon for the bridge with permanent installed monitoring system. The studies have been made on how to take full advantage of on-line monitoring data for the purpose of evaluating fatigue damage of bridge-deck sections under normal traffic loading (Chan et al 2000 and Li et al 2000), which consists of both the railway and road traffic, is defined as the traffic loading on the bridge at normal working conditions. This paper presents how to evaluate typhoon induced fatigue damage based on the structural health monitoring data. The strain-time histories measured by the system permanently installed on the Tsing Ma Bridge during a typical typhoon under the hoisting of Typhoon Signal No. 10 are investigated. The increment of fatigue damage due to the typhoon is then evaluated by applying the fatigue models based on the Miner's law and the continuum damage mechanics (CDM) respectively.

TYPHOON YORK

Typhoon "York" developed as a tropical depression about 420km northeast of Manila on 12 September 1999, and strengthened into a severe tropical storm on 14 September. The No. 8 NORTHWEST Gale or Storm Signal was hoisted at 3.15 a.m. on 16 September. Winds strengthened rapidly in the next few hours. The Increasing Gale or Storm Signal No. 9 was hoisted at 5.20 a.m. and the Hurricane Signal No. 10 at 6.45 a.m. The signal was in force for 11 hours. Winds of hurricane force, firstly northeasterly and then southwesterly, buffeted Hong Kong on 16 September. Local winds experienced a temporary lull during the eye's passage. The eye of York was closest to the Hong Kong Observatory Headquarters at around 10 a.m.

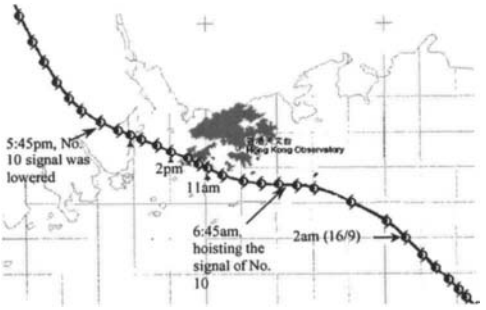

Fig. 1. Track of York over Hong Kong

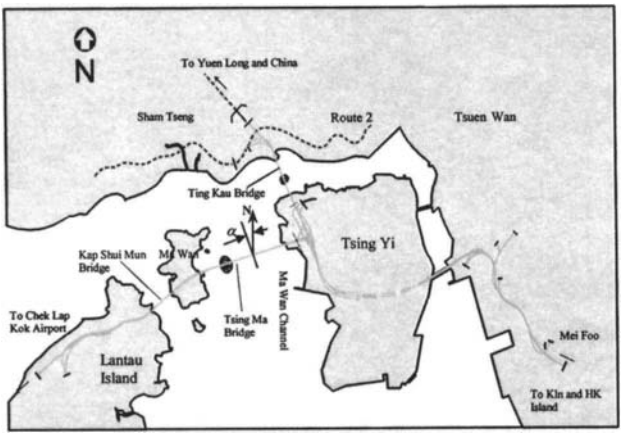

Fig. 2. Location plan of Tsing Ma Suspension Bridge

when it was about 20 km to the south-southwest. As shown in Figure 1, York crossed over Hong Kong from southeast to northwest. The alignment of the deck of the Tsing Ma Bridge (TMB) deviates from the east-west axis for about 17° anti-clockwise (see Figure 2). Actually most of the Hong Kong major typhoons including York will follow a track affecting the bridge in a way as a direct hit. From the above points of view, York is typical for investigating the effect of typhoons crossing Hong Kong on the Tsing Ma Bridge.

www.EngineeringEBooksPdf.com

WIND AND STRAIN RESPONSE MONITORING

The Tsing Ma Bridge (TMB) is the longest suspension bridge in the world that carries both highway and railway traffic. It can be seen from Figure 2 that the bridge serves as the main portion of the Lantau Link supporting highway and railway transport between Tsing Yi Island and Lantau Island. For safety assurance, a structural monitoring system - Wind And Structural Health Monitoring System (WASHMS) has been devised by the Highway Department of the Hong Kong SAR Government (Lau et al, 2000) to monitor the integrity, durability and reliability of the bridge (Figure 3). The bridge has a double deck configuration with the expressway on the upper deck and the railway below. Structurally, the deck section of the Tsing Ma Bridge is a hybrid arrangement combining both truss and box forms Lau et al (1997).

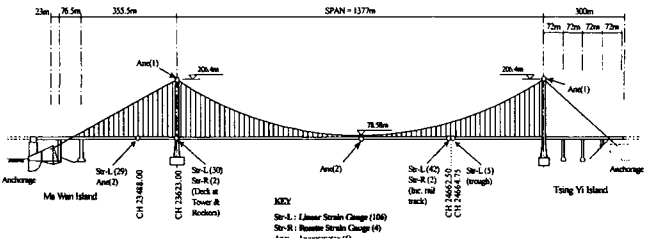

Fig. 3. Sensors layout of the Tsing Ma Bridge

The WASHMS for the Tsing Ma Bridge includes six anemometers including two digital ultrasonic anemometers installed on the north side and south side of the bridge deck at the mid-span, specified respectively as WITJN01 and WITJS01 (Figure 5). Each ultrasonic aneometer can measure three components of wind velocity simultaneously. Figures 4(a) and (b) show variations of 10-minute-averaged mean wind speed and direction, respectively, for the data obtained from the north anemometer "WITJN01". In the figures, the x-coordinate is the local time (HKT) and the measured data start from 00:00 HKT, 16 September 1999 and end at 20:00 HKT of the same day. In Figure 4(b), the direction angle α is measured from North anti-clockwise as shown in Figure 2. It can be seen that the mean wind blew, approximately from the south, across the bridge in the time region shown in Figure 4. The max. 10 min mean wind speed measured by "WITJN01" was 28.4 m/s at about 8:40 HKT, 16 September 1999.

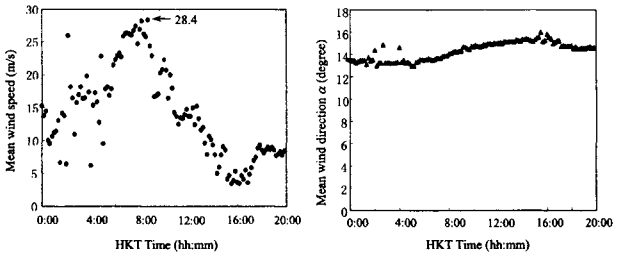

Fig. 4. Mean wind speed and direction from the anemometer "WITJN01": (a) 10 min mean speed, (b) 10 min mean wind direction

STRAIN-TIME HISTORY DURING THE TYPHOON "YORK"

Strain-time history has been recorded at locations of strain gauges installed on the decks of TMB since the bridge was commissioned. It is a useful database for on-line fatigue analysis of the bridge. Especially, the data recorded by the monitoring system for the bridge under typhoon is invaluable for the analysis of typhoon induced fatigue since these data are very limited up to now. In order to catch the particular features of typhoon induced strain history, strains distributed at several critical locations in a deck section are firstly studied in this section.

www.EngineeringEBooksPdf.com

The most vulnerable zones may be different for different types of loading. By dealing with many other data measured at different locations and comparing, the locations vulnerable both for normal traffic and typhoon for comparison are selected for the present study. According to the criticality and vulnerability ratings review by Flint & Neill Partnership (Flint & Neill Partnership, 1998), the most vulnerable zones are those under the outermost traffic lanes carrying local loads from vehicular traffic. Although the road traffic on the upper deck was stopped during periods of the typhoon "York", still the locations at two sides of the outmost of a deck may be critical from the point of view of aerodynamics. Railway beams made up of two inverted T-beams welded to flange plates are subjected to local loading from trains and to effects of composite interaction with the main deck girders. They are prone to fatigue damage from railway loading. Based on the above review, strain histories measured by three strain gauges, set at locations A, B and G shown in Figure 5 are selected in the study. As shown in Figure 5, the strain gauge "SSTLN-01" locates on the top chord of the north outer longitudinal truss, "SPTLS-02" is on the left diagonal bracing of the south outer longitudinal truss and "SPTLS-09" on the lower bracing of the cross frame underneath the railway. The analysis of fatigue damage under normal traffic loading has shown that the effective stress range at the above locations takes a comparatively large value, which means these locations are critical when the bridge serves under normal traffic and they also should be paid special attention for analysis of typhoon fatigue damage. It is observed that the strain history at "SPTLS-09" takes most large amplitude strain range among the three locations. Considering the train cross over the bridge to Hong Kong airport was still in service during typhoon "York" over Hong Kong, the above observation is understandable and the strain recorded at "SPTLS-09" has actually included the strain due to the interaction of running train and the bridge under typhoon.

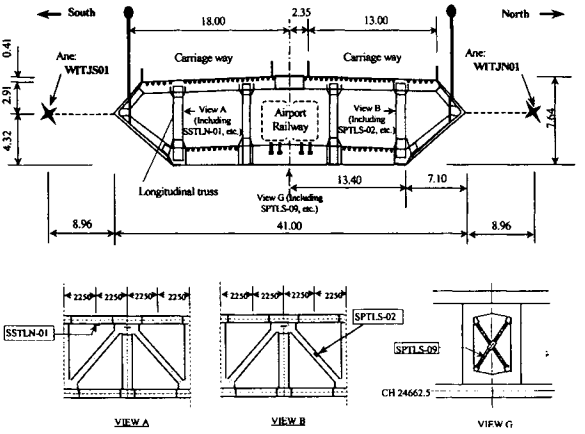

Figure 5 Locations of strain gauges and anemometers in the cross frame

It is also observed that the strain history due to typhoon, when there was no railway service and the road was closed, has a pattern different from that due to normal traffic. The normal traffic induced strain time curve in one hour can be considered to be composed of many small pulse of strain and some of higher pulses as shown in Figure 6 (b). Each higher pulse corresponds approximately to the passage of a train. The typhoon induced strain time curve has much more cycles of strain range with large amplitudes than that for higher pulse corresponding to train passing in Figure 6.

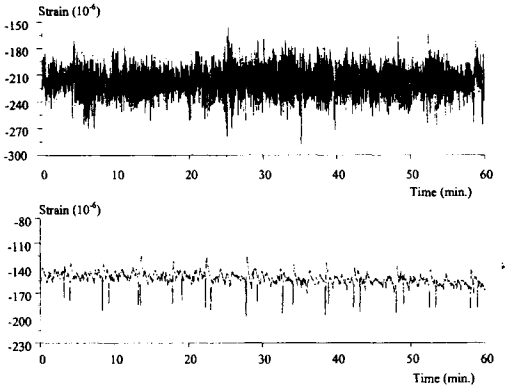

Figure 6 Hourly strain histories (14:00~15:00) at "SPTLS-09 for (a) Typhoon "York" and (b) Normal Traffic

www.EngineeringEBooksPdf.com

STRESS RANGES IN HOURLY STRESS HISTORY DUE TO THE TYPHOON

The strain-time histories shown in Figure 6 are composed of complicated variable-amplitude cycles. The stress-time histories can be obtained from these strain histories. In this work, the rain-flow counting method developed by Downing (1972) is used to count closed stress-strain hysteresis loops as cycles at different level of stress range and mean stress in a block of cycles. The 3-D histograms of rain-flow counting for a block of cycles are given in Figure 7, in which Figure 7(a) shows stress cycles at the location of the strain gauge "SSTLN-01" for hourly stress history under "York" during the hour 14:00~15:00. For the purpose of comparison, the histogram of stress spectrum at the same location for daily stress history at normal traffic is also shown in Figure 7(b). It is observed that typhoon induced stress cycles are distributed in the stress range from 3MPa to 21MPa, and most of the stress cycles with mean stress vary from 0~6MPa. Only very small cycles are in the region of the mean stress over 6MPa. It is different from the normal traffic induced stress cycles with significant variation in the value of the mean stress from -8MPa to 24MPa (see Figure 7b). The above observations suggest that typhoon induced stress cycles do not have significantly fluctuating mean stress. Therefore the effect of mean stress on fatigue damage can be neglected.

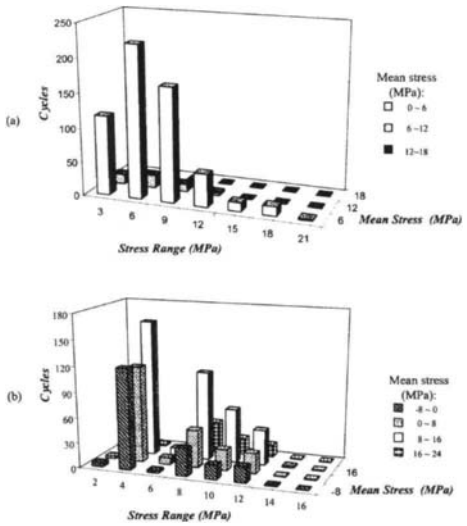

Figure 7 Rainflow counted cycles distribution w.r.t. stress range and mean stress at "SSTLN-01" for (a) hourly stress history under "York" and (b) daily stress history at normal traffic

Figure 8 shows 2-D histogram of rain-flow counted stress spectrum at the location "SPTLS-09" for (a) hourly stress history under typhoon "York" 14:00~15:00 and (b) daily stress history at normal traffic. It can be seen that the stress spectrum for typhoon induced stress cycles has more cycles in higher stress range than that induced by normal traffic. It can also be observed that the stress spectrum for typhoon induced stress history has a pattern different from that induced by normal traffic, and Figure 7(a) and Figure 8(a) show a pattern of approximate Rayleigh distribution.

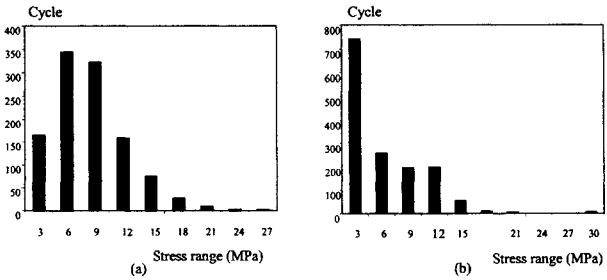

Figure 8 Stress ranges occurred at "SPTLS-09" for (a) hourly stress history under Typhoon "York" and (b) daily stress history at normal traffic

The effective stress range for a variable-amplitude stress spectrum is defined as the constant-amplitude stress range that would result in the same fatigue life as the variable-amplitude spectrum (Schilling, 1978). The formula for calculating the effective stress range can be written as:

www.EngineeringEBooksPdf.com

$$\Delta\sigma_{ef} = \left[\frac{1}{N_T}\sum_i n_i \Delta\sigma_i^m\right]^{\frac{1}{m}} \quad (1)$$

in which, n_i is the number of cycles of stress range $\Delta\sigma_i$; $\Delta\sigma_i$ is variable amplitude stress range; N_T is the total number of cycles (= $\sum_i n_i$); and m is the slope of corresponding constant amplitude S-N line. The effective stress range of the variable amplitude stress spectrum, $\Delta\sigma_{ef}$ from the above equation is equal to the root mean square (RMS) if m is taken as 2. If m is taken as the slope of the constant amplitude S-N curve for the particular detail under consideration, the equation is equivalent to Miner's law, and for most structural details, m is about 3. The effect of the mean stress in each cycle of the variable-amplitude stress spectrum on the effective stress range is not considered in the above equation. The value of the effective stress range for a variable-amplitude spectrum can be considered as a representative value of fatigue behavior generated by the variable-amplitude spectrum at the location to be considered. It cannot be expressed as a constant-amplitude stress range as the situation of stress-time history under normal traffic loading in which the effective stress range is obtained as a constant stress range for daily stress spectrum. It is therefore necessary for the typhoon loading that the effective stress range for hourly stress spectrum is used as a constant stress range and this constant stress range can be calculated based on the original variable-amplitude stress spectrum.

EVALUATION OF FATIGUE DAMAGE DUE TO TYPHOON

Fatigue in bridge members is a cumulative process under high-cycle where stress fluctuation is usually low so that the deformation in the structure is elastic. Fatigue damage in the region of fatigue crack initiation and growth of cracks in micro-scale can be well described by the concept and theory of continuum damage mechanics (CDM). Based on thermodynamics and potential of dissipation, the rate of damage for high-cycle fatigue has been expressed as a function of the accumulated micro-plastic strain, the strain energy density release rate and current state of damage (Krajcinovic & Lemaitre, 1987). The calculation of the increment of fatigue damage is carried out for the location of "SSTLP-09" Figure 9 shows normalized results of fatigue damage increment induced by typhoon in which the results are normalized by the constant result of fatigue damage increment due to normal traffic.

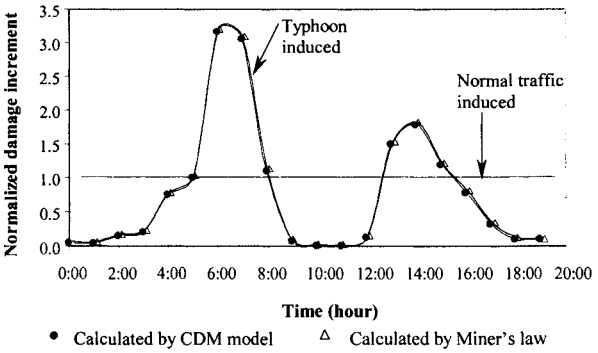

Figure 9 Normalized fatigue damage increment induced by typhoon and normal traffic

It can be observed from the figure that, first, the results calculated by CDM model are similar to that by Miner's law; second, the increment of fatigue damage generated by the typhoon at different hours varies significantly at different hours. The maximum value is over 3 times of the value for normal

www.EngineeringEBooksPdf.com

traffic loading and occurred at the hourly block between 06:00~07:00. It should be noticed that, although the increment of fatigue damage calculated by the CDM model and Miner's law has the similar results, the values of accumulative fatigue damage would be different for these two models. The miner's law is a linear accumulative fatigue damage model and history independent while the CDM model has been verified as a nonlinear accumulative model of fatigue damage under normal traffic loading (Li et al 2001 and Chan et al 2001). The accumulation of fatigue damage is history dependent, i.e. the accumulative value of fatigue damage depends not only the rate of fatigue damage under the present loading but also the present value (or initial value) of fatigue damage. In the view of physical mechanism of fatigue damage, fatigue accumulation is due to fatigue crack initiation and growth. The accumulative rate of fatigue damage depends on the service conditions and deteriorating status of the structure. Therefore, from the view of physical mechanism of fatigue damage, the nonlinear accumulation of fatigue damage is more reasonable, which shows the accumulative rate of fatigue damage to be small at the beginning of the bridge service then becoming large at later period of the service. In order to show the accumulation feature of fatigue damage under typhoon loading, the fatigue damage accumulated on the process of the action of the typhoon is calculated by using Miner's law and the CDM model respectively. The calculated results are shown in Figure 10. In the calculation, the present value (or initial value) of fatigue damage before the action of the typhoon is assumed as 0.2. It can be seen that the values of fatigue damage accumulated on the process of the action of the typhoon are different for the results calculated by Miner's law and the CDM model, and the latter is smaller than the former. The accumulative feature showed in Figure 10 are similar to the situation for the same bridge deck under normal traffic loading (Li et al 2001 and Chan et al 2001) and at the beginning of the bridge service since the fatigue condition is at the beginning period in the calculation.

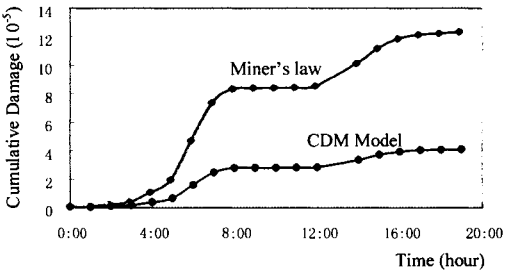

Fig.10. Curves of cumulative fatigue damage versus time calculated by the CDM model and Miner's law

CONCLUSIONS

This work studied the effect of a typhoon on fatigue damage of the deck of the Tsing Ma Bridge based on the structural health monitoring system. The measured data of wind and strain response during the typhoon York on 16 Sept. 1999, the strongest typhoon since 1983 and the typhoon of longest duration on record in Hong Kong, were analyzed in this paper for evaluating wind characteristics and typhoon induced fatigue damage of the bridge. The hourly strain-time history of the bridge during the typhoon "York" has been investigated and compared with that under normal daily traffic loading. The calculation has been made to obtain the increment of fatigue damage induced by the typhoon. It is found that the results calculated using the CDM model is much smaller than that using Miner's law.

ACKNOWLEDGMENTS

Funding support to the project by National Nature Science Foundation of China (Project Code: 50178019) and the Research Grants Council of the Hong Kong government (Project Code: B-Q514) is gratefully acknowledged. The writers wish to thank the Highways Department of the Hong Kong SAR Government for their support throughout the project.

www.EngineeringEBooksPdf.com

REFERENCES

Aktan, A. E., Grimmelsman, K. A. & Helmicki (1998), A.J., Issues and opportunities in bridge health monitoring, *Proceedings of the Second World Conference on Structural Control*, June 28 to July 2, 1998 Kyoto, Japan, ed. Takuji K. et al, Vol. 3, pp. 2359-2368

Chan, T.H.T., Ko, J.M. and Li, Z.X., Fatigue analysis for bridge-deck sections under blocked cycles of traffic loading, *Nondestructive Evaluation of Highways, Utilities, and Pipelines IV*, Proceedings of SPIE, 7-9 March 2000, Vol. 3995, ed. Aktan, A.E. & Gosselin, S.R., 358-369

Chan, T.H.T. Li, Z.X., and Ko, J.M., Fatigue Analysis and Life Prediction of Bridge with Structural Health Monitoring Data – Part II: Application, *International Journal of Fatigue*, 2001, 23(1): 55-64

Dowling, N. E., Fatigue failure predictions for complicated stress-strain history, *Journal of Materials*, JMLSA, 1972, 7(1), 71-87

Flint & Neill Partnership, *Lantau Fixed Crossing and Ting Kau Bridge, Wind and Structural Health Monitoring Criticality and Vulnerability Ratings Review*, Highways Department, Government of Hong Kong, Jan. 1998

Gurney, T., *Fatigue of Steel Bridge Decks*, HMSO at Edinburgh Press, London, 1992

Virlogeux, M., Wind design and analysis for the Normandy Bridge, in: Larsen, A. (Ed.), *Aerodynamics of Large Bridges*, Balkema, Rotterdam, 1992, 183-216

Gu, M., Xu, Y.L., Chen, L.Z. and Xiang, H.F., Fatigue life estimation of steel girder of Yangpu cable-stayed Bridge due to buffeting, *Journal of Wind Engineering and Industrial Aerodynamics*, 80, 1999, 384-400.

Krajcinovic, D. & Lemaitre, J., *Continuum Damage Mechanics: Theory and Applications*, Springer, Vienna, 1987

Lau, C. K., Wong, K. Y. and Flint, A. R. (2000), The structural health monitoring system for cable-supported bridges in Tsing Ma control area, *Proceedings of Workshop on Research and Monitoring of Long Span Bridges*, April 2000, Hong Kong, pp. 14-23

Lau, C. K. and Wong, K. Y., Design, construction and monitoring of the three key cable-supported bridges in Hong Kong, *Structures in the New Millennium*, P.K.K. Lee (ed.), A. A. Balkema, Rotterdam, Netherlands, 1997, 105-115

Li, Z.X., Chan, T.H.T. and Ko, J.M., Health monitoring and fatigue damage assessment of the bridge deck sections, *Nondestructive Evaluation of Highways, Utilities, and Pipelines IV*, Proceedings of SPIE, 7-9 March 2000, Vol. 3995, ed. Aktan, A. E. & Gosselin, S. R., 346-357

Li, Z.X., Chan, T.H.T. and Ko, J.M., Fatigue Analysis and Life Prediction of Bridge with Structural Health Monitoring Data – Part I: Methodology and Strategy, *International Journal of Fatigue*, 2001, 23(1): 45-53

Schilling, C. G., et al, Fatigue of welded steel bridge members under variable-amplitude loadings." *NCHRP Report 188,* National Academy Press, Washington D. C., 1978

www.EngineeringEBooksPdf.com

Advances in Steel Structures, Vol. II
Chan, Teng and Chung (Eds.)
© 2002 Elsevier Science Ltd. All rights reserved.

FATIGUE STRESS ANALYSIS OF SUSPENSION BRIDGES USING FEM

Tommy H. T. Chan[1], L. GUO[2] and Z. X. Li[2]

[1]Department of Civil and Structural Engineering, The Hong Kong Polytechnic University, Hung Hom, Kowloon, Hong Kong
[2]College of Civil Engineering, Southeast University, Nanjing, China, 210096

ABSTRACT

Fatigue is an important failure mode for large suspension bridges under traffic loadings. However, large suspension bridges have so many attributes that it is difficult to analyze their fatigue damage using experimental measurement methods. Numerical simulation is a feasible method of studying such fatigue damage. In British standards, the finite element method (FEM) is recommended as a rigorous method for steel bridge fatigue analysis. This paper aims at developing a model of a large suspension steel bridge using finite element methods (FEM) for fatigue stress analysis. The Tsing Ma Bridge (TMB) is selected for a case study and the corresponding finite element model is presented. The verification of the model is carried out with the help of the measured bridge modal characteristics and the online data measured by the structural health monitoring system installed on the bridge. The results show that the constructed FE model is efficient for bridge dynamic analysis. Global structural analyses using the developed FE model are presented to determine the components of the nominal stress generated by railway loadings and some typical highway loadings. The critical locations in the bridge main span are also identified with the numerical results of the global FE stress analysis. It could be seen that the FR model could be served as a basis for evaluating fatigue damage and the remaining life of the bridge could then be evaluated.

KEYWORDS

Finite element model, suspension bridge, fatigue damage, dynamic response, stress spectrum, critical location, traffic loading

INTRODUCTION

Fatigue is an important failure mode for steel structures. In fact, 80-90% of failures in steel structures are related to fatigue and fracture (ASCE, 1982). Nowadays, more and more large steel bridges are built worldwide, and some are expected to be vulnerable to fatigue-related problems. It is important to study fatigue damage in these bridges. Fatigue analysis for an existing bridge is predominantly based on stress analysis, to get the distribution of stress in structures. Recently, some important works on

www.EngineeringEBooksPdf.com

fatigue analysis for bridges have been found (Pullin et al, 1999). In those works, short or medium span bridges were the focus, and, the finite element method (FEM) was used to decide the critical locations due to fatigue damage. Field tests were then conducted for assessment of the stress range in these critical locations. However experimental techniques successful for structural identification of short and medium span bridges cannot simply be scaled-up to long span bridges (Barrish et al, 2000). Therefore, numerical simulation is a feasible method to study such fatigue damage.

The finite element method (FEM) is recommended by the British standards (BSI, 1982) as a rigorous method for structural fatigue stress analysis. Recent studies have shown that FEM has become a highly valuable tool as a basis for evaluation of fatigue behavior (Nowack & Schulz, 1996). The latest work by Lin and Smith (1999) describes the finite element modeling of fatigue crack growth of surface cracked plates, and provides an accurate evaluation of the fatigue life of the structures. However, it is very complicated to establish a FE model of a large practical structure for fatigue damage analysis, as the FE model should embody the sectional properties of structural members. Moreover, in considering that fatigue damage is a local failure mode and often occurs in welded regions, the weld detail should also be included in the FE model. There is no related work found in literature about the study of fatigue damage of large suspension bridges using FEM.

The Tsing Ma Bridge (TMB), which is 2.2 kilometers in total length and has a main span of 1377m, as shown in Figure 1, is the longest suspension bridge in the world, carrying both road and rail traffic. A structural health monitoring system has been devised and installed to monitor the integrity, durability and reliability of the bridge. This monitoring system comprises a total of approximately 350 sensors, including accelerometers, strain gauges, displacement transducers, level sensors, anemometers, temperature sensors and weigh-in-motion (WIM) sensors, installed permanently on the bridge. The strain gauges were installed to measure stresses at bridge-deck sections. By use of the online strain time history data, some important work (Chan et al, 2001, Li et al, 2001) on the fatigue damage analysis and service life prediction of the bridge-deck section of the TMB has been carried out. However, the locations of the monitoring sensors setting in the bridge were selected for general purposes and such locations might not be critical to fatigue damage. The analysis of the TMB global dynamic response and the stress time history under traffic loading in the members are needed. Moreover, if the bridge is subjected to some disastrous conditions, such as during or after an earthquake, the online data measured by the health monitor system will not be able to directly predict the degree of damage. In this paper, a large FE model of the TMB (depicted in Figure 1(b)), embodying the properties of almost all the structural members, is developed.

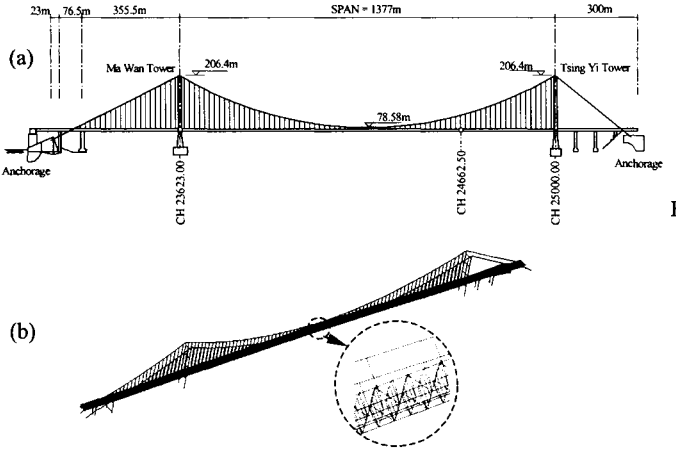

Fig. 1: (a) Configuration of the Tsing Ma Bridge and (b) FE model

www.EngineeringEBooksPdf.com

TMB FINITE ELEMENT MODEL

Bridge fatigue is a high-cycle fatigue problem where stress fluctuations are so low that the deformation in the structure is elastic except at notches and welded joints where local stresses are concentrated. Consequently, an elastic finite element model was needed for global stress estimation of the bridge in virgin state due to traffic loading, so that critical locations due to fatigue damage could be identified. As shown in Figure 1, the TMB is a double deck suspension bridge. It contains about twenty thousand structural members, including longitudinal trusses, cross frames, deck plates, tower beams, main cables, hangers, etc. In recognizing that the conventional modeling procedure for cable supported bridges by approximating the bridge deck as analogous beams or grids is not applicable for accurate fatigue stress analysis, a precise finite element model of the TMB was developed.

In the developed FE model, longitudinal trusses in the bridge deck, comprising chords, posts and diagonal bracings, were modeled as 3D, two-node iso-parametric beam elements having 6 degrees of freedom (DOF) at each node. Bending, torsional and axial force effects were all considered in each space beam element. The section details were also embodied in the corresponding elements: the top and bottom chords which are box section members, were modeled as space beam elements with box sections; vertical posts and, diagonal bracings were represented by space I-beam elements, as they are all fabricated H-sections. Considering their H-sections, crossframes in the deck were also modeled as 3D I-beam elements.

The main cables and hangers, generally simulated as truss elements, were still modeled as two-node space beam elements with circular cross sections as truss element having just 3 DOF at each node would make it difficult to connect with other typical elements. If truss elements were used to model the cables and hangers, some penalty elements should be required for the connection to other element types. To avoid the FE model being too complicated, the space beam elements were adopted to present the cables and hangers. Additionally, the space beam elements here are similar to the truss elements when the three rotational displacements (torsional and flexural displacements) in the elements were too small to be neglected. Highway pavements were modeled by 3D four-node doubly curved shell elements with reduced integration to control the hourglass. For convenient connection with the beam elements, the 6 DOF at each node were also selected in the shell elements. Railway beams are made up of two inverted T-beams welded to flange plates. They act as continuous longitudinal beams supporting a track bed. Correspondingly, each rail track was represented by continuous beam elements with I-section. The Tsing Yi and Ma Wan Towers are made of reinforced concrete and are supported by hard foundations. They were modeled as rigid bodies. Some two nodes flexible joint elements with 6 DOF at each node were used to simulate the relative joint-connections, such as bearings.

It is complicated to simulate large practical structures such as the TMB. As the aforementioned analysis shows, the welded regions are vulnerable to fatigue damage. Therefore an efficient FE model for fatigue analysis should be able to output the stress at these locations. When the stress histories in the elements around a welded connection were obtained, using a proposed local FE model, the hot spot stress in the welded region could be calculated. The fatigue damage and the remaining fatigue life in the region could be analyzed correspondingly. The proposed FE model should be adequate to calculate the normal stress history and/or internal forces in the relative elements adjacent to the regions for hot-spot stress analysis. In the deck of the TMB, almost all the structural members are welded together, so the elements were meshed at the corresponding connected points. On the other hand, considering the limit of the computational cost, the element meshes in the FE model could not be too fine. In the established TMB FE model, a practical structural member was just modeled as an element. For instance, a diagonal bracing or a vertical post was modeled as an I-beam element. The chords and the cross frames were modeled at the relative connected points of the structural members. The spatial configurations of the original structure are remained in the model. More than 7300 nodes and 19000 elements are included in the TMB FE model.

www.EngineeringEBooksPdf.com

VERIFICATION OF THE MODEL

The modal properties of the TMB under free vibration and its dynamic stresses under the train loading were studied with the developed FE model. Comparison of the computed results with the measured data was used to verify the efficiency of the FE model.

Modal Properties

The periods of the first 80 modes of free vibration were computed with FEM ranging from 2.305 to 0.134s. Some free-vibration frequencies were measured separately by the Tsing Hua University (THU) in China, the Hong Kong Polytechnic University (HK PolyU) and the Hong Kong Highways Department (HKHD). The designer Mott MacDonald Hong Kong Ltd (MMHK) and the checker Flint & Neill Partnership of UN (FNP) of TMB also analyzed theoretically the first few frequencies (Lau et al, 1999). Table 1 gives a comparison between the first few measured and analytical natural frequencies. In Table 1, the "mean" data in the 7th column are the mean values of frequencies of the 2nd to 6th columns, which include measured and theoretically results. The difference = (FEM-Mean)/FEM *100%. The maximum relative difference is 9.7%, which shows that the frequencies calculated by the constructed FE model compare well with the measured and the analyzed ones.

TABLE 1: The few free-vibration frequencies of TMB, unit (Hz)

MODE	MMHK	FNP	TH U.	HK POLYU.	HKHD	MEAN	FEM	DIFFERENCE (%)
Lateral								
First	0.065	0.064	0.069	0.069	0.070	0.0674	0.069	+2.3
Second	0.164	0.149	0.161	0.164	0.170	0.1616	0.161	-0.4
Vertical								
First	0.112	0.112	0.114	0.113	0.114	0.1130	0.117	+3.4
Second	0.141	0.133	0.137	0.139	0.133	0.1366	0.144	+5.1
Torsion								
First	0.259	0.253	0.265	0.267	0.270	0.2592	0.262	+1.1
Second	0.276	0.268	0.320	0.320	0.324	0.3016	0.332	+9.2

Comparison of the Computed Stress Responses with The Monitoring Data

The effectiveness of the FE model was studied before it was used to analyze the dynamic response of the TMB. The TMB carries both highway and railway traffic. Relatively, its dynamic response is caused by the combination of truck or highway loading and train loading. The truck loading is very complex because it varies with traffic flow, vehicle types, the road roughness and the vehicles' lateral positions, etc. There are many uncertainties in the truck loading model. Conversely, a train has fixed axle spacings and known axle loading. The train loading model is more reliable in this sense than the truck loading model. Being the first step of the research, the dynamic response of the bridge under a running train was considered.

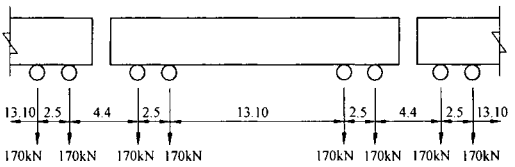

Fig. 2 Configuration of a Train, Unit (m)

A typical train model (Xia et al, 2000) is shown in Figure 2: each axle loading of

www.EngineeringEBooksPdf.com

the train is about 170kN while the train is fully loaded. A train with 10 cars full of passengers was adopted in this model. To calculate the bridge dynamic response, the equivalent nodal forces are needed. When the equivalent nodal force was added to the FE model, the dynamic response of the TMB was analyzed. The modal superposition method was adopted to study the dynamic response. Comparison of the computed results with the measured online data was needed to validate the efficiency of the FEM. The online dynamic response of the TMB was measured by a structural health monitoring system permanently installed on the bridge. Forty-seven strain gauges were installed on the frame CH-24662.5 to measure the strain-time history. Some typical locations of strain gauges are shown in Figure 3.

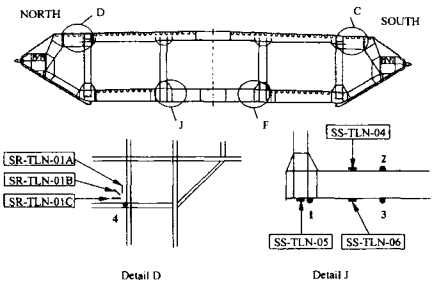

Figure 3: Typical Locations of Strain Gauges in the Bridge Deck

Generally, the measured strain-time data is the response of the bridge under both rail loading and truck loading, but the computed results are the response just under rail loading. In normal conditions, it is not easy to take a control test to measure the bridge dynamic response under rail loading only. Occasionally, the highway on the bridge will be closed, but the railway will still be opened under some emergent conditions, e.g. when the bridge is attacked by a typhoon. On September 16, 1999, typhoon York directly hit Hong Kong and the highway on the TMB was closed. The eye of York was closest to the TMB at 10 a.m. that day. Within a typhoon eye, there is almost no wind effect to the structure. During the two hours taken for the eye of York to get past the TMB, given that hardly any vehicle traffic passed along the bridge, the TMB could reasonably be considered to be under train loading only. The measured data from 10 a.m. to 11 a.m. were selected for comparison with the computed results.

The strain-time history selected from the online data recorded by the strain gauges (as shown in Figure 3) located at detail "D" and detail "J" were considered, where the strain gauge "SR-TLN-01" is a strain rosette, and the corresponding principle stresses in the location were computed for comparison. Because the TMB is symmetrical about the bridge centerline, the strain-time histories recorded by the strain gauges in details "C" and "F" are similar to those in details "D" and "J", and were not studied separately. With the strain-time history data, the stresses versus time in the locations could be obtained easily using Hooke's law (where the Young's modulus is 200GPa).

A comparison between the computed results and the measured data was carried out. To be more distinct, the related stresses due to the passage of a train were selected. The stresses should not be compared with the computed results directly because the measured stresses are affected by many factors, including traffic loading, temperature change, and the initial conditions during the installation of the strain gauges. However, being the most important factor to cause structural fatigue damage, the stress fluctuation is mainly caused by traffic loading (Chan et al, 2001). The stresses recorded by strain gauges should be calibrated for comparison with the computed data, i.e. the selected stress peak should be moved to locate at the same time as the computed data, and the measured stress value to be equal to the computed datum at time zero. The relevant stress response output points are shown in Figure 3. The comparison of output stresses at points "4", "1" and "2" with the recorded data by "SR-TLN-01", "SS-TLN-05" and "SS-TLN-04" are shown in Figure 4. As shown in Figure 4, there is just a stress cycle within the passage of a train by FE analysis. However, with the measured data, there is a main block stress cycle that consists of some small stress cycles. The small stress cycles reflect the local dynamic response of the bridge and correspond to much higher modes that cannot be included in the

www.EngineeringEBooksPdf.com

limited modal superposition analysis. However, in the analysis of high cycle fatigue damage, the main stress cycle is most important and the small stress cycle can be neglected. Figure 4 shows that the computed stress spectrum compared well with the recorded data.

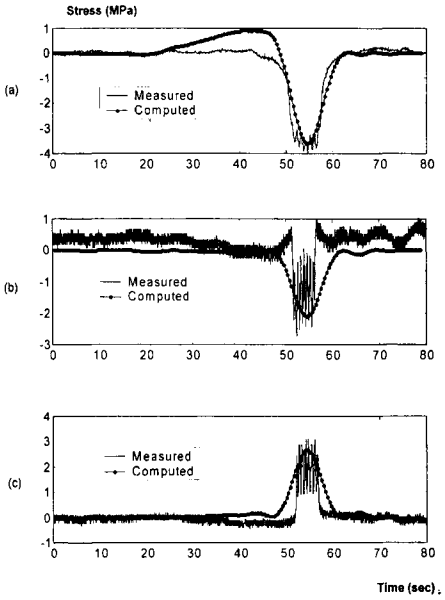

Fig. 4 Comparison of the Computed Stress Histories with measured data at (a) "SR-TLN-01", (b) "SR-TLN-05", (c) "SR-TLN-04"

DYNAMIC RESPONSE OF THE TMB UNDER TRAFFIC LOADING

In the case of bridges carrying both highway and railway loadings, the total fatigue damage should be determined for each loading condition separately [3]. Because there is only a single rail track passing through the TMB in each direction, the additional combined stress history by more than two trains could be neglected. The computed stress history should be used directly to calculate the fatigue damage in the TMB. With the volume of train passages in a block (i.e. the stress cycle numbers in a block due to train loadings should be known) (Li et al 2001), using the Palmgren-Miner rule (BSI, 1982), the fatigue damage under train loadings in a block could be obtained. In British standards, individual truck passages were considered to control fatigue behavior for short and medium span bridges. However, it would not be appropriate to simply adopt the same procedure in a fatigue evaluation for long span bridges. The TMB carries a double three-lane highway. To study the fatigue damage due to highway loading, the combined stress history under vehicles in the same direction should be studied. As mentioned earlier, it is more complicated to study the dynamic response of the bridge under truck loading than under train loading. In addition, when a truck was running on the bridge, the local response of the bridge was dominant and a much higher modal state was activated. It was still not convergent when 120 modals were adopted to calculate the bridge response under truck loading. Therefore, the modal superposition method is unsuitable for studying the bridge dynamic response caused by trucks. Here, the direct implicit integration method was adopted to compute the response. However, it is still too expensive to compute the bridge dynamic response in the whole process of a truck passing through the bridge. In normal conditions, the affected time in an element with a passage of a truck is less than two seconds, which could be found in a typical stress time history curve from online data, as shown in Figure 5 (a).

To calculate the stress time history caused by highway loading in an element, only the period of a truck affecting the element was considered. Correspondingly, the computing time was significantly reduced. It is an efficient way to compute the bridge local response. Computed stress time histories at CH24662.5 under a single truck are depicted in Figure 5(b), where the truck is a standard British fatigue truck (BSI, 1982) running in the shoulder lane, and its speed is chosen as 25m/s. As shown in Figure 5(b), the measured affecting time of an element accords well with the computed result. However, the stress spectra could not be compared because the axle load and configuration of the corresponding truck and its lateral location on the bridge could not be determined accurately.

The stress analysis here provides a base for studying the bridge fatigue damage. To obtain the total damage under the railway and highway loadings, the probability of coexistence of the two types of

www.EngineeringEBooksPdf.com

loading should be taken into account. The fatigue damage calculation will be reported in a separate paper.

THE CRITICAL FATIGUE LOCATION IN THE TMB

It is significant to decide the critical locations due to fatigue damage in practical bridges. In the aforementioned stress analysis, the bridge responses under highway loading and under railway loading were studied separately. The critical location due to fatigue damage under these two types of loading could then be analyzed. The computed bridge response under truck loading is just the local response at CH24662.5 and it can be seen that the critical locations are the outmost part of the upper chord and the bottom cross frame between the rail tracks. The critical locations due to fatigue damage under rail loading were also identified and it was found that the critical locations in the deck unit are at the outmost part of the upper chord, which is similar to the critical locations under truck loading. The stress distributions in other deck units are similar to ones at CH24662.5.

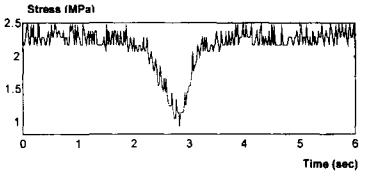

(a) Measured Stress versus Time under Truck Loading

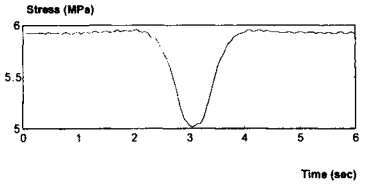

(b) Computed Stress versus Time under Truck Loading (Load 1)

Fig. 5 Stress versus Time under Truck Loading

As the local responses under truck loading are similar, the critical locations due to fatigue damage in the whole main span are mainly decided by rail loading. When a train passed through the TMB along the outbound Airport track, the stress spectra in the outmost of the upper chords along the bridge longitudinal direction were studied to determine the fatigue critical locations in the whole bridge.

The stress spectra in the left outmost part of the upper chords along the main span are depicted in Figure 6. The y-axis denotes the dimensionless stress spectra, which equals $\Delta\sigma$, the stress spectrum in the focused location divided by $\Delta\sigma^*$, the stress spectrum in the chord outmost at CH24662.5. Obviously, the critical location is not at the CH24662.5, where the strain sensors were installed. Figure 6 shows that the stress spectra in many frames are higher than the one in the frame at CH24662.5. The stress spectrum at CH23893 is about 1.2 times the stress spectrum at CH24662.5. To analyze the fatigue damage in the TMB, the stress spectrum in this location will be adopted and the remaining life of this location would be simulated.

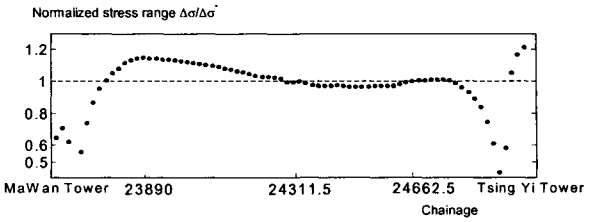

Fig. 6 Stress Range along the Main Span of the TMB

CONCLUSIONS

A large FE model of a long suspension bridge was developed in this paper. In order to be suitable for fatigue stress analysis, the developed FE model embodied the spatial configurations of the original

www.EngineeringEBooksPdf.com

structure and weld-connection details. The verification of the model was carried out with the help of the measured data. With the comparison of the computed first few modal eigenvalues with the measured ones, the main modal properties of the TMB has been included in the developed FE model. With the developed FE model, the dynamic responses of the bridge under the running train were also studied using the modal superposition method. The computed results agree well with the online data measured by the structural health monitoring system installed on the bridge. These results show that the proposed FE model in this paper is efficient for fatigue stress analysis.

The dynamic responses of the bridge under the highway and railway loading were studied with the developed FE model. During the extraction of the bridge responses under highway loadings, the effects of groups of trucks were considered. The computed stress spectra in the bridge deck could be used for subsequent fatigue damage analyses.

Critical fatigue locations within the bridge main span were also decided by FE analysis. In any cross frame, the elements at the two outmost of the upper chord are more critical to fatigue damage. Along the main span, the critical fatigue locations do not have any strain sensors installed.

All the above results provide the basis for evaluating fatigue damage in the bridge and predicting its remaining service life. The developed FE model could also be used to simulate the dynamic response of the bridge under some disastrous conditions.

ACKNOWLEDGEMENTS

Funding supports for this project by the Hong Kong Polytechnic University and the Nature Science Founding of China (No.50178019) are gratefully acknowledged. Appreciation is extended to the Highways Department of the Hong Kong SAR Government, which provided the data measured by the health monitoring system and relevant documents.

REFERENCES

ASCE (1982). Committee on fatigue and fracture reliability of the committee on structural safety and reliability of the structural division, fatigue reliability 1-4. J. of Structural Engineering 108, 3-88.

Barrish R.A., Grimmelsman A.K., Aktan A.E. (2000). Instrumented monitoring of the Commodore Barry Bridge. Proceedings of SPIE. Nondestructive Evaluation of Highways, Utilities, and Pipelines IV 3995, 112-126.

BSI, 1982 BS5400: Part 10, Code of Practice for Fatigue.

Chan T.H.T., Li Z. X., and Ko J.M. (2001). Analysis and Life Prediction of Bridges with Structural Health Monitoring Data- Part II: Application. International Journal of Fatigue 23(1), 55-64.

Lau C.K. , Mak W.P., Chan W.Y., Man K.L., and Wong K.F. (1999). Structural Performance Measurements and Design Parameter Validation for Tsing Ma Suspension Bridge. Advances in Steel Structures ICASS'99, Hong Kong, 487-496.

Li Z.X., Chan T.H.T., and Ko J.M. (2001). Fatigue Analysis and Life Prediction of Bridges with Structural Health Monitoring Data - Part I: Methodology and Strategy. International Journal of Fatigue 23 (1), 45-53.

Lin X.B., and Smith R.A. (1999). Finite element modeling of fatigue crack growth of surface cracked plates Parts I - III. Engineering Fracture Mechanics 63, 503-556.

Nowack H., and Schulz U. (1996). Significance of finite element methods in fatigue analysis. Fatigue 96, Pergamon, Oxford 2, 1057-1068.

Pullin R., Carter D.C., and Holford K.M. (1999). Damage assessment in steel bridges. Key Engineering Materials 167-168, 335-342.

Xia H., Xu Y.L., and Chan T.H.T. (2000). Dynamic Interaction of Long Suspension Bridges with Running Trains. Journal of Sound and Vibration 237, 263-280.

www.EngineeringEBooksPdf.com

Advances in Steel Structures, Vol. II
Chan, Teng and Chung (Eds.)
© 2002 Published by Elsevier Science Ltd.

CURVED STEEL BOX-GIRDER BRIDGES AT CONSTRUCTION PHASE

G. C. M. Lee[2], K. M. Sennah[1], and J. B. Kennedy[2]

[1] Civil Engineering Department, Ryerson University, 350 Victoria St., Toronto, Ontario, Canada M5B 2K3
[2] Department of Civil & Environmental Engineering, University of Windsor, Windsor, Ontario, Canada N9B 3P4

ABSTRACT

A critical design stage for curved composite concrete deck-steel box girder bridges occurs during casting the concrete bridge deck, when the non-composite steel box section must support the wet concrete and the entire construction loading. Although a composite box girder has a high torsional stiffness in the completed bridge, the open section during construction is relatively flexible in torsion. A horizontal truss system is usually installed at the top flange level to increase the torsional stiffness. While the different North American Specifications for bridges refer to the construction stage loading, they do not specify design procedures. Therefore, the aim of this paper is to provide the practicing engineers with a better understanding of the structural behavior of such curved bridges under construction loading. This paper presents a summary of an extensive parametric study, using the finite-element method, on which straight and curved single-cell steel bridges with different configurations were analyzed. The key parameters considered herein include degree of curvature, vertical cross-bracing system and top horizontal bracing system. This paper focuses on the stresses and deflections at the mid-span section as well as support reactions. Since most current design methods neglect the effects of girder bending and torsional stresses on the horizontal and vertical bracings, particular attention is given to the horizontal forces in the top horizontal bracings as well as those vertical bracings due to pure bending or combined bending and torsion.

KEYWORDS

Bridges; curved; box-girder; construction loading; finite-element; bracing system; design; evaluation.

www.EngineeringEBooksPdf.com

INTRODUCTION

During construction, the bottom flanges and webs of single-cell steel box-girder bridges, shown in Figure 1, are very flexible in torsion. Thus, due to construction loads, significant distortion or twist can occur. In straight bridges, cross frames and diaphragms act as secondary members to maintain structural integrity. While, in horizontally curved bridges, the interaction of bending and torsion causes these components to become major load-carrying elements. Most recently, Sennah and Kennedy (2001, 2002) presented state-of-the-art analysis and design of straight and curved box girder bridges.

In 1969, the fourth Danube Bridge in Vienna was damaged during construction. Latter, the Milford Haven Bridge in Wales, the Yarra Bridge in Australia and the Rhine River Bridge in Koblens all suffered disasters due to failures during erection (Branco 1981). These failures lead to question the basis for design of box girder bridges. Mcdonald et al. (1976) tested elastically two single-cell steel girder models, of different number of cross-bracings, and under concentric and eccentric loading. Top lateral bracing was used in the models. The open cross-section with top lateral bracing was analyzed as a closed section with an equivalent top plate, utilizing the equivalent box section concept introduced by Dabrowski (1968). The United State Steel (1978) reported some difficulties encountered in box girder construction and case histories about the changes in geometry and excessive rotation of girders before and during the placement of the concrete deck. Branco and Green (1985) undertook a series of scale model studies of simple-span torsionally open and quasi-closed cross-section beams to examine the effects of construction loading, as well as the bracing configurations, on the overall stability and deformation of single and interconnected box girder bridges. The results from these tests were used to check those from an analytical study, based on both the finite-strip method and the torsion-bending analysis of open and quasi-closed sections. Sennah and Kennedy (1999) investigated warping stresses in top flanges of straight and curved non-composite (open-section) steel cellular bridges under self-weight, considering only vertical bracing systems. The main objective of this paper is to study, using the finite-element method, the effects of the presence of the vertical bracing and the top lateral horizontal bracing on the structural behavior of straight and curved single-cell steel girder bridges at construction phase.

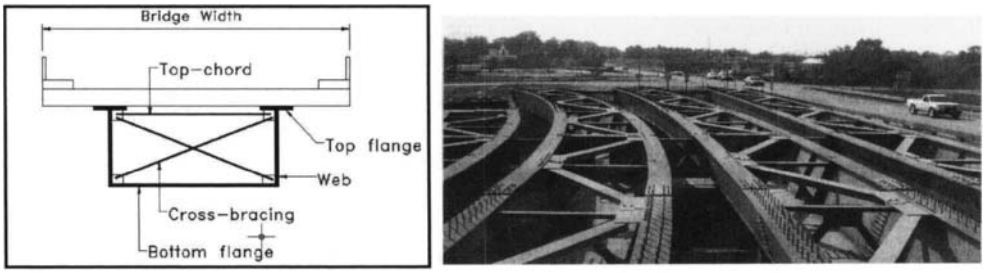

a) Single-cell bridge cross-section

b) View of horizontal bracing system (Civil Engineering Magazine, 2001)

Figure 1. Bracing systems in composite box-girder bridges

www.EngineeringEBooksPdf.com

BRIDGE AND MATERIAL MODELLING

The finite-element modeling of straight and curved single-cell steel box girder bridges was conducted using the commercially available "ABAQUS" software. Shell elements were used to model the webs, bottom flanges and solid end-diaphragms. While three-dimensional beams elements were utilized to model the top flanges, vertical bracing system and horizontal bracing system. Simple support boundary constraints were used in modeling the simply-supported bridges. Elastic material behavior was considered for steel, with modulus of elasticity of 200,000 MPa and possion's ratio of 0.3.

PARAMETRIC STUDY

In order to accurately determine the parameters affecting the structural response of straight and curved non-composite single-cell girder bridges, it was necessary to define the geometric parameters that may affect their behavior. These parameters include cross-type horizontal bracing at the level of top flanges, vertical cross-bracing and top-chord systems and degree of curvature. For this study, straight non-composite single-cell bridges were considered on which the span length of the bridges ranged from 20 m to 100 m, representing medium span bridges. The width of cell was taken as 3.0, 3.8, and 4.65 m. The span-to-depth of the web ration was taken as 25. The curved bridges considered in this study are assumed to have constant radii of curvature and concrete decks with constant elevations. The degree of curvature can be defined by the span-to-radius ratio, L/R, where the span of the bridge, L, is the arc length along the center line of its cross-section and the radius of curvature, R, is the distance from the origin of the circular arc to the center line of the cross-section. The L/R ratios used in this study ranged from 0.0 to 2.0. Solid end-diaphragms considered in this study were provided at both ends of the bridge in the radial direction. To simulate the dead load due to self-weight, the concrete deck was subjected to a uniform load of 5.4 kN/m^2, which is equivalent to a concrete density of 2.4 kN/m^3. To simulate the dead load due to self-weight of the steel section, the GRAV option in ABAQUS was used to account the dead load of the structure through gravity action.

LOAD DISTRIBUTION FACTORS

A parametric study was conducted on simply-supported curved non-composite steel single-cell bridge prototypes to investigate the influence of key parameters affecting the moment, reaction, and deflection distribution as well as axial force in bracing members throughout the bridge. The single-cell cross-section was defined by inner web, the closer to the center of curvature, and outer web, the farther from the center of curvature. In order to determine the moment distribution factor carried by the curved single-cell girder, the maximum moment was calculated for a simply-supported girder subjected to dead load as a line load per meter long of the bridge. The moment of inertia of this girder was calculated based on the open cell section. Then, the longitudinal stress at the bottom fibers of the cross-section was calculated using the elastic equation for flexural stress. The moment distribution factor was calculated as the ratio between the stress from the finite-element analysis to that obtained from simple-beam analysis. Similarly, The reaction distribution factor is the ratio between the reaction value obtained from the finite-element analysis and that obtained from simple-beam analysis of idealized straight girder. The deflection distribution factor considered herein is the ratio between the deflection values obtained from finite-element analysis for a curved bridge and the corresponding straight bridge.

www.EngineeringEBooksPdf.com

RESULTS

Axial force in horizontal bracings

Most current design methods neglect the effects of box-girder bending stresses on the horizontal top steel flange bracings. This type of horizontal truss fastened to the box near the top steel flanges is commonly used to increase torsional stiffness of the steel section during construction. Figure 2 shows the distribution of axial forces in the horizontal bracing of 100-m span single-cell bridges. While Figure 3 shows the distribution of axial forces in the diagonal members of the cross-type horizontal bracing of the same bridge but for span-to-radius of curvature ratio of 1.4. It should be noted that 17 vertical cross-bracings were utilized in the cell, with 36 panels of top horizontal cross-bracings and top-chords. It can be observed that the maximum design force in horizontal bracings is located close to the mid-span section. However, it is located close to the support line due to the effect of torsional moments associated with curvature. It can also be observed that torsional moment causes one diagonal member to be in compression, while the other diagonal member in the same truss panel is in tension.

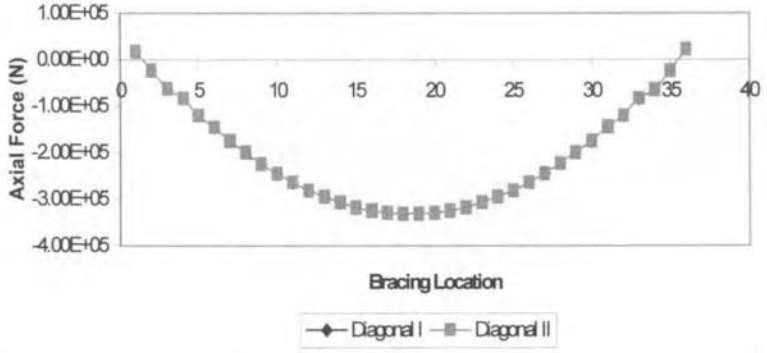

Figure 2: Axial forces in diagonal members of horizontal bracings in a straight bridge

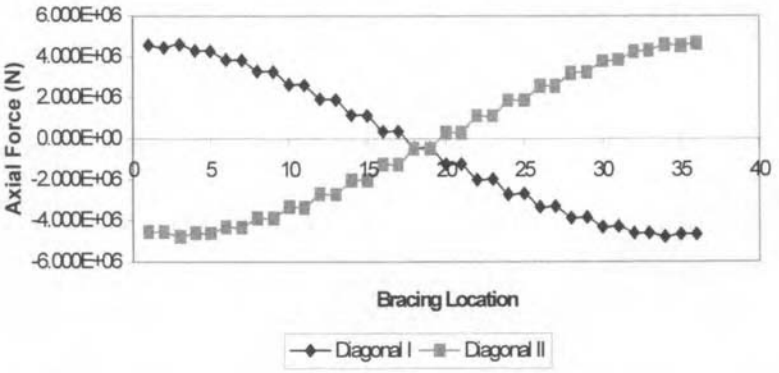

Figure 3: Axial forces in diagonal members of horizontal bracings of a curved bridge

www.EngineeringEBooksPdf.com

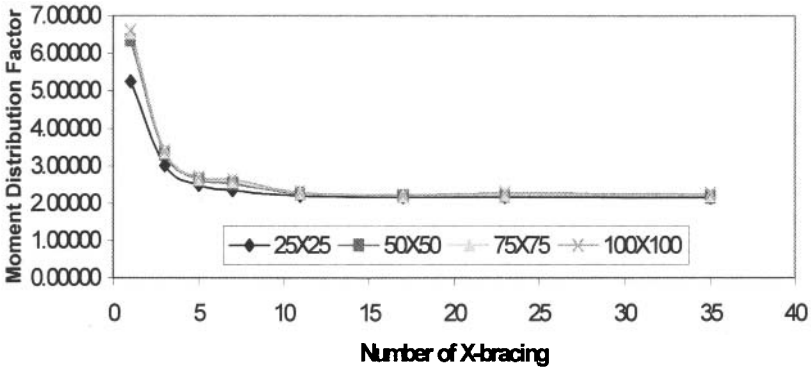

Figure 4: Cross-bracing effect in longitudinal moment distribution factor of a curved bridge

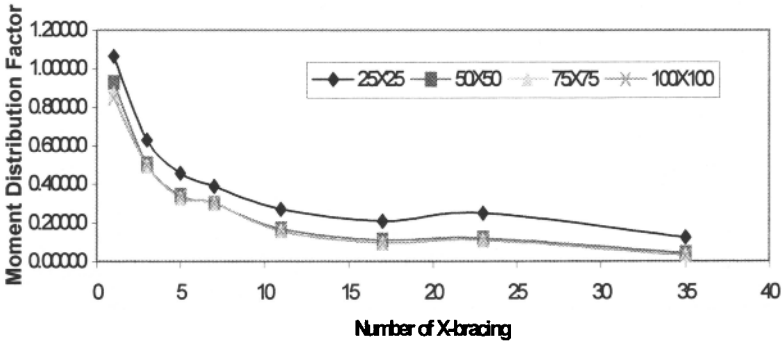

Figure 5: Cross-bracing effect in transverse moment distribution factor of a curved bridge

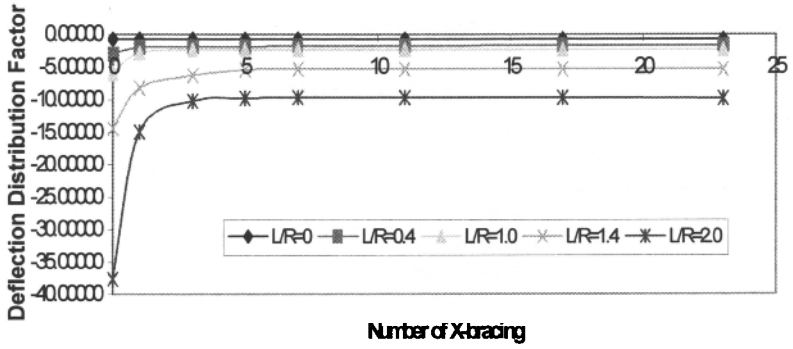

Figure 6: Effect of vertical cross-bracings on deflection distribution factor

www.EngineeringEBooksPdf.com

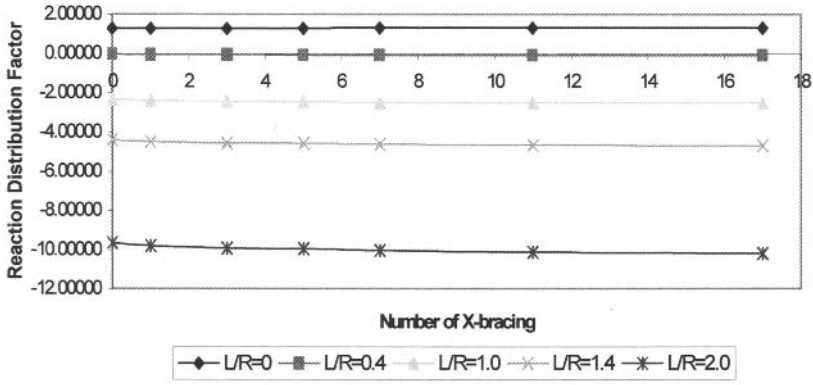

Figure 7: Reaction distribution factors for bridges with different number of cross-bracings

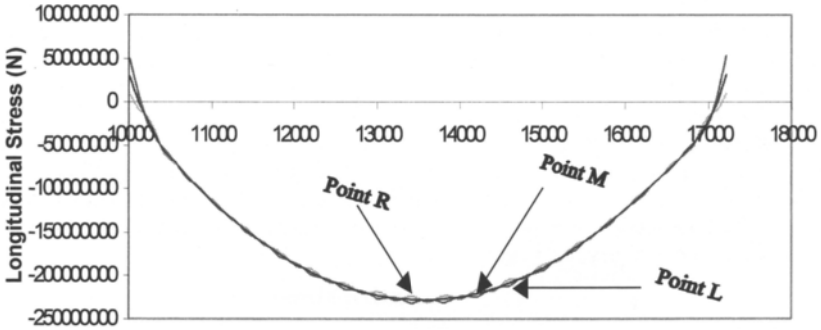

Figure 8: Longitudinal stresses in steel top flange of box girder with horizontal bracing

Vertical Bracing System

Vertical cross-bracings as are commonly installed in steel box girders to maintain the shape of the box during construction and at service. In this paper, the effect of the presence of cross-bracings at the construction phase on other straining actions was investigated. Vertical cross-bracings, shown in Figure 1, are usually installed in the radial direction at equal internals between the support lines. Figure 4 shows the effect of the number and area of cross-bracings members on the longitudinal moment distribution factor of 100-m span bridge of span-to radius of curvature of 2. It should be noted that horizontal bracings were present when investigating the effect of cross-bracings. The area of cross-bracing members was changed from 25×25 mm to 100×100 mm cross-section. It can be observed that the moment distribution factor of the single-cell bridge cross-section decreases with increase in number of cross bracings from 1 to 8. No further decrease is observed for number of cross-bracings behind 8. It can also be observed no significant change was observed with the

www.EngineeringEBooksPdf.com

change in the cross-sectional area of bracing members. Figure 5 shows the effect of number and cross-sectional area of vertical cross-bracings in the moment distribution factor for transverse stresses in the box section at the mid-span. It can be observed that similar behavior to that of the longitudinal moment is observed.

Figure 6 shows the effect of the number of vertical cross-bracing system on the vertical deflection distribution factor at the mid-span section of 80-m span bridges of different curvature. It can be observed that the presence of vertical cross-bracings has no effect in case of straight bridges. However, it decreases with increase in number of cross-bracings with increase in curvature. Figure 7 shows the effect of the presence of cross-bracing system on reaction distribution factor of the inner web, close to the center or curvature, of 60-m span bridges. It can be observed the presence of cross-bracing system between the support lines has an insignificant effect on the reaction distribution, irrespective of the degree of curvature. Similar behavior was observed in case of the outer web, faraway from the center of curvature.

Warping Stresses.

Sennah and Kennedy (1999) warping stresses in open-cell box-girder bridges at construction phase is high when compared to the limiting warping-to-bending stress ratio of 0.5 provided by different North American Specifications for bridges. In this paper a horizontal cross-bracing system is introduced very close to the top steel flange to provide a quasi-closed section to help reducing stresses associated with curvature. Figure 8 shows the normal stress distribution in the outer steel top flange of 100-m span bridge of span-to-radius of curvature ratio of 1.4. Curves for points R, M and L represent the normal stress distribution along the span length of the outer, middle, and inner points of the steel flange, respectively. It can be observed that there is no significant difference between the values of the longitudinal stress at the mid-point of the steel flange and those at the ends. This may be translated to very low warping stresses associated with curvature as well as with the presence of horizontal top bracings.

CONCLUSION

This paper investigates the effect of the presence of the horizontal truss close to the top steel flange as well as the vertical cross-bracings on the straining actions used in design curved box-girder bridges at construction phase. It can be observed that the presence of horizontal bracings near the top steel flanges significantly reduces the warping stresses in the top steel flanges. However, axial forces in the members of this horizontal truss should be considered in design based on a finite-element analysis until a new empirical method of axial force calculations is developed. In addition to minimizing transverse stresses in box-girder cross-section, the presence of vertical cross-bracing system between the support lines significantly reduce the vertical deflection and hence enhance bridge serviceability.

ACKNOWLEDGEMENTS

The Natural Science and Engineering Research Council of Canada, NSERC, supports this research work through individual research grants.

www.EngineeringEBooksPdf.com

REFERENCES

Branco, F. A. (1981). Composite box girder bridge behavior. Thesis presented to the University of Waterloo, Waterloo, Ontario, Canada, in partial fulfillment of the requirements for the degree of Master of Science.

Branco, F. A., and Green, R. (1985). Composite box girder bridge behavior during construction. *ASCE Journal of Structural Engineering*, **111(3)**: 577-593.

Dabrowski, R. (1968). Curved thin-walled girders, Theory and analysis. Springer, New York.

Hibbitt, H. D., Karlson, B. I., and Sorenson, E. P. 1996. ABAQUS version 5.6, finite element program. Hibbitt, Karlson & Sorenson, Inc, Providence, R. I.

Mcdonald, R. E., Chen, Y., Yilmaz, C., and Yen B. T. (1976). Open steel box sections with top lateral bracing. *ASCE Journal of the Structural Division*, **102(ST1)**: 35-49.

Sennah K. and Kennedy, J. (1999). Response of simply supported composite concrete deck-steel multi-cell bridges at construction phase. Proceedings of the 27th Canadian Conference for Civil Engineers, Canadian Society of Civil Engineering, Regina, Canada, Vol. 1, 175-194.

Sennah, K. and Kennedy, J. (2002). Literature review in analysis of box-girder bridges. *Journal of Bridge Engineering*, American Society of Civil Engineering, **7(2)**: 134-143.

Sennah, K. and Kennedy, J. (2001). State-of-the-art design of simply-supported curved composite box-girder bridges. *Journal of Bridge Engineering*, American Society of Civil Engineering, **6(3)**: 159-167.

United States Steel. (1978). Steel/concrete composite box girder bridges - A construction manual. Pittsburgh.

www.EngineeringEBooksPdf.com

Advances in Steel Structures, Vol. II
Chan, Teng and Chung (Eds.)
© 2002 Elsevier Science Ltd. All rights reserved.

NUMERICAL STUDY OF CHARACTERISTIC BEHAVIOR OF STEEL PLATE GIRDER BRIDGES

E. Yamaguchi[1], K. Harada[1], M. Nagai[2] and Y. Kubo[1]

[1]Department of Civil Engineering, Kyushu Institute of Technology,
Kitakyushu 804-8550, JAPAN
[2] Department of Civil Engineering, Nagaoka University of Technology
Nagaoka 940-2188, JAPAN

ABSTRACT

The conventional design for a steel plate girder bridge is based on the simple beam and grid theories. Since a steel plate girder bridge is a complicated structure, consisting of main girders, a concrete slab and a stiffening system, the conventional design does not necessarily reflect the real behavior of a steel plate girder bridge. For example, the role of each stiffening member is not captured well in such a conventional design approach and indeed it has not been clearly understood yet. Against this background, the three-dimensional finite element analyses of steel plate girder bridges are conducted in this study. Three levels of stiffening systems are considered. The results thus obtained indicate that cross beams and vertical stiffeners are not playing an important role under vertical load and that vertical stiffeners can suppress the deformation of the web under lateral load as good as cross beams. Therefore, it may be concluded that there is a good chance of removing cross beams, whereas care must be taken for the further removal of vertical stiffeners, since a steel plate girder bridge without any stiffening system may suffer from rather large deformation under wind load.

KEYWORDS

Steel plate girder bridge, stiffening system, cross beam, vertical stiffener, L-load, wind load, finite element method, three-dimensional analysis.

INTRODUCTION

A steel plate girder bridge consists of main girders, a concrete slab and a stiffening system that includes cross beams, cross frames, horizontal stiffeners, vertical stiffeners, lower laterals and so on. This kind of bridge is therefore a very complicated structure. Nevertheless, the conventional design of a steel plate girder bridge has been exclusively based on the beam theory and the grid theory for simplifying the design computation and thus reducing the design cost. Therefore, the conventional bridge design does not necessarily reflect the real behavior of a bridge. As a matter of fact, the stress

www.EngineeringEBooksPdf.com

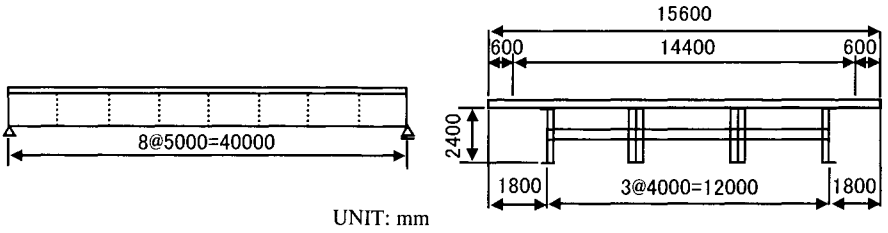

(a) Side view (b) Cross section

Figure 1: Basic bridge model (Bridge A)

actually acting in a bridge often turns out to be about a half of the stress expected in the design.

The role of each stiffening member cannot be captured well by the conventional design approach, either. Indeed, it has not been clearly understood yet. This implies that a conventional plate girder bridge may not be a very efficient structure. In fact, it has been pointed out that lower laterals are not always needed (Natori et al. 1992) and some bridges constructed in recent years in Japan have omitted lower laterals.

The recent advancement of computer technology is very rapid. The progress of finite element software is also considerable. Now, the analysis of complicated structures can be carried out much more easily and cheaply than in the past. Then, it may be no longer a difficult task to evaluate the real behavior of a bridge by the three-dimensional finite element analysis.

Against the background of the above information, the three-dimensional finite element analyses of steel plate girder bridges are conducted in this study. Three levels of stiffening systems are considered. Based on the results thus obtained, the roles of stiffening members, in particular cross beams and vertical stiffeners, are discussed. We also shed some light on the difference between the behaviors of composite and noncomposite bridges.

BRIDGE MODELS

The basic bridge model is shown in Figure 1. This steel bridge consists of a reinforced-concrete slab and four plate girders. The dimensions of plate girders, cross beams and vertical stiffeners are summarized in Table 1. The symbols in this table are illustrated in Figure 2. As for the slab, the thickness is 25 cm; Young's modulus and Poisson's ratio are 1/7 of the modulus of steel and 0.167, respectively. This basic bridge model is taken from the work of Nagai et al. (1997) and is called Bridge A in this study.

Two other bridge models, Bridges B and C, are also considered. Bridge B has no cross beams, but otherwise it is the same as Bridge A. Bridge C is the model where vertical stiffeners are removed from Bridge B, thus it has no stiffening systems.

For the analyses of these bridge models, the finite element method is employed. The slab is modeled by 8-node solid elements whereas 4-node shell elements are applied to plate girders and vertical stiffeners. The cross beam at the mid-span is modeled by 4-node shell elements and the other cross beams are by 2-node beam elements so as to reduce computational time. In total, 67272 elements with

www.EngineeringEBooksPdf.com

TABLE 1
DIMENSIONS OF CROSS SECTIONS

	Main Girder	Cross Beam	Vertical Stiffener
Bu (mm)	600	400	—
tu (mm)	20	20	—
Hw (mm)	2400	600 (1800)	300
tw (mm)	12	9	9
Bl (mm)	600	400	—
tl (mm)	50	20	—
A (cm^2)	708	214 (322)	27
Ix (cm^4)	6.943E+06	1.700E+06 (1.762E+06)	1.823E+00
Iy (cm^4)	1.260E+05	2.134E+04	2.025E+03

( ): value of the end cross-beam when different from that of the intermediate cross-beam

(a) Girder and cross beam (b) Vertical stiffener

Figure 2: Notation in Table 1

81645 nodes, 65712 elements with 80478 nodes and 58800 elements with 73566 nodes are used respectively for the analyses of Bridges A, B and C.

Two sets of analyses are conducted in what follows. In one set, the bridge is assumed composite while it is noncomposite in the other. The noncomposite bridge is modeled by introducing very weak springs between the slab and the plate girders.

NUMERICAL RESULTS

Vertical Loads

The eccentric vertical loads shown in Figure 3 are first considered. This loading condition is also employed in the work of Nagai et al. (1997). It is based on the L-load defined in the Japanese design specifications of highway bridges (1997), representing vehicle loads.

As a numerical result, the distributions of the normal stress in the longitudinal direction in the web of

www.EngineeringEBooksPdf.com

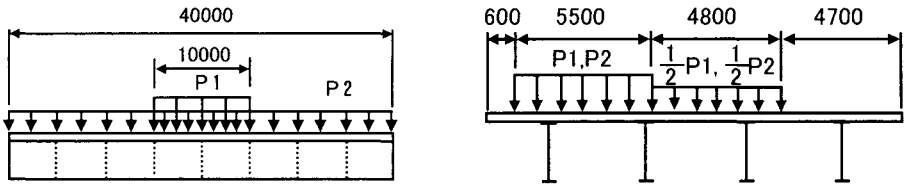

UNIT: mm

(a) Side view (b) Cross section at midspan

Figure 3: Vertical loads

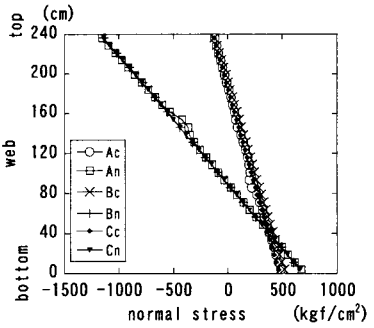

(a) at 0.1m

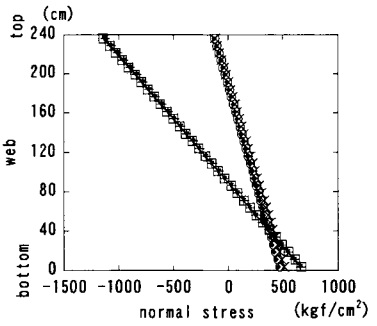

(b) at 1.3m

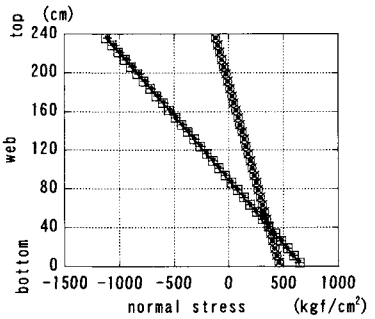

(c) at 2.5m

Figure 4: Normal stress in the longitudinal direction in the web of the outside girder (vertical loads)

the outside girder at the distances of 0.1 m, 1.3 m and 2.5 m from the midspan are presented in Figure 4. The combination of two characters given in this figure indicates an analyzed bridge model: the first character shows the type of an analyzed bridge model and the second character specifies either composite or noncomposite. For example, Ac stands for a composite plate girder bridge of Bridge A while Bn is a noncomposite plate girder bridge of Bridge B.

www.EngineeringEBooksPdf.com

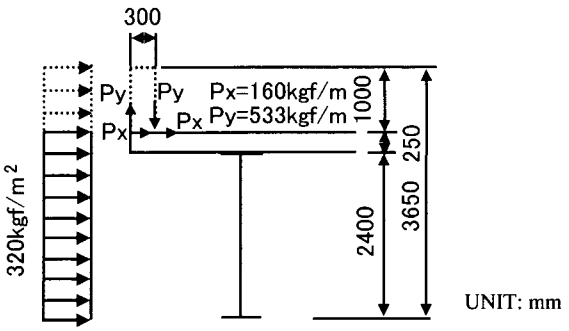

Figure 5: Lateral loads

The differences in the stress distributions among the bridge models are insignificant for both composite and noncomposite girder bridges. Also it is noted that a similar stress state is obtained regardless of the distance from the midspan (stiffener). The effect of connecting girders and a slab is obvious: the neutral axis of the composite bridge is much higher than that of the noncomposite bridge. The symmetric loading of the L-load is also considered, and the same observation is made. From these results, it may be concluded that the cross beams and the vertical stiffeners are not necessary as far as the vertical load is concerned.

Lateral Loads

The lateral loads due to wind are taken into account. Referring to the Japanese design specifications of highway bridges (1997), 320 kgf/m^2 is applied to one side of the bridge. The loads on a handrail are transformed to the combination of the horizontal force and the torsional moment at the foot of the handrail, as has been done in the work of Nagai et al. (1997). The lateral loads thus applied are illustrated in Figure 5.

The numerical results in the form of the distribution of the normal stress (bending stress) in the vertical direction in the web are summarized in Figure 6. Only small stress is observed in the region close to the midspan in the case of Bridges A and B. This phenomenon indicates that the vertical stiffener can suppress the deformation of the web as good as the cross beam. The web of Bridge C that has neither vertical stiffeners nor cross beams undergoes bending deformation due to the wind, and rather large normal stress occurs in the web at the midspan.

As the distance from the midspan (stiffener) is longer, the normal stresses taking place in the webs of Bridges A and B become larger. Yet the difference between composite and noncomposite bridges and the discrepancy between Bridges A and B are not very significant. The stress in Bridge C is greater than those in Bridges A and B in all the cases of Figure 6. In the behavior of Bridge C, the effect of connecting girders and a slab is clearly observed: the signs of the bending stress at the top and the bottom of the web change, implying that the deformed configurations of the composite and noncomposite girder bridges are different from each other.

CONCLUDING REMARKS

In the present study, plate girder bridges were analyzed by the three-dimensional finite element method. As for vertical loads, the eccentric and symmetric L-loads were considered. In all the

www.EngineeringEBooksPdf.com

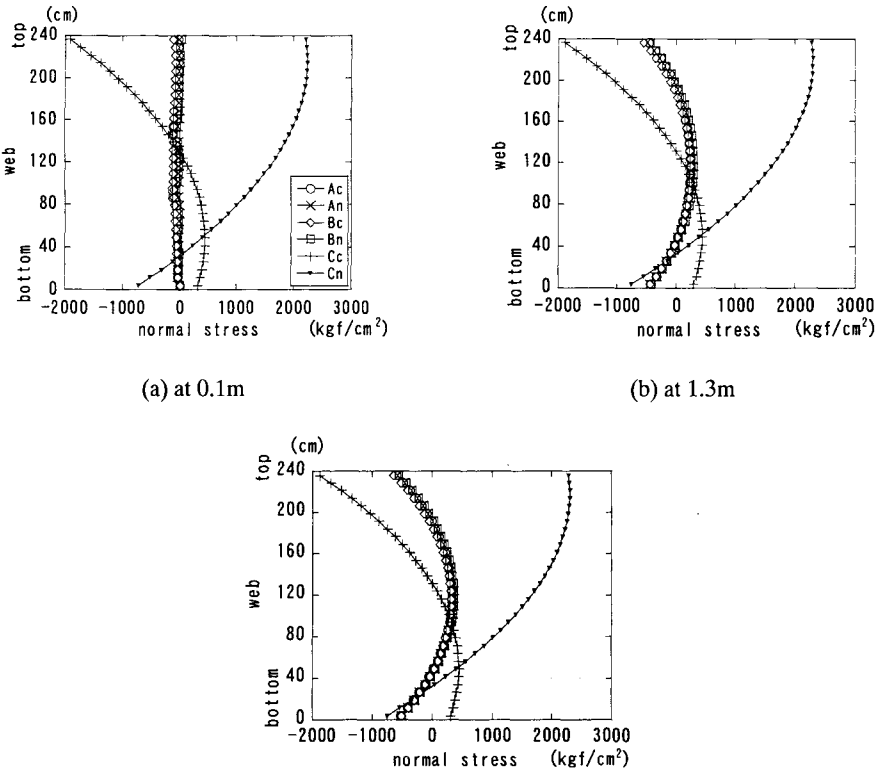

(a) at 0.1m

(b) at 1.3m

(c) at 2.5m

Figure 6: Bending stress in the vertical direction in the web of the outside girder (Lateral loads)

analyses, the difference among Bridges A, B and C were insignificant, while the structural behavior of a composite girder bridge was found different than that of a noncomposite counterpart. This leads to a conclusion that cross beams and vertical stiffeners are not playing an important role under vertical loads. In other words, it may be stated that a concrete slab has a sufficient capacity to distribute vertical loads to main girders, even when it is noncomposite.

Regardless of composite or noncomposite, the difference between Bridges A and B was not large under wind load, either. This result indicates that vertical stiffeners can suppress the deformation of the web under lateral load as good as cross beams. On the other hand, Bridge C underwent much larger deformation than the other two types of bridge. It is also noted that whether a girder bridge was composite or noncomposite made considerable difference in the structural behavior of Bridge C.

This study confirms that the conventional steel plate girder bridge design practice, where only cross beams are assumed to distribute loads to main girders, is not necessarily based on the real behavior of the bridge. It further suggests that there is a good chance of removing cross beams, whereas care must be taken for the further removal of vertical stiffeners, since a steel plate girder bridge without any stiffening system may suffer from rather large deformation under wind load.

www.EngineeringEBooksPdf.com

ACKNOWLEDGEMENTS

The authors would like to thank Mr. T. Matsumoto, Kyushu University, and Mr. Y. Murata, Kyushu Institute of Technology, for their assistance in conducting the present research.

REFERENCES

Japan Road Association (1997). *Design Specifications of Highway Bridges: Part I*, Maruzen, Tokyo, Japan.

Nagai, M., Yoshida, K. and Fujino, Y. (1997). Three Dimensional Structural Characteristics of Steel Multi I-girder Bridges with Simplified Stiffening Systems. *Journal of Structural Engineering* **43A**, JSCE, 1141-1151.

Natori, T., Akehashi, K. and Oshita, S. (1992). Study on Elimination of Lateral Bracings and Intermediate Cross Frames. *Technical Report (Giho) of Yokogawa Bridge* **21**, 13-30.

www.EngineeringEBooksPdf.com

This Page Intentionally Left Blank

www.EngineeringEBooksPdf.com

Advances in Steel Structures, Vol. II
Chan, Teng and Chung (Eds.)
© 2002 Elsevier Science Ltd. All rights reserved.

NONLINEAR SEISMIC RESPONSE ANALYSIS OF A DECK-TYPE STEEL ARCH BRIDGE

Toshitaka YAMAO[1], Hidenori HARADA[2] and Yuki Muramoto[3]

[1] Dept. of Civil Engineering and Architecture, Kumamoto University
2-39-1 Kurokami, Kumamoto, 860-8555, JAPAN
[2] Hara Design Office
799-3-105 Nagaoka, Tikushino, 818-0066, JAPAN
[3] Yokogawa Bridge Co. Ltd., Civil Engineer
2-3 Tikkou-shinmachi, Sakai, 592-8331, JAPAN

ABSTRACT

The seismic behavior of a deck-type steel arch bridge composed of parallel twin ribs with lateral members was investigated. The restoring force model incorporating the interaction curves of stiffened short arch ribs subjected to compression by in-plane and out-of-plane bending moments was analyzed numerically using MARC. A nonlinear seismic response analysis of a deck-type steel bridge arch was carried out, by which the effects of a RC floor slab stiffness and interaction curves were examined. The influence of interaction curves on the interpretation for yield resultant forces was shown to be a significant factor in the seismic behavior of arches.

KEYWORDS

3-dimensional seismic behavior, deck-type steel arch bridge, natural frequency, interaction curves, nonlinear seismic response analysis, stiffened box section, bending moment, compression

INTRODUCTION

The Hyogo-Ken Nanbu Earthquake in Japan (1995) caused severe damage in a great number of buildings, highway arch bridges and railway facilities, which emphasizes the importance of constructing deck-type bridge arches with high seismic capacity. Ordinarily, arch bridges are composed of parallel twin ribs braced with lateral members consisting of truss or transverse beams. Thus, it is necessary to conduct nonlinear seismic analyses using the restoring force model for the design of these deck-type arch bridges. A seismic analysis method of these bridges is required to establish an inelastic response design method that involves bending moment (M)-

www.EngineeringEBooksPdf.com

curvature (ϕ) relations of the stiffened steel box-section members of an arch rib. Although cyclic bending behavior and interaction curves of stiffened box-section members have been investigated experimentally and theoretically (Kitada et al. 1994, Iwatsubo et al. 1998), few studies have been made involving nonlinear seismic analyses of arch bridges (Lui and Hikosaka 2000, Okumura and Goto 2001).

The objective of this research is to investigate the effects of various factors on the 3-dimensional seismic analysis of a deck-type arch bridge composed of parallel twin ribs with lateral members. To meet this objective, the restoring force model incorporating the interaction curves of stiffened short arch ribs subjected to compression by in-plane and out-of-plane bending moments was utilized. Numerical static analyses were conducted using the finite element package MARC (*MARC* 1997) by changing the width-to-thickness ratio parameters of the plate panel of stiffened steel box-section members. Based on numerical results, the interaction curves for yield resultant forces (N, My and Mz) of stiffened short arch ribs were derived. In addition, a nonlinear seismic response analysis of a deck-type steel bridge arch was carried out using the restoring force model incorporating the interaction curves and significance of these factors on the design of deck-type arch bridges was discussed.

FEM ANALYSIS OF ARCH RIB

Analytical Model

In this study, an arch rib composed of a box-profile cross-sectional member was considered. A member of unit length with a box cross section subjected to an axial force (N) and a uniform bending moment (M) was as shown in Figure1. The analytical model consisted of a steel box cross-sectional member with two or four stiffeners positioned symmetrically about one axis with respect to member geometry and support conditions. Accordingly, the finite element analysis was only performed on a quarter or a half section of this member in all cases.

The material was assumed to be SM490Y (JIS) with a yield stress (σ_y) of 353 Mpa; Young's modulus (E) of 206 GPa; and Poisson's ratio (ν) of 0.3. The stress-strain curve was assumed to be multi-linear, where strain hardening first occurs at a strain 10 times that of the yield strain and the hardening modulus (E_{st}) is $E/30$. The profile of the cross section was rectangular (B=*1.2 m*, D=*2.1 m*) and the aspect ratio (H/D) was 1.0, at which the lowest maximum strength is expected. The width-to-thickness ratio parameter (R_R) of the plate panel surrounded by longitudinal stiffeners varied from 0.3 to 0.7 as determined by:

$$R_R = \frac{B}{t}\sqrt{\frac{\sigma_y}{E}\frac{12(1-\nu^2)}{k\pi^2}} \qquad (1)$$

$$\gamma^*/\gamma = -0.969 + 4.847R_R \qquad (2)$$

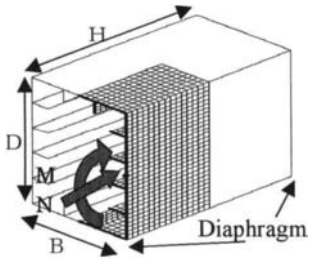

Figure 1: Analytical model

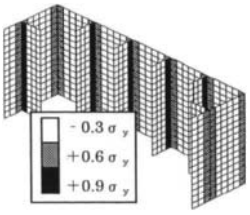

Figure 2: Distribution residual stresses

www.EngineeringEBooksPdf.com

where B is plate width, t is plate thickness and k is the buckling coefficient (k = 4.0 n^2 and n = number of plate panels). In this study, γ/γ^* is the rigidity of longitudinal stiffeners compared to a plate panel (γ = relative flexural rigidity of one stiffener and γ^* = optimum value of γ obtained from linear buckling theory; JSHB, Part II, 1996) and was determined by Eqn. 2, which was developed from the profile of the cross-sections of arch ribs of actual deck-type arch bridges.

Residual stresses distributed in a trapezoidal pattern were assumed to be $\sigma_{rt} = 0.9\sigma_y$ and $\sigma_{rc} = -0.3\sigma_y$ as shown in Figure 2. The initial patterns of crookedness of both the plate panel surrounded by longitudinal stiffeners and the outer plate were assumed to be of a sinusoidal half-wave shape in the transverse direction as was shown by Yamao et al. (2001).

The loading was adjusted by controlling the displacement of a central point on the plate that was assumed to be rigid, i.e., fastened on the edges. Thus, uniform longitudinal displacement was used in place of axial force (N) and the planar rotation of the rigid plate at the central point was used in place of bending moment (M). The values of N and M were computed from resultants of reactions at the edge nodes. The incremental displacements and the rotation were applied by changing the ratio β_I, which is defined as:

$$\beta_I = (\theta / \theta_y)/(u/u_y) \tag{3}$$

in which θ_y is yield rotation and u_y is yield displacement. Thus, pure axial force is defined as $\beta = 0$ and pure bending moment, as $\beta = \infty$. The curvature (ϕ) of a stiffened box cross-sectional member was computed as $\phi = 2\theta/H$, where H is the length of the member. Though the analytical model figure subjected to the in-plane bending moment (My) and the out-of-plane bending moment (Mz) is not shown here, the FEM analysis was performed using the same loading method.

Interaction Strength Curves

Based on the results of FEM analyses, the interaction formula for yield resultant forces (N, My and Mz) of stiffened short arch ribs is proposed by Eqn. 4. Figure 3 shows the interaction strength curves and the behavior of models where $R_{RF} = R_{RW} = 0.7$ when loading forces N, My and Mz are changed. It was found that the proposed interaction curves given by Eqn. 4 show good agreement with the ultimate strengths obtained by numerical analysis.

$$\sqrt{\left(\frac{My}{My_u}\right)^2 + \left(\frac{Mz}{Mz_u}\right)^2} + \left(\frac{N}{N_u}\right)^{1.5} = 1.0 \tag{4}$$

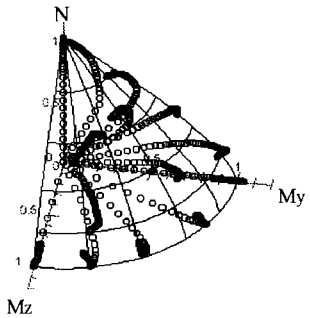

Figure3: N-My-Mz interaction curve ($R_{RF} = R_{RW} = 0.7$)

TABLE 1
STRUTURAL AND MATERIAL PROPERTIES OF THE ANALYTICAL MODEL

Structural Properties	Bridge length	(m)	180.0
	Span length of arch rib L	(m)	126.0
	Arch rise	(m)	20.0
	Thickness of RC floor slab	(mm)	210.0
Material Properties	Arch rib, stiffening girder, longitudinal girder		SMA50 Steel
	Other members		SMA41 Steel

www.EngineeringEBooksPdf.com

NONLINEAR SESMIC RESPONSE ANALYSIS

Arch Bridge Model

The structural properties and configuration of the arch bridge studied herein were as shown in Table 1 and Figure 4, respectively. The arch bridge consisted of two arch ribs and 16 columns with stiffened box sections, stiffening girders, longitudinal girders and I-section struts. The analytical model was composed of arch ribs, stiffening girders, columns with 3-dimensional beam elements and a floor slab with plate elements as shown in Figure 4. This model, in which columns are hinged to the arch ribs at both ends, constitutes one arch rib span length (L=126.0 m) with an arch rise of 20.0 m. The arch rib has a pinned end at both arch springings and the stiffening girders have horizontally movable bearings at both ends. The coordinate axes are shown in Figure 5.

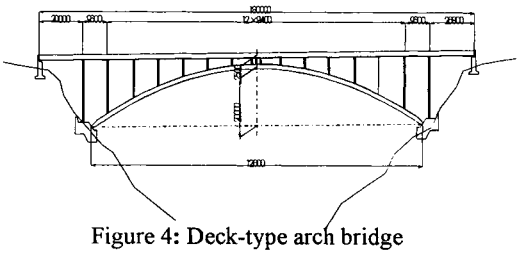

Figure 4: Deck-type arch bridge

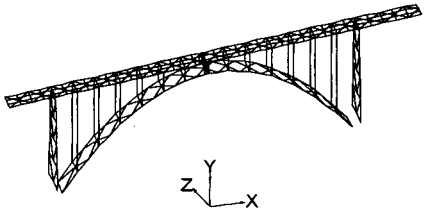

Figure 5: Analytical model

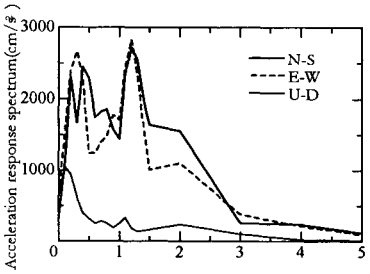

Figure 6 : Acceleration response spectrum

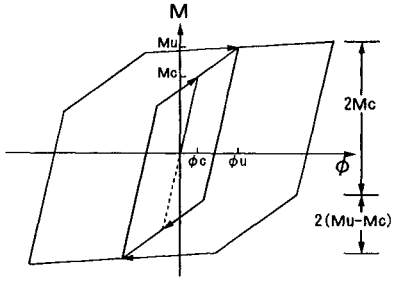

Figure 7 : Restoring force model

Ground Motion Input and Numerical Analysis

In this study, the ground acceleration wave data recorded in the Kobe earthquake were used. These were recorded at the Japanese Railway Takatori Station (JRA) and correspond with earthquake wave propagation under relatively soft ground conditions. The acceleration response spectrum of the JRA wave data is shown in Figure 6, from which it can be seen that the acceleration response spectrum of the N-S and E-W components of the JRA wave data has a maximum peak during the period of 1.1 ~1.3 s. However, the acceleration response spectrum of the U-D component is smaller than those of the N-S and E-W components.

Numerical analyses were conducted using the Newmark-β method (β = 0.25) where the equations of motion are integrated with respect to time taking into account geometrical non-linearity. A constant time

www.EngineeringEBooksPdf.com

TABLE 2
NATURAL PERIOD OF AN ARCH BRIDGE

Order of natural period	Natural period (sec)	
	Without effect of RC floor slab stiffness	With effect of RC floor slab stiffness
1	2.044	2.038
2	1.405	1.146
3	0.927	0.926
4	0.767	0.571
5	0.623	0.522
6	0.521	0.518
7	0.509	0.405
8	0.405	0.391
9	0.391	0.338
10	0.373	0.327

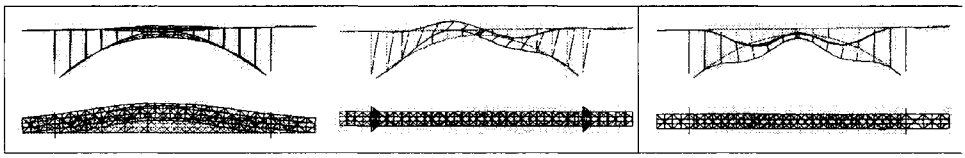

(a) 2-nd mode (out-of-plane deflection) (b) 4-th mode (longitudinal deflection) (c)7-th mode (in-plane deflection)

Figure 8: Natural mode shapes of an arch bridge

step of 0.001 s and a damping model (Rayleigh type) calibrated to the initial stiffness and mass were utilized. The seismic response analysis with ground acceleration input (N-S, E-W and U-D components) and a constant dead load was performed using the nonlinear FEM program RESP (*RESP-T* 1998), which is capable of taking into account geometric and material non-linearity. Figure 7 shows the restoring force model used for the hysteretic curve analysis by the RESP program.

RESULTS AND DISCUSSIONS

Effect of the Stiffness of the RC Floor Slab

The eigenvalue analysis was conducted to determine the effect of RC floor slab stiffness on the natural period of a deck-type steel arch bridge. The natural period of an arch bridge model with and without the effect of stiffness of the RC floor slab is presented in Table 2. It can be seen from Table 2 that the effect of stiffness on the natural period is significant at the 2nd, 4th and 7th modes of the arch bridge model and the values of the natural periods are approximately 20% shorter with the effect of stiffness included. Thus, the effect of stiffness of the RC floor slab may have a significant influence on the high-order natural period of a deck-type steel arch bridge.

Figure 8 shows the natural mode shapes of in-plane, out-of-plane and longitudinal deflections of the deck-type arch bridge. In these figures, the upper sketch is a side view and the lower one is a plane view.

www.EngineeringEBooksPdf.com

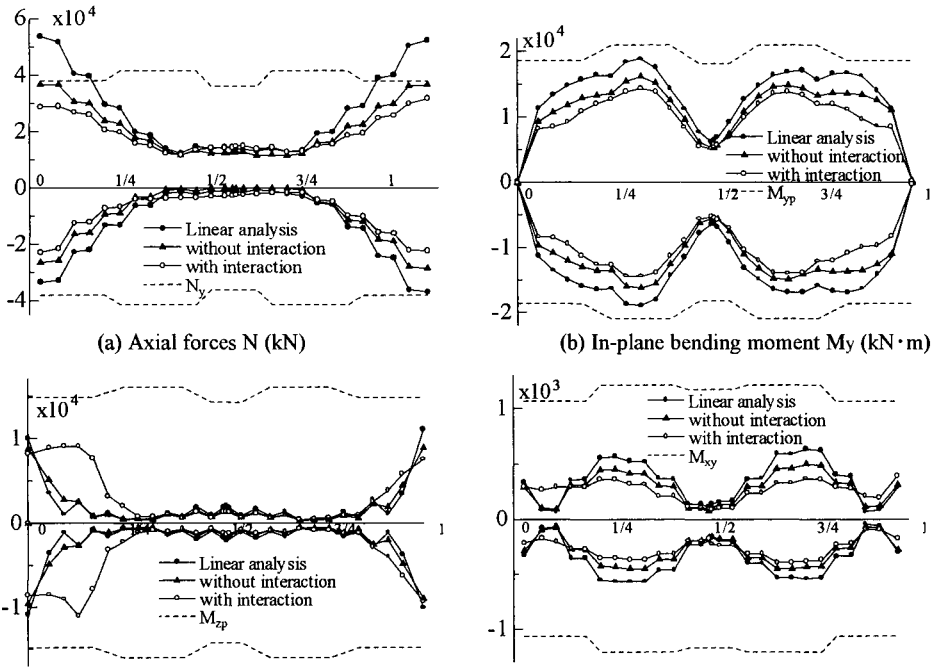

(a) Axial forces N (kN)

(b) In-plane bending moment My (kN·m)

(c) Out-of-plane bending moment Mz (kN·m)

(d) Torsion moment Mx (kN·m)

Figure 9 : Maximum response of resultant forces (N, My, Mz) on an arch rib

Effect of Interaction Curves

The maximum responses of resultant forces, axial force N, in-plane bending moment My, out-of-plane bending moment Mz, and torsional moment Mx of an arch rib with respect to arch span length L are shown in Figure 9. The elastic response analysis, and the nonlinear response analysis with and without the effect of interaction curves (Eqn. 4) were conducted in this study. From figure 9(a), the axial force response (+, compression; -, tension) at both arch springings for the elastic response analysis can be compared with the yield axial force Ny, which was up to four times greater than the axial force yielded by the dead load.

As shown in Figure 9, the maximum responses of the in-plane bending moment My occurred at the L/4 or 3L/4 points (Figure 9(b)), but those of the out-of-plane bending moment Mz were concentrated at both arch springings (Figure 9(c)). This is because the out-of-plane deflection of an arch rib is resisted by the lateral bracing and strut members. However, the maximum responses of the resultant forces decreased more in the nonlinear seismic response analysis including the effect of interaction curves than in the analysis without the interaction curves. Thus, with effect of interaction curves the material yield occurred sooner. The effect of interaction curves in the nonlinear seismic analysis of resultant forces of arch ribs were thus clearly recognized.

As shown in Figure 9(d), the maximum responses of the torsional moment Mx also occurred at the L/4 or 3L/4 points as they did for the out-of-plane bending moment My. The values of Mx were 20 % ~30% of the yield torsinal moment Mxy.

www.EngineeringEBooksPdf.com

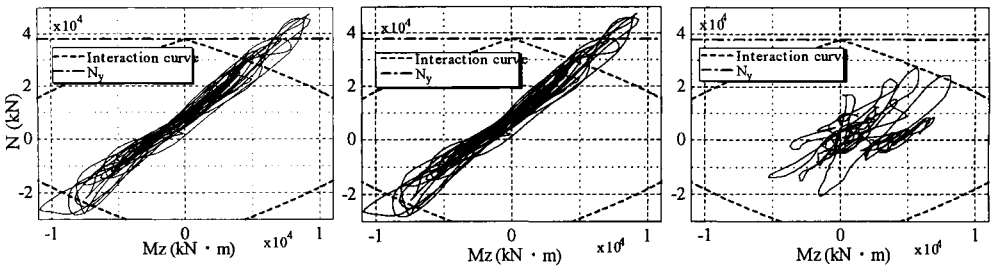

(a) Linear analysis

(b) Nonlinear analysis without interaction curve

(c) Nonlinear analysis with interaction curve

Figure 10: Mz-N hysteretic response curves at arch springings

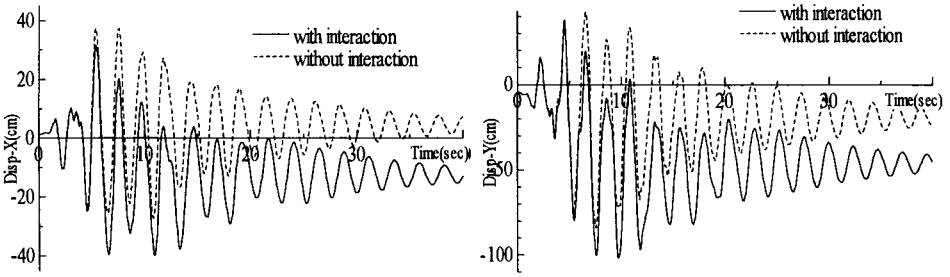

(a) Longitudinal displacement

(b) Out-of-plane displacement

Figure 11: Displacement response at L/4 point

Figure 10 shows hysteretic response curves of the relationships between the out-of-plane bending moment Mz and the axial force N at the arch springings for the elastic response analysis and the nonlinear response analysis with and without the effect of interaction curves. The axial force N in the linear analysis and in the nonlinear analysis without the effect of interaction curves was proportional to the out-of-plane bending moment Mz. However, the Mz-N hysteretic response curves are scattered in the nonlinear response analysis with the effect of interaction curves. As can be seen from these figures, the effects of interaction curves on the Mz-N hysteretic response curves at the arch springings is very pronounced.

The time histories of the longitudinal and out-of-plane displacements at the quarter point of the arch span are shown in Figure 11. The vertical axis represents the displacement response and the horizontal axis shows the elapsed time. A large difference of the displacements in both directions occurs 5 sec after the input of ground acceleration. From these results, it is can be seen that the effect of interaction curves on the residual displacement of an arch bridge with ground motion is quite large.

CONCLUSION

The 3-dimensional seismic analysis of a deck-type arch bridge composed of parallel twin ribs

www.EngineeringEBooksPdf.com

with lateral members subjected to ground acceleration was theoretically analyzed. A parametric study was conducted using the FEM analysis and nonlinear seismic response analysis methods by considering the effect of interaction curves on yield resultant forces and the nonlinear seismic behavior of a deck-type arch bridge. From this study the following conclusions can be drawn:

1) The stiffness of the RC floor slab may have a pronounced influence on the high-order natural period of a deck-type steel arch bridge compared to that of ordinary deck-type bridges that are composed of parallel twin ribs.
2) The effect of interaction curves on the nonlinear seismic analysis of resultant forces of arch ribs were clearly recognized.
3) It was found from numerical analyses that the effect of interaction curves on the Mz-N hysteretic response curves at the arch springing is very significant.
4) It was evident that the effect of interaction curves on the residual displacement of an arch bridge after the onset of ground motion is quite large.

ACKNOWLEDGMENT

The financial support provided by the Ministry of Education, Science, Sports and Cultures of Japan (Grand-in-Aid for Science Research (C)) is gratefully acknowledged.

REFERENCES

Iwatsubo K., Yamao T., Ogushi M. and Okamoto T. (1998), Cyclic bending behavior of stiffened steel members, *Procs. of the Second Symposium on Nonlinear Numerical Analysis and its Application to Seismic Design of Steel Structures*, **2**, 233-240. (in Japanese)

Japan Road Association (1996), *Design Specifications for Highway Bridges,* Part Ⅱ, Steel Bridge and Part V Seismic Design. (in Japanese)

Kitada T., Nakai H., Kunihiro M. and Harada, N. (1994), Study on interaction curve for ultimate strength of unstiffened and stiffened thin-walled box cross section subjected to compression and bending, *Journal of Structural Engineering*, **40A**, 331-342 (in Japanese)

KOOZO KEIKAKU ENGINEERING, INC. (1998), *RESP-T User Manual*

Liu Y. and Hikosaka H.(2000), Nonlinear seismic response analysis of deck-type pipe arch bridge, *Procs. of the Third Symposium on Nonlinear Numerical Analysis and its Application to Seismic Design of Steel Structures*, **3**, 173-178. (in Japanese)

NIPPON MARC (1997) *MARC K7 User Manual*, A-E.

Okumura T. and Goto Y. (2001), Ultimate in-plane behavior of upper-deck type steel arch bridges under seismic loads, *Proceedings of First International Conferences on Steel & Composite Structures*, Pusan, Korea, 1565-1572.

Yamao T., Muramoto Y. and Harada H. (2001), Ultimate strength and cyclic bending behavior on stiffened steel box-section members under high axial compression, *Proceedings of Sixth Pacific Structural Steel Conference*, Beijing, China, 345-350.

www.EngineeringEBooksPdf.com

Advances in Steel Structures, Vol. II
Chan, Teng and Chung (Eds.)
© 2002 Elsevier Science Ltd. All rights reserved.

THE UNIT LOAD METHOD - SOME RECENT APPLICATIONS

D. Janjic[1], M. Pircher[2], H. Pircher[1]

[1] TDV GesmbH, Gleisdorfergasse 5, 8010 Graz, Austria

[2] Centre for Construction Technology and Research, University of Western Sydney, Locked Bag 1797, Penrith South DC, NSW 1797, Australia

ABSTRACT

The Unit Load Method has originally been proposed as a procedure to optimise the tensioning process for the stay-cables in cable-stayed bridges and has been implemented in a well-established bridge-design software package for this purpose. The implementation of this method takes into account all relevant effects for the design of cable stayed bridges including construction sequence, second order theory, large displacements, cable sag and time-dependent effects such as creep and shrinkage or cable relaxation.

The underlying ideas of this method can also be applied to other optimisation problems in structural engineering. This paper gives an overview about the wide range of possible applications for which this method can be used and finishes with examples from practical experiences with the Unit Load Method.

KEYWORDS

Structure optimisation, unit load method, cable stayed bridge, concrete arch bridge, incrementally launched bridge

INTRODUCTION

Cable-stayed bridges with multiple stays are highly redundant structures. The stiffness of the load-bearing elements – the pylon, the deck and the cable stays – governs to a large degree the distribution of forces within the structure. The slenderness of the bridge girders in modern cable-stayed bridges has made it imperative for the bending moments to remain within tight limits throughout the construction process. Moreover, it is also very important to achieve a desired optimal moment distribution in the finished structure under dead load. The requirement to achieve a given moment distribution in the main girder and the pylon has led to the practice of adjusting

www.EngineeringEBooksPdf.com

the tension of the stay cables during the individual construction stages. However, adjusting the tension force in the stay-cables is expensive and tensioning strategies must be optimised not only for structural but also for financial reasons. Due to the high redundancy of the structural systems tensioning one single cable also affects the forces in all other cables, the pylon and the bridge deck. Time-dependent processes such as creep and shrinkage also play an important role where parts of the bridge are made of concrete. Moreover, different construction techniques call for different tensioning strategies and impose different boundary conditions onto the structural system. For example, where temporary supports are being used, a constellation could occur where the deck is lifted off its temporary supports during the tensioning process.

Recently a method called the Unit Load Method has been presented for cable-stayed bridges (Janjic et al. 2002) which allows the definition of a desired moment distribution in the final structure under dead-load and then computes the tensioning strategy which will achieve exactly that distribution taking into account construction methods, changes in the structural system (for example due to the individual construction stages), time-dependent effects such as creep and shrinkage or relaxation of pre-stressing tendons and also geometrically non-linear behaviour.

This method is in fact a general algorithm to achieve a desired distribution of section forces in any structure by adjusting certain constraints of the system. Such constraints include, for example, a change in boundary condition (jacking of a support condition), tensioning of cables (e.g. stay cables or pre-stressing tendons) or application of loads. A short summary of this method in combination with three examples demonstrating some of the many possible applications of this method is given in this paper.

THE UNIT LOAD METHOD

In the following the underlying idea of the Unit Load Method will be explained using a simple example (Bruer et al. 1999). Consider a cable-stayed bridge with a structural system as shown in Figure 1a. The desired moment distribution for this example (M^A, M^B, M^C ... M^I) is given in 9 points (A, B, C ... I) along the main girder as outlined in Figure 1b. The constraints which will be used in this example to achieve this distribution are tensioning of 8 cables (X_1 to X_8) and jacking of the support (X_9) as shown in Figure 1a.

The structure is analysed for a unit load case for each constraint and the results are stored, specifically the results for the bending moments in the points for which the desired bending distribution is given. The system is also analysed for loading with the specified dead-load. With these results a system of linear equations can be established with one equation for each point A to I in Figure 1:

$$M^A = M_P^A + M_{T_1}^A \cdot X_1 + M_{T_2}^A \cdot X_2 + ... + M_{T_9}^A \cdot X_9$$

$$M^B = M_P^B + M_{T_1}^B \cdot X_1 + M_{T_2}^B \cdot X_2 + ... + M_{T_9}^B \cdot X_9$$

:

:

$$M^I = M_P^I + M_{T_1}^I \cdot X_1 + M_{T_2}^I \cdot X_2 + ... + M_{T_9}^I \cdot X_9$$

or, more compact

$$M^K = M_P^K + \sum_{m=1}^{n} M_{T_m}^K \cdot X_m \qquad (1)$$

in which M_L^K is the moment in point K (in the current example $K = A \ldots I$) caused by action L. $L = T_m$ signifies each single unit loading case with m ranging from 1 to n (with $n = 9$ for the current

www.EngineeringEBooksPdf.com

example) and X_m is the unknown multiplication factor for the unit load causing the particular unit load cases. The lower index $L = P$ signifies the load case of dead-load on to the final system. This system of equations can be directly solved for the unknown factors X_m which in turn give the exact values for the forces to be applied at the chosen "degrees of freedom" in order to achieve the desired moment distribution. It should also be noted that the equation system as laid out in Equation 1 is non-symmetric and may contain zero-pivots which must be considered when solving for X_m.

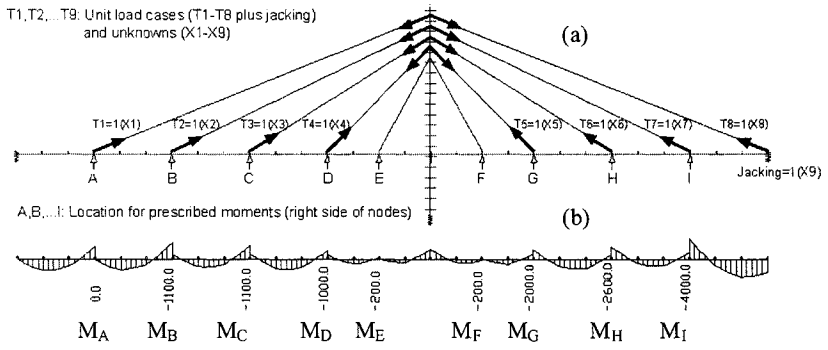

Figure 1. Unit loading cases and desired moment distribution.

This example gives the simplest application of the Unit Load Method. The underlying assumptions include linear-elastic structural behaviour, no time-dependent material properties, and tensioning of the cables on the final system. The equation system in Eqn. 1 is linear only under these assumptions. In order to apply the system in practical design situations, it has been expanded to include these effects (Janjic et al. 2002).

IMPLEMENTATION

The Unit Load Method as described above has been generalised and incorporated into the computer program *RM2000* (TDV, 2001) and has been used successfully in the analysis and design of numerous bridges in many countries. The software is centred around an object-orientated data base. Various pre- and post-processing tools support the input into the system and the processing of results from the system. Most importantly, all functionality is provided to exactly define the planned construction schedule including all changes in the structural system and the exact time frame for all actions to enable an automatic computation of time-dependent effects relevant for the structural behaviour of the structure. A powerful solver module is provided to analyse the structural data and generate results which are again stored into the central data base. Various interface functions allow the import and export of data from the data base for use with other computer programs such as spread sheet software or CAD-packages. The graphic user interface follows the common conventions of modern interactive computer programs.

CABLE-STAYED BRIDGE – VERIGE BRIDGE / MONTENEGRO

The Verige Bridge in Montenegro (Pircher, 2001) is a cable stayed bridge which is currently being designed by Gradis/Maribor of Slovenia using the Unit Load Method as implemented in the *RM2000* software (TDV, 2001). The three cable-stayed main spans (130m, 450m and 130m) are connected on one side to an approach viaduct and on the other side to a support structure on the main land and are supported by two diamond-shaped pylons of 168m height (Figure 2). The cross-section of the superstructure consists of three cells which are separated from each other by vertical

www.EngineeringEBooksPdf.com

webs. The width of the superstructure is 22.9m, the height is 2.8m and the girder is made entirely from pre-stressed concrete. The pylon and the superstructure are to be connected monolythically. The bridge is to be erected segmentally and the exact tension of the stay-cable was determined in such a way that no sub-sequent adjustments were necessary and the desired moment-diagram in the bridge girder was achieved (Figure 4). Stress limits during the construction stages (Figure 3) were also kept within the given limits. The bridge will be located in a seismically extremely active region and to complicate matters, a fault line is situated between the two pylons.

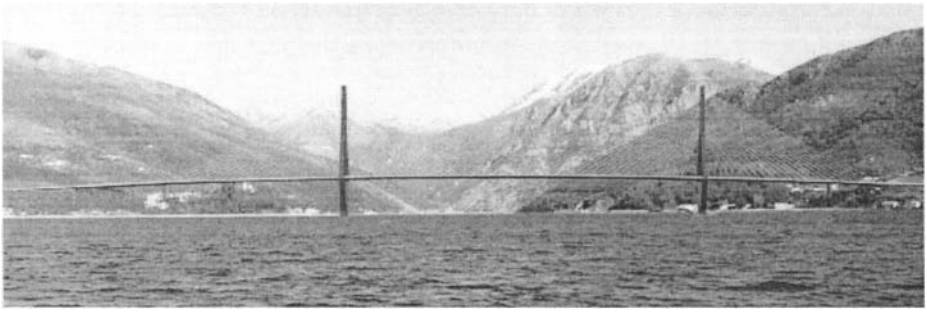

Figure 2. Artists impression of the Verige Bridge.

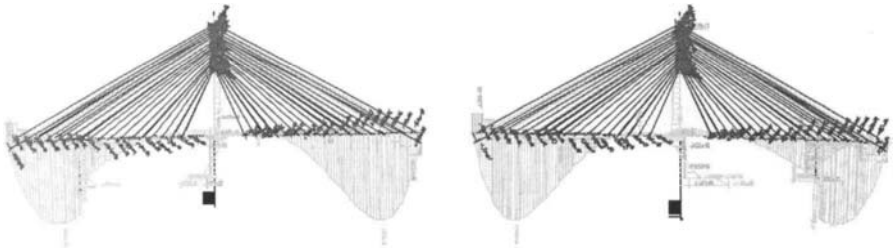

Figure 3. Bending moments, normal and shear forces during construction of the Verige Bridge.

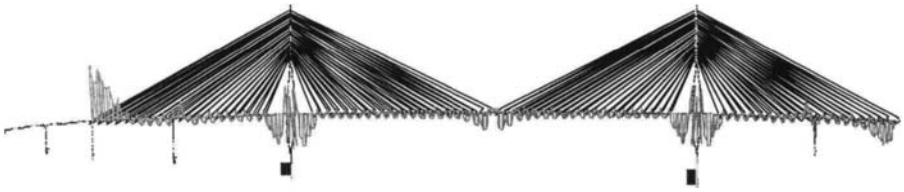

Figure 4. Optimised bending moments upon completion.

www.EngineeringEBooksPdf.com

ARCH-BRIDGE – PITZ VALLEY / AUSTRIA

During the construction of a large concrete arch (169m span) for a bridge in the Pitz-Valley in Austria (Kargel & Geisler 1983) a novel technique to erect the concrete arch was pioneered. Rather than using large scaffolds to support the arch during construction, the arch was built segmentally and supported by temporary stay-cables. The exact position, the number and the tension forces in the stay-cables had to be adjusted in such a way that the bending moments in the arch remained within tight limits. After closure of the arch, the stay cables were removed and the bridge deck and connecting columns added. A preliminary version of the Unit Load Method was employed to determine an optimal tensioning regime for the stay-cables. Due to this optimisation the stay cables were only tensioned once. Costly and time-consuming adjustments in these tension forces could be avoided.

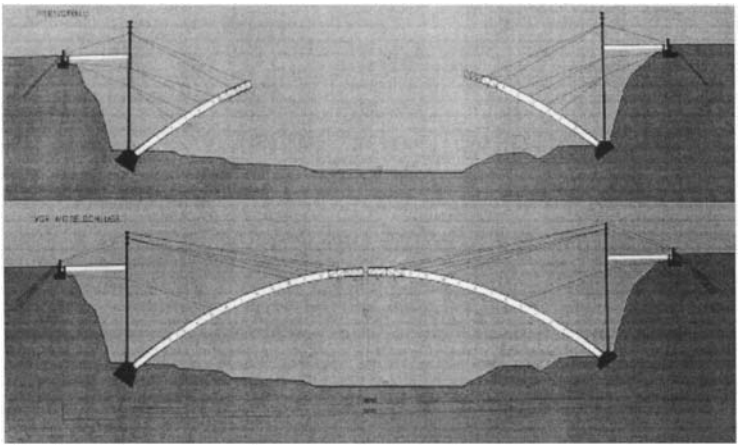

Figure 5. Construction of the arch for the Pitz-Valley Bridge (Kargel & Geisler 1983).

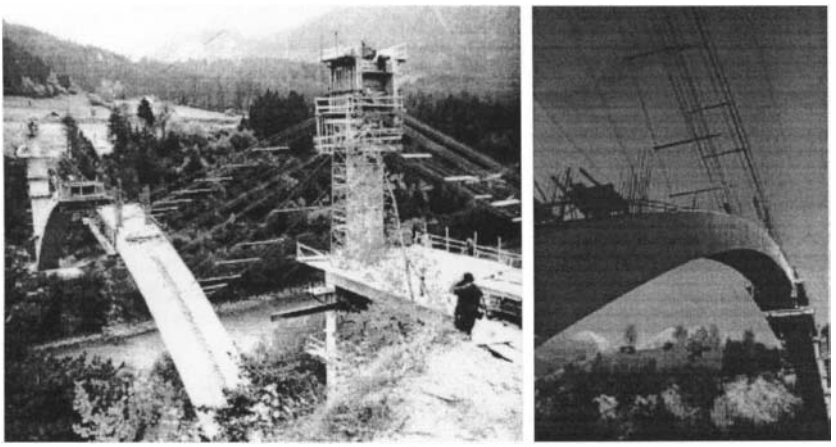

Figure 6. Arch of the Pitz-Valley Bridge during construction (Kargel & Geisler 1983).

www.EngineeringEBooksPdf.com

SIMULATION OF INCREMENTAL LAUNCHING OF BRIDGES

When a bridge is built using the Incremental Launching Method (ILM), segments of the bridge girder are assembled (steel) or cast (concrete) in a stationary assembly or casting yard at one side of the construction site. The existing portion of the bridge girder is prolonged with the newly manufactured segments and the girder is then moved longitudinally across the intended alignment of the bridge under construction. This process is repeated until the structure is completed. A flexible nose is usually attached to the front of the launched girder to facilitate the connection with piers.

During construction each part of the girder therefore alternates between the loading situation at mid-span (sagging moment) and the loading situation above the supporting pier (hogging moment, see point A in Figure 7). If pre-stressed concrete is used for the girder, this means that the deck is pre-stressed centrally during construction and often more post-tensioned tendons are added upon completion to counteract the section forces of the completed continuous beam (Rosignoli 1999). The moment envelope of the girder during construction must stay within given limits. The deflections of the front of the girder have to be controlled in such a way that the girder reaches each pier at the desired level. This can be achieved by a suitable fabrication shape and/or by jacking of the girder at the previous piers. The exact computation of these parameters is in fact rather complicated due to the changes in structural system and especially when time-dependent material behaviour (creep and shrinkage) is involved. *RM2000* has incorporated an automatic procedure to design bridges built using the ILM which takes advantage of the Unit Load Method.

In this procedure the structure at all points during construction is modelled as a statically determined system (eg. a cantilever). The piers at the respective support points are replaced by "unit loads" and a desired deflection-profile is entered which fits the boundary conditions imposed by the piers and the jacks on the piers if present. The process as described above is then used to determine the jacking regime and a suitable pre-camber of the bridge girder. Due to the repetitive nature of the ILM, the input for this procedure can be generated automatically and the design can be sped up considerably. A considerable number of changes in the structural system can be simplified into a number of loading cases onto one statically determined system. The automatic generation of the moment envelope and the exact fabrication shapes is also supported by this system.

CONCLUSIONS

The Unit Load Method has been developed to achieve a pre-defined target configuration of section forces in cable-stayed bridges by optimising the tensioning of the stay-cables. Recently, the method has been developed further into a versatile design tool that allows the definition of a target distribution of section forces or deflections in any structure. Using the Unit Load Method the necessary adjustments in a pre-determined set of constrains are computed to achieve exactly this distribution. This paper briefly describes the method and gives three application examples where this method has been used: a cable-stayed bridge, a concrete arch and the application of this method to the automated simulation of the incremental launching process of bridges. Many other possible applications of the Unit Load Method exist.

www.EngineeringEBooksPdf.com

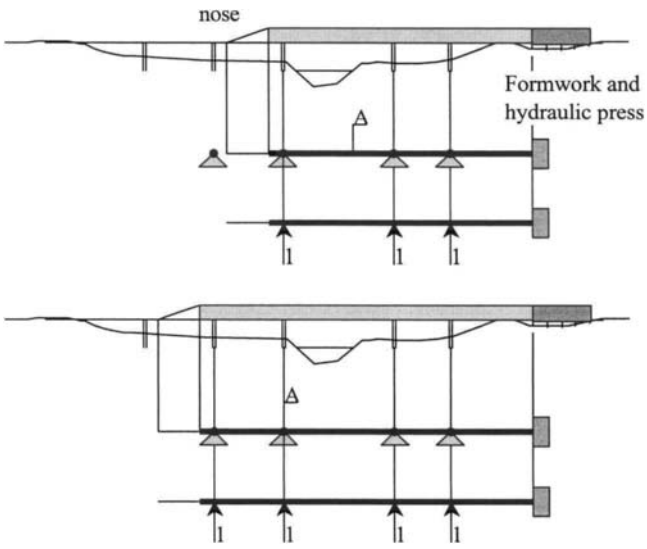

Figure 7. Schematic view of launching procedure.

REFERENCES

Bruer A., Pircher H., Bokan H. (1999). Computer Based Optimising of the Tensioning of Cable-Stayed Bridges. *Proceedings: IABSE Conference*, International Association for Bridge and Structural Engineering, Zürich, Switzerland

Janjic D., Pircher M., Pircher H. (2002) Optimisation of Cable Tensioning in Cable-Stayed Bridges. *Journal of Bridge Engineering, ASCE*, awaiting publication

Kargel E., Geisler P. (1983). Die Pitztalbrücke, Freivorbau des 169m weit gespannten Bogens. *Mayreder Zeitschrift* **28**, 6-28

Bruer A., Pircher H., Bokan H. (1999). Computer Based Optimising of the Tensioning of Cable-Stayed Bridges. *Proceedings: IABSE Conference*, International Association for Bridge and Structural Engineering, Zürich, Switzerland

Pircher H. (2001) Bay Watch. *Bridge Design & Engineering*, **22**, 64-67

Rosignoli M. (1999) Prestressing Schemes for Incrementally Launched Bridges. *Journal of Bridge Engineering, ASCE*, **4**(2), 107-115

TDV GesmbH. (2001). *RM200 – Technical Description*. Graz, Austria

www.EngineeringEBooksPdf.com

This Page Intentionally Left Blank

www.EngineeringEBooksPdf.com

Advances in Steel Structures, Vol. II
Chan, Teng and Chung (Eds.)
© 2002 Elsevier Science Ltd. All rights reserved.

GLOBAL ANALYSIS OF STEEL AND COMPOSITE HIGHWAY BRIDGES – DEVELOPMENT OF IMPROVED SPATIAL BEAM MODELS

H. Unterweger

Department of Steel Structures, Technical University Graz
Lessingstrasse 25, A- 8010 Graz, Austria

ABSTRACT

Nowadays exact modelling of a complete steel or composite bridge structure - using Finite Elements (FE) - is possible, because of the rapid development of computer power. Nevertheless this leads in general to nonacceptable costs in practical work, due to the fact of the enormous amount of data - caused e.g. by a lot of traffic load cases in complex structures. Therefore simple beam models for the whole bridge structure are useful combined with local FE - models if necessary. In the paper a simple spatial beam model of bridge decks built with two webs (open or box section) is shown, allowing for effects of section distortion and local bending between deformable intermediate diaphragms. Two examples show the accuracy and efficiency of the model, by comparing the stresses with results of more refined FE - models.

KEYWORDS

Steel Bridges, Composite Bridges, Global Analysis, Bridge Deck Modelling

INTRODUCTION

A major problem in the structural analysis of steel and composite bridges is the modelling of the bridge deck, consisting of an immense number of individual elements, such as plates, stiffeners, cross beams and diaphragms. The current design procedure in practice is therefore a combination of a global model, consisting of the whole structure including its bearings and foundations, and local models for individual parts of the structure. In Unterweger (2001) the requirements on global analysis of bridges are worked out, particularly the consistency with the local models for member resistance and for additional local stresses (e.g. for local deck bending). The main feature was the development of improved spatial beam

www.EngineeringEBooksPdf.com

models with a minimum of elements for all types of steel and composite bridge decks. The following aspects are taken into account:

- Linear elastic analysis; this allows superposition of individual load cases which is very important due to the enormous amount of traffic load cases. Second order effects (e.g. arches, truss chords) can be approximately considered if the maximum compressive axial forces of a prior first order calculation are taken into account in the stiffness of the elements in the global analysis.
- The complex global behaviour including • distortion of the bridge deck, • deformation of diaphragms, • warping of the bridge deck, • global bending effects of the slab (in case of multiple girders) and • local girder bending due to discrete distances of the diaphragms should be represented.
- Simple models for easy practical work with conventional software packages, including shear deformations and modules for automatic superposition of load cases, in contradiction to suggested comprehensive models from other authors (e.g. *Hambly* (1991), *Volke* (1999)).

The scope of the paper is focused on the presentation of models for the most common bridge sections (Fig. 1) with two webs – I- plate girder and single box girder bridges respectively with symmetry to its vertical axis. Continuous spans as well as bridges with complex support conditions (e.g. a central support at piers only), including deformable diaphragms between the supports, can be taken into account using the same type of model. The calculation of the basic natural frequencies - using lumped masses - is also possible as well, adding some further elements in the model.

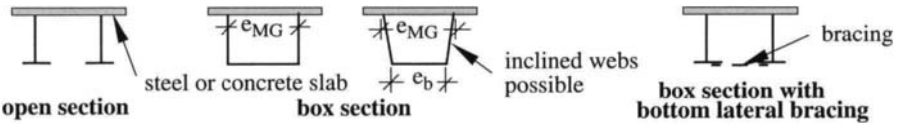

Figure 1 : Bridge cross sections covered in the paper.

BRIEF PRESENTATION OF THE BEAM MODEL

Beam elements with relevant stiffnesses

For reasons of simplicity in the following all stiffnesses are written without Young's modulus E_s for steel. For concrete slabs the procedure based on the reduction equal to the modular ratio $n = E_s / E_c \approx G_s / G_c$ between steel and concrete has to be considered for stiffness and stress calculation of the slab (long time effects in Unterweger (2001)). The effect of vertical loads is divided in symmetric and antisymmetric load part (Fig. 2), only for reason of easier explanation. The beam model with the relevant stiffnesses and internal forces is shown in Fig. 3, valid for open and box sections.

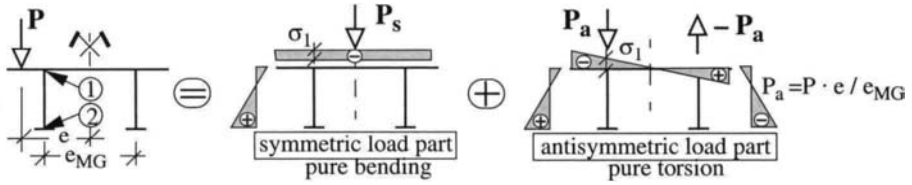

Figure 2 : Definition of vertical load parts with principal stress fields.

The bridge section is represented by only three beams with specific reduced stiffnesses. The two *main girders* (MG) placed in plane of the webs are specified by a vertical bending (I_y) and shear stiffness (shear area corresponds to the web area) only. The effective width b_{eff} of the slab (for I_y) is chosen in such a way that for pure torsion (Fig. 2), without diaphragms between the supports, the vertical deflections and stresses in web plane are exactly the same as using folded plate theory - *Resinger* (1956). For a bottom plate of a box section ($b_{ges} \approx e_{MG}$) it results in the minimum of $b_{eff} = e_{MG} / 6$. For open sec-

www.EngineeringEBooksPdf.com

tions and sections with bottom lateral bracing only the flange area is considered. Longitudinal ribs can be taken into account, using the smeared thickness t_{eff}. The *central beam* (CB) comprises the whole extensional and horizontal bending stiffness of the section (A, I_z), the whole horizontal shear stiffness - if relevant (shear area $A_{sy} \approx$ slab area) - and the torsion constant I_x, treating the section as a thin walled section. For open sections I_x may be neglected ($I_x \approx 0$); for a box section, using the terms of Fig. 1 & 3, we end up for the well known formula of Bredt with Eqn. 1. For boxed sections with bottom lateral bracing the equivalent shear thickness t_b^* is used. For vertical webs e_b is equal to e_{MG} .

$$I_x = \frac{(e_{MG} + e_b)^2 \cdot h^2}{e_{MG}/t_s + 2 \cdot h/t_w + e_b/t_b} \qquad (1)$$

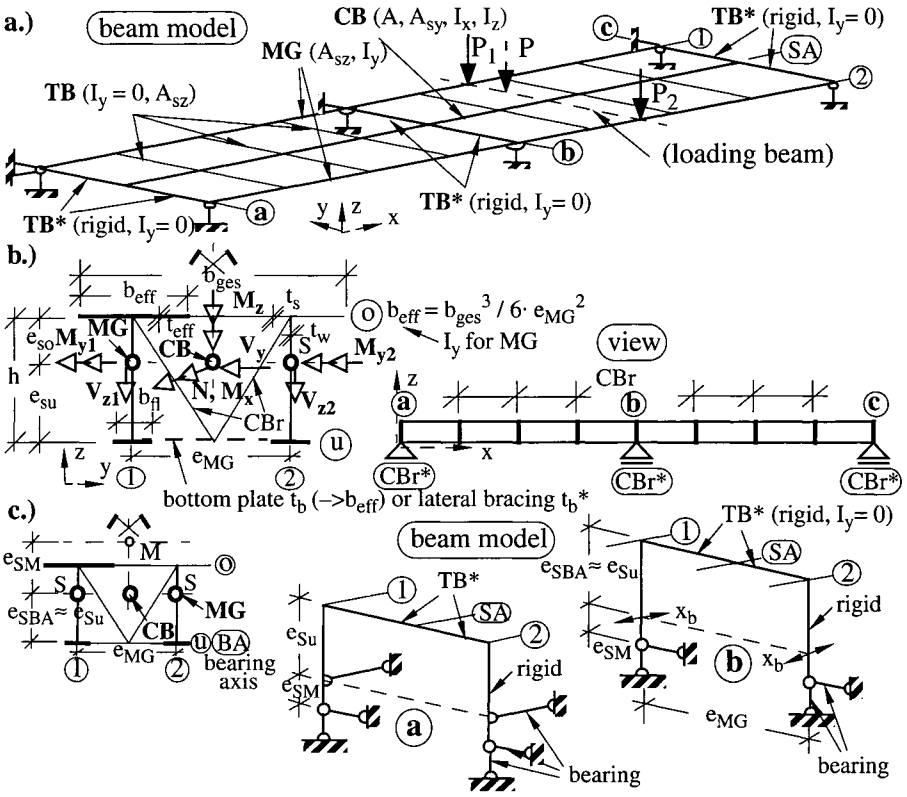

Figure 3 : Spatial beam model for bridge deck with two webs (open and box section).

The diaphragms are represented in the model by *transverse beams* (TB) with shear flexibility in vertical direction. All types of diaphragms, shown in Fig. 4, can be treated in a similar way. The shear stiffness of an isolated sway bracing or a sway frame can be expressed as an equivalent thickness t* of a diaphragm. Important is the fact that for vertical webs the shear area of the isolated diaphragm ($A_{sz} = h \cdot t^*$) must be doubled, since the stresses are halfed due to the unloading effect of the primary torsional shear T_{SV} , shown in Fig. 4. For inclined webs (Fig. 1) the unloading effect gets higher. Instead of a "load factor" $f_{ld} = 1 / 2$ we end up with $f_{ld} = e_b / (e_{MG} + e_b)$, leading to a shear stiffness factor of $f_{st} = 1 / f_{ld} = (e_{MG} + e_b) / e_b$. The diaphragms at the supports (axis *a*, *b*, *c* in Fig. 3) represented by the *transverse*

www.EngineeringEBooksPdf.com

beams TB* are assumed to be rigid. All transverse beams have no torsion stiffness (I_y=0) to allow individual bending of the MG. If the bridge deck gets no relevant axial forces all beams are in - plane.

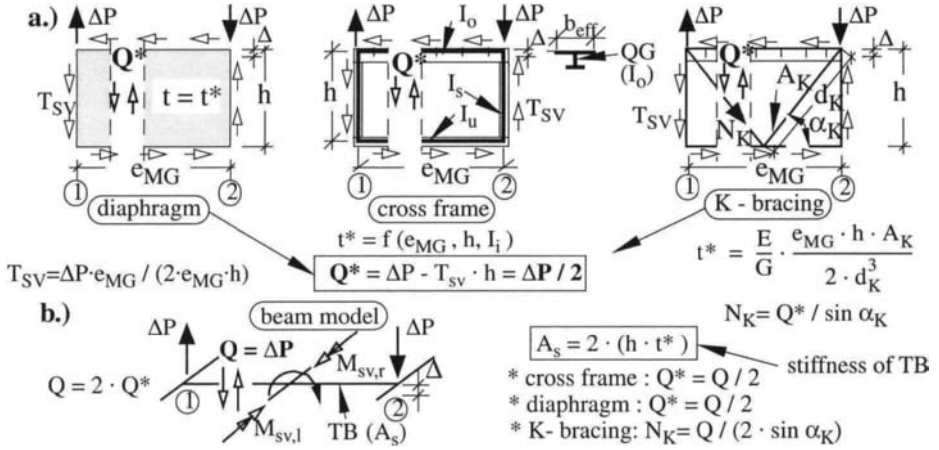

Figure 4 : Modelling of diaphragms

Modelling of special effects and stiffnesses of supports

The simplest model in Fig. 3a with all beams in - plane, can't represent longitudinal movements of the bearings - neither due to vertical bending nor due to torsion (warping). Also the vertical bearing forces due to horizontal loads are missing. By adding frames in all support axis (*a*, *b*, *c* in Fig 3c) these effects can be taken into account. Worth mentioning is the fictitious vertical extension at the frames (e_{SM} equal to the distance of centroid of MG to the flexural center) to carry out the correct vertical bearing forces. The longitudinal movements x_b and the associated restraint forces are still in level of the bearings.

Due to the specific effective width definition for calculation of the vertical bending stiffness of the two main girders (MG), their sum is in general smaller than the total vertical bending stiffness of the bridge deck. Therefore in continuous bridge decks the calculated stress resultants are to low for actions proportional to the bending stiffness (e.g. vertical temperature gradient, bearing settlements). To overcome this deficiency the addition of a *fictisious central beam* CB* in the model is necessary, which is connected only with the main girders by *rigid transverse beams* T* (Fig. 5). This central beam CB*, located in the same axis as the central beam CB, gets the difference in vertical bending stiffness ($\Delta I_y = I_{y,deck} - 2 \cdot I_{y,MG}$) as well as the torsion constant $I_{x,slab}$ of the slab if relevant (concrete slabs). The additional transverse beams T* are necessary to prevent the transverse beams from nonoccuring stresses. If bearings or foundations have no infinit stiffnesses, the truss boundary elements in Fig. 3 are replaced by springs. If necessary, slender piers are also added in the model.

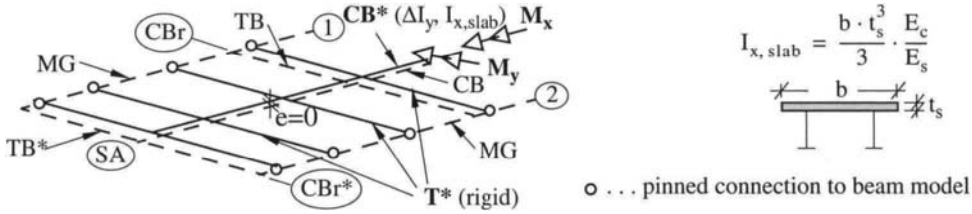

Figure 5 : Additional elements (CB*, T*) in the beam model.

Modelling of loading

Vertical loads act in the axis of the main girders. For automatic modelling of loadings, due to individual traffic lanes, additional loading beams, supported at the main girders only, can be arranged (Fig. 3a).

www.EngineeringEBooksPdf.com

The horizontal loads, acting on the central beam, are applied only in the diaphragm axis. The torsional effect due to the eccentricity to the flexural centre M of the whole bridge section is considered by vertical forces P_v (Fig. 6). The local stress effect between the diaphragms must be considered separately.

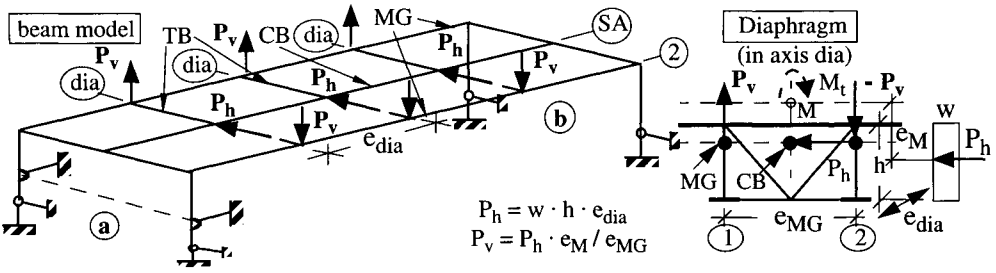

Figure 6 : Equivalent loads due to horicontal loading (wind).

Stress calculation

Normal stresses: The calculation has to be done for points at the edges of the web - shown in the following for edge 1 (Fig. 2) - with the bending moment M_y of the appropriate main girder. Based on these results the stress distributions of the whole section can be established. The moments in the main girders (M_{y1}, M_{y2}) include local bending, global bending and distortion, therefore the usage of the section modulus ($I_{y,\,MG}$) for the global analysis alone gives nonacceptable results. As a practical approach the following procedure is useful: If the shear lag effect is relevant (high b_{ges} / span length ratios) the appropriate effective width in the codes should be the assumption of the stress calculation ($I^*_{y,MG}$, e^*_o). For edge 1 it leads to Eqn. 2, allowing for the bending moment $M_{y,CB*}$ in the central beam CB* as well.

$$\sigma_1 = \frac{(M_{y1} + 0,5 \cdot M_{y,\,CB*})}{I^*_{y,\,MG}} \cdot e^*_o + \frac{N}{A} + \frac{M_z}{W_{z1}} \qquad (2)$$

If the shear lag effect can be neglected ($b_{eff} \approx b_{ges} / 2$) the stresses due to the symmetric part of $M_{y1} = 0,5 \cdot (M_{y1} + M_{y2} + M_{y,CB*})$ should be calculated using the entire width ($0,5 \cdot b_{ges}$) instead of $I_{y,\,MG}$. The last two terms in Eqn. 2 consider global axial force and horizontal bending, represented by the central beam CB, based on the behaviour of the whole bridge deck (area A, section modulus W_{z1}).

Shear stress in the web: Assuming equal stresses in the web we end up with (Eqn. 3):

$$\tau = \frac{V_{z1}}{A_{web}} + \frac{M_{x,\,CB}}{2 \cdot h \cdot e_{MG} \cdot t_w} \qquad (3)$$

The first term, based on the shear force in the appropriate main girder, represents local and global shear forces in the section as well as secondary effects due to torsion. The second term represents primary shear stresses due to torsion, based on the moment M_x in the central beam.

Shear stress in the slab and bottom plate: The proportioning of the global horizontal shear force V_y in the central beam to slab and bottom plate is equal to the consideration as an isolated section. For the primary shear stresses due to torsion the procedure is similar to the webs. The shear stresses due to vertical shear forces (local and global), distortion and secondary torsion effects - negligible for bottom bracings - are calculated considering the equilibrium condition with the normal stresses in longitudinal direction, based on the normal stress distribution in the section. If the local torsion stiffness of the slab is built in the model by using the central beam CB*, this stress component must be considered in design, based on $M_{x,\,CB*}$ as well.

Stresses in the diaphragms. The shear forces in the TB, reduced by $f_{ld} = 0,5$ for vertical webs, are the basis to determine the stresses in all types of diaphragms, as shown in Fig. 4. For the diaphragms at the supports this procedure fails if horizontal shearing forces V_y act too. Now the stress resultants of the next central beam (M_x, V_y) are the basis for the calculation.

www.EngineeringEBooksPdf.com

EXAMPLES ON GLOBAL BRIDGE DECK MODELLING

The aim of the two selected examples is to show the great efficiency of the presented simple spatial beam models, particularly when local bending, section distortion and warping effects are relevant. To clarify the structural behaviour, simplified load patterns are used. The main results are presented and compared with more exact solutions (FE - models elaborated with software package ABAQUS).

Example 1: Railway box girder bridge with deformable cross bracings

Example 1 (Fig. 7) is a single span railway box girder bridge with one or three deformable intermediate cross bracings loaded by simplified live loads on one track, investigated by Resinger (1956). The load case can be divided into two parts. Under the symmetrical part (LC1) only bending of the whole bridge deck occure, which is not shown in the following. The antisymmetrical load part (LC2) was used for a study, where the number of intermediate cross bracings (one or three) and their stiffnesses, expressed in form of an equivalent thickness t* of a diaphragm, was varied.

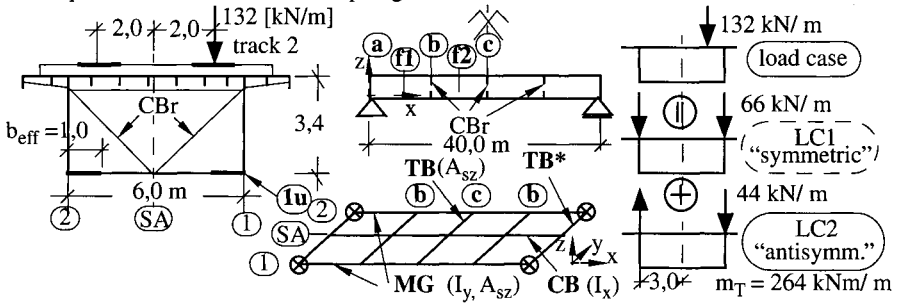

Figure 7 : Example 1; System, load cases and simple beam model.

For this system the simpliest model configuration, consisting of main girders, central beam and transverse beams gives adequate results. In Fig. 8 the normal stress distribution for LC2 at the bottom of the web (axis *1u*) is illustrated for different stiffnesses of three and one intermediate diaphragms respectively. The results of the model are compared with results of comprehensive FE - models ("exact").

In general the beam model gives conservative results, since it underestimates the favourable stress peaks at the intermediate diaphragms. However the increase of the normal stresses due to more deformable diaphragms is reproduced quite good. The obviously high differencies - particularly for three diaphragms (e.g. + 60 % in *f2*) - can be neglected if the whole load case is considered. Hence the overestimation is less than 5 %, which further decreases if the dead loads are also considered.

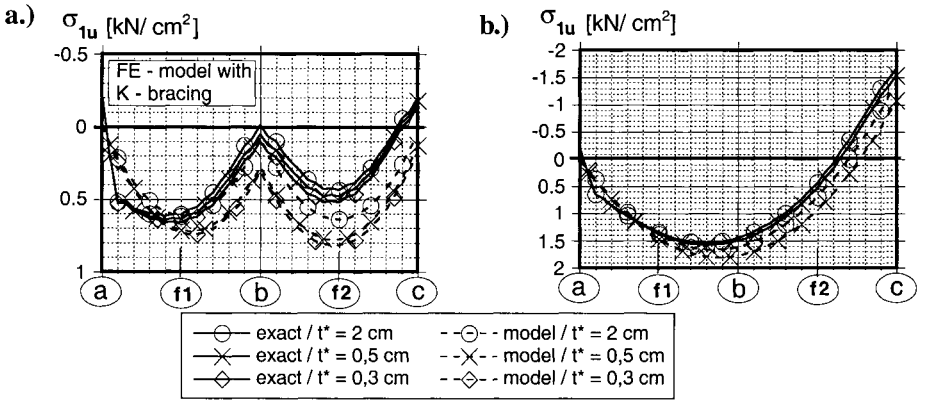

Figure 8 : Example 1; Normal stresses σ at axis *1u* due to load case LC2 for system with a.) three , b.) one, intermediate cross bracings.

www.EngineeringEBooksPdf.com

Important to mention is the good agreement of the stresses in the diaphragms. Due to the fact that the beam model in general underestimates the stresses (about – 2 ÷ 6 % compared to FE- model) an increase of the calculated stresses of + 10 % is proposed. In Fig. 9a the influence of the diaphragm deformability on some representative results for load case LC2 is shown, which is obviously nonlinear. The increase of the maximum vertical web deflection (w_{1c} in axis *c*) is similar to the normal stress between the diaphragms (axis *f2*). The minor changes of the axial force in the bracing is due to distributed loading only. In Fig. 9b the influence lines, using different diaphragm stiffnesses, for the bracing in axis *c* are presented. In the beam model they can be easily determined, using the "kinematic method". Also the common practice, ignoring the interaction of the diaphragms with the bridge deck, is illustrated (simple model). Increasing the deformability leads to a stress reduction for direct vertical single loads.

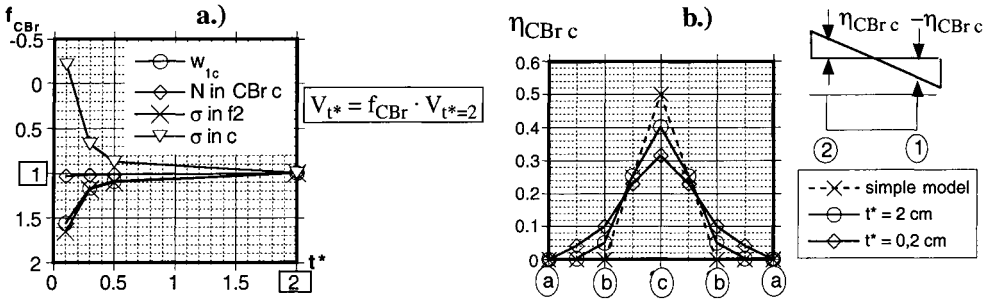

Figure 9 : Example 1; a.) Influence of the diaphragm stiffness on main results, b.) Influence Line for shear forces in cross bracing *c*.

Example 2: Plate girder bridge; Restraint bearing forces due to warping of the cross section

Example 2 (Fig. 10) deals with a single span highway composite plate girder bridge with two fixed bearings in longitudinal direction on one abutment, investigated by Resinger (1971). Due to the relevant traffic load configuration for girder 1, nonnegligible longitudinal restraint forces A_{hx} on the fixed bearings are introduced, because of warping of the open section. These forces also lead to horizontal bearing forces A_{hy} and horizontal bending of the bridge deck.

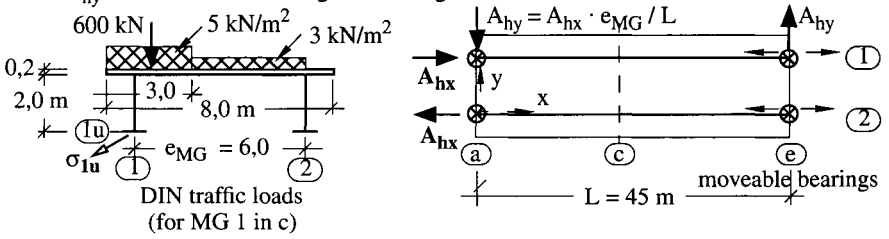

Figure 10 : Example 2; Highway composite plate girder bridge under traffic loads.

Beside Model 4T (including torsion constant for the concrete slab), a reduced Model 4 without transverse beams ($I_x = 0$) and a model with the central beam in height of the shear center was used (model 3, proposed in Resinger (1971)). Due to missing torsion stiffness I_x of the open section, the intermediate diaphragms are ineffective and are neglected in the beam models. In Table 1 the relevant results, • warping deformation between bearings in axis 1 if warping is free, • restraint bearing forces A_{hx} and • maximum normal stress $\sigma_{1u,\,c}$ in girder 1 (bottom flange at midspan) are listed and compared with an "exact" FE - model. The results show the very high bearing forces A_{hx} and on the first glance the surprisingly high influence of the torsion constant of the concrete slab on the warping behaviour (model 4 / 4T), leading to reduced stresses and warping deformations. Model 3 with the central beam in the shear centre gives inaccurate results; the warping deformations are highly overestimated, whereas the bearing

www.EngineeringEBooksPdf.com

forces A_{hx} are too small. In Table 1 also the influence of the fixed bearings on the stresses of the structure can be seen. In comparison to one fixed bearing in axis *a* the maximum stresses decrease about 10 %. Therefore the fixing of both girders in axis *a* is relevant for the design of the bearings only.

TABLE 1
EXAMPLE 2; COMPARISON OF THE MAIN RESULTS

warping - axis a	quantity	model 3	model 4	model 4T	FEM
free	$x_{a,\,1\text{-}2}$ [mm]	16,1 (+96,3%)	10,3 (+25,6%)	8,29 (+1,1%)	8,20 (±0%)
fixed	A_{hx} [kN]	1102 (-16,5 %)	1520 (+15,2%)	1352 (+2,4%)	1320 (±0%)
free	$\sigma_{1u,\,c}$ [kN/ cm^2]	23,2 (+7,5%)	23,2 (+7,5%)	21,7 (+0,4%)	21,6 (±0%)
fixed		19,5 (+2,1%)	19,7 (+3,2%)	19,2 (+0,3%)	19,1 (± 0%)

In general the proposed beam model (4T) shows very good accuracy compared to a comprehensive FE - model, however for normal stress calculation the different section modulus for the symmetric and antisymmetric part of M_{y1} must be considered.

CONCLUSIONS

The main objective of this paper was to show that also complex bridge deck behaviour can be modelled by the use of simple spatial beams with equivalent stiffnesses.

The deformation of intermediate diaphragms and warping effects of the bridge deck can be taken into account. The paper covers bridge decks with two webs only. For more than two webs the appropriate beam models are given in Unterweger (2001). An example for a complex structure with additional axial forces in the bridge deck (central arch highway bridge) is presented in Unterweger (1999).

References

Hambly E.C. (1991). *Bridge Deck Behaviour*, 2nd edition, E & FN Spon.

Resinger F. (1956). *Der dünnwandige, einzellige Kastenträger mit einfachsymmetrischem, verformbarem Rechteckquerschnitt*, phD. thesis, Technical University Graz / Austria.

Resinger F. (1957). Ermittlung der Wölbspannungen an einfachsymmetrischen Profilen nach dem Drillträgerverfahren. *Der Stahlbau* **26: 11**, 321 - 326.

Resinger F. (1971). Längszwängungen - eine Ursache von Brückenlagerschäden. *Der Bauingenieur* **46: 9**, 334 - 338.

Unterweger H. (1999), Modelling of Bridge Decks including Cross Section Distortion using simplified Spatial Beam Methodes, *2nd European Conference on Steel Structures, Technical University Prag.*

Unterweger H. (2001). *Global Analysis of Steel and Composite Bridges - Efficiency of simple Beam Models*, Habilitations - theses, Technical University Graz / Austria (in german language).

Volke E. (1999). *Die Beanspruchung stählerner Brückentragwerke nach üblichen Modellannahmen und nach genaueren Untersuchungen*, phD. theses, Technical University Vienna/ Austria.

www.EngineeringEBooksPdf.com

DYNAMICS

www.EngineeringEBooksPdf.com

This Page Intentionally Left Blank

www.EngineeringEBooksPdf.com

Advances in Steel Structures, Vol. II
Chan, Teng and Chung (Eds.)
© 2002 Elsevier Science Ltd. All rights reserved.

FIELD COMPARATIVE TESTS OF CABLE VIBRATION CONTROL USING MAGNETORHEOLOGICAL (MR) DAMPERS IN SINGLE- AND TWIN-DAMPER SETUPS

Y. F. Duan[1], J. M. Ko[1], Y. Q. Ni[1], Z. Q. Chen[2]

[1]Department of Civil and Structural Engineering, The Hong Kong Polytechnic University, Hung Hom, Kowloon, Hong Kong
[2]Department of Civil and Architectural Engineering, Central South University, Changsha 410075, P. R. China

ABSTRACT

A total of 312 semiactive magnetorheological (MR) dampers have recently been installed on the cable-stayed Dongting Lake Bridge for wind-rain-induced vibration control of the stay cables. This is the world's first time implementation of MR-based smart damping technique in bridge structures. Before the full implementation, a series of in-situ vibration experiments have been conducted for a few typical cables to understand the control effectiveness of this unprecedented damping technique and to determine the best damper setup. This paper reports the field comparative tests of the cable-damper system under different damper installation setups. In this testing phase, one utmost stay cable of the bridge, about 150 m in length, was tested without damper and with single-damper and twin-damper installations respectively. Sinusoidal-delay excitation was imposed to excite the cable vibration with different levels of response and in different frequencies. A spectrum of voltage inputs was applied to the MR damper(s) during the testing to relate the system damping behaviour with voltage strength. A Hilbert transform based identification method is used to identify amplitude-dependent frequencies and damping of the cable-damper system and to determine the optimal voltage that achieves the maximum system damping. The research emphasis is laid on the comparison of in-plane as well as out-of-plane damping performance of the system between the single- and twin-damper setups.

KEYWORDS

Bridge stay cable, vibration control, smart damping technology, magnetorheological (MR) damper, in-situ vibration test, damper installation configuration.

INTRODUCTION

The Dongting Lake Bridge, as shown in Figure 1, is a three-tower, cable-stayed bridge in Hunan, China. It has a total length of 880 m consisting of two main spans of 310 m each and two side spans of 130 m each. Since its open to traffic in the end of 2000, the bridge has experienced severe wind-rain-

www.EngineeringEBooksPdf.com

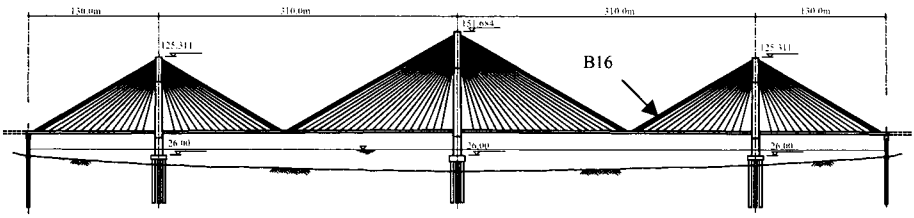

Figure 1: Elevation of Dongting Lake Bridge

induced cable vibration more than three times within half a year. Although this kind of vibration has been observed on a number of cable-stayed bridges worldwide, it is very uncommon for an existent bridge to experience wind-rain-induced cable vibration so frequently, which has caused great concern of the bridge administrative authority and management engineers.

With the objective of mitigating the wind-rain-induced vibration, implementation of semiactive MR dampers to a total of 156 stay cables in the Dongting Lake Bridge has been completed recently (Ko et al. 2002a). To the authors' knowledge, this is the world's first time implementation of MR-based smart damping technology to civil engineering structures. In order to realize this pioneering application, a series of in-situ trial tests have been conducted for a few typical cables before the full implementation to understand actual dynamic performance of the cables before and after installation of MR dampers, to determine the best damper setup, and most importantly, to demonstrate to the bridge owner control effectiveness of this unprecedented damping technique (Chen 2001; Duan 2001; Zheng 2001; Ko et al. 2002b; Ni et al. 2002). This paper reports the last phase of trial tests before the full implementation, aiming at identifying and comparing the damping performance of using single-damper setup and twin-damper setup in both in-plane and out-of-plane directions. In recognizing the nonlinearity of MR damper, a Hilbert transform based identification method is adopted to identify amplitude-dependent frequencies and damping of the cable-damper system under a wide spectrum of voltage inputs.

DESCRIPTION OF FIELD TESTS

The tested cable, designated as B16, is the utmost stay cable in one main span stretching from the side tower as indicated in Figure 1. The main properties of the cable are shown in Table 1, where L, h, l denote the total, horizontal and vertical length of the cable; D_o is the diameter of the cable including outer cover; D_s and A_s are the diameter and area of the steel bundle; E is the elastic modulus; m is the mass per unit length of the cable.

Figure 2 illustrates the single- and twin-damper setups for the cable testing. The MR damper used is Type RD-1005 from Lord Corporation. The dampers are installed between the cable and bridge deck at the position of 4.3 m (2.9% of the cable length) away from the cable lower end through the use of a supporting pole. In the single-damper setup, one damper is attached perpendicular to the cable axis within the cable plane. In the twin-damper setup, two dampers are diagonally installed in the angle of 72 degrees with each other, both being perpendicular to the cable axis. During the tests, displacement transducers are attached to the dampers for measurement of the damper piston movement.

TABLE 1
MAIN PROPERTIES OF TESTED CABLE B16

L (m)	h (m)	l (m)	D_o (mm)	D_s (mm)	A_s (cm^2)	E (MPa)	m (kg/m)
147.272	73.697	127.506	159	135.3	120.457	2.0×10^5	98.7

www.EngineeringEBooksPdf.com

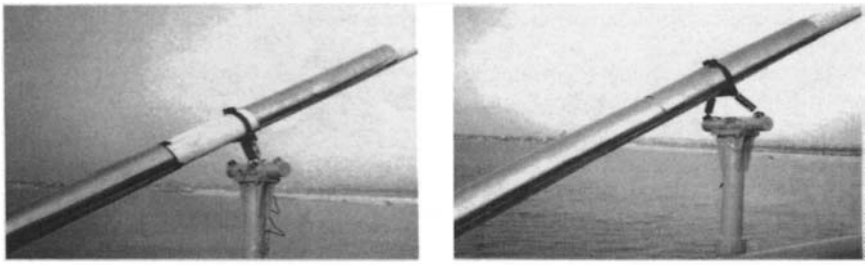

(a) Single-damper setup (b) Twin-damper setup

Figure 2: Damper setups for testing of cable B16

Figure 3 shows the schematic diagram of vibration testing and data acquisition. Sinusoidal-delay testing is conducted to excite the cable with different vibration amplitudes and in different vibration frequencies. Following this method, an electric exciter is used to produce a sinusoidal excitation on the cable to achieve a steady-state single-mode vibration by tuning the exciting frequency to a specific resonant frequency. A trigger device is then motivated to remove the sinusoidal excitation suddenly and free vibration decay is generated to determine the damping ratio of the specific mode. The cable vibration is monitored in both in-plane and out-of-plane directions with two accelerometers at 7.8 m (5.3% of the cable length) away from the cable lower end, while the excitation point is at 8.5 m (5.8% of the cable length) from the lower end. A notebook-PC-based DH5937/8 data acquisition system is used for field measurement. Signals from accelerometers and displacement transducers are acquired simultaneously at a sampling frequency of 500 Hz after passing an anti-aliasing filter with a truncating frequency of 100 Hz.

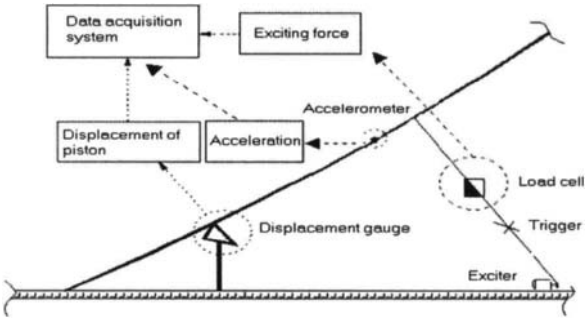

Figure 3: Schematic diagram of field vibration testing

IDENTIFICATION AND RESULT ANALYSIS

Due to the geometric nonlinearity of cable and the hysteretic nonlinearity of MR damper, the natural frequencies and modal damping of the cable-damper system are dependent on the vibration level (amplitude). In this study, a Hilbert transform based identification method (Bernal and Gunes 2000; Yang and Lei 2000) is utilized to identify the amplitude-dependent frequencies and damping of the cable-damper system. For a time-domain signal $u(t)$, its Hilbert transform can be expressed as

$$v(t) = -\frac{1}{\pi}\int_{-\infty}^{\infty}\frac{u(\eta)}{\eta - t}d\eta = \frac{1}{\pi t} * u(t) \tag{1}$$

www.EngineeringEBooksPdf.com

where * denotes the convolution operation. The essential characteristic of the Hilbert transform is to change the phase angle by 90^0 but keep the amplitude unchanged. By taking the original data (a real signal) as real part and the Hilbert transform of the original data as image part, we get a complex signal called analytic signal. For a narrow-band signal

$$u(t) = A(t)\cos(\omega t + \phi) \tag{2}$$

where ϕ is the initial phase, when the highest frequency of $A(t)$ is far smaller than ω, its Hilbert transform can be expressed as

$$v(t) = A(t)\sin(\omega t + \phi) \tag{3}$$

and the analytic signal is

$$Y(t) = A(t)\cos(\omega t + \phi) + jA(t)\sin(\omega t + \phi) = A(t)e^{j(\omega t + \phi)} \tag{4}$$

When the free decay response signal of a multi-degree-of-freedom system is dominated by single-mode vibration, it can be approximated as

$$u(t) = e^{-\xi\omega t}\cos(\omega_d t + \phi) \tag{5}$$

where ξ is the modal damping ratio; ω is the modal frequency; and ω_d is the damped modal frequency. Based on the above definition, the analytic signal through the Hilbert transform can be expressed as

$$H(t) = e^{-\xi\omega t} \cdot e^{j(\omega_d t + \phi)} = |H(t)| \cdot e^{j\theta(t)} \tag{6}$$

where the amplitude

$$|H(t)| = e^{-\xi\omega t} \quad \text{or} \quad \ln[|H(t)|] = -\xi\omega t \tag{7a, b}$$

and the phase angle

$$\theta(t) = \omega_d t + \phi \tag{8}$$

Therefore the damped frequency ω_d can be estimated from the slope of the linearly fitted straight line in $\theta(t)$ versus t plane, whereas $-\xi\omega$ is estimated from the slope of the linearly fitted straight line in $\ln[|H(t)|]$ versus t plane. With ω_d and $\xi\omega$ being estimated, the corresponding natural frequency ω and damping ratio ξ of the concerned mode can be obtained using the following formulas

$$\omega = \sqrt{\omega_d^2 + (\xi\omega)^2} \quad \text{or} \quad \xi = \sqrt{1 - (\omega_d / \omega)^2} \tag{9a, b}$$

$|H(t)|$ and $\theta(t)$ are varying with time t. If we divide the curve into sufficient pieces for piecewise-linear least-square fitting, the instantaneous frequencies and damping ratios, which are dependent on vibration level, can be obtained. By taking the in-plane vibration of the tested cable under 12 volts input to the twin-damper as an example, Figure 4 illustrates the free decay response and its envelop obtained as the amplitude $|H(t)|$ of the analytic signal by the Hilbert transform, when the frequency is tuned to the second in-plane mode. Figures 5 and 6 show the relationships of the phase $\theta(t)$ of the analytic signal and the natural logarithm $\ln[|H(t)|]$ of the amplitude versus time t, respectively. According to the above derivation, the slope of the curve in Figure 5 indicates the value of the damped frequency (ω_d), and that in Figure 6 indicates the value of the minus product of frequency and damping ratio ($-\xi\omega$).

Therefore, we need only to find the critical points which indicate obvious change of the curve slope and then make piecewise-linear least-square fitting to obtain the relations of frequency and damping ratio versus vibration amplitude. Because the curve of $\theta(t)$ versus t shown in Figure 5 is almost a

www.EngineeringEBooksPdf.com

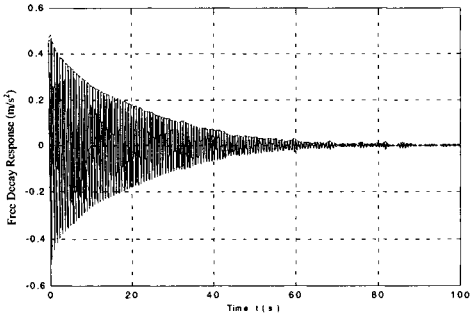

Figure 4: Free decay response and its envelop $|H(t)|$

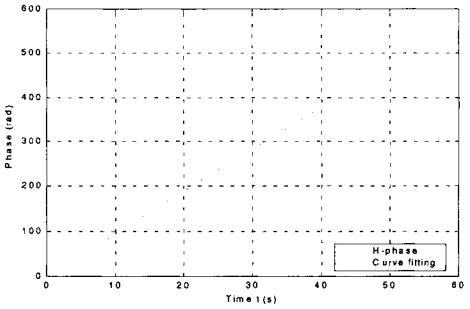

Figure 5: Phase of analytic signal

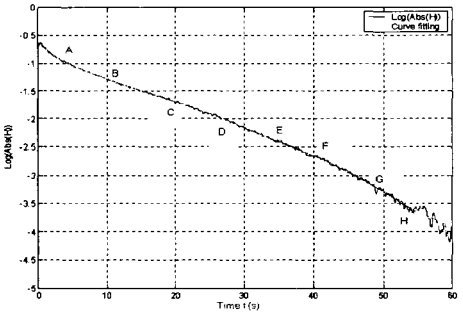

Figure 6: $\ln[|H(t)|]$ versus t and piecewise fitting

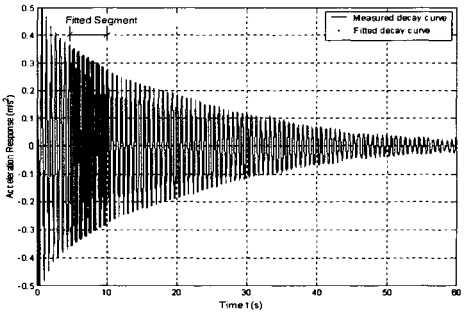

Figure 7: Curve fitting by time-domain method

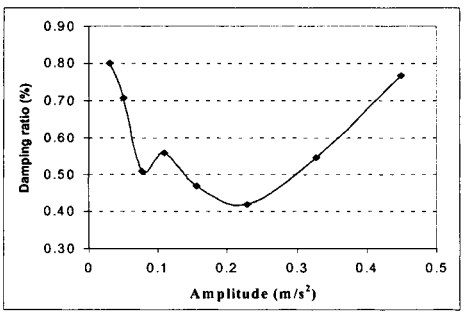

Figure 8: Damping ratio versus vibration amplitude

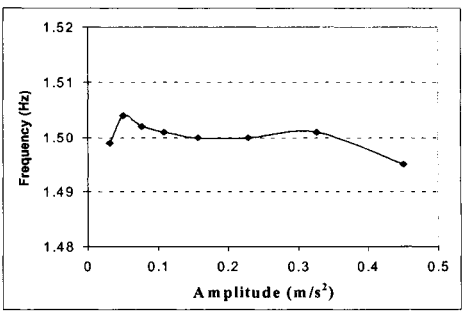

Figure 9: Frequency versus vibration amplitude

straight line, we separate the signal of the first 55 seconds into 8 pieces according to the slope change of the curve of $\ln[|H(t)|]$ versus t, designated by A to H as shown in Figure 6. Figures 8 and 9 show the identification results of the damping ratio and frequency versus vibration amplitude. In order to verify the identification accuracy of the present method, a time-domain nonlinear least-square curve fitting method is also conducted to obtain the damping ratio and frequency by fitting the free decay signal with Eq. (5) directly. Figure 7 illustrates a segment of the fitted response curve by this method corresponding to piece AB shown in Figure 6. Table 2 provides a comparison of the identification results by using the present method and the time-domain fitting method. A good agreement between the results from the two methods is observed.

www.EngineeringEBooksPdf.com

TABLE 2
COMPARISON OF IDENTIFICATION RESULTS FROM DIFFERENT METHODS

Time Duration (s)	Average Amplitude (m/s^2)	Frequency (Hz)		Damping Ratio (%)	
		Present method	Time-domain fitting	Present method	Time-domain fitting
0.0~4.0 (OA)	0.450	1.495	1.494	0.768	0.770
4.0~10.0 (AB)	0.327	1.501	1.501	0.545	0.545
10.0~20.0 (BC)	0.229	1.500	1.500	0.420	0.425
20.0~28.0 (CD)	0.157	1.500	1.500	0.468	0.465
28.0~35.0 (DE)	0.109	1.501	1.501	0.558	0.559
35.0~42.0 (FF)	0.077	1.502	1.501	0.510	0.518
42.0~50.0 (FG)	0.051	1.504	1.504	0.707	0.698
50.0~55.0 (GH)	0.031	1.499	1.500	0.801	0.821

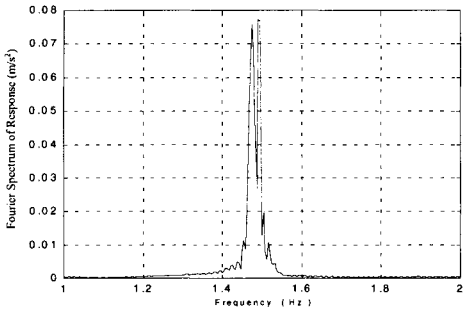

Figure 10: Double peaks in response spectrum

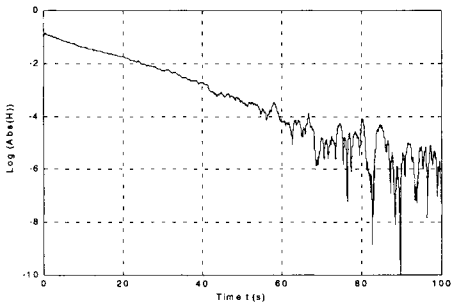

Figure 11: Visual indication of noise corruption

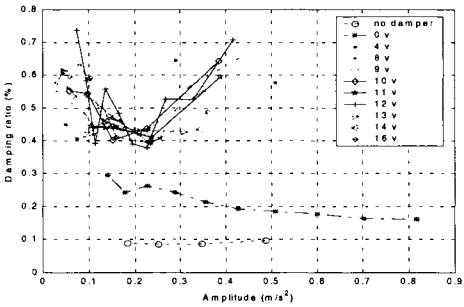

(a) Second in-plane mode

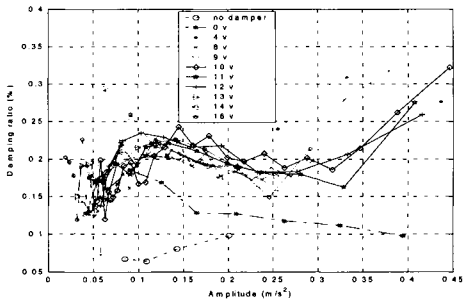

(b) Second out-of-plane mode

Figure 12: Damping ratio of tested cable with twin-damper under different voltages

The present piecewise-linear least-square fitting method based on the Hilbert-transform holds several salient advantages: (i) It automatically indicates the critical points for the change of frequency and damping ratio so that the relations of frequency versus amplitude and damping ratio versus amplitude are obtained in a phenomenological manner. The traditional frequency- and time-domain identification methods fail to do this; (ii) It improves the identification accuracy and saves computational effort by using linear least-square fitting instead of nonlinear curve fitting. The latter approach may fail to

www.EngineeringEBooksPdf.com

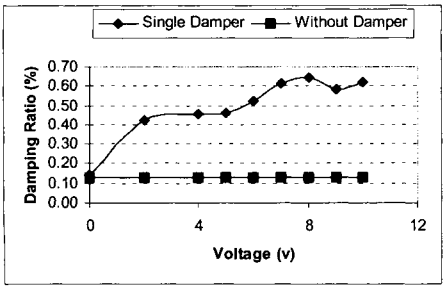

(a) Single-damper setup

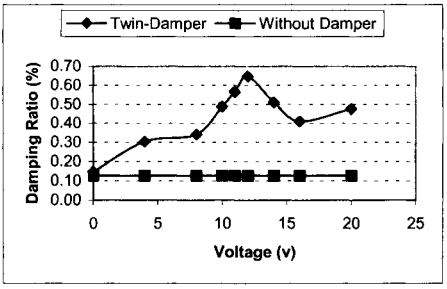

(b) Twin-damper setup

Figure 13: Damping ratios of first in-plane mode under vibration amplitude 0.04~0.07 m/s^2

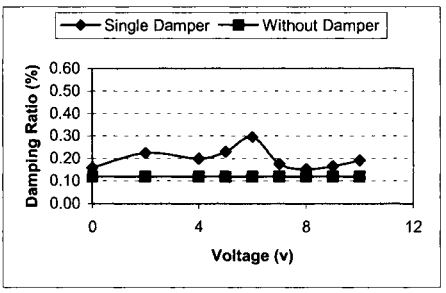

(a) Single-damper setup

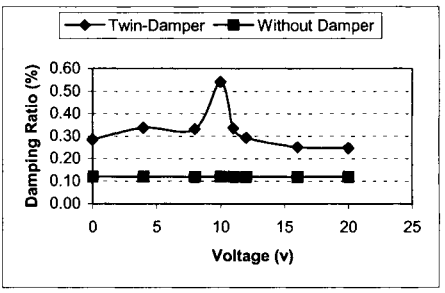

(b) Twin-damper setup

Figure 14: Damping ratios of first out-of-plane mode under vibration amplitude 0.04~0.07 m/s^2

converge when improper initial guesses are used; (iii) It circumvents the problem of double-peaks frequently encountered in the Fourier spectrum as shown in Figure 10. This abnormal phenomenon may occur in discrete Fourier transform due to time-varying behaviour and improper frequency resolution; (iv) It can give a visual indication of which signal segment is seriously polluted by noise. As shown in Figure 11, from the curve of $\mathbf{ln}[|H(t)|]$ versus t, the signal segment during 55 to 100 s was found with low signal-to-noise ratio and therefore was excluded from the identification use. It is very difficult to find the noise-corrupted segment from time-domain response curve or Fourier spectrum.

It found from Figure 9 that the maximum frequency variation among different vibration amplitudes is only about one percent. The research interest in this study is the enhanced damping of the cable due to attached MR dampers. Figure 12 shows the cable damping ratios of the second in-plane and out-of-plane modes under a wide spectrum of voltage inputs for the twin-damper setup. Figures 13 and 14 give a comparison of the first mode damping ratios using the single-damper setup and the twin-damper setup under specific vibration amplitude and a series of voltage inputs. It is found that for the first in-plane mode, the maximum damping ratio achieved in the single-damper setup is almost the same magnitude as that achieved in the twin-damper setup. However, for the first out-of-plane mode, the achievable maximum damping ratio in the single-damper setup is much less than that in the twin-damper setup. Similar consequences are also observed for the second and third modes (the damping identification results for high modes are absent here due to the limited space). It is therefore concluded that if the MR dampers are used for equally controlling cable vibration in both in-plane and out-of-plane directions, the twin-damper setup is preferable.

www.EngineeringEBooksPdf.com

CONCLUSIONS

Forced vibration tests have been conducted to experimentally determine the damping performance of a Dongting Lake Bridge cable attached with MR dampers in the single-damper setup and twin-damper setup, respectively. A new identification method based on the Hilbert transform has been applied to identify the amplitude-dependent frequencies and damping. Modal damping ratios of the cable-damper system under different vibration amplitudes and various voltage inputs are experimentally determined for both the single- and twin-damper setups. This experimental study draws the following conclusions: (i) No matter whichever damper setup is used, the frequencies and damping ratios are dependent on the vibration amplitude. The variation of frequency is negligible because it is within one percent for most cases, whereas the variation of damping ratio is appreciable; (ii) For in-plane vibration modes, the single-damper setup can provide almost the same maximum damping ratios as those provided by the twin-damper setup. However, for out-of-plane vibration modes, the maximum damping ratios achieved from the single-damper setup are much less than those achieved from the twin-damper setup; (iii) The optimal voltage input that achieves maximum system damping is different for different modes and different vibration amplitudes, as well as for different damper setups.

ACKNOWLEDGEMENTS

The work described in this paper was supported in part by a grant from the Research Grants Council of the Hong Kong Special Administrative Region, China (Project No. PolyU 5045/00E) and partially by a grant from Hong Kong Polytechnic University through the Area of Strategic Development Programme (Research Centre for Urban Hazard Mitigation). These support are gratefully acknowledged.

References

Bernal D. and Gunes B. (2000). An examination of instantaneous frequency as a damage detection tool. *Proceedings of the ASCE 14th Engineering Mechanics Conference*, Austin, USA.

Chen Y. (2001). Field vibration testing of a stay cable attached with MR dampers on Dongting Lake Bridge. *Report No. DLB-003*, Department of Civil and Structural Engineering, The Hong Kong Polytechnic University, 89p.

Duan Y.F. (2001). In-situ monitoring and control on wind-rain-induced vibration on Dongting Lake Bridge. *Report No. DLB-004*, Department of Civil and Structural Engineering, The Hong Kong Polytechnic University, 77p.

Ko J.M., Ni Y.Q., Chen Z.Q. and Spencer B.F., Jr. (2002a). Implementation of MR dampers to Dongting Lake Bridge for cable vibration mitigation. *Proceedings of the 3rd World Conference on Structural Control*, Como, Italy.

Ko J.M., Zheng G., Chen Z.Q. and Ni Y.Q. (2002b). Field vibration tests of bridge stay cables incorporated with magneto-rheological (MR) dampers. *Smart Structures and Materials 2002: Smart Systems for Bridges, Structures, and Highways*, S.C. Liu and D.J. Pines (eds.), SPIE Vol. 4696.

Ni Y.Q., Duan Y.F., Chen Z.Q. and Ko J.M. (2002). Damping identification of MR-damped bridge cables from in-situ monitoring under wind-rain-excited conditions. *Smart Structures and Materials 2002: Smart Systems for Bridges, Structures, and Highways*, S.C. Liu and D.J. Pines (eds.), SPIE Vol. 4696.

Yang J.N. and Lei Y. (2000). Identification of tall buildings using noisy wind vibration data. *Advances in Structural dynamics*, J.M. Ko and Y.L. Xu (eds.), Oxford, Elsevier, 1093-1100.

Zheng G. (2001). Ambient vibration test of six stay cables on the Dongting Lake cable-stayed bridge. *Report No. DLB-002*, Department of Civil and Structural Engineering, The Hong Kong Polytechnic University, 37p.

www.EngineeringEBooksPdf.com

Advances in Steel Structures, Vol. II
Chan, Teng and Chung (Eds.)
© 2002 Elsevier Science Ltd. All rights reserved.

EVALUATION OF RIDE COMFORT OF ROAD VEHICLES RUNNING ON A CABLE-STAYED BRIDGE UNDER CROSSWIND

W.H. Guo and Y.L. Xu

Department of Civil and Structural Engineering,
The Hong Kong Polytechnic University, Hung Hom, Kowloon, Hong Kong

ABSTRACT

This paper presents a framework for evaluation of ride comfort of road vehicles running on a cable-stayed bridge under crosswind. A road vehicle is idealised as a combination of a number of rigid bodies connected by a series of springs and dampers. A cable-stayed bridge is modelled using the conventional finite element approach taking into account the geometric nonlinearity. The vertical roughness of bridge deck surface is assumed to be a zero-mean stationary Gaussian random process. The wind forces acting on the bridge include mean wind force, buffeting force, and self-exciting force. The equations of motion of a coupled vehicle-bridge system under crosswind are then established using a fully computerised approach and solved using a direct integration method. The ride comfort of the vehicle in both vertical and lateral directions is evaluated in accordance with the ISO 2631. The numerical computation taking a real cable-stayed bridge and high-sided road vehicles as an example is performed, and extensive parametric studies are carried out to assess the effects of vehicle speed and road roughness on the ride comfort of the road vehicles.

KEYWORDS

Ride comfort, Road vehicle, Cable-stayed bridge, Crosswind, Road roughness, Numerical computation

INTRODUCTION

There have been many long span cable-stayed bridges built throughout the world in recent years to carry high-speed heavy road vehicles. Heavy road vehicles running on a long span cable-stayed bridge may significantly change local dynamic behaviour and affect fatigue life of the bridge. The vibration of the bridge may in turn affect the ride comfort of road vehicles in addition to the effects of road surface roughness. If such a long span cable-stayed bridge is built in wind prone area, the ride comfort of road vehicles running on an oscillating cable-stayed bridge subjected to crosswind is of great concern, for it will greatly affect the fatigue and handling performance of the driver and the safety of the vehicle.

Most of the previous studies focus only on the ride comfort of road vehicles running on the ground other than a long span cable-stayed bridge subjected to crosswind. Wang and Hu (1998) suggested an

www.EngineeringEBooksPdf.com

approach in the frequency domain for assessing the ride comfort of a truck-full trailer running on the ground of various road surface conditions. The effects of crosswind on ride comfort of road vehicles were not considered. The ride comfort was evaluated in terms of the acceleration responses at the location of driver seat and the human comfort criteria. Various human comfort criteria have been proposed and implemented to assess the ride comfort of the driver. Wang and Hu (1988) adopted the comfort criteria stipulated in the International Standard Organization ISO 2631 (1978), which offers the specifications for ride comfort of the driver in both vertical and lateral directions.

This paper presents a framework for evaluation of ride comfort of road vehicles running on a long span cable-stayed bridge subjected to crosswind. A road vehicle is idealised as a combination of a number of rigid bodies connected by a series of springs and dampers. A cable-stayed bridge is modelled using the conventional finite element approach taking into account the geometric nonlinearity. The vertical roughness of bridge deck surface is assumed to be a zero-mean stationary Gaussian random process. The wind forces acting on the bridge include mean wind force, buffeting force, and self-exciting force. The equations of motion of a coupled vehicle-bridge system under gust wind are established using a fully computerised approach and solved using a direct integration method (Guo and Xu, 2001). The ride comfort of the vehicle in both vertical and lateral directions is evaluated in accordance with the ISO 2631 in terms of the root mean square (RMS) accelerations at the driver seat in the form of one-third octave band spectrum. The numerical example using a real cable-stayed bridge and high-sided road vehicles is provided. Extensive parametric studies are carried out to assess the effects of vehicle speed and road roughness on the ride comfort of high-sided road vehicles.

MODELLING OF ROAD VEHICLE

The trucks that frequently run on cable-stayed bridges are taken as typical high-sided road vehicles investigated in this study. A truck model comprises 5 rigid bodies: one for the truck body, two for the front axle set, and two for the rear axle set (Fig. 1). Each rigid body in the either the front axle set or the rear axle set is connected to the truck body through two suspension units. It is assumed that the truck runs at a constant velocity over the bridge and thus the vibration of the truck in the X-direction is not considered. The truck body is assigned five degrees of freedom with respect to its gravity centre: the vertical displacement (Z_v), the lateral displacement (Y_v), the rotation about the Y-axis (pitch angle θ_v), the rotation about the X-axis (roll angle ϕ_v), and the rotation about the Z-axis (yaw angle φ_v). Each rigid body in either the front axle set or the rear axle set is assigned two degrees of freedom in the Z-direction (Z_{si}) and the Y-direction (Y_{si}). The total degrees of freedom of one truck are thus 13.

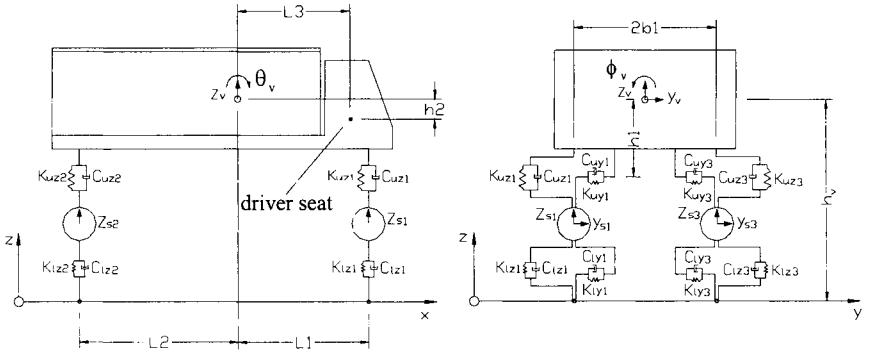

Figure 1: Truck model

www.EngineeringEBooksPdf.com

MODELLING OF CABLE-STAYED BRIDGE ANF ROAD ROUGHNESS

A real long span cable-stayed bridge is taken as an example investigated in this study. The concerned triple-tower cable-stayed bridge has an overall length of 1,177m with the two main spans measured at 475m and 448 m and the two side spans of 127 m each (Fig. 2). The three bridge towers are all single leg concrete towers. The bridge deck is separated into two carriageway structures, and each carriageway structure is formed by two longitudinal steel plate girders (Fig. 3). The cross-girders are extended at 13.5m intervals to link the two separated carriageway structures. A three-dimensional dynamic finite element model is established for the bridge. The modal analysis of the bridge shows that the natural frequencies of the bridge are spaced very closely. The fundamental frequencies in the lateral, vertical, and torsional directions are 0.216 Hz, 0.189 Hz, and 0.387 Hz, respectively. In predicting dynamic response of the coupled road vehicle and cable stayed bridge system under crosswind, the damping ratios of the bridge are taken as 1%.

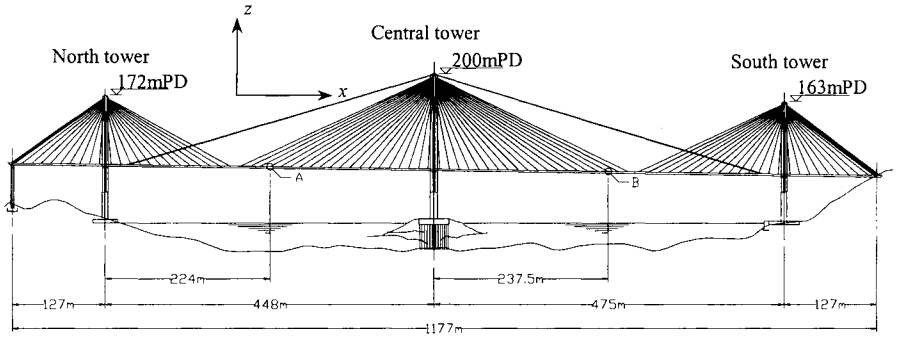

Figure 2: Configuration of long span cable-stayed bridge

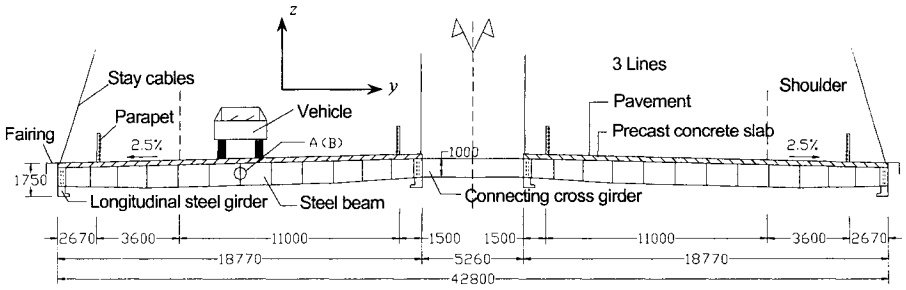

Figure 3: Typical deck cross section of bridge

Many investigations have shown that the road roughness is an important factor that affects the ride comfort of vehicles. The bridge deck surface roughness is assumed as a zero-mean stationary Guassian random process in this study, which can be generated through an inverse Fourier transform from a given power spectrum of road roughness.

WIND FORCES ON CABLE-STAYED BRIDGE AND ROAD VEHICLE

This study concerns the normal operation condition of road vehicles running on a cable-stayed bridge under crosswind. The tires of a road vehicle remain in contact with the bridge deck at all times and there is no sideslip or overturning of the vehicle. The three major components of the wind force acting on the bridge deck are included in the dynamic analysis: the steady-state force due to mean wind, the

www.EngineeringEBooksPdf.com

buffeting force due to wind turbulence, and the self-excited force due to aeroelastic interaction between motion of bridge and wind velocity. The time-histories of lateral and vertical wind fluctuating components, u(t) and w(t), at the various position of the bridge deck are generated based on a fast spectral representation method proposed by Cao et al (2000). In consideration of the compatibility with the wind forces acting on the bridge deck and the complex nature of the problem investigated, the aerodynamic wind forces acting on the road vehicle are determined using the quasi-steady approach (Baker 1986; Coleman and Baker 1990).

EQUATIONS OF MOTION OF SYSTEM

The use of the fully computerized approach(Guo and Xu, 2001) can easily lead to the equations of motion of coupled road vehicle and stayed-cable bridge system under crosswind in the following form, established from the static equilibrium position of the system.

$$\begin{bmatrix} \mathbf{M}_b + \mathbf{M}_{bbv} & 0 \\ 0 & \mathbf{M}_v \end{bmatrix} \begin{Bmatrix} \ddot{\mathbf{v}}_b \\ \ddot{\mathbf{v}}_v \end{Bmatrix} + \begin{bmatrix} \mathbf{C}_b + \mathbf{C}_{bbv} & \mathbf{C}_{bv} \\ \mathbf{C}_{vb} & \mathbf{C}_{v1} + \mathbf{C}_{v2} \end{bmatrix} \begin{Bmatrix} \dot{\mathbf{v}}_b \\ \dot{\mathbf{v}}_v \end{Bmatrix} + \begin{bmatrix} \mathbf{K}_b + \mathbf{K}_{bbv} & \mathbf{K}_{bv} \\ \mathbf{K}_{vb} & \mathbf{K}_{v1} + \mathbf{K}_{v2} \end{bmatrix} \begin{Bmatrix} \mathbf{v}_b \\ \mathbf{v}_v \end{Bmatrix} = \begin{Bmatrix} \mathbf{P}_{bvg} + \mathbf{P}_{bvr1} + \mathbf{P}_{bvr2} + \mathbf{P}_{bvr3} + \mathbf{P}_{bw} \\ \mathbf{P}_{vvr2} + \mathbf{P}_{vvr3} + \mathbf{P}_{vw} \end{Bmatrix} \tag{1}$$

In Eq. (1), $\mathbf{v}_b, \dot{\mathbf{v}}_b, \ddot{\mathbf{v}}_b$ are the nodal displacement, velocity, and acceleration vectors of the bridge, respectively; $\mathbf{v}_v, \dot{\mathbf{v}}_v, \ddot{\mathbf{v}}_v$ are the displacement, velocity, and acceleration vectors of the vehicles, respectively. The matrix $\mathbf{M}_{bbv}$ is related to the inertia forces of all the masses of the vehicles at the contact points due to the bridge accelerations. The matrix $\mathbf{M}_v$ corresponds to the inertia forces of all the rigid bodies of the vehicles, excluding the masses at the contact points. The inertia forces of all the masses of the vehicles at the contact points due to the road surface roughness constitute the force vector $\mathbf{P}_{bvr1}$. For the dampers of which the relative velocities are the function of the degrees of freedom of the vehicles only, the damper forces lead to the matrix $\mathbf{C}_{v1}$. For the dampers connected to the contact points, their relative velocities depend on not only the degrees of freedom of the vehicles but also the degrees of freedom of the bridge and the deck surface roughness. As a result, the coupled damping matrices $\mathbf{C}_{bv}$ and $\mathbf{C}_{vb}$, the additional damping matrix $\mathbf{C}_{bbv}$ to the bridge damping matrix $\mathbf{C}_b$, the additional damping matrix $\mathbf{C}_{v2}$ to the vehicle damping matrix $\mathbf{C}_{v1}$, the additional force vector on the bridge $\mathbf{P}_{bvr2}$ due to the deck surface roughness, and the additional force vector on the vehicles $\mathbf{P}_{vvr2}$ due to the deck surface roughness are generated. Similarly, for the springs of which the relative displacements are the function of the degrees of freedom of the vehicles only, the spring forces lead to the matrix $\mathbf{K}_{v1}$. From the springs connected to the contact points, the stiffness matrices $\mathbf{K}_{bv}, \mathbf{K}_{vb}, \mathbf{K}_{bbv}, \mathbf{K}_{v2}$ and the additional force vectors due to deck surface roughness $\mathbf{P}_{bvr3}$ and $\mathbf{P}_{vvr3}$ are constituted. The external forces on the bridge due to the gravity forces of the vehicles are denoted by the force vector $\mathbf{P}_{bvg}$. $\mathbf{P}_{bw}$ is the total wind force vector on the bridge deck and it is the sum of the mean wind force, the buffeting force, and the self-excited force. $\mathbf{P}_{vw}$ is the wind force vector on the vehicles.

RIDE COMFORT

Several vibration criteria are in use for defining human tolerance to whole-body vibration. The International Standard Organisation (ISO) 2631 (1978) may be one of the most popular criteria used in practice. The ISO 2631 takes the form of root mean square (RMS) acceleration spectra in one-third octave band. The RMS acceleration of the driver seat of the vehicle at a given central frequency f_c in one-third octave band can be determined by:

www.EngineeringEBooksPdf.com

$$\ddot{v}_{1/3-RMS} = [\int_{f_l}^{f_u} S_{\ddot{v}\ddot{v}}(f)df]^{1/2} \quad (2)$$

where $S_{\ddot{v}\ddot{v}}(f)$ is the acceleration power spectral density function at the driver seat; f_u is the $2^{1/6} f_c$ upper band frequency; and f_l are the $2^{-1/6} f_c$ lower band frequency. Therefore, the RMS values of vertical and lateral accelerations of the vehicle at the driver seat in one-third octave band can be computed and compared with the reduced comfort boundaries proposed in the ISO 2631 to evaluate the ride comfort.

NUMERICAL RESULTS

In the case study, a traffic flow consisting of five identical trucks arranged in line at interval of 10 meters is considered to run on the bridge. The first two natural frequencies of the truck in the lateral direction are 0.980Hz and 1. 184 Hz while the first two natural frequencies in the vertical direction are 1.806Hz and 3.291Hz, respectively. The equations of motion of the system are a set of coupled second order differential equations with time-vary coefficients. The Wilson-θ method is thus used in this study, and the θ value and the time interval used in the computation are 1.4 and 0.01 second, respectively. To eliminate the effect of suddenly applied wind forces on the dynamic response of the truck, the first truck is positioned at 200m away from the end of the bridge deck as an initial position in the computation, but only the dynamic response of the truck running on the bridge deck is used for evaluation of ride comfort and for calculation of standard deviation responses. The computation lasts until the last truck leaves the bridge deck without wind forces acting on it.

Ride Comfort

Displayed in Fig. 4 are the vertical and lateral RMS accelerations of the truck at the driver seat in the form of one-third octave band for different vehicle speeds. The mean wind speed perpendicular to the bridge and truck is 10m/s. The bridge deck surface in the vertical direction is assumed to be in good condition as specified in the ISO. The roughness of the bridge deck surface in the lateral direction is not considered because of lack of information. The allowable values from the ISO comfort criteria in the vertical and lateral directions are also plotted in Fig.4 for 1 hour, 16 minutes and 1 minute, respectively. It is seen that the RMS accelerations of the truck increase slightly with the increase of vehicle speed in either direction. The ride comfort of the truck satisfies the criteria at all vehicle speed levels concerned, in particular in the lateral direction.

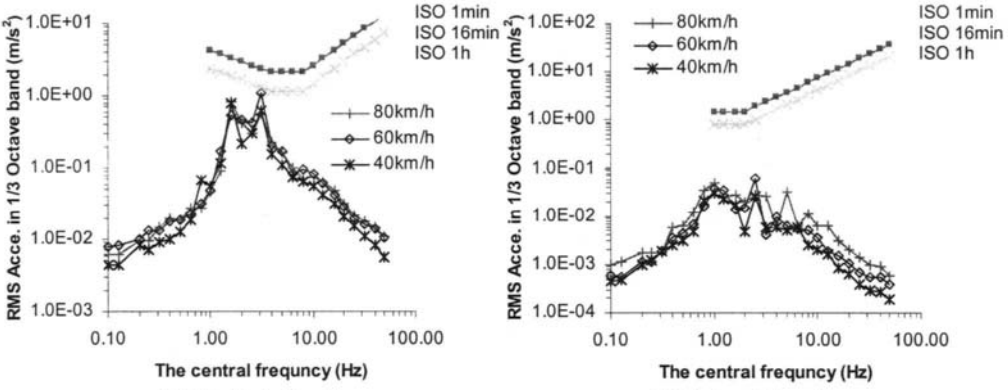

Figure 4: RMS accelerations of vehicle at the driver seat in 1/3 octave band for different vehicle speed

www.EngineeringEBooksPdf.com

The standard deviations of the vertical, lateral and rotational acceleration of the truck at the driver seat for different vehicle speeds and road conditions are listed in Table 1. It is seen that the standard deviation of lateral acceleration increases considerably with the increase of vehicle speed. However, the standard deviations of vertical and rotational acceleration do not increase always with the increase of vehicle speed. Moreover, the road roughness affects the vertical response of the truck only.

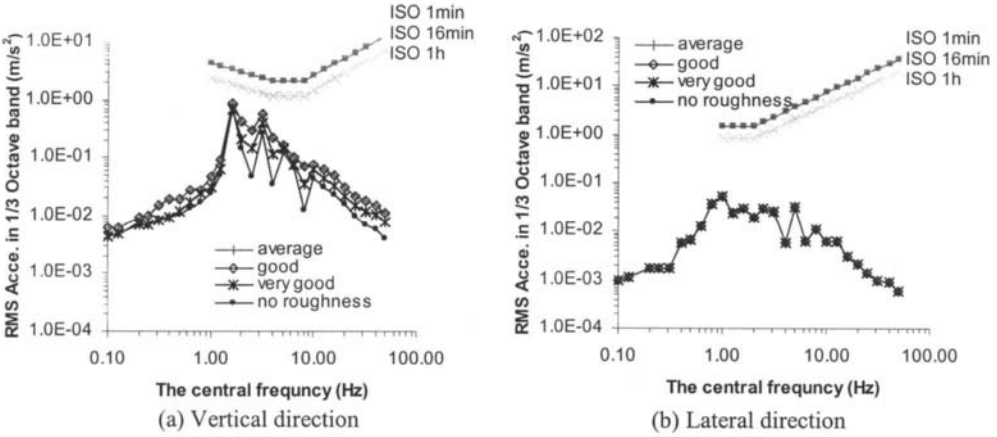

Figure 5: RMS accelerations of truck at the driver seat in 1/3 octave band for different road conditions

Displayed in Fig. 5 are the vertical and lateral RMS accelerations of the truck at the driver seat in the 1/3 octave band for different road conditions (the ISO road class: average, good, very good, no roughness). The vehicle speed is 80km/h and the mean crosswind speed is 10m/s. It is seen that the ride comfort in all the cases is within not only the 1minute comfort limit but also in the 16 minutes and 1 hour comfort limits, as stipulated in the ISO 2631. The vertical RMS accelerations vary with road condition as expected. The vertical road roughness has no effect on the lateral RMS acceleration.

TABLE 1
The Standard Deviation Acceleration Responses of Truck for Different Vehicle Speeds and Road Conditions

	Speed (km/h) (Road class: good)			ISO road class (Vehicle speed: 80km/h)			
	40	60	80	average	good	very good	no roughness
$\sigma_{\ddot{Z}_{VS}}$ (m/s^2)	1.1108	1.4327	1.1820	1.8867	1.1820	0.8582	0.8052
$\sigma_{\ddot{Y}_{VS}}$ (m/s^2)	0.0557	0.0877	0.0940	0.0940	0.0940	0.0940	0.0940
$\sigma_{\ddot{\phi}_{VS}}$ (rad/s^2)	0.0097	0.0178	0.0153	0.0154	0.0153	0.0153	0.0153

Suspension Travel

The suspension travel is also an important parameter if the design of the truck should be improved to meet the human comfort criteria. The vertical suspension travel of the front and rear suspension of the vehicle can be determined as follows:

$$d_{u1} = Z_v - L_1\theta_v - b_1\phi_v - Z_{s1} \qquad d_{u2} = Z_v + L_2\theta_v - b_1\phi_v - Z_{s2} \tag{3}$$

$$d_{u3} = Z_v - L_1\theta_v + b_1\phi_v - Z_{s3} \qquad d_{u4} = Z_v + L_2\theta_v + b_1\phi_v - Z_{s4} \tag{4}$$

www.EngineeringEBooksPdf.com

Listed in Table 2 are the standard deviations of suspension travel at the four wheel-sets at different vehicle speeds. The mean wind speed perpendicular to the bridge and truck is 10m/s. The vertical bridge deck surface is assumed to be in good condition. It is seen that the standard deviations of the suspension travel of the windward wheel-sets (1 and 3) are larger than those of the leeward wheel-sets in general, but it is not certain that as the increase of vehicle speed, the standard deviations of the suspension travel increase. Table 2 also shows the standard deviations of suspension travel at the four wheel-sets for different road conditions. The vehicle speed used is 80km/h and the mean wind speed is 10m/s. It is seen that the standard deviations of suspension travel of the windward wheel-sets are larger than those of the leeward wheel-sets. As expected, the better the road surface condition, the lower the standard deviations of the suspension travel.

TABLE 2
The Standard Deviations of Suspension Travel for Different Vehicle Speeds and Road Conditions

	Speed (km/h) (Road class: good)			ISO road class (Vehicle speed: 80km/h)			
	40	60	80	average	good	very good	no roughness
σ_{du1} (m)	0.0024	0.0021	0.0026	0.0033	0.0026	0.0021	0.0021
σ_{du2} (m)	0.0019	0.0018	0.0016	0.0024	0.0016	0.0013	0.0013
σ_{du3} (m)	0.0025	0.0022	0.0021	0.0031	0.0021	0.0016	0.0016
σ_{du4} (m)	0.0018	0.0020	0.0022	0.0027	0.0022	0.0019	0.0019

Dynamic Contact Forces

The contact forces are related to the safety of the running vehicle. The vertical contact forces between the ith tire and the deck surface can be obtained as

$$F_{ci} = M_{ci}\ddot{Z}_{ci} + C_{lzi}(\dot{Z}_{ci} - \dot{Z}_{si}) + K_{lzi}(Z_{ci} - Z_{si}) + F_{Gi} \qquad (i=1,2,\cdots,4) \tag{5}$$

$$F_{Gi} = M_v g\frac{L_2}{2(L_1+L_2)} + (M_{si}+M_{ci})g \qquad (i=1,3) \tag{6}$$

$$F_{Gi} = M_v g\frac{L_1}{2(L_1+L_2)} + (M_{si}+M_{ci})g \qquad (i=2,4) \tag{7}$$

where F_{Gi} (i=1,2,$\cdots$,4) is the external force on the ith tire due to the gravity of the vehicle; and g is the acceleration of gravity.

TABLE 3
The Standard Deviations of Vertical Contact Forces for Different Vehicle Speeds and Road Conditions

	Speed (km/h) (Road class: good)			ISO road class (Vehicle speed: 80km/h)			
	40	60	80	average	good	very good	no roughness
σ_{fc1} (m)	1.8067	2.1898	1.9902	2.8373	1.9902	1.5995	1.5813
σ_{fc2} (m)	1.7234	2.3623	1.4943	2.6375	1.4943	1.0787	0.8954
σ_{fc3} (m)	1.9306	2.1948	1.9492	2.7969	1.9492	1.4830	1.4677
σ_{fc4} (m)	1.6492	2.5893	1.6427	2.7160	1.6427	1.2555	1.1214

Listed in Table 3 are the standard deviations of vertical contact forces for different vehicle speeds. The mean wind speed is 10m/s, and the vertical deck surface is assumed to be in good condition. It is seen that the standard deviations of the contact forces do not increase always with the increase of the vehicle speed. Table 3 also shows the standard deviations of vertical contact forces for different road

www.EngineeringEBooksPdf.com

conditions, in which the vehicle speed used is 80km/h and the mean wind speed is 10m/s. It is seen that the standard deviations of vertical contact forces on the front axle are higher than the rear axle. The standard deviations of vertical contact forces on the windward side are higher than those on the leeward side. As expected, the better the road surface condition, the lower the standard deviations of the vertical contact forces.

CONCLUSIONS

A framework for evaluation of the ride comfort of road vehicles moving through a long span cable-stayed bridge under crosswind has been established. This includes the modelling of high-sided road vehicles and long span cable-stayed bridge, the simulation of the random roughness of the bridge deck, the simulation of the buffeting force and self-exciting force on the bridge deck, the estimation of the crosswind force on the road vehicle, and the evaluation of human tolerance to whole-body vibration. The equations of motion of the coupled road vehicle-bridge system under crosswind were assembled using a fully computerized approach. The dynamic responses of both the bridge and the vehicle were determined in the time domain using the direct integration method, by which the standard deviation responses and contact forces of the vehicle components and the power spectral density functions of dynamic responses could be computed through the statistics and the Fourier transform. The root mean square values of the accelerations of the vehicle at the driver seat expressed as a function of frequency in the one-third octave band were further obtained and compared with the comfort criteria stipulated in the ISO 2631. The case study demonstrate that the proposed framework can be used to investigate the dynamic interaction among the vehicle, bridge, and crosswind and to evaluate the ride comfort of road vehicles running on a long span bridge subjected to crosswind. The numerical results from the case study also show that the truck concerned satisfies the comfort criteria stipulated in the ISO 2631. In general, the better the road surface condition, the lower the dynamic response and contact force. However, the dynamic response and contact force may not increase with the increasing vehicle speed.

ACKNOWLEDGMENTS

The writers are grateful for the financial support from the Research Grants Council of Hong Kong through a RGC grant (5027/98E) to the second writer and Drs. Richard Charles & Esther Yewpick Lee Charitable Foundation through a scholarship to the first writer.

REFERENCES

Wang B.T. and Hu P.I. (1998) The assessment of the ride quality of a truck-full trailer combination. *Heavy Vehicle Systems, Int. J. of Vehicle Design,* **5:3/4,** 208-235.

Guo W.H. and Xu Y.L. (2001) Fully computerized approach to study cable-stayed bridge-vehicle interaction. *Journal of Sound and Vibration,* **248:4,** 745-761.

ISO (1978) Guide for the evaluation of human exposure to whole-body vibration. 2nd edition, International Standard 2631-1978(E), International Organization for Standardization.

Coleman S.A. and Baker C.J. (1990) High Sided Road Vehicles in Cross Winds, *Journal of Wind Engineering and Industrial Aerodynamics*, **36:1-3,** 1383-1392.

Baker C.J. (1986) A Simplified Analysis of Various Types of Wind-Induced Road Vehicle Accidents, *Journal of Wind Engineering and Industrial Aerodynamics*, **22:1,** 69-85.

Cao Y. H., Xiang H.F., and Zhou Y. (2000) Simulation of Stochastic Wind Velocity Field on Long-Span Bridges, *Journal of Engineering Mechanics, ASCE,* **126:1**, 1-6.

www.EngineeringEBooksPdf.com

Advances in Steel Structures, Vol. II
Chan, Teng and Chung (Eds.)
© 2002 Elsevier Science Ltd. All rights reserved.

COMPARISON OF BUFFETING RESPONSE OF A SUSPENSION BRIDGE BETWEEN ANALYSIS AND AEROELASTIC TEST

Y.L. Xu, D.K. Sun, and K.M. Shum

Department of Civil and Structural Engineering, The Hong Kong Polytechnic University, Kowloon, Hong Kong, China

ABSTRACT

Full bridge aeroelastic model tests are often carried out as a final confirmation of the satisfactory behaviour of an important long suspension bridge. Such a model test can provide detailed information on structural responses such as displacement, acceleration, and bending moment at many locations on bridge deck and towers. However, the conventional frequency domain buffeting analysis yields mainly displacement and acceleration responses of bridge deck. It seldom renders internal forces of bridge deck as well as tower and cable responses. In this paper, an improved analytical approach is used to perform a fully coupled buffeting analysis of a suspension bridge, directly rendering internal forces and tower and cable responses. The analytical results are then compared with those from the full aeroelastic model test of the bridge. It turns out that the improved analytical approach can reasonably estimate not only displacement and acceleration responses but also bending moment, torsional moment and shear force responses of three major bridge components.

KEYWORDS

Buffeting analysis, suspension bridge, full aeroelastic model test, overall comparison

INTRODUCTION

While both theoretical analysis and wind tunnel simulation test of long suspension bridges have advanced to a sophisticated stage, there remain a number of issues that are yet to be fully resolved. One of them refers to an overall comparison between buffeting analysis and full aeroelastic model test. Full aeroelastic model tests are often carried out nowadays for important suspension bridges to observe aerodynamic and aeroelastic behaviour of the bridge model under a well-simulated wind environment. The complex interactions between bridge components and between various modes of vibration are included in such model tests (Irwin 1992). With a careful design and construction and instrumentation of the bridge model, the buffeting responses, including not only displacement and acceleration but also bending moment, of a prototype bridge can be estimated at many locations on bridge deck and towers.

The analytical method for the estimation of buffeting response of long suspension bridges in the frequency domain, which originated in the works of Scanlan and Sabzevari (1967), has evolved in the

www.EngineeringEBooksPdf.com

last ten years to include the contributions from multi-modes and inter-modes of vibration, the effects of aerodynamic admittance and lateral flutter derivatives, and others (e.g. Jones et al. 1998). Although this approach is very sophisticated, the buffeting responses of bridge towers and cables and the interaction between three major bridge components cannot be directly estimated. Also because this approach is built upon the random theory-based mode superposition method, the estimation of internal force responses of bridge deck, such as bending moment and shear force, is time consuming and the accuracy of the results significantly depends on higher order derivatives of mode shapes. Thus, it is difficult to make an overall comparison between buffeting analysis and full aeroelastic model test.

In this connection, a fully coupled three-dimensional buffeting analysis of long suspension bridges, featured mainly by a combination of finite element approach and a pseudo-excitation method, was presented by the writers (Sun et al. 1999) as an improvement to the currently used analytical approach in the frequency domain. The improved analytical approach is used in this paper to perform a fully coupled buffeting analysis of a long suspension bridge with emphasis on the comparison of different types of responses between buffeting analysis and full aeroelastic model test. A brief introduction to the improved approach is given first. Followed are the presentations of the main features and dynamic characteristics of the bridge, the wind environment, and the aerodynamic and aeroelastic parameters used in the comparison. The computed responses are finally compared with the full aeroelastic test results at many locations on bridge deck and towers.

METHODOLOGY AND THEORY

The following is a brief introduction to the improved analytical method for the estimation of fully coupled buffeting response of long span cable supported bridges (Sun et al. 1999). The advantages of using this method are to readily handle the bridge deck with significantly varying structural properties and wind parameters along the deck, to make good use of the finite element bridge models that are already made for the static and eigenvalue analyses, to naturally include intermode and multimode responses, and to determine buffeting responses including internal forces of the bridge deck, towers and cables at the same time.

The equation of motion of the whole bridge for buffeting analysis can be expressed as

$$\mathbf{M}\ddot{\mathbf{Y}}(t) + \mathbf{C}\dot{\mathbf{Y}}(t) + \mathbf{K}\mathbf{Y}(t) = \mathbf{R}\mathbf{P}(t) \tag{1}$$

in which $\mathbf{Y}(t)$ is the total nodal displacement vector of N dimensions including the bridge deck, towers, cables, and other components; $\mathbf{M}$ is the NxN total mass matrix; $\mathbf{C}$ is the NxN total damping matrix which consists of both aeroelastic damping matrix $\mathbf{C}_s^{ae}$ and structural damping matrix $\mathbf{C}_s^{s}$; $\mathbf{K}$ is the NxN total stiffness matrix combining the aeroelastic stiffness matrix $\mathbf{K}_s^{ae}$ with the structural stiffness matrix $\mathbf{K}_s^{s}$; $\mathbf{P}$ is the total aerodynamic loading vector of m dimensions (in general, m << N) for the bridge deck, towers, cables, and other components; and $\mathbf{R}$ is the N x m matrix consisting of 0 and 1, which expands the m dimensional loading vector into the N dimensional loading vector.

The system aeroelastic stiffness matrix $\mathbf{K}_s^{ae}$ and the system aeroelastic-damping matrix $\mathbf{C}_s^{ae}$ are assembled from the element aeroelastic stiffness matrices $\mathbf{K}_i^{ae}$ and the element aeroelastic damping matrices $\mathbf{C}_i^{ae}$, respectively. The total aerodynamic loading vector can be obtained by

$$\mathbf{P} = \sum_{i}^{n} \mathbf{T}_i \mathbf{P}_{i,e}^{b} \tag{2}$$

where $\mathbf{T}_i$ is the co-ordinate transformation matrix for the ith element with the dimensions equal to the dimension of the system nodal force vector times 12 for a beam element or 6 for a cable element; $\mathbf{P}_{i,e}^{b}$ can be either the aerodynamic force vector of the deck element or the tower element or the cable element

www.EngineeringEBooksPdf.com

in local co-ordinate; and n is the total number of the elements subject to wind loading. The spectral density function matrix of the nodal buffeting forces acting on the whole bridge in the global co-ordinate system is

$$\mathbf{S}_{pp}(\omega)=\mathbf{T}\begin{bmatrix} \mathbf{S}^{e}_{p_1p_1}(\omega) & \mathbf{S}^{e}_{p_1p_2}(\omega) & \cdots & \mathbf{S}^{e}_{p_1p_n}(\omega) \\ \mathbf{S}^{e}_{p_2p_1}(\omega) & \mathbf{S}^{e}_{p_2p_2}(\omega) & \cdots & \mathbf{S}^{e}_{p_2p_n}(\omega) \\ \vdots & \vdots & \ddots & \vdots \\ \mathbf{S}^{e}_{p_np_1}(\omega) & \mathbf{S}^{e}_{p_np_2}(\omega) & \cdots & \mathbf{S}^{e}_{p_np_n}(\omega) \end{bmatrix}\mathbf{T}^{T} \tag{3}$$

where $\mathbf{T}=\left[\mathbf{T}_1,\mathbf{T}_2,\cdots\mathbf{T}_i,\cdots\mathbf{T}_n\right]$; the superscript T means the transposition of a matrix; and $\mathbf{S}^{e}_{p_ip_j}(\omega)$ is the cross-spectral density function matrix of the nodal buffeting forces acting on the ith and jth elements. A pseudo-excitation algorithm is used to determine the spectral density function matrix of buffeting responses. The advantages of this method include the less computation effort required, the retention of all cross-correlation terms between normal modes (the complete quadratic combination (CQC) method), and the feasibility for the determination of random internal force responses. The spectral density function matrix $\mathbf{S}_{PP}(\omega)$ is usually a symmetric matrix, and thus this excitation spectral matrix can be decomposed as

$$\mathbf{S}_{PP}(\omega)=\mathbf{L}^{*}\mathbf{D}\mathbf{L}^{T}=\sum_{k=1}^{m}d_{kk}\mathbf{L}_k^{*}\mathbf{L}_k^{T} \tag{4}$$

in which $\mathbf{L}$ is the lower triangular matrix ; $\mathbf{D}$ is the diagonal matrix; $\mathbf{L}_k$ is the k-th column of $\mathbf{L}$; and d_{kk} is the k-th diagonal element of $\mathbf{D}$. The pseudo excitations can then be constituted as follows:

$$\mathbf{f}_k=\mathbf{L}_k\exp\left(i\omega\ t\right)\qquad\left(k=1,2,\ldots,m\right) \tag{5}$$

For each pseudo-excitation (harmonic excitation) vector, a pseudo displacement response vector, $\mathbf{Y}_k(\omega)$, can be easily and traditionally determined by

$$\mathbf{Y}_k=\mathbf{H}(\omega)\mathbf{R}\mathbf{f}_k \tag{6}$$

$$\mathbf{H}(\omega)=\left[-\omega^2\mathbf{M}+i\omega\mathbf{C}+\mathbf{K}\right]^{-1} \tag{7}$$

The response vector of pseudo internal forces at nodes, $\mathbf{F}_k(\omega)$, including bending moment and torsional moment and shear force, can be also readily obtained by

$$\mathbf{F}_k=\mathbf{K}_s^{s}\mathbf{Y}_k \tag{8}$$

The spectral density function matrices of the displacement and internal force responses of the bridge can be then proved to be

$$\mathbf{S}_{YY}(\omega)=\sum_{k=1}^{m}d_{kk}\mathbf{Y}_k^{*}\mathbf{Y}_k^{T} \tag{9}$$

$$\mathbf{S}_{FF}(\omega)=\sum_{k=1}^{m}d_{kk}\mathbf{F}_k^{*}\mathbf{F}_k^{T} \tag{10}$$

www.EngineeringEBooksPdf.com

Because the above equation involves one summation only, much less computation efforts are needed to calculate the response spectral density matrix. In particular, the internal force response spectral matrices can be readily obtained in parallel to the displacement and acceleration response spectral matrices. The standard deviations of the displacement, velocity, acceleration, internal forces at the node can be readily computed according to the random vibration theory after the auto spectral density functions for each node are determined.

EXAMPLE SUSPENSION BRIDGE

Main Features of Bridge

A real suspension bridge recently built in China is selected for the comparison of buffeting analysis with full aeroelastic mode test. The bridge has a main span of 1,377 m and two side spans of 300 m and 355 m in the east and west, respectively (see Fig.1). The height of the towers is 206 m, and the two main cables are 36 m apart in the north and south. The bridge deck is a hybrid steel structure continuing between the two main anchorages. It is suspended by suspenders in the main span and the side span in the west. On the east side span the deck is supported by three piers.

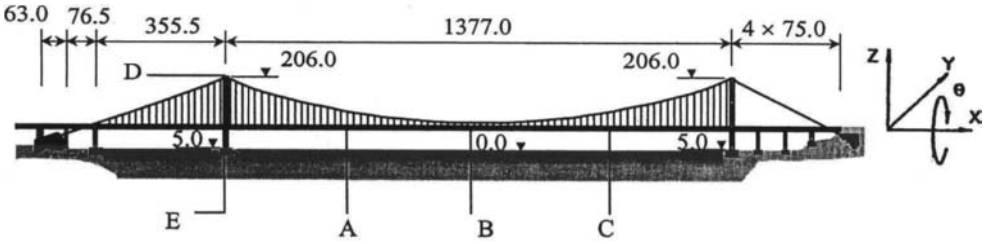

Measurement locations: A-first quarter span; B-midspan; C-third quarter span; D-west tower top; E-west tower base.

Figure 1. Elevation of bridge and wind tunnel measurement locations

Dynamic Characteristics of Bridge

A three-dimensional dynamic finite element model was established and verified against the field measurements by the writers (Xu et al. 1997). The modal analysis of the bridge showed that the natural frequencies were spaced very closely. The first 60 natural frequencies range from 0.068 Hz to 0.888 Hz only. The lowest frequency is 0.068 Hz, corresponding to the first lateral mode. The first vertical mode is almost antisymmetric in the main span at a natural frequency of 0.117 Hz while the second vertical mode is almost symmetric in the main span at a natural frequency of 0.137 Hz. The first torsional mode occurs at a natural frequency of 0.271 Hz in a half wave in the main span. The modal damping ratios measured from the bridge model tested in the wind tunnel are used in the theoretical analysis. All other modal damping ratios, which were not measured from the aeroelastic model tests, are taken as 0.5% in the theoretical analysis.

Wind Environment

The mean wind profile, turbulence intensity profile, and auto-spectra of longitudinal and vertical components of wind used in the theoretical analysis are set to those simulated in the wind tunnel for a low turbulence exposure. The logarithmic law is used to fit the mean speed profile measured in the test.

www.EngineeringEBooksPdf.com

The turbulence intensity profile is fitted by the function stipulated in ESDU (1985). The auto- spectra of longitudinal and vertical components of wind measured in the test are fitted by von Karman spectra. The auto spectrum of lateral component of wind, which was not measured in the test but used in the theoretical analysis, is also von Karman spectrum. The cross spectrum at a single point is estimated by using that suggested in ESDU (1985). The cross spectra between two points used in the analysis are obtained by using the exponential coherence function with the spectra $S_u(n)$, $S_v(n)$, $S_w(n)$, and $S_{uw}(n)$, respectively.

Aerodynamic and Aeroelastic Parameters

The aerodynamic force coefficients of the bridge deck measured from wind tunnel tests are used in the analysis. The drag, lift, and moment coefficients are 0.135, 0.090 and 0.063, respectively, at the wind incidence of 0^o with respect to the deck width of 41 m. The first derivatives of the drag, lift, and moment coefficients with respect to wind incidence at the wind incidence of 0^o are -0.253, 1.324, and 0.278, respectively. As for the aerodynamic admittance, the formula suggested by Davenport (1962) for drag is used in the analysis. The aerodynamic admittance for either lift or moment is taken as unity in the analysis. For the two bridge towers, the drag coefficient is taken as 1.5 with respect to the tower width of 9.25 m. The lift and moment coefficients for the towers as well as the first derivatives of the drag, lift and moment coefficients are not available to the writers. For the main cables, force coefficients critically depend on the Reynold's number and cable surface roughness. Conservatively, the drag coefficient of 1.0 is chosen for the cable diameter of 1.1 m.

The flutter derivatives of the bridge deck corresponding to the 0^o wind incidence without traffic and trains are used, but only the eight flutter derivatives H_i^* and A_i^* (i =1,2,3,4) were measured from the wind tunnel tests. By fitting the wind tunnel test results, the eight flutter derivatives related to vertical and torsional motions are used in the analysis. The reference width of the deck used in the tests was half the width of the deck, i.e., B/2=20.5m. When the mean wind speed at the deck level used in the analysis is above 35m/s, the flutter derivatives are extrapolated following clear trends of the curves. Flutter derivatives associated with drag force were not measured from the wind tunnel tests. The quasi-static approximations suggested by Scanlan (1987) are used in the analysis. To maintain a high spectral resolution in the interested frequency range and to avoid a poor estimate of response from numerical integration, a frequency interval about 0.00006 Hz is used within the range from 0.043 Hz to 0.950 Hz. This frequency range covers the first 60 modes of vibration of the bridge.

COMPARISONS

The full bridge aeroelastic model tests provide displacement, acceleration and bending moment standard deviation responses at several locations on the bridge deck and the west tower (see Fig.1). The peak responses are taken as 3.5 times the standard deviation responses. The results are presented as the function of mean wind speed at the deck level. To compare with the test results, the buffeting responses of the bridge are computed for the mean wind speeds at the deck level of 20m/s, 40m/s, 60m/s and 80 m/s. The computed results contain the contributions from the first 60 modes of vibration including intermode contributions. There are two cases considered in the theoretical analysis: wind excitation on the bridge deck only, and wind excitations on the whole bridge including the towers and cables.

Bridge Deck

Figs. 2a, 2b, and 2c show the peak responses of lateral, vertical, and torsional displacements of the bridge deck at the mid-main span, respectively. It is seen that the computed vertical peak displacement responses are in good agreement with the test results. The computed vertical responses for the case where wind excitation acts on the bridge deck only are almost the same as those for the case where buffeting forces act on the whole bridge. The computed torsional peak displacement responses are also

www.EngineeringEBooksPdf.com

compatible with the measured results at wind speed of 40 m/s and 60 m/s. The effects of buffeting forces on the towers and cables are not significant for the torsional displacement responses of the bridge deck. The computed lateral peak displacement responses, particularly for the case where the buffeting forces act on the whole bridge, are larger than the measured results for higher wind speeds. The inclusion of buffeting forces on towers and cables increases the lateral displacement response of the bridge significantly. This increase is almost due to the aerodynamic forces on main cables. The reasons for the difference between the computed results and measured results of lateral displacement responses need further investigation.

Figs. 3a, 3b, and 3c exhibit the peak responses of lateral bending moment (about the z- axis), vertical bending moment (about the y- axis), and torsional moment (about the x-axis) of the bridge deck at the first quarter main span, respectively. For the peak lateral bending moment response, the computed results are larger than the measured results even though the buffeting forces on the towers and cables are neglected for wind speed greater than 40 m/s. For the vertical peak bending moment response, the computed results are in good agreement with the measured results. For the peak torsional moment response, again the computed results match the measured results quite well.

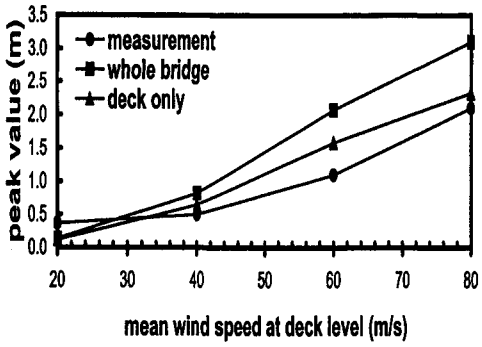

(a) lateral displacement response

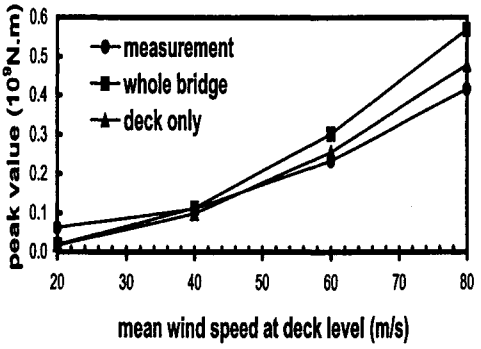

(a) lateral bending moment

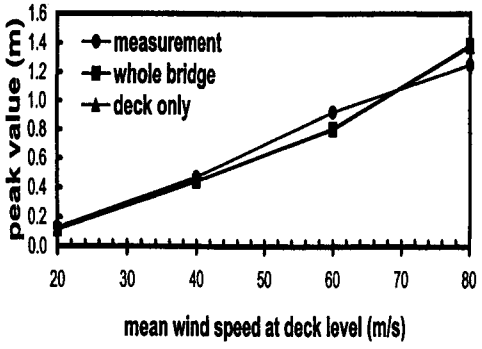

(b) vertical displacement response

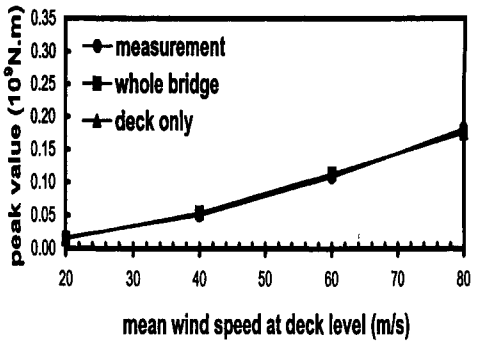

(b) Vertical bending moment

www.EngineeringEBooksPdf.com

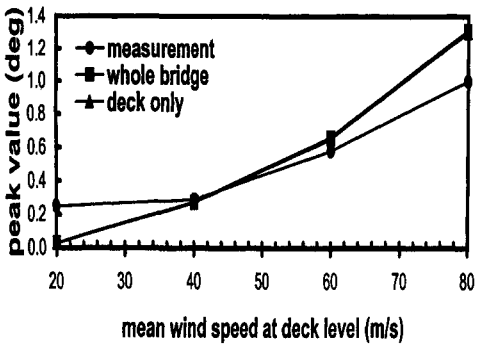

(c) torsional displacement response

Figure 2. Comparison of peak displacement responses of bridge deck at mid-span

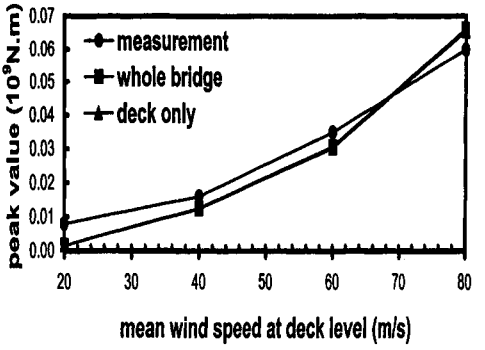

(c) torsional moment

Figure 3. Comparison of peak moments of bridge deck at 1st quarter span

Bridge Tower

Figs. 4a and 4b display the peak responses of alongwind bending moment (about the x-axis) and crosswind bending moment (about the y-axis) of the front leg of the west tower at the base. The computed peak alongwind bending moment responses with the excitation on the whole bridge match the measured results quite well. The computed responses with the excitation on the bridge deck only are significantly smaller than the measured responses in most cases. The computed peak crosswind bending moment responses are in reasonable agreement with the full aeroelastic model test results for wind speeds of 20m/s, 40m/s and 60m/s, but not for 80 m/s.

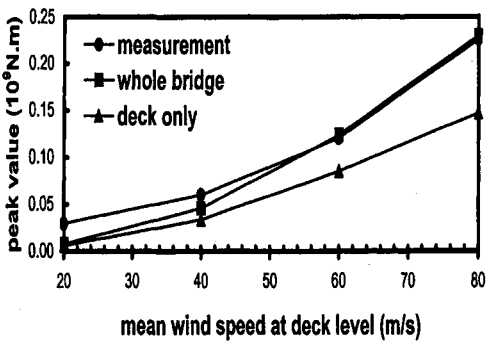

(a) alongwind bending moment

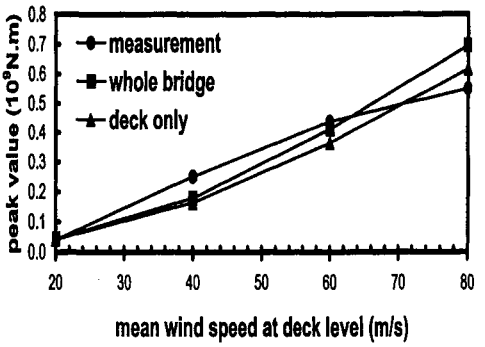

(b) crosswind bending moment

Figure 4. Comparison of peak bending moments of west tower at top

CONCLUSIONS

The fully coupled buffeting analysis of a long suspension bridge has been carried out in this paper using an improved analytical method in the frequency domain. The computed displacement, acceleration, bending moment, and torsional moment responses of both bridge deck and towers were compared with the results measured from full aeroelastic model tests. The results show that the analytical method used

www.EngineeringEBooksPdf.com

in this paper can reasonably estimate not only displacement and acceleration responses but also bending and torsional moment responses of both bridge deck and towers. The results also reveal the significant interaction between the bridge deck and bridge towers and main cables. It should be noted that though the present method can estimate different types of responses of three major bridge components, there still remain some differences between the analytical and measured results, in particular in the lateral direction. It is the writers' wish that the numerical results presented in this paper will be validated through a comparison with field measurement data in near future.

ACKNOWLEDGMENTS

The writers are grateful for the financial supports from the Hong Kong Research Grant Council through a UGC grant (CERG 5027/98E) to the first writer. The support from the relevant authorities to allow the writers to access the aeroelastic test report and other materials for academic purpose only is particularly appreciated. Any opinions and conclusions presented in this paper are entirely those of the writers.

References

Davenport, A.G. (1962). Buffeting of a suspension bridge by storm winds. *J. Struct. Div., ASCE,* **88**, 233-268.

ESDU (1985). Characteristics of atmospheric turbulence near the ground. Part 2: single point data for strong winds (neutral atmosphere). *Item No. 85020. ESDU International*, London.

Irwin, P.A. (1992). Full aeroelastic model tests. *Aerodynamics of Large Bridges*, A.Larsen (ed.), Balkema, Rotterdam, Netherlands, 99-117.

Jones, N.P., Scanlan, R.H., Jain, A., and Katsuchi, H. (1998). Advances (and challenges) in the prediction of long-span bridge response to wind. *Bridge Aerodynamics*, Larsen & Esdahl (eds), Balkema, Rotterdam, Netherlands, 59-85.

Scanlan, R.H. (1987). Interpreting aeroelastic models of cable-stayed bridges. *J. Eng., Mech., ASCE*, **113:4**, 555-575.

Scanlan, R. H. and Sabzevari, A. (1967). Suspension bridge flutter revisited. *Struct. Eng. Conf., ASCE,* Seattle, Washington, America.

Sun, D.K., Xu, Y.L., Ko, J.M. and Lin, J.H. (1999). Fully coupled buffeting analysis of long span cable-supported bridges: formulation. *Journal of Sound and Vibration*, **228 :3**, 569-588.

Xu, Y.L, Ko, J.M. and Zhang, W.S. (1997). Vibration studies of Tsing Ma suspension Bridge. *J. Bridge Engrg.*, ASCE, **3:4**, 149-156.

www.EngineeringEBooksPdf.com

Advances in Steel Structures, Vol. II
Chan, Teng and Chung (Eds.)
© 2002 Elsevier Science Ltd. All rights reserved.

DYNAMIC RESPONSE OF THE CABLE TO MOVING MASS

GUO YANLIN[1] WANG HONG[1] REN GEXUE[2]

[1]Department of Civil Engineering, Tsinghua University,
Beijing, 100084, CHINA
[2] Department of Engineering Mechanics, Tsinghua University,
Beijing, 100084, CHINA

ABSTRACT

The objective of this paper is to present a numerical study of the transient vibrations of a taut cable on which a moving mass moves at a constant speed. Based on the finite element package named ANSYS, a nonlinear finite element method is employed to analyze such a cable-mass time-varying structure. The dynamic vibration behavior of the cable-mass time-varying structure is emphasized, and the influence of some important parameters, such as the moving mass weight and velocity, the initial tension forces in the cables, is theoretically investigated in this paper. The numerical results obtained indicate that the variety of the cable mid-span deflection and maximum tension force is dependant on the moving mass velocity. The results obtained also show that the proposed analysis method can be used to predict correctly and efficiently the dynamic response of the cable-mass time-varying structural system.

KEYWORDS

Cable-mass structure, time-varying structure, dynamic response, nonlinearity, dynamic magnify factor

INTRODUCTION

Vibrations of cable structures with and without moving mass have been the subjects of many studies. Smith (1964) outlined his analytical works to investigate the dynamic behavior of a stretched string carrying a moving mass that travels along the string at constant velocity. Analytical solutions for the vibrations of the stretched string due to moving load are carried out but the interaction of string and mass is not considered in his analysis.

www.EngineeringEBooksPdf.com

Rodeman et al. (1975) analyzed the dynamic response of an infinitely long ideal cable due to the motion of the attached mass. Their results show that the dynamics of the system can be significantly affected by the inertia of the moving mass.

In this study, the objective is to present a numerical study of the transient vibrations of a taut cable on which a moving mass moves at a constant speed. The nonlinear dynamic vibration behavior of the cable-mass time-varying structure on which the moving mass moves is investigated theoretically, and the influence of some important parameters such as the moving mass weight, the initial tension force in the cable and the moving mass velocity, involved in the analysis.

ANALYSIS METHOD FOR TIME-VARYING STRUCTURE

The general nonlinear dynamic equilibrium equation of the cable-mass time-varying structure is:

$$M(t)\cdot\ddot{U}(t)+C\cdot\dot{U}(t)+F(U,t)=P(t)$$

Comparing with the classic structure, the distinct characteristic of the time-varying structure is that the mass matrix in the equation is variety with the variety of time. Because the location of the moving mass in the cable is varying with the variety of time, the cable-mass structure is a typically time-varying structure. Also, with the cable structure, the effect of the geometric nonlinearity of the cable element should be considered in the analysis.

Based on a finite element package named ANSYS, the cable element (Link10) and the mass element (Mass21) are employed to perform the dynamic analysis of the cable-mass time-varying structure, with considering the geometric nonlinearity. It is noted that the birth and death characteristic of the mass element in ANSYS is activated to trace cable behavior at any time in the vibration process.

VERIFY THE METHOD

To check the method mentioned above, a simply supported beam to moving mass is studied, and the obtained results are compared with that by using other method. The beam to moving mass is shown in figure 1.

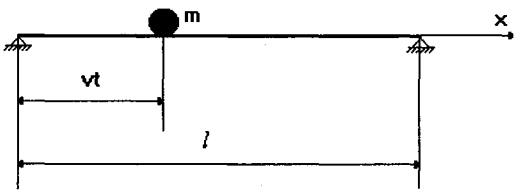

Figure 1: Simply supported beam to moving mass

Structural parameters

the beam span: L=16m.

www.EngineeringEBooksPdf.com

the beam line density: $\rho=9.36\times10^3$kg/m.

the beam bending stiffness: $EI=2.05\times10^{10}$Nm^2.

Loading

The moving mass weight: $M=6.38\times10^4$kg.

The moving mass velocity is selected as V_1=60km/h and V_2=160km/h respectively.

Results and comparison

The mid-span deflections of the beam from the REN (1993) and from this study are shown in the figure 2 and figure 3 respectively. The results obtained show that the both are in a good agreement each other. Hence, the analysis method developed in this paper is verified to be correct and it can be used to predict correctly the dynamic response of the time-varying structure.

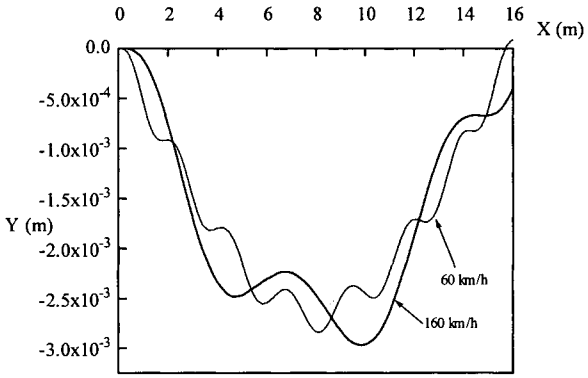

Figure 2: Results from the REN (1993)

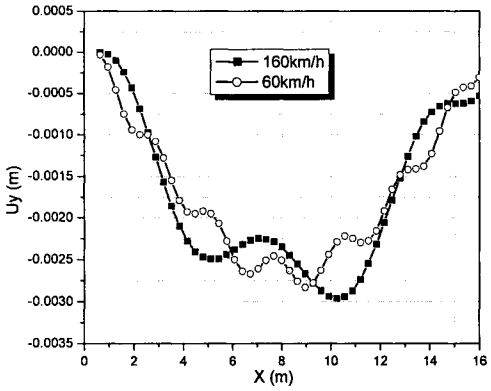

Figure 3: Results obtained in this study

www.EngineeringEBooksPdf.com

PARAMETER STUDIES OF CABLE-MASS STRUCTURE

The influence of three parameters of the cable-mass structure on its dynamical behavior, such as the moving mass weight, the initial tension force in cables and the moving mass velocity, is studied here. Figure 4 shows the cable-mass structure on which a mass moves at a constant speed. Here, the dynamic magnify factor of the mid-span deflection of the cable is denoted by DU and the maximum stress of the cable denoted by DS as:

$$DU = \frac{U_d}{U_s} \quad \text{and} \quad DS = \frac{\sigma_{d\max}}{\sigma_{s\max}}$$

Where U_d and U_s is the maximum mid-span deflection with and without considering the dynamic effect; $\sigma_{d\max}$ and $\sigma_{s\max}$ is the maximum stress of the cable with and without considering the dynamic influence.

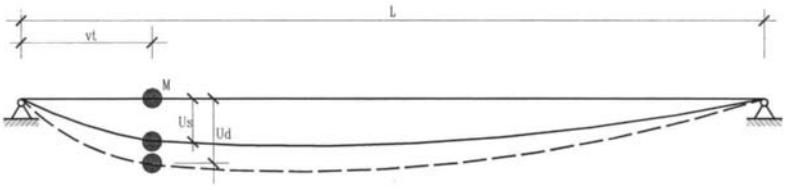

Figure 4: The cable-mass structure

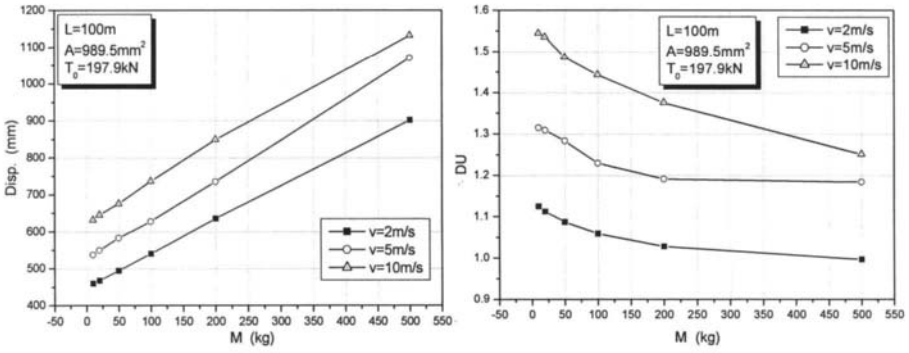

Figure 5: The mid-span deflection and DU in the cable

Effect of the moving mass weight

Six different moving mass weights, 10kg, 20kg, 50kg, 100kg, 200kg and 500kg are chosen to investigate the influence of the moving mass weight on the dynamic response of the cable-mass structure. The corresponding response and dynamic magnify factors obtained have been plotted in Figure 5 and figure 6 respectively. Obviously, the deflection and the stress in the cable increase linearly with the increase of the moving mass weight. But the DU, a dynamic magnify factor of the

www.EngineeringEBooksPdf.com

deflections, is decrease nonlinearly, and DS, a dynamic magnify factor of the stress, is increase nonlinearly, where the same initial tension in the cable keep unchanged. The results obtained also show that the dynamic effect for the deflection is larger than that for the stress.

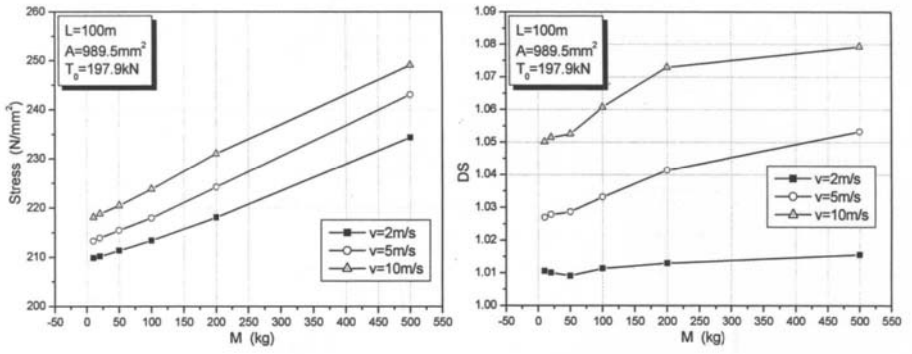

Figure 6: The maximum stress and DS in the cable

Effect of the initial tension in cable

Five different initial tension forces in the cable, namely 9.9kN, 49.75kN, 98.95kN, 197.9kN and 494.75kN, are considered. It is found from figure 7 and figure 8 that by increasing the initial tension force in the cable its mid-span deflection can reduce greatly, but it also leads to the stress increase in the cable. The dynamic magnify factors in the deflection behaves as decreasing nonlinearly for the moving mass weight above 100 kg, but it exhibits almost unchanged below 100kg. The possible reason for it is that the deflection is from the effective controlling due to a large initial tension stress. The dynamic magnify factors in the stress decreases nonlinearly significantly for the initial tension force below 200kN, and it deceases slowly above 200kN.

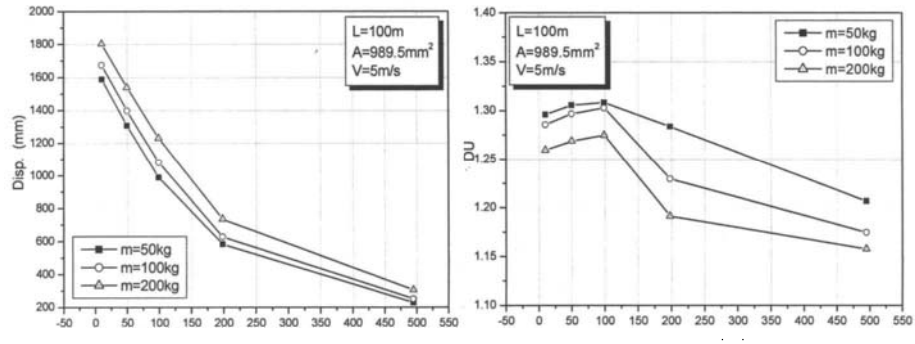

Figure 7: The mid-span deflection and DU in the cable

www.EngineeringEBooksPdf.com

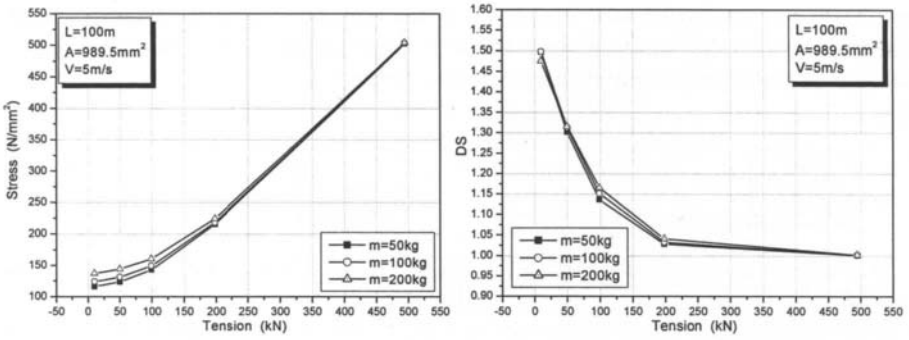

Figure 8: The maximum stress and *DS* in the cable

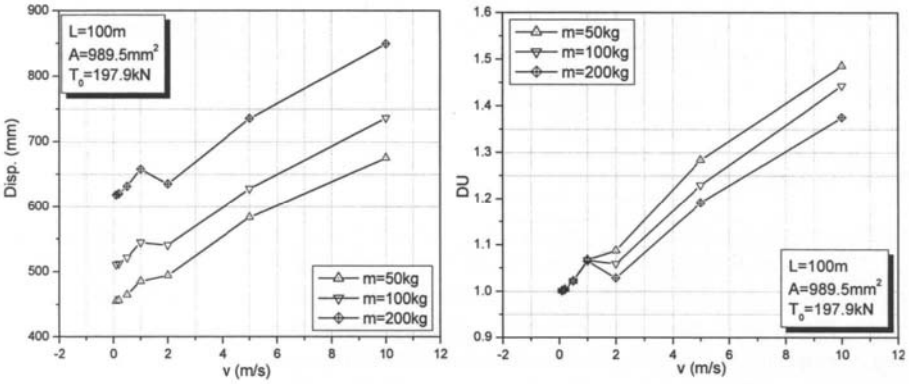

Figure 9: The mid-span deflection and *DU* of the cable

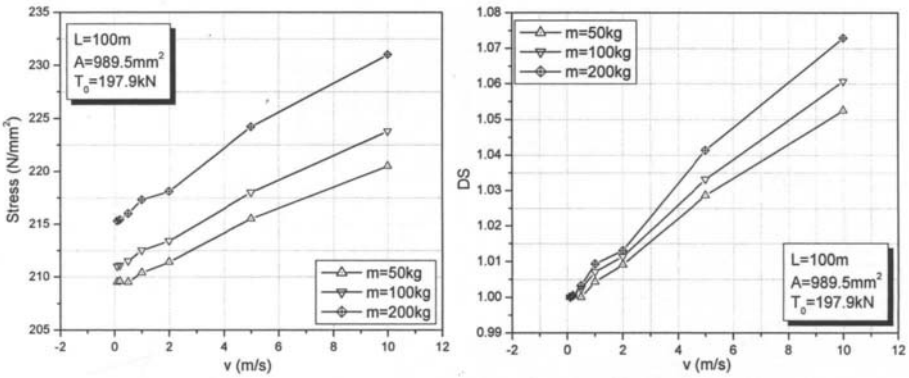

Figure 10: The maximum stress and *DS* in the cable

Effect of the velocity of the moving mass

Six different velocity of the moving mass are considered, that is, 0.2m/s, 0.5m/s, 1m/s, 2m/s, 5m/s and

www.EngineeringEBooksPdf.com

10m/s. The results obtained are shown in the figure 9 and figure 10. With decreasing the moving mass velocity, all the responses of the structure will be amplified greatly. The deflection and the stress increase linearly with the increase of the moving mass velocity. The dynamic magnify factor of deflection and stress display the same increase trend.

CONCLUSION

Based on the finite element package named ANSYS, a nonlinear finite element method is presented to analyze the dynamic response of the cable-mass time-varying structure. The influence of three important parameters, the weight of the moving mass, the initial tension force in the cable and the velocity of the moving mass, is theoretically investigated. The numerical results obtained indicate that the dynamic effect of the moving mass is very significant especially for the structural deflection. Increasing the initial tension force in the cable can greatly reduce the deflection of the structure, but leads to a large increase of the stress of the cable. Numerical studies reach a conclusion that the proposed analysis method can be used to predict correctly the dynamic response of the cable-mass time-varying structure.

ACKNOWLEDGEMENTS

The work reported here was supported by the knowledge innovation project of the Chinese Academy of Science (CAS).

REFERENCES

Smith, C.E., 1964. Motions of a stretched string carrying a moving mass particle. J. Applied Mech. 31, 29-37.

Forrestal, M.J., Bickel, D.C., Sagartz, M.J., 1975. Motion of a stretched cable with small curvature carrying an accelerating mass. AIAA J. 13, 1533-1535.

REN Gexue, 1993. Numerical methods for large scale undamped gyroscopic eigenvalue problems. Ph.D. dissertation of Tsinghua University. Beijing, CHINA.

www.EngineeringEBooksPdf.com

This Page Intentionally Left Blank

www.EngineeringEBooksPdf.com

Advances in Steel Structures, Vol. II
Chan, Teng and Chung (Eds.)
© 2002 Elsevier Science Ltd. All rights reserved.

TRAFFIC-INDUCED MICROVIBRATION MITIGATION OF HIGH TECH EQUIPMENT INSIDE A BUILDING USING PASSIVE/ACTIVE PLATFORM

Z.C. Yang[1] and Y.L. Xu[2]

[1]Department of Aircraft Engineering, Northwestern Polytechnical University, Xi'an, China
[2] Department of Civil and Structural Engineering, The Hong Kong Polytechnic University, Kowloon, Hong Kong, China

ABSTRACT

This paper investigates the possibility of using a passively or actively controlled platform to isolate a batch of high tech equipment from microvibration of the floor of a building subject to nearby traffic-induced ground motion. The governing equations of motion of the coupled platform-actuator-building system with actively controlled platform are derived in terms of the absolute coordinate to facilitate the feedback control. The performance evaluation of the platform is based on the BBN Vibration Criteria with the absolute velocity being targeted. A hybrid control system composed of passive mounts and active hydraulic actuators with a sub-optimal control algorithm is designed to actively control the platform. Hydraulic actuator dynamics are also considered in the modeling of the control system to avoid possible instability of the platform. The performance of actively controlled platform is assessed through comparisons with the cases of the building without control, the building with passively controlled platform. Simulation results indicate that passively controlled platform can be effective in reducing microvibration of high tech equipment if the parameters are properly selected. The actively controlled platform is superior to the passively controlled platform in terms of its high performance and robustness.

KEYWORDS

Microvibration, high tech equipment, actively controlled platform, passively controlled platform, traffic-induced ground motion, suboptimal control, actuator dynamics

INTRODUCTION

High tech equipment requires the building floor, on which the high tech equipment is directly installed, with extremely limited vibrations. For instance, the BBN vibration criteria [1-2] stipulate that the root mean square (rms) velocity of vibration sensitive high tech equipment should be limited from $50\mu m/sec$ to $3\mu m/sec$ within a frequency range between 8 Hz and 80 Hz. This stringent micro-scale velocity restriction makes the control of microvibration of high tech equipment inside a building subject to traffic-induced ground motion different from the control of seismic response of building structures.

www.EngineeringEBooksPdf.com

Using passive mounts (spring-damper systems) to isolate individual high tech equipment from floor vibration, which is taken as a direct base excitation, is a very common practice [3-5]. However, microvibration reduction level using passive mounts is always limited due to the nature of passive control. It is also not sufficient and economic for a large building with a great amount of high tech equipment as evidenced in many modern high tech facilities.

Recently, Yang and Agrawal [6] carried out an extensive theoretical study on the possible use of various protective systems for microvibration control of high tech facilities under horizontal traffic-induced ground motion in consideration of dynamic interaction between control system and building. The protective systems that they investigated included passive building base isolation, hybrid building base isolation, passive floor isolation, hybrid floor isolation, active control system, and passive energy dissipation system. They concluded that hybrid floor isolation could be the most effective and practical means in satisfying the design specification for microvibration of high tech equipment. Since the governing equation of motion of the building with protective systems was established in terms of relative motion to the ground, the controller was designed based on the drift and relative velocity of the floor isolator in their investigations. The use of relative velocity as feedback to control the absolute velocity of the floor may not be consistent. Furthermore, actuator dynamics were not considered in their modeling of the problem.

High tech equipment is often installed on part of the building floor such as clean rooms for semiconductor circuits manufacturing. This paper aims to investigate the possibility of isolating a batch of high tech equipment from microvibration disturbance induced by nearby traffic using actively controlled platform. The governing equations of motion of the coupled platform-actuator-building system are derived in terms of the absolute coordinate to facilitate the feedback control and performance evaluation of the platform based on the BBN vibration criteria with the absolute velocity being targeted. A hybrid control system composed of passive mounts and active hydraulic actuators with a sub-optimal control algorithm is designed to actively control the platform. The performance of actively controlled platform is assessed through comparisons with the cases of the building without control and the building with passively controlled platform.

FORMULATION IN ABSOLUTE COORDINATE

Let us consider a three-story shear building. Suppose that the building is subjected to traffic-induced horizontal ground motion (see Fig.1 (a)) and a horizontal platform is installed on the first primary floor of the building using either a passive mount (spring-damper system), as shown in Fig.1 (b), or a hybrid control system composed of a passive spring-damper system and an active hydraulic actuator, as shown in Fig. 1(c). It is noted that a batch of high tech equipment is installed on the platform for the cases shown in Figs.1 (b) and 1(c), but it is mounted on the first primary floor of the building for the case shown in Figs.1 (a).

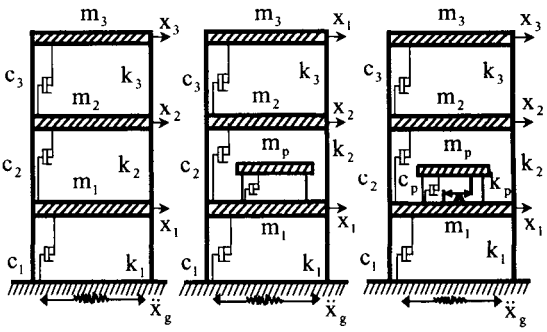

Fig.1 Building Models
(a) Plain building (b) Building with passive platform
(c) Building with active platform

Equation of motion of building without control

Microvibration control performance is assessed in terms of the absolute velocity of the platform for the cases shown in Figs. 1(b) and (c), and the absolute velocity of the first primary floor for the case shown in

www.EngineeringEBooksPdf.com

Fig. 1(a). For the building without any control device (see Fig. 1(a)), the equation of motion of the building under ground motion can be written as

$$\begin{bmatrix} m_1 & & \\ & m_2 & \\ & & m_3 \end{bmatrix}\begin{Bmatrix} \ddot{x}_1 \\ \ddot{x}_2 \\ \ddot{x}_3 \end{Bmatrix}+\begin{bmatrix} c_1+c_2 & -c_2 & \\ -c_2 & c_2+c_3 & -c_3 \\ & -c_3 & c_3 \end{bmatrix}\begin{Bmatrix} \dot{x}_1 \\ \dot{x}_2 \\ \dot{x}_3 \end{Bmatrix}+\begin{bmatrix} k_1+k_2 & -k_2 & \\ -k_2 & k_2+k_3 & -k_3 \\ & -k_3 & k_3 \end{bmatrix}\begin{Bmatrix} x_1 \\ x_2 \\ x_3 \end{Bmatrix}=\begin{Bmatrix} c_1 \\ 0 \\ 0 \end{Bmatrix}\dot{x}_g+\begin{Bmatrix} k_1 \\ 0 \\ 0 \end{Bmatrix}x_g \quad (1)$$

where m_i, k_i, c_i (i=1, 2, 3) are the mass, stiffness coefficient, and damping coefficient of the *i*th floor (*i*=1, 2, 3); x_i (i=1, 2, 3) is the absolute displacement of the *i*th floor (*i*=1,2,3); and x_g and $\dot{x}_g$ are the displacement and velocity of traffic-induced horizontal ground motion, respectively.

Equation of motion of building with passive/active platform

For the building with actively controlled platform shown in Fig. 1(c), the equation of motion of the coupled platform-building system can be written as

$$\begin{bmatrix} m_1 & & & \\ & m_2 & & \\ & & m_3 & \\ & & & m_p \end{bmatrix}\begin{Bmatrix} \ddot{x}_1 \\ \ddot{x}_2 \\ \ddot{x}_3 \\ \ddot{x}_p \end{Bmatrix}+\begin{bmatrix} c_1+c_2+c_p & -c_2 & & -c_p \\ -c_2 & c_2+c_3 & -c_3 & \\ & -c_3 & c_3 & \\ -c_p & & & c_p \end{bmatrix}\begin{Bmatrix} \dot{x}_1 \\ \dot{x}_2 \\ \dot{x}_3 \\ \dot{x}_p \end{Bmatrix}+\begin{bmatrix} k_1+k_2+k_p & -k_2 & & -k_p \\ -k_2 & k_2+k_3 & -k_3 & \\ & -k_3 & k_3 & \\ -k_p & & & k_p \end{bmatrix}\begin{Bmatrix} x_1 \\ x_2 \\ x_3 \\ x_p \end{Bmatrix}=\begin{Bmatrix} -f \\ 0 \\ 0 \\ f \end{Bmatrix}+\begin{Bmatrix} c_1 \\ 0 \\ 0 \\ 0 \end{Bmatrix}\dot{x}_g+\begin{Bmatrix} k_1 \\ 0 \\ 0 \\ 0 \end{Bmatrix}x_g \quad (2)$$

where m_p, k_p, and c_p are the mass, stiffness coefficient, and damping coefficient of the platform; x_p is the absolute displacement of the platform; and f is the control force generated by the hydraulic actuator. From the fundamental work of DeSilva [8], and experimental studies of Dyke et al. [7], the dynamic model for linear hydraulic actuator is expressed as:

$$\dot{f}=\frac{2\beta}{V}[A_0 k_q \gamma(u-x)-k_c f-A_0^2\dot{x}] \quad (3)$$

where $A_0, V, \beta, \gamma, k_q$ and k_c are specific parameters of the actuator; x is the displacement of the actuator and should be replaced by the drift of platform $(x_p - x_1)$ when incorporated into Eq. (2); u is the input displacement command of the actuator valve; and f is the actuating force of the actuator. The equation of motion of the coupled platform-actuator-building system can be expressed in state space as

$$\{\dot{z}\}=[A]\{z\}+\{B\}u+\{E_1\}\dot{x}_g+\{E_2\}x_g \quad (4)$$

where $\{z\}=\{x_1\ x_2\ x_3\ x_p\ \dot{x}_1\ \dot{x}_2\ \dot{x}_3\ \dot{x}_p\ f\}^T$ is the state vector of the coupled system; $[A]_{9\times9}=[a_{ij}]$ is the state matrix; $\{B\}_{9x1}$ is the control vector; and $\{E_1\}_{9x1}$ and $\{E_2\}_{9x1}$ are the two influence vectors related to the ground motion. It is noted that when the control force vector is deleted in Eq. (2), it becomes the governing equation of motion for the building with passively controlled platform as shown in Fig.1 (b).

Control algorithm

It is seen from Eq. (4) that the control force f is involved in the state vector of the coupled system and the control quantity is the displacement command u associated with the actuator valve. In the practice of control, it is necessary to replace the state vector {z} by an incomplete state measurement vector {y} for

www.EngineeringEBooksPdf.com

easy implementation of the control, leading to so-called sub-optimal control [9]. To obtain the desired small absolute velocity and drift of the platform, the measurement vector {y} should be chosen as

$$\{y\} = \{x_p - x_1 \quad \dot{x}_p\}^T = [C]\{z\} \tag{5}$$

where $[C] = \begin{bmatrix} -1 & 0 & 0 & 1 & 0 & 0 & 0 & 0 & 0 \\ 0 & 0 & 0 & 0 & 0 & 0 & 0 & 1 & 0 \end{bmatrix}$ is called the measurement matrix.

Using the minimum norm method of the sub-optimal control theory [9], one may have the sub-optimal displacement demand u determined by

$$u = -[F]\{y\} \tag{6}$$

where

$$[F] = [K][C]^T([C][C]^T)^{-1} \tag{7}$$

in which [K] is the optimal feedback matrix determined by minimizing the performance function

$$J = \frac{1}{2}\int_0^\infty (\{z\}^T[Q]\{z\} + uRu)dt \tag{8}$$

subject to the constraint of Eq. (4). The scalar R is the positive weighting factor for the displacement demand u, and the matrix [Q] is the positive semi-definite weighting matrix for the state vector {z}.

TRAIN-INDUCED GROUND DISTURBANCE

A modified Kanai-Tajimi power spectral density with an envelope function is suggested by Yang and Agrawal [6], to represent train-induced uniformly modulated non-stationary random horizontal ground disturbance encountered by high tech facilities.

$$S_{\ddot{x}\ddot{x}}(\omega) = \frac{[1 + 4\zeta_{g1}^2(\omega/\omega_{g1})^2](\omega/\omega_{g2})^2 s_0^2}{\{[1-(\omega/\omega_{g1})^2]^2 + 4\zeta_{g1}^2(\omega/\omega_{g1})^2\}\{[1-(\omega/\omega_{g2})^2]^2 + 4\zeta_{g2}^2(\omega/\omega_{g2})^2\}} \tag{9}$$

$$\psi(t) = \begin{cases} t^2/t_1^2 & 0 < t \le t_1 \\ 1 & t_1 < t \le t_2 \\ (t_f - t)^2/(t_f - t_2)^2 & t_2 < t \le t_f \end{cases} \tag{10}$$

where ω_{g1}, ζ_{g1}, ω_{g2} and ζ_{g2} are the ground motion parameters; s_0 is the ground acceleration intensity to be selected to match the measured ground acceleration; and t_f is the time duration of the ground acceleration. The parameters in Eqs. (9) and (10) used for the present work are the same as used by Yang and Agrawal [6] in their study: $\omega_{g1} = 6\text{Hz}$; $\omega_{g2} = 35\text{Hz}$; $\zeta_{1g} = 0.58$; $\zeta_{2g} = 0.45$; $t_1 = 5$ sec.; $t_2 = 10$ sec.; and $t_f = 15$ sec. The parameter s_0 is chosen such that the peak ground acceleration is 7.18 gals.

As described above, the time histories of ground displacement and velocity rather than ground acceleration are needed for simulation studies. Thus, velocity and displacement time histories are obtained by integrating the acceleration time history, but this process will create shift in velocity and displacement time histories. To solve this problem, a high pass digital filter with 1Hz threshold, which is much lower than the first natural frequency of the building, is applied to the acceleration time history before integration. The effectiveness of this treatment is verified by examining the responses of a SDOF benchmark building model subjected to the same ground motion and calculated using both absolute and

www.EngineeringEBooksPdf.com

relative coordinates. Figs. 2(a), 2(b) and 2(c) display the simulated time histories of the ground acceleration, velocity and displacement, respectively.

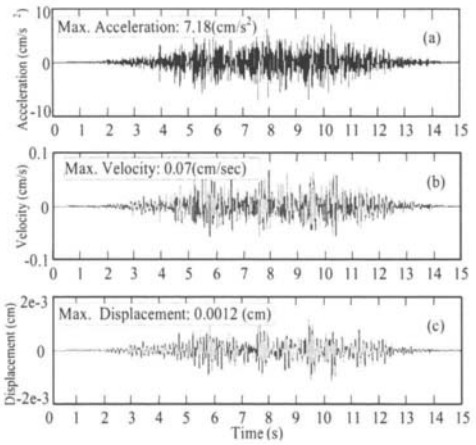

Fig.2 Train-Induced Ground Motion
(a) Time history of ground acceleration
(b) Time history of ground velocity
(c) Time-history of ground displacement

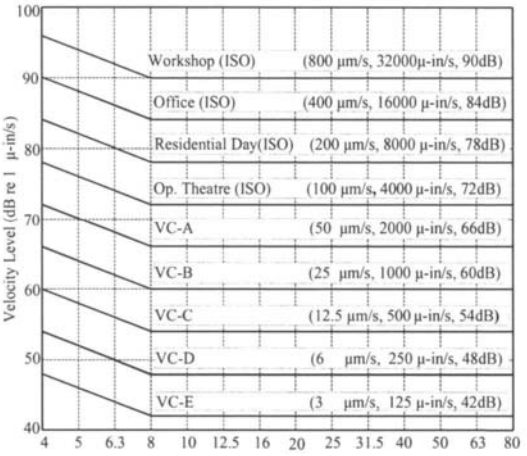

Fig.3 BBN Vibration Criteria for High Tech Equipment

BBN VIBRATION CRITERIA FOR HIGH TECH EQUIPMENT

The BBN (Bolt Beranek & Newman) vibration criteria (BBN VC) may be one of the most popular criteria used for microvibration control of high tech equipment in practice [1-2]. The criteria take the form of a set of one-third octave band velocity spectrum curves labeled by VC-A to VC-E, as shown in Fig.3. The spectrum is actually the root mean square (rms) velocity converted from the velocity time history in the one-third-octave band expressed in dB referenced to 1μ-inch/sec. To use the BBN VC, any velocity response time history $\dot{x}(t)$ should be converted into its one-third octave band velocity spectrum values $\dot{X}_{1/3}(n_c)$ by its Fourier transform $X(n)$ [6] using the following equation.

$$\dot{x}_{1/3}(n_c) = \left[\sum_{0.89\, n_c}^{1.12\, n_c} \left| \dot{X}(n) \right|^2 \Delta n \right]^{\frac{1}{2}} \tag{11}$$

where Δn is the resolution of FFT; n is the frequency in Hz; and n_c is the center frequency. Then $\dot{X}_{1/3}(n_c)$ is expressed in dB referenced to V_0=1μ-inch/sec by

$$V(n_c) = 20\log_{10}[\dot{x}_{1/3}(n_c)/V_0] \tag{12}$$

MICROVIBRATION MITIGATION WITH CONTROLLED PLATFORM

To evaluate microvibration control performance of actively controlled platform and passively controlled platform, numerical simulations are performed on a three-story shear building described in section 2. The numerical simulations are conducted using the MATLAB-Simulink tools. The parameters of the building used by Yang and Agrawal [6] are adopted here:
(i) $m_1 = 350250\text{kg}$, $m_2 = 262690\text{kg}$ and $m_3 = 175130\text{kg}$, (ii) $k_1 = 4728400\,\text{kN/m}$, $k_2 = 315230\text{kN/m}$ and $k_3 = 157610\text{kN/m}$, (iii) $c_1 = 4369\text{kN.sec/m}$, $c_2 = 291.3\text{kN.sec/m}$, $c_3 = 145.6\text{kN.sec/m}$. The three

www.EngineeringEBooksPdf.com

natural frequencies of the building are computed as 3.447, 7.372 and 19.155 Hz, respectively. The three modal damping ratios of the building are 1%, 2.14% and 5.56%, respectively.

Building without control

For the building without controlled platform, the absolute velocity response time history of the first building floor obtained from the simulation is converted to the one-third octave plot (the velocity response spectrum). The velocity response spectrum of the primary first floor is then evaluated with the BBN vibration criteria (see Fig. 4). It is observed that the vibration level of the primary first floor exceeds the specification for any type of high tech equipment within a wide frequency range between 6 Hz and 35 Hz. If a batch of high tech equipment is installed on this floor, it does not meet the requirement of any type of BBN VC microvibration criterion. To solve this problem, one may use the conventional building base isolation technique. However, the building base isolation may make the building have the excessive drift that results in low resistance to disturbance generated by in-building activities. It is also costly to use isolation technique to isolate the whole building. Therefore, an alternative microvibration control scheme is investigated in this paper.

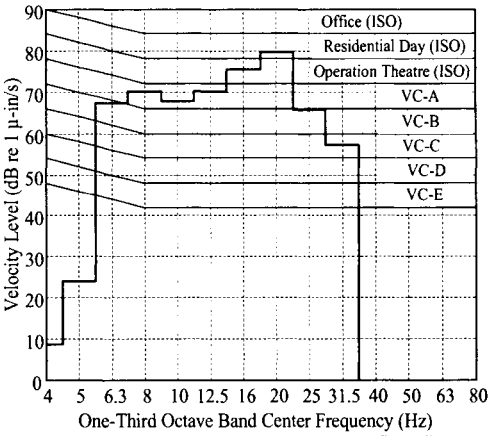

Fig.4 Velocity Spectrum of Primary first floor of Building without Control

Building with passively controlled platform

Let us consider a passively controlled platform mounted on the primary first floor of the building through a spring-damper system. The mass of the platform is taken as 87560kg, which is 25% of the mass of the primary first floor. The frequency of platform is calculated as $n_p = (k_p/m_p)^{1/2}/2\pi$ and the damping ratio of platform is taken as $\zeta_p = c_p/(4\pi m_p n_p)$. By changing the stiffness coefficient k_p and damping coefficient c_p, one may perform a parametric study to see the effects of platform frequency and damping ratio on microvibration control performance of the platform. In this connection, the velocity response spectra (one-third octave plots) of the platform are calculated for the isolator frequency from 0.2 Hz to 4 Hz and the isolating damping ratios of 1%, 2%, 3% and 4%. The maximum velocity in dB is then identified from each velocity response spectrum and is plotted against the isolator frequency and damping ratio. The results are shown in Fig. 5(a) together with the VC-B and VC-E levels between 8 Hz to 80 Hz. It is seen that the microvibration level of the platform increases with increasing isolating frequency. When the frequency of platform is below 1.4 Hz, the platform satisfies the specification for all types of high tech equipment. If isolating frequency is above 1.4 Hz, the microvibration level of the platform exceeds the VC-E level but it is still below the VC-B level. It

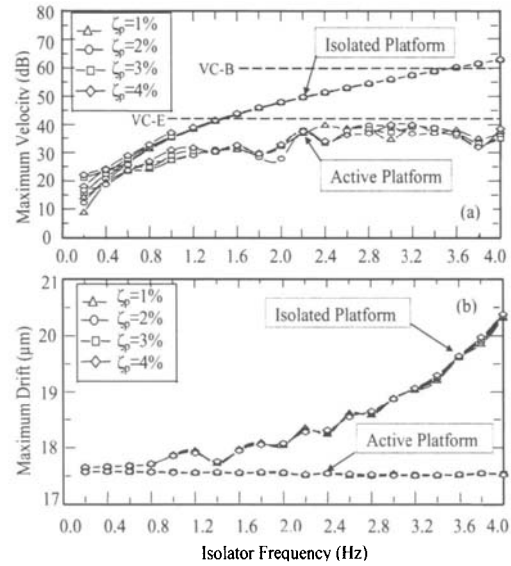

Fig.5 Variations of Active Platform Performance with Isolator Frequency
(a) Maximum velocity; (b) Maximum drift

www.EngineeringEBooksPdf.com

is also seen that the effects of damping ratio on the performance are very small, except for a low frequency range below 0.8 Hz where smaller damping ratio leads to lower vibration level.

The maximum drift of the platform is also calculated in this study based on the computed displacement time histories of the platform and the primary first floor, and the results are also depicted in Fig.5 (b). It is observed that the maximum drift of the platform increases slightly with increasing isolator frequency from 17.6 μm at 0.2 Hz to 20.3 μm at 4Hz.

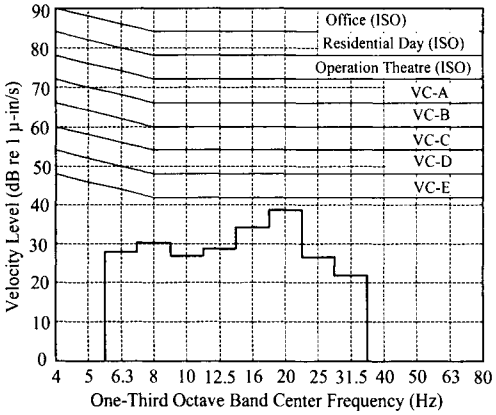

Fig.6 Velocity Spectrum of Actively

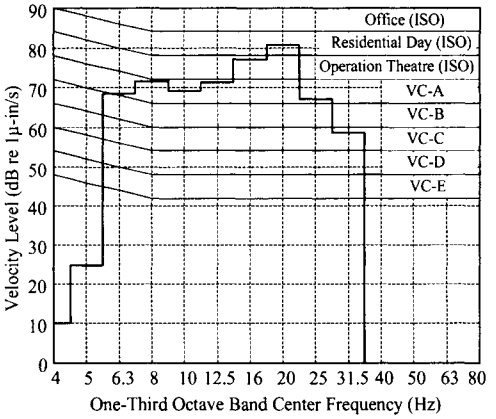

Fig.7 Velocity Spectrum of Primary first floor of Building with Actively Controlled Platform

Building with actively controlled platform

When studying the microvibration of building with actively controlled platform, the parameters of the building remain unchanged. The parameters of the hydraulic actuator are taken as $\gamma = 2.5$, $A_0/k_q = 0.15$, $A_0 k_q/k_c = 25$ and $V/2\beta k_c = 0.015$. The hydraulic actuator model used in this study with the selected parameters was tested by Dyke et al. [7]. The mass of the actively controlled platform is the same as that used in the passively controlled platform. The frequency and damping ratio of the platform attributed to passive mounts are also altered to see their effects on the performance of actively controlled platform. Fig. 6 shows the velocity response spectrum of the platform with n_p=2.6Hz and ζ_p=2%. The weighting matrix [Q] and weighting factor R in Eq. (9) are selected leading to the feedback gain matrix $[F] = [1.8574 \times 10^6, 1.0267 \times 10^6]$ for this case. It is seen that with this feedback gain matrix, the maximum velocity response of actively controlled platform is around 40dB, which satisfies the BBN specification for all types of high tech equipment. The passively controlled platform with the same isolator parameters cannot achieve the same vibration reduction level. With such a high control performance, the maximum control force required is 0.5435kN, which is only 0.063% of the platform weight. To examine if the installation of actively controlled platform has adverse effects on the building, the velocity response spectrum of the primary first floor is also computed and presented in Fig.7 together with the BBN vibration criteria.

It is found that the velocity response of the primary first floor with actively controlled platform increases a little in comparison with that of the primary first floor without any control (Fig.4). To investigate the effects of isolating frequency and damping ratio on the performance of actively controlled platform, the velocity response spectra (one-third octave plots) of the platform are computed for a series of isolating frequencies and damping ratios. The achieved maximum velocity response of the actively controlled platform is also depicted in Fig. 5(a) together with that of the passively controlled platform. Fig. 5(a) demonstrates that as isolating frequency increases, the maximum velocity response of the platform

www.EngineeringEBooksPdf.com

increases but keeps below the VC-E level stipulated in the BBN vibration criteria. This indicates that the actively controlled platform is not only of high performance but also robustness. This feature can also be seen from the maximum drift of the platform (Fig. 5(b)), The control performance of the actively controlled platform is almost independent of the isolating frequency and damping ratio. Nevertheless, the control force required increases with increasing isolating frequency, but the maximum control force is less than 1.5 kN, as shown in Fig.8.

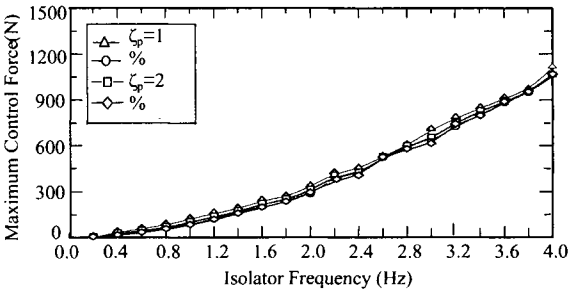

Fig.8 Variations of Active Control Force with Platform Frequency

CONCLUSION

Using actively and passively controlled platforms to isolate a batch of high tech equipment from the primary floor of a building subject to train-induced ground motion has been investigated. The actively controlled platform is installed on the primary floor through passive mounts and active hydraulic actuators with sub-optimal control algorithms. For actively controlled platform scheme, the governing equations of motion of the coupled platform-actuator-building system, have been established in terms of the absolute coordinate to facilitate the feedback control and performance evaluation of the platforms based on the BBN vibration criteria. Extensive computer simulations were carried out on a three-story high tech facility to assess the control performance of actively and passively controlled platforms. The simulation results show the passively controlled platform can be effective in reducing microvibration of all types of high tech equipment to the specified level when the isolator frequency of platform is below 1.4 Hz. The actively controlled platform can, however, achieve high control performance within a wide range of isolator frequency and damping ratios. It is superior to the passively controlled platform in terms of its high performance and robustness.

ACKNOWLEDGEMENTS

The writers are grateful for the financial support from The Hong Kong Polytechnic University through its Area Strategic Development Programme in Structural Control.

References

[1] Gordon, C.G. (1991). Generic criteria for vibration sensitive equipment. *Proc. SPIE* **1619**, 71-85.
[2] Amick H. (1997). On the generic vibration criteria for advanced technology facilities. *Journal of the Institute of Environmental Sciences* **XL 5**, 35-44.
[3] Serrand, M. and Elliott, S.J. (2000). Multichannel feedback control for the isolation of base-excited vibration. *Journal of Sound and Vibration* **234:4**, 681-704.
[4] Nakamura, Y. et al. (1999) Development of 6-DOF microvibration control system using giant magnetostrictive actuator. *Proc. SPIE* **3671**, 229-240.
[5] Yoshioka, H., et al. (2001) An active microvibration isolation system for hi-tech manufacturing facilities. *Journal of Vibration and Acoustics, ASME* **123**, 269-275.
[6] Yang, J. N. and Agrawal, A.K. (2000) Protective systems for high-technology facilities against microvibration and earthquake. *Journal of Structural Engineering and Mechanics* **10:6**, 561-567.
[7] Dyke, S.J., Spencer Jr., B.F., Quast, P., and Sain, M.K. (1995) Role of control-structure interaction in protective system design. *Journal of Engineering Mechanics, ASCE* **121:2**, 322-338.
[8] DeSilva, C. W. (1989) *Control Sensors and Actuators.* Prentice Hill, Inc., New Jersey.
[9] Kosut R.L. (1970) Suboptimal control of linear time-invariant systems subject to control structure constraints. *IEEE Trans. on Automatic Control* **15:5**, 557-563.

www.EngineeringEBooksPdf.com

Advances in Steel Structures, Vol. II
Chan, Teng and Chung (Eds.)
© 2002 Elsevier Science Ltd. All rights reserved.

DYNAMIC ANALYSIS OF COUPLED TRAIN-BRIDGE SYSTEMS UNDER FLUCTUATING WIND

Y.L. Xu[1], H. Xia[2], and Q.S. Yan[3]

[1]Department of Civil and Structural Engineering, The Hong Kong Polytechnic University, Kowloon, Hong Kong, China
[2] School of Civil Engineering, Northern Jiaotong University, Beijing, China
[3]College of Transportation, South China University of Technology, Guangzhou, China

ABSTRACT

A framework is presented for predicting dynamic response of a long suspension bridge to fluctuating wind and running trains. A three-dimensional finite element model is used to represent a suspension bridge. Wind forces acting on the bridge, including both buffeting and self-excited forces, are generated in the time domain using a fast spectral representation method and measured aerodynamic coefficients and flutter derivatives. Each 4-axle vehicle in a train is modeled by a 27-degrees-of-freedom dynamic system. The dynamic interaction between the bridge and train is realized through the contact forces between the wheels and track. By applying a mode superposition technique to the bridge only and taking the measured track irregularities as known quantities, the number of degrees of freedom of the train-bridge system is significantly reduced and the coupled equations of motion are efficiently solved. The proposed formulation are then applied to a real wind-excited long suspension bridge carrying a railway inside the bridge deck of closed cross section. The results show that the formulation presented in this paper can efficiently predict dynamic response of the coupled train-bridge system under fluctuating wind. The extent of interaction between the bridge and train depends on wind speed and train speed.

KEYWORDS

Dynamic interaction, long suspension bridge, running train, track irregularity, buffeting force, self-excited force, mode superposition, computer simulation

INTRODUCTION

To meet the needs of modern society for advanced transportation systems, more and more long suspension bridges carrying both highway and railway have been built throughout the world. These bridges are very slender and low damped, and they are often located in a unique wind environment. Under high winds, they may suffer large deflections due to mean wind force and considerable vibration because of buffeting and self-excited forces. If high-speed trains run over the bridge, the deflection and oscillation of the bridge may be further exaggerated. The large deflection and oscillation of the bridge may in turn affect the running safety of trains and the comfort of passengers.

www.EngineeringEBooksPdf.com

Little information is publicly available on this subject. Most researchers focus on either wind effects on suspension bridges without considering high-speed trains [1] or dynamic interaction between bridge and trains excluding high winds [2]. It is believed that investigations on the subject were carried out in Japan in 1970s in connection with the Honshu Shikoku Bridge, but the information is not publicly accessible and the most up-to-date research achievements were too late to be included in that early study.

This paper thus presents a framework for investigating dynamic interaction of a wind-excited long suspension bridge with running trains using the most up-to-date information in the areas of both wind-bridge interaction and bridge-train interaction. As a first stage of study, the bridge deck considered here is of closed cross-section and there are no wind forces directly acting on the trains running inside the bridge deck. To examine the proposed formulation together with the associated computer program, a real wind-excited long suspension bridge with running trains is taken as a case study.

EQUATIONS OF MOTION OF COUPLED TRAIN-BRIDGE SYSTEM

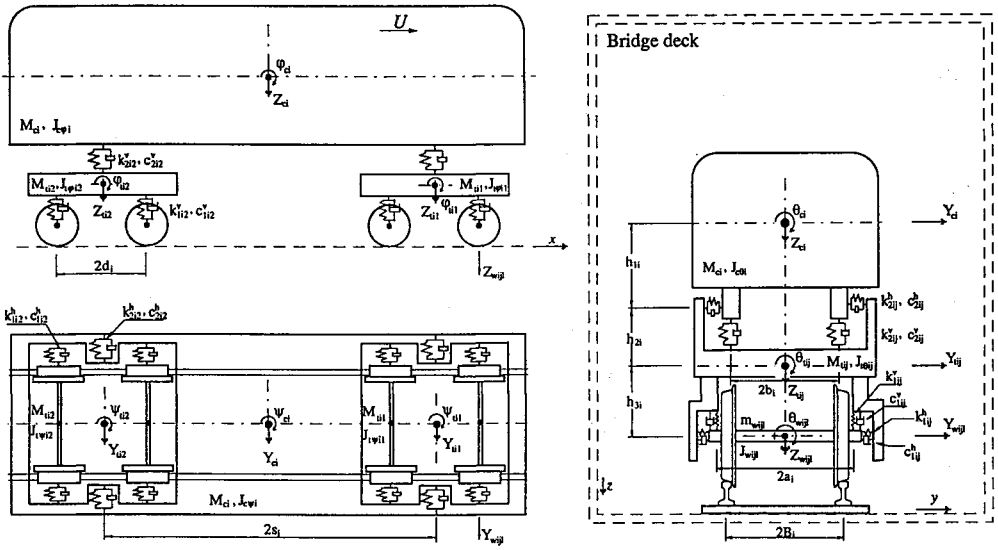

Fig 1. Dynamic Model of Vehicle

A train consists of mainly several locomotives, passenger coaches, freight cars, or their combinations. Each vehicle is in turn composed of a car body, bogies, wheel-sets, and the connections between these components. In the modeling of a vehicle, the car body, bogies and wheel-sets are usually regarded as rigid components. The connections between a car body and a bogie and between a bogie and a wheel-set are often represented by linear springs and viscous dashpots in both horizontal direction and vertical direction. In this study, each 4-axle vehicle in a train is modeled by a 27-degrees-of-freedom dynamic system (see Fig.1). The vibration amplitude of each component in a vehicle is assumed to be small. A long suspension bridge consists of mainly bridge towers, bridge deck, cables, suspenders, and anchorages (see Fig.2a). When the bridge carries a railway, the track will be laid on the bridge deck and the forces from the wheels of a train will be transmitted to the bridge deck through the track (see Fig.2b). The bridge is modeled as a three-dimensional system using the finite element method [3]. The deviations of the real rail from the ideal rail of perfect geometry are mainly considered in terms of wheel hunting and track irregularity. They are two self-excitations in the bridge-train system in addition to the moving load of the train. In this study, the wheel hunting displacement (in the lateral direction) is assumed as a

www.EngineeringEBooksPdf.com

sinusoid function with a random phase. The track irregularities consist of the lateral irregularity, vertical irregularity, and rotational irregularity.

By applying the mode superposition technique to the bridge only and taking the measured track irregularities as known quantities, the equations of motion of a train-bridge system can be derived as

$$\begin{bmatrix} \mathbf{M}_{vv} & 0 \\ 0 & \mathbf{M}_{bb} \end{bmatrix} \begin{Bmatrix} \ddot{\mathbf{X}}_v \\ \ddot{\mathbf{X}}_b \end{Bmatrix} + \begin{bmatrix} \mathbf{C}_{vv} & \mathbf{C}_{vb} \\ \mathbf{C}_{bv} & \mathbf{C}_{bb} \end{bmatrix} \begin{Bmatrix} \dot{\mathbf{X}}_v \\ \dot{\mathbf{X}}_b \end{Bmatrix} + \begin{bmatrix} \mathbf{K}_{vv} & \mathbf{K}_{vb} \\ \mathbf{K}_{bv} & \mathbf{K}_{bb} \end{bmatrix} \begin{Bmatrix} \mathbf{X}_v \\ \mathbf{X}_b \end{Bmatrix} = \begin{Bmatrix} \mathbf{F}_v \\ \mathbf{F}_b \end{Bmatrix} \tag{1}$$

where the subscripts "v" and "b" represent the vehicles and bridge, respectively. If the number of vehicles on the bridge is N_v and the number of concerned vibration modes of the bridge is N_b, the sub-displacement vectors can be expressed as

$$\mathbf{X}_v = \begin{bmatrix} \mathbf{X}_{v1} & \mathbf{X}_{v2} & \cdots & \mathbf{X}_{vN_v} \end{bmatrix}^T, \ \mathbf{X}_b = \begin{bmatrix} q_1 & q_2 & \cdots & q_{N_b} \end{bmatrix}^T \tag{2}$$

in which the sub-matrix $\{\mathbf{X}_{vi}\}$ is the displacement vector of the ith vehicle of 27 degrees of freedom; and q_i is the ith generalized coordinate of the bridge. The details of the other sub matrices in Eq. (1) can be found in the literature [4]. Eq. (1) is the second-order linear nonhomogeneous differential equation with time-varying coefficients. Wind forces acting on the bridge should be considered in the time domain.

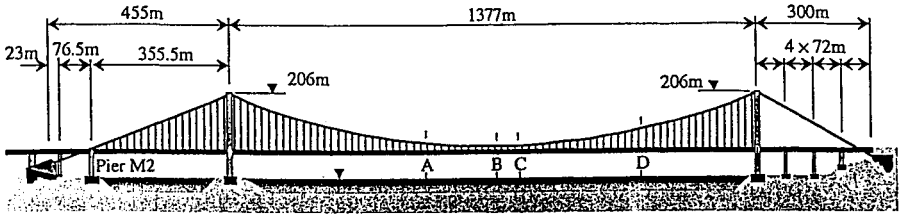

(a) Bridge elevation

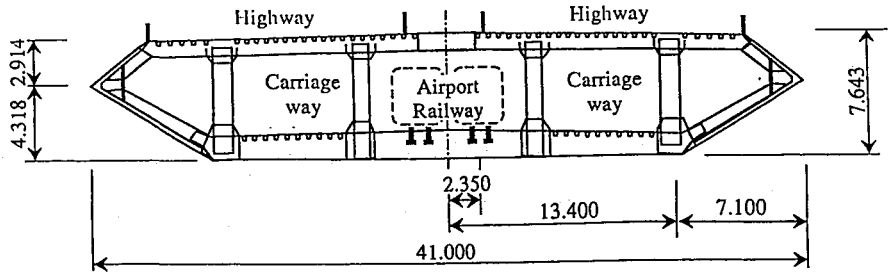

(b) Deck cross-section

Fig.2 Configuration of Suspension Bridge Used in Case Study

MODAL WIND FORCES

Wind forces acting on a long suspension bridge are mainly the static wind forces due to mean wind, the buffeting forces due to turbulent wind, and the self-excited forces due to interaction between wind and bridge motion. The mean deformation of the bridge caused by the static wind forces can be readily

www.EngineeringEBooksPdf.com

determined using the drag coefficients measured from wind tunnel tests and carrying out a static analysis. Only the buffeting forces and self-excited forces are thus considered in this study.

Modal buffeting forces

By assuming no interaction between buffeting and self-excited forces and using quasi-steady approach, the buffeting forces on the ith node of bridge deck can be expressed as [5]

$$\mathbf{F}_i^{bf} = \mathbf{A}_i^{bf}\mathbf{q}_i \tag{3}$$

$$\mathbf{F}_i^{bf} = \begin{Bmatrix} f_{Di}^{bf} \\ f_{Mi}^{bf} \\ f_{Li}^{bf} \end{Bmatrix};\ \mathbf{q}_i = \begin{Bmatrix} u_i \\ w_i \end{Bmatrix} \tag{4}$$

where f_{Di}^{bf}, f_{Mi}^{bf}, and f_{Li}^{bf} are the buffeting drag, moment, and lift, respectively, on the ith node of the bridge deck; $u_i(t)$ and $w_i(t)$ are the horizontal and vertical components of fluctuating wind, respectively; and $\mathbf{A}_i^{bf}$ is the aerodynamic force coefficient matrix for the ith node of the bridge deck. Let $\phi_{hi}^n, \phi_{\theta i}^n$, and ϕ_{vi}^n denote, respectively, the values of the lateral, rotational, and vertical components of the nth bridge mode at the ith node and let N be the total node number of the bridge deck. The modal buffeting forces of the bridge can be determined by

$$\mathbf{F}^{bf} = \begin{Bmatrix} F_1^{bf} \\ F_2^{bf} \\ \vdots \\ F_{N_b}^{bf} \end{Bmatrix} \tag{5}$$

$$F_n^{bf} = \sum_{i=1}^{N} \{\Phi_i^n\}^T \{F_i^{bf}\} = \sum_{i=1}^{N} \{\phi_{hi}^n \quad \phi_{\theta i}^n \quad \phi_{vi}^n\} \begin{Bmatrix} f_{Di}^{bf} \\ f_{Mi}^{bf} \\ f_{Li}^{bf} \end{Bmatrix},\ n=1,2,\ldots N_b \tag{6}$$

A fast spectral representation method proposed by Cao et al [6] is adopted here for the digital simulation of time histories of wind components u(t) and w(t).

Modal self-excited forces

The self-excited forces on the bridge deck can be expressed in terms of convolution integrals between the bridge deck motion and the impulse response functions [7]. The impulse response functions can be obtained using the flutter derivatives measured from wind tunnel tests and the rational function approximation approach. The self-excited forces at the ith node of the bridge deck can be expressed as

$$\mathbf{F}_i^{se} = \mathbf{E}_i\mathbf{X}_i + \mathbf{G}_i\dot{\mathbf{X}}_i + \mathbf{H}_i\ddot{\mathbf{X}}_i + \hat{\mathbf{F}}_i^{se} \tag{7}$$

$$\mathbf{F}_i^{se} = \begin{Bmatrix} f_{Di}^{se} \\ f_{Mi}^{se} \\ f_{Li}^{se} \end{Bmatrix},\quad \mathbf{X}_i = \begin{Bmatrix} p_i \\ \alpha_i \\ h_i \end{Bmatrix},\quad \hat{\mathbf{F}}_i^{se} = \begin{Bmatrix} \hat{f}_{Di}^{se} \\ \hat{f}_{Mi}^{se} \\ \hat{f}_{Li}^{se} \end{Bmatrix} \tag{8}$$

where $p_i(t), \alpha_i(t), h_i(t)$ are the lateral, torsional, vertical displacement of the ith node of the bridge deck, respectively; $\mathbf{E}_i, \mathbf{G}_i$, and $\mathbf{H}_i$ are the aeroelastic stiffness, damping, and mass coefficient matrices,

www.EngineeringEBooksPdf.com

respectively; and the matrix $\hat{\mathbf{F}}_i^{se}$ is obtained using a recursive algorithm. The modal self-excited forces can be then determined by

$$\mathbf{F}^{se} = \begin{Bmatrix} F_1^{se} \\ F_2^{se} \\ \vdots \\ F_{N_b}^{se} \end{Bmatrix} \tag{9}$$

$$F_n^{se} = \sum_{i=1}^{N} \{\Phi_i^n\}^T \{F_i^{se}\} = \sum_{i=1}^{N} \{\Phi_i^n\}^T \{\mathbf{E}_i \mathbf{X}_i + \mathbf{G}_i \dot{\mathbf{X}}_i + \mathbf{H}_i \ddot{\mathbf{X}}_i + \hat{\mathbf{F}}_i^{se}\} = \sum_{i=1}^{N} \{\phi_{hi}^n \quad \phi_{\theta i}^n \quad \phi_{vi}^n\} \begin{Bmatrix} f_{Di}^{se} \\ f_{Mi}^{se} \\ f_{Li}^{se} \end{Bmatrix} \tag{10}$$

Since the nodal displacements of the bridge can be expressed in terms of the modal coordinates of the bridge,

$$p_i(t) = \sum_{n=1}^{N_b} (\phi_{hi}^n q_n); \quad \alpha_i(t) = \sum_{n=1}^{N_b} (\phi_{\theta i}^n q_n); \quad h_i(t) = \sum_{n=1}^{N_b} (\phi_{vi}^n q_n) \tag{11}$$

Equation (9) can be thus further written as the function of the modal coordinates of the bridge.

$$\mathbf{F}^{se} = \Psi_E \mathbf{X}_b + \Psi_G \dot{\mathbf{X}}_b + \Psi_H \ddot{\mathbf{X}}_b + \hat{\mathbf{F}}^{se} \tag{12}$$

EQUATIONS OF MOTION OF COUPLED TRAIN-BRIDGE SYSTEM UNDER WINDS

In consideration that the train runs inside the bridge deck and wind forces act on the bridge deck only, the equations of motion of a wind-excited suspension bridge with running trains can be expressed as

$$\begin{bmatrix} \mathbf{M}_{vv} & 0 \\ 0 & \mathbf{M}_{bb} \end{bmatrix} \begin{Bmatrix} \ddot{\mathbf{X}}_v \\ \ddot{\mathbf{X}}_b \end{Bmatrix} + \begin{bmatrix} \mathbf{C}_{vv} & \mathbf{C}_{vb} \\ \mathbf{C}_{bv} & \mathbf{C}_{bb} \end{bmatrix} \begin{Bmatrix} \dot{\mathbf{X}}_v \\ \dot{\mathbf{X}}_b \end{Bmatrix} + \begin{bmatrix} \mathbf{K}_{vv} & \mathbf{K}_{vb} \\ \mathbf{K}_{bv} & \mathbf{K}_{bb} \end{bmatrix} \begin{Bmatrix} \mathbf{X}_v \\ \mathbf{X}_b \end{Bmatrix} = \begin{Bmatrix} \mathbf{F}_v \\ \mathbf{F}_b \end{Bmatrix} + \begin{Bmatrix} 0 \\ \mathbf{F}^{bf} + \mathbf{F}^{se} \end{Bmatrix} \tag{13}$$

Substituting Eq. (12) into Eq. (13) and having some manipulations yield

$$\begin{bmatrix} \mathbf{M}_{vv} & 0 \\ 0 & \overline{\mathbf{M}}_{bb} \end{bmatrix} \begin{Bmatrix} \ddot{\mathbf{X}}_v \\ \ddot{\mathbf{X}}_b \end{Bmatrix} + \begin{bmatrix} \mathbf{C}_{vv} & \mathbf{C}_{vb} \\ \mathbf{C}_{bv} & \overline{\mathbf{C}}_{bb} \end{bmatrix} \begin{Bmatrix} \dot{\mathbf{X}}_v \\ \dot{\mathbf{X}}_b \end{Bmatrix} + \begin{bmatrix} \mathbf{K}_{vv} & \mathbf{K}_{vb} \\ \mathbf{K}_{bv} & \overline{\mathbf{K}}_{bb} \end{bmatrix} \begin{Bmatrix} \mathbf{X}_v \\ \mathbf{X}_b \end{Bmatrix} = \begin{Bmatrix} \mathbf{F}_v \\ \overline{\mathbf{F}}_b \end{Bmatrix} \tag{14}$$

$$\overline{\mathbf{M}}_{bb} = \mathbf{M}_{bb} + \Psi_H; \quad \overline{\mathbf{C}}_{bb} = \mathbf{C}_{bb} + \Psi_G; \quad \overline{\mathbf{K}}_{bb} = \mathbf{K}_{bb} + \Psi_E; \quad \overline{\mathbf{F}}_b = \mathbf{F}_b + \mathbf{F}^{bf} + \hat{\mathbf{F}}^{se} \tag{15}$$

Equations (14) and (15) reflect the dynamic interaction of a wind-excited suspension bridge with trains running inside the bridge deck. It is solved using the Newmark implicit integral algorithm with $\beta = 1/4$.

CASE STUDY

A computer program is written based on the formulation derived above and used to perform a case study. The case study concerns a long suspension bridge carrying a railway inside the bridge deck (see Figs. 2a and 2b). The main span of the bridge is 1377 m and the height of the tower is 206m. A three-dimensional finite element model of the bridge was established. The computed natural frequencies and mode shapes were verified through the comparison with the measured results and the details can be found in Xu et al [3]. The first twenty natural frequencies up to 0.38 Hz and the associated mode shapes

www.EngineeringEBooksPdf.com

are used in this case study. The damping ratios in the lateral and vertical modes of vibration of the bridge are taken as 1% while the damping ratios in the torsional modes of vibration are 0.5%.

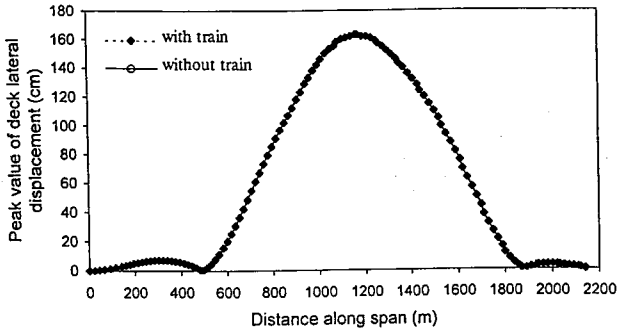

(a) Lateral displacement response

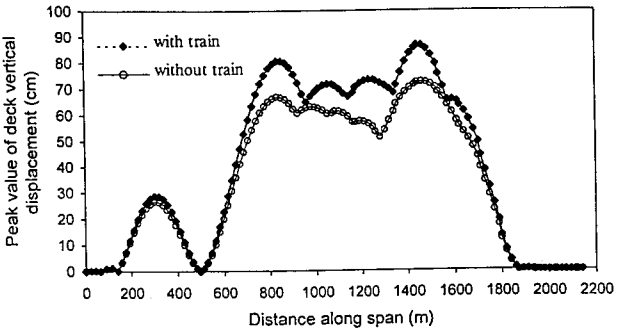

(b) Vertical displacement response

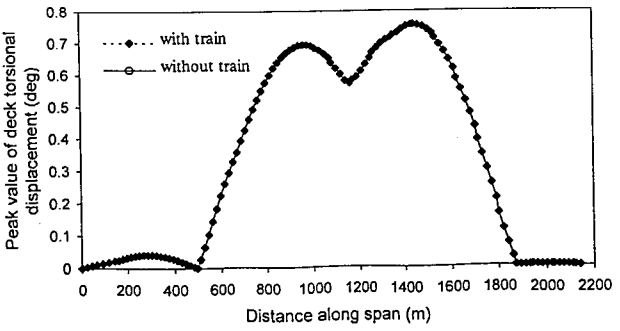

(c) Torsional displacement response

Fig.3 Maximum Displacement Responses of Bridge (U=60m/s)

The train concerned in the case study consists of 8 passenger coaches and it runs inside the bridge deck at constant speed of 70 Km/h. Each coach has two identical bogies and each bogie is supported by two identical wheel-sets. The eight passenger coaches are assumed to be identical. The average static axle loads are 10144kg (tare) and 13250kg (crush). The main parameters of the coach used in the case study can be found in Xia et al [4]. The principal vibration mode frequency of the coach is about 1.04 Hz in the vertical direction and 0.68 Hz in the lateral direction. The track vertical, lateral and torsional irregularities are taken into consideration by using the measured data from one of the main railways in China because no measurement data are available for the concerned train-bridge system. The length of the measured data used is 2500 m for vertical, lateral, and torsional irregularities, respectively. The

www.EngineeringEBooksPdf.com

effect of wheel hunting displacement on both bridge and vehicle responses is found so small that it is neglected in this case study. In the simulation of buffeting forces, the von Karman longitudinal and vertical auto-spectra are adopted [5].

The average elevation of the bridge deck and the mean wind speed at the deck level are taken as 60 m and 60 m/s, respectively. The friction velocity of wind u_* is selected as 1.15m/s for wind flow over the sea at which the bridge is located. The corresponding turbulent intensity at the deck level is about 12%. The exponential decay coefficient λ is selected as 16 [5]. The drag, lift and moment coefficients of the bridge deck measured from wind tunnel tests are 0.135, 0.090, and 0.063, respectively, at the zero wind angle of attack with respect to the deck width of 41m [8]. The first derivatives of the drag, lift, and moment coefficients with respect to wind angle at the zero wind angle of attack are –0.253, 1.324, and 0.278, respectively. The sampling frequency and duration used in the simulation of wind speeds are, respectively, 20 Hz and 10 minutes. The frequency interval and the total number of frequency interval are, respectively, 0.001 Hz and 1000. Due to the lack of wind tunnel test results, only the vertical and rotational motions of the bridge deck are taken into account in the simulation of self-excited forces. Furthermore, for the concerned bridge the coupled terms have smaller effects on the self-excited forces and accordingly they are neglected. As a result, a total of 12 frequency independent coefficients are determined by using the measured flutter derivatives and the least squares fitting method with 4 terms included in each rational function.

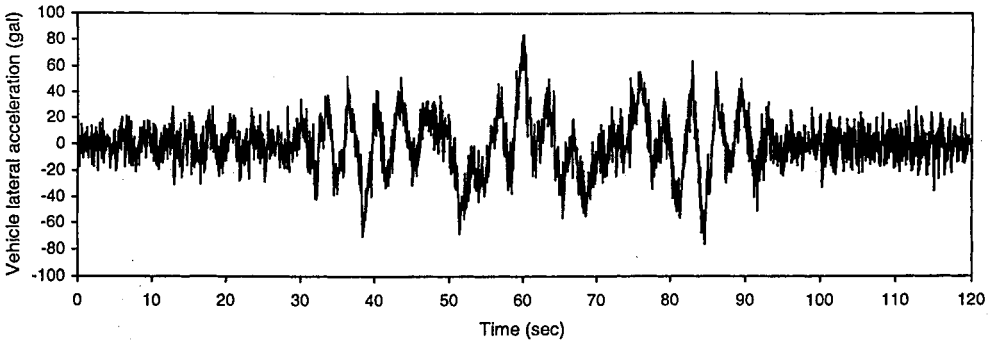

(a) Lateral acceleration

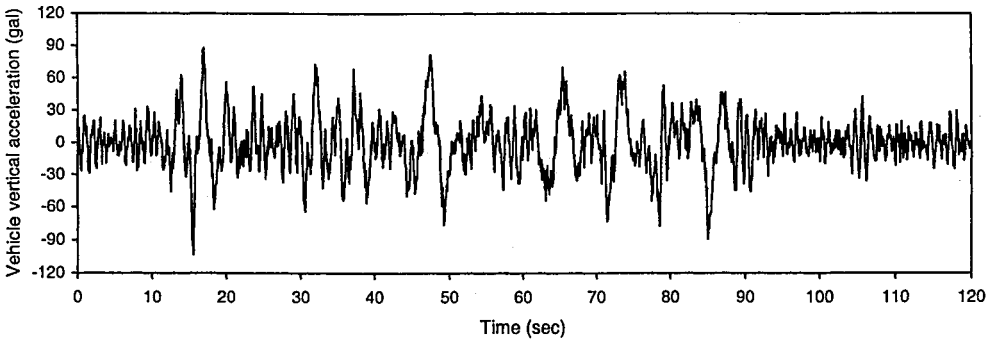

(b) Vertical acceleration

Fig.4 Acceleration Response of First Car Body

Figures 3a, 3b, and 3c show the distributions of the maximum lateral, vertical and torsional displacement responses, respectively, along the bridge deck. The maximum displacement responses of the bridge deck under high winds without trains are also computed and presented in the figures. It is seen that the

www.EngineeringEBooksPdf.com

maximum lateral and torsional displacement responses are totally controlled by high winds, and the curves from the case without the running train overlap with the curves from the case with the running train. The running train only moderately affects the maximum vertical displacement response of the bridge deck when the train runs over the main span. However, if the mean wind speed is reduced to 25 m/s while the train speed remains 70 km/h, the bridge vertical response is dominated by the running train while the bridge lateral and torsional responses are still dominated by wind forces.

Figures 4a and 4b show, respectively, the lateral and vertical acceleration responses of the first car body in the train that runs on the bridge at a constant speed of 70 km/h. The mean wind speed at the bridge deck level is 60 m/s. By comparing these responses with those without wind effects [4], it is found that when the train runs over the main span of the bridge, both the lateral and vertical acceleration responses of the first car body are significantly increased due to the motions of the bridge deck under high winds. This indicates that the large motion of the long suspension bridge under strong winds may affect the safety of train and the comfort of passengers.

CONCLUSIONS

A framework has been presented for investigating the dynamic interaction of a long suspension bridge with running trains under high winds. A real long suspension bridge carrying a train inside the bridge deck of closed cross-section was taken as a case study. The results showed that the formulation presented in this paper could predict dynamic response of the coupled train-bridge system under high winds. Under a mean wind speed of 60 m/s, the dynamic responses of the bridge were dominated by wind forces. The running train only moderately affected the vertical response of the bridge deck. However, the bridge motions due to high winds affected the safety of the train and the comfort of passengers considerably. It was also found that if mean wind speed was reduced to 25m/s, the running train then dominated the bridge vertical response but not the bridge lateral and torsional responses.

ACKNOWLEDGMENTS

The writers are grateful for the financial supports from the Hong Kong Research Grants Council through a RGC grant (PolyU 5043/01E) and the Hong Kong Polytechnic University through an internal research grant. The support from the MTR Corporation Hong Kong Limited to provide the writers with the relevant vehicle information is particularly appreciated.

References

[1] Jones, N.P., Scanlan, R.H., Jain, A. and Katsuchi, H. (1998). Advances (and challenges) in the prediction of long-span bridge response to wind. *Bridge aerodynamics,* Larsen & Esdahl, eds., Balkema, Rotterdam, Netherlands, 59-85.

[2] Fryba, L. (1996). *Dynamics of Railway Bridges*. Thomas Telford, London, England.

[3] Xu, Y.L, Ko, J.M. and Zhang, W.S. (1997). Vibration studies of Tsing Ma suspension Bridge. *J. Bridge Engrg.*, ASCE, **3:4**, 149-156.

[4] Xia, H., Xu, Y.L. and Chan, T.H.T. (2000). Dynamic interaction of long suspension bridges with running trains. *J. Sound and Vib.*, **237:2**, 263-280.

[5] Simiu, P.D. and Scanlan, R.H. (1996). *Wind Effects on Structures*. Third Edition, John Wiley & Sons, New York.

[6] Cao, Y. H., Xiang, H.F., and Zhou, Y. (2000). Simulation of stochastic wind velocity field on long-span bridges. *J. Engrg. Mech.,* ASCE, **126:1**, 1-6.

[7] Lin, Y.K. and Yang, J.N. (1983). Multimode bridge response to wind excitations. *J. Engrg. Mech.*, ASCE, **109:2**, 586-603.

[8] Xu, Y.L., Sun, D.K., Ko, J.M. and Lin, J.H. (2000). Fully coupled buffeting analysis of Tsing Ma suspension Bridge. *J. Wind. Engrg., Ind. Aerodyn.*, **85**, 97-117.

www.EngineeringEBooksPdf.com

Advances in Steel Structures, Vol. II
Chan, Teng and Chung (Eds.)
© 2002 Elsevier Science Ltd. All rights reserved.

MODAL PARAMETER IDENTIFICATION OF TSING MA BRIDGE DURING TYPHOON VICTOR: EMD-HT APPROACH

J. Chen[1], Y. L. Xu[1] and R. C. Zhang[2]

[1]Department of Civil and Structural Engineering, The Hong Kong Polytechnic University
Hung Hom, Kowloon, Hong Kong, China
[2]Engineering Division, Colorado School of Mines
Colorado, Golden, CO 80401-1887, USA

ABSTRACT

Modal parameters of the Tsing Ma Bridge are identified from the bridge responses measured during Typhoon Victor using the newly-emerged empirical mode decomposition (EMD) method in conjunction with the Hilbert-transform (HT) technique. Natural frequencies and modal damping ratios identified by the EMD-HT approach are first compared with those obtained by the traditional fast Fourier transform (FFT) method. The EMD-HT approach is then used to examine bridge modal parameters identified from different sensors at different locations. Finally, the EMD-HT approach is used to investigate variations of natural frequency and total modal damping ratio of the Bridge with vibration amplitude and mean wind speed. It is demonstrated that the EMD-HT approach is applicable to modal parameter identification of large civil structures using field measurement data, and the EMD-HT approach is better than the FFT method.

KEYWORDS

Modal parameter identification, Tsing Ma Bridge, Typhoon Victor, Field measurement data, Empirical mode decomposition, Random decrement technique, Hilbert transform.

INTRODUCTION

There are several methods available for identifying modal parameters of a civil structure from its field measurement data. The most popular approach is the fast Fourier transform (FFT) method, in which the natural frequencies of a structure are identified from its response spectra while the modal damping ratios are estimated by the half power bandwidth method or the curve fitting method, as used by Jones and Spartz (1990) among many others. Another widely used method, especially for modal damping ratio identification, is the random decrement technique (RDT) (Tamura and Suganuma, 1996). Though these two methods are popular, the FFT method requires the structural response to be a stationary random process in theory. The application of the FFT method to field measured non-stationary structural responses will be questionable for the identification of modal parameters of the structure. The stationary constraint on the data source also imposes on the RDT method together with other

www.EngineeringEBooksPdf.com

requirements (Jeary, 1986). Thus, the approach suitable for the system identification of a structure with field measured non-stationary structural responses is desirable.

Recently, an EMD-HT approach, which consists mainly of the newly-emerged empirical mode decomposition (EMD) method and the Hilbert transform (HT), has been proposed by Yang et al (2000) for modal parameter identification of a linear structure. Their numerical studies indicated that the EMD-HT approach was a simple, effective and accurate tool for modal parameter identification. However, this approach has not been examined yet for modal parameter identification of a real civil structure using its field measurement data recorded during strong winds. It is the objective of this paper that applies the EMD-HT approach to the field measurement data of the Tsing Ma Bridge during Typhoon Victor to examine the applicability of this new approach.

TSING MA BRIDGE AND TYPHOON VICTOR

The Tsing Ma Bridge is a double deck suspension bridge with a main span of 1377m and an overall length of 2160m. Since the Tsing Ma Bridge is located in one of the most active typhoon prone regions in the world, a Wind and Structural Health Monitoring System (WASHMS) was installed in the Tsing Ma Bridge to monitor the structural performance and health of the Bridge.

On 2 August 1997, about three months after the opening of the Tsing Ma Bridge to public, Typhoon Victor crossed over the Bridge. The WASHMS timely recorded wind speed and bridge response time-histories of six hour duration from 18:00 to 24:00 HKT (Hong Kong Time). In this study, the acceleration response time histories recorded at three locations on the deck (ATTJD, ATTID and ATTFD see Fig.1) and one location on the cable (ABTLC, see Fig.1) are used to identify modal parameters of the Bridge using the EMD-HT approach. At each of the three locations on the deck, there are two accelerometers measuring the accelerations in the vertical direction and one accelerometer measuring the acceleration in the lateral direction of the Bridge. The position of the lateral accelerometer is close to the horizontal neural axis of the corresponding cross section. The two vertical accelerometers are symmetrically arranged about the vertical central axis of the cross section with a horizontal central space of 26m. Thus, the vertical acceleration of the deck section can be obtained by averaging the accelerations measured by the two vertical accelerometers, and the torsional one equals the difference between the two vertical responses divided by 26m. For the cable, there are two accelerometers measuring the acceleration in the lateral direction as well as in the vertical direction. The sampling frequency of all the accelerometers was preset to 25.6Hz. Detailed descriptions of the WASHMS, Typhoon Victor, and field measurements can be found in Xu et al (1999).

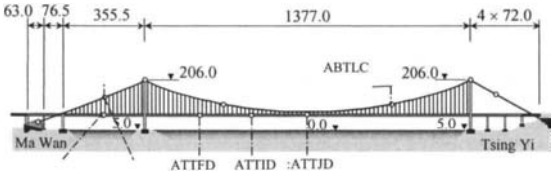

Figure 1 **Location of sensors**

The response time-history of six-hour duration measured from each accelerometer is evenly divided into six samples of one-hour duration each. As a result, there are in total $3\times3\times6=54$ samples for the bridge deck and $1\times2\times6=12$ samples for the bridge cable. Apart from this, an overlap length of half an hour is introduced between two neighboring segments to gain five more samples for each time history to investigate variations of modal parameters with vibration amplitude and mean wind speed. The hourly mean wind speed is computed from the data measured by two ultrasonic anemometers installed on the same location as ATTJD with one on the south and the other on the north.

The stationarity test of the total 66 records using the run test method (Bendat, 1986) shows that only 16%, 16% and 41% of the records from the cable and 11%, 13% and 24% of the records from the

www.EngineeringEBooksPdf.com

bridge deck can be seen as stationary records for a significance level of 0.05, 0.025 and 0.01, respectively. A large number of the records are classified as non-stationary random process that cannot be used in theory for modal parameter identification using the FFT method. The EMD-HT approach is thus applied to these records for modal parameter identification.

EMD-HT APPROACH FOR MODAL PARAMETER IDENTIFICATION

Generally speaking, the implement of the EMD-HT approach for modal parameter identification consists mainly of three steps. Firstly, the modal responses are identified from the measured response time history using the EMD method through a procedure called sifting process together with the intermittency check. The random decrement technique is then applied to each modal response time history to obtain the free response time history. Finally, the Hilbert transform is applied to the modal free response time history to identify the natural frequency and the modal damping ratio. The EMD method and the HT for modal parameter identification are briefly explained in this section.

Empirical Mode Decomposition

The empirical mode decomposition (EMD) method, developed by Huang et al (1998), is a new data processing method, which can decompose any data set into several intrinsic mode functions (IMF) by a procedure called the sifting process. Suppose $y(t)$ is the signal to be decomposed. The sifting process is conducted by first constructing the upper and lower envelope of $y(t)$ by connecting its local maxima and local minima through a cubic spline. The mean of the two envelopes is then computed and subtracted from the original time history. The difference between the original time history and the mean value, c_1, is called the first IMF if it satisfies the following two conditions: (1) within the data range, the number of extrema and the number of zero-crossings are equal or differ by one only; and (2) the envelope defined by the local maxima and the envelope defined by the local minima are symmetric with respect to the mean. The difference between $y(t)$ and c_1 is then treated as a new time history and subjected to the same sifting process, giving the second IMF. The EMD procedure continues until the residue becomes so small that it is less than a predetermined value of consequence, or the residue becomes a monotonic function. The original time history $y(t)$ is finally expressed as the sum of the IMF components plus the final residue

$$y(t) = \sum_{j=1}^{N} c_j(t) + r(t) \tag{1}$$

where N is the number of IMF components; and $r(t)$ is the final residue.

For the measured acceleration response $\ddot{x}(t)$ of the Bridge, it can be decomposed by the EMD as follows

$$\ddot{x}(t) = \sum_{j=1}^{k} \ddot{x}_j(t) + \sum_{i=1}^{N-k} c_i(t) + r_N(t) \tag{2}$$

where $\ddot{x}_j(t)$ is the jth modal acceleration response; and $c_i(t)$ is the ith IMF.

To avoid any mode mixing among $\ddot{x}_j(t)$ and make sure $\ddot{x}_j(t)$ is the response of certain vibration mode, a criterion was suggested by Huang et al (1998) to separate the waves of different periods into different modes based on the period length. The criterion, named as the intermittency check, is designed as the lower limit of the frequency that can be included in any given IMF component. It can be achieved by specifying a cutoff frequency ω_c for each IMF during its sifting process. The data having frequencies lower than ω_c will be removed from the resulting IMF. The cutoff frequencies can

www.EngineeringEBooksPdf.com

be decided by prior finite element analysis of the concerned structure, or approximately defined from the power spectrum of $\ddot{x}(t)$.

From each modal acceleration response $\ddot{x}_j(t)$, the random decrement technique is then introduced to obtain the free modal acceleration response time history as follows

$$\ddot{x}_j^f(i\Delta t) = \frac{1}{L}\sum_{k=1}^{L} \ddot{x}_j(t_k + i\Delta t); \quad i = 1,2,...,M \tag{3}$$

where
$$\ddot{x}_j(t_k) = \ddot{x}_s \tag{4}$$

and
$$\ddot{x}_j(t_k) \geq 0 \; k = 1, 3, 5, \cdots \qquad \ddot{x}_j(t_k) \leq 0 \; k = 2, 4, 6, \cdots \tag{5}$$

where $\ddot{x}_j^f(t)$ is the free modal response; L is the number of segments averaged; t_k is the starting time for each segment; $\ddot{x}_s$ is the threshold level; Δt is the sample time interval; M is an integer; and $M\Delta t = T$ is the duration of each segment. Having the free modal response $\ddot{x}_j^f(t)$ obtained, the modal parameters can be identified using the following HT identification procedure for single-degree-of-freedom (SDOF) system.

HT for Modal Parameter Identification of SDOF System

The Hilbert transform (HT) has long been used to study linear and nonlinear dynamic systems and to identify their modal parameters in the frequency-time domain. For a linear SDOF system under the impulsive loading, the impulse displacement response function of the system v(t)=0 for $t < 0$

$$v(t) = A_0 e^{-\xi\omega_0|t|} \sin\omega_d t, \quad -\infty < t < \infty \tag{6}$$

where ω_0 is the natural circular frequency of the system; ξ is the damping ratio; ω_d is the damped natural circular frequency; and A_0 is a constant depending on the intensity of impulsive loading and the mass and frequency of the system. In Eq.(6), the impulse response is already extended to the negative time domain by considering its mirror image.

According to the HT theory (Bendat, 1986), the analytical signal $z(t)$ associated with $v(t)$ is defied as

$$z(t) = v(t) + i\tilde{v}(t) = A(t)e^{-i\theta(t)} \tag{7}$$

where $\tilde{v}(t)$ is the Hilbert transform of $v(t)$. For the case in which ξ is small and ω_0 is large, the amplitude $A(t)$ and the phase angle $\theta(t)$ can be obtained as follows (Yang et al, 2000)

$$A(t) = A_0 e^{-\xi\omega_0 t} \qquad \theta(t) = \omega_d t - \pi/2 \tag{8}$$

By introducing the logarithmic and differential operators to each part of Eq. (8), one obtains

$$\ln A(t) = -\xi\omega_0 t + \ln A_0 \qquad \omega(t) = \frac{d\theta(t)}{dt} = \omega_d \tag{9}$$

Therefore, the damped natural circular frequency ω_d can be identified from the instantaneous frequency $\omega(t)$. With the identified ω_d and the slope $-\xi\omega_0$ of the straight line of the decaying amplitude $A(t)$ in a semi-logarithmic scale, the damping ratio ξ can be identified from the function $\omega_d = \omega_0\sqrt{1-\xi^2}$. Considering that the instantaneous frequency may fluctuate around its mean value due to the amplitude variation of the signal and that the requirement of small damping ratio may limit the application of the HT method, the following procedure is used for the system identification of SDOF systems based on the HT method: (1) determine the damped frequency ω_d from the slope of the phase function $\theta(t)$ by the linear least-squares fit technique; and (2) determine the damping ratio ξ by applying the linear least-squares fit technique to the decaying amplitude $A(t)$ in a semi-logarithmic

www.EngineeringEBooksPdf.com

scale. By applying the above-mentioned identification procedure to free modal response $\ddot{x}_j^f(t)$, the natural frequency and modal damping ratio of the Bridge can be easily identified.

IDENTIFIED NATURAL FREQENCIES AND MODAL DAMPING RATIOS

In this section, the EMD-HT approach is used for three purposes: (1) to compare the identified modal parameters with those from the FFT method; (2) to examine the consistency of modal parameters identified from the three sensors on the bridge deck; and (3) to find the difference of modal damping ratio between the bridge deck and the bridge cable. To fulfil the task, six major vibration modes of the Tsing Ma Bridge are considered. They are the first two lateral modes of vibration, the first two vertical modes of vibration, and the first torsional mode of vibration. The computed natural frequencies of these five vibration modes are, respectively, 0.068Hz, 0.158Hz, 0.117Hz, 0.137Hz and 0.271Hz (Xu et al, 1997). Moreover, a special vibration mode with a natural frequency of 0.23Hz, is also considered since in this mode only the main cable vibrates while the bridge deck exhibits almost no movement. For the sake of convenience of description, these six vibration modes are denoted in sequence hereafter as Lat1, Lat2, Ver1, Ver2, Tor1, and Cab1.

Comparison of Modal Parameters Identified by EMD-HT and FFT

The EMD-HT approach and the FFT method are applied to the acceleration responses of the Bridge measured from the location ATTID between 18:00 and 24:00 HKT for identifying the natural frequencies and modal damping ratios of Lat1, Lat2, Ver1, Ver2, and Tor1. The resulting natural frequencies are listed in Table1 and the resulting modal damping ratios are shown in Table 2. It is noted that the damping identified here is the total damping that consists of the net structural damping and aerodynamic damping

The maximum relative difference between the natural frequency identified by the EMD-HT approach and the computed value is 0.88%, 1.89%, 3.16%, 2.48% and 2.5% for Lat1, Lat2, Ver1, Ver2 and Tor1 respectively. For the FFT method, the maximum difference is 1.18%, 2.8%, 2.48%, 0.8% and 2.5% correspondingly. It is encouraging to see that for a given mode of vibration, the natural frequencies identified by the EMD-HT approach are very close to each other. It is also interesting to see that the natural frequencies identified by the EMD-HT approach are very close to those obtained from the FFT method no matter whether the measured acceleration response passes the stationarity test or not.

The modal damping ratios identified by the EMD-HT approach, however, are smaller than those obtained from the half-power bandwidth method in most cases with three exceptions. It is well known that for the error being accepted, an extremely long stationary record is required to estimate a modal damping ratio when the FFT-based method is applied, but it is difficult in reality to find such a long stationary record during typhoon. For the EMD-HT approach, on the other hand, it can be applied to a time history of relatively short duration (e.g. one hour). Thus, one may say that the modal damping ratios identified by the EMD-HT are more reliable than those from the FFT method.

Table1 Natural frequencies identified by EMD-HT and FFT

HKT	Lat1		Lat2		Ver1		Ver2		Tor1	
	EMD	FFT	EMD	FFT	EMD	FFT	EMD	FFT	EMD	FFT
18:00-19:00	0.0686	0.0688	0.1602	0.1625	0.1137	0.1141	0.1365	0.1359	0.2652	0.2656
19:00-20:00	0.0677	0.0672	0.1608	0.1609	0.1138	0.1149	0.1373	0.1359	0.2653	0.2656
20:00-21:00	0.0683	0.0688	0.1610	0.1609	0.1139	0.1141	0.1387	0.1375	0.2655	0.2641
21:00-22:00	0.0677	0.0672	0.1598	0.1594	0.1133	0.1141	0.1362	0.1359	0.2641	0.2641
22:00-23:00	0.0681	0.0688	0.1587	0.1594	0.1141	0.1141	0.1376	0.1375	0.2645	0.2641
23:00-24:00	0.0677	0.0672	0.1601	0.1594	0.1145	0.1141	0.1373	0.1359	0.2645	0.2641

www.EngineeringEBooksPdf.com

Table2 Modal damping ratios identified by EMD-HT and FFT

HKT	Lat1		Lat2		Ver1		Ver2		Tor1	
	EMD	FFT	EMD	FFT	EMD	FFT	EMD	FFT	EMD	FFT
18:00-19:00	0.80%	2.54%	1.27%	1.39%	0.35%	1.24%	1.01%	1.68%	0.29%	0.45%
19:00-20:00	1.52%	2.09%	0.91%	1.02%	1.27%	1.61%	0.66%	0.98%	0.75%	0.81%
20:00-21:00	0.82%	1.97%	0.81%	1.27%	1.03%	0.97%	0.78%	0.93%	0.56%	0.54%
21:00-22:00	0.55%	1.67%	0.58%	1.09%	0.68%	1.09%	0.49%	0.92%	0.35%	0.48%
22:00-23:00	1.31%	2.22%	1.07%	1.61%	0.73%	1.14%	0.94%	1.62%	0.47%	0.62%
23:00-24:00	1.58%	2.20%	1.33%	1.24%	0.89%	1.55%	0.62%	0.89%	0.47%	0.54%

Comparison of Modal Parameters from Different Sensors on Bridge Beck

For the field measurement of a large civil structure, it needs many sensors to be mounted at different locations of the structure. The consistency of modal parameters identified from the response time histories recorded at different locations is examined in this study. The EMD-HT approach is applied to the response time histories recorded at the locations ATTFD, ATTID and ATTJD of the bridge deck. The resulting natural frequencies and modal damping ratios from the response time histories between 21:00 and 22:00HKT are shown in Table 3. It is noted that for Lat2 and Ver1, the location of ATTJD is around the stationary point of the modes of vibration. Thus, the modal parameters are hard to be identified from the measurements at ATTJD. The same case occurs at the location ATTFD for Ver2.

Table3 Comparison of modal parameters from different sensors on bridge deck (21:00-22:00HKT)

Location	Lat1		Lat2		Ver1		Ver2		Tor1	
	Freq.	ξ (%)	Freq.	ξ (%)	Freq.	ξ (%)	Freq.	ξ (%)	Freq.	ξ (%)
ATTFD	0.0677	0.57%	0.1600	0.53%	0.1142	0.77%	----	----	0.2642	0.25%
ATTID	0.0677	0.55%	0.1598	0.58%	0.1133	0.68%	0.1362	0.49%	0.2641	0.35%
ATTJD	0.0677	0.54%	-----	-----	-----	-----	0.1362	0.61%	0.2636	0.45%

It is seen from Table 3 that the natural frequencies identified from the three locations are nearly identical for any given mode of vibration. The modal damping ratios in either the first or the second lateral modes of vibration are also very close to each other. Only for the vertical and torsional modes of vibration, there are some differences in the modal damping ratios identified from the three locations. This is mainly due to the complicated mechanism of both structural and aerodynamic damping. In such cases, the average of the two or three damping ratios identified may be used as the corresponding modal damping ratio.

Comparison of Modal Parameters between Bridge Deck and Cable

To answer the question if the modal parameters identified from the bridge deck are consistent with those from the bridge cable, the modal parameters identified from the bridge deck at ATTID are compared with those from the bridge cable at ABTLC. Some of the results are summarized in Table 4.

Table 4 Comparison of modal parameters between bridge deck and cable

	HKT	Lat1		Lat2		Ver1		Ver2		Cab1	
		Deck	Cable	Deck	Cable	Deck	Cable	Deck	Cable	Deck	Cable
Freq.	18:00-19:00	0.0686	0.0684	0.1602	-----	0.1137	0.1138	0.1365	0.1376	-----	0.2327
(Hz)	22:00-23:00	0.0681	0.0682	0.1587	-----	0.1141	0.114	0.1376	0.1364	-----	0.234
ξ	18:00-19:00	0.80%	0.68%	1.27%	-----	0.35%	0.71%	1.01%	1.23%	-----	0.41%
	22:00-23:00	1.31%	1.31%	1.07%	-----	0.73%	0.93%	0.94%	1.14%	-----	0.56%

In Table 4, the modes of vibration Lat1 and Ver1 and Ver2 involve the motion of both the bridge deck and cable. However, the mode of vibration Lat2 involves only the bridge deck motion while the mode of vibration Cab1 contains the bridge cable motion only. It is seen that the natural frequencies identified from the bridge deck are nearly identical to those from the bridge cable in the cases Lat1,

www.EngineeringEBooksPdf.com

Ver1, and Ver2, but there is slight discrepancy in the modal damping ratio. It is interesting to see that the modal damping ratio identified from Cab1 with cable motion only is 0.41% and 0.56% while the modal damping ratio obtained from Lat2 with bridge deck motion only is 1.27% and 1.07%. This indicates that the modal damping ratio of the bridge cable is relatively small.

VARIATIONS OF FREQUENCY AND DAMPING WITH AMPLITUDE AND WIND SPEED

In this section, the EMD-HT approach is used to investigate the variations of modal parameters with vibration amplitude and mean wind speed.

Variations of Natural Frequency with Vibration Amplitude and Mean Wind Speed

A series of response time-histories recorded at ATTID during different time periods with different vibration amplitudes are used to identify the natural frequencies and modal damping ratios of the Bridge. The variations of natural frequencies with vibration amplitude are shown in Fig. 2 (a) to (c) for Lat1, Lat2, Ver1, Ver2, and Tor1 with their linear fits, respectively. The variations of natural frequencies with hourly mean wind speed are plotted in Fig. 2 (d) to (f), correspondingly. It is clearly seen that for all the cases the natural frequencies decrease slightly with the increasing vibration amplitude and hourly mean wind speed.

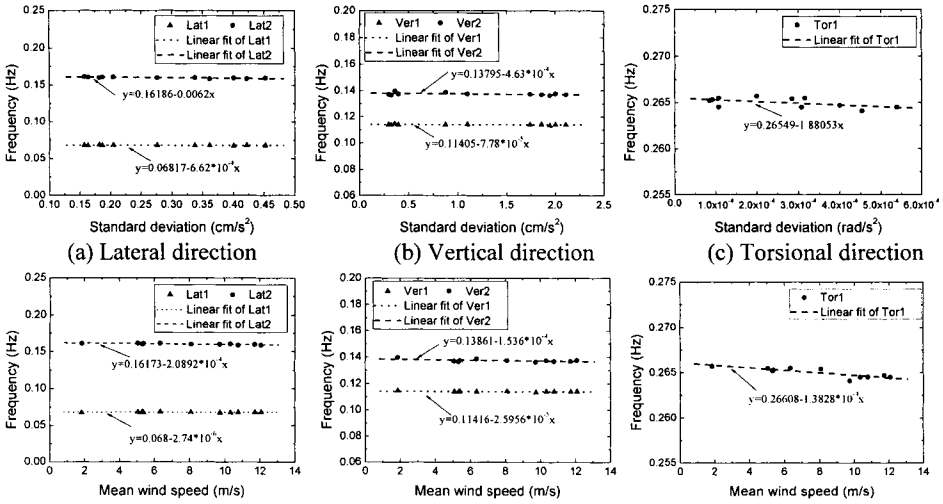

(a) Lateral direction (b) Vertical direction (c) Torsional direction

(d) Lateral direction (e) Vertical direction (f) Torsional direction

Figure 2 Variations of natural frequencies with vibration amplitude and mean wind speed

Variations of Total Damping Ratio with Vibration Amplitude and Mean Wind Speed

The total modal damping ratios identified from ATTID are shown in Fig 3(a)-(d) against vibration amplitude for Lat1, Lat2, Ver1 and Tor1, respectively. Meanwhile, the variations of the total damping ratio with hourly mean wind speed are depicted in Fig. 3(e)-(h). It can be seen that the total damping ratios have an increasing trend with the increasing vibration amplitude and mean wind speed.

www.EngineeringEBooksPdf.com

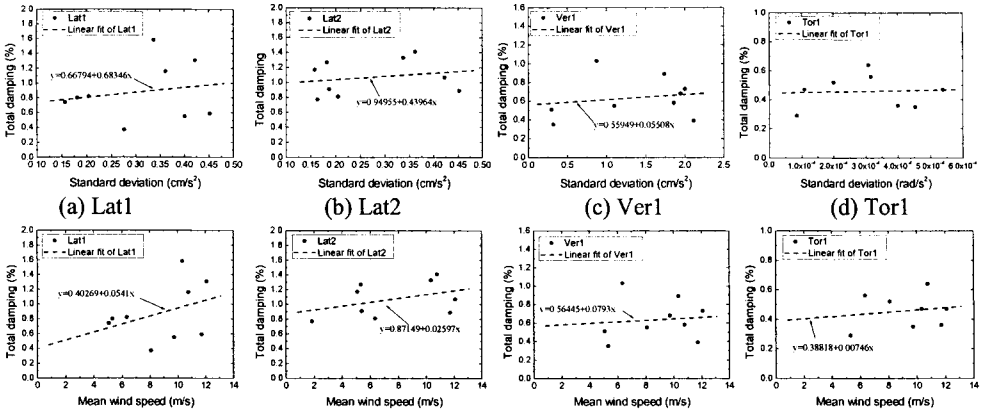

Figure 3 Variation of total damping ratio with vibration amplitude and mean wind speed

CONCLUSIONS

The modal parameters of the Tsing Ma Bridge during Typhoon Victor have been investigated using the EMD-HT approach. The results showed that the EMD-HT approach and the FFT method produced almost the same natural frequencies but the FFT method gave higher modal damping ratios than the EMD-HT approach in most cases. The consistent modal parameters were identified from different sensors at different locations. The results also demonstrated that the natural frequencies of the Bridge decreased slightly with the increase of mean wind speed and vibration amplitude. The total damping ratios, however, exhibited an increasing trend with the increase of vibration amplitude and mean wind speed.

ACKNOWLEDGMENTS

The writers are grateful for the financial support from The Hong Kong Polytechnic University through its Area of Strategic Development Programme in Structural Health Monitoring and Damage Detection and its Outstanding Young Professor Scheme to the second writer.

REFERENCES

Bendat, J. S. and Piersol, A. G., (1986), Random data: analysis and measurement procedures, 2nd Edition, John Wiley&Sons, NY

Huang, N. E., Shen, Z. , Long S. R., Wu M. C., Shih, H. H., Zheng, Q., Yen N. C. and Liu, H. H., (1998), The empirical mode decomposition and the Hilbert spectrum for nonlinear and non-stationary time series analysis, Proc. R Soc. Lond. A, 454, 903-995

Jeary, A. P. (1986), Damping in tall buildings-a mechanism and a predictor, Earthquake Engrg. Struct. Dyn. 14:5, 733-750

Jones N. P. and Spartz C. A., (1990), Structural damping estimation of long-span bridge, J. of Engrg. Mech. ASCE, 116:11, 2414-2433

Tamura, Y. and Suganuma, S.Y., (1996), Evaluation of amplitude-dependent damping and natural frequency of buildings during strong winds, J.Wind. Eng.Ind. Aerodyn. 59:2-3, 115-130

Xu, Y.L., Ko, J.M. and Zhang, W.S. (1997), Vibration studies of Tsing Ma suspension bridge, J. of Bridge Engrg, ASCE, 2:4, 149-156

Xu, Y. L., Zhu, L. D. , Wong K. Y. and Chan K. W. Y., (1999) Field measurement results of Tsing Ma suspension bridge during Typhoon Victor, Struc. Eng. And Mech., 10:6, 545-559

Yang, J. N. and Lei, Y., (2000), System identification of linear structures using Hilbert transform and empirical mode decomposition, Proc. of 18th Int. Modal Analy. Conf.: A Conference on Structural Dynamics, San Antonio, TX, Society of Experimental Mechanics, Inc. Bethel, CT, Vol1, 213-219

www.EngineeringEBooksPdf.com

Advances in Steel Structures, Vol. II
Chan, Teng and Chung (Eds.)
© 2002 Elsevier Science Ltd. All rights reserved.

DYNAMIC LOAD FROM PEDESTRIAN FOOTSTEPS

S.S. Law

Department of Civil and Structural Engineering, Hong Kong Polytechnic University
Hunghom, Kowloon, Hong Kong, China

ABSTRACT

The performance of pedestrian footbridge under environmental and pedestrian excitation has received much attention lately with the problem of resonating vibration of the Millennium Bridge in London. The dead weight of the bridge is small with increased improvement in the design method and the use of light-weight and high strength materials. Damping mechanism is seldom provided for this type of structure. This gives rise to unacceptable vibration from human or environmental excitations and causes alarm. This paper studies the vertical dynamic load generated by pedestrian footsteps on a simply supported steel bridge deck. The forces are identified using an existing algorithm on moving force identification developed by the author (Law and Fang, 2001). The identified footstep force is then generalized using a time series and the coefficients of which are obtained from collected samples of footstep forces. Further analysis on the samples collected is in process, and results would be useful for dynamic design of the performances of the pedestrian footbridge.

KEYWORDS

Force identification, pedestrian, footstep, dynamic programming, velocity, strain, steel beam.

INTRODUCTION

The recent resonating vibration of the Millennium Bridge in London (Dallard et al., 2001) raises alarm on the lack of knowledge on the dynamic behaviour of the structure when groups of pedestrian move across the bridge deck. The force generated by different group size of people varies and it could excite a light-weight bridge deck with little damping capacity into resonance.

This paper gives the dynamic loading from footstep of pedestrian as measured indirectly from the dynamic responses of the structure as an alternative approach of measurement. The interaction between the pedestrian and the bridge deck is taken into account in the identification of the footstep forces. Existing algorithm on moving force identification was used in the study (Law and Fang, 2001). The loading when compared with the pseudo-dynamic loading obtained from load cells indicates the presence

www.EngineeringEBooksPdf.com

of high frequency components and a larger magnitude due to the slow response of the load cell to dynamic load. The identified footstep force is generalized using a time series, and the coefficients of which are obtained from samples of the identified footstep forces. The results indicate the existence of higher frequency components of the impulsive footsteps which cannot be obtained from the pseudo-dynamic test by Ebrahimpour et al. (1996). These would be useful for dynamic design of footbridge under groups of moving pedestrians.

MOVING FORCES IDENTIFICATION ALGORITHM

The method to identify the moving footstep loads is adapted from previous work by the author (Law and Fang, 2001). The forces in the state-space formulation of the dynamic system are identified in the time domain using the dynamic programming technique and information from several distributed sensor measurements. Responses of the structure are reconstructed using the identified forces for comparison with the measured responses as a means of assessment the accuracy of identification. The problem formulation is briefly described below, and details on the solution of the equations are referred to Law and Fang (2001).

Assumptions

The following assumptions are made on the dynamic system model: (a) The changes in the system characteristics, i.e. the stiffness, damping and mass matrices under the passage of the force are negligible, and (b) Euler-Bernoulli beam model is used with the shear effect neglected.

Nodal Forces from an Applied Force

When a force time history f_l is applied on a two-dimensional finite beam element of length l between the ith and $(i+1)$th nodes at a point distant x from the left end, the nodal forces at each end of the beam element can be found and grouped into the global force vector as

$$\boldsymbol{P} = \boldsymbol{Y(x)} \, . \, f_l \tag{1}$$

where $\boldsymbol{P}$ is the nodal force vector and $\boldsymbol{Y(x)}$ is the vector on the location of the applied force. For the case of multi-forces acting on the beam element, the global force vector arising from the ith force is represented by

$$\boldsymbol{P}_i = \boldsymbol{Y}(x_i) \, . \, f_i \tag{2}$$

State Space Model

The finite element representation of a n-DOFs dynamic system is given by:

$$\boldsymbol{M}\ddot{\boldsymbol{u}} + \boldsymbol{C}\dot{\boldsymbol{u}} + \boldsymbol{K}\boldsymbol{u} = \boldsymbol{P} \tag{3}$$

where $\boldsymbol{u}$ is a vector containing all the displacements of the model; $\dot{u}$ is the first derivative of $\boldsymbol{u}$ with respect to time t; $\boldsymbol{M}$ is the system mass matrix; $\boldsymbol{C}$ is the system damping matrix; $\boldsymbol{K}$ is the system stiffness matrix, and $\boldsymbol{P}$ represents the system of exciting forces which is a function of the location and magnitude of the applied forces as shown in (2).

Using the state space formulation, (3) is converted into a set of first order differential equation as follows:

$$\dot{\boldsymbol{X}} = \boldsymbol{K}^* \boldsymbol{X} + \overline{\boldsymbol{P}} \tag{4}$$

www.EngineeringEBooksPdf.com

where $X = \begin{bmatrix} u \\ \dot{u} \end{bmatrix}_{2n\times 1}$, $K^* = \begin{bmatrix} 0 & I \\ -\mathrm{M}^{-1}K & -\mathrm{M}^{-1}C \end{bmatrix}_{2n\times 2n}$

$$\begin{aligned} \overline{P} &= \begin{bmatrix} 0 \\ -M^{-1}P \end{bmatrix}_{2n\times 1} \\ &= \begin{bmatrix} 0 \\ -M^{-1}Y \end{bmatrix}_{n\times n_f} f_{nf\times 1} \end{aligned} \tag{5}$$

where X represents a vector of state variables of length $2n$ containing the displacements and velocities of the nodes; n_f is the number of forces, and f is a vector of length n_f representing the unknown applied forces. These differential equations are then rewritten into discrete equations using the standard exponential matrix representation.

$$X_{j+1} = F X_j + \overline{G}_{j+1}\overline{P}_j \tag{6}$$

$$F = e^{K^*\Delta t} \tag{7}$$

and

$$\overline{G} = K^{*-1}(F - I) \tag{8}$$

where matrix F is the exponential matrix, and together with matrix $\overline{G}$ they represent the dynamics of the system; $(j+1)$ denotes the value at $(j+1)$th time step of computation; the time step Δt represents the time difference between the variable states X_j and X_{j+1} in the computation, and $\overline{G}$ is a matrix relating the forces to the system. Substituting (5) and (8) into (6) we have

$$X_{j+1} = F X_j + G_{j+1} f_j \tag{9}$$

where

$$G = \overline{G}_{2n\times 2n}\begin{bmatrix} 0 \\ -M^{-1}Y \end{bmatrix}_{2n\times nf} \tag{10}$$

Matrix G for Two Moving Forces with Known Speed

Suppose we have two forces spaced at a constant distance moving across a simply supported beam at a constant speed c. The matrices $\overline{G}$ and G in (8) and (10) respectively vary for different location of the forces. Rewrite (1) and (8) into

$$P = [Y(x_1), Y(x_2)]\begin{pmatrix} f_1 \\ f_2 \end{pmatrix} \tag{11}$$

$$\overline{G} = \begin{bmatrix} \overline{G}_{11} & \overline{G}_{12} \\ \overline{G}_{21} & \overline{G}_{22} \end{bmatrix} \tag{12}$$

and (5) becomes

$$\overline{P} = \begin{bmatrix} 0 & 0 \\ -M^{-1}Y(x_1) & -M^{-1}Y(x_2) \end{bmatrix}\begin{pmatrix} f_1 \\ f_2 \end{pmatrix} \tag{13}$$

The discrete representation of the system in (6) can then be written as

www.EngineeringEBooksPdf.com

$$
\begin{aligned}
\boldsymbol{X}_{j+1} &= \boldsymbol{F}\boldsymbol{X}_j + \overline{\boldsymbol{G}}_{j+1}\overline{\boldsymbol{P}}_j \\
&= \boldsymbol{F}\boldsymbol{X}_j + \begin{bmatrix} \overline{\boldsymbol{G}}_{11} & \overline{\boldsymbol{G}}_{12} \\ \overline{\boldsymbol{G}}_{21} & \overline{\boldsymbol{G}}_{22} \end{bmatrix} \begin{bmatrix} 0 & 0 \\ -\boldsymbol{M}^{-1}\boldsymbol{Y}(x_1) & -\boldsymbol{M}^{-1}\boldsymbol{Y}(x_2) \end{bmatrix} \begin{pmatrix} f_1 \\ f_2 \end{pmatrix} \\
&= \boldsymbol{F}\boldsymbol{X}_j + \begin{bmatrix} -\overline{\boldsymbol{G}}_{12}\boldsymbol{M}^{-1}\boldsymbol{Y}(x_1) & -\overline{\boldsymbol{G}}_{12}\boldsymbol{M}^{-1}\boldsymbol{Y}(x_2) \\ -\overline{\boldsymbol{G}}_{22}\boldsymbol{M}^{-1}\boldsymbol{Y}(x_1) & -\overline{\boldsymbol{G}}_{22}\boldsymbol{M}^{-1}\boldsymbol{Y}(x_2) \end{bmatrix} \begin{pmatrix} f_1 \\ f_2 \end{pmatrix} \\
&= \boldsymbol{F}\boldsymbol{X}_j + \boldsymbol{G}_{j+1}(x_1, x_2) \begin{pmatrix} f_1 \\ f_2 \end{pmatrix}
\end{aligned}
\tag{14}
$$

and in matrix form as

$$\boldsymbol{X}_{j+1} = \boldsymbol{F}\boldsymbol{X}_j + \boldsymbol{G}_{j+1}\boldsymbol{f}_j \tag{15}$$

where G_{j+1} is the value at $(j+1)$th time step. Note that (15) is the same as (9) but for two moving forces.

THE EXPERIMENT

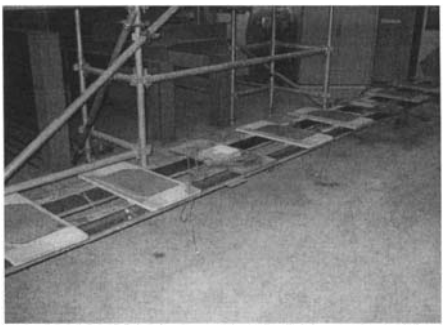

Figure 1 : Photograph on the Model Bridge Deck

The bridge model consists of two 100x55x6.9kg steel I-beams 6 metres long placed in parallel 300mm apart with steel plates and flat bars welded to the top and bottom flanges at intervals. It is supported 5.9 metres apart on rollers on top of concrete plinths. The steel plates serve as walking panels. Additional panels were formed from wooden planks fixed to the top flanges by bolts and nuts. The panels are 0.633 meters apart. A photograph of the bridge deck is shown in Figure 1.

Strain gauges were placed at the bottom of the two beams at positions $L/4$, $3L/8$, $L/2$, $5L/8$ and $3L/4$ from one end of the model, where L is the span of the bridge model. Flat steel bars were welded on the lower flange of the beams at the same positions as the gauges, and B&K 4370 accelerometers were mounted at the middle of the flat bars. Electronic triggers were mounted on the surface of the second to the ninth walking panels to monitor the exact moment when the footstep is on and off the panel. All the strain gauges and accelerometers were connected to the strain-meter KYOWA CDA230A and signal conditioner B&K 2635 respectively, and all signal were digitized with the DASP INV306 data acquisition system.

www.EngineeringEBooksPdf.com

The readings from the strain gauges were calibrated by placing and removing steel blocks on each panel in 20 kg increment up to 80 kg. The response of each strain gauge was plotted against the loading on the panel, and the slope of the lines was almost equal to the listed factor by the manufacturer.

The natural frequencies of the model bridge deck were also checked from modal analysis results obtained from 45 minutes random vibration responses of the bridge deck. The first two vertical modes are at 8.041 and 25.584 Hz, and the first three torsional modes are at 11.634, 15.167 and 34.051 Hz. The natural frequencies are low enough to allow the use of a low sampling rate of 499.7501 Hz for recording the responses. Since the vertical responses are used in the identification, the strain responses from the two beams were added and average before further processing. A person of 68 kg body weight was requested to walk on top of the bridge model starting at different panel and with different types of walking pattern.

The responses with different walking patterns from the person were measured. They are normal-walking pattern and control-walking pattern. Normal-walking pattern is the natural walking behaviour of a human step-by-step pattern. A person was asked to make a single step movement at a time on a panel with his left or right foot over one or several panels in sequence. All of these step movements were unprompted, i.e., the person was walking under normal conditions at his own pace. The control-walking pattern has one foot stepping on the panel, then stepping another foot on the same panel, i.e. with both feet located on the same panel. Next, one foot was removed from the panel and then another foot. The purpose of the later walking pattern is for reference, and it does not reflect the real walking behaviour and therefore the results are not discussed here.

To compare the results obtained from the dynamic measurement, a measurement on the footstep forces using static load cells was carried out. Three static load cells were placed at the three corners of an equilateral triangle on solid level ground with a thick wooden plank placed on top. The load cells were calibrated by placing dead weights on top of the plank from 10kg to 70kg in 10kg increments. And the calibrating voltage output of the load cells for the loading and unloading stages were noted. The same person was requested to walk on top of the wooden plank with one footstep in the normal-walking pattern to obtain the pseudo-dynamic footstep forces.

RESULTS

Single Footstep Forces

The footstep forces were identified from the measured strain responses from the five instrumented sections. Results from the use of velocity measurements are not presented here. Samples of the identified forces from single footstep are shown in Figure 2 as solid lines. The identified force exhibits a larger value close to the start and end of the time history with a smaller magnitude in the middle. They correspond to the moments when the foot is placed or removed from the panel. The larger force at the beginning of the time history in Figure 2(d) is caused by a footstep coming from a high platform thus causing a large impulsive excitation. It is noted that the samples from the left and right foot are similar indicating similar characteristics in the left and right footstep forces.

The identified force time histories are generalised by a time series consisting of the first ten harmonics (i.e. n=1, 2, 3, …., 9, 10) in the following form

$$F(t) = W_g * \{1 + \sum_{n=1}^{10} [a_n \sin(n\pi t / T)]\} \tag{16}$$

where t is the time instant, W_g is the static weight of the pedestrian which equals 68 kg in the present case, and T is the period which equals to the duration of a footstep. The curve best fitting the identified

www.EngineeringEBooksPdf.com

time history are shown as dash line in Figure 2.

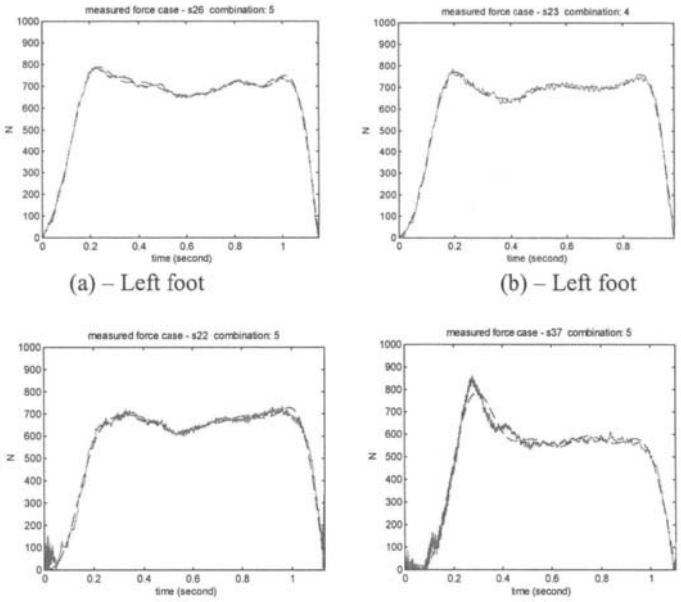

Figure 2: Results for Single Footstep

Pseudo-Dynamic Test Result

The time history of a series of footstep load from the right foot obtained from the load cells is shown below. A single sample of the load is also enlarged for reference.

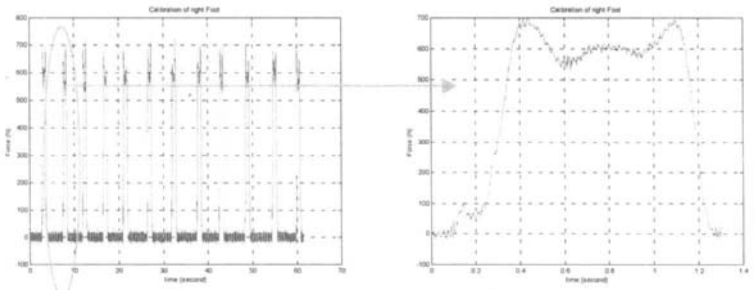

Figure 3: Footstep Load from Load Cells

Comparing the curve in Figure 3 for a single footstep and those in Figure 2 shows that they are very similar with two peaks close to the ends of the time duration. But the mean force value from load cells is 58kg while that in Figure 2 is 68kg which is the body weight of the person performing the test. This difference is due to the slow response of the static load cell giving smaller than true value of the footstep force.

www.EngineeringEBooksPdf.com

Multiple Footstep Forces

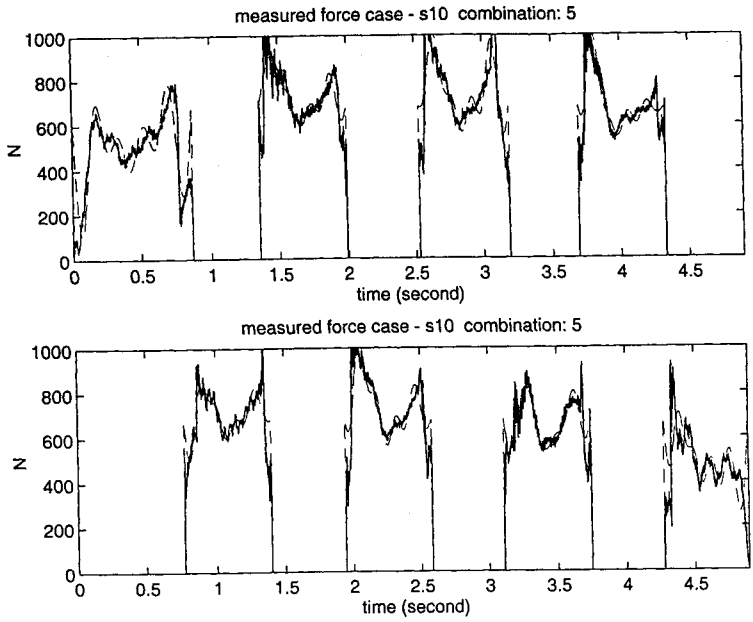

Figure 4: One Foot on Panels 2 to 9 (L-R-L-R-L-R-L-R)

A sample of multiple footstep forces is shown in Figure 4. The letter L-R etc. in bracket in the figure title indicates the sequence of left and right foot in the experiment. The identified forces are shown in solid line with high frequency components while the curved fitted using the time series are shown in dash line are smooth and close to the original time history.

The impulsive forces close to the start and end of each step is higher than those for a single footstep indicating the action of a larger impulsive force on the structure when walking continuously compared to the force from a single footstep shown in Figure 2.

The first footstep force is usually longer because of the subject needs more time in starting the walk. The last footstep force has a decreasing pattern towards the end of the period indicating the subject tends to slip off the steel deck quickly. They are not representative of the normal walking pattern and are not included in the study on the coefficients of the time series.

The average of the coefficients a_i in (16) obtained from twenty-eight samples of the forces are listed in Table 1. The samples are not coming from the starting and ending footsteps. Generally the odd coefficients are relatively larger than the other coefficients, and those from the left foot and the right food are similar. Therefore one single set of parameters is calculated for all the samples which is the characteristics of the normal walking pattern of the subject. Other pedestrian would have his or her characteristics trace of footstep forces, but the dynamic forces would have similar pattern as what we have from this experiment.

Pernica (1990) and Allen and Rainer (1976) have obtained results for moving pedestrians indicating insignificant components in the higher harmonics. His conclusion is not supported by the present set of results since the seventh and ninth harmonic has a significant component other than the first three

www.EngineeringEBooksPdf.com

components.

TABLE 1
COEFFICIENTS OF THE TIME SERIES FOR THE IDENTIFIED FORCES

	a1	*a2*	*a3*	*a4*	*a5*	*a6*	*a7*	*a8*	*a9*	*a10*
Average										
Left	0.06	0.06	0.17	0.06	0.01	0.01	-0.05	0.03	-0.08	0.00
Right	0.04	0.04	0.10	0.01	-0.08	0.00	-0.09	0.02	-0.08	0.01
Both	0.05	0.05	0.13	0.03	-0.04	0.00	-0.07	0.03	-0.08	0.00

CONCLUSIONS

A summary of experimental study on the forces produced by the footstep of a pedestrian is presented in this paper. This project measured the footstep forces acting on a bridge model by using an existing moving forces identification algorithm. The force identified has strong components in the odd harmonics of a time series as proposed in this paper where the dynamic components are expressed as a fraction of the static weight of the pedestrian. They are identified indirectly from the measured responses of the structure including the interaction effect between the pedestrian and the structure. High frequency components are retained in the final force time histories and this could not be obtained from pseudo-dynamic tests using load cells.

REFERENCES

Allen, D.E. and Rainer, J.H. (1976). Vibration criteria for long-span floors. *Canadian Journal of Civil Engineering*, 3:2, 165-173.

Dallard, P., Fitzpatrick, A.J., Flint, A., Bourva, S.Le., Low, A., Ridsdill Smith, R.M. and Willford,M. (2001). The London Millennium Bridge. *Journal of Structural Engineers*, 79:22, 17-33.

Ebrahimpour, A.Hamam, R.L. Sack, and W.N. Patten. (1996). Measuring and modelling dynamic loads imposed by moving crowds. *Journal of Structural Engineering*, ASCE. 122:12, 1468-1474

Law, S.S. and Y.L. Fang. (2001). Moving Force Identification: Optimal State Estimation Approach. *Journal of Sound and Vibration,* 239:2, 233-254

Pernica, G. (1990). Dynamic load factors for pedestrian movements and rhythmic exercises. *Canadian Acoustics*, 18:2, 3-18.

www.EngineeringEBooksPdf.com

Advances in Steel Structures, Vol. II
Chan, Teng and Chung (Eds.)
© 2002 Elsevier Science Ltd. All rights reserved.

FRICTIONAL JOINT IN THE DYNAMIC ANALYSIS OF A PORTAL FRAME

S.S. Law, Z.M. Wu and S.L. Chan

Department of Civil and Structural Engineering, Hong Kong Polytechnic University
Hunghom, Kowloon, Hong Kong, China

ABSTRACT

Most research on semi-rigid jointed frames includes only the rotational flexibility of the joint without considering the flexibility in the direction of the shear force. But in real life the tangential direction flexibility contributes significantly to the damping characteristics of the structure when under dynamic loading. This paper investigates the non-linear dynamic behaviour of a slotted-bolt-jointed portal frame. The joint is prestressed with axial tension in the bolt shank. A virtual connection spring element is included at the intersection point between the beam and the column members. The formulation of the hybrid beam-column element including the end springs is presented. Numerical simulation shows that the damping property of the structure is improved significantly with the inclusion of these frictional joints.

KEYWORDS

Frictional Joint; Semi-Rigid Connection; Beam-Column Element; Steel Frame; Cyclic Behaviour, Non-Linearity, Prestress, Slotted-bolted-joint.

INTRODUCTION

Conventional approaches in the design and analysis of steel frames commonly assume the structural components to be connected either by rigid or pinned joints. In practice, all joints are semi-rigid, in which the slope of the lateral deflected shape and rotation are discontinuous between two connected members. Most of the research so far has only studied the rotational flexibility of semi-rigid joints in steel frames (Chan and Chiu, 2000). The dynamic behaviour of steel structures with ordinary bolted frictional joints, that have flexibility in the tangential direction has received limited attention.

A frictional joint can be regarded as a typical semi-rigid connection with improved frictional damping. The improved damping is obtained since sandwiched plates are pre-loaded by high strength friction

www.EngineeringEBooksPdf.com

grip bolts installed in slotted holes. The slotted connection detail for the friction grip bolts is permitted in the design code to allow for slippage between the connected members under severe loading. This arrangement could reduce the lateral deflection of a building due to horizontal loads with improved damping behaviour enhancing the ductility of the structure.

This paper studies the dynamic behaviour of a portal frame with a hybrid finite element consisting of non-linear slotted-bolted frictional joints at its ends. The displacement function of the hybrid element is presented. Numerical simulation shows that the damping property of the structure is effectively improved through the inclusion of these frictional joints.

CONNECTION BEHAVIOUR UNDER CYCLIC LOADING

The monotonic force-deformation relation in the tangential direction of the frictional joints is first defined and then extended to the modelling of the cyclic behaviour based on Masing's rule (Herrera, 1965). The most popular existing model to describe the force-deformation relationship in a general frictional slip interface is the bilinear model, which has the disadvantage of slope discontinuity, and this is undesirable in the numerical analysis and modeling. With the assumption of an exponential distribution of peak height of spherical contact elements, Shoukry (1985) developed a microslip element to model the frictional behaviour between two metallic interfaces, by using Mindlin's spherical contact element (Mindlin, 1949) as the basic element. The force-deformation relation of the frictional interface is given by:

$$Q = \mu N[1 - \exp(\frac{-\gamma}{\sigma} v_c)] \tag{1}$$

where μ, N are the friction coefficient and normal force acting on the interface respectively; σ is the standard deviation of the peak height distribution of the contact element; and γ is a constant equal to $2(1-\nu)/[\mu(2-\nu)]$, where ν is the Poisson ratio.

With consideration of the usual configuration of a slotted bolted connection in a structural frame, a mathematical expression can be written for the load-deformation relation of a frictional joint in the tangential direction as,

$$\begin{cases} Q = Q_s[1 - \exp(-\dfrac{K_0}{Q_s} v_c)], & \text{if} \quad v_c \le v_{cl}; \\ Q = Q_s[1 - \exp(-\dfrac{K_0}{Q_s} v_{cl})] + k_l(v_c - v_{cl}), & \text{if} \quad v_c > v_{cl}; \end{cases} \tag{2}$$

where v_{cl} is the slippage threshold of the bolted hole; Q_s is the friction limit which is equivalent to μN in Shoukry's expression; K_0 is the initial stiffness, i.e. $K_0 = dQ/dv_c|_{v_c=0}$, which is equivalent to $\mu N\gamma/\sigma$ in Shoukry's expression; and k_l is the contact stiffness after the slippage threshold is reached. These properties are shown in Figure 1 where Point B is the point defining the slippage threshold. It can be seen that the stiffness of joint changes nonlinearly with the magnitude of shear loading. The joint behaves rigidly under small loading, and it softens at the application of severe loading. However when the slip threshold is reached, the bolt is in contact with the edge of the bolted hole, and the stiffness of joint is governed by the constant stiffness k_l.

Equation (2) above is physically important because the joint parameters in the loading curve, such as the initial stiffness and the frictional resistance force, are related to other physical parameters, like the normal pressure and friction coefficient. Accordingly, the joint properties can be predicted from other physical parameters, and direct testing for the force-deformation characteristics may not be necessary.

www.EngineeringEBooksPdf.com

In the following formulation, (2) is used to represent the virgin loading curve of the frictional joint in the tangential direction. The corresponding instantaneous connection stiffness in the virgin curve is given by

$$\begin{cases} r_v = \dfrac{\mathrm{d}Q}{\mathrm{d}v_c} = K_0 \exp\left[-\dfrac{K_0}{Q_s} v_c\right], & \text{if} \quad |v_c| \le v_{cl}; \\ r_v = \dfrac{\mathrm{d}Q}{\mathrm{d}v_c} = k_l, & \text{if} \quad |v_c| > v_{cl}; \end{cases} \tag{3}$$

Equation (2) can also be generalised for both the unloading and reloading curves based on the Masing rule as

$$\begin{cases} \left|\dfrac{Q - Q^*}{2}\right| = Q_s\left[1 - \exp\left(-\dfrac{K_0}{Q_s}\left|\dfrac{v_c - v_c^*}{2}\right|\right)\right], & \text{if} \quad |v_c| \le v_{cl}; \\ Q = Q^* + k_l(v_c - v_c^*), & \text{if} \quad |v_c| > v_{cl}; \end{cases} \tag{4}$$

where (v_c^*, Q^*) is the point at which load reversal occurs in the range of $|v_c| \le v_{cl}$. But, when $|v_c| > v_{cl}$, the loading and reloading process is on a straight line with slope k_l. Therefore, the corresponding instantaneous connection stiffness of both the unloading and reloading curves can be expressed as,

$$\begin{cases} r_v = \dfrac{\mathrm{d}Q}{\mathrm{d}v_c} = K_0 \exp\left(-\dfrac{K_0}{Q_s}\left|\dfrac{v_c - v_c^*}{2}\right|\right), & \text{if} \quad |v_c| \le v_{cl}; \\ r_v = \dfrac{\mathrm{d}Q}{\mathrm{d}v_c} = k_l, & \text{if} \quad |v_c| > v_{cl}; \end{cases} \tag{5}$$

in which, $v_c^* = v_{ca}^*$ when the slippage deformation happens after the reversal point A in Figure 2. If point B is the next reversal point, the reloading stiffness is obtained by replacing v_{ca}^* with v_{cb}^* in (5).

CONNECTION SPRING ELEMENT

This semi-rigid joint can be modelled as a virtual connection spring element inserted at the intersection point between a beam and a column. A typical connection spring element in the tangential direction shown in Figure 3 is used. The virtual connection spring in other directions can be described in a similar manner. The connection spring elements are located at member ends, and they are assumed infinitely small in size. The complete hybrid element includes a member and the corresponding connections. Nodes I and J are external nodes, and nodes i and j are internal nodes. The beam-column element is between nodes i and j. The connection spring elements are between nodes I and i and between nodes J and j respectively as shown in Figure 4.

In the derivation of the spring stiffness matrix, the three basic governing conditions, i.e. the compatibility, the equilibrium and the constitutive relations for an element are considered. Considering a spring with stiffness r_v, two end displacements, ${}_I v$ and ${}_i v$ on either side, and the corresponding lateral shear forces, ${}_I Q$ and ${}_i Q$, the equilibrium condition requires

www.EngineeringEBooksPdf.com

$$ {}_{J}Q + {}_{i}Q = 0 \tag{6}$$

Assuming that v_c is the relative displacement between the joint surfaces, the compatibility condition requires

$$ v_c = {}_{J}v - {}_{i}v \tag{7}$$

The constitutive relationship on the shearing action is

$$ r_v = \frac{{}_{J}Q}{v_c} = \frac{{}_{i}Q}{v_c} \tag{8}$$

Substituting (6) into (8), we have

$$ \begin{Bmatrix} {}_{J}Q \\ {}_{i}Q \end{Bmatrix} = \begin{bmatrix} r_v & -r_v \\ -r_v & r_v \end{bmatrix} \begin{Bmatrix} {}_{J}v \\ {}_{i}v \end{Bmatrix} \tag{9}$$

Therefore, the stiffness matrix of the connection element is given by:

$$ \begin{bmatrix} r_v & -r_v \\ -r_v & r_v \end{bmatrix} \tag{10}$$

SHAPE FUNCTION OF THE HYBRID ELEMENT

By using the cubic Hermitian function, the lateral deflection v in the y-direction at a location x along the center-line of a straight element can be written as

$$ v = \begin{bmatrix} (3-2\rho_1)\rho_1^2 & (3-2\rho_2)\rho_2^2 \end{bmatrix} \begin{bmatrix} v_i \\ v_j \end{bmatrix} + \begin{bmatrix} \rho_1^2 \rho_2 L & -\rho_1 \rho_2^2 L \end{bmatrix} \begin{bmatrix} \theta_i \\ \theta_j \end{bmatrix}, \qquad \rho_1 = 1 - \frac{x}{L}, \quad \rho_2 = \frac{x}{L}, \tag{11}$$

The lateral deflection v in (11) has not yet accounted for the effect of connection flexibility at the ends of the beam-column element.

The elemental stiffness matrix for the complete hybrid element is assembled from those of the end springs and the beam element. The loads Q_I, M_I and Q_J, M_J are assumed to be applied only at the global nodes I and J, and hence the shear forces Q_i and Q_j are equal to zero. We have

$$ \begin{Bmatrix} v_i \\ v_j \end{Bmatrix} = \begin{bmatrix} r_{vi} + K_{11} & K_{13} \\ K_{31} & r_{vj} + K_{33} \end{bmatrix}^{-1} \begin{bmatrix} r_{vi} & 0 \\ 0 & r_{vj} \end{bmatrix} \begin{Bmatrix} v_I \\ v_J \end{Bmatrix} - \begin{bmatrix} r_{vi} + K_{11} & K_{13} \\ K_{31} & r_{vj} + K_{33} \end{bmatrix}^{-1} \begin{bmatrix} K_{12} & K_{14} \\ K_{32} & K_{34} \end{bmatrix} \begin{Bmatrix} \theta_i \\ \theta_j \end{Bmatrix} \tag{12}$$

Using the conditions $M_i = M_I$, $M_j = M_J$, $\theta_i = \theta_I$ and $\theta_j = \theta_J$, and eliminating the internal degrees-of-freedom, the relation between the external nodal force and nodal displacements/rotations of the element can be obtained.

In assembling the elemental stiffness matrices of a structure, the element stiffness matrix is rewritten in the global coordinate system for geometrical compatibility. Substituting (12) into (11) and transforming the external nodal rotations, θ_I and θ_J, about the local axis at the ends of the element to the global nodal rotations $\bar{\theta}_i$ and $\bar{\theta}_j$, the displacement function v can be finally written as

www.EngineeringEBooksPdf.com

$$
\begin{aligned}
v = &\begin{bmatrix}(3-2\rho_1)\rho_1^2 & (3-2\rho_2)\rho_2^2\end{bmatrix}\begin{bmatrix}r_{vi}+K_{11} & K_{13}\\ K_{31} & r_{vj}+K_{33}\end{bmatrix}^{-1}\begin{bmatrix}r_{vi} & 0\\ 0 & r_{vj}\end{bmatrix}\begin{Bmatrix}v_I\\ v_J\end{Bmatrix}\\
&-\begin{bmatrix}(3-2\rho_1)\rho_1^2 & (3-2\rho_2)\rho_2^2\end{bmatrix}\begin{bmatrix}r_{vi}+K_{11} & K_{13}\\ K_{31} & r_{vj}+K_{33}\end{bmatrix}^{-1}\begin{bmatrix}K_{12} & K_{14}\\ K_{32} & K_{34}\end{bmatrix}\begin{Bmatrix}\theta_I\\ \theta_J\end{Bmatrix}+\begin{bmatrix}\rho_1^2\rho_2 L & -\rho_1\rho_2^2 L\end{bmatrix}\begin{Bmatrix}\theta_I\\ \theta_J\end{Bmatrix}\\
&=\begin{bmatrix}(3-2\rho_1)\rho_1^2 & (3-2\rho_2)\rho_2^2\end{bmatrix}\begin{bmatrix}r_{vi}+K_{11} & K_{13}\\ K_{31} & r_{vj}+K_{33}\end{bmatrix}^{-1}\begin{bmatrix}r_{vi} & 0\\ 0 & r_{vj}\end{bmatrix}\begin{Bmatrix}\bar{v}_i\\ \bar{v}_j\end{Bmatrix}\\
&+\left(\begin{bmatrix}\rho_1^2\rho_2 L & -\rho_1\rho_2^2 L\end{bmatrix}-\begin{bmatrix}(3-2\rho_1)\rho_1^2 & (3-2\rho_2)\rho_2^2\end{bmatrix}\begin{bmatrix}r_{vi}+K_{11} & K_{13}\\ K_{31} & r_{vj}+K_{33}\end{bmatrix}^{-1}\begin{bmatrix}K_{12} & K_{14}\\ K_{32} & K_{34}\end{bmatrix}\right)\\
&\times\begin{bmatrix}1/L & 1 & -1/L & 0\\ 1/L & 0 & -1/L & 1\end{bmatrix}\begin{Bmatrix}\bar{v}_i\\ \bar{\theta}_i\\ \bar{v}_j\\ \bar{\theta}_j\end{Bmatrix}
\end{aligned}
\tag{13}
$$

in which $\bar{v}_i$, $\bar{v}_j$, $\bar{\theta}_i$, $\bar{\theta}_j$ are the nodal displacements and rotations of the element referring to the global axis. The displacement function w in the z- direction can also be expressed similar to (13) when under the shear load and bending moments at the global DOFs at the ends of the member.

EQUATION OF MOTION AND ITERATION PROCEDURE

In the non-linear dynamic analysis of a structure, the equilibrium of the structure at time $t+\Delta t$ is sought on the basis of the last known equilibrium state at time t. The incremental equilibrium equations can be written as

$$[M]\{\Delta\ddot{u}\}+[C]\{\Delta\dot{u}\}+([K_{\mathrm{L}}]+[K_{\mathrm{G}}])\{\Delta u\}=\{\Delta F\}\,, \tag{14}$$

in which $[M]$ and $[C]$ are the mass and the viscous damping matrices; $[K_{\mathrm{L}}]$ and $[K_{\mathrm{G}}]$ are the linear and the geometric stiffness matrices; $[\Delta F]$ is the incremental applied force vector; and $\{\Delta u\}$, $\{\Delta\dot{u}\}$ and $\{\Delta\ddot{u}\}$ are the incremental displacement, velocity and acceleration vectors, respectively.

Expressing the velocity and the acceleration vectors at time $t+\Delta t$ in terms of the known displacement, velocity and acceleration vectors at time t, and the displacement vectors at time $t+\Delta t$ by the Newmark method (Newmark, 1959), we have

$$\{{}^{t+\Delta t}\dot{u}\}=\{{}^{t}\dot{u}\}+(1-\beta)\Delta t\{{}^{t}\ddot{u}\}+\beta\Delta t\{{}^{t+\Delta t}\ddot{u}\}\,, \tag{15}$$

$$\{{}^{t+\Delta t}\ddot{u}\}=\left(1-\frac{1}{2\alpha}\right)\{{}^{t}\ddot{u}\}-\frac{1}{\alpha(\Delta t)}\{{}^{t}\dot{u}\}-\frac{1}{\alpha(\Delta t)^2}\{{}^{t}u\}+\frac{1}{\alpha(\Delta t)^2}\{{}^{t+\Delta t}u\}\,, \tag{16}$$

where α and β are the Newmark integration parameters, and $\{{}^{t}\dot{u}\}$ and $\{{}^{t}\ddot{u}\}$ are the velocity and acceleration at time t respectively. The constant-average acceleration is obtained for $\alpha = 0.25$ and $\beta = 0.5$. The final incremental equilibrium equation for solving the unknown displacement increment $\{\Delta u\}$ at time $t+\Delta t$ can be expressed as

$$[K]_{\mathrm{eff}}\{\Delta u\}=\{\Delta F\}_{\mathrm{eff}} \tag{17}$$

where

www.EngineeringEBooksPdf.com

$$[K]_{\text{eff}} = [K_{\text{L}}] + [K_{\text{G}}] + \frac{1}{\alpha(\Delta t)^2}[M] + \frac{\beta}{\alpha \Delta t}[C] \,, \tag{18}$$

$$\{\Delta F\}_{\text{eff}} = \{\Delta F\} + [M]\left(\frac{\{{}^{t}\dot{u}\}}{\alpha \Delta t} + \frac{\{{}^{t}\ddot{u}\}}{2\alpha}\right) + [C]\left[\frac{\beta}{\alpha}\{{}^{t}\dot{u}\} + \frac{\Delta t}{2}\left(\frac{\beta}{\alpha} - 2\right)\{{}^{t}\ddot{u}\}\right], \tag{19}$$

in which $[K]_{\text{eff}}$ and $\{\Delta F\}_{\text{eff}}$ are the effective tangential stiffness and the effective load increment respectively. When the displacement increment $\{\Delta u\}$ at time $t + \Delta t$ is obtained from (17), it can be used to update the deflected shape of the structure and the displacement. The acceleration and velocity vectors are updated using (15) and (16).

Equation (17) is checked for equilibrium at each time step, and Newton-Raphson iteration on the unbalanced residual force increment vector $\{\Delta F\}_i$ at the ith step is given by

$$\{\Delta F\}_i = \left\{{}^{t+\Delta t}F\right\}_i - \left([M]\left\{{}^{t+\Delta t}\ddot{u}\right\}_i + [C]\left\{{}^{t+\Delta t}\dot{u}\right\}_i + \left\{{}^{t+\Delta t}R\right\}_i\right), \tag{20}$$

in which $\left\{{}^{t+\Delta t}F\right\}_i$ is the total applied nodal force; $\left\{{}^{t+\Delta t}R\right\}_i$ is the resisting force of the complete structure and i is the iteration number at a particular time increment. The resisting force $\left\{{}^{t+\Delta t}R\right\}_i$ is obtained by calculating the sum of internal force vectors of all elements under deformation for the current equilibrium states (Chiu and Chan, 1999).

The residual displacement increment $\{\Delta u\}_i$ due to the unbalanced residual force $\{\Delta F\}_i$ is then given by

$$\{\Delta u\}_i = [K]_{\text{eff}}^{-1}\{\Delta F\}_i \tag{21}$$

If the ratio of the Euclidean norm of $\{\Delta F\}_i$ to $\left\{{}^{t+\Delta t}F\right\}_i$, and the ratio of the Euclidean norm of $\{\Delta u\}_i$ to $\left\{{}^{t+\Delta t}u\right\}_i$ as shown in (22) are both less than a certain tolerance *TOL*, the equilibrium condition at the ith iteration is considered satisfied and no further iteration is needed. Iteration for the next time step in (17) can then be repeated.

$$\frac{\|\{\Delta F\}_i\|}{\left\|\left\{{}^{t+\Delta t}F\right\}_i\right\|} < TOL_1 ; \qquad \frac{\|\{\Delta u\}_i\|}{\left\|\left\{{}^{t+\Delta t}u\right\}_i\right\|} < TOL_2 \tag{22}$$

However, if either one of the conditions in (22) are not satisfied, the deflected shape, the displacement, velocity and acceleration of the structure are improved by the following iterative scheme for correction of equilibrium error of the system.

$$\left\{{}^{t+\Delta t}\bar{x}\right\}_{i+1} = \left\{{}^{t+\Delta t}\bar{x}\right\}_i + \{\Delta u\}_i \,, \qquad \left\{{}^{t+\Delta t}u\right\}_{i+1} = \left\{{}^{t+\Delta t}u\right\}_i + \{\Delta u\}_i \,,$$

$$\left\{{}^{t+\Delta t}\dot{u}\right\}_{i+1} = \left\{{}^{t+\Delta t}\dot{u}\right\}_i + \frac{\beta}{\alpha \Delta t}\{\Delta u\} \,, \qquad \left\{{}^{t+\Delta t}\ddot{u}\right\}_{i+1} = \left\{{}^{t+\Delta t}\ddot{u}\right\}_i + \frac{1}{\alpha(\Delta t)^2}\{\Delta u\}_i \,. \tag{23}$$

where $\{\bar{x}\}$ represents the coordinate vector of the system. The procedures in (20) to (23) are repeated until convergence is achieved. After the satisfaction of equilibrium conditions at a particular time instance, the computation for the next time increment in (17) is repeated until the desired duration of the time history is reached.

www.EngineeringEBooksPdf.com

RESPONSES OF A PORTAL FRAME

Due to the limited available publications in the design and analysis of structure with semi-rigid frictional joints, study on the effectiveness of the proposed model is referred to the performances of the structure with rigid connections. The tolerance limits in (22) are set equal to 0.001.

The proposed frictional joint model is applied to the more common portal frame of Figure 5, which is an unbraced simple portal frame made of wide flange sections as shown. A vertical uniformly distributed load of 8.2 kN/m is applied on top of the beam. Slip is permitted in the horizontal direction at joints B and C when severe horizontal motion occurs. The column and beams are divided into three and four finite elements respectively for the dynamic analysis. The fundamental natural frequency of the rigidly jointed frame is 4.1Hz. The shear force-slippage curve of the frictional connection at Point C is modelled by (4) and the parameters for the model are $Q_s = 140000$ N, $K_0 = k_l = 60000$ N/mm and $v_{cl} = 6$ mm. Lump masses from the uniform static load are distributed at the modal points of the beam elements. The excitation is from a ground acceleration of $3.8\sin(15.7t)$ m/sec^2. The time history of the lateral deflection of the frame δ is shown in Figure 6. The lateral deflection for the rigidly jointed frame (Al-Bermani et al., 1994) is also shown. The modified frame is shown to have much smaller lateral motion under the ground excitation considered in this study.

CONCLUSIONS

This paper presents a 'macro" element with slotted bolted non-linear frictional joints at the ends, which have flexibility in the tangential directions. A virtual connection spring element is inserted at the intersection point between a beam and a column to model the behaviour of a frictional joint. Numerical simulations with a portal frame showed that the inclusion of nonlinear behaviour of the connections could significantly improve the dynamic performance of these simple structures through good damping and energy-absorption characteristics

ACKNOWLEDGEMENTS

The work described in this paper was supported by a grant from the Hong Kong Research Grant Council Project No. PolyU 5054/99E.

REFERENCES

Al-Bermani, F.G.A., Li,B., Zhu,K. and Kitipornchai,S. (1994). Cyclic and seismic response of flexibly jointed frames. *Engineering structures* 16:4, 249-255

Chui,P.P.T. and Chan,S.L. (1999). Techniques in Transient Analysis of Semi-rigid Steel Frames. *Structural Dynamic Systems Computational Technique and Optimization*. Technology and Applied Science, Chapter 2, 47-98

Chan,S.L. and Chui,P.P.T. (2000). *Non-linear static and cyclic analysis of steel frames with semi-rigid connections*. Elsevier

Herrera,I. (1965). *Dynamic models for Masing type materials and structure*. Boletin Sociedad Mexicana De Ingenieria Sismica, 3:1, 1-8

Mindlin,R.D. (1949). Compliance of elastic bodies in contact. *Journal of Applied Mechanics*. ASME. 16, 259-268.

Newmark,N.W. (1959). A method of computation for structural dynamics. *Journal of Engineering Mechanics Division* ASCE. 85:3, 67- 94

www.EngineeringEBooksPdf.com

Shoukry,S.N. (1985). A mathematical model for the stiffness of fixed joints between machine parts. *Proceedings of the NUMETA'85 Conference*, Swansea, 851-858

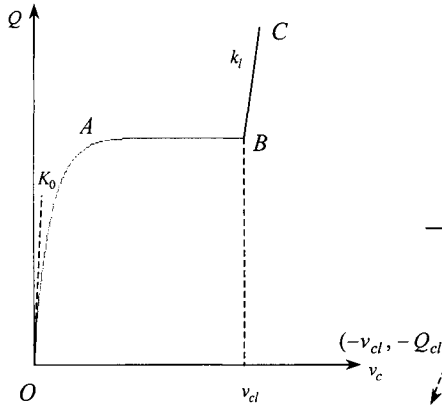

Figure 1 – Virgin loading curve of frictional joint

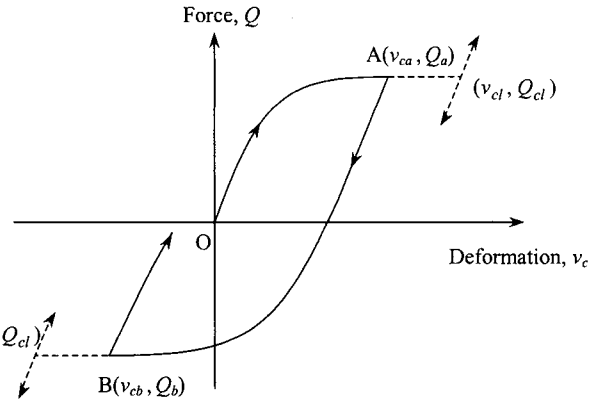

Figure 2 – Hysteresis model

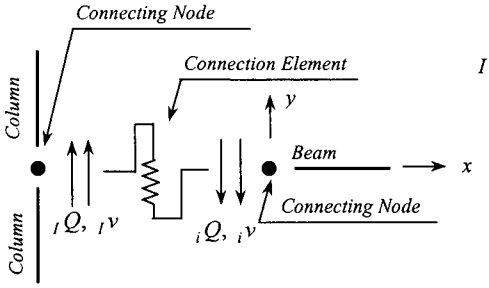

Figure 3 - Connection spring element

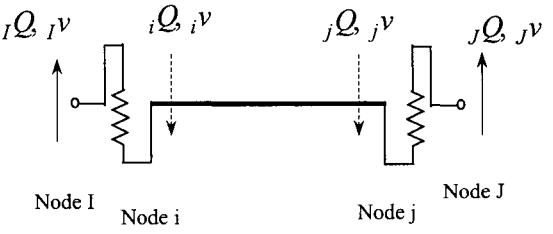

Figure 4 – The hybrid beam-column element

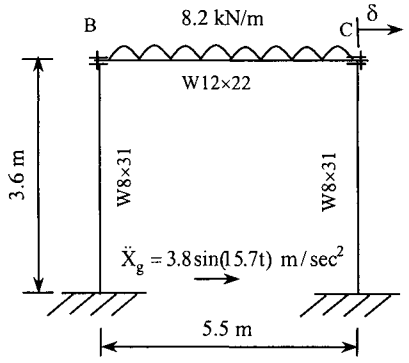

Figure 5 – The Portal frame

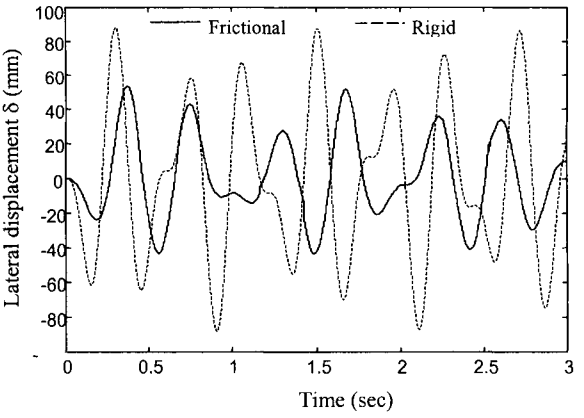

Figure 6 – Lateral Responses

www.EngineeringEBooksPdf.com

Advances in Steel Structures, Vol. II
Chan, Teng and Chung (Eds.)
© 2002 Elsevier Science Ltd. All rights reserved.

FORMULAS FOR VIBRATION PERIOD OF STEEL BUILDINGS IN TAIWAN DERIVED FROM AMBIENT VIBRATION DATA

Liang-Jenq Leu[1], Chuen-Yu Liu[2], Chang-Wei Huang[2], and Shaing-Hai Yeh[3]

[1] Professor, Dept. of Civil Engineering, National Taiwan University, Taipei, Taiwan
[2] Doctoral Student, Dept. of Civil Engineering, National Taiwan University, Taipei, Taiwan
[3]Division head, Architecture & Building Research Institute, Ministry of Interior, Taipei, Taiwan

ABSTRACT

The fundamental vibration period of a building is an important parameter for determining the design base shear. The empirical formula for calculating the fundamental vibration period given in the Specification for Seismic Design of Buildings (SSDB) of Taiwan is mainly based on that of the Uniform Building Code (UBC). However, given that the design and construction methods between Taiwan and US are not the same, it is necessary to evaluate the appropriateness of the empirical formula currently used in Taiwan. This study applies system identification techniques in analyzing the ambient vibration measurement data of 30 steel buildings located in Taipei to obtain the fundamental vibration period. On the basis of these identified periods, new empirical formulas for the translational and torsional fundamental vibration periods are then proposed. The difference between the periods predicted by the new formulas and the current empirical formula ranges from 10% to 42%.

KEYWORDS

Ambient Vibration Measurement, Steel Buildings, Fundamental Vibration Period, System Identification, Empirical Formula

1. INTRODUCTION

The fundamental vibration period of a building is an important parameter in the determination of the design base shear in building codes. For buildings with a medium or long fundamental vibration period, the design base shear is in general inversely proportional to the fundamental vibration period. In other words, the longer the fundamental vibration period the smaller the design base shear. According to SSDB of Taiwan (ABRI 1997), the fundamental vibration period of a building can be calculated using the given empirical formula or other rational analysis methods. Being a rational analysis tool for building design, the commercial software ETABS is commonly used by the structural engineers in Taiwan to obtain the fundamental vibration period. However, according to SSDB the fundamental vibration period obtained using any rational

www.EngineeringEBooksPdf.com

analysis method shall not be 1.4 times larger than that predicted by the empirical formula if it is to be used in calculating the design base shear. The value 1.4 is referred to as the upper bound factor in this study for convenience of discussion.

The objective of this paper is to propose new empirical formulas for the fundamental vibration period of steel buildings in Taiwan. This is needed since the current empirical formulas are mainly based on the UBC but the ways how steel buildings are designed and constructed in Taiwan and US are not exactly the same. To this end, ambient vibration measurements are carried out first and system identification techniques are then employed to determine the fundamental vibration periods for 30 steel buildings located in Taipei. By making use of the identified periods, new empirical formulas are proposed. Moreover, whether the value of the upper bound factor 1.4 is appropriate will be investigated in this paper.

2.EMPIRICAL FORMULAS IN BUILDING CODES

Several empirical formulas for calculating the fundamental vibration of steel buildings, T, are listed in Table 1. As can be seen, T is related to only the height of the building, h, mostly. Only the empirical formula given in UBC-70 takes the planar dimensions into account. The effects of planar dimensions will be investigated in this study.

TABLE 1
EMPIRICAL FORMULAS OF FUNDAMENTAL VIBRATION PERIOD

Building code	Empirical formula	Unit	Valid for steel buildings with	Equation number
UBC-70	$T = 0.05h/\sqrt{D}$	T: sec ; D, h: ft	General purpose	(1)
	T=0.10N	T: sec; N: number of storys	MRF	(2)
Japan BSL 1981	T=0.03h	T: sec ; h: m	General purpose	(3)
UBC-97	T=0.020 $h^{0.75}$	T: sec ; h: ft	Shear walls/braces	(4)
	T=0.030 $h^{0.75}$	T: sec ; h: ft	EBF	(5)
	T=0.035 $h^{0.75}$	T: sec ; h: ft	Others	(6)
SSDB of Taiwan	T=0.050 $h^{0.75}$	T: sec ; h: m	Shear walls/braces	(7)
	T=0.075 $h^{0.75}$	T: sec ; h: m	EBF	(8)
	T=0.085 $h^{0.75}$	T: sec ; h: m	Others	(9)

3. SPECTRAL ANALYSIS AND SENSORS DEPLOYMENT

By using the model of single input/single output in textbooks on signal processing, for example, Bendat and Piersol (1991), the relationship between the auto-correlation spectrum of the measured response S_{yy} and the auto-correlation spectrum of the external load S_{xx} can be expressed as

$$S_{yy} = |H|^2 S_{xx} \tag{10}$$

where H is the system transfer function. It is quite proper to assume that the ambient vibration signal is white noise. In this case, S_{xx} is a constant and the amplitude of the system transfer function is proportional to S_{yy} as can be seen from Eqn. 10. The auto-correlation spectrum can be calculated from the Fourier transformation as follows:

www.EngineeringEBooksPdf.com

$$S_{yy} = \lim_{T_d \to \infty} E[\frac{1}{T_d} YY^*] = \lim_{T_d \to \infty} E[\frac{1}{T_d} |Y|^2] \quad (11)$$

where E stands for the expectation operator, Y stands for the Fourier transform of $y(t)$, Y^* stands for the complex conjugate of Y, and T_d is the period for the FFT (Fast Fourier Transform). From Eqns. 10 and 11, the peaks of S_{yy} correspond to the peaks of the Fourier amplitude spectrum. Therefore, the fundamental vibration period can be identified from the peaks of the Fourier amplitude spectrum, which can be obtained by the FFT technique.

A typical deployment for the velocity sensors used in this study to record the time history of velocity at selected positions on the roof is shown in Figure 1, where sensors 2 and 3 are placed close to the floor center. The torsional response can be obtained by subtracting the responses of sensors 1 from 3; the torsional fundamental vibration period can be identified from the subtracted response using the FFT technique. The same period can be identified from the subtracted response between sensors 2 and 4. The fundamental vibration periods in the x and y directions can be identified from the responses of sensors 3 and 2, respectively, after excluding the torsional vibration periods.

4. REGRESSION FORMULAS

In this study, ambient vibration measurements are carried out for 30 steel buildings ranging from 10 stories to 50 stories in Taipei. Out of these 30 buildings, 27 are of regular shape and the other three are of irregular shape to some degree. Moreover, 10 buildings are composed of both MRF (Moment Resisting Frames) and braces, while the other 20 are MRF only. Regression formulas for the fundamental vibration period are derived from the identified results. Note that in all the formulas presented below, the vibration periods are in seconds and the dimensions are in meters.

Shortest Translational Vibration Period T_h Versus Height h

Let T_h denote the shorter period of the two translational fundamental vibration periods T_x and T_y. Since in general the shorter the fundamental vibration period the larger the design base shear becomes, the empirical formulas given in building codes usually take T_h as the fundamental vibration period for both directions for the sake of conservative design.

The proposed regression formulas are all listed in Table 2. As can be seen from the R^2 values, the exponential regression formula (Eqn. 12) fits the identified data better than the linear type (Eqn. 13). Normally higher steel buildings tend to use braces to increase the lateral stiffness so that their fundamental vibration periods will generally be shorter. This can be confirmed by using Eqns. 14 and 15, which show that for buildings with its height ranging from 50 to 120 meters the fundamental vibration periods of buildings without braces are longer than those of buildings with braces by 15% to 6%.

TABLE 2
REGRESSION FORMULAS OF T_h FOR STEEL BUILDINGS

Regression formula	Type	Classification	R^2	Height of buildings (m)	Equation number
T_h=0.0700 $h^{0.751}$	Exponential	All	0.842	30-240	(12)
T_h=0.0217 h	Linear	All	0.689	30-240	(13)
T_h=0.0432 $h^{0.845}$	Exponential	MRF + braces	0.856	50-240	(14)
T_h=0.0730 $h^{0.747}$	Exponential	MRF only	0.848	30-120	(15)

www.EngineeringEBooksPdf.com

In similar studies, Leu et al. (2001) and Yeh (2000) used the identified periods from ambient vibration measurements of 45 RC buildings to establish regression formulas for RC buildings. The formula for T_h is

$$T_h = 0.0180\, h^{0.915} \tag{16}$$

Eqn. 16 is valid for RC buildings with their heights ranging from 12 to 82 meters. The value of T_h calculated using Eqn. 12 is 2.2-1.9 times longer than that calculated using Eqn. 16 for h between 30 and 80 meters. In other words, if the height is within that range, the T_h of a steel building will be 2.2-1.9 times longer than that of a RC building. Such differences may arise from larger dimensions for RC structural members and common usage of brick walls as partition walls for RC buildings.

Torsional Fundamental Vibration Period T_t Versus T_h

As reported by Leu et al. (2001), the torsional fundamental vibration period T_t has a better relationship with the shortest translational vibration period T_h rather than with the height h. The exponential regression formula relating T_t to T_h is given in Eqn. 17 of Table 3, while the formula of the linear type is given in Eqn. 18. As a comparison, the regression formula proposed by Leu et al. (2001) for RC buildings is given in Eqn. 19; clearly, steel buildings have a better fit between T_t and T_h than RC buildings. A similar formula proposed by Satake and Yokota (1996) with respect to 31 steel buildings in Japan is given in Eqn. 20, where the R^2 value is slightly lower than that of this study.

TABLE 3
COMPARISONS OF REGRESSION FORMULAS FOR T_t OF STEEL AND RC BUILDINGS

Regression formula	Type	Classification	R^2	Height of buildings (m)	Equation number
T_t=0.890 $T_h^{0.816}$	Exponential	All steel buildings	0.908	30-240	(17)
T_t=0.770 T_h	Linear	All steel buildings	0.864	30-240	(18)
T_t=0.731 $T_h^{0.901}$	Exponential	All RC buildings	0.745	12-82	(19)
T_t=0.840 T_h	Linear	Satake and Yokota (1996), steel buildings	0.80	80-240	(20)

Effects of Planar Dimensions for Translational Fundamental Vibration Period

It is usual practice for structural engineers to use T_h as the translational fundamental period (T_x and T_y) for both directions, where x is the direction with a longer planar dimension. However, the ratio of T_x to T_y for the 30 steel buildings of this study ranges from 0.813 to 1.13, with an average of 0.971 and a standard deviation of 0.072. This ratio for RC buildings ranges from 0.410 to 1.28, with an average of 0.919 and a standard deviation of 0.176 (Yeh et al. 2000). If accurate predictions of T_x and T_y can be made, buildings can be designed more economically since different design base shears for the x and y directions may be obtained. To this end, the relationship between T_x (or T_y) and the height as well as the planar dimension is investigated. The resulting regression formula is

$$T = 0.1049\, h^{0.714}\, D^{-0.0549} \tag{21}$$

with R^2=0.851, where D is the x-direction dimension of a typical floor if T_x is concerned and the y-direction dimension if T_y is concerned. The contour plot of Eqn. 21 is shown in Figure 2. As a comparison, the formula for RC buildings is (Leu et al. 2001)

www.EngineeringEBooksPdf.com

$$T = 0.02754\, h^{0.9135}\, D^{-0.1244} \tag{22}$$

with R^2=0.765. From the above R^2 values, a better fit is obtained again for steel buildings.

5. RELATION BETWEEN PERIODS CALCULATED FROM STRUCTURAL MODELS AND IDENTIFIED FROM AMBIENT VIBRATION MEASUREMENTS

Structural designers usually use commercial software such as ETABS to establish a structural model for a building for predicting its fundamental vibration period. It is of interest to know whether such a predicted period is close enough to the one identified from the ambient vibration measurements. Out of the 30 steel buildings, there are 25 buildings whose translational fundamental vibration periods obtained using ETABS are available from the designers. However, only 15 buildings have ETABS torsional fundamental vibration periods.

For the fundamental vibration period in the direction with a longer planar dimension, T_x, the ratio of the value predicted by ETABS, T_M, to the one identified from the ambient vibration measurement, T_{am}, ranges from 0.994 to 1.667, with an average of 1.228 and a standard deviation of 0.190. For the fundamental vibration period in the direction with a shorter planar dimension, T_y, the ratio of T_M to T_{am} ranges from 0.997 to1.707, with an average of 1.263 and a standard deviation of 0.215. For the torsional fundamental vibration period T_t, the ratio of T_M to T_{am} ranges from 1.015 to 1.762, with an average of 1.264 and a standard deviation of 0.206. As a comparison, Satake and Yokota (1996) proposed the regression formula of T_M =1.37 T_{am} for 31 Japanese steel buildings; the coefficient 1.37 is close to the above average values. Longer periods predicted by structural models are reasonable because of (1) heavier mass considered in the models and (2) minor stiffness contribution due to non-structural members in real buildings.

6. RELATION BETWEEN PERIODS IDENTIFIED FROM AMBIENT VIBRATION MEASUREMENTS AND FROM EARTHQUAKE MOTIONS

The fundamental vibration period identified from ambient vibration measurements, T_{am}, is in general different from the one identified from recorded motions during earthquakes, T_{eq}. In general, T_{eq} is longer than T_{am} and the larger the magnitude of earthquakes the longer T_{eq} becomes. For steel buildings the reasons why T_{eq} is generally longer than T_{am} may include (Celebi 1996):

(1) Interaction between soil and structures, especially the rocking behavior, is more easily excited under strong excitations.
(2) Nonlinear behavior of structural members and non-structural members, for example, geometric non-linearity of beams and columns, yielding of beams and columns, cracking or damage of curtain walls and fracture of welds.

The PGA (Peak Ground Acceleration) in Taipei induced by the Chi-Chi earthquake in 1999 is approximately 100 gal. The fundamental vibration periods of four steel buildings in Taipei identified from the ambient vibration data and from the recorded motions during the Chi-Chi earthquake are listed in Table 4. From Table 4, the following formula is proposed

$$T_{eq} = 1.1\, T_{am} \tag{23}$$

www.EngineeringEBooksPdf.com

TABLE 4
FUNDAMENTAL PERIODS UNDER AMBIENT VIBRATION AND CHI-CHI EARTHQUAKE

	T_{eq} (sec)		T_{am} (sec)		T_{eq}/T_{am}	
	X direction	Y direction	X direction	Y direction	X direction	Y direction
Building 01	2.773	2.773	2.497	2.586	1.11	1.07
Building 08	2.435	2.435	2.222	2.353	1.10	1.03
Building 18	1.135	1.189	1.130	1.183	1.00	1.00
Building 29	4.224	4.827	3.380	4.712	1.10	1.02

Note: X is the direction with the longer planar dimension

7. RECOMMENDED EMPIRICAL FORMULAS

It follows from Eqn. 21 that the fundamental vibration periods for buildings with different planar dimensions but with the same height differ only about 7%. More importantly, the fundamental vibration period in the direction with a longer planar dimension is sometimes *longer* than that in the other direction for real buildings, which cannot be reflected from Eqn. 21. For the sake of conservative design, this paper suggests that the shortest translational period be used for both directions before further clarification has been done.

Two steps of correction are needed in order to let the regression formulas of T_h listed in Table 2 be used as the empirical formulas in a building code. First of all, because the regression formulas are best-fitted equations to data points, the possibility that the value of one data point is higher than the value predicted by the regression formulas is about 50%. In other words, if the regression formulas of T_h of Table 2 are used as the empirical formulas, the probability that designers overestimate the fundamental vibration period would be 50%, which is unacceptable. To be conservative, this paper suggests that the lower bound of 80% confidence level be used. By doing so, the probability that designers overestimate the fundamental vibration period is reduced to 20%. The procedure of obtaining the lower bound of 80% confidence level is described in standard textbooks on statistics, for example, Walpole and Myers (1993). The lower bounds of 80% confidence level corresponding to Eqns. 12, 14 and 15 of Table 2 are given in Eqns. 24, 25 and 26 of Table 5, respectively.

In the second step of correction, the effect of strong motion is considered, which has been discussed in Section 6. By making use of Eqn. 23, Eqns. 24, 25, and 26 are modified to become Eqns. 27, 28 and 29, respectively, of Table 5.

To avoid the possibility that structural designers use a fairly long fundamental vibration period calculated from the structural models for design, SSDB of Taiwan has imposed an upper bound of 1.4 times of the fundamental vibration period predicted by the empirical formula. Whether the value of the upper bound factor 1.4 is proper is investigated here. For the sake of simplicity, this paper proposes that a proper value, say C, of the upper bound factor is determined such that the possibility the period from the structural models is longer than C times of the period from the empirical formula will be 50%. By trial and error, the C values for Eqns. 27, 28, and 29 are 1.3, 1.35 and 1.25, respectively.

In summary, the proposed empirical formulas are as follows:

(1) If the effect of braces is not considered and the height of the building is between 30 and 240 meters, Eqn. 27 can be used. Also, the value of the upper bound factor is equal to 1.3 in this

www.EngineeringEBooksPdf.com

case. Namely, the fundamental vibration period calculated from the structural model should not be 1.3 times longer than that predicted by Eqn. 27.

(2) If the effect of braces is considered and the height of the building is between 50 and 240 meters, Eqn. 28 should be used. Also, the value of the upper bound factor is equal to 1.35 in this case. The fundamental vibration period predicted by the current empirical formula (Eqn. 7) is shorter than that predicted using Eqn. 28 by 14% to 21%.

(3) If the building consists of MRFs only and the height of the building is between 30 and 120 meters, Eqn. 29 should be used. Also, the value of the upper bound factor is equal to 1.25 in this case. The period predicted by the current empirical formula (Eqn. 9) is longer than that predicted using Eqn. 29 by 22% to 27%.

TABLE 5
TWO STEPS OF CORRECTION FOR REGRESSION FORMULAS OF T_h

Correction step	Regression formula	Classification	Height of buildings (m)	Equation number
1	$T_h=0.0606\,h^{0.746}$	All Steel buildings	30-240	(24)
	$T_h=0.0419\,h^{0.808}$	MRF with braces	50-240	(25)
	$T_h=0.0557\,h^{0.776}$	MRF only	30-120	(26)
2	$T_h=0.0667\,h^{0.746}$	All Steel buildings	30-240	(27)
	$T_h=0.0461\,h^{0.808}$	MRF with braces	50-240	(28)
	$T_h=0.0613\,h^{0.776}$	MRF only	30-120	(29)

8. CONCLUSION

This paper has proposed regression formulas for the shortest translational fundamental vibration period (T_h), torsional fundamental vibration period (T_t) and translational fundamental vibration periods (T_x and T_y) for steel buildings. The effect of planar dimensions has also been taken into account in this study. In order to let the fitted formulas, obtained from the ambient vibration measurements of 30 steel buildings, be used in building codes, two steps of correction are taken. In the first step, correction for the lower bound of 80% confidence level is carried out. In the second step, correction for the difference between the periods identified from the strong motions during earthquakes and from the ambient vibration measurements is performed. After performing these two steps of correction, the proposed empirical formulas are obtained.

It is found from this study that the fundamental vibration period predicted by the current empirical formula for steel buildings with braces is shorter than that predicted using the proposed formula by 14% to 21%. This implies that the current empirical formula for steel buildings with braces in Taiwan is too conservative. However, the fundamental vibration period predicted by the current empirical formula for purely MRF steel buildings is longer than that predicted using the proposed formula by 22% to 27%. This implies that the current empirical formula for MRF steel buildings in Taiwan is not conservative. Finally, it is found that the values of the upper bound factor are 1.35 and 1.25, respectively, for steel buildings with braces and purely MRF steel buildings. These values are different from the value 1.4 specified in SSDB of Taiwan.

www.EngineeringEBooksPdf.com

9. ACKNOWLEDGEMENTS

This research is supported by the Architecture & Building Research Institute, Ministry of Interior, Republic of China (R.O.C.) with Grant No. MOIS 902018. The authors are grateful to this support. The authors would also like to thank the National Center for Research on Earthquake Engineering of R.O.C for providing the equipment for ambient vibration measurement. Finally, special thanks go to the following graduate students, Yi-Jui Chen, Jung-Shu Tang, Shih-Chieh Lin, and Chih-Yung Lin, who assisted in performing the ambient vibration measurements reported in this study.

10. REFERENCES

Architecture and Building Research Institute (ABRI) (1997). *Specification for Seismic Design of Buildings*, Ministry of Interior, Republic of China

Bendat J.S. and Piersol A.G. (1991). *Random Data Analysis and Measurement Procedures*, 2nd Edition, John Wiley & Sons, New York, USA

Celebi M. (1996). Comparison of Damping in Buildings under Low-amplitude and Strong Motions. *Journal of Wind Engineering and Industrial Aerodynamics* **59:2-3**, 309-323.

Leu L.J., Liu C.Y., Huang C.W., Chou J.J., Lee J. H. and Yeh S.H. (2001). Formulas for Vibration Period of RC Buildings in Taiwan Derived from Ambient Vibration Data. *Proceedings (in CD-ROM) of the Eighth East Asia-Pacific Conference on Structural Engineering & Construction (EASEC-8)*, Dec.7-9, Singapore

Satake N. and Yokota H. (1996). Evaluation of Vibration Properties of High-rise Steel Buildings Using Data of Vibration Tests and Earthquake Observations. *Journal of Wind Engineering and Industrial Aerodynamics* **59:2-3**, 265-282.

Walpole R.E. and Myers R.H. (1993). *Probability and Statistics for Engineers and Scientists*, 5th Edition, Prentice-Hall, New York, USA

Yeh S.H., Leu L.J., Yang Y.B., Huang C.W., Liu C.Y., Chou J.J. and Lee J.H. (2000). *A Study on the Fundamental Period of Reinforced Concrete Buildings Using Ambient Vibration Measurement*, Research Project Report (in Chinese), MOIS 892033, Architecture & Building Research Institute, Taipei, Taiwan, Republic of China

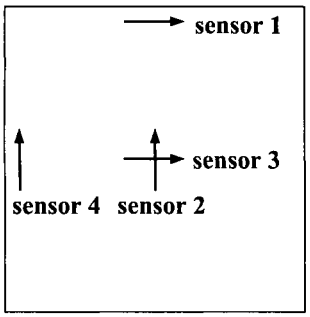

Fig.1 Sensor deployment

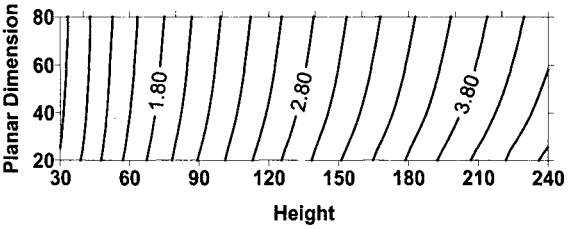

Fig.2 Effect of planar dimensions

www.EngineeringEBooksPdf.com

IMPACT MECHANICS

www.EngineeringEBooksPdf.com

This Page Intentionally Left Blank

www.EngineeringEBooksPdf.com

Advances in Steel Structures, Vol. II
Chan, Teng and Chung (Eds.)
© 2002 Elsevier Science Ltd. All rights reserved.

SOME RECENT STUDIES ON ENERGY ABSORPTION OF METALLIC STRUCTURAL COMPONENTS

G. Lu

School of Engineering and Science, Swinburne University of Technology
Hawthorn, Victoria 3122, Australia

ABSTRACT

The energy absorbing performance of metallic structures has been studied extensively with a primary aim to improving the crashworthiness performance of automobile and aircraft structures. Nevertheless, findings from these investigations are increasingly important in designing highway structures, bridges and buildings in order to minimise catastrophic failure from impact loadings. This paper summarises several recent studies of crushing of structures and materials; they include axial crushing of circular tubes, splitting of square and circular tubes, transverse piercing of square tubes, experimental determination of tearing energy, cutting of a plate by a wedge and, finally, crushing of honeycombs and aluminium foams.

KEYWORDS

Energy absorption, crushing of tubes, ductile tearing, honeycombs, metal foams

INTRODUCTION

Metallic structures posses good performance in absorbing energy by plastic deformation and ductile tearing and therefore they are frequently used as energy absorbing devices (Johnson & Reid, 1978, 1986). Conventionally these devices are incorporated in automobile and aircraft structures in order to protect their passengers during collisions. Recently there has been increasing demand for crashworthiness performance in other structures. For example, the guardrails of highways should be designed so as to absorb a sufficient amount of energy in the event of collision by a vehicle (Hui & Yu, 2000). Energy absorbing devices have been installed where potential crash occurs, such as branching region of highways and intersections in metropolitan areas. Building structures should be designed to absorb energy in the event of earthquake or disaster. In fact, the World Trade Centre might have been saved had appropriate energy absorbing devices been installed in-between floors. Incorporating the concept of crashworthiness into a wider range of structures is thus vital.

This paper selects several of our recent studies on crushing of metallic structures and materials; they include axial crushing of circular tubes, splitting of square and circular tubes, transverse piercing of square tubes, experimental determination of tearing energy, cutting of a plate by a wedge and, finally, crushing of honeycombs and aluminium foams.

www.EngineeringEBooksPdf.com

AXIAL CRUSHING OF CIRCULAR TUBES

The behaviour of thin-walled metal tubes subjected to axial compression has been studied for many years. Such tubes are frequently used as impact energy absorbers and Reid (1993) has presented a general review of deformation mechanisms. Experimentally the following modes of collapse have been observed (Fig.1): (i) axi-symmetric concertina bellowing. (ii) non-symmetric buckling (also known as diamond or Yoshimura mode), with a variable number of circumferential lobes or corners. (iii) mixed mode (combination of the two previous modes). (iv) Euler or global buckling; and (v) others (simple compression, single folds, etc.). The formation of these folds causes the characteristic fluctuation in the axial force shown in Fig. 2

Fig. 1. Collapse modes. From left to right: axi-symmetric, non-symmetric and mixed mode.

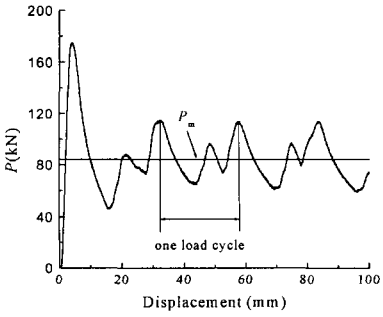

Fig. 2. A typical force-displacement curve for a tube (D=100mm, t=3mm)

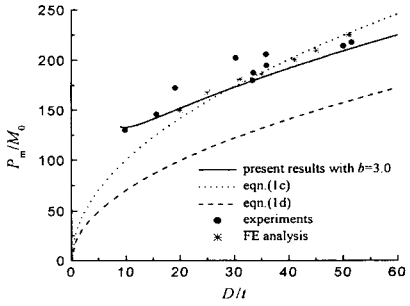

Fig. 3. Comparison of various results. (Huang & Lu, 2002)

Research on circular tubes in the past has generally concentrated on annealed aluminium or steel tubes with diameter/thickness (D/t) ratios between 10 and 150. Guillow et. al. (2001) recently undertook an experimental program to extend the range of research up to approximately D/t = 450. Of particular interest was the non-symmetric mode which has multiple corners (or lobes). For tubes with an increasing D/t ratio, the number of circumferential lobes also increased from 2 up to 5 or 6. At high values of D/t (> 200), the number of lobes often varied during testing (in one case erratically between 3, 4 and 5 lobes). The number of lobes, N, was not always an integer.

From the test results for as-received 6060-T5 aluminium tubes a mode classification chart was produced. It may be observed broadly from our chart that non-symmetric mode is present when D/t > 100, while axi-symmetric mode occurs when D/t < 50 and L/D < 2.

The average crush force Pm is most relevant to energy absorption capacity. When test results for non-dimensionalised average axial force, P_m/M_0, are plotted logarithmically versus D/t, (M_0 is full plastic bending moment per unit length), all the results (whether axi-symmetric, non-symmetric or

www.EngineeringEBooksPdf.com

mixed modes) approximately form a straight line. The following empirical relation for 6060-T5 aluminium alloy tubes was obtained $\frac{P_m}{M_0} = 72.3\left(\frac{D}{t}\right)^{0.32}$.

Theoretically, Alexander (1960) was the first researcher to propose a theory for the axisymmetric collapse mode based on the balance of external and internal work done. Several researchers further developed a model to predict the crush force. Some typical theoretical or semi-empirical formulae previously obtained are as follows:

Alexander (1960): $$\frac{P_m}{M_0} = 20.73\left(\frac{D}{t}\right)^{0.5} + 6.283 \quad [1a]$$

Abramowicz and Jones (1984): $$\frac{P_m}{M_0} = 20.79\left(\frac{D}{t}\right)^{0.5} + 11.90 \quad [1b]$$

Wierzbicki et al.(1992): for the stationary hinge model $$\frac{P_m}{M_0} = 22.27\left(\frac{D}{t}\right)^{0.5} \quad [1c]$$

and for the moving hinges model $$\frac{P_m}{M_0} = 31.74\left(\frac{D}{t}\right)^{0.5} \quad [1d]$$

Singace (1995): $$\frac{P_m}{M_0} = 22.27\left(\frac{D}{t}\right)^{0.5} + 5.632 \quad [1e]$$

All of these studies predict that the normalized mean crushing load, P_m/M_0, is roughly proportional to $(D/t)^{0.5}$ for the conventional range of D/t values. However, a curve fit to a large number of previous experimental data (Guillow et al, 2001) demonstrates that P_m/M_0 is closely proportional to $(D/t)^{0.33}$. It seems that some important characteristics have been overlooked in previous theoretical studies. To resolve this fundamental discrepancy, Huang & Lu (2002) proposed a refined collapse model where an effective hinge length proportional to tube thickness is used. This model predicts results in a better agreement with tests than previous ones over a wide range of D/t (Fig. 3).

AXIAL SPLITTING AND CURLING OF SQUARE AND CIRCULAR TUBES

Tubes can be arranged, by adopting appropriate dies, to split and curl axially (Fig. 4). From the viewpoint of energy absorption, this process produces a steady-state deformation with a constant force, which is most desirable. It has a long stroke of over 90 per cent of the total tube length. Stronge et. al. (1983) conducted experiments with square tubes split against a radius/flat die. Huang et. al. (2002a,b) further studied the splitting and curling behaviour of square and circular tubes axially compressed between a plate and a pyramidal die.

For both square and circular tubes, three energy dissipation mechanisms exist: 1) the "near-tip" tearing associated with tube splitting (crack propagation); 2) the "far-field" deformation associated with the plastic bending and possibly stretching of curls; 3) the friction as the tube interacted with the die. These are evaluated in a theoretical model presented below.

Huang et al (2002a) conducted both experiments and theoretical analysis for mild steel and aluminium tubes with pyramidal dies of various angles. An energy balance was used and force required to split and curl the tube by a die of semi-angle (α) was found to be

www.EngineeringEBooksPdf.com

$$P = \frac{4(M_0 / R + R_c t)}{1 - \mu/(\sin\alpha + \mu\cos\alpha)} \qquad [2]$$

where $M_0 = \sigma_y b t^2 / 4$ is the fully plastic bending moment for each side of tube wall, b is the tube width , t is the thickness, σ_y is the yield stress of the material, R is the curl radius, R_c is tearing energy per unit area along the cracks, μ and α are frictional coefficient and die semi-angle, respectively. The two unknown parameters, the values of which are difficult to estimate, are curl radius R and tearing energy R_c. From the experiments, curl radius R is, rather surprisingly, almost independent of tube thickness, but is affected by the die semi-angle significantly. There is no theoretical explanation for this and empirically it was found that $R = \frac{32.7}{\sin\alpha} - 25.7$, where R is in mm. R_c is largely related to plastic deformation around the ductile tearing front. Its value is dependent on loading conditions as well as material property. Lu et al (1994) measured this value for splitting square tubes and obtained an empirical equation for R_c in terms of ultimate stress and fracture strain in a uniaxial tensile test. When R and R_c are estimated in this way, Eqn 2 predicts the force reasonably well (Fig. 5).

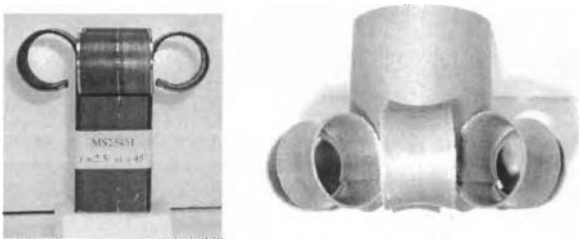

Fig. 4. Square and circular tubes split (Huang et al, 2002a; 2002b)

For circular tubes the number of cracks varies depending on the dimensions of the tube and die as well as material properties. There is a characteristic number of cracks regardless the number of initial cuts which may be made. There is a competition of possible energy dissipation mechanisms and the number of cracks is such that the total energy is a minimum. With a radius die, the final radius of curls in meridian direction has about the same value as the die radius. In a recent analysis, a critical crack opening displacement δ is used to characterise the tearing process. The number of cracks such obtained is $n = (\frac{r_0^2}{2\delta R})^{1/3}$ and the corresponding force is

$$P = 3.07\sigma_y t r_0^{2/3} \delta^{2/3} R^{-1/3} \qquad [3]$$

where r_0 is the tube radius. The coefficient of friction is taken as 0.2. The equation agrees well with the experiments by Reddy & Reid (1983) when δ is taken to be about one thickness. A theoretical model for tube splitting with pyramidal dies has been proposed and is described in detail in another paper (Huang et al, 2002b).

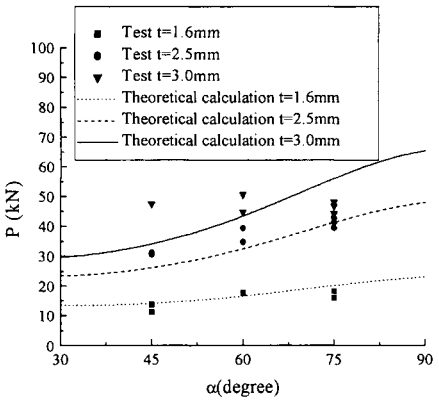

Fig. 5. Force vs. die angle for square tubes (Huang et al, 2002a)

TRANSVERSAL PIERCING OF METAL TUBES

When thin-walled tubes are subjected to impact, piercing may occurs and it is interesting to study

www.EngineeringEBooksPdf.com

energy absorption in such a process. Lu and Wang (2002) reported a study of transversal piercing of square tubes using pyramidal or conical indentors. In their studies six pyramidal punches of square or circular cross-section with 12.7mm sides or diameter was employed. The specimens tested were commercially available square hollow section, grade C350 Steel to AS1163-1991. The size of the tube section was 40 by 40mm and the wall thicknesses were 1.6mm and 2.5mm, respectively. The length of the tubes tested was varied from 40mm to 340mm.

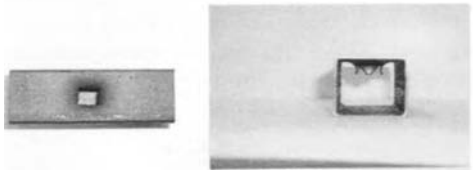

Fig. 6. Top and side view of a specimen with piercing and plastic bending (Lu & Wang, 2002).

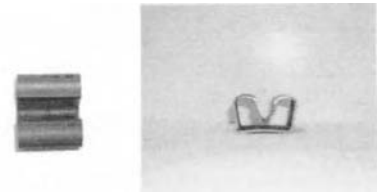

Fig. 7. Top and side view of a specimen without piercing (Lu & Wang, 2002).

Typical specimens are shown in Figs. 6 & 7, for L=2.5a and L= a (a=40 mm), respectively. Load-displacement curves are shown in Fig. 8 for tubes of four different lengths. For short tubes, no ductile tearing occurs and global structural deformation takes place. For long tubes, ductile tearing is observed to initiate and propagate along four lines. This is accompanied with localised plastic bending to accommodate the indentor. There is no deformation in the far region of the tube.

Preliminary theoretical analysis was performed. Again, three main energy dissipation mechanisms exist: plastic bending, ductile tearing and friction. The average force in the penetrating phase is shown to be

$$P = [0.05\sigma_u \varepsilon_f t + 0.5\sigma_y t^2 \beta]\frac{\sin\alpha + \mu\cos\alpha}{\cos\alpha - \mu\sin\ \alpha} \qquad [4]$$

where β is the final angle bent by tube walls, which may be assumed to be equal to the semi-angle of the pyramidal punch α. σ_u and ε_f are material ultimate stress and fracture strain, respectively. This equation compares fairly with the experiments.

Discarding the terms for plastic bending energy of tube walls and friction, the analysis should lead to an estimate for a force corresponding to the onset of crack propagation,

$$P_f = 0.05\sigma_u \varepsilon_f t \tan\alpha \qquad [5]$$

A critical length L_{cr} exists for switching between the two modes. When the length of tube is more than L_{cr}, the energy dissipation mode would be local penetration. On the other hand, when the length of tube is shorter than L_{cr}, the tube would only take a global collapse mode. Theoretically it was found to be 44mm when a=40 mm and t=1.6 mm.

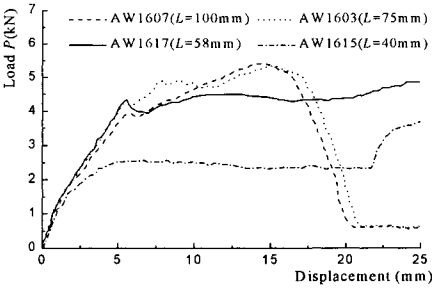

Fig. 8 Load-displacement curves for tubes of different length. t=1.6mm, a=40mm, α=30° (Lu & Wang 2002).

Quasi-static piercing of circular tubes has been reported by Johnson et al (1979).

www.EngineeringEBooksPdf.com

CUTTING OF METAL PLATES BY A WEDGE

Our next case involves cutting of metal plates by a wedge, Fig. 9 (Lu & Calladine, 1990), which has attracted research interests even recently (Paik & Wierzbicki, 1997). This problem is a simplified version of penetration of the bow of a ship into the side deck of another ship.

Depending on the inclination of plates with respect to the direction of wedge α, two distinct modes of deformation are obtained. When the plate is vertical, cutting is accompanied with forward and backward bending of flaps and the force-cutting length shows periodic fluctuation accordingly. When the plate is inclined at, say, 10^0, the two flaps bending in one direction continuously and the force increases gradually, after the initial cutting stage.

We assume that plastic deformation is dominant in this cutting process and hence the yield stress σ_y is the only material property. For a given inclination angle and a given wedge, the energy W is related to σ_y, plate thickness t, cutting length l. From the dimensional analysis, it is straightforward to see that there are two independent dimensionless groups. Here we choose $W/\sigma_y t^3$ and l/t. When all the test results are plotted accordingly, as shown in Fig. 10 for a wedge of included angle of 40^0, all the curves collapse into a single curve. This suggests that the above dimensional analysis is successful. Specifically, it appears that using the yield stress as the only one material property, as initially assumed, is sufficient in this problem; there is no real need to explicitly single out another material parameter such as tearing energy or critical crack opening displacement .

The following empirical equations for the energy were given

$$W = \begin{cases} 2.0\sigma_y l^{1.3} t^{1.7} & \text{for} \quad \alpha = 10^0 \\ 2.4\sigma_y l^{1.3} t^{1.7} & \text{for} \quad \alpha = 0^0 \end{cases} \qquad [6]$$

Further theoretical analysis has been conducted by, for example, Wierzbicki & Thomas (1993) by adopting a fracture parameter critical opening displacement. The above formulae prove applicable by a number of researchers in their subsequent studies, see Paik & Wierzbicki (1997).

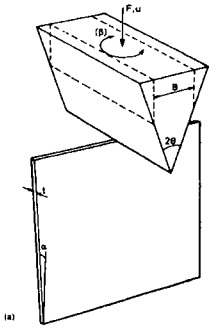

Fig. 9 Sketch of experiments (Lu & Calladine, 1990).

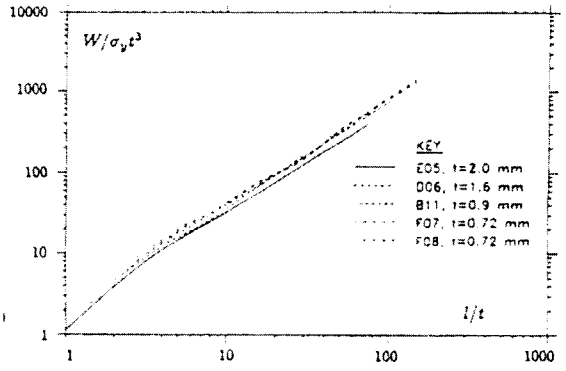

Fig. 10 Plot of dimensionless energy vs dimensionless cutting length. $\alpha = 10^0$ (Lu & Calladine, 1990).

www.EngineeringEBooksPdf.com

DYNAMIC CRUSHING OF CELLULAR SOLIDS

All the previous cases discussed above are for quasi-static loading. When loading rate is high, dynamic effects are present, usually those of strain rate and inertia. Here one finite element study on crushing honeycombs is mentioned (Ruan et al, 2002b). Such materials possess desirable characteristics for energy absorption, with a long plateau stress. Globally, honeycombs, and indeed other similar types of cellular solids such as metal foams, may be regarded as "solids". Nevertheless, the relative density (defined as the ratio of the bulk density and that of the solids for the cell walls) of these materials is very low and thus the micro-structures of each cells can be treated as beam/shell structures. Indeed analysis of these materials is largely based on structural mechanics approach.

For a block of honeycombs fully fixed at one (left) end subjected to a displacement of right hand end at a constant velocity, the deformation mode changes when the loading rate increases (Fig. 11). This leads to an increase in the overall apparent dynamic stress. Based on a large number of numerical results, it was found empirically that the dynamic plateau stress for an "I" mode is

$$\frac{\sigma}{\sigma_{ys}} = 0.8\left(\frac{h}{l}\right)^2 + \left[62\left(\frac{h}{l}\right)^2 + 41\left(\frac{h}{l}\right) + 0.01\right] \times 10^{-6} v^2 \qquad [7]$$

where σ_{ys} is the yield stress of the cell wall material, h and l are cell thickness and side length, respectively. v is the velocity of impact in m/s.

Aluminimum foams have been tested at medium and high loading rates and their results are reported (Ruan et al, 2002a; Reid et al, 2001)

Fig. 11 Honeycomb collapse modes. Left: v=3.5 m/s; "X" shaped mode; right: v=70 m/s,"I" shaped mode. (Ruan et al, 2002).

CONCLUSION

This chapter presents some studies on energy absorption of metallic structural components. The large deformation involves plastic bending/stretching, ductile tearing, friction and dynamic effects. The findings from these investigations should be significant in designing other types of structures in future where energy absorption is a consideration, as well as present applications in vehicle structures.

ACKNOWLEDGEMENT

The authors wish to thank the Australian Research Council for the financial support to undertake most of the work reported in this paper.

www.EngineeringEBooksPdf.com

REFERENCES

Abramowicz W. and Jones N. (1984). Dynamic axial crushing of circular tubes. *International Journal of Impact Engineering* **2**, 263-281.

Alexander J.M. (1960). An approximate analysis of collapse of thin-walled cylindrical shells under axial loading. *Quarterly Journal of Mechanics and Applied Mathematics* **13**, 10-15.

Guillow S.R., Lu G. and Grzebieta R.H. (2001). Quasi-static axial compression of thin-walled circular aluminium tubes. *International Journal of Mechanical Sciences* **43:9**, 2103-2123.

Huang X. and Lu G. (2002). Axisymmetric progressive crushing of circular tubes. *International Journal of Crashworthiness* (to appear).

Huang X., Lu G. and Yu T.X. (2002a). Energy absorption in splitting square metal tubes. *Thin-Walled Structures* **40**, 153-165.

Huang X., Lu G. and Yu T.X. (2002b). On the axial splitting and curling of circular tubes. *International Journal of Mechanical Sciences* (submitted).

Johnson W., Ghosh S.K., Mamalis A.G., Reddy T.Y., Reid S.R. (1979). The Quasi-static piercing of cylindrical tubes. *International Journal of Mechanical Sciences* **22**:9-20

Johnson W. and Reid S.R. (1978). Metallic energy dissipating systems. *Applied Mechanics Review* **31,** 277-288. (Its update: *Applied Mechanics Update* **39**, 315-319.)

Lu G., Ong L.S., Wang B. and Ng H.W. (1994). An experimental study on tearing energy in splitting square metal tubes. *International Journal of Mechanical Sciences* **36:12**, 1087-1097.

Lu G. and Wang X. (2002) Quasi-static piecing of square tubes. *International Journal of Mechanical Sciences* **44**, 1101-1115.

Paik J.K. and Wierzbicki T. (1997). A benchmark study on crushing and cutting of plated structures. *Journal of Ship Research*. **41**, 147-160.

Reddy T.Y. and Reid S.R. (1986). Axial splitting of circular metal tubes. *International Journal of Mechanical Sciences* **28:2**,111-131.

Reid S.R. Tan P.J. and Harrigan J.J. (2001). The crushing strength of aluminium alloy foam at high rates of strain. In *Impact Engineering and Applications*. Chiba A., Tanimura S. and Hokamoto K. eds., Elsevier, 15-22.

Ruan D., Lu G., Chen L. and Siores E. (2002a) Compressive behaviour of aluminium foams at low and medium strain rates. *Composite Structures*. In press.

Ruan D., Lu G., Wang B. and Yu T.X. (2002b). Dynamic crushing modes of honeycombs—a finite element study. *International Journal of Impact Engineering*. In press.

Singace A.A., Elsobky H. and Reddy T.Y. (1995). On the eccentricity factor in the progressive crushing of tubes. *International Journal of Solids & Structures* **32**, 3589-3602.

Stronge W.J., Yu T.X. and Johnson W. (1983). Long stroke energy dissipation in splitting tubes. *International Journal of Mechanical Sciences* **25:9-10**, 637-647.

Wierzbicki T., Bhat S.U., Abramowicz W. and Brodkin D. (1992). Alexander revisited - a two folding element model of progressive crushing of tubes. *International Journal of Solids & Structures* **29**, 3269-3288.

Wierzbicki T. and Thomas P. (1993). Closed form solution for wedge cutting force through thin metal sheets. *International Journal of Mechanical Sciences* **35**, 209-229.

www.EngineeringEBooksPdf.com

Advances in Steel Structures, Vol. II
Chan, Teng and Chung (Eds.)
© 2002 Elsevier Science Ltd. All rights reserved.

CRASH ANALYSIS OF AUTOMOBILE BUMPERS WITH PEDESTRIANS

B. Wang[1] and G. Lu[2]

[1]Department of Mechanical Engineering, Brunel University,
London, UK
[2]School of Engineering and Science, Swinburne University of Technology,
Melbourne, Australia

ABSTRACT

This paper presents simulations of the performance of a current design of car bumper system for crash with a human leg using finite element analysis as part of an on-going effort to improve road safety for pedestrians. Variations in the impact scenario are studied. The finding will help to improve the design of automobile bumper - a basic beam structure, in order to pass the new legislation on Pedestrian Impact Specification set by the European Enhanced Vehicle Safety Committee (EEVC) [1].

KEYWORDS:

Automobile, bumper, pedestrian, crash, beam, finite element analysis

INTRODUCTION

Vehicle safety in modern automotive industry is a rapidly evolving sector. In the past the sole purpose of a vehicle bumper was to prevent damage to the bodywork in minor impacts and as such strength to sustain deformation was the only consideration with typical structures being framed steel beams with vertical over-riders. In fact bumper designs were more dictated by fashion than engineering that big chrome bumpers were the must-have accessories on many cars. This attitude changed rapidly in the late 70's with the introduction of legislation in Europe

www.EngineeringEBooksPdf.com

and North America, which demanded certain crash performance from bumpers. For the first time, bumpers were considered to be a 'safety item' not just for the vehicle but for the passengers as well [2, 3].

The current designs of modern vehicles are predominated by the safety of occupants and significant improvements have been achieved with safety features being incorporated into vehicle body structure designs. However, almost no consideration is given to pedestrians. The UK government 1998 road accident statistics shows that pedestrians account for 14% of road accidents, but 27% of all road deaths. In terms of distance travelled, a pedestrian is estimated to be roughly nineteen times as likely to be killed in a road accident as a car occupant.

Detailed analysis of pedestrian accidents shows that about 80% sustained led injuries, which are non-life threatening but severe due to long term irreversible consequences. Leg injuries can be classified into several types: soft tissue (flesh) injuries, bone fractures and knee ligament injuries. Ligament injuries are of particular interest because of the consequences of permanent disability. Statistics shows that the largest number of ligament injuries occurs in the speed range of 30-50 km/h. A lower speed impact normally results in soft tissue injuries, and higher speed impacts would yield in fatalities. The injury mechanisms are mainly bending and shear. They are generally combined; however the bending moment is predominant in joint injuries and the shear force is the main issue in long bone fractures.

The developed model used in this study corresponds to an adult leg. The question of designing a child leg was considered. Accident analysis indicates that children are much less likely to sustain permanent leg injuries, and few statistic data available concerning disability in injured children suggests that their tolerance to this type of injury is higher than that of adults.

All new cars or designs are now tested by the European New Car Assessment Program (NCAP) to simulate accidents involving pedestrian impact at 40km/h, using dummy models. The results are then compared with the limits proposed for legislation by the European Enhanced Vehicle Safety Committee (EEVC). Each limit has an upper and lower performance bound. The values of the limits are summarised in Table 1 [1]. The upper limit sets a more stringent requirement for pedestrian protection. If the tested value is higher than the lower limit, permanent injuries are most likely to occur.

Table 1 EEVE WG17 Pedestrian Impact Limits

		Upper Limit	Lower Limit
Upper Leg	Bending Moment	220 Nm	400 Nm
	Sum of Forces	4.0 kN	7.0 kN
Low Leg	Tibia Deceleration	150 g	230 g
	Knee Shear Displacement	6.0 mm	7.5 mm
	Knee Bending Angle	15°	30°

Note that these limit requirements are voluntary only at the moment.

www.EngineeringEBooksPdf.com

FEM MODELLING

Only the upper and lower leg was modelled to impact with a car bumper. And a commercial code LS-DYNA version 950 [4] was used. In the simulation, the bumper was fixed as stationary and leg was assigned with an initial velocity.

The original model of leg used in this study was supplied by Ove Arup [5, 6]. It consists of two sections: femur and tibia. In between the two sections is the knee element. Fig. 1 shows the dimensions and the construction of the model. The femur and tibia inner steel tubes are modelled as rigid as the main interest is the magnitude of forces and displacements against their benchmarks in Table 1. Simulations of the detail of actual injuries are not important at this level of analysis. A 25mm layer of Confor foam surrounds these tubes, followed by rubber skin. The knee-ligament is represented by a nonlinear plastic beam in parallel with a damper with nonlinear viscosity. All internal contacts are predefined. The mass of the model is 13.4 kg. Total nodes and elements used are 7570 and 7457, respectively. External contact between the rubber skin and the bumper was defined by automatic surface to surface contact.

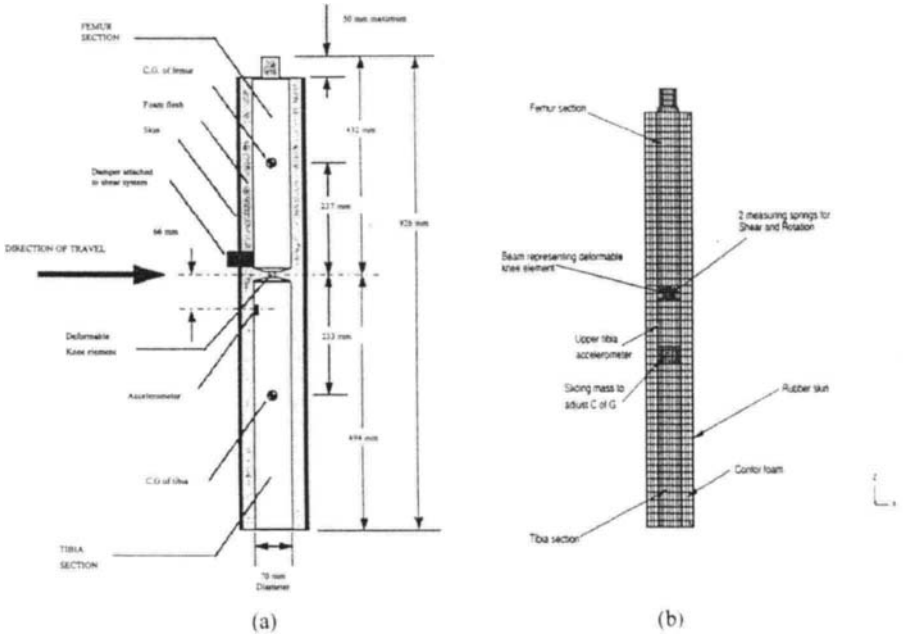

Fig.1. (a) Construction of the leg form. (b) FEM model used in the simulation. Knee element is consisted of a shear and an axial spring. A built-in accelerator at Node 125 (see Fig. 4) is used as a reference point.

www.EngineeringEBooksPdf.com

The bumper was modelled as a thin-walled hollow beam of 1.2 meter long with two chassis back supports and crushcans at 400mm each side from the centre, as shown in Fig. 2. The inserts show a magnified view of the corrugated frontal panel and the relative positions between the leg and the bumper during an impact. Hypermesh Version 5 was used to generate the mesh and shell elements were used through out. The curved hollow box beam was made from high strength steel with a yield stress of 600 to MPa, Young's modulus 210 GPa and Poisson's ratio 0.3. Rigid elements are defined as constrained nodes to represent migwelds and spot welds. Displacement of chassis back plates were fully constrained. In total 19192 elements were used with 21169 nodes.

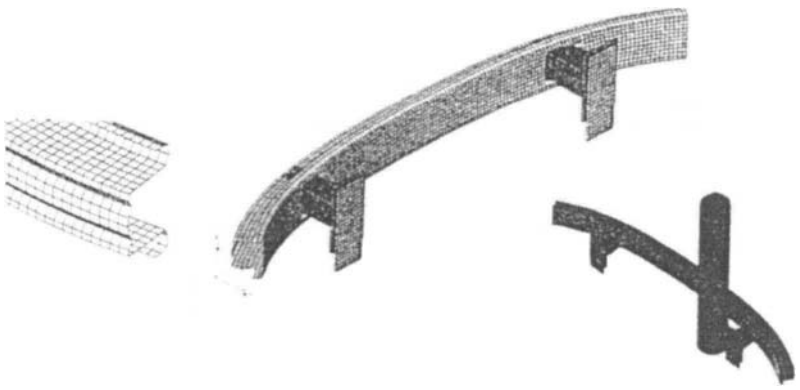

Fig. 2. FEM model of the complete bumper with the frontal corrugated panel, back plate, and supports connected to the chassis. The back plates of the support were modelled as rigid and fully constrained. The inserts show the frontal corrugated panel from a different angle, and the relative position between the leg and the bumper (Case 1).

In total eight tests runs were conducted corresponding to difference impact scenarios in terms of velocities and positions in the leg and the bumper. Time history results of the following three parameters were of particular interest from a biomedical point of view: upper tibia acceleration, knee shear displacement and knee bending angle.

RESULTS AND DISCUSSION

Fig 3 illustrates the results of Test 1 of an impact at the knee at 11.1m/s in the midpoint of the bumper. Fig. 3a shows both deformation and motion of the leg, and Fig. 3b gives the history of

www.EngineeringEBooksPdf.com

	Point 1 Time step 2, t = 0.001 sec Impactor projected at 11.1 m/s towards bumper. Impactor at maximum velocity. Impactor skin makes contact with bumper armature.
	Point 2 Time step 5, t = 0.004 sec Armature compresses Impactor skin and foam. Impactor deceleration, contact force and force upon knee at maximum value. Armature deflects backwards slightly. Impactor beginning to swing.
	Point 3 Time step 11, t = 0.010 sec Tibia section swinging heavily beneath armature. Armature deflecting back to original position. Femur section still moving in positive x direction but velocity reducing.
	Point 4 Time step 14, t = 0.013 sec Tibia section swinging back Impactor moving at constant velocity towards armature at this point. Acceleration is zero. Armature is still at original position.
	Point 4 Time step 18, t = 0.017 sec Momentum of femur causes impactor to impact with armature again. The Foam is compressed again. Causes second peak in acceleration and force acting upon knee area.

Fig. 3.a Deformation history of the leg in Case 1. Impact at the knee and the midpoint of the bumper at 40km/h

www.EngineeringEBooksPdf.com

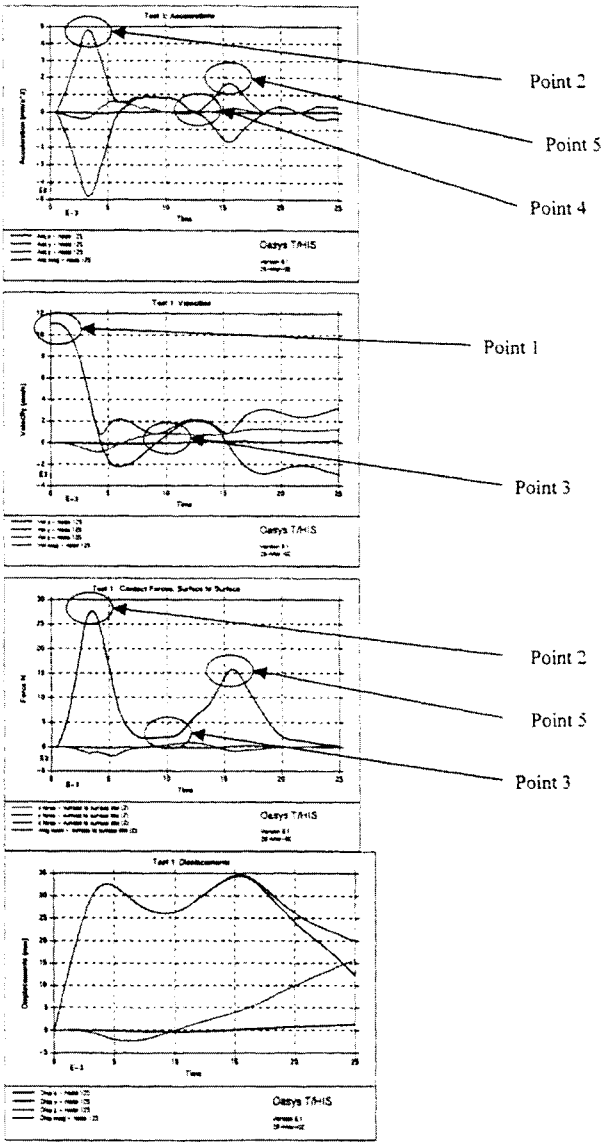

Fig. 3.b Kinematics and force history of the leg in Case 1. Impact at the knee and the midpoint of the bumper at 40km/h. Point numbers indicate time measured in ms.

www.EngineeringEBooksPdf.com

the kinematics of the reference point (node 125 - at upper tibia accelerometer, see Fig. 1) and the contact force. The acceleration and contact force curves shows that there are two peaks at 40 and 160 ms, respectively. The first peak is the initial impact between the knee and the bumper and it brings the knee to move backwards locally, then the inertia of the femur and tibia brings the knee forward again causing a second peak. For the simulation, the energy balance was checked to show that the difference is less than 1%, as seen in Fig. 4.

Table 2 summarises the key results of the total 8 different cases run, which are listed against the limits proposed by EEVC. The standard case is Case 1 where the impact occurs at the knee and in the midpoint of the bumper. Case 2 and 3 are of the same contact between the leg and the bumper, but at a lower speed of 30 and 20 km/h, respectively. Three more impact positions in leg are studied, ie, 50 mm above, 50mm and 100mm below the knee (Case 6 to 8). For the bumper, two more impact positions were 200 and 400mm from the midpoint of the span (Case 4 and 5). In all the cases except 2 and 3, the impact velocity was set at 40 km/h, or 11.1 m/s. Those satisfied with the EEVC limits are highlighted in italic font. Direct comparisons of Case 2 and 3 with the EEVE limits are not valid, as their impact velocity is lower than the required 40km/h the limits are set for. However, it clearly shows that speed has a profound effect as low speed brings to low values in all monitored parameters. It is a clear message that speed plays a key role in pedestrian injuries.

The impact position also makes a difference. The simulations show that when impact at different height of leg (Case 1, 6 to 8), none of the cases satisfies the EEVC limit requirement on maximum upper tibia acceleration. For the other two parameters, the results are mixed. Case 1 satisfies the maximum knee shear displacement, but fails the knee bend angle, while case 7 and 8 satisfy the bend angle limit, but not the shear displacement. Case 6 appears to be the worst case, indicating that bumper should not be designed higher than the knee.

For impact locations in the bumper (Case 1, 4 and 5), all fail the upper tibia acceleration and knee bending angle limits, but satisfy the shear displacement limit. This indicates that it make little difference in a central or offset impact with a pedestrian. The injuries are all unacceptably severe.

CONCLUSIONS

For all the cases simulated, stress values in the bumper never becomes close to its yield point, indicating the design used in this study is too strong for pedestrian legs. Important conclusions may be drawn from this. It may indicate that a basic steel bumper structure is not appropriate for crash protection of pedestrians. However, adopting a low-grade steel or a weak structural design has been ruled out by the industry, as high strength materials and designs bring in weight saving and provide the needed crashworthiness in non-pedestrian crashes at a much higher energy level. In fact, the current industrial philosophy for bumper design emphasises on minimising the deformation of the bodywork of the vehicle. Nevertheless, current bumper designs normally include plastic shells or skins in front of steel bumpers, but these are mainly for feature/cosmetic purposes. Possible solutions are to introduce polymer foams between the plastic shell and the steel bumper. The plastic shells can also be designed to include closed

www.EngineeringEBooksPdf.com

channels. With trapped air in the channel, the shell may provide cushioning between a pedestrian and the steel bumper structure, reducing injury severity.

With much progress having already been achieved to improve the safety of vehicle occupants, investigations on the safety of pedestrians involved in crash incidents with vehicles are urgently needed as a key issue for future development.

ACKNOWLEDGEMENT

Ove Arup & Partners are acknowledged for providing the original FE Pedestrian Impact Model for this study.

REFERENCES

1. European Enhanced Vehicle Safety Committee (1994). *Working Group 10 Report.*
2. Khalil T.B. and King, A.I. (1989). Crashworthiness and occupant protection in transportation system, ASME.
3. Macmillan R.H. (1983). *Dynamics of Vehicle Collisions*, Inderscience Enterprises Ltd, UK.
4. *LS-DYNA3D manual V950* (2000). LS-DYNA.
5. Ove Arup & Partners (2001). *Pedestrian Impact Model Version 2.*
6. Hardy, B.J. (1998). *Pedestrian Safety Testing Using the EEVC Pedestrian Impactors*, Transport Research Laboratory, UK.

Test run	Speed (km/h)	Impact position in leg from knee (mm)	Impact position in bumper from centre (mm)	Maximum upper tibia acceleration (g)	Higher/lower upper tibia acceleration limits (g)	Maximum knee shear displacement (mm)	Higher/lower knee shear limits (mm)	Maximum knee bending angle (degree)	Higher/lower knee bending limits (degree)
1	40	0	0	341.05	150-230	*1.07*	6.0-7.5	32.11	15-30
2	30	0	0	227.25		*0.57*		*23.40*	
3	20	0	0	*118.09*		*0.50*		*14.40*	
4	40	0	+400[b]	339.52		*1.04*		31.72	
5	40	0	+200[b]	344.50		*1.18*		31.95	
6	40	+50[a]	0	286.87		8.04		34.58	
7	40	-50[a]	0	288.02		11.59		*29.09*	
8	40	-100[a]	0	303.20		12.26		*21.63*	

Table 2 Summary of the simulation runs. a. "+" and "-" indicate impact point between the leg and the bumper above and below the knee. b. Impact point measured from the mid point of the bumper. Also 400mm is the position where the bumper is supported onto the chassis.

www.EngineeringEBooksPdf.com

Advances in Steel Structures, Vol. II
Chan, Teng and Chung (Eds.)
© 2002 Elsevier Science Ltd. All rights reserved.

A THEORETICAL MODEL FOR AXIAL SPLITTING AND CURLING OF CIRCULAR METAL TUBES

X. Huang[1], G. Lu[1] and T. X. Yu[2]

[1]School of Engineering and Science, Swinburne University of Technology
Hawthorn, Victoria 3122, Australia
[2]Department of Mechanical Engineering, Hong Kong University of Science
and Technology, Clear Water Bay, Hong Kong, PR China

ABSTRACT

Axial splitting and curling behaviour of circular metal tubes has been studied previously, as a potential energy absorbing system. In the experiments, mild steel and aluminum circular tubes were slowly pressed axially onto a rigid die, which was either of a radius or of a conical shape. Three main energy dissipation mechanisms exist in this process: plastic bending/stretching, ductile tearing along the axial cracks and friction. This paper presents a theoretical model, which captures these features. The plastic energy is calculated by considering bending of curved strips in-between the cracks, while the ductile tearing is accounted for by estimating the plastic stretching energy within the crack front with a critical opening displacement. Coulomb friction is assumed. Minimisation of the total energy leads to an estimate of the number of cracks, which in turn enables prediction of force etc. The model agrees with the experiments reasonably well.

KEYWORDS

Circular tubes, plastic bending, plastic stretching, ductile tearing, energy absorption

INTRODUCTION

Energy absorbing devices are employed where collision may cause serious consequences, so as to protect human as well as other important structures (Johnson & Reid, 1978, 1986). Circular tubes may be axially crushed progressively in an axisymmetric or a non-axisymmetric (or called diamond) mode by two flat plates. Alexander (1960) was the first researcher to propose a theory for the axisymmetric collapse mode based on a balance of external and internal work done. Several researchers further developed a model to predict the crush force. Recently, Guillow et. al. (2001) and Huang and Lu (2002) refined this work experimentally and theoretically.

Another collapse mode is the splitting and curling of tubes. From the viewpoint of energy absorption, this collapse mode has a long stroke of over 90 per cent of the total tube length. Stronge et. al. (1983) conducted experiments with square tubes split against a radius/flat die. Huang et. al. (2002) further studied the splitting and curling behaviour of square tubes axially compressed between a plate and a

www.EngineeringEBooksPdf.com

pyramidal die. Lu et. al. (1994) investigated the tearing energy involved in splitting square metal tubes and that in thin metal sheets (Lu et. al., 1998; Fan et. al. 2002).

In a comparative study of energy absorbers for improving occupant survivability in aircraft crashes, Ezra & Fay (1972) identified circular tube splitting and curling as an efficient system based on specific energy dissipation. Reddy & Reid (1986) and Huang et. al. (2002) studied the splitting behaviour of circular tubes compressed axially between a plate and a curved die.

A theoretical model is proposed here for the splitting and curling behaviour of circular tubes. A typical specimen and load-displacement curves are shown in Figures 1 & 2. Tubes were observed to have a number of cracks propagating along the axial direction. The strips so formed by cracks rolled up into curls with an almost constant radius. The crush force became steady after some initial fluctuations. Three energy dissipation mechanisms were involved: 1) "near-tip" tearing associated with tube splitting; 2) "far-field" deformation associated with the plastic bending and stretching of curls; 3) friction as the tube interacted with the die. These are evaluated in a theoretical model presented below.

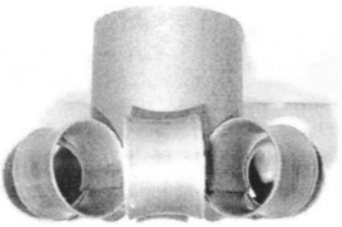

Figure 1: A typical specimen after test

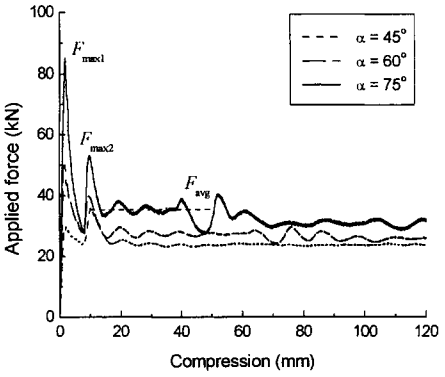

Figure 2: Force-displacement curves

THEORETICAL MODEL FOR A RADIUS DIE

Consider a tube with diameter D and thickness t pressed axially and split against a radius die (Figure 3). With the propagation the cracks, the strips so formed curl with a doubly curved face of a radius R in axial direction and about r_0 in circumferential direction. The crack tip is located at a certain point with an angle β_0 as shown in Figure 3. A number of other simplifying assumptions are made:

a) The material is regarded as rigid, perfectly plastic. There is no interaction between the resultant membrane force and the bending moments in yielding.
b) All the strips curl into rolls with a constant radius, R.
c) Plastic work in curling is calculated by considering meridional bending of a curved strip with a transversal radius r_0. Changes in transversal radius are neglected.

The apparent change in Gaussian curvature requires stretching/compression of the mid-surface (Calladine, 1983). Assumption (c) above leads to a stretching in the meridional direction only.

www.EngineeringEBooksPdf.com

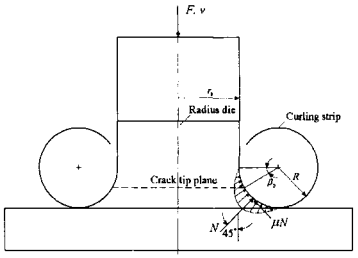

Figure 3: A model for tube splitting with a radius die

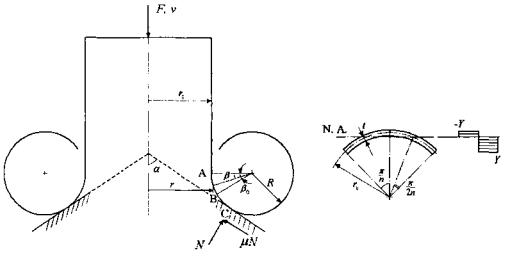

Figure 4: A model for tube splitting with a conical die

A crack opening displacement (COD) criterion is used to account for tearing, which was identified as a possible way in characterizing fracture properties of ductile sheets (Parks et. al, 1976). The crack tip is not at A but at B due to the ductility of the material; the ligament holds these assumed stripes together until a critical separation or crack opening displacement δ is reached. In the present analysis, we use a non-dimensional critical separation $\gamma = \delta/t$ as a parameter and take $\gamma = 1.0$ unless specified otherwise. Thus, β_0 can be uniquely determined from the geometry of the problem and the value of γ, as

$$\beta_0 = \cos^{-1}(1 - \frac{n\gamma t}{2\pi R}) \tag{1}$$

where n is the number of cracks (or strips).

The applied force can be calculated from energy balance. When the tube is moving downward (whilst cracks are propagating) with a speed v, the energy balance leads to

$$Fv = \dot{W}_P + \dot{W}_T + \dot{W}_F \tag{2}$$

where $\dot{W}_P$, $\dot{W}_T$ and $\dot{W}_F$ denote the rate of energy dissipation in plastic bending, tearing and friction, respectively.

In this model, all plastic bending and stretching are confined in the curved strips (with r_0) bending with a radius R. The rate of plastic bending becomes

$$\dot{W}_P = \frac{2\pi r_0 m_p}{R + r_0(1 - \cos\frac{\pi}{2n})} v \tag{3}$$

where $r_0(1-\cos\frac{\pi}{2n})$ is the increase of bending radius due to the position of the neutral axis; and the full plastic bending moment for one strip normalized with respect to the strip arc width is

$$m_p = \frac{nYr_0t^2}{2\pi}\left[\int_{\frac{\pi}{2n}}^{\frac{\pi}{n}}(\cos\frac{\pi}{2n} - \cos\theta)d\theta + \int_0^{\frac{\pi}{2n}}(\cos\theta - \cos\frac{\pi}{2n})d\theta\right]$$

$$= \frac{nYr_0t}{\pi}(2\sin\frac{\pi}{2n} - \sin\frac{\pi}{n}) \tag{4}$$

www.EngineeringEBooksPdf.com

Hence, the rate of plastic bending dissipation is

$$\dot{W}_P = 2nYr_0^2 t \frac{(2\sin\frac{\pi}{2n} - \sin\frac{\pi}{n})}{R + r_0(1-\cos\frac{\pi}{2n})} v \tag{5}$$

The tearing energy is involved in plastic work within the near-tip zone in the form of circumferential stretching ahead of the crack tip. Hence, the rate of tearing energy dissipation is

$$\dot{W}_T = \int_V \sigma_\theta \dot{\varepsilon}_\theta dV \quad \text{or} \quad \dot{W}_T = Yn\eta t^2 v \tag{6}$$

The rate of energy dissipation by friction is

$$\dot{W}_f = 2\pi r_0 \mu N v \tag{7}$$

where N is the normal force per unit length. For a conical die (Figure 4), it may be related to the applied force F and the die semi-angle as,

$$N = \frac{F}{2\pi r_0(\sin\alpha + \mu\cos\alpha)} \tag{8}$$

For a radius die, we assume the resultant normal contact force is at 45° to the horizontal; its value N can be obtained by setting $\alpha = 45°$ in the above equation.

Substituting Eqns. 5-7 to 2, and introducing three non-dimensional parameters, $f = \frac{F}{2\pi r_0 tY}$; $\phi = \frac{2r_0}{t}$; $\eta = \frac{2R}{t}$, the non-dimensional force is

$$f = \frac{\sin\alpha + \mu\cos\alpha}{\sin\alpha - \mu(1-\cos\alpha)} \left[\frac{(2\sin\frac{\pi}{2n} - \sin\frac{\pi}{n})}{\eta + \phi(1-\cos\frac{\pi}{2n})} + \frac{\gamma}{\phi^2} \right] \frac{n\phi}{\pi} \tag{9}$$

Thus, the applied force is a function of both the non-dimensional curl radius (η) and the crack number (n). For the case of a radius die, we may assume that the curl radius is the same as that of a die. Hence,

$$f = \frac{1+\mu}{1-(\sqrt{2}-1)\mu} \left[\frac{\pi^2\phi}{8n^2\eta} + \frac{n\gamma}{\pi\phi} \right] \tag{10}$$

Assume that the number of cracks is such that the total force is a minimum, i.e., $df/dn = 0$. This leads to, $n = \left(\frac{\phi^2}{4\gamma\eta}\right)^{\frac{1}{3}} \pi$. Substituting this expression into Eqn. 10 and taking the friction coefficient $\mu = 0.2$,

www.EngineeringEBooksPdf.com

the force is $f = 1.23\left(\frac{\gamma^2}{\phi\eta}\right)^{\frac{1}{3}}$ .The coefficient would be 1.58 when $\mu = 0.4$. The predicated crack number and force are plotted against the non-dimensional die (or curl) radius as shown in Figures 5 & 6, together with the test results from Reddy & Reid (1986). From the comparison in n and f, it would suggest that annealing enhanced the ductility of both aluminium and mild steel tubes with a larger value of γ: about 2 for annealed aluminium tubes and 0.5~1.0 for the rest. In these cases, the tearing energy dominates the total dissipated energy and is twice as much as the plastic bending energy.

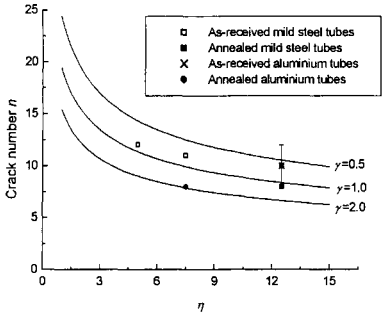

Figure 5: Number of cracks vs. die radius

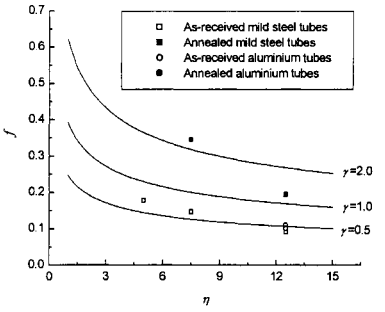

Figure 6: Force vs. die radius

THEORETICAL MODEL FOR A CONICAL DIE

For tubes with a conical die (Figure 4), previous theoretical analysis applies in a similar manner. Nevertheless, both the curl radius and crack number are unknowns. An additional equation is obtained by equilibrium consideration. Neglecting the effect of shear force, the equilibrium equation in the meridional direction is given by

$$\frac{dN_x}{d\beta} = -\frac{\sigma_\theta Rt}{r}\sin\beta \tag{11}$$

where β is an angular coordinate ($0 \le \beta \le \beta_0$), σ_θ is the hoop stress and N_x is the membrane force per unit length along the meridional direction. The development of the radius of the corresponding tube can be written, from the geometry of the model, as

$$r = r_0 + R(1-\cos\beta) \tag{12}$$

Substituting (12) into (11), the meridional equilibrium equation is re-written as

$$-\frac{dN_x}{d\beta} = \frac{YRt\sin\beta}{r_0 + R(1-\cos\beta)} \tag{13}$$

From the equilibrium of BC where $\beta = \beta_0$, the meridional membrane force at the crack tip B is

$$-N_x^B = N\sin(\alpha-\beta_0) + \mu N\cos(\alpha-\beta_0) \tag{14}$$

www.EngineeringEBooksPdf.com

where N is normal force per unit circumferential length at the contact point C. From the equilibrium of AC, the meridional membrane force at A where $\beta = 0$ can be expressed by

$$-N_x^A = N\sin\alpha + \mu N\cos\alpha \tag{15}$$

From Eqns. 13-15, the normal force per unit length is found as

$$N = \frac{Yt\ln(1+\frac{n\gamma t}{2\pi r_0})}{\sin\alpha - \sin(\alpha-\beta_0) + \mu[\cos\alpha - \cos(\alpha-\beta_0)]} \tag{16}$$

Let the bending moment at the crack tip equal to the full plastic bending moment, Eqn. 4,

$$NR\sin(\alpha-\beta_0) - \mu NR[1-\cos(\alpha-\beta_0)] = m_p \tag{17}$$

Combining Eqns. 16 and 17, the curl radius is given as

$$R = \frac{\sin\alpha - \sin(\alpha-\beta_0) + \mu[\cos\alpha - \cos(\alpha-\beta_0)]}{\sin(\alpha-\beta_0) - \mu[1-\cos(\alpha-\beta_0)]}(2\sin\frac{\pi}{2n} - \sin\frac{\pi}{n})\frac{2r_0^2}{\gamma t} \tag{18}$$

the above equations can be re-written as

$$\eta = \frac{\sin\alpha - \sin(\alpha-\beta_0) + \mu[\cos\alpha - \cos(\alpha-\beta_0)]}{\sin(\alpha-\beta_0) - \mu[1-\cos(\alpha-\beta_0)]}(2\sin\frac{\pi}{2n} - \sin\frac{\pi}{n})\frac{\phi^2}{\gamma} \tag{19}$$

where $\beta_0 = \cos^{-1}(1-\frac{n\gamma}{\pi\eta})$. This is an implicit nonlinear equation. Numerical calculations show that for small values of n, η decreases rapidly. η increases slowly when n is large.

This additional relationship is used in conjunction with Eqn. 9 in the minimisation process of the force, which leads to an estimate of crack number. The value of crack number is then substituted into Eqn. 19 to obtain the curl radius and into Eqn. 9 to obtain the force applied. Numerical results of the crack number are shown for all the cases in Figure 7. The test values seem undistinguishable for dies of different semi-angles, but they are within the theoretical curves for the semi-angles considered.

For a given die semi-angle (α) and dimensions of the tube, once the crack number is determined uniquely, the curl radius can be assessed. Figure 8 shows the variations of non-dimensional curl radius versus the die semi-angle for a typical tube with $\phi = 31$. When the curl radius and the crack number are determined as above, the force applied can be calculated theoretically. This is plotted against the ratio of the tube diameter to the thickness in Figure 9 for dies with a semi-angle $\alpha = 45°$. And the force applied almost linearly increases with the die semi-angle for α in the range of 30° to 90°, as shown in Figure 10 for a typical tube with $\phi = 31$. A general agreement between the theoretical prediction and experiments is obtained for all cases.

www.EngineeringEBooksPdf.com

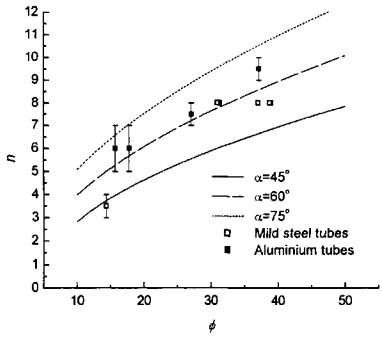

Figure 7: Number of cracks vs. tube radius

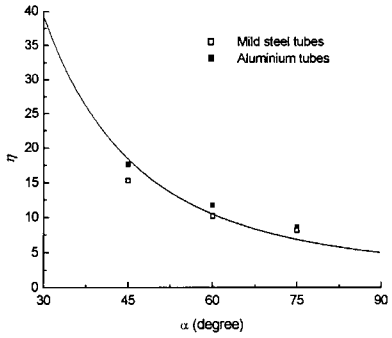

Figure 8: Curl radius vs. die semi-angle

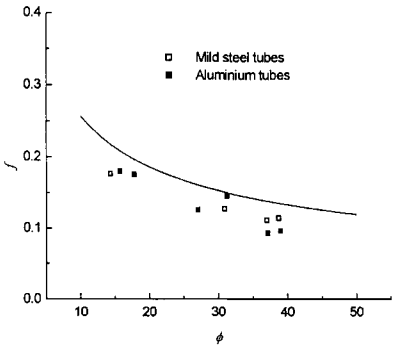

Figure 9: Force vs. tube radius

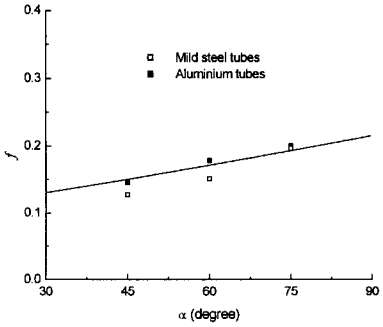

Figure 10: Force vs. die semi-angle

CONCLUSION

A theoretical model has been proposed for circular metal tubes axially split and curled with a radius or conical rigid die. Three energy mechanisms are involved: plastic bending energy, tearing energy and frictional work in this type of energy absorbers. The crack number, curl radius and force applied are reasonably predicted by this theoretical model.

ACKNOWLEDGEMENT

The authors wish to thank the Australian Research Council for the financial support to undertake this work.

REFERENCES

Alexander J.M. (1960). An approximate analysis of collapse of thin-walled cylindrical shells under axial loading. *Quarterly Journal of Mechanics and Applied Mathematics* **13**, 10-15.

www.EngineeringEBooksPdf.com

Atkins A.G. (1987). On the number of cracks in the axial splitting of ductile metal tubes. *International Journal Mechanical Sciences* **29**, 115-121.

Calladine C.R. (1983). *Theory of Shell Structures*, Cambridge University Press.

Ezra A.A. and Fay R.J. (1972). An assessment of energy absorbing devices for prospective use in aircraft impact situations. In: Herrmann G, Perone N. *Dynamic Behaviour of Structures*, Pergamon, London, 225-246.

Fan H., Wang B., and Lu G. (2002). On the tearing energy of a ductile thin plate. *International Journal of Mechanical Sciences* **44**, 407-421.

Guillow S.R., Lu G. and Grzebieta R.H. (2001). Quasi-static axial compression of thin-walled circular aluminium tubes. *International Journal of Mechanical Sciences* **43:9**, 2103-2123.

Huang X., Lu G. and Yu T.X. (2002). Energy absorption in splitting square metal tubes, *Thin-Walled Structures* **40**, 153-165.

Huang X., Lu G. and Yu T.X. (2002). On the axial splitting and curling of circular tubes. *International Journal of Mechanical Sciences* (submitted).

Huang X. and Lu G. (2002). Axisymmetric progressive crushing of circular tubes. *International Journal of Crashworthiness* (to appear).

Johnson W. and Reid S.R. (1978). Metallic energy dissipating systems. *Applied Mechanics Review* **31**, 277-288.

Johnson W. and Reid S.R. (1986). Update to: Metallic energy dissipating systems. *Applied Mechanics Update* **39**, 315-319.

Lu G., Fan H. and Wang B. (1998). An experimental method for determining ductile tearing energy of thin metal sheets. *Metals and Materials* **4:3**, 432-435.

Lu G., Ong L.S., Wang B. and Ng H.W. (1994). An experimental study on tearing energy in splitting square metal tubes. *International Journal of Mechanical Sciences* **36:12**, 1087-1097.

Parks D.M., Freund L.B. and Rice J.R. (1976). Running ductile fracture in a pressurized line pipe. *Mechanics of crack growth*, ASTM STP 590. American Society for Testing and Materials, philadelphia, 2543-2562.

Reddy T.Y. and Reid S.R. (1986). Axial splitting of circular metal tubes. *International Journal of Mechanical Sciences* **28:2**,111-131.

Stronge W.J., Yu T.X. and Johnson W. (1983). Long stroke energy dissipation in splitting tubes. *International Journal of Mechanical Sciences* **25:9-10**, 637-647.

www.EngineeringEBooksPdf.com

Advances in Steel Structures, Vol. II
Chan, Teng and Chung (Eds.)
© 2002 Elsevier Science Ltd. All rights reserved.

EXPERIMENT AND ANALYSIS OF A SCALED-DOWN GUARDRAIL SYSTEM UNDER STATIC AND IMPACT LOADING

J. T. Y. Hui[1], T. X. Yu[1] and X. Q. Huang[2]

[1]Department of Mechanical Engineering, Hong Kong University of Science and Technology, Clear Water Bay, Kowloon, Hong Kong SAR, CHINA
[2]School of Transportation Engineering, South China University of Technology, Guangzhou, CHINA

ABSTRACT

Corrugated steel W-beam guardrail system is the most popular energy absorbing system along roadside throughout the world. It helps to dissipate a vehicle's kinetic energy in impact events so as to reduce the damage to the car occupants and the car itself. Therefore, its performance and characteristics are of great importance for road safety.

In this paper, our recent experimental study on a scaled-down W-beam guardrail system is reported. Downscaled W-beam samples were tested under quasi-static and impact three-point bending to reveal its energy absorption characteristics and the large deformation mechanism. The load-deflection curves, the global flexural profiles and the cross-sectional distortion were all recorded to gain the information on the deformation mechanism and energy dissipation of the W-beams. The effects of different supporting conditions and end constraints on the large deformation behavior of the beams were also examined. The experimental observations and measurements of the samples under impact loading were compared with its static counterparts.

Furthermore, experiments were conducted on a scaled-down system consisting of a guardrail beam and two supporting posts to explore the interaction between the beam and the posts during an impact incident. This set of experiments was aimed at the examination of the energy absorbing capacities of the system and the partitioning of energy dissipation within the system when it is collided by a moving mass.

KEYWORDS

Guardrail, Energy absorbing capacity, Impact, Scaled-down testing, Cross-sectional distortion, Large deformation.

www.EngineeringEBooksPdf.com

INTRODUCTION

The most commonly used guardrail system along highways to redirect the out-of-control vehicles is steel corrugated W-beams. This energy absorbing device helps to dissipate the kinetic energy of a vehicle during an impact event so as to reduce the severity of the impact on vehicle occupants. Because of the importance of this 'life saving device', many full-scale experiments were conducted to evaluate the performance of guardrail systems and their alternatives around the world (Bank et al, 1998; Ando et al, 1995).

However, in order to reduce the cost of the experiment and to increase the flexibility in testing other possible alternatives, a series of downscaled testing procedures on the W-beams were adopted in our study. Approximately 1:3.75 downscaled W-beams were tested both statically and dynamically in the regime of large plastic deformation; for the W-beam itself as well as for a guardrail system consisting of both the W-beam and the supporting posts. The profile of the guardrail beam and the design of the system were made according to the downscale of the commonly used guardrail standard in Hong Kong. For the beam testing, three different end conditions were examined; while for the system testing, two different types of supporting posts were used to see if they would affect the performance of the guardrail beams. Details of the load carrying capacities and the cross-sectional distortions were recorded under both static and impact loadings. High-speed video was also taken during the impact experiments so that the dynamic deformation mechanism could be compared with its static counterpart.

EXPERIMENTAL SETUP

Approximately 1:3.75 downscaled specimens, with dimensions as shown in Figure 1, of conventionally used W-shaped guardrail beams were tested. The beams were tested under three-point bending for different supporting conditions, while in the system testing two different types of supporting posts were adopted. The material of the specimens was chosen to have a compatible property of the real beams. The stress-strain relationship obtained for the material was plotted in Figure 2.

Beam Testing

The downscaled specimens were subjected to quasi-static and dynamic three-point bending. The specimens were supported with one of the following three supporting conditions: (1) simply roller-supported (RS), (2) simply box-supported (BS), and (3) axially-constrained roller-supported (AR). The difference between the roller and box supports is that, at the roller support, the two ends of the cross-section of the specimen were transversely constrained, while at the box support, the two ends of the cross-section were free to move and rotate. A specimen of total length 600mm was symmetrically placed on the supports with a span L = 535mm. The specimen was loaded at the mid-span by a rigid wedge-head perpendicular to the beam axis, as shown in Figure 3.

Quasi-static tests were conducted on a Universal Testing Machine (UTM) with a loading rate of 5mm/min. The load was removed for every 10mm-interval so as to record the unloading characteristic and the cross-sectional distortion at the line of loading until a final transverse displacement of 120mm.

In the impact tests, the specimens were impact loaded under a Drop Tower with a wedge-headed drop weight assembly of 12.92kg. The specimens were struck at the mid-span with three different initial impact velocities for each of the three different supporting conditions mentioned above.

www.EngineeringEBooksPdf.com

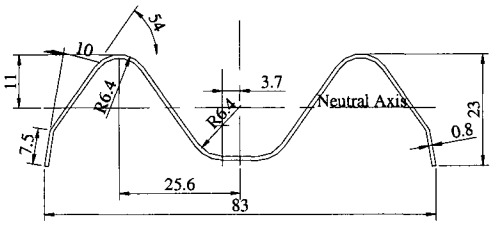

Figure 1: Cross-section of downscaled W-beam specimen

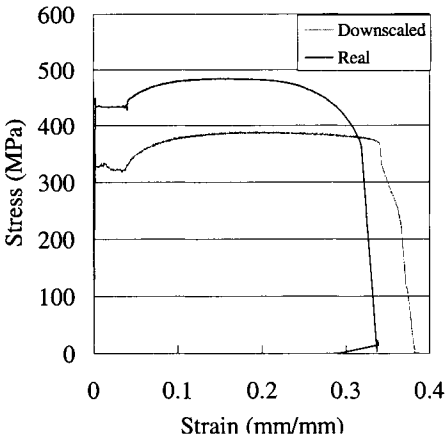

Figure 2: Typical material tensile test results for real and downscaled beams

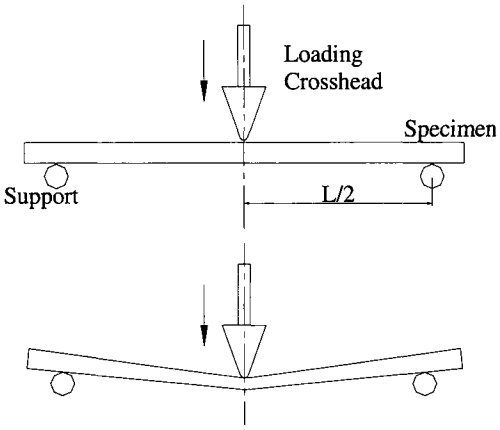

Figure 3: Schematic illustration of beam tests

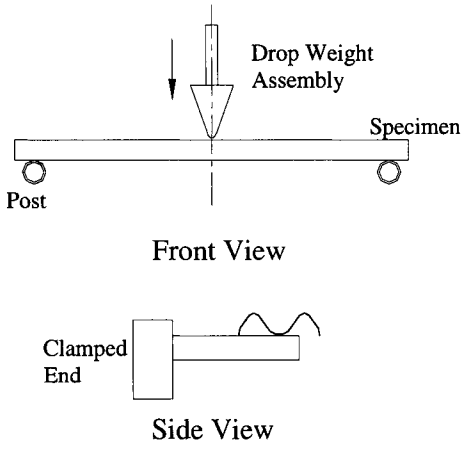

Figure 4: Schematic illustration of system tests

TABLE 1
COMPARISON OF DIMENSIONS OF CONVENTIONAL GUARDRAIL SYSTEM AND THE EXPERIMENTAL SETUP

	W-beam		Circular Hollow Post		Rectangular Hollow Post		
	Width	Thickness	Diameter	Thickness	Width	Height	Thickness
Conventional System	310-317mm	3mm	115mm	4mm	50mm	100mm	5mm
Scale-down System	81-84mm	0.8mm	30mm	0.8mm	13mm	25mm	1mm

www.EngineeringEBooksPdf.com

High-speed videos were taken during the impact tests; the global flexural deformation and the final local cross-sectional distortion were recorded. The acceleration history, and then the loading history, were obtained from the transverse displacement history recorded from the high-speed video camera.

System Testing

An approximately 1:3.75 downscaled guardrail system was designed according to the conventionally used guardrail system in Hong Kong. The experimental setup and the downscaled system dimensions were shown in Figure 4 and Table 1. The downscaled guardrail systems were impact-tested using the identical drop weight assembly as used in the beam testing. The two types of post geometry were circular hollow tubes and rectangular hollow tubes. The tubes were stainless steel type 304 extruded tubes commercially available in the market. High-speed videos were also taken during the impact tests to reveal the dynamic deformation mechanism of the guardrail system.

OBSERVATIONS AND ANALYSIS

Static Beam Testing

The load-transverse-displacement curves of W-beam samples with different supporting conditions under quasi-static three-point bending are shown in Figure 5. Generally speaking, the load-carrying capacities of the simply supported samples, either roller or box, were very similar. The load rose very quickly to a peak then decreased gradually. Along with the global flexural distortion, there was also local cross-sectional distortion right under the loading wedge. Material's strain hardening contributed to the rise in loading until the beam reached its limit instability at which the local cross-section of the W-beam started to be seriously distorted. The cross-sectional distortion resulted in a structural softening to the beam's load-carrying behavior and it also formed as a 'plastic hinge'. The corresponding local cross-sectional distortions of the W-beam samples were shown in Figure 6. Despite the similarity in load-carrying capacities, the local cross-sectional distortions for the above two types of bending were different. As observed from the measurements, although for both supporting conditions, the local cross-sections would deform through flattening of the top part then a further collapse of the whole cross-section with bulges formed at the top, there was less increase in the width of the local cross-section for the simply box-supported beams. This was mainly because for the box-supported samples, the two ends of the cross-sections were free to rotate. When larger transverse displacement was reached, the two sidewalls of the cross-sections were pushed downward. This small downward displacement of the sidewalls was not localized but occurred throughout the whole W-beam.

For the axially-constrained roller-supported W-beams, its load-carrying capacity and the local cross-sectional distortions were very similar to its counterpart without axial constraints at the early stage of the bending test. Yet, as higher transverse displacement was reached, the effect of the axial constraints was taken into effect by introducing a tension factor which competed with the structural softening effect and made the load rose again. Near the end of the test, the tension in the beam was strong enough to tear the material at the point of fixing (two holes) and led to the drops in the loading values as well as the failure of the sample just before the end of the experiment as shown in Figure 5. Also for the same transverse displacement, the collapse of the local cross-section or the increase in the width was more significant than the beam samples under other end conditions.

Impact Beam Testing

www.EngineeringEBooksPdf.com

It was observed, from the impact test results of the beam samples as shown in Figures 7 to 9, that the effect of the supporting conditions on the contact load would be less significant than the static counterpart. Only for the axially-constrained roller-supported samples, the final transverse displacement was generally smaller than the simply-supported ones for a similar impact velocity; and the response duration for a lower velocity impact was much shorter, i.e. the time for rebound was faster, than the simply-supported beams. However, the effect of the initial impact velocity, i.e. the input impact energy, was more important for the impact performances of the beam samples. It was common to see that there was a sudden increase in the load when the drop weight reached its maximum transverse displacement and just started to rebound. This phenomenon would be more noticeable when the initial impact velocity increased, resulting in a correspondingly higher peak load.

Impact System Testing

The distinction between the contact load histories for different post types was insignificant, even though the large differences in the post cross-sections and their static tip-loaded performances. Again, there were peak loads appearing at maximum transverse displacements for higher velocity impacts in both types of post configuration. The peak value increased with initial impact velocity, even the differences in maximum transverse displacements seemed to be small for higher velocity impacts.

CONCLUDING REMARKS

Scaled-down W-beam samples were static and impact tested for its basic mechanical properties and local cross-sectional deformation behaviors. The three major factors affecting the load-carrying capacity of the W-beam and the corresponding plastic dissipations were material's strain hardening, structural softening due to the local cross-sectional distortion and the tension factor due to the axial constraints. A scaled-down impact testing on the basic post-guardrail system considering the W-beam-post interaction was first attempted. However, the data shown was preliminary and more useful details of an impact to the scaled-down guardrail system could be reveled from the local cross-sectional distortions and high-speed video records.

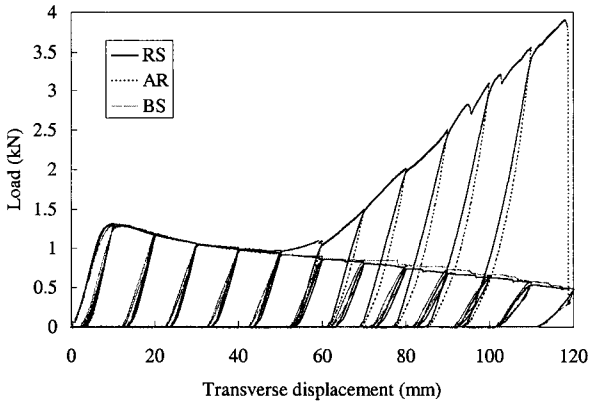

Figure 5: Load-transverse displacement curves for quasi-static three-point bending of beam samples with different supporting conditions, (a) RS-simply roller-supported, (b) AR-axially-constrained roller-supported and (c) BS-simply box-supported

www.EngineeringEBooksPdf.com

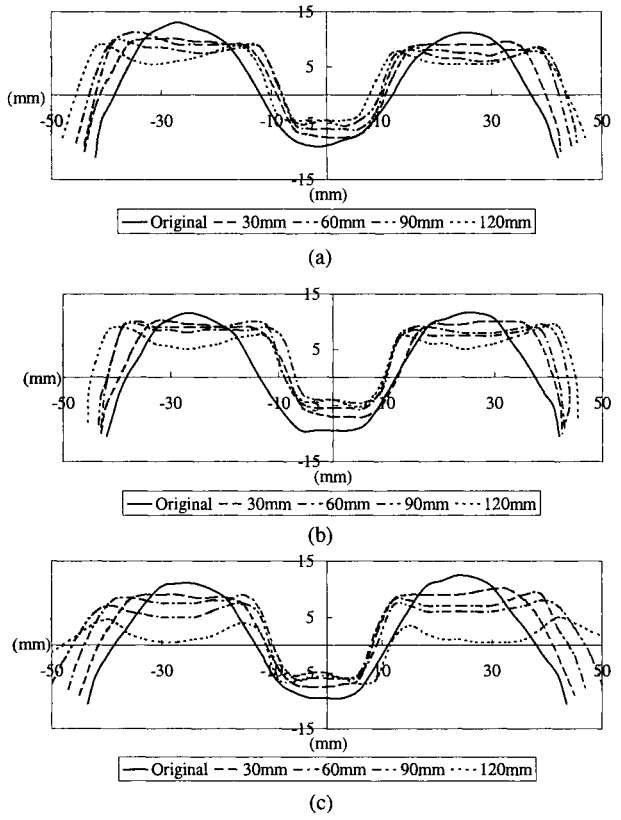

Figure 6: Local cross-sectional distortion of W-beam samples at different transverse displacement under quasi-static three-point bending with different supporting conditions - (a) RS, (b) BS and (c) AR

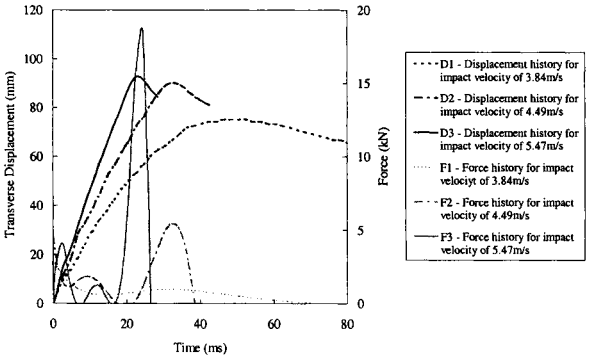

Figure 7: Force and transverse displacement history for simply roller-supported (RS) W-beam samples under impact tests with different initial impact velocities

www.EngineeringEBooksPdf.com

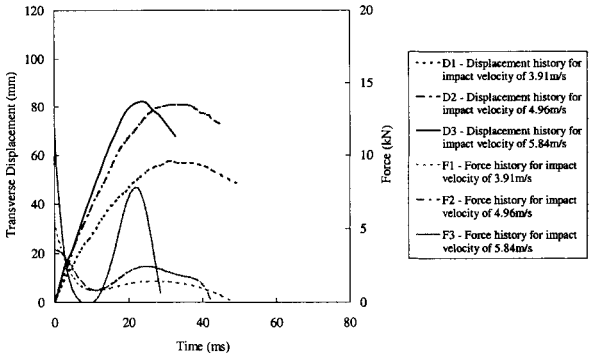

Figure 8: Force and transverse displacement history for axially-constrained roller-supported (AR) W-beam samples under impact tests with different initial impact velocities

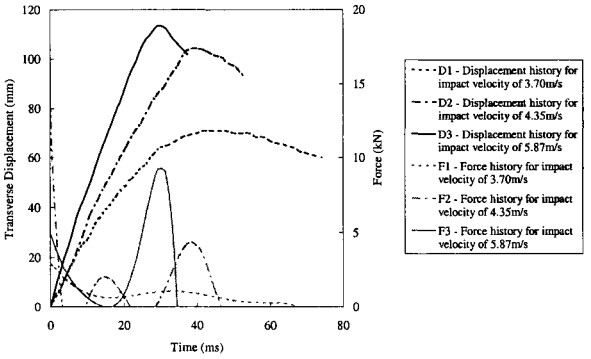

Figure 9: Force and transverse displacement history for simply box-supported (BS) W-beam samples under impact tests with different initial impact velocities

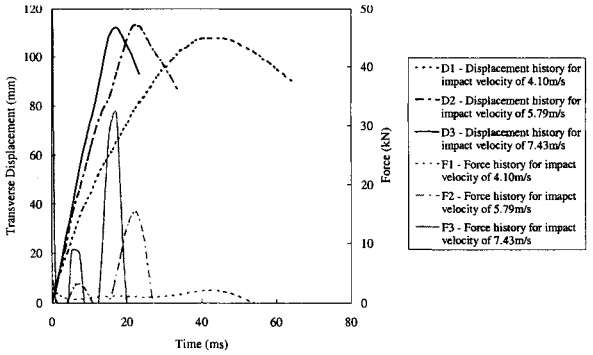

Figure 10: Force and transverse displacement history for system of W-beam samples with rectangular hollow posts under impact tests with different initial impact velocities

www.EngineeringEBooksPdf.com

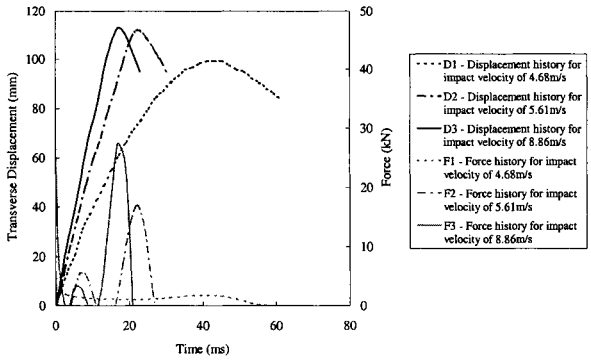

Figure 11: Force and transverse displacement history for system of W-beam samples with circular hollow posts under impact tests with different initial impact velocities

ACKNOWLEDGEMENT

The authors would like to thank to the Guangdong Province Science Foundation and the Hong Kong Research Grant Council (under grant HKUST6035/99E) for their support. The authors also wish to acknowledge the staff at the School of Transportation Engineering, the South China University of Technology for their assistance in manufacturing the scaled-down speciemens.

REFERENCES

Ando, K., Fukuya, T., Kaji, S. & Seo, T. (1995). Development of Guardrails for High Speed Collisions. *Transportation Research Record*, **1500**, 52-58.

Bank L.C., Gentry T.R. and Yin J. (1998). Pendulum Impact Tests on Steel W-beam Guardrails. *J. of Trans. Eng* **July/August**, 319-325.

Bank L.C., Hargarve M., Svenson A. and Teibei A. (1998). Impact Performance of Pultruded Beams for Highway Safety Applications. *Composite Structures* **42**, 231-237.

Hui S.K. and Yu T.X. (2000). Large Plastic Deformation of W-beams Used as Guardrails on Highways. *Proc. Of the 5th Asia-Pacific Symposium on Advances in Engineering Plasticity and Its Applications (eds. T.X. Yu, Q.P. Sun and J.K. Kim)*, 751-756, Trans Tech Publications, Uetikon, Zuerich.

Paulsen F. and Welo T. (2001). Cross-sectional Deformations of Rectangular Hollow Sections in Bending: Part I – Experiments. *Int. J. of Mech. Sci* **43**, 109-129.

Teh L.S. and Yu T.X. (1987). Large Plastic Deformation of Beams of Angle-section under Symmetric Bending. *Int. J. of Mech. Sci.* **39:7**, 829-839.

www.EngineeringEBooksPdf.com

Advances in Steel Structures, Vol. II
Chan, Teng and Chung (Eds.)
© 2002 Elsevier Science Ltd. All rights reserved.

CRASHWORTHINESS OF MOTOR VEHICLE AND LUMINAIRE SUPPORT IN FRONTAL IMPACT

Magdy Samaan[1] and Khaled Sennah[2]

[1] Department of Civil & Environmental Engineering, University of Windsor, Windsor, Canada Toronto, Canada N9B 3P4
[2] Civil Engineering Department, Ryerson University, Toronto, Ontario, Canada, M5B 2K3

ABSTRACT

In Canada, different types of collisions of vehicles are recorded each year, resulting in thousands of injuries and fatalities. The severity of these collisions depends on the aggressiveness and incompatibility in vehicle-to-vehicle, vehicle-to-pole, vehicle-to-curbs, and vehicle-to-guardrail collisions. The objective of this paper is to generate research information to enhance energy absorption characteristics in transportation infrastructures involved in vehicle crash accidents. A finite-element computer model, using the available LS-DYNA software, was developed to simulate crashes of a vehicle and a luminaire steel pole in frontal impact. The finite-element vehicle model was based on a 1991, 4-door, Ford Taurus. The steel pole was modeled using shell elements to capture the three-dimensional effect of the structure. Four configurations of steel pole supports were examined, including embedding the pole directly into the soil. Different types of solid conditions were examined to study their effects on vehicle occupant safety. The structural response focused on energy absorption as well as the deformation of the steel pole. The case of steel pole impended directly on soft clay was proved to be strong enough to offer protection under service loading, and to remain flexible enough to avoid influencing vehicle occupants, thus reducing fatalities and injuries resulting from the crash.

KEYWORDS:

Crashworthiness, finite-element analysis, frontal collision, safety, pole design, soil characteristics, energy absorption, dynamics.

www.EngineeringEBooksPdf.com

INTRODUCTION

It is considered that in the field of vehicle safety and injury prevention, there should be a strong focus on the needs of families and children. To date, this area does not appear to have considerably attracted the level of attention it deserves. A multi-disciplinary approach is advocated that links medical personnel in hospitals and rehabilitation centers to engineers and ergonomists who design and test vehicles. This approach is based on a belief that safety in automotive vehicles is fundamentally a function of both the design and function of vehicle safety systems, the design and function of highway hardware and the individuals who must make the decision to use them. As an outcome of vehicle design, vehicle occupants, involved in crash accidents with highway hardware, move out of position during or prior to vehicle collisions and thus suffer injuries, which were not foreseen during the original design of the vehicle.

Finite element models of vehicles have been increasingly used in preliminary design analysis, component design, and vehicle crashworthiness evaluation, as well as roadside hardware design. Road narrow objects (poles, U-channel sign supports, barriers, etc) are a major cause of severe injury in highway crashes. The crash event is a severe and complicated phenomenon due to the complex interactions between structural and internal behaviour. Crashed structures usually experience buckling deformation, high strain rate effects, fractures, and rapid structural unloading. This leads to highly transient response arising from non-linear stiffness and viscous characteristics of the crushed materials. One of the most important engineering parameters that engineers employ in crashworthiness is the energy absorption. This energy is used as a quantified measure to assure that the high impacts are sustained and absorbed by the structure. Therefore, the objective in crashworthiness is to build a structure on which material properties and geometrical shapes can absorb energy so that the safety regulations are achieved and more importantly the safety of the passengers is maintained. In the recent years, nonlinear explicit FE codes have advanced significantly the computer modeling and simulation of automobile crashes. This capability allows the application of the software to model and analyze the performance of the roadside objects in crashes. Among the most advanced and widely used codes, finite-element simulation using explicit code such as LS-DYNA is widely used today for modeling crash problems. The objective of this paper was to examine the energy absorption characteristics of vehicle-steel pole crash. Different structural configurations of pole supports as well as soil properties were utilized in the finite-element modeling. Recommendations to enhance occupant safety measures were drawn.

POLE DESIGN

Luminaire poles in old cities are made of wood. It was commonly known that these types of poles do not deform in crash accident, Figure 1. In contrast to wooden poles, straight round area galvanized steel poles are more flexible and offered in lengths from 2.5 to 12m. These standard poles accept a wide range of lighting configurations. The pole shaft is usually fabricated from hot rolled commercial quality carbon steel. The Canadian Highway Bridge Design Code (CHBDC, 2000) states that poles are to be designed to the minimum yield strength of the material with an adequate factor of safety and will withstand the dead loads of the structure as well as the specified wind loads. Standard finishes include

www.EngineeringEBooksPdf.com

hot-dipped galvanization, prime coat, and finish coat, both of which are available in powder or paint. The base plate is usually fabricated from structural quality weldable hot rolled carbon steel. Anchor Bolts are fabricated from hot rolled carbon steel bars with high yield strength. The threaded end is galvanized a minimum of 300 mm and each bolt is furnished with two flat washers and two hex nuts.

An increasing number of utilities are installing metal poles due to the many advantages of the metal poles over wood or concrete poles. A typical 10.4-m height steel pole is used in the current study. The diameters of the pole cross-section at the top and bottom were 133 and 333 mm, respectively. Different configurations of pole supports were utilized in this study. The first support type was the typical steel base currently used, with four anchor bolts embedded in a concrete foundation, as specified by the Canadian Highway Bridge Design Code of 2000. The second support type was similar to the first one but with stressed springs between the nuts, over and under the steel base plate. In the third case, bearing rubber pads were utilized between the base plate and the concrete foundation. In the fourth case, the steel pole was embedded 1.75 m into the soil (no concrete foundation is used). The properties of soil materials considered in this study were: 200 N/mm^2 for shear modulus and 2000 kg/m^3 for density of soil.

Figure 1: View of car impact to wooden pole (VSRC, Ryerson University, Canada)

FINITE-ELEMENT MODELING

The steel pole was modeled using shell elements to capture the three-dimensional effect of the structure. Due to its computational efficiency, the Belytschko-Lin-Tsay shell element was implemented in the modeling. Such a shell element is based on a combined co-rotational and velocity strain formulation. Also, the same element was implemented to model the steel base. 972 shell elements were utilized to model the steel pole. Eight-node solid elements were implemented to model the anchors and the anchor's head. In the first type of pole supports, the bottom nodal points of the pole

www.EngineeringEBooksPdf.com

were assumed fixed to the square steel base plate, which is fixed to the ground using four dowel bars. In the second type of supports, springs, with 50 N/mm spring coefficient, were utilized. In the third support type, dampers were considered, with a damping coefficient of 10 N.sec./mm. In the last support type, the pole was embedded over a length of 1.75 m into a cohesive soil that was represented by dampers as well as lateral and vertical springs.

A finite-element model for a midsize sedan vehicle has been used in a frontal impact (http://www.ncac.gwu.edu/archives/model/, 2002). This vehicle model is based on a 1991 Ford Taurus 4-door and has been already been validated for frontal impact scenario at impact velocity of 60 km/hr. The major characteristics of the complete FE vehicle model can be identified as follows: (1) 27874 shell elements, 303 beam elements and 349 solid elements; (2) 141 material cards, defining the material models employed, including steel, rubber, honeycomb, and glass; (3) Rigid (stone) wall for representing the ground; (4) automatic single surface contact from A-pillar to bumper; (5) tied nodes to surface contact between the column and the plate; (6) automatic nodes to surface contact between the bumper and the column; (7) conventional, spot weld, and rigid body nodal constraints; and (8) discrete springs, and discrete masses. The front-end components from bumper to A–pillar were modeled with a fine mesh, while the rear half of the vehicle had a fairly coarse mesh density. Components like bumper, front rails, upper load path beams, radiator, engine cradle, etc., were modeled to capture all significant geometric imperfections such as holes, beads and crush initiators which plays a vital role in overall crash characteristics of a vehicle.

To study the effect of soil properties on vehicle impact to steel pole, four different soil conditions were considered, namely: soft clay, stiff clay, fine sand and dense sand. The dynamic properties of these soil materials, as listed in Table 1, were calculated herein based on the available equation list elsewhere (Bowles, 1988; Peterson, 1996). Eight nodal points, along the perimeter of the steel pole cross-section at nodal levels under the ground level, were identified to simulate soil dynamic characteristics shown in Table 1. No tensile action was considered in soil behavior.

TABLE 1
DYNAMIC PROPERTIES OF SOILS CONSIDERED IN THIS STUDY

Coefficients	Soil type			
	Soft clay	Stiff clay	Fine sand	Dense sand
Horizontal spring coefficient, N/mm	1,000	5,000	10,000	20,000
Damping coefficient, N.sec./mm	15	50	75	80
Vertical spring coefficient, N/mm	4,000	24,000	48,000	73,000

DISCUSSION OF RESULTS

The finite-element simulation was performed for 100 ms using the nonlinear FE code LS-DYNA. The vehicle model was given initial velocity of 60 km/hr to impact the pole in frontal impact scenario. Figure 2 shows deformations of both the vehicle and the pole at different time increments for pole support fixed on a concrete base. While the shapes of the steel pole imbedded in soil before and after the crash are shown in Figure 3.

www.EngineeringEBooksPdf.com

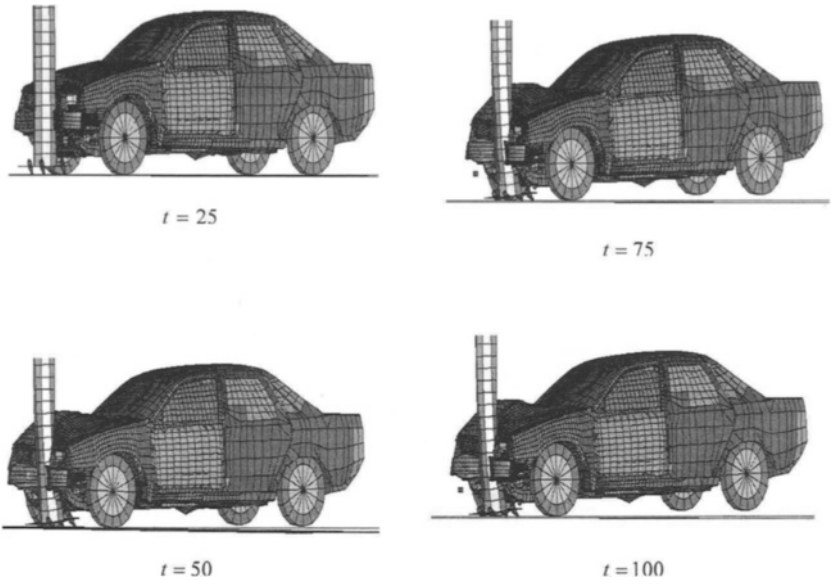

Figure 2: Deformed shapes of the vehicle and steel pole at different time increments (time in ms)

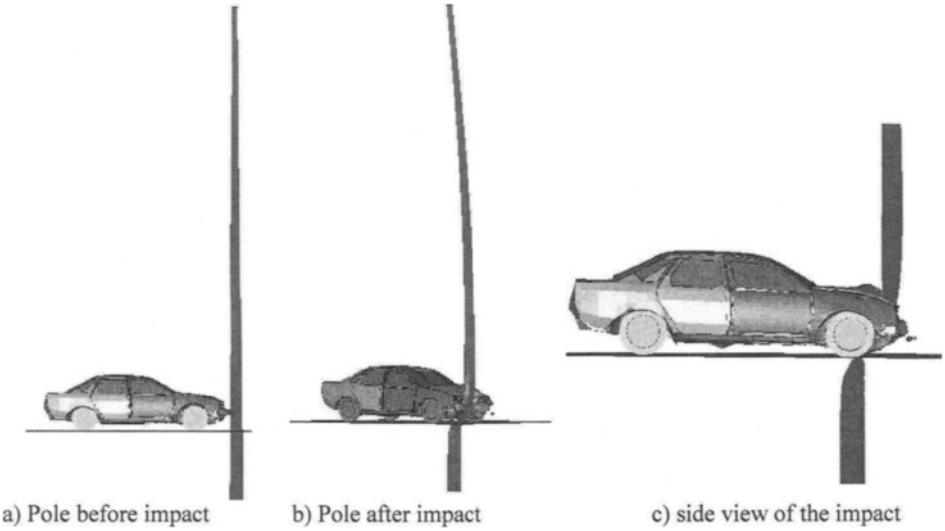

Figure 3: Vehicle impact to steel pole embedded into soil

www.EngineeringEBooksPdf.com

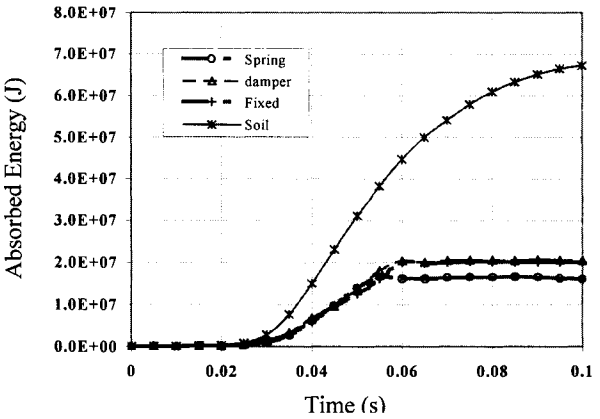

Figure 4: Absorbed energy by the steel pole for different support conditions

All types of pole supports were impacted under the same conditions. At 7 ms, it was observed the anchor bolts utilized in the first support type fractured at the ground level, shearing the steel base plate away from the ground in the same direction of vehicle motion. Then, the pole was laid on the vehicle at higher time increment. In the second support type, where the springs were used between the bolts and the base plate, the base plate also fractured and sheared away from the ground. Similar behavior was observed in case of the third support type. However, in the fourth support type, where the steel pole was embedded in the soil, the steel pole was observed to be highly deformed and did not fall down. Figure 4 shows the time-history of the change of the absorbed energy by the pole for all the support types considered in this study. It can be observed that the first three support types provide almost the same absorbed energy. However, the pole embedded in the soil absorbed much more energy so that the amount absorbed by the vehicle is considered to be much less than that for the first three support types. This may be attributed to the high deformation occurred in the pole as a result of the impact.

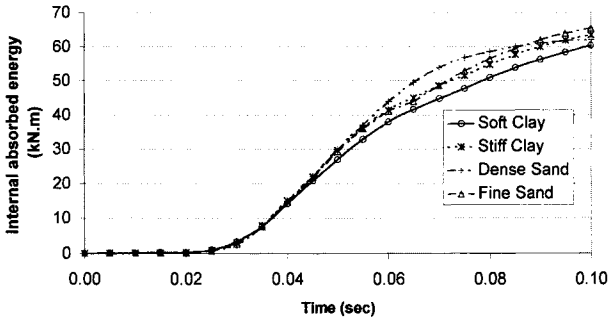

Figure 5: Absorbed energies by steel pole for different soils

www.EngineeringEBooksPdf.com

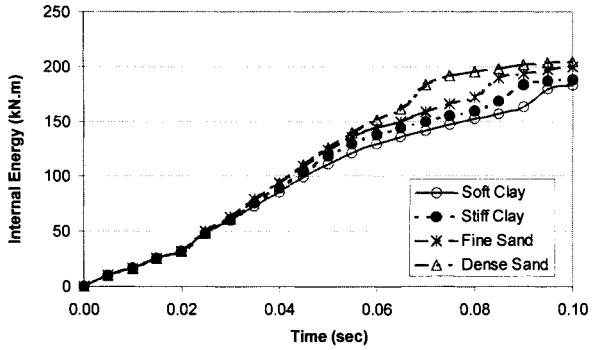

Figure 6: Energy absorption of the system for different soil conditions

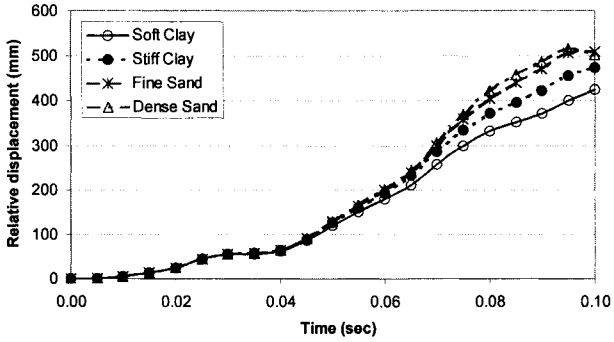

Figure 7: Relative displacement between a point on the steering wheel and corresponding point on the driver's seat

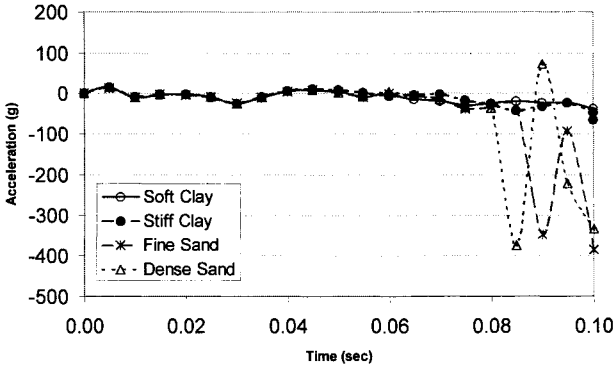

Figure 8: Acceleration-time history at a point on the driver's seat

www.EngineeringEBooksPdf.com

To study the effect of soil properties, the case of vehicle crash to steel pole embedded into soil was considered with different soil dynamic characteristics states in Table 1. Figures 5 and 6 show the absorbed energy of the steel pole and the whole system involved in vehicle crash, respectively. It can be observed that soil dynamic properties does not have significant input in the energy absorption of the pole itself of the system as a whole. However, Figures 7 shows that the relative displacement between a point on the steering wheel and the corresponding point on the driver's seat is relatively higher in case of sandy soil than in case of clayey soil. Also, Figure 8 shows the acceleration-time history of a point in the driver's seat for different soil parameters. It can be observed the acceleration values in case of clayey soil are within the acceptable value by different specifications (50 g). However, the acceleration values in case of sandy soil are more that the acceptable value. This observation will be further examined by introducing actual driver's dummy as well as child dummy on the back seat. This would provide a more reliable relative displacement and acceleration values than those obtained herein. Figure 9 shows the effect of the length of embedment of the steel pole into soil on the absorbed energy of the system. Three different cases were considered for embedment lengths were considered, namely: case I for 1.5 m, case II for 1.75 m and case III for 2 m. It can be observed that the length of embedment has insignificant effect on the energy absorbed by the system.

SUMMARY OF CONCLUSIONS

Embedding steel pole in clayey soil rather than using the conventional fixed steel base over concrete foundation is proved to be favorable in absorbing the energy resulting from vehicle-steel pole crash. This definitely assists in reducing the fatalities and injuries occurred in car accidents. Further research on crashworthiness of vehicle-steel pole impact is underway to include child and driver's dummy in both frontal and side impact to reach more reliable results.

ACKOWLEDGEMENTS

The Network of Centers of Excellence of the 21-Century Automobile, NCE of Auto21, Project No supports this research. A1 (ACI)

REFERENCES

Bowles, J. E. (1988). Foundation Analysis And Design, fourth Edition. McGraw-Hill Publishing Co., NY, pp. 901-915

Canadian Standard Association. (2000). Canadian highway bridge design code. Ontario, Canada.

http://www.ncac.gwu.edu/archives/model/. (2002). FHWA/NHTSA National Crash Analysis Center George Washington University, U.S.A.

Livermore Software Technology Corp. (1998). LS-DYNA Theoretical Manual. California, U.S.A.

Peterson, C. (1996). Dynamik Der Baukonstrukionen,"Vieweg-Verlag, Wiesbaden, Germany, pp. 784-795.

www.EngineeringEBooksPdf.com

EFFECTS OF WELDING

www.EngineeringEBooksPdf.com

This Page Intentionally Left Blank

www.EngineeringEBooksPdf.com

Advances in Steel Structures, Vol. II
Chan, Teng and Chung (Eds.)
© 2002 Published by Elsevier Science Ltd.

EXPERIMENTAL & NUMERICAL UNI-AXIAL TESTS AT HIGH TEMPERATURE – ANALYSIS OF MODELS

Yannick Vincent and Jean-François Jullien

INSA-Urgc, 20 Avenue Albert Einstein, 69621 Villeurbanne Cedex, France,

Yannick.Vincent@insa-lyon.fr, Jean-Francois.Jullien@insa-lyon.fr.

ABSTRACT

This work is concerned with the modeling of the thermal, metallurgical and mechanical phenomena encountered in the heat-affected zone (H.A.Z.) during a welding operation. It focuses particularly on the analysis of models of thermo-mechanical behavior taking into account the metallurgical effects incorporated in the calculation code SYSWELD® (E.S.I). The studies were carried out on a 16MND5 low-alloy carbon manganese steel. These studies were based on specific one-dimensional tests of the "Satoh" type, which consist of austenitizing, then cooling homogeneously the useful portion of a test piece whose longitudinal displacements are restrained. In this case, virtually all thermo-mechanical and thermo-metallurgical phenomena observable in the H.A.Z. are present simultaneously. For that reason, the Satoh tests are very useful in validating the constitutive relations used to describe the mechanical evolution in the H.A.Z. In carrying out the Satoh tests, we considered two types of thermal loading which lead to different types of transformations during heating and cooling. The comparative analyses of the calculations and the experiments enabled us to test the kinematic and isotropic models included in the program and to analyze the sensitivity of the various significant phenomena, such as transformation induced plasticity.

KEYWORDS

Phase transformation, Thermal-Mechanical testing, Constitutive behaviour, Transformation induced plasticity, Welding, Finite elements.

INTRODUCTION

A welding operation yields thermal, metallurgical and mechanical phenomena resulting in non-uniform strain and stress fields. These phenomena can affect the quality and the mechanical strength of the welded component dramatically. Therefore, the knowledge of the stress state is useful for damage evolution analysis. Uni-axial tests of the "Satoh" type can be used to induce all these observable phenomena in the H.A.Z during a welding operation. This, along with the simplicity associated with the one-dimensional aspect, led us to choose this type of test in the framework of this study for the analysis of mechanical behavior models including metallurgical effects developed by J.B. Leblond [Leblond. 89b] and implemented in the calculation code SYSWELD® (E.S.I). This type of test was performed for the first time, as implied by its name, by Kunihiko Satoh nearly 30 years ago [Satoh. 72a, 72b]. The Satoh test consists of austenitizing, then cooling homogeneously the useful portion of a test piece

www.EngineeringEBooksPdf.com

whose longitudinal displacements are restrained (the useful portion being defined as the zone being measured within which the temperature and stress fields are homogeneous). Thus, the metallurgical transformations occur simultaneously at all points of the measured zone. Since the overall deformation is prescribed to be zero throughout the thermal cycle, an axial stress develops. Then, by comparing the evolutions of calculated and measured stresses, one can analyze, among other phenomena, those related to transformation-induced plasticity, relief from strain hardening and the particular behavior of phase mixtures.

EXPERIMENTAL METHOD

Carrying out tests of the Satoh type required the design of a specific experimental device [Cavallo. 98] consisting of a dilatometer enabling us to perform thermal and mechanical tests simultaneously. The test pieces were tubes made of low-alloy ferritic steel of the 16MND5 type (AFNOR Norm). The test pieces were heated by Joule effect. This setup enabled rates of temperature increase on the order of 100°C/s up to a maximum temperature greater than 1,100°C. During the cooling stage, at low cooling rates, heat input by Joule effect was required. At higher rates, cooling was forced by a flow of nitrogen inside the test piece. These two processes provided rates of temperature decrease between -0.1°C/s and -15°C/s. The high-temperature use of argon helped control the oxidation of the test piece. The mechanical loading device allowed prescribed-force and prescribed-strain cycles to be carried out. The loading consisted of uniaxial traction or compression applied via a 100kN servo-hydraulic jack. During a Satoh test, because of the temperature rise and metallurgical transformations, the characteristics of the material evolve, which requires an automated adaptation of the regulation parameters in order to control the load in terms of both force and displacement [Vincent. 02].
The test program was designed in such a way that all thermal, metallurgical and mechanical phenomena occurring in the H.A.Z. during a welding operation would be present. However, a precise knowledge of the thermo-metallurgical and mechanical characteristics of the metallurgical constituents being studied is necessary in order to interpret the test results and derive a detailed comparison with the calculations. In addition, other tests were included besides Satoh tests: traction-compression tests at different temperatures and free dilatometer tests [Vincent. 02]. The latter tests enabled us to identify the kinetic of the metallurgical transformations and the volume changes. For the Satoh tests, we considered repeated thermal cycles with decreasing maximum temperatures. The heating rate was prescribed at 80°C/s. During the first two thermal cycles, the maximum temperatures reached were 1,100°C and 900°C respectively ($T > Ac'3 \cong 850°C$). The cooling temperatures were controlled between 800°C and the ambient temperature. For the last two cycles, the maximum temperatures reached were 670°C and 400°C respectively ($T < Ac'1 \cong 735°C$).

NUMERICAL ANALYSIS

Thermo-Metallurgical and Mechanical formulation

Both the evolution of temperature in the useful zone (which results from Satoh tests) and the kinetics of the metallurgical transformations (which results from free dilatometer tests) are known. Thus, the thermo-metallurgical calculation is not a calculation in the strict sense because the temperatures and the kinetics of the transformations are prescribed.

www.EngineeringEBooksPdf.com

The calculations involved here are elastic-plastic calculations in large strain and in large displacement. For calculations using an isotropic strain hardening law, we chose the proportionality limit as the elastic limit. For kinematic simulation, the elastic limit was set conventionally to 0.2% plastic strain. The models implemented in SYSWELD to describe the mechanical behavior are presented in [Leblond. 89b]. In order to derive the theoretical formulation of these constitutive relations, J.B. Leblond distinguishes between the small-stress case and the large-stress case. This requires the definition and the expression of a homogenized limit stress Σ^y. This stress is not relative to the first occurrence of plasticity because plasticity exists even in the absence of external stress due to the internal stresses induced by the difference of densities between the austenitic phase and the ferritic phases. Thus, a distinction is made between two plastic flow regimes. If the macroscopic equivalent stress, in Von Mises' sense, is less than this homogenized limit stress, the total plastic deformation is composed of two terms, the classical term $\dot{E}^p_{cp}$ plus an additional, so-called transformation induced plasticity (T.I.P) term $\dot{E}^p_{tp}$. Thus, below the macroscopic plasticity limit Σ^y, a classical plastic flow may occur and the behavior of the multiphase mix containing austenite is taken into account through the presence of an additional classical plastic strain term. This term is function of the variation of macroscopic stress and of the variation of temperature. The transformation induced plasticity results from the coupling between an external stress and the evolution of the proportions of the existing phases. Indeed, the application of even a small stress during the transformation yields an additional strain besides the metallurgical volumetric strain in the direction of the applied stress. J.B. Leblond developed a multiaxial and incremental formulation of the transformation induced plasticity strain. The choice of a model to represent this phenomenon was based on a theoretical as well as numerical study of Greenwood and Johnson's mechanism [Greenwood & Johnson. 65]); Magee's mechanism [Magee. 66] was neglected. This transformation induced plasticity strain rate is proportional to the applied stress, to the volume variation associated with the phase change and to the progress of the transformation, but inversely proportional to the elastic limit of the softest phase. If the homogenized limit stress is reached, Leblond's model no longer distinguishes between classical plasticity and transformation induced plasticity; the classical flow rule applies.

Test results

We will present and comment the experimental and numerical results in the following test cases:

- Satoh 0.3: Satoh test with a prescribed cooling rate of 0.3°C/s. The first thermal loading stage generates a completely bainitic transformation during cooling and the second, a double ferritic-bainitic transformation (Figure 1).
- Satoh 12: Satoh test with a prescribed cooling rate of 12°C/s. The first thermal loading stage generates a completely martensitic transformation during cooling and the second, a double bainitic-martensitic transformation (Figure 2).

Cooling rate and austenitization parameter:
For a given austenitization parameter, the cooling rate governs both the type and the kinetics of the structural transformation. The higher the cooling rate, the lower the temperatures at which the transformation starts and ends. These metallurgical transformations are accompanied by a volume expansion which counteracts the thermal contraction. Thus, different evolutions of stresses occur depending on the cooling rate. Generally, the higher the temperature at the end of the transformation, the higher the traction stress upon return to

www.EngineeringEBooksPdf.com

ambient temperature. The stress at ambient temperature may or may not exceed the elastic limit of the metallurgical constituent present.
The time during which the temperature is maintained above the equilibrium temperature of the beginning of the austenitic transformation and the maximum temperature reached determine the austenitization parameter. The higher this parameter, the larger the austenitic grain. Since this grain size has great influence on the transformations occurring during cooling, the evolution of stresses is different in the first and second thermal cycles, even though the cooling rates are identical. Rapid austenitization conditions with smaller holding times tend to favor high-temperature transformations.

Applied load:
The phase transformation kinetics was determined from free dilatometer tests just prior to the Satoh test and on the same test piece. Thus, this determination was conducted under zero loading. However, several experimental works have shown that the transformation's characteristics can be influenced by the application of a uniaxial stress ([Gautier. 85]). During a Satoh test, the stress is practically never zero. Therefore, by comparing the temperature of stress release of the Satoh test with the temperature at the beginning of the transformation determined by the free dilatometer test, we can observe, based on the following table, a significant increase in the initial temperatures of the martensitic (ΔT=56°C) and bainitic (ΔT=25°C) transformations in the case of complete transformations under stress.

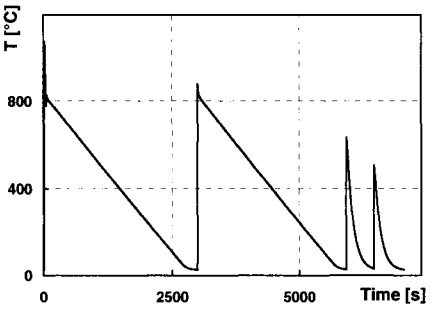

Evolution of temperature vs. time

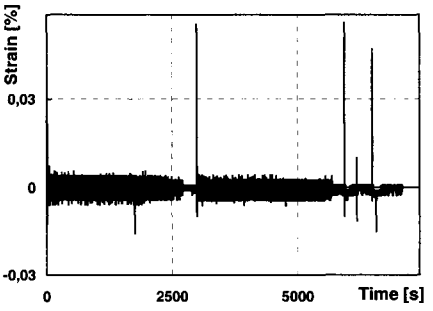

Evolution of strain vs. time

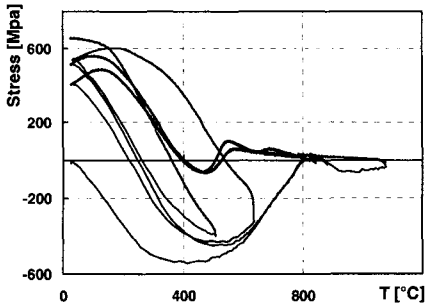

Evolution of stress vs. temperature

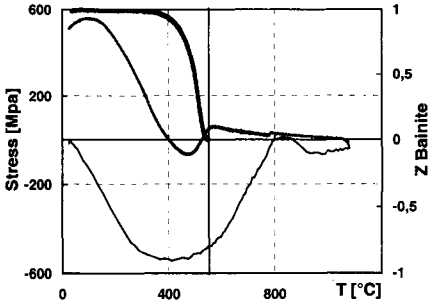

Evolution vs. temperature of:
- the stress (1st thermal cycle, Satoh test)
- the kinetics of the bainitic transformation (free dilatometer test)

Figure 1 : Experimental results for Satoh test 0.3

www.EngineeringEBooksPdf.com

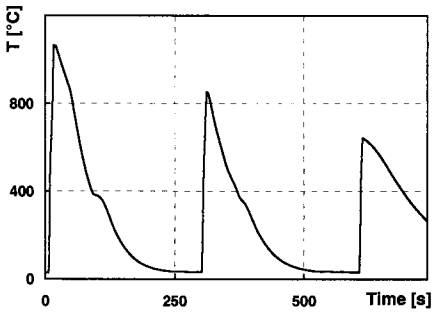

Evolution of temperature vs. time

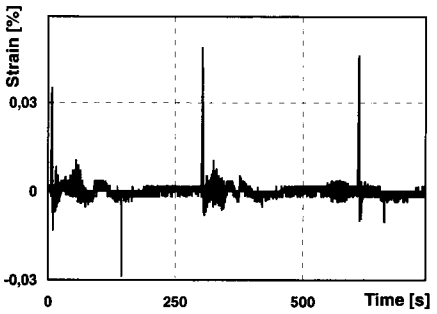

Evolution of strain vs. time

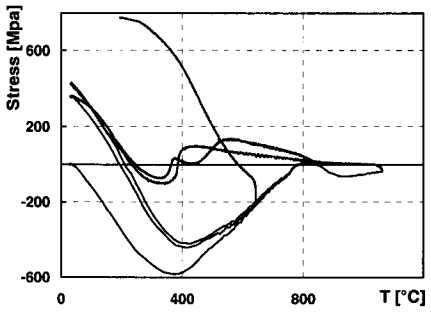

Evolution of stress vs. temperature

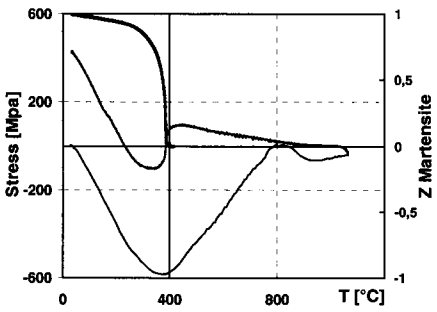

Evolution vs. temperature of:

- the stress (1st thermal cycle, Satoh test)
- the kinetics of the baintic and martensitic transformations (free dilatometer test)

Figure 2 : Experimental results of Satoh test 12

Comparative analysis

Let us compare the results from kinematic and isotropic calculations and the experimental measurements for Satoh test cases 0.3 and 12. The two constitutive relations yield somewhat different results, whether metallurgical transformations are present or not (Figure 3).

Case of high stresses: $\Sigma^{eq} = \Sigma^{y}$:
This configuration occurs particularly in the absence of phase transformation. The dominant factors are associated with the classical strain hardening law: isotropic strain hardening results in excessive final stresses and even in complete elastic adaptation after four cycles in Satoh test case 0.3. The constitutive relation with kinematic strain hardening uses a conventional elasticity limit at 0.2% plastic strain. The first and obvious drawback is that the first stages of plastic strain are not taken into account correctly. However, the Bauschinger effect is approximately represented.

Case of low stresses: $\Sigma^{eq} < \Sigma^{y}$:
This configuration occurs whenever metallurgical transformations take place during cooling. The volume expansion which coincides with the metallurgical transformation counteracts the thermal contraction. The additional plastic flow induced by the classical plastic strain and the transformation induced plasticity strain also tends to reduce the elastic strain and, consequently, the stress. For small stresses, the differences between the isotropic and kinematic constitutive relations lie in the definitions of the classical macroscopic plastic strain

www.EngineeringEBooksPdf.com

rate and of the transformation induced plasticity strain rate. These two strain rates are inversely proportional to the elastic limit of the mother phase. Thus, the first difference between the two formalisms lies in whether or not the elastic limit of the mother phase depends on the effective macroscopic isotropic strain hardening internal variable of the austenitic phase E_{γ}^{eff}. If one takes this dependency into account by updating the elastic limit of the parent phase according to its strain hardening level, one reduces the influence of transformation induced plasticity. This is one of the reasons why the stress release is greater when the isotropic formalism is used. The second difference lies in the presence or absence in the definitions of the classical plastic strain rate and transformation induced plasticity strain rate of an internal tensor variable $A\gamma$ which is subtracted from the deviatoric tensor of macroscopic stresses. The variable $A\gamma_{22}$ remains positive when the transformations occur during cooling. Thus, as long as the stress σ_{22} is positive, the quantity S_{22}-$A\gamma_{22}$ is less than S_{22}. The influence of the classical plastic strain and transformation induced plasticity strain is greater when the isotropic formalism is being used. Therefore, this formalism generates a faster stress reduction. Subsequently, the stress σ_{22} becomes negative and the quantity S_{22}-$A\gamma_{22}$ is greater than S_{22} in absolute value. This time, the influence of the classical plastic strain and transformation induced plasticity strain is greater when the kinematic formalism is being used. Thus, as soon as the stress turns to compression, the additional flow induced by the two strain rates tends to reduce the stress level, this consequence being more pronounced when the kinematic strain hardening constitutive relation is being considered. While the kinematic calculation tends to underestimate the stress decrease during the metallurgical transformation, the isotropic calculation overestimates it. Therefore, a transformation induced plasticity law associated with mixed isotropic-kinematic strain hardening could provide a better representation of the behavior of the steel being studied.

Remark: The mechanisms used to explain the transformation induced plasticity phenomenon are Greenwood and Johnson's mechanism and Magee's mechanism. While the former provides a good representation of the phenomenon occurring during diffusion transformations, it is generally thought that the latter, which takes into account the orientation of the zones transformed by external stresses, dominates when the transformation is athermal martensitic. However, although we indicated that Magee's mechanism was neglected in the calculations, the comparative results remained very good. Therefore, the idea that Magee's mechanism dominates over G&J's mechanism in a martensitic transformation is questionable.

Transformation induced plasticity strain:

It is generally accepted today that the additional flow induced by the so-called transformation induced plasticity strain plays a significant role in the evolution of the stress during structural transformations occurring in ferrous alloys. We can also verify this point. Without transformation induced plasticity the stress decreases more rapidly and the differences between the calculated results and experimental measurements are greater (Figures 14, 15). Quantitatively, toward the end of the bainitic transformation ($T \cong 400°C$: Satoh 0.3), one observes a difference of 250 Mpa between the two calculations for the first cycle. Back to ambient temperature, regardless of the cycle considered, the differences among the stress values obtained from the two calculations and the experimental values are small. The elastic limit of the monophasic or multiphasic material obtained has been reached, which yields to plastification before the end of cooling. Therefore, one can stress the fact that a correct level of residual stresses is no guarantee that the phenomena occurring during structural transformations have been modeled correctly. Indeed, plastification resulting from these transformations can partially obliterate their mechanical effects and, consequently, the lack of precision associated with the way these are accounted for.

www.EngineeringEBooksPdf.com

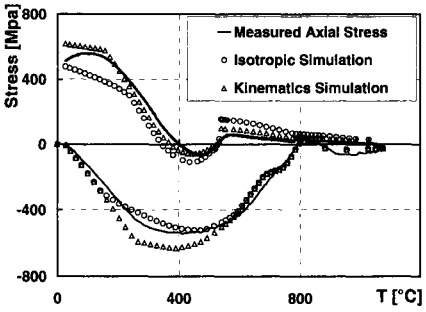

Satoh test 0.3 : 1st thermal cycle

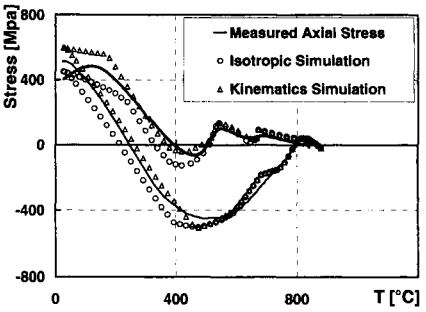

Satoh test 0.3 : 2nd thermal cycle

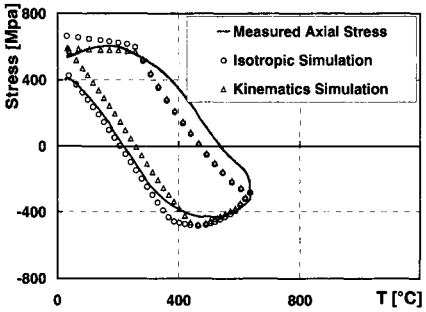

Satoh test 0.3 : 3rd thermal cycle

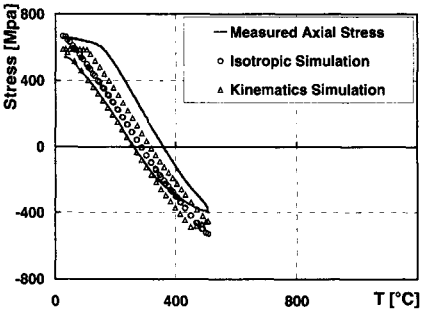

Satoh test 0.3 : 4th thermal cycle

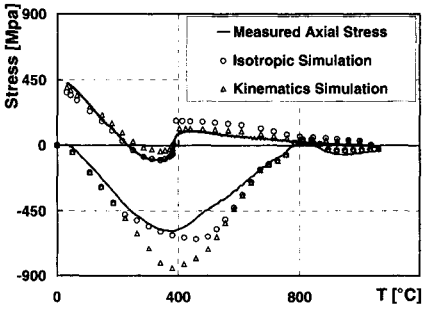

Satoh test 12 : 1st thermal cycle

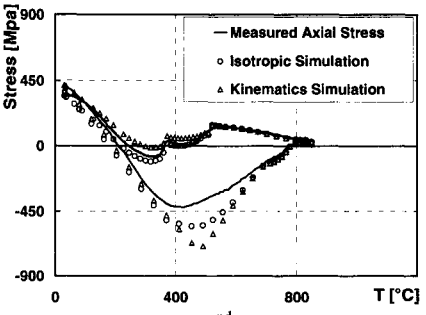

Satoh test 12 : 2nd thermal cycle

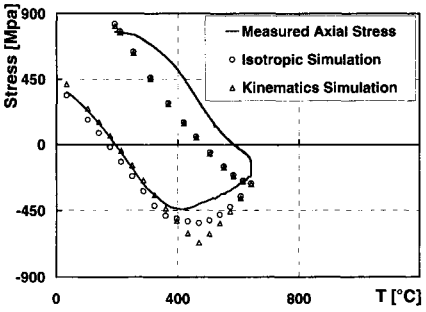

Satoh test 12 : 3rd thermal cycle

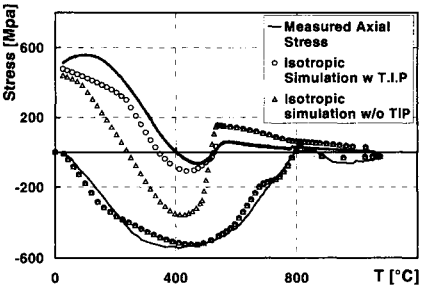

Numerical simulations with and without T.I.P effect : Satoh test 0.3 1st thermal cycle

Figure 3 : Comparison between experimental results and numerical simulations

www.EngineeringEBooksPdf.com

CONCLUSION

The objective of this study was to compare, in the case of 16MND5 steel, the prediction obtained by the models taking into account metallurgical effects which exist in the SYSWELD® code (E.S.I). The comparison was based on the numerical simulation of very specific tests of the "Satoh" type.
The comparative analyses of the calculations and the experiments enabled us to test the kinematic and isotropic models included in the program and to analyze the sensitivity of the various significant phenomena, such as transformation induced plasticity.
The analysis of the experimental results showed the mixed nature of strain hardening of the phases involved. The procedure we implemented also enabled us to pinpoint the influence of the applied stress on the characteristics of the transformations. This stress activates the transformation and a significant increase in the temperatures at which phase transformations begin can be observed.
The comparative analyzes showed the important role played by the transformation induced plasticity phenomenon. However, in certain cases, regardless of whether the transformation induced plasticity strain rate is taken into account or not, the stress at ambient temperature is more or less the same despite the very different situations of stress evolution. During structural transformations, the two formalisms, kinematic and isotropic, produce quite different results. We showed the influence of the internal variables on the evolution of the stress. While the kinematic calculation tends to underestimate the decrease of the stress during the metallurgical transformation, the isotropic calculation overestimates it. In conclusion, a mixed isotropic and kinematic strain hardening law could represent the behavior of the steel considered more accurately, whether phase transformations occur or not. As a final conclusion, the comparative analyzes showed that the idea that Magee's mechanism is more significant than Greenwood & Johnson's mechanism for the martensitic transformation is questionable.

REFERENCE

Cavallo N., 1998, "Contribution à la valiation expérimentale de modèles décrivant la ZAT lors d'une opération de soudage ", Thesis, INSA, Lyon.

Gautier E., 1985, "Transformations perlitiques et martensitique sous contrainte de traction dans les aciers", Thesis, Institut National Polytechnique de Lorraine, Nancy.

Greenwood G.W., Johnson R.H, 1965., "The deformation of metals under small stresses during phase transformation", Proc Roy Soc, vol 283, 403-422.

Leblond J.B., 1989b, " Mathematical modelling of transformation plasticity in steels, II : Coupling with strain hardening phenomena ", Int. J. Plasticity 5, 573-591.

Magee C.L., 1966, "Transformation kinetics, microplasticity and ageing of martensite in Fe-3l-Ni", Ph. D. Thesis Carnegie Mellon University, Pittsburg.

Satoh K., 1972a,"Transient Thermal Stresses of Weld Heat-Affected Zone by Both-Ends-Fixed Bar Analogy", Transactions of Japan Welding Society, Vol. 3, N°1, 125-134

Satoh K., 1972b, "Thermal Stresses Developed in High-Strength Steels Subjected to Thermal Cycles Simulating Weld Heat-Affected Zone", Transactions of Japan Welding Society, Vol. 3, N°1, 135-142.

Vincent Y., 2002, "Simulation numérique des conséquences métallurgiques et mécaniques induites par une opération de soudage - Acier 16MND5", Thesis, INSA, Lyon.

www.EngineeringEBooksPdf.com

Advances in Steel Structures, Vol. II
Chan, Teng and Chung (Eds.)
© 2002 Elsevier Science Ltd. All rights reserved.

A TWO SCALE MODEL FOR THE SIMULATION OF RESIDUAL STRESSES DUE TO WELDING OF A METALLIC MULTIPHASE MATERIAL

A Combescure, M Coret

LMC-INSA Lyon
18-20 allée des sciences
69621 Villeurbanne cedex France

ABSTRACT

This paper presents a general model for the simulation of residual stresses due to welding in a multiphase metallic material. It also presents a transformation plasticity model The model is applied to the simulation of two experiments and proves its quality to predict residual stresses, induced by the welding operation. The proposed model is based on a two scale representation of the material behaviour. The idea is to use a Taylor hypothesis to change of scale: this idea produces a very versatile way to model the phase mixing because it allows each phase to have its own material behaviour.

KEYWORDS

Two scale material model, welding, finite elements, temperatures, transformation plasticity, non linear homogenisation

1 INTRODUCTION

In this paper we present very briefly experimental results on transformation plasticity of one particular low carbon steel (16MND5) and show that this type of plasticity is governed by the second stress invariant. We then give a two scale model of the multiphase metallic material and show how to derive this class of models. We apply it to our specific steel and show the results of the application of the identified model on two experiments. The predicted residual stresses are compared to the measured ones. The influences of the viscous effects on the residual stresses appear clearly. The proposed method is an interesting alternative to the approaches of Dong for instance who systematically omits the transformation plasticity effects, or to that of Leblond

www.EngineeringEBooksPdf.com

(1989) who necessitates an important analytical work for each new type of behaviour, or of Videau and Cailletaud (1996) who proposed a complex coupled model.

2 THE EXPERIMENTS AND THE MODEL

21 Experimental results on phase transformation plasticity

We show here the main results obtained by the experimental tests on transformation plasticity of the 16MND5 steel. The details of the work are published in Coret (2002) and its PHD Work (Coret 2001) The experimental set up is displayed on the following figure 1.

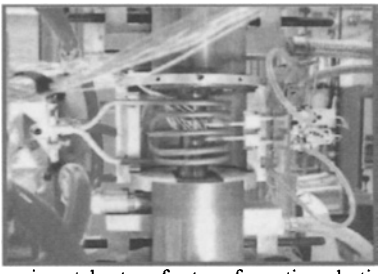

Figure 1 : Experimental set up for transformation plasticity experiments

This experimental set up allows to get heating rates of more than 100°C/s and cooling rates up to -70°C/s. It is also designed in order to apply tensile as well as torsion loads at the same time. The main experimental result is that the transformation plasticity strains rates $\dot{\underline{\underline{\varepsilon}}}^{pt}$ are proportional to the deviatoric stresses $\underline{\underline{s}}$ in case of martensitic, bainitic or austenitic transformation. The rate equation giving the transformation plasticity strain rate is hence:

$$\dot{\underline{\underline{\varepsilon}}}^{pt} = k\underline{\underline{s}} \tag{1}$$

In this equation the coefficient k depends on the type of transformation. Figure 2 gives an idea of the experimental results for bainitic transformation.

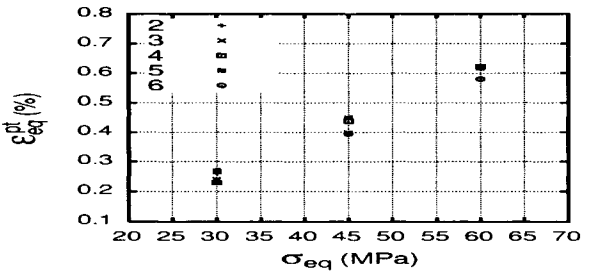

Figure 2 : Inelastic strains obtained from transformation plasticity experiments

www.EngineeringEBooksPdf.com

22 The multiphase model

We have to compute a coupled evolution problem including thermal metallurgical and mechanical variables. For the 16MND5 material it is known that the thermal and metallurgical problems are coupled but are not coupled with the mechanical problem. We can then solve first the metallurgical thermal problem and use the product of this computation (temperature fields and phase proportion fields) as inputs for the mechanical computation. The mechanical model is a two scales model is based on the following idea. Let us suppose that we have a multiphase material. We have n phases φ_i, the volumetric proportion of the phase i is denoted z_i and we suppose we known the inelastic behaviour of each phase. We have for one time step an initial inelastic state of the material (ie for each phase, the stresses, internal variables, and inelastic strains). We look for the evolution with time of the material state. When the time progresses from t_1 *to* t_2 the temperature, phase proportions and material state changes from Θ_1, z_{i1}, A_{i1} *to* Θ_2, z_{i2}, A_{i2}. We shall for simplicity suppose that the material properties (which depend on temperature) are constant during the time step and equal to their value at the end of the time step as well as the phase properties. We need now to relate the strain increment of the mixture to the strain increment of each phase. For that purpose we shall first compute the transformation plasticity strain increment:

$$\underline{\underline{\Delta E^{pt}}} = k \underline{\underline{s_2}} \left(1 - \Delta z_a\right) \tag{2}$$

Where Δz_a is the austenitic phase proportion increment. We shall then compute the mechanical strain increment:

$$\underline{\underline{\Delta E^{mech}}} = \underline{\underline{\Delta E^{total}}} - \underline{\underline{\Delta E^{pt}}} \tag{3}$$

We now apply the Taylor hypothesis to get the strain increment in each phase i:

$$\underline{\underline{\Delta \varepsilon_i^{mech}}} = \underline{\underline{\Delta E^{mech}}} \quad \forall i \tag{4}$$

We can now for each phase i use the standard non linear elasto-vico-plastic models to compute the final stress and internal variable state of the phase ($\underline{\underline{\sigma_{i2}}}, A_{i2}$), knowing the initial state, the phase strain increment, and the phase material properties. We then use the linear mixing rule to obtain the homogenised stress state $\underline{\underline{\Sigma_2}}$:

$$\underline{\underline{\Sigma_2}} = \sum_{i=1,n} z_i \underline{\underline{\sigma_{i2}}} \tag{5}$$

This homogenised stress has to be in equilibrium with the applied loads. This method has been implemented in the CASTEM 2000 finite element computing tool, and tested on elementary cases. The model also need a thermo metallurgical state computation: this module was already implemented in the same code by Martinez (1999). The model chosen for the 16MND5 had 4 phases: austenitic, ferritic, martensitic, baintic. The material properties were identified for each of the 4 phases at different temperatures. The following mechanical models were chosen for the

www.EngineeringEBooksPdf.com

different phases. For the martensitic phase, an elastoplastic with kinematic hardening was chosen.

$$\left.\begin{aligned} f_m &= J_2(s_m - X_m) - \sigma^Y{}_m \\ \dot{\varepsilon}_m{}^p &= \frac{3}{2}\frac{s_m - X_m}{J_2(s_m - X_m)} \\ X_m &= \frac{2}{3} H_m \varepsilon_m{}^p \end{aligned}\right\} \tag{6}$$

The parameters σ^Y_m, H_m are the material constants for the martensite, which have been identified from experimental tests at various temperatures. For the bainite ferrite and austenite we have chosen a Chaboche-Lemaitre viscoplastic model.

$$\left.\begin{aligned} f_m &= J_2(s_i - X_i) - \sigma^Y{}_i \\ \dot{\varepsilon}_i{}^{vp} &= \frac{3}{2}\frac{s_i - X_i}{J_2(s_i - X_i)} \\ \dot{p}_i &= \left\langle \frac{J_2(s_i - X_i) - R_i - \sigma^Y{}_i}{K_i} \right\rangle^{n_i} \\ \dot{R}_i &= b_i(Q_i - R_i)\dot{p}_i \\ X_i &= C_i \alpha_i \\ \dot{\alpha}_i &= \dot{\varepsilon}_i{}^{vp} - D_i \alpha_i \dot{p}_i \end{aligned}\right\} \tag{7}$$

In this model the material constants are $\sigma^Y_i, K_i, n_i, b_i, Q_i, C_i, D_i$. These constants have to be identified for each of the 3 phases at each of the relevant temperatures. This work has been performed and is reported in details in Coret (2001). The time integration of the rate model is implicit and uses the values of the parameters at the end of the time step.

3 Examples

31 INSA Plate under laser spot.

This example is taken from experiments done at INSA and referenced in Cavallo (1998). A circular disk of 16MND5, 160mm diameter and 8mm thick is heated at its center by a laser spot for 70 seconds, then cooled by natural convection. The heat flux is applied on a circle of 60mm diameter. The experiment sketch is displayed on Figure 3.

The temperatures of the rear face of the disk have been measured as well as the vertical displacement at different points and at the center. The residual stresses at the end of the experiment have also been measured. The numerical simulation was performed with 320 linear QUA4 axisymetric finite elements. The computed temperatures and metallurgical state at the end of the heating phase are displayed in Figure 4. The displacement histories of the center of the plate are displayed in Figure 5. One see on this figure that the two scale model proposed here gives a rather good prediction of the displacement history whereas the curve denoted "loi de

www.EngineeringEBooksPdf.com

melange" (this is the Leblond elasto plastic model prediction) over estimates the maximum

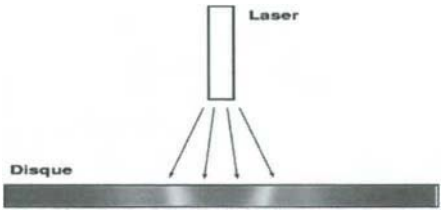

Figure 3 : INSA plate experiments

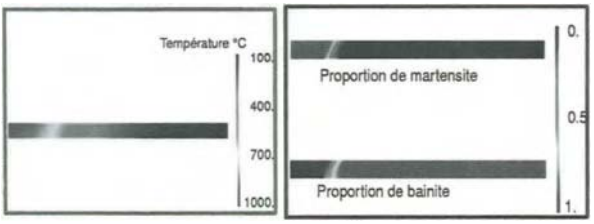

Figure 4: Computed thermal field and metallurgical fields

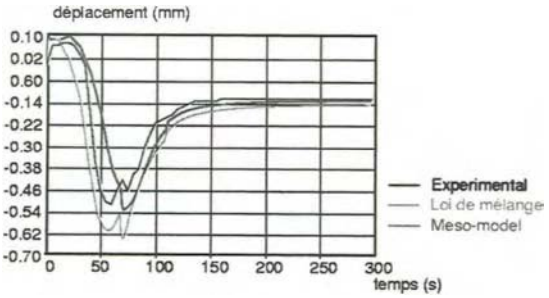

Figure 5: compared vertical displacement at the center of the plate

displacement as well as the residual displacements. Figure 6 compares the residual stresses on the upper side of the plate: here again the residual stresses are overestimated by Leblond's model.

www.EngineeringEBooksPdf.com

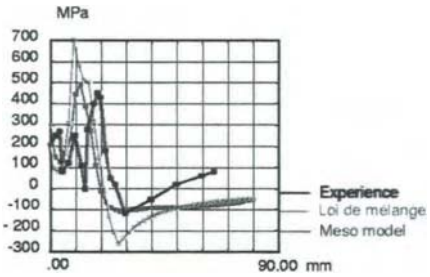

Figure 6: Comparison of residual stresses on the upper side of the plate

This is due as we could show using to the scale model to the absence of viscosity in the elastoplastic Leblond's model which do not allow the stresses to relax during the cooling phase. We see in this example the quality of the model as well as the interest of the two scale model to understand what is important for the residual stresses: here the viscous model results in a relaxation of stresses during the cooling phase.

32 friction welding of an inconel 16MND5 junction

A second example is the prediction of residual stresses produced by a friction welding of a inconel 16MND5 junction. The junction is first welded by friction then heated at 900°C during five hours and cooled until room temperature. The simulation represents the cooling phase. It has been observe d that the temperature decrease uniformly in space and linearly with time. We then have just to predict the phase changes in the 16MND5 part.

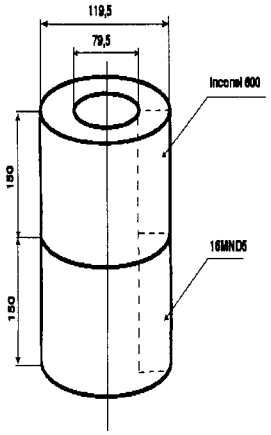

Figure 7 : Geometry of the welded junction

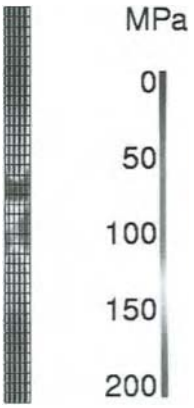

Figure 8: Residual Von Mises stress field

www.EngineeringEBooksPdf.com

The geometry is displayed in Figure 7 and the residual computed Von Mises stress field is showed on figure 8. We observe a stress of about 200MPa in the junction region. This residual stress field was also compared to measured values Figure 9 displays the comparison of the axial residual stress in the junction.

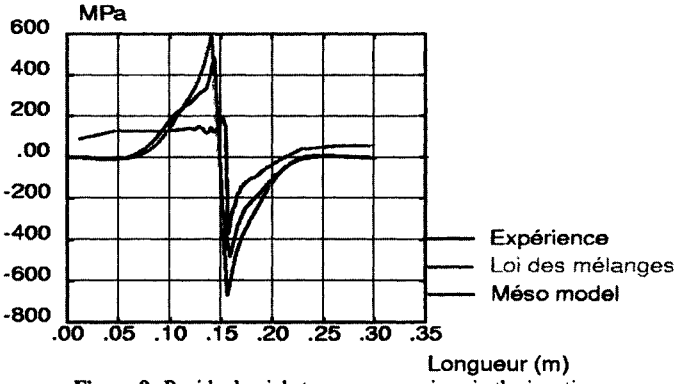

Figure 9: Residual axial stresses comparison in the junction

We observe here that the measured residual stress profile is a bit strange in the inconel because the bending moment of the residual stresses are not in equilibrium at the interface. The computed values overestimate the residual stresses in the inconel, but this is perhaps due to the fact that the inconel part was modelled using an elastoplastic model and that no viscous effect was taken into account, because no creep data were available for that material. On the 16MnD5 side the two scale model gives again a smaller residual stress: the computed values are well self equilibrated.

4 CONCLUSIONS

The simulation of residual stresses due to welding is a very difficult task. The approach presented in this paper brings two important informations. The first one is that the viscosity has a very important effect on the residual stresses even if they occur at relatively low temperatures (500°C to 600°C). The second is that the two scale models are extremely interesting to build a rather general model for phase mixtures. This model does not need any theoretical development to produce the homogenised model, hence it is a very efficient way to study a multiphase material. We have shown here in one example what are the most important physical information needed to compare with experimental results. This model has been applied to the 16MND5 steel but can be applied to any multiphase material provided that we have identified the material behaviour for each phase. The model needs a lot of internal variables in the computations (one set per phase, and per Gauss point), and also the determination of each phase material characteristics: this is an important experimental effort.

www.EngineeringEBooksPdf.com

REFERENCES

J. B. Leblond, J. Devaux, J. C. Devaux (1989)
Mathematical modelling of transformation plasticity in steels in case of ideal plastic phases
Int. J. of Plasticity, Vol 5, pp 573-591

J. C. Videau, G. Cailletaud (1996)
Experimental study of the transformation induced plasticity in a cr-ni-mo-al-ti steel.
Journal de physique, Vol 6, pp 465-473

M Coret (2001)
Etude expérimentale et simulation de la plasticité de transformation et du comportement multiphasé de l'acier 16MND5 sous chargement multiaxial anisotherme.
PHD Report : LMT ENS Cachan 61 av du president Wilson, PHD LMT 2001/15

M Coret, S Calloch, A Combescure (2002)
Experimental study of phase transformation plasticity of 16MND5 low carbon steel under multiaxial loading
Int J. of Plasticity. To be published 2002

M Martinez (1999)
Jonction 16MND5-INCONEL- 690-316LN par soudage diffusion: elaboration et calcul de contraintes résiduelles de procédé.
ENSMP PHD Thesis

N. Cavallo (1998)
Contribution à la validation expérimentale de modèles décrivant la ZAT lors d'une operation de soudage
INSA Lyon PHD Thesis april 1998

www.EngineeringEBooksPdf.com

Advances in Steel Structures, Vol. II
Chan, Teng and Chung (Eds.)
© 2002 Elsevier Science Ltd. All rights reserved.

INFLUENCE OF WELDING DETAILS ON THE PERFORMANCE OF BEAM TO COLUMN CONNECTIONS OF STEEL MRFs IN SEISMIC AREAS

D. Dubina and A. Stratan

Department of Steel Structures and Structural Mechanics, Faculty of Civil Engineering and Architecture, "Politehnica" University of Timisoara, I. Curea nr.1, Timisoara 1900, Romania

ABSTRACT:

The importance of welded connections on the behaviour of beam-to-column joints in steel moment resisting frames (MRFs) was the reason to develop an experimental program focused on the behaviour of welding details. A number of 54 "T" assembly specimens that reproduce the beam-to-column welded joints were tested. The experimental program considered the following parameters: steel grade, strain rate, welding type (fillet weld, double bevel butt weld, and single bevel butt weld), and type of loading (monotonic and cyclic pulsating). The behaviour of the different types of welds was evaluated and compared in terms of both performance and economical aspects.

KEYWORDS:

Beam-to-column joints, welded connections, fillet weld, butt weld, cyclic loading, strain rate

INTRODUCTION

Steel moment-resisting frames were traditionally used in seismic areas for low and middle-rise buildings. This structural system has the advantage of large free interior spaces and clear facades. On the other hand, steel moment resisting frames were considered advantageous from the seismic point of view, due to their inherent local and global ductility. However, the earthquakes of Northridge (1994) and Hyogoken-Nanbu (1995) revealed a series of undesirable brittle failure modes in welded beam-to-column joints that undermined the high seismic performance of steel moment-resisting frames. This fact generated concern in the scientific community for the causes of the unexpected poor behaviour of beam-to-column moment connections. Extensive laboratory studies have been carried out to study the poor performance of beam-to-column joints and to develop improved connection details and

www.EngineeringEBooksPdf.com

methodologies, SAC (1997). Among the possible causes of brittle fractures in welded joints the following ones were identified:

- workmanship (welding defects)
- detailing (stress concentration at the root or the toe of welds)
- materials (low-toughness weld metal), and
- unusually high seismic input (high strain rates).

A common failure pattern of beam-to column joints is cracking of the bottom beam flange to column weld (see Figure 1). The main causes of this type of failure are weld defects at the root of the weld (downward welding) and high stresses at the exterior of the beam flange. Weld root induced cracks can propagate either into the beam flange and web, or into the column flange. In most of the tested "pre-Northridge" joint typologies were observed reduced values of beam plastic rotation (<0.01 rad).

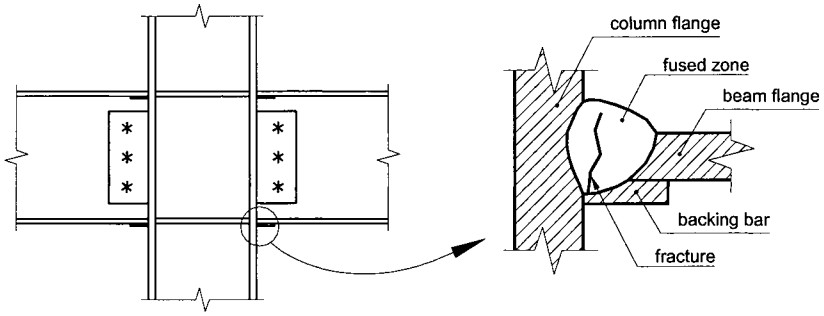

Figure 1. Weld cracking at the bottom beam flange.

The research on the causes of brittle failures of beam to column joints observed in the last earthquakes took different directions. Japan research concentrated on dynamic testing, influence of temperature on connection performance, the material properties of base and weld metal, the development of new materials, the geometry of weld copes and other details, and the elimination of these copes, while the U.S. research has attempted to better understand and nonlinear and brittle performance of steel frame structures and the properties of the material and welding, but a significant portion of the U.S. research was devoted toward developing new connection geometry, Nakashima (2000). In the same study the welding procedures in the U.S. (flux core metal arc welding – FCAW) and Japan (gas shielded metal arc welding – GMAW) are compared. It suggests that that GMAW is more costly, but it may provide greater toughness. Nakashima et al. (1998) tested 86 full scale beam-column subassemblies, with the type of connection, type of weld access holes, type of run-off tabs, and type of loading as major variables. The results of 40 specimens applied to shop-welding connection were summarized. And the primary findings indicated that the type of run-off tabs affected significantly the ductility capacity significantly and dynamic loading showed no detrimental effect on ductility compared to quasi-static loading.

El-Tawil et al. (2000) studied the effect of local geometric details and and-to-ultimate stress ratio on the inelastic behaviour of the pre-Northridge connections through finite-element analysis. Results highlighted the detrimental effect of the using steel with high yield-to-ultimate stress ratio and showed that enlarging the size of the access hole to facilitate welding increases the potential for ductile fracture at the root of the access hole.

The experimental program of Dexter et al (2000) focused mainly on the through-thickness strength and ductility of the column flanges. Forty tee-joints were tested. The results showed that, despite the high

www.EngineeringEBooksPdf.com

strain rate, high-heat input welds and several details designed to trigger fractures, the through-thickness strength or ductility of the column flanges is not a potential failure mode for welded moment connections.

Mao et al. (2001) studied the inelastic behaviour of unreinforced, flange-welded moment connections in steel seismic moment resisting frames by 3D finite-element analysis. Several issues were addressed in this study: (1) geometry and size of weld access hole, (2) control of inelastic panel zone deformation, and (3) benefit of a welded beam web. The recommendations include using a groove welded beam web attachment with supplemental fillet welds along the edges of the shear tab and a modified weld access hole geometry. The results indicate that a strong panel zone enhances inelastic connection performance, suggesting that they be used in design.

An excellent historical review of strain rate effect studies is presented in Mazzolani and Gioncu (2002), and summarised hereafter. The loading-rate effect during an earthquake was considered negligible, especially for earthquakes occurred before Northridge and Kobe events, where moderate velocities were recorded. However, after these very important and special earthquakes, when the recorded velocities were very high, many specialists consider that the loading-rate may be a possible cause of the unexpected poor behaviour of steel structures. The first research works concerning the effect of strain rate on the behaviour of metals were performed by Morrison (1932), Quinney (1934) and Manjoine (1944). Manjoine's tests were conducted at room temperature for strain rates ranging from 9.5x10-7/sec till $3x10^{2}$/sec, with testing duration between 24 h till a fraction of second. These results indicated a very important increasing of the yield stress with an increase of strain-rate, especially for strain-rate greater than 10^{-1}/sec. The increase of ultimate tensile strength is moderate, the influence of strain rate being less important than the yield stress. Consequently, the yield ratio defined by the ratio between yield stress and tensile strength, increases as far as the strain-rate increases, with the tendency to reach the value of one. A reduction of material ductility occurs, especially for strain-rate greater than 10^{-1}/sec. More recent results confirmed the previous results of Manjoine. More detailed research works showed that the modulus of elasticity is not influenced by the strain-rate variation and the upper yield stress is more strain-rate sensitive than the lower stress.

EXPERIMENTAL PROGRAM

Past experimental investigations on full-scale beam-to-column joints performed at the "Politehnica" University of Timisoara showed some undesirable failures in welds, Dubina et al. (2001). The importance of welded connections on the behaviour of beam-to-column joints led to a new experimental program focused on the detailed behaviour of some common types of welds.

The program purpose and presentation

A number of 54 specimens were prepared, that would simulate as close as possible conditions met in beam-to-column welded joints. The specimen represents a "T" assembly, and is composed of an end plate (t=20 mm) and two flanges (t=12 mm). The dimensions of the welded specimens are presented in Figure 2a. The following parameters were to be studied in this experimental program:

- Steel grade: S235 and S355.
- Strain rate: $\dot{\varepsilon}_1$=0.0001 s^{-1}; $\dot{\varepsilon}_2$=0.03 s^{-1}; $\dot{\varepsilon}_3$=0.06 s^{-1}. The first value represents a quasi-statical loading, while the other two are characteristic for steel elements under seismic conditions.
- Welding type: fillet weld, double bevel butt weld – K type, and single bevel butt weld – 1/2V type, see Figure 2b. The three types of welds were chosen due to the following reasons: the fillet weld is

www.EngineeringEBooksPdf.com

the simplest and cheapest one, the double bevel was considered to be the most reliable one, the single bevel is commonly used for site welding as it can be realised from one side only.

- Type of loading (monotonic and cyclic pulsating). Cyclic loading was considered in order to study the low-cycle fatigue phenomenon. Alternating pulses were not possible to apply due to the grips of the testing machine.

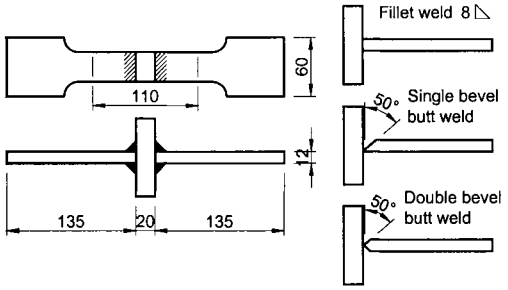

Figure 2. Welded specimens (a) and edge preparation (b)

Metal active gas (MAG) welding was used, reference number 135 according to ISO 4063-92 (Moisa et al, 2000). The welding equipment was a MIG-MAG type GLC 450-C, produced by CLOOS. The welding wire was of type G3Si1, mark IS-10, and protection gas type M21, mark CORGON 18. The welding procedure was verified for the three types of welds and two types of base metal, using the same welding material, in order to qualify the welding procedure. Tensile tests were performed on base metal (flanges and end plate), and deposited metal. Testing was performed on a 250kN universal testing machine UTS RSA 250. The universal testing machine built-in transducers, as well as external transducers were used for data acquisition.

Tensile tests on component materials

Tensile tests were performed on base metal and deposited metal in order to determine the characteristics of the materials. It was found out that the flange material (steel plate of nominal thickness of 12 mm) was not delivered according to the specifications (grades S235 and S355). Instead, flange material showed to be of S275 steel grade, according to SR EN10025. Only the end plate material (t=20 mm) was delivered as required. The deposited metal showed a resistance close to the S355 steel, but higher yield strength.

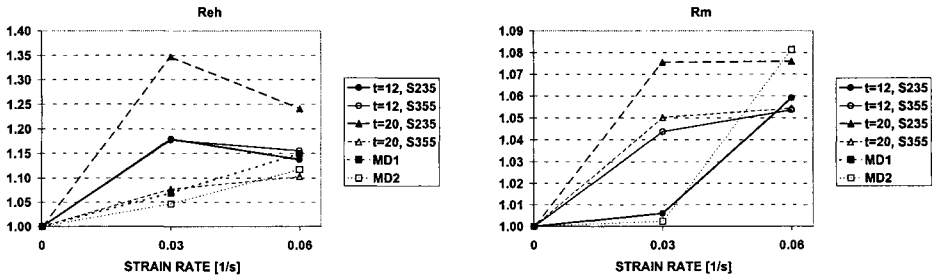

Figure 3. Variation of upper yield strength (R_{eH}) and ultimate tensile strength (R_m) for the component materials (*note: MD – deposited metal)

www.EngineeringEBooksPdf.com

The upper yield strength (R_{eH}) increases for higher strain rates (5÷35% for $\dot{\varepsilon}_2$) and (10÷24% for $\dot{\varepsilon}_3$). The maximum increase in the upper yield strength was found out for the mild steel (S235). The ultimate tensile strength (R_m) increases too for higher strain rates (0÷8% for $\dot{\varepsilon}_2$) and (5÷8% for $\dot{\varepsilon}_3$). The maximum influence is again observed for the mild steel (S235). Variation of these two parameters could be observed in Figure 3, where on the ordinate are presented normalised values of the parameters with respect to the quasi-static loading. Typical values of the ratio between the tensile strength and the yield strength (SGV=R_m/R_{eH}) are 1.2÷1.55, and the ratio is decreasing for higher strain rates (2÷20% for $\dot{\varepsilon}_2$) and (0÷13% for $\dot{\varepsilon}_3$). The total elongation at rupture (L_{ar}) is not influenced by strain rate, implying that strain rates of the magnitude of 0.03-0.06 s^{-1} does not reduce the ductility of the base and deposited metals.

Tests on welded specimens

The parameters used to evaluate the behaviour of welded specimens were basically the same used for analysis of component materials, with small exceptions. The upper yield strength (R_{eH}) was replaced by the conventional yield strength (R_{p02}), for an offset elongation of 0.2%, and the total elongation at rupture (L_{ar}) – by the total deformation at rupture (D_{er}).

It was not possible to analyse in the intended extent the *influence of the steel grade*, due to delivery of different base metal grades than the required ones (S275 instead of S235 and S355 for flanges). The differentiation of the steel grades was only in the steel grade of the end plate.

High *strain rate* caused an increase of the conventional yield strength (R_{p02}) of about 6÷18% for $\dot{\varepsilon}_2$ and 10÷19% for $\dot{\varepsilon}_3$ (see Figure 4). It could be observed that the yield strength of welded specimens is less sensitive to the influence of high strain rate than is the yield strength of component materials. The ultimate strength of the welded specimens (R_m) increases slightly with higher strain rate for the monotonically loaded specimens (4÷8% for $\dot{\varepsilon}_2$ and 6÷10% for $\dot{\varepsilon}_3$). An exception is the 5VM specimen, which failed by brittle fracture in the weld and is characterised by an important increase of R_m (40% for $\dot{\varepsilon}_3$). In the case of cyclically loaded specimens, the ultimate strength is less sensitive to the strain rate (-1÷+5%). Strain rate affects the ultimate strength of welded specimens approximately in the same extent as observed in case of component materials. The ratio of R_m/R_{eH}=SGV is characterised by values of 1.5÷1.6 for $\dot{\varepsilon}_1$, and decreases for higher strain rates (1÷11% for $\dot{\varepsilon}_2$ and 4÷10% for $\dot{\varepsilon}_3$), with the exception of 5VM specimen. The total deformation at rupture (D_{er}) diminishes for higher strain rates (exception 5CM). Contrary to component materials, a higher strain rate does imply a reduction of the ductility for monotonically loaded welded specimens. In the case of cyclic loading, high strain rate leads generally to an increase in the connection ductility, but also a decrease of D_{er} was observed in several cases, the results being rather scattered. The trend of increase of ductility under high strain rates cyclic loading could be attributed to the specimen heating, as noted elsewhere (Suita et al., 1998). Scattered results were obtained for the ductility of welded specimens monotonically tested by Beg et al. (2000) . However, the problem is a matter of controversy and further research seems to be necessary.

www.EngineeringEBooksPdf.com

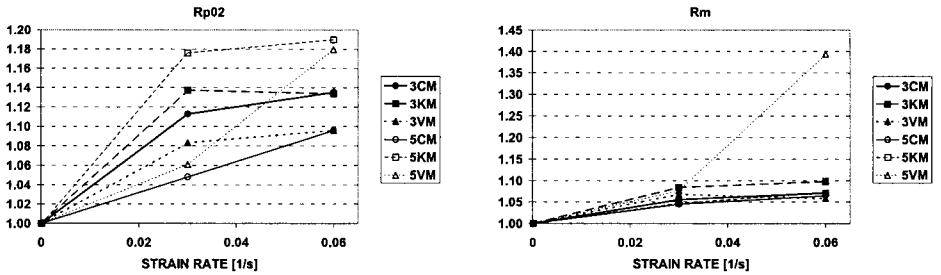

Figure 4. Variation of conventional yield strength (R_{p02}) and of the ultimate strength (R_m) for the monotonically loaded specimens.

Denomination of welded specimens is as follows: 3 – S235, 5 – S355; C – fillet weld, V - single bevel weld, K – double bevel weld; M – monotonic loading, C – cyclic loading.

It was not possible a direct comparison of the three types of welds from the point of view of *type of welding*, due to certain defects of the welds (the fillet weld size was smaller than the specified one – 5.5 mm instead of 8.0 mm, while the single bevel weld was characterised by incomplete penetration at the root of the weld). It was observed that generally, double bevel weld specimens were characterised by higher values of ultimate strength and ductility, in comparison with fillet and single bevel welds. Two *failure types* were observed for the welded specimens: rupture in the base metal and rupture in the weld. Generally, rupture occurred in the base metal (BM); the overview of failure types could be followed in TABLE 1.

TABLE 1.
FAILURE TYPE OF WELDED SPECIMENS.

specimen	failure type	specimen	failure type	specimen	failure type
3CM1	BM	3CC11	BM	3CC12	BM
3CM2	BM	3CC21	BM	3CC22	BM
3CM3	BM	3CC31	S	3CC32	N/A
3KM1	BM	3KC11	BM	3KC12	BM
3KM2	BM	3KC21	BM	3KC22	BM
3KM3	BM	3KC31	N/A	3KC32	N/A
3VM1	BM	3VC11	BM (weld cracking)	3VC12	BM
3VM2	BM	3VC21	S	3VC22	BM
3VM3	BM	3VC31	N/A	3VC32	N/A
5CM1	BM	5CC11	BM	5CC12	BM
5CM2	BM	5CC21	S	5CC22	BM
5CM3	BM	5CC31	S	5CC32	N/A
5KM1	BM	5KC11	BM	5KC12	BM
5KM2	BM	5KC21	BM	5KC22	BM
5KM3	BM	5KC31	N/A	5KC32	N/A
5VM1	S	5VC11	S	5VC12	S
5VM2	S	5VC21	S	5VC22	BM
5VM3	S	5VC31	N/A	5VC32	N/A

Note: BM – failure in base metal; W – failure in connection (weld or Heat Affected Zone – HAZ); N/A – test was stopped before specimen failure due to problem at the grips.

Failure of *double bevel weld* specimens was located in the base metal of the flanges, for both types of loading, and for all three strain rates. Tests showed detachments of the deposited metal from the base metal at the weld corners and growth of some weld defects, such as lack of fusion between beds, observed on the lateral faces of the welded connections.

www.EngineeringEBooksPdf.com

Rupture of all monotonically loaded *fillet weld* specimens occurred in the flange base metal, while during cyclic loading, three specimens ruptured in the welds. Tests on fillet weld specimens showed also such phenomena as growth of the gap between the end plate and flanges, crack initiation from the corners of the gap, initiation of detachments of the deposited weld metal from the base metal, and crack initiation at the weld corners. The rupture in the weld zone was caused by the undersized fillet welds, as well as by the reduced deformation capacity under cyclic loading of the HAZ, where crack initiation occurred.

Single bevel weld specimens failed both in base metal (see Figure 5a) and in the welds (see Figure 5b). Failures of specimens marked "3" occurred mainly in the base metal, at high deformations, close to the ones observed for the fillet weld specimens. At the same time, growth of weld defects (such as lack of fusion between beds, Moisa, 2000) was observed during the load application. Specimens marked "5" were characterised by failure in the weld. Failures were initiated either from the defects of incomplete penetration at the root of the weld, observed along the width of specimens, or from HAZ due to reduced ductility and strength. The dimension h of the defect type partial penetration, SR EN 25817 (1993) varied at these specimens between 3 and 6 mm, which is not admissible according to the above standard. Figure 5b shows the rupture of the 5VC11 specimen. It can be observed that rupture initiated at the incomplete penetration at the root of the weld, and continued into the HAZ, extending into the weld through fragile structures and internal weld defects (lack of fusion between beds). Different types of failure of single bevel weld specimens marked "3" and "5" under monotonic loading reveal the fact that there were some variations of technological parameters during specimens manufacture.

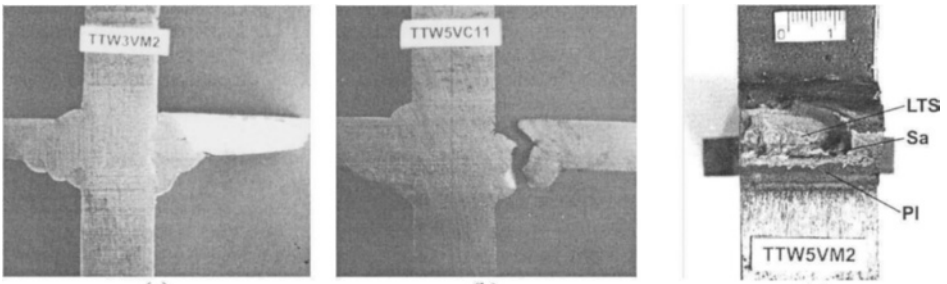

Figure 5. Failure of single bevel weld specimens: in the base metal (a), in the weld (b), types of observed defects (c).
Note: LTS – lack of fusion between beds, Sa – oblong sulphides, PI – incomplete penetration.

As can be observed in TABLE 1, *cyclic loading* increases the probability weld failure for fillet weld and single bevel specimens. In the case of fillet weld specimens, the correlation between the type of failure (base metal vs. weld) and the type of loading (monotonic vs. cyclic) is not so evident, due to small dimensions of the fillet weld specimens that failed in the welds. Failures of single bevel weld specimens were mainly due to weld defects at the root of the weld.

CONCLUSIONS

The experimental tests performed in the frame of the present research showed once again the importance of quality of welding. From the three types of welds studied (double bevel, fillet, and single bevel), the "ideal" behaviour (rupture in the base metal) was observed for the double bevel welds. This fact is attributed to the lack of defects for this welding procedure, in comparison to the other two procedures. Fillet weld specimens were characterised by an intermediary behaviour, the main cause of failures in welds being the undersized welds. This fact demonstrates one of the

www.EngineeringEBooksPdf.com

disadvantages of this type of welding, which is the difficulty to control and verify the weld size, particularly on the building site. Single bevel weld specimens had in general an unsatisfactory behaviour, due to defects of the type incomplete penetration at the root of the weld, which initiated cracks in the weld region. The behaviour of the three weld types should be analysed in conjunction with the technological and economical aspects of welding. Single bevel and double bevel welds require supplementary mechanical operations (edge preparation), while double bevel and fillet welds require overhead position in the case of site welding. The following recommendation are proposed for the particular case of beam-to-column joints in moment-resisting steel frames:

- Double bevel and fillet welds are recommended for shop welding of the subassemblies, with the condition of strict verification of weld size in the case of fillet welds.
- Single bevel welds are adequate for site welding, but rewelding of the root is compulsory in order to eliminate defects at the root of the weld.

A strain rate in the range of $0.03 \div 0.06\ s^{-1}$ (typical for steel members yielding under seismic action) has as effect the increase in the yield strength and, in a lower extent, of the ultimate strength of welded connections. Additionally, a reduction of ductility (up to 27%) is present in the case of high strain rates for monotonic loading, which is an essential characteristic for an adequate seismic performance of beam-to-column joints. However, a decrease of ductility due to high strain rates is not straightforward for cyclic loading, were the results are rather scattered. Cyclic loading increases the probability of weld fracture for partial resistant joints (undersized fillet welds in the present study), and for welds with defects (single bevel welds). It should be noticed that the alternating cyclic loading, which was not possible to be applied in this research, could have an even worse influence on the behaviour of welded connections. It is to be stressed that weld defects such as undersized fillet welds and incomplete penetration single bevel welds were observed both for past beam-to-column joints tests, as well as for welded connection tests in the present study. This fact shows the need for strict control of welding quality.

The support through the Romanian National Education Ministry - World Bank C/16 Grant "Reliability of Buildings Located in Strong Seismic Areas in Romania" is gratefully acknowledged.

REFERENCES

Beg D, Plumier A, Remec C, Sanchez L (2000). Cyclic behaviour of beam-to-column bare steel connections: Influence of strain rate, Chapter 3.1 in: *Moment Resistant Connections of Steel Building Frames in Seismic Areas* -, (Mazzolani F.M. ed.), E&FN SPON, London.

Dexter RJ, Melendrez MI (2000). Through-thickness properties of column flanges in welded moment connections. *Journal of Structural Engineering, ASCE*, **126:1**, 24-31.

Dubina D, Ciutina A, Stratan A (2001). Cyclic Tests of Double-Sided Beam-to-Column Joints, *Journal of Structural Engineering*, **127:2**, 129-136.

El-Tawil S, Mikesell T, Kunnath SK (2000). Effect of local details and yield ratio on behaviour of FR steel connections. *Journal of Structural Engineering, ASCE*, **126:1**, 79-87.

Mao C, Ricles J, Lu LW, Fisher J (2001). Effect of local details on ductility of welded moment connections. *Journal of Structural Engineering, ASCE*, **127:9**, 1036-1044.

Mazzolani FM and Gioncu V (2002). *Ductility of Seismic-Resistant Steel Structures*. SPON PRESS, London, 464 pp.

www.EngineeringEBooksPdf.com

Moisa T, Romanu R, Dragoi S (2000). *Experimental study of welded specimens from steel structures under seismic action – preparation of specimens*, Report No. 25/2000. Institute of Welding and Testing of Materials Timisoara - ISIM (in Romanian).

Nakashima M, Roeder CW, Maruoka Y (2000). Steel moment frames for earthquakes in United States and Japan. *Journal of Structural Engineering, ASCE*, **126:8**, 861-868.

Nakashima M, Tateyama E, Morisako K, Suita K (1998). Full-Scale test of beam-column subassemblages having connection details of shop-welding type. *Structural Engineering Worldwide, Elsevier Science (CD-ROM), Paper Ref. T158-7.*

SAC (1997). *Interim Guidelines Advisory No. 1. Supplement to FEMA-267 Interim Guidelines: Evaluation, Repair, Modification and Design of Welded Steel Moment Frame Structures.* SAC Joint Venture, Report No. SAC-96-03, Sacramento, California, USA.

SR EN 25817 (1993). *Arc-welded joints in steel. Guidance on quality levels for imperfections.* European Committee for Standardisation – CEN (in Romanian).

Suita K, Nakashima M, Morisako K. (1998). Tests of Welded Beam-Column Subassemblies. II: Detailed Behaviour, *Journal of Structural Engineering, ASCE*, **124:11**, 1245-1252.

www.EngineeringEBooksPdf.com

This Page Intentionally Left Blank

www.EngineeringEBooksPdf.com

FATIGUE AND FRACTURE

www.EngineeringEBooksPdf.com

This Page Intentionally Left Blank

www.EngineeringEBooksPdf.com

Advances in Steel Structures, Vol. II
Chan, Teng and Chung (Eds.)
© 2002 Elsevier Science Ltd. All rights reserved.

CORRELATION OF FATIGUE LIFE OF FILLET WELDED JOINTS BASED ON STRESS AT 1 MM IN DEPTH

Zhi-Gang XIAO[1], Kentaro YAMADA[2]

[1]Department of Civil Engineering, Nagoya University,
Furocho, Chikusa-ku, Nagoya 464-8603, Japan
[2]Division of Environmental Engineering and Architecture, Graduate School
of Environmental Studies, Nagoya University,
Furocho, Chikusa-ku, Nagoya 464-8603, Japan

ABSTRACT

Fillet welds are widely used to connect attachments, such as gussets or cover plates, to steel structures. The geometric discontinuity caused by the introduction of fillet weld and the attachments leads to stress concentration. Fatigue cracks may form at weld toe at the end or edge of the attachment when the structure is subjected to cyclic loadings. In this study, stress distribution around weld toe region is studied with a non-load-carrying cruciform joint. It is found that the weld toe shape, i.e., weld toe angle and weld toe radius, is crucial in affecting stress concentration at weld toe, but the affecting region is limited with 1 mm in depth. The effect of weld size (leg length) of the weld bead is less significant than that of weld toe shape. The stress at 1mm in depth in the cross section of the main plate passing weld toe is taken as an indication of geometric effects of the welded joints. If fatigue test results of fillet welded joints are expressed in terms of stress range at 1 mm in depth, which contains effect of geometry of welded joint except that of weld bead, the scatter of test data will only reflect the effect of weld profile. Thus correlation between different types of fillet welds can be established by means of stress at 1mm in depth. Fatigue test results are collected for non-load-carrying cruciform joints with about 10 mm thick of main plate and attachment. In these joints, the geometric effect of transverse attachment is rather small, and FEM analyses also show their stresses at 1 mm in depth to be around unity. The scatter band of these test data matches well with those of test data of in-plane and out-of-plane gussets plotted in terms of stress range of 1 mm in depth.

KEYWORDS

Fatigue, fillet weld, stress concentration factor, local stress, FEM, FEA, gusset, attachment, cruciform joint.

ONE-MILLIMETER APPROACH

The flexibility that fillet welds allow in arrangement of material in a structure leads to the unthinking use of gussets, brackets, cover plates, and other attachments, which may give rise to stress

www.EngineeringEBooksPdf.com

concentration at the end or edge of these attachments. The existence of fillet weld bead also contributes to stress concentration. Because of severe stress concentration, fatigue cracks may form at weld toe when the structure is subjected to cyclic loadings, Fig.1. Fatigue life of typical welded details can be evaluated by referring to fatigue design codes or recommendations, such as JSSC (1995) and Hobbacher (1995). Fatigue evaluation of complex details or normal details under complex loading conditions has to use hot spot stress (HSS) method, linear elastic fracture mechanics approach (LEFM), or other local stress based approaches. For plate structure, many proposals concerning the determination of HSS have been suggested, but none of them has been universally accepted (Tveiten, 2000). The great computational effort associated with LEFM and other local stress based approaches also impedes their application (Niemi, 2002). With these in consideration, this study aims to provide an approach to evaluating fatigue life of fillet welds even in complex configurations or under complex loadings.

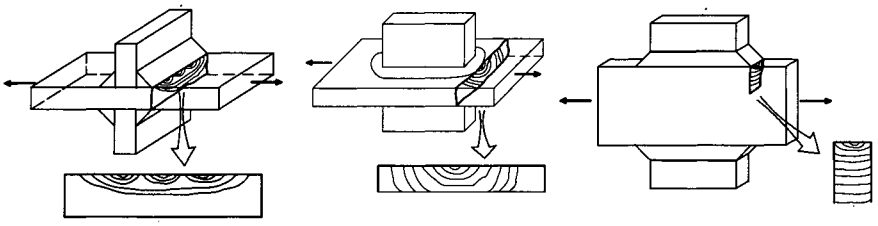

(a) Non-load-carrying cruciform joint (b) Out-of-plane gusset (c) In-plane gusset

Fig.1 Fillet welded joints and fatigue cracks

Stress Concentration in Fillet Welded Details

Stress concentration at weld toe accounts for fatigue crack initiation and propagation in fillet welded details. Both the geometry of structural elements (including attachments) and the weld bead contribute to stress concentration at weld toe, Eqn. 1.

$$K_t = K_{t,local} \times K_{t,global} \quad (1)$$

Where, K_t indicates whole stress concentration at weld toe, and $K_{t,local}$ and $K_{t,global}$ designate stress concentration coming from weld profile and structural elements, respectively.

In production, it is nearly impossible to have an exact control on the profile of weld bead. The shape and size of weld bead vary from one location to the other even in the same weld joint. This variation can partially explain the scatter of the fatigue test data. To study the local stress concentration, a non-load-carrying cruciform joint as shown in the inset of Fig.2 is analyzed with 2D plane strain finite element models. FEM analyses show that, except in extreme cases, the convex or concave of the weld surface is insignificant in affecting the stress concentration at weld toe. Therefore, the fillet weld is just modeled with a flat surface. Effects of weld toe shape and weld size are investigated.

Weld toe parameters

First, the effects of weld toe shape, i.e., weld toe radius ρ, and weld toe angle θ, are investigated. Five models with different combinations of weld toe radii and angles are analyzed. All the finite element analyses (FEA) of this study are conducted with the software package Cosmos/M 2.6, S.R.A.C. (2000). The length of the weld leg along the main plate is set at 6mm. Stress distributions around weld toe region are plotted in Fig. 2 along the surface and across the thickness of the main plate. It can be seen that stress concentration at weld toe location is very sensitive to the changes of weld toe parameters. It

www.EngineeringEBooksPdf.com

increases with the increase of weld toe angle and/or the decrease of weld radius. However, the stress value at 1 mm in depth in the cross section passing through weld toe (hereinafter referred to as weld toe section) does not change with weld toe parameters. It can be asserted that the affected region of weld toe parameters is limited with 1 mm in depth. Along the surface, it can be seen that the affecting region of weld toe parameters extends to about 2 mm away from weld toe, where the stress value declines to unity and does not change significantly with weld toe parameters.

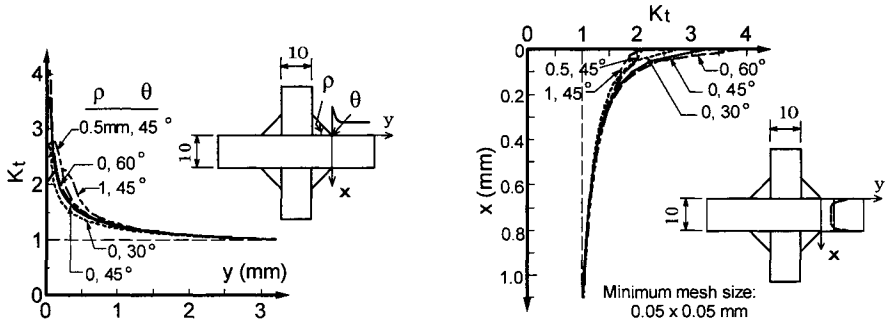

(a) Stress distribution along surface (b) Stress distribution in thickness direction

Fig. 2 Effects of weld profile

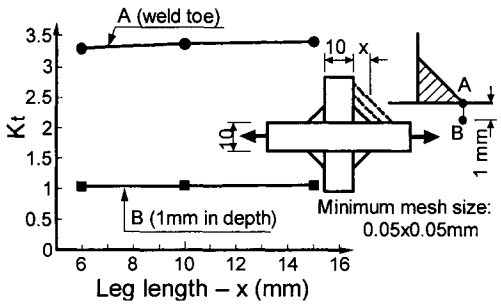

Fig. 3 Effects of leg length

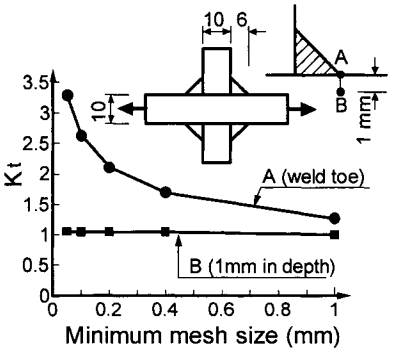

Fig. 4 Effects of mesh size

Leg length of weld

Effect of weld size is investigated with the previous non-load-carrying cruciform joint, with values of weld toe radius and weld angle being set at 0 mm and 45 degrees, respectively, Fig.3. Values of 6, 10 and 15 mm are assigned to leg length, *x*, for the three models studied. Changes of stress concentration with leg length are plotted for two separate locations. One is weld toe, Point A in the inset of Fig.3, and the other is 1mm in depth, Point B. At weld toe, stress concentration increases slightly with leg length, while, at 1mm in depth, stress value almost remains unchanged. It can be concluded with the comparison of Fig. 2 and 3, that the effect of weld size (leg length) on stress concentration is less significant than that of the weld toe shape, and that the affecting region is also limited with 1 mm in depth.

www.EngineeringEBooksPdf.com

Effect of mesh size

At critical point where exists severe stress concentration, stress results obtained from FEA are highly dependent on mesh size. Here, the sharp notch case of zero-radius weld toe is used to study effect of mesh size. Again, the previous non-load-carrying cruciform joint with 10mm thick main plate and attachments is analyzed. Weld toe angle of fillet is set at 45 degrees, and leg length at 6 mm. Five sizes of minimum mesh, 0.05, 0.1, 0.2, 0.4, and 1mm, are used to model the critical point (weld toe) region. Changes of stress value with mesh size are plotted for two locations, weld toe and 1mm in depth, in Fig. 4. At weld toe, as mesh size decreases, the stress value increases significantly. This is in agreement with the singular feature at a sharp notch tip, which is proved by Lazzarin (1998). From Fig. 4, it is seen that, at 1mm in depth, the stress value is less affected by mesh size.

One-Millimeter Approach

The abovementioned analyses have shown that the local effect of weld bead, including weld size and weld toe shape, is limited within 1 mm in depth. It seems reasonable to use the stress at 1 mm in depth to indicate the geometric effect of structural element. It is in essence the same with hot spot stress or geometric stress, which also includes effects of structural elements and excludes weld profile, and is usually solved by extrapolation of surface stress outside the affecting region of weld profile. The stress at 1mm in depth is less than geometric stress at weld toe (plate surface). But the former may be better than the latter in evaluating fatigue life, since the relatively large value of the latter is more suitable for expressing initiation life of fatigue crack, while the moderate value of the former might give a comprehensive evaluation on both initiation and propagation of fatigue crack.

Another preferable feature of 1 mm in depth is that the stress value at this location is insensitive to mesh size. This implies that, in FEA, rather stabilized results maybe assured by relative coarse mesh. The problem of balancing accuracy and computational cost, which is always present in solving problems of stress concentration, is avoided.

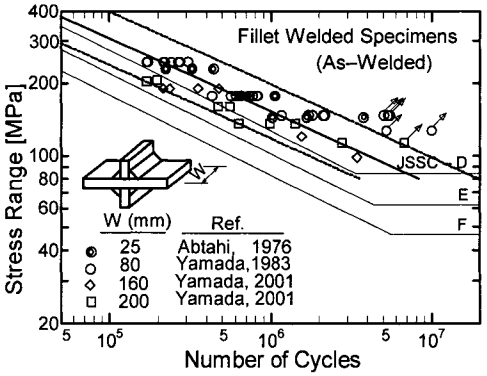

Fig. 5 Fatigue test data of reference detail

The stress of 1mm in depth for the non-load-carrying cruciform joints studied is slightly larger than unity, around 1.04. This implies that the stress raising effect of the 10 mm thick transverse attachment is rather small and is less significant compared with the local effect of weld bead. Thus, the scatter of fatigue test data of non-load-carrying cruciform joints with comparable size to the ones studied, i.e., about 10 mm thick main plate and attachments, can be attributed primarily to the variation of weld bead. Several sets of fatigue test data of such non-load-carrying cruciform joints are summarized in Fig. 5 along with the lines of mean and mean±2s (s, standard deviation).

www.EngineeringEBooksPdf.com

If fatigue test results of other fillet welded joints are expressed in terms of stress range at 1 mm in depth, which contains only effect of geometry of welded joint, the scatter of the test data will also only reflect the effect of weld profile. Therefore, these fatigue test data expressed in terms of stress range at 1 mm in depth are expected to have the same scatter range as that of the non-load-carrying cruciform joints shown in Fig. 5. If the expectation is verified by fatigue test results, then it can be said that correlation between any fillet welded joints can be established by means of non-load-cruciform joints and stress at 1 mm in depth. In this sense, the non-load-carrying cruciform joints with about 10 mm thick transverse attachments and main plate serve as a reference benchmark for expression of local effect of weld profile, and are hereinafter termed reference details. The test data and S-N curve associated with them are called as reference data and reference S-N curve, respectively.

CORRELATION OF IN-PLANE GUSSETS WITH REFERENCE DETAILS

Stress at 1 mm in depth includes only effects of structure elements (including attachments). Fatigue test data plotted in terms of stress at 1 mm in depth will only reflects local effects of weld bead, thus correlation of fillet welds with reference details, distribution of whose test data also mainly demonstrate local effects of weld bead, might be established by means of stress at 1 mm in depth. The first case to be studied is a normal weld detail, in-plane gusset.

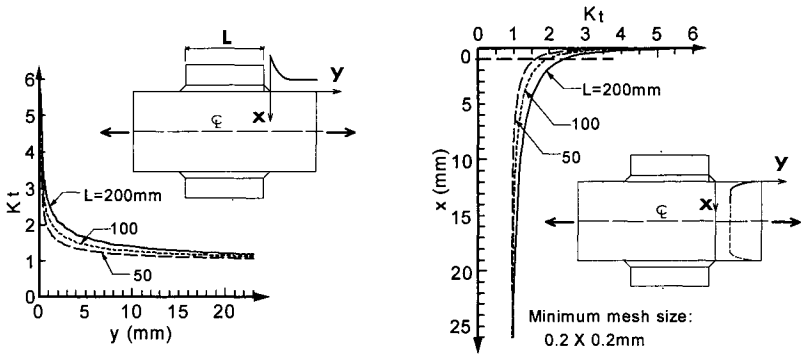

(a) Stress distribution along surface (b) Stress distribution in thickness direction

Fig. 6 Stress concentration of in-plane gusset

In in-plane gussets, Fig.1(c), the side plates are usually butt-welded to the main plate, and the weld is normally continued around the ends of the side plates for the purpose of corrosion protection. The sealing weld at the end of gusset is similar to a fillet weld in shape. The stress concentration at the toe of sealing weld is the direct reason of stress initiation and propagation. Fatigue cracks are initiated at weld toe and penetrate into the width direction of the main plate. Specifically, in the case of in-plane gusset the stress at 1mm in depth should be referred to as stress at 1 mm in width. However, to be consistent with other cases, it is still called stress at 1 mm in depth even with the real meaning of 1 mm in width.

To study the stress concentration at the end of side plate, three models of 2D plane stress elements are analyzed, and the stress distributions across the weld toe section and along the edge of the main plate are shown in Fig. 6. Fillet weld is modeled with zero radius and 6mm leg length. The lengths of gusset in these three models are 50, 100, and 200 mm, respectively. The width of gusset and main plate is 100

www.EngineeringEBooksPdf.com

and 200 mm. These dimensions are set in accordance with the test specimens whose results will be shown later. It is demonstrated by FEA that stress concentration at the end of side plate increases with gusset length.

Several sets of test data of in-plane gussets are summarized in Fig. 7. It is shown that test data are widely scattered. The distinctions between test data of different gusset lengths are evidently shown. Test data of longer gusset are distributed in the lower strength region, while those of shorter gusset in the higher strength region.

The stresses at 1 mm in depth for these three lengths of specimens are obtained from FEM analyses at 1mm in width of the main plate in the weld toe section. With these stresses at 1 mm in depth, the test results in Fig.7 are re-plotted in Fig.8 in terms of stress range at 1 mm in depth, i.e., the nominal stress range multiplied by $K_{t,global}$. In this figure, the distinction caused by lengths of gusset, which is actually reflected by $K_{t,global}$, does not show evidently. Besides, nearly all re-plotted data fall within the data range of reference detail. This indicates that correlation between in-plane gusset and the reference detail can be established by stress at 1 mm in depth.

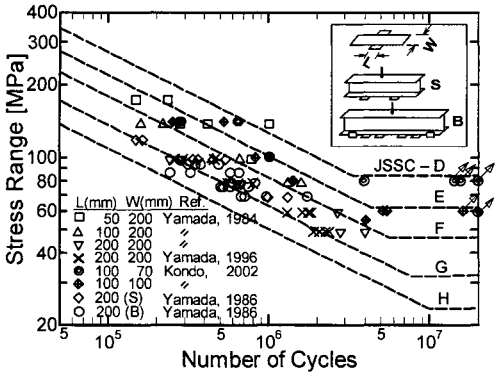

Fig. 7 Fatigue test data of in-plane gusset

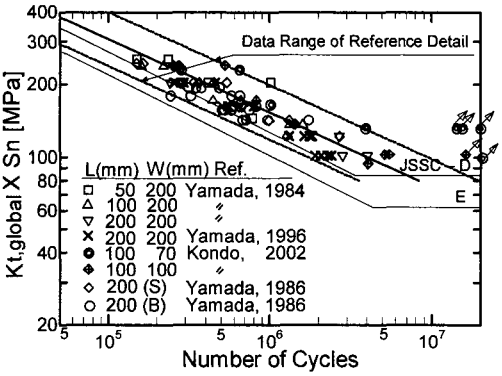

Fig. 8 Re-plotted data in terms of stress at 1 mm in depth

CORRELATION OF OUT-OF-PLANE GUSSETS WITH REFERENCE DETAILS

Models of out-of-plane gussets corresponding to test specimens to be summarized later are created with 3D eight-node solid elements. In Fig.9, stress distributions around the critical point region, i.e., weld toe at gusset end, are summarized for two models in three perpendicular directions, i.e., along transverse direction on the surface, along longitudinal direction on the surface, and through the thickness of the main plate. Factors affecting stress at 1 mm in depth (geometric stress) include the length of the gusset, the width of the main plate, and the thickness of the main plate. As these dimensions increase, stress concentration at weld toe at gusset end also increases, Yamada et al. (2002). Stress at 1 mm in depth is obtained from FEA results.

Data of five sets of fatigue tests are summarized in Fig.10. Separation between different sets of data caused by affecting factors of stress at 1 mm in depth, such as length of gusset, is evidently shown. As with the in-plane gussets, test data are re-summarized in terms of stress range at 1 mm in depth, Fig. 11. It can be seen that test data of different sets are interchangeably distributed, and the vast majority of data fall within the scatter band of the reference detail. The stress at 1mm in depth demonstrates again the good correlation between the out-of-plane gussets and the non-load-carrying cruciform joints.

www.EngineeringEBooksPdf.com

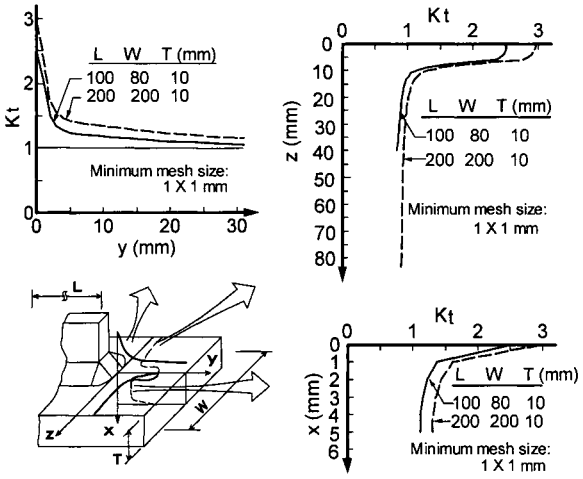

Fig. 9 Stress concentration of out-of-plane gusset

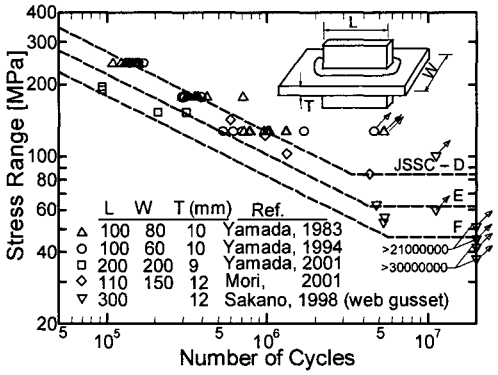

Fig. 10 Fatigue test data of out-of-plane gusset

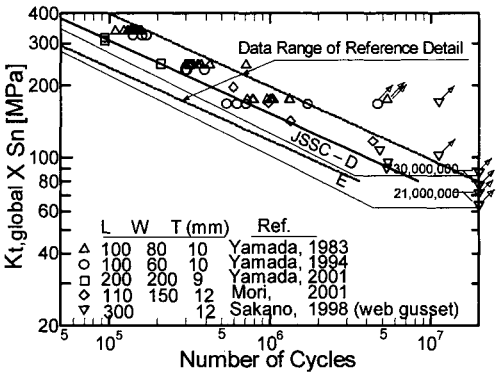

Fig. 11 Re-plotted data in terms of stress at 1 mm in depth

CONCLUSIONS

Both the geometry of structural elements (including attachments) and the profile of fillet weld bead contribute to stress concentration at weld toe region. The local effects of weld bead are limited within 1 mm in depth. This is the main reason for taking stress at 1 mm in depth as the indication of geometric effect of fillet welded joints. Other considerations for representing geometric effect with stress at 1 mm in depth include the insensitivity to mesh size of stress at 1 mm in depth and its comprehensive indication of crack initiation and propagation. The reference S-N curve to be used with stresses at 1mm in depth fatigue life evaluation is determined with test data of fillet welded non-load-carrying cruciform joints with restricted dimensions.

The correlation between fillet welded non-load-carrying cruciform joints and the other types of fillet welded details by means of stress at 1 mm in depth has been shown by fatigue test results of in-plane

www.EngineeringEBooksPdf.com

and out-of-plane gussets. This implies that the fatigue strength of fillet welded joints can be evaluated with the reference S-N curves of non-load-carrying cruciform joints after the stress at 1 mm in depth is obtained through FEA. Fatigue life of fillet welds in complex configurations or under complex loading conditions may be evaluated in the same way.

ACKNOWLEDGEMENT

The authors wish to thank the Hori Information Science Promotion Foundation for financial support. This research was also partially supported by Nagoya Expressway Public Corporation and the Ministry of Education, Science, Sports and Culture, Grant-in-Aid for Scientific Research (B), 50109310, 2002.

REFERENCES

Hobbacher, A. (1995). *Recommendations on Fatigue of Welded Components*, IIW document XIII-1539-95/XV-845-95

JSSC (Japanese Society of Steel Construction). (1995). *Fatige Design Recommendations for Steel Structures [English Version]*.

Lazzarin P., Tovo R. (1998). A notch stress intensity factor approach to the stress analysis of welds. *Fatigue and Fracture of Engineering Materials and Structures*, Vol.21, 1089-1103.

Niemi, E., and Marquis, G. (2002). Introduction to the Structure Stress Approach to Fatigue Analysis of Plate Structures, *Proc. of the IIW Fatigue Seminar,* Tokyo Institute of Technology, Japan, 73-90.

S.R.A.C. (Structural Research and Analysis Corp.) (2000). *Cosmos/M User's Guide*, Cosmos/M 2.6 online help documents.

Tveiten, B. W., and Moan T. (2000). Determination of structural stress for fatigue assessment of welded aluminum ship details, *Marine Structures*, Vol. 13, 189-212.

van Wingerde, A. M., Packer, J. A., and Wardenier, J. (1995). Criteria for the fatigue assessment of hollow structural section connections, *J. Construct. Steel Research*, Vol. 35, 71-115.

Yamada, K., Xiao, Z. G., Kim, I. T., and Tateishi, K. (2002). Re-analysis of fatigue test data of attachments based on stress at fillet weld toe, *J. of Struct. Engrg,* JSCE, Vol.48(A), 1047-1054. (In Japanese)

www.EngineeringEBooksPdf.com

Advances in Steel Structures, Vol. II
Chan, Teng and Chung (Eds.)
© 2002 Elsevier Science Ltd. All rights reserved.

FATIGUE STRENGTH PREDICTION FOR MISALIGNED WELDED JOINTS BY STRESS FIELD INTENSITY METHOD

Guan Deqing[1,2], Yi Weijian[1] and Li Li[2]

[1] School of Civil Engineering, Hunan University,
Changsha, 410082,China
[2] Department of Power Engineering, Changsha University of Electric Power,
Changsha, 410077, China

ABSTRACT

Based on the theory of stress field intensity method, a predicting model of effective stress concentration factor for misaligned welded joints is presented. The model is taken account of the effects of material properties, type of loading, value of misalignment, stress gradient, stress ratio and residual stress on the fatigue strength respectively. The effective stress concentration factors of a few of misaligned welded joints are estimated. Examples show that good agreement is achieved between the estimations and experiments. It may be greatly decreased fatigue tests with the method. Therefore the model has significance for engineering application.

KEYWORDS

Fatigue strength, Fatigue notch factor, Effective stress concentration factor, Stress field intensity method, Prediction model, Misaligned welded joint

INTRODUCTION

Fatigue failure is a main destruction form for welded joints under cyclic loading. The research of the fatigue strength property of welded joints is significant for safety assessment of engineering structures. Usually fatigue strength of welded joints may be obtained from tests, which are time-consuming and costly. Therefore predicting the fatigue strength of welded joints will certainly be useful in engineering

www.EngineeringEBooksPdf.com

application and helpful in gaining economic efficiency. Fatigue notch factor is an important parameter for fatigue strength of notch specimens, which may be estimated by some empirical formulae (Peterson, 1974, Smith and Miller, 1987). These formulae of the fatigue notch factor take the local point stress at the point of stress concentration as the parameter. However, research into fatigue failure mechanisms has shown that fatigue failure is caused by damage accumulation in the local damage zone. Some methods with zone, which including stress field intensity method (Zheng C. H., 1984, Yao W. X., 1993), critical-distance method (Taylor D., 2001), area and volume method (Taylor D. and Wang G., 1999), have been developed to predict the fatigue strength of notch specimens. The stress field intensity method is defined field intensity only takes peak-value stress and stress gradient into consideration. The approach has been becoming an efficient method to estimate the fatigue behaviors of notch specimens. Unfortunately stress intensity approach remained undeveloped to welded joints. The misalignment often exists in welded joints, it will certainly influence the fatigue strength of the weld. The paper (Andrews, 1996) studied the effect of misalignment on the fatigue strength for welded cruciform joints. An Estimating model of fatigue strength and a predicting method of S-N curve for misaligned welded joint were developed (Guan Deqing and Wang Guanghai, 1994, Guan Deqing, 1996). In the paper, the effective stress concentration factor of misaligned welded joints, which may be defined the ratio between the fatigue endurance limit of the smooth specimen and that of a welded joint is introduced. Based on the theory of stress field intensity method, a predicting model of effective stress concentration factor for misaligned welded joint is presented. The model is taken account of the effects of material properties, type of loading, value of misalignment, stress gradient, stress ratio and residual stress on the fatigue strength for misaligned welded joint respectively. The effective stress concentration factors of a few of misaligned welded joints are estimated. Examples show that good agreement is achieved between the estimations and experiments. It may be greatly decreased fatigue tests with the method. Therefore the model has significance for engineering application.

FATIGUE NOTCH FACTOR WITH STRESS FIELD INTENSITY METHOD

According to the theory of stress field intensity method, fatigue failure is caused accumulation in the local damage zone. With a section at notch root, the stress field intensity parameter, σ_{FI}, is defined as follows

$$\sigma_{FI} = \frac{1}{V}\int_{\Omega} f(\sigma_{ij})\varphi(\vec{r})dV \tag{1}$$

where Ω is the fatigue failure region. With micromechanicl studies, Ω can be considered a circle or a sphere and its size is determined by fitting of experimental results. V is the volume of Ω. $\varphi(\vec{r})$ is weight function and $f(\sigma_{ij})$ is the equivalent stress function.

Fatigue notch factor K_f is an important parameter to describe the notch specimen fatigue strength. Generally, it can be expressed from long life fatigue tests as the ratio of unnotched to notched fatigue

www.EngineeringEBooksPdf.com

strength.

$$K_f = \frac{\sigma_{-1}}{\sigma_{-1N}} \tag{2}$$

where σ_{-1} and σ_{-1N} are the fatigue endurance limit of the smooth specimen and notch specimen respectively. K_f is concerned with the material properties, geometric shape of notch , type of loading and stress gradient. The expression of fatigue notch factor with stress field intensity method may be written as follows

$$K_f = \frac{1}{V}\int_{\Omega} f(\overline{\sigma_{ij}})\varphi(\vec{r})dV \tag{3}$$

As for flat consideration, Eqn. 4 can be obtained.

$$K_f = \frac{1}{A}\int_{D} f(\overline{\sigma_{ij}})\varphi(\vec{r})dA \tag{4}$$

where D is plane stress field intensity region. A is area of region D. $f(\overline{\sigma}_{ij})$ is defined as follows

$$f(\overline{\sigma_{ij}}) = f(\sigma_{ij}/\sigma_{-1N}) \tag{5}$$

Fatigue notch factor of welded joints may be calculated with Eqn. 3 or Eqn. 4 due to there is a notch in the weld toe.

ESTIMATING MODEL OF EFFECTIVE STRESS CONCENTRATION FACTOR FOR MISALIGNED WELDED JOINT

A definition is introduced that the effective stress concentration factor β_R is the ratio between the fatigue endurance limit σ_R of the smooth specimen and that of a misaligned welded joint σ_{RW} when the stress ratio equals to R..

$$\beta_R = \frac{\sigma_R}{\sigma_{Rw}} \tag{6}$$

here β_R is an important parameter for the fatigue strength of misaligned welded joint. It is influenced

www.EngineeringEBooksPdf.com

by many factors such as material properties, type of loading, geometric shape, stress ratio, stress gradient, residual stress in notch root of misaligned welded joints.

The stress ratio R between the minimum cyclic stress σ_{min} and the maximum cyclic stress σ_{max} is defined as follows

$$R = \frac{\sigma_{min}}{\sigma_{max}} \tag{7}$$

Based on Morrow's equation with mean stress correction and considered the effects of material properties, type of loading, geometric shape, stress ratio, residual stress in notch root of welded joints, an estimating equation of β_R was developed (Guan Deqing, 1997) as follows

$$\beta_R = \frac{K_f + \frac{1+R}{1-R}(2N_L)^b}{1+\frac{1+R}{1-R}(2N_L)^b} \frac{\sigma'_f}{\sigma'_f - \sigma_r} \tag{8}$$

where σ'_f is the fatigue strength coefficient. b is the fatigue strength exponent. σ_r is residual stress in welded joint. N_L is cyclic number corresponding to the fatigue endurance limit, it may be chosen 2×10^6 for welded joints.

When R=-1, for symmetrical cyclic stress, Eqn. 8 becoming:

$$\beta_{-1} = \frac{\sigma'_f}{\sigma'_f - \sigma_r} K_f \tag{9}$$

where β_{-1} is effective stress concentration factor related to R=-1. Substituting Eqn. 3 into Eqn. 8, a relationship of β_R can be obtained as follows

$$\beta_R = \frac{\frac{1}{V}\int_\Omega f(\bar{\sigma}_{ij})\phi(\bar{r})dV + \frac{1+R}{1-R}(2N_L)^b}{1+\frac{1+R}{1-R}(2N_L)^b} \frac{\sigma'_f}{\sigma'_f - \sigma_r} \tag{10}$$

Eqn. 10 is an estimating formula of the effective stress concentration factor with stress field intensity method for misaligned welded joints. The effects of material properties, type of loading, geometric

www.EngineeringEBooksPdf.com

shape, stress gradient, residual stress in misaligned welded joints on the fatigue strength are considered in the equation respectively. As for plane consideration, substituting Eqn. 4 into Eqn. 10, we can obtain another predicting formula as follows

$$\beta_R = \frac{\frac{1}{A}\int_D f(\bar{\sigma}_{ij})\phi(\vec{r})dA + \frac{1+R}{1-R}(2N_L)^b}{1+\frac{1+R}{1-R}(2N_L)^b}\frac{\sigma'_f}{\sigma'_f - \sigma_r} \tag{11}$$

Substituting Eqn. 3 and Eqn. 4 into Eqn. 9 respectively, two estimating formulae of effective stress concentration factor may be derived.

$$\beta_{-1} = \frac{\sigma'_f}{(\sigma'_f - \sigma_r)V}\int_\Omega f(\overline{\sigma_{ij}})\varphi(\vec{r})dV \tag{12}$$

$$\beta_{-1} = \frac{\sigma'_f}{(\sigma'_f - \sigma_r)A}\int_D f(\overline{\sigma_{ij}})\varphi(\vec{r})dA \tag{13}$$

The conclusions may be derived from Eqns. 3, 4, 12 and 13 as follow: when $\sigma_r > 0$, σ_r is tensile residual stress, $\beta_{-1} > K_f$; when $\sigma_r < 0$, σ_r is compressive residual stress, $\beta_{-1} < K_f$; when $\sigma_r = 0$, σ_r is released $\beta_{-1} = K_f$.

According to the results as above, it is shown that tensile residual stresses make fatigue strength decrease while compressive residual stresses make it increase. The conclusion agrees with the fatigue experiments.

COMPARISON OF ESTIMATIONS WITH EXPERIMENTS OF EFFECTIVE STRESS CONCENTRATION FACTORS

According to the prediction method of the effective stress concentration factor for misaligned welded joints, by means of Eqn. 10 or Eqn. 11 or Eqn. 12 or Eqn. 13, we can estimate the effective stress concentration factor. In order to investigate the accuracy of the prediction model, we compare the predicted results with the experimental results of four groups of misaligned welded joints.

The fatigue experiments of four groups of misaligned welded joints made of low alloy structural steel have been carried out. Specimens of misaligned welded joints and load are shown in Figure 1. Their misalignment δ=0.15, 0.30, 0.60, 1.08mm, respectively. The fatigue life is controlled with stress amplitude. The maximal (minimal) load and the maximal (minimal) stress amplitude are 56*KN* (10

www.EngineeringEBooksPdf.com

KN) and 304*MP*a (54*MP*a) respectively. Material mechanical properties of tested specimens are ultimate strength *S*u=548*MP*a, yield strength σ_s =441*MP*a. Material constants σ'_f =894*MP*a, $\sigma_{0.0}$ =193*MP*a, b = –0.0854. Other data are t=4mm, σ_r=441*MP*a, R=0.0. The fatigue strength of four groups of misaligned welded joints is obtained from experiments.

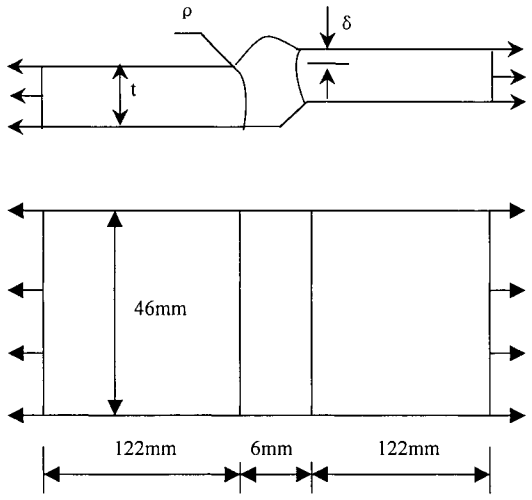

Figure 1: Misaligned welded joint

A few of appropriate approximations are adopted in calculation with stress field intensity approach.

(1) Von Mises equivalent stress is for stress function $f(\overline{\sigma_{ij}})$;

(2)Weight function is chosen relating to $|\vec{r}|$ and direction angle θ as follows

$$\varphi(\vec{r}) = 1-(1-\frac{\sigma_i}{\sigma_{\max}})r(1+\sin\theta) \tag{14}$$

here σ_i is the stress in point $\vec{r}$. $\sigma_{\max}$ is the most stress in weld toe. $\varphi(\vec{r})$ physically means the contribution of stresses at a point to peak value stress at $\vec{r}$=0. Generally, the most serious stress concentration lies at the notch root. Therefore $\varphi(\vec{r})$ is the generalized monotone decreasing function

www.EngineeringEBooksPdf.com

about $|\vec{r}|, 0 \le \varphi(\vec{r}) \le 1$. Weight function $\varphi(\vec{r})$ is 1 at point $\vec{r} = 0$. When stress gradient equals to zero, that is $\sigma_i \equiv \sigma_{\max}$, $\varphi(\vec{r}) \equiv 1$.

We assume that the fatigue failure region Ω is a circular plane intensity area. The diameter of stress field D may be regarded as a material constant, and its size is determined by fitting of experimental results. Because the stress field in misaligned welded joints is very complex, the method of finite element to compute the parameter of stress field intensity is adopted. The square eight nodes isoparameter element is used. In computing the K_f of a certain material, the error between calculated and experimental values of different type of notch specimen and magnitudes may be dealt with least square method for accumulated errors in the same field diameter, which is taken as the expected value of the D. Through calculation to notch specimens of the material, D=0.27mm was obtained. The estimating and experimental effective stress concentration factors of four groups of misaligned welded joints are located in Table 1 respectively.

TABLE 1
ESTIMATIONS AND EXPERIMENTS OF EFFECTIVE STRESS CONCENTRATION FACTORS

Misalignment	R	β_R (estimation)	β_R (test)
δ =0.15(mm)	-1.0	2.86	2.78
	0.0	2.51	2.41
δ =0.30(mm)	-1.0	3.42	3.34
	0.0	2.86	2.85
δ =0.60(mm)	-1.0	4.02	4.08
	0.0	3.52	3.44
δ =1.08(mm)	-1.0	4.90	4.96
	0.0	4.02	4.13

We have obtained that the predicted β_R of four groups of misaligned welded joints are in agreement with the experimental results from Table 1.

CONCLUSIONS

Based on the essential principle of stress field intensity method, a prediction model of the effective stress concentration factor for misaligned welded joints is developed. The effects of material properties, type of loading, geometric shape, stress gradient, stress ratio, residual stress in misaligned welded joints on the fatigue strength are considered in the estimating equations.

The relationship of effective stress concentration factor with the fatigue notch factor and residual stress can be shown that tensile residual stress makes the fatigue strength decrease and compressive residual stress makes the fatigue strength increase.

www.EngineeringEBooksPdf.com

The fatigue experiments of four groups of misaligned welded joints are carried out. Good examples of predicting the effective stress concentration factors have been obtained. It may be greatly decreased fatigue tests with the estimating model. Therefore the method has significance for engineering application.

ACKNOWLEDGEMENT

The authors gratefully acknowledge the research support for this work provided by Provincial Natural Science Fund of Hunan, China.

REFERENCES

Peterson R. E. (1974). *Stress Concentration Factor,* John Wiley and Sons, New York

Smith K. A. and Miller K. J.(1987). Prediction of fatigue regimes in notched components, *International Journal of Mechanical Sciences* **20:** 201-206.

Zheng C. H.(1984). *The research on stress field intensity approach of a new high cycle fatigue design,* PhD thesis, Tsinghua University, P. R. China

Yao W. X.(1993). Stress field intensity approach for predicting fatigue life, *International Journal of Fatigue* **15:3,** 243-245.

Taylor D.(2001). A mechanistic approach to critical-distance method in notch fatigue, *Fatigue & Fracture of Engineering Materials & Structures* **24:10,** 215-224.

Taylor D. and Wang G. (1999). A critical distance theory which unifies the prediction of fatigue limits for large and small cracks and notches, *Proceedings of the Seventh International Fatigue Congress* **1:** 579-584, Edited by Wu X. R. and Wang Z. G., Higher Education Press, Beijing, China and Engineering Materials Advisory Services Ltd. UK

Andrews R. M. (1996).The effect of misalignment on the fatigue strength of welded cruciform joints, *Fatigue & Fracture of Engineering Materials & Structures* **19:**755-768.

Guan Deqing. (1994). A method of estimating misaligned welded joints fatigue strength, *Chinese Journal of Engineering Mechanics* **11:1,**118-124.

Guan Deqing. (1996). A method of predicting the fatigue life curve for misaligned welded joints, *International Journal of Fatigue* **18:4**, 221-226.

Guan Deqing. (1997). An estimating method of fatigue strength for welded joint under general stress ratio, *Chinese Journal of Applied Mechanics* **14:1,** 54-59.

www.EngineeringEBooksPdf.com

Advances in Steel Structures, Vol. II
Chan, Teng and Chung (Eds.)
© 2002 Elsevier Science Ltd. All rights reserved.

FAILURE OF A STEEL PLATE CONTAINING A CIRCULAR RIVET HOLE WITH AN EMANATING CRACK

K.T. Chau and S.L. Chan

Department of Civil and Structural Engineering, The Hong Kong Polytechnic University, Kowloon, Hong Kong, China

ABSTRACT

Sudden catastrophic crack propagation in steel structures has led to numerous disasters. In civil engineering, collapse of temporary scaffolding occurs all the time in Hong Kong. Fatigue crack propagation is highly susceptible in these accidents. Although fracture mechanics has been developed quite substantially since 1920, the use of it among practitioners is not common, especially in the field of civil engineering. Therefore, the main objective of this paper is to provide a simple example to illustrate how to use of the results of fracture mechanics in designing steel structures jointed by rivet systems. In particular, a finite steel strip containing a circular hole is under far field tension and near field rivet load. Elastic solution of stress concentration and the fracture mechanics solution on a radial crack emanating from the hole are utilized to estimate the yield as well as fracture strength. The critical size of the crack that leads to catastrophic fracture can be estimated. Fatigue crack growth is also incorporated into our analysis.

KEYWORDS

Cracks, Rivet hole, Tension, Yielding, Fracture mechanics

INTRODUCTION

Despite careful detailed-design, practically any structure contains stress concentration due to holes. This is particularly true for steel structures, in which bolt holes and rivet holes are necessary at joints and connections between beams and columns. Although very sophisticated finite element programs, which can consider both material and geometric nonlinearities, have been used daily in design offices, the consideration of cracking from these rivet holes is rare. In reality, the majority of service cracks nucleate in the area of stress concentration at the edge of a hole, and are found responsible for many structural failure of steel structures.

www.EngineeringEBooksPdf.com

Sudden catastrophic crack propagation in steel structures has led to numerous disasters. For example, on April 28, 1988, when the fuselage of a 19-year-old Boeing 737 of the Aloha Airlines ripped open in flight over Hawaii and one flight attendant died. The cause of the accident is due to a fatigue crack propagation from a rivet hole at the fuselage (main body) of the 737 jet. Figure 1 shows a photograph of the aircraft after it landed on Maui 13 minutes later. That accident focused the industry's attention on the issue of deterioration in aging planes and resulted in mandated repairs to the aluminum airframe on a strict timetable. In 1985, an incorrect bulkhead repair by Boeing Company on the bulkhead of a Japan Air Lines 747 caused the tail section to crack open, triggering a 1985 crash that killed 520.

In civil engineering, collapse of temporary steel scaffolding occurs all the time in Hong Kong. Fatigue crack propagation is highly susceptible in these accidents. The reluctance of Hong Kong engineers applying fracture mechanics principles to analyze cracks emanating from holes and their daily design works is mainly due to the prerequisite knowledge on fracture mechanics that is normally not covered in the curriculum of the degree program in Civil Engineering and Structural Engineering in Hong Kong. For example, stress intensity factor and fracture toughness are important concepts need to be known.

Therefore, the main objective of the present paper is to demonstrate the use of the existing results and knowledge of fracture mechanics. First, we review some of the existing solutions for the stress intensity factors for cracks emanating from a hole of finite width. The applied stress leads to crack growth will be compared to the yield stress. In the process, some new approximate solutions will be proposed for practical and daily use.

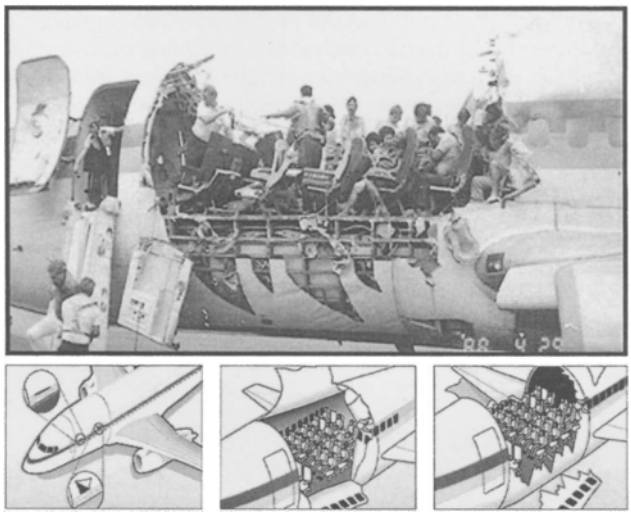

Figure 1: The 1988 Aloha Airlines disaster occurred over Hawaii.

CRACK EMANATING FROM HOLE IN FINITE STRIP UNDER TENSION

Stress concentration at a circular hole in a strip of finite width

www.EngineeringEBooksPdf.com

It is always informative to compare the stress concentration at a rivet hole without crack to those with emanating cracks. If there is no crack emanating from the circular hole in Fig. 2(a), Howland's (1929) solution for the maximum tensile stress at the edge of the hole can be approximated by:

$$\sigma_s = F_s \sigma_1 = \frac{\sigma_1[2+(1-c/b)^3]}{(1-c/b)} \tag{1}$$

which is an approximation of the solution by Howland (1929) proposed by Heywood (1952). The strip starts to yield around the rivet hole when σ_s equals σ_Y.

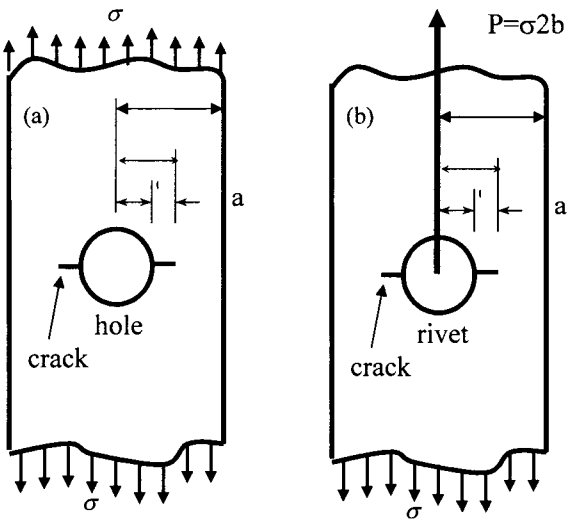

Figure 2: Cracks emanating from a hole in an infinite strip: (a) under tension; and (b) under rivet load

Stress intensity factor of emanating cracks from a circular hole in a strip of finite width

When there are horizontal cracks emanating from both sides of the hole, the following empirical formula was developed by Fuhring (1973) using finite element method:

$$K_I = F\sigma_2\sqrt{\pi a} = 1.6257\sigma_2\sqrt{\pi a}(3\beta^{2P/3} - 2.55\beta^P)\times$$
$$(\frac{\pi}{\pi-1})\left\{\sqrt{\frac{1}{\overline{\alpha}}[\tan\overline{\alpha} + 0.03325\sin(2\overline{\alpha})]}\left[1+\frac{\varepsilon^2(2-\varepsilon^2)}{(1-\varepsilon)}\right]-1.03199\right\} \tag{2}$$

where

$$\beta = \frac{\alpha-\gamma}{1-\gamma}, \quad P = -\frac{0.31656}{\log_{10}[\gamma/(1+\gamma)]}, \quad \overline{\alpha} = \frac{\pi}{2}\alpha, \quad \varepsilon = 0.344\alpha, \quad \gamma = c/b, \quad \alpha = l/b \tag{3}$$

The accuracy of this formula is typically less than ±5% and the application range are: $0.1 \le \gamma \le 0.8$ and $\gamma \le \alpha \le 0.95$. Figure 3 plots F versus l/b for various values of c/b, together with the experimental results by Cartwright and Ratcliffe (1972) for this case of c/b=0.5. The dotted line is the experimental

www.EngineeringEBooksPdf.com

results by (4) below. It should be noted that Fig. 3 is essentially the same as that given on p.292 of volume 1 of Murakami (1997).

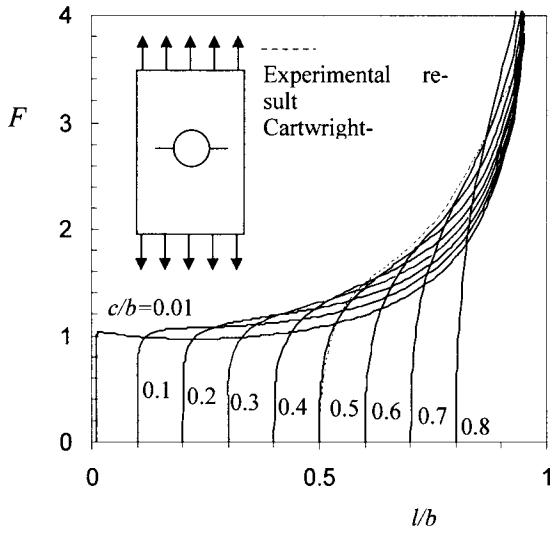

Figure 3: The stress intensity factor coefficient F given in equation (2) for various values of c/b. The dotted line is the experimental result by Cartwright and Ratcliffe (1973) for c/b=0.5.

Comparison with experiments

Experiments have been conducted by Cartwright and Ratcliffe (1972) for this case of two radial cracks emanating from a hole in an infinite strip. To check the validity of (2-3) given above, the following experimentally obtained formula for the case of c/b=0.5 is used (Cartwright and Ratcliffe, 1973):

$$K_I = \sigma\sqrt{\pi a}\,2\left[\frac{\lambda}{\pi(1+\lambda)}\{15.65-34.92\lambda+47.24\lambda^2\}\right]^{1/2} \tag{4}$$

where $\lambda=a/c=(b/c)(l/b)-1$. This solution agrees generally with the prediction of (2-3), as shown in Fig. 3.

Special cases: Hole in an infinite plate

If the hole is small relative to the width of the strip, we have $c/b \to 0$. This problem has been solved by Bowie (1956), and such problem is sometimes referred as Bowie's problem. For practical usage, various approximation formulas exist and are compiled as:

Approximation I (Tada et al., 1985):

$$K_I = \sigma\sqrt{\pi a}\left\{\frac{1}{2}(3-s)[1+1.243(1-s)^3]\right\} \tag{5}$$

www.EngineeringEBooksPdf.com

Approximation II (Kanninen and Popelar, 1987):

$$K_I = \sigma\sqrt{\pi a}\left\{1 + 2.365(1-s)^{2.4}\right\} \tag{6}$$

Approximation III (Grandt, 1975):

$$K_I = \sigma\sqrt{\pi a}\left\{\frac{0.6865(1-s)}{0.2772(1-s)+1} + 0.9439\right\} \tag{7}$$

where $s=a/c/(1+a/c)$. Figure 4 compares the predictions of (5-7), and, as shown, they are comparable. Thus, any one of these can be used for engineering purposes.

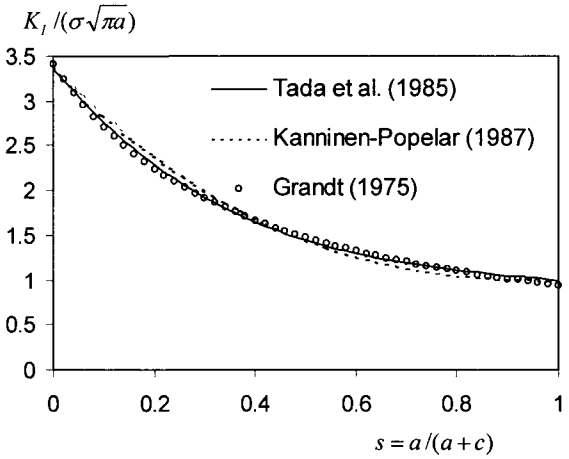

Figure 4: The stress intensity factor for Bowie's problem (crack emanating from a hole in an infinite plate). The three solutions are approximations.

Crack criterion

Crack propagation begins when the mode I (tensile mode) K_I equals to the fracture toughness:

$$K_I = K_{IC} \tag{8}$$

The typical values of K_{IC} for steel are from 30 to 150MPa$\sqrt{m}$. There are various standard techniques in determining K_{IC} experimentally, such ASTM and others. It should be borne in mind that although K_{IC} is considered as a material constant. The experimentally determined values are highly sample size and crack size dependent. Appropriate values should be selected or established carefully for the particular problem in mind.

www.EngineeringEBooksPdf.com

Comparison of yield stress versus fracture stress

The yield stress given in (1) can be compared to the fracture stress required for crack growth, which can be estimated from (3) as:

$$\mu = \frac{\sigma_2}{\sigma_1} = \frac{1}{\sqrt{\pi a}}\left(\frac{K_{IC}}{\sigma_Y}\right)\frac{F_s}{F(c/b, l/b)} \tag{9}$$

where F is defined in (2) and F_s is defined in (1). If μ is larger than 1, plastic yielding is the main mechanism. Otherwise, brittle fracture controls. Thus, a stress envelop can be developed for plastic yield and brittle cracking. In addition, a nonlinear relation for the critical crack length above which the strength is expected to be limited by brittle fracture can also be developed. For the case of AISI 1144 steel with yield stress of $\sigma_Y = 540\text{MPa}$ and fracture toughness of $K_{IC} = 66\text{MPa}\sqrt{m}$ and b=50mm, c/b=0.5, we found that the crack propagation will control the failure mechanism if the crack length a=16.2mm, otherwise yielding will occur first. Internal pre-existing cracking in steel is unlikely to be of 16.2mm. It is unlikely that such large crack remains unnoticed. For more brittle steel (say $K_{IC} = 6.6\text{MPa}\sqrt{m}$ and all other parameters remain the same), the critical crack length is about 1mm. Such crack length is more likely to leave unnoticed. Note that the critical crack size changes nonlinearity with K_{IC}/σ_Y. Thus, for more brittle steel, it is possible that cracking from the rivet hole controls the failure. However, the present result does not account for the possibility of nonlinear fracture (i.e. plastic deformation around the crack tip is not accounted for). However, steel structural member containing rivet hole is also subject to prolonged loading as well as repeated load cycles. Therefore, fatigue crack growth may occur such that initially undetectable cracks by visual, x-ray photography and reflection of ultrasonic waves, may eventually grow to a sizable length. Therefore, relation like the Paris law can be used to estimate the crack length increase with the number of load cycles as:

$$\frac{da}{dN} = C(\Delta K)^m \tag{10}$$

where C and m are material constants. For SI unit, C is typically 5.11×10^{-10} and m is 3.24 for AISI 4340 steel. In which, N is the number of the loading cycles and ΔK is the change in the stress intensity factor in each loading cycle. In the design stage, we may have to establish a S-N curve to apply both "factor of safety in stress" (i.e. shift down the S-N plot) as well as "factor of safety in life" (i.e. shift left the S-N curve). Note in this formula that ΔK increases with the increase of crack size a, which makes the crack growth very unstable as crack continues to grow.

CRACK EMANATING FROM A HOLE IN FINITE STRIP UNDER TENSION

For the case that the stress concentration is induced by a pinned rivet load, as shown in Fig. 2(b), the following formula for the stress intensity factor can be used (Cartwright and Ratcliffe, 1972):

$$K_I = \sigma\sqrt{\pi a}\,\frac{b/c}{\left[\pi(1+\lambda)\right]^{1/2}}\left[F_R(b/c, \lambda)\right]^{1/2} \tag{11}$$

where $\lambda = a/c = (b/c)(l/b) - 1$. The values of F_R are given in Table 1 below for various b/c. This formula is an empirical formula obtained from experiments.

www.EngineeringEBooksPdf.com

TABLE 1

FUNCTION IN THE STRESS INTENSITY FACTOR FOR CRACKING EMANATING FROM A HOLE IN AN INFINITE STRIP UNDER RIVET LOAD SHOWN IN FIG. 2(B)

b/c	$F(b/c,\lambda)$	Range of λ
2	$17.71\lambda - 80.75\lambda^2 + 174.6\lambda^3 - 111.0\lambda^4$	$0<\lambda<0.6$
4	$2.51\lambda - 4.115\lambda^2 + 2.791\lambda^3 - 0.563\lambda^4$	$0<\lambda<1.8$
5	$0.975\lambda - 0.66\lambda^2 + 0.18\lambda^3$	$0<\lambda<2.5$

Regarding the stress concentration at the hole in an infinite strip under rivet load shown in Fig. 2(b), the solution was given by Theocaris (1956). But detailed discussion on the interplay between plastic yield and brittle fracture similar to that of the previous section will not be given here. The results of (11) together with Table 1 are plotted in Figure 5 below. For the purpose of comparison, Fuhring's (1972) solutions for the case of applied stress at infinity are also plotted for comparison. The curve for rivets loads are similar to that of the far field tension case. As discussed by Cartwright and Ratcliffe (1972), the differences are caused by the combined effects of crack growth, stress concentration and proximity of boundary surfaces.

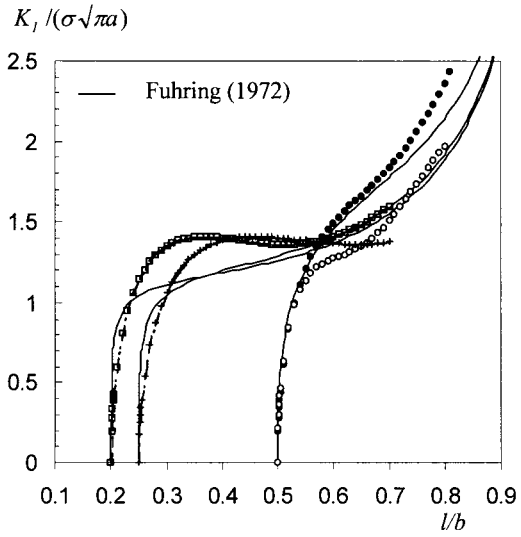

Figure 5: The experimental formulae by Cartwright and Ratcliffe (1972) for a hole under rivet load shown in Fig. 2(b) are plotted as squares, cross and open circles. The Fuhring (1973) results for the applied stress at infinity given in Fig. 2(a) are also given for comparison (the solid circles are results experimental results by Cartwright and Ratcliffe (1972).

www.EngineeringEBooksPdf.com

CONCLUSION

In this paper, we only consider two simple problems given in Fig. 2 of rivet loads. For other loading and crack geometry, stress intensity factors can be looked up from handbooks of stress intensity factor (e.g. Tada et al., 1985; Rooke and Cartwright, 1976; Murakami, 1997). The basic objective of the present paper is to demonstrate that simple formulas can be used found or established from handbooks to design rivet hole against both plastic yielding and brittle fracture. Fatigue crack propagation was also mentioned. Further useful results on the crack growth problems from a rivet hole can be found from Broek (1974) and Grandt (1975); and for elastic stress concentration at rivet holes, one can refer to the handbook by Peterson (1974) before using finite element package.

For the cases that the crack at the hole is three-dimensional, the situation is more complicated but graphical solutions have been compiled in Chapter 14 of Broek (1974). Thus, no such discussion will be given here due to space limitation.

ACKNOWLEDGEMENTS

The research was partially supported by the Hong Kong Polytechnic University.

REFERENCES

Broek D. (1974). *Elementary Engineering Fracture Mechanics*, Noordhoff, Leyden.

Cartwright D.J., Ratcliffe G.A. (1972). Strain energy release rate for radial cracks emanating from a pin loaded hole. *International Journal of Fracture*, **8:2**, 175-181.

Fuhring H. (1973). Approximation function for K-factors of cracks in notches. *International Journal of Fracture* **9**, 328-331.

Grandt Jr. A.F. (1975). Stress intensity factors for some through-cracked fastener holes. *International Journal of Fracture,* **11:2**, 283-294.

Heywood R.B. (1952). *Designing by Photoelasticity*. Chapman and Hall, New York.

Howland R.C.J. (1929). On the stresses in the neighborhood of a circular hole in a strip under tension. *Phil. Trans. Roy. Soc. (Lon),* **A 229**, 67.

Kanninen J. and Popelar J. (1987). *Advanced Fracture Mechanics.* Pergamon, Oxford.

Murakami Y. (1997). *Stress Intensity Factors Handbook*, Vol. 1-3, Pergamon, Oxford.

Peterson R.E. (1974). *Stress concentration factors*. Wiley, New York.

Rooke D.P., Cartwright D.J. (1976). *Compendium of Stress Intensity Factors*. Her Majesty's Stationery Office, London.

Tada H., Paris P.C., Irwin, G.R. (1985). *The Stress Analysis of Cracks Handbook*, 2nd Edition, Del Research, St. Louis.

Theocaris P.S. (1956). The stress distribution in a strip loaded in tension by means of a central pin. *Journal of Applied Mechanics ASME* 78.

www.EngineeringEBooksPdf.com

Advances in Steel Structures, Vol. II
Chan, Teng and Chung (Eds.)
© 2002 Elsevier Science Ltd. All rights reserved.

A METHOD TO ESTIMATE P-S-N CURVE OF WELDED JOINTS UNDER GENERAL STRESS RATIO

Guan Deqing[1,2], Yi Weijian[1] and Wang Qi[2]

[1] School of Civil Engineering, Hunan University,
Changsha, 410082,China
[2] Department of Power Engineering, Changsha University of Electric Power,
Changsha, 410077, China

ABSTRACT

It is taken account of the effects of material properties, type of loading, geometric shape, stress ratio, residual stress in notch root of welded joints on the fatigue strength respectively. By means of the concept of the worst-case notch and an estimating formula of effective stress concentration factor, based on two groups of the fatigue experimental results under high stress level, a predicting method of the fatigue life curve with arbitrary survival rate under general stress ratio for welded joints is presented. P-S-N curves of six types of welded joints under general stress ratio have been successfully estimated. It may be decreased greatly fatigue experiments to obtain P-S-N curves of welded joints with the method.

KEYWORDS

Fatigue strength, Fatigue life curve, Survival rate, Fatigue notch factor, Effective stress concentration factor, General stress ratio, Welded joint

INTRODUCTION

Fatigue is a principal mode of failure for welded structures under cyclic loads. In the assessment of the fatigue life one of the important relations is the fatigue life curve with survival rate (P-S-N curve), which is generally obtained from experiments (Maddox S J.,1991). However, the P-S-N curve will be

www.EngineeringEBooksPdf.com

time-consuming and costly from the fatigue tests. Therefore to develop a predicting method of the P-S-N curve for welded joints will certainly be useful in engineering application and helpful in gaining economic efficiency (Guan Deqing, 1996). Adopted the worst-case notch concept of welded joints (Yung J.Y. and Lawrence F.V., 1985), assuming that the slope of the fatigue life curve with arbitrary survival rate of misaligned welded joints remains constant, an estimating method of P-S-N curve for misaligned welded joints was developed (Guan Deqing, 1999). The method is efficient for estimating the fatigue life curve with survival rate of misaligned welded joints under symmetrical cyclic loading. In the paper, we take account of many influencing factors on fatigue strength such as material properties, type of loading, geometric shape, stress ratio and residual stress respectively. By means of Peterson's fatigue notch factor equation and the worst-case fatigue notch concept, using the predicting formula of the effective stress concentration factor and the estimating model of P-S-N curve for survival rate p=50% for welded joints under general stress ratio (Guan Deqing, 1997), adding two groups of the fatigue experiments under high stress level, a prediction method of the fatigue life curve with arbitrary survival rate under general stress ratio for welded joints is presented. The P-S-N curves of four groups of misaligned welded joints and "T" type of welded plate joint and welded cruciform joint have been successfully predicted.

EFFECTIVE STRESS CONCENTRATION FACTOR UNDER GENERAL STRESS RATIO

The fatigue notch factor K_f may be determined from long life fatigue tests as the ratio of unnotched to notched fatigue strength or may be calculated by Peterson's Eqn. 1

$$K_f = 1 + \frac{K_t - 1}{1 + \frac{a}{r}} \tag{1}$$

where K_t is elastic stress concentration factor. r is notch root radius. a is Peterson's material parameter. A general form K_t of welds is

$$K_t = A + B\left(\frac{t}{r}\right)^{\lambda} \tag{2}$$

where A, B, λ are constants, whose values are determined by geometric shape of welds and the types of loading. t and r are the thickness of the plate and notch root radius. The constants A and λ are usually 1 and 0.5 respectively. When the worst-case notch concept is adopted, we have

$$K_{fm} = 1 + \frac{B}{2}\sqrt{\frac{t}{a}} \tag{3}$$

where K_{fm} is the maximum value of K_f.

A definition is introduced that the effective stress concentration factor β_R is the ratio between the fatigue endurance limit σ_R of the smooth specimen and that of a welded joint σ_{RW} when the stress

www.EngineeringEBooksPdf.com

ratio is R. Where R is ratio between the minimum cyclic stress σ_{min} and the maximum cyclic stress σ_{max}.

$$\beta_R = \frac{\sigma_R}{\sigma_{RW}} \tag{4}$$

According to the paper (Guan Deqing, 1997), an estimating relationship between β_R and K_{fm} is

$$\beta_R = \frac{K_{fm} + \frac{1+R}{1-R}(2N_L)^b}{1+\frac{1+R}{1-R}(2N_L)^b} \cdot \frac{\sigma_f'}{\sigma_f' - \sigma_r} \tag{5}$$

where σ_f' is the fatigue strength coefficient. b is the fatigue strength exponent. σ_r is residual stress in the notch root of welded joint. N_L is the fatigue life corresponding to the fatigue endurance limit. Usually N_L may be chosen 2×10^6 for welds. The effects of material properties, type of loading, geometric shape, stress ratio, residual stress in welded joint on fatigue strength are considered in the relationship.

PREDICTING MODEL OF S-N CURVE UNDER GENERAL STRESS RATIO

The equation of fatigue life curve (S-N curve) for the middle cyclic number range when survival rate is 50% can be expressed as follows

$$\lg N = C - m \lg \sigma_a \tag{6}$$

where N is the fatigue life. σ_a is stress amplitude. C is intercept of the fatigue life curve. m may be regarded as the slope of the fatigue life curve. Based on experimental S-N curves of welded joints (Guan Deqing, 1996), we may assume as follows: when R=constant, all fatigue life curves under general stress ratio for different types of welded joints and different β_R values intercross at the same point in the low cyclic number range.

On the basis of the assumption, m and C in Eqn. 6 are functions of β_R and R. As long as m and C are determined, the fatigue life curves for survival rate p=50% can be obtained. According to the principle, two equations were given (Guan Deqing, 1997) as follow

$$m = \frac{1}{-b + 0.2776\lg\beta_R + 0.2776\lg\dfrac{1+\frac{1+R}{1-R}(4\times10^6)^b}{1+\frac{1+R}{1-R}(1\times10^3)^b}} \tag{7}$$

www.EngineeringEBooksPdf.com

$$C = 6.301 + m \lg \frac{\sigma_f^{'} (4\times10^6)^b}{\left[1+\frac{1+R}{1-R}\left(4\times10^6\right)^b\right]\beta_R} \tag{8}$$

By means of Eqns. 3, 5, 7, 8, we may estimate the fatigue life curve when survival rate is 50% under general stress ratio for welded joints.

ESTIMATION OF P-S-N CURVE UNDER GENERAL STRESS RATIO

The fatigue life curve with arbitrary survival rate (P-S-N curve) under general stress ratio for welded joints may be expressed as Eqn.9.

$$\lg N_p = C_p - m_p \lg \sigma_a \tag{9}$$

where N_p is fatigue life for arbitrary survival rate p; C_p, m_p are constants related to survival rate p.

The relationship between mean square deviation of logarithmic fatigue life and stress amplitude has been verified by a lot of fatigue tests as follows

$$S(\sigma_a) = C_0 - m_0 \lg \sigma_a \tag{10}$$

here C_0 and m_0 are constants. $S(\sigma_a)$ may be calculated from experimental results.

$$S(\sigma_a) = \sqrt{\frac{\sum_{i=1}^{n}(\lg N_i)^2 - \frac{1}{n}\left(\sum_{i=1}^{n}\lg N_i\right)^2}{n-1}} \tag{11}$$

where N_i is fatigue life for specimen number i. n is number of specimen.

We assume that logarithmic fatigue life under determining stress level agrees with normal distribution. Therefore

$$\lg N_p = \lg N + \mu_p S(\sigma_a) \tag{12}$$

where μ_p is standard normal deviation rated to survival rate p. Two relationships can be obtained from Eqns. 6, 9, 10 and 12.

$$m_p = m + m_0 \mu_p \tag{13}$$

$$C_p = C + C_0 \mu_p \tag{14}$$

here m and C may be calculated from Eqn. 7 and Eqn. 8 respectively.

www.EngineeringEBooksPdf.com

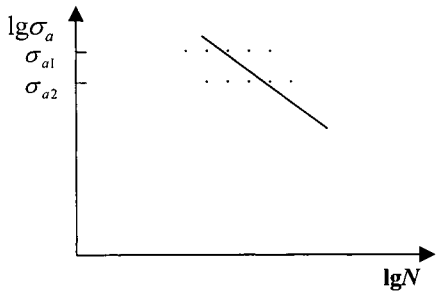

Figure 1: Arrangement of specimens

In order to determine m_0 and C_0, we may add two groups of the fatigue experiments at high stress level. Specimens may be arranged as shown in figure 1. According to the requirements of believable degree and relating error, the number of minimum specimens is chosen. Substituting stress amplitude σ_{a1} and σ_{a2} into Eqn. 10 respectively, we can obtain the mean square deviations of logarithmic fatigue life as follow

$$S(\sigma_{a1}) = C_0 - m_0 \lg \sigma_{a1} \tag{15}$$

$$S(\sigma_{a2}) = C_0 - m_0 \lg \sigma_{a2} \tag{16}$$

The expressions of m_0 and C_0 can be derived from Eqn. 15 and Eqn. 16.

$$m_0 = \frac{S(\sigma_{a2}) - S(\sigma_{a1})}{\lg \sigma_{a1} - \lg \sigma_{a2}} \tag{17}$$

$$C_0 = S(\sigma_{a1}) + \frac{S(\sigma_{a2}) - S(\sigma_{a1})}{\lg \sigma_{a1} - \lg \sigma_{a2}} \lg \sigma_{a1} \tag{18}$$

By means of the results of adding two groups of fatigue tests, $S(\sigma_{a1})$ and $S(\sigma_{a2})$ may be calculated through Eqn. 11. Using Eqn. 17 and Eqn. 18, m_0 and C_0 may be obtained. m_p and C_p can be estimated from Eqn. 13 and Eqn. 14 for determining survival rate. So we may predict the P-S-N curve with arbitrary survival rate under general stress ratio for welded joints. Because the fatigue life is shortly at high stress level, the adding fatigue tests can be accomplished conveniently.

COMPARISON OF PREDICTIONS WITH EXPERIMENTS

To investigate the exactness of the prediction method, we predict P-S-N curves of four groups of misaligned welded joints (misalignment δ=0.15, 0.30, 0.60, 1.08mm) in figure 2 and "T" type of welded plate joint as shown in figure 3 and cruciform welded plate joint as shown in figure 4. Comparison of experiments with predictions has been accomplished.

www.EngineeringEBooksPdf.com

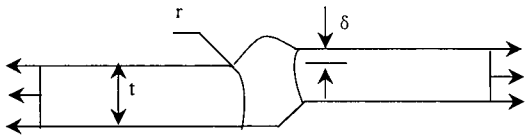

Figure 2: Misaligned welded joint

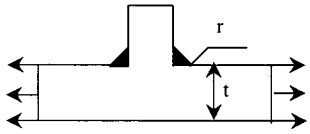

Figure 3: "T" type of welded plate joint

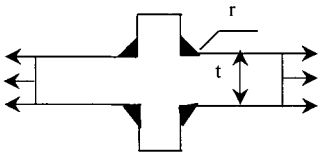

Figure 4: Cruciform welded plate joint

A few of formulae of elastic stress concentration factor have been obtained from three-dimension finite element method (Guan Deqing, 1996) as follow

For misaligned welded joint

$$K_t = 1 + [0.27 + 2.45(\frac{\delta}{t})^{1.13}](\frac{t}{r})^{0.5} \tag{19}$$

For "T" type of welded plate joint

$$K_t = 1 + 0.272\left(\frac{t}{r}\right)^{0.5} \tag{20}$$

For cruciform welded plate joint

$$K_t = 1 + 0.35\left(\frac{t}{r}\right)^{0.5} \tag{21}$$

The fatigue experiments of misaligned welded joints and "T" type of welded plate joint and cruciform welded plate joint made of low alloy structural steel have been carried out. Material mechanical properties are ultimate strength Su=548MPa, yield strength σ_s=441MPa. The material constant and other data are σ_f' = 894MPa, a = 0.361 mm, b = –0.0854, σ_r = 441MPa, t=4mm, misalignment δ=0.15, 0.30, 0.60, 1.08mm, respectively. R=0.2 for "T" type of welded plate joint and cruciform welded plate joint and R=0.08 for misaligned welded joints.

According to Eqn. 7 and Eqn. 8, m and C of six types of welded joints are estimated. For misaligned welded joints, adding two groups of the fatigue tests at stress amplitude σ_a = 190MPa and σ_a = 200 MPa respectively. For "T" type of welded plate joint and cruciform welded plate joint, at stress

www.EngineeringEBooksPdf.com

amplitude σ_a = 110MPa and σ_a =120MPa to add two groups of tests, respectively. Number of each group specimens is seven. By means of Eqn. 11, Eqn. 17 and Eqn. 18, m_0 and C_0 of experiments are obtained. According to the survival rate to be demanded, adopted Eqn. 13 and Eqn. 14, m_p and C_p are calculated. Standard normal deviation μ_p is −1.645 for survival rate p = 95%, and μ_p is −3.091 for p = 99.9 %. Experimental and predicting results of misaligned welded joints and "T" type of welded plate joint and cruciform welded plate joint are located in Table 1.

TABLE 1

m_p AND C_p OF ESTIMATIONS WITH EXPERIMENTS

Type of welded joint	p	m_p (test)	C_p (test)	m_p (estimation)	C_p (estimation)
Misaligned welded joint (δ =0.15mm)	95%	4.36	13.57	4.49	14.32
	99.9 %	4.02	13.06	4.40	13.49
Misaligned welded joint (δ =0.30mm)	95%	4.04	13.70	4.32	14.01
	99.9 %	4.02	13.42	4.28	13.75
Misaligned welded joint (δ =0.60mm)	95%	4.01	13.01	4.05	13.46
	99.9 %	4.00	12.76	4.02	13.19
Misaligned welded joint (δ =1.08mm)	95%	3.76	12.66	3.59	12.42
	99.9 %	3.47	12.40	3.44	12.23
"T" type of welded plate joint	95%	5.56	14.98	5.90	15.90
	99.9 %	5.54	15.61	5.86	15.82
Cruciform welded plate joint	95%	5.59	15.32	5.61	16.02
	99.9 %	5.56	15.16	5.59	15.79

It can be shown that the predicted m_p and C_p for six types of welded joints are in agreement with the experimental results from Table 1. So we may predict P-S-N curve of welded joint with the method.

CONCLUSIONS

A method to predict the fatigue life curve with arbitrary survival rate under general stress ratio for welded joints is developed. The expressions of m_p and C_p in the equation of P-S-N curve have been obtained respectively. m_p and C_p are related to effective stress concentration factor, β_R, stress ratio, R, and standard normal deviation, μ_p. The effects of many factors such as material properties, type of loading, geometric shape, stress ratio, residual stress in welded joint on fatigue strength are considered in the method. Although two groups of fatigue experimental results is required with the method, it's

www.EngineeringEBooksPdf.com

consuming will be minority on account of the tests are accomplished at high stress level. A few of good examples of the P-S-N curves with different survival rate for misaligned welded joints and "T" type of welded plate joint and cruciform welded plate joint have been presented. It can be greatly decreased fatigue tests to obtain P-S-N curve of welded joints with the predicting method.

ACKNOWLEDGEMENT

The authors gratefully acknowledge the research support for this work provided by Provincial Natural Science Fund of Hunan, China.

REFERENCES

Maddox S. J. (1991). *Fatigue Strength of Welded Structures* (*second edition*), Abington Publishing, Cambridge, UK

Guan Deqing. (1996). *Fatigue Fracture and Life Prediction of Welded Structures*, Hunan University Press, Hunan, China

Yung J.Y. and Lawrence F.V.(1985). Analytical and graphical aids for the fatigue design weldments, *Fatigue & Fracture of Engineering Material & Structure* **8:3,** 223-241.

Guan Deqing. (1999). A method to estimate P-S-N curve for misaligned welded joints, *Advances in Steel Structures* **2:** 999-1004, edited by Chan S. L. and Teng J. G., Elsevier Science Ltd Publishing

Guan Deqing. (1997). An estimating method of fatigue strength for welded joint under general stress ratio, *Chinese Journal of Applied Mechanics* **14:1,** 54-59.

Peterson R.E. (1974). *Stress Concentration Factor*, John Wiley and Sons, New York

Fuchs H. O. and Stephens R. I. (1980). *Metal Fatigue in Engineering*, John Wiley & Sons, New York

Guan Deqing. (1996). A method of predicting the fatigue life curve for misaligned welded joints, *International Journal of Fatigue* **18:4,** 221-226.

www.EngineeringEBooksPdf.com

Advances in Steel Structures, Vol. II
Chan, Teng and Chung (Eds.)
© 2002 Elsevier Science Ltd. All rights reserved.

FATIGUE CRACK PROPAGATION OF TUBULAR T-JOINTS UNDER COMBINED LOADS

S.P. Chiew, S.T. Lie & Z.W. Huang

School of Civil and Environmental Engineering
Nanyang Technological University, Singapore

ABSTRACT

Experimental fatigue studies are conducted on three identical steel tubular T-joints subjected to in-plane bending (IPB), combination of IPB and out-of-plane bending (OPB) and combination of axial loading (AX), IPB and OPB respectively. The fatigue performances of the joints subjected to these basic and combined load cases are investigated, and the Alternating Current Potential Drop (ACFD) technique is used to monitor their joint crack growth and crack shape developments. The test results confirmed that the tubular joint fatigue design S-N curve which is based on single axis test data is still valid for T-joints subjected to combined load cases. The specimens are also simulated numerically using a modelling procedure which can include a semi-elliptical surface crack located at any position and any length along its brace-chord intersection within the joint finite element model. The numerical results are validated against those obtained from experiments using the Paris' law equations. Good agreement between these results confirmed that the proposed modelling procedure is reliable and appropriate for fracture mechanics analysis.

INTRODUCTION

Fatigue failure is the most important failure mode for offshore steel jacket structures. The fatigue crack is always initiated at the weld toe of the brace to chord joint intersection areas where high level stress concentrations are induced due to structural discontinuity. Some test programs (e.g. ECSC research programs) have been conducted to provide a database of tubular joint fatigue test results which were used to produce a set of fatigue life design curves (S-N curves). These fatigue curves have now been included in many important international design codes. However, most of these curves were based on fatigue tests conducted on joints subjected to only basic load case, and the crack is always located either around the crown or saddle location. In reality, the cracks may be located anywhere around the brace and chord intersection due to the fact that loadings are usually multi-axes in practice. Hence, there is a need to investigate further the fatigue behavior of tubular joints subjected to multi-axes loadings. In addition, the S-N curves can only give the total fatigue life of a tubular joint; they cannot be used when crack is detected in service in a tubular joint because they do not give any further information on the crack propagation phase. Consequently, fracture mechanics method is often used to assess the joint component with crack-like defect. It can estimate the crack propagation behavior and

www.EngineeringEBooksPdf.com

used a fundamental parameter, the stress intensity factor (SIF), for analyses. Many researchers have proposed some models based on the finite element method to determine the SIF of the cracked joints. However, because of the complex geometry and loading conditions, the accurate numerical modelling of the tubular joint with a crack is still an extremely difficult task.

In this paper, three identical tubular T-joints subjected to IPB, combination of IPB and OPB and combination of AX, IPB and OPB respectively are tested to failure. The crack shape development is monitored throughout the tests using the Alternating Current Potential Drop (ACPD) technique. A systematic FE modeling procedure for cracked tubular T-joints is also presented. The joint can contain a crack which can be of any arbitrary length and located at any position along the weld toe between the brace and the chord member. This way of modelling is appropriate for joint fatigue analysis when the crack shifts from crown or saddle location. The experimental results were then used to validate the numerical results and the UK DEn (1993) tubular joint fatigue design S-N curve.

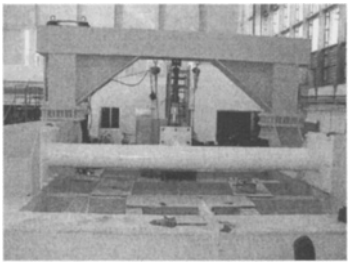

Fig. 1 General View of Test Rig

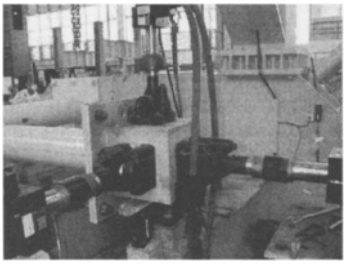

Fig. 2 The Three Actuators

EXPERIMENTAL INVESTIGATION

Test Rig and Load System

A test rig is designed specifically for the T-joints subjected to AX, IPB, OPB and any combinations of these three basic load cases as shown in Fig. 1. The rig is capable of applying static loads to determine the hot spot stress (HSS) distributions in the joint as well as cyclic loads to study its fatigue life and fracture behavior. Three actuators are used to apply loads along three mutually perpendicular axes as illustrated in Fig. 2. The actuators can be operated individually or concurrently to effect a multi-axes load condition. Each chord end of the joint specimen is mounted on the rig using eight bolts creating a fixed condition at the chord end. In the experimental tests, a sufficiently long chord greater than 6 chord diameters is used to ensure that the stresses at the brace/chord intersection are not affected by the end conditions.

Specimen Details

The three identical T-joint specimens were fabricated from API 5L Grade B steel pipe sections. The dimensions and geometric ratios of the joints are given in Fig. 3. The mechanical properties of the steel are: yield strength is 302MPa, ultimate strength is 493MPa and the elongation is 32.3%. The weld profile and the specimen preparation were carried out in accordance with the American Welding Society Codes D1.1-96 (1996) specifications. The ultrasonic technique is used to confirm the weld quality and compliance with standard specifications.

www.EngineeringEBooksPdf.com

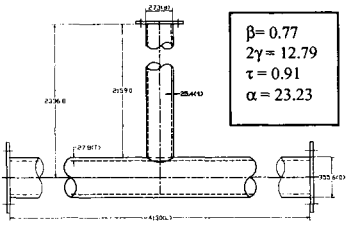

Fig. 3 Specimen Dimensions and Geometrical Ratios

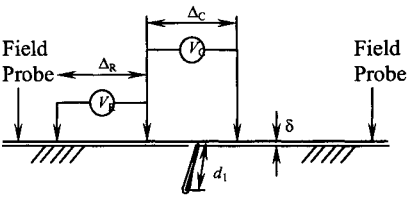

Fig. 4 The ACPD Theory and Notation

Fatigue Test

Alternating Current Potential Drop (ACPD) Technique

ACPD technique is used to monitor the shape and depth of the growing fatigue cracks on the specimens in the fatigue tests. This technique utilizes the so-called "skin effect" whereby a high frequency alternating current is confined to a thin layer when flowing through ferrous materials as shown in Fig. 4. In the Fig. 4, V_C is the cross-crack potential drop, V_R is the potential drop adjacent to reference-crack, Δ_C and Δ_R are probe spacing, and d_1 is the one dimension crack depth.

If an alternating current is forced to flow across a surface-breaking defect, the current will flow down one crack face and up the other side. Since a linear potential gradient is assumed to exist on the metal surface and on the crack faces, measurement of the potential drop across the crack and adjacent to the crack allows the calculation of the one dimension crack depth as follows:

$$d_1 = (\Delta_R/2)\{V_C/V_R - \Delta_C/\Delta_R\} \tag{1}$$

A modification factor can be used to correct the crack depth for the real situation. Fatigue cracks in tubular joints have been found in practice to maintain a low aspect ratio, often with $d_1/2c \approx 0.1$. The modification factors have been shown to be less than 1.05 for cracks of this shape and hence the d_1 estimate can be used without any modification.

Test Conditions and Load Applications

Three identical specimens are tested in room ambient temperature under a constant amplitude cyclic loading. The three servo-hydraulic actuators shown in Fig. 2 are used to apply the fatigue, i.e. Actuator 1 with 25 ton capacity for axial loading, Actuator 2 with 25 ton capacity for IPB and Actuator 3 with 10 ton capacity for OPB. A tension loading is defined as positive and a compression is defined as negative loading for all the actuators. The actuators loadings can be controlled by the RS Console software developed for the Instron Labtronic 8800 digital controller. The actual cyclic loadings applied to the three specimens are given in Figs. 5-7. Actual nominal stresses caused by cyclic loadings are calculated using 4 midway brace member strain gauges readings and are also tabulated in Table 1. During the tests, all the actuators were under load control.

www.EngineeringEBooksPdf.com

Table 1. Actual Nominal Stresses caused by Cyclic Loading

	Specimen 1		Specimen 2		Specimen 3	
	σ_{max}	σ_{min}	σ_{max}	σ_{min}	σ_{max}	σ_{min}
AX	0	0	0	0	5.41	0
IPB	36.75	0	36.53	0	16.37	0
OPB	0	0	0	-22.78	0	-7.24

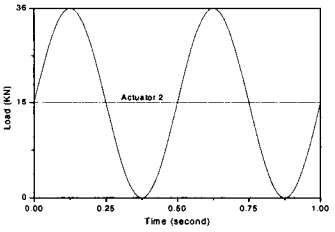

Fig. 5 Cyclic Load applied to Specimen 1

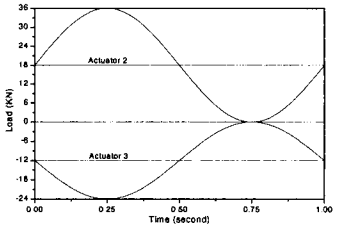

Fig. 6 Cyclic Load applied to Specimen 2

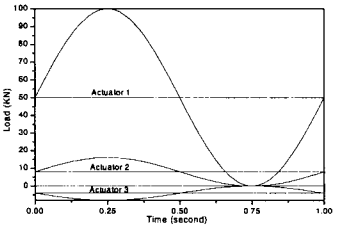

Fig. 7 Cyclic Load applied to Specimen 3

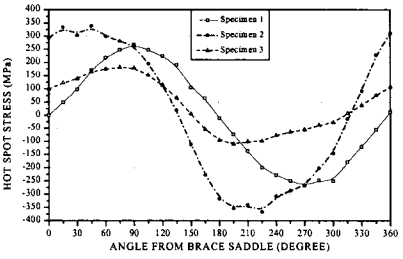

Fig. 8 HSS Distribution around the Chord

Crack Growth Monitoring

The fatigue crack development in the tubular joints is monitored by taking the ACPD crack depth measurements at fixed points around each expected crack location. Thus, the positioning of the fixed ACPD Probes requires careful consideration in order to capture the data. Crack growth is expected to initiate at the peak HSS location and the deepest point of the crack is expected to remain in this region. Therefore, the probes should be concentrated around this region to obtain meaningful results.

Based on the loadings applied, the superposition method was used to determine the peak HSS positions in each specimen by using the stress concentration factor (SCF) distributions obtained from the static tests which were carried out before the fatigue tests. The stress distributions on the chords of each specimen under these applied loadings are shown in Fig. 8. In specimen 1 and specimen 3, it can be seen that both their peak HSS are located near to the crown of the chord. In specimen 2, the peak HSS location shifts from the crown or saddle of the joint and is located at almost 45° between the crown and saddle. The ACPD probes are then fixed around these locations. Figure 9 shows the probe positions for Specimens 1 and 3 while Fig. 10 shows those of Specimen 2.

www.EngineeringEBooksPdf.com

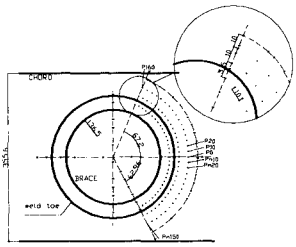

Fig. 9 A Plan View of the ACPD Probes Location in Specimens 1 and 3

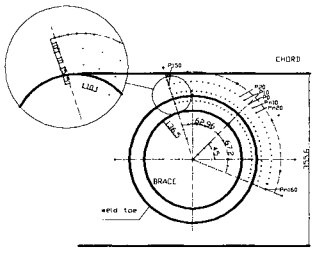

Fig. 10 A Plan View of the ACPD Probes Location in Specimen 2

All the probes are connected to a crack microgauge equipment called U10. This U10 is a modular and portable equipment utilising the ACPD technique to detect the size of defects. The U10 was then connected to a computer and is controlled by the Flair software, which is written specifically for use with U10 to provide automated instrument control, data storage facilities and dedicated graphical output under the PC WINDOWS environment. During the test, the interval of crack scanning is set to 500 seconds, and the test and scanning automatically stop when the crack has penetrated the crack depth set by Flair software.

Fatigue Test Results

A FORTRAN program had been written to analyze the ACPD raw crack depth readings, and subtract the initial crack depth readings on the uncracked joints from all the scans. The ACPD crack development plots of the three specimens are shown in Figs. 11 to 13. In order to visually compare the crack shape with the ACPD measurement, the joints were split into two parts along the crack surface after the tests. These typical crack surfaces of the three specimens are shown in Figs. 14 to 16.

It can be seen clearly that in Specimen 1, several small cracks first initiated and then coalesced one by one. In the depth direction, the position Pn20 (refer to Fig. 9) kept the deepest position during the crack propagation. In the width direction, the propagation appeared to be a process of small crack coalescing, and hence this has resulted in the propagation rate in this direction to be discontinuous. The same situation is also found in both Specimens 2 and 3. However, the crack propagation in Specimen 2 is somewhat peculiar. Several small cracks first initiated and then coalesced into two main cracks at position around Pn70 and P50 (refer to Fig. 10), but then they appeared to be propagating independently. The sites near the peak HSS position at P0 (please refer to Fig. 10) always could not become the deepest position of the crack according to the ACPD readings. This problem was only discovered after the joint is torn out and the crack surface visually examined. The reason why these two cracks propagating to the position near site P0 (refer to Fig. 10) could not meet together is because they are located at different layers as shown in the marked area in Fig. 15, and this affected the ACPD readings of the crack depth near this position. The two main cracks all stopped there and did not propagate continuously in this direction. This may be due to the existence of another crack. Two cracks propagating independently may be the reason why the crack length in this specimen is also very long. Another interesting point to note about the crack surface is the actual deepest point of crack is almost near the position P0 (refer to Fig. 10) even though the crack had penetrated the chord wall first at position P50 (refer to Fig.10) according to the ACPD readings. The crack propagation in Specimen 3 is the same as that in Specimen 1. Several small cracks initiated first and then jointed together, but the deepest position of the crack shifted between Pn10 and P20 (refer to Fig. 9) during the crack propagation.

www.EngineeringEBooksPdf.com

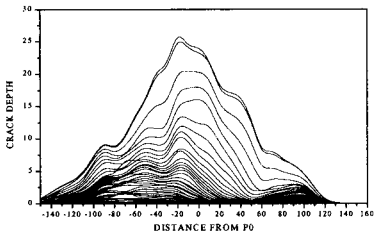

Fig. 11 ACPD Crack Shape Development in Specimen 1

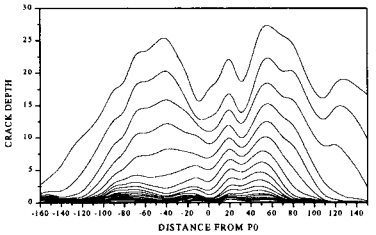

Fig. 12 ACPD Crack Shape Development in Specimen 2

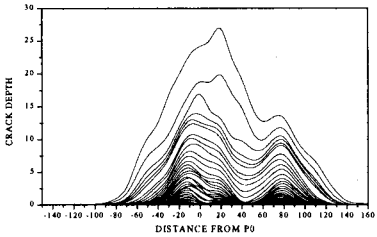

Fig. 13 ACPD Crack Shape Development in Specimen 3

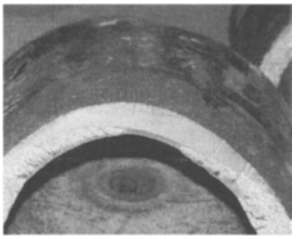

Fig. 14 Crack Surface of Specimen 1

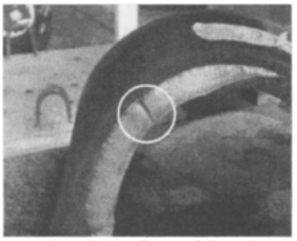

Fig. 15 Crack Surface of Specimen 2

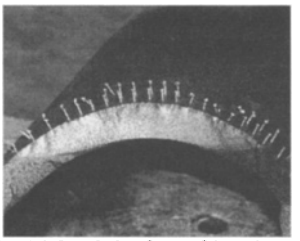

Fig. 16 Crack Surface of Specimen 3

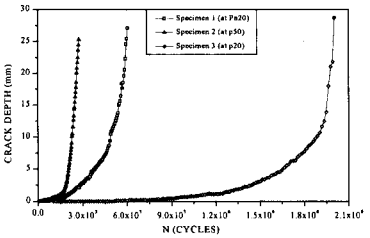

Fig. 17 Crack Growth Curves

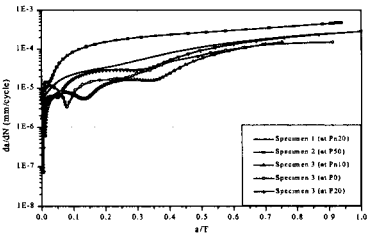

Fig. 18 Crack Growth Rates

The crack growth curves at these positions where the cracks penetrated the chord wall first according to the ACPD readings are plotted in Fig. 17 for the 3 specimens. The crack growth rates of these deepest points are also shown in Fig. 18. Figure 19 shows the plot of the fatigue design S-N curve (Zhao et al. 2000) for a thickness of 27.8 mm, and also the fatigue life of the three specimens. It can

www.EngineeringEBooksPdf.com

be seen that the design S-N curve is still valid for T-joints subjected to multi-axes loadings and for crack position not initiating at either the crown or saddle location.

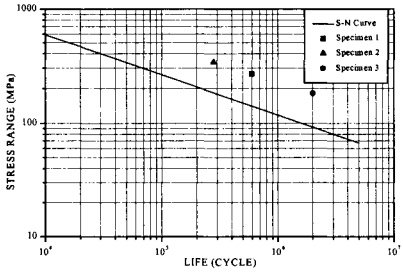

Fig. 19 S-N Test Data

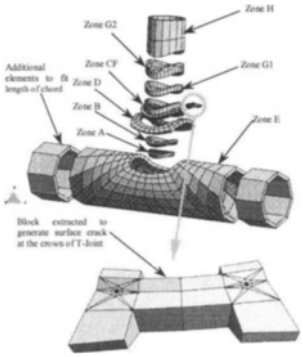

Fig. 20 Mesh Generation for T-Joint with Surface Crack

NUMERICAL MODELLING OF T-JOINT WITH SURFACE CRACK

In order to generate geometrical model that could be used in the analysis of a wide range of tubular joints, an automatic geometrical modelling technique for generic cracked Y- and T-joints is first developed. The intersecting angle of the joint can range from 30° to 90° and the welding details along the brace-chord intersection are compatible with the AWS (1996). Furthermore, the joint can contain semi-elliptical surface cracks which can be of arbitrary length and located at any position along the weld toe between the brace and the chord. The modelling procedure can be divided into two major steps. They are, namely, the modelling of brace-chord intersection and welding details and the definitions of surface cracks. Details of this modelling procedure have been reported earlier in details by the authors (Lie et al. 2000 and Chiew et al. 2001).

Based on the geometrical modelling of the cracked T-joints, the mesh model of the joints can be generated. In the mesh generation, the T-joints model is sub-divided into distinct zones as shown in Fig. 20. Each of these zones consists of different density element. In the far field (Zones A, E and H), only one layer of 3D elements will be employed. Finer meshes with more than one layer of elements will be generated near the intersection (Zone CF) of the joint to capture the stress concentration near the intersection. Between the refined regions and the far field regions, transitions regions (Zones B, D & G1) are used to connect them. When generating FE mesh for surface crack, part of the sub-mesh in Zone CF will be extracted, and a combination of tetrahedral, hexahedral, prism and pyramid elements are used to model the crack in this blocks of elements. After this block of elements is generated, it will then be merged to the mesh in Zone CF.

EVALUATION OF STRESS INTENSITY FACTORS

After the mesh model is generated and analyzed using the ABAQUS (2001) program, the SIF of the crack can be evaluated. There are several well-established procedures for this purpose, for example, the commonly used J-integral method and the method of displacement extrapolation used by Chong Rhee et al. (1991) and Bowness and Lee (1995). In this paper, another method called the interaction integral method which is provided by ABAQUS (2001) is used to extract the individual SIFs directly

www.EngineeringEBooksPdf.com

for a crack under the mixed mode loading conditions. This method is based on the work by Shih and Asaro (1988), and it has the advantage of being rather insensitive to mesh refinement and can be applied easily under the mixed mode situations. Detailed derivations of the equations for this method can be found in the ABAQUS (2001) manuals and Shih and Asaro (1988).

COMPARISONS OF EXPERIMENTAL AND NUMERICAL RESULTS

The above proposed mesh generation technique is used to produce the FE models for the specimens tested earlier. The geometry and the material properties of the numerical models are exactly the same as those of the test specimens. The crack profiles, the loading conditions of the models are all based on the information obtained from the specimens and experimental settings as shown in Table 2. The meaning of α_1, α_2 and α_m is explained in Fig. 21, a/t_c is the ratio of crack depth to chord thickness, c is the half-length of semi-elliptical crack, and the applied loadings are obtained from the readings of strain gauge on the brace directly. $\alpha_1$and α_2 are determined by the crack length and the crack location. The crack deepest point position α_m is located at the middle of α_1 and α_2 because the semi-elliptical shape was used to model the crack surface. During the analysis, the boundary conditions are that two ends of the chord are fixed rigidly, and the end of the brace is free. The contact surfaces using the master and slave arrangements within ABAQUS are also defined on the crack surfaces.

Table 2. FE Models Generated for Comparison with Experimental Results

Specimen	Crack	Crack Locations		Crack Deepest Point Position	a/t_c	c (mm)	Loading (kN)		
		α_1	α_2	α_m			F1	F2	F3
FE models for Specimen 1	Crack 1	-41.3	55.3	7.0°	0.20	132.0	0	0	-38.2
	Crack 2	-42.3	56.3	7.0°	0.34	135.0			
	Crack 3	-44.1	58.1	7.0°	0.49	140.0			
	Crack 4	-45.8	59.9	7.0°	0.66	145.0			
	Crack 5	-46.9	61.0	7.0°	0.80	148.0			
FE models for Specimen 2	Crack 1	-98.1	0.9	-49.5°	0.20	133.5	0	23.7	-37.9
	Crack 2	-105.8	7.4	-56.6°	0.35	152.0			
	Crack 3	-106.6	8.6	-57.6°	0.52	154.5			
	Crack 4	-107.3	12.4	-59.9°	0.64	160.5			
	Crack 5	-108.8	21.7	-65.3°	0.79	175.0			
FE models for Specimen 3	Crack 1	-38.8	20.8	-9.0°	0.27	80.0	106.8	7.5	-17.0
	Crack 2	-44.1	26.3	-8.9°	0.35	95.0			
	Crack 3	-47.6	31.7	-7.9°	0.5	107.5			
	Crack 4	-49.3	33.5	-7.9°	0.65	112.5			
	Crack 5	-56.3	38.8	-8.8°	0.80	130.0			

No contact problem was found in these models summarized in Table 2. The SIFs (K_I, K_{II} and K_{III}) are then obtained from the ABAQUS (2001) output file. It is noted that these results are the average values of the results from the different contours except that from the first contour abutting the crack tip because numerical tests have shown that this contour cannot provide highly accurate results (ABAQUS, 2001). For the sake of comparison, the K_I, K_{II} and K_{III} from numerical analyses are combined together and represented by an equivalent SIF called K_e, which is assumed as a crack driving force parameter for a mixed mode fracture problem (Chong Rhee et al., 1991). The relationship between K_e and K_I, K_{II}, K_{III} is

www.EngineeringEBooksPdf.com

$$K_e = [K_I^2 + K_{II}^2 + K_{III}^2/(1-\nu)]^{1/2} \quad (2)$$

where ν is Poisson's ratio. The experimental results were also converted to SIFs by using Paris' law,

$$da/dN = C(\Delta K)^m \quad (3)$$

where da/dN is crack growth rate which can be obtained from the experimental rests, ΔK is the range of SIFs, C and m are the material constants, and $C = 1.45\times10^{-11}$(m/cycle)(MPa*m$^{1/2}$)$^{-2.75}$ and m = 2.75 which are provided by material supplier, are used in this study.

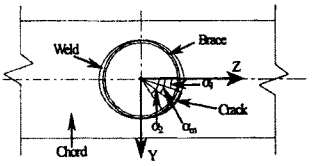

Fig. 21 Location of the Surface Crack

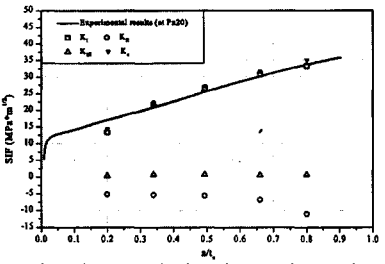

Fig. 22 Numerical and Experimental Results of Specimen 1

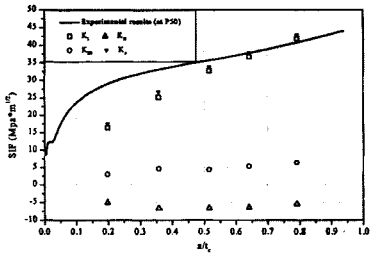

Fig. 23 Numerical and Experimental Results of Specimen 2

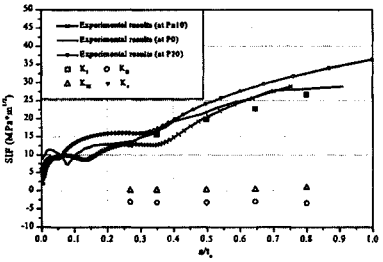

Fig. 24 Numerical and Experimental Results of Specimen 3

The comparisons of the numerical and experimental results are shown in Figs. 22 to 24. The positions Pn20 in Fig. 22 and the positions Pn10, P0 and P20 in Fig. 24 are illustrated clearly in Fig. 9. The position P50 in Fig. 23 can be found in Fig. 10. It can be seen from Fig. 22, the numerical SIF results at the deepest position agree well with the experimental results at position Pn20 in Specimen 1. In Specimen 2, as a result of the problem of the two cracks first initialized and developed independently at position Pn 70 (refer to Fig. 10) and P50, and did not coalesce together when they propagated at the position near P0, the ACPD data are not accurate near this position. Thus, the experimental results at the P50, where the crack first penetrated the chord wall according to the ACPD readings, are used in the model. Also, in the numerical model of this specimen, the length of crack covers these two cracks. The numerical SIFs at the same position as P50 in the crack model are calculated and compared with the experimental results in Fig. 23. It can be seen that in the small crack depth, the numerical results are lower than the experimental results. However, when the crack depth is large enough, the numerical results agree well with the experimental results. In Specimen 3, the numerical SIF results at the deepest position are compared with the experimental results in Fig. 24. The numerical results still agree well with the experimental results, especially the results at position P0. The comparisons show

www.EngineeringEBooksPdf.com

that the proposed mesh generation technique proposed in this paper is appropriate for fracture mechanics analysis of cracked tubular joints.

CONCLUSIONS

Three identical tubular T-joints are tested to failure under basic and combined loads. The ACPD technique is used to monitor and record the detail information of the crack propagation in the tubular T-joints. The S-N test data obtained from the experimental tests showed that the UK DEn tubular joint fatigue design S-N curve (Zhao et al. 2000) can still be used safely to predict the total fatigue life of the T-joints under combined loads even though the crack had shifted from the crown or saddle position.

A systematic FE modelling procedure for cracked T-joints is also proposed. The FE models generated by this procedure are analyzed and their SIFs results compared with those obtained from the fatigue tests. The good agreement between these results confirmed that this modelling procedure is appropriate for further fracture mechanics analyses of cracked tubular joints.

REFERENCES

ABAQUS Theory and User Manuals, Version 6.2, (2001), Hobbit, Karlsson & Sorensen Inc., USA.

American Welding Society (AWS). (1996). "ANSI/AWS D1.1-96 Structural Welding Code-Steel." American Welding Society, Inc., Miami, USA.

Bowness, D. and Lee, M.M.K., (1995). "The Development of an Accurate Model for the Fatigue Assessment of Doubly Curved Cracks in Tubular Joints", *International Journal of Fracture*, Vol. 73, pp. 129-147.

Chiew, S. P., Lie, S. T., Lee, C. K., and Huang, Z. W. (2001). "Stress Intensity Factors of Through-Thickness and Surface Cracks in Tubular Joints," *Proceedings of the 11th International Offshore and Polar Engineering Conference (ISOPE 2001),* Stavanger, Norway, Vol. IV, pp 30-34.

Chong Rhee, H., Han, S. and Gipson, G. S., (1991). "Reliability of Solution Method and Empirical Formulas of Stress Intensity Factors for Weld Toe Cracks of Tubular Joints." *Proc. 10th Offshore Mechanics and Arctic Engineering Conference*, ASME, v3-B, pp. 441-452.

DEn (1993). "Background to New Fatigue Design Guidance for Steel Joints in Offshore Structures," Department of Energy, London, UK.

Lie, S. T., Chiew, S. P., Lee, C. K., Wong, S. M., and Huang, Z. W. (2000). "Modelling Arbitrary Through-thickness Crack in a Tubular T-joint," *Proceedings of the 10th International Offshore and Polar Engineering Conference (ISOPE 2000)*, Seattle, USA, Vol. IV, pp 53-58.

Shih, C. F., and Asaro, R. J. (1988). "Elastic-Plastic Analysis of Cracks on Bimaterial Interfaces: Part I—Small Scale Yielding," *Journal of Applied Mechanics*, pp 299-316.

Zhao, X.L, Herion, S., Packer, J.A., Puthli, R., Sedlacek, G., Wardenier, J., Weynand, K., van Wingerde, A. and Yeomans, N., (2000). "Design Guide for Circular and Rectangular Hollow Section Joints under Fatigue Loading". CIDECT, TUV Germany.

www.EngineeringEBooksPdf.com

Advances in Steel Structures, Vol. II
Chan, Teng and Chung (Eds.)
© 2002 Elsevier Science Ltd. All rights reserved.

HIGH-CYCLE FATIGUE BEHAVIOUR OF WELDED THIN SHS-CHS T-JOINTS UNDER IN-PLANE BENDING

F.R. Mashiri[1], X.L. Zhao[1], L.W. Tong[2] & P. Grundy[1]

[1]Department of Civil Engineering, Monash University, Clayton, VIC 3800, AUSTRALIA
[2]Department of Building Engineering, Tongji University, Shanghai, 200092, P.R. China

ABSTRACT

T-joints made up of square hollow section (SHS) chords and circular hollow section (CHS) braces are used in the road transport and agricultural industry. The hollow sections are thin-walled with thicknesses less than 4mm. Static tests were carried out on welded thin-walled SHS-CHS T-joints under in-plane bending load to determine the linear response between applied load and deformation. The loads corresponding to the linear part of the load-deformation curves were used in subsequent fatigue tests and resulted in a high cycle fatigue response. A formula for determining the maximum linear response moment in an SHS-CHS T-joint is derived as a function of brace diameter to chord width ratio, β and chord width to chord wall thickness ratio, 2γ. Fatigue tests were carried out to determine through-thickness fatigue life (N3) and an end of test fatigue life (N4). The fatigue data from the welded thin-walled SHS-CHS T-joints is compared to the S-N data of welded thin-walled SHS-SHS T-joints and found to be within the same scatter band. An analysis has been carried out in terms of the classification method and shows that there is a minimal difference between the fatigue design S-N curve obtained by using N4 instead of N3, when the inherent scatter in fatigue data is taken into account.

KEYWORDS

Static strength, load-deformation curves, fatigue strength, failure mode, thin-walled sections

INTRODUCTION

Welded thin-walled hollow sections with thicknesses less than 4mm are used in the manufacture of equipment and structural systems in the agricultural and road transportation industries. Fatigue design rules of these structural details are not available in current fatigue guidelines (IIW 2000, Zhao et al 2000, AWS 1998, API 1991, Department of Energy 1990). This paper investigates the fatigue behaviour of welded thin-walled SHS-CHS T-joints under in-plane bending. The SHS-CHS T-joints are made up of square hollow sections (SHS) chords and circular hollow section (CHS) braces of thicknesses less than 4mm. One of the advantages of using SHS-CHS T-joints instead of CHS-CHS T-joints is that no profile cutting of the brace is required, since the circular hollow section brace is

www.EngineeringEBooksPdf.com

welded to the flat face of the square hollow section chord. The SHS-CHS T-joints also have an advantage over SHS-SHS T-joints since they have been found to have lower stress concentration factors under axial loading compared to SHS-SHS T-joints (Gandhi and Berge 1998).

Static tests were performed on the welded thin-walled SHS-CHS T-joints under in-plane bending. The moment versus angle of inclination (M-θ) and moment versus deflection at point load (M-δ) graphs were used to determine the maximum linear response moment ($M_{linear.max}$) in each of the connections tested. The maximum linear response moment is the moment below which a linear relationship is obtained between load and deformation. The maximum linear response moment, like static strength (M_{ip}) of the SHS-CHS T-joints was found to be dependent on the brace diameter (d_1) to chord width (b_0) ratio, β and on the chord width (b_0) to chord wall thickness (t_0) ratio, 2γ but independent of the brace wall thickness (t_1) to chord wall thickness (t_0) ratio, τ. A ratio, μ, of $M_{linear.max}$ to M_{ip} for these connections is therefore dependent on β and 2γ. A formula was derived to predict the ratio, μ as a function of β and 2γ. The ratios of $M_{linear.max}$ to M_{ip} predicted by the equation, $\mu_{pred.}$, are compared to the experimentally determined values, $\mu_{exp.}$. Fatigue tests were subsequently carried out based on the values of maximum linear response moment determined experimentally. All the fatigue tests failed after 10,000 cycles, showing that a high-cycle fatigue response had been obtained from the applied loads. Through-thickness fatigue life (N3) and an end of test fatigue life (N4) were measured during the fatigue tests. The ratios of N3 to N4 from the thin-walled SHS-CHS T-joints are compared to the corresponding values from previous research. The S-N data from the thin-walled SHS-CHS T-joints is compared to the S-N data from thin-walled SHS-SHS T-joints expressed in terms of the nominal stress range (classification method), and is found to lie within the same scatter band. An analysis of the data using N4 instead of N3 shows that there is a minimal difference in the class (nominal stress range at 2 million cycles) obtained, when the inherent scatter associated with fatigue life is taken into account.

SPECIMENS AND MATERIAL PROPERTIES

The parameters of the six different series of SHS-CHS T-joint specimens tested in this investigation are given in Table 1. Both the square and circular hollow sections used in the manufacture of the T-joints were of grade C350LO and conform to AS1163-1991 (SAA 1991). The C350LO tubes have a specified minimum yield stress of 350MPa and a specified minimum tensile strength of 430MPa. Since both static and fatigue failures occurred in the chord member, only the measured yield stresses for the 100x100x3SHS and 75x75x3SHS chords are reported here. They are 432.5MPa and 395.0MPa respectively. The gas-metal arc-welding process, also known as MIG was used in fillet-welding the circular hollow section braces to the square hollow section chord flange.

LOADS FOR HIGH-CYCLE FATIGUE RESPONSE

The set-up of the static tests for the SHS-CHS T-joints is shown in Figures 1(a) and 1(b). The tests were performed in a 500kN capacity Baldwin Universal testing machine. Typical moment versus deflection and moment versus angle-of-inclination graphs obtained for the SHS-CHS T-joints are shown in Figures 2(a) and 2(b). The maximum linear response moment below which the connection behaves elastically was determined from the linear portion of the moment versus deflection and the moment versus angle-of-inclination graphs, for each connection tested. The graphs shown in Figures 2(a) and 2(b) show that for each connection tested the M-θ and M-δ graphs give values of maximum linear response moment that are very close to each other.

www.EngineeringEBooksPdf.com

TABLE 1: Maximum linear response moment ($M_{linear.max}$) and static strength (M_{ip}) and μ values

Joint	Chord Member $h_0xb_0xt_0$ (mm)	Brace Member d_1xt_1 (mm)	β	τ	2γ	$M_{linear.max}$	M_{ip}	$\mu \left(= \frac{M_{linear.max}}{M_{ip}} \right)$		$\frac{\mu_{pred.}}{\mu_{exp.}}$
								$\mu_{exp.}$	$\mu_{pred.}$	
S3C1	100x100x3	48.3x2.9	0.48	0.97	33	0.20	0.651	0.31	0.37	1.19
S3C2	100x100x3	48.3x2.3	0.48	0.77	33	0.25	0.651	0.38	037	0.96
S3C4	100x100x3	33.7x2.6	0.34	0.87	33	0.10	0.476	0.21	0.23	1.11
S3C5	100x100x3	33.7x2.0	0.34	0.67	33	0.14	0.476	0.29	0.23	0.79
S6C1	75x75x3	48.3x2.9	0.64	0.97	25	0.35	0.606	0.58	0.58	1.00
S6C2	75x75x3	48.3x2.3	0.64	0.77	25	0.35	0.606	0.58	0.58	1.00
									MEAN	1.01
									COV	0.12

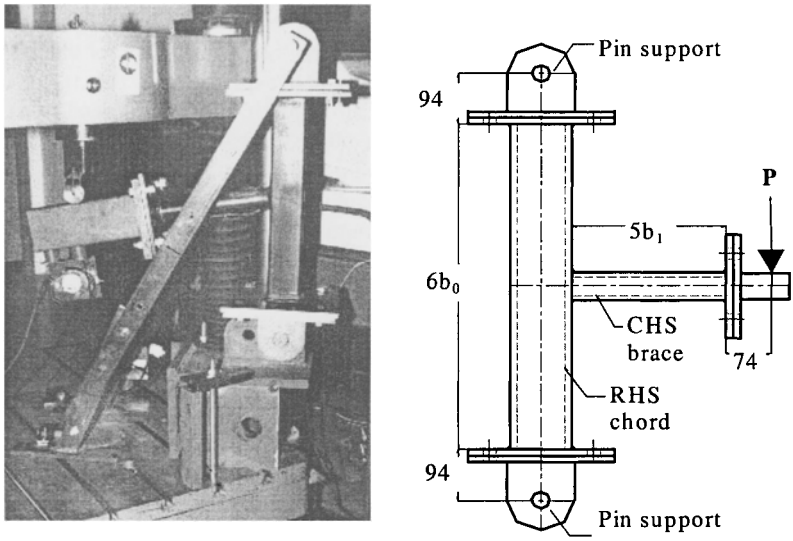

(a) (b)

Figure 1: (a) Test setup for thin-walled SHS-CHS T-joints static tests, (b) Schematic diagram for thin-walled SHS-CHS T-joint static test.

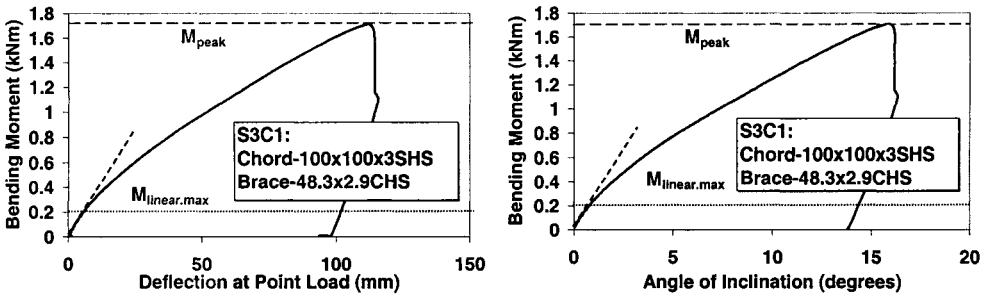

(a) (b)

Figure 2: (a) Moment versus deflection at point load graph, (b) Moment versus angle of inclination graph.

www.EngineeringEBooksPdf.com

Table 1 shows the maximum linear response moment ($M_{linear.max}$) and the static strength of the SHS-CHS connections under in-plane bending load (M_{ip}). The static strength of the SHS-CHS T-joints is determined from the formula derived by Mashiri et al (2002). The static strength of an SHS-CHS T-joint under in-plane bending load is:

$$M_{ip} = \frac{f_{y0} t_0^{\,2} d_1}{2}\left[9.95\beta^2 - 10.427\beta + 9.6434\right] = \frac{f_{y0} t_0^{\,3}}{2}(2\gamma)\cdot\beta\left[9.95\beta^2 - 10.427\beta + 9.6434\right] \qquad (1)$$

where f_{y0} is the yield stress of the chord and t_0 is the tube wall thickness of the chord, d_1 is the external diameter of the circular hollow section brace and β is the brace diameter (d_1) to chord width (b_0) ratio. The values of the maximum linear response moment and the static strength of the SHS-CHS T-joints show a dependence on the non-dimensional parameters, β and 2γ, similar to that reported by Packer et al (1992). Packer *et al* (1992), reported that both the strength and flexural rigidity of unstiffened vierendeel connections made up of square hollow sections, decrease as the chord slenderness ratio (b_o/t_o) increases and as the bracing to chord width ratio (b_1/b_o or β) decreases.

Since the values of the maximum linear response moment and the static strength of the SHS-CHS T-joints, show a dependence on β and 2γ, it implies that the ratio of experimentally determined maximum linear response moment to the static strength of SHS-CHS T-joints, also vary depending on the non-dimensional parameters β and 2γ. This trend can be observed from the ratios of experimentally determined maximum linear response moment to the static strength, $\mu_{exp.}$, shown in Table 1. The ratio of the experimentally determined maximum linear moment to static strength, $\mu_{exp.}$ in these connections show that, in general, $\mu_{exp.}$ increases with the brace to chord width ratio, β. The results in Table 1 also show that, in general, a connection with a higher 2γ value has a lower ratio of experimentally determined maximum linear response moment to static strength ($\mu_{exp.}$). The results from Table 1 also show that τ does not have a pronounced effect on the ratio between maximum linear response moment and static strength for connections with the same β and 2γ values. This is in agreement with static strength of SHS-CHS T-joints as determined by the formula given in equation 1 and shown in Table 1, which shows that for given β and 2γ values, static strength remains the same for connections with different τ values.

An equation for predicting the ratio between maximum linear response moment and static strength, $\mu_{pred.}$ for SHS-CHS T-joints under in-plane bending can therefore be derived as a function of β and 2γ, for connections with the range of non-dimensional parameters tested in this investigation:

$$\mu_{pred.} = f(\beta, 2\gamma) \qquad (2).$$

The method used by Soh and Soh (1990) for determining equations for stress concentration factors (SCFs) as a function of β, 2γ and τ, is used in this paper to determine the equation relating $\mu_{pred.}$ to β and 2γ. A formula for $\mu_{pred.}$ is obtained using a graphical method in which the variations of the ratio, $\mu_{exp.}$ with respect to each of the non-dimensional parameters is assumed to be in the form of a parameter raised to a power (Soh and Soh 1990). A plot of the ratio, $\mu_{exp.}$ versus the appropriate parameter on a log-log scale yields a straight line whose slope is interpreted as the power to which that parameter is raised. The empirical equation for predicting the ratio between maximum linear response moment and static strength, in welded thin-walled SHS-CHS T-joints made up of tubes of wall thicknesses less than 4 mm, μ_{pred} as a function of β and 2γ is:

$$\mu_{pred.} = \frac{M_{linear.max}}{M_{ip}} = b\cdot\beta^{m_1}\cdot(2\gamma)^{m_2} = 2.4571\cdot\beta^{1.3199}\cdot(2\gamma)^{-0.2668} \qquad (3).$$

The tested specimens in this investigation lie within the range of non-dimensional parameters: $0.34 \le \beta \le 0.64$; $25 \le 2\gamma \le 33$ and $0.67 \le \tau \le 0.97$. This is the validity range for equation 3. More details on determining load levels for high cycle fatigue response will be reported somewhere else (Mashiri et al 2003). A comparison of the predicted and experimentally determined values of the ratio

www.EngineeringEBooksPdf.com

between maximum linear response moment and static strength is shown in Table 1. The ratio $\mu_{pred.}/\mu_{exp.}$ has a mean value of 1.01 and a coefficient of variation (COV) of 0.12. This shows that the derived equation can predict the ratios between maximum linear response moment and static strength reasonably accurately. The loads corresponding to the maximum linear response moment and below can be applied to a connection as cyclic load and produce a high cycle fatigue response.

FATIGUE TESTS

Fatigue tests of thin-walled SHS-CHS T-joints were carried out using a multiple fatigue test rig as shown in Figure 3(a). Cyclic loading is applied through the use of air-cylinders at a rate of 1 cycle per second. The maximum and minimum loading levels in a cycle are regulated by valves connected to the air-cylinders and measured by a load cell and load cell exciter. Cycle counting is monitored through the use of a programmable logic controller (PLC).

Two different modes of failure have been used to define the fatigue failure of thin-walled SHS-CHS T-joints under cyclic in-plane bending. The number of cycles corresponding to a through-thickness crack (N3) has been determined for each connection. The number of cycles corresponding to an end of test failure criterion (N4) was also determined. The value of N4 was considered as the number of cycles corresponding to the development of a surface crack of length equal to half of the circumference of the weld toe in the chord on the brace-chord junction, (i.e. $\pi(d_1+2t_{wh})/2$, where d_1 is the diameter of the CHS brace and t_{wh} is the horizontal weld leg length). The number of cycles corresponding to a through thickness crack (N3) were determined through the use of a pressure gauge and pressure switch system as shown in Figure 3(b). Higher stress concentrations occur in the chord and results in fatigue cracks initiating and propagating at the chord weld toes. The pressure switch was therefore mounted onto the chord member. The pressure switch acts as a break detector and was set to automatically stop the cycling of the specimen when the pressure had dropped. A typical graph of pressure versus number of cycles is shown in Figure 4(a). A similar approach in measuring through thickness fatigue life was reported by Gandhi and Berge (1998). Figure 4(b) shows a specimen whose crack has developed to a length corresponding to the end of test failure criterion. At the stage when the crack length corresponds to the end of test failure criterion, it is evident that there is a separation between the brace and chord member along the weld toe in the chord as shown in Figure 4(b).

A summary of the fatigue test results is shown in Table 2. Eleven thin-walled SHS-CHS T-joints have been tested. The results include the through thickness fatigue life (N3), end of test fatigue life (N4), stress ratio (R), and nominal stress range ($S_{r\text{-}nom}$), and the location of the crack that results in failure. Failure of the SHS-CHS T-joints was observed to occur due to cracks developing along the weld toes in the chord on the side under tension. This type of failure was observed in SHS-SHS T-joints, Mashiri et al (2001) and was called the chord-tension-side failure mode. Unlike the SHS-SHS T-joints where different crack patterns, such as chord-tension-side, chord-and-brace-tension-side, brace-tension-side and chord-compression-side caused the failure of the joints, only chord-tension-side failure was observed in the tested SHS-CHS T-joints. This is an indication that the SCF in the brace may be significantly reduced when the section is changed from a square to a circular hollow section. This may reduce the chances of cracks developing in the brace as was observed in SHS-SHS T-joints.

A graph of the S-N data from the thin-walled SHS-CHS T-joints under cyclic in-plane bending is plotted in Figure 5 for the classification method (i.e. using the nominal stress range). The number of cycles corresponding to a through thickness crack (N3) and the number of cycles corresponding to the end of test failure criterion (N4) are both shown in Figure 5 for comparison. Data from SHS-SHS T-joints from previous research (Mashiri et al 2001) is also shown in Figure 5 for comparison. The S-N

www.EngineeringEBooksPdf.com

data from the thin-walled SHS-CHS T-joints lie within the same scatter-band as the SHS-SHS T-joint S-N data.

The ratio, N4/N3 ranging from 1.03 to 2.47 has been found for the thin-walled SHS-CHS T-joints data as shown in Table 2. A mean value of N4/N3 of 1.50 has also been obtained for the SHS-CHS T-joints which is similar to an average ratio of N4/N3 of 1.49 for tubular joints of thicknesses equal to and greater than 4mm, reported by van Wingerde et al (1997). Ratios of N4/N3 as high as 3.0 were also reported by van Wingerde et al (1997). The range of N4/N3 values found for the thin-walled SHS-CHS T-joints are therefore comparable to those found in thicker walled joints. Using the S-N data from the SHS-CHS T-joints, it can be demonstrated that the difference in design curves obtained through the use of N4 instead of N3 is minimal. The analyses are carried out for both N3 and N4 by: (1) using the natural slope of the S-N data to derive the S-N curves and (b) adopting a slope of –3. Mean-minus-two-standard-deviations S-N curves defined by the following equations and and their corresponding classes (stress ranges at 2 million cycles) were obtained and are also shown in Figure 5:

(a) Based on N3 and natural slope; $\log N = 10.4708 - 4.0339 \cdot \log S_{r-nom}$, yielding a class of 10.8.

(b) Based on N4 and natural slope; $\log N = 10.9212 - 4.2391 \cdot \log S_{r-nom}$, yielding a class of 12.3.

(c) Based on N3 and slope of -3; $\log N = 8.8623 - 3 \cdot \log S_{r-nom}$, yielding a class of 7.1.

(d) Based on N4 and slope of -3; $\log N = 8.9788 - 3 \cdot \log S_{r-nom}$, yielding a class of 7.8.

For the natural slope, the use of N4 gives a class that is 1.1 times larger than the class obtained when N3 is used. For the slope of –3, the use of N4 also gives a class that is 1.1 times larger than the class obtained when N3 is used.This shows that the difference in design life obtained when N4 is used instead of N3 is minimal when the inherent scatter of S-N data is taken into account. Van Wingerde (1997), similarly pointed out that the overall error of using N4 rather than N3 must be deemed small compared to the inherent scatter in S-N data for welded tubular joints of thicknesses equal to and greater than 4mm.

Current fatigue design standards for hollow section joints give fatigue design curves in terms of the hot spot stress method (IIW 2000, Zhao et al 2000, AWS 1998, API 1991, Department of Energy 1990). To enable comparison of the SHS-CHS T-joints fatigue data with current fatigue design standards for hollow section joints, stress concentration factors (SCFs) will be determined to allow the fatigue data of SHS-CHS T-joints to be analysed in the hot spot stress method.

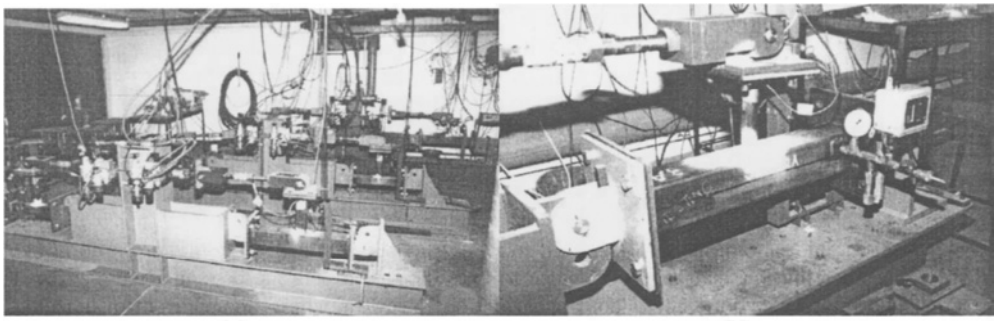

(a) (b)

Figure 3: (a) Test setup of thin-walled SHS-CHS T-joints for fatigue test in multiple fatigue test rig, (b) Setup of fatigue test showing pressure gauge and pressure switch used in detecting through-thickness fatigue life

www.EngineeringEBooksPdf.com

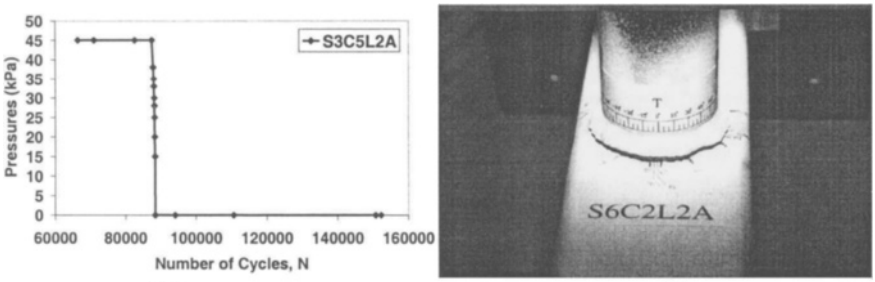

(a) (b)

Figure 4: (a) Pressure versus number of cycles (e.g. S3C5L2A), (b) Failed specimen showing extend of crack growth (e.g. S6C2L2A).

Table 2: Fatigue test data for thin-walled SHS-CHS T-joints under in-plane bending

Joint	Through Thickness Fatigue Life, N3	End of Test Fatigue Life, N4	N4/N3	Nominal Stress Range, $S_{r\text{-}nom}$, (MPa)	Stress Ratio, R	Failure
S3C1L2A	134638	332248	2.47	26.33	0.10	Chord-Tension-Side
S3C1L3A	703908	851461	1.21	19.75	0.10	Chord-Tension-Side
S3C2L2A	102073	114049	1.12	31.96	0.10	Chord-Tension-Side
S3C4L2A	97297	160380	1.65	36.54	0.10	Chord-Tension-Side
S3C4L3A	1338447	1693910	1.27	24.36	0.10	Chord-Tension-Side
S3C5L2A	88355	152266	1.72	45.12	0.10	Chord-Tension-Side
S3C5L3A	7456261	8864693	1.19	22.56	0.10	Chord-Tension-Side
S6C1L2A	16433	18490	1.13	52.66	0.10	Chord-Tension-Side
S6C1L3A	959466	1407265	1.47	19.75	0.10	Chord-Tension-Side
S6C2L2A	35559	36455	1.03	63.91	0.10	Chord-Tension-Side
S6C2L3A	3944565	8835429	2.24	23.97	0.10	Chord-Tension-Side
		MEAN	1.50			
		COV	0.32			

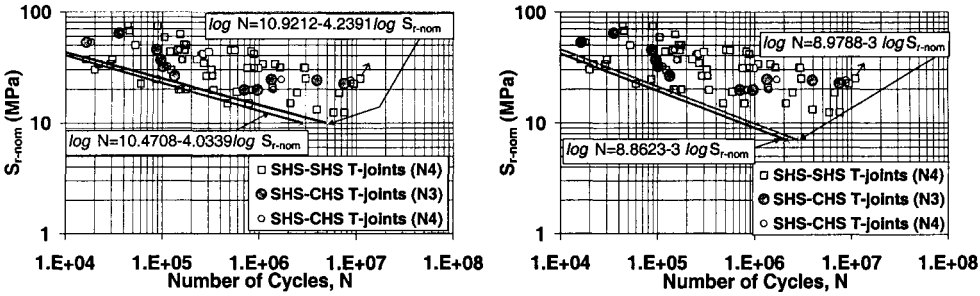

(a) (b)

Figure 5: (a) S-N curves with natural slope and, (b) with slope of –3 in the classification method

CONCLUSIONS

Static tests of welded thin-walled SHS-CHS T-joints, under in-plane bending, have been used to produce load-deformation curves from which the maximum linear response moment of a connection has been determined. The loads corresponding to the maximum linear response moment and below

www.EngineeringEBooksPdf.com

have been applied during cyclic loading and found to produce a high-cycle fatigue response in the SHS-CHS T-joints. A formula has been derived for predicting the ratio between maximum linear response moment and static strength as a function of the non-dimensional parameters β and 2γ. The fatigue data of the welded thin-walled SHS-CHS T-joints was found to lie within the same scatter-band as the S-N data of thin-walled SHS-SHS T-joints. An analysis of the S-N data of the thin-walled SHS-CHS T-joints using N4 instead of N3, shows that there is a minimal difference in the design curve obtained by using N4, when the inherent scatter in fatigue data is taken into account.

ACKNOWLEDGMENTS

The authors wish to thank the Monash University, Civil Engineering laboratory staff, Mr. Roy Goswell, Mr. Roger Doulis, Mr. Graham Rundle and Mr. Don McCarthy, for their help and support with the testing. Thanks to OneSteel Market Mills, Australia, for providing the tubes used in these tests. This project was funded by CIDECT.

REFERENCES

1. API 1991, "Recommended practice for planning, designing and constructing fixed offshore platforms", American Petroleum Institute Recommended Practice 2A (RP 2A), 19th Edition, August 1991, Washington, USA
2. AWS 1998, Structural Welding Code-Steel, ANSI/AWS D1.1-98, American Welding Society, Miami, USA.
3. Department of Energy, 1990, " Offshore Installations: Guidance on design, construction and certification", Fourth Edition, London, HMSO, UK.
4. Gandhi P. and Berge S. 1998, *J. of Struct. Eng.*, ASCE, Vol. 124, No. 4, April 1998, pp. 399-404
5. IIW 2000: Fatigue Design Procedures for Welded Hollow Section Joints, IIW Doc. XIII-1804-99, IIW Doc. XV-1035-99, Editors: Zhao X.L. and Packer J.A., Abington Publishing, Cambridge, UK
6. Mashiri F.R, Zhao. X.L., Grundy P. 2001, "Fatigue behaviour of thin-walled tube-to-tube T-joints under in-plane bending" In: *Tubular Structures IX*, Düsseldorf, Germany, ISTS9, Editors: Puthli R.& Herion S., 3-5 April 2001, pp. 259-268
7. Mashiri F.R., Zhao X.L., Grundy P. and Tong L. 2002, "Ultimate Strength of Welded Thin-Walled SHS-CHS T-Joints under In-Plane Bending", In: *Advances in Steel Structures*, ICASS'02, Editors: Chan S.L. and Teng J.G., 9-11 December 2002, Hong Kong, China.
8. Mashiri F.R., Zhao X.L. and Grundy P. 2003, "Load Levels for High Cycle Fatigue Response in Welded Thin Cold-formed Square Hollow Section (SHS) T-joints under In-Plane Bending", In: *Advances in Structures: Steel, Concrete, Composite and Aluminium*, ASSCCA'03, Editors: Hancock G.J. and Bradford M., 23-25 June 2003, Sydney, Australia
9. Packer J.A., Wardenier J., Kurobane Y., Dutta D. and Yeomans N. 1992, "Design Guide for Rectangular Hollow Section (RHS) Joints under Predominantly Static Loading" CIDECT Construction with Hollow Steel Sections, Verlag TUV Rheinland, Cologne, Germany.
10. SAA 1991, Structural Steel Hollow Sections, AS1163-1991, Standards Association of Australia.
11. Soh A.K. and Soh C.K. 1990, *Journal of Constructional Steel Research*, No. 15, pp. 173-190
12. van Wingerde A.M., van Delft D.R.V., Wardenier J. & Packer J.P., 1997: Scale Effects on the Fatigue Behaviour of Tubular Structures. *IIW International Conference on Performance of Dynamically Loaded Welded Structures*, July 14-15, San Francisco, U.S.A, pp. 123-135
13. Zhao, X.L., Herion, S., Packer, J.A., Puthli, R.S., Sedlacek, G., Wardenier, J., Weynand, K., van Wingerde, A.M. and Yeomans, N. F. (2000), Design Guide for Circular and Rectangular Hollow Section Welded Joints under Fatigue Loading, CIDECT-series "Construction with hollow steel sections", Serial no. 8, Verlag TÜV Rheinland, Cologne, Germany

www.EngineeringEBooksPdf.com

Advances in Steel Structures, Vol. II
Chan, Teng and Chung (Eds.)
© 2002 Elsevier Science Ltd. All rights reserved.

ON THE ANALYSIS OF FRACTURE PHENOMENA OBSERVED IN STEEL STRUCTURES DURING THE KOBE EARTHQUAKE

Hideyuki Fujiwara, Yoshiaki Goto and Makoto Obata

Department of Civil Engineering, Nagoya Institute of Technology,
Gokiso-cho, Showa-ku, Nagoya 466-8555, Japan

ABSTRACT

During the Kobe earthquake, brittle fracture occurred in some of the steel structures. From the observation of fracture surface, the process of the brittle fracture is considered to occur as a sequence of three events, that is, ductile crack initiation, ductile crack growth and brittle crack propagation. This implies that the ductile crack initiation plays an important role on the brittle fracture. Herein, as a first step to assess the brittle fracture, we examined the applicability of a FEM analysis based on the void damage theory to the simulation of the initial ductile failure. To deal with the ductile fracture under cyclic loads such as seismic loads, the conventional void damage theory based on the Gurson model is modified to take into account the kinematic hardening rule in addition to the isotropic hardening rule for the constitutive relation of the base material. By the comparison between the FEM analysis and experiment, it is shown that the location of the ductile fracture in steel columns can be predicted by the FEM analysis based on the void damage theory. However, there is some discrepancy between the analysis and experiment regarding the magnitude of the displacement that causes the initial ductile fracture.

KEYWORDS

ductile fracture, damage theory, local buckling, thin-walled column, numerical analysis

INTRODUCTION

Various types of damages were observed in steel structures during the Kobe earthquake. Up to the present, a lot of efforts have been made to simulate these damages. As a result, most of the damage types including the cyclic local buckling of thin-walled structures have been simulated successfully. However, the brittle fracture that occurred in steel structures as shown in Fig. 1 has not been analytically assessed yet. From the observation of fracture surface, the process of the brittle fracture is considered to occur as a sequence of three events, that is, ductile crack initiation, ductile crack growth and brittle crack propagation. This implies that the ductile crack initiation plays an important role on the brittle fracture. Herein, as a first step to assess the brittle fracture, we examined the applicability of a FEM analysis based on the void damage theory to the simulation of the initial ductile

www.EngineeringEBooksPdf.com

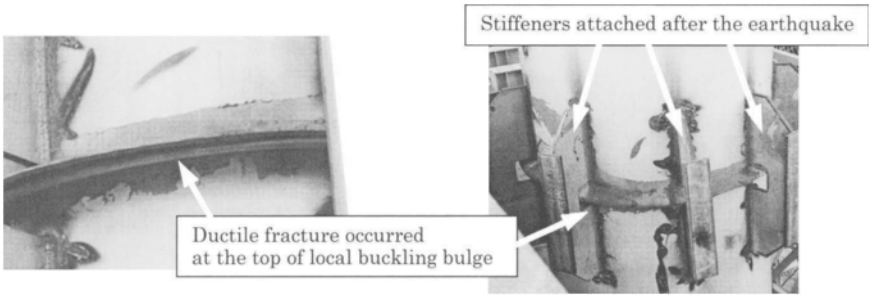

Fig. 1 Ductile fracture of thin-walled circular steel column observed in the Kobe earthquake

failure. To deal with the ductile fracture under monotonic loading, Tvergaard(1981) modified the Gurson model(Gurson 1977) where the isotropic hardening rule is utilized to express the hardening behavior. However, the isotropic hardening rule is not appropriate to express the hardening behavior of the base material subjected to cyclic loads such as seismic loads. Herein, the Gurson model modified by Tvergaard (1981) is further modified to take into account the kinematic hardening rule for the constitutive relation of the base material. This void damage theory is implemented in ABAQUS(ABAQUS *Users manual* 1999) by the USER SUBROUTINE feature. The applicability of the developed damage theory-based FEM analysis to the prediction of the ductile fracture under cyclic loads is examined by carrying out alternate loading tests on thin-wall steel columns. Specifically, we examine the validity of using the kinematic hardening rule for the constitutive relation of the base material instead of using the isotropic hardening rule.

MODIFIED GURSON'S MODEL AND IMPLEMENTATION OF KINEMATIC HARDENING RULE IN THE CONSTITUTIVE RELATION OF BASE MATERIAL

We use the basic concept of the modified Gurson model (Tvergaard (1981, 1982)) to predict the ductile fracture of steel members. The Gurson model of plasticity incorporates the effect of nucleation and the growth of voids in ductile metals that plays essential role in ductile fracture. This is one of the most widely used models among this class of plasticity theory. In the modified Gurson model, the isotropic hardening rule is assumed to express the hardening behavior of the base material. The isotropic hardening rule may be acceptable to analyze the ductile fracture under monotonic loading, but the hardening rule of this type is inaccurate to express the behavior under cyclic loading. Therefore, the modified Gurson model is further modified to take into the kinematic hardening rule(Obata 1999) in order to deal with the ductile fracture under seismic loads. The outline of the proposed constitutive model is as follows. The yield function is assumed to be given by

$$\phi = \frac{3}{2}\left(\frac{B'_{ij}B'_{ij}}{\sigma_y^{\,2}}\right) + 2fq_1\cosh\left(\frac{q_2 B_{ii}}{2\sigma_y}\right) - \left\{1 + q_1 f^2\right\} = 0 \tag{1}$$

where σ_y is the yield strength of the base material. $B_{ij} = \Sigma_{ij} - A_{ij}$ where Σ_{ij} and A_{ij} is the true stress and the back stress, respectively. $B'_{ij} = (\Sigma_{ij} - \delta_{ij}\Sigma_{kk}/3) - (A_{ij} - \delta_{ij}A_{kk}/3)$ where δ_{ij} is the Kronecker delta. q_1, q_2 and q_3 are the modification coefficients introduced by Tvergaard (1981). For theses coefficients, $q_1 = 1.5$, $q_2 = 1.0$ and $q_2 = q_1^2 = 2.25$ are assumed here, following Needleman and Tvergaard(1984). f is the volume fraction of microvoid. The increment of the void volume fraction f is the sum of the growth rate of the existing void and the nucleation rate of the new void as given by

$$df = df_{growth} + df_{nuc} \tag{2}$$

www.EngineeringEBooksPdf.com

where $df_{growth} = (1-f)D^p_{kk}$, while df_{nuc} is assumed to be expressed as below, following Needleman and Tvergaard (1984).

$$df_{nuc} = \bar{A} d\varepsilon^P_M \tag{3}$$

where $d\varepsilon^p_M$ is the incremental equivalent plastic strain of base material and $\bar{A}$ is given by

$$\bar{A} = \frac{f_N}{s_N\sqrt{2\pi}} \exp\left\{-\frac{1}{2}\left(\frac{\varepsilon^p_M - \varepsilon_N}{s_N}\right)^2\right\} \tag{4}$$

where f_N is the volume fraction of void nucleating substance contained initially in the material. ε_N and s_N are the mean plastic strain and the standard deviation for the nucleation of micro void. Based on our previous research, $f_N = 0.04$, $\varepsilon_N = 0.209$ and $s_N = 0.155$ are used. In the following analysis, A has non-zero value only when the hydrostatic stress is positive.
Normality rule is used to derive the plastic part of the deformation tensor D^p_{ij} from the Gurson's yield function as

$$D^p_{ij} = \lambda \frac{\partial \Phi}{\partial \Sigma_{ij}} \tag{5}$$

The stress and strain components of the Gurson model are assumed to be related to those of the base material as

$$B_{ij}D^p_{ij} = (1-f)\sigma_F d\varepsilon^p_M \quad , \quad \frac{\partial \Phi}{\partial A_{ij}} dA_{ij} = -H_k d\varepsilon^p_M , \quad D^p_{ij} dA_{ij} = (1-f) d^p_{ij} d\alpha_{ij} \tag{6a~c}$$

where σ_F, α_{ij}, H_k and d^p_{ij} are equivalent stress, back stress, kinematic hardening coefficient and plastic part of the deformation tensor , respectively, of the base material. Herein, Ziegler's rule is used as a kinematic hardening rule for base material. The modified Gurson constitutive model for kinematic hardening material, proposed herein, is implemented in the general-purpose FEM package program ABAQUS by USER SUBROUTINE feature.

DUCTILE FRACTURE OF THIN-WALLED COLUMN UNDER LATERNATE LOADING

Experiment

To examine the validity of the proposed FEM based-numerical method, alternate loading test is performed on a thin-walled circular steel column model with a fixed base to initiate a ductile fracture. As illustrated in Fig. 2, the column model is made of a structural carbon steel pipe (STK400, $\phi 216.4 \times thk$ 8.2) by scraping the outer surface of the pipe such that the thickness of the pipe becomes 2.0mm in the range of 50mm~550mm from the column base. In this range, the radius-to-thickness ratio parameter of the column model is $R_t = \sqrt{3(1-\nu^2)}\frac{\sigma_y}{E}\frac{R}{t} = 0.142$. The thickness of the hollow column is determined by considering the fact that the damages during the Kobe earthquake were observed in the circular steel columns with $R_t \geq 0.085$. For this model, specified alternating horizontal load is quasi-statically applied under displacement control at the top of the column with keeping the vertical compressive force P constant. The magnitude of P is 39.8kN that is 10% of the yield axial force $\sigma_y A$, where σ_y and A are yield stress and cross-sectional area, respectively, of the

www.EngineeringEBooksPdf.com

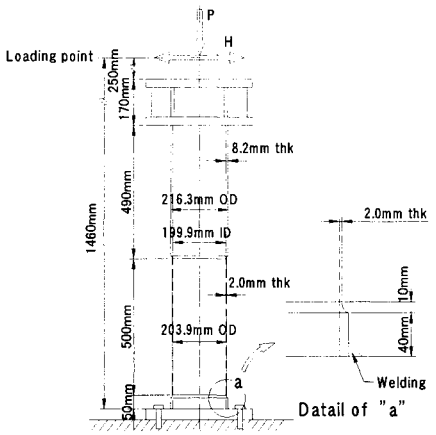

Fig. 2 Column model for experiment

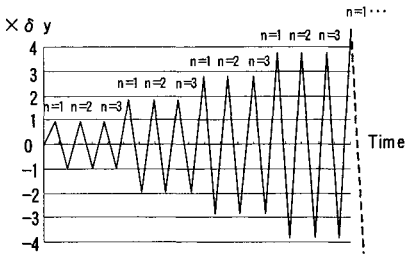

Fig. 3 Cyclic loading pattern

column. The alternating loading program is shown in Fig. 3, where δ_y=7.91mm is the horizontal displacement of the loading point when the column model begins to yield. δ_y is calculated by $\delta_y = \dfrac{H_y h^3}{3EI}$ in which $H_y = (\sigma_y - P/A)z/h$ =horizontal force corresponding to δ_y; and *h*, *EI*, and *z* = the height, the bending rigidity and the second modulus, respectively of the column. This alternating loading program is continued until the local buckling deformation referred to as elephant foot bulge becomes so large that the buckled surfaces of the thin-walled column come into contact with each other. After the alternating loading program is finished, the top of the column is pulled up in the vertical directions in order to accelerate the occurrence ductile fracture.

Numerical Analysis and Modeling

The finite-element discretization for the column model is illustrated in Fig.4. Only half of the column is discretized by virtue of the symmetry of the geometry and the boundary conditions. For the computational efficiency, only the lower part of the column where localized deformations and ductile fracture occurred is represented by the 4-node double-curved thick shell elements(S4R) and the 8-node solid elements(C3D8I). The solid elements are used specifically in the range of 40~130mm from the column base where ductile fracture was observed. In this range, 4 solid elements are used through the thickness of the thin-walled column. The rest of the lower part is discretized by the shell elements. The upper part of the column is represented by shear flexible beam element (B31). The accuracy of this model is confirmed by comparing with full shell element discretization in terms of local buckling behavior. The number of finite elements is determined, based on the convergence of solutions. At the column base, all the degrees of freedom are fixed.

The uniaxial stress-plastic strain relation for the base material of the circular column is assumed to be expressed by the power law as

$$\begin{aligned} \sigma &= \bar{h}\{\varepsilon^p - \varepsilon_{st}^p + (\sigma_y/\bar{h})^{1/n}\}^n \qquad (\varepsilon^p \geq \varepsilon_{st}^p) \\ \sigma &= \sigma_y \qquad (0 \leq \varepsilon^p < \varepsilon_{st}^p) \end{aligned} \tag{7}$$

where ε_{st}^p is the length of yield plateau. Parameters *h* and *n* including ε_{st}^p are identified such that the uniaxial stress-strain relation obtained by the tensile coupon test is best curve-fitted by Eqn. (7). For this curve fitting, the stress-strain relation up to $\varepsilon = 0.2$ is used, because the specimens in this test

www.EngineeringEBooksPdf.com

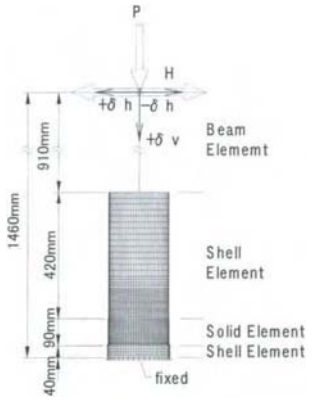

Fig. 4 Finite-element discretization for analysis model

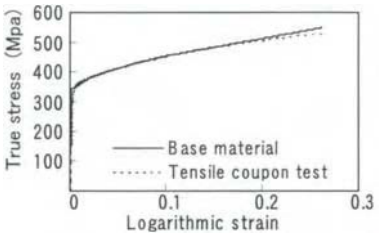

Fig. 5 Uniaxial stress-strain relation of base material

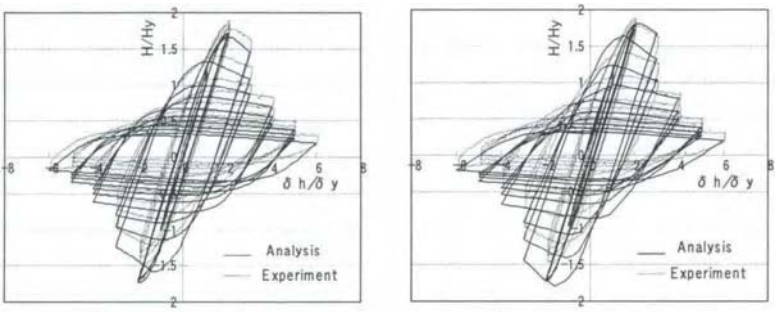

(a) Kinematic hardening (b) Isotropic hardening

Fig. 6 Horizontal load-displacement hysterisis curves

exhibit homogeneous deformation up to this strain value and the growth of the micro voids is not so significant. The material parameters so identified are $\overline{h} = 654MPa$, $\sigma_y = 340MPa$, $\varepsilon_{st}^{p} = 0.04$ and $n = 0.182$. In. Fig. 5, the stress-strain relation of the base material expressed by Eqn.(7) is compared with those obtained by the tensile coupon test.

In the Gurson model, the occurrence of the ductile fracture may be predicted by the values of the void volume fraction f.

Hysteretic behavior under horizontally applied alternating loads

Fig. 6 illustrates the hysteretic horizontal load-displacement curves at the top of the column obtained by experiment and the analyses using two types of the modified Gurson models. One analysis adopts the kinematic hardening rule as the constitutive relations of base materials and the other adopts the isotropic hardening rule. In addition, the predicted localized deformation patterns by the two types of the modified Gurson models at the end of the alternating loading step are shown in Fig. 7 in comparison with that observed in experiment. From Figs 6 and 7, it is observed that the analysis using the kinematic hardening base material predicts both the hysteretic curves and the localized buckling pattern of the column with relatively good accuracy. In contrast, the analysis with the isotropic hardening base material overestimates the magnitude of the localized deformation, although the hysteretic curve obtained by this analysis is in good agreement with that obtained by experiment.

www.EngineeringEBooksPdf.com

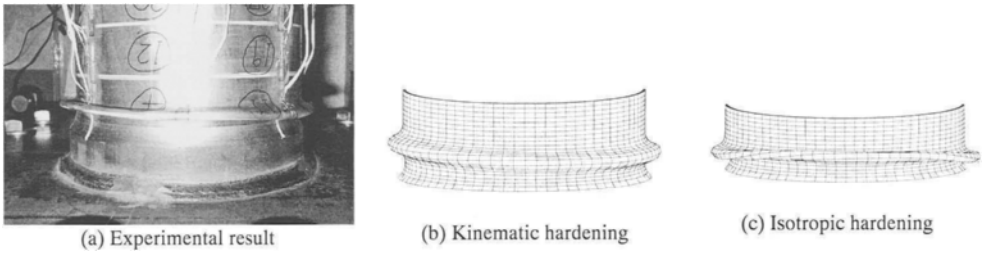

Fig. 7 Local buckling deformation ($\delta = \pm 6\delta_y, n = 1$)

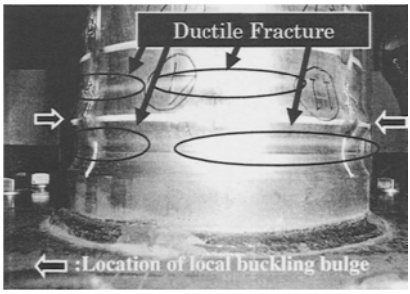

Fig.8 Ductile fracture of column mode ($\delta_v = 0mm$)

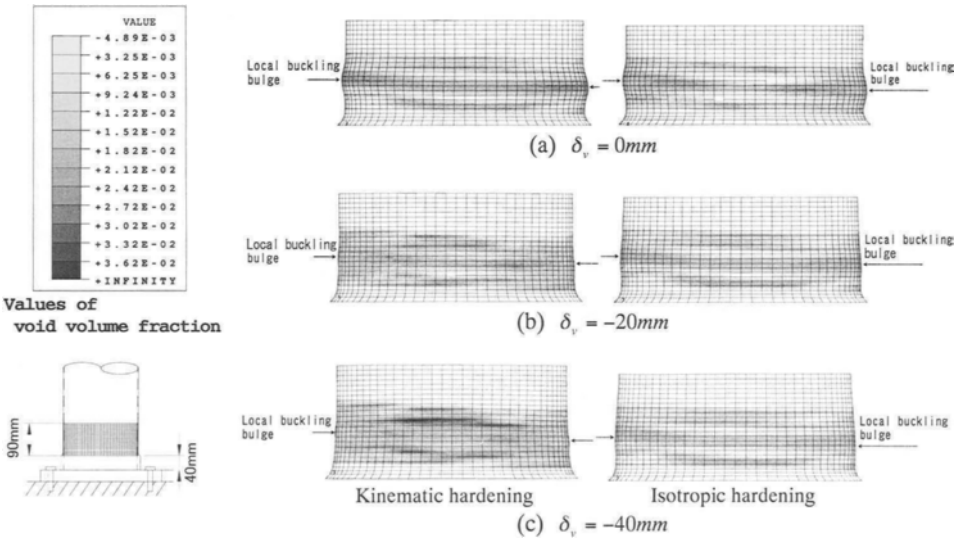

Fig. 9 Change of void volume fraction during pull-up process

www.EngineeringEBooksPdf.com

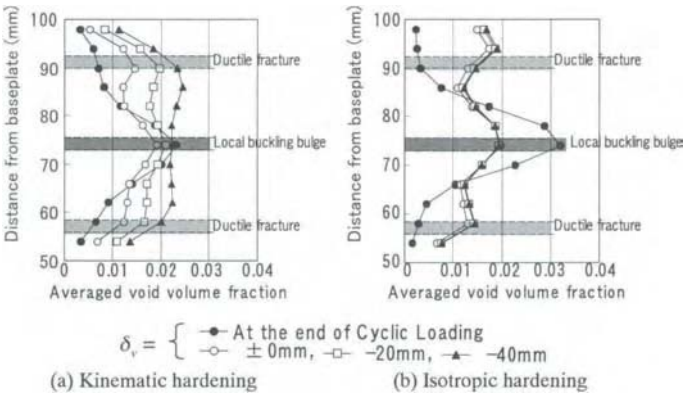

Fig.10 Distribution of void volume fraction averaged over the circumferential direction

Ductile fracture pattern

At the end of the alternating loading step in the experiment, no evident ductile fracture was detected in the localized buckle. So, the top of the column was monotonically pulled up to accelerate the initiation of ductile fracture. The locations of the ductile fracture observed in experiment are shown in fig. 8 where the vertical displacement δ_v measured from the initial state is zero. This implies that the vertical compressive plastic deformation resulted from the alternate loading is removed at this stage. From this figure, the ductile fracture is observed in the two locations just above and below the local buckling bulge. As the results of the numerical analysis with the two types of base material, the changes of the distribution of the void volume fraction on the outer-surface of the column during the pull-up process are illustrated in Fig. 9. Furthermore, the change of the void volume fraction averaged over the circumference is shown in Fig. 10 in order to show the quantitative distribution in the longitudinal directions more clearly. It may be possible to assume that the ductile fracture initiates from the locations with larger values of void volume fractions.

Regarding the conventional analysis with the isotropic hardening base material, the void volume fraction at $\delta_v = 0$ becomes the highest at the top of the local buckling bulge. This location is different from those where the ductile cracks were observed in the experiment. Furthermore, the distribution of the void volume fraction obtained by the analysis with the isotropic hardening base material remains almost the same, even if the vertical displacement δ_v is increased in the negative direction. In this case, the maximum value of the void volume fraction in the pull-up process is smaller than that at the end of the alternating loading step. Therefore, the conventional Gurson model with the isotropic hardening base material totally fails to simulate the process of ductile fracture.

In contrast, the void volume fraction obtained by the analysis with the kinematic hardening base material changes according to the magnitude of the vertical displacement, although its distribution at $\delta_v = 0$ is almost the same as that obtained by the analysis with the isotropic hardening base material. That is, with the increase of δ_v in the negative direction, the void volume fraction obtained by the analysis with the kinematic hardening base material increases at the two locations just above and below the local buckling bulge that are similar to the locations where the ductile fracture was observed

www.EngineeringEBooksPdf.com

in the experiment. On the other hand, the void volume fraction at the top of the local buckling bulge decreases. Finally, the void volume fraction becomes the highest at these two locations when $\delta_v = -40mm$. In this way, the ductile crack is predicted to occur at the magnitude of the vertical displacement in the negative direction that is larger than that observed in the experiment. This may be partly caused by the fact that the analysis with the kinematic hardening base material underestimates the vertical displacement as $\delta_v = 18mm$ that occurs at the end of the alternate loading step, compared with that observed as $\delta_v = 26mm$ by the experiment. As a result, the incremental vertical displacement in the negative direction to reach $\delta_v = 0$ is smaller for the analysis with the kinematic hardening base material than that for the experiment. This implies that the present analysis to predict the ductile fracture may be improved, if the vertical compressive displacement at the end of the alternate loading step is accurately evaluated by more sophisticated constitutive relations intended primarily for the cyclic plasticity of steel.

From the comparison between the analysis and the experiment, it may be concluded that the qualitative aspects of the void-volume growth under cyclic loading that leads to the ductile fracture can be assessed by the newly proposed modified Gurson model with the kinematic hardening base material. However, there still remains a room to be improved in order to predict quantitatively the process of the ductile fracture under cyclic loading.

SUMMARY AND CONCLUDING REMARKS

The ductile crack initiation caused by the cyclic loads plays an important role on the brittle fracture. Herein, as a first step to assess the brittle fracture during the earthquake, we examined the applicability of a FEM analysis based on the void damage theory to the simulation of the initial ductile fracture. To deal with the ductile fracture under cyclic loads such as seismic loads, the conventional void damage theory based on the Gurson model is modified to take into account the kinematic hardening rule in addition to the conventional isotropic hardening rule for the constitutive relation of the base material. By the comparison between the FEM analysis and experiment, it is shown that the location of the ductile fracture in a thin-walled steel column can be predicted in terms of the void volume growth by the newly proposed modified Gurson model with the kinematic hardening base material. However, there is some discrepancy between the analysis and experiment regarding the magnitude of the displacement that causes the ductile crack initiation. This implies that there still remains a room to be improved in order to predict quantitatively the process of the ductile fracture under cyclic loading. For this purpose, we have to use a more refined constitutive relation that can accurately express the cyclic hardening behavior of the base material.

References

Gurson, A. L.(1977). Continuum theory of ductile rupture by void nucleation and growth: Part I-yield criteria and flow rules for porous ductile media, ASME J. Engng Materials Technol. Vol.99, pp.2-15.
Tvergaard, V.(1981). Influence of voids on shear band instabilities under plane strain conditions, Int. J. Fracture, Vol.17, pp.389-407.
Tvergaard, V.(1982). Influence of void nucleation on ductile shear fracture at a free surface, J. Mech. Phys. Solids, Vol.30, pp.399-425.
ABAQUS Users Manual 5.8(1999). HSK. Inc.
Needleman, A., Tvergaard, V.(1984). An analysis of ductile rupture in notched bar, *J. Mech. Phys. Solids*, Vol.32, pp.461-490.
Obata, M. (1999). Identification of plastic behavior of structural steel at very large deformation, Reports for the research project, Grand-in-aid for Scientific Research.

www.EngineeringEBooksPdf.com

FIRE PERFORMANCE

www.EngineeringEBooksPdf.com

This Page Intentionally Left Blank

www.EngineeringEBooksPdf.com

Advances in Steel Structures, Vol. II
Chan, Teng and Chung (Eds.)
© 2002 Elsevier Science Ltd. All rights reserved.

ASSESSMENT OF STRUCTURES FOR FIRE SAFETY – INSIGHTS ON CURRENT METHODS AND TRENDS

J. Y. Richard Liew and H X Yu

Department of Civil Engineering, National University of Singapore,
Blk E1A, 1 Engineering Drive 2, Singapore 117576. (cveljy@nus.edu.sg)

ABSTRACT

Building code for fire safety can be divided into two kinds: Prescriptive codes and Performance-based codes. It is now widely recognized that performance-based codes obtain great advantages over traditional prescriptive codes in that it allows designers to use the fire engineering methods to assess the fire safety of the structure. However, as the assessment of the whole structure performance is not easy, most codes currently used are still prescriptive codes or a combination of prescriptive codes and performance-based codes. The key feature for implementing the performance-based fire design codes is the assessment of the fire resistance of the structure. This paper provides an overall view on performance-based code and the approach for designing structure in fire. Various fire models and heat transfer analysis methods are reviewed and discussed. The basis to modelling of plasticity and creep effects using Eurocode 3 stress-strain curves in plastic hinge analysis is explained. Finally, structural response calculations from simplified hand calculation method to advanced numerical procedures are presented. Future trends for research are identified.

KEYWORDS

Creep effect; fire modelling; fire resistance; fire safety; nonlinear analysis; performance-based design; steel structures.

PERFORMANCE-BASED DESIGN APPROACH

A rational approach to fire safety assessment is to relate functional requirements, such as prevention of spread of heat and smoke, safe evacuation and rescue etc., to fire resistance considering both local and global stability of structures. In a performance-based design, the designers have the freedom to choose the design methods provided that the risk to personnel and/or assets due to fire hazards can be reduced to a minimum. The main considerations for assessing the performance of a structure in fire are

i) to identify various fire scenarios which could occur during the service life of the structure,
ii) evaluate the likelihood and consequences of such scenarios, and

www.EngineeringEBooksPdf.com

iii) establish appropriate performance criteria by ensuring effective evacuation, escape and rescue and to prevent injury arising from a fire event.

Although the governing criteria for impairment of the main safety functions are often non-structural (for example exposure to heat, temperature, toxic gases etc.), it is, however, a functional requirement that the structure would remain stable to allow safe evacuation and rescue. Therefore a quantitative assessment on fire resistance of a structure is necessary and this opens up the opportunity in using advanced numerical simulation tools and techniques developed in the recent research work.

A flow chart showing the process of assessing the resistance of a structure exposed to a complete burnout of a fire compartment is shown in Fig 1. The process of calculating structural fire behavior has three essential component models: a fire model, a heat transfer model, and a structural model.

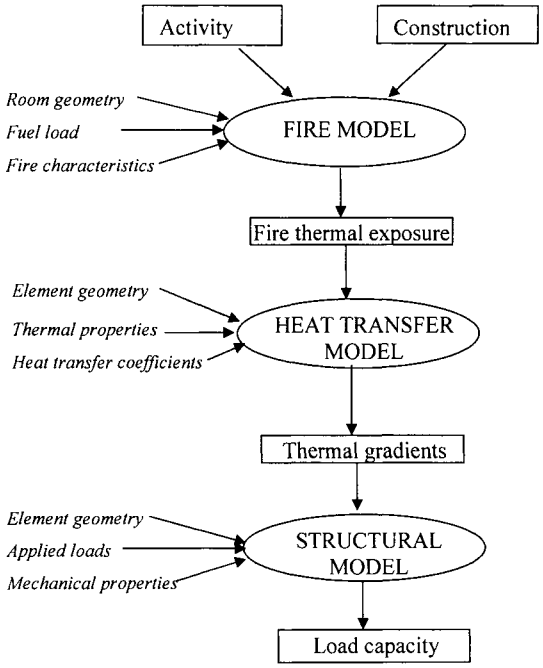

Fig.1 Flow chart for calculating the load capacity of a structure exposed to fire[1]

FIRE MODEL

A fire model is a mathematical simulation of the fire conditions in a compartment and is capable of giving information on those parameters for which it has been designed. The fire development in a room normally involves three phases: pre-flashover, flashover and post-flashover, as shown in Fig. 2. Among them, the post-flashover fire has most influence on structural design with very high temperature and radiant heat fluxes produced in this phase. Commonly used fire models include empirical models, zone models, and computational fluid dynamics (CFD) analysis.

www.EngineeringEBooksPdf.com

Empirical models yield accurate and reliable predictions provided that conditions are similar to those in the underlying assumptions. Standard fire curves such as ISO-834 do not represent the real fire in a compartment and serve only as criteria to evaluate the fire resistance capacity of single structural members. Simplified code prescribed method often assumes that the fire has a constant temperature throughout the burning period as shown in Fig .3. Factors such as fuel load, opening factor, height of opening, etc are considered to compute the maximum temperature and duration of burning period.

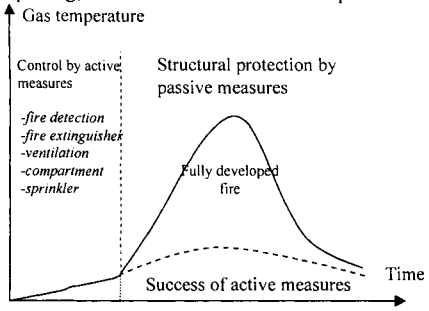

Fig .2 Natural fire concept

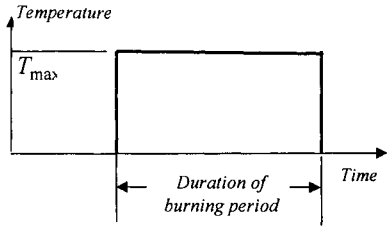

Fig.3 design fire with constant temperature

It is also possible to scale temperatures off published curves, which have been derived from computer calculations, e.g., Swedish curves, etc.

Eurocode parametric fires[2] are generally more in line with real fires occurred in a compartment. They consist of two phases - heating phase and cooling phase - while taking into account the main parameters such as fire load density, size of the compartment, opening condition, boundary material properties, etc.

Zone models represent more of the phenomenological behaviour of fire. They solve the conservation equations for distinct and relatively large regions. Computer program COMPF2 may be the best-known among them. It is a single-zone model, which solves the heat balance equations to generate gas temperatures. There are several options for calculating the heat release rate, based on ventilation control, fuel control, or the porosity of wood crib fuels[3]. The other computer models include ZONE, CSTBZ1, CFAST, BANZFIRE, etc [Ref. 4]. Loss Prevention Council[5] gives a full list of computer programs and evaluations to them. But none of them is widely used for all applications. Schleich[6] developed a realistic fire evolution model, which not only take into account the physical factors, but also the influence of active protection measures in the structure.

Neither the empirical nor the zone models have the capability to model and predict the combustion process. CFD models both the steady-state and transient state of fire based on the principles of conservation of mass, momentum and energy, and supplemented by models for turbulence generation and dissipation, soot formation and combustion chemical reactions. The outcome of a CFD analysis includes radiative and convective heat flux to surrounding structures and also smoke production and movement. Current models for predicting a fire process are suitable for well defined fuels or burning materials such as gas and oil, but less suitable for building materials for which the combustion process is not well established. Nevertheless, CFD analysis provides the most fundamental understanding of the fire processes, but its use requires huge computer resources. Significant progress has been made in recent years, but further research is still needed in order to improve the "exactness" and capability of current models.

www.EngineeringEBooksPdf.com

HEAT TRANSFER ANALYSIS

The process of heat transfer between a fire and a structure can be described by the balance between the net incident thermal radiation and convective heat flux and the rate of heat conducted in the material. There are two kinds of heat transfer models: simplified calculation model and advanced computational models.

Simplified Calculation Model

Different standards or specifications give similar way to calculate the net heat flux and temperature development in the steel member. The heat flux due to convection is proportional to the temperature gradient between the ambient gas temperature and temperature of the steel member. The heat flux due to radiation is proportional to the temperature gradient of the forth order of the ambient gas temperature and the steel temperature. ECCS[7] uses a single expression to represent the total heat flux as

$$\dot{Q} = K \cdot F \cdot (T_t - T_s) \tag{1}$$

where F = surface area of the member per unit length exposed to heating
T_t = ambient gas temperature at time t
T_s = temperature of the steel member
K = coefficient of total heat transfer

Based on this heat flow law, the temperature development in non-insulated steel member:

$$\Delta T_s = \frac{\dot{Q}}{c_s \rho_s \cdot V} \cdot \Delta t \tag{2}$$

where c_s =specific heat of steel
ρ_s =density of steel
V =volume of the member per unit length
Δt =time interval

Calculation of the temperature development in insulated members varies according to insulation materials.
Eurocode 3[2] gives a more rational estimation of the steel temperature development by considering the section factor and discriminating between internal steelwork and external steel work. For example, the formula for temperature development of unprotected internal steelwork is

$$\Delta T_s = \frac{A_m / V}{c_s \rho_s} \dot{Q} \Delta t \tag{3}$$

where A_m / V is the section factor, $\dot{Q}$ is the design value of the net heat flux per unit area.

Although the techniques for solution of the heat transfer problem are relatively well established, several complicating factors exist. For examples, physical properties such as thermal conductivity, specific heat, emissivity/absorbtivity and heat transfer coefficients vary w ith temperature. Surfaces may also be exposed to re-radiation from other surfaces. The fraction of the emitted radiation received is governed by the configuration factor, which may be tedious to calculate, especially if shadowing of other members are present. Numerical method is often used to improve the accuracy of the heat transfer analysis.

www.EngineeringEBooksPdf.com

Advanced Computational Model

There are two kinds of computational models: commercial computer programs such as ABAQUS, ANSYS, etc and specific heat transfer analysis programs such as CEFICOSS, FAHTS, etc. The former is very powerful in that they are able to analyze any 3D model with non-uniform temperature distributions both over the cross section and along the length of the structural member. But these programs are complicated to operate and not suitable for design implementation. Specific heat transfer analysis programs are based on restrictive assumptions. For example, CEIFICOSS[8], which is a 2D model, assumes uniform temperature distribution along the length of the member but allows any temperature distribution over the cross section by a rectangular mesh of the cross section. FAHTS[9] is a 3D model, which allows temperature load such as ambient gas temperature, point heat source and line heat source to be applied directly. It also considers the insulation effect. But exposure surfaces of the elements are presumed and temperature distribution over the cross section is normally assumed to be linear.

MAERIAL MODELLING AT ELEVATED TEMPERATURE

Experimental evidence shows that the stiffness and strength of steel deteriorate at elevated temperatures. Typical stress-strain curve of steel at elevated temperatures is shown in Fig. 4. The stress-strain relationship at elevated temperature does not exhibit a distinctive yield plateau.

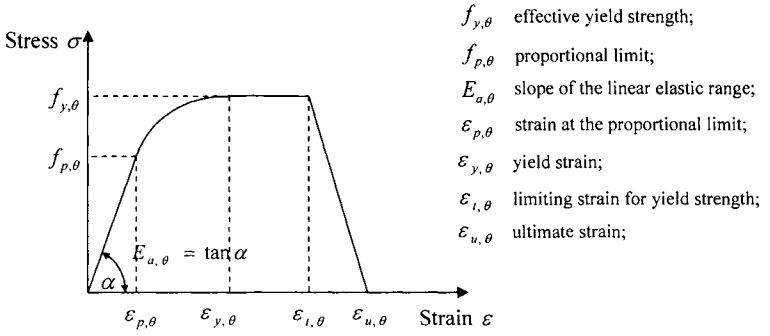

Figure 4 Stress-strain relationship of steel at elevated temperature according to Eurocode 3 [Ref. 2]

Therefore, the yield stress, or 0.2% proof stress, which is conventional design strength for steel at ambient temperature, loses its relevance because of the nonlinearity of the stress strain curve. Since fire is considered to be an accidental situation, large plastic strains are allowed. Hence, an effective yield stress is used, which is attainable when the strain is considerably larger than the elastic limit at normal temperatures. Eurocode 3 (1993) adopts a yield strain of 2% to define the effective yield stress. The temperature dependence of the proportional limit, the effective yield strength as well as the elastic modulus recommended by Eurocode 3 are shown in Fig. 5.

www.EngineeringEBooksPdf.com

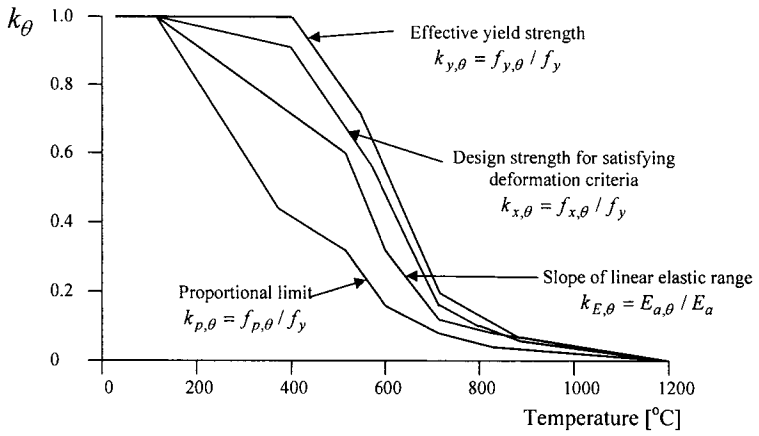

Figure 5 Reduction factor according to Eurocode 3 [Ref. 2]

Creep may be of importance in a fire situation where a cross section is subjected to high temperature (above 400 ^{0}C) and high stress for a long period of time. The stress-strain curves given in Eurocode 3 are based on measurements at constant temperature within a two-hour period to allow creep to take place in the tests. Therefore, creep effect is included in the effective yield strength used for design. In other words, when the design is based upon code values, creep does not need to be considered explicitly. If the temperature and load history is such that a structural component remains at high temperature or is highly stressed for only a short period, the prediction using the code values should yield conservative results.

When the plastic-hinge analysis is used[10-12], it is assumed that cross section is compact and the full plastic capacity can be achieved. At elevated temperature, the plastic strength surface should follow the effective yield stress and its temperature reduction curve $k_{y,\theta}$ for yield, as illustrated in Fig. 5. The elastic modulus also degrades at elevated temperature following the temperature degradation curve for the slope of linear elastic range $k_{E,\theta}$ as in Fig. 5.

STRUCTURAL RESPONSE ANALYSIS

Structural model calculates the structural performance under the temperature development obtained from thermal transfer analysis.

Simplified methods are applicable for assessing individual members in a frame subassembly. Eurocode 3 gives formula for computing resistance of tension members, beams, columns, and beam-columns. In the case of a braced frame in which each storey comprises a separate fire compartment with sufficient fire resistance, the buckling length of a column may be taken as those shown in Fig. 6. However, guidance is not given for sway frames in which storey buckling and overall stability may dominate the design of individual member. Wang et al.[13] offered simplified methods to analyse the performance of steel frames. They study the effect of continuity on the fire resistance of columns in both sway and non-sway steel frame and suggested some restraint stiffness values at the end of the column due to the continuity of the sub-frame from the parametric study.

www.EngineeringEBooksPdf.com

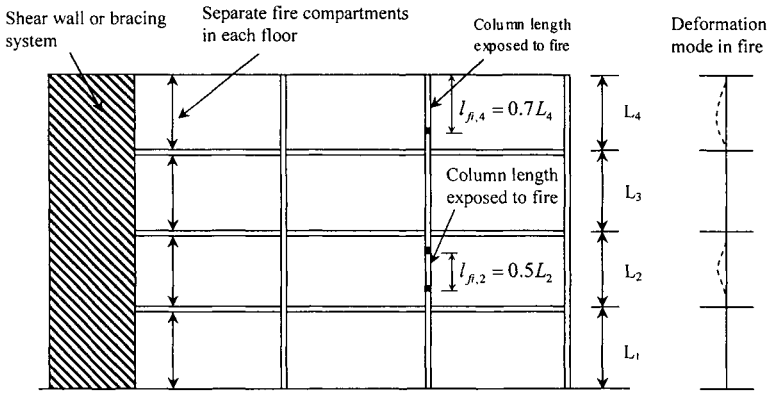

Figure 6 Buckling length of columns in braced frames [Ref. 2]

General commercial programs such as ABAQUS, ANSYS, NASTRAN, may be used for analysing structures exposed to fires. They take the advantages of full validation, powerful ability to model different kinds of problems and availability of second development so that they can almost suffice all needs. But they are rather inconvenient to use for being both time-consuming and complicated to operate since the structural analysis under fire condition is highly non-linear and transient. After Cardington test, the research group developed a rigorous computational model, ADAPTIC, for parametric studies and calibrated with the test results[13].

The beam-column plastic hinge method is a very efficient tool for progressive collapse analysis of large structures[15]. But for fire analysis, it is found to give coarse results. When the structure is modelled with beam elements, the beam model must be re-meshed for the heat transfer analysis. The fineness of the mesh depends upon the cross-sectional thermal gradients. Large temperature gradients over the cross section may occur due to partly protected cross sections or uneven fire exposure. Coarser mesh may be used when the temperature differences across the section are small. Finer mesh is required to model three sides exposed beams[12]. In the analysis of large structures, "mixed elements" could be used in which spread-of-plasticity elements are used for fire-exposed areas and beam-column elements are used for areas not exposed to fire.

Another method of including the thermal effect is to find an ambient-temperature elastic section, which is equivalent to the heated one. The equivalent section can be obtained by reducing the thicknesses of all plates of the steel cross-section using the modular ratio E_T / E_{20}[16]. Based on this theory, Bailey [7,18] developed a program INSTAF for inelastic analysis of plane frames. The program uses two-node one-dimensional elements in which the cross-section of each element is divided into a set of plate segments by sampling points. Given a reference strain distribution over the cross-section, and a stress-strain curve appropriate to each segment, the thickness of each segment is scaled by the modulus ratio E_t / E. Later, VULCAN was developed to model the steel beams and concrete beams within composite steel-framed building by a layered procedure[19]. Higher-order iso-parametric element and total Lagrangian approach are adopted so that the membrane effect of the slab is included.

www.EngineeringEBooksPdf.com

NARR2 is a two-dimensional computer program based moment-curvature method taking into account material non-linearity, geometric non-linearity, in-plane frame instability. It is based on the theory that any equilibrium state of a non-linear system can be described by a set of linear equations, provided that they are expressed in terms of the non-linear deformations. To achieve this, the beam is divided into line elements small enough to justify the assumption that internal deformations and forces are uniform along their lengths. The flexural stiffness of each element is expressed as the ratio of its total moment to its total curvature[20]. Geometrical non-linearity is considered by adding a geometrical matrix to the member stiffness matrix. A semi-rigid connection is included by directly modifying the stiffness matrix and the vector of fixed-end forces of an element.

Other commonly used computer programs include ADAPTIC, SAFIR, CEFICOSS, etc. Each has its own characteristics. Detailed descriptions of which can be found in Refs [9, 21 and 22].

CONCLUSIONS AND FUTURE WORK

The existing prescriptive fire resistance rating method does not provide sufficient information to determine how long a structure and the components in a structural system can be expected to perform in an actual fire. A method of assessing performance of structural components and the entire structural system in building fires is needed. The behaviour of the structural system under fire conditions should be considered as an integral part of the structural design. It is essential to develop design tools, including an integrated model that predicts heating conditions produced by the fire, temperature rise of the structural component, and structural response. This paper provides an insight into available methods including simple calculation methods for design and advanced computer models used for rigorous assessment.

General commercial programs are not suitable for design. Most research programs are written for specific purpose and wide range of use for design is to be validated or further developed. Future trends for structural fire research are likely to focus more on the development of integrated tools for performance-based design. Modelling of composite structures including composite slab, beams, columns and joint behaviour in fire is a step forward to unlock the benefit of composite design and their effects on the overall performance of buildings in fire. An integrated analysis of fire and blast is of great interest because of global terrorism and its impact on tall building design. Analysis of large structures exposed to attack fire is still prohibiting and therefore simplified model such as the plastic hinge-based method will be preferred. For large structures, robustness and redundancy of the structural framing are design features that have been identified as key to the building's ability to withstand extreme loads to allow safe evacuation of building occupants. Modelling of passive fire protection (PFP) is a challenging task because the thermal properties of PFP are different from those of steel and concrete, and their properties may change drastically during a fire. Performance criteria and test methods for fireproofing materials relative to their durability, adhesion, and cohesion when exposed to attack fire need further study.

RFFERENECS

1 Buchanan, Andrew H., *Structural Design for Fire Safety*, John Wiley & Sons, Ltd.
2 Eurocode 3 :*Design of steel structures- part 1.2: General rules—Structural fire design* 1993-1-2:2001
3 Feasey, R. and Buchanan, A., Post-falshover fires for structural design, *Fire Safety Journal*, 37 (2002), 83-105.
4 SFPE, handbook of fire protection engineering, third edition.
5 Loss Prevention Council, *Report on the state of the art of Compartment fire modeling*, 1994.

www.EngineeringEBooksPdf.com

6 Schleich, J. B., A natural fire safety concept for buildings -1, *Fire, Static and Dynamic Tests of Building Structures*, E & FN SPON, 1996
7 ECCS, *European Recommendations for the Fire Safety of Steel Structures*, ECCS-Technical Committee 3-Fire Safety of Steel Structures
8 Franssen, J.M, Cooke, G.M.E., and Lathan, D. J., Numerical Simulation of a Full Scale Fire Test on a Loaded Steel Framework, *Journal of constructional steel research* 35 (1995) 377-408
9 Tore Holmas, *FAHTS- Fire and Heat Transfer Simulations of Frame Structures*, SINTEF Structures and Concrete
10 Liew, J.Y.R, Ling Kan Tang, Tore Holmuas and Y S Choo, Advanced analysis for the assessment of steel franes in fire. *Journal of Constructional Steel Research*, 47, no. 1-2 (1998): 19-45.
11 Liew J.Y.R., Tang LK and Choo YS, Advanced analysis for performance-based design of steel structures exposed to fires, *J of Structural Engineering*, ASCE, USA (2002), In Press.
12 Liew JYR and Ma KY (2002), Advanced analysis of steel framework exposed to accidental fire, ,In Proceedings of Second International Workshop on Structures in Structures, Christchurch, New Zealand, 18-19 March, 2002, 303-318.
13 Wang, Y.C., Lennon T, and Moore, D.B., The behavior of steel frames subject to fire, *Journal of constructional steel research* 35 (1995) 291-322
14 PIT Project, *Behaviour of steel framed structures under fire conditions*, MAIN REPORT, the University of Edinburgh, 2000.
15 Liew JYR, State-of-the-art of advanced analysis of steel and composite frames, *Int J Steel and Composite Structures*, Techno-Press 1(3), 2001,341-254.
16 Najjar SR, *Three-dimensional analysis of steel frames, sub-frames in fire*, Ph.D. Thesis. UK: University of Sheffield, 1994
17 C.G. Bailey, Development of computer software to simulate the structural behavior of steel-framed buildings in fire, *Computers and Structures*, 67 (1998) 421-438
18 Colin Bailey, Computer modeling of the corner compartment fire test on the large-scale Cardington test, *Journal of Constructional Steel Research*, 48 (1998) 27-45
19 Zhaohui Huang, Ian W, Burgess, Roger J. Plank, Non-linear structural modeling of a fire test subject to high restraint, *Fire Safety Journal* 36 (2001) 795-814
20 Ei-Rimawi, J. A., Burgess, I. W., and Plank, R. J, The analysis of Semi-rigid Frames in Fire- a Secant Approach, *Journal of constructional steel research,* 33 (1995) 125-146
21 Elghazouli, A.Y., Izzuddin, B.A. and Richardson, A.J., Numerical modeling of the structural fire behavior of composite buildings, *Fire Safety Journal* 35 (2000) 279-297
22 Becker, R., Structural behavior of simple steel structures with non-uniform longitudinal temperature distributions under fire conditions, *Fire Safety Journl,l* 37 (2002) 495-515.

www.EngineeringEBooksPdf.com

This Page Intentionally Left Blank

www.EngineeringEBooksPdf.com

Advances in Steel Structures, Vol. II
Chan, Teng and Chung (Eds.)
© 2002 Elsevier Science Ltd. All rights reserved.

WORLD TREND FOR THE DEVELOPMENT OF PERFORMANCE-BASED FIRE CODES FOR STEEL STRUCTURES

M. B. Wong

Department of Civil Engineering, Monash University, Melbourne, 3800, Australia

ABSTRACT

The global trend towards developing a rational concept for fire engineering design of buildings has started to take effect on code development in many countries. This trend is accompanied by a large amount of research which results in the publication of performance-based codes by various countries in recent years. These performance-based codes are to replace gradually those with obsolete prescriptive requirements. As a result, we should expect to see a number of new fire codes and amendments to existing ones in the coming years. In fact, this process has been going on for a number of years. A performance-based approach to design requires structures to satisfy certain requirements based upon the behaviour of the structures in fire under realistic situations. A prescriptive-based approach to design only requires the satisfaction of certain prescribed requirements under prescribed conditions irrespective of the actual conditions that the structures are subject to in fire. Among all types of codes related to structural design, performance-based fire code for steel structures is at the forefront of development. For instance, the Eurocode for fire design of steel structures is among the first to be released in 2003. In this paper, an account of the significant development in fire engineering design codes, with particular reference to structural steel design, in some countries are given. The description of this development does not preclude the fact that a large amount of work in this area is still being done in many other countries which may not have been mentioned. However, effort has been made to include countries involving major fire code development although such list can never be exhaustive.

KEYWORDS

Fire engineering, steel structures, fire code development, performance-based design, fire research

GLOBAL TREND OF FIRE ENGINEERING

A performance-based fire code encompasses a range of requirements for whole building performance, such as structural stability, smoke control, fire spread, fire detection, fire suppression, means of escape,

www.EngineeringEBooksPdf.com

fire brigade response, etc. Structural design for fire is one of the key requirements for achieving a satisfactory fire safety environment for buildings. The introduction of performance-based fire safety codes has seen an opportunity for the engineering industry to reduce the construction cost by, among other things, reducing the cost in fire protection of structural members. It also leads to innovation in implementing active fire preventive measures such as sprinkler systems as well as a total rethinking of the structural design process and principles of building components on the basis of the structure's performance in fire.

For instance, the common practice in structural design is that structural engineer would assess the strength of the structural members, leaving the fire safety engineer to consider the fire protection requirements of the members. This process for structural design and fire protection design may be carried out by the two engineers independently without knowing what the other is doing. However, in a performance-based design environment, this design procedure may not be acceptable. The structural engineer must assess the fire resistance of the structural members in terms of the failure temperature or time. This information is the basis for the fire safety engineer to design fire protection, rather than using some arbitrary chosen failure temperature to determine, for example, the thickness of the fire protection material. To optimise the design, the two engineers must constantly exchange information regarding parameters for fire engineering design.

Ideally, the whole structural design process for members under fire condition should be carried out by engineers within a single discipline so that the whole design process becomes transparent to the designers and efficiency can be achieved. It also seems logical that structural engineers will play a major role in carrying out the fire design for structural members. Unfortunately, our undergraduate courses at universities have yet to reflect this trend.

In the following, a description of the major development of fire engineering requirements for steel structures in steel design codes in some countries or regions is given. This development not only reflects the trend for the integration of both the structural design and fire engineering design processes, it also gives indication to the research effort that individual organizations and countries have contributed to the development of performance-based fire codes. The following description does not preclude the fact that a large amount of work in this area is still being done in many other countries which may not have been mentioned. However, effort has been made to include countries involving major fire code development although the list can never be exhaustive.

The performance-based design process for structural members under fire conditions may involve a series of procedures, the complexity of which depends on how the design code is written. For instance, the strength capacity of a member in fire can be derived on the basis of property degradation at elevated temperatures, or can be tabulated on the basis of experimental results. For comparison purposes, the design process is divided into three major steps as shown in Figure 1.

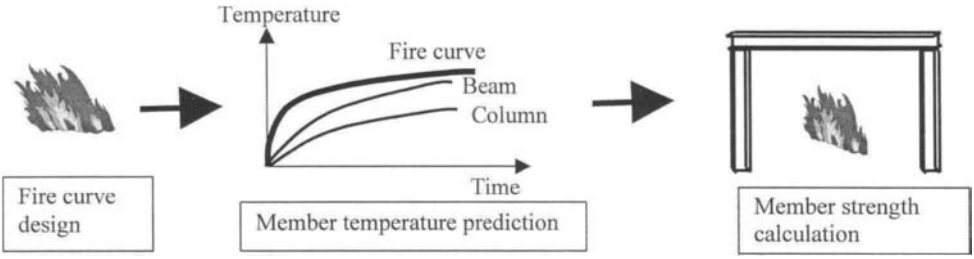

Figure 1: Design process for structural members in fire

www.EngineeringEBooksPdf.com

The first step is the fire curve design. It could be based on the theory of fire science or simply based on some arbitrary standard fire curves which assume the fire to grow indefinitely. In the second step, the temperature prediction can be performed for steel members, fire protected or unprotected, using the fire curves obtained. On the basis of the temperature distribution obtained, the strength of the structure can be assessed in the third step. The performance-based fire engineering design requirements for structures are always evolved around these three steps. For instance, the failure temperature of a steel member could be based on a prescribed value, such as 180°C according to past practice without any sound scientific justification. However, it can also be derived from analytical solution using heat transfer theory or from more sophisticated fire dynamics theory, such as the zone or field models. The latter can be said to be performance-based methods but the accuracy depends on the sophistication of the theory.

It should be noted that the requirements in steel design codes described below might be overridden by other national documents such as the national building code which is not included in the current context.

AUSTRALIA

The first major event invoking concerted effort to look into fire engineering technology in Australia is the formation of a working party under the banner of The National Committee on Structural Engineering, Institution of Engineers Australia in 1987. A few reports related to fire safety were published by different authors in subsequent years. The establishment of the Fire Code Reform Centre by industry and research organizations with sponsorship from the government in the nineties reinforced the commitment of Australia to performance-based fire safety reform.

In Australia, there is no single design code exclusively for steel structures under fire conditions. The design criteria are included in one of the seventeen sections in the steel structures design code AS4100 (SA, 1998).

Fire Curve Design

All calculations and experimental results are based on the ISO 834 standard fire curve. No provisions for other fire curves are envisaged.

Member Temperature Prediction

The temperature prediction procedure has been omitted by directly linking the steel limiting temperature to the time to failure using established experimental results from standard fire tests. The data is valid for unprotected steel temperatures up to 750°C.

For steel with fire protection, a regression analysis technique is employed to relate the steel limiting temperature to the time to failure. The coefficients for such relationship for any fire protection material must be established by fire tests which define a window of interpolation limits for such material.

Member Strength Calculation

Partial load factors for dead and live loads are used for the fire limit state. The deterioration rates for both yield stress and modulus of elasticity are provided. The determination of limiting steel temperature is based on the load ratio method which is a general derivation from the yield stress deterioration formulation. No specific method for the determination of design actions on the members is given.

www.EngineeringEBooksPdf.com

CHINA - MAINLAND

Major research on the structural behaviour and design of structures subject to fire started in, amongst others, Tongji University, Shanghai in the early nineties. In 1998, a draft fire code on steel structures was published by Tongji University (Li, et al, 1999) and, in 2000, the Technical Code on Fire Safety of Steel Building Structures was compiled (Li & Lou, 2001). This code stipulates the temperature, loading and strength requirements for steel elements subject to fire.

Fire Curve Design

All calculations are based on ISO 834 standard fire curve.

Member Temperature Prediction

Analytical solutions for temperature prediction of steel members including those with insulation are given. However, the formulation is valid for ISO 834 standard fire only.

Member Strength Calculation

Partial load factors for dead, live and wind loads are used. The deterioration rates for both yield stress and modulus of elasticity are provided. Semi-empirical formulations with appropriate temperature dependent parameters are provided for both bending and axially loaded members under increasing temperature. Both strength and deformation limit states are stipulated.

CHINA - HONG KONG SPECIAL ADMINISTRATIVE REGION (HKSAR)

The government of HKSAR has started to move towards reviewing its existing fire safety regulations with a view to possibly adopting a performance-based approach for design on the basis of sound engineering principles. Since 1990 when review on existing codes of practice related to fire engineering got underway, four codes of practice (Means of Escape Code 1996, Fire Resisting Construction Code 1996, Means of Access for Fire Fighting and Rescue Purpose Code 1995, Minimum Fire Service Installations and Equipment 1994) have been published. These codes allow a performance-based approach to be adopted for the design or alteration of buildings to meet the fire safety requirements stipulated in the Building Regulations.

In early 1998, a Fire Safety Committee of the Building Department in Hong Kong was established to oversee the building fire safety design with performance-based approach. Review of key areas of fire safety codes has been carried out and identified. A general description of the status-quo, current review and research activities, and the future directions in the development of performance-based fire codes can be found in Chow (1999). The steel structures design requirements in Hong Kong still follow the British practice.

EUROPE

A large number of countries in Europe have been conducting fire engineering research for a number of years. A concerted effort is being made to promote the use of unified codes through the European Community. In 1979, a working group was set up by the Commission of the European Communities to prepare a set of Eurocodes on construction and buildings to be used in all European Community member states as alternatives to the different national codes. The work was transferred to the European Committee for Standardisation (CEN) in 1990. In 1988, the Construction Product Directive (CPD) and

www.EngineeringEBooksPdf.com

its Interpretative Document (IP) were issued. One of the six essential requirements given in CPD is "Safety in case of fire" which contains the basic principles to be adopted, leaving the requirement details to the member states. Fire resistance can be verified through tests or calculations. Tests are based on ISO 834 standard fire curve but natural fire concepts are stated as alternative. The Eurocodes are given the status of European Standards (ENs), administered by CEN. It is expected that ENs will eventually replace all national codes. At present, the whole suite of the draft Eurocodes (ENV) is being converted into EN status, due for completion in 2004. The standards are to be adopted by each member state in EC. The ENV for steel structures has since been named as EUROCODE 3 (EC3), with conversion to EN being started in September 1999. A full EN status for fire structural design for steel, concrete composite, timber and masonry structures is expected in late 2002.

EC3 embraces the results of the most recent fire research carried out mainly in Europe. It contains design features which are distinctively different from other steel fire codes.

Fire Curve Design

The code stipulates two categories of fire curves: nominal fire curves and natural fire curves.

Nominal fire curves include the ISO 834 standard fire, the hydrocarbon fire which gives a more severe fire scenario than the standard one under certain circumstances such as offshore platform structures, and the external fire for structural members external to the main structure.

Natural fire curves, termed parametric fire curves in EC3, simulate the behaviour of a real fire which grows to a peak with a peak temperature, followed by a decay period when the fuel gradually burns out. The severity of a fully developed natural fire depends mainly on the fire load, ventilation characteristics and the thermal properties of the compartment. A special feature in this part of the code is that the amount of fuel load depends on a number of partial factors, the values of which are derived from probability consideration.

Member Temperature Prediction

Analytical solutions, based on heat transfer theory including convection, radiation and conduction properties of heat, are used to predict the temperature rise of a steel member. However, in order to match the results of fire tests for individual states, partial factors are being used in the formulations. These factors are considered as "fudge factors" which may vary from one country to another. Because of the routine nature of the calculation procedure, spreadsheet is usually used for such computation. Both protected and unprotected steel members are envisaged.

Member Strength Calculation

Contrary to many other fire codes, the design actions in fire can be related to the design actions at room temperature through a reduction factor for different fire situation, which varies with the ratio of the live and dead loads. Rather than using yield stress degradation rate in fire, a complete stress-strain curve at a specific temperature is defined. The thermal properties of steel, including temperature dependent specific heat and thermal conductivity, are also given. The calculation of the member strength can be carried out according to the mechanical properties at elevated temperatures.

SWEDEN

It must be mentioned that Sweden is one of the few countries which have a long history in developing performance-based structural fire design codes. A performance-based fire engineering design code for

www.EngineeringEBooksPdf.com

steel structures (SBI, 1976) was published with comprehensive guidance to the detailed design procedures for steel structures. The format is similar to that of Eurocode. A full performance-based building code was introduced into Sweden in 1994.

Fire Curve Design

Both standard fire and natural fire curves can be specified. A typical natural fire designed to EC3 and the Swedish code is shown in Figure 2, together with the ISO 834 standard fire curve.

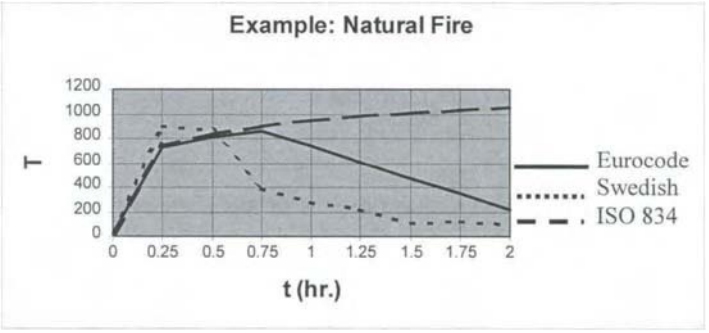

Figure 2: Fire curves

Member Temperature Prediction

Analytical solutions based on heat transfer theory are used. Both protected and unprotected steel members are included.

Member Strength Calculation

Numerical methods can be used for strength calculation of members according to the deterioration rates of steel properties. Use of plastic design method at elevated temperatures is also demonstrated.

UNITED KINGDOM

In 1990, a 3-year contract, administered by BSI and funded by the Department of Trade and Industry, was awarded to a group of fire safety engineers to prepare a draft Code of Practice on life safety. This document subsequently led to the publication of a Draft for Development (DD) by BSI.

In 1993, the Department of the Environment commissioned Bickerdike Allen Partners to produce an illustrated text on the fire safety principles underlying current UK legislation. Subsequently, a document "Design principles of fire safety" (DoE, 1996) was published. This document contains general principles rather than numeric details. Chapter 5 of this document gives detail on the functional requirements for fire resistance of structural elements. Structural design requirements for steel structures in fire are given in BS5950, Part 8 (BSI, 1990).

Fire Curve Design

The tabulated data for structural design are established from standard fire tests. However, consideration of natural fires is allowed when numerical methods are used for fire resistance assessment.

www.EngineeringEBooksPdf.com

Member Temperature Prediction

Semi-empirical formulation is used to relate the time of heating to the properties of the steel members derived from fire test results. This procedure can be omitted when fire resistance is assessed with tabulated data.

Member Strength Calculation

The fire resistance of structural members at elevated temperatures can be assessed with tabulated data from fire tests or by numerical methods.

UNITED STATES

The difficulty in developing a unified fire code in the United States is due to the fact that the 50 sovereign states make their own regulatory decisions empowered by the local "Authority Having Jurisdiction", or AHJ (Snell, 1993). Effort is being made to rectify this situation, with the National Institute of Standards and Technology (NIST) and the National Fire Protection Association (NFPA) playing a pivotal role.

Although there is no formal fire code for structural design in the United States, the publication of the ASCE Manual on structural fire protection (Lie, 1992) gives detailed design guides and formulas for fire design of structural elements using various construction materials. It is an excellent tool for structural design of members using performance-based criteria. The design criteria are both experimental and empirical, and fire curves are based on heat transfer theory.

SOUTH AMERICA

Not much is known about the development of fire safety codes in South America. Brazil claims to be the first in South America to develop the fire safety engineering codes for structural design.

Brazil

In 1996, a study group consisting of the Brazilian Association of Technical Standards and experts from a number of universities presented a draft related to the design of structural components in fire. Subsequently, in 1999, two standards were approved for adoption in structural design for fire (Silva & Fakury, 2002):

1. NBR 14432 "Fire Resistance Requirements for Building Construction Elements".
2. NBR 14323 "Steel Structures Fire Design".

The NBR 14323 standard allows the use of performance-based methods for steel design. The basis of the design procedures is largely adopted from Eurocodes 3 and 4 for steel and steel/concrete composite structures respectively.

CONCLUSION

There are many other countries, such as Japan, New Zealand, Canada, Russia and many European countries, which are conducting fire research, resulting in the publication of fire design codes. This paper gives some typical examples of national codes for design of steel structures in fire. Naturally, the process of publishing and amending these codes is on-going and more countries are expected to get

www.EngineeringEBooksPdf.com

involved in this process in the near future. A summary of the design characteristics for steel structures in fire stipulated in the fore-mentioned steel codes is given in Table 1 for comparison purposes.

TABLE 1
SUMMARY OF STRUCTURAL DESIGN FOR FIRE BY VARIOUS COUNTRIES

Region	Fire curve design		Temperature prediction		Strength calculation	
	Standard	Natural	Experimental	Analytical	Experimental	Numerical
Australia	✔		✔		✔	
Brazil	Similar to Eurocode					
China	✔			✔		✔
Europe	✔	✔		✔		✔
Sweden	✔	✔		✔		✔
UK	✔	✔	✔		✔	✔
USA	✔	✔		✔		✔

REFERENCES

BSI (1990). *BS5950 – Structural Use of Steelwork in Building. Part 8. Code of Practice for Fire Resistant Design.* British Standards Institution.

Chow W.K. (1999). Preliminary Discussion on Engineering Performance-based Fire Codes in the Hong Kong Special Administrative Region. *International Journal on Engineering Performance-based Fire Codes*, Vol. 1, No. 1, 1-10.

Department of the Environment (1996). *Design Principles of Fire Safety.* UK.

ENV 1993-1-2 (1995). *Design of Steel Structures – Structural Fire Design.* CEN.

Li G.Q., Jiang S.C. and He J.L. (1999). The First Code on Fire Safety of Steel Structures in China. *Proceedings of The Second International Conference on Advances in Steel Structures*, December, Hong Kong, 1031-1038.

Li G.Q. and Lou G.B. (2001). The Principles of Fire Resistance for Steel Structures in China. Proceedings of the International Seminar on Steel Structures in Fire, December, Shanghai, China, 29-39.

Lie T.T. (Editor) (1992). *Structural fire protection*, ASCE Manuals and Reports on Engineering Practice No. 78.

SA (1998), *AS4100 – Steel Structures*, Standards Australia.

SBI (1976). *Fire Engineering Design of Steel Structures*, Swedish Institute of Steel Construction.

Silva V.P. and Fakury R.H. (2002). Brazilian Standards for Steel Structures Fire Design. *Fire Safety Journal*, 37, 217-227.

Snell J.E. (1993). Status of Performance Fire Codes in the USA. *Nordic Fire Safety Engineering Symposium: Development and Verification of Tools for Performance Codes*, Espoo, Finland, August.

www.EngineeringEBooksPdf.com

Advances in Steel Structures, Vol. II
Chan, Teng and Chung (Eds.)
© 2002 Elsevier Science Ltd. All rights reserved.

A NEW METHOD TO DETERMINE THE ULTIMATE LOAD CAPACITY OF COMPOSITE FLOORS IN FIRE

A.S.Usmani and N.J.K.Cameron
School of Civil and Environmental Engineering, University of Edinburgh,
Edinburgh, EH9 3JN, UK

ABSTRACT

This paper presents a new method for determining the ultimate load capacity of composite floors systems in multi-storey building fires. Collapses of composite frame buildings in fire are an extremely rare event (event of September 11, 2001 were clearly extraordinary), therefore the manner of structural failure is not well understood. One of the main contributions to the robust performance of such structures is due to the tensile membrane mechanism in the composite deck slab. The research group at Edinburgh has discovered that the development of tensile membrane mechanism in fire is much more reliable relative to ambient conditions. This is because a large amount of thermal strain allows composite floor systems to assume highly deflected shapes while limiting the magnitude of damaging tensile mechanical strains, thereby retaining the ability to carry loads for much longer. Clearly, if the limits of the additional load capacity through the tensile membrane mechanism was reliably quantified, a powerful design tool would become available to engineers. Some previous work exists in this regard, but there are fundamental flaws in these approaches. Essentially these methods project ideas from tensile membrane behaviour at ambient temperature and do not take adequate account of the thermal response. This work introduces a new three-step method to analyse the ultimate capacity of laterally restrained composite floor slabs in fire.

KEYWORDS

Composite floors in fire, restrained thermal expansion, thermal bowing, ultimate capacity

INTRODUCTION

Over the last decade a great deal of new knowledge has been generated towards understanding the behaviour of structures if fire. This is particularly true for composite steel framed structures with concrete deck floor systems. The impetus for this accelerated development was initially provided by the Broadgate fire [1], followed by the full scale fire tests at BRE's Large Building Test Facility (LBTF) at Cardington [2]. This research has shown that composite floor systems in such structures possess considerably greater fire resistance than accounted for in design procedures [3–5]. The reinforced concrete slab (constructed compositely with steel beams) continues to provide viable load paths after unprotected steel beams have lost adequate strength and stiffness. The authors have developed a new method to quantify the ultimate membrane capacity of slabs in fire using a failure criterion based on a limiting reinforcement strain [6]. This paper develops this method to include the catenary capacity of secondary beams.

The Cardington fire tests and subsequent modelling work has shown that tensile membrane action in the floor system is the final resisting mechanism in a building fire before collapse. This fact is implicitly recognised by a number of authors [7,8] and they have proposed methods to enable quantification

www.EngineeringEBooksPdf.com

of the load carrying capacity at the fire limit state. Whereas these methods are of considerable practical benefit, they do not account for the correct shape of the floor system under the influence of heating. This is because these methods develop previous work [9,10] quantifying the enhancement to load carrying capacity by membrane effects, but for ambient conditions. Therefore, in effect they extend the ambient temperature failure shapes based on flexural failure (yield line mechanism) to apply to the fire situation. This is erroneous as it can be shown that at the fire limit state the bending resistance of slabs is practically negligible and the eventual failure will not occur in the manner of a yield line failure (which is essentially a low-deflection mechanism). The correct deflected shape of the slab resulting from accommodating the large thermal strains (extension and curvature) provides much enhanced membrane capacity. As this mechanism becomes more and more dominant with heating and larger deflections, failure will most probably occur in the manner of a tensile rupture of reinforcement (most likely at the supports).

Incorporating the correct deflected shape and failure mechanism to quantify the membrane capacity in fire conditions requires several new developments. The first is to develop a reliable estimate of the temperature distribution in the reinforced concrete floor slab, followed by determining the correct deflected shape and the ultimate load carrying capacity based on an assumed failure mechanism.

ASSUMPTIONS

The analysis procedure is based on a number of simplifying assumptions based on the authors understanding of floor panel behaviour in fire.

1. The slab is assumed to be rectangular in plan and restrained against lateral translation at all boundaries and free to rotate about the axes coincident with each boundary
2. Anchorage to tensile membrane forces in the slab is available at the perimeter
3. Temperature distribution in the slab varies only through the depth and the slab deflected shape is entirely governed by the temperature distribution in the slab
4. The failure during the heating phase of the fire is assumed to occur in a ductile manner (runaway) and no localisation of strain occurs in the reinforcement
5. The compartment perimeter beams are assumed to deflect much less than the centre of the slab.
6. Tensile membrane capacity is derived entirely from the reinforcement
7. Reinforcement temperature is identical to the surrounding concrete and so is its thermal expansion coefficient.

The proposed analysis is carried out in three stages, each requiring a considerable amount of effort and is separately discussed in the following sections.

THERMAL INPUT

One of the key conclusions from the research so far is that structural response to fire depends upon the rate of heating as well as the temperature of the structure, and that different fires can produce very different stress/strain patterns in composite floor systems [3]. This is because most of the pre-failure response of structural members depends upon the two geometric effects produced by heating, a mean temperature increase and a mean thermal gradient [11]. The material effects of reduction in strength and stiffness with temperature increase also require accurate estimates of the temperature distribution. The following subsections discuss the three part procedure adopted here for calculating accurate thermal input.

www.EngineeringEBooksPdf.com

Fire scenario

The fire scenario can be obtained using a number of different approaches. The simplest of these will be to adopt one of a number of standard fires, *i.e.* BS476 or ASTME119. If however the details of the fire compartment are known (or can be be estimated as part of design data, including geometry, ventilation and thermal characteristics of the wall linings and fuel load) then a better approach is to use a natural fire. This can be based on Eurocode 1 parametric relationships [12] (as chosen here) or any other suitable method.

Temperature distribution over slab depth

A 1D finite element program was written to calculate the temperature distribution. Exposition of this work is outside the scope of this paper, however for general details of finite elements for heat transfer, refer to [13]. The program developed was applied to 100 mm thick lightweight concrete slab subjected to an Eurocode 1 parametric fire. The fuel load was assumed to be 750 MJ/m^2, the opening factor was 0.08 $m^{\frac{1}{2}}$ and the thermal inertia of the wall lining was 1100 $Jm^2s^{\frac{1}{2}}K$. Figure 1 shows the variation of temperature over the depth of the slab at various times during the fire scenario, both during the heating and cooling phases (before and after peak fire temperature). Figure 2(a) shows the time evolution of the Eurocode 1 parametric fire chosen here.

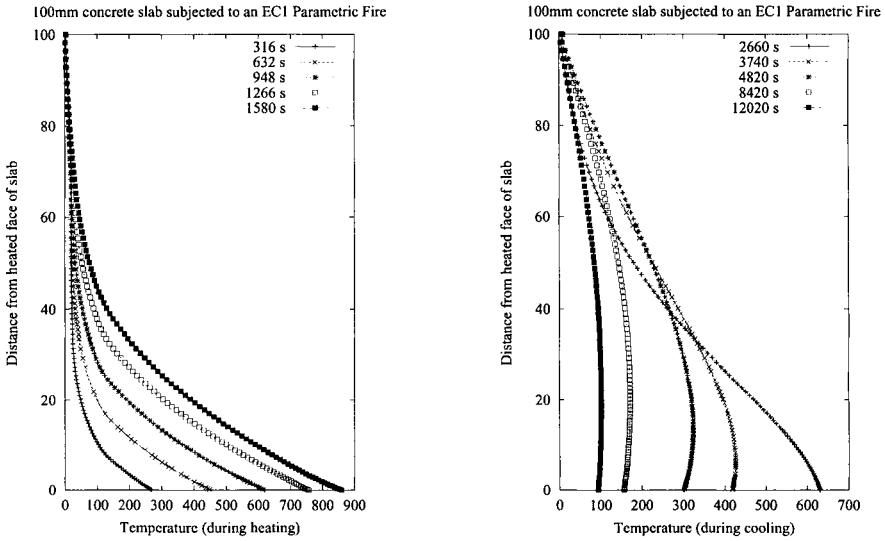

(a) Heating phase

(b) Cooling phase

Figure 1: Temperature distribution in the slab over the whole fire scenario

Estimation of equivalent temperature effects on the model

Given that the cross-sections of composite structural members and the temperature distributions over their depths can be quite complicated, the issue of equivalent thermal loading that must be applied to the members is not straightforward. A procedure developed specifically for this purpose [6] is applied to the chosen 100 mm lightweight concrete slab subjected to the fire specified earlier. Figure 2(a)

www.EngineeringEBooksPdf.com

shows various temperatures against time (including the mean slab temperature). Figure 2(b) shows the equivalent temperature gradient variation over time.

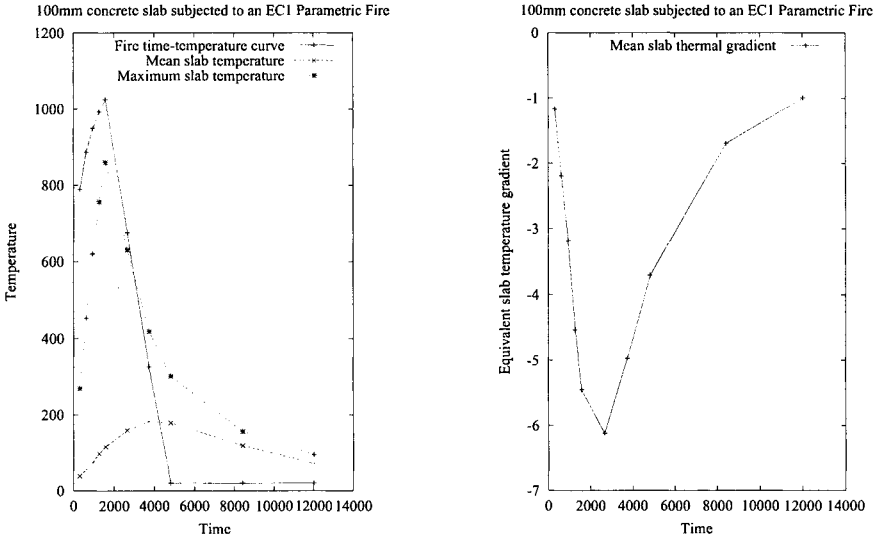

(a) Mean temperatures

(b) Equivalent slab temperature gradient

Figure 2: Time variation of temperatures and equivalent thermal gradient over slab depth

DETERMINATION OF THE SLAB DEFLECTION PROFILE AND STRESS STATE

In this section a method is presented for determining the deflection of a slab and the resulting stress and strain distribution due to the thermal loading only. The analysis is geometrically nonlinear, however, the material behaviour is linear i.e. material degradation is not considered. Although material softening does play an important role in the behaviour of a structure in a fire, its importance is not as great as traditionally thought. Full details of the method and derivation appear in [6], only a brief outline is provided here.

Thermal loading

The thermal loading is caused by the thermal gradient $T_{,z}$ and the thermal expansion ΔT. These cause a thermal moment M^T and a thermal force N^T respectively which can be calculated:

$$M^T = E\alpha \int_{-h/2}^{h/2} T(z) z \, dz = E\alpha T_{,z} \frac{h^3}{12} \tag{1}$$

$$N^T = E\alpha \int_{-h/2}^{h/2} T(z) \, dz = Eh\alpha\Delta T \tag{2}$$

Governing equations

To calculate the distribution of membrane stresses within a slab (in the $x-y$ plane) subjected to thermal loading there are two governing differential equations which must be solved. For stresses

www.EngineeringEBooksPdf.com

under large deflections to be obtained it is necessary to retain the nonlinear terms. The two equations to be solved are the equilibrium equation and the compatibility equation [14] which, for an isotropic flat slab subject to thermal loading, can be written as,

$$D\left(\frac{\partial^4 w}{\partial x^4}+2\frac{\partial^4 w}{\partial x^2 y^2}+\frac{\partial^4 w}{\partial y^4}\right)-h\left(\frac{\partial^2 F}{\partial y^2}\frac{\partial^2 w}{\partial x^2}+\frac{\partial^2 F}{\partial x^2}\frac{\partial^2 w}{\partial y^2}-2\frac{\partial^2 F}{\partial x \partial y}\frac{\partial^2 w}{\partial x \partial y}\right)+\frac{1}{1-\nu}\left(\frac{\partial^2 M^T}{\partial x^2}+\frac{\partial^2 M^T}{\partial y^2}\right)=0 \tag{3}$$

$$h\left(\frac{\partial^4 F}{\partial x^4}+2\frac{\partial^4 F}{\partial x^2 y^2}+\frac{\partial^4 F}{\partial y^4}\right)-Eh\left[\left(\frac{\partial^2 w}{\partial x \partial y}\right)^2-\frac{\partial^2 w}{\partial x^2}\frac{\partial^2 w}{\partial y^2}\right]+\frac{\partial^2 N^T}{\partial x^2}+\frac{\partial^2 N^T}{\partial y^2}=0 \tag{4}$$

where w is the deflection function for the slab (along the z-axis), F is the Airy stress function, E is the Young's modulus, ν is the Poisson's ratio, D is the flexural rigidity of the slab, M^T is the thermal moment and N^T is the thermal force. The slab is assumed to be restrained against lateral translation but free to rotate along all four boundaries.

Solution and calculation of stresses and strains

Representing the thermal deflection (w_T) and the thermal moment M^T as Fourier series expressions and solving the differential equations leads to a series solution for the thermal deflection [6]. A practically useful approximation to w_T can be obtained using the first term of the series solution:

$$\begin{aligned}&\frac{3}{4}\left\{(3-\nu^2)\left(1+\frac{L^4}{B^4}\right)+4\nu\frac{L^2}{B^2}\right\}\left(\frac{w_T}{h}\right)^3\\&\left\{\left(1+\frac{L^2}{B^2}\right)^2-12\frac{L^2(1+\nu)N^T}{\pi^2 Eh^3}\left(1+\frac{L^2}{B^2}\right)\right\}\left(\frac{w_T}{h}\right)\\&-192\frac{L^2(1+\nu)M^T}{\pi^4 Eh^4}\left(1+\frac{L^2}{B^2}\right)=0\end{aligned} \tag{5}$$

For a slab subjected to heating the total strain consists of two components:

$$\varepsilon_{\text{total}}=\varepsilon_{\text{mechanical}}+\varepsilon_{\text{thermal}} \tag{6}$$

The total strain $\varepsilon_{\text{total}}$ is governed by the deflection of the slab, however, not all of this strain is converted into mechanical stress. Whether the stress state in the slab is elastic or plastic is governed by the mechanical strains. The membrane stress distribution along the boundary of the slab for any deflection w can be calculated using the Airy stress function:

$$\sigma_{xx} = \frac{\partial^2 F}{\partial y^2}=\frac{w^2\pi^2 E}{8(1-\nu^2)}\left(\frac{1}{L^2}+\frac{\nu}{B^2}\right)-\frac{w^2\pi^2 E}{8L^2}\cos\frac{2\pi y}{B}-\frac{E\alpha\Delta T}{1-\nu} \tag{7}$$

$$\sigma_{yy} = \frac{\partial^2 F}{\partial x^2}=\frac{w^2\pi^2 E}{8(1-\nu^2)}\left(\frac{1}{B^2}+\frac{\nu}{L^2}\right)-\frac{w^2\pi^2 E}{8B^2}\cos\frac{2\pi x}{L}-\frac{E\alpha\Delta T}{1-\nu} \tag{8}$$

These equations can be used to determine the stress in a slab due to a deflection w. In this instance we are interested in the stress in the reinforcement so the the Young's modulus should be that of the steel (E_s).

Equations 7 and 8 can be rearranged to provide the membrane mechanical strains:

$$\varepsilon_{xx,\text{mech}} = \frac{w^2\pi^2}{8L^2}\left(1-\cos\frac{2\pi y}{B}\right)-\alpha\Delta T \tag{9}$$

$$\varepsilon_{yy,\text{mech}} = \frac{w^2\pi^2}{8B^2}\left(1-\cos\frac{2\pi x}{L}\right)-\alpha\Delta T \tag{10}$$

www.EngineeringEBooksPdf.com

The values of x and y chosen should correspond to the positions of the reinforcement along the edge so that a mechanical stress and mechanical strain can be calculated for each bar. These will be defined as σ_{w_T}, ε_{w_T}. Should the calculated mechanical stress be greater than the yield stress then, $\sigma_{w_T} = \sigma_{y,T}$ where $\sigma_{y,T}$ is the yield stress of the reinforcement at a temperature T.

DETERMINATION OF THE ULTIMATE MEMBRANE CAPACITY

Design philosophy

The total deflection of the slab w_t will be considered to consist of two components; the deflection caused by the thermal load, w_T, and the deflection caused by the design load, w_q, such that,

$$w_t = w_T + w_q \tag{11}$$

w_T is calculated as shown in the last section. It is possible to calculate w_q once a failure criterion is defined. The ultimate load (q_{ult}) will be calculated by equating the change in internal and external work done as the slab moves through the deflection w_q.

Failure criterion

Geometrical limits such as $span/20$ have often been used to define failure, this is highly unsatisfactory for assessing structural capacity in fire. A better approach is to apply a limiting value for the mechanical strain based on the ductility of the reinforcing bars. EC2 [15] recognises two classes of ductility, high ductility (H) and normal ductility (N). According to the properties given in Eurocode 2, where ε_{uk} is the characteristic value of the elongation at maximum load, the value of ε_{uk} is 5.0 for 'High' and 2.5 for 'Low' ductility. Eurocode 2 further states that reinforcement with a bar size of 16mm or above can be treated as being highly ductile whereas if the bar size is 12mm or less then normal ductility should be assumed.

For the purposes of this design method it will be assumed that the ultimate load has been reached when any of the reinforcing bars reaches this mechanical strain limit. The total strain ε_{total} at which this point is reached is calculated by considering the ductility class and the thermal expansion such that:

$$\varepsilon_{total} = \varepsilon_{uk} + \alpha\Delta T \tag{12}$$

The limiting deflection w_t at which this total strain value is reached can be calculated using Eqn.10 as the shortest span will reach the mechanical yield strain limit first. By setting $\varepsilon_{mech} = \varepsilon_{uk}$ and $w = w_t$ and rearranging:

$$w_t = \frac{B}{\pi}\sqrt{4(\varepsilon_{uk} + \alpha\Delta T)} \tag{13}$$

Calculation of stress-strain distribution due to combined loading

At the limiting deflection w_t there will be tensile membrane forces throughout most of the slab and so some cracking of the concrete will occur. Eurocode 2 [15] states that for concrete in tension with cracks, Poisson's ratio should be taken as zero. In calculating the stress in the reinforcement at the deflection w_t it is therefore necessary to modify Eqns. 7 and 8 slightly to take account of this such that:

$$\sigma_{xx} = \frac{w_t^2\pi^2 E_s}{8L^2}\left(1 - \cos\frac{2\pi y}{B}\right) - E_s\alpha\Delta T \tag{14}$$

$$\sigma_{yy} = \frac{w_t^2\pi^2 E_s}{8B^2}\left(1 - \cos\frac{2\pi x}{L}\right) - E_s\alpha\Delta T \tag{15}$$

www.EngineeringEBooksPdf.com

If the reinforcement bars are at a temperature that will cause the steel properties to degrade then appropriate reduced values of E_s and $\sigma_{y,T}$ should be chosen. The mechanical strains can be calculated using Eqns.9 and 10. Again, a mechanical strain and mechanical stress should be calculated for every reinforcing bar and values of x and y should be chosen accordingly. The mechanical stress and mechanical strain at this deflection will be defined as σ_{w_t}, ε_{w_t}.

External work

Calculation of the external work done by the load is straightforward, and can be calculated as:

$$\begin{aligned} \Pi_{ext} &= \int_0^L \int_0^B q_{\text{ult}} w_{\text{q}} \sin\frac{\pi x}{L} \sin\frac{\pi y}{B} \mathrm{d}x\,\mathrm{d}y \\ &= q_{\text{ult}} w_{\text{q}} \frac{4LB}{\pi^2} \end{aligned} \tag{16}$$

Internal work

The internal work must be calculated for every reinforcing bar. The total internal work can be defined as the energy required to move from the stress-strain state σ_{w_T}, ε_{w_T} at a deflection of w_T due to the thermal loading to the stress-strain state σ_{w_t}, ε_{w_t} at a deflection of $w_t = w_T + w_q$ due to the combined loading. If V is the volume of a reinforcing bar then the total internal work done can be defined as:

$$\Pi_{int} = \sum_{n=1}^{\text{no. rebar}} \int^V \Delta\sigma \Delta\varepsilon \,\mathrm{d}V \tag{17}$$

where

$$\Delta\sigma = \sigma_{w_t} - \sigma_{w_T} \tag{18}$$

$$\Delta\varepsilon = \varepsilon_{w_t} - \varepsilon_{w_T} \tag{19}$$

Comparing the internal and external work the ultimate load (q_{ult}) that the slab is capable of carrying can be calculated:

$$q_{\text{ult}} = \frac{\Pi_{int}}{w_{\text{q}} \frac{4LB}{\pi^2}} \tag{20}$$

Each reinforcing bar in the slab has a residual amount of tensile membrane capacity which can be used to carry load. The utilisation factor ξ of a reinforcing bars tensile capacity can be defined as:

$$\xi = \frac{\Delta\sigma}{\sigma_{y,T}} \tag{21}$$

where $\Delta\sigma$ was defined in Eqn.18 and $\sigma_{y,T}$ is the yield stress of a reinforcing bar at temperature T.

DESIGN EXAMPLE

To illustrate the proposed new design method a 9m x 9m laterally restrained slab was analysed. A depth of 100mm was assumed and reinforcement was taken to be a standard A142 mesh positioned at mid-height. Ambient yield strength of 600N/mm^2 and Young's modulus of 210,000N/mm^2 were assumed for the mesh reinforcement. Young's modulus of E=40,000N/mm^2 was assumed for the concrete.

The slab was subjected to a Eurocode 1 parametric fire as described in Section . Two situations were considered; Load Case 1 has the highest thermal gradient at an earlier time in the fire scenario, while Load Case 2 has the highest thermal expansion at a later time (see Figure 2). Both load cases were analysed using the method presented previously to determine their ultimate collapse load. The

www.EngineeringEBooksPdf.com

Load case	Time (s)	ΔT (°C)	$T_{,z}$(°C)/mm	$w_T(mm)$	w_t (mm)	q_{ult} (kN/m^2)
1	3000	150	-6.1	252	927	6.91
2	4000	200	-5.0	282	934	7.09

Table 1: Results of two load cases for the design example

mesh reinforcement has a bar diameter of less than 16mm, therefore normal ductility was used. The results of the analysis are tabulated in Table 1. Table 1 shows that the lowest capacity corresponds to Load Case 1 with an ultimate load of 6.91kN/m^2. There is only a slight difference between the two load cases considered. Both of the calculated capacities were greater than a typical design load of 6.1kN/m^2 for a slab of this size and geometry [16].

Contribution of unprotected composite secondary beams

At the limit state it can be reasonably assumed that unprotected secondary beams will retain very little flexural stiffness. Axial stiffness (as a catenary) will provide the only available contribution. Furthermore, it can be assumed that the deflection profile of unprotected secondary beams will depend entirely on the slab profile. It can also be assumed (conservatively) that the mean temperature of the unprotected beam is close to the atmosphere temperature during the heating phase of the fire. In the cooling phase, the steel temperature will quickly become higher than the atmosphere and the steel will begin to regain strength. At this stage, provided that the steel member connections are sufficient to resist the large tensions generated, the overall load carrying capacity will significantly increase, and no further checks are necessary. Finally, as the beam is constrained to the deflection profile imposed by the slab, it is quite reasonable to assume that the additional load capacity provided by the beam is governed by the compatibility principle. These assumptions provide a simple and natural modification of the internal work expression of Eqn.17, as:

$$\Pi_{int} = \sum_{n=1}^{\text{no. rebar}} \int^{V} \Delta\sigma\Delta\varepsilon \, dV + \sum_{n=1}^{\text{no. beams}} \int^{V} \Delta\sigma_B\Delta\varepsilon_B \, dV \tag{22}$$

where

$$\Delta\sigma_B = \sigma_{beam,w_t} - \sigma_{beam,w_T} \tag{23}$$

$$\Delta\varepsilon_B = \varepsilon_{beam,w_t} - \varepsilon_{beam,w_T} \tag{24}$$

Calculation of stress-strain in unprotected composite secondary beams

The equations below are written assuming the secondary beams span across the short direction (B). If the thermal expansion of the beam is defined as ΔT_b, the mechanical stress and strain in the secondary beams after the thermal loading can be calculated:

$$\sigma_{beam,w_T} = \frac{w_t^2\pi^2 E_b}{8B^2}\left(1-\cos\frac{2\pi x}{L}\right) - E_b\alpha_b\Delta T_b \tag{25}$$

$$\varepsilon_{beam,w_T} = \frac{w^2\pi^2}{8B^2}\left(1-\cos\frac{2\pi x}{L}\right) - \alpha_b\Delta T_b \tag{26}$$

At the limiting deflection the mechanical stress and strain in the beam(s) can be calculated as:

$$\sigma_{beam,w_t} = \frac{w_t^2\pi^2 E_b}{8B^2}\left(1-\cos\frac{2\pi x}{L}\right) - E_b\alpha_b\Delta T_b \tag{27}$$

$$\varepsilon_{beam,w_t} = \frac{w^2\pi^2}{8B^2}\left(1-\cos\frac{2\pi x}{L}\right) - \alpha_b\Delta T_b \tag{28}$$

www.EngineeringEBooksPdf.com

No.of beams	Capacity ignoring beams (kN/m^2)	Capacity including beams(kN/m^2)
1	6.91	7.96
2	7.09	8.46

Table 2: Effect of secondary beams on limit capacity of slab under Load Case 1

An appropriate reduced value of E_b and yield stress σ_{y,T_b} should be chosen based on the temperature T_b of the secondary beams. The value of x chosen should correlate with the position of the secondary beams under the slab. By applying Eqns.25, 26, 27 and 27 in Eqn. 22, the contribution of the beam to the limit capacity can be calculated.

Contribution of unprotected composite secondary beams to limit capacity

For the design example chosen, two structural layouts were considered; the first consisted of a secondary beam situated across the midspan of slab dimension L, the second comprised two beams situated at 3m and 6m along L (in this example $L = B$). All secondary beams were taken to be grade S275 305x165x46 universal beams.

Load Case 1 occurred at a time of approximately 2,000 seconds into the fire. At this point in time the atmosphere temperature was 880^{o}C. The atmosphere temperature at the time of Load Case 2, 4,000 seconds, was only 400^{o}C. It is clear that the first load case is the one to be checked. Table 2 shows the effect of secondary beams on the limit capacity of the slab under Load Case 1. If one secondary beam is positioned at the midspan of the slab then the limit capacity increases by 1.05kN/m^2. Including two beams has a greater effect, however, proportionally the increase is much less, the limit capacity increases only by 1.37 kN/m^2. The calculations can be confirmed independently by calculating the tension in the beams based on the deflection and thermal expansion [11] and using catenary formulas to approximate the uniformly distributed load on the beam(s) equivalent to the calculated tension. The numbers match quite closely.

CONCLUSIONS

A new design method for assessing the ultimate load carrying capacity of composite floor slab systems in fire has been presented. A logical failure criterion has been assumed, unlike the commonly used limiting deflection criteria which are entirely inappropriate in assessing the structural capacity of such floor systems. However, this does not mean that limiting deflection criteria may not used in the context of other design requirements, such as egress, fire fighter access and so on. The method is based on the authors understanding of the fundamental principles that govern the behaviour of composite structures in fire, and the output generated is fully consistent with these principles. Despite the rigorous nature of the background theory used, the authors believe that the method presented is reasonably straightforward and consistent with good engineering judgment and can potentially become a reliable engineering tool. A number of outstanding issues still need to be addressed. These include further development issues, to cover a larger range of practical situations, such as, profiled concrete slabs and slabs composite with unprotected steel beams. But more importantly, there are fundamental issues, such as the assumption of material linearity with temperature (in the thermal deflection calculation), although there are good reasons why this may not be very significant. The greatest issue is the validation of the method, which can be achieved by comparing a number of sophisticated computational predictions and available experimental data. The computational validation work will begin soon as the most important next step, in order to establish that the method is both reliable and conservative.

www.EngineeringEBooksPdf.com

REFERENCES

[1] Structural fire engineering investigation of Broadgate phase 8 fire. Technical report, Steel Construction Institute, Ascot, UK, 1991.

[2] D.M.Martin and D.B.Moore. Introduction and background to the research programme and major fire tests at BRE Cardington. In *National Steel Construction Conference*, pages 37–64, May, 1997.

[3] Behaviour of steel framed structures under fire conditions. Technical Report Main Report, DETR-PIT Project, School of Civil and Environmental Engineering, University of Edinburgh, 2000. available at www.civ.ed.ac.uk/research/fire/project/technicalreports.html.

[4] M.Gillie, A.S.Usmani, and J.M.Rotter. A structural analysis of the first Cardington test. *Journal of Constructional Steel Research*, 57:581–601, 2001.

[5] M.Gillie, A.S.Usmani, and J.M.Rotter. A structural analysis of the Cardington British Steel Corner Test. *Journal of Constructional Steel Research*, 58:427–443, 2002.

[6] A.S.Usmani and N.J.K.Cameron. Limit capacity of reinforced concree floor slabs in fire. *Cement and Concrete Composites Journal*, 2002. For the special issue on "Fire Resistance of Concrete", invited pater, submitted July 2002.

[7] Y.C. Wang. Tensile Membrane Action in Slabs and its Application to the Cardington Fire Tests. Technical report, Building Research Establishment, 1996. Paper presented to the second Cardington Conference 12-14 March 1996.

[8] C.G.Bailey and D.B.Moore. The structural behaviour of steel frames woth composite floor slabs subject to fire: *Part 1*: Theory. *The Structural Engineer*, 78:19–27, 2000.

[9] R.Park. Ultimate Strength of Rectangular Concrete Slabs under Short Term Uniform Loading with Edges Restrained Against Lateral Movement. *Proceedings of the Institution of Civil Engineers*, Vol. 28:125–150, May-August 1964.

[10] K.O.Kemp. Yield of a Square Reinforced Concrete Slab on Simple Supports Allowing for Membrane Force. *The Structural Engineer*, Vol.45(7):235–240, 1967.

[11] A.S.Usmani, J.M.Rotter, S.Lamont, A.M.Sanad, and M.Gillie. Fundamental principles of structural behaviour under thermal effects. *Fire Safety Journal*, 36:721–744, 2001.

[12] Eurocode 1: Basis of design and actions on structures. Technical Report ENV 1991-2-2, Brussels, European Committee for Standardisation, 1996.

[13] H.C.Huang and A.S.Usmani. *Finite Element Analysis for Heat Transfer - Theory and Software*. Springer-Verlag, London, 1994.

[14] D.J.Johns. *Thermal Stress Analysis*. Pergamon Press, 1965.

[15] Eurocode 2: Design of concrete structures. Technical Report ENV 1992-1-1, Brussels, European Committee for Standardisation, 1992.

[16] C.G.Bailey and D.B.Moore. The structural behaviour of steel frames woth composite floor slabs subject to fire: *Part 2*: Design. *The Structural Engineer*, 78:28–33, 2000.

[17] British Standard Insitution. *BS5950 Part 8: Code of Practice for Fire Resistant Design*, 1990.

www.EngineeringEBooksPdf.com

Advances in Steel Structures, Vol. II
Chan, Teng and Chung (Eds.)
© 2002 Elsevier Science Ltd. All rights reserved.

GRAPHICAL METHOD FOR DESIGN OF STEEL STRUCTURES IN FIRE

M. B. Wong

Department of Civil Engineering, Monash University, Melbourne, 3800, Australia

ABSTRACT

The design of steel structures in fire is always a daunting task because of the complexity involved in carrying out such process. The whole process can be divided mainly into three parts: (1) Establishing the temperature–time curve for the fire which may include standard fire and natural fires; (2) Establishing the temperature-time curves for the steel members; this process involves heat transfer calculations based on analytical solution; (3) Checking the strength requirements of the steel members on the basis of the temperatures attained. In essence, the design process involves three parameters: time, temperature and strength, all of which have to be assessed individually in order to satisfy the fire resistance requirements as stipulated in most building codes. In this paper, a method is proposed to link the three parameters together so that the design process can be carried out efficiently. The three parameters are expressed on a design chart from which design information, such as the required steel section properties, temperatures attained and the time required, for all the members in a steel structure can be extracted. The forces in the members are obtained from simple elastic theory based on a previously published method for steel structures in fire. An example is given to demonstrate the use of this method.

KEYWORDS

Fire engineering, design, steel structures, temperature, heat transfer, fire curve.

STRUCTURAL DESIGN FOR FIRE

The development of performance-based fire engineering design often requires consideration of fire situation for which engineering computations on the basis of sound engineering principles are performed. The computational process for designing structures under fire conditions is often a complex one, requiring multi-disciplinary consideration in order to achieve a satisfactory solution to the total issue of fire safety. When applying to structural design, these engineering principles constitute a lengthy design process (Lie, 1992) including fire modelling, material performance in fire, temperature prediction, structural performance in fire, fire resistance level, temperature-time relationship, etc. It is common practice for design engineers to conduct such design process in an efficient manner with the

www.EngineeringEBooksPdf.com

aid of design charts and tables. Design charts and tables relating the characteristics of fire to the temperatures of steel have been described by, for instance, Thor, et al (1977) and are available in design codes (for instance, SBI, 1976).

For structural design alone, the design process requires separate consideration of the following major steps:

(1) Determine of fire resistance level (in minutes) according to building regulations;
(2) Select a suitable fire curve corresponding to certain fire scenario;
(3) Relate the fire curve to the temperature-time curve of the structural members; hence, determine the maximum temperature (T_s) of the structural members corresponding to the required fire resistance level;
(4) Determine the failure temperature (T_c) that the structural members of the structure in fire can attain;
(5) If $T_s < T_c$, the structure satisfies the strength requirements under fire conditions, otherwise design modification needs to be made and the above process repeated.

The objective of this paper is to present a concept, based on the use of design charts, whereby the structural design process as described above can be performed in an integrated manner. The concept is illustrated with an example for the design of structures using unprotected steel sections under standard fire curve. Although the scope of illustration is restrictive, it serves as a guide to the use of the concept which could be extended to design of steel structures under real fire curves using different types of steel sections.

TEMPERATURE PREDICTION OF STEEL MEMBERS

Fire curves are used to describe the fire temperatures which structural members are subject to over a period of time. For standard fire tests carried out according to ASTM E119 or ISO 834, a standard fire curve is used so that the temperature of the structural member under testing is increasing until failure occurs. This standard fire curve is commonly adopted for fire tests although real fire curves are becoming popular to simulate realistic fire situation. A structural member is said to satisfy the fire resistance level when it meets all the design criteria over a specified period of time without failure.

To determine the fire resistance level, the relationship between the standard fire curve and the structural member's temperature-time curve needs to be established. As fire tests are costly, it is common practice for engineers to obtain the temperature-time curves for various steel sections by computations. The details for carrying out such computations can be found in Wong, et al (1998). In essence, the computations are based on the heat transfer theory between gases and steel. For steel sections, the temperature varies with the section factor, H/A, the ratio of the perimeter of the cross-section to its area. Using this approach, the temperature variation of steel sections with a range of H/A = 50 m^{-1} to 350 m^{-1} is plotted in Figure 1. These values of H/A cover the practical range for most steel sections.

RELATIONSHIP BETWEEN BENDING MOMENT CAPACITY AND SECTION FACTOR

To relate the bending moment capacity of steel sections to the range of H/A given in Figure 1, it is necessary to group the sections into different types with different grades of steel so that a general trend of the relationship can be visualised. For instance, the bending moment capacity of the universal beam (UB) sections with nominal yield strength of 300 MPa being used in Australia is plotted against H/A as shown in Figure 2. In order to ensure safety in design, it is desirable to have a lower-bound curve so

www.EngineeringEBooksPdf.com

that conservative solutions obtained for design would lie within the safe zone. This lower-bound curve has been found to be

$$y = 3100 - 23.09x + 0.043x^2 \quad (1)$$

where $y = M_{20}$ = moment capacity at room temperature and x = H/A. Similar curves for other types of sections, such as universal columns and tubular sections, can be established in this way.

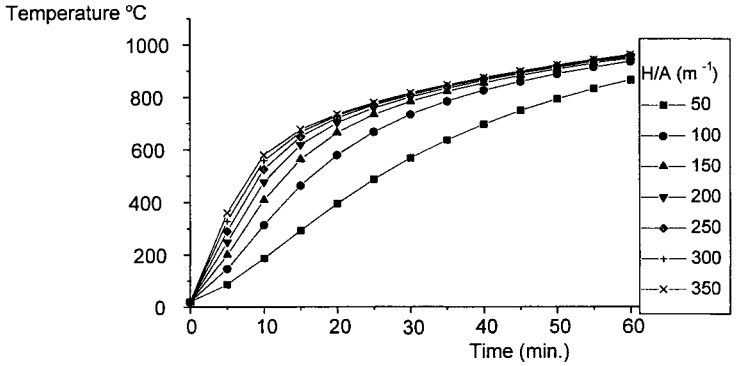

Figure 1: Temperature-time curves for steel sections

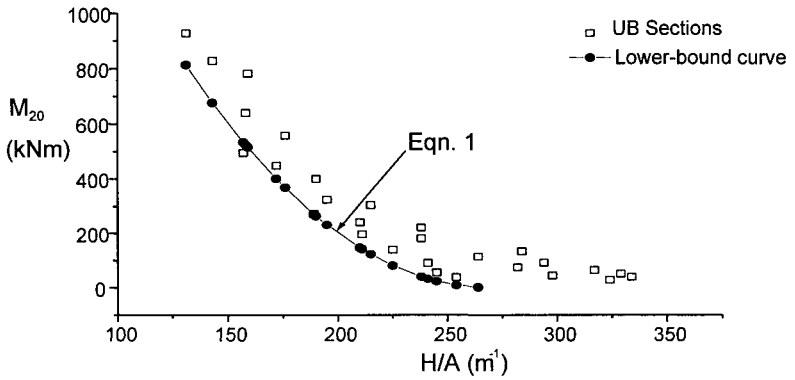

Figure 2: Relationship between moment capacity and section factor for UB sections

FAILURE TEMPERATURE CALCULATIONS

The strength of a structural member in fire is usually expressed in terms of its load ratio at elevated temperatures. The load ratio is a ratio of the design action to the capacity. For the present purpose, the design action of bending moment is used in the following discussion. The general expression relating the bending moment and temperature in a structural member is given by

www.EngineeringEBooksPdf.com

$$\frac{M^*(T)}{M_{20}} \leq \frac{f_{yT}}{f_{y20}} = \phi_{yT} \tag{2}$$

where $M^*(T)$ is the bending moment at temperature T, M_{20} is the moment capacity at room temperature, f_{yT} and f_{y20} are the yield stresses at temperature T and room temperature respectively. The symbol ϕ_{yT} represents the rate of deterioration of the yield stress with temperature. Eqn. 2 can be expressed as a function of temperature and H/A by replacing M_{20} by Eqn. 1. That is,

$$f(T, H/A) = M^*(T) - (a + bx + cx^2)\phi_{yT} = 0 \tag{3}$$

where $y = a + bx + cx^2$ is the general expression representing Eqn. 1. Eqn. 3 contains two unknowns, T and H/A, while the design action $M^*(T)$ can be obtained from structural analysis. For the case of a simply supported beam with a point load acting at mid-span, $M^*(T)$ is simply the maximum bending moment at mid-span. The problem remaining is to find a suitable section for the structural member satisfying Eqn. 3. This is done in the following.

GRAPHICAL SOLUTION

To provide a solution to Eqn. 3, a chart depicting the relationship between T and H/A for all steel sections is first produced. This relationship can be found by re-plotting Figure 1, showing the variation of T with H/A and the resulting chart is shown in Figure 3. The solution is then obtained by plotting Eqn. 3 on Figure 3. The main advantage of using Figure 3 is that it provides a general 3-dimensional view (fire resistance level, temperature, section factor) for the solution to the problem and the selection of appropriate steel sections can be readily made from Figure 3.

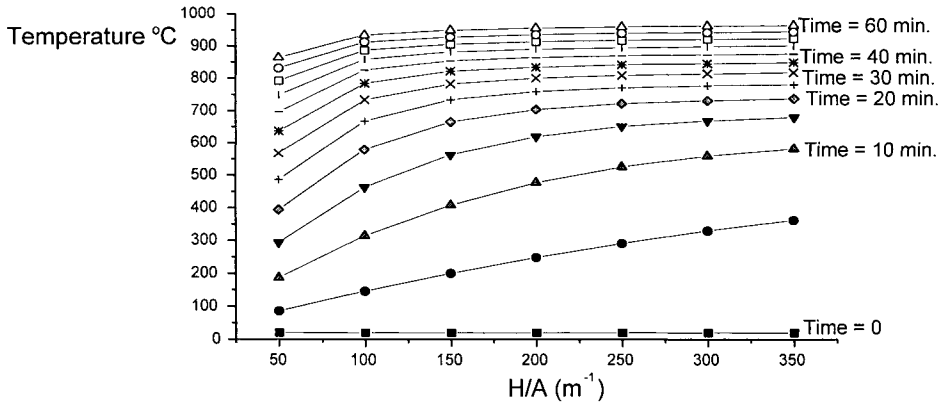

Figure 3: Variation of Temperature with H/A

www.EngineeringEBooksPdf.com

EXAMPLE

Simply-supported beam

A simple illustration for the use of Figure 3 is given using a simply-supported beam example which has a span of 6 m with a design load of 40 kN acting at mid-span. The beam was subject to a fire following the ISO 834 standard fire curve. In this case, $M^*(T)$ = 60 kNm.

According to Australian steel structures code AS4100 (SA, 1998), the function for the variation of the yield stress of steel with temperature is

$$\begin{aligned} \phi_{yT} &= \frac{905 - T}{690} && \text{for } 215°C \le T < 905°C \\ &= 0 && \text{for } T < 215°C \end{aligned} \tag{4}$$

If UB steel sections are used, Eq. (3) then becomes

$$60 - (3100 - 23.09x + 0.043x^2)\left(\frac{905 - T}{690}\right) = 0 \tag{5}$$

Eq. (5) in conjunction with Figure 3 is plotted in Figure 4 and the following observations are made.

(a) If a steel UB section with H/A = 150 m^{-1} is used, the failure temperature T_c of the beam is found to be about 830°C at about 35 minutes.
(b) If the fire resistance level of 60 minutes is required, a steel UB section with H/A = 60 m^{-1} is required where the failure temperature is about 870°C.
(c) If, for some reasons, the maximum temperature of the compartment is expected to be 700°C, then a minimum steel UB section with H/A = 200 m^{-1} is required.

It is clear that the graphical method illustrated in Figure 4 provides a number of solution options for the design engineers. All the graph plotting and internal calculations can easily be carried out using spreadsheet.

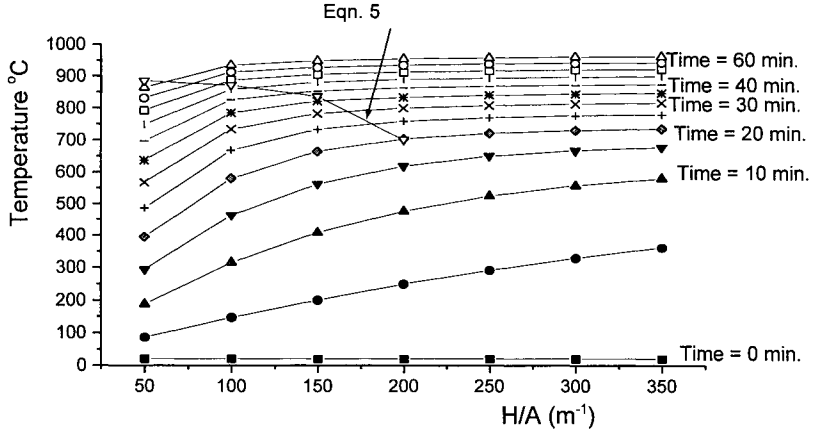

Figure 4: Graphical solution for steel sections at elevated temperatures

www.EngineeringEBooksPdf.com

For steel frames subject to elevated temperatures, the bending moment $M^*(T)$ in members consists of two components: M_L^* due to the static loading and M_T^* due to the thermal loading. It can be shown that $M^*(T)$ can be expressed as a function of the temperature T and the procedure to calculate M_L^* and M_T^* has been described in Wong (2001).

CONCLUSION

A graphical method for the design of steel structures under fire conditions is presented. The concept has been illustrated using structures with unprotected steel sections in fire. Standard fire curve has been used in the illustration. The method provides the design engineers with more information about the choice of steel section and fire resistance level at high temperatures. Although the scope of illustration is restrictive, the concept can be extended to

1. Other types of steel sections, fire protected and unprotected;
2. Other grades of steel;
3. Any structural analysis techniques for member force calculations;
4. Other structural failure criteria;
5. Other types of fire curves such as real fire curves.

REFERENCES

Lie T.T. (Editor) (1992). *Structural Fire Protection*, ASCE Manuals and Reports on Engineering Practice No. 78.

Thor J., Pettersson O. & Magnusson S.E. (1977). A Rational approach to Fire Engineering Design of Steel Buildings. *Engineering journal, American Institute of Steel Construction*, Vol. 14, No. 3, 108-113.

Pettersson O., Magnusson S.E. & Thor J. (1976). *Fire engineering design of steel structures*, Swedish Institute of Steel Construction, 1976.

Wong M.B., Ghojel J.I. & Crozier D.A. (1998). Temperature-time Analysis for Steel Structures Under Fire Conditions. *An International Journal on Structural Engineering and Mechanics*, 6, No. 3, April, 275-289.

SA (1998). *AS4100 – Steel Structures*, Standards Australia.

Wong M.B. (2001). Elastic and Plastic Methods for Numerical Modelling of Steel Structures Subject to Fire. *Journal of Constructional Steel Research*, Vol. 57 (1), 1-14.

www.EngineeringEBooksPdf.com

Advances in Steel Structures, Vol. II
Chan, Teng and Chung (Eds.)
© 2002 Elsevier Science Ltd. All rights reserved.

HIGH TEMPERATURE TRANSIENT TENSILE PROPERTIES OF FIRE RESISTANT STEELS

W. Sha and T.M. Chan

Metals Research Group, School of Civil Engineering, The Queen's University of Belfast, Belfast BT7 1NN, UK

ABSTRACT

Fire resistance of steel for safety and economy has been the subject of extensive investigation in recent years. Preventive and protective measures are needed to minimise loss of life and properties from fire hazard. Fire resistance is governed by steel strength, the member section factor, types of protective measure taken, and load. To improve fire resistance, Nippon Steel of Japan has developed some fire resistant steels based on niobium and molybdenum. This project is to determine the properties of fire resistant steels, at high temperatures using transient tensile test. In such tests, the load on a steel specimen is maintained constant while its temperature is increased at a given rate and the changes in gauge length are constantly recorded. A comparison was drawn between the strength reduction factors, the elongation and the failure temperatures in three Nippon steels. The most heavily alloyed steel clearly outperforms the other two steels in all three of these categories. Overall, these three steels performed in a very consistent manner at high range temperatures and their strength reduction factors have higher values than the factors of conventional structural steels from Eurocodes or British Standard. The factors are higher for experimental steel containing 0.58 percentage niobium, much more than the Nippon fire resistant steels. The strength reduction factors obtained from steady-state tests are slightly higher than the factors obtained from transient tests. Without reference to similar steel from transient tests, the factors from steady-state tests could give rise to misleading answers when used in a fire engineering analysis. From the structural engineers' point of view, the result from the transient tensile testing is useful for steel structural design.

KEYWORDS

Fire resistance, steel, transient tensile test, high temperature, strength, elongation, failure temperature, strain, materials properties.

INTRODUCTION

Steel is the most important metallurgical material available to civil engineers worldwide. Interest in the area of fire resistance of steel for safety and economy has rapidly grown in the last two decades. The development of fire resistant steels is one aspect of the effort to enhance building safety in fire.

www.EngineeringEBooksPdf.com

This effort has been mainly from Nippon Steel, where some fire resistant steels have been developed containing niobium and/or molybdenum [Sakumoto et al. (1992)]. These steels have increased yield strength at elevated temperatures, believed to be especially for meeting the requirements of Japanese building regulations. The aim of this project was to determine the properties of three variants of fire-resistant steels at high temperatures using transient tensile testing. Each country requires a similar minimum standard performance from structure during a fire over a specified period. For example when designing a structure for use by the public, in some specific situations that structure must be able to withstand a fire for two hours without major structural failure occurring. This means that structural steel members must usually be able to withstand gas temperatures in excess of 1000°C over the required period.

The importance of metals as constructional materials is almost invariably related to their load bearing capacity in either tension or compression and their ability to withstand deformation without fracture. It is usual to assess these properties by tensile tests in which the modulus of elasticity, the yield or proof stress, the tensile strength and the percentage elongation are determined. A stress-strain curve is plotted using stress obtained by dividing the load by the original cross-sectional area of the specimen, and strain obtained as the extension divided by the original heated length [Dieter (1988)]. This curve is known as an engineering stress-strain curve and rises to a maximum stress level and then falls off with increasing strain until it terminates as the specimen breaks. The maximum stress level is known as the tensile strength of the specimen. Stress-strain curve shows a linear relationship from the origin up to the proportional limit point, also called elastic limit. This initial linear deformation is the elastic deformation of the material. This deformation is recovered once the load is removed from the specimen. This behaviour is called the elastic behaviour. The point at which the line begins to deviate from this linear characteristic is known as the elastic limit. After this point, any deformation that occurs will be plastic and so it is not recoverable.

In many structures, it is common for a loaded steel component to be in fire situation subjected to a change in temperature and it is important to know how the resulting deformation of the material will develop. For this reason, tensile tests under transient heating conditions have been devised [Copier (1972), Ruge & Winkelmann (1977), Ruge & Winkelmann (1980), Skinner & Stevens (1972), Twilt (1982), Witteveen & Twilt (1972)]. In such tests, the load on a steel specimen is maintained constant while its temperature is increased at a given rate and the changes in gauge length are constantly recorded. In work by Kirby and Preston (1988) typical tensile curves are shown up to 2% strain for a Grade 43A steel derived from transient tests at a heating rate of 10°C per minute. The principal features comprise a small initial elastic extension, when the load was applied at room temperature, followed by a very gradual increase in length as the temperature was increased. For the purpose of fire engineering design, strength reduction factors can be derived from the transient tensile curves. These factors can be found by dividing the stresses at 2%, 1.5% and 0.5% strains by the yield strength of the material at room temperature (approximately 20°C). Then strength reduction factor versus temperature curves can be plotted. The relationship between the elongation at fracture and temperature also can be derived from the transient tensile data.

COMPOSITION AND YIELD STRENGTH OF FIRE RESISTANT STEELS

JIS G3106, "Rolled steels for welded structures" specifies chemical composition and mechanical properties at room temperature and does not specify mechanical properties at high temperature. Fire resistant steel satisfies specification on JIS G3106. The three fire resistant steels, Nb-Mo steel, Mo steel (1) and (2) were made by Nippon Steel. The compositions of the steels are given in Table 1. The yield strength, tensile strength and elongation are also shown in Table 1, compared with the normal requirement for structural steel of a yield strength between 300 and 400 MPa and an elongation of 20%. A brief of description of each alloying element used in the steels is shown in Table 2. Nb-Mo

www.EngineeringEBooksPdf.com

steel and Mo steel (2) are G3106 SM490A with tensile strength at room temperature higher and equal to 490 MPa because of the amount of Mn in their chemical composition. Mo steel (1) is G3106 SM400A with tensile strength at room temperature higher and equal to 400 MPa. As structural steel should satisfy the weldability, weld test like maximum hardness test in welded heat-affected zone (HAZ) was carried out by Nippon Steel. The hardness of the heat-affected zone is lower for the fire resistant steel than the conventional steel [Chijiiwa et al. (1995)].

TABLE 1
COMPOSITIONS OF Nb-Mo, Mo (1) AND (2) FIRE RESISTANT STEELS

Steel	C	Mn	Si	Mo	Nb	Yield strength (MPa)	Tensile strength (MPa)	Elongation (%)
Nb-Mo	0.11	1.14	0.24	0.52	0.03	350	552	20
Mo (1)	0.1	0.64	0.1	0.51	-	380	507	21
Mo (2)	0.11	1.13	0.23	0.56	-	448	562	24
P8240	0.014	0.28	0.28	0.21	0.58	214	389	29

TABLE 2
BRIEF DESCRIPTION OF EACH ALLOYING ELEMENT USED IN THE FIRE RESISTANT STEELS

Element	Description
C, Carbon	An essential ingredient in steel. Higher carbon content increases the yield point and hardness and reduces ductility and weldability.
Si, Silicon	Higher silicon content increases the strength of the steel at high temperatures by raising the ferrite-austenite transition temperature.
Mn, Manganese	Manganese is similar in many ways to iron and is widely used in steel as a deoxidant. Manganese can contribute to temperature embrittlement. It lowers the ferrite-austenite transition temperature and can therefore be used to stabilise silicon content in steel.
Mo, Molybdenum	The principal use of molybdenum worldwide is in alloy steel. It can help to reduce temper brittleness in steel. Molybdenum raises the high temperature strength and creep resistance of steel, but reduces the yield strength at room temperature. It does this by reducing the austenite-pearlite transformation temperature.
Nb, Niobium	Niobium improves the steel strength at room temperature and at high temperature without affecting weldability. It also improves creep strength.

PROCEDURE

Preparation of Samples for Transient Tensile Testing

The fire resistant steels were obtained as hot rolled plates from Nippon Steel of Japan, the compositions of which were given in Table 1. It was decided that flat rectangular samples rather than cylindrical samples would be more appropriate because of the limited material available. The gauge length of samples was 80 mm and the cross sectional area of the gauge was 25 mm^2 with a square section of 5 × 5 mm, for Nb-Mo and Mo (1) steels. These samples were prepared using the traditional cutting method of spark erosion and then machining. The cross sectional area of Mo steel (2) samples was 28 mm^2 with a rectangular section of 6.1 × 4.6 mm because the thickness of the original steel plate

www.EngineeringEBooksPdf.com

is 6.1 mm. These samples were cut by a laser machine. This cutting method is more efficient. The finishing of surface area of the gauge length of these samples was acceptable but they were not as smooth as the other samples. All the samples have a clearance of 140 mm allowed at each end to permit them to be gripped outside the furnace while the gauge length stayed completely within the furnace. An 8-mm diameter hole was drilled in each end of the sample at an end distance of 5 mm to allow a pin to pass through. This pin transferred the load from the tensile testing machine to the sample. The dimensions of the samples of Nb-Mo and Mo (1) fire resistant steels are shown in Figure 1. The gauge length was narrower than the clearance, to ensure that deformation and failure occurred along the gauge. Six samples of each of the Nb-Mo and Mo (2) steels and three samples of the Mo steel (1) were prepared to these specifications.

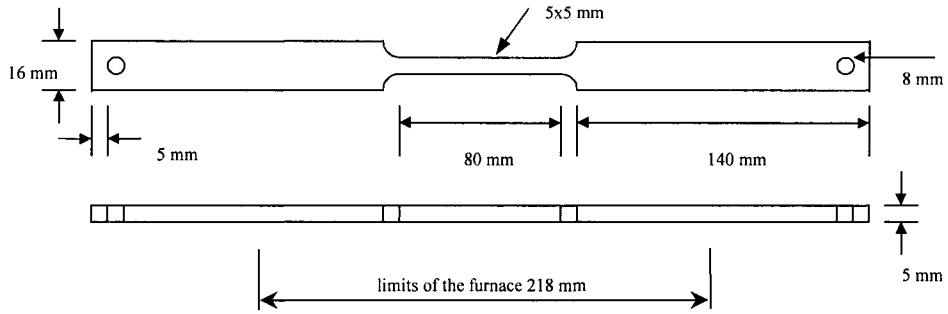

Figure 1: Transient tensile test sample dimensions of Nb-Mo and Mo (1) fire resistant steels

Transient Tensile Test

The sample was fed down through the furnace and fixed at both ends by placing pins through the holes that were described previously. The spaces at the ends of the furnace were packed with refractory ceramic fibres to reduce heat loss and protect the load cell from heat. A thermocouple was placed inside the furnace to monitor the temperature. The specimen temperature was assumed equal of temperature measured in the furnace. There was no direct measurement on the steel specimen. There is likely longitudinal heat loss in the specimen but at present, there are quantitative data on this.

A transient tensile test is to heat a tensile sample with a constant heating rate while being held under a constant load. The prescribed load was transmitted to the specimen by means of Nimonic pull rods, passing through the ends of the furnace and hydraulically gripped in the machine before the experiment starts. The constant load applied to the sample was chosen based on six different strength reduction factors (applied stress/yield strength) which were set to be tested, 0.23, 0.37, 0.51, 0.65, 0.79 and 0.93. The Mo (1) fire resistant steel was only tested at the ratio of 0.37, 0.65 and 0.93.

The load cell had to be kept at a low temperature to ensure that the readings obtained from the test were accurate. The sample was heated up at a constant rate of 10°C per minute. The stroke readings were shown on a large electronic display (LED) and the specimen strain can be monitored, from the displacement at the platens of the machine. The furnace has an upper limiting temperature over 1000°C. The test was carried out until failure occurred. The two halves of the failed sample were then removed from the furnace and placed end to end to enable a measurement of elongation to be taken (after cooling down).

In addition to the strain due to deformation under load, there was an additional increase in length arising from thermal expansion that was deducted before the strain against temperature curves were plotted. The specimens tested have a gauge length of 80 mm but the actual length of the furnace is 218

www.EngineeringEBooksPdf.com

mm so thermal expansion had to be accounted for over this length. An average value of 13.5×10^{-6} K^{-1} was taken as the coefficient of thermal expansion because the values of coefficient of thermal expansion do not vary significantly over the test temperature range. Although this calculation does not consider the fact that the ends of the specimen are colder, this is compensated to some extent by the neglected expansion immediately outside the furnace. This, and the possible different and variable coefficients of expansion of the steels studied, introduces errors in the strain measurement. Fortunately enough, the procedure was the same in all tests and the qualitative comparison is still valid.

Deriving Results from Transient Tensile Test Data

As has been described in the previous section, at the end of each transient test a strain against temperature graph was plotted. Then the curves can be shown to 2%, 1.5% and 0.5% strain. From these graphs, the strength reduction factor at different temperature for each steel sample can be found.

Because the calculated deformation due to thermal expansion was greater than the actual extension at the initial part of the test, an assumption had to be made before plotting the graph. Because these samples were carrying a tension load, the values of strain cannot be negative. In the initial part of the graph, if the actual extension value was less than the thermal expansion deformation then the strain was assumed equal to zero.

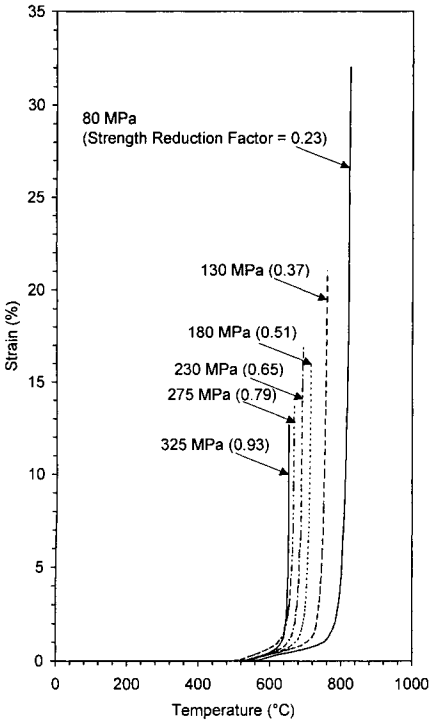

Figure 2: Strain – temperature curves for Nb-Mo steel obtained from transient tensile tests

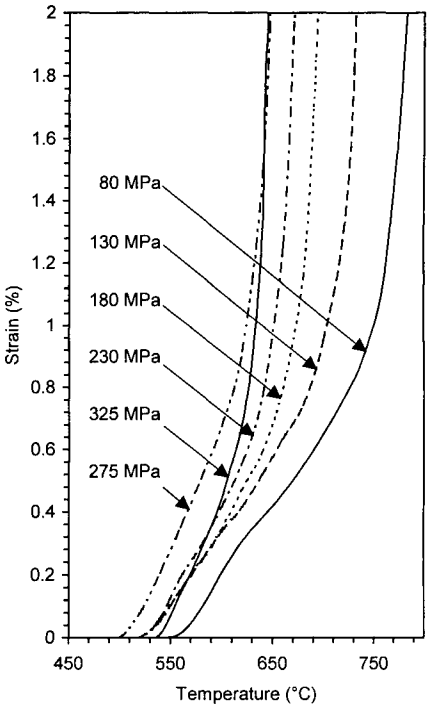

Figure 3: Strain – temperature curves of Nb-Mo steel up to 2% strain

www.EngineeringEBooksPdf.com

RESULTS AND DISCUSSION

Figure 2 shows the strain – temperature curves of Nb-Mo steel samples. Figure 3 shows the strain – temperature curves of the Nb-Mo steel up to 2% strain. The graphs of the strength reduction factor against temperature derived are shown in Figures 4–6. Data for conventional structural steels from Eurocodes or British Standard [Lawson et al. (1996)] and a prototype fire resistant steel development by the authors' group, P8240, are included for comparison. The P8240 steel is not an existing heat resistant steel for boiler tubes, etc.

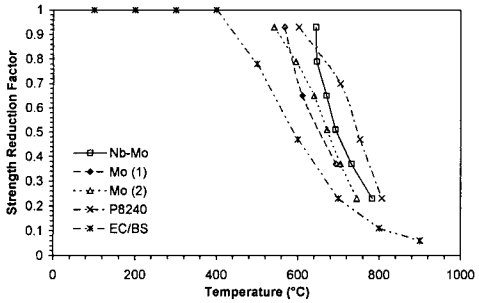

Figure 4: Strength reduction factor against temperature at 2% strain

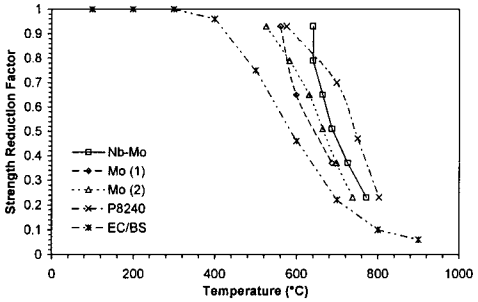

Figure 5: Strength reduction factor against temperature at 1.5% strain

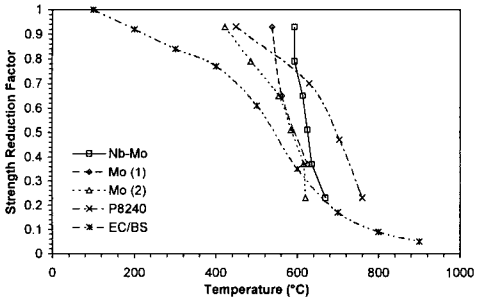

Figure 6: Strength reduction factor against temperature at 0.5% strain

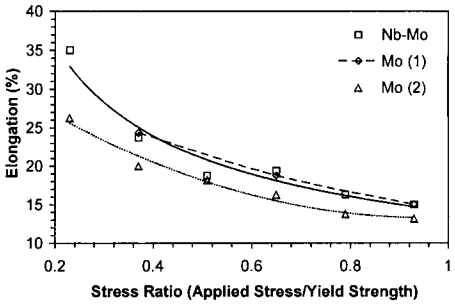

Figure 7: Elongation against stress ratio

From Figures 4 to 6, it is observed that the strength reduction factors of the Nb-Mo steel at 2%, 1.5% and 0.5% strains at high range temperatures are higher than the factors for the Mo steel (1) and (2). This may be explained with the composition and possibly the manufacturing process of the steel. The Nb-Mo steel is the only steel tested containing small amount of niobium that improves strength at high temperatures. In addition, molybdenum improves strength at high temperatures. Because Mo steel (2) contains slightly more molybdenum, at the higher temperature end of the scale, it can be seen from Figures 4 and 5 that the performance of this steel exceeds the Mo steel (1). Compared with the factors of P8240 steel the strength reduction factors of the three fire resistant steels at 2%, 1.5% and 0.5% strains at high range temperatures are lower. This is because P8240 steel contains 0.58 niobium, which is much more than Nb-Mo steel. However, the trend is the opposite at low range temperatures, in that the steel temperature of P8240 at strength reduction factor 0.93 shows remarkably low value compared to that on other strength reduction factors. This is probably because this steel does not have as much the in-situ precipitation strengthening capability at the low range temperatures as the Nippon Steels.

www.EngineeringEBooksPdf.com

The factors of the three fire resistant steels are higher than the factors of conventional steels from Eurocodes or British Standard.

Figures 7 and 8 show that there are relationships between elongation at failure, stress ratio and failure temperature. The lower the stress ratio the higher the elongation and the higher the failure temperature. Out of the three fire resistant steels, the Nb-Mo steel has the best performance, as it has the highest failure temperature. Figure 7 shows that the Mo steel (2) failed at each stress ratio with the shortest elongation, indicating that this steel is more brittle than the other two fire resistant steels.

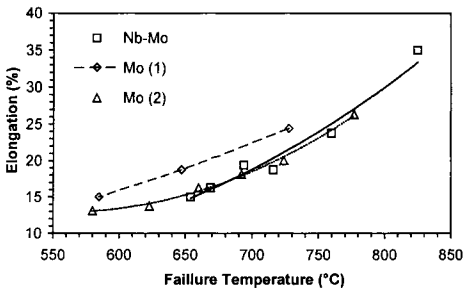

Figure 8: Elongation against failure temperature

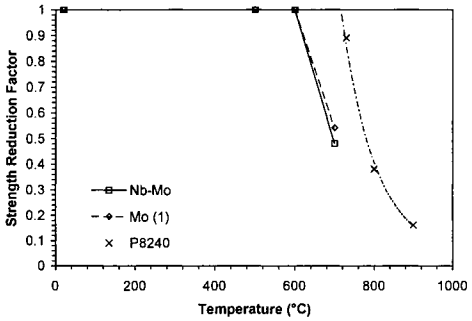

Figure 9: Strength reduction factors from steady-state tests

Strength reduction factors can be also derived from tensile tests under steady-state heating condition (constant temperature). In this type of test an unloaded sample is brought into thermal equilibrium at a certain temperature and it is then strained at a uniform rate while the resulting loads experienced by it are recorded as a function of extension. Nb-Mo and Mo (1) steels have been tested by using this method at the Queen's University of Belfast in previous years. Figure 9 shows the strength reduction factors at 2% strain for these steels under this test method [Sha (1998), Sha et al. (2000)].

Comparing Figures 4 and 9 shows that the strength reduction factors at 2% strain obtained from transient tests are slightly lower than the factors obtained from tests under steady-state conditions. During fire accidents, the temperature does not stay at the same level all the time. Therefore, the factors obtained from steady-state tests are more optimistic than the factors obtained from transients tests.

CONCLUSIONS

From the transient tensile testing of the fire resistant steels, a comparison was drawn between the strength reduction factors, the elongation and the failure temperatures in the Nb-Mo, Mo (1) and (2) steels. The Nb-Mo steel clearly outperforms the other two fire resistant steels in all three of these categories due to alloying elements. Overall, these three steels performed in a very consistent manner at high range temperatures and their strength reduction factors are greater than the factors of conventional structural steels from Eurocodes or British Standard. Because P8240 steel contains 0.58 niobium, much more than other fire resistant steels, its factors are higher than the factors of the Nippon steels.

The strength reduction factors obtained from steady-state tests are slightly higher than the factors obtained from transient tests. Without reference to similar steel from transient tests, the factors from steady-state tests could give rise to misleading answers when used in a fire engineering analysis. From

www.EngineeringEBooksPdf.com

the civil engineers' point of view, the result from the transient tensile testing is useful for steel structural design.

ACKNOWLEDGEMENT

The writers would like to thank Dr. Kazutoshi Ichikawa of Nippon Steel Corporation for supplying Nippon fire resistant steels.

REFERENCES

Chijiiwa R., Tamehiro H., Yoshie A., Funato K., Yoshida Y., Horii Y. and Uemori R. (1995). Development and Practical Application of Fire-resistant Steel for Buildings. *HSLA Steels'95 Conference Proceedings*, ed: G. Liu, H. Stuart, H. Zhang and C. Li, China Science and Technology Press, Beijing, pp. 584–589.

Copier W.Y. (1972). *Rep. No. BI-72-73/05.3.11.640*, Institute TNO for Building Materials and Building Structures, Delft, Netherlands.

Dieter G.E. (1988). *Mechanical metallurgy*, SI metric Ed., McGraw-Hill, London.

Kirby B.R. and Preston R.R. (1988). High Temperature Properties of Hot-rolled Structural Steels for Use in Fire Engineering Design Studies. *Fire Safety Journal*, **13:1**, 27–37.

Lawson R.M. and Newman G.M. (1996). *Structural Fire Design to EC3 and EC4, and Comparison with BS 5950*, Steel Construction Institute, Ascot, UK, p. 22.

Ruge J. and Winkelmann O. (1977). *Materialpruf*, **19:8**, 295–299.

Ruge J. and Winkelmann O. (1980). *Brandvershatten von Bauteilen, Sonderforschungsbereich* 148, Arbeitsbericht 80, 1978, Part II, Braunschweig, pp. 147–192.

Sha W. (1998). Fire resistance of Floors Constructed with Fire-resistant Steels. *Journal of Structural Engineering*, **124:6**, 664–670.

Sha W., Kelly F.S., Blackmore S.P.O. and Leong, K.H.J. (2000). Design and Characterisation of Experimental Fire Resistant Structural Steels. *HSLA Steels'2000*, Metallurgical Industry Press, Beijing, pp. 578–583.

Skinner D.H. and Stevens A.G. (1972). *Rep. MRL 6/8*, Broken Hill Proprietary Co. Ltd. (BHP), Melbourne Research Laboratories.

Sakumoto Y., Yamaguchi T., Ohashi M. and Saito H. (1992). High-temperature Properties of Fire-resistant Steel for Buildings. *Journal of Structural Engineering*, **118:2**, 392–407.

Twilt L. (1982). *Proceedings of the CIB/RILEM Symposium on Material Properties*, Delft, Netherlands.

Witteveen J. and Twilt, L. (1972). On the Behaviour of Steel Columns at Elevated Temperatures. *Proceedings of the Colloquium on Column Strength*, International Association for Bridge and Structural Engineering, Paris.

www.EngineeringEBooksPdf.com

Advances in Steel Structures, Vol. II
Chan, Teng and Chung (Eds.)
© 2002 Elsevier Science Ltd. All rights reserved.

MECHANICAL PROPERTIES OF STRUCTURAL STEEL AT ELEVATED TEMPERATURES

J. OUTINEN and P. MÄKELÄINEN

Laboratory of Steel Structures,
Department of Civil and Environmental Engineering,
Helsinki University of Technology
P.O. Box 2100, FIN-02015 HUT, Finland
http://www.hut.fi/Units/Civil/Steel/

ABSTRACT

A wide research program has been carried out since 1994 in the Laboratory of Steel Structures at Helsinki University of Technology in order to investigate mechanical properties of different structural steels at elevated temperatures by using mainly transient state tensile test method. Some main test results from the high-temperature tests of structural steels S350GD+Z and S355J2H are presented here with a short description of the testing facilities. Structural steel S350GD+Z is a commonly used steel grade used in thin-walled steel structures and S355J2H is a common steel material used in tubular steel structures.

The aim of the research presented in this paper is to produce accurate material data for the use in different structural analyses. The main test results are public and they are available for other researchers.

The mechanical properties of structural steel after cooling down, i.e. the residual strength was also shortly examined and these test results are given in this report.

The test results were used to determine the temperature dependencies of the mechanical properties, i.e. yield strength, modulus of elasticity and thermal elongation, of the studied steel material at temperatures up to 950°C. The test results are compared with the material model for steel according to Eurocode 3: Part 1.2.

KEYWORDS: elevated temperature, fire, high-temperature, mechanical properties, steel, structural steel, cold-formed steel, steady-state, transient-state, tensile testing.

INTRODUCTION

The behaviour of mechanical properties of different steel grades at elevated temperatures should be well known to understand the behaviour of steel and composite structures at fire. Quite commonly simplified material models are used to estimate e.g. the structural fire

www.EngineeringEBooksPdf.com

resistance of steel structures. In more advanced methods, for example in finite element or finite strip analyses, it is important to use accurate material data to obtain reliable results.
To study thoroughly the behaviour of certain steel structure at elevated temperatures, one should use the material data of the used steel material obtained by testing. The tests have to be carried out so, that the results can be used to evaluate the behaviour of the structure, i.e. the temperature rate e.g. should be about the same that is used in the modelling assumptions.

Extensive experimental research has been carried out since 1994 in the Laboratory of Steel Structures at Helsinki University of Technology in order to investigate mechanical properties of several structural steels at elevated temperatures by using mainly the transient state tensile test method. The basic material research programme is still going on, but the main test results so far were published in 2001 in the Laboratory of steel structures' publication series, Outinen, Kaitila, Mäkeläinen (2001).

The test results have recently been used in some research projects studying the behaviour of e.g. cold-formed steel members in fire, Feng, Wang, Davies (2001); Kaitila (2002). The results seem to work quite well with the structural analyses carried out within these projects.

In this paper the transient state test results of structural steel grades S350GD+Z and S355J2H are presented with a short description of the testing facilities and comparisons with ENV1993-1-2.

In addition to the original plan, some tests were also carried out for structural steel material taken from that has been tested at elevated temperatures. This was to find out the residual strength of the material after fire. The preliminary test results are presented in this paper.

STUDIED MATERIALS

The studied materials were commonly used structural steel grades. The actual yield strength varied significantly from the nominal values and this has to be taken into account. The materials are listed in the Table 1 below with the nominal and measured values at room temperature.

TABLE 1
STUDIED STEEL GRADES

Steel Grade	Nominal f_y [N/mm^2]	Measured f_y [N/mm^2]	Material Standard
S350GD+Z	350	402	SFS-EN 10 147
S355J2H	355	539-566*	SFS-EN 10219-1

* The measured yield strength values are for test specimen taken from the face of square hollow sections 50x50x3, 80x80x3 and 100x100x3.

TEST METHODS

Two types of test methods are commonly used in the small-scale tensile tests of steel at high temperatures; transient-state and steady-state test methods. The steady state tests are easier to carry out than the transient state tests and therefore that method is more commonly used than the transient state method. However, the transient state method seems to give more realistic test results especially for low-carbon structural steel and that is why it is used in this research

www.EngineeringEBooksPdf.com

project as the main test method. A series of steady state tests were also carried out in this project.

TESTING DEVICE

The tensile testing machine used in the tests is verified in accordance with the standard EN 10 002-2. The extensometer is in accordance with the standard EN 10 002-4. The oven in which the test specimen is situated during the tests was heated by using three separately controlled resistor elements. The air temperature in the oven was measured with three separate temperature-detecting elements. The steel temperature was measured accurately from the test specimen using temperature-detecting element that was fastened to the specimen during the heating.

TEST RESULTS OF STRUCTURAL STEEL S350GD+Z

On the basis of the transient state test results of steel S350, a suggestion concerning the mechanical properties of the studied material was made to the Finnish national norm concerning the material models used in structural fire design of unprotected steel members. The test results were fitted to ENV1993-1-2 material model and the results are illustrated in Table 2.

TABLE 2
REDUCTION FACTORS FOR MECHANICAL PROPERTIES OF STRUCTURAL STEEL S350GD+Z AT TEMPERATURES 20°C-1000°C. VALUES BASED ON TRANSIENT STATE TEST RESULTS

Steel Temp. θ_a [°C]	Reduction factor for the slope of the linear elastic range $k_{E,\theta} = E_{a,\theta}/E_a$	Reduction factor for proportional limit $k_{p,\theta} = f_{p,\theta}/f_y$	Reduction factor for satisfying deformation criteria **(informative only)** $k_{x,\theta} = f_{x,\theta}/f_y$	Reduction factor for yield strength $k_{p0,2,\theta} = f_{p0,2,\theta}/f_y$	Reduction factor for yield strength $k_{y,\theta} = f_{y,\theta}/f_y$
20	1.000	1.000	1.000	1.000	1.000
100	1.000	0.970	0.970	1.000	0.970
200	0.900	0.807	0.910	0.863	0.932
300	0.800	0.613	0.854	0.743	0.895
400	0.700	0.420	0.790	0.623	0.857
500	0.600	0.360	0.580	0.483	0.619
600	0.310	0.180	0.348	0.271	0.381
700	0.130	0.075	0.132	0.106	0.143
800	0.090	0.000	0.089	0.077	0.105
900	0.068	0.000	0.057	0.031	0.067
950	0.056	0.000	0.055	0.023	0.048
1000	0.045	0.000	0.025	0.014	0.029

In Figure 1 the experimentally determined yield strength f_y is compared with ENV1993-1-2 material model. In Eurocode, the nominal yield strength is assumed to be the constant until 400°C, but in the real behaviour of the studied steel it starts to decrease earlier.

www.EngineeringEBooksPdf.com

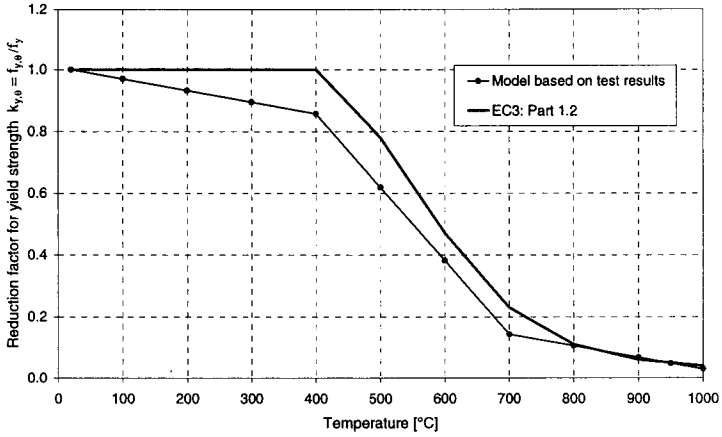

Figure 1: The reduction factor for effective yield strength $f_{y,\theta}$ of structural steel S350GD+Z determined from test results compared with the values given in Eurocode 3: Part 1.2

Additionally, tensile tests were also carried out at ambient temperature for material taken from members that have been tested at elevated temperatures. This was to find out the remaining strength of the material after fire. In Figure 2 the tensile test results are compared with the test results for unheated material.

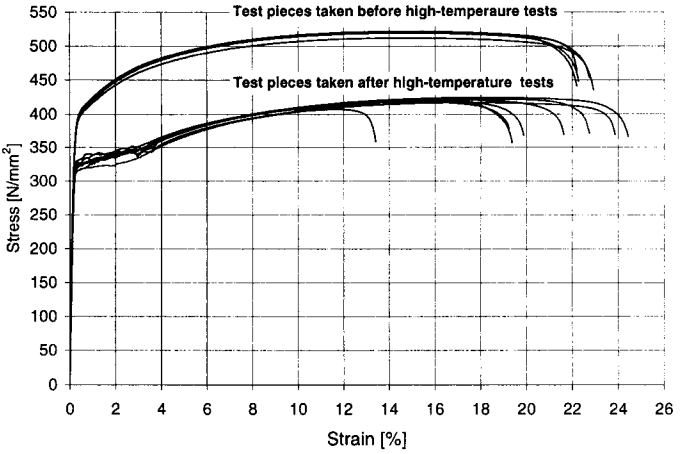

Figure 2: Tensile test results for structural steel S350GD+Z. Test pieces taken before and after high-temperature compression tests

From Figure 2 it can be seen that the increased yield strength of the material due cold-forming has decreased back to the nominal yield strength level of the material. It has to be noted that the material has reached temperatures up to 950°C in the compression tests. The compression tests were carried in a research project of VTT, the Techcnical Research Centre of Finland (not published yet).

www.EngineeringEBooksPdf.com

The members that were in the compression tests were quite distorted after the tests. Despite this, the mechanical properties of the steel material were preserved in the nominal strength level of the material. This kind of phenomenon should be taken into account when considering the load bearing capacity of steel structures that have been in fire and are otherwise still usable, i.e. not too badly distorted. In a research done by Corus Group, the researchers came to the same conclusion.

TEST RESULTS OF STRUCTURAL STEEL S355J2H

The test results for yield strength at ambient temperature for steel S355J2H are illustrated in Table 3. It can be seen from the test results that the increased strength caused by cold-forming is significant for all studied hollow sections. The nominal yield strength for the material is 355N/mm^2. Tensile tests were also carried out for the specimens taken from the corner part of the section SHS 50x50x3. The average yield strength fy for these specimens was 601 N/mm2.

TABLE 3:
TENSILE TEST RESULTS FOR STRUCTURAL STEEL S355J2H AT ROOM TEMPERATURE
TEST PIECES FROM SHS CROSS-SECTIONS

	Yield strength f_y [N/mm^2]	Yield strength $R_{p0.2}$ [N/mm^2]	Yield strength $R_{t0.5}$ [N/mm^2]
50x50x3	566	520	526
80x80x3	544	495	502
100x100x3	539	490	497

A test series of over 100 tensile tests was conducted for the material taken from SHS-tubes 50x50x3, 80x80x3 and 100x100x3. The heating rate in the tests was 20°C/minute. Some tests were also carried out with a heating rate 10°C/minute and 30°C/minute. A small test series was also carried out with a heating rate 45°C/minute.

The tensile tests for structural steel S355J2H were carried out using test specimens that were cut out from SHS-tubes 50x50x3, 80x80x3 and 100x100x3 longitudinally from the middle of the face opposite to the welded seam. A small test series with test specimen taken from the corner parts of the SHS-tube 50x50x3 was also carried out as an addition to the original project plan. The test results have been fitted into the EC3: Part 1.2 material model using the calculation parameters determined from the transient state tests.

The high-temperature tensile testing has to be carried out using the rules given in testing standard SFS-EN 10002 : Metallic materials. Tensile testing. Parts 1-5. In this standard there are limitations for the strain rate and the loading rate used in high temperature tensile testing. The test results that are given in this report are based on tests carried out according this testing standard.

From the test results it was clearly seen, that with this used heating rate 20°C/minute the increased strength caused by cold forming starts to vanish in temperatures 600°C-700°C. For the test specimen with a higher heating rate the increased strength seems to remain to higher temperatures. The test results (SHS 50x50x3) at temperatures 20°C – 1000°C are illustrated in Table 4.

www.EngineeringEBooksPdf.com

TABLE 4
MECHANICAL PROPERTIES OF STRUCTURAL STEEL S355J2H AT ELEVATED TEMPERATURES
TEST PIECES FROM SHS 50x50x3

Temp. [°C]	Modulus of Elasticity E [N/mm^2]	Proportional limit f_p [N/mm^2]	Yield strength f_y [N/mm^2]	Yield strength $R_{p0.2}$ [N/mm^2]	Yield strength $R_{t0.5}$ [N/mm^2]
20	210000	481.1	566	520	526
100	210000	481.1	566	520	526
200	189000	441.48	549.02	485	496
300	168000	367.9	537.7	439	455
400	147000	311.3	481.1	381	399
500	126000	169.8	367.9	255	280
600	65100	67.92	181.12	118	132
700	27300	39.62	101.88	66	72
750	23100	28.3	67.92	46	51
800	18900	19.81	42.45	29	33
850	16537.5	11.32	31.13	20	23
900	14175	6.792	22.64	13	17
950	11812.5	5.66	19.81	12	14
1000	9450	4.528	22.64	10	11

The test results with heating rates 10°C/minute and 20°C/minute did not differ much from each other, even the heating rate 30°C/min seemed to give slightly higher test results. This led to the decision to try tests with even higher heating rate. Three small test series were carried out. One with corner specimens with a heating rate 20°C/minute, one with corner specimen with a heating rate 45°C/minute and one with flat specimen with a heating rate 45°C/minute. The test results at temperature 700°C are illustrated in Figure 3.

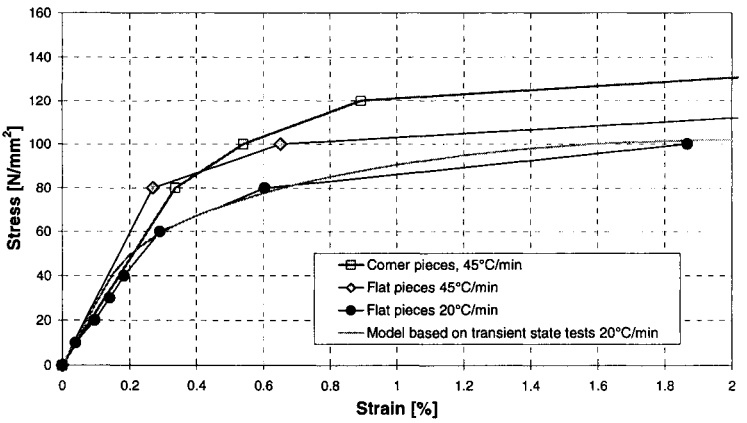

Figure 3: Stress-strain curves of structural steel S355J2H. Test results with different specimens and different heating rates at temperature 700°C

The difference between the test results with heating rates 20°C/minute and 45°C/minute seemed not to be as big as was assumed before for the specimens taken from the face of the square hollow section. Also the difference between the test results with flat specimens and corner specimens with a heating rate 20C/minute was not very big. The test results for the corner pieces are significantly higher with heating rate 45°C/minute.

www.EngineeringEBooksPdf.com

Some tests for structural steel S355J2H were carried out at room temperature with test specimens that had been heated unloaded up until temperature 950°C and let cool down to ambient temperature after that. The mechanical properties of the material were near the nominal values of structural steel S355 as seen in Figure 4.

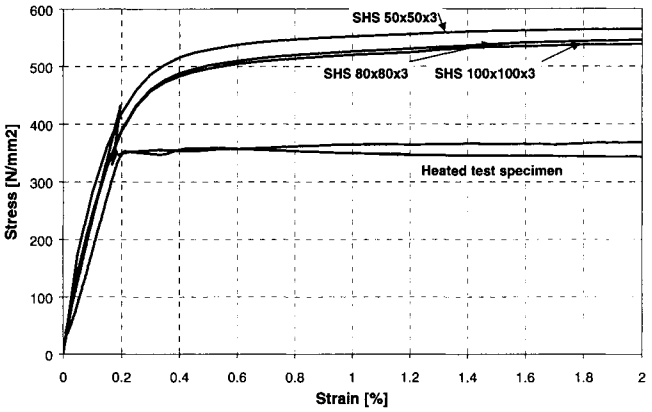

Figure 4: Comparison between the tensile test results of heated and non-heated test specimen on structural steel S355J2H at room temperature.

In addition to this project a small tensile test series was carried out to determine the yield strength of the material used in high-temperature stub column tests. The specimens were taken out from SHS 50x50x3 tubes after they had been tested at elevated temperatures (max. temperature was 710°C). The average yield strength of the material before high-temperature tests was 529N/mm^2 and the nominal yield strength 355N/mm^2. The test results are illustrated in Figure 5.

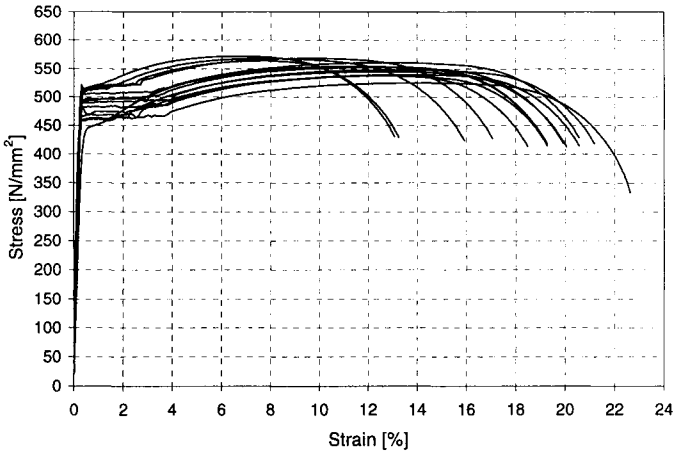

Figure 5: Tensile test results at ambient temperature for structural steel S355J2H. Test coupons taken from SHS 50x50x3 tubes after high-temperature stub column tests

www.EngineeringEBooksPdf.com

CONCLUSIONS

A short overview of the test results for structural steels S350GD+z and S355J2H were given in this paper. The high temperature test results were fitted to the 'Eurocode 3 model' to provide the data in a useful form to be used in e.g. finite element modeling of steel structures. The aim of this research is mainly to get accurate information of the behaviour of the studied steel grades and to provide useful information for other researchers.The test data is presented more accurately in Report by Outinen, Kaitila, Mäkeläinen (2001), which can be downloaded free from: *http://www.hut.fi/Units/Civil/Steel/Publications/jsarj.html.*

The behaviour of structural steel S350GD+Z differed from the EC3 model and a new suggestion was made on the basis of the high-temperature tests. The mechanical properties after heating seemed to be near the nominal values of the material, which is good, when thinking of the residual strength of steel structures after fire.

The behaviour of steel S355J2H seemed also to be very promising. The increase of strength due to cold-forming seemed to remain quite well at elevated temperatures. This should naturally be taken into account when estimating the behaviour of cold-formed steel structures. Also the strength after high-temperature tests seemed to remain quite well.

ACKNOWLEDGEMENTS

The authors wish to acknowledge the support of the company Rautaruukki Oyj, and the National Technology Agency (TEKES) and also the co-operative work of VTT Building and Transport, Finnish Constructional Steelwork Association and Tampere University of Technology making this work possible.

REFERENCES

Outinen, J., Kaitila, O., Mäkeläinen, P. (2001), *High-Temperature Testing of Structural Steel and Modelling of Structures at Fire Temperatures*, Laboratory of steel structures publications, TKK-TER-23, Finland

Outinen J., Kaitila O., Mäkeläinen P. (2000), *A Study for the Development of the Design of Steel Structures in Fire Conditions*, 1st International Workshop of Structures in Fire, Copenhagen, Denmark

Feng,M., Wang,Y.C., Davies,J.M. (2001), *Behaviour of cold-formed thin-walled steel short columns under uniform high temperatures,* Proceedings of the International Seminar on Steel Structures in Fire, pp.300-312, Tongji University, China

Kaitila, Olli (2002). *Imperfection sensivity analysis of lipped channel columns at high temperatures*, Journal of Constructional Steel Research, 58:3, 333-351

EN1993-1-2 (1993) *Eurocode 3: Design of steel structures, Part 1.2 : Structural fire design*, European Committee for Standardisation (CEN), Brussels

SFS-EN 10002 : *Metallic materials. Tensile testing. Parts 1-5*

Reinstatement of Fire Damaged Steel and Iron Framed Structures. Published by Corus, Swinden Technology Centre, Moorgate, Rotherham, UK

www.EngineeringEBooksPdf.com

Advances in Steel Structures, Vol. II
Chan, Teng and Chung (Eds.)
© 2002 Elsevier Science Ltd. All rights reserved.

STRUCTURAL RESPONSE OF A STEEL BEAM WITHIN A FRAME DURING A FIRE

Z. F. Huang[1], K. H. Tan[2], S. K. Ting[3]

1. Research Fellow,
2. Associate Professor., Ph.D., MACI, MIES, MASCE,
3. Associate Professor, Sc.D. (MIT)
School of CEE, Nanyang Technological University, Block N1, #01A-37,
50 Nanyang Avenue, Singapore, 639798.

ABSTRACT

Tradition steel beam fire resistance tests were conducted on a simply-supported beam subjected to constant lateral load and ISO fire curve. Under such conditions, the beam fails when a plastic hinge forms along the beam length. Nonetheless, such tests do not represent the real picture for a steel beam within a building, in which case, the beam is normally axially-restrained. To investigate the full collapse stage of axially-restrained beams under fire conditions, beams with slenderness ratio of $\lambda = 50$ are analysed with visco-elasto-plastic finite element program FEMFAN. All beams are subjected to constant external loads and monotonically increasing temperature. Some dominant parameters are studied, namely, external load utilisation factor, axial restraint ratio and cross-sectional thermal gradient. Numerical results reveal that (1) all beams experience catenary actions at the later heating stage, which are provided by their boundary axial restraints. (2) Due to the catenary action, the beam failure temperature is irrelevant to its external load level. These observations, which agree well with the Cardington fire test, show the possibility to relax current code for determining the steel beam critical temperature according to the one-twentieth of span rule-of-thumb requirement. In addition, the whole development of member cross-sectional stress distribution, as well as the strain rate, are also presented.

KEYWORDS

Fire, Steel beam, Axial restraint, Catenary action, Strain rate, Creep

www.EngineeringEBooksPdf.com

INTRODUCTION

This paper investigates the behaviour of steel beams within a frame in a compartment fire. Current design codes for the fire resistance of a steel beam are based on the experiments performed on simply supported beams subjected to ISO834 fire curve. Obviously, these 'standard' fire tests do not represent well the real situation: a compartment fire in a complete building. During a compartment fire, normally, a heated beam is subjected to slowly developed fire and is boundary restrained. Generally, the structural response of such a steel beam under fire conditions is substantially affected by various factors, such as the external load level, boundary restraints and creep, etc. Regarding the boundary restraints, (1) the rotational restraints are contributed by adjoining beam-to-column connections, and (2) the axial restraint is offered by the adjacent structure. If a heated beam within a fire compartment is isolated for analytical purpose, its boundary restraints can be represented by a linear elastic spring attached at its right end (see Fig. 1). (Because the Cardington fire tests showed that most heated beams experienced local buckling in their bottom flanges (Bailey, 1996), the complicated rotational restraint effect will be considered in future.)

During the past several years, there were several published works focusing on the influence of axial restraint on the behaviour of steel beams in fire (El-Rimawi et al., 1999; Usmani et al., 2001). For instance, through investigating the key factors governing the behaviour of composite frame structures in fire, Usmani et al. (1999) found that the axial restraint can significantly retard beam collapse by catenary action.

In this paper, numerical studies are conducted on simply supported axially-restrained steel beams subjected to a rising temperature (Fig. 1). Visco-elasto-plastic 2-D finite element program FEMFAN (Tan et al., 2002) is used as the analytical tool. The parameters under investigations include the axial restraint ratio and load utilisation factor, whose definitions are respectively shown in Eq. (1) and (2). The developments of stress and strain across the beam section are also presented.

It is found that due to the axial restraint, all beams investigated experience catenary action, which dominates the structural response of beams toward the end of heating. Moreover, the degree of axial restraint controls the magnitude of member axial force developed during the heating. Lastly, creep effect begins to be significant beyond 400°C.

SCOPE OF ANALYSIS

A schematic of a heated beam with an axial restraint is shown in Fig. 1. The spring stiffness k_l is assumed to be constant during heating. The *axial restraint ratio* β_l is used to evaluate the degree of axial restraint and expressed as:

$$\beta_l = \frac{k_l}{E_0^{20} A_b / l_b} \tag{1}$$

where E_0^{20} is the elastic modulus of steel at 20°C (MPa);
A_b is the cross-sectional area of beam (m^2);
l_b is the length of beam (m).

www.EngineeringEBooksPdf.com

The value of ratio β_l ranges from 0.02 to 1.0, representing weak-to-strong axial restraints. However, its practical range is relayed on extensive relevant experimental investigations.

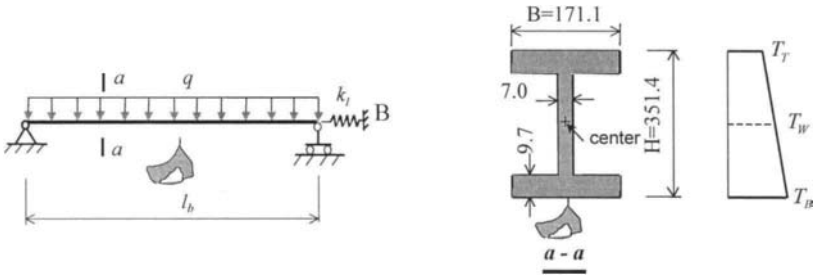

Fig. 1 Isolated Beam Model

Beam 'AB' is made of UB356×171×45 section and have a slenderness ratio $\lambda = 50$ (Fig. 1). Only bending behaviour about the major axis is investigated. The steel grade is ASTM A36.

For steel beams (Fig. 1) sustaining uniformly distributed load (hereafter UDL) q, the load utilisation factor μ^M (superscript 'M' denotes moment) is defined (CEC, 1995) at the beginning of heating as:

$$\mu^M = \frac{M_{mid}}{M_p^{20}} = \frac{M_{mid}}{f_y^{20} W_p} \tag{2}$$

where $M_{mid} = q l_b^{\,2} / 8$ denotes the beam mid-span bending moment (kNm);

$M_p^{20} = f_y^{20} W_p$ denotes the plastic moment capacity of cross-section for ambient temperature design, in the absence of shear force (kNm);

f_y^{20} is the steel yield strength at ambient temperature (MPa);

W_p denotes the plastic section modulus (m^3).

In this study, factor μ^M takes on 0.20 and 0.70, respectively representing the practical lower and upper bound of design value.

Regarding the heating scheme, this study assumes:

(i) The beam bottom flange temperature T_B is equal to $20 + 10t$ (cf. Fig. 1), in which t denotes time (min) and T_B is in Celsius degree.

(ii) The temperature through the depth of beam section is linearly distributed with $T_T = 0.7 T_B$ (Fig. 1).

(iii) The temperature along the beam length is uniform.

www.EngineeringEBooksPdf.com

RESPONSE OF STEEL BEAMS AT ELEVATED TEMPERATURE

Internal Axial force and Mid-span Deflection

Figure 2 illustrates the development of beam internal axial force P, while the corresponding mid-span deflections v_{mid} are shown in Fig. 3. In each figure, the load utilisation factor μ^M takes on 0.20 (dashed curves) and 0.70 (continuous curves), while the axial restraint ratio β_l ranges from 0.02 to 1.00. In Fig. 2, $N_p = f_y^{20} A_b$ denotes the axial plastic capacity at ambient temperature.

Figure 2 shows that due to the axial restraint against thermal expansion, the internal axial force P experiences three stages throughout the heating for most cases. At the first stage, force P grows with temperature as the beam tries to expand. Thus, the linear spring exerts an increasing compression force on the beam. The growth rate will slow down and then eventually starts to decrease, due to the degradation of steel elastic modulus E_0^T and the onset of beam yielding. The maximum value of P, which is denoted as P_u in this paper (Fig. 2), marks the beginning of the second stage, at the end of which P reduces to zero. This marks the beginning of the last stage, which is identified by the catenary action. This means that the linear spring hauls up the beam to prevent it from collapsing. Clearly, no 'run-away' collapse occurs, as is the case for a simply-supported beam without axial restraint.

Catenary action has two effects on heated beams. Firstly, it prevents a heated beam from premature failure. Thus, compared to the simply supported beams without any axial restraint (for example, conventional fire resistance beam tests), a beam with axial restraint can undergo much higher temperatures. This phenomenon has been observed in the Cardington fire tests (Bailey et al., 1996). Secondly, as long as catenary action takes place, a heated beam will experience some horizontal movement at its ends. The unfavourable movement may induce substantial $P-\Delta$ effects on the adjoining columns. However, numerical analyses also show that compared to the horizontal expansions at the first or second heating stage, the horizontal contractions at the third stage are small. This can be perceived indirectly from the development of axial force P in Fig. 2, since the horizontal movement is directly proportional to the value of axial force P, based on the linear elastic spring assumption.

Furthermore, Fig. 3 demonstrates that at the third stage, the mid-span deflections v_{mid} do not develop at an accelerating rate, which implies that the responses of beams are largely dominated by the axial restraints at this stage. This conclusion seems somewhat against the traditional assumptions. In the traditional assumptions, material strength continues to deteriorate, which leads to increasing deflection until the structure no long sustains the applied loads. This is true for simple determinate structures (such as standard fire resistance tests) or redundant structures once all load carrying paths have been exhausted.

Moreover, due to the beneficial effects of catenary action, numerical analyses illustrate that all beams under high load level ($\mu^M = 0.7$) remain stable well beyond 750°C (Fig. 3). For clarity, Fig. 3 does not show the developments of v_{mid} up to the ultimate collapse temperatures. To sum up, the load level normally has only slight influence on the beam 'collapse' temperature, but greater influence on their deformation history.

www.EngineeringEBooksPdf.com

Sectional Stresses and Strains

Figures 4a and 4b respectively show the distribution of mid-span sectional stress under utilisation factor $\mu^M = 0.20$ and 0.70 for beams with $\beta_l = 0.20$. Figure 4a illustrates that under a monotonically rising temperature, the beam changes from elastic to plastic stress while the top flange undergoes compression to tension. At the later heating stage, the whole section is in tension resulting from catenary action. Simultaneously, the neutral axis (associated with zero stress) moves from the mid-depth point 'a' down to its lowest position 'b', and then climbs up to position 'c'. Similar observation is revealed in Fig. 4b.

Moreover, for the beam of Fig. 4b with $\mu^M = 0.70$, the variations of the strain rates at the mid-span are shown in Fig. 5. Only the top and bottom layers are shown. Figure 5a demonstrates that at the beginning of heating, the thermal strain $\dot{\varepsilon}_{th}$ and mechanical strain rate $\dot{\varepsilon}_{ep}$ govern the total strain rate $\dot{\varepsilon}_{Tol}$. However, beyond 400°C (Fig. 5a) or 300°C (Fig. 5b), the creep strain rate $\dot{\varepsilon}_{cr}$ dominates the total strain rate $\dot{\varepsilon}_{Tol}$.

In terms of the effect of linear spring on the internal axial force P, clearly, enhancing the axial restraint results in an increase of P (Fig. 2). On the other hand, P_u, the ultimate value of P developed at the beginning of second stage (Fig. 2), is proportional to the axial restraint ratio β_l. This indicates that during a fire, the beam thermal expansion and the subsequent internal force redistribution will significantly influence the behaviour of adjoining structural components.

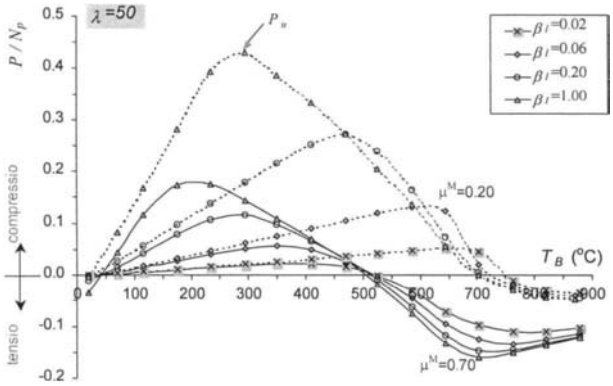

Fig. 2 Development of Beam Internal Axial Force

www.EngineeringEBooksPdf.com

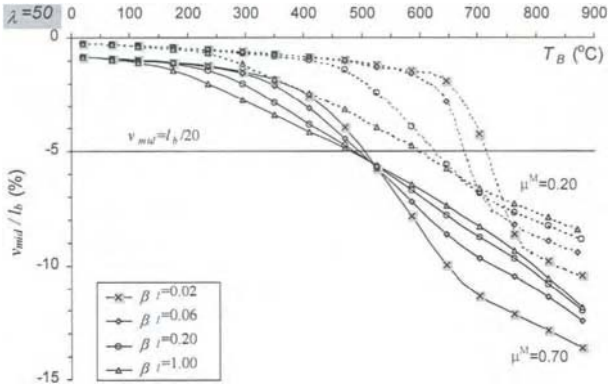

Fig. 3 Development of Beam Mid-span Deflection

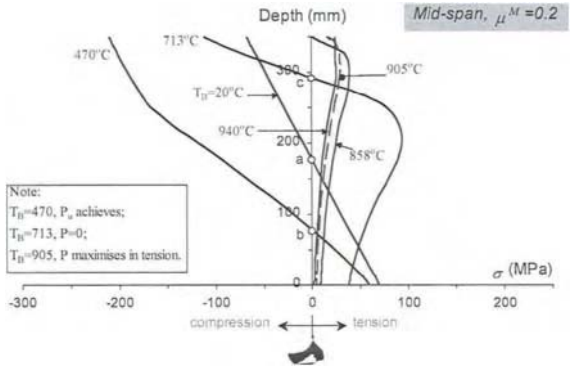

Fig. 4a Development of Stress in Beam Mid-span Section under $\mu^M = 0.2$ ($\beta_l = 0.20$)

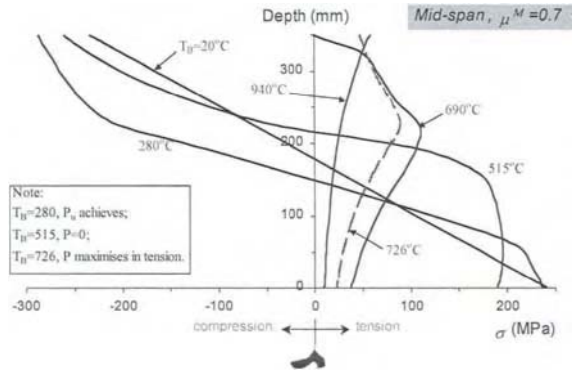

Fig. 4b Development of Stress in Beam Mid-span Section under $\mu^M = 0.7$ ($\beta_l = 0.20$)

www.EngineeringEBooksPdf.com

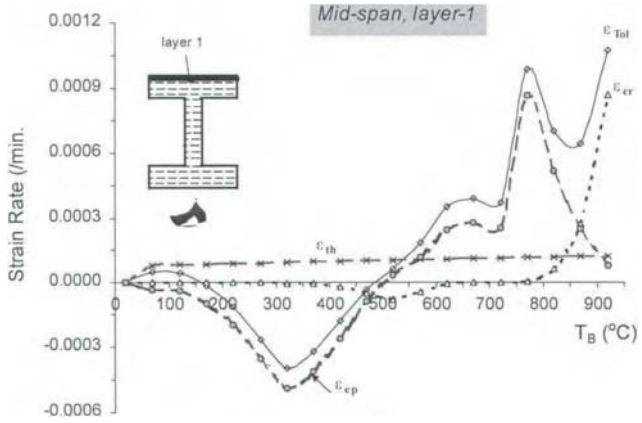

Fig. 5a Development of Strain Rates at *Layer-1* in Beam Mid-span Section ($\mu^M = 0.7$, $\beta_l = 0.20$)

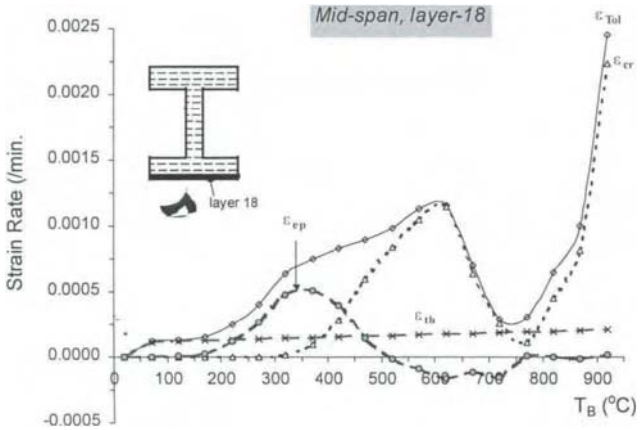

Fig. 5b Development of Strain Rates at *Layer-18* in Beam Mid-span Section ($\mu^M = 0.7$, $\beta_l = 0.20$)

CONCLUSIONS

This paper studies the general behaviour of a thermal-restrained steel beams under a fire condition. The governing factors under consideration comprise the load utilisation factor, slenderness ratio and axial restraint ratio.

Numerical analyses demonstrate that instead of the load utilisation factor, it is beam axial restraint that substantially influences the response of beam towards the end of heating. This is due to the catenary action that is experienced by all beams under study. Most importantly, numerical study shows that the deflections which develop under an increasing temperature, are not controlled by the steel material

www.EngineeringEBooksPdf.com

degradation (which is true for a determinate structure), but by member axial restraints. At very high temperature, the plastic and creep strain in together with post-buckling large displacement, retard the failure of a restrained beam.

Creep is found to dominate the thermal response of steel beams at a temperature as low as 400°C.

REFERENCES

1. Bailey, C. G., Burgess, I. W., Plank, R. J. (1996), "Computer simulation of a full-scale structural fire test", *The Structural Engineers,* **74(6),** 93-100.
2. (**B**ritish **S**tandard **I**nstitution) BSI (1987), *British Standard BS476, Part 20:* Method for determination of the fire resistance of elements of construction. London, UK.
3. (**C**ommission of **E**uropean **C**ommunities) CEC (1995), "Design of Steel Structures: Part 1.2: General Rules – Structural Fire Design (EC3 Pt.1.2)". *Eurocode 3*, Brussels, Belgium.
4. EI-Rimawi, J. A., Burgess, I. W. and Plank, R. J. (1999), "Studies of the Behaviour of Steel Subframes with Semi-Rigid Connection in Fire", *Journal of Constructional Steel Research,* **49,** 83-98.
5. Tan, K. H., Ting, S. K. & Huang, Z. F. (2002), "Visco-Elasto-Plastic Analysis of Steel Frames in Fire", *Journal of Structural Engineering*, ASCE, **128(1),** 105-114.
6. Usmani, A. S., Rotter, J. M., Lamont, S., Sanad, A. M. & Gillie, M. (2001), "Fundamental Principle of Structural Behaviour under Thermal Effects", *Fire Safety Journal.* **36,** 721-744.

www.EngineeringEBooksPdf.com

Advances in Steel Structures, Vol. II
Chan, Teng and Chung (Eds.)
© 2002 Elsevier Science Ltd. All rights reserved.

EFFECT OF EXTERNAL BENDING MOMENT ON THE RESPONSE OF BOUNDARY-RESTRAINED STEEL COLUMN IN FIRE

K. H. Tan[1], Z. F. Huang[2]

1. Assoc. Prof., Ph.D., MACI, MIES, MASCE,
School of CEE, Nanyang Technological University, Block N1, #01A-37,
50 Nanyang Avenue, Singapore, 639798.
2. Research Fellow,
School of CEE, Nanyang Technological University, Block N1, #B1b-09,
50 Nanyang Avenue, Singapore, 639798.

ABSTRACT

Traditionally, fire resistance of a steel column is determined by the standard fire resistance test conducted on a pin-roller column subjected to ISO fire curve. Under such conditions, the external bending moments at the column ends were found to significantly decrease the column critical temperature. However, a steel column within a frame is axially and rotationally restrained. To investigate the influence of bending moments on the column behaviour in fire, in this study, columns of slenderness ratio $\lambda = 100$ are analysed with visco-elasto-plastic finite element program FEMFAN. All columns are subjected to constant external loads and monotonically increasing temperature. Some dominant parameters are considered, namely, external load utilisation factor, axial and flexural restraint ratios. Extensive analyses show that (1) the column end moments substantially affect both the structural responses of columns with and without flexural restraints during the heating; (2) the end moments significantly reduce the critical temperature of a column without any flexural restraints, while they have limited effects on one with flexural restraints. This is due to the restoring effect of flexural restraints towards the end of heating. Based on this study, it shows that the load utilisation factor, which is used to predict the column critical temperature as proposed by EC3 Pt.1.2, will overestimate the influence of external bending moment if a flexually-restrained column is concerned.

KEYWORDS

Fire, Steel column, External bending moment, Flexural restraint, Critical temperature

www.EngineeringEBooksPdf.com

INTRODUCTION

During a fire, there is significant moment redistribution among heated members and its adjoining cool members. This is mainly due to a substantial reduction of stiffnesses of heated members at elevated temperature, as well as member thermal expansions. Both EC3 Pt.1.2 (CEC, 1995) and BS5950 Pt.8 (BSI, 1990) suggest column critical temperature is solely a function of load utilisation factor μ_0 (equivalent to *load level* in BS5950 Pt.8). The term μ_0 is defined as a ratio of design effect of actions relative to the corresponding design value of load bearing resistance at the beginning of heating (20°C). For a column with class 1 (or class 2) cross-section (classification refers to CEC, 1992) subjected to both in-plane bending moment and axial load (Fig. 1), its utilisation factor μ_0 is expressed as:

$$\mu_0 = \mu^N + \mu^M = \frac{N_{fi,Ed}}{N_{b,fi,0,Rd}} + \frac{k_y M_{y,fi,Ed}}{M_{p,y}} \tag{1}$$

where $\mu^N = N_{fi,Ed} / N_{b,fi,0,Rd}$ is the contribution of axial force;

$\mu^M = k_y M_{y,fi,Ed} / M_{p,y}$ is the contribution of in-plane bending moment (subscript 'y' denotes $y-y$ axis, i.e., major axis);

$N_{fi,Ed}$ is the column service load at the beginning of heating (kN), in which the subscript 'fi' represents fire conditions, the subscript 'Ed' represents design value of external load action. In this study, $N_{fi,Ed}$ is the column internal axial force at 20°C (cf. P^{20} in Fig. 2);

$N_{b,fi,0,Rd}$ is the column buckling resistance at time $t=0$ (kN), in which the subscript 'b' represents buckling, '0' represents at $t=0$ (i.e., the beginning of heating) and 'Rd' represents load bearing resistance;

k_y is amplifying factor (see Eq. (5.51) in CEC, 1992);

$M_{y,fi,Ed}$ is the column in-plane (i.e., about major axis) bending moment at the beginning of heating (kNm);

$M_{p,y} = W_{p,y} f_y$ is the rigid-plastic moment capacity about major axis at 20°C (kNm);

$W_{p,y}$ is the plastic section modulus about major axis (m^3).

The column critical temperature T_{cr} proposed by EC3 Pt.1.2 is expressed as:

$$T_{cr}^{EC3} = 39.19 \ln\left(\frac{1}{0.9674\mu_0^{3.833}} - 1\right) + 482 \tag{2}$$

where μ_0 is utilisation factor.

It should be noted that Eq. (2) is based on numerous traditional fire resistance tests on columns with idealised boundary conditions, such as pined and fully fixed. The validation of Eq. (2) should be verified against the axially-restrained column with/without flexural restraint, which is commonly encountered in design practice. This is because Eq. (2) will yield a smaller T_{cr} for a column subjected

www.EngineeringEBooksPdf.com

to an additional bending moment besides an axial load. However, Wang et al. (1995) observed that as columns approach failure, the internal bending moments at the ends of heated columns reduce rapidly. This implies that the external bending moment may not exert significant influence on column T_{cr}.

The objective of this paper is to examine the effects of external moments on heated columns with and without rotational restraint.

SCOPE OF ANALYSIS

A schematic of a heated column with boundary restraints is shown in Fig. 1, in which the linear (or rotational) elastic spring represents the axial (or flexural) restraint. The stiffness k_l and k_R are assumed to be constant during heating. The *axial restraint ratio* β_l and *rotational restraint ratio* β_R are respectively used to evaluate the degree of axial and flexural restraint. Their definitions are as follows:

$$\beta_l = \frac{k_l}{E_0^{20} A_c / l_c} \tag{3}$$

$$\beta_R = \frac{k_R}{4E_0^{20} I_c / l_c} \tag{4}$$

where A_c is the cross-sectional area of column (m^2);
$E_0^{20} A_c / l_c$ and $4E_0^{20} I_c / l_c$ are the elastic axial stiffness and flexural stiffness of the column 'AB' at ambient temperature, respectively.

In this study, the value of ratio β_l takes on 0.01 and 0.25, representing practical extremely weak to extremely strong axial restraints. The rotational restraint ratio β_R takes on 0.0 (without restraint) and 1.353 (with weak restraint).

All beam 'AB' are made of 356×171UB45 section (Fig. 1). Only bending behaviour about the major axis is investigated, and all beams are of the same slenderness ratio $\lambda = 100$. The steel grade is ASTM A36.

In this study, factor μ^N takes on 0.20.

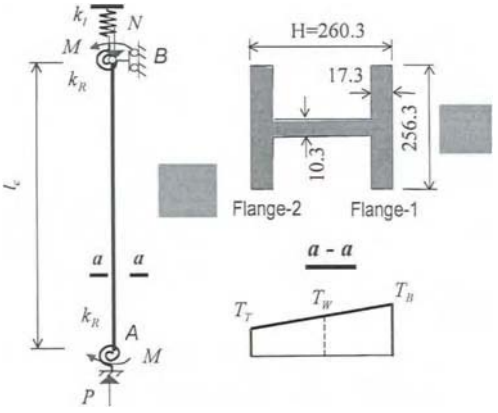

Fig. 1 Isolated Column Model

Regarding the heating scheme, this study assumes:

(i) The temperature of flange near fire T_B rise at a rate of 10°C/min. (Fig. 1).

www.EngineeringEBooksPdf.com

(ii) The temperature through the width of column section is linearly distributed with $T_T = 0.7T_B$ (Fig. 1).
(iii) The temperature along the column height is uniform.

Finite element program FEMFAN (Tan et al. 2002) is used in this study.

COLUMN CRITICAL TEMPERATURE

For a heated thermal restrained column, its internal axial force P is used as an index to judge column failure. Fig. 2 shows a typical development of force P under a rising temperature, which can be divided into three stages. At the first stage, axial force P grows with temperature as the column expands. The axial restraint therefore exerts a compression force on the column at this stage (Fig. 1). At the second stage, force P decreases due to the degradation of steel elastic modulus E_0^T and the large lateral displacement. Normally, the column will enter into the third stage, which is identified by $P < P^{20}$ (here, P^{20} denotes the service load at the beginning of heating). This means that part of the initial load carried by this heated column is transferred to its surrounding cool structure; that is, the heated column ceases to sustain its assigned load at room temperature. Therefore, this study assumes column *critical temperature* T_{cr} is corresponding to $P = P^{20}$.

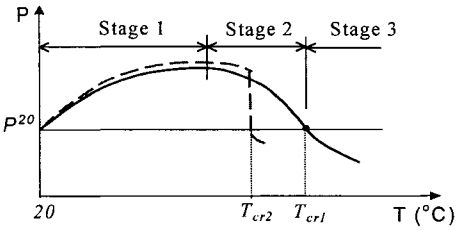

Fig. 2 Typical Development of Column Internal Axial Force

However, it is also observed some columns experience buckling failure at stage2 (see Table 1 or Neves, 1995). Under such situation, the buckling temperature is taken as T_{cr}.

RESPONSE OF STEEL COLUMNS AT ELEVATED TEMPERATURE

In Fig. 1, the external moment at the each end of column takes on such a value that when each of them acts solely on the straight column, the internal bending moment at that end is equal to $0.2M_{p,y}$. Here, factor 0.20 is denoted as μ^M (see Eq. (1)).

The predictions of column critical temperatures are listed in Table 1, in which critical temperature in shade denotes column buckles at stage 2.

Table 1 shows that the critical temperatures of those columns without rotational restraint are substantially reduced by external bending moment. However, for those columns with rotational restraints, their T_{cr} is little affected if external bending moment is included. As such, it is expedient to investigate the relationship between column internal forces and rising temperature. Fig. 3 displays all positive internal forces under study, in which superscripts 'B' and 'SP' denote node 'B' and rotation spring, respectively, and subscript '*mid*' denotes mid-height.

www.EngineeringEBooksPdf.com

		μ^N= 0.20		μ^N= 0.35		μ^N= 0.50		μ^N= 0.70	
without bending Moment	0.01	605	699	518	639	442	583	336	520
	0.04	585	668	502	616	420	566	302	498
	0.10	578	654	495	604	416	558	302	493
	0.25	573	647	491	596	416	550	302	488
		+ μ^M= 0.20							
with bending Moment	0.01	531	693	441	630	344	572	217	500
	0.04	519	664	437	611	343	558	217	486
	0.10	512	652	436	600	343	552	217	483
	0.25	507	645	434	593	343	545	217	479

TABLE 1 COLUMN CRITICAL TEMPERATURES WITH OR WITHOUT EXTERNAL BENDING MOMENT UNDER UNIFORM HEATING (°C)

Note: a: P.R. denotes pin-roller.

Columns without Flexural Restraint

Firstly, the influence of external bending moment on columns without flexural restraint is examined. Figs. 4a and 4b show the developments of column internal forces under a rising temperature, pertaining to axial restraint ratio β_l of 0.01 and 0.25, respectively. All columns are subjected to axial load of $\mu^N = 0.20$. Both Fig. 4a and Fig. 4b illustrate that throughout the heating, the axial force P including external bending moment M is consistently lower than the axial force P excluding moment M. Therefore, the relevant column critical temperatures are reduced by external bending moment.

Furthermore, throughout heating, the internal bending moment at the column bottom end (Fig. 1) follows the same direction as that at the mid-height (Fig. 4). This implies that under the proposed load pattern as shown in Fig. 1, a pin-roller column bends in a single curvature (convex to fire) throughout heating, irrelevant to if column is subjected to external bending moments.

The effect of external moment on the column lateral deflection is studied also. For column in Fig. 4a, Fig. 5 shows the variation of mid-height lateral displacement u_{mid} during the heating, with and without actions of external bending moments M. Clearly, moment M accelerates the development of u_{mid} and consequently, hastens the 'collapse' of column (see P in Fig. 4a).

Besides, it is noteworthy that in this study, the external bending moments M at the column ends are arranged such that this column bends in a single curvature towards fire source. This is the most unfavourable condition. However, if the imposed bending moments M are arranged such that a column bends in double curvature, it is predicable that the T_{cr} will be increased subsequently.

www.EngineeringEBooksPdf.com

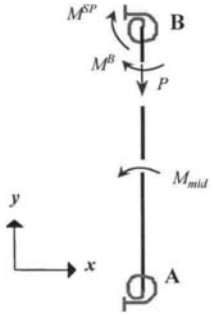

Fig. 3 Internal Forces of Sub-frame

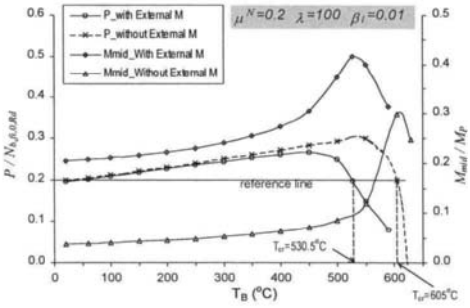

Fig. 4a Development of Column Internal Forces With or Without External Bending Moment (Pin-roller, $\mu^N = 0.2$, $\beta_l = 0.01$)

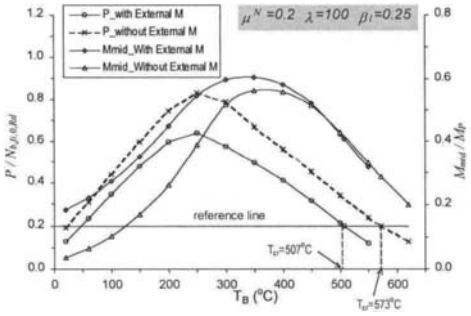

Fig. 4b Development of Column Internal Forces With or Without External Bending Moment (Pin-roller, $\mu^N = 0.2$, $\beta_l = 0.25$)

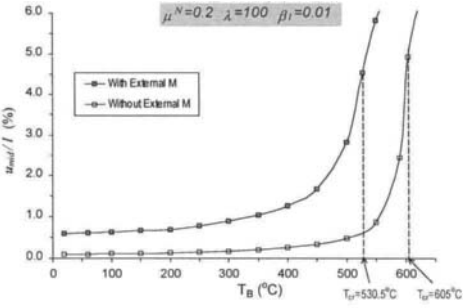

Fig. 5 Development of Column mid-height deflection With or Without External Bending Moment (Pin-roller, $\mu^N = 0.2$, $\beta_l = 0.01$)

Columns with Flexural Restraints

So far, the effects of external bending moment on pin-roller columns have been explored. The following examines the effects on flexurally-restrained columns. It is more valuable to do so since most columns in a frame receive flexural restraints.

The developments of internal forces (see Fig. 3) are illustrated in Figs. 6a and 6b. These columns are of weak rotational restraints of β_R=1.353 and axial restraint of β_l=0.01 to 0.25. The utilisation factor μ^N is maintained at 0.20. For comparison purpose, the development of axial force P without any external bending moment are also included in Figs. 6a and 6b.

Both Fig. 6a and Fig. 6b show that under a monotonically rising temperature, the absolute value of M^B decreases gently and eventually, M^B reverses its direction and develops gradually at a small

www.EngineeringEBooksPdf.com

accelerating rate. At the later heating stage, M^B attains its ultimate value and then decreases smoothly. This trend becomes more pronounced as the axial restraint ratio β_l increases. With respect to the column mid-height moment M_{mid}, both Figs. 6a and 6b show clearly that with the inclusion of external bending moment, the magnitude of M_{mid} is increased from the beginning of heating, compared to those M_{mid} without any external bending moment. However, at the later heating stage, M_{mid} is greatly negated by M^B (see Figs. 6a and 6b). Consequently, two curves of M_{mid} with or without consideration of external bending moments, merge together.

Besides, the comparison of axial force P with and without the action of external bending moment M, shows clearly that there exists indiscernible differences between the two predictions (Fig. 6a to 6b). Thus, the corresponding critical temperatures are very close. This is a common observation for all investigated columns with rotational restraints (Table 1).

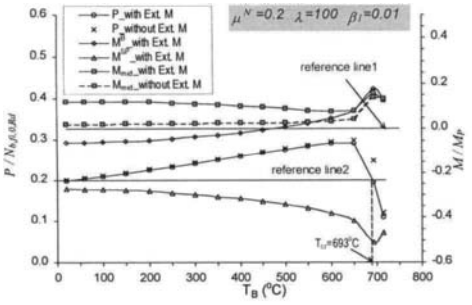

Fig. 6a Development of Column Internal Forces With or Without External Bending Moment ($\beta_R=1.353$, $\mu^N=0.2$, $\beta_l=0.01$)

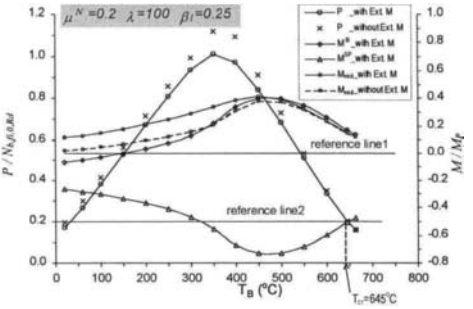

Fig. 6b Development of Column Internal Forces With or Without External Bending Moment ($\beta_R=1.353$, $\mu^N=0.2$, $\beta_l=0.25$)

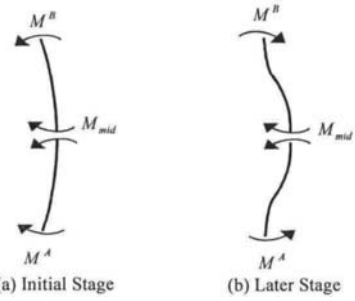

Fig. 7 The Deflection Profiles of Heated Column Attached by Rotational Springs

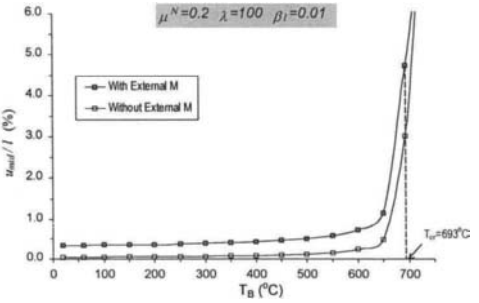

Fig. 8 Development of Column mid-height deflection With or Without External Bending Moment ($\beta_R=1.353$, $\mu^N=0.2$, $\beta_l=0.01$)

www.EngineeringEBooksPdf.com

In short, at the initial heating stage, the flexurally-restrained column bends in a single curvature, which is indicated by the same direction of M^B and M_{mid} as shown in Fig. 7. However, at the later heating stage, the column bends in triple curvature (see Fig. 7b), which is indicated by the opposite direction of M^B and M_{mid}. Bending in triple curvature at the later stage, the development of its lateral deflection is significantly retarded. This behaviour is markedly different from that of a pin-roller column, which keeps on bending in a single curvature throughout the heating.

Fig. 8 shows the development of mid-height lateral deflection u_{mid} for the column of Fig. 6a. It can be seen that unlike columns without flexural restraint (Fig. 5), the inclusion of external bending moments only slightly hastens the lateral deflection under a rising temperature. This explains why two curves of axial force P with and without consideration of external moments, follow closely each other throughout the heating (Fig. 6a).

CONCLUSIONS

Based on the preceding numerical analyses, it can be concluded that for a normal steel column with rotational restraints, it is unrealistic for EC3 Pt.1.2 to suggest a critical temperature which is solely determined by the load utilisation factor that includes the full contribution of internal bending moment at the beginning of heating (cf. Eq. (2)). Numerical analyses show that the development of column internal forces change substantially with temperature and do not remain static.

In brief, this study finds:

- For columns without flexural restraint, external bending moments not only affect the developments of internal forces at elevated temperatures, but also significantly reduce column critical temperatures.
- For columns with flexural restraint, external bending moments only affect the developments of internal forces at elevated temperatures; with regard to column critical temperature, the influence is very limited.

REFERENCES

1. BSI (1990), "Code of Practice for Fire Resistant Design: Structural Use of steelwork in Building. Part 8, BS5950". London, UK.
2. (**C**ommission of **E**uropean **C**ommunities) CEC (1992), "Design of Steel Structures: Part 1.1: General Rules and Rules for Buildings (EC3 Pt.1.1)". *Eurocode 3*, Brussels, Belgium.
3. CEC (1995), "Design of Steel Structures: Part 1.2: General Rules – Structural Fire Design (EC3 Pt.1.2)". *Eurocode 3*, Brussels, Belgium.
4. Neves, I. Cabrita (1995), "The Critical Temperature of Steel Columns with Restrain Thermal Elongation", *Journal of Constructional Steel Research.* **24,** 211-227.
5. Tan, K. H., Ting, S. K. & Huang, Z. F. (2002), "Visco-Elasto-Plastic Analysis of Steel Frames in Fire", *Journal of Structural Engineering*, ASCE, **128(1),** 105-114.
6. Wang, Y. C., Lennon, T. and Moore, D. B. (1995), "The Behaviour of Steel Frames Subjected to Fire", *Journal of Constructional Steel Research.* **35,** 291-322.

www.EngineeringEBooksPdf.com

Advances in Steel Structures, Vol. II
Chan, Teng and Chung (Eds.)
© 2002 Elsevier Science Ltd. All rights reserved.

CONCRETE-FILLED HSS COLUMNS AFTER EXPOSURE TO THE ISO-834 STANDARD FIRE

Lin-Hai Han[1] Jing-si Huo[1] & You-Fu Yang[2]

[1]College of Civil Engineering and Architecture, Fuzhou University, Fuzhou, Fujian, 350002, China
[2]School of Civil Engineering, Harbin Institute of Technology, Haihe Road 202, Harbin, 150090,China

ABSTRACT

The behavior of eighteen concrete-filled HSS (hollow structural steel) columns with or without fire protection after exposure to the ISO-834 standard fire subjected to axial or eccentric loads has been experimentally investigated and the results presented in this paper. A mechanics model is developed in this paper for concrete-filled HSS columns after exposure to the ISO-834 Standard Fire, and is a development of the analysis used for ambient condition (Han et al, 2001b). The predicted load versus mid-span deflection relationship for the composite columns is in good agreement with test results. Based on the theoretical model, influence of the changing strength of the materials, fire duration time, sectional dimensions, steel ratio, load eccentricity ratio and slenderness ratio on the residual strength index (*RSI*) is discussed. It was found that, in general, the slenderness ratio, sectional dimensions and the fire duration time have a significant influence on the residual strength index (*RSI*). However, the steel ratio, the load eccentricity ratio and the strength of the materials have a moderate influence on RSI. Finally, formulas suitable for incorporation into building code, for the calculation of the residual strength of the concrete-filled HSS columns after exposure to fire are developed based on the parametric analysis results.

KEYWORDS

Concrete-filled HSS columns, standard fire curve, mechanics model, residual strength, fire duration time, residual strength index

1. INTRODUCTION

Filling hollow steel columns with concrete can increase the load bearing capacity of the column due to concrete filling. In addition, a high fire resistance can be obtained compared with bare steel tubular columns. Concrete-filled HSS columns also have much better endurance characteristics than conventional RC columns under fire conditions as the steel casting prevents spalling of the concrete. Another benefit is that the tubular form of the steel eliminates the need for formwork. These advantages have led to the increased use of such columns in the recent tall buildings in China. In the past, although there are a large number of research studies on realistic performance of concrete-filled HSS columns under fire conditions, such as British Steel and Pipes (1990); Klingsch (1985); Hass (1991); O'Meagher et al (1991); Falke (1992); Lie and Stringer (1993); Kim, et al (2000); Wang (1999); Kodur (1999); Han (2001), there is very little research work on post-fire behavior of this kind of composite columns.

The residual strength of a composite column may be used to assess the potential damage caused by fire

www.EngineeringEBooksPdf.com

and help to establish an approach to calculating the structural fire protection for minimum post-fire repair. The main objectives of these studies in this paper are thus fourfold: firstly, to describe a series of tests on composite columns after exposure to the ISO-834 standard fire (ISO-834, 1975). Secondly, to develop a mechanics model for concrete-filled HSS columns after exposure to Fire. Thirdly, to analyze the influence of the changing strength of the materials, fire duration time, sectional dimension, steel ratio, load eccentricity ratio, and slenderness ratio on the residual strength. And finally, to establish a simplified model for calculating the residual strength of concrete-filled HSS columns after exposure to the ISO-834 standard fire based on the parametric analysis.

2. EXPERIMENTAL PROGRAM

2.1 Specimen Preparation

Eighteen concrete-filled HSS columns were tested. Test parameters were section types, slenderness ratio and load eccentricity ratio. The details of each column are listed in Table 1, where a is the fire protection thickness, L is the calculated length of the specimen. e is load eccentricity; e/r is load eccentricity ratio, in which $r=D/2$, D is the diameter of CHS (circular hollow section), width or depth of SHS (square hollow section) or RHS (rectangular hollow section) respectively. λ is defined as slenderness ratio, $\lambda=4L/D$ for specimens with circular sections, $\lambda=2\sqrt{3}L/D$ for specimens with square or rectangular sections.

TABLE 1
SUMMARY OF TEST INFORMATION

Section Type	No.	Specimen Number	Sectional Dimension (mm)	L (mm)	λ	e (mm)	e/r	f_{sy} (MPa)	a (mm)	N_{ue} (kN)	N_{uc} (kN)	N_{uc}/N_{ue}
CHS	1	C1	ϕ 108×4.32	600	22.2	0	0	356	0	632	408	0.65
	2	C2	ϕ 108×4.32	600	22.2	15	0.28	356	0	387	319	0.83
	3	C3	ϕ 108×4.32	1200	44.4	0	0	356	0	362	341	0.94
	4	C4	ϕ 108×4.32	1200	44.4	15	0.28	356	0	227	251	1.11
	5	CP1	ϕ 108×4.32	900	33.3	0	0	356	25	779	866	1.11
	6	CP2	ϕ 108×4.32	900	33.3	15	0.28	356	25	485	625	1.29
SHS	1	S1	□-100×100×2.93	600	20.8	0	0	294	0	416	248	0.60
	2	S2	□-100×100×2.93	600	20.8	15	0.30	294	0	259	203	0.78
	3	S3	□-100×100×2.93	1200	41.6	0	0	294	0	227	219	0.96
	4	S4	□-100×100×2.93	1200	41.6	15	0.30	294	0	158	164	1.04
	5	SP1	□-100×100×2.93	900	31.2	0	0	294	25	455	427	0.94
	6	SP2	□-100×100×2.93	900	31.2	15	0.30	294	25	302	314	1.04
RHS	1	R1	□-100×80×2.93	1200	41.6	0	0	294	0	214	201	0.939
	2	R2	□-100×80×2.93	1200	41.6	15	0.3	294	0	148	149	1.007
	3	R3	□-120×90×2.93	1200	34.6	0	0	294	0	218	240	1.101
	4	R4	□-120×90×2.93	1200	34.6	18	0.3	294	0	209	183	0.876
	5	RP1	□-100×80×2.93	900	31.2	0	0	294	25	398	334	0.839
	6	RP2	□-120×90×2.93	900	26.0	0	0	294	25	358	358	1.000

Strips of the steel tubes were tested in tension, the average yield strength (f_{sy}) of steel in the circular tube was found to be 356 MPa and the modulus of elasticity was about 201,000 MPa. The average yield strength (f_{sy}) of steel in the square or rectangular tube was found to be 294 MPa and the modulus of elasticity was about 195,000 MPa. Two types of concrete were used. The details of the concrete mix are given in Table 2. The concrete mix in the circular tube was designed for a compressive cubic strength (f_{cu}) at 28 days of approximately 70.2 MPa, The modulus of elasticity (E_c) of concrete was measured, the average value being 31100 MPa. The average cubic strength at the time of test was 71.3 MPa. The concrete mix in the square and rectangular tube was designed for a compressive cubic strength at 28 days of approximately 34.4 MPa, The modulus of elasticity of concrete was found to be 27440 MPa. The average cubic strength at the time of test was 34.8 MPa.In all the concrete mixes, the fine aggregate used was silica-based sand, the coarse aggregate was carbonate stone.

Each tube was welded to a square or rectangular (for specimens with square or rectangular sections) or

www.EngineeringEBooksPdf.com

circular (for specimens with circular sections) steel base plate 10 mm thick. The concrete was filled in layers and was vibrated by poker vibrator. The specimens were placed upright to air-dry until heating. During curing, a very small amount of longitudinal shrinkage of 1.4 mm or so occurred at the top of the column. A high-strength epoxy was used to fill this longitudinal gap so that the concrete surface was flush with the steel tube at the top. Two semi-circular holes with 20 mm in diameter, located at the junctions between the tube and the top plate as well as the bottom plate were drilled in the section wall. They were provided as vent holes for the water vapor pressure produced during fire exposure.

TABLE 2
MIXTURE OF CONCRETE (kg/m^3)

Concrete Strength f_{cu} (MPa)	Water	Cement	Sand	Aggregate
70.2	176	536	1099	589
34.4	206	457	1129	608

The spray material used was specified in "CECS24:20 Design Regulation for the Fire Protection of Steel Structures"(CECS24:20,1990).The spray material used for the fire protection of the columns with the thermal conductivity, water content, specific heat and density of 0.116W/m.k, 0.01,1.047$\times$ 10^3J/kg.k and 400$\pm$20kg/m^3 respectively. Table 1 shows the fire protection thickness of the columns.

2.2 Test Apparatus

Prior to testing, the specimens were heated by exposing the columns to heat in a furnace specially built for testing columns in Tianjin, China. The ambient temperature at the start of the test was about 20 °C. During the test the column was exposed to heating controlled in such a way that the average temperature in the furnace followed as closely as possible the ISO-834 standard fire curve (ISO-834, 1975). The fire duration time (t) for specimens without fire protection were set to be 90 min., for specimens with fire protection were set to be 180 min. (shown in Table 1).

All of the specimens were tested for residual strength after exposure to the ISO-834 standard fire (ISO-834, 1975). Displacement transducers were used to measure: (a) longitudinal deformation over the test region at the top and bottom of the specimens; (b) vertical displacements at the pins, load application points and the centre of the specimens; as well as (c) the overall shortening of the specimens. Strain gauges were used to determine the longitudinal and circumferential strains at the centre of the specimens.

The test specimens behaved in a relatively ductile manner and testing proceeded in a smooth and controlled way. The axial thrust versus extreme fibre compressive strains ranging from 0.00768 to 0.0148 for circular columns, 0.00793 to 0.0118 for square columns, and 0.0062 to 0.01528 for rectangular columns. Typical failure mode was overall buckling failure. When the load was small, the lateral deflection at middle height is small and approximately proportional to the applied load. When the load reached about 60% to 70% of the maximum load, the lateral deflection at middle height started to increase significantly. All specimens failed at the mid-height by rupture of the steel casing in tension zone after substantial cracking of the concrete in the tension zone and buckling of the steel in the compression zone at the tested curves of load versus lateral deflection (u_m) are shown in Figure 1.

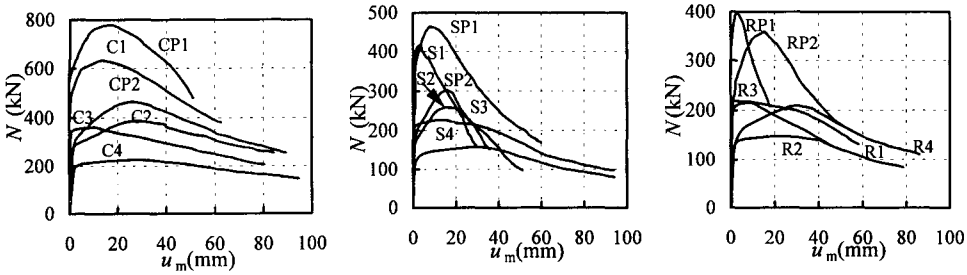

(a) Circular specimens (b) Square specimens (c) Rectangular specimens

Figure 1: Load (N) versus mid-span lateral deflection (u_m) curves

www.EngineeringEBooksPdf.com

Because of the infill of concrete, the circumferential deformation and ovalization of the composite cross sections were prevented, resulting in higher stiffness and larger critical buckling loads. The enhanced structural behavior of the concrete filled columns can be explained in terms of "composite action" between the steel tube and the concrete core.

3. MECHANICS MODEL

3.1 Load versus Mid-Span Deflection Relations

The calculation of the residual strength of the composite column involves the calculation of the temperatures of the fire, to which the column is exposed, the temperature in the column and its deformations and strength after exposure to fire.

After exposure to fire, the strength of the beam-column decreased with the duration of exposure. The stress-strain relations of the steel and core concrete after exposure to high temperatures were given in Huo（2001）and Han, et al (2000, 2001a).

A numerical model was worked out for the analysis of the residual strength of the composite columns after exposure to ISO-834 standard fire, and is a development of the analysis used for normal temperature condition (Han, et al, 2001b). The model allows a differentiated consideration of all physical and geometrical non-linearity. In this method, The column temperatures can be calculated by finite element method (Han, 2001). For the calculation of column residual strength, similar assumptions were made as Han et al (2001b):

The load (N) versus mid-span deflection (u_m) relations can be established by using the method for normal temperature condition. The model has been described in detail in Han (2001).

In order to obtain a basis of comparison for the effects of fire on the residual strength of the composite columns, the fire is defined as a time versus temperature relationship by the ISO-834 Standard fire curve (ISO-834, 1975).

It was found that the ultimate strength of a column after exposure to the ISO-834 standard fire is reduced and less than the corresponding value under normal temperature condition. In the calculations, a small arbitrary load eccentricity of $L/1000$, reflecting a nearly ideal straight in axis of the column, has been selected for the initial eccentricity (Han, 2000).

Figure 2 gives schematic view of load versus mid-span lateral deflection curves, where $N_u(t)$ is the residual strength corresponding to the fire duration time (t) of the composite columns, and N_u is the ultimate strength of the composite columns at ambient temperatures. u_{mu} and $u_{mu}(t)$ are the deflection in the mid-height of the composite columns corresponding to N_u and $N_u(t)$ respectively. It can be found from this figure that, after exposure to fire the increase in curvature with time t due to fire exposure results in an increase in column deflection and reduced the column stiffness. In effect, the ultimate strength of a column after exposure to fire is reduced and less than the corresponding value under ambient condition.

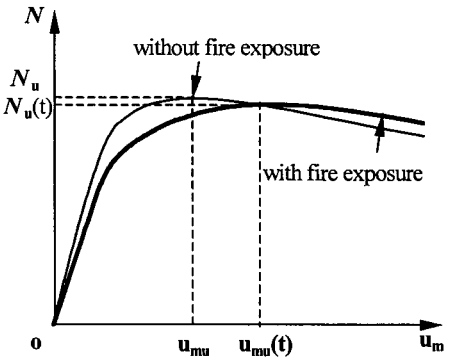

Figure 2: Schematic view of axial load (N) versus mid-span lateral deflection (u_m) curve

The predicted curves of load versus lateral deflection (plotted in dashed lines) are compared in Figure 3 with experimental curves. A good agreement is obtained between the predicted and tested curves.

www.EngineeringEBooksPdf.com

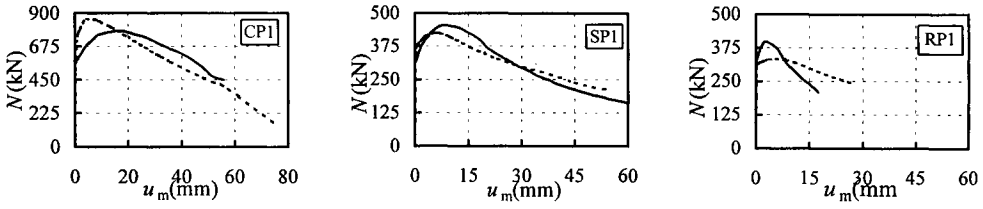

(a) (b) (c)

Figure 3: Axial load(N) versus mid-span lateral deflection (u_m) curves
(Experimental curves are shown in solid lines; Predicted curves are shown in dashed lines)

3.2 Maximum Loads in Beam-Columns

The predicted maximum strengths (N_{uc}) are compared in Table 1 with those obtained in tests (N_{ue}). A mean ratio (N_{uc}/N_{ue}) of 0.947 is obtained with a COV of 0.169.

Figure 4 shows the typical calculated axial load (N) versus mid-span deflection (u_m) relations and their changes due to fire exposure.

Figure 5 illustrates the typical calculated interaction relationship between compression strength (N) and bending strength (M) of the composite columns with different fire duration time.

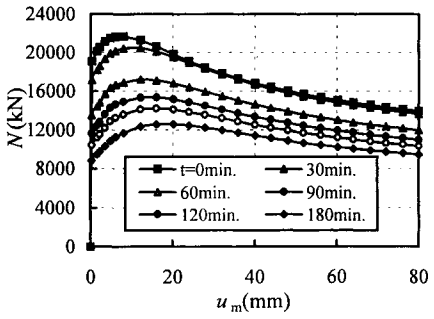

Figure 4:Axial load (N) versus mid-span lateral deflection (u_m) curves

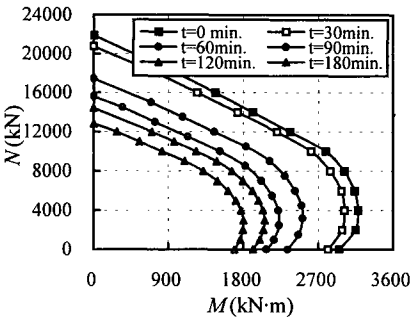

Figure 5: Compressive strength (N) versus bending strength (M) interaction curves

(Tube: □–600×600×14 mm, L=4000mm, f_{sy}=345MPa, f_{ck}=26.8MPa)

Figure 4 and 5 make it clear that the critical load bearing strength decreases considerably after exposure to fire. The consequence is a progressive loss of load bearing capacity of the composite columns by increasing duration of fire exposure (t).

4. PROCEDURE FOR THE DEVELOPMENT OF FORMULAS

4.1 Important Parameters

For convenience of analysis, residual strength index (RSI) is defined to quantify the strength of the concrete-filled HSS columns after exposure to ISO-834 standard fire. It is expressed as:

$$RSI = \frac{N_u(t)}{N_u} \tag{1}$$

where, $N_u(t)$ is the residual strength corresponding to the fire duration time (t) of the composite

www.EngineeringEBooksPdf.com

columns, and N_u is the ultimate strength of the composite columns at ambient temperatures.

The residual strength index (*RSI*) determined by using of Equation (1) can be plotted against the fire duration time (t) under different parameters, such as fire duration time, sectional dimensions, slenderness ratios, steel ratios, load eccentricity ratios, strength of concrete and steel. Figure 6 shows typical examples. The basic parameters in the calculations are: Tube □–600×600mm; α=0.1; λ=40; e/r=0; f_{sy}=345MPa; f_{ck}=26.8MPa.

It can be seen from Figure 6 that the residual strength index (*RSI*) increases when the sectional dimension (D) increases, decreases as the slenderness ratio (λ) increases. *RSI* decreases as fire duration time t increases. However, other parameters, such as steel ratio (α=A_s/A_c, in which, A_s is the cross-section area of steel tube, A_c is the cross-section area of concrete), load eccentricity ratio (e/r), strength of the concrete (f_{ck}=0.67f_{cu}) and the steel (f_{sy}) have moderate influence on the residual strength index (*RSI*).

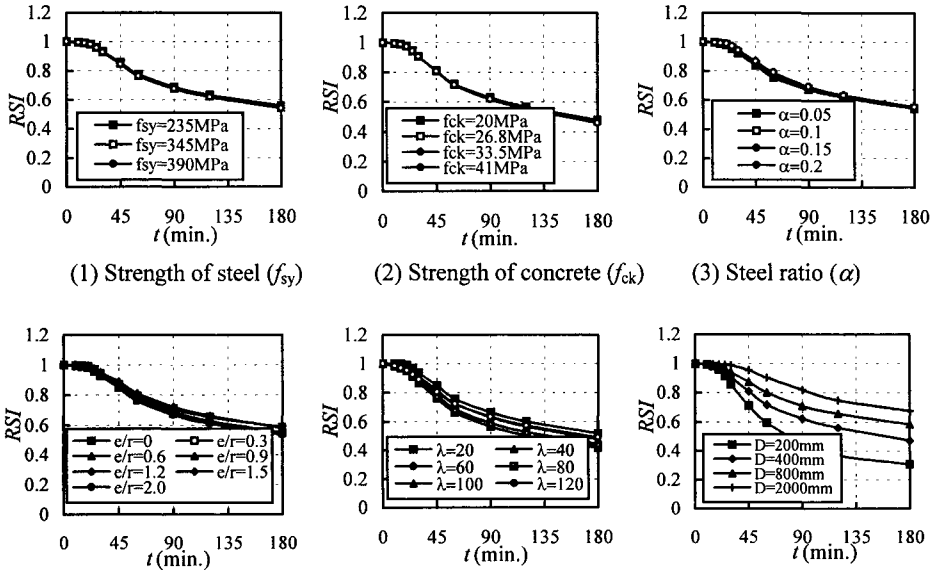

(1) Strength of steel (f_{sy}) (2) Strength of concrete (f_{ck}) (3) Steel ratio (α)

(4) Load eccentricity ratio (e/r) (5) Slenderness ratio (λ) (6) Sectional dimension (D)

Figure 6: *RSI* versus t relations under different parameters

4.2 Residual Strength Index (RSI) Formulas for the Composite Columns

Using the relations between the residual strength index (*RSI*) and the various parameters that determine it, the following formula for the residual strength index (*RSI*) of the composite columns without fire protection, filled with plain concrete can be obtained by using regression analysis method, i.e.
For concrete-filled HSS columns with circular sections:

$$RSI = \begin{cases} (1+0.15t_o-2t_o^2+2t_o^3)\cdot f(C_o)\cdot f(\lambda_o) & t_o \le 0.6 \\ (1-0.39t_o+0.095t_o^2)\cdot f(C_o)\cdot f(\lambda_o) & t_o > 0.6 \end{cases} \quad (2a)$$

For concrete-filled HSS columns with square and rectangular sections:

$$RSI = \begin{cases} (1-0.036t_o-0.59t_o^2)\cdot f(C_o)\cdot f(\lambda_o) & t_o \le 0.6 \\ (1-0.46t_o+0.117t_o^2)\cdot f(C_o)\cdot f(\lambda_o) & t_o > 0.6 \end{cases} \quad (2b)$$

www.EngineeringEBooksPdf.com

where,

$$f(C_o)=\begin{cases} a\cdot C_o^2+b\cdot C_o+c & C_o\le 1 \\ d\cdot(C_o-1)+1 & C_o>1 \end{cases} \quad (3)$$

in which $a=-0.73t_o+0.087; b=1.41t_o-0.14$; $c=-0.68t_o+1.05; d=0.039\ln t_o+0.09$.

The function of $f(\lambda_o)$ in Equation (2a) and (2b) can be expressed as:

$$f(\lambda_o)=\begin{cases} e\cdot\lambda_o+f & \lambda_o\le 1.875 \\ g\cdot\lambda_o+h & \lambda_o>1.875 \end{cases} \quad (4)$$

in which $e=0.05t_o^2-0.17t_o+0.018; f=-0.05t_o^2+0.18t_o+0.98; g=-0.06t_o^2+0.25t_o-0.039;$ $h=0.1t_o^2-0.58t_o+1.09$; $t_o=t/100$; $C_o=D/600$ or $(D+B)/1200$ for columns with circular or rectangular sections respectively.

The units for time (t) and sectional dimension (D and B, where B is the width of the SHS or RHS) are minute and mm respectively.

The validity limits of Equation (2a) and (2b) are: $t\le$180min; D= 200 mm to 2000mm; α=0.04 to 0.2; λ=15 to 80; e/r=0 to 3.0; f_{sy}=200MPa to 500 MPa; f_{ck}=20MPa to 60 MPa.

To verify the validity of the formulas, the residual strength index *RSI* calculated with the formula were compared with those calculated with the mathematical model, which, as shown in Figure 7, predicts the calculated *RSI* by using formula (2a) and (2b) with reasonable accuracy. The residual strength calculated with the formula is compared with the experimental strength determined by the authors of this paper in Figure 8. It can be found that the accuracy with which the formula predicted the experimental strength is reasonable.

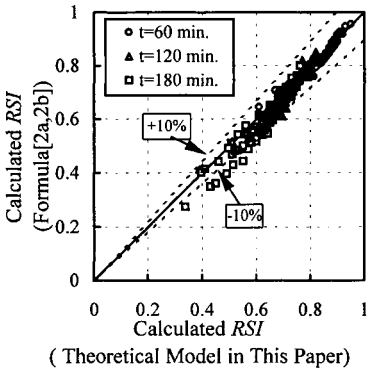

Figure 7: Comparison of calculated *RSI* between theoretical model and formula [2]

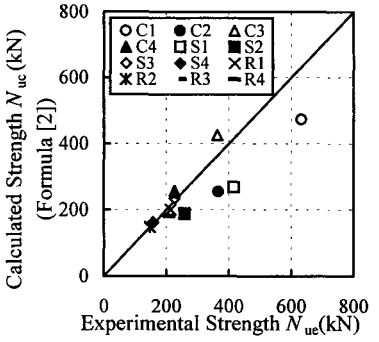

Figure 8: Comparison of calculated residual strength between formula [2] and tests

5. CONCLUSIONS

Based on the analytical results of this study, the following conclusions can be drawn:

(1) Because of the infill of concrete, the tested concrete-filled HSS columns under after exposure to ISO-834 standard fire behaved in a relatively ductile manner and testing proceeded in a smooth and controlled way. The enhanced structural behavior of the columns can be explained in terms of "composite action" between the steel tube and the concrete core.

(2) Fire exposure increases the deflections and decreases the strength of concrete-filled HSS columns. There is no strength reduction due to fire exposure for a fire duration time less than 10 minutes.

(3) The fire duration time, column section size and the slenderness ratio have significant influence on

www.EngineeringEBooksPdf.com

the residual strength ratio (*RSI*) of the column after exposure to ISO-834 Standard fire. However, other parameters, such as steel ratio, load eccentricity ratio, strength of the concrete and the steel have moderate influence on the residual strength index (*RSI*).

(4) Formulas suitable for incorporation into building codes, for the calculation of the residual strength of concrete-filled HSS columns after exposure to ISO-834 Standard Fire are presented. It is evident from the comparisons between the results calculated with the formulas and the mathematical model that the calculated results with reasonable accuracy.

ACKNOWLEDGEMENTS

The research work reported herein were made possible by the Fujian Provincial Natural Science Foundation of China (No.E0120001) and Fujian Province International Cooperation Project (No.2001I020the financial support is highly appreciated. The authors also express special thanks to Mr. Yu-Cheng, Feng, Dr. Jiu-Bin Feng, and Dr. Lei Xu for their assistance in the experiments.

REFERENCES

[1] British Steel Tubes and Pipes (1990). *Design for SHS Fire Resistance to BS5950: Part 8*. London, 1990.
[2] CECS24:20 (1990). *Design Regulation for the Fire Protection of Steel Structures*. Chinese Planning Press, (in Chinese).
[3] Falke, J. (1992). Comparison of Simple Calculation Methods for the Fire Design of Composite Columns and Beams. *Proc. of an Engineering Foundation Confer on Steel-Concrete Composite Structure*, ASCE, New York, 226-241.
[4] Han L. H. (2000). *Concrete Filled Steel Tubular Structures*. Science Press, Peking (in Chinese).
[5] Han L. H. (2001). Fire Performance of Concrete Filled Steel Tubular Beam-Columns. *Journal of Constructional Steel Research-An International Journal*, **57:6**, 697-711.
[6] Han, L. H., Yang, H. and Cheng, S. L. (2001a). Residual Strength of Concrete Filled RHS Stub Columns after Exposure to High Temperatures. *Advances in Structural Engineering-An International Journal*, **5:2**,123-134.
[7] Han, L. H., Zhao, X. L. & Tao, Z. (2001b). Tests and Mechanics Model of Concrete-Filled SHS Stub Columns, Columns and Beam-Columns. *Steel & Composite Structures-An International Journal*, **1:1**, 51-74.
[8] Hass, R. (1991). *On Realistic Testing of the Fire Protection Technology of Steel and Cement Supports*." Translation of BHPR/NL/T/1444, Melbourne, Australia.
[9] ISO-834 (1975). *Fire Resistance Tests-Elements of Building Construction*. International Standard ISO 834.
[10] Huo Jing Si(2001).Behaviors of Concrete-Filled Steel Tubular Beam-Columns after Standard Fire [D]. *Dissertation for the Master Degree,* Harbin Institute of Technology.
[11] Kim, D. K., Choi, S. M. and Chung, K. S. (2000). Structural Characteristics of CFT Columns Subjected Fire Loading and Axial Force. *Proceedings of the 6th ASCCS Conference*, Los Angeles, USA, 271-278.
[12] Klingsch, W. (1985). New Developments in Fire Resistance of Hollow Section Structures. *Symposium on Hollow Structural Sections in Building Construction*, ASCE, Chicago Illinois.
[13] Kodur, V. K. R. (1999). Performance-Based Fire Resistance Design of Concrete-Filled Steel Columns." *Journal of Constructional Steel Research* **51**, 21-26.
[14] Lie, T. T. and Stringer, D. C. (1994). Calculation of the Fire Resistance of Steel Hollow Structural Section Columns Filled with Plain Concrete. *Can. J. Civ. Eng.*, **21**, 382-385.
[15] Okada, T., Yamaguchi, T., Sakumoto, Y. and Keira, K. (1991). Load Heat Tests of Full-Scale Columns of Concrete-Filled Tubular Steel Structure Using Fire-Resistant Steel for Buildings. *Proc. of the Third International Conference on Steel-Concrete Composite Structures (I)*, ASCCS, Fukuoka, 101-106.
[16] O'Meagher, A. J.,Bennetts, I. D.,Hutchinson, G. L. and Stevens, L. K. (1991). *Modelling of HSS columns filled with concrete in Fire*. BHPR /ENG/R/91 /031/ PS69, Melbourne, Australia.
[17] Wang, Y. C. (1999). The Effects of Structural Continuity on the Fire Resistance of Concrete Filled Columns in Non-Sway Frames. *Journal of Constructional Steel Research* **50**, 177-197.

www.EngineeringEBooksPdf.com

Advances in Steel Structures, Vol. II
Chan, Teng and Chung (Eds.)
© 2002 Elsevier Science Ltd. All rights reserved.

AN EXPERIMENTAL STUDY AND CALCULATION ON THE FIRE RESISTANCE OF CONCRETE-FILLED SHS AND RHS COLUMNS

Lin-Hai Han[1] Lei Xu[2] & You-Fu Yang[2]

[1]College of Civil Engineering and Architecture, Fuzhou University, Fuzhou, Fujian, 350002, China
[2]School of Civil Engineering, Harbin Institute of Technology, Haihe Road 202, Harbin, 150090,China

ABSTRACT

The main objectives of this paper are threefold: firstly, to report a series of fire tests on concrete-filled steel SHS (square hollow section) and RHS (rectangular hollow section) columns with square and rectangular sections. Secondly, to analyze the influence of several parameters, such as fire duration time, sectional dimension, slenderness ratio, load eccentricity ratio, strength of steel and concrete on the residual strength index (*RSI*) of the composite columns. Finally, to develop formulas for the calculation of the fire resistance and the fire protection thickness of the concrete-filled steel SHS and RHS columns, such formulas are suitable for incorporation into building codes. The concept of this paper were used to provide data on the necessary fire protection measures for the concrete-filled steel SHS columns used in a high-rise building, Ruifeng, Shangye Building in China.

KEYWORDS

Concrete-filled SHS or RHS, column, standard fire curve, temperature, fire resistance, fire protection

Nomenclature

a	Fire protection thickness, in mm
A_s	Steel cross-sectional area
A_c	Concrete cross-sectional area
B	Width of rectangular steel tube
C	Perimeter of SHS or RHS section
D	Depth of rectangular steel tube
e	Eccentricity of load
e/r	Load eccentricity ratio, $r=D/2$ or $B/2$
f_{sy}	Yield strength of steel
f_{cu}	Concrete cubic strength
f_{ck}	Characteristic concrete strength ($=0.67f_{cu}$)
L	Effective buckling length of column in the plane of bending
R	Fire resistance, in minute
RSI	Residual strength index ($RSI= N_u(t)/ N_u$)
t	Fire duration time, in minute
T_{cr}	Limiting temperature, in °C
α	Steel ratio ($=A_s / A_c$)
β	Depth to width ratio, $\beta=D/B$
λ	Slenderness ratio, given by $2\sqrt{3}L/B$ or $2\sqrt{3}L/D$

www.EngineeringEBooksPdf.com

1. INTRODUCTION

An important criterion for the design of concrete-filled steel square hollow section (SHS) or rectangular hollow section (RHS) columns, besides the serviceability and critical load bearing capacity, is fire resistance. Bare hollow steel tubular columns filled with plain concrete with high load levels often cannot achieve the desired fire resistance time for tall buildings. At present, the most economical solution to the design of a fire resistant concrete-filled SHS or RHS column in China is to design for the maximum structural efficiency and to obtain the required fire resistance by application of a conventional insulating system. This method removes the need to use fiber or bar reinforcement in the concrete core (British Steel Tubes and Pipes, 1990), and has been used in the practical engineering projects in China. In the past, most of the columns designed according to the regulations for steel construction (GB50045-95, 2001) due to a lack of design codes for composite columns in China.

In the past, there are a large number of research studies on the fire resistance of concrete-filled steel tubular columns, such as British Steel and Pipes (1990); Klingsch (1985); Hass (1991); O'Meagher et al (1991); Lie and Stringer (1994); Wang (1999); Kodur (1999); Han (2001), and etc.

The behaviors of concrete-filled steel SHS and RHS columns with or without fire protections subjected to axial or eccentric loads have been experimentally investigated and the results presented in this paper. The differences of this test program compared with the similar studies carried our by other researchers mentioned above are:

(1) Both concrete-filled steel columns with square and rectangular sections were tested, seldom concrete-filled steel RHS columns under fire were reported.
(2) Both concentrically and eccentrically loaded columns were performed, seldom eccentrically loaded concrete-filled steel SHS or RHS columns were performed.
(3) Both columns with fire protection and without fire protection were performed, seldom fire tests on such columns with fire protection were performed.
(4) Load ratio is greater than 0.7 (in the past, the load ratio was generally less than 0.5).

The main objectives of this paper were thus threefold: firstly, to report a series of fire tests on composite columns; Secondly, to analyze influence of several parameters, such as sectional dimension, slenderness ratio and protection thickness on the fire resistance of the composite columns. Finally, to develop formulas for the calculation of the fire resistance and the fire protection thickness of the concrete-filled SHS and RHS columns, such formulas are suitable for incorporation into building codes.

2. EXPERIMENTAL PROGRAM

A total of eleven specimens were tested. For each column, the axial shortening versus fire exposing time, fire resistance, temperatures of the steel and concrete at difference locations in the cross section are recorded

Test parameters were section types, tube depth-to-width ratio, slenderness ratio and load eccentricity ratio. The details of each column are listed in Table 1, where t_s is thickness of the steel tube.

2.1 Specimen Preparation

To determine the steel material properties, tension coupons were cut from a randomly selected steel tube, three coupons were cut. The coupons were tested in tension, from these tests, the average yield strength (f_{sy}) as well as the Young's modulus of elasticity were shown in Table 1.

Two types of concrete were used. The details of the concrete mix are given in Table 2. For each batch of concrete mixed, three 100 mm cubes were also cast and cured in conditions similar to the related specimens. The composite columns were tested at an age of 28 days after concrete casting. The average compression cube strengths (f_{cu}) at that age were 18.7 MPa and 49.0 MPa respectively. The modulus of elasticity (E_c) of concrete was measured, the average values being 26,700 MPa and 30,200 MPa respectively. In all the concrete mixes, the fine aggregate used was silica-based sand, the coarse aggregate was carbonate stone.

www.EngineeringEBooksPdf.com

TABLE 1
SUMMARY OF TEST INFORMATION

Specimen Number	Sectional Dimension $D\times B\times t_s$ (mm)	β	f_{sy} (MPa)	E_s ($\times 10^5$) (MPa)	f_{cu} (MPa)	a (mm)	Test Load N_p (kN)	e/r	R_{test} (min)	T_{cr} (°C)	Fail Mode
R-1	□-300×200×7.96	1.5	341	1.87	47.3	0	2486	0	21	639	C
R-2	□-300×200×7.96	1.5	341	1.87	47.3	0	2233	0.15	24	636	C
R-3	□-300×150×7.96	2.0	341	1.87	47.3	0	1906	0	16	750	B
R-4	□-300×150×7.96	2.0	341	1.87	47.3	0	1853	0.15	20	786	C
RP-1	□-300×200×7.96	1.5	341	1.87	47.3	13	2486	0	104	790	C
RP-2	□-300×200×7.96	2.0	341	1.87	47.3	20	2486	0	146	506	C
RP-3	□-300×150×7.96	2.0	341	1.87	47.3	13	1906	0	78	530	B
RP-4	□-300×150×7.96	2.0	341	1.87	47.3	22.6	1906	0	122	529	B
SP-1	□-219×219×5.30	1.0	246	2.00	18.7	17	950	0	169	668	B
SP-2	□-350×350×7.70	1.0	284	1.83	18.7	11	2700	0	140	504	B
SP-3	□-350×350×7.70	1.0	284	1.83	18.7	7	1670	0.3	109	586	C

Notes- Failure Mode: B = Buckling; C= Compression

The spray material used was specified in "CECS24: 20 Design Regulation for the Fire Protection of Steel Structures" (CECS24:20,1990). The spray material has a thermal conductivity (λ_p) of 0.116 W/m.k, a specific heat (c) of 1.047×10^3 J/kg.k, a density (ρ) of 400 ± 20 kg/m^3 and a water content of 1 percent. Table 1 shows the fire protection thickness (a) of the specimens with fire protection coats.

TABLE 2
MIXTURE OF CONCRETE (kg/m^3)

Concrete Strength f_{cu} (MPa)	Modulus of Elasticity E_c (MPa)	Water	Cement	Sand	Aggregate
18.7	26,700	171	318	636	1275
47.3	30,200	170	425	630	1175

The tubes were all manufactured from mild steel sheet, with four plates cut from the sheet, tack welded into a square or a rectangular shape and then welded with a single bevel butt weld at the corners. The components of the column were dimensioned so that their length was 3810 mm including the plate thickness. Two semi-circular holes with 20 mm in diameter, located at the junctions between the tube and the top plate as well as the bottom plate were drilled in the section wall. They were provided as vent holes for the water vapor pressure produced during the experiment. Three thermocouples were mounted at mid-height of the specimen for measuring temperatures of the steel and concrete at different locations in the cross section.

2.2 Test Apparatus

The tests were carried out by exposing the columns to heat in a furnace specially built for testing loaded columns in Tianjin, China. The test furnace was designed to produce the conditions to which a member might be exposed during a fire, i.e. temperatures, structural loads, and heat transfer. All columns were designed as the same load ratio (ratio of the applied forces N_p in fire conditions to those used in the design of the member at room temperature N_d) for the purpose of parametric analysis. Since fire in building is a rare occurrence and for calculating purposes is usually treated as a form of 'accidental' loading, the values of the load ratios (N_p/N_d) were selected as 0.77 (Han, 2000). The design loads N_d were determined by the use of Chinese code GJB4142-2000 (2001). The equations were listed in detail in Han, Zhao and Tao (2001). The real applied loads N_p were shown in Table 1.

The ambient temperature at the start of the test was about 20 °C. During the test the column was exposed to heating controlled in such a way that the average temperature in the furnace followed as

www.EngineeringEBooksPdf.com

closely as possible the ISO-834 Standard (ISO-834, 1975) curve. Temperature readings were taken at each thermocouple location at intervals of 1 minute. Axial shortening was also measured.

The current failure criterion specified in ISO-834 Standard is adopted in this paper, which is based on the amount of contraction and the rate of contraction (ISO-834,1975).

3. EXPERIMENTAL RESULTS AND SPECIMEN BEHAVIOR

It was observed that the tested specimens all failed by compression or overall buckling (shown as in Table 1). Specimen RP-1 and Specimen RP-2 are selected to demonstrate the typical failure mode of the tested columns, shown as in Figure 1. Typical measured axial shortening (Δ) versus time (t) relations is shown in Figure 2.

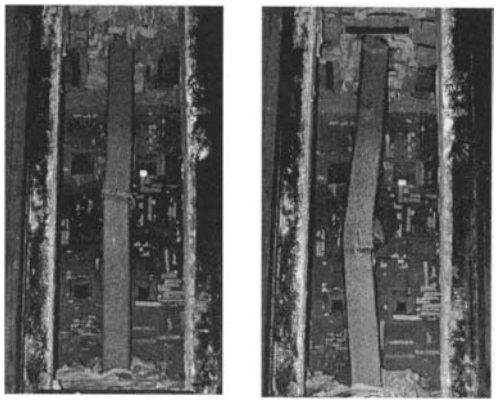

(a) Compression (RP-1) (b) Buckling (RP-2)

Figure 1: Typical failure mode of the specimens

It was found that because of the infill of concrete, the tested specimens behaved in a relatively ductile manner and testing proceeded in a smooth and controlled way. The enhanced structural behavior of the columns can be explained in terms of "composite action" between the steel tube and the concrete core. It is expected that the steel tube starts expand at the early stage of heating, compressive stress in the concrete core will be decreased, then the steel may locally buckle, which transfers additional load onto the core concrete. In the finally limit state, the steel may does nothing but to confine core concrete, until the concrete core fails in a brittle manner. The tendency is clearly indicated by the rapid increase of shrinkage right before collapse as shown in Figure 2

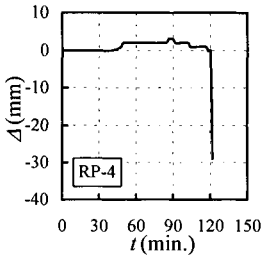

Figure 2: Δ versus t relation

The test results are summarized in Table 1, which indicates that the fire resistance (R) of the members with fire protections were significantly great than those of the columns without fire protections.

The temperature of the critical element at which the member would fail under the given fire and loading conditions is defined as "limiting temperature" T_{cr} (British Steel Tubes and Pipes, 1990). The limiting temperatures (T_{cr}) of the specimens so determined for the current test are listed in Table 1. It can be found that the T_{cr} of the specimens for the current test ranged from 506 °C to 790° C. In the regulation of BS5950: Part 8 (British Steel Tubes and Pipes, 1990), unfilled SHS structures in practice, data on fire protection material can be based on keeping the steel below 550 °C (620 °C for intumescent coatings on beams). At these temperatures virtually any member designed to BS5950 would be adequately protected. It can be found that the limiting temperatures T_{cr} of the majority of the specimens in the current tests are very close to that of the unfilled

TABLE 3
COMPARISON BETWEEN TESTED AND DESIGNED PROTECTION THICKNESS

Specimen Number	Fire Resistance R (min.)	a_{code} (mm)	a_{test} (mm)	$\frac{a_{test}}{a_{code}}$
RP-1	104	25	13	0.52
RP-2	146	40	20	0.50
RP-3	78	21	13	0.62
RP-4	122	30	22.6	0.75
SP-1	169	46	17	0.37
SP-2	140	37	11	0.30
SP-3	109	26	7	0.27

www.EngineeringEBooksPdf.com

SHS structures specified in the regulation of BS5950. Table 3 shows the comparisons between the protection thickness of the current tested specimens (a_{test}) and the designed thickness according to GB50045-95 (2001) (a_{code}). It can be found that the ratio of a_{test} / a_{code} in Table 3 ranges from 0.3 to 0.75. The comparisons clearly show that the design method of fire protection thickness for steel columns in GB50045-95 (2001) is not applicable for concrete-filled SHS or RHS columns. The protection thickness can be reduced about 25% to 70% for concrete-filled SHS or RHS columns.

4. PROCEDURE FOR THE DEVELOPMENT OF FORMULAS

4.1 Comparison between Calculated and Experimental Results

Using the mathematical model described by Han (2001), calculations were made on the fire resistance of the concrete-filled steel columns. The calculated values are compared in Figure 3 with the current experimental results. The comparison shows reasonable agreements between the calculated and tested results.

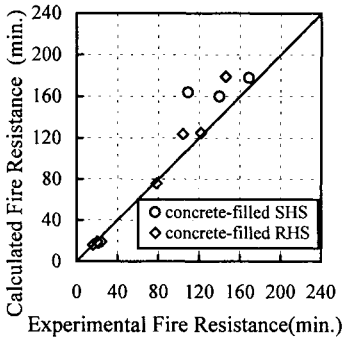

Figure 3: Comparison of fire resistance between theoretical model and tests

4.2 Important Parameters

For convenience of analysis, residual strength index (*RSI*) is defined to quantify the strength of the concrete-filled SHS or RHS columns subjected to ISO-834 standard fire. It is expressed as:

$$RSI = \frac{N_u(t)}{N_u} \qquad (1)$$

where $N_u(t)$ is the ultimate strength corresponding to the fire duration time (t) of the composite columns, and N_u is the ultimate strength of the composite columns at ambient temperatures (Han, Zhao and Tao, 2001).

The residual strength index (*RSI*) so determined are plotted in Figure 4 against the fire duration time (t). It can be seen from this figure that *RSI* increases when the sectional dimensions (C) increases, decreases as the slenderness ratio (λ) increases. *RSI* increases as fire duration time t increases. However, other parameters, such as steel ratio (α), load eccentricity ratio (e/r), strength of the concrete (f_{ck}) and the steel (f_{sy}) have moderate influence on the *RSI*.

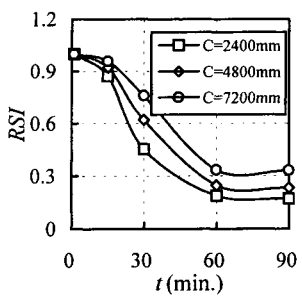

(a) Diameter (C)

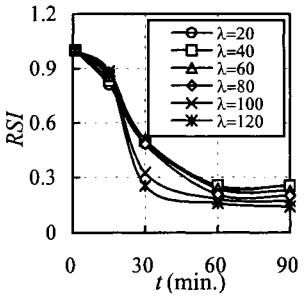

(b) Slenderness ratio (λ)

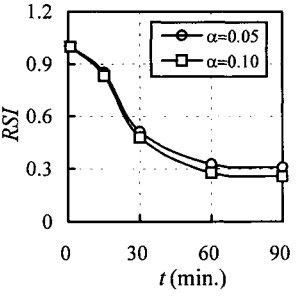

(c) Steel ratio (α)

www.EngineeringEBooksPdf.com

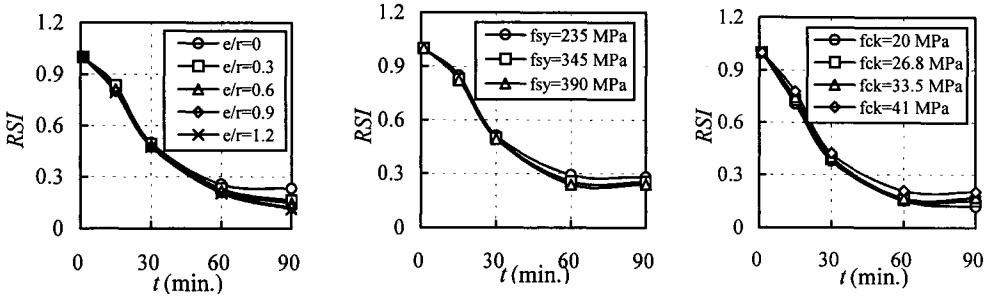

(d) Load eccentricity ratio (e/r) (e) Strength of steel (f_{sy}) (f) Strength of concrete (f_{ck})

Figure 4: Residual strength index (RSI) versus fire duration time (t)

4.3 Fire Resistance Time Formula

Using the relations between the residual strength index (RSI) and the various parameters that determine it, the following formula for the strength index (RSI) for concrete-filled steel SHS and RHS columns without fire protections, can be obtained by using regression analysis method, i.e.

$$RSI=\begin{cases}1/(1+a\cdot t_0^2) & t_0\le t_1\\ 1/(b\cdot t_0^2+c) & t_1<t_0\le t_2\\ k\cdot t_0+d & t_0>t_2\end{cases} \qquad (2)$$

where $a=(0.05\lambda_0^3-0.28\lambda_0^2+0.33\lambda_0+0.93)\cdot(-2.56B_0+16.08)$;

$b=(-0.19\lambda_0^3+1.48\lambda_0^2-0.95\lambda_0+0.86)\cdot(-0.19B_0^2+0.15B_0+9.05)$; $c=1+(a-b)\cdot t_1^2$;

$d=1/(b\cdot t_2^2+c)-k\cdot t_2$; $k=0.0336\lambda_0^2-0.2\lambda_0+0.0744$;

$t_1=0.38\cdot(0.02\lambda_0^3-0.13\lambda_0^2+0.05\lambda_0+0.95)$;

$t_2=(0.03B_0^2-0.13B_0+0.71)\cdot(0.03{\lambda_0}^2-0.29\lambda_0+1.21)$; $t_0=t/100$; $B_0=C/1600$; $\lambda_0=\lambda/40$.

The validity limits of Equation (2) are: $R\le 180$ min; C = 800 mm to 8000 mm; α = 0.04 to 0.2; λ = 15 to 80; f_{sy} = 200 MPa to 500 MPa and f_{ck} = 20 MPa to 60 MPa.

To verify the validity of the formulas, the fire resistance (R) calculated with the formula were compared with those calculated with the mathematical model, it was found that the calculated fire resistance with reasonable accuracy. The fire resistance (R) calculated with the formula were compared with the experimental values in Figure 5. It can be found that the accuracy with which the formula predicted the experimental fire resistance is reasonable, and in general, the predictions are somewhat conservative.

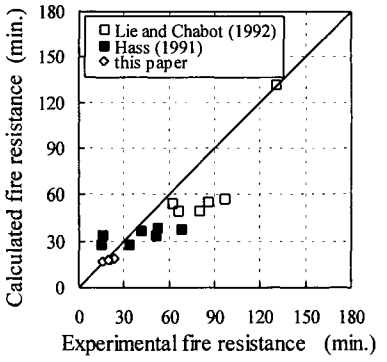

Figure 5: Comparison of calculated and experimental fire resistance

4.4 Fire Protection Thickness Formula for the Composite Columns

Under design loads, concrete-filled steel SHS or RHS columns filled with plain concrete without fire protection often cannot achieve the desired fire resistance. At present, the most economical solution to the design of a fire resistant concrete-filled SHS or RHS columns in China, is to design for the

www.EngineeringEBooksPdf.com

maximum structural efficiency and to obtain the required fire resistance by application of a kind of spray material which is specified in "CECS24: 20 (1990). By the use of the mathematical model (Han, 2001), influence of the changing protection thickness (a), sectional dimensions, steel ratio, slenderness ratio, load eccentricity ratio, strength of the concrete and the steel on the fire resistance (R) were analyzed (Han, 2001). It had been found that the protection thickness, the dimensions and the slenderness ratios have significantly influence on the fire resistance of the columns. Other parameters have moderate influence on the fire resistance of the columns when the columns have the same load ratios (Han, 2001).

Using the relations between the protection thickness (a) and the various parameters that determine it, the following formula for the protection thickness of the composite columns with any desired fire resistance (R) can be obtained by using regression analysis method, i.e.

$$a=(2.5R+22)\cdot C^{-(0.42+0.0017\lambda-2\times10^{-5}\lambda^2)} \quad (3)$$

where R is in min; the perimeter of the column section C is in mm.

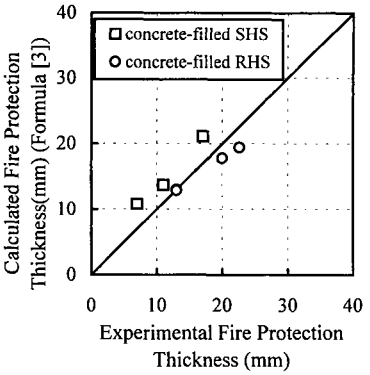

Figure 6: Comparison of calculated fire protection between formula [3] and tests

Equation (3) has the same validity with Equation (2). To verify the validity of the formulas, the fire protection thickness (a) calculated with the formula was compared with those calculated with the mathematical model, it was found that the calculated fire protection thickness with reasonable accuracy, and in general, the predictions are somewhat conservative. The fire protection thickness calculated (a) with the formula were compared with the present experimental fire protection thickness in Figure 6. It can be found that the accuracy with which the formula predicted the experimental fire protection thickness is reasonable.

5. PRACTICAL ENGINEERING

The concept described above was used to calculate the fire resistance of concrete-filled steel SHS columns used in actual buildings. One example is the Ruifeng, Shangye Building (Figure 7), which is a 24-storey Grade A office block with a four-level basement. The main structure is 89.7 m in height. The total construction area is 51,095 m^2 .The tower is designed as a composite structure with reinforced concrete core and external concrete-filled steel SHS columns. The most interesting part of the construction is the column construction, with only a small number of buildings known to be constructed using similar methods anywhere in the world.

Figure 7: A general view of Ruifeng, Shangye Building during construction

The columns were required to have a minimum fire resistance rating of 180 min under full design loads according to Chinese code (GB50045-95, 2001). A kind of spray material similar to the fire protection used in the current tests was adopted. The protection thickness is 50 mm according to the conventional approaches to fire protection of steel columns (GB50045-95, 2001). The average value of the column fire protection thickness of Ruifeng, Shangye Building is 20mm. It can be found that this protection thickness is significantly smaller than 50 mm. Figure 8 shows elevation of the columns during protection material spraying.

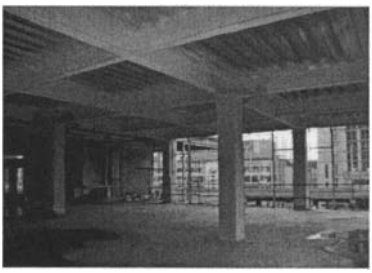

Figure 8 Elevation of the columns during fire protection material spraying

www.EngineeringEBooksPdf.com

6. CONCLUSIONS

Based on the analytical results of this study, the following conclusions can be drawn:

(1) The fire resistance of the concrete-filled steel SHS and RHS columns, with high load ratios, can be enhanced through the use of fire-protection coat.

(2) The fire protection thickness for concrete-filled steel SHS and RHS columns can be reduced about 25 to 70% of that for bare steel columns specified in GB50045-95 (2001).

(3) Formulas suitable for incorporation into building codes, for the calculation of fire resistance and fire protection of concrete-filled steel SHS and RHS columns are presented.

(4) The concept in this paper were used to provide data on the necessary fire protection measures for the concrete-filled steel SHS columns used in a high-rise building, Ruifeng, Shangye Building in Hangzhou City, South of China.

ACKNOWLEDGEMENTS

The research work reported herein were made possible by the financial support from Fujian Provincial Natural Science Foundation of China (FPNSFC, No.E0120001) and and Fujian Province International Cooperation Project (No.2001I020), the financial support is highly appreciated. The authors also express thanks to Professor Jian-Sheng Jin, Professor Yu-Cheng, Feng, and Mr. Hai-Xiu Zhang for their assistance in the experiments. The authors also express special thanks to Hangzhou Hangxiao Steel Construction CO., LTD, for providing information, photographs and other details on the concrete-filled steel SHS columns used in the Ruifeng, Shangye Building.

REFERENCES

[1] British Steel Tubes and Pipes (1990).*Design for SHS Fire Resistance to BS5950: Part 8*. London, 1990.
[2] CECS24:20 (1990). *Design Regulation for the Fire Protection of Steel Structures*. Chinese Planning Press (in Chinese).
[3] GB50045-95 (2001). *Code for Fire Protection Design of Tall Buildings*. Chinese Planning Press (in Chinese).
[4] GJB4142-2000 (2001). *Technical Specifications for Early-Strength Model Composite Structures, Part 8*. Peking, China (in Chinese).
[5] Han L. H. (2000).*Concrete Filled Steel Tubular Structures*. Science Press, Peking (in Chinese).
[6] Han L. H. (2001). Fire Performance of Concrete Filled Steel Tubular Beam-Columns. *Journal of Constructional Steel Research-An International Journal* **57:6**, 697-711.
[7] Han, L. H., Zhao, X. L. & Tao, Z. (2001).Tests and Mechanics Model of Concrete-filled RHS Stub Columns, Columns and Beam-Columns. *Steel & Composite Structures-An International Journal*, **1:1**, pp.51-74.
[8] Hass, R. (1986). On Realistic Testing of the Fire Protection Technology of Steel and Cement Supports. *Translation of BHPR*/NL/T/1444, Melbourne, Australia.
[9] ISO-834 (1975). *Fire Resistance Tests-Elements of Building Construction*. International Standard ISO 834.
[10] Klingsch, W.(1985). New Developments in Fire Resistance of Hollow Section Structures. *Symposium on Hollow Structural Sections in Building Construction*, ASCE, Chicago Illinois.
[11] Kodur, V. K. R. (1999). Performance-Based Fire Resistance Design of Concrete-Filled Steel Columns. *Journal of Constructional Steel Research* **51:1,** 21-26.
[12] Lie, T. T. and Stringer, D. C. (1994). Calculation of the Fire Resistance of Steel Hollow Structural Section Columns Filled with Plain Concrete. *Can. J. Civ. Eng.* **21:3,** 382-385.
[13] O'Meagher, A. J., Bennetts, I. D.,Hutchinson, G. L. and Stevens, L. K. (1991). *Modelling of HSS columns filled with concrete in Fire. BHPR* /ENG/R/91 /031/ PS69.
[14] Wang, Y. C. (1999). The Effects of Structural Continuity on the Fire Resistance of Concrete Filled Columns in Non-Sway Frames. *Journal of Constructional Steel Research* **50:3,** 177-197.

www.EngineeringEBooksPdf.com

ANALYSIS AND DESIGN

www.EngineeringEBooksPdf.com

This Page Intentionally Left Blank

www.EngineeringEBooksPdf.com

Advances in Steel Structures, Vol. II
Chan, Teng and Chung (Eds.)
© 2002 Elsevier Science Ltd. All rights reserved.

A UNIFIED ANALYSIS METHOD TO PREDICT LONG-TERM MECHANICAL PERFORMANCE OF STEEL STRUCTURES CONSIDERING CORROSION, REPAIR AND EARTHQUAKE

Yoshiaki Goto[1] and Naoki Kawanishi[2]

[1] Department of Civil Engineering, Nagoya Institute of Technology, Gokiso-cho, Showa-ku, Nagoya 466-8555, Japan
[2] Department of Civil Engineering, Toyota National College of Technology, Eisei-cho,Toyota 471-8525, Japan

ABSTRACT

A unified structural analysis method is developed in order to take into account the effects of the histories of corrosion loss of material and repair on their long-term mechanical performance of steel structures in addition to the histories of the damages caused by excessive external loads, e.g. big seismic loads. This analysis method is characterized by the point that the volume change in material due to corrosion or repair is adopted as a new controlling parameter along with the conventional parameters such as load and displacement. With this new parameter, the residual stress and residual deformations of structures that are determined by the histories of corrosion loss of material, past repair and seismic damage can be accurately predicted at an arbitrary point of their lifetime. As a result, the long-term mechanical performance of steel structures can be accurately assessed.

KEYWORDS

Corrosion, Repair, Ultimate behavior, Dynamic analysis, Earthquake, Steel bridge, Life cycle

INTRODUCTION

In addition to the histories of the damages caused by excessive external loads, e.g. big seismic loads, the histories of corrosion loss of material and repair have a big influence on the long-term mechanical performance of steel structures. This long-term mechanical performance is schematically shown for a bridge in Fig.1 in terms of its strength. In the conventional analysis to estimate the strengths of the existing steel bridges, the corroded or repaired structural members are simply represented by elements with geometrically reduced or increased volume of material. However, in this conventional analysis, the residual stress distribution and residual deformation of the bridges that are determined by the histories of corrosion loss of material, past repair and seismic damage are usually ignored. The repair work for the corroded or damaged bridges is commonly conducted under dead load. As the result of

www.EngineeringEBooksPdf.com

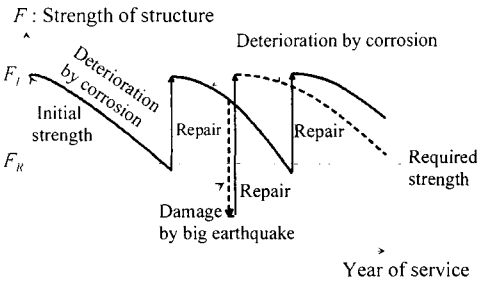

FIG. 1. Deterioration curve for a steel bridge

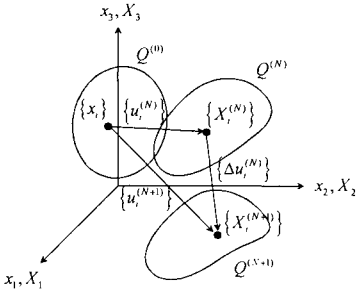

FIG. 2. Definition of coordinates

this repair work, the residual stress and residual deformations existent in the bridges are different from those in the virgin bridge. Therefore, in order to assess the long-term mechanical performance of bridges accurately, the residual stress distribution and deformations have to be identified by considering the histories of corrosion, seismic damage and repair. Herein, we develop a unified structural analysis method that can take into account the effects of the histories of corrosion and repair in addition to the seismic damages on the long-term mechanical performance of steel structures. This new analysis method is characterized by the point that the volume change of structural members due to corrosion or repair is adopted as a new controlling parameter in addition to the conventional controlling parameters such as load and displacement. With the introduction of the new controlling parameter, the change of residual stress and residual deformation caused by corrosion or repair can be accurately evaluated at an arbitrary point of their lifetime.

ANALYSIS OF STEEL STRUCTURES CONSIDERING VOLUME CHANGE OF MEMBERS DUE TO CORROSION AND REPAIR

We here present a new structural analysis method where the volume change of structural members due to corrosion or repair is adopted as a new controlling parameter in addition to the conventional controlling parameters such as load and displacement. The introduction of this new parameter enables us to carry out a unified analysis considering corrosion and repair in addition to earthquake.

We shall employ the updated Lagrangian approach where the updated coordinates $(X_1^{(N)}, X_2^{(N)}, X_3^{(N)})$ at the state $Q^{(N)}$ are defined as follows to locate a material point of a body under the incremental deformation from the state $Q^{(N)}$ to the state $Q^{(N+1)}$ (Fig.2).

$$X_i^{(N)} = x_i + u_i^{(N)} \tag{1}$$

where (x_1, x_2, x_3) are the rectangular Cartesian coordinates of a material point defined at the initial configuration of the body and $u_i^{(N)}$ is the i-th component of the translational displacement of the material point at the state $Q^{(N)}$. It is assumed that the state of the body changes from the state $Q^{(N)}$ to the state $Q^{(N+1)}$ as a result of the changes in material volume, body forces, external forces and displacements from $V^{(N)}$, $\overline{b}_i^{(N)}$, $\overline{t}_i^{(N)}$, $u_i^{(N)}$ to $V^{(N)} + \Delta V^{(N)}$, $\overline{b}_i^{(N)} + \Delta b_i^{(N)}$, $\overline{t}_i^{(N)} + \Delta t_i^{(N)}$, $u_i^{(N)} + \Delta u_i^{(N)}$. The volume change of material inevitably causes the change in the body surface from $S^{(N)}$ to $S^{(N)} + \Delta S^{(N)}$. Then, the principle of virtual work for the state $Q^{(N+1)}$ is expressed as

$$\int_{V^{(N)}+\Delta V^{(N)}} \rho^{(N)} \frac{\partial^2 (u_i^{(N)} + \Delta u_i^{(N)})}{\partial t^2} \delta \Delta u_i^{(N)} dV + \int_{V^{(N)}+\Delta V^{(N)}} \left(\sigma_{ji}^{(N)} + \Delta \Pi_{ji}^{(N)} \right) \frac{\partial \delta \Delta u_i^{(N)}}{\partial X_j^{(N)}} dV$$

$$= \int_{S_\sigma^{(N)}+\Delta S_\sigma^{(N)}} (\overline{t}_i^{(N)} + \Delta \overline{t}_i^{(N)}) \delta \Delta u_i^{(N)} dS + \int_{V^{(N)}+\Delta V^{(N)}} (\overline{b}_i^{(N)} + \Delta \overline{b}_i^{(N)}) \delta \Delta u_i^{(N)} dV \tag{2}$$

www.EngineeringEBooksPdf.com

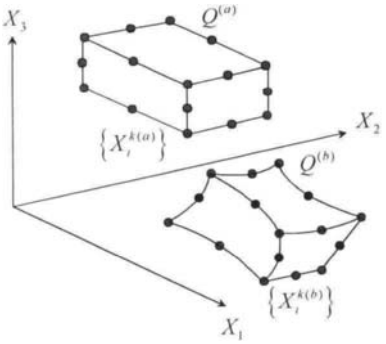

FIG. 3. Nodal coordinates of a brick element at $Q^{(a)}$ and $Q^{(b)}$ states

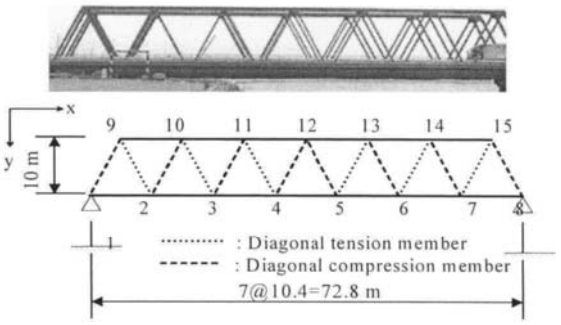

FIG. 4. Warren truss bridge for numerical analysis

where $\sigma_{ji}^{(N)}$ is the Cauchy stress and $\Delta\Pi_{ji}^{(N)}$ is the nominal stress increment defined in terms of the coordinates $(X_1^{(N)}, X_2^{(N)}, X_3^{(N)})$. $\rho^{(N)}$ is the density of the body at the state $Q^{(N)}$. Subscript σ of $S_\sigma^{(N)}$ denotes the surface of the body where boundary conditions are prescribed by external forces.

Based on the principle of virtual work given by Eq.(2), we derived a quadratic isoparametric brick element with 20 nodes shown in Fig. 3 and a Bernoulli-Euler beam element with 2 nodes. The brick element is evaluated by $3 \times 3 \times 3$ Gaussian integration points, while the beam element has 2 integration points in the longitudinal direction and 21 integration points on the cross section. These elements are implemented in ABAQUS(*ABAQUS Users manual* 1999) as user elements.

NUMERICAL EXAMPLE

Existing Corroded and Repaired Warren Truss Bridge

A Warren truss bridge constructed in 1950s that is illustrated in Fig. 4 is chosen as a bridge model for the present analysis. The member details including yield stress are summarized in Table 1. These members are rigidly connected at truss joints. The diagonal tension members with H section are so arranged in the bridge that their flange planes are parallel to the x-y plane. Corrosion loss of material is observed at the location of the diagonal members embedded in the concrete floor slab as shown in Fig.5. The corrosion of the diagonal tension members with H section is more serious, compared with the compression members with box section. Therefore, the corroded parts of the diagonal tension members were repaired with splice plates bolted to their web in order to increase cross sectional areas.

Bridge Model for Numerical Analysis

Here, we examine the ultimate behavior of the repaired Warren truss bridge in comparison with the corresponding virgin bridge. Corrosion pattern considered in the present analysis is shown in Fig. 6 where the lower parts of the diagonal tension members embedded in the concrete floor slab are assumed to be corroded uniformly along the length. This corrosion pattern is determined by simplifying the pattern observed in the real structure. The constitutive relation of member material is assumed to be expressed by the kinematic hardening plasticity model with a constant plastic modulus that is 1% of its elastic modulus ($E = 2.06 \times 10^5 (Mpa)$). The dead load assumed to distribute along the length of the bridge with the magnitude of 0.0358MN/m is concentrated on the joints of lower chord

www.EngineeringEBooksPdf.com

members. For each member of the bridge, an initial deflection expressed in the form of a half sine wave is introduced such that its amplitude of the crookedness in the middle of the member is 0.1% of the member length. Residual stress existent in the virgin bridge is ignored. Each truss member is discretized into 30 beam elements in view of the convergence of solutions.

Corrosion Process

First, the corrosion progress under dead load is analyzed. To express the magnitude of the corrosion loss of the member cross-sectional area, we introduce the corrosion loss ratio β defined as $\beta = \Delta A / A_0$ where ΔA and A_0 are the lost cross-sectional area and the virgin cross sectional area, respectively, of the member. In the present analysis, the corrosion loss ratio of the corroded parts of the diagonal tension members are monotonically increased from $\beta = 0$ to $\beta = \beta_f$ with keeping the dead load constant. Final corrosion loss ratio β_f considered herein is 0.9. Due to this corrosion, plastification occurs in the corroded range of all the diagonal tension members.

Repair Process

At the corrosion loss ratio of $\beta = \beta_f$, the corroded parts of the diagonal tension members are repaired. It will be ideal for the corroded members to be fully restored to their original geometrical shapes. This repair method is herein referred to as "full repair method". However, for the ease of the repair work, it often happens in general practice that only the cross-sectional area of the web in the corroded members with H section is simply increased by splice plates such that the increased area coincides with the total area that is lost in the H section due to corrosion(Fig.5). This repair method herein referred to as "partial repair method" is based on an understanding that the restoration of the tensile rigidity and strength of the corroded members will be enough in case of the diagonal tension members where buckling will not occur. The cross sections of corroded diagonal tension members repaired by the above two methods are illustrated in Fig.7. Here, we examine the validity of the two repair method .

The repair work for corroded members is usually conducted under dead load without jacking up bridges, unless the deflections of the bridges caused by the corrosion are significant. As the result of this repair work, the deflections caused by the corrosion loss of material, however, remain in the repaired bridges. Furthermore, the large stress acts on the uncorroded parts in the corroded members, while no stress acts on the newly restored parts of the members until live load or seismic load is applied. This repair method is herein referred to as "repair method without jacking-up process". To remove the deflection due to corrosion, the bridges have to be jacked up before repairing the corroded member. The jacking-up methods considered herein are two. Method I is to jack up all the nodes 2~7 of the lower chord members to remove the concentrated dead loads acting on these nodes. Method II is to jack up the two nodes 4 and 5 located near the center of the span such that the vertical deflections of these two nodes become zero under dead load.

Ultimate behavior of repaired bridge

In the previous section, several possible repair methods are explained. Herein, we examine the effect of these repair methods on the ultimate behavior of the repaired truss bridge in comparison with the corresponding virgin bridge. For the repaired bridges, we examine their ultimate behavior under two loading types, that is, a statically applied live load and a dynamically applied seismic load.

In the analysis under the statically applied live load, the live load pattern shown in Fig. 8 is used such that the member 4-11 becomes critical under this load pattern. The ultimate behavior of the repaired

www.EngineeringEBooksPdf.com

TABLE 1. Member details of Warren truss bridge

Member	Seciton	Web	U. flange	L. flange	σ y
1 - 9	BOX	400×15	450×14	360×13	317
2 - 9	H	326×9	360×12	360×12	317
2 - 10	BOX	360×13	332×13	332×13	235
3 - 10	H	300×13	360×12	360×12	235
3 - 11	BOX	340×12	300×9	300×9	235
4 - 11	H	330×9	250×11	250×11	235
4 - 12	BOX	230×9	340×9	340×9	235
1 - 2	BOX	360×9	360×11	450×9	235
2 - 3	BOX	360×9	360×11	450×9	317
3 - 4	BOX	360×12	360×14	450×11	317
4 - 5	BOX	360×14	360×14	450×11	317
9 - 10	BOX	400×12	450×13	360×12	235
10 - 11	BOX	400×16	450×18	360×17	317
11 - 12	BOX	400×19	450×22	360×22	317
		(mm)	(mm)	(mm)	(MPa)

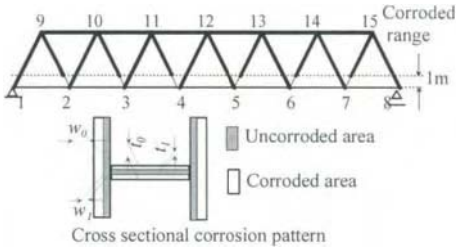

FIG 6. Corrosion patterns of Warren truss bridge

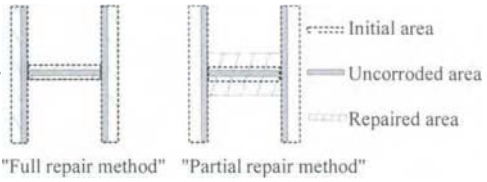

FIG.7. Repair methods for diagonal tension members

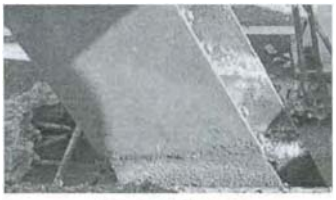

Corroded flanges

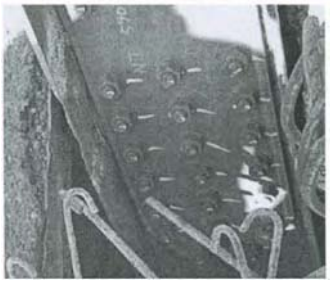

Corroded web repaired with splice plates

FIG.5. Corroded and repaired diagonal tension members

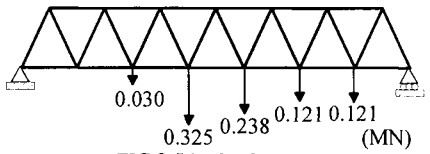

FIG.8 Live load pattern

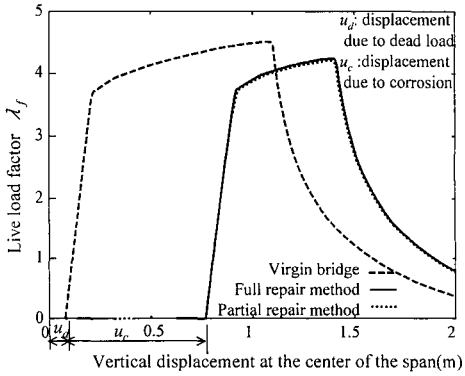

FIG.9. Ultimate behavior of bridges with differently repaired diagonal tension members

bridge is analyzed by the arch-length control method with keeping the dead load constant.

In the dynamic analysis under the seismic load, we determine the input horizontal acceleration wave by magnifying twice the N-S component of the waves recorded by Japan Metrological Agency (JMA) during the 1995 Kobe earthquake. The nonlinear dynamic response analysis is carried out with keeping the dead load constant. The density of steel considered for members is 7850kg/m^3. The masses of the floor slab assumed to distribute along the length with the magnitude of 2410kg/m are lumped on the connections of the lower chord members. The Newmark's β method (β=0.25) is used for the numerical integration with respect to time. The maximum time interval adopted in the numerical integration is 0.01. This value is decreased in case of poor convergence.

www.EngineeringEBooksPdf.com

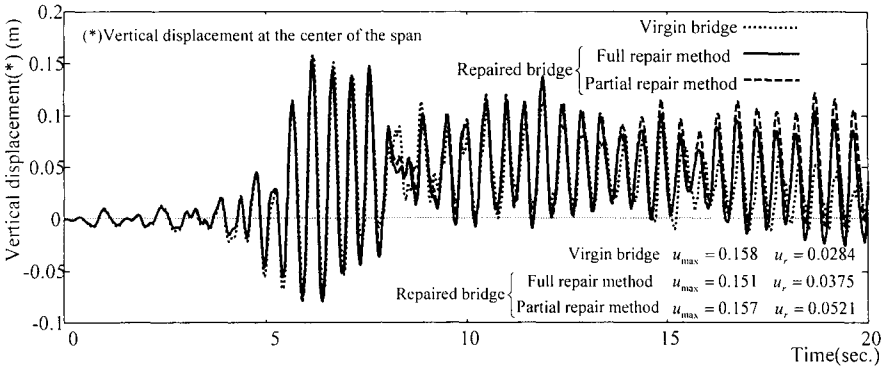

FIG.10. Vertical displacement response histories for bridges with differently repaired diagonal tension members

Effect of repair methods for corroded diagonal tension members

The corroded diagonal tension members of the truss bridge are here assumed to be repaired under dead load without using jacking-up process. This implies that the displacements caused by corrosion are not removed during the repair process. Two methods shown in Fig.7 are considered for repairing the diagonal tension members. One is the "full repair method". The initial stress distribution and deformation of the corroded bridge so repaired are, however, different from those of the virgin bridge, because the members are repaired under dead load. The other is the " partial repair method". The ultimate behaviors of the repaired bridges and the corresponding virgin bridge under the statically applied live load are shown in Fig.9, expressed in terms of the relation between the live load factor λ_l and the vertical displacement at the center of the bridge span. Live load factor λ_l is defined here as the ratio between the applied live load and the live load pattern shown in Fig.8. It is observed from Fig.9 that the ultimate behaviors of the repaired truss bridges are virtually the same, regardless of the repair methods. However, the maximum loads of the repaired bridges become a little smaller than that of the virgin bridge. This is caused by the initial deflection of the repaired bridges caused by the corrosion.

As the results of the dynamic analysis under seismic loads, the vertical displacement response histories obtained for the repaired bridges are shown in Fig.10 in comparison with that for the virgin bridge. As seen from Fig.10, the dynamic behaviors of the repaired bridges are somewhat different from that of the virgin bridge. Although the maximum response deflections u_{max} of the repaired bridges are almost the same as that of the virgin bridge, the repaired bridges tend to exhibit larger residual deflections u_r. Specifically, the bridge repaired by the "partial repair method" exhibits the largest residual displacement. This residual displacement is caused by the bending deformation occurred in the repaired part of the diagonal tension members. This shows the inadequacy of the conventional repair philosophy that the restoration of the tensile rigidity and tensile strength will be enough for the corroded diagonal tension members where bending deformation is not significant under static loads.

Effect of jacking-up methods during repair work

To remove the deflections due to corrosion, the bridge has to be jacked up before repairing the corroded members. The jacking up methods considered herein are two, that is, Method I and Method

www.EngineeringEBooksPdf.com

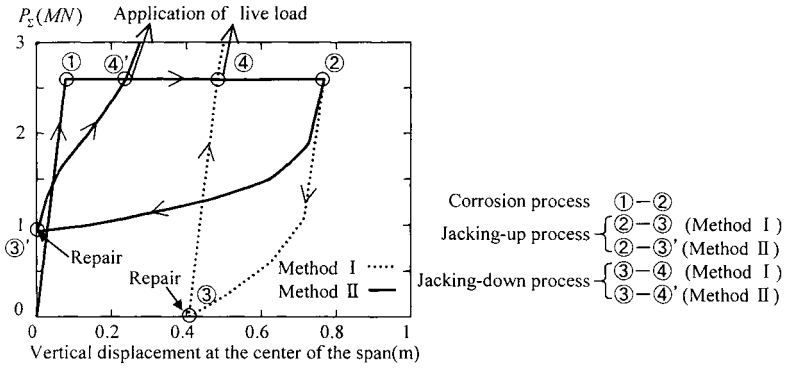

FIG.11. Equilibrium curves during jacking-up and jacking-down processes

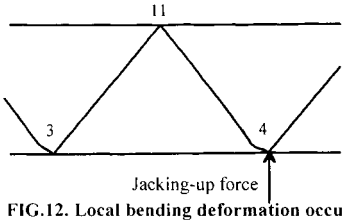

FIG.12. Local bending deformation occurred in Method II after jacking-up process

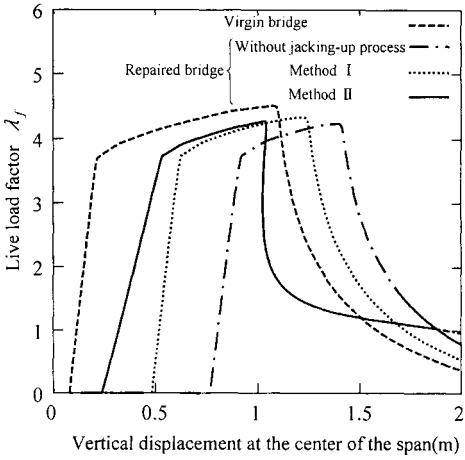

FIG.13. Ultimate behavior of repaired bridges with different jacking-up methods

II. For the above two jacking-up methods, we show in Fig.11 the relation between the displacement of the span center and the sum of the vertical loads acting on the corroded bridge during the jacking-up process. As can be seen from Fig.11, although the vertical loads are completely removed by Method I, the vertical displacement caused by corrosion cannot be removed due to the plastification of members during corrosion process. In Method II where two nodes near the center span are jacked up to remove the displacements of these nodes, the local bending deformation occurs at the lower part of the diagonal tension members 3-10 and 4-11, as illustrated in Fig.12. After the bridge is jacked up, all the corroded members are assumed to be geometrically restored to their original shapes by the "full repair method".

The ultimate behaviors of the repaired bridges and the corresponding virgin bridge under the statically applied live load are shown in Fig.13. In this figure, the behavior of the bridge repaired under dead without jacking-up process is also shown for comparison. It can be seen from Fig.13 that the maximum load of the bridge repaired by Method I is a little higher than that of the bridge repaired without jacking–up process but a little lower than the virgin bridge. In spite of the jacking-up process, the maximum load of the bridge repaired by Method II does not increase, compared with that of the bridge repaired under dead load without jacking-up process.

www.EngineeringEBooksPdf.com

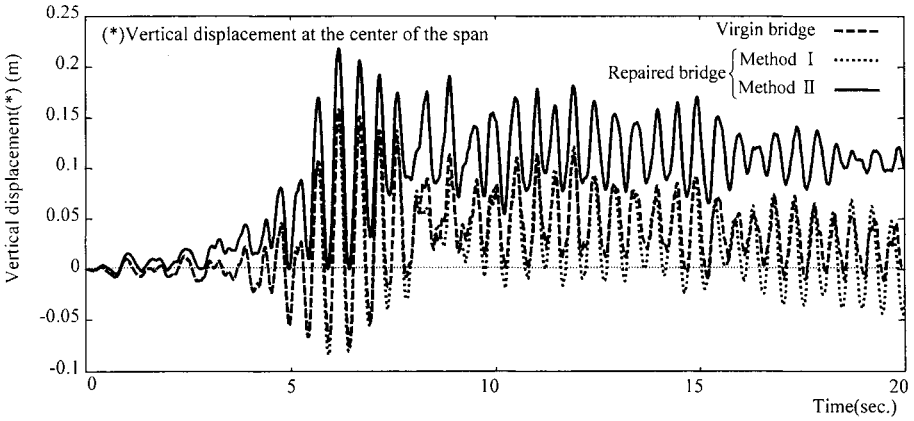

FIG.14 Vertical displacement response histories for repaired bridges with different jacking-up methods

The dynamic responses of the bridges repaired by Methods I and II are shown in Fig. 14, in comparison with that of the virgin bridge. From this figure and Fig.10, it can be seen that the dynamic behavior of the bridge repaired by Method I is almost comparable to that of the virgin bridge or to the bridge repaired without jacking-up process. However, the bridge repaired by Method II exhibits a considerably large maximum response displacement and residual displacement. This is caused by the buckling behavior of the diagonal tension members with the initial localized bending deformations that occurred during the jacking-up process. The jacking-up Method II to remove the initial deflections has a bad effect on the dynamic behavior of the repaired bridge. It can be concluded from the present dynamic analysis that the repair method without jacking-up process is most adequate both from the mechanical and economical reasons, as long as the deflections caused by the corrosion process are allowable in terms of the serviceability of the bridge.

SUMMARY AND CONCLUDING REMARKS

A unified structural analysis method is presented in order to take into account the histories of corrosion loss of material and repair on their long-term mechanical performance of steel structures in addition to the histories of the damages caused by excessive external loads, e.g. big seismic loads. This analysis method is characterized by the point that the volume change of material due to corrosion or repair is adopted as a new controlling parameter in addition to the conventional parameters such as load and displacement. With the introduction of this new parameter, the histories of corrosion and repair process are precisely simulated. By a numerical example, it is examined how the ultimate behavior of a corroded Warren truss bridge is influenced by its repair methods. Under static loads, the ultimate behavior of repaired bridges are almost comparable to the corresponding virgin bridge, regardless of the difference of the repair methods. In contrast, under dynamic loads, the jacking-up process to remove the deflections of the bridge caused by the corrosion results in local deformations that have an unfavorable effect on the ultimate behavior of the repaired bridge.

REFERENCES

ABAQUS Users Manual 5.8 (1999). HKS, Inc.

www.EngineeringEBooksPdf.com

Advances in Steel Structures, Vol. II
Chan, Teng and Chung (Eds.)
© 2002 Elsevier Science Ltd. All rights reserved.

A HIGHER ORDER FORMULATION FOR GEOMETRICALLY NONLINEAR SPACE BEAM ELEMENT

Jian-Xin GU[1], Siu-Lai CHAN[1] and Zhi-Hua ZHOU[2]

[1] Department of Civil and Structural Engineering, The Hong Kong Polytechnic University, Kowloon, Hong Kong, China
[2] College of Civil Engineering, Southeast University, Nanjing, 210018, China

ABSTRACT

This paper describes a consistent incremental tangent stiffness matrix for geometrically nonlinear analysis of space beam element. In this refined finite element formulation, two deformation matrices due to axial force and moment, which represent the higher order effects of the deformations in element, are derived. These matrices are the functions of element deformations and incorporated with the coupling among axial, lateral and torsional deformations. These proposed matrices are used together with linear and geometric stiffness for beam elements to analyze deflection behavior of space frames comprising members with negligible sectorial warping. Numerical examples show that the proposed element is accurate and efficient in predicting the nonlinear behavior, such as axial-torsional and lateral-torsional buckling of space frame even when less elements are used to model a member.

KEYWORDS

Beam element, Space frames, Geometrically nonlinear analysis, Tangent stiffness matrix, Flexural-torsional analysis, Large displacement analysis

INTRODUCTION

Geometric nonlinearity is important for investigating the ultimate strength of beams that fail by axial-torsional and flexural-torsional buckling. The conventional beam-column approach cannot predict the lateral–torsional buckling because some coupling terms among axial, flexural and torsional displacements are lost in tangent stiffness matrix. Thus, the development of new and efficient formulations for nonlinear analysis of space beam structures has attracted the study of many researchers. In the context of space frames, the study of geometric non-linearity effects has always been complicated because of the fact that

www.EngineeringEBooksPdf.com

rotations in three-dimensional space cannot be treated as vectors, i.e., the commutative property is not satisfied. Argyris, et al (1978) introduced the semitangential moment and semitangential rotation and derived the geometric stiffness matrix of the space beam element using natural mode technique. Conci and Gattas (1990) investigated geometric nonlinear problems of thin-walled space frames using a natural approach. Kuo, et al.(1993) presented a nonlinear analysis of space frame considering finite rotations. Teh and Clarke (1997,1999) pointed out the awkwardness of a quasitangential and semitangential moment from the true behavior of internal moment and non-symmetry of the element tangent matrix, and they introduced a fourth kind of conservative moment and vectorial rotation. Kim, et al (2001a,b) addressed the similarity and difference between Rodriguez' rotation and semitangential rotations and argued for adopting the semitangential definition for the nodal rotational degree of freedoms and internal moments.

Bathe and Bolourchi (1979) developed a large deflection finite element formulation and pointed out that the updated Lagrangian formulation is computationally more effective. Yang and McGuire (1986), Chan and Kitiporchai (1987), Kim, et al (2001b) developed stiffness matrix for the analysis of thin walled beams in the updated Lagrangian formulation. Pi and Trahair (1994) used position vector analysis to model the geometric nonlinearities for large deflection and rotations and presented a treatment of the total Lagrangian formulation for nonlinear analysis of thin-walled beam-columns. Oran (1973) presented a co-rotational formulation for angular displacements. Later Crisfield (1990), Izzuddin (1993), Teh and Clarke (1998), Hsiao and Lin (2000) extended this concept to buckling and postbuckling analysis of three-dimensional beams. Chan (1992) pointed out that the updated Lagrangian approach is a very efficient and reliable procedure as far as the iterative convergence rate and its ability to prevent divergence are concerned, and the co-rotational approach requires less elements per member to obtain an accurate solution.

In most researches, cubic Hermite element is extended to the nonlinear analysis of space beams. Incremental secant stiffness matrix including the geometric stiffness with the linear stiffness matrix is often linearised into the tangent stiffness matrix. Meek and Tan (1984) allowed for higher order terms due to axial force in their element formulations. Al-bermani and Kitipornchai (1990) proposed an improved analysis technique using less elements to model a member via the introduction of deformation stiffness matrix. Yang and Leu (1991) accounted for higher order nonlinear effects in force recovery procedure in 2-D nonlinear analysis and obtained better results than conventional equations. Liew, et al (2000) obtained a geometric stiffness matrix based on stability interpolation functions for improved nonlinear analysis of space frame structures, and some higher order effects are included in their matrix.

In this paper, a refined finite element allowing for higher order effects of element deformations for geometrically nonlinear analysis of space beam is derived. The development is entirely based on the principle of stationary total potential energy. Two derived deformation matrices due to axial force and moment are functions of element deformations and incorporate the coupling among axial, lateral and torsional deformations. These proposed matrices are used together with linear and geometric stiffness for beam elements to analyze deflection behavior of space beams. As for rotational degrees of freedom, they are still represented by displacement derivatives. And the tangent stiffness matrix is corrected by the introduction of joint moment matrix, to make displacement derivatives equivalent to the

www.EngineeringEBooksPdf.com

commutative rotational degrees of freedom. Numerical examples have shown that the proposed element is accurate and efficient in predicting the nonlinear behavior, such as axial-torsional and lateral-torsional buckling, of space frames even when less elements are used to model a member.

ASSUMPTIONS

The following assumptions are made in this study:

(1) The beam is slender, and the Euler-Bernoulli hypothesis is valid;
(2) The beam element is doubly symmetric and prismatic;
(3) The material remains elastic within the loading rang;
(4) The load is conservative and nodal, and shear deformations are negligible;
(5) The influence of sectorial warping in the section can be neglected. Strains are small but displacements and rotations can be large.

NONLINEAR FORMULATION

Applying the principle of stationary potential energy can derive the element stiffness matrix. The incremental nodal force and incremental nodal displacement vectors {f} and {u} at the two ends of the element are given as follow,

$$\{f\} = [\, f_{x1},\, f_{y1},\, f_{z1},\, m_{x1},\, m_{y1},\, m_{z1},\, f_{x2},\, f_{y2},\, f_{z2},\, m_{x2},\, m_{y2},\, m_{z2}]^T \tag{1}$$

$$\{u\} = [\, u_1,\, v_1,\, w_1,\, \theta_{x1},\, \theta_{y1},\, \theta_{z1},\, u_2,\, v_2,\, w_2,\, \theta_{x2},\, \theta_{y2},\, \theta_{z2}]^T \tag{2}$$

Total Potential Energy of Element

The total potential energy of a general element subjected to the above actions is given by

$$\Pi = U - V \tag{3}$$

in which U is the strain energy stored in the element and V is the external work done.

$$\begin{aligned} U = {} & \frac{1}{2}\int_0^L \left[EA(u')^2 + EI_z(v'')^2 + EI_y(w'')^2 + GJ(\theta_x')^2\right]dx \\ & + \int_0^L \frac{F_x}{2}(v'^2 + w'^2)\,dx + \int_0^L \frac{F_x r_I^2}{2}(\theta_x')^2\,dx \\ & + \int_0^L \left[F_y(\theta_x w' - u'v') - F_z(\theta_x v' + u'w')\right]dx \\ & - \int_0^L M_y(v'\theta_x')\,dx - \int_0^L M_z(w'\theta_x')\,dx + \frac{1}{2}\int_0^L M_x[v''w' - v'w'']\,dx \end{aligned} \tag{4}$$

www.EngineeringEBooksPdf.com

in which E is the elastic modulus, G the shear modulus, L the length of element, A the cross-sectional area, I_y and I_z moment of inertia, $r_1^2 = (I_y + I_z)/A$ the polar radius of gyration about the shear center, J the tosional constant, u the axial displacement, θ_x the angle of twist, v,w the lateral displacement, a prime represents a derivative with respect to x. The forces at the internal cross-section x can be expressed in terms of those at the element ends:

$$F_x = P, \quad F_y = -(M_{z1} + M_{z2})/L, \quad F_z = (M_{y1} + M_{y2})/L, \tag{5,6,7}$$

$$M_x = M_{x2}, \quad M_y = -M_{y1}(1 - x/L) + M_{y2}(x/L), \quad M_z = -M_{z1}(1 - x/L) + M_{z2}(x/L) \tag{8,9,10}$$

The work of element nodal force increments under nodal displacement increments is given by

$$V = \{u\}^t \{f\} \tag{11}$$

Linear interpolation functions are adopted for the axial displacement, u, and the angle of twist, θ_x. Cubic interpolation functions are used for the lateral displacements, v and w. Subtituting these functions into Eqn. 4 and 3, the expression for the total potential energy may be defined in terms of the incrmental nodal displacements at the two ends of the element.

The Incremental Tangent Stiffness Matrix for Predictor and Error Corrector

The secant equilibrium equation of the beam element can be formulated from the principle of stationary potential energy

$$\delta\Pi = \delta U - \delta V = 0 \tag{12}$$

which leads to the element secant stiffness matrix in updated Lagrangian formulation. This incremental stiffness matrix is often linearised into the tangent stiffness matrix in the literature. For a single frame element, the induced moment matrix $\mathbf{k_i}$ should be added to the stiffness matrix, because of the quasitangential properties of the bending moments M_y and M_z and the semitangential property of the torque M_x, hence to yield the true equilibrium condition that satisfies the rigid body test. So incremental secant equation can be given as,

$$\{f\} = \left([k_e] + [k_g] + [k_i] \right) \{u\} \tag{13}$$

The linear stiffness matrix $\mathbf{k_e}$ and geometric stiffness matrix $\mathbf{k_g}$ are available in standard text and the induced moment matrix $\mathbf{k_i}$ can be found in text (Yang, 1994).

The axial force P can be obtained in terms of total element deformations from co-rotational approach as,

$$P = EA\left[\frac{e}{L} + \frac{2}{30}(\Theta_{z1}^2 + \Theta_{z2}^2) - \frac{1}{30}\Theta_{z1}\Theta_{z2} + \frac{2}{30}(\Theta_{y1}^2 + \Theta_{y2}^2) - \frac{1}{30}\Theta_{y1}\Theta_{y2} + \frac{r_1^2}{2L^2}(\Theta_x)^2\right] \tag{14}$$

www.EngineeringEBooksPdf.com

where Θ_{y1}, Θ_{y2}, Θ_{z1} , Θ_{z2} are the total end rotations, Θ_x the total twist and e the relative axial displacement.

Incremental tangent stiffness matrix can be derived by the differentiation of force increments with respect to displacement increments after complex mathematics manipulation as,

$$K_{ij} = \frac{\partial f_i}{\partial u_j} + \frac{\partial f_i}{\partial P}\frac{\partial P}{\partial u_j} + \sum_{k=1}^{4}\frac{\partial f_i}{\partial M_k}\frac{\partial M_k}{\partial u_j} = k_e + k_g + k_i + k_P + k_m + k_{mi} \tag{15}$$

in which $\mathbf{k_p}$ is the component due to axial force which is a function of total element deformation, $\mathbf{k_m}$ the component due to internal bending moments which is a function of the element deformation increments..

For a single and discrete element, $\mathbf{k_i}$ is asymmetric due to the lack of conjugation between bending moments and displacement derivatives, which have been used as the commutative rotational degrees of freedom. The symmetry will be restored when the element is connected to the other elements. As a result, only the symmetric potion of induced portion of induced moment matrix, which is referred to as the joint moment matrix $\mathbf{k_j}$ (Yang 1994), needs to be assembled to form to the structure tangent stiffness matrix. So also does the matrix $\mathbf{k_{mi}}$. In the nonlinear load-deflection analysis of spatial frame, $\mathbf{k_e}$, $\mathbf{k_g}$, $\mathbf{k_j}$ and $\mathbf{k_p}$ are used in 'predictor' phase which involves solution of structural displacement increments from the total equations of equilibrium. And all the components of $\mathbf{K_{ij}}$ are used in 'corrector' phase, which is concerned with recovery of the element forces from the element displacement increments obtained in predictor phase.

Once the element displacement increments are obtained, the element force increments can be evaluated by the natural deformation approach as

$$\{f\} = \left([k_e] + [k_g] + [k_i] + [k_P] + [k_m] + [k_{mi}]\right)\{u_n\} \tag{16}$$

where $\{u_n\}$ denotes the natural deformations obtained by excluding the rigid body motions from the element displacement vector $\{u\}$ defined by Eqn. 2. The updated internal forces in an element can thus be obtained as

$$\{^{i+1}F\} = \{^{i}F\} + \{f\} \tag{17}$$

in which $\{^{i}F\}$ is the internal forces at ith configuration.

NUMERICAL EXAMPLES

Axial-torsional Buckling of a Column

Fig.1 shows a column with rectangular cross-section under the action of an axial force. The two ends of the bar are rigidly built-in. The material and section properties are $E = 2.0\times10^{11}$ N/m^2, $G = 7.69\times10^{10}$ N/m^2, $A = 4.706\times10^{-3}$ m^2, $I_y = 6.992\times10^{-6}$ m^4, $I_z = 1.954\times10^{-5}$ m^4, J =

www.EngineeringEBooksPdf.com

1.944×10^{-7} m^4, L = 4.0 m. The theoretical axial-torsional buckling force can be predicted as $P_{cr} = GJ / r_1^2 = 2.6516$ MN. In the geometrical nonlinear analysis, a disturbing torque of $M_t = 0.001P$ is applied at mid-span of the bar to initiate the displacement and the twist. The bar is modeled by two and four proposed elements, and, for comparative purpose, by the conventional cubic elements. As seen in Figure 1, same results are obtained by two and four present elements which are also in good agreement with the results from Timoshenko's theory (1961). The results by two or more conventional cubic elements cannot accurately predict the nonlinear behavior because the incremental secant equation does not allow for higher order terms in twist deformations. The results by two elements proposed by Al-bermani, et al's method (1990) are also plotted in the same figure, which show that their results are excellent in small and moderately large deformation range with twist less than 0.4.

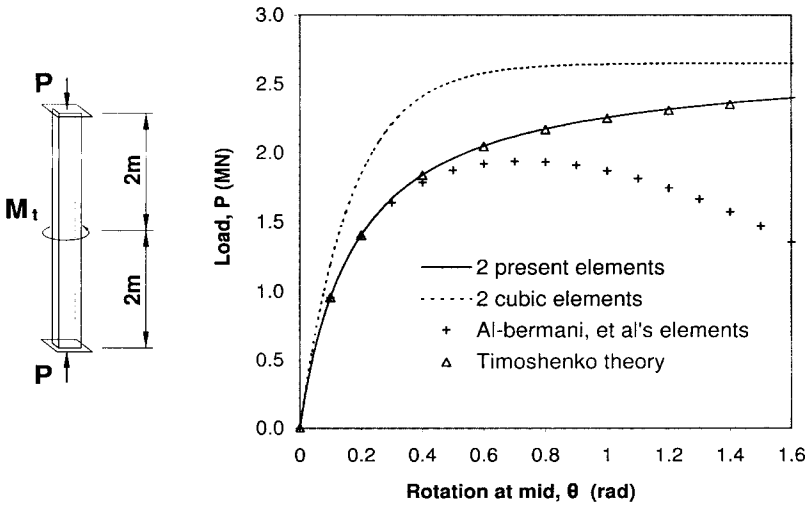

Figure 1. Load-displacement curves of axially compressed column

CONCLUSIONS

This paper derives a refined finite element for geometrically nonlinear analysis of space frames in updated Lagrangian framework. A new incremental tangent stiffness matrix, which allows for high order effects of element deformation, replaces the conventional incremental secant stiffness matrix. Two deformation matrices due to axial force and moment are derived. They are the functions of element deformations and incorporated with the coupling among axial, lateral and torsional deformations. These proposed matrices are used together with the linear and geometric stiffness for beam elements to analyze the deflection behavior of space frames. Numerical examples demonstrate that the proposed element is accurate and efficient in predicting the nonlinear behavior, such as axial-torsional and lateral-torsional, of space frames even when less elements are used to model a member.

www.EngineeringEBooksPdf.com

ACKNOWLEDGEMENT

The authors are thankful to the financial support by The Research Grant Council, Hong Kong SAR Government under the project "Analysis and design of steel frames allowing for beam warping and lateral-torsional buckling (B-Q233) ".

REFERENCES

Al-Bermani F.G.A. and Kitipornchai S. (1990). Nonlinear analysis of thin-walled structures using least element/member, *Journal of Structural Engineering, ASCE* **116:1**, 215-234.

Argyris J.H., Dunne P.C. and Scharpf D.W. (1978). On large displacement-small strain analysis of structures with rotation DOF, *Comput. Methods Appl. Mech. Engrg.* **14,** 401-451; **15,** 99-135.

Bathe K.J. and Bolourchi S. (1979). Large displacement analysis of three dimensional beam structures, *International Journal fo Mumer. Methods Engrg.* **14,** 961-986.

Chan S.L and Kitipornchai, S. (1987). Geometric nonlinear analysis of asymmetric thin-walled beam-columns, *Engrg. Struct.* **9:4**, 243-254.

Chan S.L. (1992). Large deflection kinematics formulations for three-dimensional framed structures. *Comput. Methods Appl. Mech. Engrg.* **95,** 17-36.

Conci A. and Gattass M.(1990). Natural approach for geometric non-linear analysis of thin-walled frames. *International Journal for Numerical Methods in Engineering,* **30,** 207-231.

Crisfied M.A. (1990). A consistent co-rotational formulation for non-linear three-dimensional beam elements. *Comput. Methods Appl. Mech. Engrg.* **81**:131-150.

Hsiao K. M. and Lin W.Y. (2000): A co-rotational finite element formulation for buckling and postbuckling analysis of spatial beams. *Comput. Methods Appl. Mech. Engrg.* **188,** 567-594.

Izzuddin, B.A. and Elnashai, A.S. (1993) Eulerian formulation for large-displacement analysis of space frames, J. Engrg. Mech., ASCE **117,** 549-569.

Kim M.Y. Chang S.P. and Park H.G. (2001a). Spatial postbuckling analysis of nonsymmetric thin-walled frames. I: Theoretical considerations based on semitangential property. *J Eng. Mech. ASCE* **127:8,** 769-778.

Kim M.Y. Chang S.P. and Kim S.B. (2001b). Spatial postbuckling analysis of nonsymmetric thin-walled frames. II: Geometrically nonlinear FE procedures. *J Eng. Mech. ASCE* **127:8,** 779-790.

Kuo S.R., Yang Y.B. and Chou J.H.,(1993). Nonlinear analysis of space frames with finite rotations. *Journal of Structural Engineering, ASCE* **119:1,** 1-15.

Liew J.Y.R., Chen H., Shanmugam N.E. and Chen W.F. (2000). Improved nonlinear plastic hinge analysis of space frame structures. *Engineering Structures,* .**22**, 1324-38.

Meek J.L and Tang H.S. (1984). Geometrically nonlinear analysis of space frames by an incremental iterative technique. *Comput. Methods Appl. Mech. Engrg.* **14,** 401-451.

Oran C. (1973). Tangent stiffness in space frames. *Journal of Structural Engineering, ASCE,***99: ST6,** 987-1001.

www.EngineeringEBooksPdf.com

Papadrakakis M. and Ghionis A. (1986). Conjugate gradient algorithm in nonlinear structural analysis problems. *Comput. Methods Appl. Mech. Engrg.* **59,** 11-27.

Pi Y.L. and Trahair N.S. (1994). Nonlinear Inelastic analysis of steel beam columns. I:theory. *Journal of Structural Engineering ASCE* **120:7,** 2041-61.

Teh LH and Clarke M.J. (1997). New definition of conservative internal moments in space frames. *J Eng. Mech. ASCE* **123:2,** 97-106.

Teh L.H. and Clarke M.J. (1998). Co-rotational and Lagrangian formulations for elastic three-dimensional beam finite elements. *J Constr. Steel Res.* **48:2-3,** 123-144.

Teh L.H. and Clarke M.J. (1999). Symmetry of tangent stiffness matrices of 3D elastic frame. *J Eng. Mech. ASCE* **125:2,** 248-251.

Timoshenko S.P. and Gere J.M. (1961). Theory of elastic stability, 2nd edition. McGraw-Hill, New York.

Yang Y.B. and Kuo S.R.(1994). Theory & analysis of nonlinear framed structures, Prentice Hall, Singapore

Yang Y.B. and Leu L.J. (1991). Force recovery procedures in nonlinear analysis. *Computers and Structures* **41:6,** 1255-61.

Yang Y.B. and McGuire W. (1986). Stiffness Matrix for geometric nonlinear analysis. *Journal of Structural Engineering, ASCE* **112:4,** 853-877.

www.EngineeringEBooksPdf.com

Advances in Steel Structures, Vol. II
Chan, Teng and Chung (Eds.)
© 2002 Elsevier Science Ltd. All rights reserved.

UNIFIED ANALYTICAL METHOD OF GLIDING CABLES IN STRUCTURAL ENGINEERING - FROZEN-HEATED METHOD

Y.L. Guo and X.Q. Cui

Department of Civil Engineering, Tsinghua University, Beijing, China

ABSTRACT

This paper presents a new, efficient and unified structural analytical method for solving the internal forces and deformations of a structure with gliding cable elements. This method is called "the frozen-heated method"(FHM). With the gliding cable elements in engineering structures, it is difficult to obtain its mechanical behavior easily only by using traditional analytical method because of cable gliding during the loading process. It is the frozen-heated method that provides an efficient approach for analyzing this kind of structure. Several numerical examples are presented to verify its validity and efficiency.

KEYWORDS

Gliding cable, frozen-heated method, virtual temperature load, mechanical behavior, compatibility condition, equilibrium state

INTRODUCTION

Cable components [1] play a very important role in steel structures, and they are combined with other steel elements to form many new hybrid structures, such as ropeway, suspended cable structures, cable truss structures, cable dome structures, cable membrane structures etc. In the steel structures combined with cable elements, there are two kinds of cable joint connection forms. One is the fixed joint where the cables cannot produce relative gliding, and the other is gliding joint where the individual cable may move independently in the common joint. The internal forces and the deformations analysis in steel structures without gliding cable is relative simple, and many papers published are concerned with their

www.EngineeringEBooksPdf.com

behavior studies [3]. Recently, more and more gliding joints in cable structures are applied in some structural forms, such as cable supported structure [2]. But the analysis to such a structure with gliding cable is very difficult, and only few papers presented it [3-9]. In general, FE analysis package, for example ANSYS, contains the contact element that can be directly used to analyze this kind of structure with gliding cables. But this method is very complex and cannot be understood easily. Another method, named "changing cable original length method", was brought out to solve this problem [4], but this method is only suitable when the force of the end of the cable is known; Similarly, another two methods, named "power searching method" and "dynamic relaxing method" can be used to solve this problem also when only the end force of cable is known [5,6]; Based on this consideration, a gliding cable element method was brought out. The numerical results obtained indicate that this method is very efficient, but its disadvantage is that the complex gliding stiffness matrix must be solved.

Currently, the authors developed a new, efficient and unified structural analytical method to solve this problem, named "frozen-heated method". The basic principle of this method is that a virtual temperature-increasing load is introduced in one side of the cable of the gliding joint, and a virtual temperature-decreased load is applied in the other side cable of the gliding joint. Finally a nonlinear finite element analysis is employed to find out the forces and deformations by using an iterative method. The application of this method is demonstrated by some numerical examples.

COMPUTATIONAL STEPS OF FROZEN-HEATED METHOD

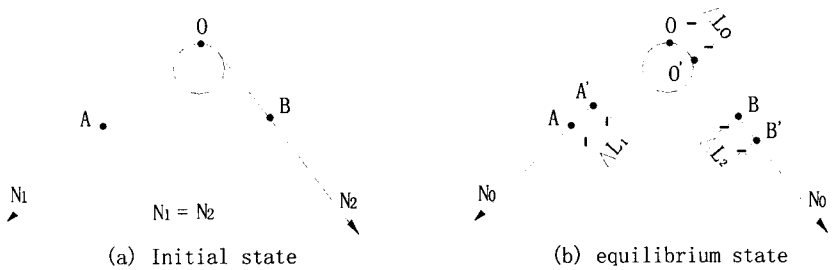

Figure 1: Frozen-heated method concept ional diagram

As shown in figure 1, a cable will be gliding around the pulley when the tension forces of the cables on two sides of the pulley are not equal ($N_1 \neq N_2$). Just when they become equal, the structure will be in the equilibrium state. It is very clear that during the loading process the cable gliding length on one side should be equal to the cable gliding length on the other side, regardless of the structure approaching its equilibrium state or not, namely:

$$\Delta L_1 = \Delta L_2 = \Delta L_0$$

Based on the above consideration, in the frozen-heated method a virtual temperature-decreased load Δt_1 is applied on the left cable element, reducing its length with Δl ; Simultaneously, a virtual

www.EngineeringEBooksPdf.com

temperature-increasing load Δt_2 is put on the right cable element, increasing its length with the same value. Further, a nonlinear finite element analysis is employed to compute the two side cable elements' tension forces. If the two forces are not equal, the above iterative steps must be continued. Obviously, when there are more than one pulley, the same steps must be repeated on every pulley until the global structure approaches the equilibrium state.

For the cable elements located on the two sides of the pulley, the virtual temperature loads can be derived by the following equations:
Because of

$$\Delta l = L_1 \cdot \alpha \cdot \Delta t_1 = L_2 \cdot \alpha \cdot \Delta t_2 \tag{1}$$

$$\Delta l = \frac{\Delta F_1 \cdot L_1}{E \cdot A_1} = \frac{\Delta F_2 \cdot L_2}{E \cdot A_2} \tag{2}$$

So,

$$\Delta t_1 = \frac{\Delta F}{E \cdot A_1 \cdot \alpha} \quad ; \qquad \Delta t_2 = -\frac{L_1 \cdot \Delta t_1}{L_2}$$

where, ΔF is the tension force difference of cable elements on the two sides of the pulley. ΔF is the function of ΔN ($\Delta N = N_1 - N_2$) and is defined as $\frac{\Delta N}{\beta}$, where β is distributional coefficient of the difference in internal forces N_1 and N_2. And then,

$$\Delta t_1 = \frac{1}{E \cdot A_1 \cdot \alpha} \cdot \frac{\Delta N}{\beta} \tag{3}$$

In general iterative strategy, β is considered a constant and the computational steps are shown in appendix.

The symbols used in the above are as follows:

l_{i1}、l_{i2}: two side cable elements' lengths of (i)th pulley, respectively;

$\Delta t_{i1}^{'}$、$\Delta t_{i2}^{'}$: virtual temperature loads on two side cable elements of (i)th pulley of (K-1)th iterativeness, respectively;

N_{i1}、N_{i2}: two side cable elements' tension forces of (i)th pulley of (K)th iterativeness, respectively;

ε_i: the different value of two side cable elements' tension forces of (i)th pulley of (K)th iterativeness;

ε_t: the relative different value of total out of forces of (K)th iterativeness;

E、A_i、α: the cable's elastic modulus, the cable element's sectional areas and the thermal expansion

www.EngineeringEBooksPdf.com

coefficient of (i)th pulley, respectively;

β : distributional coefficient of the difference in internal forces N_1 and N_2.

NUMERICAL EXAMPLES

Example 1

To verify the validity and efficiency of the frozen-heated method, three different cases are first selected, as shown in fig (2). For the first case, the frozen-heated method is used to analyze its internal forces and deformations. For second case, the point B is considered as not gliding, namely a fixed point. For third case the point B is treated as gliding but keeping a constant horizontal force unchanged. The nonlinear finite element analysis is employed to solve their internal forces and deformations, and the result obtained is listed in table 1.

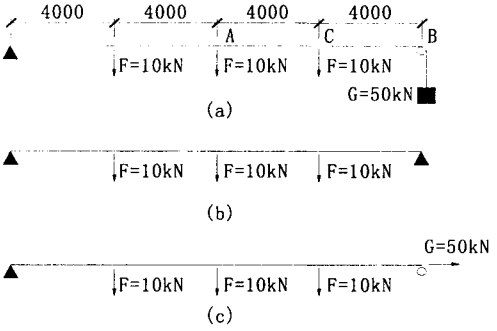

Figure2: Computational model of single cable

It is very clear from the table 1 that if the gliding of the cable is not considered in the analysis, very large error in load reliving system will result [3].

Table 1: Results compared with of the three methods

Contents	Figure 2(a)	Figure 2(b)	Figure 2(c)
Vertical displacement of node A(mm)	-1227.0	-606.4	-1549.0
Horizontal displacement of node A (mm)	-149.0	-	-178.2
Horizontal displacement of node B(mm)	-	-	-356.4
Cable gliding length(mm)	301.6	-	-
Cable tension force of CB segment (kN)	50.4	133.1	52.2

Example 2

As shown in figure 3, one I-section steel cantilever with 3.16kN/m uniform loads is pulled by a pair of cables that around a pulley. The frozen-heated method is used to analyze its internal forces and deformations and the results obtained are compared with those without considering cable gliding.

www.EngineeringEBooksPdf.com

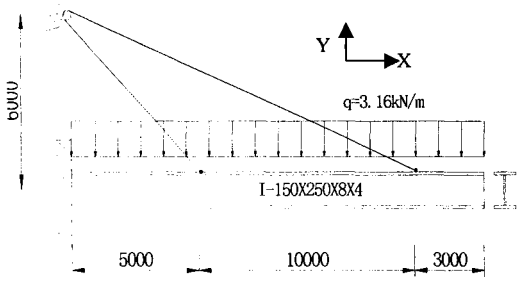

Figure 3: Cable stayed beam

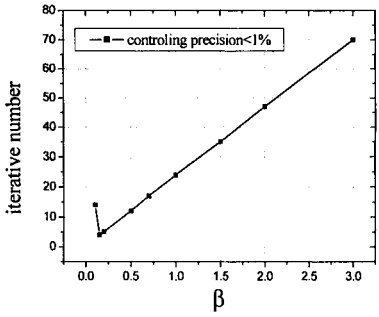

Figure 4: Curve of iterative number with β

Table 2: Results comparison with and without consideration of cable gliding

gliding or not?	Uy (mm)		Mz (kN.m)		Cable Fx (kN)	
	Max	Min	Max	Min	Short	Long
No	0	-56.2	15.6	-27.3	37.0	66.4
Yes	18.7	-150.2	40.4	-56.9	58.6	59.1

Obviously, without considering cable gliding will get large errors in analyzing the cantilever with cable elements. Therefore, the frozen-heated method used to analyze gliding cables can estimate accurately the real structural behavior. Figure 4 shows the relationship between iterative number and β value.

In this case, the convergence of this method is very good when β is close to 0.2. But when β is greater than 0.2, the iterative number will increase linearly and quickly. The searching for an optimal β during iterative process is under way.

Example 3

As shown in figure 6, that load reliving system was tested in South-Eastern University of China [6]. The numerical results were computed by dynamic relaxing method. FHM was employed to analyze it again, and the results were compared to those of both the experiment results and dynamic relaxing method. This structure is a cable net structure, and the plane is square. The geometric parameters were shown in figure 6. All the boundary joints are pulleys with cables around them (total 20 joints). The weight of each suspending poise is 20N, and concentrated load (P=200N) was applied on the mid-joint of the structure. The diameter of each cable is 1.2mm, and the elastic modulus is 54400N/mm^2.

The load-deflection curve of joint O is shown in figure 6. It is obvious that the FHM can solve the gliding cable question in structural engineering efficiently, and it has good precision. Compared with the experiment results, the error precise to be less 5%. The errors appear only because the friction forces were not taken into consideration [6].

www.EngineeringEBooksPdf.com

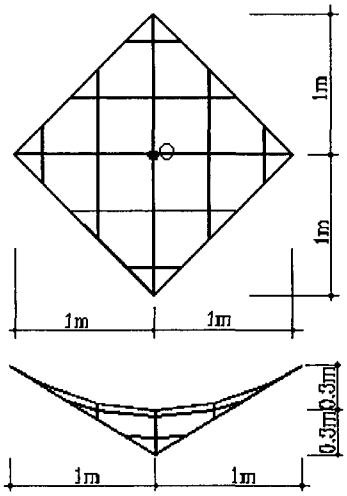

Figure 5: Experiment model

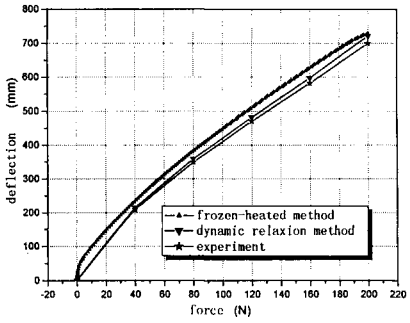

Figure 6: Mid-point deflection VS load

CONCLUSIONS

1) Frozen-heated method is a unified, efficient structural method to analyze the gliding cable structures. It can be also employed for analyzing efficiently the static behavior of the load reliving structure.

2) The examples employed in this study demonstrate a good convergence while using frozen-heated method; The convergence depends upon β that will vary during iterative process and has different values in different type of structures. Therefore, one should pay much attention to improve its convergence while utilizing this method.

REFERENCES

1. H. Yan (1994). Application and development of hybrid structure system. Industrial construction. 6, 10-16.
2. G. B. Xu, L. Cui (2000), New cable supported structure, Spatial structures, 1, 27-34.
3. L X Zhang, Z Y Shen (2000), Numerical models for cable elements in pre-stress cable structures, Spatial structures, 6:2, 18-23
4. X.M. Wang (1992). Cable computation of changing original length, Computational structural mechanics and application, 9:2, 135-139.
5. S. Jian, J. Yi, Q.G. Qin (1997). Study and application of load relieving system. Proceedings of 8th space structure conference, 311-316.
6. S. Jian etc (1999) Mechanical behavior study on load relieving system, Engineering mechanics, 16:3, 38-43
7. G.Y. Wang (2000). On mechanics of time-varying structures, Journal of civil engineering.33:6,

www.EngineeringEBooksPdf.com

105-108.
8. C. Melbourne, P.Bullman (1987) Load relieving system, Proc. Int. Conf, on Non-Conventional Structures, London, 2. 1-6.
9. H. Li, X.L. Liu (2000). A new kind of structure-load relieving system, Proceedings of 9th spatial structures conference, 555-562.

APPENDIX: COMPUTATIONAL STEPS

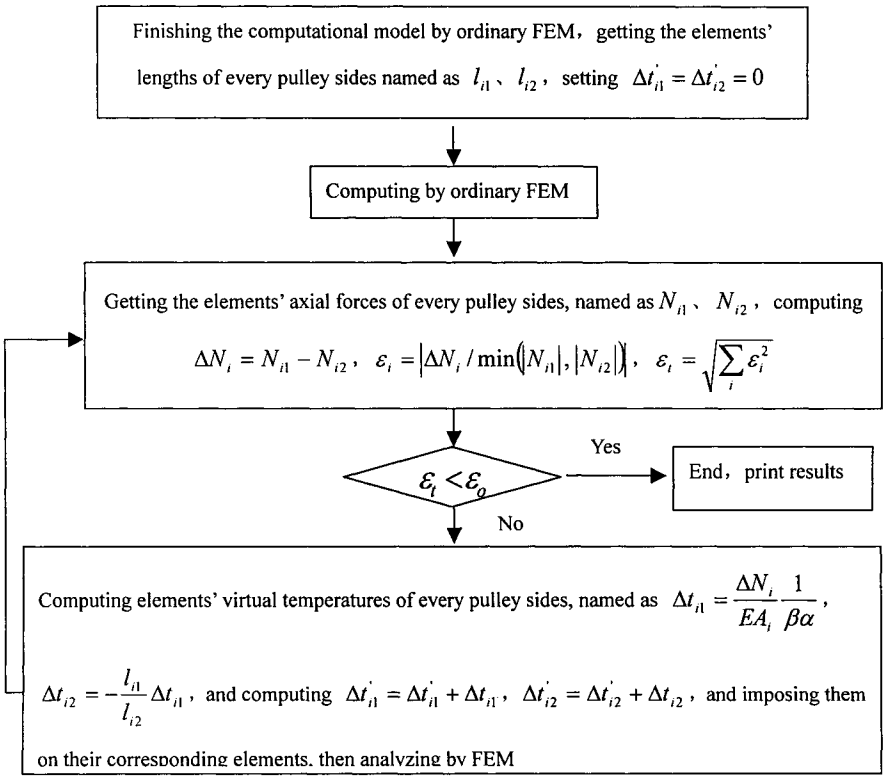

www.EngineeringEBooksPdf.com

This Page Intentionally Left Blank

www.EngineeringEBooksPdf.com

Advances in Steel Structures, Vol. II
Chan, Teng and Chung (Eds.)
© 2002 Elsevier Science Ltd. All rights reserved.

Large Deflection Analysis of Tensioned Membrane Structures Allowing for Support Flexibility

Jin-Jun Li and Siu-Lai Chan

Dept. of Civil and Structural Engineering, the Hong Kong Polytechnic University, Hung Hom, Kowloon, Hong Kong, China

ABSTRACT

Tensioned membrane structures are normally reinforced with pretensioned cables, and they are then supported by metal space frames of light weight. Conventional analysis and design for tensioned membrane structures are based on two assemblages, fixing the support positions and determining the equilibrium shape of the cable-membrane at first and checking the adequacy of the metal frames against support reactions. Under this methodology, the interaction between the cable-membrane and the metal frame is neglected. An integrated nonlinear FE analysis, including cable element, membrane element and beam element in the FE library, is proposed in this paper for large deflection analysis of membrane structures allowing for support flexibility. The interaction between the support structure and the cable-membrane is examined through numerical study of a saddle shade pavilion structure. Results of integrated analysis were noted to deviate considerably from those obtained in an isolated analysis, which reveals that an integrated analysis is necessary for structural engineers to determine whether or not the effects of elastic deformations of supports should be taken into account in the design of tensioned membrane structures.

KEYWORDS

Tensioned membrane, Cable-membrane, Support flexibility, Integrated analysis, Large deflection, Shape finding, Loading analysis, Saddle shade pavilion

INTRODUCTION

Tensioned membrane structures have been become increasingly popular. The nature of tensioned membrane structures is such that the structural stiffness is achieved by means of special geometric shapes with initial prestressing in the membranes and cables. Design of tensioned membrane structures is more dependent upon computers than most other structural systems. Typical steps for the computer design of tensioned membrane structures comprise shape finding, loading analysis and cutting pattern generation. Currently, main algorithms for shape finding and loading analysis in practical use include nonlinear FEM with incremental-iterative procedure, force density method and

www.EngineeringEBooksPdf.com

dynamic relaxation method (Meek and Xia, 1999).

Many tensioned membranes and their cables functioning as reinforcement are supported by light-weight metal frames. According to the conventional design method such structures are divided into two assemblages, the cable-membrane and the support, and their designs are carried out separately. At first, the initial and loaded equilibrium shapes of the cable-membrane are determined by fixing all of the support points, based on which the cable-membrane can be designed. The support structure is checked and designed, using the obtained support reactions of the cable-membrane as external loads. Under this conventional methodology, the interaction between the cable-membrane and the support structure can not be considered and is therefore neglected in the design. Although some publications indicated such analysis of the cable-membrane with the support structure is available (Wakefield, 1999; Tabarrok and Qin, 1992), no special investigation has been found on effects of the interaction in the analysis and design of tensioned membrane structures.

In practical cable structures, influences of flexible supports, or boundary effects, were studied. Substructuring concept was employed in many researches, where cable and support structures analyzed separately and the interactions were considered by iterating cable forces and support-node displacements (Majowiecki et al., 1984; Shan et al., 1993). Nonlinear finite element analysis with both cable and beam elements can also be found in the studies on cable supported or guyed structures (Desai et al., 1988; Chu et al., 1976). In addition to above-mentioned methods, some authors investigated optimization techniques for the analysis of cable structures with flexible supports (Stefanou et.al., 1995; Buchholdt, 1999). Cables are affected by the flexibility of their supports in tensioned membrane structures. In practical engineering of tensioned membranes, size-optimized supports with reasonable flexibility is desired as well and variation of membrane behavior due to elastic deformations of supports should be checked carefully. Since no example is found on this topic, numerical study is conducted in this paper. Along this direction, this paper presents an integrated nonlinear FE large deflection analysis for the tensioned membrane supported by metal frames and examines their interaction through a practical structure.

FEM DESCRIPTION

The detailed formulation of cable, membrane and beam finite elements should be referred to the work by Tabarrok and Qin (1992), Tan (1989), Levy and Spillers (1995) and others. For completeness, however, the following gives the basic descriptions of the finite elements and the numerical scheme employed in this study.

Cable Element

The cable element employed is a three-dimensional line element with two end nodes and six degrees of freedom. Linearly elastic constitutive law is assumed and only tensile stresses are resisted by this element. Fig. 1 shows a cable element with its end nodes I and J in the global structural coordinate (X_1, X_2, X_3). The elongation of the cable element is the unique natural deformation. Analyzing the relationship of elongation with tension force and incorporating the coordinate transformation, the incremental elastic stiffness matrix for the cable element can be written as,

$$[K_e]_{Cable} = \frac{EA}{l_0}\begin{bmatrix} CC^T & -CC^T \\ -CC^T & CC^T \end{bmatrix} \tag{1}$$

www.EngineeringEBooksPdf.com

where E is the material modulus, A and l_0 are respectively the sectional area and the original length of the cable, and C is the direction cosine vector. The components of C are given by,

$$C_i = \frac{1}{l_0}(X_{Ji} - X_{Ii}) \tag{2}$$

where the index i takes on value 1, 2, 3 corresponding to the respective global axes.

The geometric stiffness furnishes the relationship between the change in the global nodal force components and the global nodal displacements when the element natural tension is held invariant. Hence, by examining these nodal tension components before and after imposition of the nodal displacement, the geometric stiffness can be expressed as,

$$[K_g]_{Cable} = \frac{T}{l_0}\begin{bmatrix} I_3 - CC^T & -(I_3 - CC^T) \\ -(I_3 - CC^T) & I_3 - CC^T \end{bmatrix} \tag{3}$$

where T is the cable tension and I_3 is a 3×3 unit matrix.

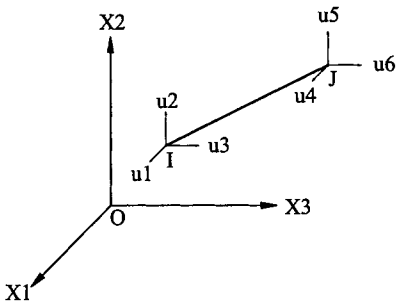

Fig. 1: Cable element in the global coordinate

Membrane Element

A triangular facet element of constant strain with three nodes and nine degrees of freedom is employed in this study and shown in Fig. 2 in its local (x, y) and global (X_1, X_2, X_3) coordinates. From analytical geometry, the lengths of its three sides uniquely define the configuration of a triangle. The geometry of the triangular element after deformation therefore can be defined by the elongation along its three sides. By analyzing the correlation of the nodal force with side elongation and considering the coordinate transformation, the elemental elastic matrix in global coordinate (X_1, X_2, X_3) can be expressed as,

$$[K_e]_{Membrane} = AtT_G^T T_N^T D T_N T_G \tag{4}$$

where

A and t are respectively the area and thickness of the element,

D is the intrinsic constitutive matrix,

www.EngineeringEBooksPdf.com

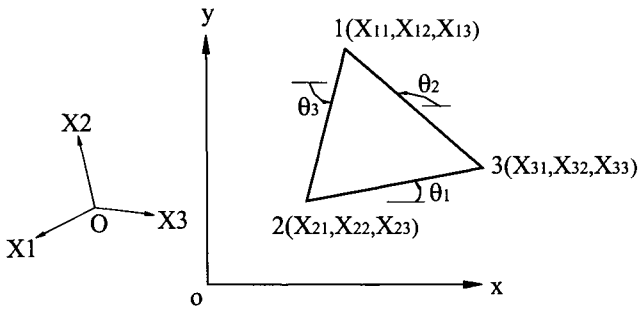

Fig. 2: Membrane element in local and global coordinate

$$D=\frac{E}{1-\nu^2}\begin{bmatrix}1 & \nu & 0\\ \nu & 1 & 0\\ 0 & 0 & \frac{1-\nu}{2}\end{bmatrix}$$

E and ν are respectively the Young's modulus and the Poisson's ratio of the membrane material, T_N is the transformation matrix for nodal deformations to strains,

$$T_N=\Psi^{-1}L_{0d}^{-1}$$

$$L_{0d}=diag\left[l_{023},l_{031},l_{013}\right]$$

l_{0ij} is the initial length of side containing element corner i and j,

$$\Psi=\begin{bmatrix}a_1 & b_1 & c_1\\ a_2 & b_2 & c_2\\ a_3 & b_3 & c_3\end{bmatrix}$$

$$a_i=\cos^2\theta_i,\ b_i=\sin^2\theta_i,\ c_i=\sin\theta_i\cos\theta_i\ \ (i=1,2,3)$$

θ_i is the angle of inclination to the local x axis of triangle side ($i=1,2,3$, see Fig. 2),

T_G is the transformation matrix for global displacements to natural stresses,

$$T_G=\begin{bmatrix}0 & 0 & 0 & -\alpha_{23} & -\beta_{23} & -\chi_{23} & \alpha_{23} & \beta_{23} & \chi_{23}\\ \alpha_{31} & \beta_{31} & \chi_{31} & 0 & 0 & 0 & -\alpha_{31} & -\beta_{31} & -\chi_{31}\\ -\alpha_{12} & -\beta_{12} & -\chi_{12} & \alpha_{12} & \beta_{12} & \chi_{12} & 0 & 0 & 0\end{bmatrix},$$

$$\alpha_{ij}=\frac{X_{j1}-X_{i1}}{l_{0ij}},\ \beta_{ij}=\frac{X_{j2}-X_{i2}}{l_{0ij}},\ \chi_{ij}=\frac{X_{j3}-X_{i3}}{l_{0ij}}$$

X_{ij} is the global coordinate for node i in the direction of j ($j=1$, 2 or 3) axis.

The geometric stiffness for the constant strain triangular element can be obtained conveniently by referring to the derivation of the geometric stiffness for the cable element. It can be written as,

$$\left[K_g\right]_{Membrane}=\begin{bmatrix}B_{12}+B_{31} & -B_{12} & -B_{31}\\ -B_{12} & B_{12}+B_{23} & -B_{23}\\ -B_{31} & -B_{23} & B_{23}+B_{31}\end{bmatrix} \tag{5}$$

www.EngineeringEBooksPdf.com

where

$$B_{ij} = \frac{P_{ij}}{l_{ij}}\left[I_3 - C_{ij}C_{ij}^T\right]$$

C_{ij} is the direction cosines vector for the side containing corner node i and j and is evaluated as,

$$C_{ij} = \frac{1}{l_{0ij}}\left\{\left(X_{j1} - X_{i1}\right)\ \left(X_{j2} - X_{i2}\right)\ \left(X_{j3} - X_{i3}\right)\right\}^T$$

P_{ij} is the tension force along the triangle side with node i and j.

Beam Element

For tension structures, the space support, unlike the cable-membrane, undergoes small deflections due to its relatively larger rigidity. Accordingly it is appropriate to adopt linear beam element with small deflections. Since the formulation of such beam element is available in many textbooks, its elastic stiffness matrix will be omitted here.

Numerical Scheme

Newton-Raphson method is used as the incremental-iterative strategy for solving large deflection problem in this paper.

NUMERICAL EXAMPLE: A SADDLE SHADE PAVILION

Shape Finding

The nonlinear FEM above-described is adopted as the numerical tool for shape finding as well as loading analysis of tensioned membrane structures. A shade pavilion structure with a saddle membrane supported by a space steel frame is studied here. The flat mesh generated for the shape finding is shown in Fig. 3. The governing node coordinates of the mesh and the material properties are also shown in Fig. 3. Material properties include tensile stiffness (Et), Poisson ratio (v), weight density (w_1) for membrane material, and Young's modulus (E), sectional area (A) and weight density (w_2) for cable material are given in the same figure. The steel support frame of this shade pavilion is given in Fig. 4 with its isometric view. Nodal coordinates, member sections and material properties of this space frame are given in Fig. 4. For this steel support frame, all the members are rigidly connected except that the ties and struts are pinned at both ends. The pretensions of the edge cables are assumed to be 1 kN and the prestresses of the membrane elements are 4.0 kN/m.

A trial shape is obtained through elevating 1 and 3 corner points to a height of 1.216m while 2 and 4 corner points are fixed in the flat mesh (see Fig. 3). The stresses in membrane and cable elements due to large elastic strains are not accumulated in this process and space supports are not considered in this step. When the trial shape of tensioned cable-membrane is obtained, it is attached to the steel structure at the supporting points in the FE model and a series of numerical iterations are activated until system equilibrium is achieved. The same material properties of the steel structure are adopted and the prestress pattern of the cable-membrane is maintained in this process. The initial equilibrium shape found is plotted in Fig. 5(a).

www.EngineeringEBooksPdf.com

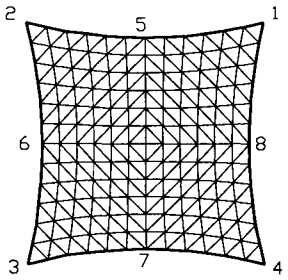

Coordinates:
1 (1.946, 1.946)
2 (-1.946, 1.946)
3 (-1.946, -1.946)
4 (1.946, -1.946)
5 (0.000, 1.703)
6 (-1.703, 0.000)
7 (0.000, -1.703)
8 (1.703, 0.000)

Membrane properties:
Et=1000 kN/m
v=0.2
w1=0.0147 kN/m2

Cable properties:
E=1.568E8 kN/m2
A=2.166E-4 kN/m
w2=0.018 kN/m

— pretensioned cable segment

Fig. 3: Flat mesh and material properties of membrane and cable

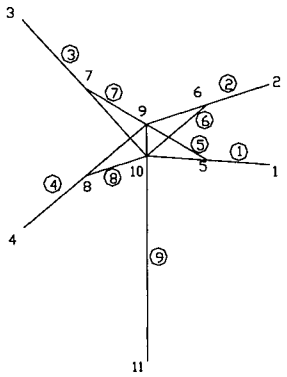

Coordinates:
1 (1.946, 1.946, 5.216)
2 (-1.946, 1.946, 4.000)
3 (-1.946, -1.946, 5.216)
4 (1.946, -1.946, 4.000)
5 (1.000, 1.000, 4.625)
6 (-1.000, 1.000, 4.313)
7 (-1.000, -1.000, 4.625)
8 (1.000, -1.000, 4.313)
9 (0.000, 0.000, 4.625)
10 (0.000, 0.000, 4.000)
11 (0.000, 0.000, 0.000)

Sections:
Spars ① ~ ④:
CHS 168.3ø X 10
Tie & Strut ⑤ ~ ⑧:
CHS 114.3ø X 5
Column ⑨:
CHS 273ø X 12.5

Material Properties:
E=2.058E8 kN/m2
v=0.3
w3=78.5 kN/m3

Fig. 4: Details of steel support frame

Loading Analysis

Four loading types are analyzed for this shade pavilion structure to simulate the actions from different directions. In the vertical loading case, surface pressures of 4.8 kPa are applied upward and downward. In horizontal loading case, nodal loads of 0.26 kN per node in the cable-membrane are applied in the X and Y direction respectively. The magnified deformation of the integrated structure are respectively shown in Fig. 5(b~e) for those four loading cases.

A comparison between the analysis results of the tensioned membrane structure with and without the support frame is tabulated in Table 1. It can be seen from Table 1 that the horizontal loads, both in X and Y directions, rather than the vertical upward and downward loads lead to more deviated results in the tensioned membrane structure when flexibility of structural steel supports is considered. The fact that the horizontal stiffness of the space support frame is relatively small is the cause for the large deviation.

The maximum values of internal cable tensions in the saddle membrane structure are lowered when the flexible supports are considered (see Table 1). In the horizontal loading cases, the maximum cable

www.EngineeringEBooksPdf.com

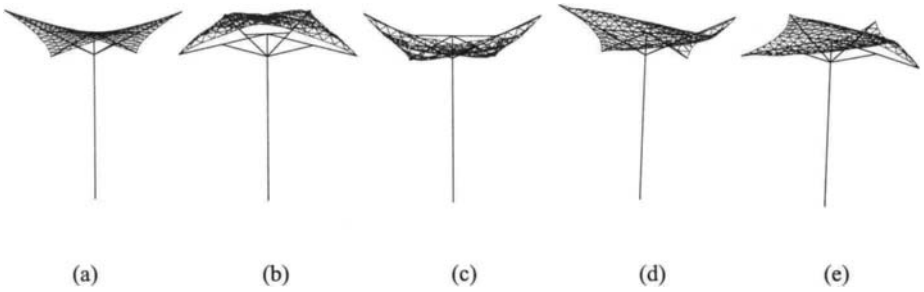

Fig. 5: Equilibrium shapes in shape finding and loading analysis, (a) initial equilibrium shape; (b) deformed shape under upward loads; (c) deformed shape under downward loads; (d) deformed shape under X-directional loads; (e) deformed shape under Y-directional loads

tension reduces nearly 1/3 due to the large support displacements. Maximum membrane stresses experience less variations and indicate a slight increase when supports become flexible.

TABLE 1
RESULT COMPARISONS BETWEEN FLEXIBLE AND FIXED SUPPORTS CONSIDERED

Loading direction		Upwards		Downwards		X direction		Y direction	
Support type		Flexible	Fixed	Flexible	Fixed	Flexible	Fixed	Flexible	Fixed
Max. cable tension (kN)		60.3	67.6	65.4	67.6	45.1	66.3	44.2	66.3
Max. membrane stress (kN/m)		33.6	27.5	29.6	27.5	13.5	11.2	13.1	11.2
Maximum support displacement (mm)	X	2.2	None	0.6	None	90.3	None	5.8	None
	Y	2.2	None	0.6	None	5.5	None	89.3	None
	Z	16.3	None	3.0	None	51.2	None	51.2	None

CONCLUSION

In reality, the tensioned membrane structures are supported by flexible space structures of light weight. To develop a criterion of determining whether the interaction between the tensioned structures and the space supports should be considered or not is non-trivial at present. However, a practical tool to consider the inclusion of these interactions should be available to structural engineers.

This paper presents an integrated analysis of tensioned membrane structures with flexible space supports, and examines the effects of the elastic deformations of supports on the tensioned membrane

www.EngineeringEBooksPdf.com

and cables through a practical structure. Numerical results demonstrate that the flexibility of space frame supports should be taken into account.

REFERENCE

1. Buchholdt H. A. (1999), *An introduction to cable roof structures, second edition*, Thomas Telford, London
2. Chu K. H. and Ma C. C. (1976), Nonlinear cable and frame interaction, *Journal of Structural Division, ASCE*, 102: 569-589
3. Desai Y. M., Popplewell N., Shan A. H. and Buragohain D. N. (1988), Geometric nonlinear static analysis of cable supported structures, *Computers & Structures*, 29: 6, 1001-1009
4. Levy R. and Spillers W. R. (1995), *Analysis of geometrically nonlinear structures*, Chapman & Hall, New York
5. Majowiecki M. and Zoulas F. (1984), On the elastic interaction between rope net and space frame anchorage structures, in: *Proceedings of 3rd International Conference on Space Structures*, 778-784, Nooshin, H. (eds), Sep. 11-14, Guildford, UK
6. Meek J. L. and Xia X. (1999), Computer shape finding of form structures, *International Journal of Space Structures*, 14: 1, 35-55
7. Shan W, Yamamoto C. and Oda K. (1993), Analysis of frame-cable structures, *Computers & Structures*, 47: 4/5, 673-682
8. Stefanou C. D. and Moossavi Nejand S. E. (1995), A general method for the analysis of cable assemblies with fixed and flexible elastic boundaries, *Computers & Structures*, 55: 5, 897-905
9. Tabarrok B. and Qin Z. (1992), Nonlinear analysis of tension structures, *Computers & Structures*, 45: 5/6, 973-984
10. Tan K. Y. (1989), *The computer design of tensile membrane structures*, PhD thesis, Department of Civil Engineering, The University of Queensland
11. Wakefield D. S. (1999), Engineering analysis of tension structures: theory and practice, *Engineering Structures*, 21: 680-690

www.EngineeringEBooksPdf.com

Advances in Steel Structures, Vol. II
Chan, Teng and Chung (Eds.)
© 2002 Elsevier Science Ltd. All rights reserved.

TORSIONAL ANALYSIS OF ASYMMETRIC PROPORTIONAL BUILDING STRUCTURES USING SUBSTITUTE PLANE FRAMES

W. P. Howson and B. Rafezy

Cardiff School of Engineering, Cardiff University,
PO Box 925, Cardiff CF24 0YF, UK

ABSTRACT

An approximate method for determining the nodal deflections of multi-bay, multi-storey asymmetric buildings is described, in which the structure is simplified before it is analysed. This has the advantage that it gives useful structural insights into the behaviour of the structure and enables modifications and re-analysis to be undertaken quickly, without the information overload that can be generated when analysing such complex structures. The approach uses a well-established method for reducing multi-bay, multi-storey, orthogonally framed structures to two equivalent substitute frames lying parallel to the axes of the original frames. Each substitute frame is a single bay, multi-storey frame that has the same number of storeys and the same storey heights as the original frame but is symmetric and carries symmetric vertical loads comprising only in-plane stiffness. It is shown that each of these frames can be used independently to determine the sway deflection of the original structure when it is loaded horizontally through the centre of pressure. It is further shown that, with little additional effort, the components of the two substitute frames can be combined in a different way so that the torsional deflection of the original building can be determined using a general plane frame program. The overall displacements of the original frame can then be determined straightforwardly. The model makes the usual assumption of inextensible members and rigid in-plane stiffness of the floors and is appropriate for sway frames, although it can account for light bracing or cladding stiffness. The destabilising effect of axial load in the columns can be accounted for, as can the effect of shear deformation, although the latter is likely to be negligible in comparison with the approximations inherent in developing the model. The assumptions of the model are tested against the results of an 'exact' three-dimensional computer program

KEYWORDS

Proportional building structures, planar modelling, substitute frames, torsional analysis.

INTRODUCTION

The ability to analyse complex, multi-bay, multi-storey structures to a high degree of accuracy has become commonplace due to the widespread availability of powerful desktop computers and a variety of inexpensive finite element software. However, while such approaches are ideal for analysing final designs, their automatic selection in every case should be questioned. For example, the task of data

www.EngineeringEBooksPdf.com

preparation and checking can quickly become excessively onerous for complex structures, while the results will often be so voluminous that it is difficult to gain a clear picture of what is happening. In addition, such generalised methods use the same procedures to solve many different types of problem which were previously solved using problem-oriented solutions. Thus, little understanding of the problem is required to achieve satisfactory answers; the likelihood that gross errors will therefore be missed is high, and the engineer will not necessarily have been required to assess the important behavioural characteristics of the structure. In a number of cases, a feasible alternative is to use an 'approximate' technique that can sometimes offer solutions of sufficient accuracy for definitive checks and is virtually the only choice for intermediate checks during scheme development.

Approximate techniques for solving building structures have been given much attention over the years and many references, together with an extensive bibliography, are given by Stafford-Smith and Coull (1991). In addition, the problem of solving for the torsional displacements in a number of building structure types using planar techniques has been addressed by a number of authors, see Coull and Stafford-Smith (1973), Stafford-Smith and Cruevellier (1990) and Rutenberg and Eisenberger (1983,1986).

In the remainder of this paper, a substitute frame technique is developed for calculating the nodal displacements of a three-dimensional, multi-bay, multi-storey skeletal sway frame. It is based on the Principle of Multiples; requires only the use of a standard plane frame computer program and can yield almost exact solutions for certain combinations of structural topology and member properties.

SUBSTITUTE FRAMES AND THE PRINCIPLE OF MULTIPLES

The Principle of Multiples applies to unbraced, rigidly jointed, multi-bay, multi-storey plane frames and is exact on the basis of inextensible member theory. Its link to substitute frames is probably attributable to Grinter (1937) and is explained in some detail below.

Figure 1 applies to deflection calculations due to lateral load F. It is usual to perform the lateral load calculations with W = 0, but non-zero values of W can be used if the designer wishes to allow for the magnifying effect that vertical loads have on horizontal deflections caused by lateral loading. The Principle of Multiples proves that the frames of Figures 1(a)-(d) share the same horizontal deflections for lateral loading problems. The reasons are as follows.

In Figure 1, the k's are values of EI/L for the members, where EI is the flexural rigidity and L is length. Additionally, values are identical when the subscripts are identical, so that the frame of Figure 1(a) is symmetrical. Note also that the vertical loading is symmetric and the lateral loading is anti-symmetric i.e. the F of Figure 1(a) can be replaced by F/2 at the left hand end of the top team and F/2 at the right hand end of the top beam etc. Therefore the frame will sway with an anti-symmetric deflection pattern. Hence any frame which is identical to frame (a) must have the same deflected shape. Therefore any frame obtained by superposing N (which need not be integer) such frames, in the sense implied by frames (b) and (c), must also share the deflected shape of frame (a), even if the frames are all clamped together. Hence putting N=2 and N=4 gives the required proofs for frames (b) and (c), respectively. Moreover, frame (d) can be obtained by fastening together two frame (a)'s and a frame (b), which are situated side by side in the appropriate way. Since frames (a) and (b) share the same anti-symmetric deflection pattern, the process of fastening them together to form frame (d) leaves the deflections unaltered.

Most multi-bay, multi-storey, plane frames do not obey the Principle of Multiples, Horne and Merchant (1965), Lightfoot (1956). However, a well established method exists for reducing them to single bay multi-storey 'substitute' frames which can then be used to obtain approximate lateral loading results for

www.EngineeringEBooksPdf.com

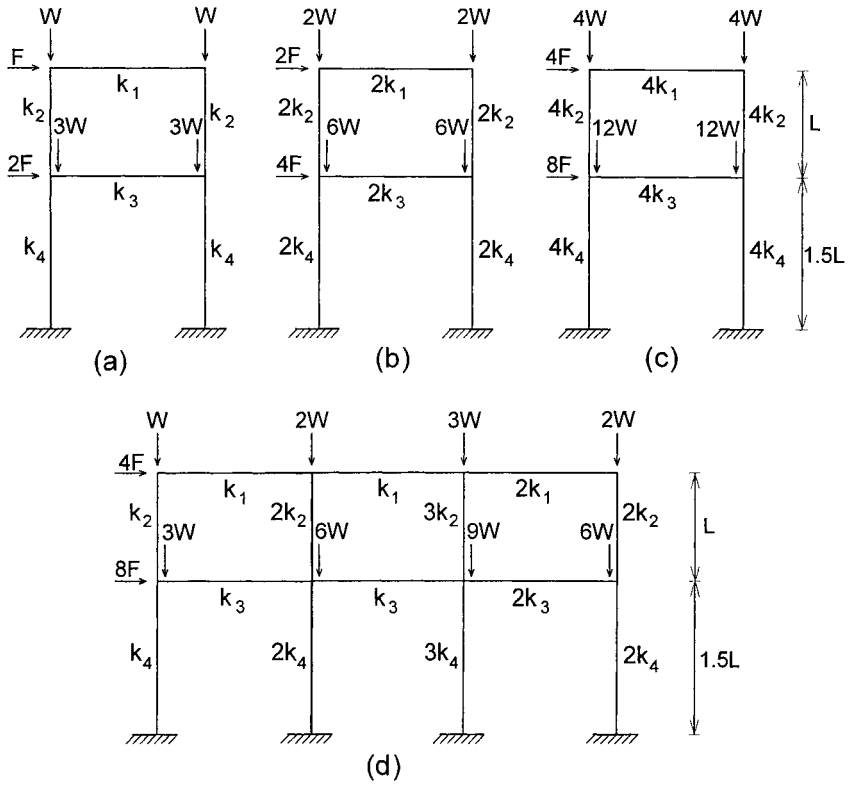

Figure 1. Frames (a) to (d) comply with the Principle of Multiples

the multi-bay case. The substitute frame has the same number of storeys and the same storey heights as the actual frame, but differs in that it has only one bay, is symmetric and carries symmetric vertical loads. The required details of the substitute frame are found from the actual frame as follows: the substitute column k is equal to half the sum of the k's for all actual columns at the same storey level; the substitute beam k is equal to the sum of the k's for all beams at the same storey level; the horizontal loads at the nodes at both ends of a beam are equal to half of the sum of the horizontal loads at all actual nodes at that storey level; and the values of W for the substitute columns are equal to half the sum of the axial forces in all actual columns at the same storey level.

Applying the above rules to the frame of Figure 1(d) gives the frame of Figure 1(c), on which the forces 4F and 8F can be replaced by anti-symmetrical pairs of forces. Hence it can be deduced that when a frame obeys the Principle of Multiples the rules yield a substitute frame which gives exactly correct results for the actual frame, remembering that inextensible member theory is assumed.

REMARKS AND ASSUMPTIONS

Before progressing to the development of the required substitute frames, the following remarks and assumptions should be noted.

www.EngineeringEBooksPdf.com

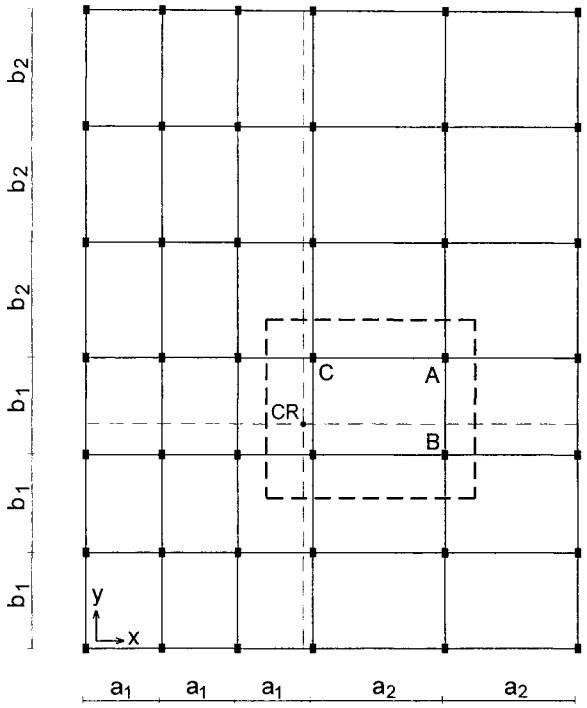

Figure 2. Typical floor plan with North-South direction vertical.
The dashed rectangle is expanded in Figure 3

The centre of pressure, CP, is the point at which the resultant horizontal load acts at each floor level. The horizontal distribution of the normal load on the structure is arbitrary, but is assumed to remain proportional with height. The centre of pressure at each floor thus lies on a single vertical line through the building. In similar fashion, the centre of rigidity, CR, at each floor level is the point through which the resultant horizontal forces at each floor level must be applied for the floors to translate without torsion. If a pure torsional moment is applied to the floor, the displacement occurs about the centre of rigidity. In order that the centre of rigidity for each floor should lie on a single vertical line through the building, it is necessary that the resisting frames are arranged such that their principal axes form an orthogonal grid in plan and are connected at each floor level by a rigid diaphragm. Furthermore, the frames lying in any one direction, see Figure 2, need to be proportional i.e. each frame needs to be a multiple of a reference frame, where the reference frame in the N-S direction need not be the same as that for the E-W direction. It is also assumed that inextensional member theory is used.

As noted previously, very few frames will approach such ideal conditions, but there is evidence to suggest that the method is not especially sensitive to structural approximations and solutions for typical building structures can be expected to produce results which are at least sufficiently accurate for preliminary design purposes. Thus, irregularities such as 'off-grid' beams and columns or skewed stiffness elements, etc. can be included by moving them to 'on-grid' locations with their stiffnesses factored appropriately to conform as far as possible to the theory of the following sections. In similar fashion, light bracing or cladding stiffness can be included, together with frames that do not conform precisely to the requirements of proportionality. However, care must be exercised to ensure that the final results are sufficiently accurate for their intended purpose.

www.EngineeringEBooksPdf.com

SUBSTITUTE PLANE FRAMES FOR THREE DIMENSIONAL STRUCTURES

Substitute Frames for Sway

Figure 2 shows the plan view of a multi-storey structure idealised as a set of plane frames running in the N-S and E-W directions. If we consider only a typical frame, frame i, running in the N-S direction, it is clear that we can develop an equivalent substitute frame with stiffness $\mathbf{s}_i$, using the procedure described earlier, in which the beam stiffnesses and column axial loads allow for the effect of the floor slabs. The corresponding force vector $\mathbf{p}_i$, is merely the vector of external loads deemed to be carried by the original frame. Thus the stiffness relationship for the typical substitute frame i is given by

$$\mathbf{p}_i = \mathbf{s}_i \mathbf{d}_i \tag{1}$$

where $\mathbf{d}_i$ is the corresponding vector of nodal displacements. It is then clear that if we add together the substitute frames arising from all such frames running in the N-S direction, we obtain a further substitute frame whose stiffness is given by

$$\mathbf{S}_{NS} = \sum_{i=1}^{n} \mathbf{s}_i \tag{2}$$

where n is the number of plane frames running in the N-S direction i.e. the individual substitute frames have been clamped together as described earlier. The corresponding force vector is given by

$$\mathbf{P}_{NS} = \sum_{i=1}^{n} \mathbf{p}_i \tag{3}$$

An identical argument enables us to write the equivalent expressions for the stiffness and force vector of the m frames running in the E-W directions as

$$\mathbf{S}_{EW} = \sum_{j=1}^{m} \mathbf{s}_j \tag{4}$$

and

$$\mathbf{P}_{EW} = \sum_{j=1}^{m} \mathbf{p}_j \tag{5}$$

The pure sway displacements $\mathbf{D}_{NS}$ and $\mathbf{D}_{EW}$, in the N-S and E-W directions, respectively, can now be found by solving the stiffness relationships

$$\mathbf{P}_{NS} = \mathbf{S}_{NS} \mathbf{D}_{NS} \tag{6}$$

and

$$\mathbf{P}_{EW} = \mathbf{S}_{EW} \mathbf{D}_{EW} \tag{7}$$

These displacements correspond to the equivalent original frame displacements, remembering that inextensional member theory is assumed. If the torsional deformation of the original structure is deemed to be negligible, this completes the analysis.

www.EngineeringEBooksPdf.com

Substitute Frames for Torsion

The moment resisted by a typical N-S substitute frame, shown in Figure 3 as AB, is

$$\mathbf{p}_i \, l_{xi} = \mathbf{s}_i \, \mathbf{d}_i \, l_{xi} \tag{8}$$

where $\mathbf{p}_i$ is the external force vector acting on the substitute frame corresponding to the original N-S plane frame i and $\mathbf{s}_i$ and $\mathbf{d}_i$ are the corresponding stiffness matrix and displacement vector, respectively, and l_{xi} is the distance of the substitute frame from the centre of resistance, CR.

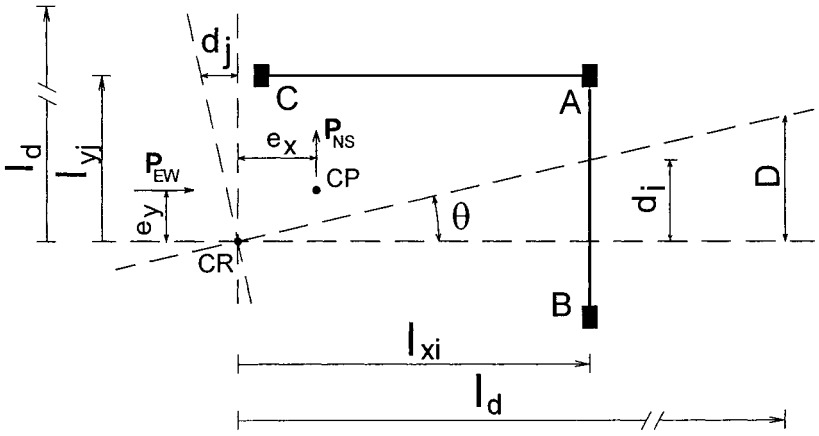

Figure 3. The expanded rectangle form Figure 2 showing two typical orthogonal substitute frames.

It is now convenient to refer this substitute frame to a convenient datum location a distance l_d from the centre of resistance along the x axis. Since its effect must remain unchanged we may write

$$\mathbf{s}_i \, \mathbf{d}_i \, l_{xi} = \mathbf{s}_i' \, \mathbf{d}_d \, l_d \tag{9}$$

where $\mathbf{s}_i'$ is the equivalent stiffness at location l_d and $\mathbf{d}_d$ is the corresponding displacement vector.

Now since the floor plates are assumed to be rigid in their plane

$$\mathbf{d}_d \, l_{xi} = \mathbf{d}_i \, l_d \tag{10}$$

Substituting (10) into (9) gives

$$\mathbf{s}_i' = \mathbf{s}_i \left(\frac{l_{xi}}{l_d} \right)^2 \tag{11}$$

Thus the effective stiffness of all such N-S substitute frames is given by

$$\mathbf{S}_{NS}' = \frac{1}{l_d^2} \sum_{i=1}^{n} \mathbf{s}_i \, l_{xi}^2 \tag{12}$$

where n is the number of N-S frames. In an exactly similar way, a typical E-W substitute frame, shown in Figure 3 as AC, resists a moment

www.EngineeringEBooksPdf.com

$$\mathbf{p}_j \, l_{yj} = \mathbf{s}_j \, \mathbf{d}_j \, l_{yj} \tag{13}$$

where the symbols have equivalent meaning to the previous derivation.

Again we refer the substitute frame to a datum location distance l_d from the centre of resistance, but this time along the y axis. The equivalent stiffness is then given by

$$\mathbf{s}'_j = \mathbf{s}_j \left(\frac{l_{yj}}{l_d} \right)^2 \tag{14}$$

and the effective stiffness of all such E-W substitute frame is given by

$$\mathbf{S}'_{EW} = \frac{1}{l_d^2} \sum_{j=1}^{m} \mathbf{s}_j \, l_{yj}^2 \tag{15}$$

Since both sets of frames resist the applied moment and their effective stiffnesses have been calculated for the same effective datum they can be added directly to give the total effective stiffness as

$$\mathbf{S}' = \mathbf{S}'_{NS} + \mathbf{S}'_{EW} = \frac{1}{l_d^2} \left\{ \sum_{i=1}^{n} \mathbf{s}_i \, l_{xi}^2 + \sum_{j=1}^{m} \mathbf{s}_j \, l_{yj}^2 \right\} \tag{16}$$

The vector of applied moments, **M**, can then be written down as

$$\mathbf{M} = \mathbf{S}' \, \mathbf{D} \, l_d \tag{17}$$

where **D** is the vector of in-plane substitute frame displacements corresponding to **S**′. In turn it can be seen from Figure 3 that

$$\mathbf{M} = \mathbf{P}_{NS} \, e_x - \mathbf{P}_{EW} \, e_y \tag{18}$$

and

$$\mathbf{D} / l_d = \boldsymbol{\theta} \tag{19}$$

where e_x and e_y are the eccentricities of the applied force vectors and θ is the required vector of torsional displacements. Hence, substituting (16), (18) and (19) into (17) gives

$$\mathbf{P}_{NS} \, e_x - \mathbf{P}_{EW} \, e_y = \left\{ \sum_{i=1}^{n} \mathbf{s}_i \, l_{xi}^2 + \sum_{j=1}^{m} \mathbf{s}_j \, l_{yj}^2 \right\} \boldsymbol{\theta} \tag{20}$$

EXAMPLE

The preceding theory will now be clarified by analysing a five storey building which has equal storey heights of 4.0m and a typical floor plan given by Figure 2 when $a_1 = 6.0$m, $a_2 = 10.5$m and $b_1 = b_2 = 7.5$m. The second moment of area for the beams is $I_x = 0.0072\text{m}^4$ and for the columns are $I_x = 0.009\text{m}^4$ and $I_y = 0.00625\text{m}^4$. The resultant horizontal forces acting in both the N-S and E-W directions at each storey level are $\mathbf{P}_{NS} = \mathbf{P}_{EW} = [3375 \quad 2700 \quad 2025 \quad 1350 \quad 675]^T$ kN and the eccentricity of the loads are $e_x = 2.25$m and $e_y = 0$, see Figure 3. Young's modulus for all members is taken as E=2.1E10 N/m^2. The second moment of area for the beams and columns in the substitute frame for sway parallel to the x direction are calculated as, respectively, $I_{beam} = (3\times7\times0.0072)+(2\times7)(6/10.5)\times0.0072 = 0.2088$ and

www.EngineeringEBooksPdf.com

$I_{column} = 0.5(6\times7\times0.00625) = 0.13125$, where the 7 represents the number of substitute frames to be added together, the 0.5 divides the total column I value between the two columns of the substitute frame and the ratio 6/10.5 factors the I value of a 10.5m beam to its equivalent for a 6.0m beam, thus enabling member properties to be summed for a datum beam length, L, since the required stiffness is proportional to I/L. This datum length is arbitrary but involves slightly more work if it does not correspond to an original member length. The equivalent values for sway in the y direction are given by $I_{beam} = 6\times6\times0.0072 = 0.2592$ and $I_{column} = 0.5(6\times7\times0.009) = 0.189$. The corresponding values for torsional motion, based on equation (16), are

$$I_{beam} = (6\times0.0072/21.75^2)(17.25^2+11.25^2+5.25^2+0.75^2+11.25^2+21.75^2) + [(0.0072/22.5^2)\times (3(7.5^2+15^2+22.5^2)\times2+2(7.5^2+15^2+22.5^2)\times2\times(6/10.5))\times(22.5^2/21.75^2)]\times(7.5/6) = 0.2202$$

and

$$I_{column} = 0.5[((7\times0.009)/21.75^2)(17.25^2+11.25^2+5.25^2+0.75^2+11.25^2+21.75^2) + (6\times0.00625/22.5^2)(7.5^2+15^2+22.5^2)\times2\times(22.5^2/21.75^2)] = 0.13247.$$

These values can then be used with other data in a general plane frame program, which in addition may be able to account for the destabilising effect of member axial force, shear deflection etc., to obtain the results in columns 2-4 of Table 1 below. The results can then be converted easily to displacements in the original structure, columns 6, 8 and 10, where they are compared with the equivalent results from an 'exact' three-dimensional program, columns 5, 7 and 9. Note that all results assume inextensional member theory which can be simulated in a general program by multiplying the cross-sectional area of the original member by 10^3.

Table 1. Comparative results for the above data.

	Deflection of the substitute frames in the x , y and θ directions			Displacement comparison for Real and Substitute Frames					
				Displacements at point (x=0, y=0) on Figure 2					
Storey level	δ_x	δ_y	θ	δ_x		δ_y		θ	
				Real	Sub.	Real	Sub.	Real	Sub.
5	.09012	.07845	.00047	.1043	.1007	.0712	.0703	.0005	.0005
4	.08067	.06982	.00042	.0933	.0902	.0633	.0626	.0004	.0004
3	.06415	.05508	.00033	.0741	.0717	.0499	.0493	.0003	.0003
2	.04217	.03560	.00022	.0486	.0471	.0322	.0318	.0002	.0002
1	.01752	.01418	.00009	.0200	.0195	.0128	.0127	.0001	.0001

CONCLUSIONS

The Abstract can be read as a statement of the conclusions.

REFERENCES

Coull A. and Stafford-Smith B. (1973). Torsional Analysis of Symmetric Building Structures. *J. Struct. Div. ASCE* **99:1**, 229-233.

Grinter L.E. (1937) *Theory of Modern Steel Structures*, Vol. 2., Macmillan, N.Y.

Rutenberg A. and Eisenberger M. (1983). Torsion of Tube Structures: Planar Formulation. *Comp. Struct.* **17:2**, 257-260.

Rutenberg A. and Eisenberger M. (1986). Simple Planar Modelling of Asymmetric Shear Buildings for Lateral Forces. *Comp. Struct.* **24:6**, 885-891.

Stafford-Smith B. and Cruevellier M. (1990). Planar Modelling Techniques for Asymmetric Building Structures. *Proc. Instn. Civ. Engrs.* **89**, 1-14.

Stafford-Smith B. and Coull A. (1991). *Tall Building Structures: Analysis and Design*, Wiley, N.Y.

www.EngineeringEBooksPdf.com

Advances in Steel Structures, Vol. II
Chan, Teng and Chung (Eds.)
© 2002 Elsevier Science Ltd. All rights reserved.

ON SOME PROBLEMS OF ANALYTICAL AND PROBABILITY APPROACHES TO STRUCTURAL DESIGN

J. J. Melcher

Civil Engineering Faculty, Brno University of Technology
Brno, CZ-662 37, Czech Republic

ABSTRACT

This paper deals with topical problems of improvement of structural design procedures by probabilistic approaches based on elaboration and evaluation of real measured data on strength and geometric characteristics of steel products. Traditionally, the design development process can be characterized through progressive transition from the analysis of ideal member incorporated into the ideal structure towards the analysis of actual members with initial imperfections embodied into the real structural system. Nevertheless, recently the essential advancement in structural design development proceeds from progressive transition away of the deterministic understanding of structural system behaviour towards the statistic and probabilistic approaches to structural reliability considering the random distribution of action and resistance characteristics. The reliability-based approach to structural analysis presents an efficient instrument for calibration and verification of practically used design criteria. Presented paper deals with general classification of material characteristics and presents examples of real product data and their distribution. Some questions of probability evaluation of design procedures are discussed through selected illustrative examples of reliability studies, namely the necessity of complex parallel study of both the action and resistance parameters in the specified design criterion, the problem of variable and not steady balanced values of reliability index of semi-probabilistic (limit state) design concept and finally the problem of expedient definition of steel grade not just by characteristic resistance but also through other material parameters. The paper illustrates both the general ideas and detailed examples of probability approaches to steel structural design.

KEYWORDS

Structural design, Probability, Resistance, Strength, Design criterion, Limit state, Partial safety factor.

INTRODUCTION

Traditionally, during the last decades, the development of design procedures of structural members had been based on the analysis of the ultimate (design) strength corresponding to the initially imperfect

www.EngineeringEBooksPdf.com

real member and structural system. Through improved analytical or numerical approaches and using the results of experimental techniques, all of the major load cases, section types and other decisive parameters are now explicitly accounted in the design requirements, namely the geometry and material characteristics together with real boundary conditions. Thus that design development process can be described by leading tendency characterized through progressive **transition from the analysis of ideal member incorporated into the ideal structure to the analysis of actual members with initial imperfections embodied into the real structural system** considering member restraints and mutual influence among various primary and secondary constructional parts.

The analytical solutions are important as a basis of specified regulations that should be written in a lucid and close form needed for practical designing. They also enable the transparent studies of different parameter influence to the results of structural design outcomes and issues.

In general, not even nowadays the analytical approaches can be held for the enclosed proposition accounting both the detailed specified provisions and general design concepts. Some supplementary solutions for lateral beam buckling of prevailing cases characterized by at least monosymmetric sections loaded transversely to their plane of symmetry has been presented by Melcher (1994, 1999), for example. Also some general ideas concerning the design limit state concept and their criteria has been discussed - see Melcher (1996), for example.

Nevertheless, another fundamental tendency represents recently the essential advancement in structural design development, namely the progressive **transition from the deterministic understanding of structural system behaviour towards the statistic and probabilistic approaches to structural reliability** considering the random distribution of action and resistance characteristics.

While the analysis of actual structural system is a problem of adequate calculation model of a certain constructional arrangement and its solution, the probability concept create general basis for design methods and criteria that are assigning for conventional (specified) level of structure reliability.

Despite significant development of probabilistic methods and theory of reliability, together with essential improvement of numerical analysis and computer techniques during last two decades, in most countries the background of contemporary and progressive codes predestinated for practical designing proceeds from the level of semi-probabilistic approaches - see also some starting information presented by Chen, W.F. and Atsuta, T. (1976). The lack of necessary real data on action and resistance characteristics and their distribution and especially the difficulties in solution of reliability problems of complex structural systems with various action combinations are restraining, for the time being, the use of full-probabilistic approaches mainly to very desirable calibration and verification studies of practical design procedures. Thus the statistical and probabilistic studies - in our understanding - represent an important tool for the development and verification of more sophisticated but simple and lucid provisions used in the steel design practice. Specifically, the reliability-based approach to the analysis of structure behaviour presents an efficient instrument for verification of design criteria including the relation of defined extreme (maximal) action to defined extreme (minimal) resistance of structural system. Parallel advance in full-probabilistic design methods should be contemplated.

In this paper some general ideas and problems of probability approaches to structural design will be illustrated, also through the measured data and real characteristics of steel structural members.

MATERIAL AND CROSS-SECTION CHARACTERISTICS OF STRUCTURAL PRODUCTS

Real strength capacity of a structural member depends primarily on its material and cross-sectional characteristics (i.e. on actual strength parameters and the tolerances of plate elements and section

www.EngineeringEBooksPdf.com

shape). While the general principles of the probability approach to structural design has been elaborated up to systematically perfected JCSS (2001) model code, the actual data on strength and geometry of different materials and large assortment of shapes and profiles are published rarely and deficiently, especially taking into account the time continuity. Moreover, some specified procedures defining very basic structural strength parameters could be confusing from the point of view of strictly conceived probability design concept.

So, for example, the member tensile design resistance $R_d = R_k / \gamma_M$ is, in general, defined through characteristic strength $R_k = A \,.\, f_y$ in which A is the cross-section area, f_y is the yield strength and γ_M is the partial safety factor relating to material strength. Currently accepted characteristic and design values generally correspond to 5 % and 0.1% fractile of the statistical distribution of resistance, respectively (see scheme in Figure 1). Thus the partial safety factor, covering the variability of the yield strength, as well as that of section properties, has to comply with the condition $\gamma_M > 1.0$.

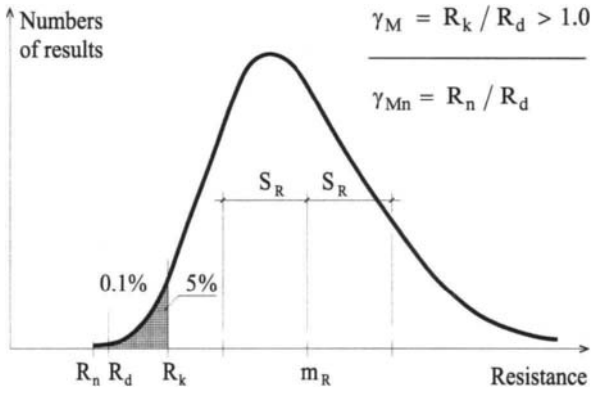

Figure 1: Distribution curve for steel member tensile resistance

The European standard practice takes the characteristic yield strength as corresponding to the specified guaranteed (nominal) minimum value for yield strength $f_y \equiv R_{eH}$ given in the relevant product standard for structural steels. For convenience, the nominal value characterizes the steel grade and basic plate thickness range. In reality this is not the true characteristic strength which in practice will clearly be higher.

Studies on recent production samples in the EU countries show that the mean value of the yield strength is about 15 to 20 % higher than the nominal value and minus plate thickness tolerances hardly get near maximum of 1 % (cross-sectional area A is approximately equal to its nominal value). Thus considering the nominal resistance value $R_n = A \,.\, R_{eH}$ for conventional characteristic value, the corresponding material partial safety factor $\gamma_{Mn} = R_n / R_d$, based on nominal value R_n and covering through statistical analysis of R_d the actual distribution of yield strength and plate thickness tolerances, depends on real quality of steel product and generally could be even less then 1.0.

According to recent statistical evaluation of basic European steel assortment, in the frame of conversion of European Prestandards to European Standards for design of steel structures, the value of $\gamma_{Mn} \equiv \gamma_{M0} = 1.0$ is being expected to be proposed for resistance of cross-sections to excessive yielding including local buckling and maybe also for resistance of members to instability assessed by member checks.

www.EngineeringEBooksPdf.com

The verification and evaluation of the quality and reliability of actual steel production is essentially significant for international trade and economic cooperation. Already during 1955-1975, in Czechoslovakia, the statistical evaluation of quality of steel production had been started with the view of assessment of the steel design strength defined according to principles of limit state design - see the fundamental work of Mrazik (1987) . At present, in the Czech Republic, the probability approaches to structural design are newly emphasized both in the frame of theoretical studies and analysis of large sets of real product data. The report on some recent results has been published by Fajkus et all. (2002). For illustration, some typical examples of that data demonstrating the steel production of dominant Czech producer in 1999-2001 will be presented further in this paper.

Figure 2 gives the example of statistical elaboration of results for plates made of steel grade S 235. The substitution of histogram by different types of distribution is shown.

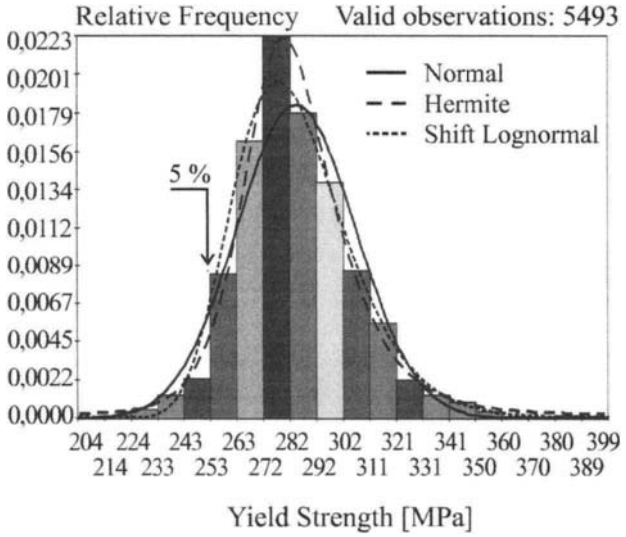

Figure 2: Distribution of plate yield strength made of steel S 235

The mean value of yield strength m_{fy} = 284.5 MPa and the standard deviation S_{fy} = 21.5 MPa have been determined. The distribution skewness is SK_{Md} = 0.60239 and kurtosis KU_{Md} = 4.5991. The characteristic value taken as 5% quantile is not sensitive to the distribution type. Using Hermite distribution the characteristic value is R_k = 252.8 MPa and the design value R_d = 212.8 Mpa.

Figure 3 shows the distribution of yield strength for IPE shapes made of steel S 235. The specimens were taken from section flanges. The results correspond to dimensions from IPE 160 to IPE 220.

TABLE 1
CHARACTERISTIC AND DESIGN VALUES FOR IPE SHAPES

	Characteristic value (5 % quantile)			Design value (0.1 % quantile)		
Distribution Type	Normal	Hermite	Shift Lognorm	Normal	Hermite	Shift Lognorm
Value	269.6 MPa	275.2 MPa	271.2 MPa	245.3 MPa	263.4 MPa	252.5 MPa

www.EngineeringEBooksPdf.com

Again as the most fitting distribution is taken the Hermite distribution. The mean value of the yield strength is m_{fy} = 297.3 MPa and the standard deviation S_{fy} = 16.8 MPa. The distribution skewness is SK_{Md} = 0.32462 and kurtosis KU_{Md} = 2.5415. The corresponding characteristic and design values are summarized in Table 1.

Undoubtedly, the statistical analysis of strength data based on the samples taken just from flanges of the rolled shapes gives results acceptable for the member resistance under bending. In case of tension higher yield strength values in thin profile web can contribute to increase of the load-carrying capacity of steel member remarkably. Thus the problem of yield strength variability along the cross-section of hot rolled shapes and the mutual correlation studies among different parts of the section needs also more attention.

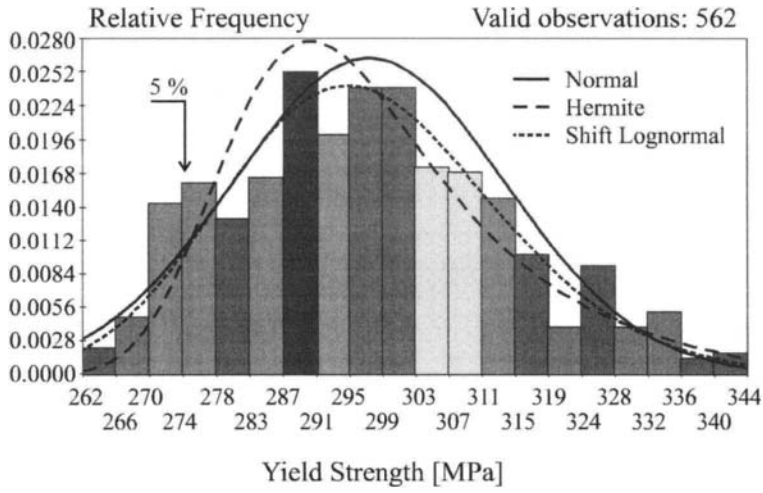

Figure 3: Distribution of yield strength for IPE shapes made of steel S 235

The value of the design resistance R_d takes into account both the distribution of the yield strength and section area depending on tolerances of the plated section elements. So besides the member strength characteristics also the actual geometrical section parameters should be contemplated when collecting basic data for statistical approach to structural design.

In the frame of the real geometric data elaboration the dimensions of all of the plated member elements and also the weight of the steel products were evaluated. When analyzing the cross-section geometry the application of the relative cross-section area is expedient. That parameter is defined by ratio of actual cross-section area to nominal area.

In Figure 4 some results of statistical evaluation of geometric data measured on hot-rolled shapes IPE are presented through histograms of area A and plastic section modulus W_{pl} . For tolerances of product weight the limit deviation assigned by corresponding code (EN 10034:1993 - Structural steel I and H sections. Tolerances on shape and dimensions) is ± 4 % for both the individual members and the gross delivery. The measurements have shown that 2% of resulting data are outside that limitation. In Table 2 basic geometric section parameters, namely the mean value m_X , the standard deviation S_X , the skewness SK_X and the kurtosis KU_X , are summarized. Together 371 valid observations have been analyzed.

www.EngineeringEBooksPdf.com

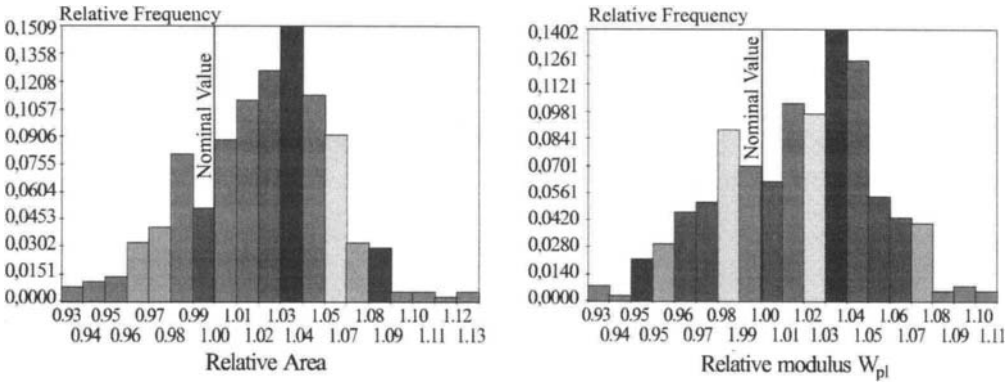

Figure 4: Histograms of area A and plastic section modulus W_{pl} of IPE shapes

TABLE 2
RELATIVE CROSS-SECTION CHARACTERISTICS OF IPE SHAPES

Value	m_X	S_X	SK_X	KU_X
A	1.025	0.03245	-0.2152	3.076
W_{pl}	1.019	0.03347	-0.2583	2.650

PROBLEMS OF COMPLEX PROBABILITY ANALYSIS OF ACTIONS AND RESISTANCE

For a steel member with action effect S_d and resistance R_d, the basic design criterion expressed in the semi-probabilistic (limit state) format can be presented through permanent (G), leading variable (Q_L) and accompanying variable (Q_{Ai}) actions in general form of

$$S_d = \gamma_G\, G_k + \gamma_{Q,L}\, Q_{L,k} + \sum \psi_A\, \gamma_{Q,Ai}\, Q_{Ai,k} \leq A \cdot f_{y,k} / \gamma_M = R_d \,, \qquad (1)$$

where subscript k stands for the appropriate characteristic value and γ are appropriate partial safety factors of action and material, respectively. The combination factor ψ_A allows for the resulting action of simultaneously affecting accompanying variable loading.

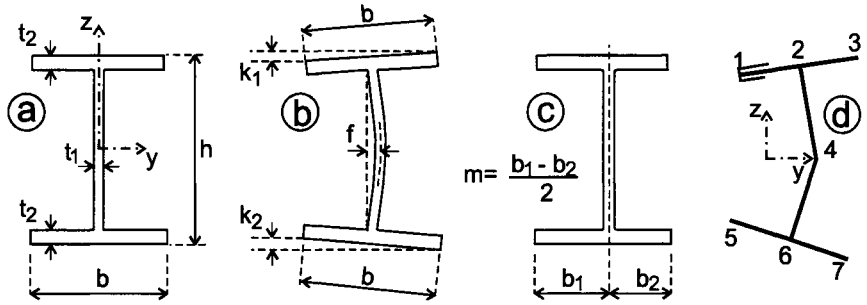

Figure 5: Typical initial geometric imperfections

www.EngineeringEBooksPdf.com

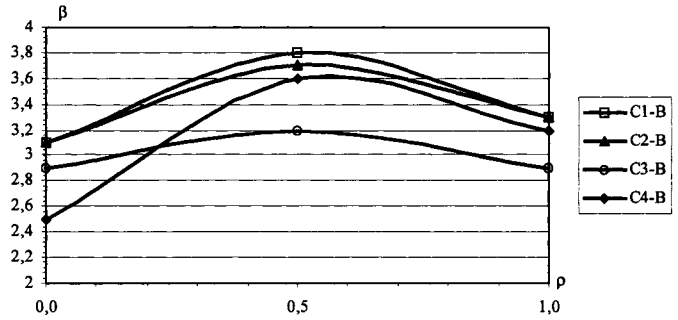

Fig. 6 Reliability index β relating with action parameter ρ

For the verification of the member reliability the complex consideration of both action and resistance sides in the Equation (1) is necessary. Moreover probabilistic studies should take into account the random set of initial imperfections and their distribution parameters. Thus for the solution of the reasonable calculation model, based usually on plated structural system elaborated by FEM, the statistical analysis is being introduced applying the advanced procedure of Monte Carlo simulation. The possibilities of the probability approach to structural design verification have been demonstrated in paper of Melcher J., Kala Z. and Kala J. (2000), for example. In Figure 5 the corresponding typical initial geometric imperfections introduced in calculations are illustrated.

At present also the problem of the choice of suitable values of partial safety factors of loads and material in Equation (1) is discussed, specifically considering the ratio of permanent to variable actions expressed through parameter $\rho = Q_k / (G_k + Q_k)$. Four cases C_i (γ_G ; γ_Q), namely C_1 (1.35 ; 1.50), C_2 (1.20 ; 1.60), C_3(1.10 ; 1.40) and C_4(1.00 ; 1.00) have been analyzed within the study of the compression member presented by Melcher (2002). From the results presented in Figure 6 it can be seen that the reliability concept of limit state design, in general, is not steady balanced and the selection of partial safety factors could contribute to discrimination or preference the constructional system with predominant permanent or variable type of loading actions.

For the classification of the steel grade considering the probability approach to structural design not just the material characteristic value but also its variation coefficient and skewness should be evaluated. This problem illustrated by Figure 7 has been opened in paper of Kala and Melcher (2002).

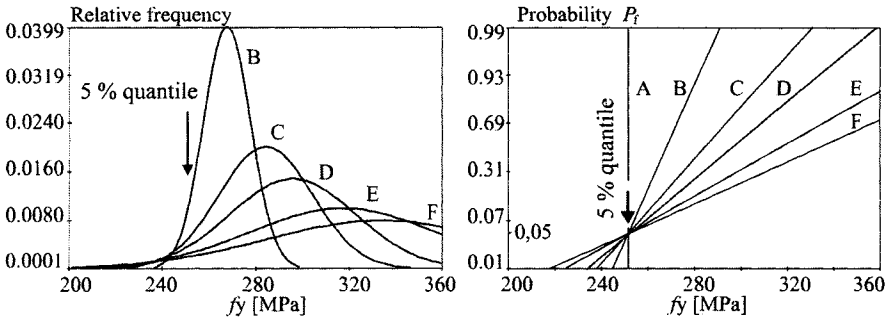

Fig. 7 The variety in yield strength distribution

www.EngineeringEBooksPdf.com

CONCLUSIONS

The reliability-based approach to structural analysis presents an efficient instrument for calibration and verification of practically used design criteria. Presented paper deals with general classification of material characteristics and presents examples of real data on yield strength and cross-section parameters and their distribution. Some questions of probability evaluation of design procedures are discussed through selected illustrative examples of reliability studies, namely the necessity of complex parallel study of both the action and resistance parameters in the specified design criterion, the problem of variable and not steady balanced values of reliability index of semi-probabilistic (limit state) design concept depending on ratio of permanent to variable loading and finally the problem of definition of steel grade not just by characteristic material resistance but also through its variation coefficient and skewness parameter. The evaluation of real data on action and resistance characteristics and their distribution create the precondition for the future effects of full-probabilistic design methods.

Acknowledgements

This paper has been elaborated under grant support of projects Reg. No. MSM 261100007 and GACR 103/00/0758. Author would like to acknowledge the participation of Dipl.-Eng. M. Fajkus and Dr. Z. Kala in the elaboration of data for probabilistic studies.

REFERENCES

Chen, W.F. and Atsuta, T. (1976). *Theory of Beam-Columns*, Vol. 1 and Vol. 2, McGraw/Hill, Inc., New York, 461 - 491.

Melcher J. (1994). Note to the Buckling of Beams with Monosymmetric Section Loaded Transversely to its Plane of Symmetry. In: *Proc. of the SSRC 1994 Annual Technical Session*, SSRC / Lehigh University, Bethlehem, 61 - 75.

Melcher, J. (1999). Kippen von Trägern als Stabilitätsproblem zweier Gruppen von Querschnittypen, *Stahlbau*, **Heft 1:68**, 24 - 29.

Melcher J. (1996). Design Limit State: Reality or (Science) Fiction?. In: *Proc. of the Int. Conference on Advances in Steel Structures ICASS '96 held in Hong Kong*, PERGAMON / Elsevier Science Ltd, Oxford, 579 - 584.

JCSS (2001). *Probabilistic Model Code*, Vrouwenvelder, T. and Faber, M. (Editors), Joint Committee on Structural Safety (JCSS), 12th draft, Part 1 - Part 3.

Mrazik, A. (1987). *Teoria spolahlivosti ocelovych konstrukcii (Theory of Reliability of Steel Structures)*, VEDA - SAV Publisher, Bratislava (in Slovak Language).

Fajkus, M., Melcher, J., Holicky, M., Rozlivka, L. and Kala, Z. (2002). Design Characteristics of Structural Steels Based on Statistical Analysis of Metallurgical Products, In: *Proc. of the Int. Conference EUROSTEEL 2002*, Coimbra (in print).

Melcher, J., Kala, Z. and Kala, J.(2000). The Analytical and Statistical Approaches to Lateral Beam Buckling, In: *Proc. of the SSRC Annual Technical Session and Meeting held in Memphis*, University of Florida - SSRC, 246 - 261.

Melcher, J. (2002). The Problems of Probabilistic Approaches to Structural Stability, In: *Proc. of the 15th ASCE Mechanics Conference*, Columbia University, New York (in print).

Kala, Z. and Melcher, J. (2002). Problems of Statistic Steel Grade Definition, In: *Proc. of the Int. Conference EUROSTEEL 2002*, Coimbra (in print).

www.EngineeringEBooksPdf.com

Advances in Steel Structures, Vol. II
Chan, Teng and Chung (Eds.)
© 2002 Elsevier Science Ltd. All rights reserved.

DESIGN OF STEEL FRAMES USING CALIBRATED DESIGN CURVES FOR BUCKLING STRENGTH OF HOT-ROLLED MEMBERS

S. L. Chan and S. H. Cho

Department of Civil and Structural Engineering, The Hong Kong Polytechnic University, Hong Kong, China

ABSTRACT

This paper presents a method of designing steel frames allowing for various sections. An analytical investigation was carried out to study the behaviour of a column member with both ends pinned and with various imperfection-to-length ratios. From the obtained results, the magnitudes of imperfection-to-length ratios of various sections are suggested for design and analysis of steel frames allowing for member buckling strength based on the Perry Robertson formula.

KEYWORDS

Column buckling, initial imperfection, residual stress, stocky column effect

INTRODUCTION

In the conventional design method of steel structures, linear theory is commonly adopted. The assumptions of a linear design procedure are that the members are perfectly straight in analysis and the buckling strength is checked separately by the design code such as BS5950 (2000).

All practical members contain imperfections that neither the Euler's buckling load nor the squash load is the actual failure load. The process of checking member strength separately implies an inconsistency in analysis and in design since the former analyses a frame with perfectly straight members.

Due to the availability of low-cost personal computers in the last decade, structural analysis using computer program is widely adopted. However, it is felt that, linear analysis does not normally meet our requirements to date. Instead, the second-order analysis allowing for practical features of external forces, structural geometry and imperfections is becoming a trendy design method. This paper describes an imperfection calibration exercise and concept in making the second-order analysis to have a consistent result with the buckling strength curves in the design code, BS5950 (2000).

www.EngineeringEBooksPdf.com

OBJECTIVES AND SCOPES

The investigation is aimed to determine the initial imperfection to be input in Nida (2002) to produce the buckling strength curves of various sections which fulfil the design rules given in BS5950 (2000). The sections to be investigated include universal beams (UB), universal columns (UC), circular hollow sections (CHS), square hollow sections (SHS), rectangular hollow sections (RHS) and channels. The magnitudes of initial imperfection are also determined and tabulated for use in conjunction with Nida (2002) for practical analysis of steel frames with various hot-rolled sections.

METHODOLOGY

As shown in Figure 1, the model used in the present investigation is a column with both ends pinned. The buckling or the effective length will be simply equal to the member length. The values of imperfection-to-length ratios (δ_0/L) of various sections in order to obtain the same buckling design curves given in BS5950 (2000) are determined analytically. The buckling design curves of these sections are generated using Nida by inputting designated values of δ_0/L. Then comparisons are made between the BS5950 curves and the curves by Nida to ensure these curves are close but conservative to the buckling curve in BS5950 (2000).

Figure 1: Simple column model for calibration studies

www.EngineeringEBooksPdf.com

CODE APPROACH

Design by BS449 (1969)

In the allowable stress design code BS449 (1969), the buckling design curve was derived from the expression derived theoretically as:

$$(p_E - p_c)(p_y - p_c) = \eta\, p_E p_c \tag{1}$$

in which p_y = design strength
p_c = compressive strength
p_E = Euler strength
η = a parameter defining the possible straightness of the member

The smaller root of the above formula can be obtained as:

$$p_c = \frac{p_E p_y}{\varphi + (\varphi^2 - p_E p_y)^{1/2}} \tag{2}$$

where $\varphi = \dfrac{p_y + (\eta + 1)p_E}{2}$

and η can be expressed as:

$$\eta = \frac{\delta_0 y}{r^2} = \frac{\delta_0}{L} \cdot \frac{y}{r} \cdot \frac{L}{r} = \frac{\delta_0}{L} \cdot \frac{y}{r} \cdot \lambda \tag{3}$$

where r = radius of gyration
y = distance from the centroid of the section to the extreme fibre of the section
λ = slenderness ratio $= L_E / r$

The initial imperfection could be taken as 0.1% of the member length. Consequently, the parameter η becomes:

$$\eta = 0.001 \cdot \frac{y}{r} \cdot \lambda \tag{4}$$

It is obvious that the parameters and thus the buckling strength are dependent of the geometry of the section only. The use of a lower bound value of 0.001y/r, however, did not take several other effects into consideration such as residual stress and stocky column effect. To cope with these effects, the new design code BS5950 makes the following modification.

Design by BS5950 (2000)

It is an ultimate limit state design code to replace the BS449 (1969). The major differences between BS5950 (2000) and BS449 (1969) regarding column buckling strength are:

1. The inclusion of section shape variation (i.e. the use of four compressive strength tables)

www.EngineeringEBooksPdf.com

2. The allowance for locked-in stresses (i.e. residual stresses)
3. The allowance for stocky column effect

Unlike the BS449 curve, which was derived theoretically, the four BS5950 curves were calibrated from experiment. Modifying the slenderness, the four buckling design curves were produced more accurately and η turned out to be a curve fitting parameter:

$$\eta = 0.001a(\lambda - \lambda_0) \tag{5}$$

where λ_0 = limiting slenderness = $0.2\pi\sqrt{E/p_y}$

a = Robertson constant = 2.0 for curve a
= 3.5 for curve b
= 5.5 for curve c
= 8.0 for curve d

EQUIVALENT IMPERFECTION BY Nida

When calculating compressive strength p_c, Nida takes into account the residual stress and initial imperfection via the use of centre initial imperfection of the member. Therefore, these effects are controlled by the value of δ_0/L, which are calculated using Eqn. 3 and Eqn. 5 as follows.

$$\eta = \frac{\delta_0}{L}\cdot\frac{y}{r}\cdot\lambda = 0.001a(\lambda - \lambda_0) \approx 0.001a\lambda \tag{6}$$

Note that this approximation tends to be more accurate for larger value of λ. Rearranging terms will give:

$$\frac{\delta_0}{L} = 0.001\frac{a}{y/r} \tag{7}$$

From Eqn. 7, it can be seen that the δ_0/L value depends on the section type, the axis of bending and the geometry of the section. In other words, for the same type of section and axis of bending, the value of δ_0/L is maximum if the section has the minimum value of y/r. Therefore, in order to obtain the lower bound solution of δ_0/L for each section type and axis of bending, a section having the smallest value of y/r (the critical section) is used. Table 1 summarizes the critical section for each section type and axis of bending and its corresponding value of δ_0/L calculated according to Eqn. 7.

www.EngineeringEBooksPdf.com

TABLE 1
CRITICAL SECTIONS FOR VARIOUS TYPES OF SECTION AND AXIS OF BENDING

Type of Section (S275 Steel)	Axis of Bending			
	x-x		y-y	
	Section	$\delta_0/L \cdot 1000$	Section	$\delta_0/L \cdot 1000$
UB	305x165x40	1.697	127x76x13	1.685
UC	356x368x129	3.076	356x406x634	2.860
CHS	508.0x10.0	1.389	-	-
SHS	300x300x6.3	1.598	-	-
RHS	300x200x6.3	1.513	500x200x8.0	1.732
Channel	Any axis:		152x89	4.474

With the above information, the buckling design curves of various critical sections are plotted using Nida. Figures 2 to 4 present the buckling design curves of these critical sections along with the BS5950 (2000) curves "a" to "c". The discrepancy between the curves by Nida and BS5950 is largely because of the negligence of the limiting slenderness in Eqn. 6 as it can be seen that in each figure two curves tend to converge with increasing slenderness. It can also be observed the discrepancy is larger in ascending order for curves a, b and c, of which the latter possess a larger value of Perry constant.

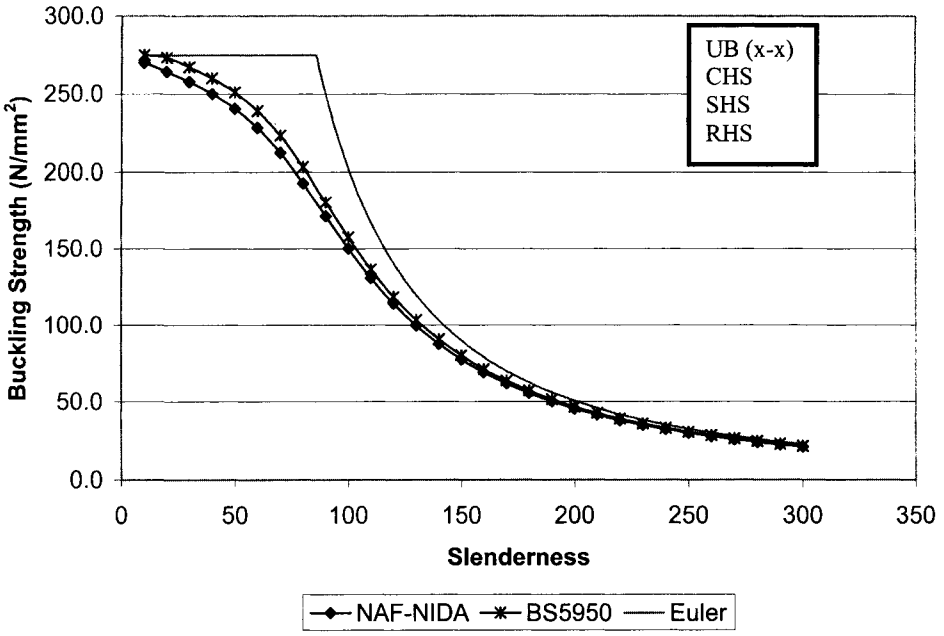

Figure 2: Buckling design curves (Curve a)

www.EngineeringEBooksPdf.com

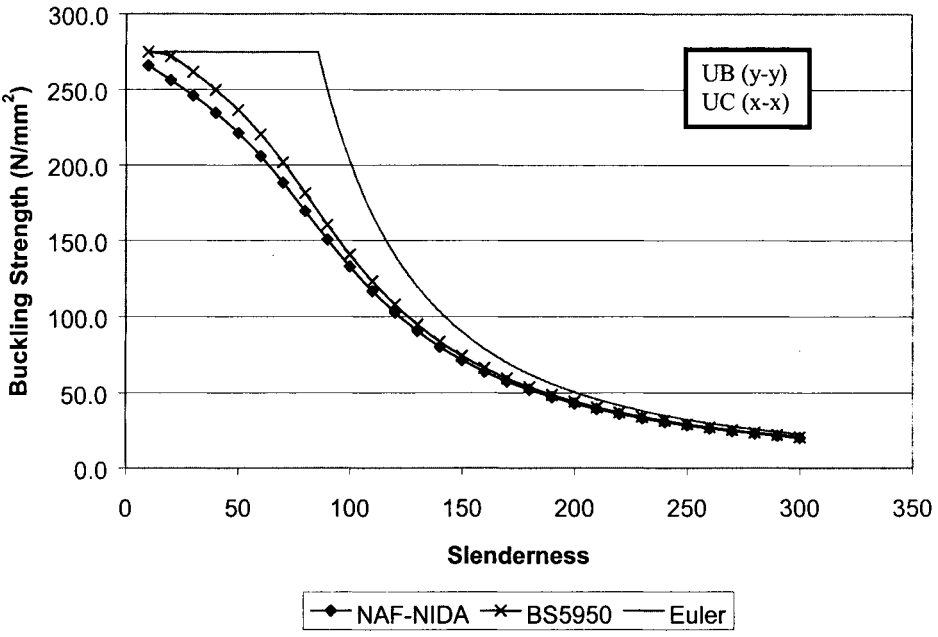

Figure 3: Buckling design curves (Curve b)

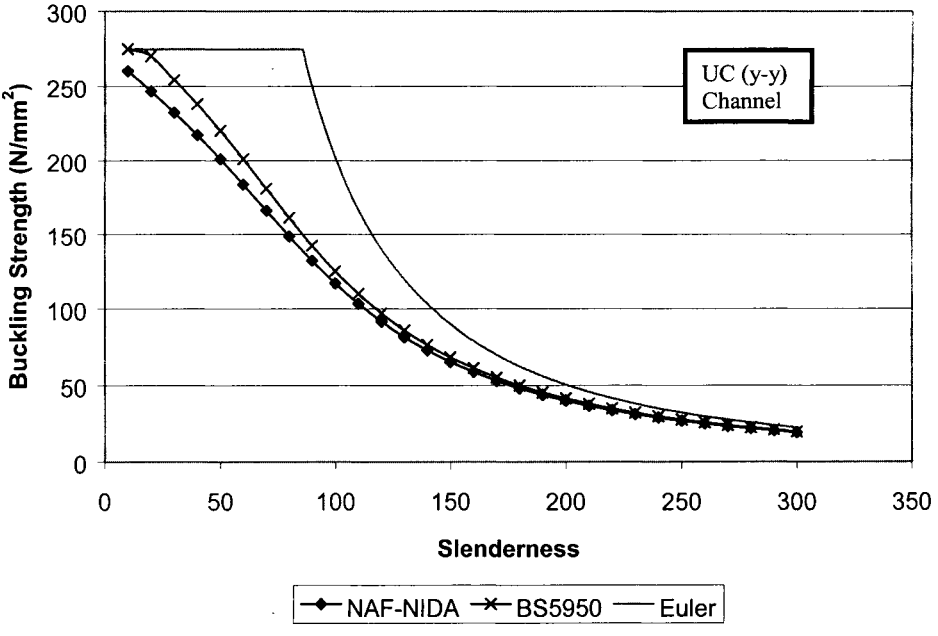

Figure 4: Buckling design curves (Curve c)

www.EngineeringEBooksPdf.com

REFINED SECOND-ORDER ANALYSIS METHOD FOR DESIGN

When designing imperfect steel frames using various section types of various dimensions using Nida, the tabulated non-dimensional values of imperfections, δ_0/L, listed in Table 1 should be used. These values will always give a lower bound compressive strength of compressive members.

CONCLUSION

Whilst the P-Δ effect can be considered by geometry update, the P-δ effect is included for various members by the procedure proposed in this paper. The discrepancy between the BS5950 curves and the Nida curves can be further minimized by fine tuning of the non-dimensional δ_0/L value. However, the present small and conservative discrepancy is considered as acceptable in practical design.

ACKNOWLEDGEMENT

The authors acknowledge the financial support of "Advanced Analysis and Design of Steel Frames Allowing for Beam-column Inelastic Buckling (Project no. PolyU5054/01E)" by the Research Grant Council grant from the Hong Kong SAR Government.

REFERENCES

British Standards Institution (1969). *BS449, Part 2 Specification for the Use of Structural Steel in Building*, BSI, London, England

British Standards Institution (2000). *BS5950, Part 1 Structural Use of Steelwork in Buildings*, BSI, London, England

Chan S.L. and Chui P.P.T. (2000). *Non-linear Static and Cyclic Analysis of Steel Frames with Semi-rigid Connections*, Elsevier

Chen W.F. and Chan S.L. (1995). Second Order Inelastic Analysis of Steel Frames using Element with Mid-span and End Springs. *Journal of Structural Engineering* **123:3,** 530-541

NIDA, Version 5 (2002). *Non-linear Integrated Design and Analysis Computer Program Manual*, HKPU

The Steel Construction Institute (1988). *Introduction to Steelwork Design to BS5950: Part 1*, SCI Publication

www.EngineeringEBooksPdf.com

This Page Intentionally Left Blank

www.EngineeringEBooksPdf.com

Advances in Steel Structures, Vol. II
Chan, Teng and Chung (Eds.)
© 2002 Elsevier Science Ltd. All rights reserved.

ANALYSIS OF THE BENDING STRENGTH OF U-SECTION STEEL SHEET PILES CRIMPED IN PAIRS

M.P. Byfield and R.J. Crawford

Cranfield University, RMCS Shrivenham, Swindon, SN6 8LA, UK

ABSTRACT

U-section steel sheet piles are one of the largest structural sections available and are a popular product for constructing large retaining walls throughout Europe and Asia. U-section piles have been widely used throughout the 20th Century. However, in recent years their bending strength has been an issue of uncertainty because they are connected together by interlocking joints located along the pile wall centreline. As the piles resist bending moments, inter-pile movement can significantly increase bending stresses. When this occurs, the wall is said to have exhibited reduced modulus action, also known as clutch slippage. U-shaped piles are normally driven in pairs and the common interlock may be crimped or welded to prevent this inter-pile movement. The resulting pair of piles is asymmetric in cross-section and may exhibit a reduced bending strength due to oblique (biaxial) bending. The recently introduced Eurocode 3 Part 5 has taken this into account and applies a reduction factor to the bending strength. The work presented herein has been carried out to determine suitable values for the reduction factor. The work has involved the experimental testing 1/6th scale U-piles and the research shows that freedom of lateral movement is essential to the development of oblique bending, and piles that are restrained against lateral movement will not exhibit significant oblique bending.

KEYWORDS

Codes & standards, piles & piling, retaining walls, substructures, steel structures, structural Eurocodes.

INTRODUCTION

The problem of reduced modulus action was first examined by Lomeyer (1934), although more recent investigations by Williams and Little (1992) and Schillings and Boeraeven (1996) have confirmed that interpile movement reduces the bending strength of U-piles below the fully composite bending strength normally assumed during design. The British Standard BS8002 (1994) provides useful information to designers as to which soil conditions one can expect will lead to reduced modulus action, although a large proportion of the U-section pile walls constructed in Europe and Asia have been designed without consideration of the problem and have experienced no adverse side-effects. In situations that BS8002 defines as likely to result in significant interpile movement engineers are advised to drive the piles in "crimped pairs" (Figure 1), whereby the common pile interlocks are

www.EngineeringEBooksPdf.com

pressed together to preventing inter-pile movement. Welding of the common pile interlock can also be carried out, although this is generally a more expensive solution. Furthermore, a numerical method has been developed for quantifying the effect of the discontinuities in shear transfer if crimp spacing is widened, Crawford and Byfield (2001). Piles may also be crimped into triples or quadruples, although this is not generally a preferred option because pile driving can be problematic.

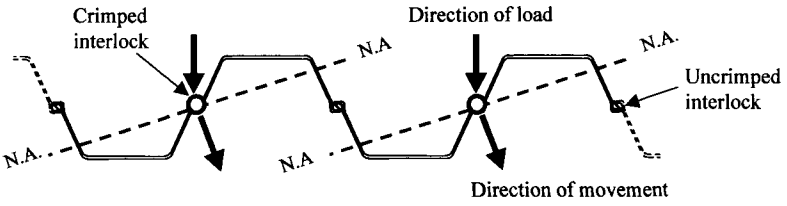

Figure 1: Crimped pairs of U-piles exhibiting oblique bending

It had been the UK design practice to assume that U-piles crimped in pairs achieved the full composite bending strength, however, work by Hartmann-Linden *et al* (1997) and Schmitt (1998) carried out in support of Eurocode 3 Part 5 (CEN, 1996) showed that crimped pairs of U-piles may not achieve their full composite bending strength because of a phenomenon termed "oblique bending". This results in the neutral axis of bending becoming inclined from the centre-line of the pile wall (Figure 1) and Eurocode 3 now stipulates that the bending strength of crimped pile pairs should be downgraded using a factor β_b, where the reduced bending strength, $M_{c.Rd}$, is given by:

$$M_{c.Rd} = \beta_B W_{pl} f_y / \gamma_{M0} \quad (1)$$

for class 1 and 2 cross-sections. For class 3 cross-sections:

$$M_{c.Rd} = \beta_B W_{el} f_y / \gamma_{M0} \quad (2)$$

Where:
W_{el} is the plastic section modulus determined for a continuous wall
W_{pl} is the elastic section modulus determined for a continuous wall
f_y is the yield stress
γ_{M0} is partial safety factor

Eurocode 3 and the UK National Application Document to Eurocode 3 propose values of β_B ranging from 0.8 to 1.0, reserving a value of $\beta_B = 1.0$ to the use of piles crimped into triples. Importantly oblique bending does not only increase bending stresses, it also creates significant lateral movement, as shown in Figure 1. Laboratory tests carried out by Hartmann-Linden *et al* (1997) on piles free to displace sideways under loading have clearly demonstrated this lateral movement, however, piles forming practical retaining walls are unlikely to be free to displace sideways due to factors such as the soil structure interaction.

The Effect of Lateral Restraint on Oblique Bending

The behaviour of laterally restrained piles is arguably more relevant to designers than laterally unrestrained piles, because the soil structure interaction *inter alia*, will limit freedom of sideways movement. The theoretical effect of oblique bending on crimped pairs of U-section piles restrained against lateral movement will therefore be considered. To do this the behaviour of crimped pairs of

www.EngineeringEBooksPdf.com

piles that are free to displace laterally should be examined, Figure 2A. In accordance with conventional stress analysis theory, the moment M_x applied about the centre line of the pile wall can be represented in terms of the partial moments $\overline{M}_x$ and $\overline{M}_y$, i.e.:

$$M_x = \sum\left(\overline{M}_x + \overline{M}_y\right) \tag{3}$$

where

$$\overline{M}_x = \frac{M_x}{1-\left(I_{xy}^2 / I_x I_y\right)} \tag{4}$$

and

$$\overline{M}_y = \frac{-M_x\left(I_{xy} / I_x\right)}{1-\left(I_{xy}^2 / I_x I_y\right)} \tag{5}$$

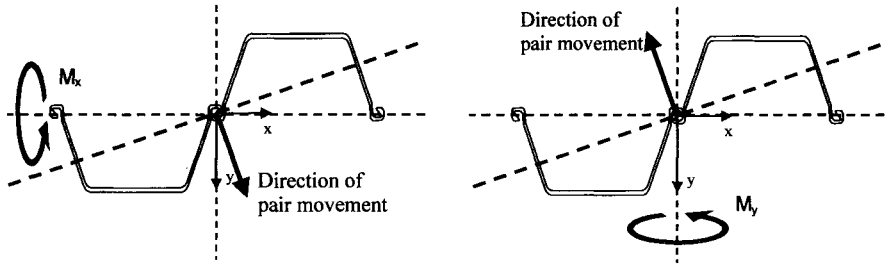

A: Behaviour of an unrestrained pile pair

B: Movement of wall due to lateral restraining moment

Figure 2

Importantly, the partial moment $\overline{M}_y$ causes lateral movement (normal to the y-y axis). If the piles are laterally restrained then the lateral restraining force will generate a moment M_y, Figure 2B. The resulting moment can be represented as the sum of the partial moments $\overline{M}_x^*$ and $\overline{M}_y^*$, each of which is defined as:

$$\overline{M}_x^* = \frac{-M_y\left(I_{xy} / I_x\right)}{1-\left(I_{xy}^2 / I_x I_y\right)} \tag{6}$$

and

$$\overline{M}_y^* = \frac{M_y}{1-\left(I_{xy}^2 / I_x I_y\right)} \tag{7}$$

The partial moment $\overline{M}_y^*$ will result in lateral movement and if full restraint against lateral movement is present the total lateral displacement must be zero. It follows that:

$$\sum\left(\overline{M}_y + \overline{M}_y^*\right) = 0 \tag{8}$$

Given this balance of moments about the y-y axis then the lateral restraining moment M_y can be defined, i.e.:

www.EngineeringEBooksPdf.com

$$M_y = M_x\left(\frac{I_{xy}}{I_x}\right) \tag{9}$$

Since M_y is defined, then the total moment about the major axis can be determine, i.e:

$$\sum\left(\overline{M}_x + \overline{M}_x^{\bullet}\right) = \frac{M_x}{1-\left(I_{xy}^2/I_xI_y\right)} + \frac{-M_y\left(I_{xy}/I_y\right)}{1-\left(I_{xy}^2/I_xI_y\right)} = M_x \tag{10}$$

Therefore, since the sum of the partial moments about the y-y axis is zero, oblique bending will not occur if crimped pairs of piles are restrained against lateral movement. Given that the section properties are constant along the length of the pile pair, then the lateral restraining force is given by the second derivative of equation 9, i.e.:

$$T = N\left(\frac{I_{xy}}{I_x}\right) \tag{11}$$

Where T is the lateral force required to prevent lateral movement
N is the force normal to the plane of the wall
I_x is the moment of inertia of the crimped pair about the x-x axis
I_{xy} is the product second moment of area

This demonstrates that the restraining force must be greater than the load applied normally to the wall by the factor I_{xy}/I_x, where values of I_{xy}/I_x range from 1.6 for the LX20 pile and 2.3 for the LX8 pile. Experimental tests carried on full-scale LX20 and LX8 piles reported by Hartmann-Linden *et al* (1997) confirm the theory, where the restraining force was found to be between 1.6 and 2.4 times the normal load.

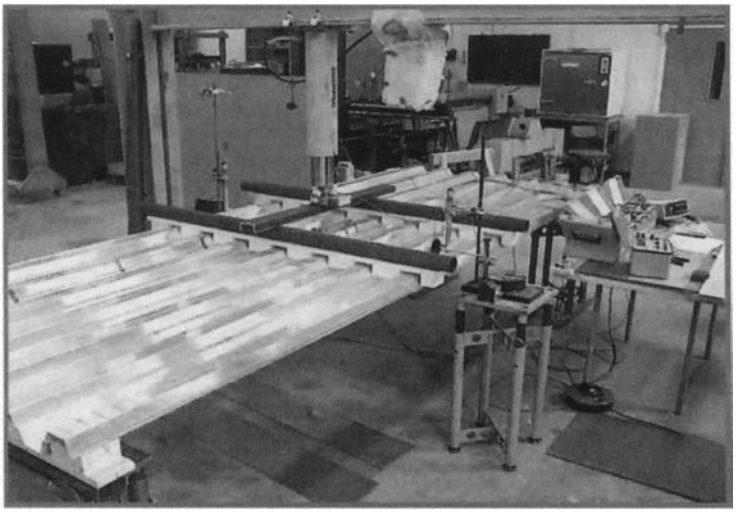

Figure 3: The test set-up

www.EngineeringEBooksPdf.com

EXPERIMENTAL TESTING

The experimental tests carried out in support of the development of Eurocode 3 typically comprised of a single pair of 6m long piles that were either completely free to displace sideways under load or were laterally restrained at reaction and load points only. The experimental tests presented herein were carried out in order to establish if a greater degree of lateral restraint would effect the development of oblique bending. In order to simulate the restraint provided in practical pile walls, panels of $1/6^{th}$ scale replica LX20 U-piles were tested. The tests simulated 20m long U-piles set in bays of up to 7.2m wide (at full-scale), see Figures 3 and 4. In order to demonstrate the main contention of the paper four separate tests are reported herein. These tests include Test 1 (laterally unrestrained) carried out on panel comprising 6 crimped pairs of piles with the freedom to translate sideways under load. Test 2 (partially restrained laterally) carried out on 6 crimped pairs that were laterally restrained at loading and reaction points only. The Test 3 (fully laterally restrained) was identical to Test 2 but for the provision of restraint against lateral movement along the complete length of the piles. Finally, Test 4 (fully composite) carried out on 6 single piles with all the interlocks crimped, preventing inter-pile movement and providing a benchmark test. The lateral restraint applied in Tests 2 and 3 was achieved by arranging two groups of three crimped pile pairs adjacent to one another, with one group mirroring the other. The arrangement was such that lateral movement from one group of pile pairs was equal and opposite to the movement from the opposite set of piles, in effect providing mutual restraint, Figure 5. No significant lateral deflection was recorded during these tests.

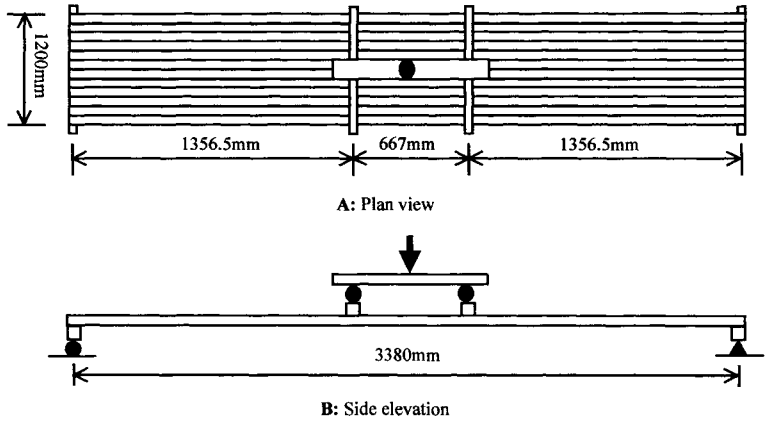

Figure 4: Side elevation of test set up

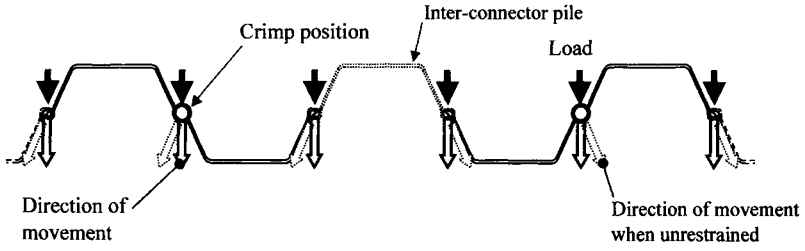

Figure 5: Provision of lateral restraint for tests 2 and 3

www.EngineeringEBooksPdf.com

The test piles were formed from aluminium extruded from a high precision, specially commissioned die, Figure 6. The elastic modulus of the piles was 70.81kN/mm^2 for the stress range applied during the tests. Crimping was simulated using 4.0mm diameter blind-rivets inserted through 4.2mm holes drilled through the pile interlocks. During each of the tests a single, centrally located pile pair was strain gauged. Gauge locations were chosen such that the complete stress distribution for a pile pair could be established, with 4 gauges on the outer pans, and 4 adjacent to the interlocks. All these gauges were located at mid-span. The data from gauges were used for graphically plotting the experimental stress distributions sketched in Figure 7. The theoretical stress distribution sketched for test 1 (unrestrained) assumes full oblique bending. For the tests 2, 3 and 4 all the theoretical stress distributions assume full composite action, i.e. no oblique bending.

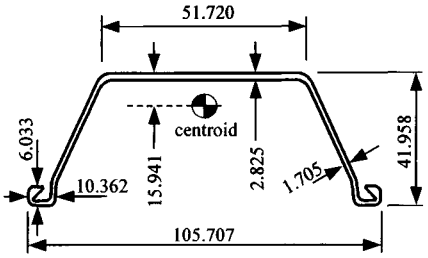

Figure 6: Test pile dimensions

RESULTS AND DISCUSSION

Test 1: Piles Laterally Unrestrained

The experimentally recorded stresses conformed extremely closely to the oblique bending stresses predicted from theory. These results are in accordance with findings previously reported, with oblique bending resulting in a 75% increase in bending stress over that predicted for full composite action, with the neutral axis inclined at an angle of 17° from the horizontal. As predicted from theory, lateral movement of up to 30% of the downward movement was observed under the vertically applied load and based on this test the β_b factor for laterally unrestrained pile pairs should be calculated assuming full oblique bending. However, it is unlikely such freedom of movement would be present in a permanent retaining wall, given that the soil structure interaction, together with the capping beam and tie rods would be likely to restrain sideways movement.

Test 2: Piles Partially Restrained Laterally

The partial restraint against lateral movement reduced the extent of oblique bending, although experimental stresses still significantly exceeded those stresses expected for fully composite action. Comparison between the maximum experimental stress and the maximum theoretical stress, assuming full composite action, reveals a β_b factor of 0.78, which is close to the lower-bound figure of 0.8 recommended in Eurocode 3.

Test 3: Piles Fully Laterally Restrained

The comparison between experimental and theoretical stresses, Figure 7, reveals that the additional restraint has been important in preventing oblique bending, which can be seen to have had a minor

www.EngineeringEBooksPdf.com

effect in the interlocks, but little effect in the pile pans (flanges). Comparison between the maximum theoretical and experimental stresses produces a β_b factor of 0.94.

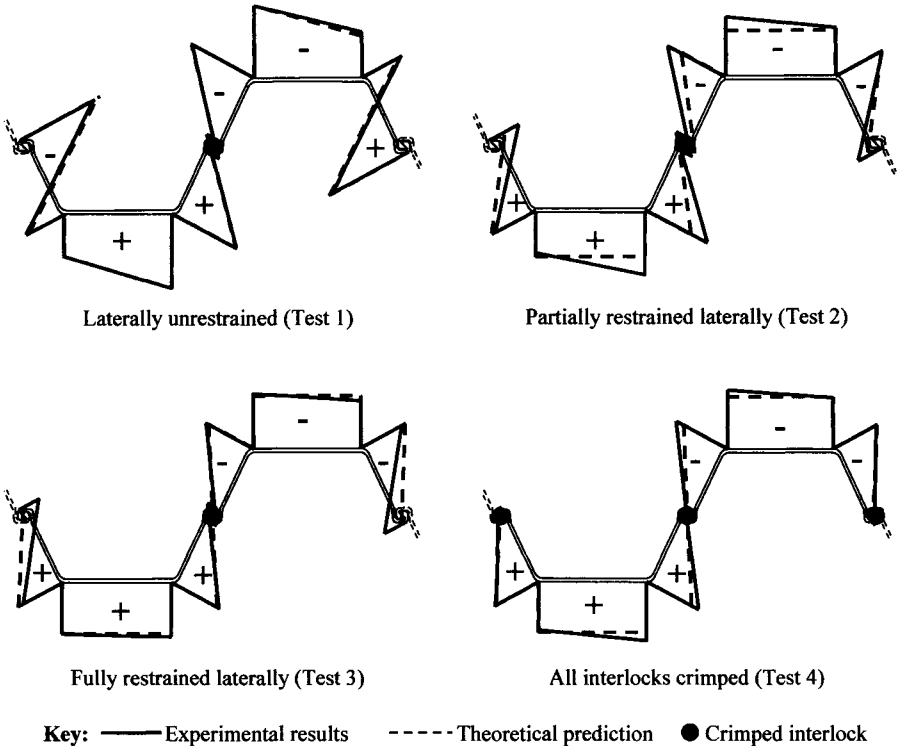

Figure 7: Experimentally observed stress distributions compared with theoretical stress predictions

Test 4: Piles Fully Composite

This final test, whereby all the interlocks were crimped, produced a very similar stress distribution to that for test 3, confirming that oblique bending has been largely prevented.

Given that the comparison between experimental data from test 3 showed no significant difference to the data from test 4, in which all interlocks were crimped, a β_b of 1.0 would seem to be justified for piles with adequate restraint against lateral movement. Alternatively, if the retained soil has low strength in shear the β_b factor of 1.0 may still be used, providing lateral restraint is provided by another means. A practical method to provide lateral restraint would be to use the restraining method demonstrated in test 3, whereby crimped pairs are arranged in bays, separated by single interconnecting piles, see Figure 8. Thus, piles provide mutual restraint against lateral movement, as is the case for Z-section steel sheet piles.

www.EngineeringEBooksPdf.com

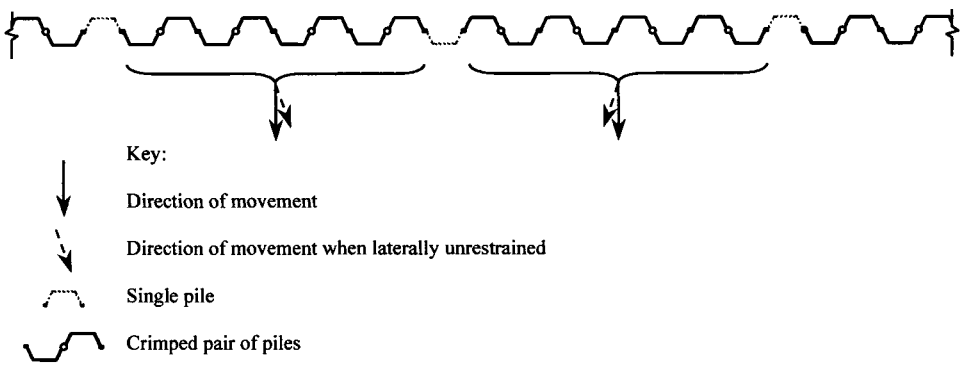

Figure 8: A practical method of providing lateral restraint

CONCLUSIONS

This paper reports a series of tests that assess the effect that freedom of lateral movement has on the development of oblique bending, which has been shown to be largely prevented where piles are fully restrained against lateral movement. The test reported on partially restrained piles confirm the findings from similar tests carried out in support of the development of the Eurocode 3-Part 5, i.e. that the provision of only partial restraint against lateral movement would not prevent oblique bending. In practice, restraint against lateral movement may be provided by a combination of the soil-structure interaction, capping beam and tie rods *inter alia*. However, where concern exists regarding the degree of restraint available, then an alternative arrangement of piles can be used, similar to that used to restrain the piles during the experimental testing described herein.

REFERENCES

British Standards Institute (1994). BS 8002: Earth retaining structures, BSI, London.

CEN (1996). Eurocode 3: Design of steel structures, Part 5: Piling. BSI, London, UK.

Crawford, R. J. and Byfield, M. P. (2001). A numerical model for predicting the bending strength of Larssen steel sheet piles. Proc. Conf. on Structural Engineering, Mechanics and Computation (SEMC), Capetown, 393-400.

Hartmann-Linden, R. et al, (1997). Development of unified design rules for steel sheet piles and introduction into Eurocode 3, Part 5. RWTH, Aarchen, Germany.

Lohmeyer E. (1934). Discussion to 'Analysis of sheet pile bulkheads' by P. Baumann. *Proc. Am. Soc. Civ. Engrs,* Vol. 61, No. 3, 347-355.

Schillings, R. and Boeraeve, P. (1996). Design Rules for Steel Sheet Piles – ECSC Project 7210-SA 127/523/840. CRIF Dep. of Steel Con., Liège, Belgium.

Schmitt, (1998). Bending behaviour of double U sheet piles. International Sheet Piling Company, ProfilARBED – Luxembourg.

Williams, S.G.O. and Little, J.A. (1992). "Structural behaviour of sheet piles interlocked at the centre of gravity of the combined section". *Proc. ICE Structures and Buildings*, Vol. 94 Issue 2.

www.EngineeringEBooksPdf.com

Advances in Steel Structures, Vol. II
Chan, Teng and Chung (Eds.)
© 2002 Elsevier Science Ltd. All rights reserved.

A TEXTBOOK FOR THE NEW CANADIAN STANDARD-*STRENGTH DESIGN IN ALUMINUM*

D. Beaulieu

Département de génie civil, Faculté des sciences et de génie
Université Laval, Québec, QC Canada, G1K 7P4

ABSTRACT

The fourth edition of the Canadian Standard CAN/CSA-S157, *Strength Design in Aluminum* and its Commentary are due for publication in year 2002. This edition, based on the concept of limit states design is primarily for applications in buildings, but is written in a form that will find use for all types of aluminum load-bearing components and assemblies. In order to assist the designers in their calculations and the educator in their teaching of structural aluminum, a comprehensive 800 page textbook has been written based on this new Standard, and incorporates supplement excerpts from corresponding American and European Standards, This accompanying manual is meant to be highly practical since it not only covers the theory but also contains numerous well detailed design examples covering every single aspect of strength and stability design of aluminum structures. In this respect, it should appeal to all. The book is published both in French and English and comes with a teaching tool on CD-ROM. The paper presents the principal characteristics of the Standard, and the content and particularities of the textbook.

KEYWORDS

Aluminum, analysis, codes, design, education, stability, standards, strength, structures, textbook.

INTRODUCTION

The Canadian Standard for the design of aluminum structures has not been updated since 1983 (CSA, 1983). This is a very long period considering the rapid growth of the industry in many fields of application, especially in Europe and in America. New and comprehensive design standards have been produced in Europe (ECS, 1998) and in the United States (AA, 2000) in the last few years, leaving Canada way behind. An attempt to update the Canadian Standard has been made in the early 1990 but the resulting draft has never been adopted for obscure reasons. The draft was based on an ISO document (ISO, 1995) developed in Europe during the same period.

www.EngineeringEBooksPdf.com

The 1992 Draft was finally resurrected and updated into CAN/CSA-S157-2001, *Strength Design in Aluminum* (CSA, 2001 a) which is due for publication in 2002, together with a Commentary (CSA, 2001 b).

The best Codes and Standards are the short ones with a thick commentary, from the eye of the principal users: the practitioners. It is even better when a Design Handbook is published alongside to the Standard and its Commentary. This is the case in the United States, for instance (AA, 2000).

The next best situation is the publication of a comprehensive textbook on the same material, which could be written in such a way as to appeal to both the educators and the practitioners. This is what is happening in Canada.

The objective of this paper is to introduce a new book on the design of aluminum structures which is in its editorial phase and which is likely to be available approximately at the same time as the Standard itself.

THE CANADIAN STANDARD

The fourth edition of CAN/CSA-S157 supersedes earlier editions that were issued in 1962, 1969 and 1983. The first two were based on working stress design in imperial units and the 1983 edition used limit states design and SI units.

Requirements to satisfy the ultimate limit state form the core of the new Standard. As a document referenced by the *National Building Code of Canada* (CNRC, 1995), the load factors and resistance factors specified by that Code are given. However, because the design expressions predict the characteristic resistance of components and connections, the Standard will find use in any field of engineering in which known applied loads are to be supported.

Serviceability limit states depend on the desired behavior under service load for each particular application, and are not specified in the Standard. For components used in buildings, for instance, reference is made to the *National Building Code of Canada*.

The procedures to determine the resistance to the various modes of buckling (flexural, torsional, lateral-torsional, shear, etc.) have been unified, making use of formulas relating the normalized slenderness to the normalized buckling stress. From research, it has become evident that the straight-line buckling formula did not provide a reasonably uniform margin of safety over the full range of slenderness and it has been replaced by a modified Perry-type formula, which is a more widely accepted model.

The unification of the buckling curves is probably the single most important item making the use of the new standard a simple exercise. A simple set of normalized curves, shown in Figures 1 and 2 is used throughout the Standard for the evaluation of the compressive resistance of plates and members. All stiffened plate and member buckling conditions are treated in the same manner, as long as the slenderness (λ),which characterizes a given condition, is known. The slenderness is normalized to give $\overline{\lambda}$ which, in turn, gives the normalized buckling stress $\overline{F}$ when the proper curve is used. Below $\overline{\lambda}_o$, buckling does not occur.

The normalized buckling stress is used in Equation 1 to give the buckling stress F_c:

$$F_c = \overline{F}\, F_o \tag{1}$$

www.EngineeringEBooksPdf.com

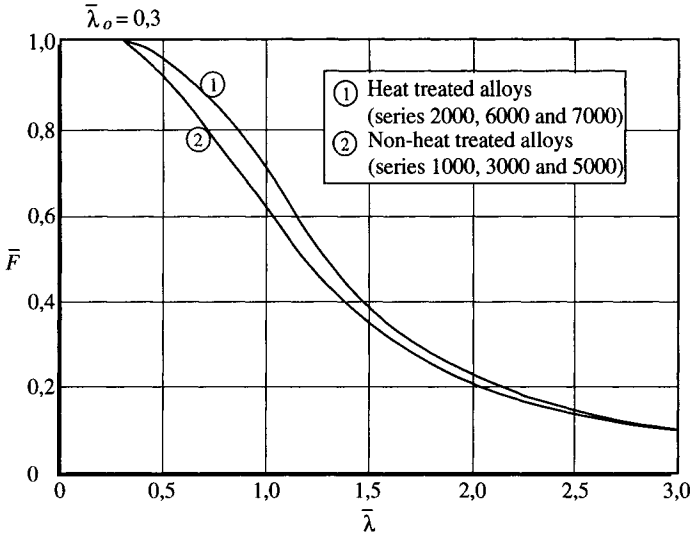

Figure 1 : Normalized buckling stress for columns and beams

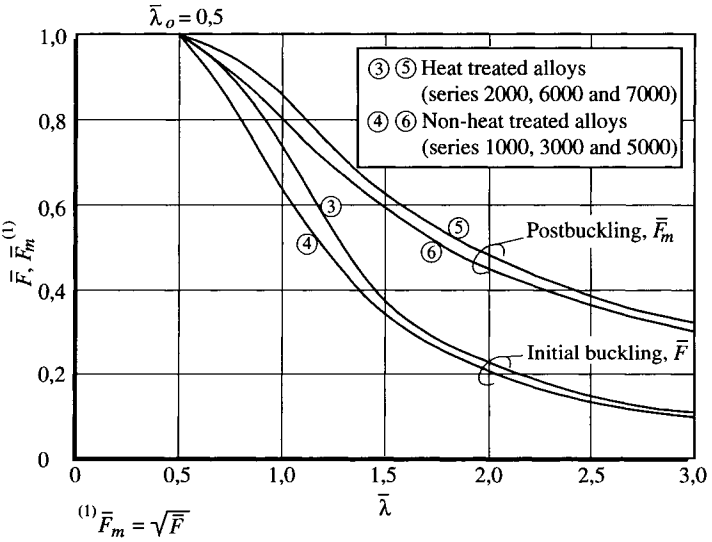

Figure 2 : Normalized buckling stress and postbuckling strength for plates

The limiting stress (F_o) allows, among others, to account for different types of local plate buckling and welding conditions. It is generally equal to the yield strength of the base metal (F_y), especially for plates. In this manner, the influence of welds and local buckling on the capacity of columns and beams is fully accounted for. Means have been introduced to make use of the basic buckling curve for each alloy type in the design of flat elements with postbuckling strength, a subject which is much more thoroughly treated in the new standard,

The design of welded joints has also been expanded.

www.EngineeringEBooksPdf.com

A NEW TEXTBOOK

Structural aluminum is not used as much in Canada as it is in many other countries or as it should. The reasons are obvious: it is no taught in universities but with a few exceptions, the designers are not properly informed, the standard is too old, the industry is passive in this field of application, and there is barely any design material available (textbook, handbook, software, etc.). Consequently, the Canadian engineers must often rely on material published elsewhere to do their design or they use their own.

To address this important problem, a design Standard will be published along with a comprehensive textbook (Beaulieu, 2002 b). The handbook will come later and hopefully, the situation will improve. Meanwhile, it is urgent to give the educators in colleges and universities the material required to teach the students all they need to know about aluminum as a material and how to use aluminum in structural applications, and to give the technicians and engineers in practice enough information for them to become acquainted with this new material and the tools they need to perform their designs.

The book contains nine chapters for a total of more than 800 pages. Since it is written in a simple language for the students, it is easy to read and to understand. The book is presented in a manner very similar to previous books co-authored by the same author on structural steel design (Picard and Beaulieu, 1981; Picard and Beaulieu, 1991). These textbooks have been used in universities for many years and they are used *very intensively* by practicing engineers, since they contain simple descriptive information and, above all, several comprehensive design examples covering the whole theory. It might be interesting for the reader to know that the third edition of this book is in preparation and is due to come out in 2003 (Beaulieu et al., 2003). It will be published for the first time both in French and in English.

The textbook on structural aluminum will also be published in the two languages. It has been written in French and is presently being translated by the Chair of the *CSA Technical Committee on Strength Design in Aluminum* himself. The English version will hopefully be available at the end of 2003, a full year after the publication of the French version.

The book is based on the new Canadian Standard CAN/CSA-S157-2001 but is *self-contained and is code independent*. In other words, it never directly refers to a specific clause of the standard and it does not follow the same order. Each concept is explained, followed by the resulting design equations and illustrated by a design example.

The book also heavily refers to the American (AA, 2000) and European (ECS, 1998) Standards. However, once again, no reference is made to specific clauses. This was considered necessary in order to present the best of three universes in a single document. The textbook can therefore be regarded as a tentative draft for a uniform Standard. This was probably the most difficult challenge, considering the different philosophy of each Standard. Duplications and unnecessary comparisons were to be avoided in order to prevent the "pizza effect". The chapter on fatigue, for instance, compares the different details and *S-N* curves of each standard but finally demonstrates that the basic theory is the same. In this sense, it opens the door to a uniform Standard, a dream which should come true.

To ease the teaching of the whole content of the textbook, since it all comes down to education, a CD-ROM will be prepared using an appropriate format (Acrobat Reader and PowerPoint), for different types of presentations (short and long ones).

To give an idea of the scope of the textbook and a means to appreciate its usefulness, the content of each chapter is introduced and is lightly described in the following paragraphs.

www.EngineeringEBooksPdf.com

Chapter I – Introduction (8 p.)

This short chapter is general in content. It introduces aluminum by presenting its history and listing the main characteristics of the materials.

Chapter II – Characteristics of structural aluminum (130 p.)

This is a basic and important chapter which is written for those who have never used aluminum as a structural material. This is the reason why it has also been published as a separate document (Beaulieu, 2000 a). The potential users of this document do not have to be civil or mechanical engineers. However, since it is not meant to be a thesis on metallurgy, it might no appeal to experienced metallurgists.

The chapter covers the production and transformation of aluminum, the classification of the different alloys, the basic metallurgical treatments, the influence of welding, the surface treatments, the physical, mechanical and chemical properties, the fire resistance, the weldability, and the corrosion resistance of aluminum, in that order.

Chapter III – Design Principles (95 p.)

This chapter is more general in nature. It contains sections on the management of a project, on limit states (ultimate and serviceability) and other design approaches (Standards are compared), on loads and load combinations, and on all types of stability considerations. Simple methods to account for P-Δ effects are presented, followed by two detailed design examples.

Chapter IV – Tension members (41 p.)

Chapter IV is the first of a series covering the behavior of structural members. It describes the behavior or tension members, accounting for net sections, eccentricities and the influence of welding. It contains four design examples.

Chapter V – Plates and members in compression (110 p.)

Chapter V covers what is generally considered as a difficult topic and, through seven detailed design examples, makes the design of stiffened plates and members loaded in compression look simple.

Its content includes a discussion on failure modes, on factors susceptible to affect buckling, on plate and standard member buckling, and on the compression resistance of built-up members, stiffened panels, curved plates, tubes and sandwich panels. The torsional buckling modes are given special attention.

Chapter VI – Members in pure and combined flexure (110 p., estimated)

This most important and basic chapter describes the flexural resistance of standard members (cross-sectional resistance and lateral-torsional buckling), the shear and compressive resistances of stiffened webs, the behavior of members loaded in flexion-tension and flexion-compression (beams-columns), the design of stiffened girders and composite (aluminum-concrete) beams, and the shear resistance of various types of sections, like stiffened panels, sandwich panels, curved plates and tubes. This is all illustrated in eight design examples.

www.EngineeringEBooksPdf.com

Chapter VII – Mechanical Connections (100 p., estimated)

Chapter VII is a very detailed chapter on the design of various types of mechanical connections.

It covers detailing, the resistance of bolts (zinc-coated or cadmium-plated steel bolts, stainless steel bolts and aluminum bolts), rivets and screws, the resistance of mechanically joined plates, the resistance of contact and friction-type connections, the resistance of concentric or eccentric connections loaded in shear or tension, and the resistance of screwed connections. It also describes other type of connections most suited for repetitive industrial applications, and glued connections. A total of seven design examples concludes the chapter.

Chapter VIII – Welded connections (90 p., estimated)

Many types of welding techniques are described in this chapter but the GTAW, GMAW and PAW processes receive more attention. The resistance of butt welds (full and partial penetration) and fillet welds is covered in detail. The design of concentric and of different types of eccentric fillet welded connections is described in full. The design of welded connections looks simple through the six design examples provided.

Chapter IX – Fatigue (120 p., estimated)

Fatigue is not a simple subject, especially in aluminum structures. Chapter IX is a practical chapter which integrates the recommendations of the three referenced Standards in order to provide the designer with the best and most complete available information for fatigue design considerations. It contains a large amount of details with an objective: to make the student or the designer aware of the importance of structural detailing in structures subjected to cyclic loading.

Basic fracture mechanics principles are presented in order to describe fatigue crack growth. All factors susceptible to affect fatigue resistance are discussed. Concepts related to fatigue cracking, like inspection, detail improvement, prevention, repair and reinforcement, are introduced. Chapter IX contains five design examples including one on the "Hot Spot" method.

CONCLUSION

The Canadian designers, educators and students alike now have appropriate tools to consider aluminum as an interesting alternative to other structural materials in applications requiring lightness or corrosion resistance: a new Standard and a new comprehensive Handbook. The handbook is self-contained and code independent, which means that it can be used effectively in any other countries.

References

Aluminum Association (The). (2000). Aluminum Design Manual, *Specifications for Aluminum Structures — Building Load and Resistance Factor Design*. Part 1 b., Washington D.C., USA.

Beaulieu, D. (2002a). *Les Caractéristiques de l'aluminium structural*. Les Presses de l'Université Laval, Québec, Canada, 132 p.; *The Characteristics of Structural Aluminum* (English version to be published in early 2003).

www.EngineeringEBooksPdf.com

Beaulieu, D. (2002b). *Calcul des charpentes d'aluminium*. Les Presses de l'Université Laval, Québec, Canada, 800 to 850 pages (expected, since being edited at the time of the submission of this paper); *Design of Aluminum Structures* (English version to be published in 2003).

Beaulieu, D., Picard, A., Grondin, G., Tremblay, R., and Massicotte, B. (2003). *Design of Steel Structures*, (in preparation), Canadian Institute of Steel Construction, Willowdale, Ontario, Canada, 1600 p. (estimated).

Canadian National Research Council. (1995). *National Building Code — Canada*. Ottawa, Ontario, Canada.

Canadian Standards Association. (1983). *Strength Design in Aluminum*. CAN3-S157-M83, Rexdale, Ontario, Canada.

Canadian Standards Association. (2001a). *Strength Design in Aluminum*, CAN/CSA-S157-2001, Rexdale, Ontario, Canada.

Canadian Standards Association. (2001b). *Commentary on CSA Standard CSA-S157-2001, Strength Design in Aluminum*, Rexdale, Ontario, Canada.

European Committee for Standardization. (1998). *Eurocode 9 : Design of Aluminium Structures – Part 1-1 : General Rules – General Rules and Rules for Buildings*. ENV1999-1-1: 1998E. Brussels, Belgium.

International Organization for Standardization. (1995), *Aluminium Structures — Material and Design — Ultimate Limit State Under Static Loading*. ISO/TR 11069 : 1995, Genève, Switzerland.

Picard, A, and Beaulieu, D. (1981). *Calcul aux États Limites des Charpentes d'Acier*. Canadian Institute of Steel Construction, Willowdale, Ontario, Canada, 450 p.

Picard, A. and Beaulieu, D. (1991). *Calcul des Charpentes d'Acier*. Canadian Institute of Steel Construction, Willowdale, Ontario, Canada, 850 p.

www.EngineeringEBooksPdf.com

This Page Intentionally Left Blank

www.EngineeringEBooksPdf.com

INDEX OF CONTRIBUTORS

Volumes I and II

Albermani, F. 429
Al-Mahaidi, R. 245
Anderson, J.C. 221
Ansourian, P. 713

Bakht, B. 773
Bambach, M.R. 617
Batista, E. 341
Bauer, D.B. 181
Beale, R.G. 303, 461
Beaulieu, D. 1209
Bechara, E. 205
Benaddi, A. 181
Berry, P.A. 487, 495
Bezkorovainy, P. 617
Bradford, M.A. 95, 625
Bridge, R.Q. 479, 511, 519, 667
Burns, T. 617
Bursi, O.S. 81
Byfield, M.P. 139, 261, 1201

Cameron, N.J.K. 1079
Camotin, D. 331, 341
Chan, S.L. 321, 543, 913, 1017, 1153, 1169, 1193
Chan, T.H.T. 791, 799
Chan, T.M. 1095
Chau, K.T. 1017
Chen, G.D. 641
Chen, H. 213, 285
Chen, J. 897
Chen, J.F. 755
Chen, S.F. 559
Chen, Z.Q. 849
Chiew, S.P. 1033
Chilton, J.C. 755
Chin, G.P.W. 351
Cho, S.H. 1193
Choy, S.C. 543
Chu, K. 763
Chung, K.F. 121, 351, 437, 445, 649
Chusilp, P. 69
Combescure, A. 659, 981
Coret, M. 981
Couchman, G.H. 261
Crawford, R.J. 1201
Cui, X.Q. 1161

da S. Vellasco, P.C.G. 253
Davies, J.M. 57, 401
Detandt, H. 783
Dezi, L. 535
Dhanalakshmi, M. 139, 261
Ding, X. 599
Dong, S.L. 15
Du, X.X. 453
Duan, J.X.J. 221
Duan, Y.F. 849
Dubina, D. 409, 989
Dundu, M. 383
Dymiotis, C. 321

Elchalakani, M. 567
Emi, T. 189
Espion, B. 783

Fang, Z.Z. 551
Feifel, E. 683
Fish, R.A.D. 357
Fujiwara, H. 1051
Fulop, L.A. 409

Gardner, L. 43
Ge, H.B. 607
Girão Coelho, A.M. 277
Gläsle, M. 713
Godley, M.H.R. 303, 461
Goto, Y. 171, 1051, 1145
Greiner, R. 667
Grundy, P. 237, 1043
Grzebieta, R.H. 567
Gu, J.X. 1153
Guan, D.Q. 1009, 1025
Guo, L. 799
Guo, W.H. 857
Guo, Y.J. 453
Guo, Y.L. 147, 155, 163, 551, 641, 873, 1161

Han, L.H. 583, 591, 1127, 1135
Han, Q.H. 229
Han, Y. 155, 551
Hancock, G. 3, 311, 421
Hao, W.Q. 155
Harada, H. 823
Harada, K. 815
Ho, H.C. 437, 445
Holst, J.M.F.G. 729
Hosain, M.U. 527
Howson, W.P. 1177
Huang, C.W. 921
Huang, X. 947
Huang, X.Q. 955
Huang, Z.F. 1111, 1119
Huang, Z.W. 1033
Hui, J.T.Y. 955
Huo, J.S. 1127

Iguchi, T. 197

Janjic, D. 831
Javidruzi, M. 755
Jullien, J.F. 675, 973

Kawanishi, N. 1145
Kemp, A.R. 383
Kennedy, J.B. 807
Kihara, S. 197
Kitipornchai, S. 429
Ko, C.H. 121
Ko, J.M. 791, 849
Kozlowski, A. 269
Kubo, Y. 815

Lam, D. 503
Law, S.S. 905, 913
Lee, G.C.M. 807
Lee, M. 357
Legay, A. 659
Leoni, G. 535
Leu, L.J. 921
Li, G.Q. 599
Li, J.J. 1169

www.EngineeringEBooksPdf.com

Li, K. 453
Li, L. 1009
Li, Z.F. 213, 285
Li, Z.X. 791, 799
Liang, Q.Q. 625
Lie, S.T. 1033
Liew, J.Y.R. 1061
Lim. J.B.P. 391
Limam, A. 675
Lin, X. 737
Ling, T.W. 245
Liu, C.Y. 921
Liu, T. 155, 163
Liu, W. 583
Liu, X.L. 229
Liu, Y. 365
Lu, G. 931, 939, 947

Mäkeläinen, P. 1103
Mashiri, F.R. 237, 1043
Melcher, J.J. 1185
Mikami, I. 633
Milojkovic, B. 303
Miyazaki, Y. 633
Mufti, A.A. 773
Muramoto, Y. 823
Mursi, M. 575

Nagahama, K. 341
Nagai, M. 815
Namba, H. 189
Nethercot, D.A. 43, 391
Neves, L.C. 253
Ni, Y.Q. 849
Nip, T.F. 503
Niwa, K. 633

Obata, M. 171, 1051
Oehlers, D.J. 471
Outinen, J. 1103

Pan, Y. 147
Pashan, A. 527
Patrick, M. 511, 519
Petrovski, T. 205
Pi, Y.-L. 95
Pircher, H. 831
Pircher, M. 375, 667, 831
Prola, L.C. 331

Quispe, L. 421

Rafezy, B. 1177
Rasmussen, K.J.R. 357, 617
Ren, G.X. 873
Rotter, J.M. 27, 729
Rubal, M. 205

Saal, H. 683
Sakurai, T. 763
Samaan, M. 963
Sennah, K.M. 807, 963
Seracino, R. 471
Sha, W. 1095
Shen, Z.Y. 105
Shi, Y.J. 213, 285, 295
Shum, K.M. 865
Silvestre, N. 341
Simões da Silva, L. 253, 277
Song, C.Y. 693, 703
Song, Z.S. 105
Staquet, S. 783
Stratan, A. 989
Sun, D.K. 865
Susantha, K.A.S. 607

Tabuchi, M. 189, 197
Tadros, G. 773
Tan, H.B.A. 575
Tan, K.H. 1111, 1119
Tanaka, T. 189, 197
Tao, Z. 591
Teng, J.G. 693, 703, 721, 737, 745
Ting, S.K. 1111
Tong, G.S. 129
Tong, L.W. 237, 1043

Ukur, A. 567
Unterweger, H. 839
Usami, T. 69, 607
Usmani, A.S. 1079
Uy, B. 575, 625

Vafai, A. 755
Vaux, S. 311
Vincent, Y. 973
Vitali, A. 535
Voutay, P.A. 401

Wang, A.J. 649
Wang, B. 939
Wang, H. 873
Wang, Q. 1025
Wang, Y.Q. 213, 285, 295
Wang, Z. 295
Wheeler, A. 375, 479
Wilkinson, T. 205
Wong, C. 311
Wong, H.T. 745
Wong, M.B. 1071, 1089
Wong, Y.L. 543
Wright, H.D. 625
Wu, Z.M. 913

Xia, H. 889
Xiao, R.Y. 351
Xiao, Y. 221
Xiao, Z.G. 1001
Xu, L. 1135
Xu, Y.L. 857, 865, 881, 889, 897

Yamada, K. 1001
Yamaguchi, E. 815
Yamao, T. 823
Yan, Q.S. 889
Yang, D. 3
Yang, Y.F. 583, 1127, 1135
Yang, Z.C. 881
Yeh, S.H. 921
Yi, W.J. 1009, 1025
Young, B. 365
Yu, H.X. 1061
Yu, T.X. 947, 955

Zandonini, R. 81
Zhang, L. 129
Zhang, R.C. 897
Zhao, X.L. 237, 245, 567, 1043
Zhao, Y. 15, 721
Zhong, J.H. 559
Zhou, X.M. 599
Zhou, Z.H. 321, 1153

www.EngineeringEBooksPdf.com

KEYWORD INDEX

Volumes I and II

Actively controlled platform, 881
Actuator dynamics, 881
AIJ-SRC, 543
Aluminum, 1209
Ambient vibration measurement, 921
Analysis, 1209
Anisotropy, 617
Antisymmetric, 95
Application, 15
Arches, 95
Arching, 773
Attachment, 1001
Automobile, 939
Axial compression, 737
Axial restraint, 1111
Axisymmetric, 659

Bare steel tubes, 479
Beam, 129, 939
Beam-column, 155, 163, 591
Beam-column connection, 213
Beam-column element, 913
Beam element, 1153
Beam-to-column joints, 989
Bearing capacity, 583
Bending load, 675
Bending moment, 823
Biaxial bending, 559
Biaxial compression, 625
Bifurcation analysis, 357
Bolted moment connections, 437
Bolted steel shells, 745
Bonded, 543
Box-girder, 807
Box section, 69, 163
Braced frame, 269
Bracing system, 807
Bridge deck, 773
Bridge deck modelling, 839
Bridges, 495, 535, 807
Bridge stay cable, 849
Buckle, 155
Buckling, 27, 57, 69, 95, 321, 401, 461, 575, 683, 693, 703, 721, 729, 737, 745, 755, 763
Buckling resistance, 703
Buffeting analysis, 865
Buffeting force, 889
Bumper, 939
Butt weld, 989

Cable-mass structure, 873
Cable-membrane, 1169
Cable-stayed bridge, 831, 857
Camber, 783
Cassettes, 57
Catenary action, 1111
Chimneys, 27
Circular tubes, 245, 947
Cladding, 429
Closed steel ribs, 511
Code and standards, 1201
Codes, 1209
Cold-formed, 429
Cold-formed section, 453
Cold-formed steel, 57, 205, 365, 391, 421, 461, 1103
Cold-formed steel beams, 331
Cold-formed steel cassette section, 401
Cold-formed steel C-section, 351
Cold-formed steel members, 341
Cold-formed steel purlins, 445
Collapse criteria, 229
Collapse properties, 229
Column buckling, 1193
Columns, 365, 575, 583, 1135
Combined loads, 675
Compatibility condition, 1161
Component method, 253, 277
Composite, 503
Composite beam, 487, 495, 511, 519, 551
Composite bridge(s), 783, 839
Composite columns, 559
Composite connections, 261
Composite construction, 261, 625, 745
Composite floor, 269
Composite floors in fire, 1079
Composite floor systems, 527
Composite steel-concrete girders, 535
Composite structures, 575
Compression, 3, 57, 401, 823
Computer simulation, 889
Concrete arch bridge, 831
Concrete-filled, 253
Concrete-filled HSS columns, 1127
Concrete-filled SHS or RHS, 1135

www.EngineeringEBooksPdf.com

Concrete-filled steel column, 607
Concrete filled steel tube, 591
Concrete-filled steel RHS, 583
Concrete-filled tubes, 479, 567
Concrete shells, 745
Connection deformability, 535
Connections, 205
Constitutive behaviour, 973
Construction loading, 807
Contact elements, 351
Continuous composite beam, 487, 495
Contraflexure, 487
Corrosion, 1145
Corrugation, 713
Coupled instability, 57, 401
Cracks, 755, 1017
Cramping force, 189
Crash, 939
Crashworthiness, 963
Creep, 535, 583, 1111
Creep coefficient, 583
Creep effect, 1061
Critical location, 799
Critical moment, 129
Critical temperature, 1119
Cross beam, 815
Cross-section classification, 43
Cross-sectional distortion, 955
Cross stiffener, 641
Crosswind, 857
Cruciform joint, 1001
Crushing of tubes, 931
Cuplok, 311
Curved, 807
Cyclic, 409
Cyclic behaviour, 913
Cyclic loading, 763, 989
Cylinders, 683, 737
Cylindrical shells, 675, 713, 729, 737, 755
Cylindrical steel pier, 763

Damage, 221
Damage cumulation, 105
Damage theory, 1051
Damper installation configuration, 849
Deck slab, 773
Deck-type steel arch bridge, 823
Deformation capacity, 277
Deformation limit, 237
Design, 321, 421, 461, 745, 1089, 1209
Design criterion, 1185
Design development, 121, 445
Design evaluation, 807
Design method, 583
Design philosophy, 27
Design suggestions, 453
Destructive mechanism, 453
Development, 15
Dimple, 729
Direct strength, 421
Direct strength approach, 401
Distortional buckling, 341, 649
Distortional post-buckling, 331
Double-angle, 181
Double skin composite panels, 625
Double-skin composite sections, 567
Ductile crack, 197
Ductile fracture, 1051
Ductile tearing, 931, 947
Ductility, 69, 253, 261, 277, 591, 633, 763
Dynamic analysis, 409, 607, 1145
Dynamic interaction, 889
Dynamic magnify factor, 873
Dynamic programming, 905
Dynamic response, 799, 873
Dynamics, 755, 963

Early age shrinkage, 535
Earthquake, 1145
Eaves, 383
Eccentric discharge, 693, 703
Education, 1209
Effective flexural rigidity, 445
Effective stress concentration factor, 1009, 1025
Efficient algorithms, 659
Elastic analysis, 487, 495
Elastic buckling, 675
Elasticity, 95
Elastic-plastic analysis, 487,
Elasto-plastic analysis, 599
Elevated temperature, 1103
Elongation, 1095
Empirical formula, 921
Empirical mode decomposition, 897
Energy absorbing capacity, 955
Energy absorption, 931. 947, 963
Energy-dissipation, 591
ENV 1993-1-4, 43
Equilibrium state, 1161
Eurocode 3, 253
European, 27
Experimental, 253
Experimental investigation, 365
Experimental research, 213
Experimental study, 479
Experiments, 721, 737

www.EngineeringEBooksPdf.com

Extended end plate, 253
External bending moment, 1119

Fabrication misfit, 729
Factors of safety, 303
Failure mode, 1043
Failure temperature, 1095
Falsework, 311
Fatigue, 1001
Fatigue damage, 791, 799
Fatigue life curve, 1025
Fatigue notch factor, 1009, 1025
Fatigue strength, 1009, 1025, 1043
FEA, 189, 197, 1001
FEM, 1001
Fiber model, 607
Field measurement data, 897
File protection, 1135
Fillet weld, 989, 1001
Finite element analysis, 285, 625, 939, 963
Finite element method, 105, 277, 551, 815
Finite element model, 799
Finite elements, 401, 617, 659, 675, 807, 973, 981
Finite shell element, 163
Finite strip analysis, 357
Fire, 1103, 1111, 1119
Fire code development, 1071
Fire curve, 1089
Fire duration time, 1127
Fire engineering, 1071, 1089
Fire modelling, 1061
Fire research, 1071
Fire resistance, 1061, 1095, 1135
Fire safety, 1061
First yield criteria, 641
Fixed/warping-free members, 341
Flexible supporting system, 295
Flexural behaviour, 383
Flexural buckling, 357
Flexural failure, 437
Flexural loading, 375
Flexural restraint, 1119
Flexural strength, 479
Flexural-torsional analysis, 1153
Flush end plate, 253
Footstep, 905
Force identification, 905
Formwork, 311
Fractionated casting, 535
Fracture, 205
Fracture failure, 213
Fracture mechanics, 1017
Frames, 321
Frictional joint, 913
Frontal collision, 963
Frozen-heated method, 1161
Full aeroelastic model test, 865
Full size tests, 527
Fundamental vibration period, 921

GBT, 401
GBT distortional buckling formulae, 341
General stress ratio, 1025
Generalised Beam Theory (GBT), 341
Generic lapped sections, 437
Geometric non-linear, 295
Geometrically nonlinear analysis, 1153
Girders, 69
Gliding cable, 1161
Global analysis, 839
Guardrail, 955
Gusset, 1001

Headed stud shear connectors, 527
Health monitoring, 791
Heat transfer, 1089
High performance steel, 633
High-strength bolt, 189
High strength concrete, 783
High strength steel, 3, 245, 575
High tech equipment, 881
High temperature, 1095, 1103
High-temperature,
Hilbert transform, 897
Hollow core slab, 503
Hollow section, 253
Honeycombs, 931
Hot-rolled girder, 783
Houses, 409
Hysteretic behavior, 591
Hysteretic model, 607

Impact, 955
Imperfections, 721, 729, 737
Imperfection sensitivity, 693
Imperfection shape, 375
Imperfection size, 375
Incremental method, 295
Incrementally launched bridge, 831
Initial imperfection(s), 375, 1193
In-plane bending, 237
In-situ vibration test, 849
Integrated analysis, 1169
Interaction buckling, 357
Interaction curves, 823

www.EngineeringEBooksPdf.com

Interactive buckling, 147
Interface friction, 471
Internal pressure, 675
I sections with slender webs, 649

Joints, 253

Lapped connections, 445
Large deflection, 1169
Large deformation, 295, 955
Large displacement analysis, 1153
Lateral torsional buckling, 383, 391, 649
Life cycle, 1145
Light gauge steel, 409
Limit state, 1185
Limit state design, 27
Lipped channel beams, 331
L-load, 815
Load-deformation curves, 1043
Loading analysis, 1169
Local buckling, 3, 43, 197, 357, 375, 383, 453, 479, 625, 1051
Local forces, 683
Local moments, 683
Local plate buckling, 147, 391
Local stress, 1001
Long suspension bridge, 889
Longitudinal fillet welds, 245
Longitudinal shear, 511, 519
Long-span bridge, 791
Long-span structures, 15
Long-term sustained load, 583
Low cycles fatigue, 105

Magnetorheological (MR) damper, 849
Materials properties, 1095
Materials testing, 139
Mathematical modelling, 139
Maximum displacement demand, 607
Mechanical behavior, 1161
Mechanical properties, 453, 1103
Mechanics model, 1127
Metal deck, 773
Metal foams, 931
Microvibration, 881
Mill tests, 139
Misaligned welded joint, 1009
Modal parameter identification, 897
Mode superposition, 889
Modular construction, 745
Moment-connections, 391
Moment-curvature, 383
Moment resistance of connections, 437
Moment resistance ratios, 445
Moment-rotation. 383
Moment-rotation behaviour, 253

Narrow ribbed metal deck, 527
Natural frequency, 823
Non-composite, 471
Non-linear analysis, 303, 311, 321, 351, 429, 1061
Nonlinear buckling, 659
Non-linear homogenisation, 981
Nonlinearity, 873, 913
Nonlinear seismic response analysis, 823
Nozzle, 683
Numerical analysis, 1051
Numerical computation, 857
Numerical integration, 139
Numerical modelling, 783

Optimal design, 269
Overall buckling, 3
Overall comparison, 865

Pallet racks, 461
Parametric analysis, 583
Parametric instability, 755
Partial interaction, 471
Partial safety factor, 1185
Passively controlled platform, 881
Patch loading, 683
Patch loads, 351, 693, 703
Pedestrian, 905, 939
Perforated beams, 121
Perforated section approach, 121
Performance-based design, 1061, 1071
Phase transformation, 973
Piles and piling, 1201
Pinned/free-to-warp members, 341
Planar modelling, 1177
Plastic behaviour, 383
Plastic bending, 947
Plastic mechanism, 237
Plastic stretching, 947
Plasticity, 617
Plate rotation restraint, 331
Plates, 69, 617
Point supported glass curtain wall, 295
Pole design, 963
Post buckling, 401
Post-local buckling, 625
Precast, 503

www.EngineeringEBooksPdf.com

Prediction model, 1009
Prestress, 913
Prestressed, 543, 551
Prestressing, 783
Pretensioned structures, 15
Probability, 1185
Proportional building structures, 1177
Prospects, 15
Pseudo-dynamic test, 171
Purlins, 421
Purlin-sheeting, 429
Push-out tests, 527

Rack-section columns/beams, 341
Random decrement technique, 897
Ratio of component plates, 147
Rectangular plate, 633
Reentrant open steel ribs, 511
Regression analysis, 527
Reinforcement, 683, 763
Reinforcing steel, 511, 519
Reliability, 659
Repair, 221, 1145
Residual displacement demand, 607
Residual strength, 1127
Residual strength index, 1127
Residual stress, 729, 1193
Residual stresses, 737
Resistance, 277, 1185
Restrained thermal expansion, 1079
Retaining walls, 1201
Retrofit, 221
Rib punch-through failure, 511, 519
Rib shearing failure, 511, 519
Ride comfort, 857
Rings, 721
Rivet hole, 1017
Road toughness, 857
Road vehicle, 857
Roofs, 745
Roof systems, 437
Rotation capacity, 261
Running train, 889

Saddle shade pavilion, 1169
Safety, 963
Scaffold, 303, 311
Scaffolding, 321
Scale down model, 599
Scaled-down testing, 955
SDOF analysis, 607
Second-order analysis, 321
Seismic behavior, 221
Seismic design, 763
Seismic design of bridge, 171
Self-excited force, 889
Semi-continuous composite beam, 487
Semi-rigid, 303
Semi-rigid connection, 913
Semi-rigid joint, 269
Shaking table test, 599
Shallow arch, 95
Shape finding, 1169
Shear, 57, 69, 409
Shear-carrying capacity, 641
Shear connector, 511, 519
Shear contribution, 543
Shear lag, 181
Shear-moment interaction curves, 121
Shear studs, 503
Shell elements, 351
Shells, 27, 659, 693, 703, 721, 745
Shrinkage, 583
SHS, 365
Silo loading codes, 693, 703
Silos, 27, 667, 693, 703, 713, 729, 737
Simplified approach, 599
Simplified design method, 559
Simulated earthquakes, 599
Slab, 773
Slab-on-girder beams, 471
Slenderness ratio, 163
Slip load, 189
Slotted-bolted-joint, 913
Smart damping technology, 849
Snap-through, 95
Soil characteristics, 963
Solid concrete slab, 527
Space frames, 1153
Spline finite strip method, 331
Stability, 3, 129, 311, 421, 461, 551, 667, 713, 721, 1209
Stability design, 69
Stainless steel, 43, 365, 617
Standard fire curve, 1127, 1135
Standards, 27, 1209
Static strength, 237, 1043
Statistical analysis, 783
Stay-in-place form, 773
Steady-state, 1103
Steel, 303, 503, 543, 1095, 1103
Steel beam-column connection, 285
Steel beams, 139, 261, 905, 1111
Steel bridge, 839, 1145
Steel buildings, 921
Steel column, 1119
Steel-concrete columns, 559
Steel frame, 913

www.EngineeringEBooksPdf.com

Steel-free deck slab, 773
Steel hollow sections, 237, 567
Steel plate girder bridge, 815
Steel plate shear wall, 641
Steel plates, 625
Steel roof truss, 453
Steel silos, 721
Steel space structures, 15
Steel structures, 139, 181, 213, 261, 295, 321, 357, 575, 1061, 1071, 1089, 1201
Steel-concrete hybrid structure, 599
Stiffened box section, 823
Stiffener, 401, 713
Stiffener buckling, 391
Stiffening system, 815
Stiffness, 277
Stocky column effect, 1193
Strain, 905, 1095
Strain hardening, 139
Strain-hardening gradient, 633
Strain rate, 989, 1111
Strains distribution, 453
Strength, 285, 383, 591, 625, 1095, 1185, 1209
Stress, 285
Stress analysis, 139
Stress concentration factor, 1001
Stress field intensity method, 1009
Stress spectrum, 791, 799
Stress-strain model, 583
Structural analysis, 269
Structural design, 365, 503, 559, 1185
Structural engineering, 43
Structural Eurocodes, 1201
Structural hollow sections, 205
Structural instability, 649
Structural members, 3
Structural stability, 365
Structural steel, 1103
Structure optimisation, 831
Structures, 303, 1209
Stub columns, 567
Stud shear connectors, 625
Suboptimal control, 881
Substitute frames, 1177
Substructures, 1201
Support flexibility, 1169
Survival rate, 1025
Suspension bridge, 799, 865
Sway frame, 311
Symmetric, 95
System identification, 921

Tall buildings, 575
Tangent stiffness matrix, 1153
Tanks, 27, 667, 683, 729
Tapered, 155
Tapered I-columns, 147
Tapering ratio, 147
Tee section approach, 121
Temperatures, 981, 1089, 1135
Tendons, 543
Tensile testing, 1103
Tension, 205, 1017
Tensioned membrane, 1169
Tension web member, 181
Testing, 409
Tests, 357, 617
Textbook, 1209
Thermal bowing, 1079
Thermal-mechanical testing, 973
Thin-walled column, 1051
Thin-walled cylinder, 667
Thin-walled sections, 129, 237, 245, 1043
Thin walled steel tubes, 375
Three-dimensional analysis, 815
Three-dimensional degenerated curved shell element, 229
Time-varying structure, 873
Torsional analysis, 1177
Torsional buckling, 357
Torsional-flexural, 155
Towers, 27
Track irregularity, 889
Traffic-induced ground motion, 881
Traffic loading, 799
Transformation induced plasticity, 973
Transformation plasticity, 981
Transient-state, 1103
Transient tensile test, 1095
Transition junctions, 721
Transverse reinforcement, 503
Truss, 181
Tsing Ma bridge, 897
T-stub model, 277
Tubular members, 365
Two scale material model, 981
Typhoon, 791
Typhoon Victor, 897

Ultimate bearing capacity, 453
Ultimate behavior, 69, 1145
Ultimate capacity, 1079
Ultimate compression capacity, 229
Ultimate load capacity, 147
Ultimate strength, 237
Ultimate tension capacity, 229
Uniaxial compression, 633

www.EngineeringEBooksPdf.com

Unit load method, 831
Unpropped construction, 261

Velocity, 905
Vertical stiffener, 815
Vibration, 755
Vibration control, 849
Virtual temperature load, 1161
Virtual work, 95

Wall panels, 409
Walls, 57
Warping effects, 331
Warping restraint, 331
WBFW connection, 189
Web openings of various shapes and sizes, 121
Weld connection, 197
Weld overlay, 221
Welded beams, 495
Welded connection, 181, 221, 989
Welded girder, 783
Welded hollow spherical joint, 229
Welded joint, 1025
Welding, 205, 973, 981
Wet concrete loading, 745
Wide ribbed metal deck, 527
Width-thickness ratio, 163
Width-to-thickness ratio, 197
Wind load, 667, 815

Yield line theory, 237
Yield plateau length, 633
Yielding, 713, 1017

Z-sections, 357

3-dimensional seismic behavior, 823

www.EngineeringEBooksPdf.com

This Page Intentionally Left Blank

www.EngineeringEBooksPdf.com